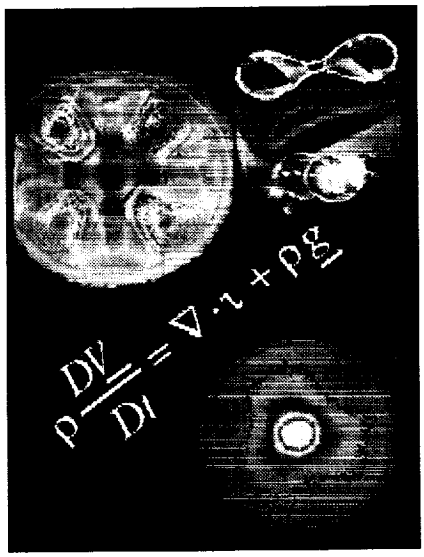

Proceedings of the Fourth Microgravity Fluid Physics & Transport Phenomena Conference

August 12 - 14, 1998
Cleveland, Ohio

Sponsored by:
The NASA Office of Life and Microgravity Science & Applications

Hosted and organized by:
The National Center for Microgravity Research on Fluids and Combustion and NASA Lewis Research Center

Under the auspices of:
The Microgravity Fluid Physics and Transport Phenomena Discipline Working Group

Table of Contents

Session 7A:
Bubbles and Drops

Session 7B:
Liquid Bridges

Session 7C:
Interfacial Phenomena III

PREFACE AND ACKNOWLEDGMENTS

The Fourth Microgravity Fluid Physics and Transport Phenomena Conference provides us the opportunity to view the current scope of the microgravity Fluid Physics and Transport Phenomena Program and conjecture about its future. The program currently has a total of 106 ground-based and 20 candidate flight principal investigators. A look at the collection of papers in this document clearly shows both the high quality and the breadth of the ongoing research program. One can easily notice many established world class scientists as well as investigators who are early in their career poised to achieve that stature. We hope that many of the participants in this conference will perceive it as an exciting and rewarding area of research and choose to participate in the upcoming NASA Research Announcement expected to be released in Fall of 1998.

As we look to the future, we find ourselves amidst a sea of changes, most of them positive. The International Space Station (ISS) is about to be launched this year, providing the microgravity research community with a tremendous opportunity to conduct long-duration microgravity experiments which can be controlled and operated from their own laboratory. Frequent planned shuttle trips will provide opportunities to conduct many more experiments than were previously possible. NASA Lewis research Center is in the process of designing a Fluids and Combustion Facility (FCF) to be located in the Laboratory Module of the ISS that will not only accommodate multiple users but allow a broad range of fluid physics and transport phenomena experiments to be conducted in a cost effective manner.

NASA is in the process of defining strategy for exploring Mars and other planets in the "Better, Faster, Cheaper" framework. These missions pose considerable challenge in that they require humans and associated systems to be subjected to prolonged exposure to microgravity during the interplanetary transit phase and in reduced gravity while on the planet's surface. Knowledge of how these extraterrestrial gravitational environments affect various systems and processes is vital to the success of these missions. NASA's Microgravity Research Program and its participating research community have emerged as primary sources of expertise in this unique area of research. In order to fully utilize this expertise, the Microgravity Research Division of NASA's Office of Life and Microgravity Science organized a workshop in August 1997 to identify factors/issues critical to enabling research and technology development needs of the long-duration space explorations. The proceedings of this workshop have been published as NASA CP-1998-207431 and will be available at the conference.

As one might expect, fluid physics and transport phenomena play a major role in many of the research and technology development needs identified in the workshop. The Microgravity Research Division has developed specific performance goals that support these needs. The performance goals represent new opportunities for the Microgravity Fluid Physics and Transport Phenomena Community and are listed below:

1. Advance the state of knowledge sufficiently to enable dust control technologies and bulk material handling for extraterrestrial habitats and/or in situ resource utilization.
2. Advance the state of knowledge sufficiently to allow development of reliable and efficient heat transfer technologies for space and extraterrestrial operations.
3. Advance the state of knowledge sufficiently to allow development of effective fluid management technology for space and extraterrestrial and industrial applications.
4. Establish the knowledge base required to design chemical process systems for exploration missions.

This conference itself has undergone a number of changes and innovations. In consultation with the Fluid Physics and Transport Phenomena Discipline Working Group chaired by Professor Paul Neitzel, we decided to produce a prepublication of the conference proceedings using an electronic medium. The abstracts are already on the World Wide Web at the website http://www.ncmr.org and we plan to post the complete papers on the web shortly after the conference. In this regard we acknowledge the support of our principal investigators who have provided us timely inputs of their papers and abstracts and

accommodated our format requirements. This cooperation was necessary to accomplish this and is much appreciated.

The Discipline Working Group has provided the much needed guidance in planning the content and the format of this conference. Their advice and guidance were essential for the success of this conference.

The establishment of the National Center for Microgravity Research on Fluids and Combustion represents another significant milestone for the program. The mission of the Center is to lead a national effort to increase the number of microgravity researchers and quality of research. The Center's primary role is to support the principal investigators in the program and promote not only dialogue but also working interactions among diverse groups and communities that are essential for continued success and growth of the program.

This conference has been organized and hosted by the National Center under the leadership of its Director, Professor Simon Ostrach. I would like to acknowledge the extensive efforts of members of the Center in planning, organizing, and hosting the conference and in preparing the proceedings and Conference materials. The first electronic publication and web based registration were major challenges that the Center staff handled skillfully. Sincere appreciation is offered to the authors for providing the papers in a timely manner and to the members of the Microgravity Fluids Physics Branch of NASA Lewis Research Center for their many contributions.

Finally I would like to express my gratitude to all of the Conference participants for their contributions to the success of this Conference.

Dr. Bhim S. Singh,
Fluid Physics Discipline Lead Scientist
Mail Stop 500-102
NASA Research Center
21000 Brookpark Road
Cleveland, OH 44135
Phone (216) 433-5396 or fax (216) 433-8660
E-mail: bhim.s.singh@lerc.nasa.gov

This conference was made possible by the efforts of many people. We acknowledge the contributions of the following individuals:

Fluid Physics and Transport Phenomena Discipline Working Group
- G. Paul Neitzel (chair), Georgia Institute of Technology
- Bhim Singh (vice-chair), NASA Lewis Research Center
- Sanjoy Banerjee, University of California-Santa Barbara
- S. George Bankoff, Northwestern University
- Bradley Carpenter, NASA Headquarters
- Stephen Davis, Northwestern University
- Joe Goddard, University of California--San Diego
- Joel Koplik, City College of the City University of New York
- Michael Moldover, NIST
- Harry Swinney, University of Texas at Austin
- Matthew Tirrell, University of Minnesota

Session Chairs
Plenary Sessions:
- Jack Salzman, Chief, Microgravity Science Division, NASA Lewis Research Center
- Dr. David Weitz ,University of Pennsylvania
- Dr. Iwan Alexander, National Center for Microgravity Research on Fluids and Combustion/Case Western Reserve University

Parallel Sessions (In Session Order):

Hasan Oguz, Johns Hopkins University
Robert Davis, University of Colorado at Boulder
Iwan Alexander, NCMR/Case Western Reserve University
Mark McCready, University of Notre Dame
Paul Chaikin, Princeton University
Dan Rosner, Yale University
Andrea Prosperetti, Johns Hopkins University
Joe Goddard, University of California at San Diego
Joel Koplik, City College of the City University of New York
Ain Sonin, Massachusetts Institute of Technology
Ashok Sangani, Syracuse University
Yasuhiro Kamotani, Case Western Reserve University
Peter Wayner, Rensselaer Polytechnic Institute
Alice Gast, Stanford University
Gareth McKinley, Massachusetts Institute of Technology
Vijay Dhir, University of California at Los Angeles
Eric Shaqfeh, Stanford University
Hossein Haj-Hariri, University of Virginia
Luis Bernal, University of Michigan
Mike Schatz, University of Texas at Austin
Kathleen Stebe, Johns Hopkins University

National Center for Microgravity Research on Fluids and Combustion

Dr. Simon Ostrach, Director
Thomas Cochran, Deputy Director
Ann Heyward, Outreach Programs Manager and Conference Lead
Iwan Alexander, Fluids Senior Scientist

Conference Team:	Ann Heyward, Chair	Iwan Alexander
	Judith Andersson	Tom Barkis
	Christine Gorecki	Annmarie Jones
	Beatrix Norton	Terri Rodgers
	Melissa Rogers	Norman Weinberg

The Logistics and Technical Information Division and its support service contractors, particularly Gregory Patt and Patricia Webb.

Jennifer Barovian and John Kizito of Case Western Reserve University.

Session 1A

Multiphase Flow I

MECHANISM OF ATOMIZATION IN A TWO-LAYER COUETTE FLOW.

R. M. Roberts, H. -C. Chang and M. J. McCready, Department of Chemical Engineering,
University of Notre Dame, Notre Dame, IN, 46556, USA, mccready.1@nd.edu

1. INTRODUCTION

Atomization of liquids in gas-liquid or liquid-liquid flows is one of the basic processes that determines the configuration of the phases and the overall behavior of the flows. Here we are defining atomization as the removal of liquid droplets from a flowing layer of a more viscous phase by shearing action of the (necessarily) faster-moving, less-viscous phase.

Atomization rates are an important issue in the design and operation of many industrial devices. For large diameter hydrocarbon transportation pipelines, that are oriented close to horizontal and operated at large gas-liquid flow ratio, a stable oil film is needed on the top portion of the pipe to protect the pipe from corrosion caused by CO_2 combined with condensed water. Even though waves are expected to occur for most flow situations, these do not get large enough to wet the top of the pipe. Consequently, a protecting film will occur only if a sufficient rate of atomized oil droplets impact the top wall. The ability to predict pressure drop in pipelines is crucial to their design. Fore and Dukler (1994) state that up to 20% of the pressure drop is from the atomization and deposition process. In heat transfer applications, knowledge of the entrained liquid fraction is crucial to assure that the remaining liquid film can accommodate the imposed heat flux without causing dryout. Asali et al. (1985) present data demonstrating up to 30-40% liquid entrainment in vertical annular flow but with a strong effect of flow rates. Numerous chemical processing operations rely on emulsification or atomization to create the interfacial area necessary for efficient reaction or contacting. Phase mixing is typically affected by agitation or pumping through nozzles. However, both of these processes are relatively inefficient. A fundamental study of the atomization mechanism can hence allow us to optimize these existing processes or suggest a more efficient new process, such as shearing a two layer configuration.

For the air-water system, photographic experiments by Woodmansee and Hanratty (1969) and Whalley et al. (1979) have directly linked atomization to large waves – liquid is removed by some mechanism from the crest of large solitary or roll waves. The connection between atomization and waves is important because wave properties vary significantly if gravity is not present to drain liquid from the waves (which occurs in all orientations on earth). Experiments done by Dukler and coworkers (Colin et al., 1991; Dukler et al. 1988; Bousman and Dukler, 1993) indicate that solitary waves in μg have much larger amplitude/substrate ratios than similar flows in earth gravity. Consequently, based on the Woodmansee and Hanratty (1969) mechanism, it is expected that atomization will occur more readily under microgravity conditions. As such, it becomes a fundamental consideration for the design of two-phase flow devices in spacecraft, space stations and lunar bases. Two-phase energy loops have not yet been implemented in spacecraft. However, the advantages in terms of weight and thermal capacity make them very attractive — but only if they can be understood sufficiently well. Wang et al. (1990) mention that future satellites will need higher power requirements, perhaps as high as 100 kW as opposed to current levels of 5-10 $k\,W$. Consequently, even for unmanned spacecraft, the ability to transfer more energy with lower ΔT and flow rates and ultimately less weight than for single phase systems is quite desirable.

The importance of knowing the fraction of liquid entrained in gas-liquid flows has been recognized for many years. Studies originally focused on measuring the entrained fraction and developing empirical correlations (e.g. Dallman et al., 1984; Asali et al., 1985). However as explained by Schadel and Hanratty (1989), a better approach is to measure and correlate the atomization and deposition rates separately. Unfortunately, this still has not produced a general predictive relationship valid for all flows. This is perhaps because their correlations do not reflect the fundamental mechanism. For earth conditions, the qualitative scenario leading to atomization in gas-liquid flow is expected to be as follows. Waves grow due to a flat-film shear instability (Hanratty, 1984) when the liquid phase is sheared by the gas. Under sufficiently severe conditions, the waves evolve into large, localized solitary waves (Jurman and McCready, 1989). If these are breaking waves, they are called roll waves (Andreussi et al., 1985) and atomization occurs when liquid is sheared from the crest of these waves (Woodmansee and Hanratty, 1969). However, this envisioned "lifting and shattering" process of Woodmansee and Hanratty (1969) occurs too rapidly and at too small a spatial scale for gas-liquid flow on earth for even modern high-speed video cameras to adequately capture the phenomenon. Consequently, confirmation of the speculated mechanisms (e.g., combined capillary and shear instability) and the ability to validate fundamental theory remain elusive.

This paper describes our initial attempts to circumvent the time scale problem by conducting experiments in a liquid-liquid flow, that because of the matched densities of the liquids, also has no effect of gravity drainage. The primary issues to be addressed are the overall mechanism and specific issues such as what affects the quantitative aspects of atomization (e.g. drop size and rate) as viscosity, density and flow

ratios, orientation and the presence of gravity are changed. Further we are interested in developing a fundamental theory to accurately describe atomization and allow prediction for situations outside the available range of data. Because atomization occurs at the crests of solitary waves, the behavior of such waves is of fundamental importance.

2. EXPERIMENT

To gain more insight into the process of atomization, experimental studies are performed in the two-layer Couette device shown in Figure 1. Two neutrally buoyant immiscible fluids with different viscosities are placed in the cell where the outer cylinder rotates with a constant speed. Mercury is placed at the bottom of the cell to provide a shear-free interface. The viscosity ratio of the inner phase to the outer phase and the surface tension is kept constant at m=0.0159 and σ=0.01 N/m respectively. Vertically crested waves can form at the interface between these two liquids depending on the speed and the depth ratio. Data are obtained using direct video imaging illuminated with both studio lighting and sheets of laser light. More complete description of the experiment and how it is performed is given by Gallagher (1996) and Gallagher et al (1997).

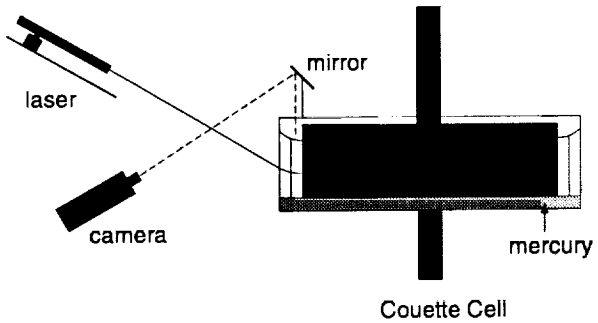

Figure 1: Two-layer Couette experiment showing the high speed video camera set-up.

3. RESULTS

For an inner depth of $l > l^*$ (l is the depth of the less viscous fluid and l^* denotes the depth at the instability boundary), long waves are unstable (see Gallagher et al., 1997) and a number of different wave structures can be formed. Figure 2 shows these patterns as a function of the outer speed and the depth of the inner fluid. For low speeds, no waves are present. It must be emphasized that this is in the unstable region for all rotation rates and our experiments have been run for very long times. Even accounting for the need of a wave to "fit" inside the device, it is not known precisely why a rotation rate of sufficiently high value is needed for waves to form. However as the plate speed is increased, at most conditions, periodic waves are formed with a constant wavelength and wave speed. While we cannot check every possible value of l^*, this transition appears to always be supercritical (subject to the limitations of using weakly-nonlinear bifurcation theory of Sangalli et al. (1997) for a long wave instability). Generally the initial waves are periodic

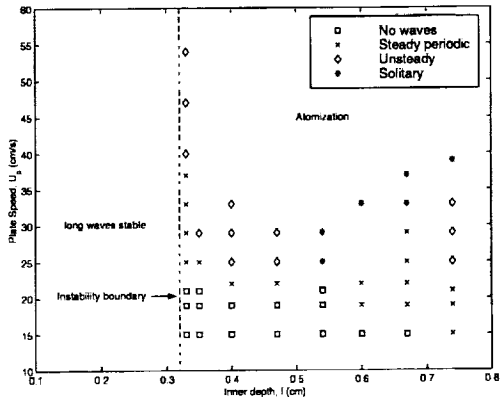

Figure 2: Plate speed U_p as a function of the inner depth l showing different wave structures in the long wave unstable regime.

and remain at small amplitude and finite wavelength if the rotation rate is not too large. However, if the rotation rate is increased, the initial waves suffer an unsteady modulation instability that precipitates wave coalescence and evolution towards longer and larger waves. In some cases, the coalescence events cease forming solitary wave-like structures. However as the plate speed is increased even further, these solitary waves are unstable leading to the regime of atomization.

As mentioned above, for gas-liquid systems this process involves the shearing of liquid droplets from the crests of the waves. However, for the two layer Couette system, a different mechanism is obtained that leads to the formation of droplets. To provide a better understanding of this mechanism, a high speed video camera (Ekta-Pro, 1000) is used to observe the wave structures. The corresponding wave amplitudes are usually measured with a horizontal laser sheet. But since this only provides a two-dimensional picture of the process, the camera is focused from above the device directly in line with the two phases and the interface (see Figure 1). The waves are tracked at a rate of 1/500 sec per image for a specific outer speed and inner depth.

Figure 3 displays a solitary wave-like structure resembling a roll wave for an inner depth of l=0.66 cm and a plate speed of U_p= 84 cm/s. The top of the image represents the more viscous upper phase and the

bottom represents the inner less viscous phase. The boundary separating the two phases denotes the interface, and the lengths of the image in the tangential and normal directions are $x \sim 0.8\ cm$ and $y \sim 0.6\ cm$ respectively. However, at this particular plate speed, these roll waves are unstable and may form elongated crests. Since gravity is not present to drain liquid from these waves, the elongations eventually lead to sheet-like structures as seen in Figure 4 which leads to quite a different mechanism for atomization.

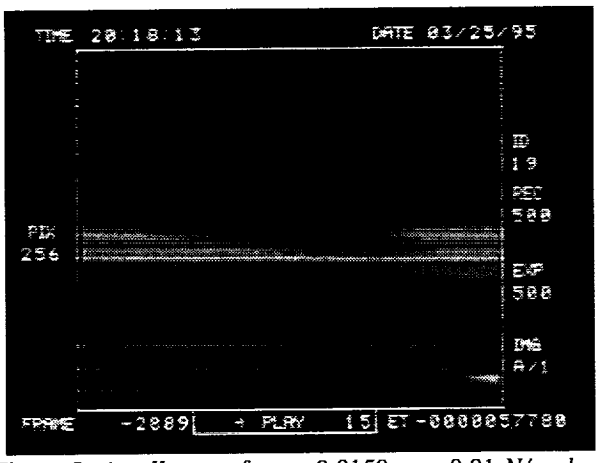

Figure 3: A roll wave for m=0.0159, σ = 0.01 *N/m*, l = 0.66, and U_p = 84 *cm/s*.

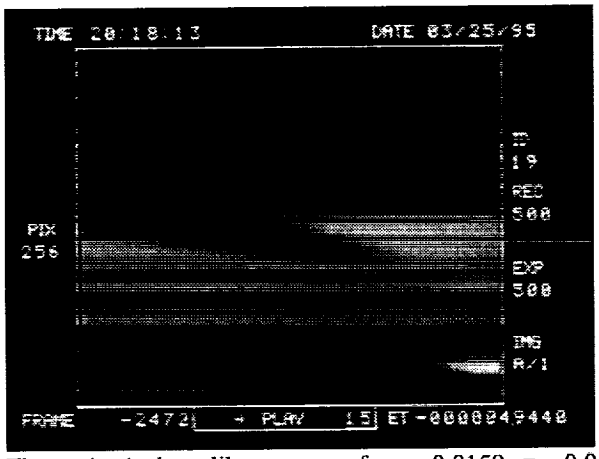

Figure 4: A sheet-like structure for m=0.0159, σ = 0.01 *N/m*, l = 0.66, and U_p = 84 *cm/s*.

For a viscosity ratio $m<<1$, the upper more viscous phase approximately travels with the speed of the outer cylinder. However, the inner less viscous phase travels slower as the velocity profile decays linearly to 0 at the wall of the inner cylinder. Therefore, as the crest becomes more elongated, the speed differential between the bottom and top of the crests stretches the sheet even further. This leads to a decrease in the cross-sectional distance d as the sheet becomes thinner. This process eventually leads to the sheet "snapping" off in the middle as d becomes too small to sustain this structure. Figure 5 shows an elongated sheet just prior to break off (one cannot see that the sheet is attached to the upper phase since the tangential distance of the image is too small). As the sheet snaps off, one part remains attached to the outer phase and the other part forms the droplets usually associated with atomization.

To investigate the thinning process in more detail, the change in the height of the sheets, d/d_0 ($d_0 \sim O(0.4\ mm)$ represents the initial height), is measured as a function of time. Since the cross-sectional area of the sheet must remain constant, d/d_0 should decay linearly in time as shown in Figure 6. Moreover, the speed differential is used to estimate a shear rate of $\gamma \sim 0.045\ (ms)^{-1}$ and this analytical prediction compares quite closely to the experimental data.

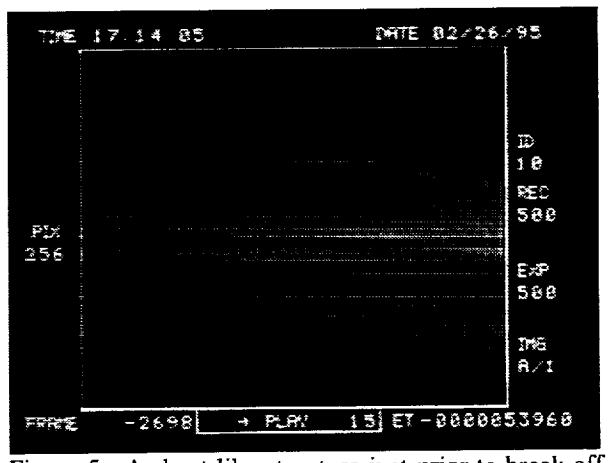

Figure 5: A sheet-like structure just prior to break off for m=0.0159, σ = 0.01 *N/m*, l = 0.66, and U_p = 84 *cm/s*.

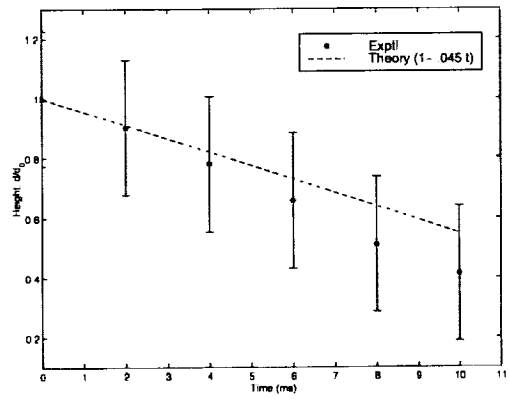

Figure 6: The change in the height of the sheet d/d_0 as a function of time.

4. DISCUSSION

The results presented provide new insight into the mechanism of atomization however several issues remain unresolved. First is the nature of the initial transition to waves for depths $l > l^*$ where long waves are unstable for any rotation rate. Sensibility (that is experience with well-defined supercritical bifurcations that lead to waves, e.g., Sangalli et al., 1995) tells us that we would expect to require that a wavelength that can "fit" inside the space be unstable with some reasonable growth rate. However since long waves are unstable, the bifurcation point occurs at 0 wavenumber which is not convenient for analysis by other than a longwave analysis. Unfortunately, the waves that are seen first are periodic with a finite wavenumber so this method does not seem appealing. If we use the weakly-nonlinear analysis of Sangalli et al. (1997), we need to pick a wavelength and a rotation rate. The choice of wavelength could be the waves that are observed but the rotation rate would be arbitrary because we can't use the experimental value for rotation that produces measurable waves. Nevertheless if these choices are made, the transition is predicted to be supercritical for all $l>l^*$. Since this is so, there is still a unresolved question: why are no periodic waves seen at $l = \sim 0.54$? Further work is need to answer this.

The formation of the sheets as a function of the inner depth and the plate speed is also unknown. It may simply be related to the ratio a/H where a is the amplitude of the wave and H is the depth of the top phase. For larger amplitude waves, the unsteady or solitary waves become unstable leading to sheet-like structures. A specific value of ratio a/H could provide the necessary criterion for this phenomenon. Future experiments will produce a phase regime map showing the experimental boundary leading to these structures. Moreover, the viscosity ratio will be varied to elucidate the effect of viscous forces on this process. Finally, it will be necessary to perform numerical simulations of the 2-D Navier Stokes equations to compliment the experimental and theoretical efforts by producing these sheets for any set of experimental parameters.

5. REFERENCES

Andreussi, P., J. C. Asali and T. J. Hanratty, "Initiation of roll waves in stratified gas-liquid Flows", *AIChE J.* **33**, 119-129 (1985).

Asali, J. C., G. W. Leman and T. J. Hanratty, "Entrainment Measurements and their Use in Design Equations", *Physicochemical Hydrodynamics*, **6**, 207-221 (1985).

Bousman, W. S. and A. E. Dukler, "Studies of gas-liquid flow in microgravity: Void fraction, pressure drop and flow patterns", *Proc. ASME Winter Meeting*, (1993).

Colin, C., J. Fabre and A. E. Dukler, "Gas-liquid flow at Microgravity Conditions", *Int. J. Mult. Flow*, **17**, 533-544 (1991).

Dallman, J. C., J. E. Laurinat and T. J. Hanratty, "Entrainment for Horizontal annular Gas-Liquid Flow", *Int. J. Mult. Flow*, **10**, 677-690 (1984).

Dukler, A. E., J. A. Fabre, J. B. McQuillen and R. Vernon, "Gas-Liquid flow at microgravity conditions: Flow patterns and their transitions", *Int. J. Mult. Flow*, **14**, 389-400 (1988).

Fore, L. B. and A. E Dukler, "The Impact of Droplet Entrainment on Momentum Transfer in Gas-Liquid Annular Flow", submitted *AIChE J.*, (1994).

Gallagher, C. T., D. T. Leighton and M. J. McCready, "Experimental investigation of a two-layer shearing instability in a cylindrical Couette cell", *Phys. Fluids,*. **8**, 2385-2392 (1996).

Gallagher, C. T., "Experimental investigation of a two-layer shearing instability", Ph.D. Thesis, University of Notre Dame (1996).

Hanratty, T. J., "Interfacial instabilities caused by an air flow over a liquid layer", in *Waves on fluid interfaces*, ed. R. Meyer, Academic (1984).

Jurman, L. A., and M. J. McCready, "A study of waves on thin liquid films sheared by turbulent gas flows", *Phys. Fluids A*, **1**, 522-536 (1989).

Schadel, S. A. and T. J. Hanratty, "Interpretation of Atomization Rates of the Liquid Film in Gas-Liquid Annular flow", *Int. J. Mult. Flow*, **15**, 893-900 (1989).

Sangalli, M., C. T. Gallagher, D. T. Leighton, H.-C. Chang and M. J. McCready, "Finite amplitude wave evolution at the interface between two viscous fluids", *Phys. Rev. Let*, **75**, 77-80 (1995).

Sangalli, M., M. J. McCready and H.-C. Chang, "Stabilization mechanisms of short waves in gas-liquid flow", *Phys. Fluids*, **9**, 919-939 (1997).

Wang, L. P., V. P. Carey, R. Greif and D. Abdollahian, "Experimental Simulation and Analytical Modeling of Two-Phase Flow under zero-gravity conditions", *Int. J. Mult. Flow*, **16**, 407-419 (1990).

Whalley, P. B., G. F. Hewitt and J. Terry, "Photographic studies of two-phase flow using a parallel light technique", *UKAEA Report*, AERE-R9389 (1969).

Woodmansee, D. E. and T. J. Hanratty, "Mechanism for the removal of droplets from a liquid surface by a parallel air flow", *Chem. Eng. Sci.*, **24**, 299-307 (1969).

STUDIES ON NORMAL AND MICROGRAVITY ANNULAR TWO PHASE FLOWS.

V. Balakotaiah[1], S. S. Jayawardena[2] and L. T. Nguyen[3],
Department of Chemical Engineering, University of Houston, Houston, TX 77204-4792
[1]Bala@uh.edu, [2]Subash@uh.edu, [3]LJN96442@jetson.uh.edu

ABSTRACT

Two-phase gas-liquid flows occur in a wide variety of situations. In addition to normal gravity applications, such flows may occur in space operations such as active thermal control systems, power cycles, and storage and transfer of cryogenic fluids.

Various flow patterns exhibiting characteristic spatial and temporal distribution of the two phases are observed in two-phase flows. The magnitude and orientation of gravity with respect to the flow has a strong impact on the flow patterns observed and on their boundaries. The identification of the flow pattern of a flow is somewhat subjective. The same two-phase flow (especially near a flow pattern transition boundary) may be categorized differently by different researchers.

Two-phase flow patterns are somewhat simplified in microgravity, where only three flow patterns (bubble, slug and annular) have been observed. Annular flow is obtained for a wide range of gas and liquid flow rates, and it is expected to occur in many situations under microgravity conditions. Slug flow needs to be avoided, because vibrations caused by slugs result in unwanted accelerations. Therefore, it is important to be able to accurately predict the flow pattern which exists under given operating conditions.

It is known that the wavy liquid film in annular flow has a profound influence on the transfer of momentum and heat between the phases. Thus, an understanding of the characteristics of the wavy film is essential for developing accurate correlations.

In this work, we review our recent results on flow pattern transitions and wavy films in microgravity.

FLOW PATTERN TRANSITIONS IN MICROGRAVITY

The absence of gravity reduces the number of observed flow patterns to three and it also reduces the number of dimensionless groups needed to characterize two-phase flows by two. For microgravity two-phase flows in a smooth pipe, there are five relevant dimensionless groups:

$$\text{Gas Reynolds number, } Re_{GS} = \frac{\rho_G U_{GS} D}{\mu_G}$$

$$\text{Liquid Reynolds number, } Re_{LS} = \frac{\rho_L U_{LS} D}{\mu_L}$$

$$\text{Weber number, } We_{LS} = \frac{\rho_L U^2_{LS} D}{\sigma}$$

$$\text{Ratio of gas to liquid densities, } = \frac{\rho_G}{\rho_L}$$

$$\text{Ratio of gas to liquid viscosities, } = \frac{\mu_G}{\mu_L}$$

Here, U_{LS} is the superficial velocity of the liquid based on a single phase flow and U_{GS} is the superficial gas velocity. The viscosity, density and surface tension are denoted by μ, ρ and σ, respectively. When the last two ratios are small, the flow pattern transition boundary may be assumed to be a weak function of these two ratios. The number of dimensionless groups may be further reduced to two by combining Re_{LS} and We_{LS} and ignoring the influence of We_{LS} alone.

For microgravity two-phase flows, (using experimental data from various systems) we developed a pair of dimensionless flow pattern transition maps shown in Figs. 1 and 2 (Jayawardena *et al.*, 1997). These maps suggest the importance of Suratman number ($Su = \frac{Re^2_{LS}}{We_{LS}} = \frac{\rho_L \sigma D}{\mu^2_L}$) in determining the transitions between the flow patterns.

BUBBLE-SLUG TRANSITION

The bubble-slug flow pattern transition occurs at a particular value of the ratio (Re_{GS}/Re_{LS}). This transitional value, $(Re_{GS}/Re_{LS})_t$, depends on the Suratman number as given below:

$$(Re_{GS}/Re_{LS})_t = K_1 Su^{-2/3}. \quad (1)$$

SLUG-ANNULAR TRANSITION

It is found that when the Suratman number is less than 10^6, slug-annular flow pattern transition occurs at a particular value of the ratio (Re_{GS}/Re_{LS}). This transitional value, $(Re_{GS}/Re_{LS})_t$, was found to depend on the Suratman number as given below:

$$(Re_{GS}/Re_{LS})_t = K_2 Su^{-2/3}. \quad (2)$$

When the Suratman number is greater than 10^6, slug-annular flow pattern transition was found to be a function of the gas Reynolds number, Re_{GS}. This transitional value, $(Re_{GS})_t$, was found to depend on the Suratman number as given below:

$$(Re_{GS})_t = K_3 Su^2. \quad (3)$$

Experimental data shown in Figs. 1 and 2 suggest the following numerical values:

$K_1 = 464.16,$ (4a)

$K_2 = 4641.6,$ (4b)

$K_3 = 2x10^{-9}$. (4c)

The Suratman number is determined by the tube diameter and physical properties of the fluid. Thus, the proposed maps can be used to identify the flow pattern for any given two-phase system, even when there are no prior experimental microgravity flow pattern data.

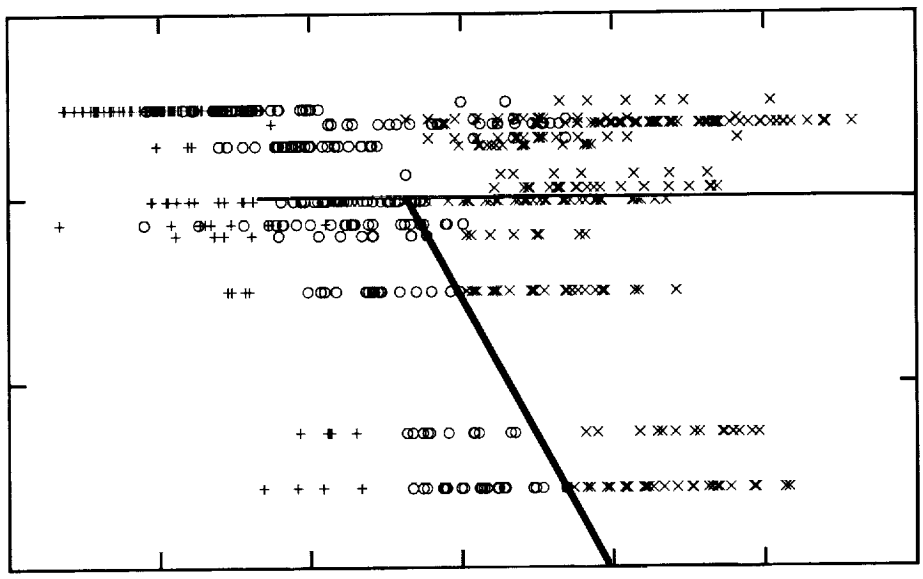

Figure 1. Dimensionless flow pattern map for microgravity two-phase flows. (For slug-annular transition for $Su > 10^6$ and for bubble-slug transition).

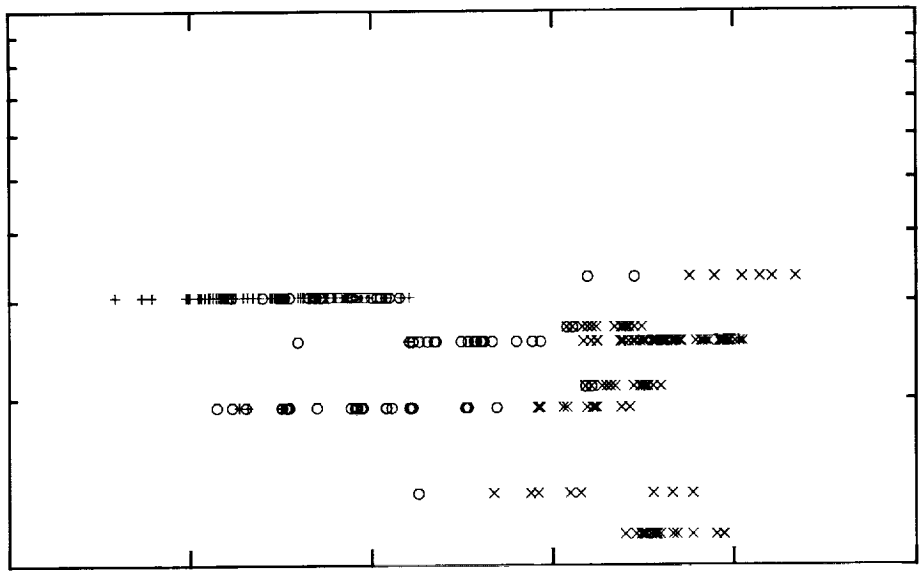

Figure 2. Dimensionless flow pattern map for the slug-annular transition in microgravity two-phase flows (for Su > 10^6).

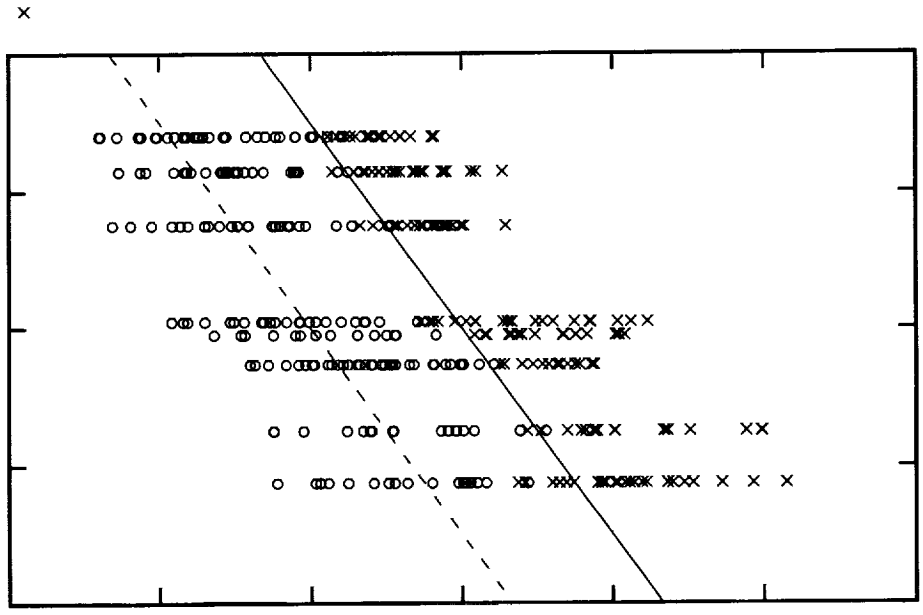

Figure 3. Results of recent microgravity two phase flow tests conducted using various fluids as shown in table 1.

VALIDATION OF PROPOSED MAP

We have collected new flow pattern data on micro-gravity two phase flows. These tests were done using the same test rig used by Bousman (1994), but with different working fluids. The Suratman number was changed by reducing the surface tension and/or by increasing the viscosity using a surfactant and/or glycerin. Figure 3 shows these new data points. The fluid properties and corresponding Suratman numbers are listed in Table 1.

These new experiments confirmed that the slug-annular transition boundary given by Eq. (2) extends to low values of the Suratman number (10^2 < Su < 10^4). However, they did not verify the bubble-slug transition boundary. The proposed boundary may not applicable for low Suratman number bubble-slug transitions. On the other hand, due to experimental limitations, the flow visualization was done after 85 pipe diameters. Since the feed section generated annular flow. It is possible that the flow development length was not sufficient to distribute the phases to achieve bubble flow.

When we planned these experiments, our aim was to validate the slug-annular transition for various two phase flows in microgravity and we could do that with flows having Suratman numbers as low as 770.

Table 1. Properties of the fluids used in these tests.

Test Fluid (Wt % of Glycerin)	Su	Properties		
		ρ_L	μ_L	σ
AWG (70)	1800	1181	23.00	64.6
AWGZ (70)	770	1181	23.00	27.0
AWG (60)	8900	1153	10.66	68.9
AWGZ (50)	11000	1125	6.03	27.0
AWG (24)	250000	1056	1.98	72.2
AWG (64)	5400	1164	13.63	68.4
AWG (32)	140000	1077	2.63	71.8
AWGZ (32)	56000	1077	2.63	28.5

(weight percentage of glycerin is given in parentheses)

Key: AW = air-water,
AWG = air-water-glycerin,
AWZ = air-water-Zonyl,
AWGZ = air-water-glycerin-Zonyl,

Units: ρ_L (kg/m^3), μ_L (cP) and σ (dyne/cm),

SYSTEM SPECIFIC, DIMENSIONAL FLOW PATTERN MAPS

Some system specific flow pattern maps (for a given fluid in a selected tube size) are plotted using the two-phase quality vs. mass flow rate. Such maps are useful for single-component, two-phase system. Our flow pattern boundaries may be used to create such system specific flow pattern maps.

The two-phase quality x, is defined as

$$x = \frac{(\rho_G U_{GS})}{(\rho_G U_{GS} + \rho_L U_{LS})} . \qquad (5)$$

Combining Eqs. (1), (5) and material balance on the two-phase flow gives the following expressions for the bubble-slug flow pattern boundary for any Suratman number:

$$x_{t,B\text{-}S} = \frac{K_1 \frac{\mu_G}{\mu_L} Su^{-2/3}}{(1 + K_1 \frac{\mu_G}{\mu_L} Su^{-2/3})} \qquad (6)$$

This transitional quality, $x_{t,B\text{-}S}$, is independent of the total mass flow rate.

The criteria for the slug-annular transition depends on the Suratman number of the system. The following expression (from Eqs. (2,) (5) and material balance) gives the slug-annular flow pattern boundary when the Suratman number is smaller than 10^6:

$$x_{t,S\text{-}A} = \frac{K_2 \frac{\mu_G}{\mu_L} Su^{-2/3}}{(1 + K_2 \frac{\mu_G}{\mu_L} Su^{-2/3})} \qquad (Su < 10^6) \quad (7))$$

This transitional quality, $x_{t,S\text{-}A}$, is also independent of the total mass flow rate.

Combining Eqs. (3), (5) and material balance gives the following slug-annular flow pattern boundary when the Suratman number is larger than 10^6:

$$\dot{m}\, x_{t,S\text{-}A} = K_3 \frac{\pi D^3}{4} \frac{\sigma^2 \rho_L^2}{\mu_L^4} \mu \qquad (Su > 10^6) \quad (8)$$

where $\dot{m}$ is the total mass flow rate of the two-phase flow. Equation (8) suggests that it is possible to obtain slug flow at higher values of quality, provided mass flow rate of the two-phase flow is low.

An example of such a single-component, two-phase system is a refrigerant flowing in a tube. In such cases, the total mass flow rate and the quality are the preferred variables to prepare flow pattern maps. Figure 4 shows the flow pattern boundaries on a two-phase quality vs. mass flow rate map, for a selected two-phase system in microgravity.

The bubble flow pattern is observed in an extremely small range of quality. The value for $x_{t,B\text{-}S}$

at that transition is about 0.04%. For most flow conditions in microgravity, annular flow is observed.

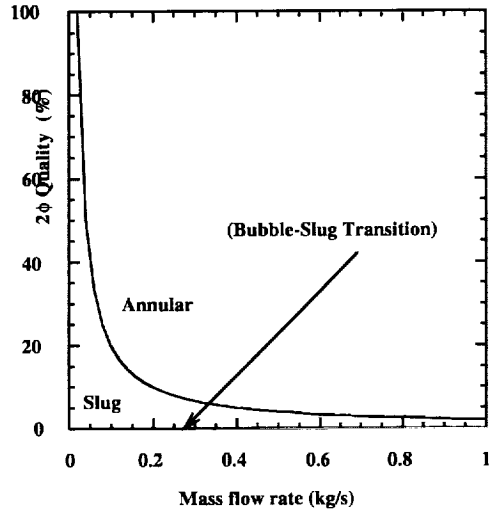

Figure 4. Dimensional, system specific flow pattern map for a single component microgravity two-phase flow. (For refrigerant R134a at 70°F in 25.4 mm ID tube, Su = 4.5×10^6)

The system specific flow pattern map for a low ($<10^6$) Suratman number system consists of two straight lines, since the two-phase quality at the flow pattern boundary is independent of the total mass flow rate. A detailed discussion including the critical void fraction of a two component systems is given in Jayawardena and Balakotaiah (1997).

WAVY FILMS IN MICROGRAVITY

We now study characteristics of the wavy films in microgravity annular flows. Bousman (1994) collected data on wavy film profiles in microgravity using air-water, air-water-glycerin and air-water-Zonyl systems. His film thickness data are shown in Fig. 6. Where the dimensionless film thickness is defined as

$$h^+ = \frac{h\,u^*}{\nu_L}, \qquad u^* = \sqrt{\frac{\tau_w}{\rho_L}}. \tag{9}$$

Since wall measured shear stress (τ_w) is not accurate, we estimate τ_w using measured pressure gradient:

$$\tau_w = \left(\frac{dP_G}{dx}\right)\left(\frac{D}{4}\right) \tag{10}$$

where τ_w is the average interfacial stress and D is the tube diameter. The liquid Reynolds number Re_L is defined as

$$Re_L = \left(\frac{4\Gamma}{\nu_L}\right), \tag{11}$$

where Γ is the flow rate in the film per unit perimeter. Since film flow rate is not measured, we approximate Re_L by Re_{LS}, assuming negligible entrainment.

A relationship between h^+ and Re_L is derived by assuming a velocity profile. The following velocity profile is assumed in the film for laminar flow

$$u^+ = y^+. \tag{12}$$

For the turbulent flow, the universal velocity profile

$$u^+ = y^+ \qquad 0 < y^+ < 10$$
$$u^+ = 2.78 \ln y^+ + 3.60 \qquad 10 < y^+ \tag{13}$$

where, u^+ is the dimensionless friction velocity in the film ($u^+ = u/u^*$) is assumed in the liquid film.

These equations gives

$$Re_L = 2\,(h^+)^2 \qquad 0 < h^+ < 10$$
$$Re_L = 3.28\,h^+ + 11.12 \ln h^+ - 88.8 \qquad 10 < h \tag{14}$$

A plot of this equation is shown in Fig. 5 as the solid line. The agreement with data is good. The mean film thickness of normal and microgravity two phase flows are not fundamentally different.

Since we expect the surface tension effects to dominate under microgravity conditions, it is of interest to compare the rms values of the film thickness under normal and microgravity conditions. (Note: The rms film thickness is actually the standard deviation since we subtract the mean film thickness. However, we are following here the literature terminology.)

The rms values of the film thickness fluctuations is normalized using the same length scale defined using the friction velocity u^*, and it is denoted as h^+_{rms}. When h^+_{rms} is plotted against Re_{LS}, it shows a large amount of scatter, partly due to the fact that these data points were collected at different gas velocities ranging from about 5 m/s to about 25 m/s. Experimental observations show that the annular flow liquid film becomes smoother at higher gas flow rates.

The following correlation predicts measured h^+_{rms} values for various flow conditions used in these tests:

$$h^+_{rms} = A\,Re_{LS}^{0.7} \tag{15}$$

Here A is a coefficient which depends only on the gas flow rate. The available data suggests:

$$A = (0.135\text{-}0.0033\,U_{GS}). \tag{16}$$

Figure 6 is a comparison of the predicted h^+_{rms} values with the experimental values. One dilemma here is that our intuition suggests that h^+_{rms} should be affected by the surface tension, where as Eq. (15) indicates the contrary.

Another quantity of interest is the enhancement in the friction factor. Here we compare the friction factor based on the interfacial stress with that of a corresponding single phase gas flow. The friction factor is defined as

$$f_i = \frac{\tau_i}{\frac{1}{2}\rho_G U^2_{GS}} \quad (17)$$

Asali *et al.* (1985) have analyzed data for co-current down flow and presented a correlation of the form

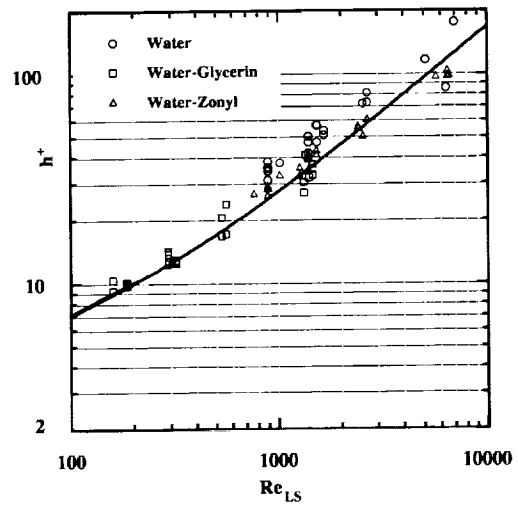

Figure 5. Dependence of normalized liquid film thickness on the liquid Reynolds number for microgravity annular two-phase flow and the comparison with the proposed correlations.

$$\left(\frac{f_i}{f_s} - 1\right) Re^{0.2}_{GS} = 0.45\,(h^+_G - 4) \quad (18)$$

Here, f_s is the gas phase friction factor that would exist in a smooth tube and

$$h^+_G = \frac{h}{\nu_G}\sqrt{\frac{\tau_w}{\rho_G}} \quad (19)$$

The microgravity data is shown in Fig. 7 along with the correlation given by Eq. (20). Though the data is more scattered, it is clear that the enhancement in the interfacial friction factor is higher in microgravity than in normal gravity.

If we use all the available micro-gravity data, then the interfacial shear stress can be represented by the following equation:

$$\left(\frac{f_i}{f_s} - 1\right) Re^{0.2}_{GS} = 0.42\, h^{+\,1.18}_G \quad (20)$$

When we eliminated data points close to the slug annular transition, the following two correlations are obtained.

$$\left(\frac{f_i}{f_s} - 1\right) Re^{0.2}_{GS} = 0.16\, h^{+\,1.3}_G \quad (21)$$

for water and water-glycerin mixtures and

$$\left(\frac{f_i}{f_s} - 1\right) Re^{0.2}_{GS} = 0.25\, h^{+\,1.3}_G \quad (22)$$

for water-Zonyl mixture. (Zonyl reduces the surface tension by about a factor three). That indicates that surface tension influences the interfacial structure of the waves.

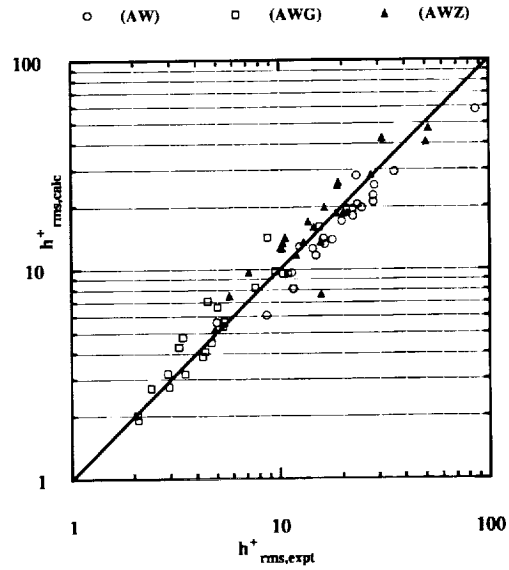

Figure 6. Comparison of calculated h^+_{rms} values with the experimental data.

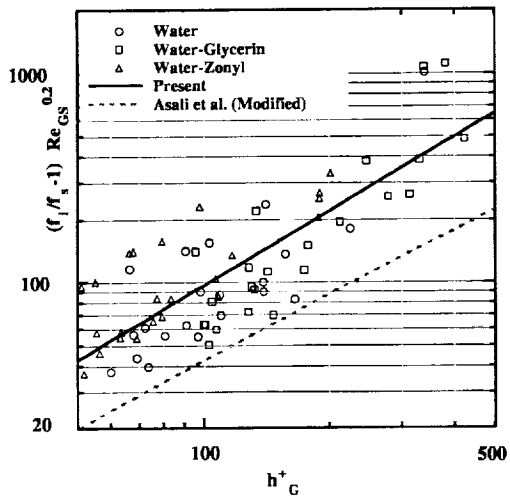

Figure 7. Comparison of the friction factor for the interfacial shear stress in microgravity annular flows with the existing normal gravity annular flow correlation of Asali *et al.* (1985) (Dashed line) with the new correlation (solid line).

CONCLUSIONS AND DISCUSSION

The recently proposed flow pattern map was verified at low Suratman number systems. Experiments confirmed the applicability of the proposed slug-annular flow pattern transition boundary for two phase flow systems with a low Suratman number.

System specific, dimensional flow pattern boundaries can be obtained for microgravity two phase flows. For a wide range of two-phase qualities, slug flow can be observed in such a system if the total mass flow rate is small, provided Suratman number is large. Bubbly flow exists in microgravity only at extremely low two-phase qualities.

The dimensionless parameter affecting the slug-annular transition changes at a Suratman number of about 10^6. Thus, we expect a dramatic change in the mechanism governing the slug-annular transition. It is very important to study liquid film characteristics, pressure gradients and drop entrainment measurements for high Suratman number two-phase flows in microgravity.

When properly non-dimensionalized using the pressure gradient, the mean film thickness of an annular flow depends only on the liquid Reynolds number, irrespective of gravity. Agreement between experimental data and the prediction suggests that entrainment of liquid droplets in microgravity annular flows to be small. This speculation needs experimental validation.

The differences between the normal and microgravity annular liquid films are apparent when we compare the interfacial friction factors. It is found that the friction factor enhancement is higher in microgravity conditions than in normal gravity downward annular flows. In microgravity annular flows, the enhancement to the friction factor is surface tension dependent.

ACKNOWLEDGMENTS

This work is supported by a grant from the NASA-Lewis Research Center (NAG3-1840), a NASA Lewis GSRP grant to Luan Nguyen and the UH-JSC aerospace post-doctoral fellowship program.

REFERENCES

Asali. J. C., Hanratty, T. J. and Andreussi, P., 1985, "Interfacial Drag and Film Height for Vertical Annular Flow", *AIChE J*, **31**, (6), 895.

Bousman, W. S., 1994, "Studies of Two-Phase Gas-Liquid Flow in Microgravity", Ph. D. dissertation, University of Houston.

Jayawardena, S. S., Balakotaiah, V., and Witte, L. C., 1997, "Flow Pattern Transition Maps for Microgravity Two-Phase Flows", *AIChE J.* , **43**, (6), 1637-1640.

Jayawardena S. S. and Balakotaiah, V., 1997 "Studies on Flow Pattern Transitions and Wavy Films in Gas-Liquid Two-Phase Flows in Microgravity", Proceedings of the ASME Winter Annual Meeting, Dallas, Texas, 1997.

EXPERIMENTAL AND ANALYTICAL STUDY OF TWO-PHASE FLOW IN MICROGRAVITYS

D. Abdollahian, S. Levy, Inc.
J. Howerton, F. Barez, San Jose State University
John McQuillen, NASA Lewis Research Center

Please refer to the Conference Book of Abstracts or the NCMR Website at http://www.ncmr.org

MEASUREMENT OF TWO-PHASE FLOW CHARACTERISTICS UNDER MICROGRAVITY CONDITIONS

E. G. Keshock[1], C. S. Lin[2], M. E. Harrison [3], L. G. Edwards [2], J. Knapp[2], and X. Zhang [4]
[1] Cleveland State University, E. 24th and Euclid Ave., Cleveland, OH 44115, e.keshock@csuohio.edu,
[2] Analex Corporation, 3001 Aerospace Parkway, Brookpark, OH 44135, sclin@lerc.nasa.gov

SUMMARY

This paper describes the technical approach and initial results of a test program for studying two-phase annular flow under the simulated microgravity conditions of KC-135 aircraft flights. A helical coil flow channel orientation was utilized in order to circumvent the restrictions normally associated with drop tower or aircraft flight tests with respect to two-phase flow, namely spatial restrictions preventing channel lengths of sufficient size to accurately measure pressure drops. Additionally, the helical coil geometry is of interest in itself, considering that operating in a microgravity environment vastly simplifies the two-phase flows occurring in coiled flow channels under 1-g conditions for virtually any orientation. Pressure drop measurements were made across four stainless steel coil test sections, having a range of inside tube diameters (0.95 to 1.9 cm), coil diameters (25 - 50 cm), and length-to-diameter ratios (380 - 720). High-speed video photographic flow observations were made in the transparent straight sections immediately preceding and following the coil test sections. A transparent coil of tygon tubing of 1.9 cm inside diameter was also used to obtain flow visualization information within the coil itself. Initial test data has been obtained from one set of KC-135 flight tests, along with benchmark ground tests. Preliminary results appear to indicate that accurate pressure drop data is obtainable using a helical coil geometry that may be related to straight channel flow behavior. Also, video photographic results appear to indicate that the observed slug-annular flow regime transitions agree quite reasonably with the Dukler microgravity map.

INTRODUCTION

General

The presence of an earth gravitational environment can enormously complicate a two-phase liquid/vapor flow, resulting in a variety of perturbations, instabilities, and generally undesirable unsteady features. As a result, even though two-phase flows have been studied extensively under earth gravity conditions, the accuracy of multiphase predictive tools is quite poor in comparison to those available for single-phase systems. Studying two-phase flow systems in a microgravity environment, can remove such undesirable flow complications, perhaps enabling the development of (1) more accurate predictive methods applicable in our earth gravity environment, and (2) accurate correlations that may be applied to the design of two-phase systems intended to operate under the microgravity conditions of space.

Parabolic aircraft trajectories have been used to obtain data for a very broad range of phenomena for reduced gravity periods of up to about 20 seconds duration. However, in the case of obtaining accurate measurements of two-phase flow behavior and characteristics under such low-gravity conditions, a virtually insurmountable impediment, or restriction, exists because of space limitations alone. This major impediment arises because of the long lengths of flow channel required to avoid entrance or exit effects, particularly insofar as they affect accurate measurements of pressure drop.

Typically, long, extended lengths of straight channel are required to insure a developed flow. Such requirements, using conventional experimental approaches, cannot be accommodated in KC-135 (or smaller) aircraft testing because of spatial constraints. These constraints are even more extreme in facilities available for space experiments.

Early Studies

In early studies of two-phase flow in aircraft parabolic trajectories, observation of flow patterns and their details have been reasonably successful, but associated pressure drop measurements have proven much more difficult to obtain, primarily due to flow channel length limitations. For example, in one of the early studies by Hepner et al [1] flow pattern observations and pressure drop measurements were made of air-water two-phase flow in a 2.54 cm diameter tube. However, since the length-to-diameter ratio (L/D) was only 20, the pressure drop measurements obtained were of little use.

More than a decade later, Chen et al. [2, 3] obtained the most extensive pressure drop data obtained to that time, for adiabatic two-phase flow of R-114 in the low-gravity conditions of KC-135 aircraft flight. Flow occurred in a 1.58 cm diameter and 1.83 m long straight tube, with pressure differential measurements made over a channel length of almost 120 diameters. The results were used to develop a new correlation for the prediction of two-phase pressure drop in a reduced gravity environment, based upon an annular flow model and using an interfacial friction factor developed from their test data. Nevertheless, the magnitudes of the pressure drops upon which the correlation was based were small, so that

measurement errors were a significant fraction of the pressure drops measured.

Accordingly, to circumvent the restrictions upon channel length imposed by drop tower and aircraft spatial restrictions, the present study utilizes a flow channel configured in a helical coil arrangement. This geometric arrangement permits a considerable length of flow channel to be "packed into" a compact space having very modest overall dimensions. The substantially larger pressure drop occurring over a much larger length of flow channel are thus much more easily measured with accuracy.

Since the studies of Chen et al cited earlier, a variety of additional studies have been conducted [4 - 8] using smaller channel (tube) sizes, and in both horizontal and vertical configurations, but at the expense of modification of the two-phase flow characteristics. Most recently, efforts have been made to identify conditions (involving tube size and fluid characteristics) that would justify obtaining "zero-g" data by conducting tests in a 1-g environment [9].

Coil Curvature Effects

In single phase flows the friction factor for flow in coils differs from that in a straight geometry under earth gravity conditions because of secondary flows induced by the curved channel geometry. It should be expected that for two-phase flows a coiled flow path would also induce secondary flows within each of the phases, that are not present in a straight-channel geometry. The detailed structure of secondary flows in two-phase flow in curved channels is not well defined. Not surprisingly, the relationship between two-phase pressure drops in coiled and straight flow channels is likewise not well defined. Some of the first results of this type have been obtained by Yan [10], for the vertical up-flow of air-water in circular cross-section (0.325 inches I.D.) helical coils of 3.125 inches coil diameter. A number of two-phase flow studies in helical coil geometries under 1-g conditions are listed in references [11-16].

EXPERIMENTAL PHASE

Coil test sections of small curvature (large coil diameter) were designed to minimize complexities induced by curvature (secondary flow effects), so that the flows would not differ substantially from straight-channel flows. Also, small channel diameters were considered undesirable due to the potential of distorted flow pattern observations, e.g. a single small bubble occupying the entire cross-section of a small diameter tube, so as to give the appearance of a slug flow condition instead. Larger tube sizes are also likely to be more advantageous in detecting entrance and developmental effects.

Four stainless coils of different sizes and lengths, as summarized in Table 1, were designed for use in the present study. A typical coil test section is illustrated in Figure 1. Two of the test sections are of the same inside diameter, 1.91 cm., but one was of more than 13 meters length, while the second was only about half that length. The longer length coil was considered to be of greatest benefit in aircraft flight tests. Its substantial length would insure an easily measurable, large pressure drop, even for such a large tube cross-sectional area. The smaller length test section was utilized to greatest advantage in laboratory ground testing, where it was essential to relate curved channel results to straight tube results – in effect, a correlation factor. The 3.76 meter length for this coil is compatible with the length of a straight channel that may be accommodated in the ground laboratory.

However, there is no justification in terms of physical phenomenological considerations that would justify the use of the same "modification factor" in low-g conditions as in 1-g conditions. Therefore, a fourth test section was designed that could be tested under low-g conditions and which would allow a relationship between straight-channel and curved channel flows. Due to spatial restrictions of the KC-135 flight apparatus, however, a much shorter straight length of flow channel can be utilized for comparisons to a coil configuration. Therefore, a smaller tube diameter is necessitated in order to create a large enough pressure drop in the straight length to be readily measurable. Due to the smaller tube diameter dictated, the coil diameter must also be correspondingly smaller in order to preserve the Dean number scaling parameter, and the d/D ratio contained therein. Accordingly, the fourth test section is of 0.95 cm. I.D., with a coil diameter of 25.40 cm., such that d/D = .0374, as with coils 1 and 2, Table 1.

Both the inlet and exit ends of the tubing were connected to instrumented straight lengths of tubing of the same diameter in which pressure transducers were located, as indicated in the diagram of Figure 1.

All tests were conducted with the coil axes being oriented vertically. In almost all cases, the air/water flows were in the downward direction, primarily because of constraints imposed in accommodation of the test sections to the flight apparatus developed by NASA specifically for two-phase aircraft flight experiments. The range of air/water flows studied under flight conditions was set by the design limitations of the flight test apparatus. Accordingly, liquid superficial liquid velocities were between 0.1 and 1.1 m/s, and superficial gas velocities between 0.1 and 25 m/s. Although the primary focus of the study has been upon annular flow, it was important to establish the con-

ditions under which the slug-annular flow regime transition occurred.

For flow visualization within the curved passages of the coil itself it was necessary to design a transparent coil (50.80 cm coil diameter) of tygon tubing (1.90 cm I.D.), as described more fully in [17]. As with the largest stainless steel coil, the pitch angle is only about 1 degree.

MEASUREMENTS AND RESULTS

Flow patterns were observed in the straight inlet and exit sections immediately preceding and following the coiled test sections, respectively, using high speed video photography, both in 1-g and aircraft flight tests. Comparisons of the observed flow patterns were made with the Choe-Weinberg-Weisman [18] and Taitel-Dukler [19] maps for 1-g conditions and with the Dukler et al [20] map developed specifically for microgravity conditions. Results for the ground laboratory tests indicated good agreement with the Choe et al map for the slug-annular transition. With the limited data obtained from a single set of flight tests, it appears that the slug-annular transition is reasonably well predicted by the Dukler et al [20] flow pattern map developed for straight-channel flows under microgravity conditions, which apparently indicates that the small curvature of the coils did not have an appreciable influence upon this flow pattern transition. Some of these limited initial results are shown in Figure 2.

Representative data for measured pressure traces are shown in Figures 3 and 4 for 1-g and microgravity conditions. Pressure drop values were obtained from taking the difference between the measured pressures across the coil at a sampling rate of 1 kHz. In Figure 3 the differing pressure traces at the coil inlet and exit appear to reflect the changes in flow structure that occurs as the two-phase mixture traverses through the coil. Such changes could very reasonably be expected to occur in long sections of straight flow channels also, however. The inlet and exit traces shown in Figure 4 for an annular flow pattern do not show a marked difference since the opportunity for bubble coalescence or other major flow modifications do not exist in this case.

Measured pressure drop values for a limited number of test conditions are presented in Figure 5, and are compared with values predicted by the Lockhart-Martinelli and homogeneous methods. Far more important will be the comparisons between the coiled and straight lengths of flow channel, both in 1-g and microgravity conditions. A large amount of data is now available from the first successful flight tests. Only these initial representative results can be presented at the time of the writing of this paper. These limited initial results appear very promising and of great interest, both from a practical and a scientific view, but a complete validation of the experimental approach must await the collecting and analysis of a considerable amount of additional data, not only from these first flight tests, but from additional tests to be conducted in the next six-month period.

ACKNOWLEDGMENTS

This work, which was supported through NASA Grant NAG3-1922, is gratefully acknowledged and appreciated.

REFERENCES

1. Hepner, B. B., King, C. DE., and Littles, J. W., "Zero-G Experiments in Two-Phase Flow Regimes, ASME Paper TS-ENAs-24, ICES Conf., San Francisco, 1975.

2. Chen, I. Y., Downing, R. S., Parish, R. and Keshock, E. G., "Observed Flow Regimes and Pressure Drops of Vapor and Liquid Flow in Adiabatic Piping," AIChE Symposium Series, Vol. 84, No. 263, 1988, pp. 203-216.

3. Chen, I.Y., Downing, R.S., Keshock, E.G., and Alsharif, M., "Measurements and Correlation of Two-Phase Pressure Drop Under Microgravity Conditions," AIAA Jnl. Thermophysics, Vol. T, No. 4, October, 1991.

4. Lambert, A., "KC-135 Zero-Gravity Two-Phase Flow Pressure Drop Experiments and Modeling," M. S. Thesis, Texas A& M University, College Station, TX, 1990.

5. Hill, W. S., and Best, F. R., "Microgravity Two-Phase Flow Experiment and Test Results," SAE Tech. Paper Series 911556, 21st Int. Conf. on Environmental Systems, San Francisco, 1991.

6. Bousman, W. S., and Dukler, A. E., "Studies of Gas-Liquid flow in Microgravity: Void Fraction, Pressure Drop and Flow Patterns," Proc. of ASME Winter Ann. Mtg., New Orleans, AMD-Vol. 174 / FED-Vol. 175, Dec., 1993.

7. Best, F. R., and Huang, D. S., "Microgravity Two Phase Flow Pressure Drop Experiments in the NASA KC-135," Proc. 7th Symp. on Space Nuclear Power Systems, Albuquerque, NM, Jan., 1990.

8. Miller, K. M., Ungar, E. K., Dzenitis, J. M., and Wheeler, M., "Microgravity Two-Phase Pressure Drop Data in Smooth Tubing," Proc. ASME Winter Ann. Mtg., New Orleans, AMD-Vol. 174 / FED-Vol. 175, Dec., 1993.

9. Ungar, E. K., Chen, I. Y., and Chan, S. H., "Selection of Gravity Insensitive Ground Test Fluid and Test Configuration to Allow Simulation of Two-Phase Flow in Microgravity," Seventh AIAA/ASME Joint Thermophysics and Heat Transfer Conference, Albuquerque, NM, June 15-18, 1998.

10. Yan, A., "Study of Two-Phase Flow Patterns and Frictional Pressure Drop in Helical and Spiral Coils," M.

S. Thesis, Mech. and Aerospace Eng. Dept., Univ. of Tennessee, Knoxville, TN, 1992.
11. Whalley, P. B., "Air-Water Two-Phase Flow in a Helically Coiled Tube," Int. Jnl. Multiphase Flow, Vol. 6, pp. 345-356, 1980.
12. Uddin, A. K. M., "A Model to Predict Two-Phase Flow Patterns in Helically Coiled Tubes," Particulate Phenomena and Multiphase Transport, Hemisphere Publ. Corp., 1988.
13. Saxena, A. K., Schumpe, A., Nigam, K. D. P., and Deckwer, W. D., "Flow Regimes, Hold-Up and Pressure Drop for Two Phase Flow in Helical Coils, Can. Jnl. of Chemical Eng. , Vol. 68, Aug., 1990.
14. Awwad, A., Xin, R. C., Dong, Z. F., Ebadian, M. A., and Soliman, H. M., "Flow Patterns and Pressure Drop in Air/Water Two-Phase Flow in Horizontal Helicoidal Pipes," Trans. ASME, Vol. 117, Dec., 1995, pp. 720-725.
15. Xin, R. C., Awwad, A., Dong, Z. F., and Ebadian, M. A., "Heat Transfer of Air/Water Two-Phase Flow in Helicoidal Pipes," Trans. ASME, Vol. 118, May, 1996, pp. 442-448.
16. Yan, A., Keshock, E. G., Omrani, E. G., and Downing, R. S., paper presented at AIChE Annual Meeting, Nov., 1995.
17. Keshock, E. G., Lin, C. S., and Edwards, L. G., "Design of Helical Coil Apparatus for Study of Two-Phase Flow in DC-9 Microgravity Flight Tests," Proc. Sixth Int'l. Symp. on Gas-Liquid Two-Phase Flows, ASME Fluids Eng. Div. Mtg., June, 22-26, 1997, Vancouver, BC, Canada
18. Choe, W. G., Weinberg, L., and Weisman, J., Two-Phase Transport and Reactor Safety, Hemisphere Publishing, Co., 1978.
19. Taitel, Y., and Dukler, A. E., "A Model for Predicting Flow Regime Transitions in Horizontal and Near-Horizontal Cocurrent Gas-Liquid Flow," AIChE Journal, Vol. 22, pp. 47-55, 1976.
20. Dukler, A.E., Fabre, J.A., McQuillen, J.B., and Vernon, R., "Gas-Liquid Flow at Microgravity Conditions: Flow Patterns and Their Transitions," Int. J. Multiphase Flow, V. 14, N. 4, pp. 389-400, 1988.

Coil	Tube O.D. (cm)	Tube I.D. (cm)	Coil Dia. (cm)	Coil Pitch (cm)	Coil Length (cm)	Coil Length-to-Dia. Ratio
No. 1	2.54	1.91	50.80	3.02	1356	710
No. 2	2.54	1.91	50.80	3.02	718	376
No. 3	1.59	1.27	50.80	3.02	718	565
No. 4	1.59	0.95	25.40	1.59	678	714

Table 1. Specifications for Stainless Steel Coil Test Sections.

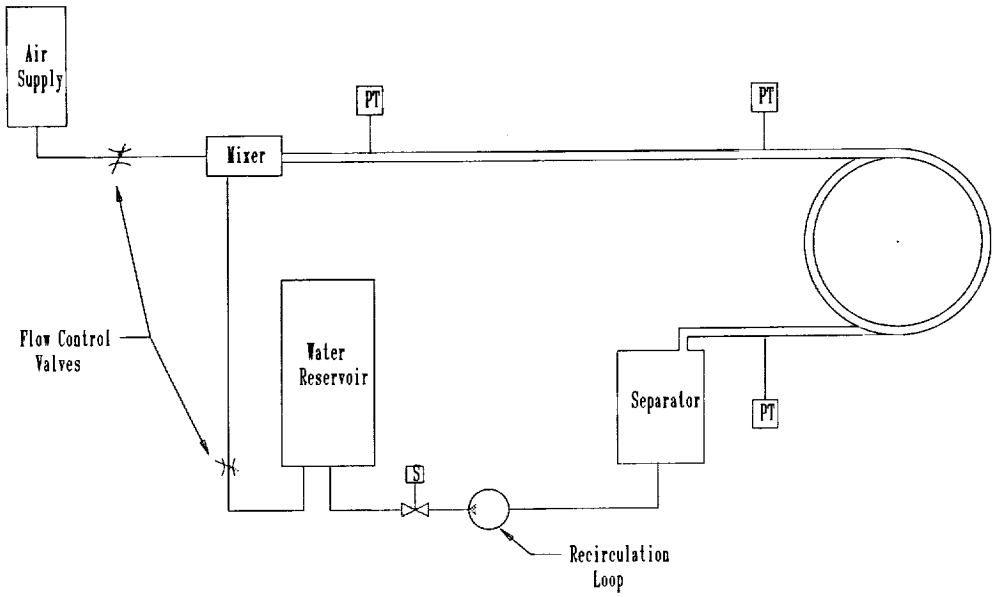

Figure 1. Schematic of aircraft two-phase test apparatus.

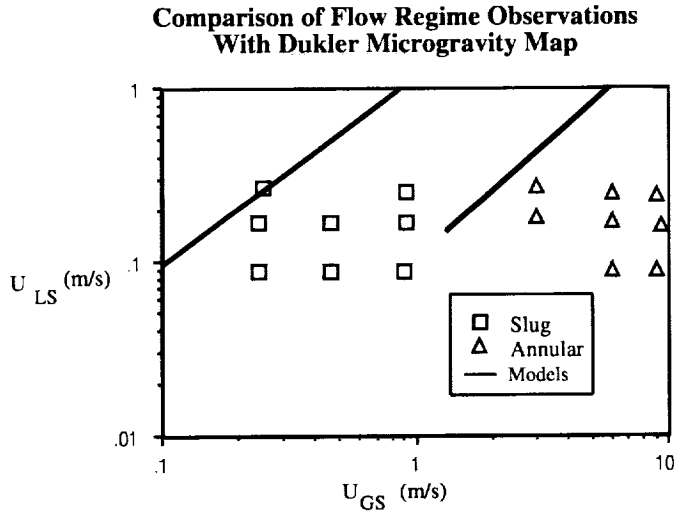

Figure 2.

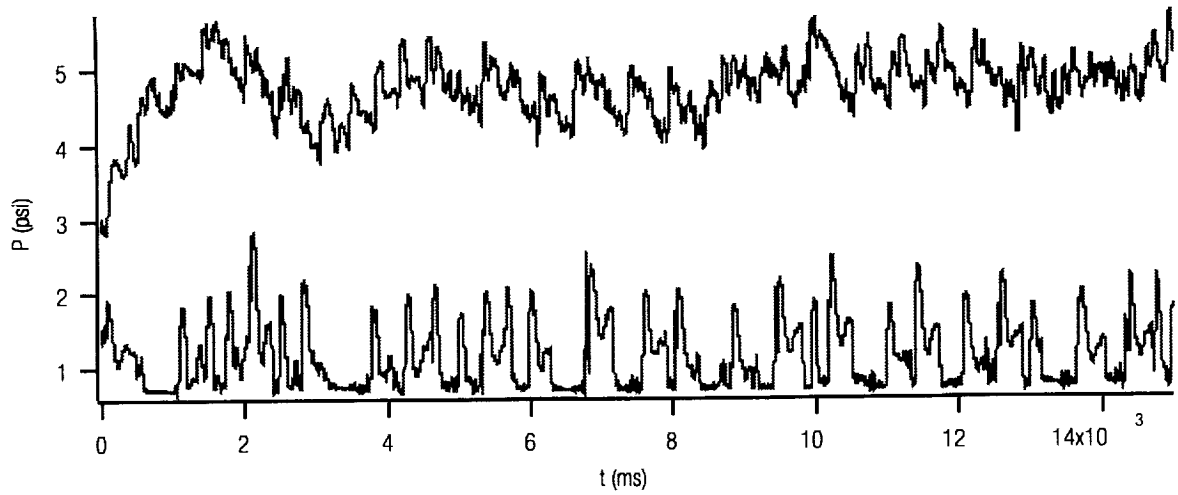

Figure 3. Pressure traces during flight parabola (slug/bubble flow).

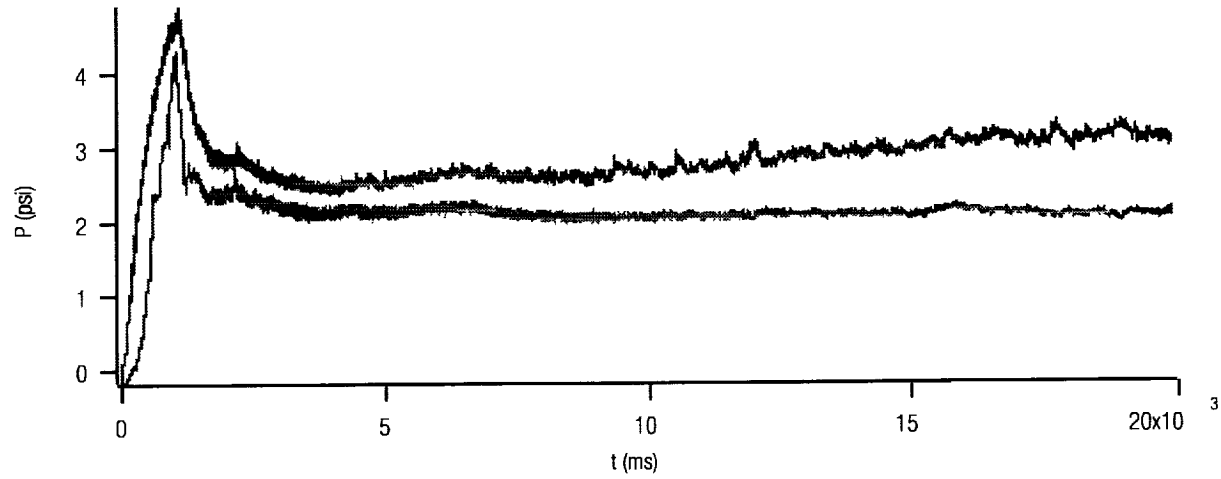

Figure 4. Pressure traces during flight parabola (annular flow).

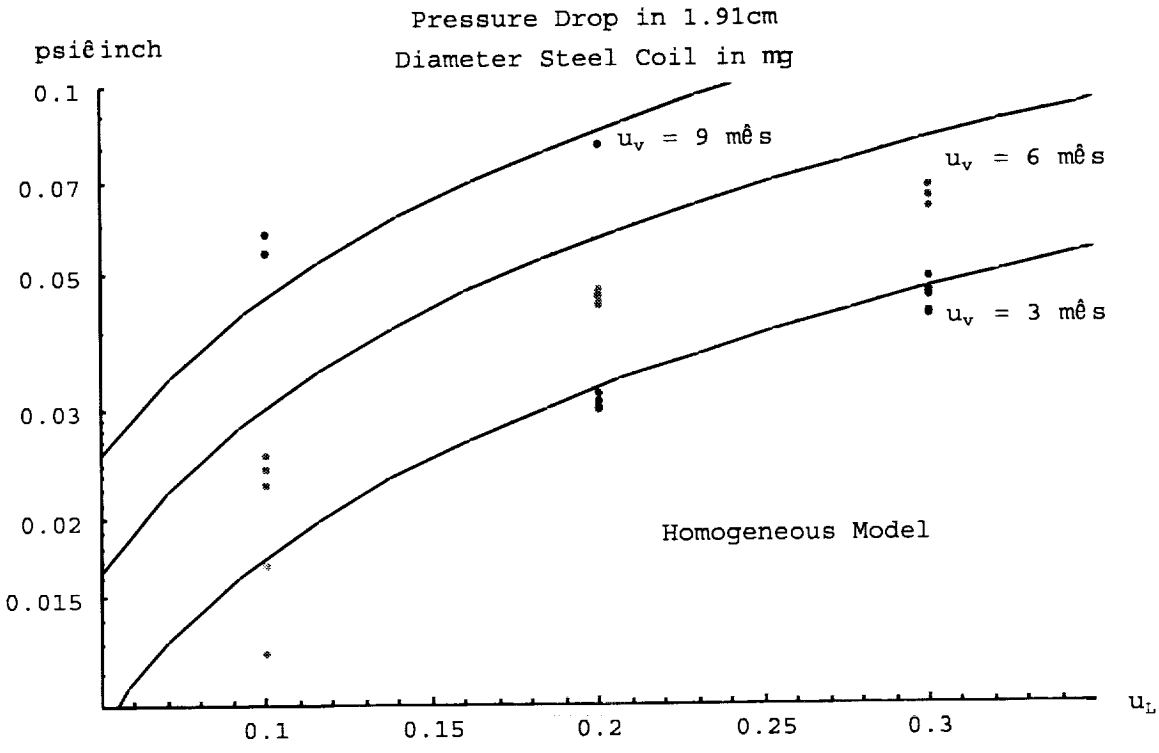

Figure 5. Representative measured Δp values compared with Lockhart-Martinelli predictions.

INDUSTRIAL PROCESSES INFLUENCED BY GRAVITY.

J. P. Kizito[1], F.B. Weng[2], Y. Kamotani[3] and S. Ostrach[4] [1,2,3,4](Department Of Mechanical and Aerospace Engineering, Case Western Reserve University, Cleveland, Ohio, 44106) [3]e-mail: yxk@po.cwru.edu.

PART I[2]: ROTATING ELECTROCHEMICAL SYSTEMS.

INTRODUCTION

The development and commercialization of a Ni/Zn battery system has been hindered for decades mainly due to the limited cycle-life of the Zn electrode during multiple recharging procedures. The problem has been traced to: (i) formation and propagation of zinc dendrites which lead to cell shorting, and (ii) redistribution of zinc active material on the electrode (shape change), which causes gradual capacity loss. It is known that a rotating Ni/Zn battery can provide very high energy and long life-cycle [1]. The main objective of our effort is to obtain a better understanding of convection in a rotating battery in order to improve Ni/Zn battery performance and life-cycle.

The rotating Ni/Zn battery system can be considered as a rotating electrolyte solution inside a shallow electrochemical cell subjected to an axial concentration difference (see Fig. 1). With superimposed rotating motion in the charging cell, solutal buoyancy induces a swirling secondary flow through the coupling of centrifugal, Coriolis, gravitational acceleration and density variations in the electrolyte solution.

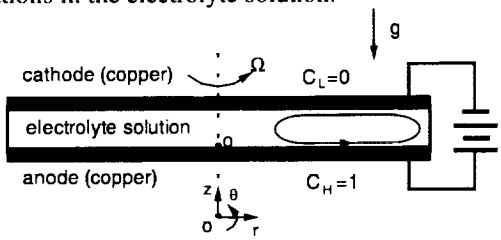

Fig. 1 Configuration of a rotating electrochemical cell.

In the present work, solutal convection in shallow vertical rotating electrochemical cells is studied analytically, experimentally and numerically. Scaling analysis for the boundary layer regime is performed to determine the flow and solutal boundary layer characteristics [2]. The proper dimensionless parameters are derived. The analysis also provides physical insight into the nature of the interaction among centrifugal, Coriolis forces and mass transport process in rotating battery. The experiment investigates the mass transfer rate in the rotating electrochemical systems by utilizing the limiting current method [2]. A correlation of mass transfer rate is obtained, which helps to design rotating Ni/Zn battery optimally. The detailed flow and solutal fields as well as mass transfer rate are investigated numerically. The results from scaling analysis and experimental investigations of mass transfer are used to validate this numerical study. The results from this study are discussed in terms of dendrite formation and shape change on the electrode and how these processes can be prevented and controlled by the rotation of the battery.

SCALING ANALYSIS

The scaling laws for the boundary layer regime are tabulated in Table 1. There are two important cases depending on the relative magnitude of δ_v (Ekman

		Case A, $\delta_v >> \delta_s$ ($ScRo_s>>1$)	Case B, $\delta_v << \delta_s$ ($ScRo_s<<1$)
Solutal layer thickness, δ_s		$(\nu/\Omega)^{1/2}(ScRo_s)^{-1/4}$	$(\nu/\Omega)^{1/2}(ScRo_s)^{-1}$
Ekman layer thickness, δ_v		$(\nu/\Omega)^{1/2}$	$(\nu/\Omega)^{1/2}$
Vel. u	$z<\delta_1$	$\Omega R(Ro_S/Sc)^{1/2}$	$\Omega R Ro_S$
	$z<\delta_2$	$\Omega R(Ro_S/Sc)^{1/2}$	$\Omega R Sc^2(Ro_S)^3$
Vel. v	$z<\delta_1$	$\Omega R/Sc$	$\Omega R Ro_S$
	$z<\delta_2$	$\Omega R(Ro_S/Sc)^{1/2}$	$\Omega R Ro_S$
Sh number: H/δ_s, or R/δ_s		$Ek^{-1/2}(ScRo_s)^{1/4}$ or $(Ra_{\Omega R})^{1/4}$	$Ek^{-1/2}(ScRo_s)$
ratio of two layer, δ_v/δ_s		$(ScRo_s)^{1/4} >> 1$	$(ScRo_s)^{-1} << 1$

Table 1 Scaling laws in boundary layer regions along horizontal surfaces of a flat rotating cylinder.

layer thickness) and δ_s (solutal boundary layer thickness). In Case A, $\delta_v >> \delta_s$, the solutal boundary layer development, and thus the mass transfer rate, is controlled by the centrifugal buoyancy, while in Case B, $\delta_v << \delta_s$, it is controlled by the Ekman layer flow and the associated axial flow. In that sense, the convection in Case A is analogous to natural convection in a rectangular container without rotation. The above scaling analysis shows that the mass transfer rate in the rotating cell is governed by $Ek^{-1/2}$ and $ScRo_S$ or $(ScRo_S)^{1/4}$, depending on the convection regime. Also, the $ScRo_S$ number is the most important parameter to determine the two convection regimes. In battery applications, we generally have $Ek<<1$ and $ScRo_S>>1$ so that the rotating electrochemical cell has a large inviscid core, and the mass transfer rate is primarily controlled by centrifugal buoyancy.

In the present configuration the radial velocity component is outward along the bottom wall and inward along the top wall. Then, the azimuthal velocity component, which is induced by the Coriolis force, is

against the cylinder rotation direction near the bottom wall and in the direction of rotation near the top wall. Since the centrifugal buoyancy force acts mainly in the region δ_S, the radial velocity has a peak near the edge of δ_S and its magnitude decreases away form that location due both to viscous retardation and to the Coriolis force. Along the bottom wall the total mass flux in the velocity boundary layer increases in the flow direction as the radial velocity increases with increasing radius. Consequently, an axial fluid motion is induced toward the wall by entrainment.

EXPERIMENTAL AND NUMERICAL RESULTS

Figure 2 shows the relations between current density and overpotential at rotating speeds between 150 rpm and 400 rpm for a 0.08M concentration difference. As seen in the figure, the current is independent of the rotation rate when the overpotential is below 200 mV. This is because the current is controlled by the electrochemical reaction and overpotential, since the convection is still very weak and the fluid is nearly

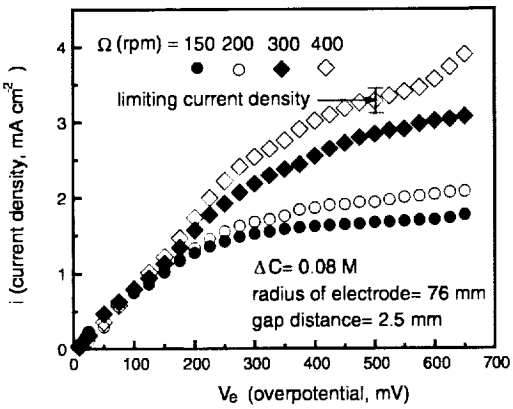

Fig. 2 Current density vs. overpotential in rotating cells.

in solid body rotation. The figure also shows that the limiting current density is increased with increasing rotation rate. This is due to the fact that larger centrifugal body forces increase the convection and enhance the mass transfer rate. In the present work the limiting current is considered to lie in the region where the curvature of the current-overpotential curve is reduced to a relatively small value but below the current at which the slope starts to increase due to hydrogen generation. For example, Fig. 2 indicates the limiting current value so determined for the 400 rpm curve, together with a range of uncertainty. The uncertainty is about ± 10 % for that case. The uncertainty is smaller in other tests.

To validate scaling laws, the mass transfer data are plotted as $\overline{Sh}\,Ek^{1/2}$ versus $ScRo_S$ in Fig. 3. In the present experiment the value of $ScRo_S$ is larger than unity so that the situation is closer to Case A than Case B.

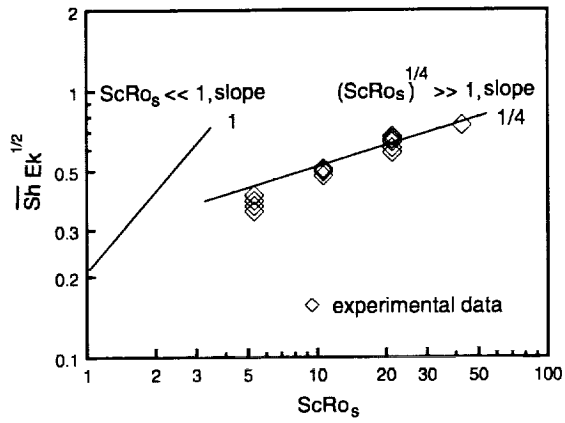

Fig. 3 $\overline{Sh}\,Ek^{1/2}$ vs. $ScRo_S$ number for Ar=0.033.

However, since the value of $(ScRo_S)^{1/4}$ ranges from 1.5 to 2.6, which is near unity, the centrifugal convection regime is not expected to be very well established. The data in Fig. 3 show the slope of the $\overline{Sh}\,Ek^{1/2}$ - $ScRo_S$ curve is close to ¼ for large values of $(ScRo_S)^{1/4}$, as predicted by the scaling analysis. The data for $ScRo_S$=5.3 deviate from the power law because the value of $(ScRo_S)^{1/4}$ is near unity (1.5). The results also indicate that the Coriolis force has a minor effect for inhibiting the mass transfer rate in the rotating electrochemical cells.

Fig. 4 shows the computed effect of the Coriolis force on the Sherwood number as a function of $ScRo_S$ for a fixed value of Ek. The Coriolis force reduces the radial velocity because it opposes the centrifugal buoyancy. Therefore, the mass transfer rate is also reduced by the Coriolis force in the parametric range where the Coriolis force is not negligible compared to the centrifugal buoyancy. With increasing $ScRo_S$, the solutal boundary becomes thinner relative to the Ekman layer so that the mass transfer rate is affected less by the Coriolis force. The results agree with scaling analysis. In the case of zero Coriolis force there is no azimuthal velocity, hence the flow recirculates in a fixed radial plane. Thus, the centrifugal convection

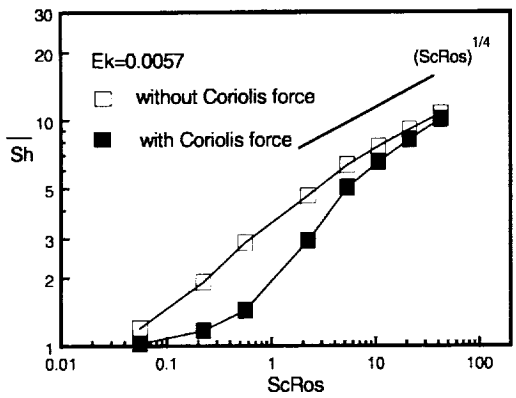

Fig. 4 Total Sherwood number vs. ScRos for Ek=0.0057, with and without Coriolis force.

in that situation is similar to buoyancy-driven convection so that Sh is proportional to the 1/4th power of $ScRo_S$ for a given Ek , as can be seen in Fig. 4.

On the other hand, when $ScRo_S$ is relatively small, the flow regime is close to the Ekman flow convection and the reduction of Sh due to the Coriolis force becomes more important. The maximum reduction of Sh is about 50% for $ScRo_S$ around unity according to Fig. 4. Therefore, one practical way to increase the mass transfer rate is to reduce the azimuthal flow by using, for example, partitions inside the test cells.

Figure 5 shows the effect of Coriolis force on the velocity and solutal fields. A comparison of (a) and (b) in Fig. 5 reveals that the Coriolis force interacts with centrifugal force and changes the flow and the

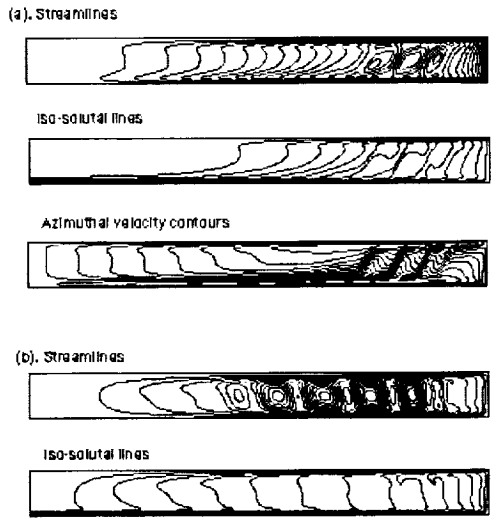

Fig. 5 Streamlines, iso-solutal lines and azimuthal velocity contours for Ek=0.0057, ScRos=10.63, Ar=0.03, (a) with Coriolis force and (b) without Coriolis force.

solutal patterns. The Coriolis force suppresses the flow rate in a rotating cell especially close to the central axis. The reverse secondary cells in case (a) are induced by the Coriolis force. Without the Coriolis force, the suction flows does not exist and the flow direction of secondary cells is the same as that of the primary flow. These cells are similar to natural convection in a tall cavity. The viscous boundary layers become thick and non-uniform in the absence of the Coriolis force.

Finally, some important implications of the present results to rotating battery applications are discussed. Generally, the dendrites appear when the charging current is close to the limiting current. When the battery rotates at high speed, the limiting current is increased several times over that of a stationary battery. Therefore, one can charge the battery efficiently at a charging current that is below the current for dendrite formation. Moreover, the convection may be used to control the shape change phenomenon. Although the mechanism of shape change is still unclear, the basic shape change phenomenon is that the zinc material depletes from the edge area to the center during the multiple recharge procedure [3]. In the present experiment, the rough-red deposition is seen near the edge of electrode and the smooth-pink deposition near the center area [4]. Such deposition pattern is caused by the fact that the high centrifugal field in the rotating cells causes more mass transfer in the edge area than near the center area. Therefore, the centrifugal convection may provide efficient means of compensating the mass transfer rate near the edge area of the zinc electrode thereby prolonging the battery cycle-life.

REFERENCES

[1]. Tamminen P, Salkind AJ, High power longlife bipolar nickel-zinc batteries in power source 12 proc. International power source conference 16, Brighton, England, 1988.

[2]. Weng F-B, Kamotani Y, Ostrach S. Mass transfer rate study in rotating shallow electrochemical cells, accepted by International Journal of Heat and Mass Transfer.

[3]. Einerhand, R. E. F., Visscher, W., de Gocij, J. J. M. and Barendrecht, E., Zinc Electrode Shape Change II. Process and Mechanism, Journal of The Electrochemical Society, 1991, V.138, No.1, pp. 7-17.

[4]. Weng, F.-B., Mass Transport Process in Rotating Shallow Electrochemical Cells, Case Western Reserve University, Cleveland, Ohio, Ph.D. Thesis, January, 1997.

PART II[1]: STABILITY OF COATING FLOWS.

INTRODUCTION

Industrial coating processes involve covering surfaces with one or more uniform liquid layers, which are subsequently cured or dried to form films. Productivity reasons strive for high-speed applications, and several discrete film layers are at times applied simultaneously. Because of such demands, attempts to use a specific coating process for a given application frequently fail. The cause of coating process failure is due to film instability leading to temporal or spatial growth of surface waves, resulting eventually in the rupture of the film. Therefore, it is important to identify the type of instability, establish the cause of the undesirable phenomena, and implement a control strategy minimizing the undesirable phenomena.

Recently, new economically significant technologies have emerged that use coating operations such as in the manufacture of semiconductor components, magnetic information storage systems and photoresist microelectronics. This has caused a renewed interest in coating processes. Correspondingly, there is a need to improve productivity, economy and uniformity in the traditional processes. These processes include the manufacture of photography films and paper, X-ray films, welding, galvanized steel and laminated composites.

Considerable work exists on coating films, summarized in the review article by Ruschak (1985). Although, numerous authors have studied falling thin films for example Liu et al., (1993), rising films are uniquely different, as demonstrated by Kheshgi et al. (1992).

The present work investigates, in more detail than in the past work, the nature and conditions under which interfacial film instability occurs in coating flow.

Consider a substrate withdrawal at a steady rate from an applicator of wetting liquid results in a liquid film on the substrate. The principles of conservation of mass and momentum describe the flow in the coating applicator and on the moving substrate. The boundary conditions are as follows. The no slip and impermeability conditions exist at the liquid-solid interface. At the liquid air interface the continuity of velocity and shear stress holds, and the surface tension force must balance a jump in the normal stress. In addition, the kinematic interface condition must always hold. From the above conditions, the non-dimensional parameters are derived to give insight into the dominant physical forces. Non-dimensional parameters are helpful because they demonstrate the sensitivity of the flow variables to the property values, and thereby, indicate the kind of accuracy required for the property values in the experimental work.

The non-dimensional for the coating phenomena are $\mu U_o/\sigma$, $\rho g h_c^2/\mu U_o$, and $\rho U_o h_c/\mu$. Also, Re_r (Relative Reynolds number = $\rho^2 g h_o^3/3\mu^2$) is used to describe the shear stress in the film. The first parameter is called the capillary number, $Ca = \mu U_o/\sigma$, which represents the ratio of viscous to surface tension forces. Kizito et al. (1998) showed that in the region where the thickness is constant, the viscous and gravity forces are balanced. So one can define a characteristic film thickness by setting the second parameter to unity, namely $h_c = (\mu U_o/\rho g)^{1/2}$. The actual final film thickness (h_o) non-dimensionalized by h_c is $T_o = h_o/h_c = (\rho g h_o^2/\mu U_o)^{1/2}$. Also, $Po = \mu(g/\rho\sigma^3)^{1/4}$ is used which is a function of Ca/Re with the capillary rise $(\sigma/\rho g)^{1/2}$ used as the length scale. Although Po does not represent a ratio of forces, it is a convenient parameter because it is constant for a given fluid. In certain situations, the bulk flow in the applicator influences the film flow. However, in the present study, the applicator is much deeper than the film thickness so that the applicator dimensions do not influence the film flow.

A typical low Ca coating process would involve fluids like molten glass at low substrate speed. High Ca coating flows involves fluids like thick adhesives, heavy oils or molten glass at a high substrate speed. Coating flows at high Re occur with fluids like liquid metals and molten semi-conductor materials. In the present investigation, the non-dimensional parameter ranges deemed relevant to current industrial applications are Ca (1.0×10^{-3} to 10.0) and Re (3.0×10^{-3} to 20.0).

BACKGROUND

Stability of the film depends on whether a small perturbation imposed on the fluid in its primary will grow or dampen. One source of instability arises by the crinkling of the interface by the shear that is always present in normal gravity. The present study assumes that the interfacial perturbations are caused disturbances of all wavelengths and the disturbance having the maximum growth rate dominates the interface. Since the maximum growth rate will dominate the interfaces and can originate at any point along the interface, it is reasonable to assume that only those formed at the farthest upstream distance are dominant the coating substrate.

To accomplish the stability studies numerically, a direct simulation of the flow field subject to an initial disturbance is preformed using a Nekton code. If the extended basic flow is stable, then, the perturbations, including the perturbed interface, eventually decay. The simulation uses supercritical steady state solutions as the initial condition. Then, the free surface pertur-

bation at the interface has an amplitude equal to 0.0065% of the mean film thickness.

EXPERIMENTAL METHOD

The real-time monitoring, diagnostic, and experimental apparatus are described in detail elsewhere (Kizito et al. 1996). The primary test fluid used is silicone oil (Dow Corning).

The temporal film thickness measurements are made using an ultra high accurate laser proximity probe which displays a local sensitivity of about two hundredth of a micron. The position of the probe is 0.85 m above the bottom of the applicator. This position is chosen because belt wobbling and lateral movements are minimal. All measurements are made after sufficient time has elapsed to attain steady state conditions at the applicator. The proximity probe, which is manufactured by Keyence, is of a laser reflective type (LC-2430) with a sampling rate of 50kHz, a resolution of 0.02 μm, response time of 100 μs, and linearity of ±0.05%. Each reading is averaged over a bin of 2024 data points. The data are ported to computer using an RS-232C at 4800 bytes per second. The combined uncertainty using the root-sum-square method in the determination of the Ca is ±1.2%, Re is ±1.23%and Po is ±1.3%.

RESULTS AND DISCUSSION

As the Re of the flow increases, beyond a certain critical Re the interface becomes wavy. At large Re, the main wave and its accompanying small waves become so randomly mixed that the individual wave fronts are indistinguishable. Eventually, scattered on the interface are a large number of waves that subsequently merge to form teardrops.

The chronological and spatial development of a wavy coating film by means of numerical simulations of a two-dimensional flow field subjected to an initial disturbance is describe first. Numerical simulation uses a periodic model with a control volume length more than thirty times the film thickness. The simulation starts with an initial arbitrary infinitesimal perturbation at the in-flow boundary condition.

Figure 2 shows a simulation of a wavy film at a non-dimensional time ($t = T\ U_o/h_c$) of t = 192. Figure 2a shows the region occupied by the wavy film. This figure demonstrates that the lead wave is the largest, therefore indicating the direction of spatial growth. These results agree with experimental observation by Kizito et al. (1996).

Figure 3 shows the Re_r when waviness is first observed anywhere in the film. In all cases, the film becomes unstable after the final film becomes independent of the Ca. The fact that the film thickness attains the maximum value before it becomes wavy implies that the appearance of waves relates to the diminishing importance of surface tension as a stabilizing force in the meniscus region. This figure shows that at about Re_r equal to unity the coating film becomes wavy.

The major difference between wavy and non-wavy flow is that in the former, capillary and viscous forces have a principal role in damping small disturbances in the final thickness region. The fact that the effect of surface tension is relatively small when Ca is large and when the film becomes wavy, seems to suggest that certain small disturbances generated in the meniscus region may propagate downstream to trigger instability.

A comparison between a falling film and a coating film reveals the following about the final film region of coating flow. The flow of liquid relative to the belt is similar to that of the falling film although the direction of gravity is different. Contrary to falling films that become unstable at $Re_r = 0$, for a vertical case, a coating film becomes unstable only after a certain Re_r.

Figure 4a shows the temporal film thickness measured by laser proximity probe. The test condition are for Po=0.1 fluid at two conditions, namely, Re_r=0.5, Ca=0.155, T_o=0.64 and Re_r=2.7, Ca=0.31 and T_o=0.84. Figure 4b shows the power spectrum of the above measurements using Lomb's FFT algorithm to give frequencies at significance levels of the $O(10^{-6})$. The frequencies represented by **"ff"** are the forcing frequencies due to the mechanical vibration. These frequencies are measured without the liquid film at the same operating conditions. These figures show that below a critical Re_r, the dominant frequency is that due to natural noise inherent in the system. Conversely, above the critical Re_r, the natural wave formation on the interface dominates the coating substrate. When the probe is moved downstream at the same operating condition, the magnitude of the average film-thickness increases by 26% over a distance of 0.1m.

CONCLUSION

The present methods and techniques described above are suitable for describing the first phase of coating film stability. The new aspects and phenomena of importance to coating flow found in the present work are the following. Beyond a certain $Re_r = 1$, when T_o exceeds 0.67, the coating film on a moving substrate becomes wavy. This situation is different from a falling film whose critical Re_r =0 and T_o greater than unity. Direct numerical simulations show that the waves are convective in nature. In addition, experimental results show that the amplitude of the waves increases downstream thus confirming the numerical observations. The instability is due the crinkling of the interface induced by shear due to gravity.

REFERENCES

Kheshgi HS; Kistler SF; Scriven LE (1992) Rising and Falling Film Flows: Viewed From A First-Order Approximation. Chem. Eng. Sci.: 47; 3, 683-694.

Kizito JP; Ostrach S; Kamotani Y (1991) Coating flow in Microgravity: MS Thesis, Case Western Reserve University, Cleveland, OH USA.

Kizito JP; Ostrach S; Kamotani Y (1996) Coating flow at High Capillary and Reynolds numbers. Ph.D. Thesis, Case Western Reserve University, Cleveland, OH USA.

Kizito JP; Kamotani Y; Ostrach S (1998) Experimental Free Coating Flows at High Capillary and Reynolds Number. Experiments in Fluids. Submitted.

Liu, J.; Paul, JD; Gollub JP (1993) Measurements of the Primary Instabilities of Films Flows. J Fluid Mech.: 250; 69-101.

Ostrach S (1988) Industrial Processes Influenced by Gravity. NASA CR-182140, C-21066-G.

Ostrach S; Kizito JP; Kamotani Y (1994) Free Coating flow at High Capillary and Reynolds numbers. AMD-184, Two Fluid Flows - With or Without Phase Change ASME, 1-11.

Ruschak KJ (1985) Coating Flows. Ann. Rev. Fluid Mech.: 17, 65-89.

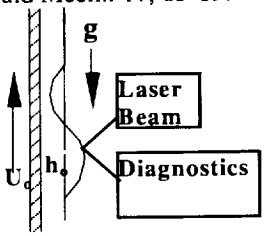

Figure 1 : Schematic of the experimental setup

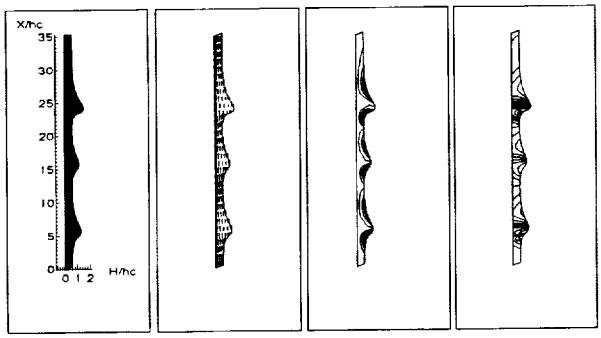

Figure 2: Simulation of a wavy film at t = 192; Ca = 4.05 and Re = 6.58. The region occupied by the wavy film, the velocity vectors plot, transverse velocity contour and the pressure contour respectively.

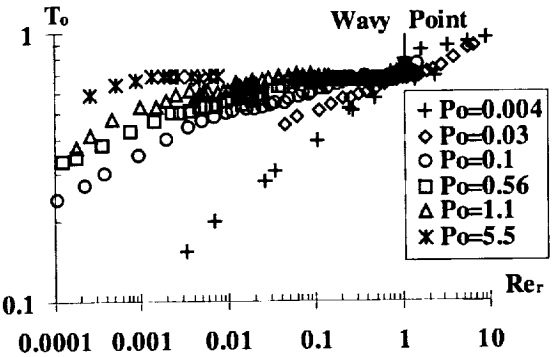

Figure 3: Non-dimensional final film thickness as a function of Re_r.

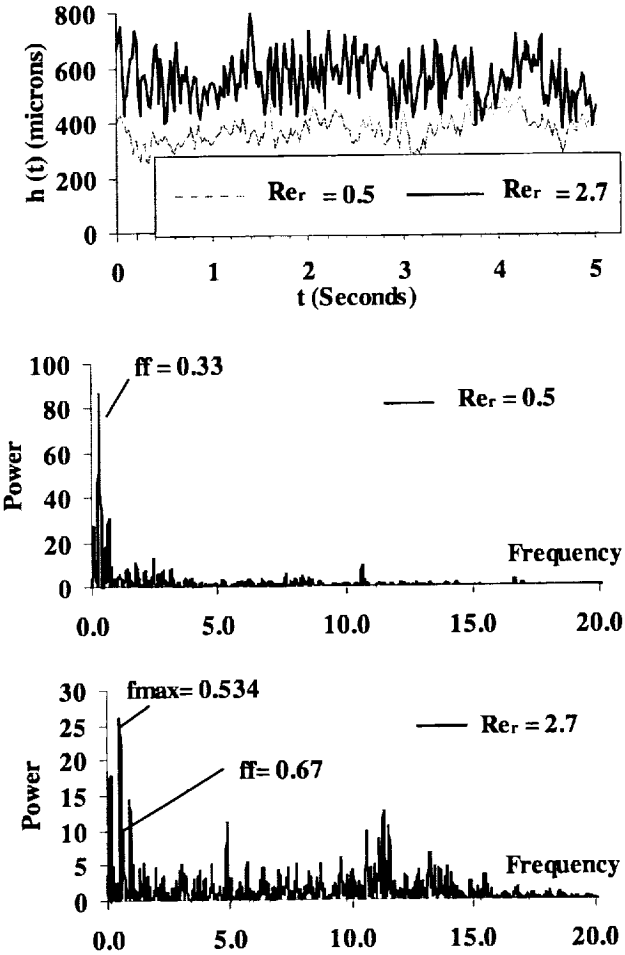

Figure 4: The temporal film thickness measurement and the resulting power spectrum.

Session 1B

Electric and Magnetic Effects

WAVES IN RADIAL GRAVITY USING MAGNETIC FLUID.

D. R. Ohlsen[1], J. E. Hart[2], and P. D. Weidman[3],

[1]Program in Atmospheric and Oceanic Sciences, University of Colorado, Boulder, CO 80309-0311, ohlsen@fluida.colorado.edu

[2]Program in Atmospheric and Oceanic Sciences, University of Colorado, Boulder, CO 80309-0311, hart@tack.colorado.edu

[3]Department of Mechanical Engineering, University of Colorado, Boulder, CO 80309-0427, Patrick.Weidman@colorado.edu

INTRODUCTION

Terrestrial laboratory experiments studying various fluid dynamical processes are constrained, by being in an Earth laboratory, to have a gravitational body force which is uniform and unidirectional. Therefore fluid free-surfaces are horizontal and flat. Such free surfaces must have a vertical solid boundary to keep the fluid from spreading horizontally along a gravitational potential surface. In the absence of terrestrial gravity, surface tension forms fluid masses into spherical balls without solid boundaries, as demonstrated on the Space Shuttle in the Drop Physics Module [1]. A fundamentally different problem is the behavior of fluids with a *body* force rather than a surface force that generates the spherical geometry. In many atmospheric, oceanic, or stellar fluid flows, the horizontal scale is large enough that sphericity is important in the dynamics. Further, fluids in spherical geometry can cover an entire domain without any sidewall effects, i.e. have truly periodic boundary conditions. We describe novel spherical body-force laboratory experiments using ferrofluid.

Ferrofluids are dilute suspensions of magnetic dipoles, for example magnetite particles of order 10 nm diameter, suspended in a carrier fluid [2]. A surfactant coating keeps the particles separate so that thermal Brownian motions in the fluid are sufficient to overcome both gravity and particle-particle attraction to keep the dipoles in suspension. For flows in which external magnetic field variations and the bulk fluid motions are slow compared to the time for the magnetic fluid particles to rotate ($\sim 10^{-6}$ s), the fluid magnetization, $\boldsymbol{M}$, is parallel to the applied magnetic field, $\boldsymbol{H}$. If there is a gradient in $H = |\boldsymbol{H}|$, then there will be a systematic body force owing to the slight but persistent correlation of field strength and pole sense. With this additional body force term, the momentum equations become [2]:

$$\frac{d\boldsymbol{u}}{dt} + \boldsymbol{u}\cdot\nabla\boldsymbol{u} + 2\Omega\times\boldsymbol{u} = -\frac{\nabla p}{\rho} + \boldsymbol{g} + \frac{M\nabla H}{\rho} + \upsilon\nabla^2\boldsymbol{u} \quad (1).$$

The superparamagnetic ferrofluid response is complicated by the fact that $M = M(H)$ unlike ρ which is independent of g for the gravitational case. As the applied magnetic field, H, increases, more of the ferrofluid dipoles line up with the field resulting in a linear increase in ferrofluid magnetization, M, for small H but saturating at M_s for large H. Figure 1 shows an example measurement of the field-averaged magnetization,

$$\overline{M} \equiv \frac{1}{H}\int_0^H M dH'$$

that shows this effect.

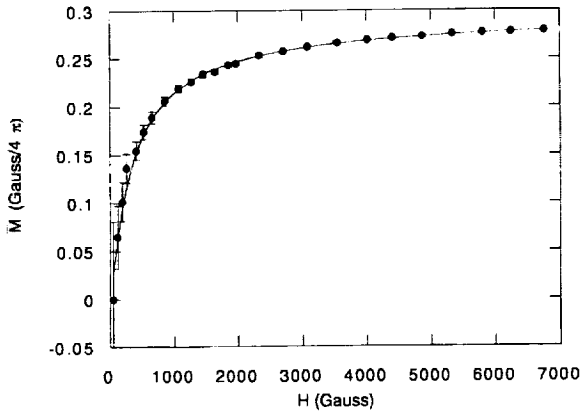

Figure 1. Field averaged magnetization vs. magnetic field for diluted water-based ferrofluid. The curve is a least-squares fit to a theoretical Langevin function prediction [2, 3].

In the experiments described below, the magnetic fields are less than 400 Gauss so M is nearly proportional to H. We have made careful measurements of M vs. H for $H < 500$ Gauss and fit them empirically to polynomials in H to use in theoretical predictions of the body force, $M\nabla H$.

APPROACH

The present study improves on the laboratory technique introduced in [3]. Figure 2 shows a schematic of the experiment. The apparatus is cylindrically axisymmetric. A cylindrical ceramic magnet is embedded in a smooth, solid, spherical PVC ball. The body force on the water-based ferrofluid depends only on the field strength and gradient from the interior magnet. The geopotential field (surfaces of constant $|H^2|$) and its gradient, the body force, were made nearly spherical by careful choice of magnet height-to-diameter ratio and magnet size relative to the PVC ball size. Terrestrial gravity is eliminated from Equation (1) by immersing

the "planet" and its ferrofluid "ocean" in an immiscible silicone oil/Freon mixture of the same density. Thus the earth gravity is removed from the dynamics of the ferrofluid/oil interface and the only dynamically active force there is the radial magnetic gravity. The entire apparatus can rotate, and waves are forced on the ferrofluid surface by exterior magnets.

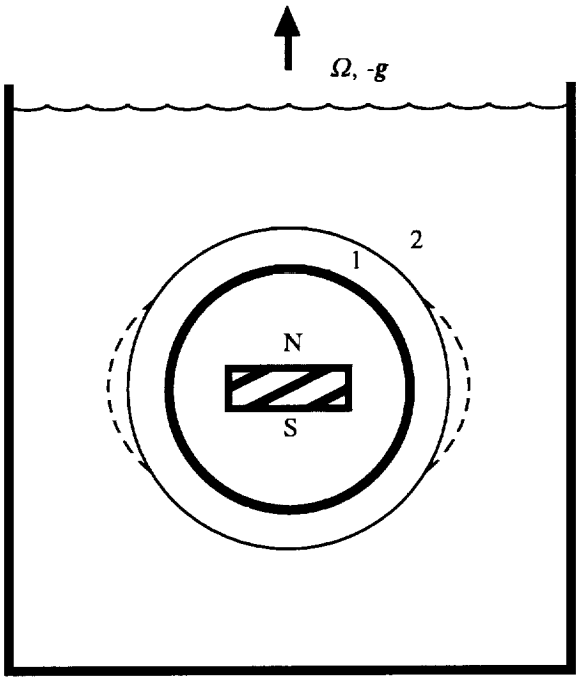

Figure 2. Side view schematic cross section of the cylindrically symmetric experiment. A cylindrical tank holds a silicone oil and Freon mixture (2) surrounding a water-based ferrofluid layer (1) that is held by the magnetic body force onto the surface of a PVC ball covering a cylindrical permanent magnet. $\rho_1 = \rho_2$ to eliminate terrestrial gravity. The entire apparatus rotates at angular frequency, Ω.

Figure 3 is a perspective view photograph of the apparatus. The external disk-shaped magnet at left forces a wave with maxima symmetrically displaced off the equator and a local minimum on the equator. Waves with a single maximum on the equator can be forced by inverting the forcing magnet polarity. A Plexiglas wall just visible on the right side in the black ferrofluid serves as a continental boundary for the ferrofluid ocean for studies of wave reflection discussed below. The entire ferrofluid ball is about 35cm in diameter, twice the size of reference [3], and the surrounding oil/Freon mixture has a viscosity 1/5 as large, giving more than an order of magnitude reduction in viscous effects. Careful temperature control of the water in the outer square box is required to maintain uniform density between the ferrofluid and oil/freon mixture as the expansion coefficients of the two fluids are different.

The biggest improvement in technique over [3] is in the wave visualization. Fluorescing dye is added to the oil/Freon mixture and an argon ion laser generates the horizontal light sheet visible in Figure 3. This sheet can be scanned vertically. Viewed from above, the experiment is a black circle with wave deformations surrounded by a light background. A contour of the image intensity at any light sheet position gives the surface of the ferrofluid "ocean" at that "latitude". Radial displacements of the waves as a function of longitude are obtained by subtracting the contour line positions from a no-motion contour at that laser sheet latitude. The experiments are run by traversing the forcing magnet with the laser sheet height fixed and images are frame grabbed to obtain a time series at one latitude. The experiment is then re-run with another laser-sheet height to build up a full picture of the three-dimensional wave structure in the upper hemisphere of the ball as a function of time

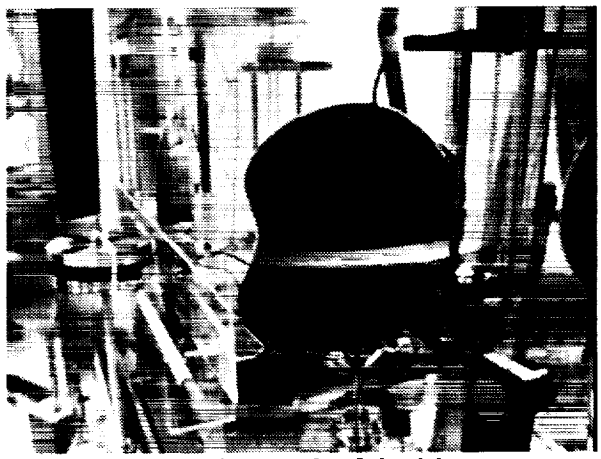

Figure 3. Photograph of the laboratory experiment. See text above for a description.

RESULTS

We concentrate here on results of laboratory studies of waves that are important in Earth's atmosphere and especially the ocean. In large scale atmospheric and oceanic fluid dynamics, only the local vertical projection of the planetary rotation, $f = 2\Omega\sin(\text{latitude})$, is important because the atmosphere and ocean are very thin compared to their horizontal extent and stratification effects further inhibit vertical motions. An important class of waves in geophysical fluid dynamics depends on the latitudinal variation of f [4, 5]. These Rossby waves are evident for example in the structure and dynamics of the atmospheric jet stream and Atlantic Gulf Stream. At the equator f changes sign, and a special class of these waves is trapped to equatorial latitudes but carry energy and momentum east and west [5]. These equatorial Kelvin and Rossby waves are an integral part of the dynamics of El Niño. This ferrofluid experimental technique is the only laboratory realization of these equatorial waves. To get oceanic

scaling in the laboratory, the experiment must rotate rapidly (4-second rotation period) so that the wave speed is slow compared to the planetary rotation speed as in the ocean.

In [3] observations of equatorial Kelvin and Rossby waves were compared to theoretical predictions [4, 5] and satellite observations [6, 7]. These experiments were conducted on the full sphere with visualization of wave height only on the equator. Using the improved experiment with lower friction and better visualization, we have extended the results in [3] to verify the latitudinal shape of the westward propagating equatorial Rossby waves. These waves have their largest signal off the equator, something like the wave shown in Figure 3.

In the Pacific Ocean, eastward propagating Kelvin waves eventually run into the South American coast. Theory predicts that some of the wave energy should scatter into coastal-trapped Kelvin waves that propagate north and south along the coast [8]. Some of this coastal wave energy might then scatter into *mid-latitude* Rossby waves that propagate back westward. Satellite observations of the Pacific Ocean sea-surface temperature and height seem to show signatures of westward propagating Rossby waves at 20N to 50N latitude, 5 to 10 years after the 1982-83 El Niño [9]. The observational data is difficult to interpret unambiguously owing to the large range of motions that fill the ocean at shorter timescales.

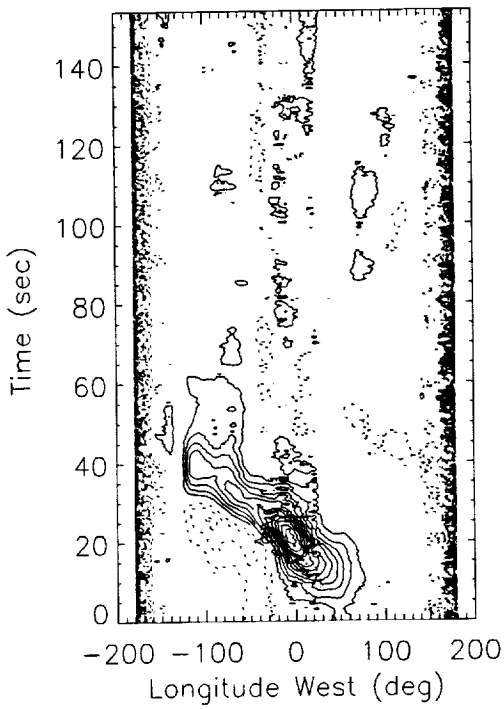

Figure 5. Wave height at 0°N latitude for 4-second rotation period experiment.

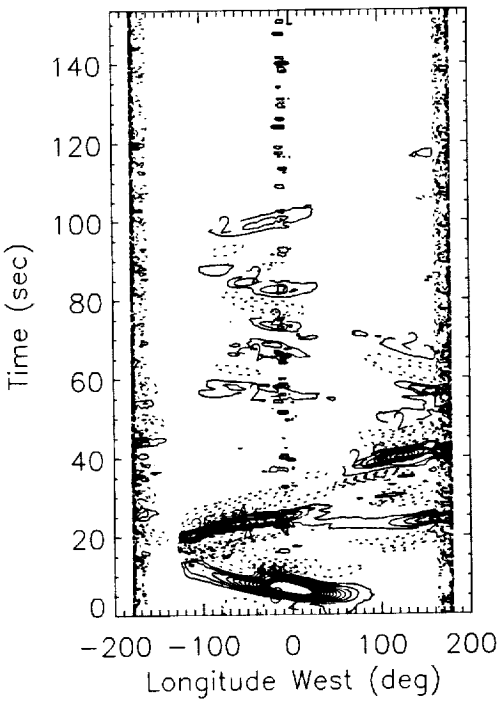

Figure 4. Wave height at 0°N latitude for non-rotating experiment.

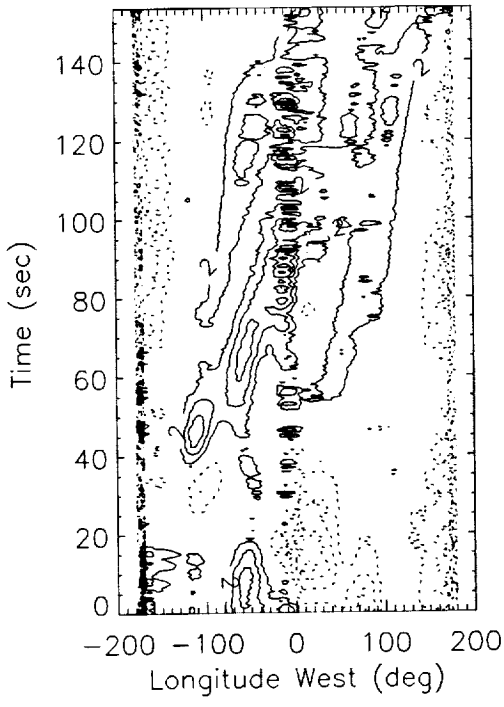

Figure 6. Wave height at 60°N latitude for 4-second rotation period experiment.

This series of reflections giving eastward, northward, and then westward traveling waves is observed cleanly in the laboratory experiments, confirming the theoretical expectations. Figures 4, 5, and 6 are all contours of wave height vs. longitude and time for experiments with a vertical wall (continent) placed at longitude −130°W. In the experiments, a wave with maximum amplitude on the equator is forced by an external magnet moving in the co-rotating direction (eastward). The magnet is closest to the experiment at 0°W longitude. Gaps in the laser-light sheet projection system give rise to the contour noise from −20°W to 10°W and 160°W to −170°W longitudes. In Figure 4 the experiment is not rotating and the wave height on the equator is plotted. The wave reflects from the wall and propagates at the same speed back to the west. Much of the wave energy propagates toward the pole in the non-rotating case (not shown). In contrast for the rapidly rotating case (Figures 5 and 6), the eastward wave propagates to the wall along the equator in Figure 5 and then disappears at about 40 seconds. Plots at higher latitude show the wave propagating northward until in Figure 6 at 60°N, the wave reaches maximum amplitude along the wall at 45 seconds and then propagates westward, more slowly than the eastward wave. This westward propagation at speeds slower than the equatorial Kelvin wave speed fits the classic long Rossby wave signature.

FUTURE WORK

The linear and nonlinear characteristics of traveling or standing waves on a liquid surface are a classic problem in fluid dynamics. Lateral boundaries have a strong effect on the spatial structures (fronts, pulses, solitons, etc.) observed in nonlinear propagating wave systems [10, for an extensive review]. It is of great theoretical interest to contrast wave behavior with and without lateral boundaries. With our spherical magnetic body force, a straight circumferential channel formed by boundaries at ± latitudes is an experimental system for free-surface capillary-gravity waves that has periodic boundary conditions in one direction. Similarly, the entire spherical surface is boundary-less and periodic in two-dimensions. In an equatorial channel geometry, the contact lines are of the same length (as opposed to in an annular geometry) and this symmetry makes comparison to theory easier. We plan next to study various capillary-gravity waves using this apparatus which is the laboratory version of the standard theoretical periodic-boundary construct.

Standing capillary-gravity waves are excited if the gravitational force oscillates in time. This is normally accomplished by vibrating a fluid container vertically. These "Faraday waves" have become, along with Rayleigh-Benard convection, a canonical system for studies of non-equilibrium pattern formation, spatio-temporal evolution, and chaos [10]. Our spherical geometry, with parametric oscillation obtained by oscillating the magnetic field, is a very clean system for investigating such parametrically excited waves, without complications of boundary shapes and contact angles which can determine patterns and mode competition dynamics even very far from the boundaries [11]. We've designed an electromagnet version of the apparatus of Figures 2 and 3 to provide an oscillating "gravity". We should have sufficient electromagnetic driving strength in the frequency range 0.01 to 10 Hz, to generate Faraday wave patterns by parametric excitation with up to a few tens of waves in a circumference on the sphere or somewhat fewer fitting around inside a polar basin. The spherical system has the periodic boundaries of the standard theoretical development [11] but which have not been previously possible experimentally.

Continuing the geophysical applications, ferrofluid experiments offer the potential for conducting laboratory studies of thermally driven oceanic flows over a substantial part of a sphere. These slow deep overturning oceanic motions are highly constrained by the dynamical influence of planetary vorticity advection. Such effects cannot be studied in the terrestrial laboratory, when the all-important case of continuous thermal stratification is considered, because of the strong gravity induced cells that have no oceanic analogs. Previous GFFC-type [12] experiments are also ill suited to oceanic flow modeling because they are too viscous (thin gaps). We will address the key **technical** issues in building a relatively simple but effective microgravity based experiment to enable laboratory study of continuously stratified spherical flows in complex basins spanning a latitude range of at least plus or minus 60 degrees. We realize that such an experiment must be conducted in microgravity, and our terrestrial demonstration experiment will be contaminated by terrestrial gravity induced flows. The main technical issues to explore are: 1) how to get a large enough magnetic buoyancy frequency in an apparatus of sufficient size, 2) how to stratify and force motion in the experiments, and 3) how to visualize the flows effectively.

ACKNOWLEDGEMENTS

This work is supported by NASA grant NAG3-1848 and NSF grants OCE-9416661 and OCE-9709338. Scott Kittelman and Dr. Navid Borhani built the apparatus and Scott Kittelman has been instrumental in conducting all the experiments.

REFERENCES

1. Wang, T.G., A.V. Anilkumar, C.P. Lee, and K.C. Lin: *J. Fluid Mech.*, **276**, 389-403, 1994.
2. Rosensweig, R.E.: *Ferrohydrodynamics*. Cambridge University Press, 1985.
3. Ohlsen, D.R. and P.B. Rhines: *J. Fluid Mech.*, **338**, 35-58, 1997.

4. Gill, A.E.: *Atmosphere-Ocean Dynamics*. Academic Press, 1982.
5. Philander, S.G.: *El Niño, La Niña, and the Southern Oscillation*. Academic Press, 1990.
6. Chelton, D.B. and M.G. Schlax: *Science*, **272**, 234-238, 1996.
7. Delcroix, T., J. Picaut, and G. Eldin: *J. Geophys. Res.*, **96 (Suppl.)**, 3249-3262, 1991.
8. Clarke, A.J.: *J. Phys. Oceanogr.*, **13**, 1193-1207, 1983.
9. Jacobs, G.A., H.E. Hurlburt, J.C. Kindle, E.J. Metzger, J.L. Mitchell, W.J. Teague, and A.J. Wallcraft: *Nature*, **370**, 360-363, 1994.
10. Cross, M.C. and P.C. Hohenberg: *Rev. Mod. Phys.* **65**, 851-1112, 1993.
11. Miles, J. and D. Henderson: *Annu. Rev. Fluid Mech.*, **22**, 143-165, 1990.
12. Hart, J.E., G.A. Glatzmaier, and J. Toomre: *J. Fluid Mech.*, **173**, 519-544, 1986.

Control Of Flowing Liquid Films By Electrostatic Fields In Space

E. M. Griffing[1], S. G. Bankoff[1], [1]Chemical Engineering, Northwestern University, Evanston IL, 60208-3120, USA, e-griffing@nwu.edu, R. A. Schluter[2], [2]Physics and Astronomy, Northwestern University, Evanston IL, 60208-3120, USA , M. J. Miksis[3], [3]Engineering Science and Applied Mathematics, Northwestern University, Evanston IL, 60208-3120, USA

INTRODUCTION

Future space missions will benefit greatly from light weight radiators capable of rejecting large amounts of heat. The generation of $1MW$ of electric power requires a compact source such as a nuclear reactor, which produces as much as $1.5MW$ of waste heat [11]. This heat must be radiated into space. Most current designs utilize high pressure heat pipes, which employ redundancy and possibly armor to protect against damage from micrometeorites. These radiators make up about a third of the system weight. New designs which safely incorporate thinner walls and lower the need for redundancy will dramatically reduce weight. Because of the expense of moving a given mass out of earth gravity, this weight savings translates directly into cost savings.

The Electrostatic Liquid Film Radiator (*ELFR*) was proposed by Kim, Bankoff, and Miksis [8] in 1991. This design utilizes thin film flow to carry heat over a large membrane. Low internal pressures allow for thin, lightweight, membrane walls. The heavy armor is dispensed with by allowing for holes due to micrometeorites. Coolant leakage is then prevented by the application of an internal electric field local to the 'leak' hole. The electric field creates a pressure drop across the fluid interface. If this pressure drop is greater than the internal pressure of the radiator and any normal gravitational force, *both free design parameters*, the pressure within the liquid at the radiator wall will be negative and leaks will be suppressed.

Redundancy in an *ELFR* is reduced, because the radiator can be operated with most micrometeorite holes. Current heat pipe designs, on the other hand, use 28% redundancy [11]. The radiator is partitioned, and a leak is stopped by turning off the damaged section. Several *ELFR* designs, such as a tubular radiator, and a spinning conical radiator are explored in Kim, Bankoff, and Miksis [9, 10]. Assuming the same operating temperature as used in the heat pipes, the conical radiator design, shown in figure 1 could in principle achieve a reduction in weight over present designs of the order of 90% [4]. This remains to be explored in detail, but clearly a vigorous effort is justified. These designs assume the radiator to be operating in zero g, but other designs may allow for operation on the moon or Mars.

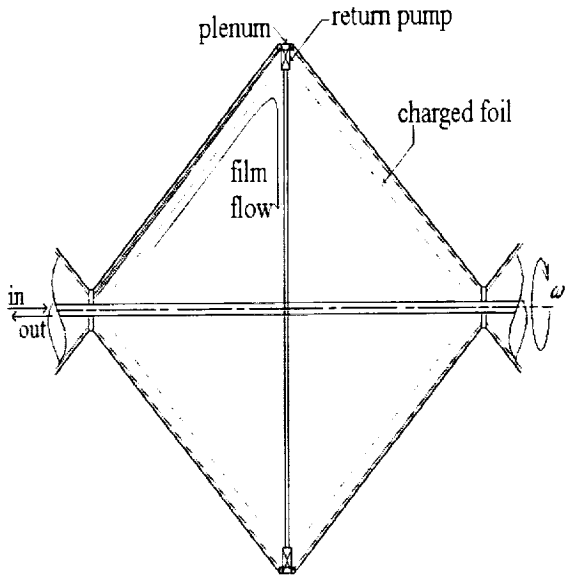

Figure 1: In this conical *ELFR* design, radiator fluid is distributed among multiple rotating cones. The cone angle, B, and rotation rate, w are used to set an artificial acceleration. Fluid flows radially along each cone, is collected by a plenum at the outer edge, and returned to the center by a small mechanical pump.

In order for a safe design and failure analysis to be made, more has to be learned about the fundamental behavior of a fluid film as it passes under an electrode. The film height and the electric field are coupled. This produces a mechanism whereby the fluid can touch the electrode and cause a breakdown of the field. Further complicating the situation, traveling waves are expected to form in the radiator. The interaction of these traveling waves with the field also needs to be studied. The dynamics of the fluid within a 'leak' hole present a complicated free surface problem which can affect leak rates, especially for lunar or Mars based applications.

The effect of an electric field on fluid interfaces is the subject of extensive study as it bears on ink jet printing, spray painting, emulsifying, etc. In 1964, Taylor and McEwan [13] derived a linear stability result for a stationary inviscid fluid of infinite depth under

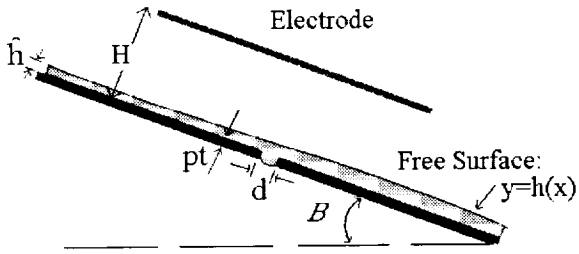

Figure 2: Coordinate scheme of flow under an electrode.

an infinite electrode. These results compare well with their experiments, which show the formation of 'Taylor cones' at a critical voltage. These cones form jets which touch the electrode and short the circuit when the fluid is a conductor. Other authors studying pattern formation and stability of horizontal interfaces in the presence of electric or magnetic fields include Silber and Knobloch [12], and Deyirmenjian et al.[1].

Work involving electric fields and thin moving films has been far less common. For this problem, Kim, et al. [7, 9] and Gonzalez and Castellanos [3, 2] have used long wave theory. Both authors calculate the stability of the Nusselt flow for an infinite electrode and show the field to be purely destabilizing. In the case of flow down an inclined plane with no field, the long wavelength instabilities are often not seen experimentally, as observable amplitudes are slow to develop. For an *ELFR*, the flow only has to be stable for the length of a radiator, so that only instabilities with a short enough characteristic development time are important. Kim, et al. use lubrication theory, Karman-Polhausen theory, the Korteweg-de Vries equation and Marker and Cell *SOLA* [5] algorithm to obtain $2D$ height and pressure profiles of a thin film in the presence of a fixed electric field for various geometries. The stability of these primary flows as they pass under an electrode and the coupling of the field and the fluid interface, in close proximity to the electrode, remain to be studied.

In the current work the flow under a finite electrode down a vertical plate is studied experimentally. Fluid height profiles and critical voltages for instability can be used to test theoretical predictions. Pressure profiles are obtained with a manometer, and leak rates are studied as a function of pressure driving force for various hole shapes and film Reynolds numbers.

EXPERIMENT

We consider a thin liquid layer flowing down an inclined plate as shown in figure 2. The height and

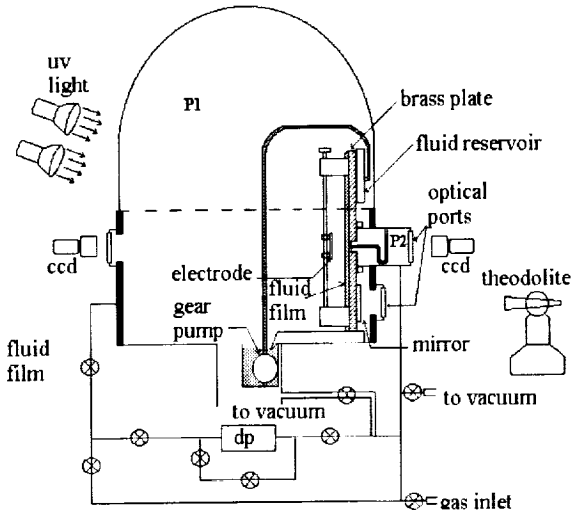

Figure 3: The experimental apparatus is used to measure fluid height and pressure profiles, instability voltages, and leak rates.

length of the electrode are given as H and l. The height of the fluid layer and the length of a typical disturbance are given as $\hat{h}$ and L. The diameter of the 'leak' hole and the plate thickness are given as d, and pt. Typical experimental values of H, l, $\hat{h}$, d, and pt are 1.5 cm, 5 cm, 0.05 cm, 0.1 cm, and 0.1 cm respectively. Because $d << l$ and $\hat{h} << H$, the effect of the hole on the flow dynamics is negligible.

The experimental apparatus, shown in figure 3, consists of a vertical brass plate, fluid reservoir, pump, and electrode inside a vacuum chamber. The vacuum is used to reach high fields without electrical breakdown. Fluid flows continuously down the plate passing under the electrode. The whole apparatus can be tilted to a desired angle $85° < B < 95°$, which is measured with a theodolite. This allows for a normal component of gravity of $-100\,cm/s^2 < g_n < 100\,cm/s^2$. A manometer is used to measure pressure profiles, and a fluorescence imaging method [6] is used to measure height profiles. The electrode is held on threaded rods so that it can be moved in the direction of flow to vary the relative position of the 'leak' hole, and normal to flow to vary H.

The primary flow velocity profile without the field is parabolic. Several primary flow height profiles for an uncoupled electrostatic field, as calculated by Kim, et al., are shown in figure 4. The amplitude of the steady standing wave decreases as the Reynolds number increases. This is due to a momentum flux balance

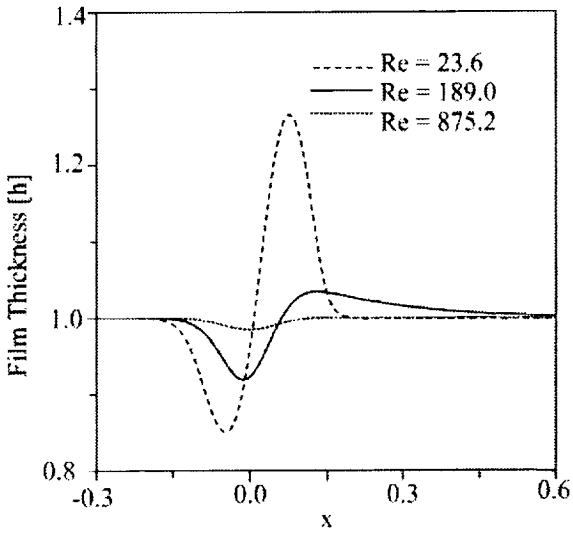

Figure 4: Reprinted from Kim, et al.[7]. The steady state wave amplitude is shown to decrease as Re is increased.

between the pressure exerted by the field and convection away from the electrode due to the flow. As the electric field is increased past some critical voltage, a new type of electrohydrodynamic instability, *EHI*, is observed experimentally. This instability is similar to Taylor cones, but is more complex. The fluid changes from a $2D$ shape to a distorted moving $3D$ cone which emits a liquid jet in less than a tenth of a second. In the case of a dielectric fluid, the liquid jet passes under the electrode harmlessly. In the case of a conductor, the jet induces breakdown and causes the system to fail.

In the horizontal static film case, the formation of the cones is governed by a balance of the destabilizing electric force with the stabilizing gravitational and surface tension forces. The surface tension and the gravitational forces then form a selection mechanism making most dangerous wavelengths of approximately 1.6 cm for water and 1.1 cm for organic oils [13]. In the experiment with a vertical plate, there is no normal gravitational force, the fluid is of finite depth with velocity, and the electrode is finite. Linear stability theory for an infinite electrode shows the longest waves to be the most unstable, but also the slowest growing [14]. In this case, the observed lengths of the *EHI* are less than 2 cm.

Because the *EHI* can cause the failure of the system, the critical voltage of the onset of the instability represents the limit of the force which can be exerted by the field. The coupling of the field and the fluid interface in the horizontal case was shown significantly to reduce the critical field for electrode heights $H < 1$ cm. For $H = 1.5$ cm and $5 < Re < 40$, the *EHI* is observed at $V \approx 15$ Kv. This corresponds to a pressure of ≈ 50 $dynes/cm^2$. The vapor pressure of lithium, a suggested radiator fluid, is 9 $dynes/cm^2$ at $700K$. Using these figures, an artificial acceleration as large as ≈ 0.5 g could be overcome with the electric field.

The fluid height is measured by the fluorescence imaging method, the details of which are given in Johnson et al.[6]. A fluorescent dye is introduced into the working fluid, and incident ultraviolet light induces fluorescence in the visible range. A digital camera held normal to the fluid is then used to record the fluorescence intensity produced by a patch of fluid. The intensity is then correlated with fluid height through a model equation. Preliminary experiments show that the steady state profiles in the parameter ranges of the experiment are smaller than the accuracy of the imaging system, which is roughly 2 % of the film depth. A more accurate 16 bit camera will be used in future work to obtain the height profiles.

The pressure profiles are obtained with a manometer, which taps the vertical plate and uses the working fluid, so that only one fluid interface affects the measurement. A traveling microscope is then used to measure the displacement of the interface. The pressure is obtained as a function of position in the direction of flow by moving the electrode with respect to the manometer. Because g_n is zero, lubrication theory shows that for low Re, dP/dy is zero to first order. The pressure exerted by the electrode at the interface is then transmitted across the fluid film. Figure 5 shows the experimental pressure profiles for various Re and A, the aspect ratio of the hole, pt/d, as compared with the pressure profiles predicted by an uncoupled calculation of the electrostatic field. These data confirm that the pressure drop across the film is within the error of the measurement, 3 $dynes/cm^2$. For the case of a dielectric fluid, the thickness of the brass plate, or A, will affect the field within the 'leak' hole and possibly the measured pressure.

To measure leak rates, the fluorescent imaging system is again used. In this case, a macroscopic lens is used to focus on the back of the leak hole. Depending on flow conditions, either a single or a double rivulet forms as the leaking fluid drains down the plate. By getting the height profile of these rivulets in the transverse direction and assuming a parabolic profile, we can instantaneously estimate the relative flow rate of the leak. Figure 6 shows an example image of a double rivulet leak and the transverse flow rate profile. Figure

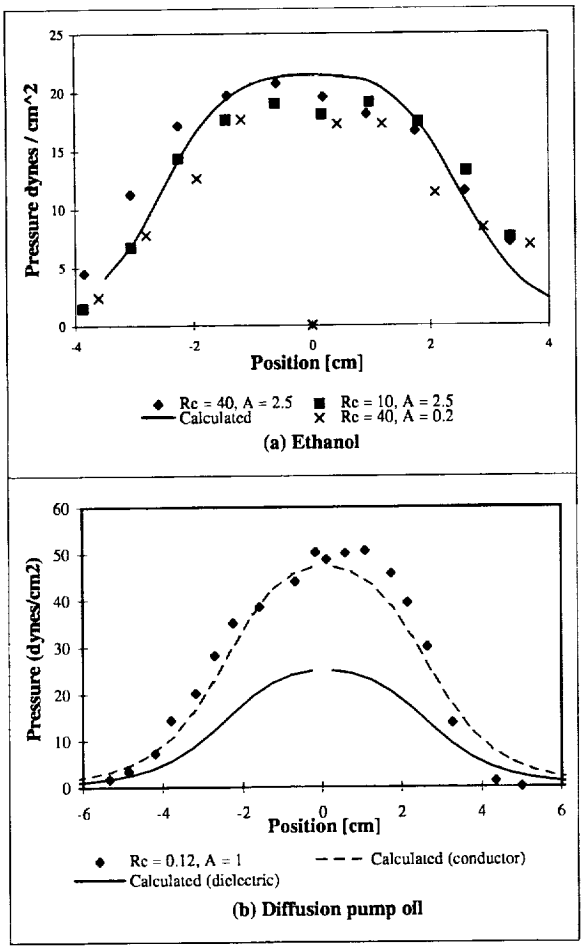

Figure 5: Measured pressure profiles confirm that the pressure exerted by the field at the fluid / vapor interface is transmitted across the film with unmeasurable hydrodynamic effects.

7 shows the flow rate decrease to zero as a voltage of $\approx 11\ Kv$ is approached. The Reynolds number, Re, was varied over $5 < Re < 40$, and no significant change in the critical voltage required to stop a leak was observed.

Several important aspects of this experiment should be noted. The effect of gravity is to make a pressure drop from the top to the bottom of the leak hole of 77 $dynes/cm^2$, significantly affecting leak stopping experiments on earth. Also, the fluid in this case is ethanol, which wets the brass plate. Capillary forces therefore induce leaking, and cause a complicated moving contact line problem at the back of the hole. Future experiments will determine the effect of wetting and possibly gravity on leak rates. Finally, the interface at the back of the hole in a non-leaking situation is observed to vibrate at a frequency which is greater than 24 Hz. The g force associated with this vibration has not been measured. In all future experiments of this nature, the whole apparatus is to be suspended by a $2m$ chain to suppress these high-frequency oscillations.

The major result here is that it has been shown experimentally that leaks from a low-volatility fluid (lithium at 700 K and gallium or diffusion pump oil at 525 K) pumped-loop *ELFR* can be stopped by application of an electric field well below the critical value for the *EHI* under space conditions. Weight comparisons for equivalent power with a conventional heat-pipe radiator are difficult to make, since the two radiator systems are quite different. However, purely on a basis of estimated weight per kilowatt at a radiator temperature of 525 K, for a 1675 Kw radiator, the *ELFR* has been roughly estimated to be well below one by Mason et al. in 1989 [11, 4].

A major source of difficulty in conducting a leakage experiment in earth gravity is the tendency for the fluid to drain down the back side of the plate. In a space experiment, gravity will be nearly zero, or else radially outwards, so that the meniscus at a round hole will remain symmetric with no preferred direction for leakage.

ACKNOWLEDMENTS

This work is supported by NASA. The contribution of Mr. R. Gwinner under a grant from the German government for the design phase of the work is acknowledged with thanks.

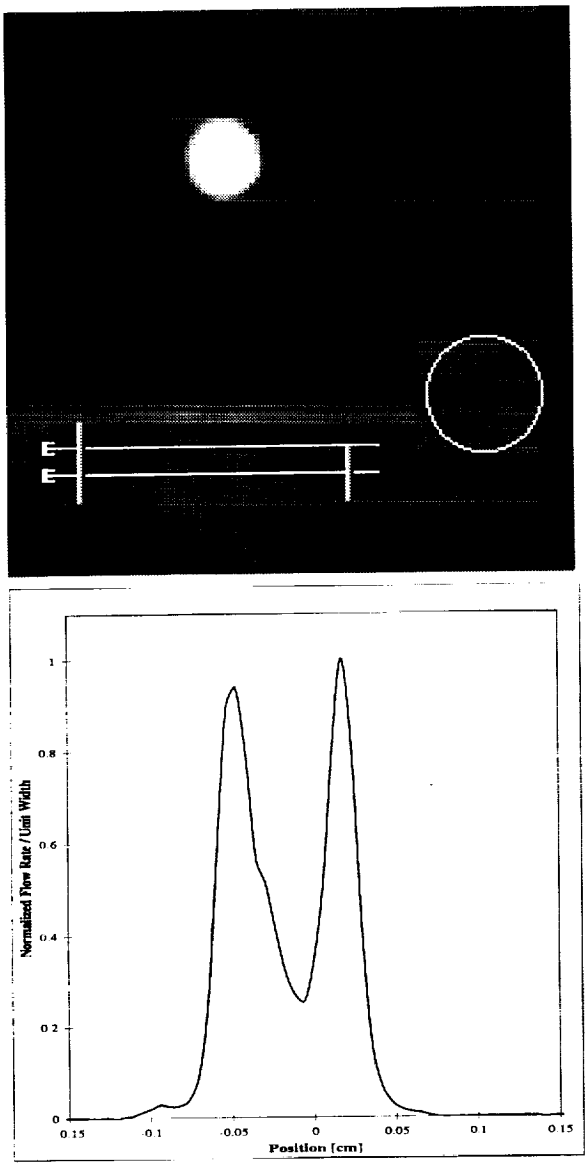

Figure 6: Leak rates are measured with the fluorescence imaging method. The bright circle is the 1 *mm* leak hole. The flow rate is calculated as the integral of the flow rate profile across the rivulet at the horizontal lines. The area within the circle is used to normalize the incident light intensity.

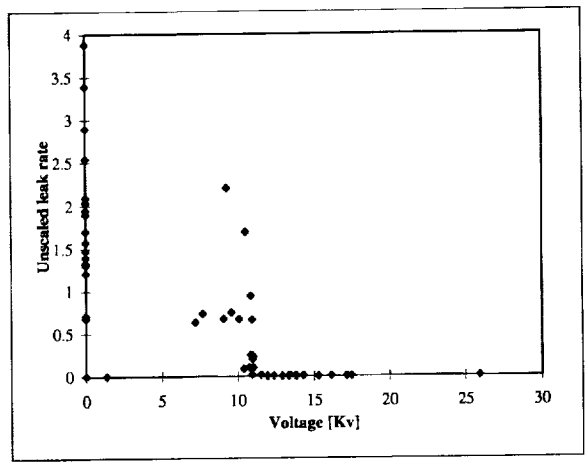

Figure 7: The leak rates measured as in Figure 6 decrease to zero as a critical voltage is reached.

References

[1] V.B. Deyirmenjian, A.D. Zahir, and S. W. Morris. Weakly nonlinear analysis of electroconvection in a suspended fluid film. *Physical Review E*, 56(2), 1997.

[2] A. Gonzalez and A. Castellanos. Korteweg-de Vries-Burgers equation for surface waves in non-ideal conducting liquids. *Physical Review E*, 49(4), 1993.

[3] A. Gonzalez and A. Castellanos. Nonlinear electrohydrodynamic waves on films falling down an inclined plane. *Physical Review E*, 53(4), 1995.

[4] R.R. Gwinner and S.G. Bankoff. Design study of an electrostatic liquid film space radiator. Unpublished technical report, chemical engineering, Northwestern university, 1992. Contact gbankoff@nwu.edu.

[5] C.W. Hirt, B.D. Nichols, and N.C. Romero. SOLA - A Numerical solution algorithm for transient fluid flows. Technical report, Los Alamos Scientific Laboratory of the Univ. of California, Los Alamos, 1975.

[6] M.F.G Johnson, R.A. Schluter, and S.G. Bankoff. Fluorescent imaging system for global measurement of liquid film thickness and dynamic contact angle in free surface flows. *Rev. Sci. Instrum.*, 68(11), 1997.

[7] H. Kim, S.G. Bankoff, and M.J Miksis. The effect of an electrostatic field on film flow down an inclined plane. *Phys. Fluids*, 1991.

[8] H. Kim, S.G. Bankoff, and M.J Miksis. Lightweight space radiator with leakage control by internal electrostatic fields. In *Proc. Eighth Symp. On Space Nuclear Power Systems*, CONF. -910116, 1991.

[9] H. Kim, S.G. Bankoff, and M.J Miksis. Interaction of an electrostatic field with a thin film flow within a rotating conical radiator. *AIAA Journal*, 1992.

[10] H. Kim, S.G. Bankoff, and M.J Miksis. Cylindrical electrostatic liquid film radiator for heat rejection in space. *J. of Heat Trans.*, 1994.

[11] Lee S. Mason, Harvey S. Bloomfield, and Donald C. Hainley. SP-100 power system conceptual design for lunar base applications. Technical Report TM 102090, NASA Lewis Research Center, Cleveland, OH 44135, 1989.

[12] M. Silber and E. Knobloch. Pattern Selection in Ferrofluids. *Physical Review D*, 30, 1988.

[13] G.I. Taylor and A.D. McEwan. The stability of a horizontal fluid interface in a vertical electric field. *J. Fluid Mech.*, 22(1), 1965.

[14] C.S. Yih. *Fluid mechanics: a concise introduction to the theory.* West River Press, Ann Arbor, Mich, 1988.

CELL AND PARTICLE INTERACTIONS AND AGGREGATION DURING ELECTROPHORETIC MOTION

Robert H. Davis, Shulin Zeng and Paul Todd, Department of Chemical Engineering,
University of Colorado, Boulder, Colorado 80309-0424

ABSTRACT

The stability and pairwise aggregation rates of small particles undergoing electrophoretic migration are predicted in the presence of gravitational motion for large particles and Brownian motion for small particles. The particle aggregation rates may be enhanced or reduced by appropriate alignment and strength of the electric field. Density gradient zone electrophoresis experiments to quantify particle aggregation are also described.

INTRODUCTION

Electrophoresis refers to the motion of charged particles, droplets or molecules in response to an applied electric field. When particles have different surface charge densities or potentials, they will migrate at different velocities in an electric field. This leads to the possibility that they will collide and aggregate, thereby preventing separation (Todd and Hjertén, 1985; Nichols *et al.*, 1995).

Electrophoresis is widely used on the analytical scale (and sometimes on the preparative scale) for the separation of biological molecules such as proteins and nucleic acids. In order to improve the separation and reduce convection due to electrical heating, such separations are usually done in a gel matrix or a capillary tube. A suspension of particles or cells would clog a gel matrix or very fine capillary, however, and so electrophoretic separation of such suspensions is performed as "free" electrophoresis in a wider chamber or column without a gel. In this case, the separation efficiency may be affected by three factors: (i) free convection or mixing due to thermal gradients, (ii) particle sedimentation, and (iii) particle aggregation. This research focuses on particle aggregation due to electrophoretic motion with and without gravity sedimentation. The ground-based experiments are designed to minimize free convection, but it is anticipated that a low-gravity environment will be needed to study electrophoretic aggregation in the absence of sedimentation and convection.

In addition to having general scientific and engineering significance, our fundamental study of particle aggregation in electric fields is expected to have practical application to electrically-controlled cell flocculation for cell separation and recycle in space-based bioreactors, where gravity cannot be employed. Similarly, an extension of the proposed study to drop interactions and coalescence would provide an understanding of electrically-driven demixing of two liquid phases, such as those encountered in biphasic aqueous extraction of biological cells and molecules under reduced gravity when buoyancy-driven demixing is weak.

RESULTS AND DISCUSSION

A theoretical study of pairwise aggregation of particles undergoing combined electrophoretic and gravitational motion has been completed (Wang *et al.*, 1997). Depending on its relative strength and orientation, the presence of an electric field may enhance or reduce the gravitational aggregation rate. For antiparallel alignment of gravitational and electrophoretic motion, with the former dominant, a "collision-forbidden" region of parameter space is predicted due to the stronger hydrodynamic interaction of two particles for gravitational motion than for electrophoretic motion. This region is evident in Figure 1, which shows the predicted collision frequency (number of doublets formed per total number of particles per unit time) for a model system. Figures 2 and 3 show how one particle moves outward around the other for antiparallel alignment with gravitational motion dominant, while one particle moves inward toward the other for antiparallel alignment with electrophoretic motion dominant, respectively.

An experimental study to measure pairwise aggregation rates has been initiated. A density gradient zone electrophoresis chamber was assembled, in which a combination of a sucrose density gradient and a cooling jacket and finger is used to stabilize against free convection due to electroviscous heating. Preliminary experiments have been performed in which a band of faster-moving particles passes through a band of slower-moving particles, resulting in aggregate formation (Figure 4). In the initial experiments, polystyrene latex particles of 3.5 μ m diameter and two different surface charges (due to different surface coverages of sulfate groups) were used. Aggregation was observed and quantified, but it could not be determined if homoaggregates or heteroaggregates formed, since the particles are physically indistinguishable. In more recent experiments, polystyrene latex particles of 2.3 μ m diameter and 3.5 μ m were used. As shown in Figure 5, heteroaggregates were formed when a band of faster-moving particles passed through a band of slower-moving particles. As expected, increasing the particle concentrations gave a higher relative amount of aggregation (Figure 6). However, a major difficulty is that the two original bands do not completely separate, leaving open the possibility that aggregates form during sampling from the region of band overlap. One reason that the bands do not completely separate is that they experience considerable spreading due to variation in surface potentials within a single

particle type and due to hydrodynamic interactions. Another reason is that the band of faster-moving particles experiences collective sedimentation as it reaches the upper regions of the column where the fluid density is lower.

A macroscopic theory was also developed to predict the evolution of the aggregate size distribution with time and position, based on population dynamics balances. Typical results for zone electrophoresis with two initial bands of single particles which pass through each other to form a third band of dimers is shown in Figure 7. The theory gives results which are qualitatively similar to the experimental observations. However, the spreading of the bands in the experiments is greater than predicted by the current theory which does not account for hydrodynamic interactions and the distributions of surface potentials.

The mobility functions for two interacting spheres of different size and surface potential undergoing electrophoresis with arbitrary separation and orientation of the line of centers relative to the electric field have been determined using bispherical coordinates. This method of calculating mobility functions is highly accurate and efficient, even for particles in close contact and with arbitrary size ratio. These mobility functions are being used to predict pairwise aggregation rates of very small particles experiencing combined electrophoresis and Brownian motion at arbitrary Péclet numbers.

FUTURE RESEARCH

We plan to measure pairwise aggregation rates of additional particles with different surface potentials undergoing electrophoretic motion. Different ionic strengths will be employed, to cover ranges in which aggregation and no aggregation are expected. A variety of particles (or cells) will be screened for aggregation properties, and the effects of particle concentration will be quantified. The simulations to interpret these experiments will be extended to include nonuniformity in the surface potential of particles within each band, and to incorporate varying solution properties due to the density gradient. In addition, the average mobility and spreading of each band will be quantified and interpreted in terms of electrophoretic and hydrodynamic effects.

Calculations of the aggregation of colloidal particles due to the combined effects of Brownian motion and electrophoretic motion will also be completed. These calculations will employ the two-sphere mobility functions which we have recently determined for arbitrary separations and size ratios. Population dynamics balances will then be used to predict the growth of the aggregate size distribution in a suspension of colloidal particles when an electric field is applied.

REFERENCES

Wang, H., Zeng, S., Loewenberg, M. and Davis, R. H. (1997) Particle aggregation due to combined gravitational and electrophoretic motion, *J. Colloid Interf. Sci.* **187**, 213-220.

Nichols, S. C., Loewenberg, M. and Davis, R. H. (1995) Electrophoretic particle aggregation, *J. Colloid Interf. Sci.* **176**, 342-351.

Todd, P. and Hjertén, S. (1985) Free zone electrophoresis of animal cells. I. Experiments on cell-cell interactions. In *Cell Electrophoresis*. (ed. Schütt, W. and Klinkman, H.), Walter deGruyter and Co., Berlin, pp. 23-31.

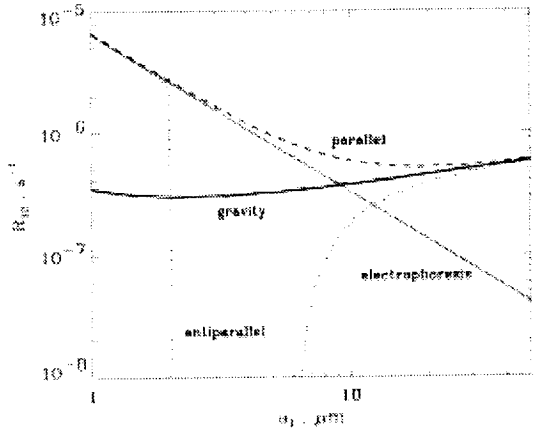

Figure 1 - The aggregation frequency as a function of the radius of the larger particle for a model system with gravitational motion alone, electrophoretic motion alone, parallel combined motion, and antiparallel combined motion. For antiparallel combined motion, the collision forbidden region is evident for $2\ \mu$ m $< a_1 <$ $6\ \mu$ m.

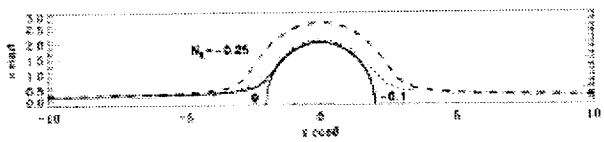

Figure 2 - The grazing relative trajectory for gravitational motion ($N_{E\_}$= 0) and relative trajectories with the same impact parameter for antiparallel combined motion when electrophoresis is weak (N_E is the ratio of electrophoretic motion to gravitational motion).

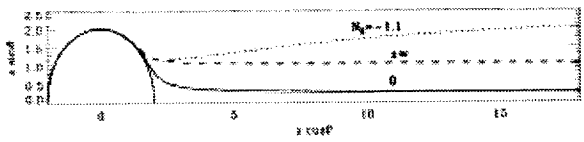

Figure 3 - The relative trajectories for electrophoretic (dashed curve), gravitational (solid curve), and anti-parallel combined motion (dotted curve) when electrophoresis is stronger than gravity.

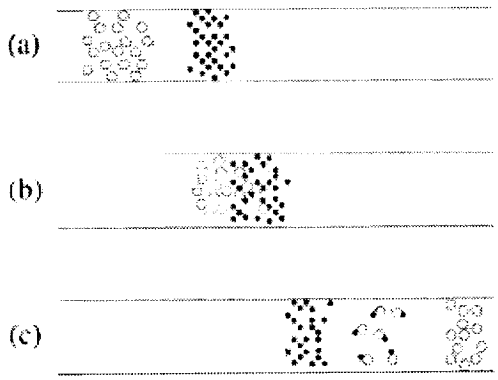

Figure 4 – Schematic of aggregation during zone electrophoresis of a high-mobility band passing through a low-mobility band.

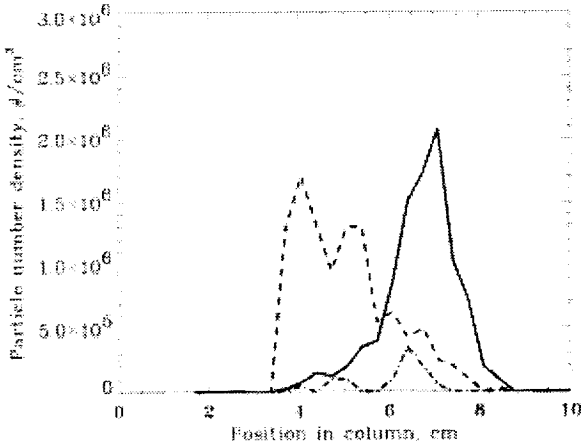

Figure 5 - Particle number density distribution in the column after electrophoresis of 0.01% 2.3 μm particles (dashed line) and 0.03% 3.5 μm particles (solid line) to form heteroaggregates (dashed-dotted line).

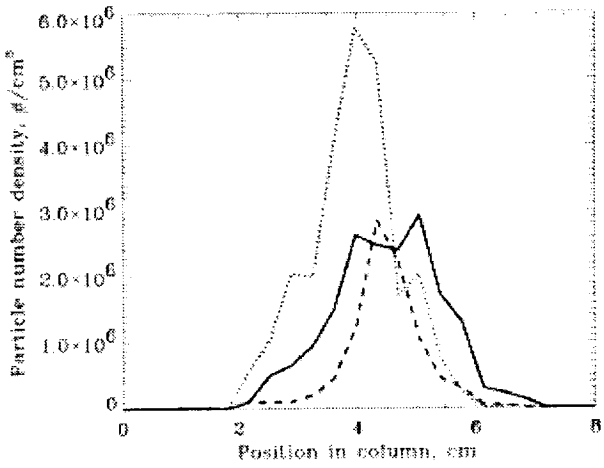

Figure 6 - Particle number density distribution in the column after electrophoresis of 0.02% 2.3 μm particles (dotted line) and 0.05% 3.5 μm particles (solid line) to form heteroaggregates (dashed line).

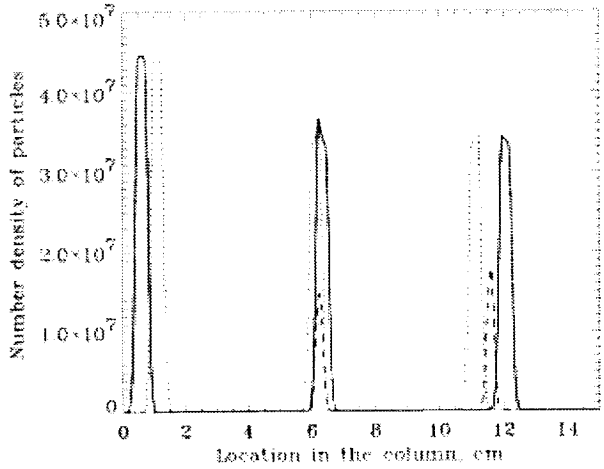

Figure 7 - Simulation results for density gradient zone electrophoresis of faster (solid lines) and slower (dotted lines) particles which form heteroaggregates (dashed lines).

Magnetic control of convection in electrically nonconducting fluids

Jie Huang[1], Donald D. Gray[1], [1]*Department of Civil and Environmental Engineering, West Virginia University, Morgantown, WV 26506-6103, USA, un072134@wvnvms.wvnet.edu*, Boyd F. Edwards[2], [1]*Department of Physics, West Virginia University, Morgantown, WV 26506-6315, USA, bedwards@wvu.edu*

Abstract

Inhomogeneous magnetic fields exert a body force on electrically nonconducting, magnetically permeable fluids. This force can be used to compensate for gravity and to control convection. The effects of uniform and nonuniform magnetic fields on a laterally unbounded fluid layer heated from below or above are studied using a linear stability analysis of the Navier-Stokes equations supplemented by Maxwell's equations and the appropriate magnetic body force. For a uniform oblique field, the analysis shows that longitudinal rolls with axes parallel to the horizontal component of the field are the rolls most unstable to convection. The corresponding critical Rayleigh number and critical wavelength for the onset of such rolls are less than the well-known Rayleigh-Bénard values in the absence of magnetic fields. Vertical fields maximize these deviations, which vanish for horizontal fields. Horizontal fields increase the critical Rayleigh number and the critical wavelength for all rolls except longitudinal rolls. For a nonuniform field, our analysis shows that the magnetic effect on convection is represented by a dimensionless vector parameter which measures the relative strength of the induced magnetic buoyancy force due to the applied field gradient. The vertical component of this parameter competes with the gravitational buoyancy effect, and a critical relationship between this component and the Rayleigh number is identified for the onset of convection. Therefore, Rayleigh-Bénard convection in such fluids can be enhanced or suppressed by the field. It also shows that magnetothermal convection is possible in both paramagnetic and diamagnetic fluids. Our theoretical predictions for paramagnetic fluids agree with experiments. Magnetically driven convection in diamagnetic fluids should be observable even in pure water using current technology.

I. Introduction

In a recent experiment, Beaugnon and Tournier[1] have successfully levitated various diamagnetic solids and liquids using a strong nonuniform static magnetic field. Recent experiments [2,3] also observe the strong enhancing and suppressing effects of an applied inhomogeneous static magnetic field on thermal transport in a gadolinium nitrate solution heated from below, indicating that the thermal gradient induced buoyancy-driven convection in this paramagnetic fluid is controllable via the applied magnetic field. We provide here the theory of magnetically controlled convection in a horizontal, electrically nonconducting fluid layer heated from either above or below. We show that the convective fluid flow can be effectively controlled by placing the layer in a non-uniform magnetic field, which can promote or inhibit convection for both upward and downward thermal gradients. This phenomenon has a great potential to be utilized to enhance or to suppress the gravitational effect in terrestrial experiments and to control the flow of nonconducting fluids in a microgravity environment. This effect can be utilized to increase the efficiency of heat-transfer devices.

When a magnetically permeable fluid is placed in a static magnetic field $\vec{H}$, Landau and Lifshitz [4] calculate the volume forces on the fluid [Eq. (34.3) in Ref. 4 converted to SI units],

$$\vec{f} = -\nabla p_0 + \frac{1}{2}\nabla\left[H^2\rho\left(\frac{\partial\mu}{\partial\rho}\right)_T\right] - \frac{H^2}{2}\nabla\mu + \mu\vec{j}\times\vec{H}\ , \quad (1)$$

where p_0 is the pressure in the absence of the field, ρ the density of the fluid, T the temperature, μ the magnetic permeability of the fluid, and $\vec{j}$ the electric current density in the fluid. For electrically nonconducting fluids, $\vec{j} = 0$, and therefore the last term vanishes. As $\mu = \mu_0(1+\chi)$, $\vec{M} = \chi\vec{H}$, and $\nabla \times \vec{H} = 0$ in nonconducting diamagnetic or paramagnetic fluids, we can rewrite Eq. (1) as

$$\vec{f} = -\nabla p_0' + \mu_0\vec{M}\cdot\nabla\vec{H}\ , \quad (2)$$

where μ_0 is the permeability of free space, χ the volumetric susceptibility of the fluid, p_0' the modified pressure including magnetic contribution, and $\vec{M}$ the magnetization (the magnetic moment per unit volume). The first term on the right side of Eq. (2) has no contribution to convection since $\nabla\times\nabla p_0' = 0$. Paramagnetic fluids contain atoms or molecules that have intrinsic magnetic moment, and their magnetic susceptibilities satisfy Curie's law [5], *i.e.*, $\chi = C\rho/T$, where C is a positive constant. Unlike paramagnetic fluids, diamagnetic fluids contain atoms or molecules that have no intrinsic magnetic moment. When a static magnetic field is applied to these fluids, the change of the field induces a magnetic moment for each atom or molecule. Diamagnetic susceptibilities satisfy $\chi = \chi_m\rho$, where χ_m is the susceptibility per unit mass, a negative constant. The last term in Eq. (2) is the Kelvin body force [6] $\vec{f}_m = \mu_0(\vec{M}\cdot\nabla)\vec{H}$, which arises from the interaction between the local magnetic field $\vec{H}$ within the fluid and the molecular magnetic moments characterized by the magnetization $\vec{M}$. An imposed thermal gradient produces a spatial variation in the magnetization through the temperature-dependent

magnetic susceptibility for paramagnetic fluids and through the temperature-dependent mass density for diamagnetic fluids, and therefore renders the Kelvin body force density $\vec{f}_m$ nonuniform spatially. This thermal gradient induced inhomogeneous magnetic body force density $\vec{f}_m$ can promote or inhibit convection in a manner similar to the gravitational body force.

II. Governing Equations

To study magnetically controlled convection in electrically nonconducting fluids, we consider an incompressible horizontal layer of such fluids heated on either top or bottom in the presence of an external nonuniform magnetic field. We choose our coordinate system by defining $|z| < d/2$ with $\hat{z}$ pointing up, where d is the layer thickness. We assume that the external field satisfies $\vec{H}^{ext} = \vec{H}_0 + (\vec{r}\cdot\nabla)\vec{H}^{ext}$, where $\vec{r} = x\hat{x} + y\hat{y} + z\hat{z}$ is the position vector. Here the vector $\vec{H}_0$ is the field at the center of the layer, and the field gradient $\nabla\vec{H}^{ext}$ is a constant tensor. Maxwell's equations require this tensor to be symmetric and traceless.

The fluid flow is governed by the Navier-Stokes equations in addition to Maxwell's equations for the magnetic field $\vec{H}$ and magnetic induction $\vec{B} \equiv \mu_0(\vec{M} + \vec{H})$. Under the Oberbeck-Boussinesq approximation, which allows density variations only in the large gravity term of the Navier-Stokes equations, we write the dimensionless governing equations for the convective flow [7],

$$\frac{1}{Pr}\left(\frac{\partial\vec{v}}{\partial t} + \vec{v}\cdot\nabla\vec{v}\right) = -\nabla p + (R\hat{z} - \vec{R}_m)\theta + K\sin^2\varphi\theta\hat{z} + K(z-\theta)\hat{H}_0\cdot\nabla\vec{h} + \nabla^2\vec{v}\ , \tag{3}$$

$$\frac{\partial\theta}{\partial t} + \vec{v}\cdot\nabla\theta - \hat{z}\cdot\vec{v} = \nabla^2\theta + \Phi\ , \tag{4}$$

$$\nabla\cdot\vec{h} - \hat{H}_0\cdot\nabla\theta = 0\ , \tag{5}$$

$$\nabla\cdot\vec{v} = 0\ . \tag{6}$$

Here, $\vec{v}$, p, θ, and $\vec{h}$ represent the respective departures of velocity, pressure, temperature, and magnetic field from the static thermal conduction state. In these equations, $\hat{H}_0 = \vec{H}_0/H_0$ is the unit vector in the $\vec{H}_0$ direction, ϕ the angle between $\vec{H}_0$ and the horizontal, and Φ the viscous dissipation. Equation (3) involves the Prandtl number $Pr = \nu/D_T$, the Rayleigh number $R = \alpha g d^3\Delta T/\nu D_T$, the Kelvin number

$$K = \frac{\mu_0\chi_0^2\Delta T^2 d^2 H_0^2}{\rho_0\nu D_T}\times\begin{cases}1/(1+\chi_0)T_0^2 & \text{paramagnetic;}\\ \alpha^2 & \text{diamagnetic,}\end{cases} \tag{7}$$

and the vector control parameter

$$\vec{R}_m = \frac{\mu_0\chi_0 d^3\Delta T}{\rho_0\nu D_T}\left(\vec{H}\cdot\nabla\vec{H}\right)^{ext}_{\vec{r}=0}\times\begin{cases}1/T_0 & \text{paramagnetic;}\\ \alpha & \text{diamagnetic,}\end{cases} \tag{8}$$

where α is the thermal expansion coefficient, ν the kinematic viscosity, D_T the thermal diffusivity, T_0 the average temperature of the layer, ΔT the temperature difference between the bottom and the top, χ_0 the susceptibility at T_0, and ρ_0 the density at T_0.

III. Results and Implications for Experiments

The Rayleigh number R in Eq. (3) measures the strength of gravitational buoyancy relative to dissipation. In the absence of magnetic fields, the thermal convective instability in a fluid layer heated from below is determined by this parameter R, and Rayleigh-Bénard convection sets in for $R > R_c \approx 1708$. In the presence of a uniform magnetic field ($K \neq 0$ but $\vec{R}_m = 0$), the magnetic effect on convection is determined by the Kelvin number K and the angle φ. For ordinary diamagnetic fluids such as water, our linear stability analysis shows that the difference for the marginal state due to the magnetic effect is less than 0.1% for a field up to 30 Tesla, and therefore the uniform field effect on convection in these fluids might be negligible. For paramagnetic fluids, our linear stability analysis [8] shows that longitudinal rolls with axes parallel to the horizontal component of the field are the rolls most unstable to convection. The corresponding critical Rayleigh number and critical wavelength for the onset of such rolls are less than the well-known Rayleigh-Bénard values in the absence of magnetic fields. Vertical fields maximize these deviations, which vanish for horizontal fields. Horizontal fields increase the critical Rayleigh number and the critical wavelength for all rolls except longitudinal rolls.

The vector parameter $\vec{R}_m$ in Eq. (3) measures the relative strength of the magnetic buoyancy force due to the applied field gradient. Since this parameter is the only one containing the external field gradient $\nabla\vec{H}^{ext}$ in the governing equations (3-6), the effect of the field gradient on convection in a nonconducting fluid layer is completely characterized by this vector parameter. The combination of the vertical component of $\vec{R}_m$ with R in Eq. (3) shows that the gravitational effect on the convective flow can be balanced by this component of $\vec{R}_m$. Therefore, convection in electrically nonconducting fluids can be controlled by an inhomogeneous magnetic field. The application of this theory to experiments [2,3] yields a good agreement [9]. Our analysis also shows that magnetically controlled convection in diamagnetic fluids should be observable even in pure water using current technology [10].

This work shows that thermal convection in electrically nonconducting fluids can be controlled by an external inhomogeneous magnetic field through the vector parameter $\vec{R}_m$. The inhomogeneous field exerts a magnetic body force on these fluids, and this force can balance the gravitational body force in terrestrial experiments. This magnetic field induced body force can be utilized to control the flow of nonconducting fluids in a microgravity environment with possible

applications in mixing, heat transfer, and materials processing.

Acknowledgments This research was supported by NASA under Grant No. NAG3-1921.

References

1. E. Beaugnon and R. Tournier, Levitation of organic materials, Nature **349**, 470 (1991).

2. D. Braithwaite, E. Beaugnon, and R. Tournier, Nature **354**, 134 (1991).

3. E. Beaugnon, *et. al.*, J. Phys. I France **3**, 399 (1993).

4. L. D. Landau and E. M. Lifshitz, Electrodynamics of continuous media (Pergamon Press, Oxford, 1960), Chap. 4.

5. N. W. Ashcroft and N. D. Mermin, Solid State Physics (Saunders College, Philadelphia, 1976), Chap. 31.

6. R. E. Rosensweig, Ferrohydrodynamics (Cambridge Univ. Press, NY, 1985), Chap. 4.

7. J. Huang, D. D. Gray, and B. F. Edwards, Thermoconvective instability of paramagnetic fluids in a nonuniform magnetic field, Phys. Rev. E, **57**, 5564 (1998).

8. J. Huang, B. F. Edwards, and D. D. Gray, Thermoconvective instability of paramagnetic fluids in a uniform magnetic field, Phys. Fluids **9**, 1819 (1997).

9. J. Huang, B. F. Edwards, and D. D. Gray, Magnetic control of convection in nonconducting paramagnetic fluids, Phys. Rev. E Rapid Communications **57**, 29 (1998).

10. J. Huang, D. D. Gray, and B. F. Edwards, Magnetic control of convection in nonconducting diamagnetic fluids, submitted to Phys. Rev. E.

ELECTRIC FIELD INDUCED INTERFACIAL INSTABILITIES

Robert E. Kusner[1], Kyung Yang Min[2], [1,2]NASA Lewis Research Center, [1]rkusner@lerc.nasa.gov, [2]kym0270@lerc.nasa.gov, Xiao-lun Wu[3], [3]University of Pittsburgh, wu@vms.cis.pitt.edu, Akira Onuki[4], [4]Kyoto University, Kyoto, Japan

1 INTRODUCTION

Several systems exhibit an interfacial instability in response to a stress resulting from the application of an external field. Two such systems closely related to the proposed system of study are a ferrofluid/air interface in the presence of a magnetic field [1, 2], and the interface between two fluids when charged with ions [3, 4, 5, 6]. Both systems lead to the formation of a hexagonal dimple pattern. One of our collaborators, Prof. A. Onuki, has recently proposed that such an effect could be observed at the neutral two-phase interface of a critical system, such as a binary fluid near its consolute point, or a simple fluid near the critical point of its liquid/vapor transition, in the presence of an externally applied electric field [7].

An undulation instability of interfaces between two immiscible dielectric fluids was studied using an oscillating electric field. The binary system studied was a mixture of aniline and cyclohexane (AC). The aniline component is slightly polar, making the aniline rich phase significantly more conductiong than the cyclohexane rich phase. The critical electric field E_c, at the onset of instability, was measured as the frequency was varied at several different temperatures.

At lower frequencies, column-like structures were formed. When the critical field was plotted as a function of reduced temperature ϵ, it exhibited a power-law relationship, $E_c \sim \epsilon^{\zeta}$, where $\zeta \sim 0.34$. This compares well with the value $\zeta \sim 0.4$ for a system of conducting and non-conducting fluids.

At higher frequencies, the charge carriers in the conducting fluid can do not respond quick enough; the electric fields in the system are determined by its dielectric properies. In such a case, the interface becomes unstable due to the difference in the dielectric constants of the two phases. Measurement at a high frequency limit displayed two major differences from that of a lower frequency limit. First, localized elevation of interfacial surface was observed as opposed to column-like protusions, and secondly, $E_c \sim \epsilon^{\zeta}$, where $\zeta \sim 0.08$. The measured value of ζ is in good agreement with the theoretically predicted value $\zeta = 0.07$.

2 EFFECT OF ELECTRIC FIELD ON THE INTERFACE

The change in the free energy due to a capillary surface wave with wave number k is proportional to

$$G_k = \sigma k^2 - C_E k + g(\Delta\rho) \quad (1)$$

$$= \sigma(k - \frac{C_E}{2\sigma})^2 - \frac{C_E^2 - 4\sigma(\Delta\rho)g}{4\sigma}, \quad (2)$$

where σ is the surface tension, g is the gravitational acceleration, and $\Delta\rho$ is the mass density difference between the two phases, taken to be positive. The parameter C_E represents the effect of electric field on the binary system. For a cell filled with a critical binary mixture where the interface is formed at the middle of two electrodes near the critical temperature, C_E is represented by

$$C_E = \frac{1}{\pi}\frac{\varepsilon_1\varepsilon_2(\varepsilon_2 - \varepsilon_1)^2}{(\varepsilon_1 + \varepsilon_2)^3}(\frac{V}{d})^2. \quad (3)$$

Here d is the separation of electrodes, V is the applied voltage, and ε_1 and ε_2 are dielectric constants of two phases, respectively. The first and third term in Eq. (1) are the standard expressions used to describe a capillary wave on a liquid surface. The second term is the effect of the electric field and the source of the instability. Equation (2) shows that G_k takes a minimum at wave number $k^* = C_E/2\sigma$ and that the surface fluctuation at $k = k^*$ becomes unstable for $C_E^2 > 4\sigma(\Delta\rho)g$. This condition, together with eq. (3), determines the critical (or threshold) electric field E_c:

$$E_c = \frac{1}{\varepsilon_2 - \varepsilon_1}\sqrt{\frac{2\pi(\varepsilon_1 + \varepsilon_2)^3}{\varepsilon_1\varepsilon_2}}\sqrt[4]{\sigma(\Delta\rho)g}. \quad (4)$$

Upper and lower boundaries of Eq. (4) based on $\varepsilon_2/\varepsilon_1 \to \infty$ or $\varepsilon_2/\varepsilon_1 \sim 1$ represent the conducting and non-conducting limits, respectively. In this calculation, two well-known relationships were used: $\sigma \cong \sigma_0\epsilon^{2\nu}$[8, 9] and $\varepsilon_2 - \varepsilon_1 \cong \varepsilon_0\epsilon^{\beta}$ with $\nu = 0.625$ and $\beta = 1/3$[10].

1. Conducting limit ($\varepsilon_2/\varepsilon_1 \to \infty$):

$$E_c \sim \sqrt{\frac{2\pi}{\varepsilon_1}}\sqrt[4]{\sigma(\Delta\rho)g} \sim (\epsilon^{2\nu}\epsilon^{1/3})^{1/4} \sim \epsilon^{0.4}. \quad (5)$$

G. I. Taylor used alternate derivation of the first form in Eq. (4) and it was verified experimentally in a few systems (water-air, water-oil, mercury-air, and mercury-oil)[11].

2. Non-conducting limit ($\varepsilon_2/\varepsilon_1 \sim 1$):

$$E_c \sim \epsilon^{-1/3}(\epsilon^{2\nu}\epsilon^{1/3})^{1/4} \sim \epsilon^{0.07}. \qquad (6)$$

Later when figure 3 is discussed, more precise definition of the non-conducting limit will be presented.

In the case of an alternating electric field $E = E_0\cos(\omega t)$, the frequency ω influences current flow in a material with an ohmic conductivity κ in addition to its dielectric properties (dielectric const ε). In such a leaky dielectric, the polarization current is $\vec{j} = \partial(\varepsilon\vec{E})/\partial t \sim \omega\varepsilon\vec{E}$ and the current density due to the migration of free charge is $\vec{j} = \kappa\vec{E}$. The ratio of these two currents, $\omega\varepsilon/\kappa$, decides whether the system behaves as a conducting or non-conducting system[12]. At low frequency limit ($\omega \ll \kappa/\varepsilon$), the interface charge is that for a static interface and the system behaves as a conductor. At high frequency limit ($\omega \gg \kappa/\epsilon$), conducting processes should be inhibited and the free charges remain neutralized, leaving only a residual polarization charge at the interface. Therefore, the temperature dependence of the threshold electric field in the aniline and cyclohexane (AC) system will be manifested as follows:

1. When $\omega \ll \kappa/\varepsilon$, $E_c \sim \epsilon^{0.4}$.
2. When $\omega \gg \kappa/\varepsilon$, $E_c \sim \epsilon^{0.07}$.

3 EXPERIMENTAL

The sample cell was constructed of two indium/tin oxide (ITO) coated electrodes cemented to a glass spacer of rectangular shape. The separation between electrodes was 4mm. The cell was immersed in an oil bath (Dow Corning 200 fluid, viscosity=1.5 cSt), whose temperature was controlled by a surrounding water bath. The temperature of the oil bath was kept constant with a precision of ± 0.5 mK/day. For the AC binary system, the critical concentration of aniline was 0.444 mole fraction and the critical temperature was $T_c = 32.70°$C. Dielectric constants of pure cyclohexane and aniline are 2.03 and 6.86, respectively[13].

The AC system was found to be light-sensitive with its critical temperature drifting with time. Such a drift of temperature was offset by re-measuring T_c for each set of measurements. All the temperature scales described below were calibrated in this way. Due to the degradation of the sample, only four sets of measurements will be presented.

Figure 1: Instability observed at $\Delta T = 120$mK and $f = 200$Hz. The upper phase is cyclohexane-rich and the bottom aniline-rich. As the frequency increases, the pattern of strings changed from finer to coarser one.

An ac-amplifier (Trek, Inc. Model 609D-6) with a 4 kV peak ac output and a small signal bandwidth of 35 kHz was used to generate an oscillating field perpendicular to the interface. In order to observe interfacial instability, the temperature T was lowered below T_c to the desired value and frequency was set to $f = \omega/2\pi = 10$Hz. The amplitude of the field was raised gradually until instability was seen. Near the onset, even a small change of the voltage amplitude generated the instability, thus enabling the critical field E_c to be measured with an accuracy of 2%. The rms value of the critical voltage was recorded by a multimeter (Keithley, Model 2001). Next frequency was increased stepwise and the whole process was repeated for a few different temperatures.

At a lower frequency ($f \sim 10$ to $f \sim 1000$Hz), many string-like structures were formed in the cyclohexane-rich phase. This observation is very similar to what was seen in G. I. Taylor's experiment[11, 14]. There the interfacial agitation and occasional isolated points rose from the conducting to non-conducting fluid as the critical voltage for instability was approached. The string spanned the space between the interface and one of the electrodes, and had a life time of several seconds. When the field was abruptly turned off, each string split into a few pieces, all of which eventually fell to the interface in a couple of seconds.

Figure 1 shows such a structure formed at $\Delta T = 120$mK and $f = 200$Hz. Due to a bubble near the filling tube which is at the left top of figure, the field was not uniform across the cell, resulting in a localized

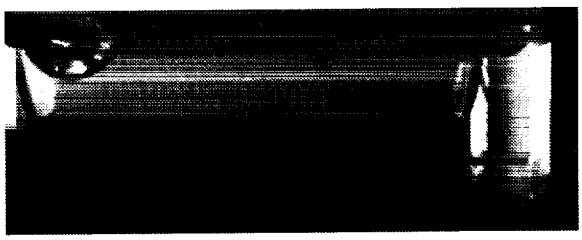

Figure 2: Instability observed at $\Delta T = 120$mK and $f = 3500$Hz. The localized convective motion of the upper fluid seen in Fig. 1 is absent for this relatively high frequency.

convective motion of the upper fluid in the left side of the cell. Nonetheless the pattern formed on the right half of the cell was almost stationary.

At a higher frequency ($f \sim 1000$ to $f \sim 13,000$Hz), many locally elevated areas (of cone shape) were formed as shown in Fig. 2. At such a high frequency, when the applied field exceeded the critical value by a small amount, a rigorous mixing of the two phases across the interface was observed.

When E_c was plotted as a function of frequency for a fixed temperature, the plot was of the sigmoidal shape with two flat regions in a low and high frequency limit, respectively. Figure 3 shows measurements for two different temperatures, $T = 31.12$°C and $T = 32.56$°C. Two additional measurements obtained at $T = 31.89$°C and $T = 32.44$°C are not shown in this figure. However, they exhibit the same shape and fall in between the two curves represented.

It is interesting to note that the sigmoidal shape observed here can be obtained by replacing ε_j with $|\varepsilon_j + 4\pi\kappa_j \cdot i/\omega|$ (j =1, 2 and $i = \sqrt{-1}$) in Eq.(4)[15]. In this theoretical approach, the non-conducting limit, $\kappa_j \to 0$ for $j = 1, 2$, is obtained by taking a limit: $4\pi\kappa_j/\omega \ll \epsilon_j$ for $j = 1, 2$ or simply $\omega \to \infty$. Obviously, such a non-conducting limit should correspond to the plateau of each curve in Fig. 3. In order to fit the curves in this figure, the magnitude and phase lag of the current should be measured as a function of frequency for this leaky dielectric[12]. However, this was not possible because of the fast degradation of the sample.

Figure 4 is a log-log plot of critical electric field E_c vs. reduced temperature ϵ for five different frequencies. It was obtained from Fig. 3 by reading E_c as a function of T for a fixed frequency (the measurements at $f = 0$ is not shown in Fig. 3). Note that the slope in this figure yields the critical exponent ζ in the relation $E_c = \epsilon^{\zeta}$.

The dependence of the critical exponent ζ on fre-

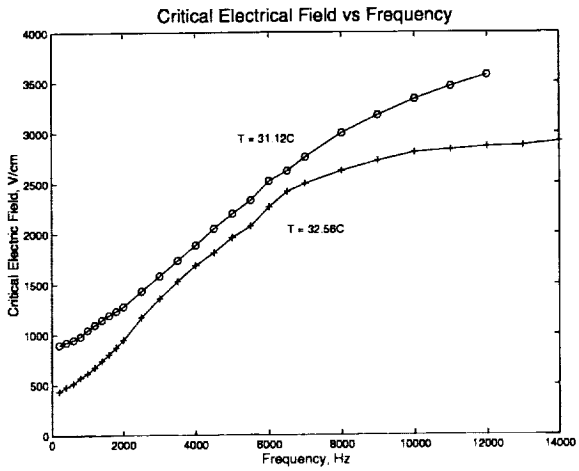

Figure 3: Plot of critical electric field vs frequency. The curve marked with '+' sign levels off for high frequencies ($f \geq 10000$Hz). In the measurement corresponding to the curve marked with '0' sign in the same figure, the critical electric fields above f =12000Hz could not be obtained, due to the instrumental limitation of the amplifier used.

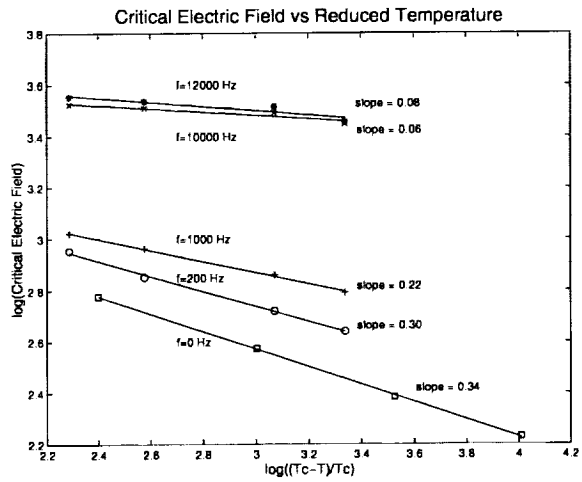

Figure 4: Log-log plot of critical electric field as a function of reduced temperature for fixed frequencies. Solid lines are linear regression fit to data.

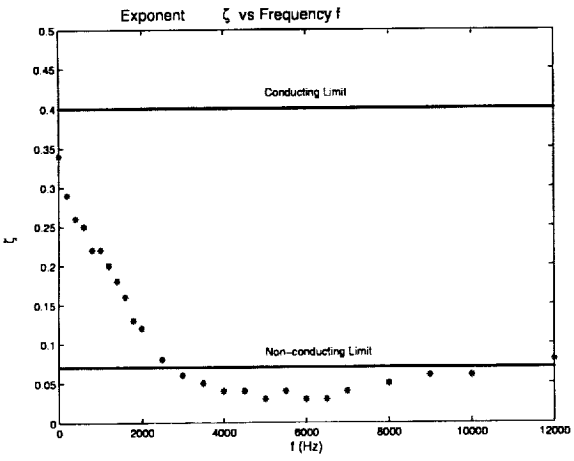

Figure 5: Critical exponent ζ vs frequency f. Two horizontal lines are the conducting and non-conducting limits, respectively. For $f \geq 2500$Hz, the critical exponent is close to the value of the non-conducting limit.

quency f is plotted in Fig. 5. The range of the frequency representing the plateau of the curves in Fig. 3 do not coincide with the range, $f \geq 2500$Hz, where the critical exponent ζ levels off in Fig. 5. This implies that the approach to the value $\zeta = 0.07$ is not a sufficient condition for the system to behave as a non-conducting medium.

4 CONCLUSION

Measurements with a time-varying electric field seems to produce substantially more instructive information about the instability than static-field measurements. With a judicious choice of a sample such as a marginally polar AC system, and by varying the frequency of the applied field, both the conducting and non-conducting limits of an interfacial instabilities could be probed in a systematic fashion. Two control parameters, temperature and frequency, allow us to effectively change the surface tension, the dielectric constant and the ohmic conductivity of each phase. Currently we are investigating similar effects with an alternate binary system, methylene iodide/cyclohexane. The dielectric constant for the methylene iodide is similar to that of aniline but without the toxicity. However certain precautions are being taken, since methylene iodide is also light-sensitive. We are building a new cell, where a copper layer on the electrode will stabilize the light-sensitive nature of methylene iodide.

5 ACKNOWLEDGEMENTS

Support to study the effect of electric field instabilities in a two phase fluid interface has been provided to General Vacuum, Inc. by the National Aeronautics and Space Administration under contract # NAS3-2789.

References

[1] M. D. Cowley and R. E. Rosensweig, J. Fluid Mech. **30**, 671 (1967).

[2] A. Gailitis, J. Fluid Mech. **82**, 401 (1977).

[3] L. P. Gorkov and D. M. Chernikova, Pis'ma Zh. Eksp. Teor. Fiz. **18**, 119 (1973) [JETP Lett. **18**, 68 (1973)].

[4] K. Mima, H. Ikezi and A. Hasegawa, Phys. Rev. **B14**, 3953 (1976).

[5] A .P. Volodin, M. S. Khaikin and V. S.Edel'man, Pis'ma Zh. Eksp. Teor. Fiz. **26**, 707 (1977) [JEPT lett. **26**, 543,(1977)].

[6] M. Wanner and P. Leiderer, Phys. Rev. Lett. **42**, 315 (1979).

[7] A. Onuki, Physica A **217**, 38 (1995).

[8] M. Moldover, Phys. Rev. A **31**, 1022 (1985).

[9] E. S. Wu and W. W. Webb, Phys. Rev. A **8**, 2077 (1973).

[10] D. T. Jacobs, J. Phys. Chem. **86**, 1995-1998 (1982).

[11] G. I. Taylor and A. D. McEwan, J. Fluid Mech. **22**, 1 (1965).

[12] W. B. Russel, D. A. Saville, and W. R. Schowalter, Colloidal Dispersions, Cambridge University Press (1989).

[13] D. Beaglehole, J. Chem. Phys. **74**, 5251 (1981).

[14] J. R. Melcher, Phys. Fluids **4**, 1348 (1961).

[15] L. D. Landau and E. M. Lifshitz, Electrodynamics of Continuous Media, vol. 8, Pergamon Press (1984).

Session 1C

G-Jitter and Stochastic Flow

FLUID PHYSICS IN A FLUCTUATING ACCELERATION ENVIRONMENT

François Drolet, Supercomputer Computations Research Institute, Florida State University, Tallahassee, Florida 32306-4130, drolet@scri.fsu.edu, Jorge Viñals, Supercomputer Computations Research Institute, Florida State University, Tallahassee, Florida 32306-4130, and Department of Chemical Engineering, FAMU-FSU College of Engineering, Tallahassee, Florida 32310-6046, vinals@scri.fsu.edu

1 Introduction

Our program of research aims at developing a stochastic description of the residual acceleration field onboard spacecraft (g-jitter) [1, 2] to describe in quantitative detail its effect on fluid motion [3, 4, 5]. Our main premise is that such a statistical description is necessary in those cases in which the characteristic time scales of the process under investigation are long compared with the correlation time of g-jitter. Although a clear separation between time scales makes this approach feasible, there remain several difficulties of practical nature: (i), g-jitter time series are not statistically stationary but rather show definite dependences on factors such as active or rest crew periods; (ii), it is very difficult to extract reliably the low frequency range of the power spectrum of the acceleration field. This range controls the magnitude of diffusive processes; and (iii), models used to date are Gaussian, but there is evidence that large amplitude disturbances occur much more frequently than a Gaussian distribution would predict. The lack of stationarity does not constitute a severe limitation in practice, since the intensity of the stochastic components changes very slowly during space missions (perhaps over times of the order of hours). A separate analysis of large amplitude disturbances has not been undertaken yet, but it does not seem difficult a priori to devise models that may describe this range better than a Gaussian distribution. The effect of low frequency components, on the other hand, is more difficult to ascertain, partly due to the difficulty associated with measuring them, and partly because they may be indistinguishable from slowly changing averages. This latter effect is further complicated by the lack of statistical stationarity of the time series.

Recent work has focused on the effect of stochastic modulation on the onset of oscillatory instabilities [6] as an example of resonant interaction between the driving acceleration and normal modes of the system, and on cavity flow [7] as an example of how an oscillatory response under periodic driving becomes diffusive if the forcing is random instead. This paper describes three different topics that illustrate behavior that is peculiar to a stochastic acceleration field. In the first case, we show that g-jitter can induce effective attractive or repulsive forces between a pair of spherical particles that are suspended in an incompressible fluid of different density provided that the momentum diffusion length is larger than the inter particle separation (as in the case in most colloidal suspensions). Second, a stochastic modulation of the control parameter in the vicinity of a pitchfork or supercritical bifurcation is known not to affect the location of the threshold. We show, however, that resonance between the modulation and linearly stable modes close to onset can lead to a shift in threshold. Finally, we discuss the classical problem of vorticity diffusion away from a plane boundary that is being vibrated along its own plane. Periodic motion with zero average vorticity production results in an exponential decay of the vorticity away from the boundary. Random vibration, on the other hand, results in power law decay away from the boundary even if vorticity production averages to zero.

2 Acceleration induced interactions between pairs of particles

Consider an ensemble of spherical particles of radii R_i and density ρ_p suspended in an incompressible fluid of density ρ_f and shear viscosity μ. If the fluid is enclosed by perfectly rigid boundaries, the buoyancy force acting on each suspended particle is $\vec{F} = \frac{4}{3}\pi\,(\rho_p - \rho_f)\,R^3\vec{g}(t)$, where $\vec{g}(t)$ is the effective acceleration field. In the frame of reference co-moving with the container enclosing the fluid, $\vec{g}(t)$ is a body force, with intensity equal to the value of the acceleration of the container. For containers of reasonable size in a microgravity environment, $\vec{g}$ can be assumed to be spatially uniform. The hydrodynamic interaction between two such particles is given in the overdamped limit of Stokes flow by [8, 9],

$$\frac{d\vec{r}}{dt} = (\omega_{21} - \omega_{11}) \cdot \vec{F}_1 + (\omega_{22} - \omega_{21}) \cdot \vec{F}_2, \qquad (1)$$

where $\vec{r}$ is the relative position of particle 2 with respect to particle 1, $\vec{F}_i$ is the force acting on the i-th particle,

and ω_{ij} are hydrodynamic mobility tensors, given, e.g., in references [8, 9]. After some straightforward algebra, the leading contribution at distances large compared to the particle radii is given by,

$$\frac{d\vec{r}}{dt} = \frac{2(\rho_p - \rho_f)}{9\mu}\left(R_2^2 - R_1^2\right)\vec{g}(t) +$$

$$\frac{(\rho_p - \rho_f)\left(R_1^3 - R_2^3\right)}{3\mu}\frac{1}{r}\left[\frac{\vec{r}\vec{r}}{r^2} + \frac{1}{2}\left(\mathcal{I} - \frac{\vec{r}\vec{r}}{r^2}\right)\right]\cdot\vec{g}(t), \quad (2)$$

where $\mathcal{I}$ is the identity tensor. The first term in the right hand side describes the relative motion of two *independent* particles of different size. Both the longitudinal and transverse components of the second term in the right hand side of Eq. (2) are of the form,

$$\frac{dr}{dt} = \frac{A}{r}g(t), \quad (3)$$

where, for the longitudinal component, $A = (\rho_p - \rho_f)(R_1^3 - R_2^3)/3\mu$.

Consider an initial interparticle separation $r_0 \gg R_i$. In this case, and for times shorter than the average time needed for the two particles to coalesce, the quantity $y = r^2/2A$ is a Wiener process if $g(t)$ is Gaussian and white ($\langle g \rangle = 0$, $\langle g(t)g(t') \rangle = 2D\delta(t-t')$), and therefore the conditional probability for r is,

$$P(r,t|r_0,t_0) = \frac{r}{|A|\sqrt{4\pi D(t-t_0)}}e^{-\frac{\left(r^2 - r_0^2\right)^2}{16DA^2(t-t_0)}}. \quad (4)$$

The ensemble average of r, $\langle r \rangle$ can be computed analytically,

$$\langle r \rangle = \sqrt{\frac{|A|}{4}}\left[2D(t-t_0)\right]e^{-\frac{r_0^4}{32A^2D(t-t_0)}}$$

$$D_{-3/2}\left(-\frac{r_0^2}{2|A|\sqrt{2D(t-t_0)}}\right), \quad (5)$$

where $D_p(z)$ is a parabolic cylinder function [10] (formula 9.240). For short times, the asymptotic form of $D_p(z)$ for large z allows the computation of $\langle r \rangle$

$$\langle r \rangle = r_0\left(1 - \frac{A^2D(t-t_0)}{r_0^4}\right), \quad (6)$$

which decreases in time regardless of the sign of A. Therefore g-jitter induces an effective hydrodynamic *attraction* between pairs of particles. The attractive interaction is not confined to short times, but it arises directly from the $1/r$ dependence in Eq. (3). By taking the average of Eq. (3), using the Furutsu-Novikov theorem [11] and the fact that the noise is Gaussian and white, one finds,

$$\frac{d\langle r \rangle}{dt} = AD\left\langle\frac{\delta 1/r(t)}{\delta g(t)}\right\rangle, \quad (7)$$

where $\delta/\delta g(t)$ stands for functional derivative with respect to g. Directly from Eq. (3), we find that $\delta(1/r(t))/\delta g(t) = -A/r^3$, and therefore,

$$\frac{d\langle r \rangle}{dt} = -A^2D\left\langle\frac{1}{r^3}\right\rangle, \quad (8)$$

identical to Eq. (6) with $1/r_0^3$ replaced by $\langle 1/r^3 \rangle$. Since r is a positive quantity, $d\langle r \rangle/dt < 0$ for all values of r. It is also interesting to note that the effective attractive interaction is not confined to the term proportional to $1/r$ in the hydrodynamic mobility, but that attractive contributions arise from higher powers of $1/r$ as well. In fact, this attraction is generic for over damped motion and multiplicative noise provided that the mobility is a decaying function of the interparticle separation [12].

The question naturally arises as to the behavior of pairs of particles near contact, or of particles near a solid wall. In either case, lubrication theory allows the calculation of the mobility tensor. The longitudinal component vanishes linearly with interparticle distance whereas the transverse component becomes non-analytic (diverges logarithmically at short distances) [9]. In both cases, the mobility *increases* with interparticle separation leading to an average repulsion ($d\langle r \rangle/dt > 0$) following the same arguments given above.

3 Stochastic resonance and bifurcations

Consider the normal form appropriate for a pitchfork bifurcation in which A is the linearly unstable mode and B is some linearly stable mode. Then,

$$\frac{d}{dt}\begin{bmatrix} A \\ B \end{bmatrix} = \begin{bmatrix} \epsilon & 0 \\ 0 & -\beta \end{bmatrix}\begin{bmatrix} A \\ B \end{bmatrix} + \begin{bmatrix} -cA^3 \\ 0 \end{bmatrix} +$$

$$\begin{bmatrix} m_{11} & m_{12} \\ m_{21} & m_{22} \end{bmatrix}\begin{bmatrix} A \\ B \end{bmatrix} g(t), \quad (9)$$

with $\epsilon \ll 1$ and the remaining coefficients of order one. We further assume that $D \sim \mathcal{O}(\epsilon)$. Close to threshold, A changes in a slow scale $T = \epsilon t$, compared with either the relaxation of B (of order one) or the noise.

If the coupling to the unstable mode B is neglected, it is known that the threshold in the stochastic case remains at $\epsilon = 0$ [13, 14]. This can be seen by averaging Eq. (9) over the fast time scale so that $\langle A(T)g(t) \rangle \approx$

$A(T)\langle g(t)\rangle = 0$. The resulting equation for $A(T)$ no longer depends on the noise. If, on the other hand, both equations are averaged over the fast time scale, we find that,

$$\langle Bg\rangle = \langle B\rangle\langle g\rangle + D\left\langle \frac{\delta B}{\delta g}\right\rangle = Dm_{21}A + \ldots \qquad (10)$$

where we have used the Furutsu-Novikov theorem [15, 16]. Therefore, the correlation of $B(t)g(t)$ itself evolves over the slow time scale T as a consequence of the fact that the equations for both A and B contain exactly the same stochastic process. The coefficient of the linear term in the equation for $A(T)$ is now $\epsilon + Dm_{21}m_{12}$ and hence the bifurcation point will occur at $\epsilon = -Dm_{12}m_{21} < 0$.

4 Flow due to a randomly vibrating plane boundary

Consider a semi-infinite fluid layer occupying the region $x > 0$ and a solid boundary at $x = 0$ which is being displaced along the y direction with a prescribed, time-dependent velocity $v_0(t)$. For an incompressible, Newtonian fluid, the y component of the velocity field in the fluid v satisfies,

$$\frac{\partial v}{\partial t} = \nu\frac{\partial^2 v}{\partial x^2}, \qquad (11)$$

with boundary conditions $v(x=0,t) = v_0(t)$ and $v(x\to\infty,t) = 0$. We consider a function $v_0(t)$ which is a stochastic process in time, and hence proceed to solve the initial value problem (11) with a stochastic boundary condition. Let $v_0(t)$ be a Gaussian, white stochastic process with mean $\langle v_0(t)\rangle = 0$ and variance $\langle v_0(t)v_0(t')\rangle = 2D\delta(t-t')$. We find that,

$$\left\langle v^2(x,t)\right\rangle = \frac{2D\nu}{\pi x^2}\left(1+\frac{x^2}{2\nu t}\right)e^{-x^2/2\nu t}. \qquad (12)$$

The velocity disturbance propagates into the fluid diffusively, with a diffusion coefficient ν. At long times, however, even though the vorticity produced at the wall averages to zero, the velocity does not decay exponentially away from the wall, but rather as a power law,

$$\left\langle v^2(x,t\to\infty)\right\rangle = \frac{2D\nu}{\pi x^2}. \qquad (13)$$

We now turn to the case in which the velocity of the boundary is not white, but a narrow band noise instead. As discussed elsewhere [2], narrow band noise provides an approximate description of the spectral components of the residual acceleration field in microgravity, as well as a convenient way to interpolate between the white noise and monochromatic noise limits. Narrow band noise is a Gaussian process that satisfies, [17]

$$\langle v_0(t)\rangle = 0, \quad \left\langle v_0(t)v_0(t')\right\rangle = v_0^2 e^{-|t-t'|/\tau}\cos\Omega(t-t'), \qquad (14)$$

where $\langle\ \rangle$ denotes an ensemble average. Ω is a characteristic angular frequency that corresponds to the peak in the spectral density of the process, and τ is a correlation or coherence time determining the width of that peak. In essence, this process describes a periodic signal of characteristic frequency Ω, but that only remains coherent for a time τ on average. The amplitudes are distributed gaussianly with variance v_0^2. The white noise limit is obtained when $\Omega\tau \to 0$ while $v_0^2\tau = D$ remains finite, whereas the monochromatic noise limit corresponds to $\Omega\tau\to\infty$ with v_0^2 finite. We do not attempt to find a general solution of Eq. (11) for an initially quiescent fluid and narrow band forcing. We focus instead on long time or statistically stationary averages. We find,

$$\left\langle v^2(x)\right\rangle = \int_{-\infty}^{\infty} d\omega P(\omega)e^{-x\sqrt{\frac{2|\omega|}{\nu}}}. \qquad (15)$$

where $P(\omega)$ is the power spectrum that corresponds to the autocorrelation function (14). The integral can be carried out explicitly in the limits of small and large τ. In the vicinity of the white noise limit, we find,

$$\left\langle v^2(x)\right\rangle = \frac{2\nu v_0^2\tau}{\pi x^2} - \frac{1}{2}\frac{v_0^2(120+4\Omega^2x^4/\nu^2)\nu^3}{\pi x^6}\tau^2 + \mathcal{O}(\tau^3). \qquad (16)$$

The first term in the right hand side is the white noise limit already given in Eq. (13). The first correction term is also a power law decaying as x^{-6} away from the wall. The low frequency part of the power spectrum dominates the decay of the velocity field at long distances and leads to a very slow rate of decay. In the opposite limit of $\tau rightarrow\infty$, we find,

$$\left\langle v^2(x)\right\rangle = \left\langle v_0^2\right\rangle e^{-x\sqrt{\frac{2\Omega}{\nu}}} + \frac{v_0^2\nu}{\pi x^2}\left\{\left[\frac{x^2}{\nu}\left(1-\frac{\pi}{2}\right)+\tau x\sqrt{\frac{2(\Omega+1/\tau)}{\nu}}\right]e^{-x\sqrt{\frac{2(\Omega+1/\tau)}{\nu}}} + \left[\frac{x^2}{\nu}\left(1+\frac{\pi}{2}\right)-\tau x\sqrt{\frac{2(\Omega-1/\tau)}{\nu}}\right]e^{-x\sqrt{\frac{2(\Omega-1/\tau)}{\nu}}}\right\} \qquad (17)$$

In the limit $\tau\to\infty$ the term within braces vanishes and one recovers the classical result that the characteristic velocity $\sqrt{\langle v^2\rangle}$ decays exponentially into the fluid with

a characteristic decay length given by $\sqrt{2\nu/\Omega}$. If, on the other hand, the spectrum of the forcing function has a finite width, the velocity field still decays exponentially, but the decay length increases to $\sqrt{2\nu/(\Omega - 1/\tau)}$.

Acknowledgments

This work has been supported by the Microgravity Science and Applications Division of the NASA under contract No. NAG3-1885. This work is also supported in part by the Supercomputer Computations Research Institute, which is partially funded by the U.S. Department of Energy, contract No. DE-FC05-85ER25000.

References

[1] W. Zhang, J. Casademunt, and J. Viñals, Phys. Fluids A **5**, 3147 (1993).

[2] J. Thomson, J. Casademunt, F. Drolet, and J. Viñals, Phys. Fluids **9**, 1336 (1997).

[3] *Fluid Sciences and Materials Sciences in Space*, edited by H. Walter (Springer Verlag, New York, 1987).

[4] E. Nelson, Technical Report No. TM 103775, NASA (unpublished).

[5] G. Martin, C. Baugher, and F. Henderson, Technical report, Acceleration Characterization and Analysis Project (ACAP), NASA (unpublished).

[6] F. Drolet and J. Viñals, Phys. Rev. E **56**, 2649 (1997).

[7] J. Thomson and J. Viñals, AIAA J. **34**, 975 (1996).

[8] G. Batchelor, J. Fluid Mech. **75**, 1 (1976).

[9] W. Russel, D. Saville, and W. Schowalter, *Colloidal Dispersions* (Cambridge University Press, New York, 1989).

[10] I. Gradshteyn and I. Ryzhik, *Tables of integrals, series and products* (Academic Press, New York, 1980).

[11] P. Hanggi, in *Stochastic processes applied to Physics*, edited by L. Pesquera and M. Rodriguez (World Scientific, Singapore, 1985), p. 69.

[12] It is important to emphasize the relevance of overdamped motion to the results presented. If the correlation time of the fluctuating force is smaller than the viscous decay time (as is the case in thermal Brownian motion), the fluctuating force enters additively in the equations of motion for the particles and the effects discussed do not arise.

[13] A. Schenzle and H. Brand, Phys. Rev. A **20**, 1628 (1979).

[14] R. Graham and A. Schenzle, Phys. Rev. A **25**, 1731 (1982).

[15] K. Furutsu, J. Res. Nat. Bur. Standards **67D**, 303 (1963).

[16] E. Novikov, Zh. Eksp. Teor. Fiz. **44**, 1919 (1964), [Sov. Phys. JETP **20**, 1290 (1965)].

[17] R. Stratonovich, *Topics in the Theory of Random Noise* (Gordon and Breach, New York, 1967), Vol. II.

THERMOCAPILLARY FLOWS WITH LOW FREQUENCY g-JITTER

P. Grassia, G.M. Homsy, *Department of Chemical Engineering, Stanford CA 94305-5025, USA.*
bud@chemeng.stanford.edu

ABSTRACT

A thermocapillary parallel flow is established in a fluid filled slot with an applied temperature gradient. Low frequency jitter is imposed in arbitrary directions. Vertical jitter proves to be relatively uninteresting, merely augmenting or opposing the basic thermocapillary flow. Streamwise jitter still produces parallel flows, but these now exhibit boundary layers or layered cellular structures for large Rayleigh number as the applied stratification alternates between stable and unstable. Runaways are possible for unstable stratification and these correspond to resonant excitation of stationary long wave Rayleigh-Bénard modes. Spanwise jitter produces fully three dimensional motion. A spanwise-streamwise circulation results for weak spanwise jitter, which advects the interfacial temperature establishing a subsidiary spanwise thermocapillary flow. This flow is strong at small Biot number when advected temperature is trapped in the slot, and has a counter-intuitive dependence on the spanwise-streamwise aspect ratio.

1 INTRODUCTION

Materials processing situations frequently involve interfaces with lengthwise temperature gradients, and are therefore susceptible to thermocapillary motions. If materials processing is conducted in space, the thermocapillary flows will also be subject to fluctuating accelerations (g-jitter) characteristic of the space based microgravity environment [1, 2, 3, 4]. While there has been a large number of studies of buoyant systems subject to gravitational modulation [5, 6, 7, 8, 9, 10], there is no equivalent body of results for thermocapillary systems under these circumstances.

The present paper considers the effect of jitter on a basic thermocapillary flow in a particularly simple geometry: a fluid layer of finite depth but infinite horizontal extent. This is the thermocapillary slot flow of Davis and coworkers [11, 12], which is sketched in Figure 1. The underlying simplicity of the slot model is such that, even when jitter is added, the problem remains amenable to analytical techniques. This permits a thorough parametric study of the system, allowing the possibility of considering several different directions of jitter, including spanwise jitter which has been little studied to date even for buoyancy driven flows. The structure of the paper is as follows. In the next section we introduce the governing equations of the slot. In §3 we present results for jitter confined to the plane, and in §4 we consider spanwise jitter. Conclusions are given in §5. Full details may be found elsewhere [13, 14].

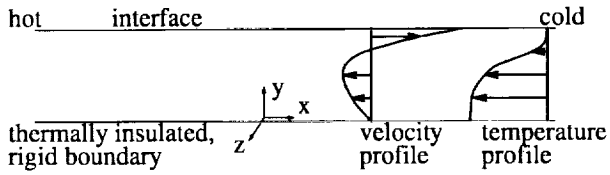

Figure 1: Thermocapillary slot return flow produced by a lengthwise applied temperature gradient. A vertically varying advected temperature profile, which balances streamwise heat convection and vertical heat conduction, is also present.

2 GOVERNING EQUATIONS

The governing continuity, momentum and thermal equations of the slot subject to g-jitter are

$$\nabla.\mathbf{u} = 0, \quad (1)$$

$$MaPr^{-1}(\mathbf{u}_{,t} + \mathbf{u}.\nabla\mathbf{u}) = -\nabla p + \nabla^2\mathbf{u} + \mathbf{G}T, \quad (2)$$

$$Ma(T_{,t} + \mathbf{u}.\nabla T) = \nabla^2 T, \quad (3)$$

where Ma is the Marangoni number, Pr is the Prandtl number and $\mathbf{G}$ represents the dimensionless jitter, consisting of a dynamic Bond number G, multiplied by an $O(1)$ vector describing the direction and time modulation of gravity. Note that the momentum equation can be recast as a vorticity equation

$$Re(\boldsymbol{\omega}_{,t} + \mathbf{u}.\nabla\boldsymbol{\omega}) = Re\boldsymbol{\omega}.\nabla\mathbf{u} + \nabla^2\boldsymbol{\omega} + \nabla T \times \mathbf{G}, \quad (4)$$

which clearly shows the role of temperature gradients in vorticity generation. The temperature field is most conveniently written $T = -x + T^a(x, y, z, t)$ where $-x$ represents the applied temperature field, that is responsible for the basic thermocapillary flow, and T^a is produced by advection.

The base of the slot $y = 0$ is an inpenetrable, no slip, thermally insulated boundary. The interface $y = 1$ is assumed to remain flat, to sustain thermocapillary stresses, and to permit heat transfer characterized by a Biot number Bi. Accordingly

$$\mathbf{u} = T^a_{,y} = 0 \text{ at } y = 0 \text{ and}$$

$$v = u_{,y} - 1 + T^a_{,x} = w_{,y} + T^a_{,x}$$

$$= T^a_{,y} + BiT^a = 0 \text{ at } y = 1. \quad (5)$$

The slot flows must also be consistent with no fluid penetration conditions which would apply on the sidewalls of a cavity

of finite extent. There are various ways of ensuring this, depending on the class of slot flow. In many cases return flow conditions will apply

$$\int_0^1 u\,dy = \int_0^1 w\,dy = 0. \qquad (6)$$

However there are also more general possibilities (to be discussed in §4).

In the absence of jitter $\mathbf{G} = 0$ the equations admit parallel flow solutions in the x direction, with the advected temperature field varying only in the vertical. The solutions are [11, 12]

$$u = \tfrac{3}{4}y^2 - \tfrac{1}{2}y, \quad T^a = -\tfrac{1}{48}Ma(3y^4 - 4y^3 + 1). \qquad (7)$$

Our goal is to calculate how these solutions are modified in the presence of jitter. For simplicity we assume throughout that the modulation occurs at some frequency Ω which is small enough to be quasistatic, allowing the neglect of time derivatives in equations (2)–(3).

3 JITTER WITHIN THE PLANE

If $\mathbf{G}$ is non-zero but confined to the xy plane, we still obtain parallel flow solutions, with advected temperature varying only in the vertical. It is clear from equation (4) that *vertical* components of gravity only produce vorticity when coupled to the applied temperature field, not when coupled to T^a. As the applied temperature is independent of any thermocapillary motion, thermocapillarity and vertical gravity operate independently of one another. If $\mathbf{G} = (0, G\cos\Omega t, 0)$ vertical gravity produces fields

$$\begin{aligned} u &= -\tfrac{1}{24}G\cos\Omega t\left(4y^3 - \tfrac{15}{2}y^2 + 3y\right), \\ T^a &= \tfrac{1}{24}Ma\,G\cos\Omega t\left(\tfrac{1}{5}y^5 - \tfrac{5}{8}y^4 + \tfrac{1}{2}y^3 - \tfrac{3}{40}\right), \end{aligned} \qquad (8)$$

additional to those of equation (7). Thus vertical gravity alternately cooperates or competes with the thermocapillary fields as $G\cos\Omega t$ executes its oscillation cycle.

Now consider the case of *streamwise* gravity given by $\mathbf{G} = (G\cos\Omega t, 0, 0)$. From equation (4) we deduce that this generates vorticity when coupled with the advected temperature field, implying an interaction will occur between thermocapillarity and streamwise gravity. We define a streamfunction ψ such that $u = \psi_{,y}$. The thermal equation (3) now relates the streamwise heat advection $Ma\,\psi$ and the vertical heat conduction $-T^a_{,yy}$. Substituting into vorticity equation (4), we deduce

$$\psi_{,yyyy} - Ra\cos\Omega t\,\psi = 0, \qquad (9)$$

where the Rayleigh number Ra equals $Ma\,G$. The boundary conditions are $\psi = \psi_{,y} = 0$ at $y = 0$, and $\psi = \psi_{,yy} - 1 = 0$ at $y = 1$.

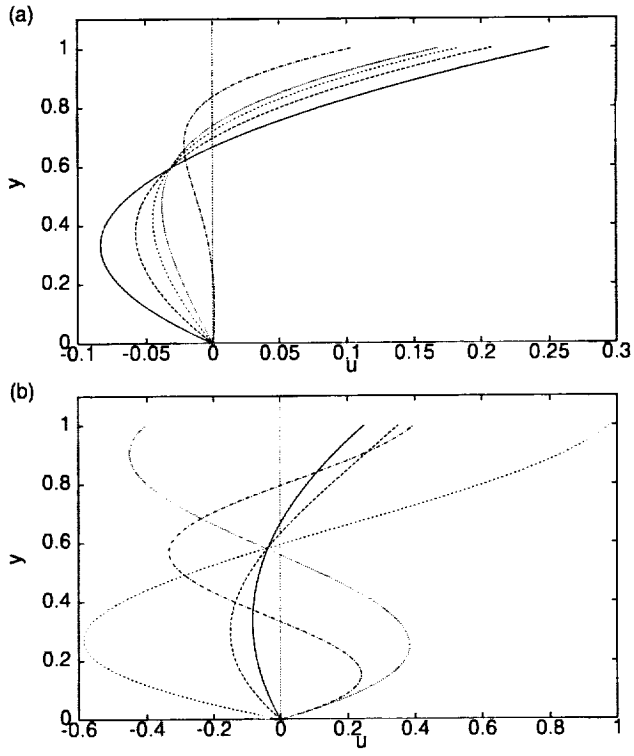

Figure 2: Velocity profiles for streamwise jitter during the (a) stable and (b) unstable part of the oscillation cycle, with solid line: $Ra|\cos\Omega t| = 0$, the base state profile; long dashes: $Ra|\cos\Omega t| = 100$; short dashes: $Ra|\cos\Omega t| = 200$; and dash-dot line: $Ra|\cos\Omega t| = 2200$. As $Ra|\cos\Omega t|$ increases, the stable case (a) tends to form an interfacial boundary layer, while the unstable case (b) forms cellular structures. Additionally in (b), the profiles obtain a large amplitude if they lie near one of the runaway values of $Ra\cos\Omega t$.

The solutions of this equation will be linear combinations of trigonometric and exponential functions. However these solutions are structurally quite different depending on the sign of $Ra\cos\Omega t$. If $Ra\cos\Omega t$ is large and negative, the solutions tend to be confined in boundary layers (see Figure 2(a)). If $Ra\cos\Omega t$ is large and positive, the solutions are highly cellular in nature (see Figure 2(b)). In both cases the thickness of the boundary layers or the wavelength of the cells scales as $\left(Ra|\cos\Omega t|\right)^{-1/4}$. There are also found to be particular positive values of $Ra\cos\Omega t$ which lead to infinitely large responses or runaways.

Physical insights into the reason for the different behaviour in the two cases can be deduced by considering the stratified slot initially in the absence of thermocapillarity. If $Ra\cos\Omega t < 0$, gravity and the applied temperature gradient are anti-parallel, meaning the slot is stably stratified in the

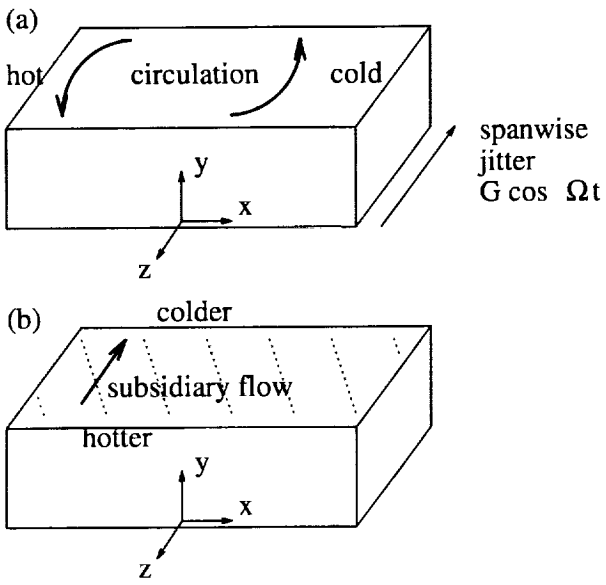

Figure 3: (a) Purely buoyant circulation flow induced by spanwise jitter in a slot with an applied temperature gradient. The circulation alternates between anticlockwise and clockwise as the jitter proceeds. (b) The circulation convects heat and rotates the isotherms (shown as dotted lines). The presence of a non-zero spanwise component of the interfacial temperature gradient drives a subsidiary thermocapillary flow.

Rayleigh-Bénard sense. If $Ra\cos\Omega t > 0$, gravity and the applied temperature gradient become parallel, corresponding to unstable stratification. If thermocapillarity is now added to the stably or unstably stratified system, it breaks the symmetry of the Rayleigh-Bénard basic state, thereby imposing directionality on the flow. The runaways in the unstable case correspond to values of the quasistatic Rayleigh number $Ra\cos\Omega t$ that support stationary, long wave Rayleigh-Bénard modes, which become resonantly excited by the thermocapillary forcing.

4 SPANWISE JITTER

If $\mathbf{G} = (0, 0, G\cos\Omega t)$ equations (1)–(5) no longer admit parallel flow solutions, and in fact a non-linear set of equations must be solved and the flows are fully 3-dimensional. For weak spanwise jitter, we pursue a perturbation expansion in powers of $G\cos\Omega t$. It is clear from equation (4) that spanwise jitter coupling to the applied temperature field generates vertical vorticity at leading order. This produces a purely buoyant circulation flow around the slot (see Figure 3(a)). We concentrate solely on the leading order results here. Results through second order, which necessarily include steady streaming flows, are given in [14].

In determining this circulation, we want to continue to exploit the horizontal spatial invariance properties that follow from the geometric simplicity of the slot model. Accordingly we assume a first order circulation flow of the form $G\cos\Omega t\,(zu_{01}(y), 0, xw_{10}(y))$ where u_{01} and w_{10} are functions to be determined. These functions are necessarily non-return flows, and in place of equation (6) we do the following. Imagine that the infinite slot models a true shallow cavity of unit depth, length A^{-1} and breadth $A_{xx}A^{-1}$. Consider a quadrant $0 \le x \le \frac{1}{2}A^{-1}, 0 \le z \le \frac{1}{2}A_{xx}A^{-1}$, located between the cavity centre and one corner. No penetration conditions on the cavity sidewalls require that the fluid flux entering the quadrant along $x = 0$ matches that leaving along $z = 0$. Applied to the assumed slot flows this requires

$$\int_0^1 w_{10}\,dy = -A_{xx}^2 \int_0^1 u_{01}\,dy. \tag{10}$$

The parameter A has cancelled from equation (10) but the spanwise-streamwise aspect ratio A_{xx} must be retained. The solutions for u_{01} and w_{01} are found to be

$$u_{01} = -\frac{1}{1+A_{xx}^2}\left(\tfrac{1}{2}y^2 - y\right), \tag{11}$$

$$w_{10} = \frac{A_{xx}^2}{1+A_{xx}^2}\left(\tfrac{1}{2}y^2 - y\right). \tag{12}$$

Clearly streamwise (spanwise) circulation flow is favoured at small (large) A_{xx}.

The circulation flow convects heat and therefore rotates the isotherms. This produces a temperature $G\cos\Omega t\, zT_{01}(y)$ where

$$T_{01} = \frac{Ma}{1+A_{xx}^2}\left(\tfrac{1}{24}y^4 - \tfrac{1}{6}y^3 + \tfrac{1}{8} + \frac{1}{3Bi}\right). \tag{13}$$

The term involving Bi accounts for the interfacial value of T_{01} and tends to be dominant even for Bi values as large as unity. A non-zero interfacial advected temperature arises here because the circulations are not return flows, and hence convect heat along the layer. If $Bi \to 0$ the convected heat has great difficulty escaping the interface, and so the temperature in the slot rises to a very high level.

As there are now additional temperature gradients along the surface in excess of the applied temperature gradient, new subsidiary thermocapillary motions are produced (see Figure 3(b)). These will be in the spanwise direction and we write them as $G\cos\Omega t\, w_{00}(y)$, where

$$w_{00} = \frac{Ma}{(1+A_{xx}^2)Bi}\left(\tfrac{1}{6}y - \tfrac{1}{4}y^2\right). \tag{14}$$

If thermocapillarity is inherently strong (Ma is large) or if heat is trapped in the slot (Bi is small) the subsidiary flow can dominate the circulation. The parametric dependence of

w_{00} on A_{zz} is counterintuitive on geometric grounds, i.e. the spanwise subsidiary flow is largest when spanwise-streamwise A_{zz} aspect ratio is small. The reason is that small A_{zz} favours the streamwise circulation that produces the isotherm rotation which in turn drives w_{00}.

5 CONCLUSIONS

The thermocapillary slot model subject to g-jitter exhibits rich physical behaviour. The simplicity of the slot geometry allows an analytic approach to the problem, facilitating a thorough parametric investigation, including the possibility of considering various directions of jitter. Vertical jitter is uninteresting because the advected temperature fields that are produced do not themselves produce any vorticity. Streamwise jitter is more interesting, and produces velocity profiles exhibiting boundary layer structures in the stable part of the cycle and cells in the unstable part. In the latter case it is possible to resonantly excite stationary long wave Rayleigh-Bénard modes for particular values of the quasistatic Rayleigh number. Spanwise jitter generates circulation flows around the slot. As the circulation advects interfacial temperature, it establishes subsidiary spanwise thermocapillary flows. At large Marangoni number or small Biot number, these subsidiary motions can become important.

ACKNOWLEDEMENTS

The authors acknowledge the support of NASA Grants NAG3-1475-S1 and NAG3-1943.

REFERENCES

[1] Alexander, J.I.D. 1990 *Low gravity experiment sensitivity to residual acceleration: A review.* Micrograv. Sci. Technol. **III**(2), 52–68.

[2] Nelson, E.S. 1991 *An examination of anticipated g-jitter on a space station and its effects on materials processing.* NASA Technical Memorandum 103775.

[3] Alexander, J.I.D., Lizée, A., Favier, J.-J. & Garandet, J.-P. 1996 *Analysis of residual acceleration effects on transport and segregation during directional solidification of tin-bismuth in the MEPHISTO furnace facility.* Third Microgravity Fluid Physics Conference, NASA Conference Publication **3338**, 461–464.

[4] Thomson, J.R., Drolet, F. & Viñals, J. 1996 *Fluid physics in a fluctuating acceleration environment.* Third Microgravity Fluid Physics Conference, NASA Conference Publication **3338**, 429–434.

[5] Gresho, P.M. & Sani, R.L. 1970 *The effects of gravity modulation on the stability of a heated fluid layer.* J. Fluid Mech. **40**, 783–806.

[6] Biringen, S. & Danabasoglu, G. 1990 *Computation of convective flow with gravity modulation in rectangular cavities.* J. Thermophysics **4**, 357–365.

[7] Biringen, S. & Peltier, L.J. 1990 *Numerical simulation of 3-D Bénard convection with gravitational modulation.* Phys. Fluids A **2**, 754–764.

[8] Farooq, A. & Homsy, G.M. 1994 *Streaming flows due to g-jitter-induced natural convection.* J. Fluid Mech. **271**, 351–378.

[9] Farooq, A. & Homsy, G.M. 1996 *Linear and non-linear dynamics of a differentially heated slot under gravity modulation.* J. Fluid Mech. **313**, 1–38.

[10] Lizée, A. & Alexander, J.I.D. 1997 *Chaotic thermovibrational flow in a laterally heated cavity.* manuscript.

[11] Sen, A.K. & Davis, S.H. 1982 *Steady thermocapillary flows in two-dimensional slots.* J. Fluid Mech. **121**, 163–186.

[12] Smith, M.K. & Davis, S.H. 1983 *Instabilities of dynamic thermocapillary liquid layers. Part 1. Convective instabilities.* J. Fluid Mech. **132**, 119–144.

[13] Grassia, P. & Homsy, G.M. 1998 *Thermocapillary & buoyant flows with low frequency jitter. Part I. Jitter confined to the plane.* Accepted for publication in Phys. Fluids.

[14] Grassia, P. & Homsy, G.M. 1998 *Thermocapillary & buoyant flows with low frequency jitter. Part II. Spanwise jitter.* Accepted for publication in Phys. Fluids.

Ground-Based Experiments on Vibrational Thermal Convection

Michael F. Schatz, Jeffrey L. Rogers, School of Physics, Georgia Institute of Technology, Atlanta, GA 30332-0430, USA, mike.schatz@physics.gatech.edu

1. INTRODUCTION

In many microgravity experiments involving fluid flow, density variations arise frequently due to, for example, temperature or concentration gradients. These variations couple to time-dependent accelerations (g-jitter) that are unavoidably present aboard spacecraft; this coupling can significantly influence outcomes in microgravity experiments. Ground-based experiments can provide insight into these effects that complements both theoretical studies and space-based experiments.

Convective flow is one class of behavior that can arise from g-jitter effects. The Rayleigh-Benard system is an important model for understanding thermal convection; thus, studies of this problem in the presence of acceleration modulations provide insight into the nature of g-jitter induced flow and of the effects of modulation and noise on non-equilibrium pattern formation.

In the following, we describe experiments on Rayleigh-Benard convection subjected to sinusoidal acceleration modulation. Theoretical investigations of this problem have been conducted by several workers [1-3]; by comparison there appears to be little previous experimental work [3].

2. DESCRIPTION OF EXPERIMENT

CO_2 gas, compressed at 3.10 E10^6 PA, is confined to a horizontal layer of depth d = 0.064 cm by a 0.5 cm thick aluminum mirror and a 2.54 cm thick sapphire window (Fig. 1). The thickness of the gas layer varies by approximately 1 μm, as measured inteferometrically. A cylindrical paper sidewall of inner diameter 2, d = 4.13 cm bounds the gas layer laterally.

The convective flow is controlled by applying a temperature difference ΔT across the layer and by oscillating the layer vertically with a sinusoidal acceleration of frequency f and amplitude a. ΔT, which typically ranges from 20 to 30 °C, is applied uniformly by heating the mirror and cooling the window. The temperature of the bottom plate fluctuates by less than 0.003 °C, while the window, whose temperature is fixed at 22.4 °C, is regulated to 0.01 °C. The dimensionless number that characterizes the heating is the Rayleigh number $R = \frac{g\alpha\Delta T d}{\nu\kappa}$ with kinematic viscosity ν, thermal diffusivity κ, temperature coefficient of volumetric expansion α and the earth's gravitational acceleration g. We describe our results in terms of a reduced Rayleigh

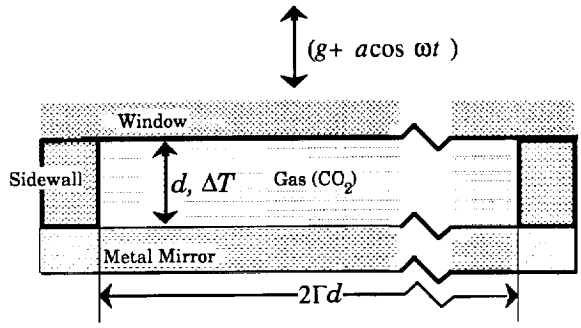

Figure 1: Geometry of Rayleigh-Bénard convection subjected to time periodic acceleration modulations.

number $\epsilon = \frac{R-R_0}{R_0}$ where R_0 = 1708 is the Rayleigh number at the onset of convection in the absence of shaking. Time dependent accelerations are applied by a hydraulic shaker table that vertically vibrates the experiment. In typical experiments, a ranges from 1 to 8 g and 8 Hz <= f <= 21 Hz; f is controlled to within 0.01 Hz and a is maintained to within 5%. The vertical diffusion time $\frac{d^2}{\kappa}$ ($\approx$ 1 s) is used to obtain the nondimensional frequency $\omega = \frac{2\pi f d^2}{\kappa}$; the oscillation amplitude is conveniently described in terms of the nondimensional displacement $\delta = \frac{a}{g\omega^2}$. The Prandtl number is fixed at 0.9 in the experiments.

The convection flow is visualized by the shadowgraph technique. Dynamics that occur over long time scales (>> $\frac{2\pi}{\omega}$) are captured using a standard NTSC video camera interfaced to a frame grabber. The camera is shuttered by a ferroelectric liquid crystal polarizer that is synchronized with the drive signal for the shaker table. Fast (< $\frac{2\pi}{\omega}$) convective dynamics can be captured using a high speed (800 frames per second) video camera. In all cases, the shadowgraph images are digitized and enhanced to improve the signal-to-noise using standard image processing techniques.

3. RESULTS

A wide variety of convective flow states are observed for fixed ω (Fig. 2). Each experimental run is performed by setting ϵ to a fixed value and slowly ramping up and then down in δ. A range of ϵ is probed by repeating this procedure at different values of ϵ. Each experimental run begins with δ = 0 where the convective flow is in

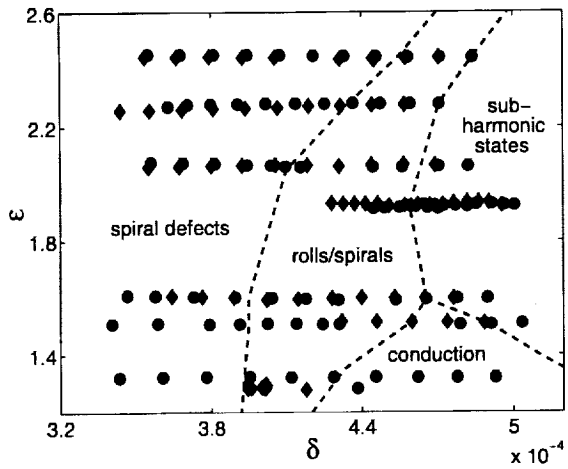

Figure 2: Phase diagram of convective flows is obtained by plotting the reduced Rayleigh number ϵ as a function of displacement amplitude δ with drive frequency $\omega = 80$. Data is obtained by fixing ϵ and varying δ; increasing δ is indicated by closed circles and decreasing δ is indicated by closed diamonds. The boundaries between flow states (dotted lines) are approximate and are drawn in to guide the eye.

the disordered, time dependent spiral defect chaos [4] for the range of ϵ described here.

As δ increases for low values of ϵ, the system passes through a sequence of increasingly ordered convective flows and returns to the conduction state (Figs. 2 and 3). Initially, the number of spiral defects decrease and the convection pattern exhibits either a single spiral (Fig. 3(b)) or a pattern of straight rolls (Fig. 3(c)). Upon further increases of δ, hexagonal patterns are observed to arise for a narrow range of δ (Fig. 3(d), but not shown on the phase diagram Fig. 2); hexagons disappear and the conduction state returns for δ sufficiently large. In this regime, all convective patterns are similar in appearance to those flows that arise in standard Rayleigh-Benard convection (the "no-shake" case) with the exception that in the presence of shaking, all convective patterns in this range of parameter are observed to oscillate synchronously with the drive frequency ω. (Patterns near onset in standard Rayleigh-Benard convection are stationary.).

The conduction state becomes unstable to new convective patterns with further increases in δ for low values of epsilon (Fig. 4). These new convective patterns are observed to oscillate at $\omega/2$, the subharmonic of the drive frequency. The subharmonic flows initially appear as

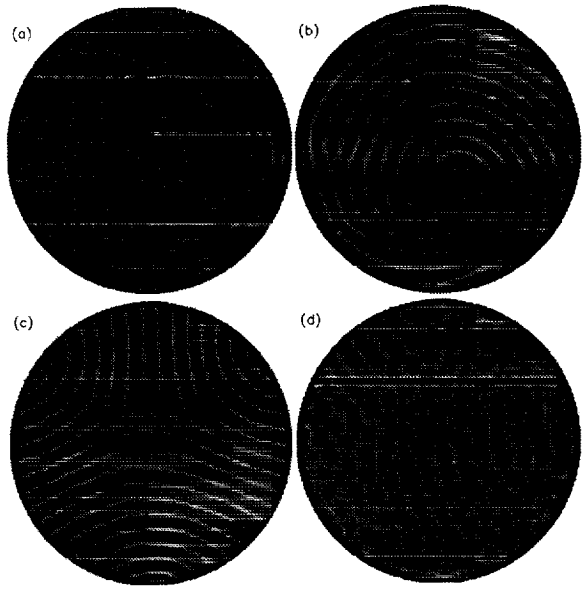

Figure 3: Transitions between convective flows with time dependence synchronous with the drive frequency ω. The convective flow exhibits spiral defect chaos in the absence of modulation, as shown in (a) for $\epsilon = 1.13$. The convective flow becomes less disordered as the displacement amplitude δ of the modulation is increased, giving rise to patterns in the form of (b) spirals ($\delta = 4.56E10^{-4}$, $\omega = 79$, $\epsilon = 2.06$), (c) stripes ($\delta = 1.58E10^{-4}$, $\omega = 181$, $\epsilon = 2.26$), or (d) hexagons ($\delta = 1.70E10^{-4}$, $\omega = 178$, $\epsilon = 2.44$). All cases of modulated convection (b-d) exhibit global rotation of the pattern. For these values of ϵ and ω, the system returns to the conduction state with further increases in δ.

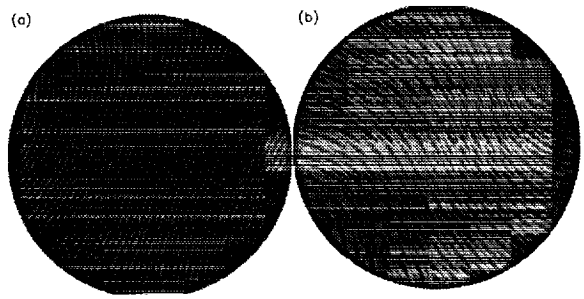

Figure 4: Convective flows with temporal response at the subharmonic $\frac{\omega}{2}$. The subharmonic patterns appear as (a) stripes ($\delta = 4.82E10^{-4}$, $\omega = 80$, $\epsilon = 1.92$), with wavelengths substantially smaller than that of unmodulated or synchronous convection (Fig. 1). Upon further increases in δ, the stripes become wavy (c). In both cases, the patterns exhibit global rotation.

nearly straight rolls with a wavelength that is significantly smaller than the synchronous roll patterns(Fig. 4(a)). With further increases in δ the subharmonic rolls become wavy along the roll direction; this waviness is accompanied by an additional frequency.

A global rotation to the pattern is observed for both synchronous and subharmonic ordered patterns. The direction of rotation depends on initial conditions; both clockwise and counterclockwise pattern rotations have been observed for all patterns. The rotation rate is observed to slow as δ approaches values near the transition to conduction.

Some aspects of these transitions can be understood drawing an analogy with the motion of a damped simple pendulum whose pivot is subjected to vertical sinusoidal oscillation [1]. In the absence of shaking, an inverted pendulum that is unstably balanced above the pivot is akin to a fluid layer where the conduction state is destabilized by heating from below. It is known that an inverted pendulum may be stabilized if the pivot is subjected to oscillations; the circumstances under which this may arise can be determined examining the stability of the equation of motion, the Mathieu equation. In the same way, it may be expected that oscillations may stabilize the conduction state in the Rayleigh-Benard problem. This analogy can be made quantitative; an approximate linear stability of the fluid layer can be performed by mapping equations of motion for the fluid layer to the Mathieu equation [1]. Both subharmonic and fundamental modes that are observed in the experiment are predicted with approximate values for the onset of convection and the wavenumbers that are consistent with the experiments.

For sufficiently large values of ϵ, there is no range of δ where the conduction state exists and the fundamental mode increases for low values of epsilon, the system can pass directly from the fundamental mode to the subharmonic mode of convection (Fig. 5.). As δ is increased, the sequence of fundamental modes are similar to those observed at smaller ϵ. For δ sufficiently large, the subharmonic modes first appear in locallized regions--typically trapped within defects of the fundamental pattern. These subharmonic can be trapped because they have a significantly smaller length scale than the fundamental mode; moreover, the subharmonics are advected with the defects in the fundamental mode and appear and disappear as the defects in the fundamental pattern appear and disappear (Fig. 5 (a)). With further increases in δ, the subharmonic pattern spreads throughout the convection cell; both patterns are seen to coexist (Fig. 5(b)). The patterns coexist

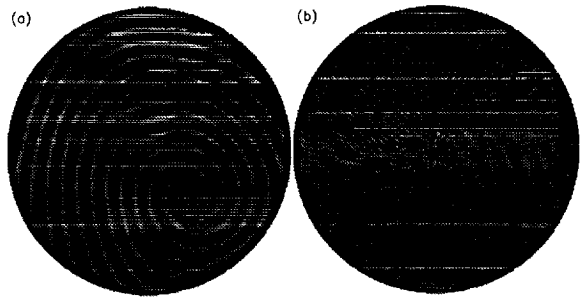

Figure 5: Competition between synchronous and subharmonic patterns. The subharmonic stripes first appear as locallized patches trapped within defects of the synchronous pattern (a) ($\delta = 4.71E10^{-4}$, $\omega = 80$, $\epsilon = 2.27$). With small changes in parameter, both subharmonic and synchronous patterns coexist over most of the apparatus (b).

for only a small range of δ with further increases in δ, subharmonic patterns of straight rolls appear.

4. CONCLUSIONS

Our experiments on Rayleigh-Benard convection with periodic acceleration modulation are permitting the study of flows that arise from two different pattern forming mechanisms. We observe flows that respond synchronously with the drive frequency ω; the patterns observed in this regime have wavenumbers and morphologies that are similar to convection in the absence of modulation, where the wavenumber selection is known to be directly related to the geometry. We also observe flows that respond at the drive frequency's subharmonic $\frac{\omega}{2}$ and have wavenumbers that are substantially smaller than those for the fundamental modes; the temporal behavior of the subharmonic patterns is akin to those observed in systems subject to parametric instability (e.g. surface waves in Faraday experiments) where wavenumbers are selected through a dispersion relation. Our experimental results for the onset of convection appear to be in agreement with preliminary computations of the approximate linear stability [1] of the conduction state; we are currently refining the computations for the exact problem [2].

To make closer connection to the effects of g-jitter in a microgravity environment, we will extend our studies to include stochastic modulations (noise). It is well-known that acceleration fluctuations aboard spacecraft exhibit both deterministic and stochastic features [5]. Our experiments on Rayleigh-Benard convection with acceleration modulation provide a general setting to

understand the effects of noise on convective flows. Specifically, recent theoretical work suggests that small amounts of noise can alter qualitatively transitions to oscillatory states [6]. We will investigate this question in future experiments.

5. *ACKNOWLEDGMENTS*

This work is supported by the NASA Office of Life and Microgravity Sciences under Grant NAG3-2006.

6. *REFERENCES*

1. P. M. Gresho and R. L. Sani, J. Fluid Mech., **40**, 783 (1970).

2. R. M Clever, G. Schubert and F. H. Busse, J. Fluid Mech., **253**, 663 (1993).

3. G. Z. Gershuni and D. V. Lyubimov, *Thermal Vibrational Convection* (J. Wiley, Chichester, England, 1998).

4 J. R. de Bruyn, E. Bodenschatz, S. W. Morris, S. P. Trainoff, Y. Hu, D. S. Cannell and G. Ahlers, Rev. Sci. Instrum., **67**, 2043 (1996) and references therein.

5. J. R. Thomson, J. Casademunt, F. Drolet, and J. Viñals, Phys. Fluids, **9**, 1336 (1997).

6. F. Drolet, and J. Viñals, Phys. Rev. E, **56**, 2649 (1997).

DIFFUSING LIGHT PHOTOGRAPHY OF CONTAINERLESS RIPPLE TURBULENCE

William B. Wright and Seth J. Putterman,
Physics Department, University of California, Los Angeles, CA 90095

When a fluid is injected with energy at long wavelength and high amplitude so as to drive it far from equilibrium it can reach a turbulent state of motion. The key problem faced by researchers is the achievement of an understanding of how energy distributes itself in turbulent flows(*1*). Two aspects which we address are the average power spectrum of the turbulent state(*2*) and the fluctuations around this average. The power spectra of turbulence and thermal equilibrium are similar in that both are proportional to powers of the wavenumber 'k' of the fluid motion (*3-6*). Turbulence and thermal equilibrium are different in that the turbulent state has a huge probability to be found in motions that are vastly different from the average flow. These fluctuations called 'intermittency' are the basis for the long standing interest in this problem among physicists and engineers.

As an example of turbulent flow we are measuring the motion of high amplitude ripples on the surface of a fluid. The equilibrium distribution of energy of capillary waves per unit area of surface per range of wavenumber is:

$$u(k) \approx (k_B T)k \qquad (1)$$

which expresses the equipartition of energy (k_B is Boltzmann's constant and T is the temperature). In comparison the steady state wave turbulent distribution of ripple energy driven by a source of power per unit area 'q' is:

$$u(k) \approx q^{\frac{1}{2}}(\rho\sigma)^{\frac{1}{4}}k^{-\frac{7}{4}} \qquad (2)$$

where ρ ,σ are the fluid density and surface tension *5,6,7*).

Most research on turbulence has focused on the long standing issue of vortex motion in a heavily stirred fluid. For this case as analyzed by Kolmogorov $u(k) \approx \rho^{\frac{1}{3}}q^{\frac{2}{3}}k^{-\frac{5}{3}}$ where q is now the power input per unit of volume by the tides into the stirring of the seas *3,4,8.9*). We are studying capillary wave turbulence because it affords us the opportunity to measure turbulence in a closed system. In particular if a spherical blob of fluid is positioned in microgravity then the ripples run around the surface and do not scatter from any boundaries. In this case all interactions are of the type that account for turbulence. This physical system will provide us with the quintessential turbulent motion that might yield an insight into the (so far) hidden paradigm of turbulence. Another advantage of microgravity is that it permits us to study capillary motions at longer wavelengths than are achievable on the ground. This expanded range of turbulent motion is essential for elucidating the properties of turbulence.

To measure the surface height as a function of position we suspend 1μm polystyrene balls in the fluid at a concentration of .04%(*10*). These particles scatter externally imposed light and enable us to take images of the surface which can be calibrated. Such a photo is

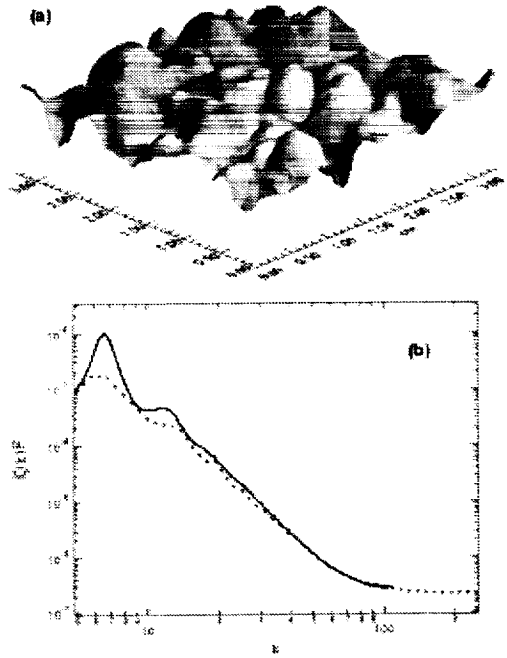

shown in Figure 1A, from our ground based research.

Figure 1: Close-up photo (A) and power spectrum (B) of the turbulent state of ripple motion.

The corresponding power spectrum of surface displacement is shown in Figure 1B, and it is in good agreement with Equation 2. In microgravity we expect to obtain an inertial range that extends down to 5 Hz so that the turbulence will exist over an extra decade of motion. Figure 1A displays a close-up of the surface that was made possible by our development of a high intensity flash lamp [4 Joules]. Figure 2 displays data for the rate of dissipation of mechanical energy into heat in the turbulent range of motion for a single snapshot of the fluid surface:

$$\frac{\dot{E}\lambda_0^2}{\sigma v} \approx \left[\lambda_0 \nabla^2 \zeta\right]^2 \qquad (3)$$

where ν, λ_0 are the kinematic viscosity and wavelength at which energy is injected.

Figure 2 represents the key problem of turbulence and the key advantage of the capillary wave realization of the issues surrounding turbulence(*10*). First note that the dissipation is focused into singular surfaces(*11*). There are large regions where the motion is strong and large regions where the motion is weak. In thermal equilibrium such singular surface and quiet pools are ruled out by exponentially suppressed probabilities.

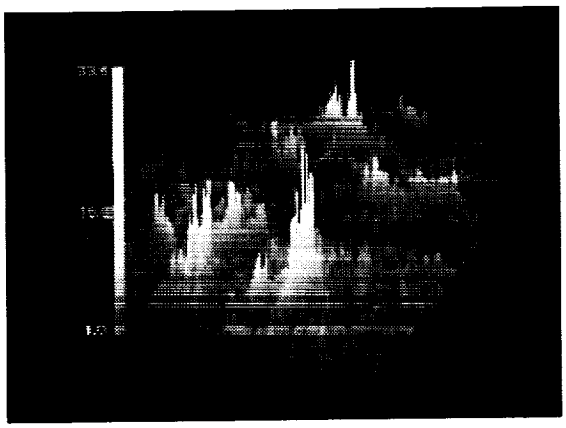

Figure 2: Data for intermittency in capillary wave turbulence.

As mentioned above an understanding of the processes which generate this type of motion is central to the problem of turbulence. The advantage of the capillary wave system is that we can (for the first time) quantitatively measure this 'intermittent' state and so pose a precise challenge for the theorists(*12*). An additional advantage is that capillary waves (in microgravity) present us with the added benefit of studying this state in its purist form: that is without the interference of walls.

The theory of the turbulent power spectrum and the criteria for turbulence can be understood in parallel with Kolmogorov's law of vortex turbulence. If E_k denotes the ripple energy per unit area between k and 2k then the rate at which nonlinear interactions cause energy to roll over (or cascade) to the range (2k,4k) is given by

$$\left.\frac{dE}{dt}\right|_+ \approx \frac{G^2 \omega_k E_k^2}{\sigma} - 4\nu k^2 E_k \qquad (4)$$

where ω is the frequency of motion of a ripple with wave number 'k'. The nonlinear coefficient of interaction is given by(*13*)

$$G^2 = \frac{8\pi^4}{13}$$

For capillary waves the dispersion law bends upwards so that

$$\omega^2 = \frac{\sigma}{\rho} k^3$$

According to this so-called decay spectrum two capillary waves can interact to create a third wave. For this reason the lowest order nonlinear term, as in Eq 4, which describes the change in the spectrum of ripples due to scattering, is quadratic in the energy. In addition to the cascade driven by this nonlinear term, energy can be lost due to linear viscous damping. Turbulence results when the reversible nonlinearities beat out the linear (viscous) damping or

$$\frac{1}{\tau_+} \equiv \frac{G^2 \omega_k E_k}{\sigma} >> 4\mu k^2$$

Another criterion for turbulence, which in fact distinguishes it from chaos, is that turbulence involves many modes. That is, there must be many modes activated within the bandwidth due to the nonlinear rollover rate $\frac{1}{\tau_+(\omega)}$. If the number of excited modes per unit frequency is $n(\omega)$ then turbulence occurs also when

$$\frac{n(\omega)}{\tau_+(\omega)} >> 1$$

{The density of capillary modes available for excitation is $n_0(\omega) = S\omega^{\frac{1}{3}} / 3\pi(\sigma/\rho)^{\frac{2}{3}}$ where S is the surface area} In the steady state and at high amplitude Eq. 4 leads to Eq. 2.

A mold which we have built to simulate the measurements that we intend to carry out in microgravity is shown in Figure 3. Here light is incident on the curved surface with a ripple and is recorded (on the opposite side) by a photodetector. These photos will enable us to calibrate the effects of curved surfaces and drift of the center of mass on the diffusing light technique.

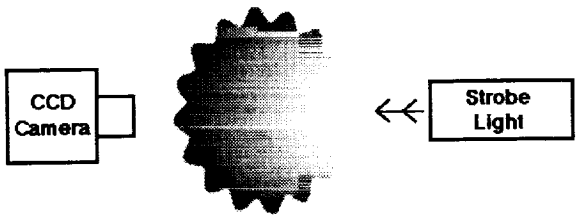

Figure 3: Model for calibrating measurements of ripples on a curved surface.

The 10cm diameter blob that we intend to measure in microgravity will be positioned by ultrasonic acoustic beam {SPACE DRUMS c/o Guigne International}. A focused sound beam of intensity 155dB provides a force of about 5mN on an area 3cm x 3cm. A array of these projectors can move the blob 1mm in about a tenth of a second in those instances where it drifts off axis. An advantage of the focused sound beam positioning arrangement is that when the fluid is in position the controlling beams can be turned off.

Successful data in microgravity will constitute a leading order challenge to theories and computer simulations of turbulence.

References:

1. W. Heisenberg; Proc. Roy. Soc. (London) A195, 402, (1948).
2. L.F. Richardson; Weather Prediction by Numerical Process, Cambridge U. Press (1922); Proc. Roy. Soc. (London) A110, 709 (1926).
3. A.N. Kolmogorov; Dokl. Akad. Nauk. SSSR 30, 301 (1941); A.M. Oboukhov; Dokl. Akad. Nauk. SSSR 32, 19, (1941).
4. L.D. Landau and E.M.Lifshitz; *Fluid Mechanics*, (Pergamon, New York, 1955)
5. V.E..Zakharov , V.S. L'vov and G. Falkovich, Kolmogorov Spectra of Turbulence, (Springer Berlin 1992).
6. R.Z. Sagdeev; Rev. Mod. Phys. 51, 1 (1979).
7. W.B. Wright, R. Budakian, S.J. Putterman; Phys. Rev. Lett. 76, 4528 (1996), and W.B. Wright; Ph.D. Thesis UCLA 1996.
8. H.L. Grant, R.W. Stewart, A. Moilliet; J. Fluid Mech. 12, 241 (1961).
9. U. Frisch, S. Orszag, Physics Today, January 1990 p. 24.
10. W. B. Wright, R. Budakian, S. Putterman; Science 278, 1609, (1997)
11. R.H. Kraichnan; Bull. Am. Phys. Soc. 42, 53 (1997);R.H. Kraichnan, in Turbulence and Stochastic Processes, ed. J.C.R. Hunt, O.M. Phillips, D. Williams (Royal Society, London 1991); Phys. Fluids 10, 2080 (1967).
12. A.N. Pushkarev, V.E. Zakharov; Phys. Rev. Lett. 76, 3320 (1996).
13. V.E. Zakharov, V.S. L'vov, G. Falkovich; *Kolmogorov Spectra of Turbulence*: [Springer-Berlin] 1992.

DROP BREAKUP IN FIXED BED FLOWS AS MODEL STOCHASTIC FLOW FIELDS

Eric S. G. Shaqfeh, Alisa B. Mosler, and Prateek Patel, Department of Chemical Engineering , Stanford University
Stanford, CA 94305-5025 (email: eric@chemeng. stanford.edu)

INTRODUCTION

Drop breakup and the criteria for drop breakup in viscous flows has been the subject of vigorous research since the early defining work of G.I. Taylor (1932, 1934)[1,2] concerning drop deformation and its effect on emulsion rheology in flow. The preponderance of work in the area has been focussed on drop deformation and breakup in steady, linear flows. In this context "breakup" refers to the nonexistence of a bound drop shape, since experiments generally show drop fragmentation only in the case of very extreme drop elongation or, more commonly, when the flow is abruptly altered.[3] There have been a host of review articles detailing studies of drop deformation and unbound growth in steady linear flows.[4,5,6] Most of these articles describe the delineation of flows as "strong" based on their ability to create unbound growth or distortion of the drop, or, in other words, cause the nonexistence of a bound shape. Most of this work also has been at least tacitly described as bearing on drop breakup in the flow through porous media.

In related studies, researchers have developed simple deterministic models for drop breakup in flow through porous media. These include the flow through a straight capillary tube,[7] flow through a contraction[8], and the flow through a converging diverging tube.[9] This previous research does not include the stochastic element of the disordered flow fields present in most porous media.

There is a growing body of literature, however which suggests that , indeed, drop breakup in time-varying flows may be qualitatively different than the "breakup" witnessed in steady flows. For example, Stone and coworkers [3,10] have shown that drop fragmentation can be incurred by drops in time varying linear flows (primarily by abruptly altering the flow field) even if the flow field remains "weak" throughout its duration by the criteria established for steady flows. Moreover a recent study of drop breakup in chaotic flows by Tjahjadi and Ottino (1991)[11] demonstrates that fragmentation can be readily induced, primarily by the "end-pinchoff" mechanism found in time dependent linear flows by Stone et al. [3,10] .

Our thesis then in the present research is that there is significant evidence that the breakup of drops in disordered, Lagrangian unsteady flows may very well be more important (i.e. more common) and governed by very different criteria than that governing the unbound growth of drops witnessed in steady elongation, for example. The mechanisms of breakup in disordered, unsteady flows are then only beginning to be examined. Criteria necessary to designate a given disordered flow field as strong, have therefore not been developed. This is the focus of the present research.

NUMERICAL SIMULATIONS

To examine drops and drop breakup mechanisms in disordered flow fields, first, we have completed large scale numerical simulation of drop breakup in disordered, Lagrangian unsteady flows as models for the flow through fixed fiber beds. The flow fields chosen were a class of anisotropic Gaussian flows, which have been shown by Shaqfeh and Koch[12] to be equivalent to the flow through a disordered, dilute fixe fiber bed if one can neglect the near field interactions of fiber and drop. Individualrealizations of these flow fields were created spectrally via a large sum of Fourier modes following a modified version of the procedure developed by Kraichnan[13] to simulate model turbulent flows. The drop evolution in these flows was then modeled using small deformation theory for the evolving drop surface. To be specific O(Ca), O(Ca^2), and O(Ca^3) small deformation theory models were used to simulate the evolution of the drop shape as it traversed the porous bed (i.e. anisotropic Gaussian flow field). Note in this context that it has been shown elsewhere[6], that these models have been very useful and are very accurate for predicting drop breakup in steady linear flows. This is true even though the drop shape and deformation near breakup are not well predicted by these models, since the deformation is very large.

The results of these simulations were very interesting and are contained in a more detailed publication elsewhere[14]. First it was demonstrated that "breakup" (defined within the context of the small deformation theory as a singularity in the deformation parameter with the latter defined originally by Taylor (1934)) did occur in the flow through the model fixed bed. In fact it was found that there was a "critical" value of the pore size Capillary number where 1 out of 2000 drops broke in flow. More complete examination of this critical condition revealed that there were rare events which caused isolated breakup events at smaller values of the critical Capillary. Therefore, a more accurate way to define a critical condition in this flow was to define a very small, standard rate of drop breakup per unit time and denote the critical condition based on the ability of the bed to cause drops to break at a faster rate than the chosen small standard. Based on this definition, we found for example that the critical capillary number was approximately 0.16 for a volume fraction of solids $\phi = 0.025$ in the bed. This value was determined using the second order small deformation theory, and was somewhat smaller using the third order theory, although as is well known the third order the-

ory does not include all terms at the same order of approximation. We also found that the critical condition was weakly decreasing as the solids volume fraction increased. Note that these values of the critical condition are comparable to those found for isolated drops in pure straining motion.

The most interesting results from these simulations were the predictions about the rates and the mechanisms associated with how the drops broke-up. First, as shown in Fig. 1, the breakup events were isolated and fairly short lived events. The deformation parameter, D_f, for single drop in a given realization of the stochastic flow, would typically oscillate in a disordered fashion until, in one to three pore lengths (or correlations lengths of the stochastic flow), it would rapidly become unbound, indicating a breakup event.

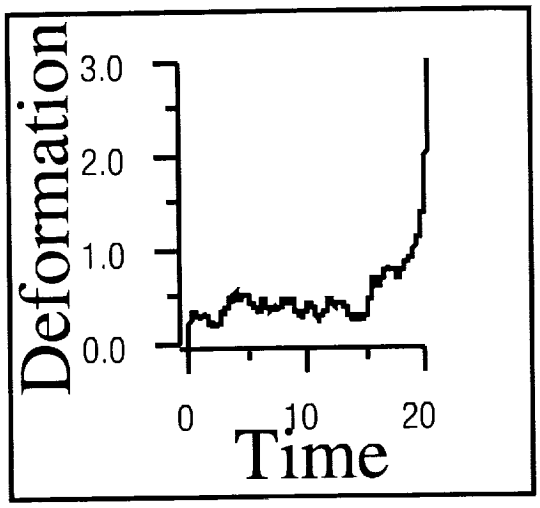

Fig. 1. The deformation parameter vs. time in a sample realization of a drop flowing through the fixed bed. Time is made dimensionless with the time it takes to flow through a pore.

Most of these events appeared to be *twist breakups* where the drop would reach a state of deformation that would not allow it to undergo the next deformation that the stochastic flow imposed without fracture. Vorticity was very often associated with breakup. Of note here is that the upon examining the drop distribution of those drops which did *not* fracture we found that breakup was not favored in any particular region of the probability density of deformation. It seemed to occur with almost equal probability over the whole range of deformations. Thus the distributions became almost Gaussian at large Capillary numbers, cf. Fig. 2.

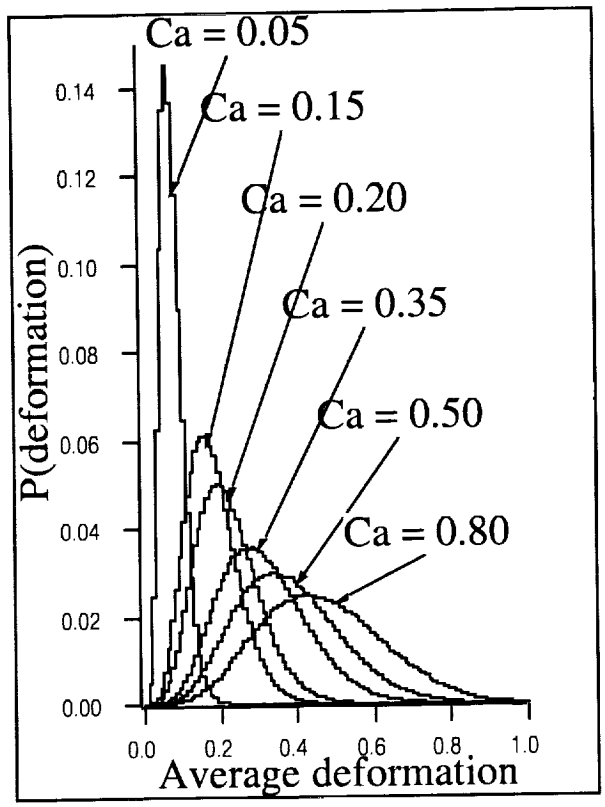

Fig. 2. Drop deformation distributions for those drops which do not break in the stochastic flow

A second notable characteristic of these breakup events was the local flow field in which they typically occurred. We examined the statistics of the type of linear flow that the drop experienced in the one to two time steps before the breakup event. The summary of this study is presented elsewhere[14] where we plot a histogram of the parameter, L, which has been used by Olbricht et al.[15] to characterize steady flows as strong or weak. Values of L> 0 contain more extensional character than vortical flow and are classified as 'strong' since they will break drops at a critical steady flow strength. Those for L<0 are alternatively classified as 'weak'. Our results show that this classification is of little use for the stochastic flow examined here, since drop breakup was noted just as readily in the weak flows as in the strong. In fact, it would appear from our visualizations of the breakup events that the local flow in which the drop breaks is not a useful test for predicting breakup events, since the deformation *before* the breakup event is as important as the flow in which the drop ultimately breaks. This is a key point to which we shall return in our discussion of ongoing work.

EXPERIMENTS

In parallel to the simulation work described in the preceding section, we have developed an ongoing experimental investigation of drop breakup in dilute fixed fiber beds. We have been motivated in this work

by recent experiments by Vinckier et al.[16] and Yang et al.[17] on the shear behavior of PDMS/polyisobutylene emulsions. These researchers created emulsions by vigorously mixng these immiscible liquids at concentrations of PDMS of approximately 1%. At that concentration, coalescence and breakup under shear act to create a steady drop size distribution which was reproducible. Upon creating this drop distribution these researchers used turbidity, dichroism and small angle light scattering measurements to examine the deformation and breakup of drops under steady simple shear. They found that form dichroism measurements were a sensitive measure of the breakup process.

We have chosen to use the same materials for our emulsions, however since our work is initially focussed on the breakup of single drops, we have chosen to use a much more dilute emulsion at PDMS concentrations of 0.01%. We have chosen to use the samelight scattering and polarimetry techniques as the Vinckier et al.[16] and Yang et al.[17] however we have added microscopy of the emulsions, which has allowed us to determine the evolution of the drop size distribution during the flow fields examined.

The emulsions were examined in two flow fields: simple shear and the flow through a dilute fixed bed of fibers. The latter flow was generated in an existing fiber bed that was constructed with known statistics at solids volume fraction of 2.5%. The bed has been used in two previous studies by our group in examinations of particle orientation and polymer stretch in fixed bed flows.[18,19] In simple shear flow, we reproduced the salient features of the experiments by Vinckier et al.[16] and Yang et al.[17] . To be specific, turbidity, small angle light scattering, and microscopy indicated that drop breakup occured even at low values of the Capillary number (Ca < 0.07) primarily because of breakup of the large drop tail in the distribution. After breaking this tail, the distribution achieved a steady state in the flow at a given capillary number which was characterizd by some degree of anisotropy in the SALS and dichroism. We could correlate directly with an average deformation parameter in the flow .

The measurements in the simple shear flow acted to benchmark our results in the flow through fixed beds. These measurements showed remarkable similarities to the shear flow measurements. Breakup from the large drop tail was found to occur at *pore size Capillary numbers* that were very low (again Ca < 0.07). However in this instance, we used time-dependent measurements to reveal that breakup was nearly uniform throughout the bed and occured after only one or two pore lengths of flow. This is in agreement with our numerical simulations. Initial measurement of the dichroism in the flowing suspension however, did indicate that it reached a steady state in the flow. This suggests that the deformation of the drop population which has not broken reaches a steady drop size distribution and then breakup events occur which do not significantly distort the distribution. The deformation parameters calculated from the dichroism in the fixed bed flow indicate deformation which may be well in excess of that in simple shear flow (cf. Fig. 3). These deformations were in excess of those calculated from our direct numerical simulations of the process and at present we are working to determine the cause of this discrepancy.

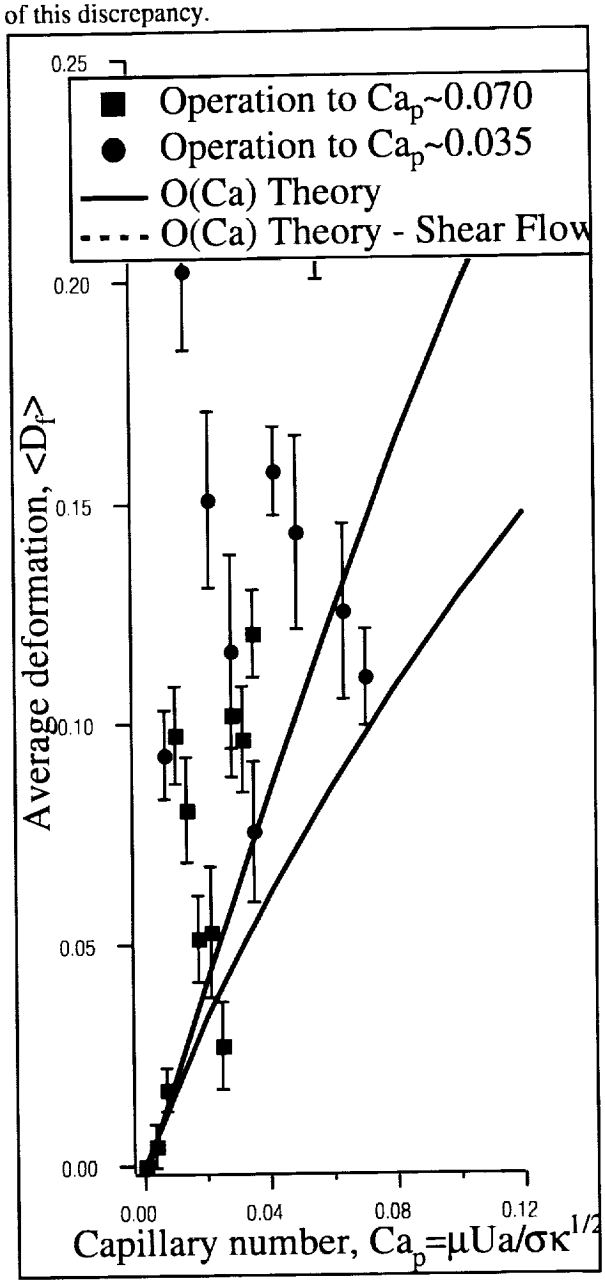

Fig. 3 Measured deformations in the flow of a PDMS emulsion through a dilute fixed fiber bed. Shown are also the simulations for fixed bed flow and the theory for shear flow.

ONGOING WORK

At present we are focussing on two parts to the research outlined above. First, we are modifying the simulations in a number of important ways. Rather than use the small deformation theories to predict drop breakup we are writing a full, boundary integral code to examind full drop deformation and change in these stochastically fluctuating fields. We feel this is important for two reasons. First, the preponderance of twist breakups in our initial simulations might be an artifact of the small deformation theory since it is well known that the detailed shapes achieved by the drops as calculated from this theory are not accurate near breakup. Thus other important mechanisms of drop breakup may inded be excluded by this small deformation theory including end pinching and capillary wave instability. Both of these mechanisms were important in the available work on breakup in chaotic flows[11]. This may be part of the reason for the reduced drop deformation parameters in our simulations as compared to the expeirmental work. A second reason for modifying our simulations is to focus on determining a reasonable criterion to predict breakup in these flows. It is now our feeling that any of the *possible two point rate of deformation correlation functions* may be useful. The reasons for this are made manifest from our previous work: these correlations contain important information concerning the strain that a drop experiences before entering a new flow region.

The second general area in which we are focussing our energies is in improving our experimental work. At present we are constructing a large fiber bed which will be index-of-refraction matched to the fluid. Thus we will be able to examine single drops as they pass through the bed, and thus witness breakup events as they happen. It is our purpose here to understand whether these twist breakups (or more generally, short time breakup events) are the major breakup mechanism in these disordered flows.

ACKNOWLEDGEMENTS

The authors would like to thank the NASA microgravity fluid physics program for funding this work through grant no. NAG3-1843

REFERENCES

1. G.I. Taylor, Proc. R. Soc. London Ser. A, 146, 501 (1934)

2. G. I. Taylor, Proc. R. Soc. London Ser. A, 138, 41 (1932)

3. H.A. Stone, B.J. Bentley, L.G. Leal, J. Fluid Mech. 173, 131 (1986)

4. A. Acrivos, 4th Int'l Conf. on Physicochemical Hydrodynamics, Ann. (N.Y.) Acad. Sci. 404, 1 (1983)

5. J. M. Rallison, Annu. Rev. Fluid Mech. 16, 45 (1984)

6. H. A. Stone, Annu. Rev. Fluid Mech. 26, 65 (1994)

7. W.L. Olbricht and D.M. Kung, Phys. Fluids A. 4, 1347 (1992)

8. C.D. Han and K. Funatsu, J. Rheol., 22, 113 (1978)

9. W.L. Olbricht and L.G. Leal, J. Fluid Mech. 134, 329 (1983)

10. H.A. Stone, and L.G. Leal, J. Fluid Mech. 206, 223 (1989)

11. M. Tjahjadi and J.M. Ottino, J. Fluid Mech. 232, 191 (1991)

12. E.S.G. Shaqfeh and D.L. Koch, J. Fluid Mech. 244, 17 (1992)

13. R.H. Kraichnan, Phys. Fluids 13, 22 (1970)

14. A.B. Mosler and E.S.G. Shaqfeh, Phys. Fluids 9, 11 (1997)

15. W.L. Olbricht, J.M. Rallison, and L.G. Leal, J. Non-Newtonian Fluid Mech. 10, 291 (1982)

16. I. Vinckier, P. Moldenauers, and J. Mewis, J. Rheol. 40, 613 (1996)

17. H. Yang, P. Moldenauers, and J. Mewis, Polymer, March 1997

18. P.L. Frattini, E.S.G. Shaqfeh, J.L. Levy and D.L. Koch, Phys. Fluids A. 3, 2516 (1991)

19. A.R. Evans, E.S.G. Shaqfeh, and P.L. Frattini, J. Fluid Mech. 281, 319 (1994)

Session 2A

Multiphase Flow II

BUBBLE GENERATION IN A FLOWING LIQUID MEDIUM AND RESULTING TWO-PHASE FLOW IN MICROGRAVITY

S. C. Pais[1], Y. Kamotani[2], A. Bhunia[3] and S. Ostrach[4], [1,2,3,4] Department of Mechanical & Aerospace Engineering, Glennan Building, Case Western Reserve University, 10900 Euclid Avenue, Cleveland, OH 44106, [2] Corresponding Author, e-mail: yxk@po.cwru.edu,

INTRODUCTION

The development of two-phase flow research under reduced and microgravity conditions is prompted by a wide range of space applications, such as, thermal energy and power generation, propulsion, cryogenic storage and long duration life support systems; necessary for programs, such as NASA's Human Exploration for the Development of Space (HEDS). Study of gas-liquid flows in reduced gravity is important for the design of two-phase thermal control systems, intended to replace conventional pumped liquid loops[1, 2]. The main advantage of a two-phase thermal control system is its reduced weight, which is of utmost importance since any weight saving for payload transfer to orbit signifies lower launch costs.

Under normal gravity conditions, when gas is injected through an orifice into a quiescent liquid medium, the bubble grows and detaches quite readily due to the buoyancy force. Under reduced gravity conditions, the detaching role of the buoyancy force is significantly diminished, giving rise to uncontrollably larger bubbles than those obtained in normal gravity. Consequently, another bubble detaching force is required in order to control bubble size and frequency of formation. A practical solution is to use flowing liquid and utilize its drag force for bubble detachment[3,4].

Two configurations generally considered for bubble dispersion in a flowing liquid are the co-flow and the cross-flow geometry. In the co-flow configuration, the dispersed phase is introduced through a nozzle in the same direction with the liquid flow; whereas in the cross-flow geometry, gas is injected perpendicular to the direction of liquid flow. Of the three major two-phase flow patterns, namely bubble, slug and annular [5], only bubble and annular flows are used in space based systems [6]. In this work, we are concentrating on the bubbly flow regime.

For normal[7, 8] and reduced gravity[9, 10], bubble generation in a quiescent liquid has been extensively studied. Reduced gravity bubble formation in the cross-flow configuration has been recently reported by several investigators[4, 11, 12]. On the other hand, the co-flow configuration has only been considered in normal gravity in order to observe the effect of liquid velocity on bubble detachment[12, 13]. Under reduced gravity conditions bubble generation and resulting two-phase flow by multiple nozzle injection along the periphery of the flow conduit has been reported by several investigators [5,6]. With multiple nozzle injection, due to unpredictable coalescence of adjacent bubbles, it is difficult to control accurately the void fraction of the ensuing two-phase flow. A better alternative is controlled bubble generation via single nozzle injection.

In this work, we investigate bubble generation by gas injection via a single nozzle in a co- and cross-flow system. Experiments using air and water are performed in parabolic flight aboard the modified DC-9 Reduced Gravity Research Aircraft at NASA Lewis Research Center. Effects of surrounding liquid velocity and two-phase flow conduit geometry on the bubble diameter and the associated void fraction are investigated. For the co-flow geometry, we have also developed a theoretical model, based on an overall balance of forces acting on the bubble. Predictions of bubble diameter and formation frequency using the present model show good agreement with our experimental results.

EXPERIMENTAL STUDY

In reduced gravity, the bubble diameter (D_B) is dependent on fluid properties, flow geometry and flow conditions.

$$D_B = f (Q_d, Q_c, D_P, D_N, \sigma, \mu_c, \mu_d, \rho_c, \rho_d)$$

where Q_d is the volumetric gas flow rate, Q_c is the volumetric liquid flow rate, D_P is the pipe diameter, D_N is the nozzle diameter, σ is the surface tension, μ_c and ρ_c are the dynamic viscosity and density of the liquid phase, while μ_d and ρ_d are the dynamic viscosity and density of the gas phase. In this study, we are investigating the effect of flow conditions (Q_d, Q_c) and flow geometry (D_P, D_N) on bubble diameter (D_B).

Apparatus and Methods

Our experiments are conducted aboard the modified DC-9 Reduced Gravity Research Aircraft which provides the investigator with 20 seconds of 0.01 g reduced gravity environment. Out of this time period an estimated 15 seconds is allotted for acquisition of experimental data. The reproducibility of data between two consecutive trajectories is within ± 5%. The present two-phase flow experiments are performed with an air-water system using three different sets of pipe diameters (D_p = 1.27 cm, 1.9 cm and 2.54 cm). In addition, two different ratios of nozzle to pipe diameters are considered ($D_n^* = D_n/D_p$ = 0.1 and 0.2). Depending on the two-phase flow pipe diameter, superficial gas ($U_{GS} = 4Q_d/\pi D_p^2$) and liquid velocities ($U_{LS} = 4Q_c/\pi D_p^2$) are varied from 8 to 70 cm/s. In general, for each data point acquired, two dive trajectories are executed.

The co-flow test section (figure 1) consists of a Plexiglas pipe, which acts as the two-phase flow conduit.

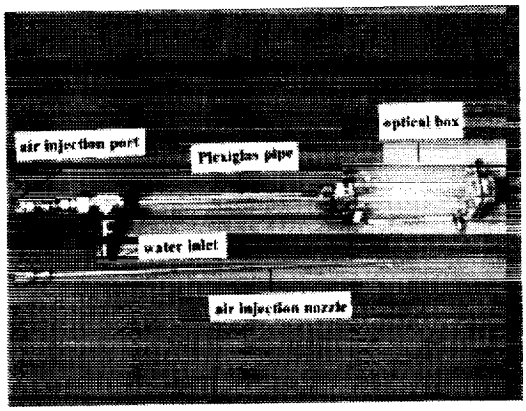

Fig 1: Co-flow experimental test section

A tee branch fitting is mounted on the inlet side of the pipe. Dry and filtered air is injected through a stainless steel tube, which acts as the gas injection nozzle and protrudes into the pipe. Distilled water is introduced through the remaining port of the tee branch fitting. The water and air mixing region is surrounded by a Plexiglas visual rectangular box filled with water, which eliminates optical distortion of the generated bubble.

The cross flow test section, shown in figure 2, is machined as a tee section from a rectangular piece of Plexiglas stock. Two orthogonally positioned, equal diameter holes are bored into the Plexiglas tee, one merging into the other. Through one of these holes, air is injected via a stainless steel tube. The other hole acts as the water inlet tube as well as the two-phase flow conduit.

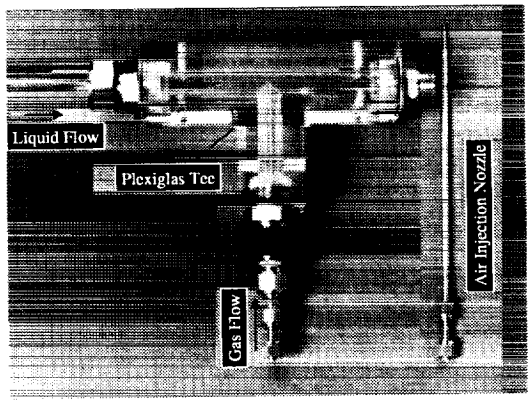

Fig 2: Cross-flow experimental test section

The complete experimental test section assembly is integrated within the Learjet Two-phase Flow Apparatus, developed and described by McQuillen and Neumann[14]. The bubble generation process is recorded with a high speed video camcorder (250 frames/sec). For every experimental run, a new batch of distilled water is used to minimize contamination at the bubble surface.

Experimental bubble diameter is obtained from the flight experiment video by using THIN 2.0© and OPTIMAS 5.1© image acquisition and processing software packages. The geometrically averaged bubble diameter for each of three consecutively detached bubbles in the vicinity of the gas injection nozzle is first calculated. The bubble diameter reported in this work is the arithmetic average of these three values. The standard deviation for bubble diameter measurement is within ± 2.5% of the mean diameter value. Uncertainty errors in flow velocity measurement have an upper limit of ± 5% of the obtained value. A more elaborate discussion on experimental procedure and data acquisition is given by Pais[15].

Co-flow Configuration Results

The important role played by the flowing liquid on bubble detachment in reduced gravity is shown in figure 3. Experimental data presented in this figure is obtained for a fixed pipe diameter of 1.9 cm and a gas flow rate of 51 cm^3/s (cc/s). Two sets of nozzle diameters (D_N = 0.19 cm and 0.38 cm) are used. For both nozzle diameters, as superficial liquid velocity is increased, the bubble diameter decreases. The drag induced by the surrounding liquid flow results in faster detachment of the bubble, thereby decreasing its size. It is further observed that bubble diameter increases with nozzle diameter, which can be explained from the fact that with a larger injection nozzle more gas is fed into the bubble.

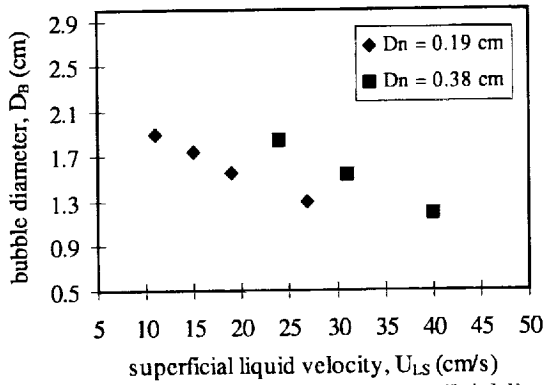

Fig 3: Effect of nozzle diameter and superficial liquid velocity on bubble diameter. Fixed Q_d = 51 cc/s and D_P = 1.9 cm.

Variation of bubble size with increasing volumetric gas flow rate and pipe diameter is displayed in figure 4. The volumetric liquid flow rate and the nozzle diameter are kept constant at Q_c = 40 cc/s and D_N = 0.19 cm. Experiments are conducted with three different pipe diameters, D_P = 1.27, 1.9 and 2.54 cm by varying the gas flow rate from 16 to 40 cc/s. It is obvious that bubble diameter increases with increasing gas flux and pipe diameter. At a fixed Q_c, an increase in pipe diameter implies a reduction in co-flowing liquid velocity and therefore liquid drag. Larger bubbles are

formed when drag induced by the flowing liquid is reduced.

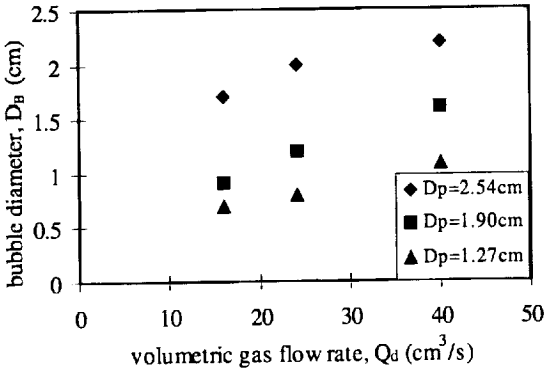

Fig 4: Variation of bubble diameter with volumetric gas flow rate and flow conduit diameter. Fixed Qc = 40 cc/s and D_N = 0.19 cm.

Figure 5 displays variation of void fraction (V_f) with volumetric gas and liquid flow rates. Void fraction is defined as the ratio of volume occupied by the gas phase to total volume of fluid within a given section of the two phase flow conduit. Mathematically, for a single bubble in the bubbly flow regime, this relationship can be written as $V_f = 2D_B^3/3D_P^2\Delta$, where Δ is the distance between the front of the detached bubble and the front of the previously detached bubble. In the bubbly flow regime the maximum value of the void fraction is 2/3 ($D_B = D_P$), beyond which formation of Taylor bubbles (slugs) occurs. In the slug flow regime, void fraction can exceed the value of 2/3, its upper limit being 1.

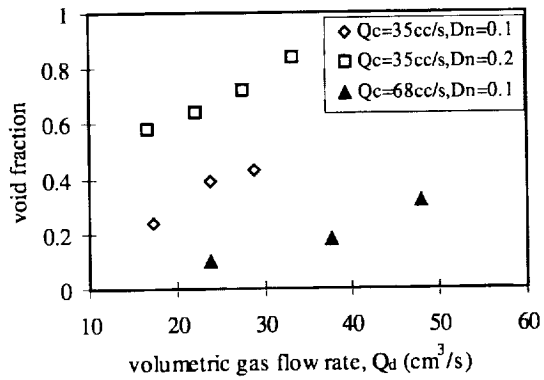

Fig 5: Dependence of void fraction on gas and liquid flow rate with respect to variation in nozzle diameter. D_P is fixed at 1.9 cm.

Void fraction, which is directly proportional to the bubble diameter, increases with gas flow rate and nozzle diameter, while decreasing with liquid flow rate. For the data presented in this graph, the pipe diameter is fixed at 1.9 cm. It is observed that at $D_N^* = 0.1$ (D_N = 0.19 cm), for two different liquid flow rates, Q_c = 35 and 68 cc/s, the void fraction is less than 2/3, indicating occurrence of the bubbly flow regime. On the other hand, for Q_c = 35 cc/s and $D_N^* = 0.2$ (D_N = 0.38 cm), the void fraction exceeds the value of 2/3 for Q_d = 29 and 33 cc/s, suggesting formation of Taylor bubbles at such flow conditions.

Cross Flow Configuration Results

In the cross-flow configuration, bubble diameter as a function of superficial liquid velocity and nozzle diameter is shown in figure 6. This plot displays data taken with the 1.27 diameter test section at a constant gas flow rate of 44 cc/s. For two different nozzle diameters (D_N = 0.127 and 0.254 cm), the superficial liquid velocity (U_{LS}) is varied from 20 to 60 cm/s. It is observed that the bubble diameter decreases with increasing superficial liquid velocity for a given gas injection geometry at a constant gas flow rate. Furthermore, it is noted that the bubble diameter increases with increasing nozzle diameter. The trends are similar to those displayed by the co-flow configuration.

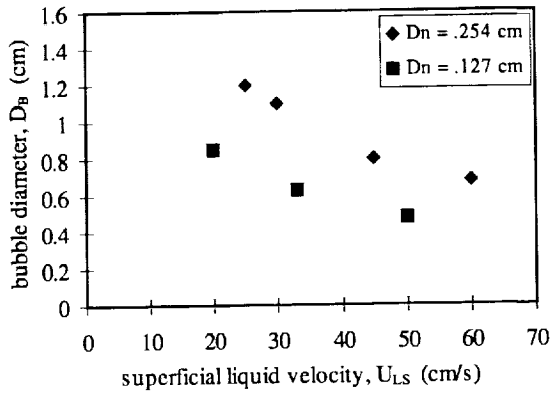

Fig 6: Effect of superficial liquid velocity and nozzle diameter on bubble size for a fixed Q_d = 44 cm^3/s and D_P = 1.27 cm.

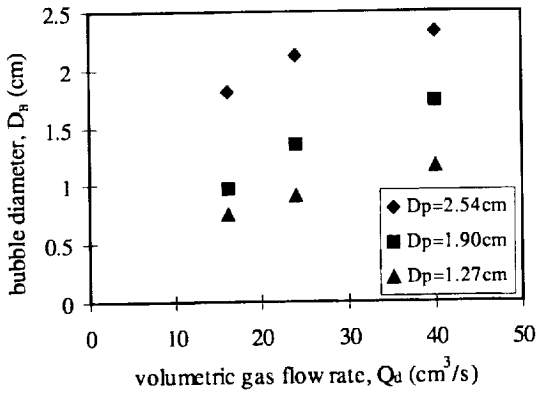

Fig 7: Variation of bubble diameter with respect to gas flow rate and pipe diameter at a fixed Q_c = 40 cm^3/s and D_N = 0.19 cm.

Figure 7 shows the variation of bubble diameter with volumetric gas flow rate and pipe diameter at a constant liquid flow rate of 40 cc/s. For acquiring this data, three distinct volumetric gas flow rates are used, namely 16, 24 and 40 cc/s. Experiments are performed

using the 1.27, 1.9 and 2.54 cm diameter test sections, keeping the nozzle diameter constant at 0.19 cm. Note that bubble size grows with increasing gas flow rate and pipe diameter at a constant liquid flow rate. Figure 4 and figure 7 display bubble diameters at identical flow geometry and conditions for co and cross flow configurations. It is interesting to observe that at similar flow conditions and geometry, somewhat larger bubbles are generated by using the cross-flow configuration rather than the co-flow configuration.

A plot of void fraction (V_f) values as a function of volumetric gas and liquid flow rates is presented in figure 8. This experimental data is obtained using the 1.9 cm diameter test section for two different nozzle diameters, D_N = 0.19 and 0.38 cm. For two different liquid flow conditions (Q_c = 51 and 68 cc/s), the gas flow rate is varied from 16 to 49 cc/s. In the cross-flow configuration, analogous to the co-flow geometry, the void fraction increases with increasing gas flow rate and decreases with increasing surrounding liquid flow. Furthermore, it is observed that V_f increases with gas injection nozzle diameter.

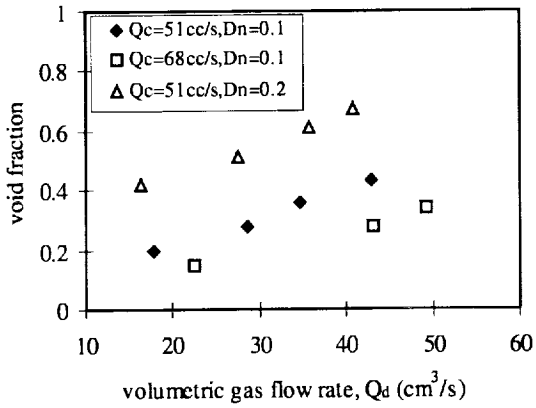

Fig. 8: Effect of volumetric gas and liquid flow rates on void fraction with respect to variation in nozzle diameter for constant pipe diameter of 1.9 cm.

Comparison of Co- and Cross-flow Configuration

Bubble diameters and void fraction obtained using the co-flow system are compared with corresponding values obtained in the cross-flow geometry. The data displayed in figure 9, is obtained using a 1.9 cm diameter test section at constant liquid flow rate of 68 cc/s with a 0.38 cm nozzle diameter. The volumetric gas flow rate is varied from 21 to 70 cc/s. It is observed that at similar values of gas and liquid flow rates as well as similar nozzle and pipe diameters, bubbles generated by using the cross-flow configuration are slightly larger in size relative to those obtained in co-flow geometry. Therefore, the void fraction of the resulting two-phase flow also follows a similar trend.

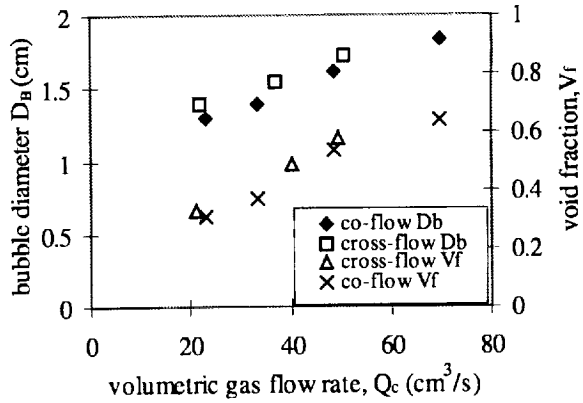

Fig 9: Comparison of bubble diameter and void fraction for co and cross-flow configuration. Fixed Q_c = 68 cc/s, D_P = 1.9 cm and D_N = 0.38 cm.

THEORETICAL STUDY

In parallel to the experimental work, we have developed a theoretical model to describe the bubble detachment process from which we obtain the detached bubble diameter and formation time in a co-flow configuration, as shown in figure 10.

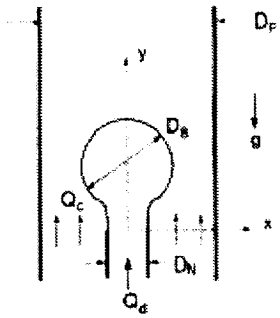

Fig. 10: Schematic of co-flow configuration.

The current model, which is valid for both normal and reduced gravity conditions at constant gas flux, is employed to investigate single bubble generation in the dynamic (Q_d = 1 – 1000 cc/s) and bubbly flow regime ($D_B < D_P$). The focus of the model is to identify the important forces involved in the process of bubble formation and their role on bubble detachment. The bubble shape is assumed spherical throughout the formation process. Hence, for constant flow conditions, the rate of change of bubble volume (V_B) is given as d V_B/d t = Q_d = constant. Various important forces involved in the bubble generation process are:

$$F_B = V_B(\rho_c - \rho_d)g$$

$$F_\sigma = \pi D_N \sigma$$

$$F_M = \rho_d \frac{Q_d^2}{(\pi/4)D_N^2}$$

$$F_D = S_D C_{DW} \frac{1}{2}\rho_c U_{eff}^2 A_{eff}$$

$$F_I = \frac{d}{dt}\left[\rho_d V_B \frac{ds}{dt} + \rho_c C_{MC} V_B U_{eff}\right]$$

where F_B, F_σ, F_M, F_D, F_I are respectively the buoyancy, surface tension, momentum flux, drag and inertia forces acting on the bubble. C_{DW} is drag coefficient of the bubble in presence of confining pipe walls; ds/dt is velocity of the bubble center away from the nozzle tip; U_{eff} is the relative velocity of bubble center w. r. t. superficial liquid velocity (U_{eff} = ds/dt – U_{LS}), A_{eff} is the effective area of the bubble on which the drag force acts; S_D is +1 or –1 for $U_{eff} < 0$ and $U_{eff} > 0$ respectively and C_{MC} is the added mass coefficient. Expressions for C_{MC}, C_{DW}, A_{eff} are given in our previous work[16].

Buoyancy and gas momentum flux always promote bubble detachment, while surface tension tries to prevent it. The inertia force has two components. Bubble inertia represented by the first term of the inertia force expression is always an attaching force. On the other hand, liquid inertia, represented by the second term, as well as the liquid drag can be either attaching or detaching, depending on whether $U_{eff} > 0$ or $U_{eff} < 0$.

Bubble generation occurs in two stages. During the first stage, defined as the expansion stage, the bubble grows radially due to incoming gas flux, however the bubble base remains attached to the nozzle. Bubble volume and growth rate during the expansion stage are respectively written as $V_B = (\pi/6)\, D_B^3(t)$ and ds/dt = ½ $dD_B(t)/dt$. A balance of the attaching and detaching forces marks the end of expansion stage ($D_B = D_{Bc}$) and the beginning of the second stage, namely the detachment stage. During the detachment stage, the bubble continues to grow in size, the bubble volume being $V_B = (\pi/6)\, D_{Bc}^3 + Q_d t$. The bubble moves away from the nozzle, but still remains attached to it via a neck region. The bubble center located at a distance Y from the nozzle tip, moves at a velocity d s/dt = d Y/d t. Bubble motion during the two stages is described by a balance of forces acting on it:

$$\mathbf{F_B + F_\sigma + F_M + F_D + F_I = 0}$$

At the end of the detachment stage, the bubble departs the nozzle base due to neck pinch-off. The neck pinches off when its length becomes equal to the nozzle diameter. Therefore, the detachment criterion is written as:

$$L_N = Y - \tfrac{1}{2} D_B \geq D_N$$

Solving the force balance equations at the two stages of bubble formation, subject to the detachment criterion leads to a non-dimensional functional expression for the detached bubble diameter:

$$D_B^* = f(Re_P, We_P, Fr_P, U_{GS}^*, D_N^*, \rho^*)$$

Various dimensionless parameters are Reynolds number $Re_P = \rho_c U_{LS} D_P/\mu_c$; Weber number $We_P = \rho_c U_{LS}^2 D_P/\sigma$; Froude number $Fr_P = \rho_c U_{LS}^2/(\rho_c - \rho_d) g\, D_P$; Dimensionless superficial gas velocity $U_{GS}^* = U_{GS}/U_{LS}$; Dimensionless nozzle diameter $D_N^* = D_N/D_P$ and density ratio $\rho^* = \rho_d/\rho_c$. Further details on the method of solution and predictions resulting from this theoretical model are discussed by Bhunia et. al.[16].

A comparison of the present reduced gravity experimental data with predictions of the numerical model is shown in figure 11. This figure displays variation of dimensionless bubble diameter with respect to non-dimensional superficial gas velocity. Two different sets of dimensionless nozzle diameter (D_N^*) and for each D_N^* two different Reynolds number conditions are considered. The numerical predictions show good agreement with the experimental data. Over a wide range of Re_P, the present computational model predicts bubble diameter within ±10% of the experimental results.

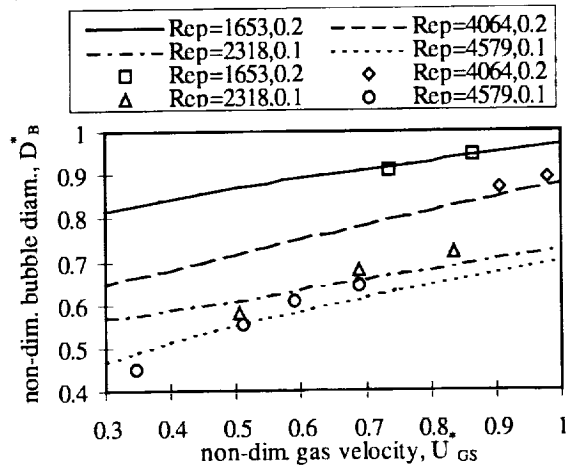

Fig. 11: Comparison of numerical predictions with experimental results. Solid and dotted line – Numerical predictions, symbols – experimental data.

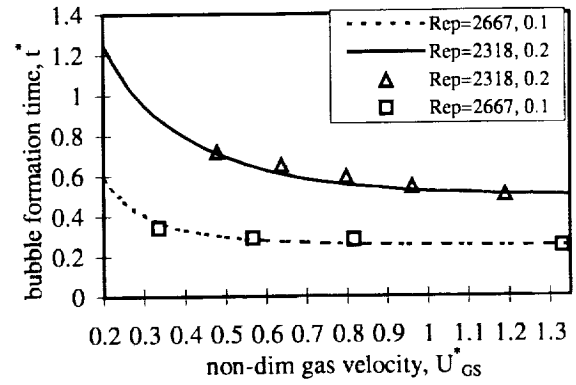

Fig 12: Comparison of computed dimensionless bubble formation time with reduced gravity experimental data. Solid and dotted line – numerical predictions, Symbols - experimental data; $D_N^* = 0.1$, Re_P = 2667, We_P = 3.8, Fr_P = 4.4; $D_N^* = 0.2$, Re_P = 2318, We_P = 3.9, Fr_P = 8.0.

The theoretical model is further validated by a comparison of the dimensionless bubble formation time ($t^* = t\, U_{LS}/D_P$) obtained from the model and the experimental data shown in figure 12. At low values of U_{GS}^*, the bubble formation time decreases sharply with increasing U_{GS}^*, until it reaches an asymptotic limit of constant time, irrespective of the U_{GS}^* value. It is fur-

ther observed that with increasing nozzle diameter when bubble size increases, it takes longer for the bubble to detach.

At higher superficial liquid velocity, the bubble deviates from its spherical shape, as assumed in this model. The present model agrees well with the experimental data up to a maximum Weber number of 30, which corresponds to a Reynolds number of 7500 for an air-water system using a 2.54 cm diameter pipe.

CONCLUSIONS

The present work focuses on bubble generation via single nozzle injection in a co- and cross-flowing liquid. This study is based on empirical data, obtained by performing experiments aboard the DC-9 Reduced Gravity Research Aircraft in parabolic flight. Effect of the flow conditions and geometry on detached bubble diameter and thereby void fraction of the resulting two-phase flow is investigated. It is shown that bubble diameter and void fraction increase with volumetric gas flow rate, pipe diameter and nozzle diameter, while they decrease with surrounding liquid flow. The important role of the continuous liquid flow in detaching bubbles under reduced gravity conditions is thus emphasized.

It is of interest to note that bubble size and corresponding void fraction are somewhat smaller for the co-flow system than for the cross-flow configuration at similar flow conditions and flow geometry. From empirical evidence it is shown that the void fraction can be readily controlled in case of single nozzle gas injection by varying the flow geometry or the flow conditions.

A theoretical model based on an overall force balance acting on the bubble during the two stages of generation is also developed. Two sets of forces, one aiding and other inhibiting bubble detachment are identified. The theoretical model predicts bubble diameter in good agreement with the reduced gravity experiments.

REFERENCES

[1]. S. Ostrach, *Industrial Processes Influenced by Gravity*, NASA CR-182140, C-21066-G, 1988.

[2]. S. Banerjee, *Space Applications*, Multiphase Flow and Heat Transfer: Bases and Application Workshop Santa Barbara, Calif., 1989.

[3]. S. C. Chuang and V. W. Goldschmidt, *Bubble formation due to a Submerged Capillary Tube in Quiescent and Co-flowing Systems,* J. Basic Eng., **92**, 1970.

[4]. I. Kim, Y. Kamotani and S. Ostrach, *Modeling Bubble and Drop Formation in Flowing Liquids in Microgravity*, AIChE Journal, **40**, 1, 1994.

[5]. C. Colin, J. Fabre and J. B. McQuillen, *Bubble and Slug Flow in Microgravity Conditions-I , Dispersed Bubble and Slug Flow*, Int. J. Multiphase Flow, **17**, 4, 1991.

[6]. A. E. Dukler, J. Fabre, J. B. McQuillen and R. Vernon, *Gas liquid Flow at Microgravity Conditions: Flow Patterns and Their Transitions*, Int. J. Multiphase Flow, **14**, 4, 1988.

[7]. N. Rabiger and A. Vogelpohl, *Bubble Formation and its Movement in Newtonian and Non-Newtonian Liquids*, in Encyclopedia of Fluid Mechanics, **3**, Gulf Pub. Houston, 1986.

[8]. H. Tsuge, *Hydrodynamics of Bubble Formation from Submerged Orifices*, in Encyclopedia of Fluid Mechanics, **3**, Gulf Pub. Houston, 1986.

[9]. O. Pamperin and H. Rath, *Influence of Buoyancy on Bubble Formation at Submerged Orifice*, Chem. Eng. Sci., **50**, 19, 1995.

[10]. H. Merte, Jr., H. S. Lee and R. B. Keller, *Report on Pool Boiling Experiment Flown on STS-47 (PBE-IA), STS-57 (PBE-IB) and STS-60 (PBE-IC)*, NASA CR-198465, 1996.

[11]. H. Nahra and Y. Kamotani, *Bubble Formation and Detachment in Liquid Flow Under Normal and Reduced Gravity*, 36th Aerospace Sciences Meeting & Exhibit, Reno, January, 1998.

[12]. H. N. Oguz, S. Takagi and M. Misawa, *Production of Gas Bubbles in Reduced Gravity Environments*, 3rd μg Fluid Phys. Conf, NASA Conf. Pub.-3338, 1996.

[13]. E. Sada, A. Yasunishi, S. Katoh and M. Nishioka, *Bubble Formation in Flowing Liquid*, Can. J. Chem. Eng., **56**, 1978.

[14]. J. B. McQuillen and E. S. Neumann, *Learjet Two Phase Flow Apparatus*, NASA TM 106814, NASA LeRC, 1995.

[15]. S. C. Pais, *Bubble Generation in a Continuous Liquid Flow Under Reduced Gravity Conditions*, Ph. D Thesis, Case Western Reserve University, 1998.

[16]. A. Bhunia, S. C. Pais, Y. Kamotani and I. Kim, *Bubble Formation in a Co-flow Configuration in Normal and Reduced Gravity*, Accepted for publication in AIChE Journal.

ACKNOWLEDGEMENT

We gratefully acknowledge support from the National Aeronautics and Space Administration, Grant number NAG3-1913, which made this work possible.

PRODUCTION OF GAS BUBBLES IN REDUCED-G ENVIRONMENTS

Hasan N. Oğuz, Jun Zeng, Department of Mechanical Engineering, The Johns Hopkins University, Baltimore, MD 21218, oguz@jhu.edu

1 Introduction

Bubbles in liquids are a common occurrence that can be found in many applications such as power generation, life support systems, cryogenic fluid handling, and chemical and biological reactors, gas-liquid mixtures (Zhao & Rezkallah 1993, Bousman et al. 1996, Kamotani 1996). Bubbles are typically produced by injecting gas into a liquid through a small orifice from which is they are removed by buoyancy. For a comprehensive review of this process see Kumar & Kuloor (1970). Under normal gravity, bubbles ascend through the liquid enabling gas transfer to occur and pop at the free surface. Both formation and removal of bubbles depend on the buoyancy force. In the absence of this force the process is quite different and the bubble may remain attached to the orifice indefinitely. Bubble formation becomes less reliable and harder to control. Other forces that may be safely neglected under normal gravity conditions become significant and may cause bubble detachment. For instance, Pamperin & Rath (1995) found that the inertia of the injected gas can lead to bubble detachment under weightlessness conditions. It is also possible to impose an electric field or a temperature field to exert an external force to the bubble. Another practical approach is to create an artificial flow around the bubble and force it out of the orifice (Kim et al 1994). In this paper, we have investigated the effect of an imposed flow on the bubble formation and detachment from underwater orifices for various cases. Experiments have been performed under normal gravity conditions and the working fluid was water. The process is modeled by axisymmetric and 3-D boundary integral techniques.

The simplest situation is when the flow is parallel to the gas injection direction so that the problem is axisymmetric. The usefulness of this idea in terms of reducing bubble size has been recognized a long time ago (Chuang & Goldschmidt 1970). The efficiency of this scheme is much better if the flow is bounded by a tube. We have studied this problem in detail and a brief description of the results is given in the next section.

2 Coaxial bubble formation in a tube

Here we report on a series of experiments of air bubble formation from a needle in a plexiglass tube filled with water. The needle is positioned coaxially in the center of the tube. The process is recorded by a CCD camera in conjunction with a 5 μsec strobe. Bubble generation frequency is measured by placing, in the path of bubbles, an infra-red beam of light carried by a fiber optic cable. Each time a bubble formed, a pulse is detected when the bubble crosses the light beam. Needles of inner diameters ranging from 100 μm to 400 μm are employed in the experiments. We have used a tube of radius 0.16 mm and also a smaller tube of radius 0.08 mm for the smallest needle.

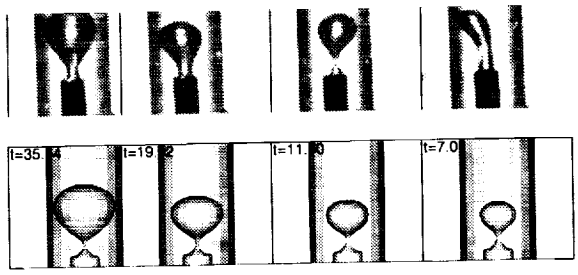

Figure 1: Comparison of bubble shapes as computed by the boundary integral simulations with experiments for four water flow rates. The tube diameter is 3.2 mm, needle O.D. 1.27 mm, I.D. 0.84 mm, Q_{air} = 0.22 ml/s, and Q_{water} from left to right 1.65, 2.69, 3.73, and 4.76 ml/s.

A remarkable characteristic of this flow is that bubble formation is quite regular with little or no variation from one bubble to another provided that water flow rate is sufficiently low. This regime is ideal for reliable production of bubbles of specified size. We have observed a substantial reduction in bubble size as the water flow rate is increased while the gas flow rate is kept constant (fig. 1). This behavior is common to other flow rates and needle sizes as well. A typical plot of bubble radius as a function of the average liquid velocity in the tube is shown in fig. 2 together with the axisymmetric boundary integral simulations. The agreement is remarkable despite the appreciable differences between the real and simulated bubble shapes at high liquid flow rates. Bubble size as a function of water velocity for smaller needles are also plotted in figs. 3,4.

The behavior of this system can be explained by using simple physical arguments. From fig 2,3 it is

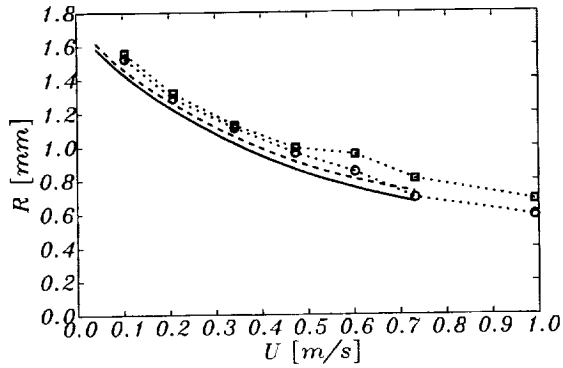

Figure 2: Bubble radius as a function of the average liquid velocity in the tube; Q_{air} circles 0.165 ml/s, squares 0.261 ml/s. boundary integral simulations (solid line for 0.165 ml/s, dotted line 0.261 ml/s), The tube diameter is 3.2 mm and the needle O.D. and I.D. are 1.27 mm and 0.84 mm respectively.

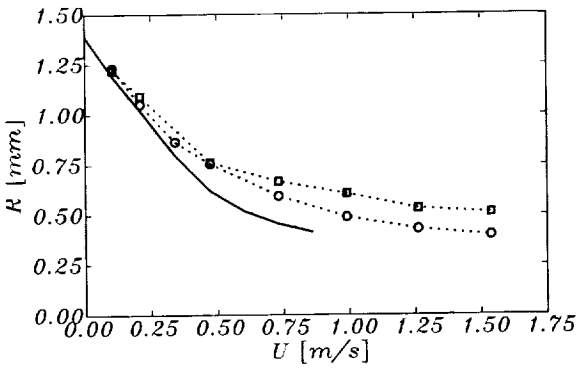

Figure 3: Bubble radius as a function of the average liquid velocity in the tube; Q_{air} circles 0.1 ml/s, squares 0.22 ml/s. boundary integral simulations (solid line for 0.1 ml/s, dotted line 0.22 ml/s), The tube diameter is 3.2 mm and the needle O.D. and I.D. are 0.7 mm and 0.4 mm respectively.

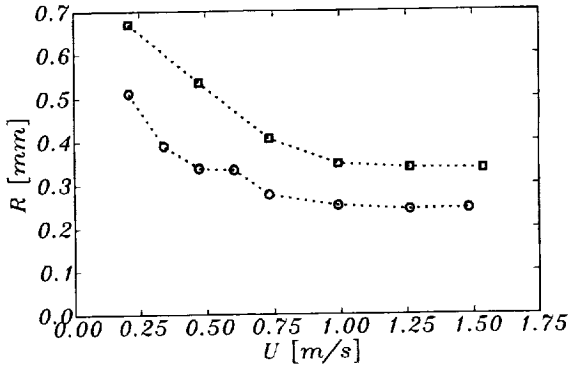

Figure 4: Bubble radius as a function of the average liquid velocity in the tube. Q_{air}: circles 0.05 ml/s, squares 0.195 ml/s). The tube diameter is 3.2 mm and the needle O.D. and I.D. are 0.4 mm and 0.2 mm respectively.

apparent that bubble size is solely determined by the liquid velocity and is relatively insensitive to the gas flow rate at low water flow rates. This is similar to the slow growth regime of Oguz & Prosperetti (1993) where the detachment size is given by a balance between surface tension and buoyancy and bubble acceleration can be neglected. In the present case, we need to consider the added mass force caused by the flow in the tube. There is a weak dependence on the gas flow rate since the bubble growth influences the magnitude of the added mass force. For the smallest needle where the tube diameter is much larger than the needle diameter, the effect of the added mass is less significant. As a result, bubble size depends on the gas flow rate as well as the water flow rate (fig. 4). When the needle size is not too small, the primary factor is the high sensitivity of the added mass force to the bubble radius. As the bubble size becomes comparable to the tube size, it is forced to follow the liquid in the tube. The fact that a very good agreement is obtained between experiments and potential-flow boundary-integral simulations shows that the dominant forces are surface tension and added mass forces in this regime. The viscous drag force acting on the bubble is typically small in comparison to other forces of the system.

As the bubble grows it remains attached to the needle due to the surface tension force. At some point the added mass force overcomes the surface tension and the bubble moves away from the needle. As a result, the neck that is formed between the bubble and the needle pinches off and the bubble departs freely in the tube. For the purpose of understanding different forces acting on the bubble a simple model for the bubble motion can be written as

$$\frac{d}{dt}\left[\rho\alpha_a V(\dot{Z}-U)\right] = \rho V g + f_v(\dot{Z}-U) - \frac{\sigma}{2\pi R_n} \quad (1)$$

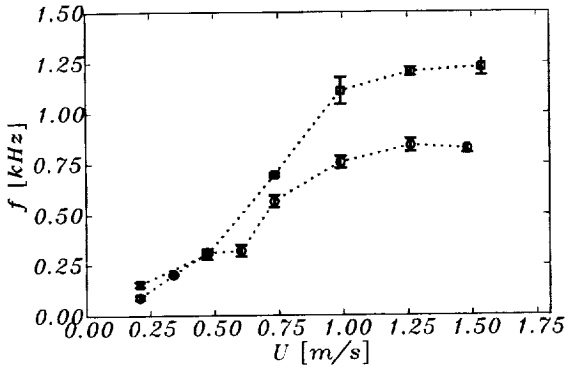

Figure 5: Bubble formation frequency as a function of the average water velocity for $Q_{air} = 0.05$ (circles) and 0.2 (squares) ml/s. The tube diameter is 3.2 mm and the needle O.D. and I.D. are 0.4 mm and 0.2 mm respectively.

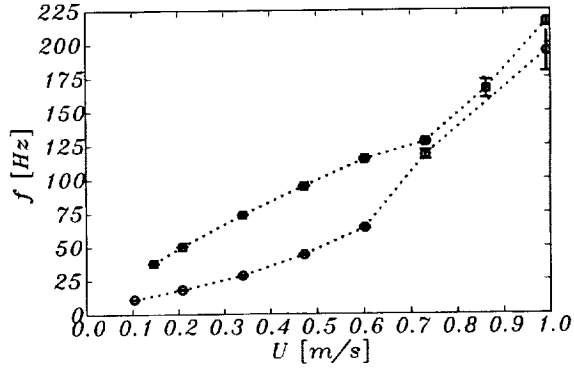

Figure 6: Bubble formation frequency as a function of the water velocity U for $Q_{air} = 0.17$ (circles) and 0.58 (squares) ml/s. The tube diameter is 3.2 mm and the needle O.D. and I.D. are 1.27 mm and 0.84 mm respectively.

where Z is the z coordinate of the bubble center, V the bubble volume, g the gravitational acceleration, f_v the viscous drag coefficient, $U = Q_{water}/\pi R_t^2$ the average water velocity in the tube, σ the surface tension, R_n the inner radius of the needle, ρ the water density. Here α_a is the added mass coefficient which is a strong function of the ratio of the bubble radius to the tube radius. For all the cases considered in this study, the liquid velocity U is always greater than the bubble center velocity $\dot{Z}$. As a result, both the added mass force and the viscous drag always act in the direction of the flow, forcing the bubble away from the needle. We have not investigated cases in which U is negligibly small because it leads to bubble coalescence and the tube fills up with gas eventually. The threshold velocity can be estimated by assuming that $\dot{R} = \dot{Z}$ assuming spherical growth. The condition $\dot{Z} < U$ (i.e. bubble lagging behind the flow) is satisfied when $U > Q_{air}/4\pi R^2$. Above this threshold bubble generation proceeds at a regular pace and becomes faster and faster as the water flow rate is increased. At some point, the pinch-off process which is governed by the surface tension cannot keep up with the flow and the reduction in bubble size stops.

There are two factors limiting the bubble size. The first one is based on a simple geometrical argument that the bubble radius cannot be smaller than the needle's outer radius, R_o. Since the needle is blocking the flow, growth always proceeds freely up to this limit. The maximum bubble frequency is therefore

$$f_b = \frac{3}{4\pi}\frac{Q_{air}}{R_o^3} \tag{2}$$

Bubble frequencies shown in figs. 5 and 6 are smaller than the values given by (2). These limits are 1430 Hz for the small needle and 158 Hz for the large needle at the smallest gas flow rates. Therefore the bubble size limits observed in figs. 2-4 are not due to the blocking effect of the needle.

The other limiting factor is the duration of the pinch-off process. The detachment of the bubble from the needle is a result of a capillary instability and it requires a very short but finite time to complete once the bubble shape becomes unstable. The pinch-off time can be estimated as

$$T_p = 2\pi\alpha_p\sqrt{\frac{\rho R_n^3}{\sigma}} \tag{3}$$

where α_p is a numerical factor of order one. If we compare this time with the characteristic time of the flow, R_n/U the ratio becomes a Weber number We, given by

$$We = \frac{\rho U^2 R_n}{\sigma}. \tag{4}$$

If We exceeds a certain critical value, bubble detachment cannot keep up with the flow. This point marks the transition from the regular bubble formation regime to the asymptotic bubble-size regime. It is difficult to determine the exact value of We_{crit} since the transition is rather smooth. Our measurements indicates that We_{crit} must be between 3 and 7.

Since T_p is the minimum time required to detach a bubble, formation frequency cannot be greater than $1/T_p$ and must reach an asymptotic value in the second regime. Indeed, we have observed that the measured bubble frequency is almost constant and only slightly affected by the gas flow rates in this regime in fig. 5. However, the frequency limit is much less apparent for the larger needles (fig. 6). We believe that this is due to

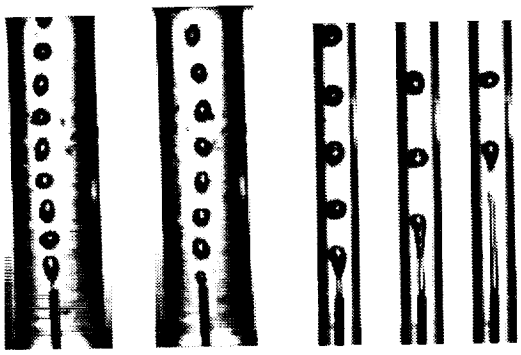

Figure 7: Bubble shapes for U = (from left to right) 126, 153 cm/s, tube diameter 3.2 mm, and 135, 188, 292 cm/s, tube diameter 1.6 mm. The gas flow rate is 0.195 ml/s and the needle O.D. and I.D. are 0.4 mm and 0.2 mm respectively.

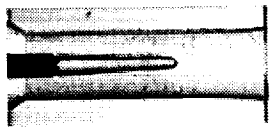

Figure 8: Steady bubble at U=2 m/s and the gas flow rate is zero. The tube diameter is 3.2 mm and the needle O.D. and I.D. are 1.27 mm and 0.84 mm respectively. This configuration can be used to create a steady gas-liquid interface in micro-gravity.

the stabilizing effect of the tube that prolongs the pinch-off process when the needle size is comparable to the tube size. As a consequence, the neck of the bubble gets longer with increasing water flow rates. The tube has little effect, on the other hand, when the needle is much smaller than the tube. The stabilizing effect of the tube is illustrated in fig. 7 where the neck of the bubble is shown to be longer under similar water flow rates for the same needle when a smaller tube is used. The bubble is more stable and, as a result, bigger bubbles are obtained in the case of the smaller tube.

At high flow rates, the bubble becomes elongated while remaining coaxial in the tube. In this regime bubbles are shed from the tip of the bubble. Even when the gas injection is stopped a stable gas cavity is observed to persist at the tip of the needle (fig 8). The shape of the bubble seems to be quite robust under these conditions. This configuration can provide a stable gas-liquid interface in micro-gravity.

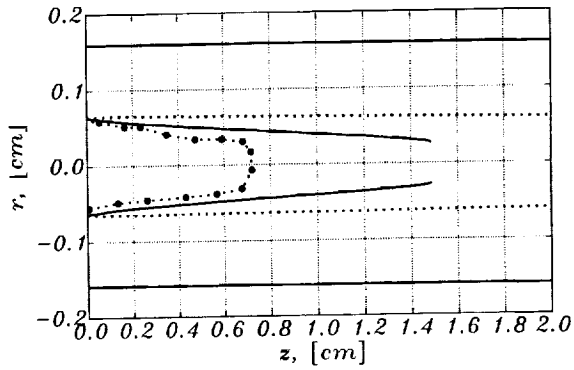

Figure 9: Comparison of elongated bubble shape as predicted by the theory (uniform initial profile solid line, parabolic profile dotted) with experiment (solid dots).

The flow field in this limit is reminiscent of the velocity profile adjustment of a viscous free jet after it exits a nozzle. The similarity is based on the fact that the boundary condition goes through an abrupt change in character as the flow passes through the needle surface and encounters the bubble surface. We have developed a new semi-analytical method to deal with a class of problems of this nature (Oğuz 1998). The application of the method to the present case is particularly interesting and is explained briefly in the following. The free surface flow shown in fig 8 can be considered as an annular jet where the outer boundary remains in contact with the tube's inner wall while the inner boundary is a free surface defining an elongated bubble. Because of the high aspect ratio of the bubble shape it can be approximated as a cylindrical gaseous region of constant pressure.

We start with the following representation of the cylindrical velocity components u, v, in the r and z direction respectively, which satisfies the boundary conditions $u = v = 0$ at $r = R_o$,

$$u = \sum_{n=1}^{\infty} a_n E_{00}(\lambda_n, R_o, r) \tag{5}$$

and

$$v = \sum_{n=1}^{\infty} b_n E_{01}(\lambda_n, R_o, r) - \frac{r}{R} E_{01}(\lambda_n, R_o, R_o). \tag{6}$$

Here we introduce the notation

$$E_{ij}(\lambda_n, R_o, r) = Y_i(\lambda_n R_o) J_j(\lambda_n r) - J_i(\lambda_n R_o) Y_j(\lambda_n r). \tag{7}$$

At the inner boundary i.e. bubble surface ($r = R_b$) the free shear condition leads to

$$E_{01}(\lambda_n, R_o, R_b) = 0 \tag{8}$$

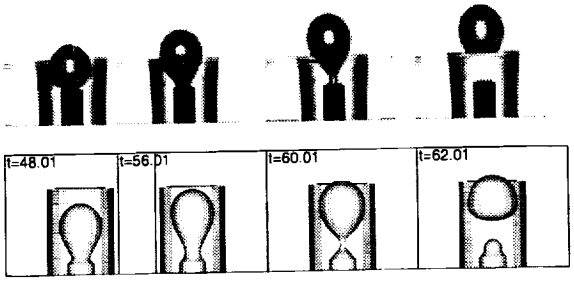

Figure 10: CCD images of of a bubble that is subject to an oscillatory flow field at 48, 56, 60 and 62 ms together with boundary integral simulations. Forcing frequency and amplitude of U are 15Hz and 13 cm/s. The tube diameter is 3.2 mm and the needle O.D. and I.D. are 1.27 mm and 0.84 mm respectively.

which constitutes an equation for λ_n.

After substituting eq (5) and (6) into the continuity equation and taking scalar products with $E_{00}(\lambda_m, R_o, r)$ we obtain an equation involving a_n, b_n, and dR_b/dz. The equation for dR_b/dz is obtained by taking the integral of the continuity equation from R_o to $R_b(z)$. The evolution equations for da_n/dz and dR_b/dz, which are essentially the scalar product of the momentum equation with the functions E_{00}, are integrated in the z direction. In fig. 9 we plot computed bubble shapes for parabolic and uniform initial velocity profiles together with the experimental shape that corresponds to that of fig. 8. The profile is straighter and therefore more stable for the parabolic case than for the uniform velocity case. The experimental profile matches the uniform-case more closely but the real bubble is much shorter than the computed one. Temporal fluctuations that are ignored by the theory may be present in the flow and destabilize the downstream end of the cylindrical bubble. A stability analysis in which the steady state is given by the present theory is required to resolve this issue.

3 Oscillatory flow

With the flow arrangement described in the previous section, we have shown that a precise control of the bubble size can be achieved at constant water flow rates. Since this setup may not be practical in some applications, an oscillatory flow in which the net water flux is zero could be a better alternative, eliminating the need of circulating liquid by means of a pump. We have conducted a

Figure 11: Comparison between experiment and boundary integral simulations for horizontal tube and eccentric needle cases. The gas flow rate is 0.22 ml/s. The tube diameter is 3.2 mm and the needle O.D. and I.D. are 1.27 mm and 0.84 mm respectively.

preliminary set of experiments in which an oscillatory flow field is imposed in the tube. Early indications show that it is possible to phase lock the bubble formation frequency to the forcing frequency under certain conditions. In the experiments the flow is actuated by a rubber membrane driven by a solenoid. In fig. 10 we show CCD images of the bubble growing from a needle and ejected in the outflow phase of the oscillation.

The principle of operation of this system can be described as follows. In the inflow phase of the oscillation, the growing bubble that is attached to the needle tip assumes an oblate shape. As a result, when the flow is reversed, the added mass force pushes the bubble away from the needle in a very efficient manner. Axisymmetric boundary integral modeling of this problem is not straightforward. The basic problem is that the flow separation at the exit of the tube is completely ignored by the potential flow theory. There have been attempts to correct this error in the past (Wjingaarden 1968). We have simply chosen to increase the tube length to account for the separation in an approximate way. In so doing, we have found a very good agreement between experiment and simulation (fig. 10).

4 Cross flow and 3-D effects

In several practical situations the process of bubble formation becomes three-dimensional. For instance, the orientation of the tube with respect to the gravitational field may cause the bubble to move off-center, towards the tube wall. The needle location with respect to the tube is another factor that renders the problem three-dimensional. The off-center placement of the needle is a typical situation of practical importance even in the absence of gravity and is considered in the present study.

We have developed a three dimensional potential-flow boundary-integral method that is applied to the cases mentioned above. For details of the problem formulation and the numerical procedure see Oğuz & Zeng

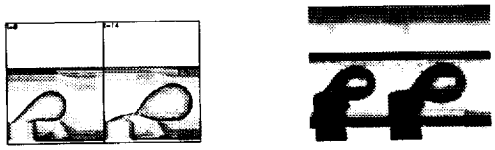

Figure 12: Cross-flow bubble formation in a tube: simulations and experiment. The average water velocity is 0.21 m/s. The tube diameter is 3.2 mm and the needle O.D. and I.D. are 1.27 mm and 0.84 mm respectively.

(1997). We have tested the model for several cases and a good agreement is found between experiment and simulations. In fig. 11 we show the last computed shapes of bubbles for the case of a horizontal tube gravity pointing downward and an off- center needle. The match between experiment and simulation is remarkable considering the complexity of the 3-D system. One problem with these cases is that the bubble tend to move towards the tube wall or to the needle surface during the simulation and the boundary integral system becomes singular. We have adopted a scheme in which an artificial force is applied to the relevant portion of the bubble surface when it gets too close to solid walls. We have found that the necessary force is comparable in magnitude to the lubrication force that would be present if we take into account the effect of viscosity.

Gas injection from a needle embedded in the tube wall is also investigated. As bubbles grow they are forced to deform in the direction of the flow due to the added mass force just as in the case of the coaxial formation of bubbles. When the shape becomes unstable the bubble neck pinches off. This case which is inherently three-dimensional and much more difficult to model than the previous ones has also relevance in micro-gravity boiling in tubes. In fig. 12 we show a comparison of the computed bubble shapes with experiment. The agreement is again remarkably good.

We plan to employ the 3-D code for problems involving multiple injection ports in various geometrical arrangements. The effect of the neighboring bubble on the growth process will be investigated. Our initial results show that simultaneous growth of several bubbles can lead to strong interaction that is independent of the inter-bubble distance. We also plan to study cases involving bubble removal by suction orifices.

The author would like to thank J. Libertini for her assistance in running the experiments. Work supported by the Micro-Gravity Science Program of NASA.

References

[1] W.S. Bousman, J.B. McQuillen, and L.C. Witte. Gas-liquid flow patterns in microgravity: effects of tube diameter, liquid viscosity and surface tension. *Int. J. Multiphase Flow*, 22:1035–1053, 1996.

[2] S.C. Chuang and V.W. Goldschmidt. Bubble formation due to a submerged capillary tube in quiescent and coflowing streams. *ASME J. Basic Engng.*, 92:705–711, 1970.

[3] Y. Kamotani. Bubble-generation in a flowing liquid medium and resulting two-phase flow in microgravity. In *Third Microgravity Fluids Conference*, NASA Lewis Research Center, Cleveland, Ohio, 1996.

[4] I. Kim, Y. Kamotani, and S. Ostrach. Modeling bubble and drop formation in flowing liquids in microgravity. *AIChE Journal*, 40:19–28, 1994.

[5] R. Kumar and N.R. Kuloor. The formation of bubbles and drops. *Adv. Chem. Engng. Edited by Drew, T.B. et al*, 8:256–368, 1970.

[6] H.N. Oguz. on the relaxation of laminar jets at high reynolds numbers. *Phys. Fluids*, 10:361–367, 1998.

[7] H.N. Oguz and J. Zeng. Axisymmetric and three-dimensional boundary integral simulations of bubble growth from an underwater orifice. *Engineering Analysis with Boundary Elements J.*, pages 319–330, 1997.

[8] O. Pamperin and H. Rath. Influence of buoyancy on bubble formation at submerged orifices. *Chem. Eng. Sci.*, 50:3009–3024, 1995.

[9] L.van Wijngaarden. On the oscillations near and at resonance in open pipes. *J. Eng. Math.*, 2:225–240, 1968.

[10] L. Zhao and K.S. Rezkallah. Gas-liquid flow patterns at microgravity conditions. *Int. J. Multiphase Flow*, 19:751–763, 1993.

VORTEX DROPLET FORMATION BY A VORTEX RING IN MICROGRAVITY

Luis P. Bernal, Pepi Maksimovic, Choongil Kim,
Department of Aerospace Engineering
University of Michigan

Please refer to the Conference Book of Abstracts or the NCMR Website at
http://www.ncmr.org

DECOUPLING THE ROLES OF INERTIA AND GRAVITY ON PARTICLE DISPERSION

D. E. Groszmann, J. H. Thompson, S. W. Coppen, and C. B. Rogers,
Tufts University, Department of Mechanical Engineering, Medford, MA 02155

ABSTRACT

Inertial and gravitational forces determine a particle's motion in a turbulent flow field. Gravity plays the dominant role in this motion by pulling the particles through adjacent regions of fluid turbulence. To better understand and model how a particle's inertia effects its displacement, one must examine the dispersion in a turbulent flow in the absence of gravity. In this paper we present the particle experiments planned for NASA's KC-135 Reduced-Gravity Aircraft, which generates microgravity conditions for about 20 seconds. We also predict the particle behavior using simulation and ground-based experiments. We will release particles with Stokes numbers of 0.1, 1, and 10 into an enclosed tank of near-isotropic, stationary, and homogenous turbulence. These particle Stoke numbers cover a broad range of flow regimes of interest. Two opposed grids oscillating back and forth generate the turbulent field in the tank with a range of turbulence scales that covers about three orders of magnitude and with turbulence intensities of about ten times the mean velocity. The motion of the particles will be tracked using a stereo image velocimetry technique.

Using a model for particle dispersion, which is supported by data from direct numerical simulations and quasi-numerical simulations, we estimate the average particle dispersion for our three Stokes numbers to be less than 20 cm after 10 seconds.

INTRODUCTION

Particle laden flows are common to both nature and man-made applications. There are many natural phenomena such as volcanic activity, sedimentation, and blood flow that involve the flow of a fluid interspersed with solid or semi-solid particles. Likewise, examples of man-made particle flows abound such as solid rocket combustion, dispersion of chemical and biological agents, paint sprays, and filtration systems. A majority of these applications occur in turbulent fluid environments that complicate the modeling process because the particles respond to the local fluid turbulence they see while moving through the fluid. Modeling these particle-laden flows is a necessary step in improving our understanding of the physics involved and consequently for designing new technologies in this area.

In addition to the inertial component, the movement of a particle in turbulent flow is greatly affected by gravity. Gravity pulls the particles through different "neighborhoods" of fluid turbulence, which complicates any experimental attempt to study its response to the surrounding fluid. That is, particles that respond to most of the fluid turbulence in the absence of gravity respond to a great deal less turbulence in the presence of gravity.

We have taken three different approaches to measure the response of the particles in order to model the effect of particle inertia on particle dispersion. First, Direct Numerical Simulation (DNS) allows us to vary the inertial effects in a simple turbulent field. Second, Quasi-Numerical Simulation (QNS), which is a hybrid numerical/experimental technique[1], allows for more complex turbulence fields but is limited to particles constrained to move in a two dimensional plane. Third, one can measure the dispersion of real particles in a turbulent airflow. This last method has the largest range of turbulence scales but provides little information on the fluid turbulence as seen by the moving particle. Traditional ground-based experiments of this type are limited because gravitational drift masks most of the inertial effects. Therefore, we have designed an experiment for tracking the motion of a single particle in a known turbulent field in the absence of gravity. The tests will be conducted onboard NASA's KC-135 Reduced-Gravity Aircraft (about 20 seconds of microgravity).

Few have been able to study these kinds of flows experimentally. Yudine[2] predicted that the particle would respond less to the turbulence than one might expect simply because gravity is pulling it through adjacent fluid neighborhoods. Csanady[3] expanded this work to show how increased drift would change the shape of the fluid velocity autocorrelation (continuity effect). Wells and Stock[4] used electrostatic charge to remove the influence of gravity. They found, for their single Stokes number case, that if the drift velocity is less than the turbulence intensity, the particle dispersion is independent of drift, implying that particle inertia does not play a dominant role. They were only able to run a single particle size, however, due to difficulties with their experimental setup. In our current set of experiments, we plan on investigating the behavior of at least 3 different particle sizes for Stokes numbers of 0.1, 1 and 10.

APPROACH

The experimental component to our research program involves studying particle dispersion through a turbulent fluid in the absence of gravity. The tests

will be conducted onboard NASA's KC-135 Reduced-Gravity Aircraft that provides about 20 seconds of microgravity. This is sufficient to achieve dispersion times of desirable length. We will release particles of various sizes in an enclosed tank of grid-generated, isotropic, and stationary turbulent airflow and track their dispersion using a stereo image velocimetry technique. Although the data collected will provide less information than our other methods regarding the turbulence seen by the particles, it will extend the range of turbulent scales experienced by the particle and include particle motion in all three dimensions.

Our experimental apparatus (see Figure 1) consists of a closed rectangular Plexiglas tank measuring 30.5 x 30.5 x 61 cm with two grids on opposite sides of the tank. The grids are moved back and forth, sinusoidally 180 degrees out of phase with each other using a pair of stepper motors and a crank-slider mechanism that are located outside of the tank. The grid's mesh size (2.54 cm), stroke length (4.5 cm), and oscillation frequency (6 Hz) have been optimized to produce a turbulent flow field with about three orders of magnitude in scales. Characterized by a near-zero mean velocity, the isotropic turbulence in this type of flow is desirable for its simplicity, with the generated turbulence in the plane parallel to the grid being homogenous and decaying in a self-similar manner relatively far downstream from the grid. The stationary and isotropic turbulent conditions are ideal for studying particle dispersion because the particles will remain in a relatively small volume, facilitating the techniques for tracking their dispersion.

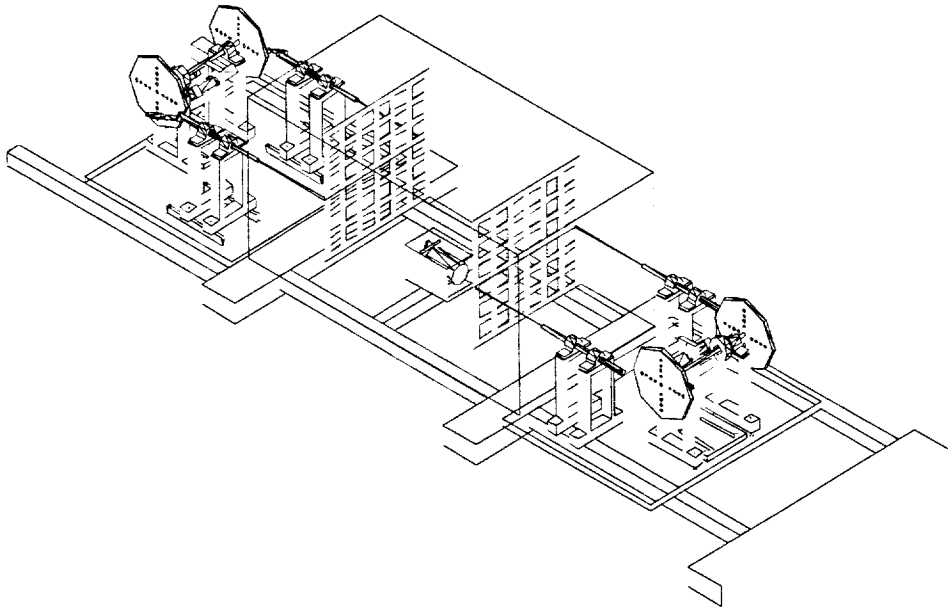

Figure 1. Experimental Apparatus

At the start of every run, we insert the particles into a desired interrogation volume in the tank using an injection system that propels one or more particles upward from the initial resting position. The injection system consists of a semi-rigid plastic dish that is hit from below by a lever operated by a DC servomotor (see Figure 2). The motor speed is regulated to place the particle at the desired tank location with a minimum in mean velocity. Any velocity imparted to the particle by the injection system will damp out in about three to four particle time constants due to the exponentially decaying nature of particle velocity.

The solid particles consist of hollow ceramic spheres (PQ Corporation) with diameters of 100 μm and 300 μm and glass beads (GlenMills, Inc.) of 500 μm to provide particle Stokes numbers of 0.1, 1, and 10, respectively. Because of the Stokes number dependence on particle mass, we are using hollow ceramic spheres to allow for larger particle diameters with the smaller Stokes numbers. The density ratio of the particle to the air is on the order of 10^3, which allows us to simplify the particle transport equation. The dominance of electrostatic forces typical for these small particles makes it necessary to place only one or few particles in the interrogation volume of the stereo image velocimetry (SIV) system at the onset of every parabolic trajectory.

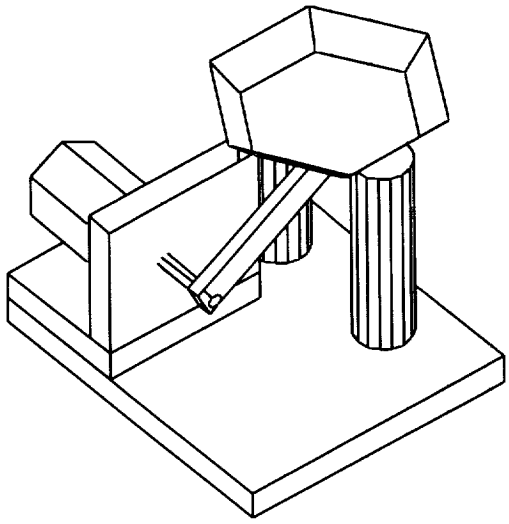

Figure 2. Particle Injector

The SIV apparatus (see Figure 3) incorporates a single color video camera and several filters and mirrors to capture orthogonal views of the particles in the tank. Light from the particles will bounce off each first-surface mirror and continue through the filters that color the image either blue or red. The two orthogonal images (red and blue) are then combined with a beamsplitter and stored via a Sony DXC-950 color video camera onto a Hi-8 cassette. The entire experimental system is housed in an equipment rack that is bolted to the floor of the KC-135 as shown in Figure 4.

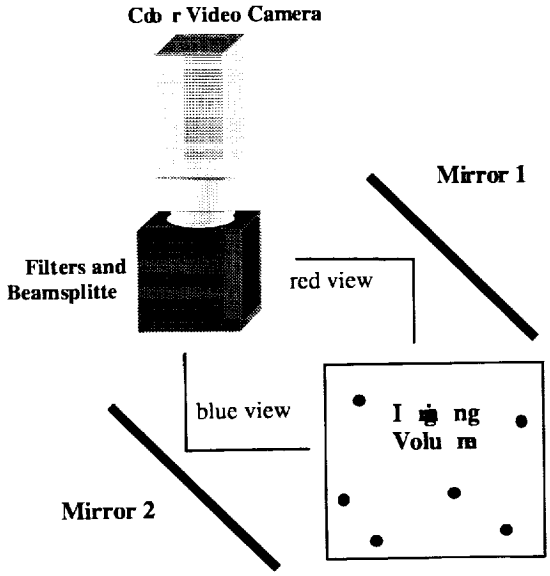

Figure 3. SIV Apparatus

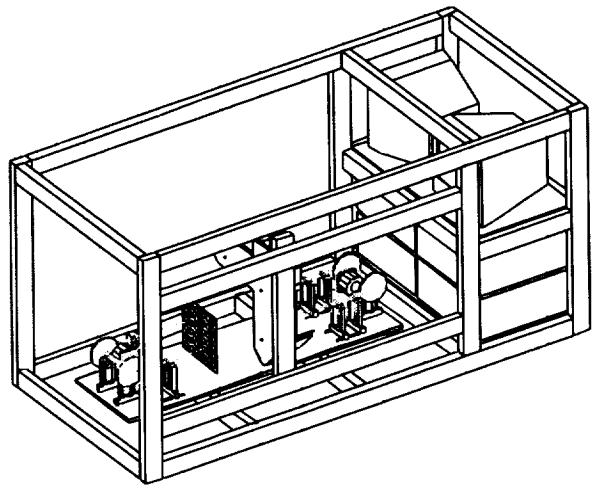

Figure 4. Equipment Rack

RESULTS

Laser Doppler Velocimetry (LDV) measurements inside the tank of grid-generated turbulence at varying distances from the grids were used to characterize the flow parameters before conducting the microgravity experiments[5]. Initially, only one oscillating grid was used to generate the turbulence in the tank. Results from these measurements, as seen in Figure 5, show that the turbulence is near-isotropic since the ratio of turbulence intensities in the forced (u') and unforced (v') directions are close to one. The data was taken while moving away from the grid (x direction) and is normalized by the grid mesh length.

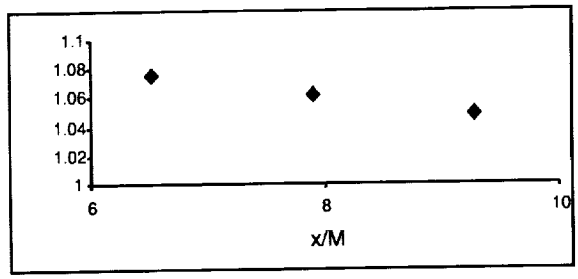

Figure 5. Ratio of u'/v' Moving Away from the Grid

A problem we encountered with the one grid approach was the presence of a mean velocity in the flow of air in the tank. Figure 6 shows the velocity profiles in the forced and unforced directions and the non-zero mean, especially in the forced direction. Preliminary results using the two-grid approach has reduced the mean velocity and increased the turbulence intensity to ten times this mean velocity, while maintaining the near-isotropy. We are currently experimenting with this grid system to improve on these results.

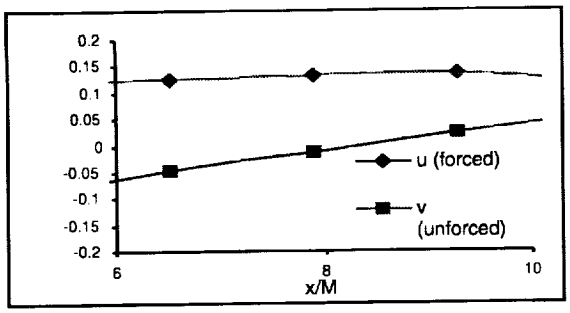

Figure 6. Mean Velocity Profiles

The goal of our upcoming microgravity experiments is to examine the dispersion of three different size particles, which characterize three regimes in particle flow. A Stokes number of 0.1 is representative of a flow where the particle closely follows the fluctuations in the velocity of the surrounding fluid. In the other extreme, a Stokes number of 10 will respond very little to the carrier fluid much like a boulder falling through air. In between, we will examine the case with a Stokes number of 1.

To estimate what we will see in the microgravity experiments, we can use results from our DNS[6] and QNS[5] techniques. Particle dispersion measurements were obtained from the DNS simulation for Stokes numbers that ranged from 1.21 to 3.44 in the absence of gravity for a Reynolds number, based on the Taylor microscale, of 42. The Stokes numbers were calculated by dividing the particle integral scale by the fluid integral scale. Particle dispersion measurements were estimated for the QNS method at a channel Reynolds number of 6600 in the absence of gravity. As expected, these data confirm that smaller particles disperse more than larger particles. The smaller the particle, the more it is affected by the variations in the fluid velocity. Larger particles have too much inertia to respond to all of the fluctuations of the flow and therefore disperse less. We can model this behavior[7] and estimate the average dispersion of our three particle sizes using the following:

$$\overline{y_2^2(t)} = 2\overline{u_f^2}T_f^2(1+St)\left\{\frac{t}{T_f(1+St)} - \left[1 - e^{\frac{-t}{T_f(1+St)}}\right]\right\}$$

where the T_f is the integral scale of the fluid velocity, $\overline{u_f^2}$ is the mean squared fluid velocity, and St is the Stokes number.

By normalizing the DNS and QNS dispersion measurements by a characteristic length of particle fluctuations, $y^* = \overline{y_2^2(t)} / 2\overline{u_p^2}T_p^2$, and normalizing the time with T_p, we can collapse all runs onto a single curve as shown in Figure 7.[5] This is true regardless of Stokes number, flow conditions and measurement method. For our microgravity experiments then, after 10 seconds, particles with Stokes numbers of 0.1, 1, and 10 will have average displacements of 19.8, 19.6, and 17.8 cm respectively.

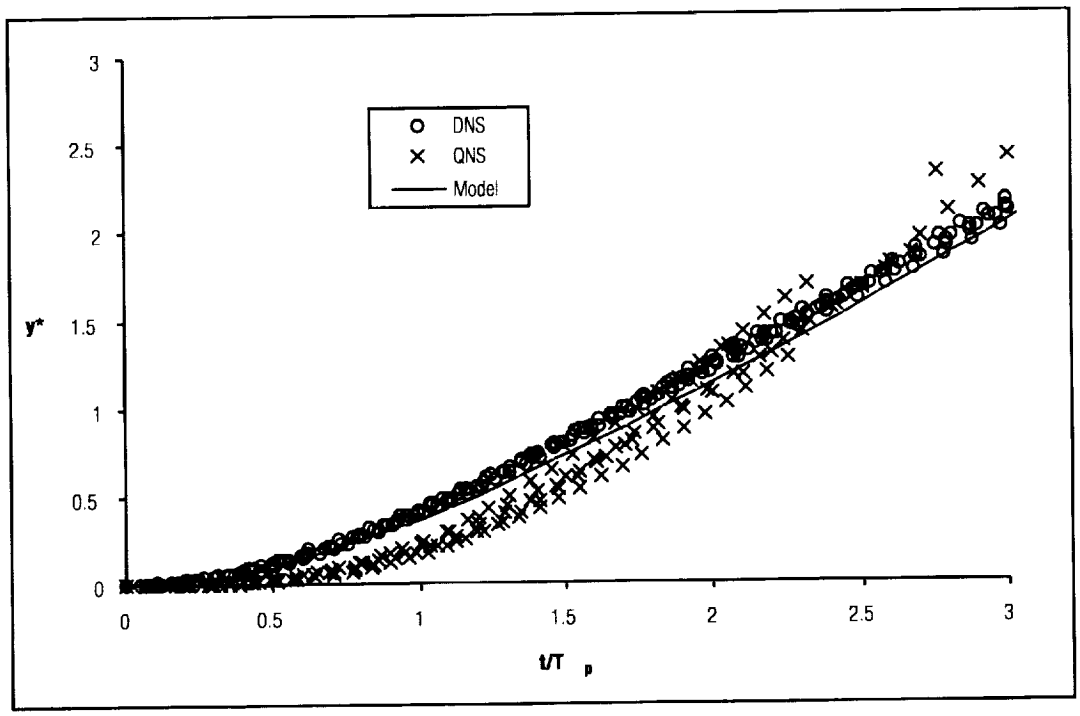

Figure 7. Particle Dispersion Comparison of DNS and QNS with the Model

CONCLUSION

Results from DNS and QNS show that particle dispersion decreases with increasing Stokes number as one might expect. In addition, for particles of constant Stokes number, greater turbulence results in more dispersion. These methods also verified the dispersion model.

Our next step is to examine the inertial effects on particle dispersion in the absence of gravity for a larger range of turbulence scales. Particles will be released inside an enclosed tank of grid-generated, isotropic turbulence while in NASA's KC-135 Reduced-Gravity Aircraft. In the 20 seconds of microgravity, we will track the dispersion of these particles, which range from 0.1 to 10 in Stokes number, using a three-dimensional stereo image velocimetry technique. Using a dispersion model verified by DNS and QNS results, we estimate that these particles will have an average dispersion of less than 20 cm. Removing the masking effects caused by gravity will allow us more insight into the role of inertia on particle dispersion.

ACKNOWLEDGEMENTS

This work was funded by NASA's microgravity research division. We would like to thank Professors K.D. Squires of the University of Arizona and V.P. Manno of Tufts University for their assistance with this research.

REFERENCES

[1] Ainley, S., Eaton, J.K., and Rogers, C.B., "Technique for Fluid Velocity measurements in the Particle-Lagrangian Reference Frame," ASME FEDSM97-3570, 1997.

[2] Yudine, M.I., "Physical Considerations on Heavy-Particle Diffusion," In Atmospheric Diffusion and Air Pollution: *Adv. Geophys*, 6, pg. 185-191, 1959.

[3] Csanady, G.T., "Turbulent Diffusion of Heavy Particles in the Atmosphere," *J. Atmos. Sci.*, 20, pg. 201-208, 1963.

[4] Wells, M.R. and Stock, D.E., "The effects of Crossing Trajectories on the Dispersion of Particles in a Turbulent Flow," *J. Fluid Mech.*, 136, pg. 31-62, 1983.

[5] Thompson, J.H., Coppen, S.W., Ainley, S.B, and Rogers, C.B., "Isolating the Role of Gravity on Particle Dispersion," AIAA98-0658, 1998.

[6] Coppen, S.W., "Particle Behavior Using Direct Numerical Simulations of Isotropic Turbulence," Doctoral Thesis, Tufts University, Medford, MA, 1998.

[7] Ainley, S., Coppen, S., Manno, V.P. and Rogers, C.B., "Modeling Particle Motion In a Turbulent Air Flow," ASME FEDSM97-3176, 1997.

BUBBLE DYNAMICS ON A HEATED SURFACE

M. Kassemi[1], N. Rashidnia[2], [1,2]NCMR, NASA LeRC, Cleveland OH 44135, Mohammad.Kassemi@lerc.nasa.gov, Nasser.Rashidnia@lerc.nasa.gov

INTRODUCTION

In this work, we study steady and oscillatory thermocapillary and natural convective flows generated by a bubble on a heated solid surface. Behavior of bubbles in terrestrial applications has been subject to extensive research especially as related to boiling processes. As a result, various procedures have been developed to minimize and control the problem of gas bubbles or exploit their properties on earth. In the microgravity environment, however, bubbles will behave in a significantly different manner and are expected to be more problematic. Therefore, understanding the intricacies of the Marangoni convection generated by bubbles is not only beneficial for terrestrial applications but may prove to be essential for controlling space processing experiments and interpreting their results.

The interaction between thermocapillary and natural convection flows can be very complicated. Experimental observations made in our Laboratory and those reported by other investigators[1] indicate that above a critical Ma number, the temperature and flow fields exhibit several complicated symmetric and asymmetric oscillatory modes. Previously, we studied the steady state thermocapillary and natural convection generated by a bubble on a heated solid surface in 1-g and low-g environments[2]. In this work, we focus on the transient flow and temperature fields generated by the bubble below and above the critical Ma number. It will be shown that below the critical Marangoni number, steady state conditions are attainable. In this situation, we compare the steady state numerical solutions predicted by our transient solver (by marching through time) with experimental results recently published by Wosniak and Wosniak[3]. Above the critical Marangoni number, we will show both numerically and experimentally that a symmetric oscillatory thermocapillary flow is generated by the bubble in 1-g. We will discuss the nature, origin, and dynamics of this oscillatory behavior in detail.

THEORETICAL BACKGROUND AND EXPERIMENTAL SETUP

Consider the enclosure containing a liquid (silicone oil) with a bubble injected and kept stationary at the inside of the top wall as shown in Fig. 1. The side walls are insulated and the temperature of the top and bottom walls are uniformly maintained at T_h and T_c, respectively. Therefore, a thermally stratified state is established in the enclosure before the bubble is introduced. Once the bubble is positioned and the interface between the air and the test liquid is formed, surface tension forces created by the temperature gradient along the interface will drive a thermocapillary convective flow. This thermocapillary flow disrupts the thermal stratification near the bubble resulting in significant temperature gradients and convection near the bubble surface.

The experimental setup designed and constructed to quantify the thermocapillary flow generated by the bubble consists of three main components; the test cell and the injector, the Mach-Zehnder Interferometer (MZI) or the Wollaston Prism Interferometer (WPI), and the laser sheet flow visualization unit. The onset of the thermocapillary and natural convection flows is determined by observing the interferometric fringe patterns created by the temperature field and visualizing the velocity field near the bubble using a laser sheet. A schematic of the test cell which is made of large optical glass widows suitable for interferometric measurements is shown in Fig. 2

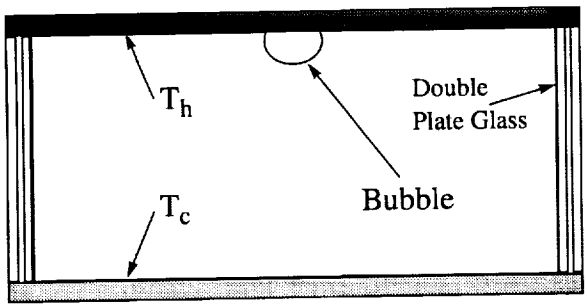

Figure 1. Schematic of The Test Enclosure.

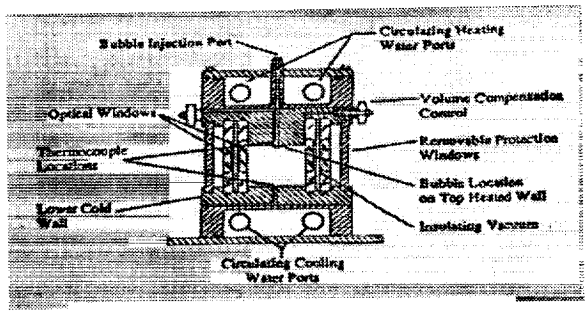

Figure 2. Schematic of The Test Cell

A transient two-dimensional model is developed which describes the fluid flow and heat transfer induced by the bubble in terms of the continuity, momentum and energy equations. For details of the numerical and experimental procedures the reader is referred to Kassemi and Rashidnia[4].

RESULTS AND DISCUSSION

Steady State Results

In order to gain insight into the flow and temperature fields generated by the bubble, we first compare steady state solutions predicted by our transient numerical model with 1-g and low-g steady state experimental results provided by Wosniak and Wozniak[3] which are included in Figs. 3 and 4. Wozniak's reduced gravity results were obtained during the European TEXUS 33 sounding rocket experiments with low-gravity conditions of about 6 minutes duration.

The numerical simulations are generated by marching through time until steady state temperature and velocity fields are achieved. In the ground-based case, the numerical simulations are performed for Re = 4300, Gr = 2400, Pr = 122. Initially a hemispherical bubble shape is assumed by the model but the bubble shape changes very fast to accommodate the forces exerted upon it. At 1g, due to the presence of the large hydrostatic force, the steady state bubble shape predicted by the model, is much flatter than its originally assumed exact hemispherical shape. In this case, because of the simultaneous action of the buoyancy and thermocapillary forces, a vigorous thermocapillary vortex coexists with two weaker vortices below the bubble as shown by the streamlines in Fig. 5. The strongest vortex driven by the thermocapillary force fills the top portion of the enclosure next to the bubble. It carries the fluid down along the surface of the bubble creating a strong boundary layer flow which is revealed by the packing of streamlines near the interface. The temperature contours around the bubble are moderately distorted by this flow as indicated in Fig 5. The steady state bubble shape and temperature and fluid fields (which prevail at t=180s and beyond) are in excellent agreement with the steady state results of Wozniak reproduced in Fig. 3a.

Next, conditions pertinent to Wozniak's microgravity experiment are considered for g = $10^{-4}g_o$, Ma = 1830, Ra = 0.25, Pr = 122. Note that a vigorous thermocapillary flow is generated next to the bubble surface. But in contrast to the terrestrial examples presented in Fig. 5, this time a natural convective flow will not ensue due to the reduced buoyancy force. As a result, the recirculating thermocapillary vortex will grow unopposed until it nearly fills the entire enclosure at steady-state. The streamlines of Fig. 6 clearly show that the microgravity flow pattern resembles a jet-like flow emanating from around the bubble and flowing downwards into the enclosure. As a result of this intense recirculating flow, the temperature field is greatly altered. Again, there is excellent agreement between our numerical predictions and the experimental results of Wozniak for bubble shape and the velocity and temperature profiles even though

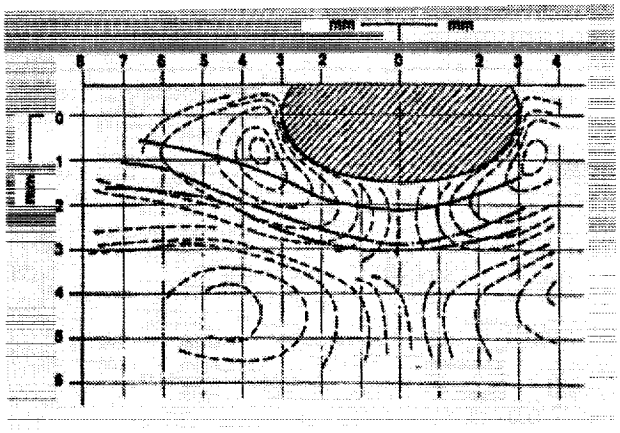

Figure 3. 1-G Experimental Temperature and Streamline Contours for Ma = 2440, Ra= 500, and Pr=122 (Wozniak and Wozniak[3]).

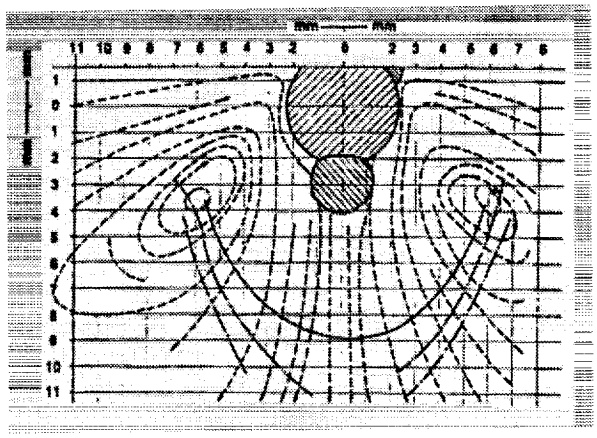

Figure 4. Low-G Experimental Temperature and Streamline Contours for Ma = 1830, Ra= 0.25, and Pr=122 (Wozniak and Wozniak[3]).

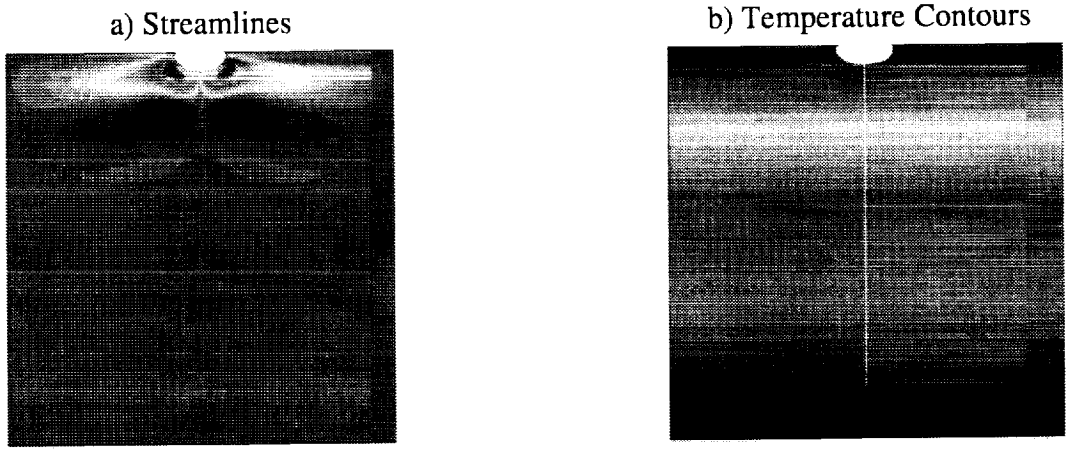

Figure 5. 1-G Numerical Predictions of a) Streamlines, b) Temperature Contours, and Bubble Shape for Ma=2440, Ra=500, and Pr=122 at t=180s.

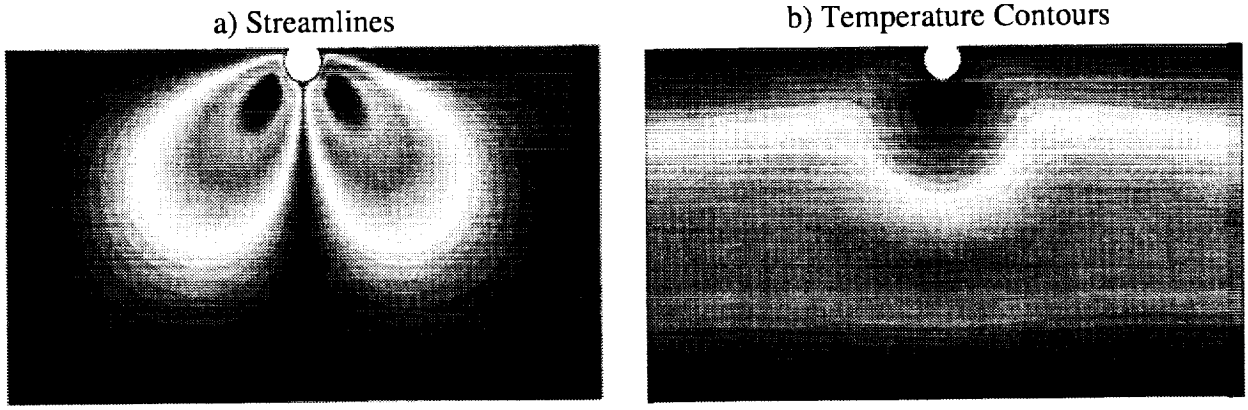

Figure 6. Low-G Numerical Predictions of a) Streamlines, b) Temperature Contours, and Bubble Shape for Ma=1830, Ra=0.25, and Pr= 122 at t=200s.

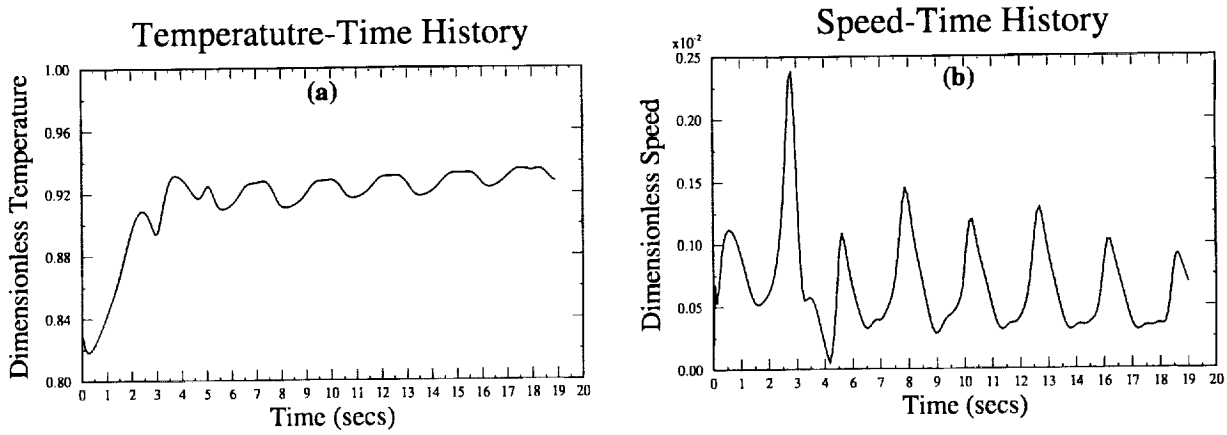

Figure 7. Temperature-Time History (a) and Velocity-Time History (b) of a Point on the Bubble Surface for Ma= 90,000, Ra=50,000, and Pr=8.4.

during the low gravity experiment an unexpected smaller bubble formed and remained attached to the larger bubble.

Unsteady Flows Beyond The Critical Ma Number

Experiments performed in our laboratory indicate that beyond a critical Ma of approximately 12,000 the flow and temperature fields undergo several oscillatory modes depending on the value of the Ma number. The interferograms (presented in Fig. 8a) show the oscillatory temperature field which occurs at Ma = 90,000, Ra = 20,000, Pr=8.4. The oscillations are symmetric and are accompanied by an up and down periodic motion in the fluid.

The temperature-time and velocity-time history of a point on the bubble surface obtained during the numerical simulation of the high Ma number case are presented in Fig. 7. In this situation, the flow and temperature fields develop much along the same lines as the 1-g low Marangoni case discussed previously but at around 6s, because of the strength of the convection, the velocity and temperature fields go into a periodic oscillatory mode. The numerical simulations of this high Marangoni case show an intricate interplay between heat and momentum transfer as depicted in Figs. 8b-c and 19a-b for one period of oscillation. Figs. 8b and c show that initially at t = 0, the vigorous thermocapillary vortex which is near the lower portions of the bubble brings the hot fluid down the surface of the bubble while taking the colder fluid from the inner regions of the enclosure up into an area close to the bubble. This flow will modify the temperature field drastically creating a cold finger near the bubble surface as shown in Fig. 8b ($t = 2\pi/5\text{-}6\pi/5$). This cold finger is the main cause of the instability. The corresponding interfacial temperature and velocity distributions are presented in Fig. 9 for one period of oscillation. At the beginning of the cycle t = 0, the temperature drops drastically near the hot wall and then monotonically decreases at a much smaller slope as the top of the bubble is approached. The interfacial velocity also achieves its maximum in the high temperature gradient region near the hot wall and monotonically decreases to zero as the top of the bubble is approached. As the cold finger forms and grows ($t = 2\pi/5\text{-}6\pi/5$), touching the bubble interface, it perturbs the interfacial temperature profile by creating a temperature dip on the surface. This increases the tangential temperature gradient in the base region as shown in Fig. 9a and creates a gradient reversal further down along the interface. Fig. 9b shows that as a result of this temperature dip, the fluid velocity is reduced to zero for a good portion along the bubble surface. The net effect of these changes is to push the center of the thermocapillary vortex up towards the hot wall as shown at $t = 4\pi/5\text{-}6\pi/5$ in Fig. 8c. At this new location, the vortex will draw from the warmer fluid near the hot wall which to-

a) Sequence of Interferogram Fringe Patterns around The Bubble During One Period of Oscillation

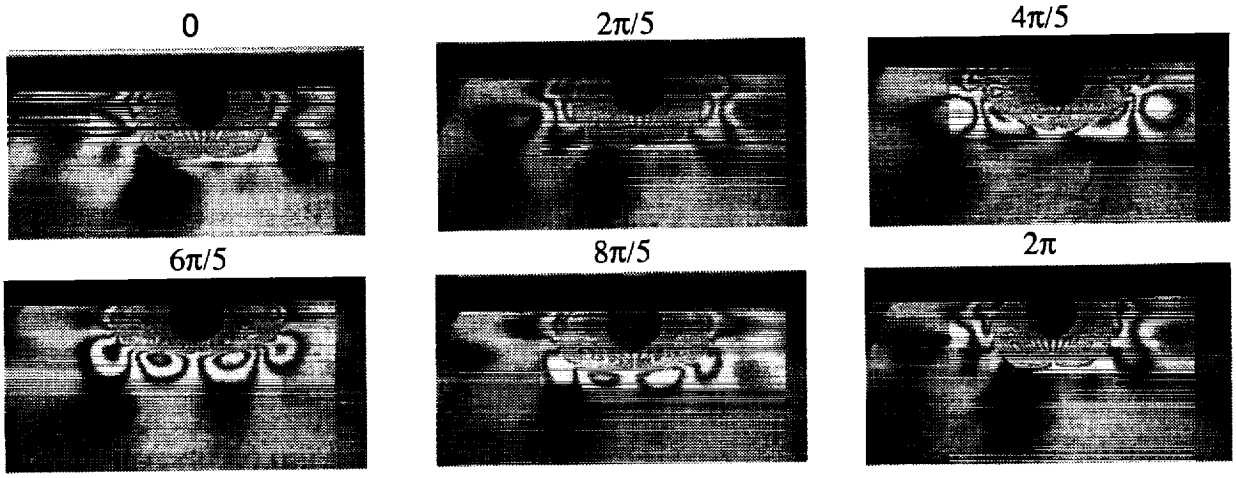

b) Numerical Predictions of Temperature Contours around The Bubble During One Period of Oscillation

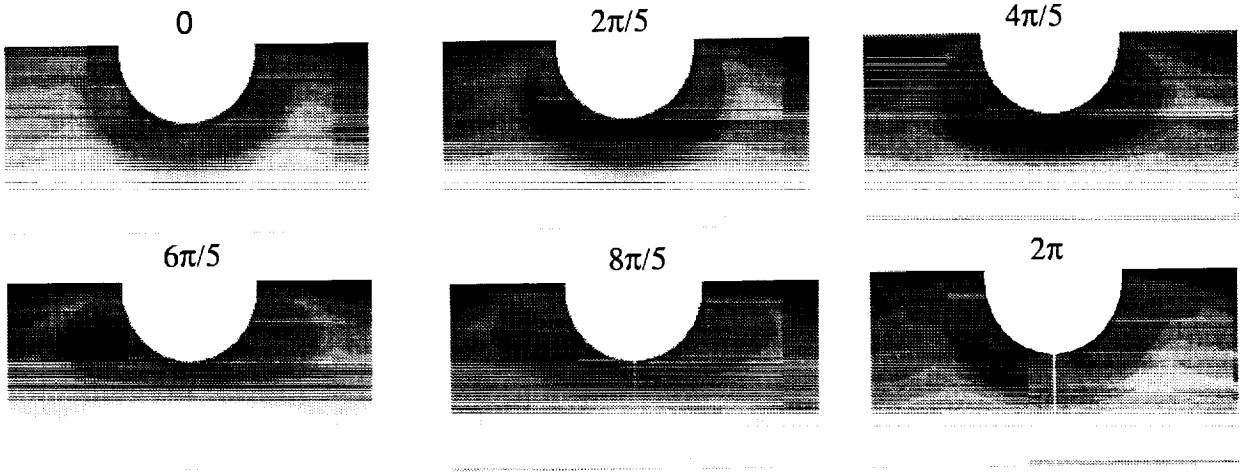

c) Numerical Predictions of Streamline Contours During One Period of Oscillation in The Entire Enclosure

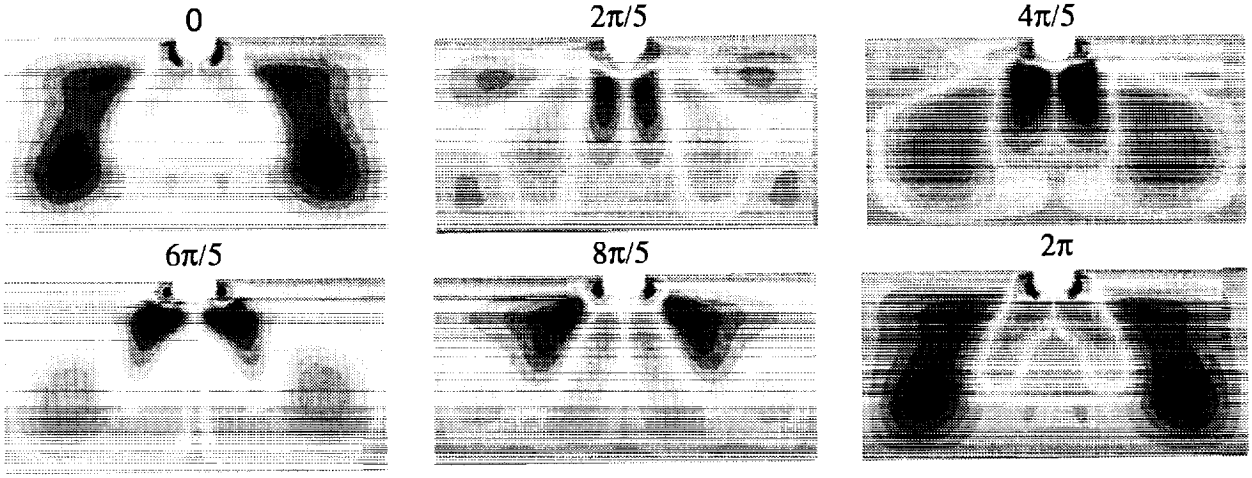

Figure 8. 1-G a) Experimental Interferograms (WPI) and Numerical Predictions of b) Temperature and c) Streamline Contours During One Period of Oscillation for Ma=90,000, Ra=50,000, and Pr= 8.4.

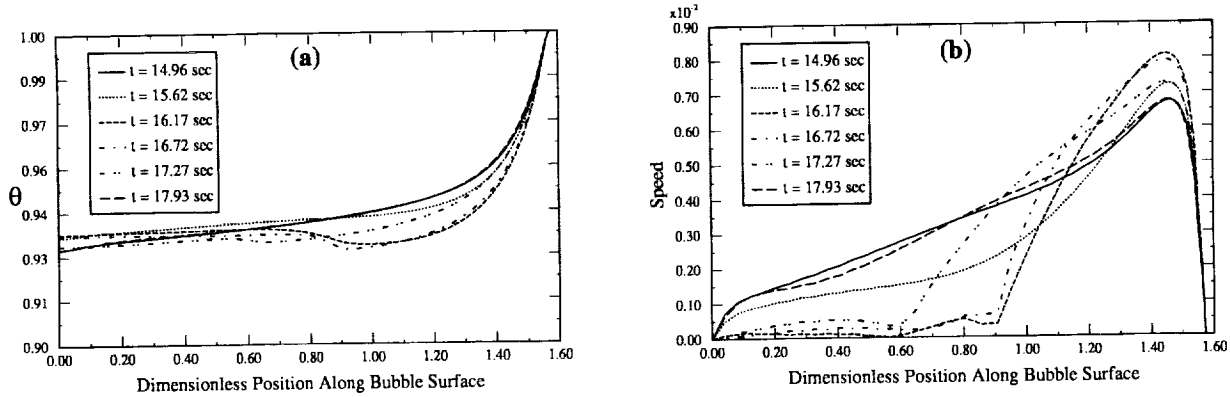

Figure 9. Interfacial Temperature (a) and Velocity (b) Profiles During One Period of Oscillation for Ma= 90,000, Ra=50,000, and Pr=8.4 (The Origin Corresponds to The Intersection of Bubble with The Centerline).

gether with the vigorous mixing action will tend to gradually diminish the cold finger as shown in time sequences $8\pi/5$-2π. As the cold finger diminishes, the temperature dip on the bubble surface disappears, relaxing temperature gradients near the base and increasing the velocity along the bubble surface. Finally, at t = 2π, the thermocapillary vortex returns to its original position near the base of the bubble and one period of oscillation is completed. The streamline contours of Fig. 8 show that this complex interplay between transport of heat and momentum results in a virtual pumping action first pushing down and then pulling up the fluid from below the bubble.

CONCLUSIONS

In this work a combined experimental-numerical approach is adopted to investigate the steady and oscillatory fluid flow and temperature fields created by a bubble attached to a heated solid surface. Both experimental observation and numerical predictions indicate that the thermocapillary flow induced by bubbles on earth is greatly influenced and affected by its inevitable interactions with buoyancy-driven convection. Below the critical Marangoni number, the steady state low-g and 1-g temperature and velocity fields predicted by the finite element model are in excellent agreement with both visualization experiments in our laboratory and recently published experimental results in the literature. Above the critical Marangoni number, the model predicts an oscillatory flow which is also closely confirmed by experiments. It is shown that the dynamics of this oscillatory flow are directly controlled by the thermal and hydrodynamic interactions brought about by combined natural and thermocapillary convection. Therefore, as the numerical simulations show, there are considerable differences between the 1-g and low-g temperature and flow fields at both low and high Marangoni numbers. This has serious implications for both materials processing and fluid management in space.

ACKNOWLEDGMENT

The authors wish to gratefully acknowledge the support provided by the Computational Microgravity Laboratory. This work was supported by NASA Microgravity Science and Applications.

REFERENCES

1. Raake, D., Siekmann, J., Chun, CH.-H., *Temperature and Velocity Fields Due to Surface Tension Driven Flow*, **Experiments in Fluids**, Vol. 7, pp. 164-172, 1989.
2. Kassemi. M. and Rashidnia, N., *Thermocapillary and Natural Convective Flows Generated by a Bubble in 1-G and Low-G Environments*, Technical Paper AIAA 96-0743, 1996.
3. Wozniak, G. Wozniak, K., and Bergelt, H., *On the Influence of Buoyancy on the Surface Tension Driven Flow around a Bubble on a Heated Wall*, **Experiments in Fluids**, Vol. 21, pp. 181-186, 1996.
4. Kassemi. M. and Rashidnia, N., *Steady and Oscillatory Flows Generated by a Bubble in 1-G and Low-G Environments*, Technical Paper AIAA 97-0924, 1997.

A THREE-DIMENSIONAL LEVEL SET METHOD FOR DIRECT SIMULATION OF TWO-PHASE FLOWS IN VARIABLE GRAVITY ENVIRONMENTS

F. Beaux, B.A. Knowlton and S. Banerjee
Chemical Engineering Department
University of California – Santa Barbara

Please refer to the Conference Book of Abstracts or the NCMR Website at http://www.ncmr.org

Session 2B

Colloids

SHEAR-INDUCED MELTING OF AQUEOUS FOAMS.

A. D. Gopal and D. J. Durian, UCLA Dept. of Physics and Astronomy.

INTRODUCTION

Aqueous foam is a nonequilibrium collection of polydisperse gas bubbles packed in a smaller amount of water containing surfactants, or other surface-active macromolecules [1-7]. These preferentially adsorb at the gas-liquid interfaces and give rise to repulsive forces which prevent bubble coalescence. The typical bubble size can range from 10 μm to 1cm, and their minimum surface separation distance, i.e. the soap film thickness, can range from 10 Å to 1 μm. The volume fraction of liquid can be as small as 0.01%, such that the bubbles are nearly polyhedral, or as large as about 8% on earth, such that the bubbles appear slightly spherical. If made wetter, however, the liquid will rapidly drain under the influence of gravity; thus, the close-packing limit of about 35% liquid, where the bubbles are perfectly spherical, cannot be reached on earth. Much is known about the behavior of surfactants at interfaces and about the behavior of soap films, including their relation to surfactant and liquid properties[8-13]; however, much less is known about the behavior at larger length scales. In particular, we do not know how to fully describe and extract the salient features of structure and dynamics at the bubble scale, or how to use this information to predict rheological behavior at the macroscopic scale. In no small part, this is because *the single-most important structural parameter –the liquid content– cannot be appreciably varied on earth.* The objective of the current ground based research and the proposed microgravity experiments is to exploit rheological and multiple-light scattering measurements in order to quantify and elucidate the unusual elastic character of foams in terms of their underlying microscopic structure and dynamics. Special interest is in determining how this elastic character vanishes, i.e. how the foam melts into a simple viscous liquid, as a function of both increasing liquid content and increasing shear strain rate. In this report, we focus on recent developments regarding the latter.

MACROSCOPIC RHEOLOGY

As a form of matter, foam is neither solid, liquid, nor vapor – yet it possesses the hallmark mechanical features of all three forms of matter. Under small applied shear forces, it can respond elastically, like a solid. Under large applied shear forces, it can flow and deform arbitrarily without breaking, like a liquid. Under pressure or temperature perturbations, it can proportionally change its volume, like a gas. This unusual rheological behavior in combination with low density and high interfacial area is the basis for our common fascination with everyday foams and for their utility in a wide variety of applications. Efforts to measure and understand the quantitative rheology of foams are reviewed in Refs. [1,14-16,3-5,17]. Since foams appear to exhibit a static shear modulus and to be shear-thinning above a yield stress, they are often described as Bingham plastics during flow and as a Kelvin solids under small deformations:

$$\sigma = \begin{cases} G_o\gamma + \eta_k\dot{\gamma} & \text{for } \gamma \ll 1 \quad \text{(Kelvin)} \\ \sigma_y + \eta_p\dot{\gamma} & \text{for } \dot{\gamma} = \text{const} \quad \text{(Bingham)} \end{cases} \quad (1)$$

The magnitude of the shear modulus and yield stress are set by surface tension, bubble size, and liquid content, while the plastic viscosity is set by interfacial- and film-level dissipation mechanisms involving surfactant transport and viscous flow.

The simple Kelvin-solid/Bingham-plastic picture provides valuable intuition, but is not necessarily correct –even qualitatively– for many reasons. First, it is difficult to ensure linear response due to neighbor-switching rearrangement of the bubbles induced by application of even very small shear; a truly linear regime may not exist. Second, the static and slow strain rate behavior can be severely affected by time evolution of the underlying packing structure via gas diffusion between bubbles (coarsening) or via drainage. Thus, for example, stress can relax after a step-strain and foam can creep under small applied stress; these features, as well as the complex dynamic shear modulus, are inconsistent with Eq.(1). Third, it is difficult to achieve a known, rheometric, velocity field due to plug-flow and wall-slip; this can invalidate analyses and render experiments irreproducible. Fourth, foams are disordered and polydisperse, and are hence difficult to characterize; this can lead to further irreproducibility. As an example, these effects combine to produce the following linear and flow rheology for a commercial shaving foam:

RESPONSE TO SMALL OSCILLATIONS:

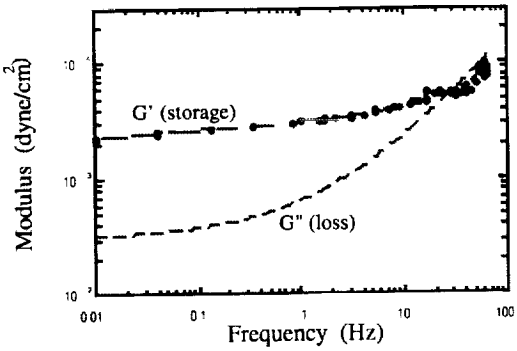

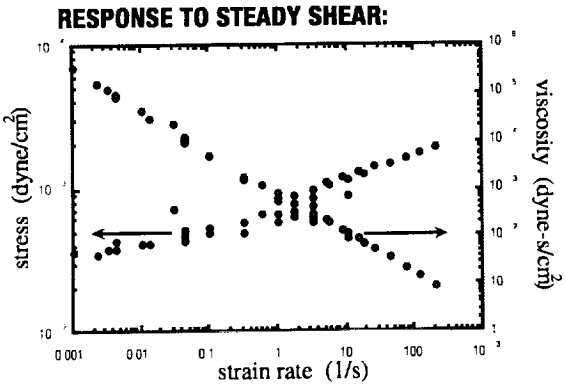

Clearly, it is not a Kelvin solid, which behaves according to Eq.(1) as $G'(\omega)=G_0$ and $G''(\omega)=\eta_k\omega$. Clearly, also, it is not a Bingham plastic, since the stress does not approach a constant at low strain rates and since the viscosity does not approach a constant at high strain rates.

As a result of the above difficulties, accurate reproducible measurements of foam rheology and systematic trends with structural parameters are still in great need. The influence of surface tension σ_S and average bubble diameter D is relatively simple to measure and predict; namely, moduli are proportional to σ_S/D. The influence of dissipation mechanisms, e.g. liquid viscosity, by contrast is very difficult to predict; however, in the context of the Bingham plastic model, the only role is simply to set the value of the plastic viscosity, η_p, and hence the key dynamical time scale, $\tau_p=\eta_p/\sigma_S$. How to predict film-level flows and the value of this time scale are difficult fluids dynamics problem of current interest.

Note that surface tension, bubble size, and liquid viscosity all affect the basic moduli and time scales, but do not alter the general nature of the behavior. The influence of liquid content, however, is much more dramatic and much less understood. Most obviously, the liquid content dictates bubble shape, i.e. whether bubbles appear approximately polyhedral or spherical and whether more liquid resides in soap films or in Plateau borders and vertices. While photographs of a foam offer no clue as to chemical composition or bubble size, the liquid content is immediately evident from bubble shape. Therefore, *the volume fraction of liquid, ϕ , is the single most important parameter (a) in affecting foam structure and also (b) in producing the widest range of behavior as it is varied.* For example, as the foam becomes wetter, the ability to support shear decreases in accord with the complex shape of the bubbles until the shear modulus vanishes at the random close-packing volume fraction. As this melting transition is approached, the film-level flows, and hence dynamical time scales, must also vary significantly. Perhaps even more importantly, the stability of the packing structure with respect to neighbor-switching rearrangements must decrease too. These crucial dynamical issues have not been at all explored, either experimentally or theoretically, in any jammed system. Another important issue that has received no attention is the dependence of foam rheology on the evolution mechanisms and time scales to be discussed next.

MICROSCOPIC DYNAMICS

The bubble-packing structure of foams is difficult to describe, due to randomness and polydispersity. It is even more difficult to measure, since bulk foams are opaque. Due to the unavoidably large refractive index mismatch between the gas and liquid, incident light strongly reflects and refracts at the bubble interfaces and this multiple light scattering gives rise to their familiar white appearance. This restricts the use of light-based microscopies to surface structure and two-dimensional foams. Besides surface observation, other available probes of structure include electrical conductivity [18-20], external pressure [21], freeze fracture [22], penetration by optical fiber [23], and either MRI [24-26] or confocal microscopy [27] applied to small samples. Without exception, these are all either indirect and open to ambiguity of interpretation, invasive and therefore not suitable for *in-situ* and time-evolution studies, and/or too slow for all but the most stable foams. The development of a superior means of quickly and noninvasively measuring the bubble-scale structure of foams would thus significantly advance our understanding of both foam rheology and foam stability. Toward this end, the PI developed a superior means of quickly, noninvasively characterizing three-dimensional foams by use of multiple-light scattering [28]. This includes diffuse-transmission spectroscopy (DTS) as a probe of bubble-scale structure and diffusing-wave spectroscopy (DWS) as a probe of bubble-scale dynamics [29-32]. Since foams are unavoidably opaque, these techniques can be applied quite generally. The PI also used these techniques to quantify the time-evolution of structure and bubble-rearrangement dynamics in a coarsening three-dimensional foam [33], to observe the nature of rearrangement dynamics during slow shear [34], and to quantify the influence of thermal fluctuations [35].

Here, we use DWS to investigate the change in the nature of the bubble dynamics as the strain rate is increased toward $1/\tau_d \equiv \sigma_y/\eta_p \cong 10\ s^{-1}$, the time scale set by the duration of rearrangement events. For small rates, the rearrangements can come to completion and the foam thus achieved macroscopic deformation via a series of stick-slip avalanche-like rearrangement events [34]. For fast rates, by contrast, the rearrangements cannot come to completion before

they must rearrange again. Since the bubbles are in constant motion, just like the molecules in a simple viscous liquid, the elastic character vanishes and the foam "melts".

This crossover from jerky to continuous motion can be seen directly in the following raw DWS data:

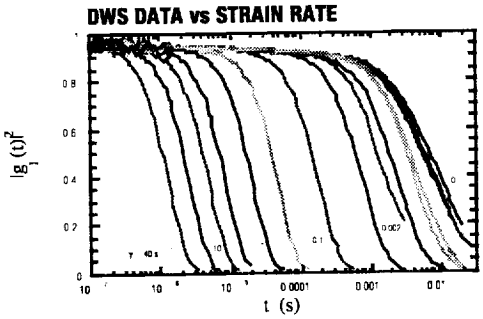

At low strain rates, the decay is slower and is exponential in time – this form is indicative of discrete localized rearrangements occurring at a rate commensurate with the decay rate. At slightly faster shear, the rates increase linearly but the form is still exponential. At much higher shear, the decay rate is still faster but more importantly is exponential in time squared – this form is indicative of smooth continuous shear flow at the bubble-scale [36].

RELAXATION DURING SHEAR

Now that we have microscopic evidence of a crossover to a "melted" state at high strain rates, we would like to observe consequences for the macroscopic rheology. Traditionally, solids and liquids can be distinguished by whether or not stress eventually relaxes to zero following the sudden imposition of a small step-strain. The new twist we introduce is to perform such experiments while steady shear is in progress, for example:

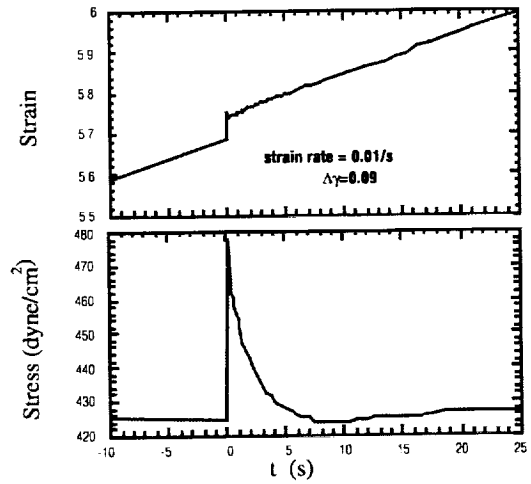

Note that the stress increases immediately after the step strain, as in a solid, but then decreases back toward the same nonzero value as before the step strain, as in a liquid. The stress jump is proportional to the size of the step-strain, as long as it is less than about 10%. In other words, the transient response is linear and is like that of a viscoelastic material. Defining a suitable shear-relaxation modulus, we observe that it vanishes smoothly as the strain rate is increased:

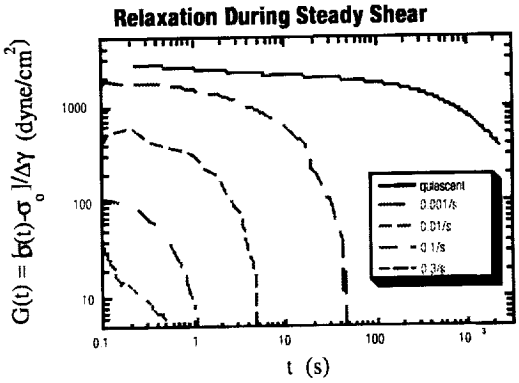

So at high strain rates, there is a crossover to purely viscous response, showing that the foam has "melted". This is a macroscopic manifestation of the crossover to smooth continuous motion at the bubble scale.

CONCLUSIONS

To summarize, we have investigated the behavior of an aqueous foam as a systematic function of increasing shear strain rate. In both the microscopic dynamics and in the macroscopic rheology we find a crossover to a "melted" state in which the elastic character has vanished. The critical strain rate for this crossover is set by the duration of the stick-slip rearrangements, easily observed under slow shear. This represents the first firm connection between dynamical behavior at bubble- and macro- scales in foams. While this is important at face value, it also represents a crucial step in our broader program to characterize the bubble-scale structure and macroscopic rheology of foams as a systematic function of increasing liquid content, where another kind of melting transition will occur.

REFERENCES

[1] J. J. Bikerman, *Foams* (Springer-Verlag, New York, 1973).

[2] D. Weaire and N. Rivier, "Soap, cells and statistics - random patterns in two dimensions," Contemp. Phys. **25**, 55 (1984).

[3] A. M. Kraynik, "Foam flows," Ann. Rev. Fluid Mech. **20**, 325-357 (1988).

[4] J. H. Aubert, A. M. Kraynik, and P. B. Rand, "Aqueous foams," Sci. Am. **254**, 74-82 (1989).

[5] A. J. Wilson, ed., *Foams: Physics, Chemistry and Structure.* Springer Series in Applied Biology , (Springer-Verlag, New York, 1989).

[6] D. J. Durian and D. A. Weitz, "Foams," in *Kirk-Othmer Encyclopedia of Chemical Technology*, 4 ed., edited by J.I. Kroschwitz (Wiley, New York, 1994), Vol. 11, p. 783-805.

[7] R. K. Prud'homme and S. A. Khan, ed., *Foams: Theory, Measurement, and Application.* Surfactant Science Series **57**, (Marcel Dekker, NY, 1996).

[8] K. J. Mysels, K. Shinoda, and S. Frankel, *Soap Films, Studies of Their Thinning and a Bibliography* (Pergamon Press, New York, 1959).

[9] I. B. Ivanov, ed., *Thin Liquid Films: Fundamentals and Applications.* Surfactant Science Series **29**, (Marcel Dekker, Inc., New York, 1988).

[10] M. J. Rosen, *Surfactants and Interfacial Phenomena*, 2nd ed. (John Wiley & Sons, New York, 1989).

[11] A. W. Adamson, *Physical Chemistry of Surfaces*, 5th ed. (John Wiley & Sons, New York, 1990).

[12] J. N. Israelachvili, *Intermolecular and Surface Forces*, 2nd ed. (Academic Press, San Diego, 1991).

[13] C. Isenberg, *The Science of Soap Films and Soap Bubbles* (Dover Publications, New York, 1992).

[14] G. R. Assar and R. W. Burley, "Hydrodynamics of foam flow in pipes, capillary tubes, and porous media," in *Gas-Liquid Flows*, edited by N.P. Cheremisinoff (Gulf Publishing Company, Houston, 1986), Vol. 3, p. 26-42.

[15] H. C. Cheng and T. E. Natan, "Measurement and physical properties of foam," in *Gas-Liquid Flows*, edited by N.P. Cheremisinoff (Gulf Publishing Company, Houston, 1986), Vol. 3, p. 3-25.

[16] J. P. Heller and M. S. Kuntamukkula, "Critical review of the foam rheology literature," Ind. Eng. Chem. Res. **26**, 318-325 (1987).

[17] D. M. A. Buzza, C. Y. D. Lu, and M. E. Cates, "Linear shear rheology of incompressible foams," J. de Phys. II **5**, 37-52 (1995).

[18] N. O. Clark, "The electrical conductivity of foam," Trans. Faraday Soc. **44**, 13-15 (1948).

[19] A. K. Agnihotri and R. Lemlich, "Electrical conductivity and the distribution of liquid in polydedral foam," J. Coll. I. Sci. **84**, 42-46 (1981).

[20] R. Phelan, D. Weaire, E. A. J. F. Peters, and G. Verbist, "The conductivity of a foam," Journal of Physics: Condensed Matter **8**, L475-482 (1996).

[21] G. Nishioka and S. Ross, "A new method and apparatus for measuring foam stability," J. Coll. I. Sci. **81**, 1-7 (1981).

[22] A. J. Wilson, "Cryo-microscopical methods for the investigation of foam structure," in *Foams: Physics, Chemistry, and Structure*, edited by A.J. Wilson (Springer-Verlag, New York, 1989), p. 69-88.

[23] C. G. J. Bisperink, A. D. Rontcltap, and A. Prins, "Bubble size distribution in foams," Adv. Coll. I. Sci. **38**, 13 (1992).

[24] C. P. Gonatas, J. S. Leigh, A. G. Yodh, J. A. Glazier, and B. Prause, "Magnetic resonance images of coarsening inside a foam," Phys. Rev. Lett. **75**, 573-576 (1995).

[25] B. A. Prause, J. A. Glazier, S. J. Gravina, and C. D. Montemagno, "Three-dimensional magnetic resonance imaging of a liquid foam," Journal of Physics: Condensed Matter **7**, L511-516 (1995).

[26] K. Kose, "3D NMR imaging of foam structures," Journal of Magnetic Resonance, Series A **118**, 195-201 (1996).

[27] M. G. Reed, C. V. Howard, and C. G. Shelton, "Confocal imaging and second-order stereological analysis of a liquid foam," Journal of Microscopy **185 pt.3**, 313-320 (1997).

[28] D. J. Durian, D. A. Weitz, and D. J. Pine, "Multiple light scattering probes of foam structure and dynamics," Science **252**, 686-688 (1991).

[29] G. Maret and P. E. Wolf, "Multiple light scattering from disordered media. The effect of Brownian motion of scatterers.," Z. Phys. B **65**, 409-413 (1987).

[30] D. J. Pine, D. A. Weitz, P. M. Chaikin, and E. Herbolzheimer, "Diffusing-wave spectroscopy," Phys. Rev. Lett. **60**, 1134-1137 (1988).

[31] D. A. Weitz and D. J. Pine, "Diffusing-wave spectroscopy," in *Dynamic Light Scattering: The Method and some Applications*, edited by W. Brown (Claredon Press, Oxford, 1993), p. 652-720.

[32] P.-A. Lemieux, M. U. Vera, and D. J. Durian, "Diffusing-light spectroscopies outside the diffusive limit: the role of ballistic transport and anisotropic scattering," Phys. Rev. E **57**, 4498-4515 (1998).

[33] D. J. Durian, D. A. Weitz, and D. J. Pine, "Scaling behavior in shaving cream," Phys. Rev. A **44**, R7902-R7905 (1991).

[34] A. D. Gopal and D. J. Durian, "Nonlinear bubble dynamics in a slowly driven foam," Phys. Rev. Lett. **75**, 2610-2613 (1995).

[35] A. D. Gopal and D. J. Durian, "Fast thermal dynamics in aqueous foams," J. Opt. Soc. Am. A **14**, 150-155 (1997).

[36] X.-l. Wu, D. J. Pine, P. M. Chaikin, J. S. Huang, and D. A. Weitz, "Diffusing-wave spectroscopy in a shear flow," J. Opt. Soc. Am. B **7**, 15-20 (1990).

DYNAMICS OF SINGLE CHAINS OF SUSPENDED FERROFLUID PARTICLES.

S. Cutillas and J. Liu, California State University Long Beach, Department of Physics and Astronomy, 1250 Bellflower Boulevard, 90840 CA, Long Beach.

Introduction

Super paramagnetic particles is a new class of magnetic materials that exhibit a susceptibility χ near the value of one while most of natural paramagnetic materials have a magnetic susceptibility at least five orders of magnitude lower. Ferrofluid emulsion is one of such systems. A collection of iron oxide nanoparticles (in our case Fe_3O_4 with a radius of 6nm) dispersed in kerosene is called a ferrofluid which has various properties [1]. The most important is that each nanoparticle has a permanent dipole moment. Due to the small size of the nanoparticles, they only have a single domain magnetization. The thermal agitation randomizes the iron oxide particles so that the total magnetization of the ferrofluid is equal to zero when no magnetic field is applied. Once an external magnetic field is applied, the nanoparticles are oriented slightly in the field direction and the ferrofluid can have a strong magnetization. Particles, having a submicronic size, (in our case 0.23μm as radius) can be made of this ferrofluid. If these ferrofluid droplets are dispersed in water, some surfactant is added to prevent aggregation, the system thus produced is called a ferrofluid emulsion.

When ferrofluid particles are suspended in water, they diffuse under Brownian forces. Applying a magnetic field to such a suspension leads to dipole-dipole interactions between particles. The amplitude of this interaction is described by a dimensionless parameter λ, which is the ratio of the magnetic dipolar energy over the thermal energy [2]:

$$\lambda = \frac{\pi a^3 \chi^2 \mu_0 H_0^2}{18 kT} \qquad (1)$$

Where a is the particle radius, μ_0 is the vacuum permeability, H_0 the applied magnetic field, k the Boltzmann constant and T the absolute temperature. When λ is greater than one, magnetic interactions dominate. Because of the strong anisotropy of the dipolar interaction, particles aggregate to form chains in the field direction (cf. Fig.1).

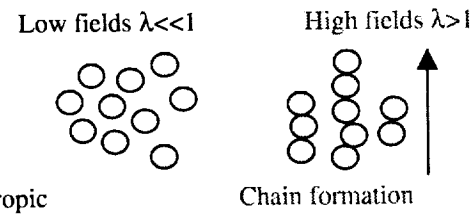

Figure 1: Magnetic field effect on a ferrofluid emulsion.

When the volume fraction is high, bigger aggregates are formed by the lateral coalescence of several chains [3,4,5]. While many studies and applications deal with the rheological properties [6] or the field-induced structural changes [3-7], this work is to better understand the chain dynamics. We will show, in the first section, that the kinetics of chain formation is a diffusion-limited aggregation. The second and the main part of this work will talk about measurements of the effective diffusion coefficient by dynamic light scattering (DLS) [8]. In particular, our experiments are able to measure two different motions. One is from the center of mass of the chain and the other is from internal motions (particle fluctuations). This is an extension of our earlier work [9,18].

Experimental conditions

Our sample consists of ferrofluid particles dispersed in water. The particle volume fraction is 10^{-5} to avoid multiply scattering as well as chain-chain lateral aggregation. The emulsion is introduced in a test tube of 2cm of diameter with care to avoid dust pollution.

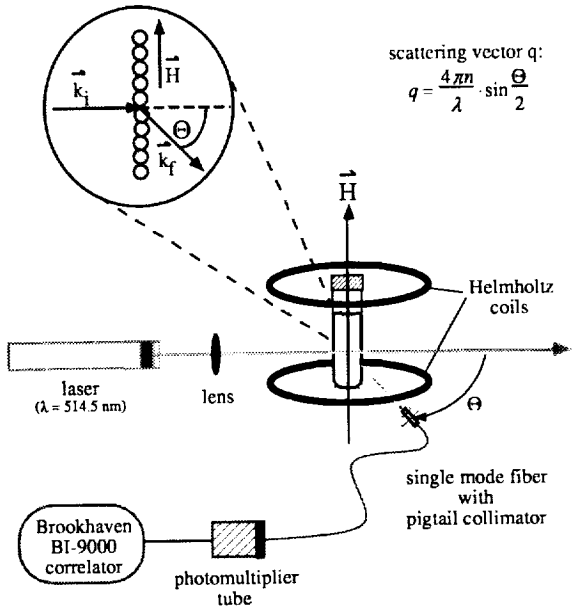

Figure 2: Experimental setup of dynamic light scattering. The onset specifies our scattering geometry, with

chains perpendicular to the scattering plane, and the definition of q is also indicated.

The tube is placed in the sample holder with an index match bath to reduce reflections. The sample holder is then put inside a pair of Helmholtz coils as shown in Fig.2.

An Ion Argon laser beam (λ_0=514.5nm) is focused through a lens (with a focal length equal to 25cm) to the sample. The detector is placed at an angle θ from the initial path that specifies the momentum transfer q, defined in the experimental setup shown in Fig.2. The scattered light is collected by a photomultiplier tube and analyzed by a digital correlator to give the intensity autocorrelation function. In self beating mode, often called homodyne mode, the intensity autocorrelation function that the correlator measures $<I(q,t)I(q,0)>$ is related to the dynamic structure factor $S(q,t)$ with the relation:

$$< I(q,t) I(q,0) > - < I^2 > = \alpha S^2(q,t) \quad (2)$$

And

$$S(q,t) = \frac{1}{V} \sum_{n,p} \exp\{iq(r_n(t) - r_p(0))\} \quad (3)$$

$<I^2>$ is the mean square amplitude of the intensity and α is a parameter that only depends on geometrical factors. V is the scattering volume and $r_n(t)$ is the position of the particle number n at time t. In general, interpretation of DLS experiments requires a model for $S(q,t)$.

In the absence of magnetic field, the suspension is isotropic without any interactions between particles and the structure factor reduces to a single exponential $S(q,t) \propto exp(-q^2 D_0 t)$. $D_0=(kT/\xi)$ is the diffusion coefficient of a particle. $\xi = 6\pi \eta a$ is the Stokes frictional coefficient of a spherical particle in a fluid of viscosity η. If interactions or polydispersity can not be ignored, an effective diffusion coefficient has to be introduced. Formally, D_{eff} is defined as:

$$D_{eff} = -\frac{1}{q^2} \frac{\partial}{\partial t} \ln(S(q,t)) \Big|_{t \to 0}$$

It reduces to D_0 if no interactions between particles are present. Therefore, without magnetic field, we can use DLS to measure particle size. The particle radius was found to be $a=0.23\mu$ m with 7% of polydispersity through a fitting procedure called cumulant expansion [8]. In this case, if we vary the scattering angle θ (and so q) we do not have any change in the measured diffusion coefficient: it is q-independent.

When a magnetic field is applied, the system consists of particles and chains. Equation 2 can still be used to fit our data if we assume $S(q,t) \sim exp(-\Omega t)$ and $\Omega = q^2 D_{eff}$. Ω measures the frequency of scatters (particles, chains).

The magnetic field is controlled by a computer (with a digital-analog converter board) connected to a remote power supply. The field was first calibrated without any magnetic material and a linear relation between the current and the field was found. Each Amp produces 67.0±0.5 Gauss. The relation giving λ for a given magnetic field strength is not simple since the susceptibility varies with the magnetic field. However, an order of magnitude can be found with the equation $\lambda=0.01B^2$, where B is the external magnetic field applied, expressed in Gauss. For 200Gauss, λ=400. Our expressions of λ, given in this paper, are rigorous solutions of the equations of the magnetic field in heterogeneous media.

Results

I) Kinetics of chain formation

When a strong magnetic field is applied (λ=406), at a fixed q, we first notice a monotonous decrease of the effective diffusion coefficient with time. Physically, this means that chains are becoming longer and longer with time (see Fig.3).

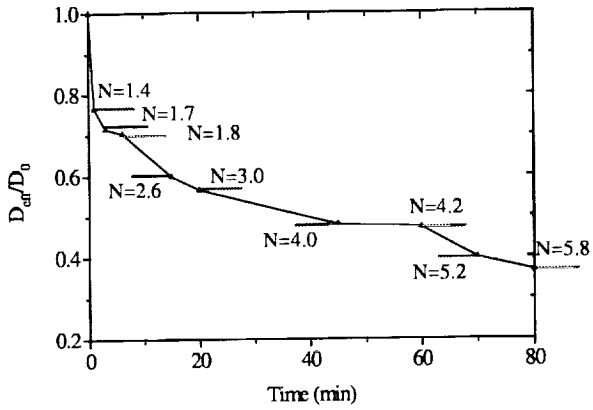

Figure 3: Normalized effective diffusion coefficient versus time. (λ=406, q= 4.2x10^6 m^{-1})

To obtain chain length from D_{eff}, a theoretical model of rigid chains of N spherical particles is used [11,12] since it agrees very well with a recent experiment [10]. The result is shown below:

$$D_{chain} = f(N) D_0$$

$$f(N) = \frac{3\ln(2N) + 1.254}{4N} \quad (4)$$

Here, we assume that the effective diffusion coefficient measures the average motion of isolated chains. In very dilute system like the one we used, this is cer-

tainly true. From equation 4, we are able to get the mean number of particles per chain, N, from the effective diffusion coefficient.

This is illustrated in the Fig.4 where the effective diffusion coefficient is normalized by that of a single particle. Figure 4 shows a Log-Log plot of the results based on measurements of Fig.3.

Calculating the value of N as a function of the time gives us information about the kinetics of aggregation (i.e. N versus time).

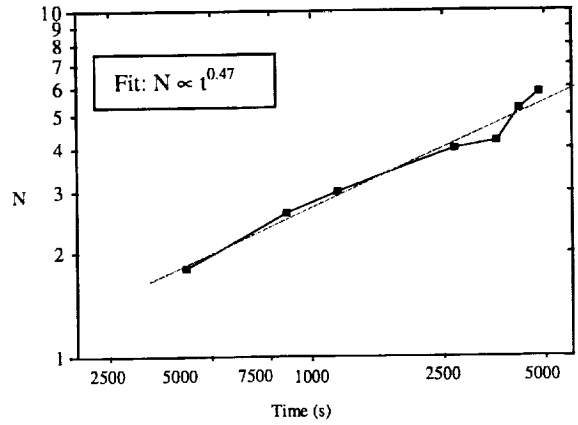

Figure 4: Mean number of particle per chain versus time, kinetics of chain formation.

Fitting the data with a power-law relation gives an exponent of 0.47±0.05. Thus, N depends on time as a square root (within our experimental uncertainties for this short chain formation). As expected, since the volume fraction is very low, the kinetics of particle aggregation into chains is a diffusion-limited aggregation. This is consistent with our earlier data and other work [9,18,13].

II) Dynamics of single chains

If we apply a magnetic field of 200 G to the sample for 6 hours, we can get chains long enough (more than 19 particles) and far away (more that 70 particle diameters) that the chain growth slow down. Now, we can do other experiments. In this case, the absolute time is no longer important since chain length is almost constant during the next 30 minutes. First, we vary θ (or q) at a constant magnetic field strength, and measure the effective diffusion coefficient.

Varying q allows us to select a window within which different length scales of motion will be probed. This can be seen in another way: q defines a characteristic length ($l=2\pi/q$) over which dominantly motion will contribute to the intensity correlation function. To be able to probe different length scales by varying the scattering angle is an important property of DLS.

In this work, the experimental range of the scattering angle is $5^\circ < \theta < 130^\circ$. The equivalent range for the scattering wave vector is $1.4\text{x}10^6 < q(\text{m}^{-1}) < 2.9\text{x}10^7$. Thus, the characteristic length scale will have the range $0.21 < l\ (\mu\text{m}) < 4.42$. In terms of the particle radius:

$$0.9a < l < 20a. \qquad (5)$$

We can see here that motions will be probed over quite a broad range in a single experiment from one particle radius up to twenty particle radii.

Next, we vary the magnetic field intensity (or λ) and repeat the q-dependence experiment.

Figure 5 shows four series of experiments performed at different magnetic field or coupling constant λ (indicated in the onset). To work with the same chain length, these four experiments are done consecutively after the 6 hours at λ=406. The first one is for λ=406, the second one is for λ=17, the third one is for λ=157 and the last one is for λ=46. Each experiment takes around 30 minutes. This procedure allows us first to decrease the magnetic energy of interaction between chains to slow down again the kinetics of aggregation and second to cool the coils which were warm after a long-time experiment. At each fixed λ value, we measure the effective diffusion coefficient D_{eff} as a function of q. D_{eff} is normalized by the single particle diffusion coefficient D_0, and $l=2\pi/q$ is normalized by the particle radius a.

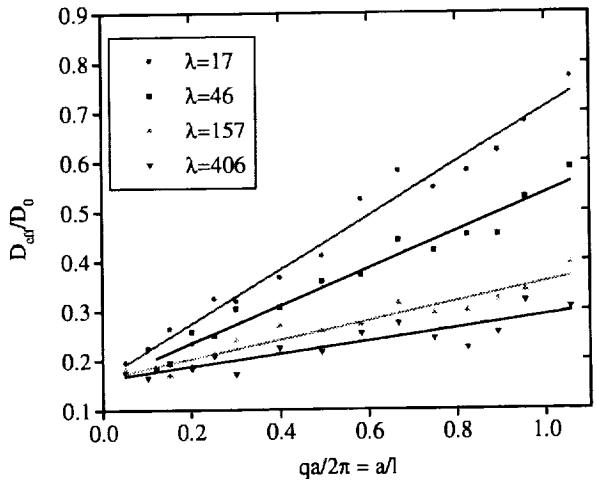

Figure 5: Dependence of the normalized effective diffusion coefficient versus the normalized scattering wave vector for different λ values.

Figure 5 shows a few interesting features. First, for all λ values, D_{eff} is linearly proportional to qa. Second,

as λ increases the slope of D_{eff} versus q decreases. But all these straight lines converge to the same point (D_{eff}/D_0=0.16) as q approaches zero.

To understand the q dependency of D_{eff}, let us look at the probing length used. In our study, the characteristic length scale probed is $l=2\pi/q$ which is in the range of $0.9<l/a<20$. When l is much larger than the particle radius ($l/a \rightarrow \infty$) we are mainly sensitive to the center of mass diffusion of the chain. D_{eff} is then the diffusion of the entire chain and depends only on N and D_0 but not on q and λ. The value D_{eff} allows us to obtain the number of particles per chain N. In the opposite limit (i.e. $l/a<1$), we are sensitive to motions on the size of individual particles. The main contributions to the measured diffusion coefficient come from internal motions of the chains (i.e. particles' fluctuations inside the chain). However, the reason for a linear dependence of D_{eff} on q is not clear.

The fact that the initial value of D_{eff}/D_0 (here equal to 0.16 when q approaches zero) does not depend on λ indicates that the straight chain configuration is well maintained even for the lowest λ values we used. This value can be used to find the number of particles per chain from the equation (4). This gives us N=19±1 as the mean number of particles in a chain (after 6 hours at λ=406).

Figure 6 shows the dependence of D_{eff} on λ based on the data in Fig.5. Since $D_{eff}/D_0 \sim k(qa)$, we plotted, in a Log-Log plot, the slope k versus λ in Fig.6. Here, a fit of power-law is obtained $D_{eff}/D_0 \propto \lambda^{\delta}$ giving the exponent $\delta = -0.47 \pm 0.05$.

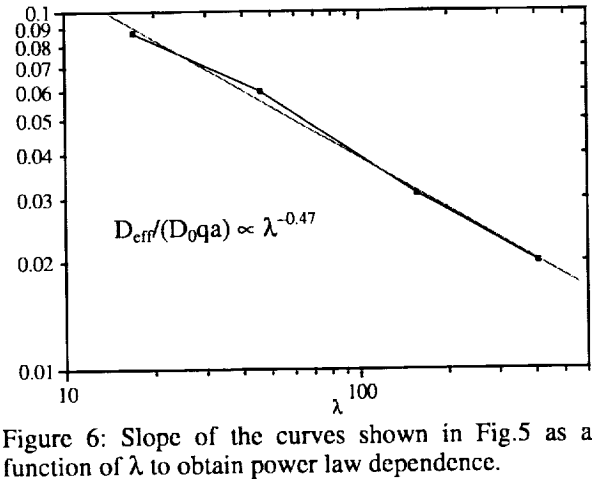

Figure 6: Slope of the curves shown in Fig.5 as a function of λ to obtain power law dependence.

We can approximate $D_{eff}/D_0 \sim 1/\sqrt{\lambda}$. We can see here that when the magnetic field increases (so λ increases) this reduces the internal motions. Therefore, based on the results of Fig.5 and 6, D_{eff}/D_0 may be written as:

$$D_{eff}/D_0 = \frac{A}{\sqrt{\lambda}} g(N)\, qa + f(N) \qquad (6)$$

This effective diffusion coefficient given by Eq.6 is consisted of two parts.
The first term is the contribution due to internal motions of the chain (particle fluctuations) while the second part is due to the whole chain motion (diffusion of the center of mass of the chain).

In Eq.6, $g(N)$ accounts for the chain length dependence. $g(N)$ and the constant A is determined from experiments described below.

We created two chain lengths to study the effect of chain length on the effective diffusion coefficient. To obtain a longer chain size than 19 particles per chain, we hold the magnetic field at λ=406 for 3 more hours (this increases the experimental time up to more than 9 hours). We then reduced the field down to λ=46 and repeated the q-dependence measurements. The result is shown in Fig.7 below where for the same value of λ (λ=46) two experiments with two different chain sizes are compared here:

Figure 7: Effect of different chain sizes on the measured diffusion coefficient versus q.

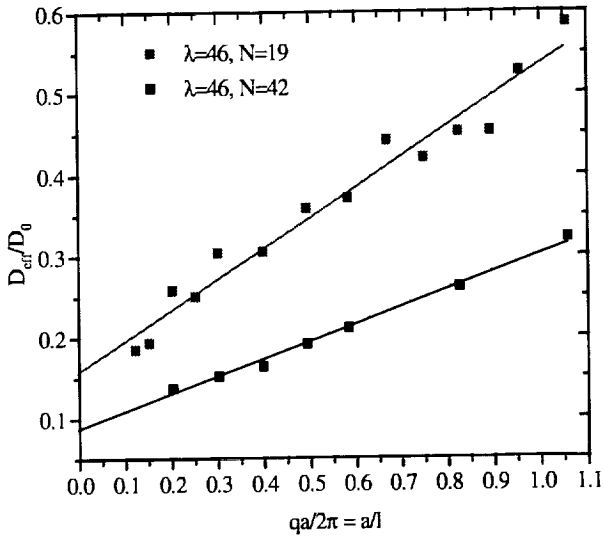

From the data shown in Fig.7, we notice that when N varies, not only the initial value is different but also the slope changes. If we also assume that $D_{eff}/D_0 \propto N^{\varepsilon}$, ε is found to (−0.7±0.1).

To summarize the results from figures 5,6 and 7, we found that the effective diffusion coefficient follows the simple relation:

$$D_{eff}/D_0 = \frac{3}{N^{0.7}\sqrt{\lambda}} qa + f(N) \qquad (7)$$

Here $f(N)$ is given by equation 4. The constant A was found equal to 3.0±0.2. It was determined experi-

mentally by finding the exact value of D_{eff}/D_0 from Fig.5 for a given qa/2π.

It is worth noting here that our experiments do not cover the whole range of probing window ($l=2\pi/q$). We were only sensitive to the most interesting range where a q dependency of D_{eff} can be observed. However, if we expand the q range toward both ends, different behavior of D_{eff} may be observed. Based on dynamics of polymers [14,15], we expect a qualitative behavior as shown in the Fig.8. Here, three dynamical regimes exist.

For small qa values, D_{eff}/D_p corresponds to the diffusion coefficient of the entire chain. In the opposite limit ($qa>2\pi$) it corresponds to the diffusion coefficient of the monomer inside a polymer chain D_p.

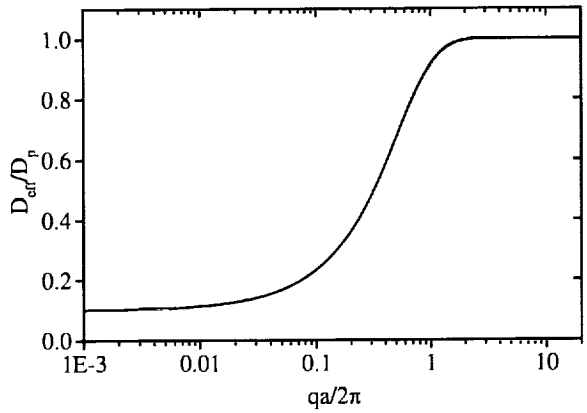

Figure 8: Universal behavior of the effective diffusion coefficient versus q in polymer physics.

In our case D_p is the diffusion coefficient of a single particle in the chain configuration. Notice that D_p is different from the case of isolated particles D_0. In both of these regions, the behavior of D_{eff}/D_p does not depend on $qa/2\pi$. If a broader range of $qa/2\pi$ was accessible we expect to see also these two others regions where D_{eff}/D_0 becomes constant.

In our experiment, the characteristic frequency [15] probed by DLS is defined as $\Omega(q)=D_{eff}q^2$.

$$\Omega(q)=\left[\frac{3}{N^{0.7}\sqrt{\lambda}}qa+f(N)\right]q^2D_0 \qquad (8)$$

The two constant regions can be obtained by setting $qa=0$ and $qa=2\pi$. When $qa=0$, $D_{eff}=D_{chain}$ or, in terms of the minimum frequency, $\Omega_{min}=q^2D_{chain}$. When $qa/2\pi$ approaches 1, the maximum frequency is obtained by replacing qa by 2π in Eq.7 for the effective diffusion coefficient. The result, valid for $q>(2\pi/a)$, is:

$$\Omega_{max}(q)=\left(\frac{6\pi}{N^{0.7}\sqrt{\lambda}}+f(N)\right)q^2D_0 \qquad (9)$$

In this work, we just reached the boundary of the two limits. If we extend qa a little large, we may see the saturation behavior. From equations (7, 8 and 9) we can see that the higher λ and N are, the lower the internal vibration frequency and the slower the diffusion motion. Increasing the magnetic interaction leads to a more rigid chain, which is reasonable. Decreasing λ reduces the dipolar binding between particles in a chain. Thus, fluctuations of higher frequency are observed. However, λ can not be reduced below the value of 1. In this case, only the motion of isolated particles will be probed (if no irreversible aggregation occurred) since chains break [16]. The N dependence indicates that when the number of particles per chain increases, internal frequencies of the chain reduce. This behavior may be explained by the fact that more vibrational modes are present for a longer chain than that of a shorter chain. If the slowest modes (or the longest wavelength) contribute mainly to the probed fluctuations, the characteristic frequency will decrease with chain length.

For $N>5$, $f(N)\approx(3/2)N^{0.75}$. Therefore, we may replace $N^{0.7}$ in Eq.6-9 by $f(N)$. Thus, equation (7) becomes:

$$D_{eff}\approx\left(\frac{2}{\sqrt{\lambda}}qa+1\right)f(N)D_0 \qquad (10)$$

We can write Eq.10 by separating the two parts. The internal part with an apparent internal diffusion coefficient D_{int}, and the global part with the diffusion coefficient of the whole chain D_{chain}.

$$D_{eff}=D_{int}+D_{chain}$$

With

$$D_{int}=\frac{2qa}{\sqrt{\lambda}}D_{chain} \quad \text{and} \quad D_{chain}=f(N)D_0$$

Equations (8) and (9) can also be expressed in a closed form:

$$\Omega(q)=\left(\frac{2}{\sqrt{\lambda}}q^3a+q^2\right)f(N)D_0 \qquad (11)$$

And, for $q>(2\pi/a)$:

$$\Omega_{max}(q)=\left(\frac{4\pi}{\sqrt{\lambda}}+1\right)f(N)q^2D_0 \qquad (12)$$

The apparent diffusion coefficient of particles in a chain configuration D_p is given in terms of the maximum frequency (term "apparent" is used since a particle does not have a real diffusion behavior inside a chain because of its bounding motion):

$$D_p=\frac{\Omega_{max}}{q^2}=\left(\frac{4\pi}{\sqrt{\lambda}}+1\right)D_{chain} \qquad (13)$$

From equation (13) we see that D_p reduces to D_{chain} when $\lambda>>(4\pi)^2=160$ and that the particle radius is completely contained in the single particle diffusion

coefficient D_0. Because of the square root dependence, even in the case $\lambda=10^4$, internal fluctuations still contribute f 12% of that of the whole chain. To reach D_{int}/D_{chain} = 1%, $\lambda=10^6$ is necessary. In practice, such a large λ value is difficult to obtain with submicronic particles, due to saturation of magnetization. In our case, if no saturation effect is taken account, the magnetic field would have the value of 1 Tesla to get a completely rigid chain. In our case, for the maximum magnetic field used, λ=406 and D_{int}/D_{chain} = 62%.

Physically, this means that in almost all experiments realized with these systems composed of submicronic super-paramagnetic particles, chain fluctuations can not be neglected. Furthermore, the only way to obtain rigid chains is to increase the particle size well above the micrometer. Since the magnetic interactions is proportional to the cube of the particle radius (cf. Eq.1), a particle diameter about 3 micrometers need to be used with a magnetic field of 300 Gauss to reach $\lambda=10^6$ (assuming the same magnetic susceptibility). The biggest problem with such particles will be their sedimentation and stability of ferrofluid droplets. Furthermore, using these particles we can test if rigid chains coalesce into bigger aggregate as theoretical prediction suggested [17]. This is our next project.

Conclusion

In conclusion, we find that DLS is a powerful technique in probing the dynamics of chains. We made quantitative measurements concerning the variation of our parameters; the coupling parameter λ, the mean number of particles per chain N and the particle radius a. For instance, we showed that the frequency of the fluctuations depend on the magnetic interaction through $1/\sqrt{\lambda}$ (the higher the field, the more rigid the chain). The dependence of the number of particle per chain also leads to slow down the characteristic frequency when the chain length increases.

We found separated motions when the scattering wave vector varies. The effective diffusion coefficient comprises two parts. The first one comes from the diffusion of the center of mass of the chain (drift motion), and the second one comes from the internal fluctuations of particles that compose the chain. These internal fluctuations can not be neglected even for the highest magnetic field used in our experiments (λ=406, D_{int}/D_{chain}=62%). This work is a basic study of the chain dynamics. It is the first step leading to a better understanding the mechanism of chain-chain lateral aggregation in the field-induced structural formation of dipolar fluids.

Acknowledgements

We gratefully acknowledge M. Hagenbuechle for the experimental setup and earlier work [9,18] on which this work is based and the NASA for the grant NAG 3-1830 supporting this work.

References

[1.] R.E. Rosensweig, Ferrohydrodynamics, Cambridge University Press, 1985.

[2.] P.G. de Gennes & P.A Pincus. (1970), *Phys Kondens Mat.*, **11**, 189.

[3.] G.A. Flores, J. Liu, M. Mohebi & N. Jamasbi, "Field induced columnar and bent-wall-like patterns in a ferrofluid emulsion", *proceeding of the 6th international conference on E.R.F. & M.R.S &A.T.* Japan (1997) To be published.

[4.] J. Liu et al, "Field-Induced Structures in Ferrofluid Emulsions", *Phys. Rev. Letters*, **74** (14), p. 2828 (1995).

[5.] S. Cutillas and G. Bossis, "A comparison between flow-induced structures in electro- and magneto-rheological fluids", *Europhys. Lett.*, **40** (4), 465 (1997).

[6.] E. Lemaire et al, "Influence of the particle size on the rheology of magnetic suspensions", *J of Rheology*, **39**(5), (1995)

[7.] S. Cutillas, G. Bossis and A. Cebers, "Flow-Induced transition from cylindrical to layered patterns in MR fluids" *Phys Rev E*, **57** (1), 804, (1998).

[8.] B.J. Berne & R. Pecora, Dynamic Light Scattering, Wiley and Sons, New York, (1966).

[9.] M. Hagenbuechle and J. Liu, "Study of chain formation and chain dynamics in a dilute magneto-rheological fluid", *Applied Optics*, **36**, p. 7664, (1997).

[10.] K. Zhan, R. Lenke and G. Maret, J. *Phys. II France*, **4**, p. 555, (1994)

[11.] H. Yamakawa, Transport properties of polymer chains in dilute solution: hydrodynamic interactions, *J. Chem. Phys.*, **53**, p.436, (1970).

[12.] G. K. Batchelor, "Slender-body theory for particles with arbitrary cross-section in Stokes flow", *J. Fluid. Mech.*, **44**, p.419, (1970).

[13.] M. Fermigier & A.P. Gast, "Structure Evolution in a Paramagnetic Latex Suspension", *J. Coll. Int. Sci.*, **154**, 522, (1992).

[14.] R. Pecora, Dynamic Light Scattering, Plenum Press, New York (1985).

[15.] P. G. de Gennes, Scaling concepts in polymer physics, Cornell University Press (1979)

[16.] S. Cutillas, G. Bossis, E. Lemaire, A. Meunier and A. Cebers, "Experimental and theoretical study of the field-induced phase separation in electro- and magnetorheological suspensions", *proceeding of the 6th international conference on E.R.F. & M.R.S &A.T.* Japan (1997) To be published.

[17.] T. C. Halsey and W. Toor, *J. of Stat. Phys.*, **61**, 1257, (1990)

[18.] M. Hagenbuechle and J. Liu, *proceeding of the 6th international conference on E.R.F. & M.R.S &A.T.* Japan (1997) To be published.

Chain Dynamics in Magnetorheological Suspensions

A. P. Gast[1], E. M. Furst[1], [1]Department of Chemical Engineering, Stanford University, Stanford, CA 94305-5025, USA, alice@chemeng.Stanford.EDU

1 Introduction

Magnetorheological (MR) fluids are colloidal suspensions of paramagnetic particles in a non-magnetic fluid. These fluids, along with their electrical analogues, electrorheological (ER) fluids, have been proposed as controllable fluids, for use in electromechanical devices such as dampers, clutches and brakes. [1] When exposed to an external magnetic field, the particles acquire dipole moments aggregate to form chains in the field direction. The fluid structure depends on the volume fraction; dilute suspensions form weakly-interacting single-particle chains, while when more concentrated, the particle chains cross-link laterally into a dense network. The latter structure is responsible for the unique rheological properties of MR fluids: the quick formation of a network in response to an external field creates a rapid liquid-to-solid transition. Aside from their practical applications, MR fluids are of fundamental interest because they allow us to probe the structure and dynamics of a suspension of particles interacting via a "tunable" anisotropic interaction.

Recently, we have studied microscopic properties, such as the kinetics of chain growth and low-energy structures [2, 3]. The suspension dynamics [4, 5] are of interest since it has been proposed that Landau-Peierls thermal fluctuations of dipolar chains could be responsible for long-range attractions between chains [6]. Rigid dipolar chains produce a transverse magnetic field that decreases approximately as $exp(-\rho/a)$ where ρ is the distance from the chain and a is the dipolar particle radius. Thus, chains separated by a distance greater than one diameter should interact weakly. In contrast, taking into account thermal fluctuations produces a mean-squared field that decreases as a power law: $\sqrt{\langle H^2 \rangle} \sim \sqrt{kTa}/\rho^2$. Thus, fluctuations may be responsible for the long-range lateral interactions in dipolar chains that greatly affect their response and final structures.

We report our initial studies of the dynamics of MR fluid suspensions using diffusing-wave spectroscopy (DWS). The application of DWS to study the dynamics of MR fluids has several advantages: first, it allows us to probe suspensions capable of forming long chains. Second, the highly multiply-scattered light probes smaller length and time scales than those accessible through single scattering experiments or microscopic observation, complementing those studies. Finally, we can probe thick samples to minimize interfacial effects on our results.

2 Experimental

We synthesized MR emulsion droplets following a method due to Bibette [7]. A ferrofluid (Rhone-Poulenc), composed of mono-domain iron oxide particles suspended in octane, is emulsified into water using sodium dodecyl sulfate, SDS (Sigma, cmc = 2.351 g/ml). The rough emulsion is fractionated by seven successive depletion aggregations with SDS micelles. We vary the particle density by manipulating the amount of octane in the ferrofluid; the particles in this study have a density of approximately 1.1g/ml. We resuspend the particles in a D_2O–SDS solution ($\rho = 1.10g/ml$) at the SDS cmc to minimize sedimentation effects in our light scattering experiments. In this study we use particles of approximately 240nm diameter, at a volume fraction, ϕ of 0.005 and an estimated magnetic susceptibility χ of 1.2.

When placed in an external magnetic field, the particles interact via an anisotropic dipolar potential

$$U(r,\theta) = \left(\frac{4\pi\mu^2}{\mu_0}\right)\frac{1-3cos^2(\theta)}{r^3} \qquad (1)$$

where θ is the angle the particle centers form with the field direction, r is the distance between particle centers, and $\mu = \frac{4}{3}\pi a^3 \mu_0 \chi H$ is the induced dipole for a particle of radius a in a field of magnitude H. We characterize the dipole strength with [8]:

$$\lambda = \frac{-U_{max}}{kT} = \frac{\pi\mu_0 a^3 \chi^2 H^2}{9kT} \qquad (2)$$

Our experiments are conducted over a range of dipole strengths: λ = 4, 7, 11, and 16.

The dynamics of our MR fluid are studied using a transmission geometry [9]. The MR fluid is placed in a spectrophotometer cuvette (Spectrocell) with a pathlength L = 10mm. The cuvette is centered in a uniform magnetic field generated by Helmholtz coils. Linearly polarized light from a 35mW HeNe (Spectraphysics) at 632.8nm is expanded to a plane wave with a 10× laser collimator and illuminates the face of the sample perpendicular to the field direction. The transmitted diffuse light is collected by two pinholes coupled to a multimode fiber optic. A cross-polarizer transmits only depolarized, highly multiply-scattered light. The intensity fluctuations are measured using a photomultiplier (Thorn EMI) with a built-in amplifier–descriminator. We use a commercial correlator (Brookhaven Instruments, BI-9000AT) to calculate the intensity autocorrelation, $g^{(2)}(t)$. The electric field autocorrelation $g^{(1)}(t)$, is found using the Siegert relation, $g^{(2)}(t) = |g^{(1)}(t)|^2$.

When the magnetic field is applied, the dipolar particles rapidly aggregate to form chains. On longer time scales, the chains experience lateral interactions and coalesce to form thicker columns. Our experimental protocols attempt to produce conditions where the fluctuations of individual chains dominate the system dynamics. First, by minimizing the density difference between our droplets and the suspending fluid, we reduce the sedimentation-induced aggregation of chains. During our dynamic studies, the chains are grown at $\lambda = 16$ and after 12 seconds, the desired field strength is applied. This provides a consistent starting point for measurements at each dipole strength in terms of the suspension structure, and avoids the initial ballistic motion when the field is turned on. Starting at 15 seconds, we collect autocorrelation data for 60 seconds. To assess the effect of the starting time, we repeat the experiments switching the field at 85 seconds and starting the autocorrelation at 90 seconds.

In the diffusion limit of light transport in turbid media, a photon executes a random walk with an average step length of l^*, characterizing the distance over which its direction is randomized. Since structure and interactions affect the value of l^* [9, 10, 11, 12], we measure the diffuse transmittance of an expanded laser beam to monitor the change in light transport properties during an experiment. Changes in l^* are taken into account in our analysis. The initial value of l^* is found from by fitting the field-off data. The characteristic photon absorption length [13] $l_a = \sqrt{l^*/3\alpha}$, where α is the absorption coefficient, is found independently by varying the pathlength and measuring the diffuse transmittance through a sample without the magnetic field.

Light transport properties are also measured by removing the collimator and focusing the incident beam to a point source on the sample cuvette face. The transmitted diffuse light is collected on a ccd array and recorded on videotape at a rate of 30Hz. Images are captured from tape by averaging 20 video frames and processed to assess the degree and evolution of anisotropic light transport in our samples after the field is applied and the magnetic chains begin growing.

3 Results and Discussion

Effects of anisotropic light transport. In diffusing wave spectroscopy, the electric-field autocorrelation is a weighted sum

$$g^{(1)}(\mathbf{r},t) = \int_0^\infty d\tau P(\mathbf{r},\tau) exp[(-c/3l^*)k_0^2\langle\Delta r^2(t)\rangle\tau] \tag{3}$$

where $\langle\Delta r^2(t)\rangle$ is the mean-squared displacement of the scatterers and c is the speed of light in the medium, and the probability $P(\mathbf{r},\tau)$ that a diffusing photon will arrive at position $\mathbf{r}$

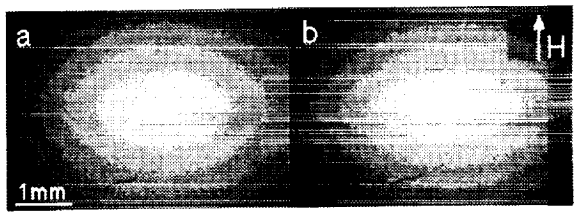

Figure 1: Images showing depolarized diffuse intensity from a point source transmitted through a 10mm sample at $\lambda = 16$. (a) Field on 45 seconds. (b) Field on 150 seconds.

and time τ, is determined by solving the diffusion equation for the experimental geometry. The MR system is complicated by the fact that the suspension structure becomes anisotropic as the particles aggregate to form chains. In this case, the diffusion equation for the light energy density U is anisotropic

$$\frac{\partial U(\mathbf{r},\tau)}{\partial\tau} = (D_\parallel\nabla^2 + D_\perp\nabla^2 + 1/\mu_a)U(\mathbf{r},\tau) \tag{4}$$

where μ_a is the characteristic time for photon absorption and $D_\parallel$ and $D_\perp$ are the light diffusion constants in the direction parallel and perpendicular to the orientation of the chains, respectively. The diffusive probability is found from $P(\mathbf{r},\tau) = U(\mathbf{r},\tau)/\int_0^\infty d\tau U(\mathbf{r},\tau)$. The anisotropic light diffusion problem may be reduced to the familiar isotropic form by rescaling the axes, such that for our geometry we have [14]

$$\left[\frac{\partial}{\partial\tau} - D\frac{\partial^2}{\partial\zeta^2} - \frac{1}{\mu_a}\right]U(\mathbf{r},\tau) = 0 \tag{5}$$

where D is the average diffusivity and $\zeta = \sqrt{D/D_\perp}x$. This equation is valid as long as the plane-wave conditions are met experimentally; that is, the component of l^* along the anisotropy is much less than the width of our expanded beam. Eq. (5) is solved using zero net-flux boundary conditions discussed elsewhere [9].

We note that Eq. (3) assumes the dynamic scattering cross-section can be approximated with its form for a dilute colloidal suspension [15]. Recently, an anisotropic multiple light scattering formalism has been developed and applied to light scattering in nematic liquid crystals [16]; however, the nature of light scattering in nematics differs from that in colloidal systems due to the smaller length-scale structures. In the future, adaption of this formalism to anisotropic colloidal suspensions may improve the analysis.

The magnitude of the light transport anisotropy is established through the steady-state transmission of a point-source through the sample. Fig. (1) shows images of the diffuse depolarized intensity collected by our ccd camera for 45 and 150

seconds after the field is applied at $\lambda = 16$. The ratio of the major and minor axes increases rapidly to 1.6 at 15 seconds as the chains are initially formed. At 45 seconds, the ratio is 1.8 and increases slowly to 2.2 at 150 seconds; this relatively small anisotropy validates the use of Eq. (5). The ratios are insensitive to switching the field strength to lower values, and the images return immediately to the isotropic values when the field is turned off.

Estimation of l^* and l_a. The absorption length l_a is $1.12 \pm 0.08mm$. Using this value and the calculated particle self-diffusion coefficient D_s, we fit the field-off autocorrelation to find $l^* = 790 \pm 10\mu m$ as shown in Fig. (2). The relatively large value of l^* compared with systems such as polystyrene spheres [10] can be attributed to the lower contrast of our droplets.

As mentioned previously, changes in the spatial arrangement and interactions of scatterers alter the diffuse transmittance through the sample. In the case of dense or interacting suspensions, l^* is proportional to the weighted average over the particle form factor $P(q)$ and structure factor $S(q)$ [9, 10, 11, 12]:

$$l^{*-1} \propto 2k_0{}^{-2} \int_{4\pi} q^2 P(q) S(q) d\Omega. \qquad (6)$$

To assess the effect of the dipolar interactions and chain structures on l^*, we monitor the diffuse transmittance through our sample and measure the normalized increase of the scattering length $\Delta l^*(t)/l^*(0)$. For $L > l_a$, the diffuse transmittance may be written as [13]:

$$T(L) = \frac{10 l^*}{3 l_a} exp(-L/l_a). \qquad (7)$$

Expanding Eq. (7) to three terms and dividing by $T(0)$, we find an expression for the normalized change in the diffuse transmittance $\Delta T(t)/T(0)$ as a function of $\Delta l^*(t)/l^*(0)$ [17].

During the experiments, $\Delta l^*(t)/l^*(0)$ increases rapidly to 0.20 ten seconds after applying the field, then increases linearly to 0.24 at 150 seconds. Thus, l^* varies by less than approximately 2% during our autocorrelation measurements and does not change when the field is stepped to lower values; it does return immediately to zero when the field is turned off. This suggests that structure dominates l^* and there is a minimal amount of structural change when the field is reduced for our dynamic measurements.

DWS results. As shown in Fig. (2), the autocorrelation $g^{(1)}(t)$ for the field-off data is well-described by the isotropic solution of Eq. (3) by fitting l^* using our measured value for l_a and calculated value for D_s. The next three curves show $g^{(1)}(t)$ measured 90 seconds after applying the field. The autocorrelations now show a shift to longer decay times, increasing with higher values of λ. Unlike the isotropic case, the autocorrelations for the dipolar systems cannot be fit using a single

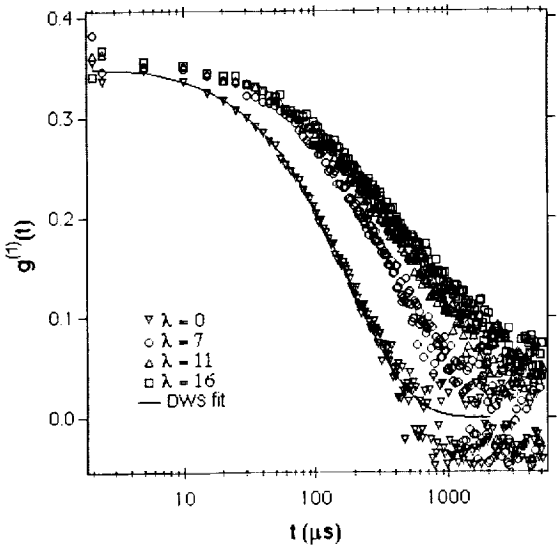

Figure 2: Measured DWS autocorrelation functions for the isotropic MR suspension and three field strengths measured 90s after applying the initial field. The solid line shows a fit of the solution to Eq. (3). Increasing λ shifts the decay to longer times.

characteristic decay time such as $(D_s k_0{}^2)^{-1}$. Instead, we calculate the mean-squared displacement with time $\langle \Delta r^2(t) \rangle$ from the solution of Eq. (3).

Fig. (3) shows $\langle \Delta r^2(t) \rangle$ scaled by the particle diameter d for each dipole strength as a function of scaled time $tD_s d^{-2}$. The straight solid line in each plot represents self-diffusion, which the field-off data follows very well. When the field is applied, the initial mean-squared displacements follow a similar slope which is less than that of free three-dimensional (3D) diffusion, but consistent with two-dimensional (2D) diffusion (the dashed, straight lines in Fig. (3)) irrespective of dipole strength. As the time increases, $\langle \Delta r^2(t) \rangle$ diverges further from the free diffusion limit, exhibiting a constrained, subdiffusive motion. The magnitude of deviation from the solid line increases as we increase the dipole strength, suggesting that the DWS experiment is sensitive to the small-wavelength motions of the dipolar chains. The chains should exhibit a spectrum of modes of motion, including short-time individual "vibrations" of each particle, collective chain motion at intermediate time-scales, and eventually the long-time diffusion of the entire chain. Since the scattering data exhibits the same initial slope, our experiments appear to measure the Brownian motion of the particles comprising the dipolar chains. Particle diffusion is hindered by constraint to the chain through the dipolar interaction with its neighbors. Movement perpendic-

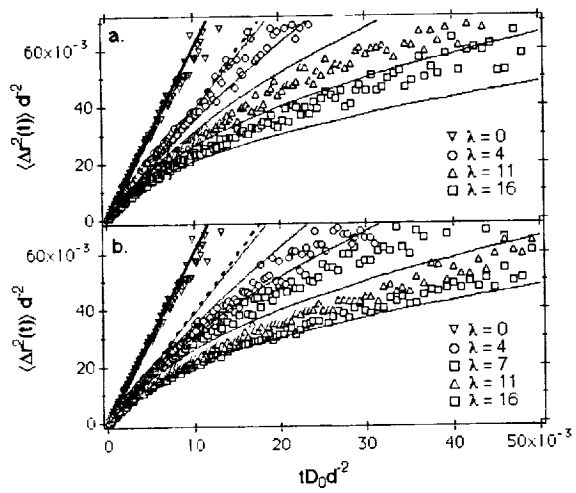

Figure 3: $\langle\Delta r^2(t)\rangle$ calculated from $g^{(1)}(t)$ using the solution to Eq. (3). The straight, solid line represents 3D self-diffusion, the dashed line represents 2D self-diffusion, and the five curved solid lines are simulation results for dipolar chains of 100 particles with $\lambda = 5, 10, 15, 20$, and 26, increasing from left to right in the figures. (a) DWS data taken 15 seconds after applying the magnetic field. (b) Data taken 90 seconds after applying the field.

ular to the chain direction dominates, indicated by the initial 2D motion, while the constraint increases as we increase the dipole strength, thereby stiffening the chains. It is also apparent that the mobility 90 seconds after applying the field is reduced further from the freely-diffusing limit than that measured 15 seconds after applying the field, possibly due to the lateral aggregation of chains with time. This is consistent with the slow increase in l^* measured through the diffuse transmittance. Lateral aggregation should stiffen the magnetic chains further, and thus decrease chain segment motion.

Brownian dynamics simulations. To test our interpretation of the DWS experiments, we conduct Brownian dynamics simulations of magnetic chains over the time scales observed in our experiments [18, 19]. Briefly, the simulations solve the equation of motion of the ν^{th} particle taking into account three forces acting on it: a dipolar force between neighboring particles $F_i^{D,\nu}$, a stochastic Brownian force $F_i^{Br,\nu}$, and an excluded volume interaction $F_i^{EV,\nu}$. Again scaling displacement with the particle diameter d and time with the characteristic time a free particle diffuses its diameter $D_s d^{-2}$, the dimensionless equation of motion, neglecting inertia, is written as:

$$q_i^\nu = \lambda F_i^{D,\nu} + F_i^{Br,\nu} + cF_i^{EV,\nu} \qquad (8)$$

where λ is the dipole strength. The simulations are conducted for $\lambda = 5, 10, 15, 20$, and 26 using ensembles of 500 chains for proper averaging. We compute the mean-squared deviation of each particle, $\langle\Delta r_\nu^2(t)\rangle$ averaged over all particles in the simulation for chains of 20 and 100 particles.

Since our experiments are most sensitive to lateral fluctuations in the chain, we extract the mean-squared displacement projected onto a plane orthogonal to the chain direction. We compare the 100 particle simulation results to the DWS data in Fig. (3). The differences in $\langle\Delta r_\nu^2(t)\rangle$ using 20 particles showed no consistent trend and did not exceed the expected accuracy. The simulations capture the qualitative aspects of the experimental results nicely; however, there are quantitative discrepancies for both the 15 and 90 second data. For instance, the simulations require a higher dipole strength to generate similar displacements with time. This could reflect the fact that the simulation neglects the local field created from the formation of the dipolar chains as well as higher moment interactions [20]. At this time we should not expect exact quantitative agreement for a variety of reasons including neglect of hydrodynamic interactions and magnetic interactions between chains.

4 Conclusions

As a class of tunable fluids, MR systems are interesting due to their fast rheological response and possible applications in mechanical systems such as brakes and clutches. In this paper, we presented initial studies of the dynamics of MR fluids using diffusing-wave spectroscopy. By accounting for changes in the light transport properties of the system, we found dynamical differences which depend on the interaction strength between the fluid particles. The DWS experiments offer the capability to measure the dynamics of the MR fluid systems on time- and length-scales that capture the short-wavelength chain motions. Brownian dynamics simulations of dipolar chains support our experimental results. Both experiments and simulations show initial particle displacements that are independent of field strength; however, at longer times, we see a constrained sub-diffusive movement that increases with the dipolar interactions. We plan to investigate the quantitative agreement between simulations and experiments by incorporating hydrodynamic interactions and chaining effects into our simulations in the near future.

5 Acknowledgements

The authors thank Patrick Doyle for his aid with the simulations, Jerome Bibette for providing the ferrofluid, and Marc Fermigier for fruitful discussions. Support by NASA (Grant

No. NAG3-1887-1) is gratefully acknowledged.

References

[1] Z. Shulman, R. Gorodkin, E. Korobko, and V. Gleb, J. Non-Newtonian Fluid Mech. **8**, 29 (1981); W. Leventon, Design News 185 (1993); J. Carlson and K. Weiss, Machine Design **Aug. 8**, 61 (1994).

[2] J. Promislow, A. Gast, and M. Fermigier, J. Chem. Phys **102**, 5492 (1995).

[3] J. Promislow and A. Gast, Langmuir **12**, 4095 (1996); Phys. Rev. E **56**, 642 (1997).

[4] M. Hagenbüchle and J. Liu, Appl. Opt. **36**, 7664 (1997).

[5] A. Silva, B. Bond, F. Plouraboué, and D. Wirtz, Phys. Rev. E **54**, 5502 (1997).

[6] T. Halsey and W. Toor, J. Stat. Phys. **61**, 1257 (1990).

[7] J. Bibette, J. Colloid Interface Sci. **147**, 474 (1991).

[8] A. Gast and C. Zukoski, Adv. Colloids Interface Sci. **30**, 153 (1989).

[9] D. Pine, D. Weitz, J. Zhu, and E. Herbolzheimer, J. Phys. **51**, 2101 (1990).

[10] D. Pine, D. Weitz, P. Chaikin, and E. Herbolzheimer, Phys. Rev. Lett. **60**, 1134 (1988).

[11] S. Fraden and G. Maret, Phys. Rev. Lett. **65**, 512 (1990).

[12] D. A. Weitz and D. J. Pine, in *Dynamic Light Scattering*, edited by W. Brown (Oxford University Press, New York, 1993), pp. 652–720.

[13] A. Z. Genack, in *Scattering and Localization of Classical Waves in Random Media*, edited by P. Sheng (World Scientific, Singapore, 1990), pp. 207–311.

[14] H. S. Carslaw and J. C. Jaeger, *Conduction of Heat in Solids*, 2nd ed. (Clarendon Press, New York, 1986).

[15] F. C. MacKintosh and S. John, Phys. Rev. B **40**, 2383 (1989).

[16] H. Stark and T. C. Lubensky, Phys. Rev. E **55**, 514 (1997); H. Stark *et al.*, J. Opt. Soc. Am. A **14**, 156 (1997).

[17] J. M. Ginder, Phys. Rev. E **47**, 3418 (1993).

[18] P. S. Doyle, Ph.D. thesis, Stanford University, 1997.

[19] H. C. Öttinger, *Stochastic Processes in Polymeric Fluids* (Springer, New York, 1996).

[20] H. Zhang and M. Widom, Phys. Rev. E **51**, 2099 (1995).

PHYSICS OF COLLOIDS IN SPACE

P.N. Segre, L. Cipelletti, D.A. Weitz
Dept. of Physics and Astronomy
University of Pennsylvania

P.N. Pusey, W.C.K. Poon, A.B. Schofield
Dept. of Physics
University of Edinburgh

Please refer to the Conference Book of Abstracts or the NCMR Website at http://www.ncmr.org

Analogies between colloidal sedimentation and turbulent convection at high Prandtl numbers

P. Tong , B. J. Ackerson, Department of Physics, Oklahoma State University, Stillwater, Oklahoma 74078, USA,
ptong@osuunx.ucc.okstate.edu

In a recent experiment, Segrè et al. [1] used the particle imaging velocimetry (PIV) technique to measure the spatial correlation function, $C(\ell) = \langle \delta v(r) \delta v(r+\ell) \rangle$, of the velocity fluctuation δv in a sedimenting suspension of non-Brownian particles over a wide range of particle concentrations and sample sizes. They found that the measured $C(\ell) \sim \exp(-\ell/\xi)$, where the velocity correlation length ξ depends on the particle radius a and volume fraction ϕ_0 in a non-trivial power-law form $\xi \simeq a\phi_0^{-1/3}$. In this paper we propose a new set of coarse-grained equations of motion to describe concentration and velocity fluctuations in a dilute sedimenting suspension of non-Brownian particles. With these equations we find that colloidal sedimentation is analogous to high Rayleigh number, high Prandtl number turbulent convection [2,3]. Our model explains the experimental results by Segrè et al. and also provides a coherent framework for the study of sedimentation dynamics in different colloidal systems.

To understand the basic principles governing the colloidal sedimentation, we consider a simple case of a dilute sedimenting suspension of hard spheres in a long cylindrical tube of radius L. To separate the velocity fluctuation δu from the mean settling velocity $\bar{v}$, we choose a uniform suspension with $\bar{v} = 0$ as our reference system. It has been suggested [1,4] that velocity fluctuations in a sedimenting suspension may arise from fluctuations of the local particle concentration. Therefore, we model the colloidal sedimentation with a coarse-grained Navier-Stokes equation. The fluid velocity $\delta\mathbf{u}$ and pressure δp at a point $\mathbf{x}$ satisfy the creeping flow equation [5]

$$\nabla \delta p(\mathbf{x}) - \eta \nabla^2 \delta\mathbf{u}(\mathbf{x}) = \mathbf{f}\delta n(\mathbf{x}), \tag{1}$$

where η is the viscosity of the fluid and δn [$= n(\mathbf{x}) - \bar{n}$] represents the fluctuation of the particle number density $n(\mathbf{x})$ about its mean $\bar{n}$. In the above, $\mathbf{f} = (4\pi/3)a^3\Delta\rho\mathbf{g}$ is the buoyancy force acting on a particle of radius a, where $\mathbf{g}$ is the gravitational acceleration and $\Delta\rho = \rho_p - \rho_s$ is the density difference between the particle (ρ_p) and the solvent (ρ_s). In writing Eq. (1) we have assumed that the fluid volume element δV is a coarse-grained volume, which is large enough to contain many particles but is small enough such that the particle distribution inside δV is uniform. In this case, we have $\mathbf{f}\delta n(\mathbf{x}) = \Delta\rho\mathbf{g}[\phi(\mathbf{x}) - \phi_0]$, where $\phi(\mathbf{x})$ is the particle volume fraction and ϕ_0 is its mean value.

Nondimensionalizing Eq. (1) with respect to the length L, the time L^2/D, and the concentration ϕ_0, we have

$$-\frac{1}{\sigma}\nabla\delta p(\mathbf{x}) + \nabla^2\delta\mathbf{u}(\mathbf{x}) = Ra\,\phi(\mathbf{x})\hat{\mathbf{z}}, \tag{2}$$

where the unit vector $\hat{\mathbf{z}}$ is directed upward opposite to the direction of $\mathbf{g}$, and the dynamic pressure δp has included a term, $-\Delta\rho g\phi_0 z$, to absorb contributions from the constant forcing term $-\Delta\rho\mathbf{g}\phi_0$. In Eq. (2) the Rayleigh number Ra is defined as

$$Ra = \Delta\rho g\phi_0 L^3/(\eta D), \tag{3}$$

where D is an effective diffusion constant of the particles. The Schmidt number σ is given by $\sigma = \nu/D$ with ν being the kinematic viscosity of the fluid. For a dilute suspension of small colloidal particles, D is approximately equal to the particle self diffusion constant $D_s = k_BT/(6\pi\eta a)$, where k_BT is the thermal energy. For large non-Brownian particles, however, the effect of thermal agitations is negligible and their diffusion-like motion is produced by the hydrodynamic interactions between the particles [6]. Nicolai et al. have shown [7] that the hydrodynamic diffusivity has the form $D_h \simeq 5aU_0$, where $U_0 = 2a^2\Delta\rho g/(9\eta)$ is the Stokes velocity.

With the hydrodynamic diffusivity D_h, Eq. (3) becomes

$$Ra = 0.9\phi_0(\frac{L}{a})^3. \tag{4}$$

It should be mentioned that while it is cancelled out in Ra, $\Delta\rho g$ is needed so that D_h can be used to describe the hydrodynamic diffusion of the settling particles at small length scales. Equation (2) together with the continuity equation for an incompressible fluid

$$\nabla \cdot \delta\mathbf{u} = 0 \tag{5}$$

and the advective mass diffusion equation

$$\partial_t\phi + (\delta\mathbf{u}\cdot\nabla)\phi = \nabla^2\varphi \tag{6}$$

complete the description of concentration and velocity fluctuations in colloidal sedimentation.

It is evident that Eqs. (2)-(6) are the same as those for buoyancy-driven convection [3]. Velocity and concentration fluctuations in colloidal sedimentation are therefore analogous to those in buoyancy-driven convection, and they are completely controlled by the two dimensionless parameters Ra and σ, once the boundary conditions are specified. We now estimate typical values of Ra and σ in colloidal sedimentation. In the experiment by Segrè et al. [1], the particle's radius $a \simeq 8\ \mu m$, Stokes velocity $U_0 \simeq 6.5\ \mu m/s$, volume fraction $\phi_0 \simeq 0.05$, and the characteristic sample size $L \simeq 1\ cm$. With these experimental values, we find $D_h \simeq 2.6 \times 10^{-6}\ cm^2/s$, $Ra \simeq 8.8 \times 10^7$, and $\sigma \simeq 3800$. The Schmidt number σ

is equivalent to the Prandtl number in thermal convection. Colloidal sedimentation is, therefore, associated with high Rayleigh number, high Prandtl number turbulent convection.

To understand the sedimentation dynamics, it is helpful to distinguish two characteristic length scales in convection: the viscous dissipation length δ_v and the diffusive dissipation length δ_d. The values of δ_v and δ_d are determined, respectively, by the transition Reynolds number $Re_c = \widetilde{\delta u}\delta_v/\nu$ and the transition Peclet number $Pe_c = \widetilde{\delta u}\delta_d/D_h$. Here $\widetilde{\delta u}$ is the rms value of the velocity fluctuation δu averaged over a volume of δ_v^3 (or $\delta_d{}^3$). It is the ratios of these lengths to each other and to the sample size L that determine the flow state of the system [2]. For high-Ra, high-σ turbulent convection, one anticipates that the flow consists of three different regions: (i) $a < \ell < \delta_d$, (ii) $\delta_d < \ell < \delta_v$, and (iii) $\delta_d < \ell < L$. In Region (i), molecular viscosity and hydrodynamic diffusivity determine the momentum and mass transport processes, respectively, and hence the particle distribution remains uniform without any large fluctuations. In Region (ii) turbulent (or eddy) diffusivity and molecular viscosity are dominant, and thus large fluctuations in particle concentration are expected but the velocity field remains relatively smooth. Finally, in Region (iii) turbulent diffusivity and viscosity both dominate over the corresponding hydrodynamic and molecular processes. In this case, one expects to see large fluctuations both in particle concentration and in velocity at different length scales.

We first discuss the length δ_d, above which velocities become large and concentration fluctuations are transported by convection. This occurs when the local Peclet number $Pe = \widetilde{\delta u}\ell/D_h$ becomes larger than Pe_c. Recent thermal convection experiments have shown [8] that while turbulent mixing creates on average an isothermal fluid in the turbulent bulk region, large temperature fluctuations still remain in the region and the characteristic length scale associated with these fluctuations is of the order of δ_d. Therefore, the velocity correlation length ξ is determined by δ_d in Region (ii). According to Kraichnan's theory [2],

$$\delta_d \simeq \left(2\pi^2 Pe_c^2\right)^{1/3} L Ra^{-1/3}, \qquad (7)$$

where the power law amplitude is expressed in terms of the numerical value of Pe_c. Priestley [9] first gave a direct argument for the $Ra^{-1/3}$ scaling. He argued that when Ra is large enough, δ_d should be a new length scale independent of the sample size L. With Eqs. (7) and (4), we immediately have $\xi \sim \delta_d \simeq LRa^{-1/3} \simeq a\phi_0^{-1/3}$. The mapping of colloidal sedimentation to turbulent convection, therefore, explains the experimental finding that $\xi \simeq 11a\phi_0^{-1/3}$. It also provides a physical interpretation for the existence of a velocity cut-off length, which prevents hydrodynamic dispersion coefficients from being divergent.

We now discuss the velocity variance $\widetilde{\delta u}$ in colloidal sedimentation. According to Kraichnan's theory [2],

$$\widetilde{\delta u} \simeq \frac{Pe_c D_h}{\delta_d} \simeq \frac{Pe_c D_h}{\left(2\pi^2 Pe_c^2\right)^{1/3} LRa^{-1/3}}. \qquad (8)$$

Eq. (8) states that at the transition Peclet number Pe_c, the mass flux due to hydrodynamic diffusion, $D_h\widetilde{\delta\phi}/\delta_d$, is approximately equal to that by convection, $\widetilde{\delta u}\widetilde{\delta\phi}$. Because $\delta_d \simeq a\phi_0^{-1/3}$ and $D_h \simeq aU_0$, we find from Eq. (8) that $\widetilde{\delta v} \sim \widetilde{\delta u} \simeq D_h/\delta_d \simeq U_0\phi_0^{1/3}$, which is independent of the sample size L. This result agrees well with the experimental finding that $\widetilde{\delta v} \simeq 2U_0\phi_0^{1/3}$ [1].

We thank P. M. Chaikin for useful discussions. This work was supported by the National Aeronautics and Space Administration under the joint grant No. NAG3-1852.

[1] P. N. Segrè, E. Herbolzheimer, and P. M. Chaikin, Phys. Rev. Lett. **79**, 2574 (1997).

[2] R. H. Kraichnan, Phys. Fluids, **5**, 1374 (1962).

[3] E. D. Siggia, Annu. Rev. Fluid Mech., **26**, 137-168 (1994).

[4] E. J. Hinch, in *Disorder and Mixing*, p. 153, edited by E. Guyon, J.-P. Nadal, and Y. Pomeau, (Kluwer, Dordrecht, 1988).

[5] R. E. Caflisch and J. H. C. Luke, Phys. Fluids, **28**, 759 (1985); D. L. Koch and E. S. G. Shaqfeh, J. Fluid Mech., **224**, 275 (1991).

[6] R. H Davis, J. Fluid Mech., **310**, 325 (1996), and references therein.

[7] H. Nicolai and E. Guazzelli, Phys. Fluids, **7**, 3 (1995); H. Nicolai et al., Phys. Fluids, **7**, 12 (1995).

[8] G. Zocchi, E. Moses, and A. Libchaber, Physica A **166**, 387 (1990).

[9] C. H. B. Priestley, *Turbulent Transfer in the Low Atmosphere*, (University of Chicago Press, Chicago, 1959).

STRUCTURE, HYDRODYNAMICS, AND PHASE TRANSITIONS OF FREELY SUSPENDED LIQUID CRYSTALS

Noel Clark
University of Colorado

Paper Unavailable

Session 2C

Interfacial Phenomena I

THE EFFECTS OF THIN FILMS ON THE HYDRODYNAMICS NEAR MOVING CONTACT LINES

K.Stoev [1], E. Ramé [2], T. Leonhardt [3], S. Garoff [4]
[1,3,4] Physics Department, Carnegie Mellon University, Pittsburgh, PA
[2] National Center for Microgravity Research in Fluids and Combustion,
c/o NASA Lewis Research Center, Cleveland, OH 44135

1. INTRODUCTION

Dynamic wetting, the displacement of one fluid by another immiscible fluid on a solid surface, controls many natural and technological phenomena, such as coating depositions and oil recovery. Modeling these processes is not trivial because an unphysical stress singularity arises at the contact line when the classical hydrodynamic assumptions (incompressible Newtonian fluids, non-deformable solids, and the no-slip boundary condition at the solid surface) are applied to the whole fluid body.[1,2] Analyses postulating an "inner" region very near the contact line with unique, non-classical hydrodynamics[3,4] remove this singularity and successfully describe the interface shape and the flow field near moving contact lines.[5-8] Many inner models have been postulated,[3,9-16] but no one has been able to directly identify the unique hydrodynamics of the inner region thus far.

Films formed ahead of an advancing or receding contact line are tempting as candidates for removing the contact line singularity because they can alter the stress on the macroscopic fluid body at the fluid-solid interface.[7,14,17] Thin films (in this paper of molecular thickness) form ahead of static or slowly advancing menisci[18-22] by slow diffusive transport or more rapidly via vapor deposition. In either case, these films can only affect the hydrodynamics if they form sufficiently fast and over a long enough spatial range that the contact line moves across a pre-existing film. Even if the film is short, it may form a "foot" in front of the moving contact line. Thicker, mobile films (in this paper on the order of microns thick) form when the receding fluid leaves behind a thin but mobile fluid layer on the solid[23] or via Marangoni-driven flows.[24]

The role films play in the hydrodynamics near moving contact lines depends on whether they behave as chemisorbed layers on the solid, as Newtonian fluids, or possess a complex, non-Newtonian response to the strain rate next to the contact line. Even the same film may exhibit a range of rheological behaviors when varying contact line speeds force it to respond over different time scales. In many technologically relevant processes, fluids are forced to move over these films; in this paper we explore how these films influence contact line hydrodynamics.

The regime where a receding contact line leaves behind a macroscopic mobile film has been widely studied. Landau & Levich[23] first predicted that the thickness, d, of a film deposited on a solid pulled vertically out of a Newtonian liquid in the limit of small capillary number, $Ca \equiv U\eta / \gamma$ (where U is the velocity of the solid, η the fluid viscosity and γ the surface tension) follows the relation $d \sim lCa^{2/3}$ where l is a length which depends on the specific geometry of the problem. Bretherton[25] analyzed the interface shape and the film thickness when a bubble moves in a capillary tube leaving behind a liquid film; he also considered the interface shape of a liquid slug advancing over a film predeposited on the capillary tube wall. Cox,[26] Ruschak[27] and Wilson[28] discuss the same problem focusing on varying conditions for the film deposition. Tuck & Schwartz[14] present a detailed numerical interface shape analysis of the evolution equation for fluid flowing down a wall precoated with a film of the same material. Park & Homsy[29] formalize Bretherton's results by an asymptotic matching process.

Many have measured the film thickness as a function of receding speed[30,31] and the critical speed for forming a macroscopic film.[32,33] To probe the effects of spontaneously formed and preexisting thin films on contact line hydrodynamics, we measure advancing and receding interface shapes near the macroscopic contact line. (A more complete discussion of this work may be found in ref. 34.) We examine to what extent films existing in front of macroscopic fluid bodies alter the fluid motion near moving contact line as described by two models, valid at low Ca. The first one is the three-region model[4,5] which correctly describes the hydrodynamics near moving contact lines but does not address the inner physics that mitigate the classic stress singularity. In this model, a film can only affect the hydrodynamics at the inner region level. The second model, derived from the Landau & Levich theory, models the hydrodynamics of receding fluids leaving behind a uniform film or fluids advancing over a pre-deposited film of the same material. Landau & Levich analyze a specific inner region; their film is the inner mechanism which removes the classic contact line singularity, with the film thickness being the inner length scale.

2. MODELS

2.1 Fluids Depositing Thick Films or Advancing Over Liquid Layers

The thickness of a film left behind by most fluids in the small *Ca* regime described by Landau & Levich[23] and Bretherton[25] is on the order of microns. Far from the contact line, the thickness of the fluid layer is uniform and the film effectively extends to infinity, thus avoiding the classic contact line singularity. We use Cartesian coordinates, with x along the solid surface, y perpendicular to it, and $y=h(x)$ being the location of the fluid/vapor interface (see Fig. 1a). The origin of the of the y axis is at the solid surface and that of the x axis is obtained via the asymptotic matching as discussed below.

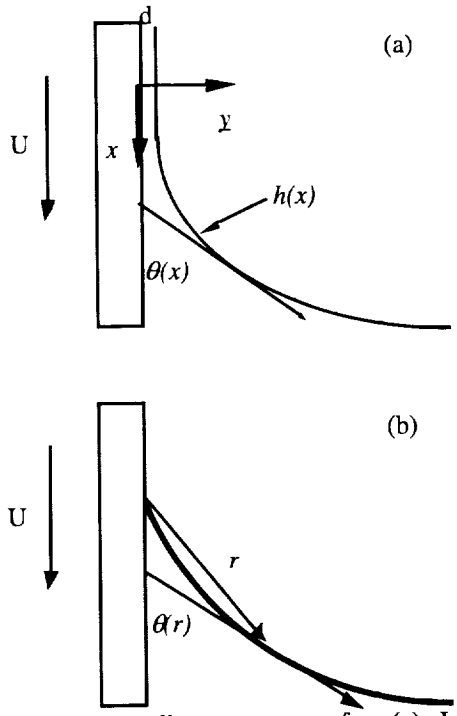

Figure 1. Coordinate systems for (a) Landau & Levich's theory. (b) three-region model.

Between the uniform film and the static meniscus there is a transition region where viscous and surface tension forces balance. Using $d\ Ca^{-1/3}$ and d as the x and y scales, the interface in recession (subscript r) asymptotes to a uniform unit thickness at $x\to-\infty$; whereas at $x\to\infty$

$$h_r \to A_r x^2 + B x + C + (18\, x\, A_r^2)^{-1} + \ldots \quad (2).^{25,29}$$

A_r is an absolute constant, found to be ~0.67. The classic result,

$$d/R = 2\, A_r\, Ca^{2/3} \quad (3)$$

follows from matching.

In our experiments, R is the radius of curvature formed by a static meniscus with zero contact angle on a cylinder of outer radius, R_T, tilted an angle δ from the vertical. When $R_T \gg a$,[5]

$$R = \left[\sqrt{2(1-\sin\delta)}\,/\,a + 0.39/R_T\right]^{-1},$$

where $a \equiv (\gamma / \rho\, g)^{1/2}$ is the capillary length, ρ is the density of the liquid and g is the acceleration of gravity. Matching of the film interface shape (2) to a static-like meniscus also requires that the macroscopic meniscus be tangent to the solid at $x=-B/2A_r$,[29] and this condition identifies the origin of x. A uniformly valid expression for the angle, θ_r, between the solid and the local tangent to the fluid/vapor interface (see Fig. 1a), is:

$$\bar{x}<0:\ \theta_f = Ca^{1/3} h_r' \ , \quad (4)$$

$$\bar{x}>0:\ \theta_f = Ca^{1/3} h_r' + f(\bar{x}Ca^{1/3}; a/R_T, \delta) - 2Ca^{1/3} A_r \bar{x} \quad (5)$$

Here f represents a static shape with a 0° contact angle rising against the cylinder; $\bar{x} \equiv x+B/2A_r$, and the primes denote $d(.)/d\bar{x}$.

As in the receding case, the advancing (subscript a) interface shape h_a approaches a unit thickness as $x\to-\infty$. In contrast, however, Bretherton[25] showed that this approach is modulated by a parameter, β , which generates a one-parameter family of solutions. The behavior of these solutions as $x\to\infty$ when $A_a(\beta)\neq 0$ is:

$$h_a \sim A_a(\beta)\, x^2 + B(\beta)\, x + C(\beta) + (18\, x\, A_a(\beta)^2)^{-1} + \ldots \quad (7)$$

For $\beta = \beta^*$ such that $A_a(\beta^*)=0$, the large-x behavior (7) becomes singular and is replaced by: [36]

$$h_a \sim x(9\ln(x))^{1/3} \quad (8).$$

In this case, the outer solution matched to (8) need not extrapolate to a 0° contact angle.

The uniform asymptotic approximation to the interface shape when $A_a \neq 0$ is analogous to (4) and (5):

$$\bar{x}<0\ \theta_a = Ca^{1/3} h_a' \quad (9)$$

$$\bar{x}>0\ \theta_a = Ca^{1/3} h_a' + f(\bar{x}Ca^{1/3}; a/R_T, \delta) - 2Ca^{1/3} A_a \bar{x} \quad (10)$$

The question of the conditions needed to achieve each of the behaviors (7) and (8) is, to our knowledge, still unresolved. On the one hand, the rear of Bretherton's bubble must behave as (7) because the thick wetting film has been deposited by the fluid receding at the front of the same bubble at the same *Ca*. On the other hand, Tuck & Schwartz[14] and de Gennes[17] select the logarithmic behavior (8) in their analyses. Below we make some observations aimed at clarifying this issue.

Because of the free parameter β, the film thickness in advance is not uniquely determined by *Ca*. These three quantities are related by:

$$d/R=2A_a(\beta)\,Ca^{2/3} \text{ as } Ca\to 0, \qquad (11)$$

so that we can fix both *Ca* and *d/R* independently within the restrictions of the model. This is feasible experimentally since we can prepare a film of any thickness and then force the meniscus forward at any *Ca*. Examination of (11) shows that, as long as $\beta \neq \beta^*$, $(d/R)Ca^{-2/3}\to \text{const}=2A_a(\beta)\neq 0$ as $Ca\to 0$, implying that polynomial behavior (7) applies. Since $A_a(\beta)\to 0$ as $\beta\to\beta^*$, we conjecture that the logarithmic behavior (8) should arise in a parameter space compatible with $(d/R)Ca^{-2/3}\to 0$ as $Ca\to 0$. This conjecture is consistent with the analysis of Wilson & Jones.[38] Thus, (8) would arise for decreasing *d/R* at a given fixed *Ca*, or at increasing *Ca* for a fixed *d/R*.

This model poses severe demands on the fluid. For the fluid in the film to behave as predicted, it must be able to develop velocity gradients of order *U/d* in a time scale $aCa^{1/3}/U$.[34] Due to interactions with the solid surface, very thin (molecular size) films may not respond in this manner.

2.2 *Menisci Moving Over Solid Surfaces*

We also compare our data to the three-region model.[5] In contrast to the cases discussed above for thick, mobile fluid films, this model describes the spreading of liquids over dry surfaces or surfaces covered with thin, adsorbed, immobile films. When a fluid spreads over such a surface, the liquid-vapor interface valid as $r/a\to 0$ is given by:

$$\theta(r) = g^{-1}\left[g(\omega_0) + Ca\,\ln r/a\right] + f(r/a;\, a/R_T,\, \delta,\, \omega_0) - \omega_0 \qquad (12),$$

where *r* is the distance from the contact line to a point on the interface (See Fig. 1b), *f* is the static shape with contact angle ω_0, with

$$g(x) \equiv \int_0^x (2y - \sin 2y)/(4\sin y)\, dy .$$

Details and restrictions of this model may be found in refs. 4 and 5.

As in earlier work,[5-8,39-41] we use video microscopy and digital image analysis to measure the liquid/air interface shape formed on the outside of a tube 1.25cm in diameter. The tube is immersed or withdrawn from a bath of a polymer liquid, Poly(dimethylsiloxane) (PDMS), at constant speeds. In our experiments we used two solid surfaces: Pyrex (a high energy surface) and Pyrex coated with Aquapel™, a perfluorinated surfactant (a low energy surface). Details of all experimental procedures and data analysis may be found in ref. 34.

3. RESULTS AND DISCUSSION

3.1 Advancing Motions Over Molecular Films

Spontaneous films of 1000cSt PDMS do form in front of static or slowly advancing contact lines on the wetting surface; but they grow extremely slowly. We have determined[34] that there is no precursing film of length greater than 2.5μm –the detectability limit of our optical microscopy at advancing velocities ≥5μm/sec. Thus, for these velocities, either a film shorter than 2.5μm exists and may relieve the stress singularity; or another mechanism must relieve the singularity for this system. However, a film mechanism may be appropriate in other systems where films grow more rapidly by vapor transport or Marangoni flow as opposed to surface diffusivity.

By comparing data to two different models, we have seen a marked contrast between contact lines moving over molecular scale and micron scale films. When the solid surface is completely free of molecules from the fluid phase, the three-region model applies and describes the data. However, the three-region model also describes two cases where molecular thin films exist. In the first of these cases, films with thicknesses on the order of a monomer unit (7Å), which grow across the surface by diffusive motion and are not chemisorbed to the solid, do not provide the hydrodynamic response required by the Landau & Levich model; but they do provide some inner scale mechanism compatible with the three-region model. In the second case, films with thickness on the order of the radius of gyration of our polymer (30Å) which are very tightly bound to the solid behave similarly. We could speculate that while such films cannot "flow", they can deform, perhaps in the time scale set by the motion of the contact line. However, the 30Å films behave in the same way as the 7Å films. In contrast, the hydrodynamics near contact lines moving over micron scale films at small *Ca* is described by the Landau & Levich as expected. Thus, the definition of what constitutes a hydrodynamic film is subtle and hinges on the ability of the material in the film to develop a velocity gradient in a time scale dictated by the speed of the contact line passage. When the film can respond fast enough, the Landau & Levich model may apply. When a very thin film cannot develop such a gradient, the hydrodynamics of a contact line moving over such a film may be described by the three-region model.

3.2 Hydrodynamic Films formed by Receding Contact Lines

Often moving contact lines deposit films on surfaces as they recede. For our system, molecular scale films are not formed behind bulk receding

menisci for

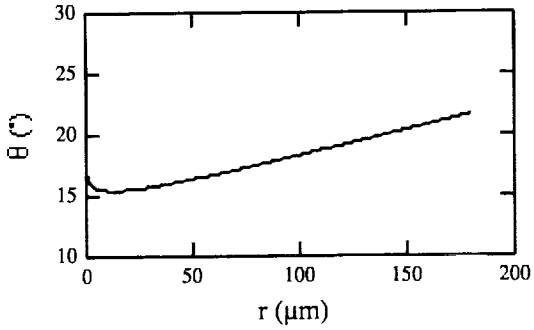

Figure 2. Fit to the data of the three-region model in recession on non-wetting surface. Ca=-2.5x10^{-4}. Solid line: best fit, ω_0=11.5°.

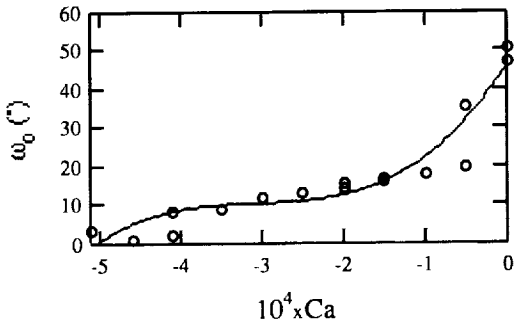

Figure 3. ω_0 vs. Ca in recession on the non-wetting surface. Solid line: 3rd order polynomial fit as guide to the eye.

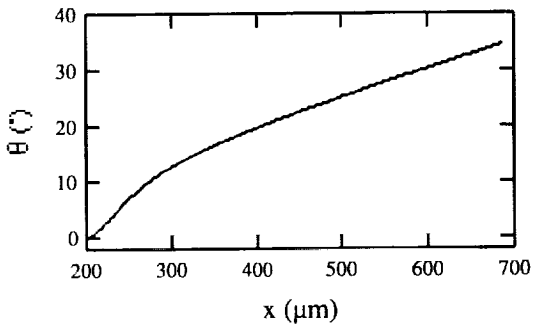

Figure 4. Fit of the Landau & Levich theory in advance. F=3.9 (Ca=1.5x10^{-3}). Solid line: best fit, d=5μm.

either the wetting or the non-wetting surfaces examined. For the wetting system (bare Pyrex solid surface), a thick film is left behind on the substrate at the smallest achievable receding speeds, ~1μm/s. For the nonwetting system (Aquapel™ coated Pyrex tube), no material (not even a molecular film was detected using breath figures) is deposited on the surface below the critical speed, U_{crit}, for drawing a thick film. Even after drawing a thick film at $|U|>|U_{crit}|$, the Young's force trying to keep the surface dry retracts the film as soon as we reduce the receding speed below U_{crit}. This lack of material deposition, even at the molecular level, is somewhat puzzling. In contrast to speculations concerning air entrainment,[45] in this case, molecular scale entrainment of the receding phase has not occurred and entrainment only occurs when receding phase has exhibited a 0° contact angle.

On a nonwetting surface, we have examined the receding interface shape as the speed is increased but before a thick film is pulled. As expected, Eq. (12), the three-region model, describes the hydrodynamics down to Ca=-2.5x10^{-4} (Figure 2). For lower Ca but before thick films are pulled (-5x10^{-4}<Ca<-2.5x10^{-4}), the model fails. This is surprising because the model does not differentiate between advancing and receding motions and all the assumptions of the model, including small curvature, are fulfilled at the same $|Ca|$ where the model works in advance. As we increase the receding speed before a film is pulled, some short-lived pinning events take place along the contact line at Ca~-3.5x10^{-4}. At Ca~-4x10^{-4}, these pinning events pull at the contact line forming an uneven thick film and the contact line becomes broken. Finally, at Ca~-5x10^{-4}, the solid drags a uniform PDMS film. When thick films are deposited, the Landau & Levich - theory correctly describes both the interface shape and the film thickness for Ca>-5x10^{-3}, which suggests this as the parameter limitation of this small-Ca theory.

In full agreement with previous work,[32,33,46] we leave behind thick films as ω_0 approaches 0°. This happens at essentially zero velocity on the wetting surface and at $U=U_{crit}$ for the nonwetting surface (Figure 3).

3.3 Contact lines advancing over Hydrodynamic Films

We deposit a hydrodynamic film on the solid by withdrawing the tube from the PDMS at a controlled speed (Ca~-2.5x10^{-4}). Under these conditions the film thickness is about 5μm. Once the film lies on the solid, we advance the fluid by immersing the tube at various speeds.

Contact lines advancing over preexisting films exhibit richer behavior than receding contact lines. As noted above, the three-region model properly describes the contact lines advancing over molecular scale films. But it fails to describe any portion of the interface shape when thick films preexist on the surface probably because the flow of fluid from the film modifies the motion of the advancing fluid over length scales larger than allowed by the model. Bretherton's advancing model,[25] whose validity is defined by F=O(1) as $Ca\to 0$ where $F\equiv aCa^{2/3}/d$, does describe the data.

We conjecture that, for F "small enough", viscous forces in the film-meniscus transition are so small that the interface emerges with static shape and a 0° contact angle. This selects for $h_a(x)$ the large-x behavior given by Eq. (7) which is the Landau & Levich theory. On the other hand for "large" F, viscous forces in the transition region prevent the interface from exiting the region as a static interface with 0° contact angle. In this regime, the large-x behavior of $h_a(x)$ is given by Eq. (8) and not by Landau & Levich's theory. We have found preliminary evidence of this conjecture. For $F<4$ the Landau & Levich theory accounts for advancing over thick preexisting films (Figure 4, $Ca<2.0\times10^{-3}$) but it begins to fail at higher F. At $F>4$, the macroscopic interface shape does not seem static in the same range of x where it is static for $F<4$. In addition, Figure 5 shows that the theory (Eq. 10) incorrectly predicts the

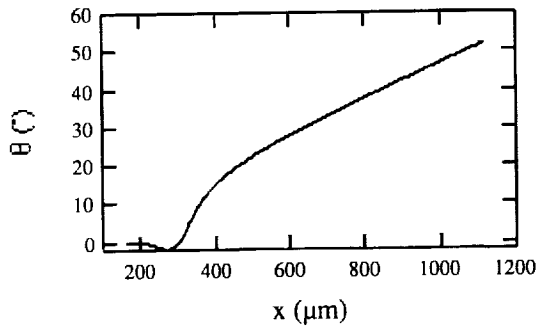

Figure 5. Fit of the Landau & Levich theory in advance. F=5.3 ($Ca=2.4\times10^{-3}$). Solid line: theory with d=5μm determined from film left behind in recession and choice of x-origin that minimizes the square difference.

viscous bending. Further, the three-region model does not fit any portion of the data, possibly because the ratio d/a=1/300 is too large to satisfy the condition $Ca\ln(d/a)=O(1)$ as $Ca\to0$ required by the model. The question remains as to whether this failure of the Landau & Levich theory represents the onset of the logarithmic behavior of Eq. (8) and whether this behavior could actually be observed at higher F values.

4. CONCLUSIONS

We have performed a quantitative study of the interface shape near moving contact lines in the presence of films of the same fluid. By examining the interface shape, we move beyond the measurement of the film thickness and provide more complete tests of the effects these films have on the hydrodynamics governing the motion of contact lines. For wetting and nonwetting surfaces, we measure the interface shape within several hundred microns from contact lines moving across preexisting and spontaneously formed films. We examine the hydrodynamics near the contact line moving across films thick enough that the fluid they contain obeys the same, Newtonian constitutive relation as the fluid in the bulk. We also examine cases where the film is very thin and fluid motion in the film is inhibited. We consider whether these thin films can be the inner scale mechanism which relieves the stress singularity associated with dynamic spreading across a dry surface.

By comparing our experimental data to two models valid in the limit of small Ca, we gain insight into the fluid behavior in the films. Spontaneously formed films on wetting surfaces have little impact on spreading except at very low spreading rates. On nonwetting surfaces, we have made the first measurements of the interface shape for a receding contact line. For receding speeds where no thick film is present, no molecular scale film forms and, although viscous bending is observable, its form is not described by the model successful in the advancing case. Our comparison of the hydrodynamics for molecular scale and micron scale films poses intriguing questions about the molecular relaxations and mobilities in very thin fluid films. For contact lines advancing or receding over micron scale films, the model treating the fluid in the film as having similar properties as in the bulk successfully describes the hydrodynamics near the contact line.

ACKNOWLEDGMENT

We wish to acknowledge the support of NASA from grant No. NCC3-465.

REFERENCES

[1] C. Huh and L.E. Scriven, J. Colloid Interface Sci. **35**, 85 (1971).

[2] E.B. Dussan V. and S.H. Davis, J. Fluid Mech. **65**, 71 (1974).

[3] E.B. Dussan V., J. Fluid Mech. **77**, 665 (1976).

[4] R.G. Cox, J. Fluid Mech. **168**, 169 (1986).

[5] E.B. Dussan V., E. Ramé and S. Garoff, J. Fluid Mech. **230**, 97 (1991).

[6] J.A. Marsh, S. Garoff and E.B. Dussan V., Phys. Rev. Lett. **70**, 2778 (1993).

[7] K.R. Willson, "The dynamic wetting of polymer melts," Doctoral Thesis, Dept. of Physics, Carnegie Mellon University, Pittsburgh, Pennsylvania, USA (1995).

[8] Q. Chen, E. Ramé and S. Garoff, J. Fluid Mech. **337**, 49 (1997).

[9] O.V. Voinov, Fluid Dynamics **11**, 714 (1976).

[10] L.M. Hocking, J. Fluid Mech. **79**, 209 (1977).
[11] C. Huh and S.G. Mason, J. Fluid Mech. **81**, 401 (1977).
[12] P.A. Thompson and M.O. Robbins, Phys. Rev. Lett. **63**, 766 (1989).
[13] P.G. de Gennes, X. Hua and P. Levinson, J. Fluid. Mech. **212**, 55 (1990).
[14] E.O. Tuck and L.W. Schwartz, SIAM Rev. **32**, 453 (1990).
[15] J.X. Yang, J. Koplik, J.R. Banavar, Phys. Rev. A **46**, 7738 (1992).
[16] Y.D. Shikhmurzaev, Int. J. Multiphase Flow, **19**, 589 (1993).
[17] P.G. de Gennes, Reviews of Modern Physics **57**, 827 (1985).
[18] W.B. Hardy, Philos. Mag. **38**, 49 (1919).
[19] W.D. Bascom, R.L. Cottington and C.R. Singleterry, Advances in Chemistry **43**, 355 (1964).
[20] F. Heslot, N. Fraysse and A. M. Cazabat, Nature **338**, 640 (1989).
[21] J. De Coninck, S. Hoorelbeke, M.P. Valignat and A.M. Cazabat, Phys. Rev. E **48**, 4549 (1993).
[22] S.F. Burlatsky, A.M. Cazabat, M. Moreau, G. Oshanin and S. Villette, "Spreading of molecularly thin wetting films on solid interfaces," to appear in *Instabilities and Non-Equilibrium Structures VI, ed. E.* Tirapegui, Kluwer Academic (1997).
[23] L.D. Landau and V.G. Levich, Acta Physicochim. URSS **17**, 42 (1942).
[24] S.M. Troian, E. Herbolzheimer, S.A. Safran, Phys. Rev. Lett. **65**, 333 (1990).
[25] F.P. Bretherton, J. Fluid Mech. **10**, 166 (1961).
[26] R.G. Cox, J. Fluid Mech. **14**, 81 (1962).
[27] K.J. Ruschak, Chem. Eng. Sci. **31**, 1057 (1976).
[28] S.D.R. Wilson, J. Eng. Math. **16**, 209 (1982).
[29] C. W. Park and G. M. Homsy, J. Fluid Mech. **139**, 291 (1984).
[30] G.I. Taylor, J. Fluid Mech. **10**, 161 (1961).
[31] D. Quéré, C. R. Acad. Sci. Paris, Sér. II, **313**, 313 (1991).
[32] R.V. Sedev and J.G. Petrov, Colloids and Surfaces **53**, 147 (1991).
[33] B.V. Derjaguin and S. M. Levi, "Film coating theory," Focal press, London. pp. 21 (1964).
[34] K. Stoev, E. Ramé, T. Leonhardt and S. Garoff, Phys. Fluids, accepted.
[35] G.F. Teletzke, H.T. Davis and L. E. Scriven, Rev. Phys. Appl. **23**, 989 (1988).
[36] C. Bender and S. Orszag, "Advanced mathematical methods for scientists and engineers," New York: McGraw-Hill, pp. 155 (1982).
[37] C. Huh and L. E. Scriven, J. Colloid Interface Sci. **30**, 323 (1968).
[38] S.D.R. Wilson and A.F. Jones, J. Fluid Mech. **128**, 219 (1982).
[39] J.A. Marsh, "Dynamic contact angles and hydrodynamics near a moving contact line," Doctoral Thesis, Dept. of Physics, Carnegie Mellon University, Pittsburgh, Pennsylvania, USA (1992).
[40] Q. Chen, "Experimental investigation of dynamic wetting models: interface shapes and velocity fields near the moving contact line," Doctoral Thesis, Dept. of Physics, Carnegie Mellon University, Pittsburgh, Pennsylvania, USA (1996).
[41] E. Ramé and S. Garoff, J. Colloid Interface Sci. **177**, 234 (1996).
[42] G.P. Lopez, H.A. Biebuyck, C.D. Frisbie, G.M. Whitesides, Science **260**, 647 (1993).
[43] H. Zhao and D. Beysens, Langmuir **11**, 627 (1995).
[44] B. Frank and S. Garoff, Langmuir **11**, 4333 (1995).
[45] T.D. Blake, "Wettability," edited by John C. Berg, New York: Marcel Dekker Inc., pp. 251 (1993).
[46] J.G. Petrov and R.V. Sedev, Colloids and Surfaces **13**, 313 (1985).

Direct Numerical Simulation of Wetting and Spreading Behavior on Heterogeneous and Roughened Substrates

Leonard W. Schwartz, Departments of Mechanical Enginering and Mathematical Sciences, University of Delaware, Newark, DE 19716, USA, schwartz@me.udel.edu

ABSTRACT

A method of calculation is presented that allows the simulation of the time-dependent three-dimensional motion of thin liquid layers on solid substrates for systems with finite equilibrium contact angles. The contact angle is a prescribed function of position on the substrate. Similar mathematical models are constructed for substrates with a pattern of roughness. Evolution equations are given, using the lubrication approximation, that include viscous, capillary and disjoining forces. Motion to and from dry substrate regions is made possible by use of a thin energetically-stable wetting layer. We simulate motion on heterogeneous substrates with periodic arrays of high contact-angle patches. Two different problems are treated for heterogenous substrates. The first is spontaneous motion driven only by wetting forces. If the contact-angle difference is sufficiently high, the droplet can find several different stable positions, depending on the previous history of the motion. A second simulation treats a forced cyclical motion. Energy dissipation per cycle for a heterogeneous substrate is found to be larger than for a uniform substrate with the same total energy. The Landau-Levich solution for plate removal from a liquid bath is extended to account for a pattern of roughness on the plate.

1. INTRODUCTION

Wetting and capillary considerations during the slow motion of liquids on solid substrates are important in both the technological and natural worlds. Applications include the spreading behavior of liquid coatings, as well as flows in oil reservoirs, chemical reactors and heat exchangers. Some biological application areas are motions in the tear film on the cornea of the eye, flows on liquid covered membranes in the lungs, and the general area of cell motility, where cell motions have many of the features of inert liquid droplets [1]. The spreading properties of agrochemicals such as pesticides and insecticides are important determinants of their effectiveness. Capillary forces are often dominant in problems of small physical dimensions; however they can also be important for large-scale phenomena when body forces are very weak, as in the microgravity environment of orbiting satellites in space.

Application of a wettability pattern or a pattern of roughness to the walls of vessels containing liquid is a possible strategy for controlling the position of the liquid in the microgravity environment of orbiting space vehicles. In the absence of gravity, liquid in a partially-filled container can assume many different configurations. Small imposed accelerations can cause large displacements of the liquid which is undesirable for a variety of reasons. Contact line dynamics will play an important role, either by "pinning" the location of the liquid on the wall or by dissipating the kinetic energy imparted to the liquid. The present results suggest that different wall wettability patterns may accomplish one or the other of these objectives.

We will briefly outline mathematical and numerical procedures for liquid motions on chemically heterogeneous or roughened substrates. These employ the long-wave or "lubrication" approximation. More complete information can be found elsewhere [2,3,4].

2. THE MATHEMATICAL MODEL

Integral mass conservation is

$$h_t = -\nabla \cdot \mathbf{Q} + w_i(x, y, t) \ . \qquad (2.1)$$

Here h is the thickness of the liquid layer and $\mathbf{Q}$ is the two-dimensional areal flux vector defined as

$$\mathbf{Q} = \int_0^{h(x,y)} (u, v)\, dz$$

where u and v are velocity components in the x and y directions respectively. Likewise ∇ is a two-dimensional operator with respect to x and y. w_i is a local injection rate that is an input function of substrate position and time.

Under the assumptions of lubrication theory [5,6], i.e. the motion is sufficiently slow that inertial forces may be neglected and the free surface is inclined at a small angle relative to the substrate, the momentum equation for an assumed Newtonian liquid may be integrated

to yield

$$\mathbf{Q} = -\frac{1}{3\mu}(h^3 \nabla p) \ . \tag{2.2}$$

Here μ is the viscosity and the pressure p is independent of the normal coordinate z. The no-slip condition for the velocity has been applied on the substrate and the liquid free surface is stress-free. The pressure in the liquid is given by

$$p = -\sigma\kappa - \Pi \approx -\sigma\nabla^2 h - \Pi \tag{2.3}$$

and the pressure above the liquid is taken to be zero without loss of generality. The first term on the right is an approximation to the free-surface curvature when the surface slope is small. The error in this curvature approximation is proportional to the square of the surface inclination. σ is surface tension and the so-called disjoining pressure is given by the two-term model [2,3,7]

$$\Pi = B\left[\left(\frac{h^*}{h}\right)^n - \left(\frac{h^*}{h}\right)^m\right] \ . \tag{2.4}$$

B and the exponents n and m are positive constants with $n > m > 1$. The local disjoining energy density

$$e^{(d)}(h) = -\int_{h_*}^{h} \Pi(h')dh' \tag{2.5}$$

has a single stable energy minimum at the thin wetting-layer thickness $h = h_*$. A local force balance near an apparent contact line gives

$$\sigma\cos\theta_e = \sigma - e^{(d)}(\infty) \tag{2.6}$$

which is the disjoining-model equivalent of the Young-Laplace equation.

The equilibrium contact angle is taken to be an arbitrarily prescribed function of position and the evolution equation for flow over a heterogeneous substrate becomes

$$h_t = -\frac{\sigma}{3\mu}\nabla\cdot\left[h^3\left(\nabla\nabla^2 h + \frac{(n-1)(m-1)}{2h_*(n-m)}\nabla\left[\theta_e^2\left(\frac{h_*^n}{h^n} - \frac{h_*^m}{h^m}\right)\right]\right)\right] + w_i(x,y,t) \tag{2.7}$$

It is possible to augmented this equation with gravity and other force terms as additional driving mechanisms. [3]

Each pressure component on the right of equation (2.3) may be identified with an integrated energy component. The free-surface energy is proportional to the area of the liquid surface and is given by

$$E^{(\sigma)} = \sigma\iint\left(\frac{1}{\cos\gamma} - 1\right)dA \approx \frac{\sigma}{2}\iint \nabla h\cdot\nabla h\, dA \tag{2.8}$$

where A is the total area of the substrate, and γ is the angle between the normal to the surface and the normal to the substrate. The total disjoining energy is

$$E^{(d)} = \iint e^{(d)} dA \ . \tag{2.9}$$

The global energy change equation is

$$\dot{E}^{(\mu)} = -(\dot{E}^{(\sigma)} + \dot{E}^{(d)}) + \dot{W} \tag{2.10}$$

which is the statement that the rate of viscous working is equal to the rate of decrease of the stored, or potential, energy components plus the rate of working on the system. Here

$$\dot{W} = \iint p\, w_i\, dA \tag{2.11}$$

may be recognized as the rate of working on the system by means of injection w_i. For cyclical motions, the drop shape returns to its original configuration and there is no change, over a cycle, in $E^{(\sigma)}$ or $E^{(d)}$. In that case the total viscous work done is the time integral of $\dot{W}$ or

$$\oint p\, dV$$

where V is drop volume, $dV = w_i\, dA$ and the special integral sign denotes a full cycle.

For the quasi-three dimensional problems treated here, numerical solutions use finite difference methods and an alternating direction implicit (ADI) technique is implemented. Developed originally for second-order elliptic and parabolic systems [8], ADI uses alternating sweeps in each direction and only a banded system of equations needs to be solved to update the discrete set of $h_{i,j}$ values.

3. VALIDATION

The model has been calibrated by comparison with several experiments. Axisymmetric spreading of a droplet on a high-energy [i.e. small contact angle] uniform substrate has been measured by several investigators and general agreement with Tanner's Law [9]

$$A \propto V^{3/5} t^{1/5}$$

has been verifed. Here A is drop area, V is volume and t is time. It can be shown that the solution for $h(r,t)$ is self-similar and the drop central height must also follow a power law in time [3]. Figure 1 shows a comparison of the similarity solution assuming a wetting layer of 30 nm thickness which agrees with experimental results [10]. Also shown is an axisymmetric simulation on a uniform low-energy substrate with a finite contact angle. It is seen that the power-law is followed until the drop has almost stabilized at a dimensionless central height $h_c \approx 1$. This spreading behavior, with finite contact angle, has been observed experimentally by Zosel [11]. Another simulation, shown as symbols in the Figure, assumes the substrate has a pattern of wettability as in Fig. 5. The substrate area-average wettability is the same as for the low-energy uniform case. It can be seen that the spreading is unaffected by the contamination pattern until the droplet slows and ultimately stops spreading. Three-dimensional simulations are limited to thick precursor layers because of the need to adequately resolve details in the contact region. Too thick a precursor layer results in a relatively weak speed discrepancy; this discrepancy is in accordance with the predicted inverse logarithmic dependence on the precursor thickness [12].

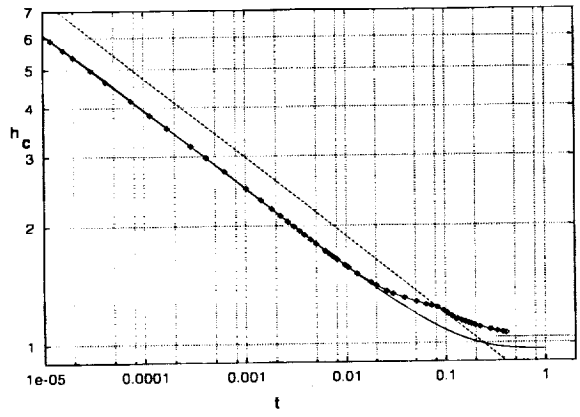

Figure 1: Drop central height h_c versus time, showing the similarity range for axisymmetric spreading. The initial drop height is 10. The straight line on this log-log plot is $h_c = 0.75t^{1/5}$ which matches experiments. The solid curve is the calculated behavior for finite contact angle on a uniform substrate, while the lines-points curve is calculated for the square wettability pattern.

We have performed a laboratory experiment to compare with drop spreading simulations [3]. A 26 μl drop of glycerin was placed near the center of a cross of 1

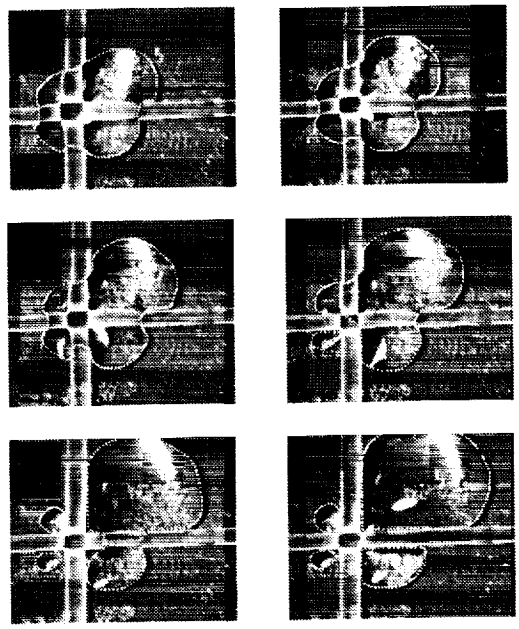

Figure 2: Video images taken from an experiment where a glycerin drop is placed near the center of a cross of 0.1 cm Teflon tape on a glass slide. These pictures may be compared with the simulation shown in Fig. 3.

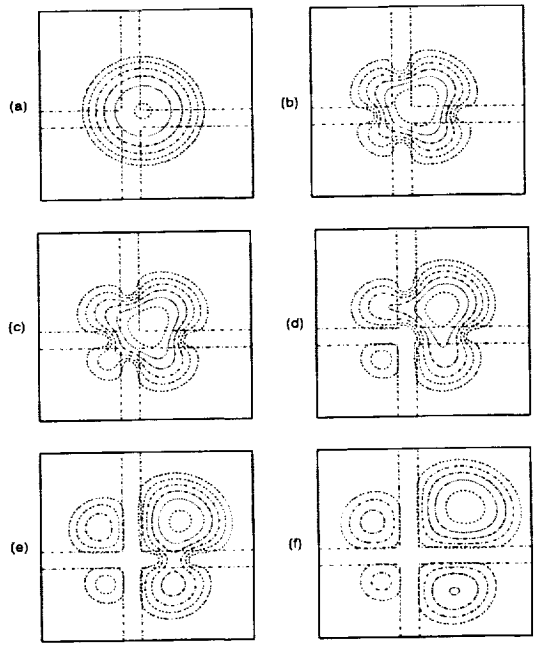

Figure 3: Contour plots from a computer simulation of break-up of a liquid drop placed on a "cross" of high-contact-angle material.

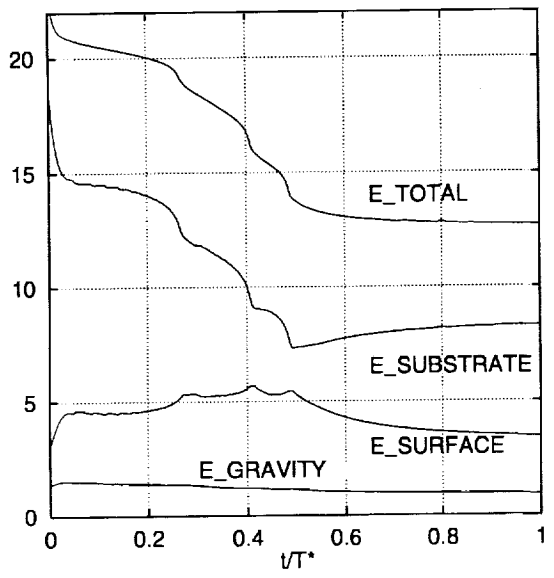

Figure 4: Energy components versus time from the drop-on-cross simulation.

mm Teflon tape that had been fixed to a horizontal glass slide. Wetting forces cause the drop to break up into unequal fragments as shown in Fig. 2. Simulation results, in Fig. 3, show detailed agreement with the experiment. However time-scale corrections need to be applied because (i) the simulation precursor layer is overly large, and (ii) the contact angles in the experiment are beyond the range of quantitative validity of the small-slope lubrication approximation. Energy component variation, from the simulation, is given in Fig. 4. The Bond number $Bo = \rho g R^2/\sigma = 2.5$ using the stabilized radius R for the drop on glass. The gravitational effect is quite minor, however, as can be seen in the Figure. Note that the motion proceeds in a "jerky" manner that is characteristic of capillary driven motions on nonuniform substrates. Each drop disconnection is reflected as a rapid decrease in the substrate energy.

4. HYSTERETIC MOTIONS ON HETEROGENEOUS SURFACES

Simulations have been performed to investigate the dissipation of energy when a liquid moves on mixed-wettable substrates. Again we consider the motion of a drop, both in spontaneous motion, driven only by wetting forces, and also in a periodic forced motion. Several periodic patterns of wettability have been considered, two of which are shown in Fig. 5. The equilibrium contact angle θ_e is larger on the dark patches than on the surrounding field. Numerical procedures for generating these and other patterns, including slight smoothing at patch boundaries to maintain derivative continuity, are given in [2].

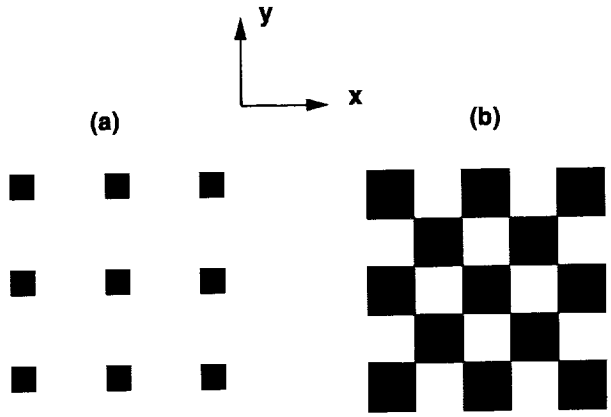

Figure 5: The substrate wettability patterns used in this study. The dark regions have larger values of contact angle than the surrounding field. (a) Isolated spot pattern; (b) Checkerboard pattern.

Figure 6 shows two different stable drop shapes obtains by allowing a drop to advance outward (left) and recede (right) from a starting profile that was either steeper or shallower than the equilibrium shapes. The contact angle on the isolated patches is about four times larger than on the field. Effective advancing and receding contact angles may be calculated using averages of local values; the effective contact angle ratio for this case is $\theta_a/\theta_r = 1.14$. This ratio is a measure of contact angle hysteresis. Figure 7 is an instantaneous picture during the receding simulation. It shows transient interior dewetting due to an instability near the receding contact line.

A schematic diagram for a notional experiment to explore energy dissipation in forced motions in shown in Fig. 8. By pumping liquid in and out via a syringe, the droplet can be forced to periodically traverse the wettability pattern. Pressure-volume plots from numerical simulation are shown in Fig. 9 where motions on a checkerboard wettability pattern are compared with a uniform substrate of the same average energy. The area of each hysteresis loop is the input work required to drive a cycle of the motion. Additional dissipation results from the presence of the pattern, the effect being more important at low speeds or long cycle times.

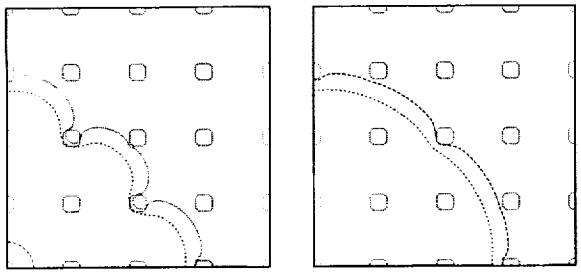

Figure 6: Contour plots of final static shapes for advanced (left) and receded (right) drops in spontaneous motion. The wettability pattern is also shown. The difference between the two cases is a measure of contact angle hysteresis.

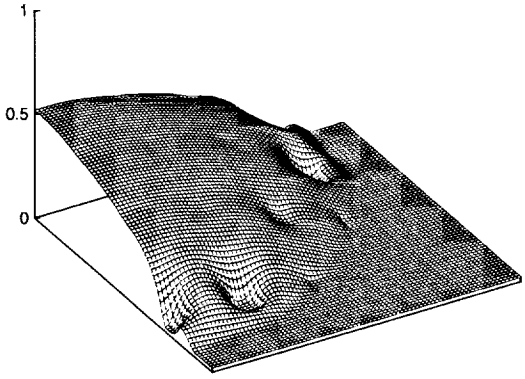

Figure 7: A frame during recede. A de-wetting instability leads to interior dry patches near the receding periphery. This is a transient effect and the drop continues to recede until the final configuration, shown in Fig. 6, is attained.

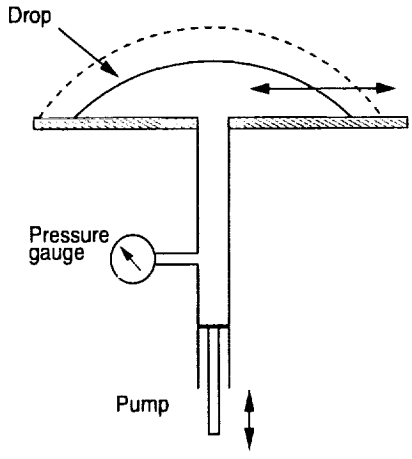

Figure 8: Schematic diagram of a notional experiment to investigate energy dissipation in a cyclic motion of a drop.

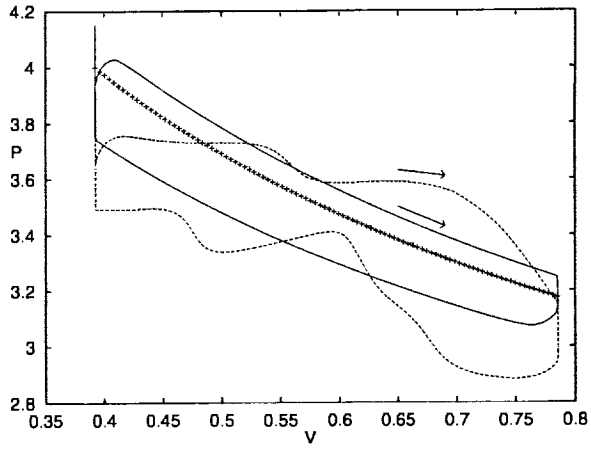

Figure 9: Dimensionless pressure P versus volume V showing hysteresis loops in cyclical motion. The solid line is for a uniform substrate, dashed line is for a checkerboard wettability pattern. The symbol curve is for the non-dissipative quasi-static theory with equation $P = 2\pi^{1/3}V^{-1/3}$.

For comparison, a quasi-static non-dissipative curve, for motion on a uniform substrate, is also shown.

5. MOTIONS ON A SURFACE WITH A PATTERN OF ROUGHNESS

It is possible to include a roughened substrate in the lubrication formulation. It may be shown [4] that the evolution equation needs only be modified by inclusion of the substrate shape function in the "permeability," *i. e.* the factor of proportionality between the flux and the pressure gradient. It is often convenient to allow the substrate to move with time while the computational window is fixed to the liquid free surface.

A model problem is an extension of the well-known Landau-Levich [13] problem for the withdrawal of a moving plate from a bath of liquid. We consider the plate to have a periodic pattern of roughness or "cells" as shown in Fig. 10. The plate moves with constant speed U to the right while the liquid meniscus is pinned at the left end of the computational window. While the Landau-Levich result is time independent, here the problem becomes time periodic with a period equal to the cell passage time. All dimensional constants can be absorbed by scaling. We let h_0 be a measure of coating thickness, such as the cell depth and substrate coordinates (x, y) are made dimensionless using the length

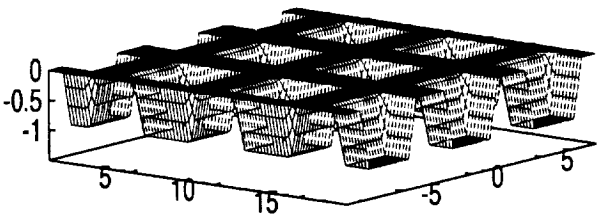

Figure 10: A periodic square array of cells on the substrate.

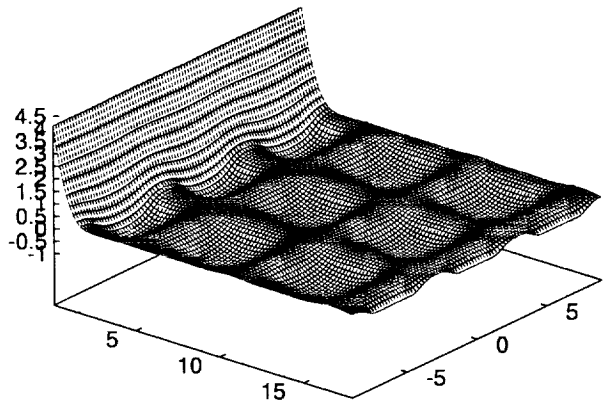

Figure 11: A liquid surface during meniscus withdrawal for the cell pattern in Fig. 10. Note how the meniscus 'scrapes out' the cells.

scale

$$L = h_0 \left(\frac{\sigma}{3\mu U} \right)^{1/3} \qquad (5.1a) .$$

The time unit is

$$T^* = \frac{L}{U}. \qquad (5.1b)$$

The long-wave model equation is

$$\frac{\partial h}{\partial t} = -\frac{\partial h}{\partial x} - \nabla \cdot (s \nabla \nabla^2 h) \qquad (5.2)$$

A function $h_1(x, y, t)$ represents the moving substrate and the permeability s in (5.2) is simply $s = (h - h_1)^3$.

As seen in Fig. 11, the downward pressure of the meniscus acts so as to "scrape" liquid from the cells. A certain residual fraction remains in each cell, determined primarily by the cell geometry. Much greater work is required to move the plate compared to a smooth-wall case. The problem is applicable to damping of periodic motions where the wall roughness is a surrogate for the chemical heterogeneity discussed above. Further details, including terrestrial applications in the coating and printing industry, where engraved or "gravure" rollers are used, are given in [4].

6. ACKNOWLEDGMENT

This work is supported by the NASA Microgravity Program, ICI, and The State of Delaware.

7. REFERENCES

1. Greenspan, H. P., *J. Fluid Mechanics* **84**, 125 - 143, 1978.
2. Schwartz, L. W., *Langmuir* 1998 (in press).
3. Schwartz, L. W. & Eley, R. R., *J. Colloid Interface Sci.* 1998 (in press).
4. Schwartz, L. W., P. Moussalli, P. Campbell, & R. R. Eley *Trans. Inst. Chem. Engrs.* **76**, 22-29 (1998)
5. Atherton, R. W. & Homsy, G. M., *Chem. Eng. Comm.* **2**, 57 (1976).
6. Benney, D. J., *J. Math. & Phys.* **45**, 150 (1966).
7. Mitlin, V. S., *J. Colloid Interface Sci.* **156**, 491 (1993).
8. Peaceman, D. W. & Rachford, H. H., *SIAM J.* **3**, 28 (1955).
9. Tanner, L., *J. Phys. (D)* **12**, 1473 (1979).
10. Lelah, M. D. & Marmur, A. M., *J. Colloid Interface Sci.* **82**, 518 (1981).
11. Zosel, A., *Colloid & Polymer Sci.* **271**, 680 (1993).
12. De Gennes, P. G., *Rev. Mod. Physics* **57**, 827 (1985).
13. Kim, J. S., Kim, S., & Ma, F., *J. Appl. Phys.* 73, 422-428, (1993).
14. Levich, V., *Physicochemical Hydrodynamics*, Prentice-Hall, Englewood Cliffs (1962).

ON THE BOUNDARY CONDITIONS AT AN OSCILLATING CONTACT LINE

L. Jiang[1], Z. Liu[2], M. Perlin[2], and W.W. Schultz[1]
[1]Mechanical Engineering & Applied Mechanics and [2]Naval Architecture & Marine Engineering
University of Michigan, Ann Arbor, MI 48109, perlin@engin.umich.edu

ABSTRACT

We investigate principally the pinned contact line and the associated flow field, adjacent surface elevation, and contact angle. A limited discussion and results for partial slip, oscillating contact lines are included also. Previous experimental results are compared to the theories of Hocking and Miles. It is shown that at low frequencies, the pinned contact line experiments agree reasonably with Hocking; however, at higher frequencies, there is a significant difference. A discussion of the present experimental setup is included; the magnification, Brewster angle, and view camera techniques used are presented. New experimental results of the flow fields and surface elevations in the pinned contact line regime are presented. Finally, the partially-pinned contact-line problem is addressed. Results from standing (Faraday) wave experiments are presented and the need for an improved contact-line model is discussed. Additionally, a comparison is presented of a modified Tanner's law with the data of Ting and Perlin.

INTRODUCTION

The contact line is the intersection between two distinct fluids and a solid. In our experiments, the fluids are water and air, the solid is glass. The contact angle, θ_c, is defined as the angle between the tangent to the fluid interface at the contact line and the water-glass interface. "Contact angle" is used in place of the more proper description "apparent contact angle." The various phenomena that occur at the contact-line boundary are very important in many fluid flows, for example, the spreading process of liquid drops and the generation and dissipation of waves interacting with a solid surface. To determine and quantify the contact-line behavior, measurements of the contact-line position and dynamic contact angle (i.e. contact angle with a moving contact line) are conducted, and to quantify the flow, velocity-field measurements are included. As opposed to their uni-directional counterparts, oscillatory contact-line boundaries have not been studied experimentally in a significant way until very recently (Ting and Perlin, 1995). We mention the following papers relevant to the work presented: Stokes (1845), Smith (1968), Hocking (1987), Miles (1990), and Cocciaro *et al.* (1993). The Stokes paper includes the solution to his so-called "second problem," that of an infinite-length, oscillating plate in a semi-infinite fluid. Smith (1968) discussed the surface waves generated by viscous forces (i.e. he contrasts the Stokes solution to the solution with a free surface present); however, no contact-line effects are included. Hocking (1987) used an oscillatory contact-line boundary condition (by using two approximations to Dussan V's model) to calculate the waves generated by a vertically oscillating, upright plate and obtained the amplitude of the radiated waves and the energy dissipation due to contact-line hysteresis. Miles (1990), addressing the same problem as Hocking, used a boundary condition along the plate (similar to that proposed by Navier) associated with a boundary condition at the contact line. Viscosity was included and a non-zero initial free-surface meniscus was also considered (in one case). Cocciaro *et al.* (1993) conducted experiments to examine the effects of the dynamic contact-line behavior on surface waves by horizontally oscillating a container.

In this work, we investigate primarily the pinned contact line and the associated flow field, adjacent surface elevation, and contact angle. A limited discussion and results for partial slip, oscillating contact lines are included also. Previous experimental results are compared to Hocking and Miles. It is shown that at low frequencies, the experiments agree reasonably with Hocking; however, at higher frequencies, there is a significant difference. A method to determine whether this is due to inviscid nonlinearity or viscous effects is discussed. The model of Smith is shown to require extension to a much larger horizontal region adjacent to the contact line. A discussion of the experimental setup used is offered including the magnification, Brewster angle, and view camera techniques used. New experimental results of the flow fields and surface elevations in the pinned contact line regime are presented. Finally, the partially-pinned contact-line problem is addressed. Results from Faraday wave experiments are presented and the need for an improved contact-line model is discussed. In addition, a comparison of a modified Tanner's law with the data of Ting & Perlin (1995) is presented.

THE PINNED CONTACT LINE AND ATTENDANT FLOW FIELD DURING OSCILLATION OF A SURFACE PIERCING VERTICAL PLATE IN A LIQUID

To determine the dissipation and wave-generation effects that the contact line has at a free surface-solid plate intersection (a free surface is where the effect of the air layer on the liquid layer is neglected), we begin with the simplest case, an oscillatory pinned contact line. Ting & Perlin has shown that the Hocking model with/without hysteresis is inadequate for the case of slip-stick motion. The questions we seek to answer are: Why, how, and to what extent and depth does the contact line modify the flow field so that surface perturbations greatly exceed those due to the assumption of a no-slip boundary condition along the rest of the plate that produces the Stokes layer? These are perplexing questions, even for the simplified problem of the pinned contact line because the boundary condition along the plate is unchanged throughout the liquid regime except as modified by slip (not necessary in pinned case). As a first step, figure 1 compares a modified theory of Hocking, with the Stokes solution (i.e. the "contact angle" of the Stokes solution is the angle of a material line that, although not at the free surface, initially has the value of the static meniscus), and the data of Ting and Perlin. Hocking's theory is based on an inviscid fluid and a contact-line condition with/without hysteresis (we choose to use the one with complete hysteresis for this comparison), i.e. $V_r=\partial\eta/\partial t-V_p=\lambda\partial\eta/\partial x$ where V_r is the relative velocity—fluid to solid, η is the contact-line position, V_p is the plate velocity, the contact angle minus 90^o equals the arctangent of the surface slope—and it has been approximated by the surface slope, and λ is a (capillary) coefficient. To obtain a variation in contact angle representative of that of water on glass that begins with a small static angle, the static contact angle measured experimentally is added to the Hocking *free-surface* angle prediction to yield a modified Hocking angle. For a pinned-end condition, V_r is zero, and so λ is set to zero. This figure shows that the modified Hocking prediction is in reasonable agreement with the lower frequency, 2 Hz, oscillation although it is a poorer predictor for the larger contact angle; however, there is significant difference between the modified Hocking prediction and the experiments at 20 Hz. The Stokes solution is presented to demonstrate the large difference that exists between its predictions and the data. It is unknown whether the larger discrepancy between the modified Hocking theory and the experiments at 20 Hz is due to nonlinearity (Hocking's solution is for linear waves and obtained through Fourier transform) or due to viscous effects. Interestingly, the waves produced during a 2 Hz oscillation at 1 mm are negligible and one can infer that the solution and experiment agree when this is the case. In the future, experiments will be conducted with increased stroke at

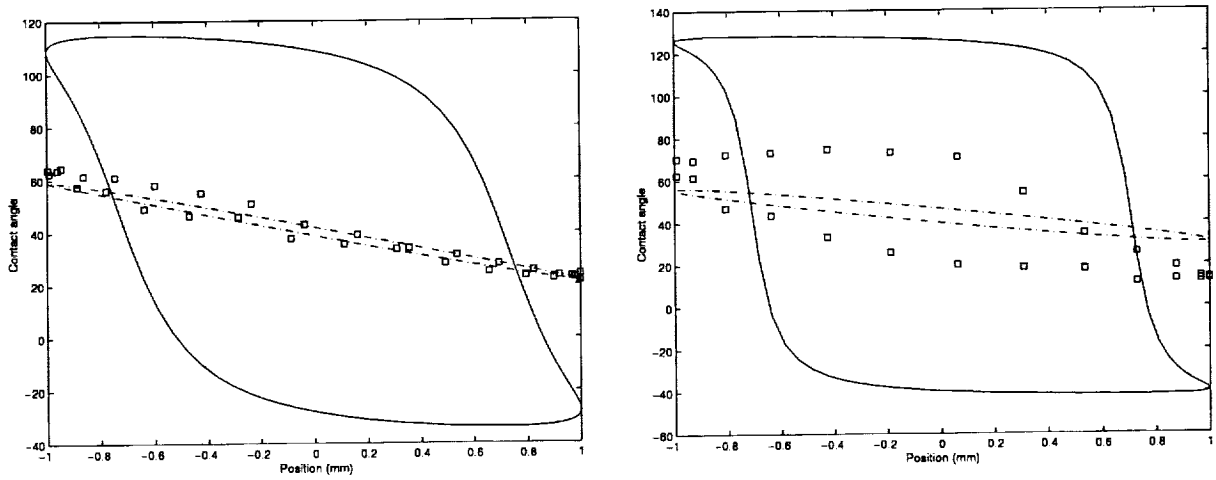

(a) (b)

Figure 1. Comparison of Ting & Perlin data (□) with a modified Hocking prediction for no contact-angle hysteresis (— · —) and the "contact angle" of the Stokes solution (——). (a) Stroke amplitude of 1 mm and oscillation frequency of 2 Hz. (b) Stroke amplitude of 1 mm and oscillation frequency of 20 Hz.

lower frequency to increase nonlinearity (ks, the wavenumber times stroke amplitude, a dimensionless measure of nonlinearity) and with decreased stroke at higher frequency to presumably reduce nonlinearity. The experimental result presented in figure 1(a) has an associated ks of 0.032 while that presented in figure 1(b) has a ks of 0.239 and is therefore more nonlinear. The experimental result in the 20 Hz experiment exhibits much larger contact angle changes than the theory predicts. We have also graphed the Miles theory (not shown) that includes a viscous boundary layer and other assumptions, and its predictions are slightly worse than those of Hocking's as modified. The future experiments will demonstrate whether the disagreement with the modified Hocking theory is due to nonlinearity or viscosity or a combination of the two. To analytically handle the nonlinear, inviscid, pinned condition, one can resort to a bispectral or even higher-order spectral treatment.

Smith (1968) treats the problem of a viscous fluid with a free surface adjacent to an oscillating vertical plate. The no-slip boundary condition is applied along the liquid-solid interface. Neither surface tension nor a meniscus were included in the analysis; however, one can trace the transition from the Stokes' solution that is valid deep in the liquid to the shear-free surface. Missing from this analysis is the capillary length, l_c,that provides a possible starting point for additional analysis. That is, the distance from the contact line where the free surface "feels" the contact angle under static conditions, l_c, greatly exceeds the boundary-layer thickness or the viscous length scale, l_v. In Smith's analysis, the transition is shown to have a second-order effect on the surface wave motion and occurs only in the corner with viscous length scale in the horizontal and vertical directions. Taking surface tension into account in this analysis may modify the results significantly.

We have conducted new experiments to measure as a function of time the flow field and surface elevation in the vicinity of a pinned contact line. The experimental setup is a vertically oscillating upright glass plate partially immersed in treated water and the longitudinal elevation view is shown in figure 2. The oscillation frequencies are 1-20 Hz; however, only two phases of the 1-Hz sinusoidal oscillation with stroke amplitude of

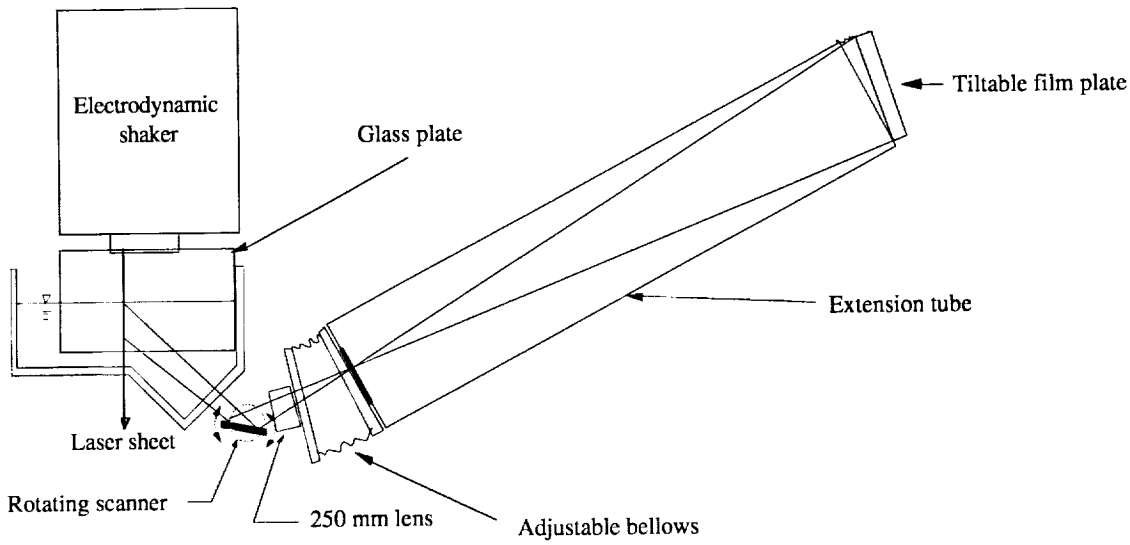

Longitudinal elevation view (not to scale)

Figure 2. Experimental setup used to obtain the flow fields and surface-elevation profiles.

0.12 mm (so that the contact line remains pinned) are presented. The Reynolds number based on radian frequency and stroke amplitude is 0.09. The primary difficulty associated with these surface-elevation and flow field measurements is that a magnification of about ten is desired at a large (about 27 cm) standoff distance—the standoff distance is required to effect the removal of the re-reflection of light scattered by particles from the free surface. The technique used is particle-image velocimetry (PIV) in conjunction with Brewster-angle viewing through a transparent angled lower wall (Lin & Perlin), although with the vertically oscillated glass plate, other reflection problems arise from the plate itself. A 4 in x 5 in (10.16 cm x 12.70 cm) view camera with a 250 mm focal-length lens and an adjustable bellows (length and angles of the lens and film plane are accommodated) is used. The object distance is 27 cm, the distance to the film plane is about 280 cm, the pulse duration of the acousto-optic modulated (i.e. triggered) argon-ion laser sheet is 4ms, the bias velocity is 0.1058 cm s^{-1} (compared to a maximum plate/contact angle velocity of 0.0747 cm s^{-1}), and the time between laser pulses is 40 ms. The magnification is 10.5.

To what depth does the contact-line effect extend or at what depth does the flow field revert to the Stokes solution is the question we would like to answer. We present in figure 3 two phases, - 26.6° and - 44.6° corresponding to plate velocities of - 0.674 mm s^{-1} and - 0.537 mm s^{-1} respectively of the 1-Hz experiment. The axes are in cm and the x-axis coordinates represent the physical distance from the face of the plate; however the velocity vectors have not been shifted according to the location of the contact line. The magnitude of the vectors in the figures represents about 0.22 mm s^{-1}. It is seen that nearly uniform flows exist in these small regions near the contact line for these phases, although their directions have changed with phase. Many additional images need to be processed, corrected for contact-line position, and analyzed before definitive conclusions can be drawn.

THE PARTIALLY-PINNED CONTACT LINE DURING FREE-SURFACE OSCILLATION AND PLATE OSCILLATION

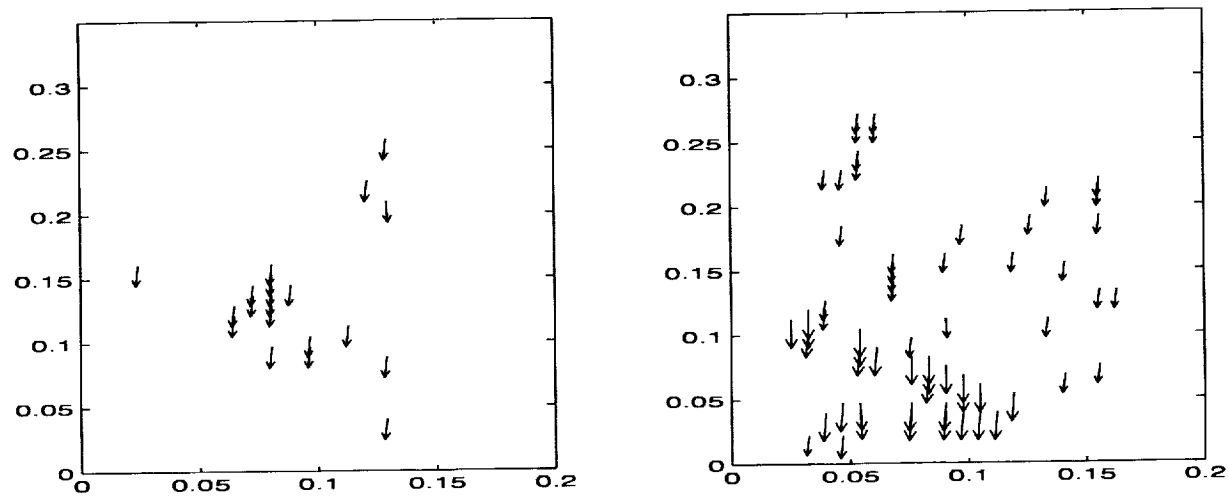

Figure 3. Experimental flow fields measured using the PIV technique. Phases of the 1-Hz sinusoidal oscillation are - 26.6° and - 44.6° corresponding to plate velocities of - 0.674 mm s^{-1} and - 0.537 mm s^{-1} respectively. The axes are in cm; however the velocity vectors have not been shifted according to the location of the contact line. The magnitude of the vectors in the figures represents about 0.22 mm s^{-1}.

In this section we discuss the frequency and damping of Faraday waves (waves generated through resonance by vertical container oscillation), and the use of an associated *ad-hoc* approach to analyze the data of Ting & Perlin when the contact line is no longer pinned. The model simplifies to Tanner's law (Tanner, 1979) if the static contact angle is very small.

We describe experimental data on the frequency and damping of Faraday water waves in glass tanks with treated water. The measured frequency detuning due to the contact-line effect is shown in figure 4. In the contact-line regime of the wave decay where the wave dissipation is dominated by contact-line effects (i.e. this is not the physical contact-line region), the averaged data follows a -2/3 power law with respect to wave amplitude a. The (viscous and contact-line) wave damping obtained from a demodulated signal also demonstrate amplitude dependence. The damping rate first increases with decreasing amplitude following a -1/3 power law (1.3 mm < a < 6 mm), then starts to decrease for smaller wave amplitude (a < 1.3 mm). Miles (1991) predicted no amplitude dependence in either frequency detuning or damping when the following Hocking condition is applied at the contact line for standing water waves

$$\eta_t = \lambda_c \eta_x \quad at \quad x = 0, \qquad (1)$$

where $\eta_x \approx \theta_c - \frac{\pi}{2}$ with θ_c the dynamic contact angle and λ_c the capillary coefficient. (We use a subscript on λ now as the tank walls are fixed in laboratory coordinates and in the analysis, i.e. V_p=0) For small difference between the actual frequency ω and the natural frequency (without contact-line effect) ω_n, Cocciaro *et al.* (1993) showed that the results of Miles (1991) can be simplified to

$$\gamma_c - \frac{F_n \lambda_c}{1 + (\lambda_c \omega l)^2}, \qquad (2)$$

$$\omega - \omega_n - \frac{F_n \omega_n}{1 + (\lambda_c \omega l)^2} - \frac{\gamma_c^2}{2\omega_n} \qquad (3)$$

where γ_c represents contact-line damping. Here λ_c is assumed to be constant. We note that if we assume $\lambda_c \sim a^{1/3}$, equations (2) and (3) give the

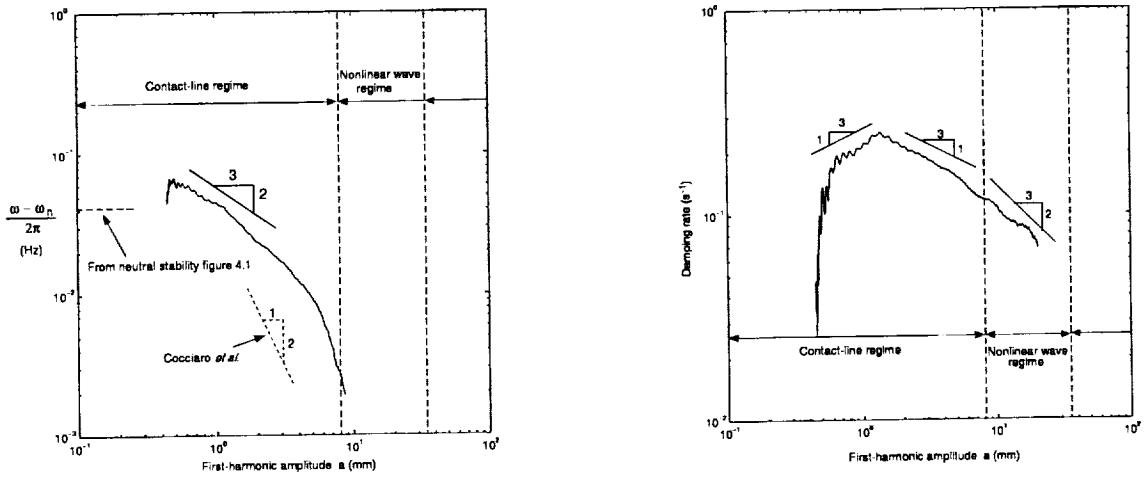

Figure 4. (a) Frequency difference $(\omega-\omega_n)/2\pi$ versus wave amplitude a. (b) Damping rate γ.

correct frequency and damping as observed in our experiments

$$\gamma_c \sim \frac{F_n a^{1/3}}{1 + a^{2/3}(\omega l)^{-2}}, \qquad (4)$$

$$\omega - \omega_n \sim \frac{F_n \omega_n}{1 + a^{2/3}(\omega l)^{-2}} - \frac{\gamma_c^2}{2\omega_n} \quad . \qquad (5)$$

The exact - 2 / 3 power shown in figure 4 between frequency shift and wave amplitude is shown in (5). And (4) implies a 1/3 power law between contact-line damping and wave amplitude for small a, and a $-1/3$ power for large a as shown in figure 4.

The above experiments are contrasted with similar experiments with Photo-Flo treated water in the same glass tank. This wetting agent usually forms a thin film of water forms on the glass even for water waves of small amplitude. The measurements suggest this is true and that the frequency of a decaying elevation approaches a value close to ω_n (without contact line effect) as amplitude approaches zero. There is no clear amplitude dependence in either the frequency shift or the damping.

More experiments are conducted for Faraday waves in a small circular cylinder (Pyrex glass, 12.8 cm diameter) with treated water, and in a large circular cylinder (plexiglass) with treated water. Both cylinders ensure uniform contact-line behavior (as compared with waves in rectangular tanks discussed above). Preliminary data suggest no amplitude dependence in the frequency and the damping rate as demonstrated earlier. However, the decaying record may be too short to provide valuable information needed in the small amplitude (contact-line dominated) range. These measurements suggest very complex contact-line influence on water waves and the sensitivity of contact-line behavior to the material of the solid and the surface property of the liquid.

The above *ad-hoc* approach for wave frequency and damping estimate does not explain the fundamental physics of the contact-line dynamics. Both Cocciaro *et al.* (1993) and Ting & Perlin (1995) find experimentally a nonlinear relation between contact-line velocity and contact angle, see figure 5. In particular, Ting & Perlin measure a time-dependent λ_c with its amplitude proportional to a^2, not $\lambda_c \sim a^{1/3}$ as assumed in (4) and (5). One could propose the following model without contact-angle hysteresis

$$\lambda_d(\theta_e - \theta_c)^3 = |V_r| \quad , \qquad (6)$$

where θ_e is the static contact angle (assumed to be 90° in (1), but is approximately 30° to 50° in experiments.) The choice of a cubic fit is inspired by the 1/3 exponent that appeared in the ad-hoc approach above. However, matching (6) directly with Ting & Perlin is difficult because of the strong hysteresis loop in the contact angle versus contact-line velocity diagram (figure 5(b)). Such hysteresis is partially caused by the large hysteresis in the static contact angle (17°), and maybe partially caused by inertial effects. However, equation (6) exhibits some qualitative features observed by Ting & Perlin. For example, both (6) and figure 5(b) show that the contact-line velocity is the largest at the smallest contact angle. (6) also predicts that if the maximum V_r is amplitude dependent (experiments show $|V_r|_{max} \sim a^{\alpha}$, $1 < \alpha < 2$), the smallest θ_c has a much weaker dependence on amplitude. Again, this agrees with figure 9 of Ting & Perlin.

Models for unidirectional, steady contact-line motion also exhibit a cubic relation $U \sim \lambda\ \theta\ (\theta^2 - \theta_e^2)$, but λ is only a function of surface tension and viscosity. For small static contact angle $\theta_e << 1$, Tanner's law $U \sim \lambda\theta^3$ is recovered. The mechanism behind Tanner's law and (6) is probably the same, i.e. the contact-angle variation is caused by hydrodynamics very close to the contact line and can be described by a balance between capillary force and viscous force. If we assume that (6) applies to Faraday waves in the rectangular tank, we can equivalently assume that the Young's force at the contact line $F = \cos\theta - \cos\theta_e$ is balanced by the viscous force near the contact line. The dissipation over one wave cycle is then proportional to $F \cdot a$ where a is again the wave amplitude. Using (6) for small contact angle θ_c, we obtain $F \sim \theta^2 \sim V_r^{2/3}$. If we further assume that $V_r \sim \omega a$, the damping rate can be estimated by

$$\gamma = \frac{F \cdot a}{Energy} \sim \frac{a\, a^{2/3}}{a^2} \sim a^{-1/3}$$

which is the amplitude dependence measured in our Faraday wave damping rate. The amplitude dependence of the wave frequency remains unresolved.

Even with some qualitative agreements with Ting & Perlin, (6) is difficult to apply in the linear eigenvalue analysis for water waves. Thus we will try to apply a more elaborate analysis with the belief that hydrodynamics can describe the wetting condition in oscillating flows, and that the viscous and capillary balance remains essential in determining the relation between contact-line velocity and (apparent) contact angles.

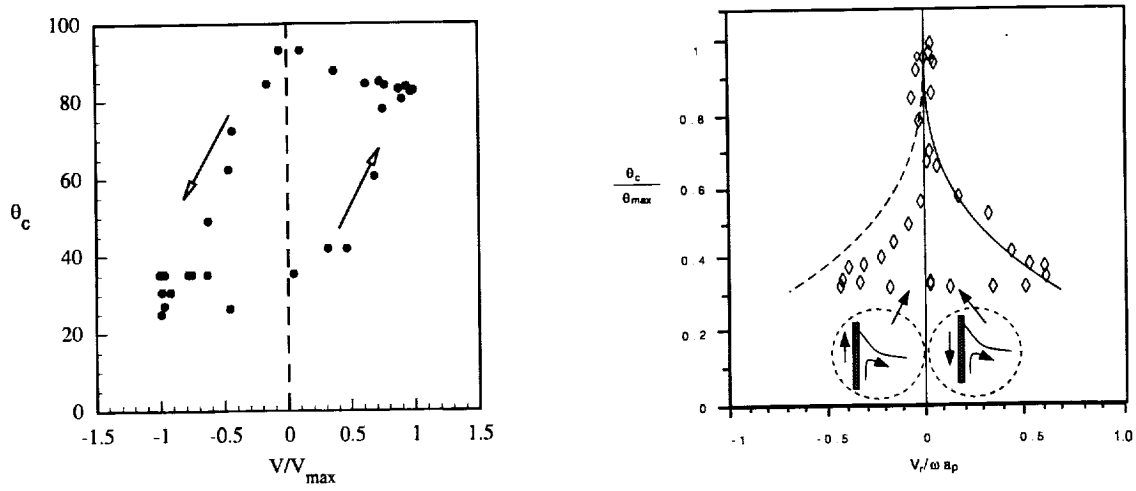

Figure 5. (a) Contact angle versus contact-line velocity inferred from Cocciaro *et al.* (1993); (b) Contact angle versus relative contact-line velocity for 2 Hz oscillation (Ting & Perlin). The inserts demonstrate the corner vortex at the maximum plate position. Stroke amplitude is 3 mm. The solid and dash curves are predicted by (1).

REFERENCES

Cocciaro, B., Faetti, S. & Nobili, M. 1993 "Experimental investigation of capillary effects on surface gravity waves in a cylindrical container: non-wetting boundary conditions," *J. Fluid Mech.* **246**, 43-66.

Hocking L. M. 1987 "Wave produced by a vertically oscillating plate," *J. Fluid Mech.* **179**, 267-281.

Jiang, L. 1997 "Nonlinear gravity-capillary water waves," Ph.D. Dissertation, Univ. Michigan.

Lin, H.J. & Perlin, M. "Improved methods for thin, boundary layer investigations," *Exper. in Fluids*, to appear.

Miles, J.W. 1990 "Capillary-viscous forcing of surface waves," *J. Fluid Mech.* **219**, 635-46.

Miles, J.W. 1991 "Capillary boundary layer for standing waves," *J. Fluid Mech.* **222**, 197-205.

Smith, S.H. 1968 "On the creation of surface waves by viscous forces," Q. J. Mech. Appl. Math., **XXI**, 439-450.

Stokes, G.G. 1845 "On the theories of the internal friction of fluids in motion," *Trans. Camb. Philos. Soc.*, **8**, 287.

Tanner, L. 1979 "The spreading of silicone oil drops on horizontal surfaces," *J. Phys. D* **12**, 1473-1484.

Ting, C.L. & Perlin, M. 1995 "Boundary conditions in the vicinity of the contact line at a vertically oscillating upright plate: an experimental investigation," *J. Fluid Mech.* **295**, 263-300.

THE MICROMECHANICS OF THE MOVING CONTACT LINE

Seth Lichter, Department of Mechanical Engineering, Northwestern University, Evanston, IL 60208-3111
s-lichter@nwu.edu

ABSTRACT

A transient moving contact line is investigated experimentally. The dynamic interface shape between 20μm and 800μm from the contact line is compared with theory. A novel experiment is devised, in which the contact line is set into motion by electrically altering the solid-liquid surface tension γ_{SL}. The contact line motion simulates that of spontaneous wetting along a vertical plate with a maximum capillary number $Ca \sim 4 \cdot 10^{-2}$. The images of the dynamic meniscus are analyzed as a function of Ca. For comparison, the steady-state hydrodynamic equation based on the creeping flow model in a wedge geometry and the three-region uniform perturbation expansion of Cox (1986) is adopted. The interface shape is well depicted by the uniform solution for $Ca \leq 10^{-3}$. However, for $Ca > 10^{-3}$, the uniform solution over-predicts the viscous bending. This over-prediction can be accounted for by modifying the slip coefficient within the intermediate solution. With this correction, the measured interface shape is seen to match the theoretical prediction for all capillary numbers. The amount of slip needed to fit the measurements does not scale with the capillary number.

Introduction

In this work, we seek to model spontaneous wetting. The experimental method to mimic spontaneous wetting makes use of electrical double layer theory. Experimental results are compared to an asymptotic theory [1] which describes the shape of the fluid interface. One of the objectives of this work is to assess the utility of this theory to the case of spontaneous wetting. Rigorous testing comparing theory and experiment has already been done for controlled wetting in which the contact line moved at constant capillary number [2, 3]. We find here that for flows with a suitably low maximum capillary, steady theory is applicable. However, for flows at higher capillary number, the measurements deviate from theoretical values. The source of this discrepancy does not appear to be due to the unsteadiness of the spontaneous wetting flow. Rather, it appears to be due to a large region of slip which invalidates theory's assumption that slip is of more limited extent.

Surface Tension Depends on Electrical Potential

In a container filled with fluid and vapor, the location where the fluid/vapor interface meets the solid container is denoted as the contact line, see Fig. 1. Young's equation

$$\gamma_{SV} = \gamma_{SL} + \gamma_{LV} \cos\theta,$$

relates the the surface tension at the solid/vapor (SV) interface to that along the solid/liquid (SL) and liquid/vapor (LV) interfaces as well as to the contact angle θ. It can also be shown [4] that

$$\left(\frac{\partial \gamma_{SL}}{\partial V_M}\right) = -\sigma_o,$$

which reveals that the surface tension at the solid/liquid interface can be modified by an applied potential V_M to the wetted solid surface; σ_o is the surface charge density. If we denote the maximum surface tension when $\sigma_o = 0$ as γ^o_{SL}, and the corresponding potential as V_o, then the above equation gives

$$\gamma_{SL} = \gamma^o_{SL} - \int_{V_o}^{V_M} \sigma_o dV.$$

The integral on the right-hand side is the electrical energy stored in the double layer at the solid/liquid interface. If we now estimate the double layer energy in terms of the Helmholtz model [5], then

$$\gamma_{SL} = \gamma^o_{SL} - \int_{V_o}^{V_M} CV dV,$$

where C is the capacitance of the double layer. Carrying out the integration yields,

$$\gamma_{SL} = \gamma^o_{SL} - \frac{C}{2}(V_M - V_o)^2.$$

The above equation provides an operational equation for the manipulation of solid-liquid surface tension. The application of a potential will alter the solid/liquid surface tension γ_{SL}; consequently, the balance of Young's equation is disrupted; the contact line then must move to a new location at which a new angle θ is established as a new equilibrium angle.

Experiment

Contact line motion takes place on a gold-mercury (Au-Hg) amalgam surface. The liquid used is a mixture of

glycerol and water to which a bit of KOH is added to enhance conductivity. A step change in surface potential is applied by a computer controlled potentiostat. The subsequent motion of the contact line is observed using a CCD camera attached to a microscope, see Fig. 2.

Asymptotic Theory

An asymptotic theory has been developed which describes the shape of the liquid/vapor interface as a function of distance from the contact line [1, 6, 7]. The interface shape is expressed in terms of the local interface angle

$$\theta = \left(\theta_d^3 + 9Ca \ln \frac{r}{L_{cap}}\right)^{1/3} + f(r) - \theta_d, \qquad (1)$$

and where θ_d is the apparent contact angle, Ca is the capillary number, $L_{cap} \equiv \sqrt{2\gamma_{LV}/\rho g}$ is the capillary length, and $f(r)$ is the static shape of the interface in the absence of motion, see Fig. 1.

Experimental Results

In response to the application of a potential V_M, the contact line is set into motion. The measured capillary number as a function of time is shown in Fig. 3. At first, the contact line moves at high capillary number and, as time proceeds, it slows down. At any selected time, that is, at any capillary number, the interface shape can be determined from the images gathered by the CCD camera, for example as shown in Fig. 4. The difference between the observed interfacial angle θ and that given by the theory of Eq. (1) can be computed, as shown in Fig. 5. In this particular figure, the agreement between the theory and measurement stretches from about $200\mu\text{m} < x < 470\mu\text{m}$. This pair of minimum and maximum values bound the interval over which the theory and experiment agree. This pair of values is gathered for an entire run in Fig. 6. While for $Ca \lesssim 5 \cdot 10^{-3}$, the theory and experiment agree over the entire field of view, at higher capillary numbers, the interval of agreement narrows. Finally, at $Ca \approx 4 \cdot 10^{-2}$, the interval of agreement has narrowed to zero.

Modified Theoretical Model

The theoretical results shown in Eq. (1) were derived under the condition that slip occurs within a molecular-sized region at the contact line. If slip is allowed over a much longer extent, then an *ad hoc* analysis shows that the theory is modified,

$$\theta = \left(\theta_d^3 + 9\beta Ca \ln \frac{r}{L_{cap}}\right)^{1/3} + f(r) - \theta_d, \qquad (2)$$

where the factor β, which appears on the right-hand side of the equation, is a measure of slip at intermediate length scales. If $\beta = 1$, then the original model is recovered. If $\beta = 0$, then slip occurs over the entire intermediate region. By fitting β, it is found that the interval over which the measurement and the modified theory, Eq. (2), agree can be made to extend over the entire field of view, see Fig. 7.

Conclusion

This work investigates spontaneous wetting. A flow which mimics spontaneous wetting is established by utilizing the variation of solid/liquid surface tension with the potential applied at the solid surface. It is found that the steady asymptotic theory holds for low values of the capillary number, even though the flow is unsteady. At higher values of the capillary number, agreement between theory and experiment fails. The discrepancy may be due to slip occurring over a large interval of the solid/liquid interface.

ACKNOWLEDGMENTS

This work has been supported by the NASA Microgravity Science and Applications Division under grant NAG3-1892. I would like to thank the Technical Officer, Dr. Mark Weislogel, for his years of advice and encouragement. The help of Chih-Yu Lin in preparing this paper is gratefully acknowledged.

References

[1] R. G. Cox. The dynamics of the spreading of liquids on a solid surface. Part 1. Viscous flow. *J. Fluid Mech.*, 168:169--194, 1986.

[2] Q. Chen, E. Ramé, and S. Garoff. The breakdown of asymptotic hydrodynamic models of liquid spreading at increasing capillary number. *Phys. Fluids*, 7:2631--2639, 1995.

[3] E. Ramé and S. Garoff. Microscopic and macroscopic dynamic interface shapes and the interpretation of dynamic contact angles. *J. Colloid Int. Sci.*, 177:234--244, 1996.

[4] J. T. Davies and E. K. Rideal. *Interfacial Phenomena.* Academic Press, 1963.

[5] Y. Y. Perng. *The unsteady moving contact line: Experimental investigation.* PhD thesis, Northwestern University, 1998.

[6] E. B. Dussan V, E. Ramé, and S. Garoff. On identifying the appropriate boundary conditions at a moving contact line: an experimental investigation. *J. Fluid Mech.*, 230:97--116, 1991.

[7] A. J. J. van der Zanden. *The hydrodynamics of a moving fluid-liquid contact line.* PhD thesis, Technische Universiteit Endhoven, 1993.

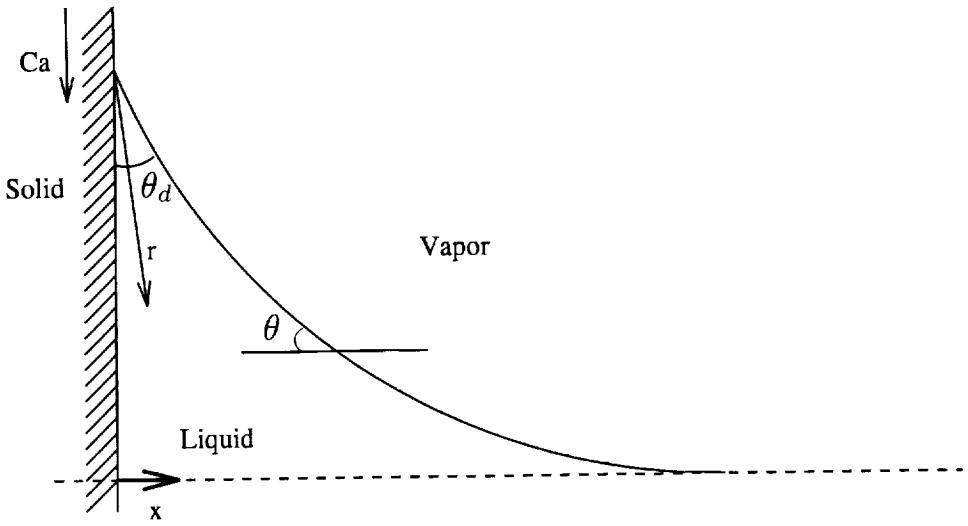

Figure 1: The moving contact line. For an advancing contact line, the wall moves relative to the fluid as shown, characterized by the capillary number Ca. In spontaneous wetting, the capillary number is a function of time. The local angle θ varies along the interface.

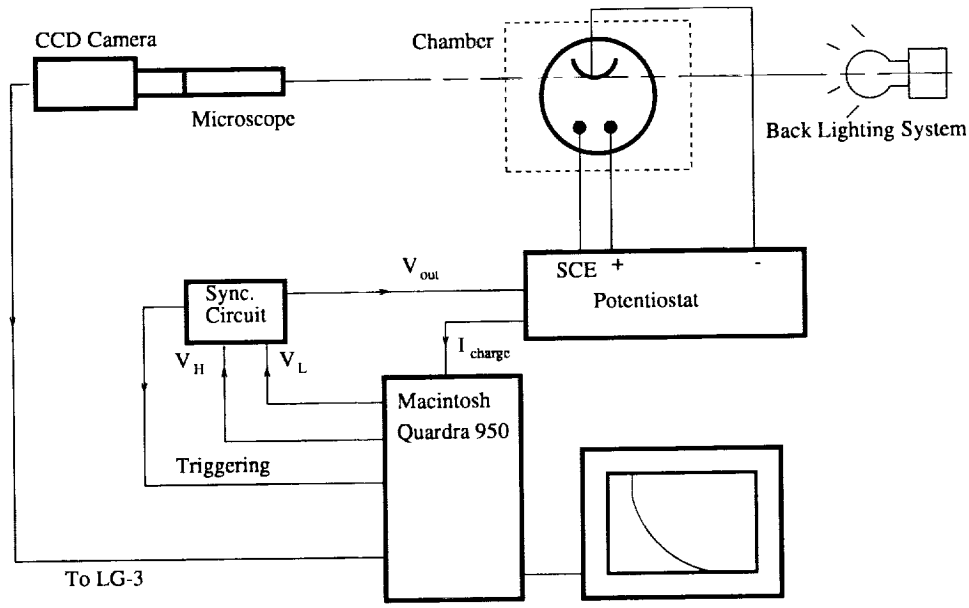

Figure 2: Schematic of the experimental set-up. The curved Au-Hg plate is immersed in KOH solution in the experimental chamber, here seen in top view. The two dots in the chamber are electrodes which apply a step change in potential to the plate. After processing, the CCD camera produces a view of the interface, as sketched here on the monitor. From this view, the interface shape can be determined.

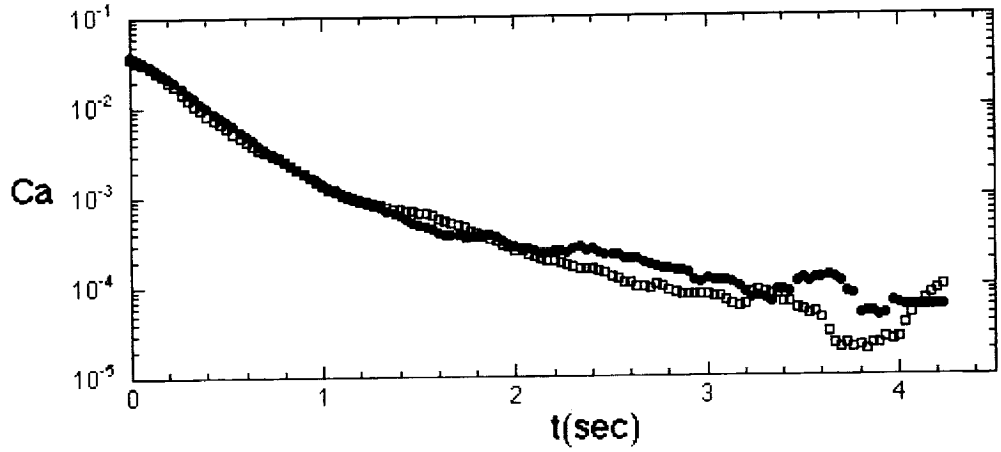

Figure 3: The capillary number as a function of time after a step change in potential is applied to the plate. Data from two runs is shown. The scatter for times greater than about 3 seconds is due to inaccuracies in measuring these low capillary numbers.

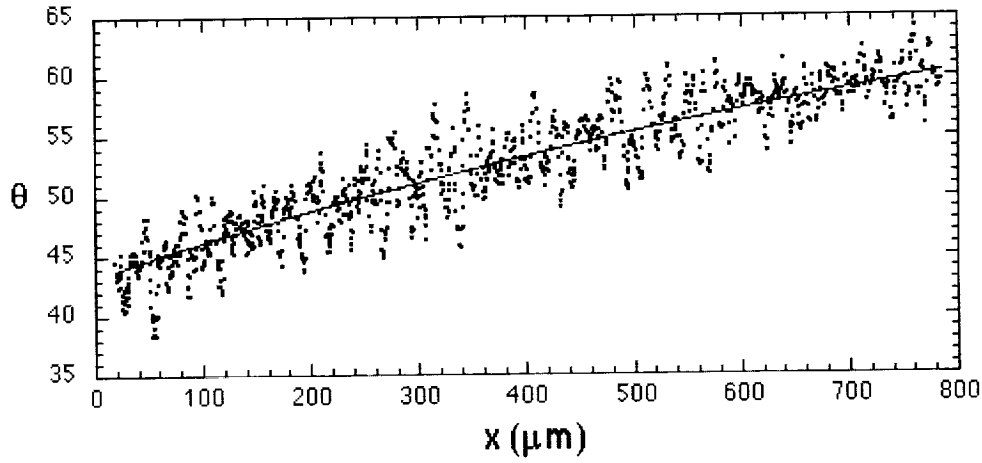

Figure 4: Dynamic profile for $Ca \sim 1.58 \cdot 10^{-3}$. Dots are data and the solid curve is the outer solution $f(r)$, see Eq. (1).

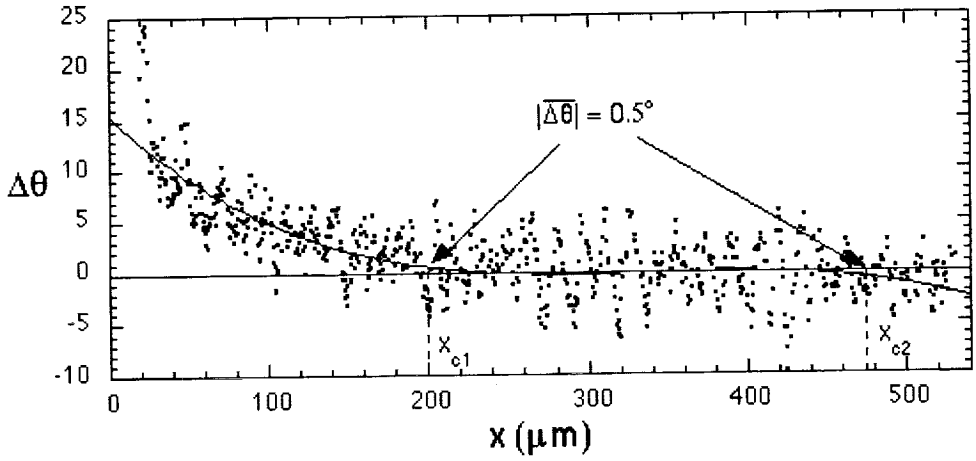

Figure 5: Difference between the measurement of interface angle and the prediction from Eq. (1) for $Ca \sim 2.06 \cdot 10^{-2}$. The equation and measurement agree over the interval in x between the dashed lines.

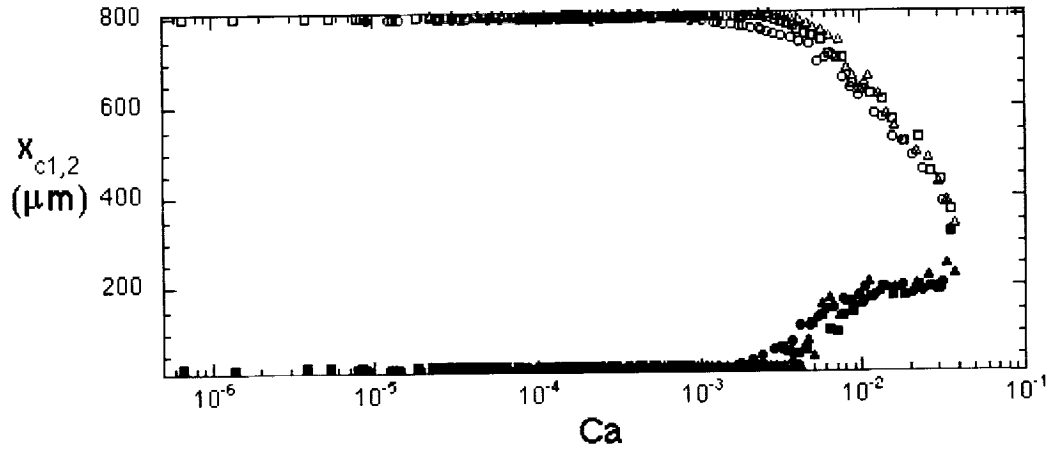

Figure 6: The extent of agreement between theory, Eq. (1), and experiment for one run. Data such as shown in Fig. 5 define the maximum (minimum) distance from the wall at which agreement is found, shown here by the open (closed) symbols. The x-distance between the symbols indicates the interval of agreement. At low capillary numbers, the agreement stretches over the entire field of view. At higher capillary numbers, the interval of agreement narrows. At the highest capillary number shown, there is no interval in which theory and measurement agree.

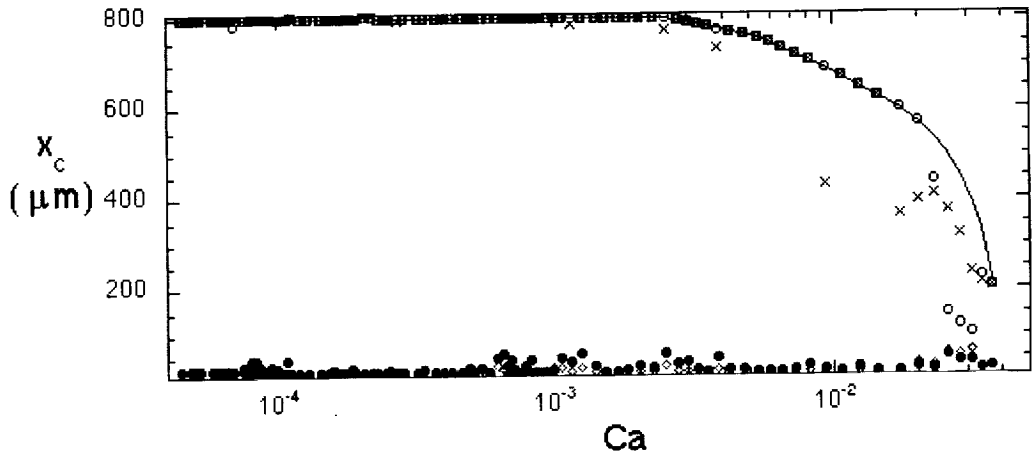

Figure 7: A similar figure to Fig. 6, however here the data is compared with the modified theory, Eq. (2). The maximum (minimum) distance from the wall at which agreement is found, is shown here by the open (closed) symbols. The line shows the outer location of the field of view. Note that for $Ca \gtrsim 5 \cdot 10^{-3}$ by using the modified theory the interval of agreement is larger than that found using Eq. (1), shown in Fig. 6.

DYNAMICS OF THE MOLTEN CONTACT LINE

Ain A. Sonin[1] (speaker), Gregg Duthaler[2], Michael Liu[2], Javier Torresola[2] and Taiqing Qiu[3]

OBJECTIVES

The moving molten contact line plays a key role in a number of applications, including certain coating processes, spin casting of metals, and various droplet based manufacturing techniques. The purpose of our program is to develop a basic understanding of how a molten material front spreads over a solid substrate that is below its melting point, arrests, and freezes. We are concerned particularly with the dynamic contact line that occurs in molten droplet deposition on cold substrates. Our hope is that the work will provide a scientific knowledge base for certain new applications, such as the "printing" of arbitrary three-dimensional objects by precise deposition of individual molten microdrops (Gao & Sonin, 1994), and at the same time contribute generally to the understanding of low Bond number, capillarity-driven liquid dynamics problems.

The main obstacle to progress at this time is our lack of knowledge of the basic processes in molten droplet deposition. We do not yet know the basic laws that govern the dynamics of the molten contact line and its eventual arrest by freezing, and consequently are not in a position to answer the most fundamental question in molten droplet deposition: given the melt and target materials, how do we choose the droplet size and deposition conditions so as to produce a suitable solid shape? The answer to this question depends on the motion and arrest of the molten contact line.

ARREST OF A MOLTEN CONTACT LINE MOVING OVER A SUBCOOLED SOLID OF ITS OWN KIND: EXPERIMENTS AND THEORY

A molten droplet usually spreads over a cold substrate much quicker than it solidifies in bulk, that is, the drop remains essentially in liquid form until the contact line arrests. The point of contact line arrest determines the final shape of the droplet. An ordinary liquid's contact line arrests at a certain "equilibrium" contact angle. When a molten material is involved, however, the spreading is typically arrested by contact line freezing. Indeed, a little reflection shows that in homologous deposition (melt and target of the same material, one above and the other below the freezing point), there exists no meaningful final equilibrium contact angle.

Using an experiment where the rate of contact line advance was externally controlled, Schiaffino and Sonin (1997a) investigated the arrest of the contact line of a molten microcrystalline wax spreading over a subcooled solid "target" of the same material. They found (Fig. 1) that contact line arrest takes place at an apparent liquid contact angle which depends primarily on the Stefan number $S=c(T_f-T_t)/L$ based on the temperature difference T_f-T_t between the fusion point and the initial target temperature, c being the specific heat and L the latent heat of fusion. Neither the melt's superheat nor the prior history of the contact line motion appeared to significantly affect the contact angle at the point where the contact line comes to a halt.

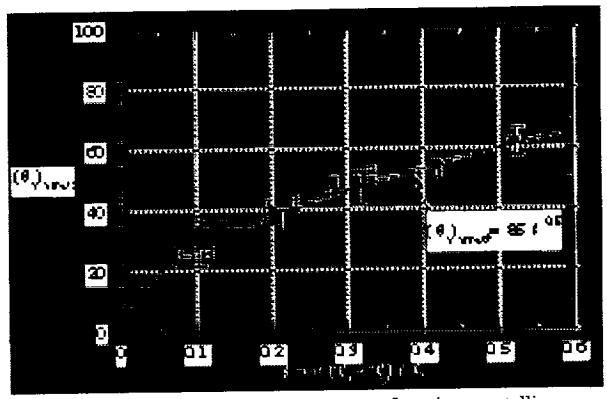

Figure 1 Apparent contact angle at arrest for microcrystalline wax

Schiaffino and Sonin proposed the following physical mechanism for contact line arrest due to freezing: arrest occurs when the liquid's dynamic contact angle approaches the angle of attack θ_s of the solidification front just behind the contact line (Fig. 2). Contact line advance is possible only as long as the liquid's contact angle θ_a exceeds θ_s.

In a second paper Schiaffino and Sonin (1997b) showed that the conventional continuum equations and boundary conditions for the slow spreading of a pure molten material over a solid of its own kind have no meaningful solution for θ_s. The quantity θ_s is deter-

[1] Professor, Department of Mechanical Engineering, Room 3-256, MIT, Cambridge, MA 02139; sonin@mit.edu
[2] Graduate Research Assistant, Department of Mechanical Engineering, Room 3-243, MIT
[3] Assistant Professor, Department of Mechanical Engineering, Room 3-158, MIT

mined by the heat flux just behind the contact line, and the heat flux in the conventional mathematical model is singular at the contact line. However, by comparing experimental data with numerical computations, Schiaffino and Sonin estimated that for microcrystalline wax, the breakdown of the conventional solidification model occurs within a distance of order 0.1-1 μm of the contact line. The physical mechanism for this breakdown is as yet undetermined, and consequently no first-principles theory exists at this time for θ_s and thus for contact line arrest. However, the functional relationship $\theta_s \approx f(S)$ can in principle be determined experimentally for each material.

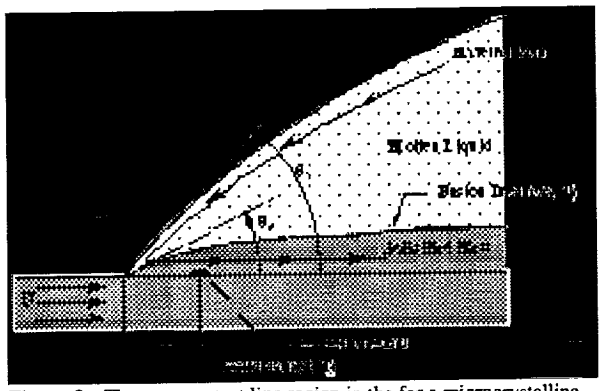

Figure 2 The near contact line region in the for a microcrystalline wax contact line reference frame.

MOLTEN DROPLET DEPOSITION: SIMILARITY LAWS AND EXPERIMENTS

A third paper by Schiaffino and Sonin (1997c) presents a study of the deposition process of molten droplets, from the instant of contact to complete solidification. This study lays down a framework for understanding low to moderate Weber number molten droplet deposition in terms of similarity laws and experimentation. The study is based on experiments with three molten materials—molten wax on solid wax, water on ice, and mercury on frozen mercury—which between them span a considerable range of the deposition/solidification similarity parameters. Based on experiments from the highly viscous limit to the inertia dominated limit, correlations are obtained for the spreading velocity, spreading time scales, the spreading factor (i.e. ratio of deposited drop's final footprint radius and the drop's initial radius), post-spreading liquid oscillation amplitudes and time scales, and bulk solidification time scales. At low to moderate Weber numbers, spreading is driven principally by interfacial forces at the contact line rather than by impact phenomena. The main *dynamic* similarity parameter is the Ohnesorge number $Z=\mu/(\rho\sigma a)^{0.5}$, where μ is the absolute viscosity, ρ is the density, σ in the surface tension, and a is the drop radius. The principal similarity parameter for contact line arrest is the Stefan number.

FURTHER EXPERIMENTS

Experiments have been carried out to (i) extend the investigation of contact line freezing to different materials and conditions, (ii) investigate the relationship between the dynamic contact angle and the contact line speed during spreading, and (iii) better define the thermal and solidification properties of the microcrystalline wax we have been using.

Contact line motion and arrest were studied by depositing molten drops with radius of order 1 mm on solid targets below the melt's fusion point, and photographing the process using high-speed video microscopy. Complete spreading, arrest and solidification events were recorded for molten wax on solid wax, for water on ice, and for molten wax deposited on inclined wax surfaces in order to investigate gravitational effects on molten contact line dynamics and arrest (Fig. 3). From the high-speed video data we obtain empirical relationships between the instantaneous values of the capillary number $Ca= \mu U/\sigma$ (U is the contact line advance speed) and melt contact angle θ_s. This relationship is discussed in the next section.

Post-arrest angles were obtained for molten solder on glass, molten solder on solid solder, and for octacosane on solid octacosane with two different (measured) surface roughnesses. Octacosane ($C_{28}H_{58}$) is a low melting point alkane with a distinct fusion point and latent heat release, and has well known thermal properties. We also investigated molten octacosane on clean glass and on glass coated with two types of self-assembled monolayers, one of which chemically resembles octacosane. These results will be discussed at the conference.

In addition, a study was completed of the thermal and solidification properties of microcrystalline wax, including its thermal conductivity k and enthalpy h(T) and specific heat c(T) at temperatures between 0°C and 115°C (Torresola, 1998). This wax has a distinct fusion point at 90° C (Schiaffino, 1996), but releases latent heat over a broad temperature range (about 20°C) below that point.

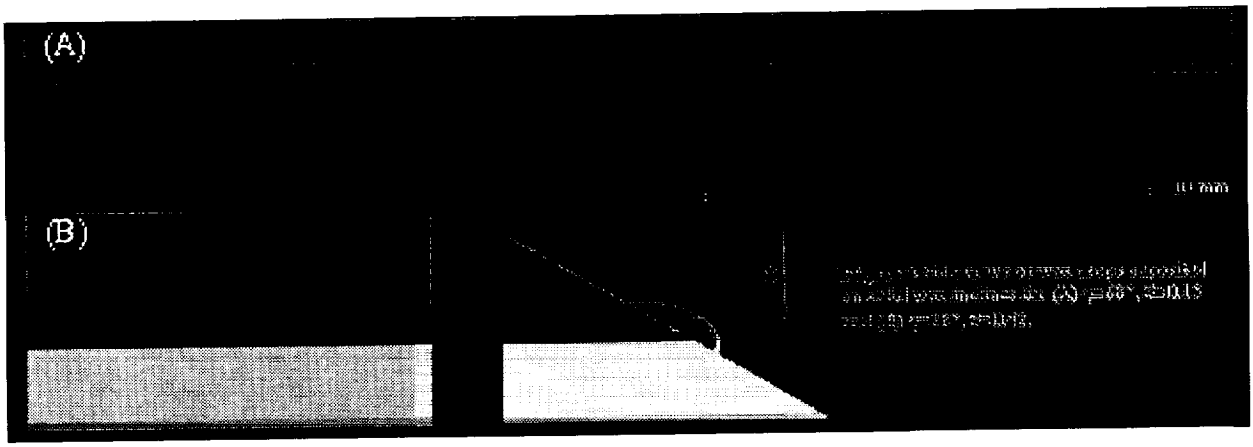

THEORY FOR VELOCITY VS. ANGLE AT A MOLTEN CONTACT LINE

A significant body of both experimental and theoretical work has built up over the past two decades on the relationship between speed and apparent contact angle at an *ordinary* liquid contact line. See for example the reviews by Dussan V. (1979), de Gennes (1985), Kistler (1993), Blake (1993), and the comments in Schiaffino & Sonin (1997a). One of the simplest approximate forms of this relationship is the Hoffman-Tanner-Voinov law for small Ca (Hoffman, 1975; Tanner, 1978; Voinov, 1976, 1978; see also Boender, *et al*, 1991),

$$Ca = \kappa\left(\theta_a^3 - \theta_m^3\right) \qquad (1)$$

where θ_m is the liquid's contact angle at the molecular scale, and is usually identified with the equilibrium angle. Hoffman's experimental value for κ is about 1.3×10^{-2} rad^3, although it does in fact depend weakly on flow system size.

Other than some results mentioned in Schiaffino and Sonin (1997a), no work has previously been done on the Ca vs. θ_a relationship for a *molten* contact line. The molten dynamic contact line problem differs significantly from the ordinary one in that a solidification front forms underneath the molten material as it moves across the subcooled solid, and the material streamlines move into the solid as sketched in Fig. 2. Schiaffino & Sonin (1997a,b) argued that the solidification front at the contact line is wedge-like with a slope θ_s relative to the "horizontal", and deduced $\theta_s(S)$ empirically.

We have adapted Voinov's methodology to the molten contact line and obtained solutions for the liquid flow field near the contact line and for Ca vs. θ_a (Duthaler, 1998). Since the actual solidification front shape near the contact line is unknown, we approximate it as piecewise continuous, with constant slope θ_s up to a cut-off distance $r=\lambda$ and zero slope thereafter (Fig. 4). The flow in the liquid region is assumed to be inertia-free and quasi-steady near the contact line, with viscous forces balancing the pressure gradient resulting from interfacial curvature. In general the equations require a numerical solution, but in the final stages of the arrest process, where $(\theta_a-\theta_s)<<\theta_s$, they yield the following surprisingly simple analytical expression

$$Ca = \frac{\kappa}{\sin\theta_s}\left[\left(\theta_a - \theta_s\right)^4 - \left(\theta_m - \theta_s\right)^4\right] \qquad (2)$$

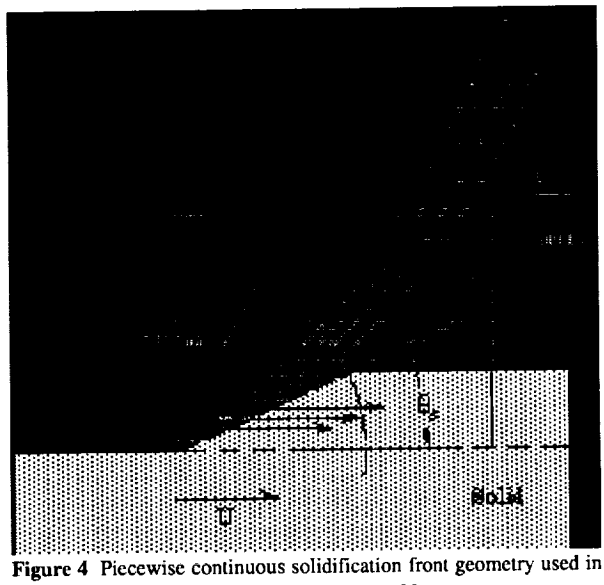

Figure 4 Piecewise continuous solidification front geometry used in modeling the molten dynamic contact line problem

Here, κ plays a role similar to the coefficient in Eq. (1), but does not have exactly the same value. Eq. (1) is in essence an analog of the Hoffman-Tanner-Voinov

law for molten materials approaching the final stage of arrest. Note that near contact line arrest, Ca scales as the 4th power of the (small) difference θ_a-θ_s. This behavior differs dramatically from that of the Hoffman-Tanner-Voinov Law, Eq. (1).

The theory can be applied, for example, to calculate the time scale associated with a molten drop spreading event. For example, in the limit of small Bond and Capillary numbers and small interfacial angles (θ_a,θ_m, θ_s<<1), we obtain

$$\frac{1}{(\theta_a - \theta_s)^3} - \frac{1}{(\theta_o - \theta_s)^3} = \frac{3\theta_s^{4/3}}{\sin\theta_s}\frac{t}{\tau} \qquad (3)$$

where θ_o is the value of θ_a at t=0,

$$\tau = \frac{\mu}{3\kappa\sigma}\left(\frac{4V}{\pi}\right)^{1/3} \qquad (4)$$

is a characteristic time, and V denotes the volume of the drop. Note that θ_a-θ_s~ $t^{1/3}$ for this case. Applying a similar scaling analysis to Schiaffino's force feed experiment (see Schiaffino and Sonin, 1997b) shows that very near the arrest of a force fed droplet, θ_a-θ_s ~ $t^{1/6}$.

The magnitude and trends predicted by the new spreading model are in basic agreement with our experimental results (Fig. 5). The plot shows empirical data for a drop deposition characterized by S=0.15, along with the predictions of various spreading models. The solid line represents the numerical solution of the new hydrodynamic equations derived for melts, based on applying Voinov's methodology to the simplified, wedge-like solidification interface of Fig. 4. We have set the wedge size λ equal to the cut-off distance computed by Schiaffino and Sonin (1997b), λ≈0.1 μm. We also take θ_s=20°, and assume that θ_m=θ_s and that the bulk of the drop remains hemispherical during the final, slow stage of spreading. The approximate solution given by Eq. (2) with θ_s=θ_m=20• is shown using long dashes. Since no *a priori* model for θ_s exists, we choose the value θ_s=20• to ensure good agreement with the experimental final arrest angle, 28.5•. For reference, Fig. 5 also shows Eq. (1) with θ_m set equal to the final arrest angle. At Ca<10^{-2} this equation overestimates Ca for given θ_a by nearly an order of magnitude.

HIGH-RESOLUTION MICROSENSORS FOR THE THERMAL PROCESSES NEAR THE MOVING CONTACT LINE

Before a useful theory for molten contact line advance and freezing can be developed, we need a realistic model for the heat flux at the contact line. One of

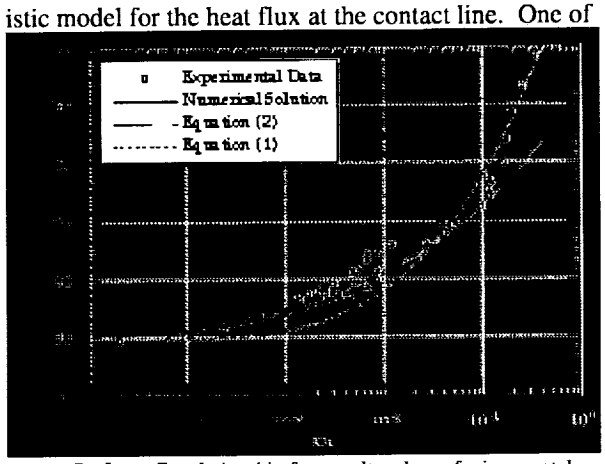

Figure 5 θ_a vs. Ca relationship for a molten drop of microcrystalline wax spreading over a solid target of the same kind. The numerical solution begins when R/a=1.64 and H/a=0.90.

the key objectives of our program is the development of micron-scale sensors for measuring the transient temperature at a point on the substrate surface as a molten contact line moves over it. The hope is that from this temperature history, we can back out information on the heat flux distribution near the contact line and obtain important clues about the nature of the thermal process in that region.

The sensors are of the thermistor type, microfabricated with silicon-based technology on either pure silicon or amorphous silicon dioxide wafers, 100 mm in diameter and 0.5 mm thick. Each wafer has room for 60 chips. Each chip has 32 sensors on its surface, 8 arrayed in a cross-pattern and spaced 400 μm apart, 8 arrayed in line with 200 μm spacing, and 16 arrayed in line with 50 μm spacing (Figs. 6 and 7). The sensors in the two coarsely spaced arrays are 2.5 μm square, and those in the fine array are 1.5 μm square. The time response is better than 10 μs. The sensing elements are made of boron-doped silicon and are electrically connected to the outside circuitry by aluminum circuit traces and gold wires. Temperature is sensed via Wheatstone bridges which detect the sensors' resistance variations due to temperature. Each individual sensor must be separately calibrated. Data is acquired with a PC 16-channel interface board, at a maximum rate of 10^6 samples/sec.

At the time of writing, the chips have been fabricated on wafers (we have several hundred chips of each of the two substrate materials), and a dozen chips have been cut and packaged. The data acquisition system has been constructed, and sensor calibration and testing is in progress. Some results on thermal

transients during contact line passage will be available for the August conference. While we expect that the data will provide information on the near-contact-line heat transfer process, we also foresee possible problems. First, small as they are, the sensors are actually slightly larger than the cutoff lengths computed by Schiaffino and Sonin (1997b), and the spatial resolution may be insufficient for resolving the near-contact-line region where the conventional model departs from reality. Second, due to the microfabrication method the conductors protrude about 0.5 μm above the substrate surface, which may be large enough to affect contact line motion. Finally, a sensor's temperature history will depend not only on the heat flux distribution into it from the fusion front, but also on the thermal properties of the substrate below it and the solidified melt between it and the fusion front (Fig. 2). The heat flux distribution in the contact line region must therefore be unfolded from computations of the overall system's transient response. Whether these potential problems are significant will become clear as the work proceeds.

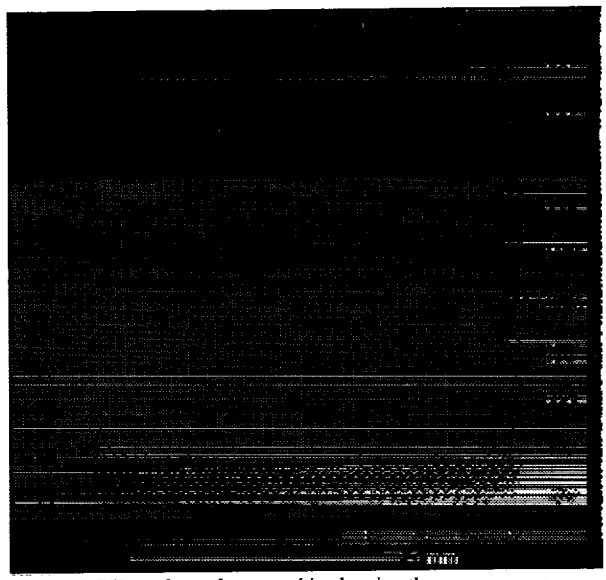

Figure 6 Silicon thermal sensor chip showing the sensor arrays

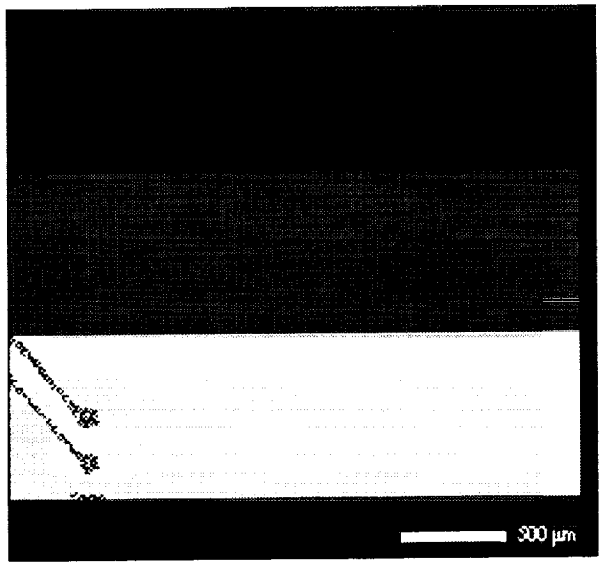

Figure 7 Close-up of the coarse cross-pattern sensor array

ACKNOWLEDGEMENTS

This research was supported by NASA under Grant NAG 3-1845 and by NSF under Grant GTS-9523764. We thank Professor Paul Laibinis and doctoral student Seok-Won Lee of the MIT Department of Chemical Engineering for their advice on materials selection and their assistance in preparing the self-assembled monolayer coatings.

REFERENCES

Blake, T. D., in *Wettability*, J. C. Berg, editor, Marcel Dekker, New York, 1993, 251-309.

Boender, W., A. K. Chesters, and A. J. J. van der Zanden, 1991, *Int. J. Multiphase Flow*, **17**, 661-676.

de Gennes, P. G., 1985, *Rev. Mod. Phys.*, **57**, 827-863.

Dussan V., E. B., 1979, *Ann. Rev. Fluid Mech.*, **11**, 371-400.

Duthaler, G., Ph.D. Thesis, Department of Mechanical Enginering, MIT, in progress.

Gao, F. and A. A. Sonin, 1994, *Proc. Roy. Soc. London A*, **444**, 533-554.

Hoffman, R. L., 1975, *J. Colloid and Interface Sci.*, **50**, 228-241.

Kistler, S. F., in *Wettability*, J. C. Berg, editor, Marcel Dekker, New York, 1993, p. 311-429

Liu, Michael, MS Thesis, Department of Mechancial Engineering, MIT, in progress.

Schiaffino, S., 1996, *The Fundamentals of Molten Microdrop Deposition and Solidification*. PhD Thesis, Department of Mechanical Engineering, MIT.

Schiaffino, S., and A. A. Sonin, 1997a, *Phys. Fluids,*. **9**, 3172-3187.

Schiaffino, S., and A. A. Sonin, 1997b, *Phys. Fluids.*, **9**, 2217-2226.

Schiaffino, S. and A. A. Sonin, 1997c, *Phys. Fluids.*, **9**, 2227-2233.

Tanner, L. H., 1979,*J. Phys D: Appl. Phys.*, **12**, 1473-1484.

Torresola, J., 1998, Solidification Properties of Certain Waxes and Paraffins. MS Thesis, Department of Mechanical Engineering, MIT.

Voinov, O. V., 1976, Translated from Izvestiya Akademii Nauk SSSR, Mekhanika Zhidkosti i Gaza, No. 5, 76-84.

Voinov, O. V., 1978, *Sov. Phys. Dokl.*, **23**, 891-893.

EFFECTIVE FORCES BETWEEN COLLOIDAL PARTICLES

Riina Tehver[1], Jayanth R. Banavar[1], [1]Department of Physics and Center for Materials Physics, Pennsylvania State University, University Park, Pennsylvania 16802, Joel Koplik[2], [2]Benjamin Levich Institute and Department of Physics, City College of the City University of New York, New York, New York 10031

Colloidal suspensions have proven to be excellent model systems for the study of condensed matter and its phase behavior [1]. Many of the properties of colloidal suspensions can be investigated with a systematic variation of the characteristics of the systems and, in addition, the energy, length and time scales associated with them allow for experimental probing of otherwise inaccessible regimes [2, 3]. The latter property also makes colloidal systems vulnerable to external influences such as gravity. Experiments performed in micro-gravity by Chaikin and Russell have been invaluable in extracting the true behavior of the systems without an external field [3]. Weitz and Pusey (private communication) intend to use mixtures of colloidal particles with additives such as polymers to induce aggregation and form weak, tenuous, highly disordered fractal structures that would be stable in the absence of gravitational forces.

Between any two colloidal particles, there is an attractive force caused by the interactions between the fluctuating dipole moments of their constituent atoms. This van der Waals force leads to irreversible aggregation of unprotected particles and it is desirable to diminish its magnitude [4] and provide a stabilization mechanism. Common mechanisms are steric stabilization and charge stabilization [1]. For steric stabilization, colloidal particles are coated with polymers so that there is a short-range highly repulsive (nearly hard core) force between two colloidal particles when their respective polymer layers are compressed. We shall consider these types of colloidal particles later.

Charge stabilization occurs when charged surface groups on colloidal particles dissociate, ionizing the particle and emitting counterions into the solution. The standard theory of interaction in these charged colloidal suspensions is due to Derjaguin, Landau, Verwey and Overbeek (DLVO) [5] and the DLVO potential includes a non-negligible screened Coulomb repulsion

$$U_{DLVO}(r) = \frac{Z^{*2}e^2}{\epsilon}\frac{\exp(-\kappa r)}{r} \qquad (1)$$

in addition to the short-range van der Waals attraction. The inverse Debye screening length, κ and the effective charge, Z^* are given by $\kappa^2 = 4\pi\rho e^2/k_BT\epsilon$, $Z^* = Z\exp(\kappa a)/(1+\kappa a)$. Here, ϵ is the dielectric constant of the solvent, ρ is the density of counterions, a is the radius of a colloidal "macroion", Z is its bare charge, k_B and T are the Boltzmann constant and temperature. The screened Coulomb potential is obtained in the mean-field linearized Poisson-Boltzmann approximation and is thus expected to have have limited applicability, although the functional form of the potential with a renormalized charge has been argued to remain valid in a wider regime [6].

Indeed, the DLVO theory has been shown to explain some experimental data [7] but fails to account for others [8]. The main experimental challenges to the theory are numerous indications of a long-range attraction between colloidal particles. The latter are evident in experiments where particles are confined near a wall or in suspensions at higher densities. When two isolated particles at a low density have been considered, no attraction has been found. Hence, many-body effects might be thought to be responsible for this unexpected attractive force.

To study the role of confinement and evaluate many-body forces, we consider a system consisting of spherical colloidal macroions, a counterion density distribution $\rho(\vec{r})$ and a homogeneous solvent of a specified dielectric constant. The effective Hamiltonian for our system can be expressed as:

$$\mathcal{H} = \frac{1}{2}\sum_I M_I \dot{\vec{R}}_I^{\,2} + \sum_{I,J<I} U(|\vec{R}_J - \vec{R}_I|) + \mathcal{F}. \qquad (2)$$

M_I and $\vec{R}_I$ are the masses and coordinates of the macroions and $U(|\vec{R}_J - \vec{R}_I|)$ is the macroion-macroion interaction energy. In the expression for the free energy of the counterions [9, 10],

$$\mathcal{F} = \int d^3\vec{r}\rho(\vec{r})[\phi_{ext} + \frac{1}{2\epsilon}\phi_{int} + \phi_{id}(\rho) + \phi_{corr}(\rho)] \quad (3)$$

we include: the macroion-counterion and counterion-wall interaction potentials, ϕ_{ext}; the Coulomb interactions between counterions, $\phi_{int}(\vec{r}) = \int d^3\vec{r}'\frac{\rho(\vec{r}')}{|\vec{r}-\vec{r}'|}$; ideal gas, ϕ_{id}, and correlation, ϕ_{corr}, contributions. The ideal gas term is $\phi_{id} = k_BT\log[\Lambda_B^3\rho(\vec{r})] - 1$, where Λ_B is the de Broglie thermal wavelength and we employ the free energy of a one-component plasma [11] in evaluating ϕ_{corr}. We use pseudopotentials for macroion-counterion interactions [10] to suppress the large variation of the counterion density near a macroion core.

Given $\mathcal{F}$, the forces between macroions due to counterions can be evaluated using the Hellmann-Feynman theorem. The total force acting on a macroion becomes:

$$F_I = -\nabla_{\vec{R}_I}\mathcal{F}(\rho(\vec{r}),\phi_{ext}) - \nabla_{\vec{R}_I}\sum_J U(|\vec{R}_J - \vec{R}_I|). \quad (4)$$

The equilibrium counterion density, $\rho(\vec{r})$, itself can be obtained from a functional minimization: $\frac{\delta\mathcal{F}}{\delta\rho} = 0$. An efficient scheme for solving a functional minimization of this type was developed by Car and Parrinello [12] in the context of quantum-mechanical electronic properties calculations and also used by Lowen, Madden and Hansen [10] for colloidal suspensions. Expressing the counterion density in terms of a wave function $\psi(\vec{r})$, $\rho(\vec{r}) = |\psi(\vec{r})|^2$, one can consider the Fourier components of $\psi(\vec{r})$, $\psi_{\vec{k}}$, to be dynamical variables in a Lagrangian:

$$\mathcal{L} = \frac{1}{2}\sum_{\vec{k}} m_{\vec{k}}|\dot{\psi}_{\vec{k}}|^2 + \frac{1}{2}\sum_I M_I \dot{\vec{R}}_I^{\,2} - \mathcal{F} - \sum_{I,J<I} U(|\vec{R}_J - \vec{R}_I|) \quad (5)$$

with a constraint: $\int d^3\vec{r}\rho(\vec{r}) = NZ$. N is the number of macroions. $m_{\vec{k}}$ are fictitious masses determining the time-scale of the dynamics of counterion density. We used this Lagrangian to solve the functional minimization by performing dynamical simulated annealing on $\psi_{\vec{k}}$ to obtain the minimum of $\mathcal{F}$ for a fixed macroion configuration.

We started out with a configuration of two macroions in a periodic cubic box of length $1\mu m$ at a temperature $T = 300K$ in water, $\epsilon = 78$. The counterion density was evaluated on a 96^3 grid and the radius and charge of a macroion were $a = 100nm$ and $Z = 200e^-$ (e^- stands for the elementary charge). The forces between macroions at a series of different separations were measured. At this low packing fraction, relatively low surface charge and counterion concentration, the DLVO pair-potential between two macroions is expected to hold. We plot the DLVO prediction for the periodic system in Fig. 1. We show our density functional minimization results in the same figure as well as the force resulting from an *optimal* fitting to a pair-potential of the DLVO form. The numerical values for the inverse screening length and effective charge for the optimal fit are presented as the first set in Table 1.

In order to check the validity of pair-wise additivity that we had tacitly assumed above, we placed three colloidal particles in a unit cell with periodic boundary conditions. Maintaining our previous pseudopotential parameters, we studied the following geometries. First, we positioned the three macroions in configurations of equilateral triangles of different sizes and calculated

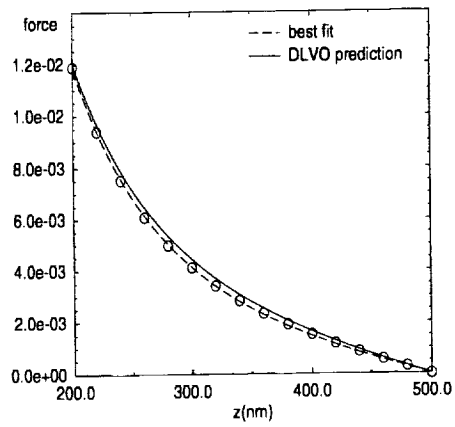

Figure 1: The total force on a macroion in a periodic system with two macroions and free counterions in the primary simulation cell. The DLVO prediction with no adjustable parameters (solid line) is compared to numerical local density approximation data (open circles) and the best fit of a DLVO-type potential is also plotted (dashed line). The force is scaled to $(e^-/nm)^2$.

the force on one of the macroions as a function of the edge of the triangle. In Fig. 2, we plot our data for the force in these configurations as a function of the distance and compare it to the force obtainable from an additive pair-potential. Secondly, we also placed the three macroions in an asymmetric triangular configuration where two macroions were close to each other (separation of $200nm$) and a third macroion was at a distance of $473nm$ from either of the two. We measure a force of $1.24\cdot10^{-2}(e^-/nm)^2 \pm 0.05\cdot10^{-2}(e^-/nm)^2$ on either one of the first macroions while pairwise additive forces predict $1.22\cdot10^{-2}(e^-/nm)^2 \pm 0.05\cdot10^{-2}(e^-/nm)^2$ for the value. Thus, we detect no three-body component in the effective forces.

To study forces between macroions in a confined system, we introduced two parallel short-range repulsive walls. We placed the macroions at different separations and distances from a wall and measured the effective forces between them. We fit our data to a DLVO-type force and the effective parameters obtainable from the fit are summarized in Table 1. Our results can be understood as follows. The introduction of repulsive walls increased the counterion density in the middle of the simulation cell, while decreasing the Debye screening length in that region (compare sets 1 and 2 in the table). On the other hand, near the walls,

	R_x (nm)	κa	Z^* (e^-)	Z (e^-)
1	-	0.374	212.5	200.9
2	500.0	0.454	220.2	203.3
3	350.0	0.444	220.5	204.2
4	200.0	0.308	213.8	205.5

Table 1: The parameters corresponding to the optimal effective pair interaction potential between macroions in different geometries. The first set of data was obtained with periodic boundary conditions while walls were introduced in the last three. R_x measures the distance from a wall. κa and Z^* are obtained from the fit, the bare charge Z is calculated from κa and Z^*. The DLVO prediction for a periodic system is: $Z = 200$, $Z^* = 205.8$ and $\kappa a = 0.258$.

the counterion density must decrease and the Debye screening length consequently increase – the latter can be seen by comparing sets 2, 3 and 4. Thus, this simple model for confinement changes the effective parameters in the DLVO potential but does not introduce any fundamentally new behavior.

Besides electrostatic interactions, entropic depletion effects that arise from (hard-core) exclusion play an important role in determining the behavior of multicomponent colloidal suspensions [13, 14]. It is well known that the addition of free polymers to a suspension of colloidal particles can cause an effective attraction. The first successful attempt to predict and explain the phenomenon was made by Asakura and Oosawa (AO) [15]. In their approach, there is an exclusion volume around each large sphere within which the centers of small ones cannot penetrate. As the entirely entropic free energy of small spheres depends on the volume accessible to them, the favored configurations are the ones where the exclusion volumes of large spheres overlap. This implies that there ought to be a force, pushing the large spheres towards each other in order to increase the entropy of the small ones. A similar mechanism explains the attraction of a large sphere towards a wall. Quantitative AO calculations ignore the interactions between the small spheres completely and even though an overall acceptable experimental agreement with the AO prediction has been reported [13, 16], the ideal gas approximation based AO theory does not provide a satisfactory description of entropic potentials and forces in dense colloidal suspensions.

To go beyond the simple geometric arguments of AO requires a detailed theory for the structure of a binary

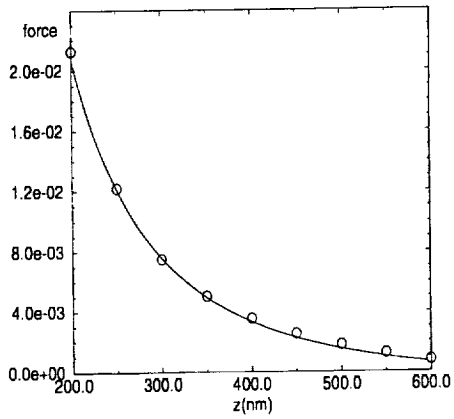

Figure 2: Test of the additivity of the effective macroion potential. Three macroions were placed in equilateral triangular configurations and the force on a macroion as a function of the edge of the triangle was measured. Open circles are our data whereas the solid line indicates the force from an additive DLVO-type potential with the parameters: $Z^* = 212.5e^-$, $\kappa a = 0.374$. The force is scaled to $(e^-/nm)^2$.

fluid. Even though significant progress has been made [17], this is a difficult task for an arbitrary binary system. We consider instead the simplest situation in which all the spheres are of the same size and study depletion forces and potentials by an analysis of the data for this system. All our numerical data were obtained from hard-sphere molecular dynamics simulations where the system evolves on a collision-to-collision basis: all particles move freely until two of them come in contact, then an elastic collision between the two occurs, after which all particles move freely until the next collision. Desired quantities are measured as equilibrium time averages in these simulations.

Let us first consider the depletion potential between two hard spheres in a "solution" of other hard spheres of the same size. The potential of mean force, W, is related to the pair correlation function, $g(x)$, as [18]

$$g(x) = \exp(-W/k_BT). \tag{6}$$

The depletion force therefore turns out to be:

$$F/k_BT = \frac{\partial \ln(g(x))}{\partial x}, \tag{7}$$

where x is the distance between two particles. An example of the depletion force between two hard spheres

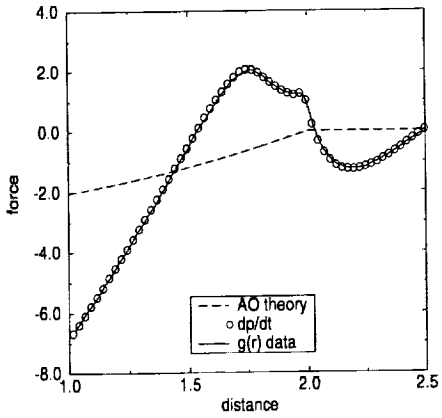

Figure 3: The depletion force as a function of the distance between two hard spheres in a mixture of other hard spheres of the same size at a packing fraction $\phi = 0.45$. The distance is measured in hard sphere diameters, σ, and the force is scaled to k_BT/σ.

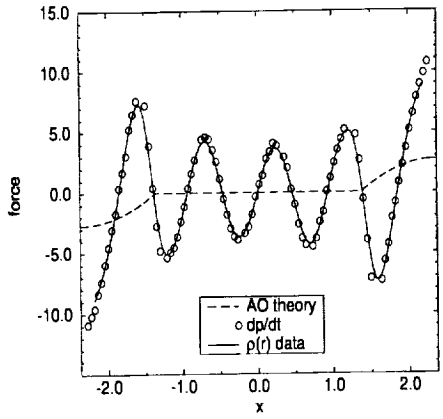

Figure 4: The depletion force between a hard sphere and a wall for the system described in the text. x is measured in hard sphere diameters and the force is scaled to k_BT/σ. The walls are parallel to the yz plane and are located at $x = \pm 2.37$. In the simulation, presented in this figure, thermal walls were used but reflecting walls result in a qualitatively similar force profile.

in a hard-sphere fluid derived from a pair-correlation function using Eq. (7) is given in Figure 3. At a packing fraction of $\phi = 0.45$, it suffices to consider 108 hard spheres in a cubic box with periodic boundary conditions to obtain the first features in the force profile. We can prove the validity of our calculation by measuring the depletion force directly by recording the total momentum transfer in a unit time on a sphere at a known distance from another one. We compare both of those force measurements to the AO prediction in Figure 3.

Similarly, the depletion force between a sphere and a wall can be obtained from the density profile:

$$F/k_BT = \frac{\partial \ln(\rho(x))}{\partial x} \qquad (8)$$

where x is the direction perpendicular to the wall and $\rho(x)$ is the local density of the hard sphere fluid. The well-known layering of fluid molecules near a wall leads again to a more complex structure for the force than AO predicts. See Fig. 4 for the force data and the AO prediction. We also plot the force obtained from momentum transfer measurements. The data was obtained with the same number of spheres at the same density as before.

Depletion forces in complex geometries with step edges and non-trivial curvature have been measured and argued to have profound consequences for cellular biology or entropic control and directed motion of colloidal particles. The AO-type calculations of entropic forces and potentials in these geometries are simple enough to carry out while more precise predictions quickly become rather laborious and, to our knowledge, have not been attempted. To go beyond the AO theory, we calculated entropic forces and potentials for a system of 324 hard spheres at a packing fraction of about 0.45 in a three-dimensional T-shaped channel. Potentials near step-edges and corners are of principal interest and are shown in Figure 5. A comparison with the AO prediction is also shown in the figure. The potential barrier repelling a hard sphere from a step-edge is simply a reflection of the density decrease near it. Analogously, the potential minimum attracting particles towards a corner and the sharp increase in density there are different manifestations of the same effect.

There is an interesting and important feature to the depletion forces that already manifests itself in the AO approach. Depletion forces need not be pairwise additive. In the AO approximation, the force between two particles arises from the overlap of excluded volumes. Three-body effects become relevant when the hard spheres are considered in configurations in which their pairwise overlap volumes themselves overlap, resulting in an over-counting of the actual overlap volume. An example could be a triangular configuration. The AO prediction for an equilateral configuration is calculable.

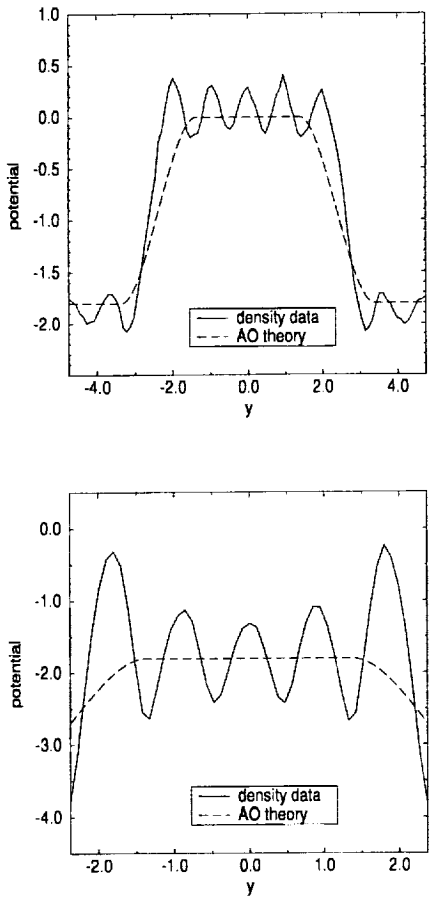

Figure 5: The effective potential profiles for a hard sphere fluid confined in a T-shaped channel. To form the channel, walls in the yz plane were placed at: $x = 4.74\sigma$; $x = 0$ for $|y| > 2.37\sigma$; $x = -4.74\sigma$ for $|y| < 2.37\sigma$; and in the xz plane at $y = \pm 2.37\sigma$ for $-4.74\sigma < x < 0$. (Periodic boundary conditions were used otherwise.) The upper figure displays the effective potential at $x = 0$, i. e. along a "step," the edges of which are located at $y = \pm 2.37\sigma$. The lower figure is the effective potential at $x = -4.74\sigma$ where the "corners" are located at $y = \pm 2.37\sigma$. The potential is given in units of thermal energy and y is measured in hard sphere diameters.

For the packing fraction $\phi = 0.45$, the AO two-body force at two sphere contact is $F_{AO} = -2.0\ k_BT/\sigma$. If forces were additive, the magnitude of the total force on a sphere in this triangular configuration would be $2F_{AO}\cos(\pi/6) = -3.5\ k_BT/\sigma$. Instead, when all overlap volumes are correctly accounted for, an AO-like analysis predicts instead a force of $-2.9\ k_BT/\sigma$. The *exact* three-body force can in principle be found from a three-point correlation function but obtaining reliable statistics for this measurement is rather time consuming. Instead, we prepared the described triangular configuration and measured the momentum transfer on each of the spheres in a simulation. The two-body force at contact for $\phi = 0.45$ is $F_{sim} = -6.8\ k_BT/\sigma$ (see Fig. 3). The actual measured force, $-10.0\ k_BT/\sigma$, is again significantly lower than the additive pairwise force: $2F_{sim}\cos(\pi/6) = -11.8\ k_BT/\sigma$. Indeed, the three-body component in this geometry for our system of hard spheres is a significant percentage of the total force.

In conclusion, we have performed calculations of effective forces between charged colloidal particles in different configurations and studied effective depletion forces in hard sphere colloids. In the first case, our data are well fit to screened Coulomb type potentials. It should be noted that in our calculations, the walls were not charged and dielectric discontinuities between the suspension and the walls were not considered. One may speculate that long-range attraction cannot be accounted for by static calculations and that they probably originate from temporal fluctuations. In the second case, a comparison of our numerical data and the Asakura-Oosawa theory indicates that the AO theory underestimates the magnitude of depletion forces at contact, ignores the complex nature of entropic interactions, consisting of several maxima and minima and underestimates the range of the interactions.

Acknowledgment: This work was done in close collaboration with Francesco Ancilotto, Amos Maritan and Flavio Toigo to whom we are grateful. We are indebted to Paul Chaikin and Dave Weitz for numerous stimulating discussions and the NASA Microgravity Program for their generous support.

References

[1] P. N. Pusey, in: Liquids, Freezing and the Glass Transition, eds. J. P. Hansen, D. Levesque and J. Zinn-Justin (North-Holland, Amsterdam, 1991). W. C. K. Poon and P. N. Pusey, in: Observation, Prediction and Simulation of Phase Transitions in Complex Fluids, eds. M. Baus, L. F. Rull and J.-P. Ryckaert (Kluwer Academic, Dordrecht, 1995).

[2] W. van Megen and S. M. Underwood, Nature (London), 362, 616 (1993). K. Schatzel and B. J. Ackerson, Phys. Rev. Lett. 68, 337 (1992). B. J. Ackerson and P. N. Pusey, Phys. Rev. Lett. 61, 1033 (1988).

[3] J. Zhu, M. Li, R. Rogers, W. Meyer, R. H. Ottewill, STS-73 Space Shuttle Crew, W. B. Russell and P. M. Chaikin, Nature (London), 387, 883 (1997).

[4] The magnitude of van der Waals forces can be reduced by index matching the solvent and the particles but this is unfortunately incompatible with density matching. A micro-gravity environment is thus essential to avoid sedimentation and resulting complications.

[5] B. V. Derjaguin and L. D. Landau, Acta Physicochim. USSR 14, 633 (1941). E. J. W. Verwey and J. T. G. Overbeek, Theory of the Stability of Lyophobic Colloids (Elsevier, Amsterdam, 1948).

[6] S. Alexander, P. M. Chaikin, P. Grant, G. J. Morales, P. Pincus and D. Hone, J. Chem. Phys, 80, 5776 (1984).

[7] J. C. Crocker and D. G. Grier, Phys. Rev. Lett. 73, 352 (1994).

[8] J. C. Crocker and D. G. Grier, Phys. Rev. Lett. 77, 1897 (1996). A. E. Larsen and D. G. Grier, Nature (London), 385, 230 (1997). A. E. Larsen and D. G. Grier, Phys. Rev. Lett. 76, 3862 (1996). B. V. R. Tata, M. Rajalakshmi and A. K. Arora, Phys. Rev. Lett. 69, 3778 (1992). B. V. R. Tata and N. Ise, Phys. Rev. B 54, 6050 (1996). B. V. R. Tata, E. Yamahara, P. V. Rajamani and N. Ise, Phys. Rev. Lett. 78, 2660 (1997). K. Ito, H. Yoshida and N. Ise, Science 263, 66 (1994).

[9] M. J. Stevens and M. O. Robbins, Europhys. Lett. 12, 81 (1990).

[10] H. Lowen, P. A. Madden and J.-P. Hansen, Phys. Rev. Lett. 68, 1081 (1992). H. Lowen, J.-P. Hansen and P. A. Madden, J. Chem. Phys. 98, 3275 (1993).

[11] M. Baus and J.-P. Hansen, Phys. Rep. 59, 1 (1980).

[12] R. Car and M. Parrinello, Phys. Rev. Lett. 55, 2471 (1985).

[13] A. D. Dinsmore, A. G. Yodh and D. J. Pine, Nature (London) 383, 239 (1996). A. D. Dinsmore, D. T. Wong, P. Nelson and A. G. Yodh, Phys. Rev. Lett. 80, 409 (1998).

[14] P. D. Kaplan, J. L. Rouke, A. G. Yodh and D. J. Pine, Phys. Rev. Lett. 72, 582 (1994). P.D. Kaplan, L. P. Faucheux and A. J. Libchaber, Phys. Rev. Lett. 73, 2793 (1994). A. Imhof and J. K. G. Dhont, Phys. Rev. Lett. 75, 1662 (1995). P. Bartlett, R. H. Ottewill and P. N. Pusey, Phys. Rev. Lett. 68, 3801 (1992).

[15] S. Asakura and F. Oosawa, J. Chem. Phys. 22, 1255 (1954). S. Asakura and F. Oosawa, J. Polymer Sci. 33, 183 (1958).

[16] Y. N. Ohshima, H. Sakagami, K. Okumoto, A. Tokoyoda, T. Igarashi, K. B. Shintaku, S. Toride, H. Sekino, K. Kabuto and I. Nishio, Phys. Rev. Lett. 78, 3963 (1997).

[17] Y. Mao, M. E. Cates and H. N. W. Lekkerkerker, Physica A 222, 10 (1995). P. Attard and G. N. Patey, J. Chem. Phys. 92, 4970 (1990). R. Dickman, P. Attard and V. Simonian, J. Chem. Phys. 107, 205 (1997). T. Biben, P. Bladon and D. Frenkel, J. Phys.: Condens. Matter 8, 10799 (1996).

[18] J. P. Hansen, I. R. McDonald, Theory of Simple Liquids (Academic Press, London, 1986).

Session 3A

Phase Change I: Boiling

CONSTRAINED VAPOR BUBBLE

J. Huang, M. Karthikeyan, J. Plawsky, P. C. Wayner, Jr., The Isermann Department of Chemical Engineering, Rensselaer Polytechnic Institute, Troy NY12180, USA, wayner@rpi.edu

ABSTRACT

The nonisothermal Constrained Vapor Bubble, CVB, is being studied to enhance the understanding of passive systems controlled by interfacial phenomena. The study is multi-faceted: 1) it is a basic scientific study in interfacial phenomena, fluid physics and thermodynamics; 2) it is a basic study in thermal transport; and 3) it is a study of a heat exchanger. The research is synergistic in that CVB research requires a microgravity environment and the space program needs thermal control systems like the CVB.

Ground based studies are being done as a precursor to flight experiment. The results demonstrate that experimental techniques for the direct measurement of the fundamental operating parameters (temperature, pressure, and interfacial curvature fields) have been developed. Fluid flow and change-of-phase heat transfer are a function of the temperature field and the vapor bubble shape, which can be measured using an Image Analyzing Interferometer.

INTRODUCTION

The CVB, which is presented in Fig. 1 for a microgravity environment, has various thin film regions that are of both basic and applied interest. Generically, a CVB is formed by underfilling an evacuated enclosure with a liquid. Classification depends on shape and Bond number. The specific CVB discussed herein was formed in a fused silica cell with inside dimensions of 3x3x40 mm and, therefore, can be viewed as a large version of a micro heat pipe. Since the dimensions are relatively large for a passive system, most of the liquid flow occurs under a small capillary pressure difference. Therefore, we can classify the discussed system as a low capillary pressure system. The studies discussed herein were done in a $1g$ environment (Bond Number = 3.6) to obtain experience to design a microgravity experiment for a future NASA flight where low capillary pressure systems should prove more useful. The flight experiment is tentatively scheduled for the year 2000. The SCR was passed on September 16, 1997. The RDR is tentatively scheduled for October, 1998.

Since the solid walls of the container constrain the shape of the vapor bubble and liquid/vapor interface, the intermolecular force fields in the thin film regions are different from that in a bulk liquid. In addition to surface tension stresses (e.g., Marangoni stresses), both

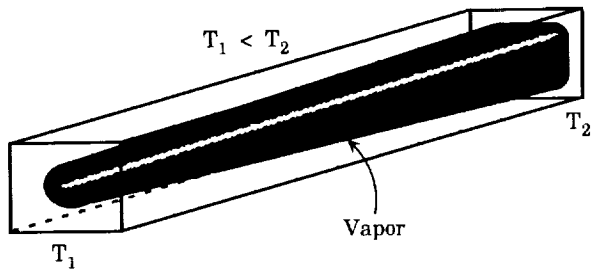

Figure 1: Vapor bubble constrained in glass cell.

disjoining pressure (due to van der Waals forces) and capillary pressure gradients are important (Potash and Wayner, 1972). For a completely wetting system with insufficient liquid to fill the cell, the liquid will coat all the walls of the container. For a particular liquid/solid system, the film thickness profile is a function of the fill ratio and temperature and concentration profiles.

Under equilibrium conditions, the CVB system has been used to study interfacial thermodynamics and characterize wetting (DasGupta *et al.*, 1995). For the non-equilibrium case presented in Fig. 1, there is an external heat input at End (2), where evaporation occurs, and heat removal near End (1), where condensation occurs. The return condensate flows from End (1) to End (2) as a result of stress gradients due to interfacial free energy (e.g., capillary and disjoining pressure gradients). For a very small cross-sectional area with a mean meniscus curvature comparable to the reciprocal of the hydraulic radius of the flow channel, and Bond number $\approx 4 \times 10^{-3}$, the system has been called a micro heat pipe, which has been extensively studied (Cotter, 1984, Peterson, 1992, and Faghri, 1995). Under some conditions, the processes are like those in other heat transfer systems, e.g., the microlayer in boiling. Therefore, the experimental and theoretical results obtained studying the CVB are of both generic and specific use.

The CVB study is multi-faceted: 1) it is a basic scientific study in interfacial phenomena, fluid physics and thermodynamics; 2) it is a basic study in thermal transport; and 3) it is a study of a heat exchanger. The research is synergistic in that CVB research requires a microgravity environment and the space program needs thermal control systems like the CVB. The objective of this paper is to present some of our ground based results.

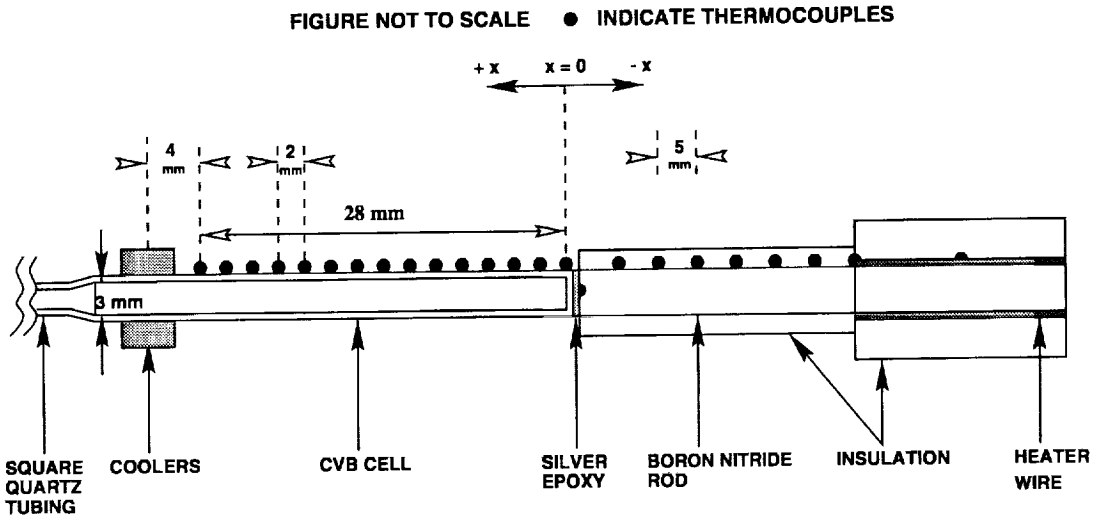

Figure 2: Experimental setup.

These results demonstrate that experimental techniques for the direct measurement of the fundamental operating parameters (temperature, pressure, and interfacial curvature fields) of the system have been developed. Fluid flow and change-of-phase heat transfer are a function of the temperature field and the vapor bubble shape, which can be measured using an Image Analyzing Interferometer. The extended Young-Laplace Equation gives the pressure field as a function of the shape.

EXPERIMENTAL METHOD

A pentane/quartz CVB was used to study transport processes under non-equilibrium conditions (Karthikeyan *et al.*, 1997 and Huang *et al.*, 1997). In Fig. 2, the experimental setup consists mainly of the fused silica CVB cell (3x3x40 mm inside dimensions with walls 1.25 mm thick), thermocouples to measure the temperature on the outside surface, T, a resistance heater, and thermoelectric coolers. Pyrex connecting tubes and a pressure transducer to measure the vapor pressure are not shown. Additional details of the experimental equipment are presented by Karthikeyan (1997). The experimental use of glass allows the profile and, therefore, the pressure gradient causing fluid flow to be optically measured using a microscope. A portion of the optical system to record the naturally occurring fringes in the top corner of the cell to obtain δ_0 and r is presented in Fig. 3. Details of this film thickness measurement technique, Image Analyzing Interferometry (IAI), are elaborated elsewhere (DasGupta *et al.*, 1995).

Experimentally, we have found that, in the low capillary pressure systems of interest, dramatically different phenomena occur on the top and bottom surfaces because of the gravitational force field. Therefore, the process on one surface interferes with the study of the process on the other process. For example, at times, boiling occurs on one surface while not on the other. A significant change in the system size to obtain a lower Bond Number by increasing the capillary pressure would also produce a significant change in the phenomena being studied. We are interested in the lower capillary pressure system with lower viscous effects due to their relatively large size.

In Fig. 2, a CVB cell is connected to a boron nitride rod. The measured boron nitride rod temperatures were fitted to the classical fin equation. The heat going out from the end of the boron nitride rod ($x = -1\ mm$), Q_{out}, was calculated from the gradient of the temperature profile. The heat input to the CVB cell at $x = 0\ mm$, Q, was obtained by deducting the calculated convective heat loss from the first mm of the CVB cell from Q_{out}. The overall uncertainties in Q, calculated using the classical propagation equation, was about 18% (see Karthikeyan, 1998).

EXPERIMENTAL RESULTS AND DISCUSSIONS

Fig. 4 shows a plot of the temperature difference, θ, between the outside surface of the CVB cell and the room, *vs.* the axial distance, x, for both the cell operating as a CVB, and as a dry evacuated cell. $x = 0$ represents the beginning of the cavity of the cell and

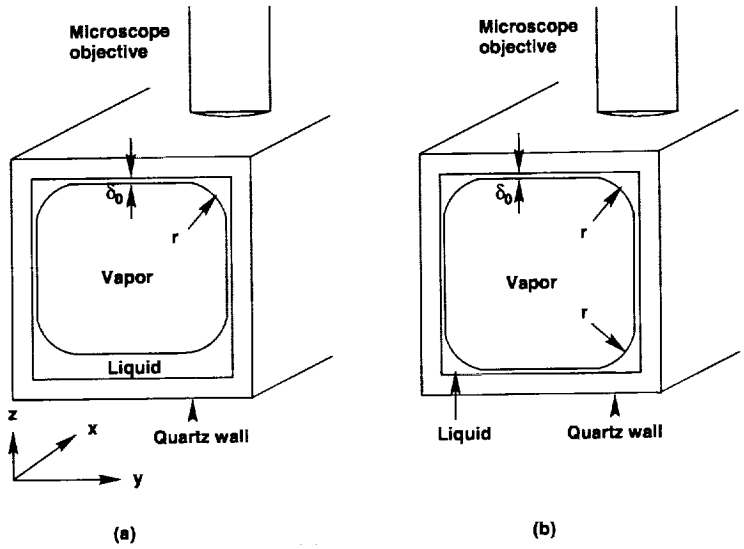

Figure 3: Location of the microscope objective with respect to the CVB cell: (a) asymmetric film in 1g environment; (b) film with Bond Number = 0.

the two dashed lines represent the 1 mm thick glass wall at the heater end of the cell. The electrical power inputs to the heater (13.4 W) and coolers were the same in both cases. However, we see a dramatic difference between the temperature profiles of the CVB and the dry run. While the temperature profile for the dry cell resembles that of a fin, the CVB temperature profile has three distinct regions (shown in Fig. 5). The heat flow rate through the CVB is almost three times that of the heat flow rate through the dry cell (1.49 W for the CVB against 0.5 W for the dry cell). We define the thermal conductance, C, as the ratio of the CVB heat input to the total temperature drop across the length of the cell,

$$C = Q/\Delta T \tag{1}$$

At Q=0.5 W, we found that the conductance for the dry cell was 0.0036 W/K versus 0.01 W/K for the CVB, a three-fold increase in the conductance for the CVB.

A comparison of the measured radius of curvature, r, profile in the upper corner for a non-isothermal CVB experiment(Q=0.81 W) to that for an isothermal CVB cell, is shown in Fig. 6. In both cases, the bubble length was 26 mm and the angle of inclination was $-4°$. The difference in the two profiles is obvious; while the radius of curvature for the isothermal case changes relatively little, the radius of curvature for the non-isothermal case increases from about 0.09 mm to more than five times as much. The increased capillary pressure gradient is needed to recirculate the working fluid. On the other hand, the change in the radius of

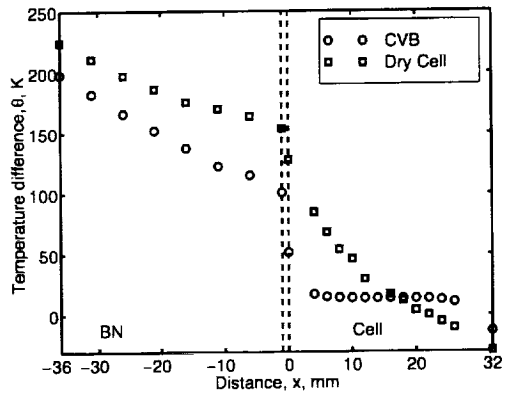

Figure 4: Temperature difference profiles of the CVB and the corresponding dry cell ($\theta = T - T_\infty$).

curvature in the isothermal case was caused solely by the gravitational force. Due to gravitational effects, the radius of curvature profile in the bottom of the cell is different. Fig. 7 shows both the experimental radii of curvature and those predicted by the model (Karthikeyan *et al.*, 1998). There is good agreement between these experimental and predicted values. Obviously, the gradient of the radius of curvature profile in higher for the higher heat flow rate experiment.

In order to characterize the variation in the effectiveness of the CVB from region to region, we define

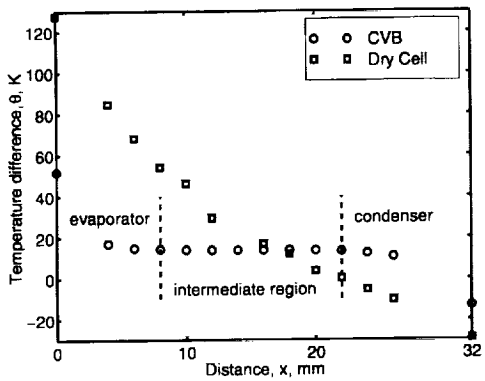

Figure 5: Temperature difference profiles in the quartz cell for the experiments shown in Fig. 4 ($\theta = T - T_\infty$).

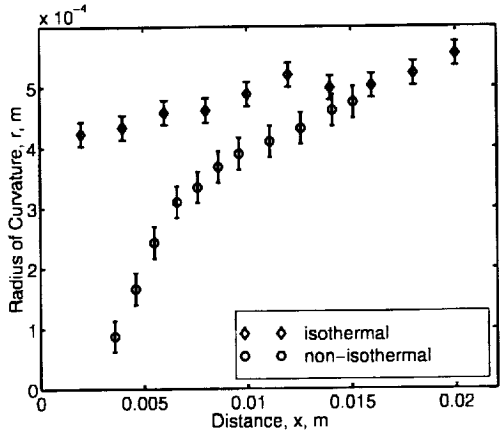

Figure 6: Corner radius of curvature profiles obtained using IAI.

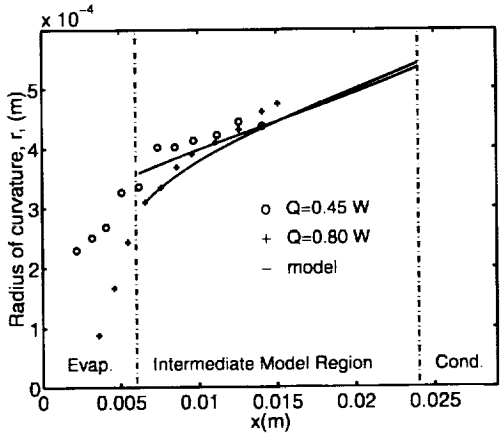

Figure 7: Radii of curvature profiles for bubble length = 26 mm and the angle of inclination = $-4°$.

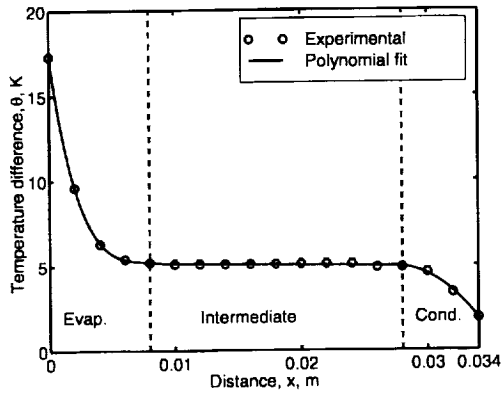

Figure 8: CVB temperature difference profile and 3-region polynomial fit ($\theta = T - T_\infty$).

the local effective thermal conductivity, $k_{eff}(x)$ as,

$$k_{eff}(x) = -\frac{q(x)}{d\theta/dx} \tag{2}$$

where

$$q(x) = \frac{Q - \int_0^x L_q h_{cell}\theta dx}{A} \tag{3}$$

where L_q is the outside perimeter of the cell, A the cross-sectional area of the cell, and the heat transfer coefficient between the cell and the environment, h_{cell}, which was obtained from an equivalent dry cell experiment. The plot of the temperature profile of one CVB experiment (Q=0.316 W) along with the polynomial fit is shown in Fig. 8, while the plot of the local effective thermal conductivity, k_{eff}, as a function of position, x, is shown in Fig. 9. Even including the area of the glass which has a very low thermal conductivity, the effective thermal conductivity (solid line in Fig. 9) in the intermediate region well exceeds the thermal conductivity of copper depicted by the dash-dot line.

Figs. 10 and 11 show the temperature profiles for CVB experiments at various heat loads with bubble length, l_b, 26 mm and $>$ 28 mm, respectively. The fixed volume of the system could be experimentally set. When the bubble length is greater than 28 mm, the bubble extends all the way to the coolers. The reduced thermal resistance in the condenser region allows a higher heat flow rate to the CVB cell. Fig. 12 shows a plot of the thermal conductance, C *vs.* the heat load, Q, for the experiments shown in Figs. 10 and 11. Since the conductance increases with an increase in the heat load, the CVB has not reached its capillary limit.

Fig. 13 shows an excellent correlation between the CVB operating temperature and the saturation temper-

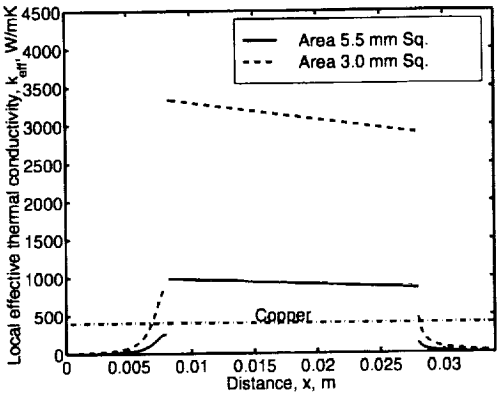

Figure 9: Local effective thermal conductivity vs. x for the CVB.

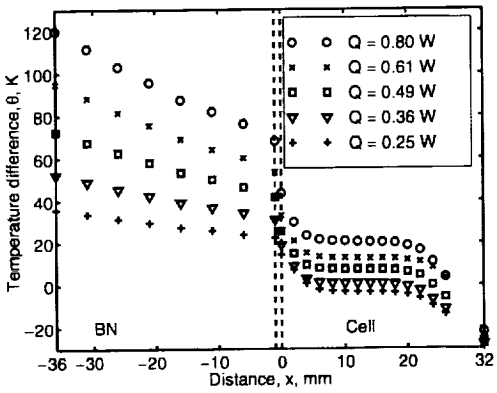

Figure 10: Temperature difference profiles of CVB for various Q, $l_b = 26$ mm ($\theta = T - T_\infty$).

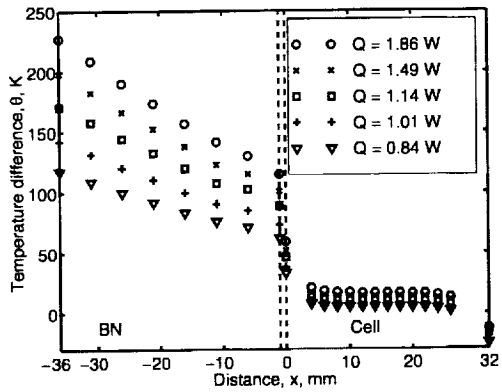

Figure 11: Temperature difference profiles for $l_b > 28\ mm$ (constant but not exactly known), ($\theta = T - T_\infty$).

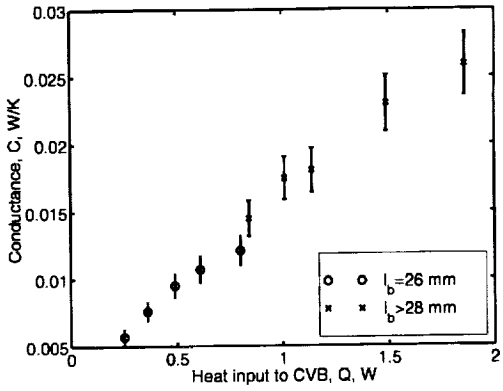

Figure 12: Thermal conductance as a function of the heat input to the CVB.

ature based on the measured pentane vapor pressures. However, it is also seen that the saturation temperature, T_{sat}, is always a little higher than the measured outside temperature in the intermediate region, T_{int}, where radial heat conduction through the glass wall is very small. This temperature difference, which never exceeds 2.5 $^\circ C$, may be due to non-condensables or the heat loss from the intermediate region. Kelvin effects at these capillary pressures are very small.

Fig. 14 shows the CVB temperature profiles for experiments conducted at various angles of inclination, under constant heater and cooler power inputs. The bubble length was also a constant at 26 mm. The negative sign of the angle means that the evaporator is at a higher level than that of the condenser, and capillary forces are hindered by the hydrostatic head in the flow of the condensate back to the evaporator. As we can see from Fig. 14, both length and temperature of the intermediate region decrease with an increase in the angle of inclination from 0° to -25°. In fact, for the experiment at -25°, the region of small temperature gradient (intermediate region) is almost non-existent. Additionally, it is seen that the heat input to the CVB decreases with an increase in the angle of inclination. This is because of the reduction in the liquid flow rate from the condenser to the evaporator due to the opposition of the hydrostatic head to liquid flow. Since the heat removal rate through the coolers remains the same, a reduction in the heat input with the increase in the angle of inclination causes a reduction in the operating pressure; consequently, the operating temperature of the CVB decreases. As expected, the thermal conductance of the CVB decreases with an increase in the angle of inclination. This trend is plotted in Fig. 15.

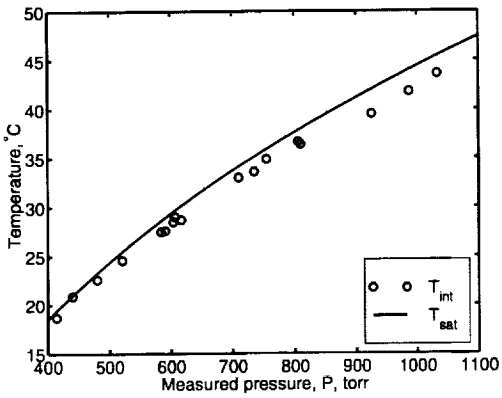

Figure 13: Variation of the CVB operating temperature with operating pressure.

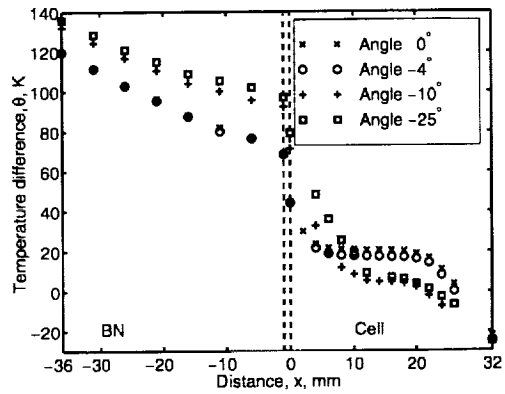

Figure 14: $\theta = T - T_\infty$ profiles (Q=0.80, 0.71, 0.48, 0.33 W, for angles = $0°, -4°, -10°, -25°$, respectively).

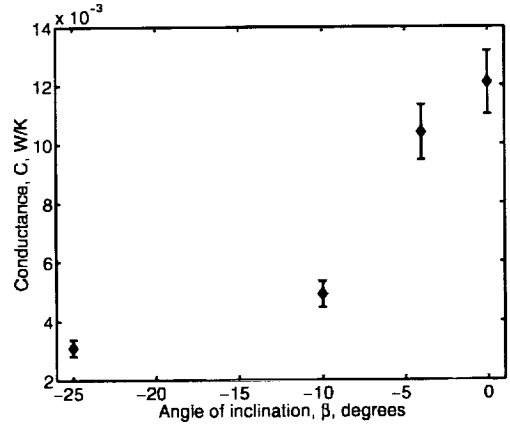

Figure 15: Variation of thermal conductance with the angle of inclination of the CVB.

CONCLUSIONS

1) Experimental techniques for direct measurement of the fundamental operating parameters (temperature, pressure and interfacial curvature fields) in the Non-isothermal Constrained Vapor Bubble (CVB) were demonstrated.

2) The CVB has an overall thermal conductivity that is extremely high in the intermediate region of the cell where heat losses to the surroundings are minimized.

3) For the heat flow rates studied, the thermal conductance of the CVB increases with an increase in the heat input.

4) The performance of the CVB is a strong function of its orientation with respect to gravity.

ACKNOWLEDGMENT

This material is based on work supported by the National Aeronautics and Space Administration under grant # NAG3-1834. Any opinions, findings, and conclusions or recommendations expressed in this publication are those of the authors and do not necessarily reflect the view of NASA.

REFERENCES

Cotter, T. P., 1984, Principles and Prospects of Micro Heat Pipes, *Proc. 5th Int. Heat Pipe Conf.*, Tsukuba, Japan, pp. 328-335.

DasGupta, S., Plawsky, J. L., and Wayner, P. C., Jr., 1995, Interfacial Force Field Characterization in a Constrained Vapor Bubble Thermosyphon, *AIChE Journal*, 41(9), pp. 2140-2149.

Faghri, A., 1995, Heat Pipe Science and Technology, First Edition, Taylor and Francis, Washington, DC.

Huang, J., Karthikeyan, M., Plawsky, J. L., and Wayner, P. C., Jr., 1997, Two-Dimensional Analysis of the Evaporator of a Constrained Vapor Bubble, *Proc. 10th Intl. Heat Pipe Conf.*(F-5), Stuttgart, Germany.

Karthikeyan, M., 1997, Experimental and Analytical Investigation of the Non-Isothermal Constrained Vapor Bubble, Ph.D. Thesis, Department of Chemical Engineering, Rensselaer Polytechnic Institute, NY

Karthikeyan, M., Huang, J., Plawsky, J. L., and Wayner, P. C., Jr., 1998, Experimental Study and Modeling of the Intermediate Section of the Non-isothermal Constrained Vapor Bubble, *J. Heat Transfer* Vol. 120, pp. 166-173.

Peterson, G. P., 1992, Overview of Micro Heat Pipe Research and Development, *Appl. Mech. Rev*, 45(5), pp. 175-189.

Potash, M. Jr. and Wayner, P. C. Jr., 1972, Evaporation from a Two-Dimensional Extended Meniscus, *Int. J. Heat Mass Transfer*, Vol. 15, pp. 1851-1863.

COMMENTS ON THE OPERATION OF CAPILLARY PUMPED LOOP DEVICES IN LOW GRAVITY

K. P. Hallinan[1] and J. S. Allen[2]
[1]University of Dayton, Dayton, Ohio, 45469-0210, khallina@engr.udayton.edu
[2]MS500-102,NASA-LeRC, 2100 Brookpark Rd., Cleveland, OH, 44135, jeff.allen@lerc.nasa.gov

ABSTRACT

The operation of Capillary Pumped Loops (CPL's) in low gravity has generally been unable to match ground-based performance. The reason for this poorer performance has been elusive. In order to investigate the behavior of a CPL in low-gravity, an idealized, glass CPL experiment was constructed. This experiment, known as the Capillary-driven Heat Transfer (CHT) experiment, was flown on board the Space Shuttle Columbia in July 1997 during the Microgravity Science Laboratory mission.

During the conduct of the CHT experiment an unexpected failure mode was observed. This failure mode was a result of liquid collecting and then eventually bridging the vapor return line. With the vapor return line blocked, the condensate was unable to return to the evaporator and dry-out subsequently followed. The mechanism for this collection and bridging has been associated with long wavelength instabilities of the liquid film forming in the vapor return line. Analysis has shown that vapor line blockage in present generation CPL devices is inevitable.

Additionally, previous low-gravity CPL tests have reported the presence of relatively low frequency pressure oscillations during erratic system performance. Analysis reveals that these pressure oscillations are in part a result of long wavelength instabilities present in the evaporator pores, which likewise lead to liquid bridging and vapor entrapment in the porous media. Subsequent evaporation to the trapped vapor increases the vapor pressure. Eventually the vapor pressure causes ejection of the bridged liquid. Recoil stresses depress the meniscus, the vapor pressure rapidly increases, and the heated surface cools. The process then repeats with regularity.

INTRODUCTION

Capillary pumped loops are closed loop phase change devices relying upon evaporation of liquid at the source of heat and then condensation of vapor at the sink of heat. The distinguishing characteristics of CPLs from other capillary pumped heat transfer devices are the macroscopically large vapor and liquid transport lines that ideally make possible the passive transport of heat over long distances. The porous media providing the capillary pumping is confined to the evaporator region.

The first Capillary-Pumped Loop (CPL) was developed in the 1960's at the NASA Lewis Research Center in Cleveland, Ohio (Stenger, 1966). Since then a significant number of low gravity evaluations have followed. The first of these was the Capillary Pumped Loop GAS Experiment (G-471), flown in June, 1985. The low-gravity results of this experiment are still unclear; though initial reports indicated success. The CApillary Pumped Loop (CAPL) experiment was flown in February, 1994 on board STS-60 as part of the Hitchhiker payload. This experiment tested a starter pump concept designed to clear the vapor lines of liquid prior to start-up of the CPL evaporators. Douglass (1997) reported that vapor penetrated the wick of the starter pump during operation yielding a temperature there above that of the system temperature. Further, the starter pump was never able to fully clear the vapor lines of liquid. The CAPL experiment was reflown as CAPL-2 with a redesigned starter pump in July, 1995 on board STS-69. Preliminary findings indicated performance within the thermal requirements of the EOS program (CAPL2, 1995). In November 1996, the Visualization In an Experimental Water Capillary Pumped Loop (VIEW-CPL) experiment was flown on the middeck of STS-80. This was the first experiment specifically designed to investigate the failure of CPL's in low gravity. The results of the VIEW-CPL are still preliminary, although the harmful presence of a vapor bubble within the core of the evaporator was reported (Kolos and Herold, 1997). Finally, the Two Phase Flow (TPF) experiment, designed to address problems encountered during the CAPL experiment, was flown in August, 1997 on STS-85 during the Technology, Application and Science (TAS) mission. The TPF experiment incorporated a new type of starter pump as well as a "capillary flow valve". Initial reports indicate some difficulties in start-up (Ottenstein, 1997).

In general, capillary-pumped loops have not been started from a cold state successfully without the use of a starter pump (Ku, 1995b). In most instances, the starter pump is a heated wicking structure that is used

to clear the vapor lines of liquid. Often, especially during startup, the temperature data has indicated that the liquid was flowing in reverse inside the evaporator. These experiments have also exhibited pressure oscillations accompanied by evaporator deprime (Ku and Huang, 1995a). The fundamental mechanism of the unstable operation, however, has not been identified.

The Capillary-driven Heat Transfer (CHT) experiment was designed and conducted to gain insight into the failure mechanisms of CPL devices in low gravity. The following describes the CHT experiment and the results that satisfy this objective.

EXPERIMENT

The main component of the Capillary-driven Heat Transfer (CHT) experiment is a Pyrex test loop shown schematically in Figure 1. The loops were designed to ideally model CPLs. All glass construction was used to permit observation of the fluid orientation within the whole of the CPL during testing.
Two such loops were fabricated and tested in low gravity. These loops were mounted within an enclosed experimental housing. Each was designed with an evaporator and condenser leg, having respective evaporator inner diameters of 1mm and 4mm and a 10mm inner diameter condenser. A partition wall was used to isolate these legs from each other. The vapor return line likewise had a 10mm internal diameter. The liquid return line was equal in diameter to the evaporator inner diameter. Within the loop a three-way valve was used to direct liquid (ethanol) from the 10cc reservoir into the condenser leg and/or the evaporator leg of the test loop. Conical transition sections connected the vapor leg to the capillary tubing. The conical sections were designed as capillary traps in low gravity and preferentially located the evaporator meniscus. The test fluid was spectroscopic grade ethanol.

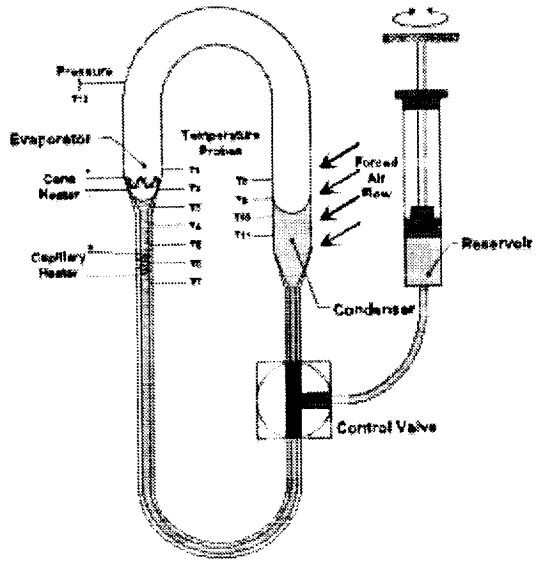

Figure 1 Schematic of experimental CPL model.

The loops were designed to prevent evaporator dry-out due to surface tension differences between the evaporator and the condenser alone even at the maximum temperature expected.

During the testing, heat could be applied to the evaporator by either of two heaters. The first, called the cone heater, was a serpentine wire attached to the evaporator conical transition section. The second, called the capillary heater, was a spiral wound wire located on the capillary tubing approximately 10 mm from the cone heater. Both heaters were constructed from 0.25mm Kanthol wire, rolled flat to insure good contact with the glass surface. A brushless fan mounted over an opening (fan vent) in the experiment module housing provided cooling for the condenser. This cooling air was exhausted through two additional openings (condenser vents) in the condenser side of the experiment module housing.

The loop was instrumented with 7 thermocouples (Type T, 40 AWG) along the length of the evaporator leg and 4 thermocouples along the length of the condenser leg. The thermocouples were located 0.25 mm from the inside wall in small diameter holes drilled into the Pyrex tubing. This proximity to the inside wall coupled with the fine gauge of the thermocouples provided a very quick response to wall temperature changes. An additional thermocouple and a pressure transducer were connected to the vapor leg to allow for a determination of the vapor properties. The loops were backlit to permit video recording of the internal phenomenon.

The output voltages from the thermocouples and pressure transducer as well as the power for the heaters and pressure transducer were fed to an LED read-out that simultaneously displayed the temperature, pressure, and heat input data. A video record of this data was obtained.

Four types of CHT experiments were conducted on the MSL-1 mission. The two relevant to the present paper were conducted as follows. In the first, liquid was added to the loop to the condenser to near the top of the straight section. Capillarity insured that the liquid in the evaporator was at the top of the evaporator conical section. Power was initiated to one of the two heaters. During the transient, evaporator meniscus stability and overall liquid orientation within the loop was observed.

The second type of experiment was referred to as the re-wetting experiments. In these, the liquid was withdrawn to the bottom of the straight section of the evaporator capillary tubing. Power was then applied to the capillary heater. After a set waiting period, the control valve was rotated to free liquid flow from the condenser to the evaporator. The subsequent re-wetting of the evaporator meniscus was then observed. Several waiting times and therefore initial temperatures were investigated.

The following sections present the results describing the dominant device failure mode - liquid slugs forming in the vapor return line that block the return of vapor to the condenser - and the related evaporator instabilities.

RESULTS

Liquid Slug Formation in the Vapor Return Lines

One of the first experimental observations was the formation of a continuous liquid film over the entire length of the vapor return leg. Immediately after applying heat, a liquid film could be seen advancing along the wall of the vapor leg on the evaporator side due to condensation of vapor on the cooler walls of the loop. Capillary forces "drain" the liquid film in the regions where the vapor tubing bends. The process of low-gravity liquid pooling in the elbow of the vapor tube and the eventual formation of a liquid slug is illustrated in Fig. 2. During each experiment run, the liquid accumulated in the outer radius of the bend in the vapor section of the test loop. This pool of liquid would collect into a lobe that would grow until a slug of liquid would form, completely bridging the vapor line.

Figures 3 and 4 show the formation of the liquid slug in the vapor leg and the subsequent recession of the condenser meniscus after the slug has formed. In Figure 3 the liquid film begins to pool in the outer radius of the bend and eventually bridges. Prior to complete bridging of the vapor line, the pooling of the liquid in the bend of the vapor leg does not adversely effect the CPL operation. However, after the liquid slug forms, condensation to the condenser meniscus is completely disrupted. Subsequently, as liquid is continually fed to the evaporator, the condenser meniscus begins to recede as shown in Figure 4. Eventually, it recedes into the capillary tube thereby eliminating the pressure difference feeding liquid into the evaporator. At this point the evaporator dries out and the system fails.

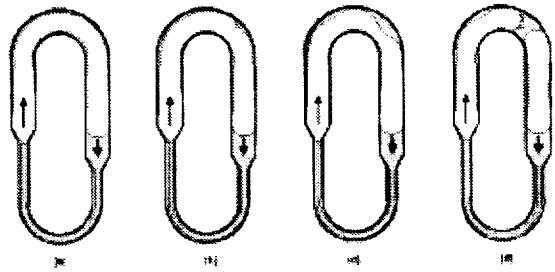

Figure 2. Illustration of liquid accumulation and slug formation in the test loop vapor leg during low-gravity CHT experiments. The arrows indicate the direction of liquid and vapor flows.

Figure 3 Formation of a liquid slug in the bend of the vapor leg.

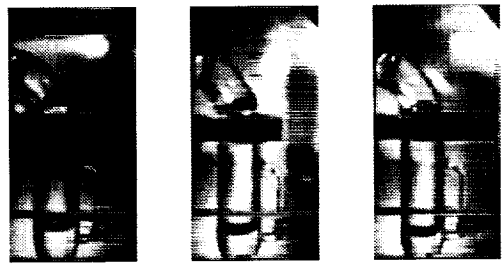

Figure 4 Recession of the condenser meniscus after formation of a liquid slug.

The formation of this slug is primarily the result of an instability arising from a long-wave disturbance of the

annular liquid film in the vapor return line. Gauglitz and Radke(1990), Aul and Olbricht (1990) and Hu and Joseph (1989) have shown that an annular film within a straight tube is fundamentally unstable to long-wave disturbances. Such a liquid film will always breakup and form periodically spaced annular lobes when the length of the liquid film exceeds a critical length. For thick liquid films, the annular liquid lobes will bridge the tube and form liquid slugs. Though this long wavelength instability is ultimately responsible for the slug formation shown in Figures 3 and 4, the liquid flow to the outer portion of the tubing bend is caused by another mechanism.

In a low Bond number (i.e., low gravity) environment, liquid in an annular film will flow from the inner to outer radius of a bend because of differences in the interfacial curvature and, therefore, liquid pressure between these two regions. These pressure differences and the liquid flow that develops are analyzed by examining four distinct regions of the annular liquid film (see Figure 5). The first region is the outer portion of the tubing bend where the liquid accumulates. Region 2 is the inside radius of the tubing bend and is located 180^0 from region 1 at the same centerline location. Regions 1 and 2 are highlighted in the cross sectional view of the annular liquid film at section A-A. Region 3 comprises the straight portion of the vapor line. Region 4 is the condenser meniscus. For the purposes of this analysis, the condenser meniscus is presumed to be far from the bend (See Allen et al., 1998, for results obtained by relaxing this requirement) and the liquid film is assumed to be of uniform thickness, h.

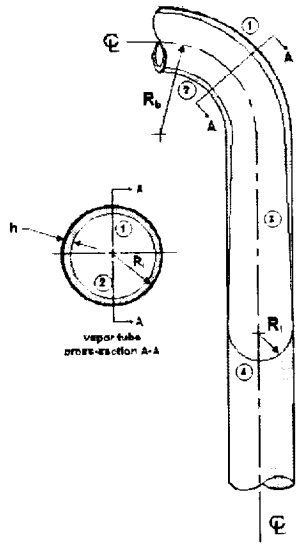

Figure 5 Geometry of the annular liquid film.

The pressure drop across a liquid-vapor interface is known from the Laplace-Young equation:

$$P_v - P_l = \sigma\left(\frac{1}{R_1} + \frac{1}{R_2}\right)$$

where P_v is the vapor pressure, P_l is the liquid pressure, R_1 and R_2 are the principal radii of curvature, and σ is the surface tension. One of the principal radii of curvature is
the same for each of the four regions and is equal to the tubing inside radius minus the film thickness, R_1 - h. The second principal radius curvature varies from region to region. In region 1 that radius of curvature is $R_b + R_1 - h$.
Similarly, $-R_b + R_1 - h$, ∞, and $R_1 - h$ are the second principal radius of curvature for regions 2, 3, and 4, respectively.

In order to simplify the analysis, a film thickness ratio is defined as $\delta = h/R$. Also, the ratio of the annular film radius to the bend radius is defined as $\Gamma = (R_1 - h)/R_b$. Substituting these and the appropriate principal radii of curvature into the Laplace-Young equation results in the following set of expressions for the pressure jump across the liquid surface for each of the four regions of the liquid film.

$P_v - P_l\|_1 = \frac{\sigma}{R_i(1-\delta)}\left(1+\frac{\Gamma}{1+\Gamma}\right)$	$P_v - P_l\|_2 = \frac{\sigma}{R_i(1-\delta)}\left(1+\frac{\Gamma}{1-\Gamma}\right)$
$P_v - P_l\|_3 = \frac{\sigma}{R_i(1-\delta)}$	$P_v - P_l\|_4 = \frac{\sigma}{R_i(1-\delta)}2$

For an isothermal system there is no vapor flow between regions 1 and 2. Likewise, for an isothermal system without significant vapor flow, the pressure drop in the vapor between each of the other regions is also assumed to be negligible. In considering a system with a condensing vapor this assumption would have to be revisited; however, in the CHT experiments before the vapor line is blocked, a majority of the condensation occurred near the condenser meniscus, so this assumption is not unreasonable. These equations are then rearranged to express the pressure drop within the annular liquid film between the various regions.

$\Delta P_l\|_{2-1} = \frac{\sigma}{R_i(1-\delta)}\left(\frac{2\Gamma}{1-\Gamma^2}\right)$	$\Delta P_l\|_{3-1} = \frac{\sigma}{R_i(1-\delta)}\left(\frac{\Gamma}{1+\Gamma}\right)$
$\Delta P_l\|_{2-3} = \frac{\sigma}{R_i(1-\delta)}\left(\frac{\Gamma}{1-\Gamma}\right)$	$\Delta P_l\|_{3-1} = \frac{\sigma}{R_i(1-\delta)}$

The potential for liquid flow can be rewritten in terms of the Capillary number. Neglecting the aspect ratio of the annular liquid film, the Capillary number is defined as $Ca = \mu U/\sigma$. Using a lubrication approximation to describe the liquid film flows, the pressure drops and

the characteristic lengths, L, between each region are combined to determine the respective velocity scales, U. The length scales and resulting capillary numbers for each of these regions are shown in Table 1.

Table 1 Length scales and Capillary numbers characterizing liquid film flows between each of the regions

Region	Length Scale	Capillary number
2-1	$\frac{\pi}{2}R_i(1-\delta)2$	$\frac{2}{\pi}\left(\frac{\delta}{1-\delta}\right)^2\left[\frac{\Gamma}{1-\Gamma^2}\right]$
3-1	$\frac{\pi}{2}R_i(1-\delta)\frac{1+\Gamma}{\Gamma}$	$\frac{2}{\pi}\left(\frac{\delta}{1-\delta}\right)^2\left[\frac{\Gamma}{1+\Gamma}\right]^2$
2-3	$\frac{\pi}{2}R_i(1-\delta)\frac{1-\Gamma}{\Gamma}$	$\frac{2}{\pi}\left(\frac{\delta}{1-\delta}\right)^2\left[\frac{\Gamma}{1-\Gamma}\right]^2$
3-4	$\frac{\pi}{2}R_i(1-\delta)$	$\frac{2}{\pi}\left(\frac{\delta}{1-\delta}\right)^2$

During the CHT experiments, the annular liquid film thickness was estimated to be 350 microns[1]. Based upon these parameters, the Capillary numbers characterizing the different regions are shown in Table 2.

Table 2 Typical Capillary numbers for the annular liquid film flow in the bend of the vapor leg during the CHT experiments.

Regions	$Ca \times 10^5$
2-1	124
3-1	20
2-3	73
3-4	361

These Capillary numbers are represented pictorially in Figure 6, where the length of the arrow is representative of the magnitude of the liquid flows. Liquid flow into the bend is much larger than the flow out of the bend. Therefore, liquid will accumulate in the outer region of the tubing bend in any low Bond number system. Also, the liquid flow into the condenser meniscus is higher than any other liquid film flows in the system. This implies that there is always significant drainage into the condenser meniscus even in low gravity systems. It also explains why the formation of the slug often took as many as 10 minutes to form. But as reported by Aul and Olbricht (1989), drainage by the meniscus will only occur over a length of $2\pi R_i$. When the condenser meniscus receded to near the conical section after a slug formed, another lobe was observed to form in region 4, since the length above the condenser meniscus to the bend approach this critical length.

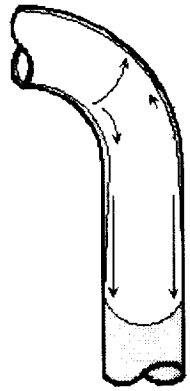

Figure 6 Vectors representing magnitude and direction of liquid film flow in CHT experiment.

The variation in the Capillary number between the various regions is a function of the geometry of the system and is not a function of the properties of the liquid (assuming constant temperature). Therefore, the liquid film flows illustrated in Figure 6 are typical of the flows in any annular liquid film within a bend in a low Bond number system where the radii ratio, Γ, is between 0.1 and 0.4. As Γdecreases below 0.1, the liquid film flow, characterized by $Ca_{2\text{-}1}$, is the dominant feature in the region of the bend, but is an order of magnitude less than the liquid flow into the condenser meniscus. At $\Gamma = 0.01$, $Ca_{2\text{-}1}$ is two orders of magnitude less than the flow into the condenser meniscus. Liquid film flows characterized by $Ca_{2\text{-}1}$ become significant relative to flows into the meniscus only when $\Gamma > 0.1$.

Characteristic Time Scales and Evaporator Meniscus Oscillations

An annular liquid film in a straight tube has been shown to be unstable when the film length exceeds a critical length of $2^{3/2}\pi R_i$ (Aul and Olbricht, 1990, Gauglitz and Radke, 1990). This long wavelength instability, driven by surface tension, results in the liquid film collecting into periodically spaced, axisymmetric "lobes". When $\delta > 0.1$ enough liquid is present that the lobes will "pinch off" and bridge the tube, forming slugs of liquid. When δ is less than 0.1, only lobes will form.

The effect of the capillary-driven flow in the bend relative to the long wavelength instability can be

[1] This estimate of the liquid film thickness is based on a uniform distribution of a volume of liquid over the entire surface of the vapor leg. The volume of liquid chosen was that which was lost from the condenser meniscus before the formation of the liquid slug

gauged through a comparison of the characteristic times for each of the flow potentials. The characteristic time associated with the long wave length instability is given by Aul and Olbricht (1989) as

$$t_\lambda = \frac{\mu_l R_i}{\sigma \delta^3},$$

where μ_l is the absolute viscosity of the liquid. This time scale characterizes the growth rate of the lobe or slug of liquid.

The circumferential flow only occurs when there is a bend in the tubing. When $\delta << 1$, the film can be treated as planar and the characteristic flow time for the circumferential flow is $\mu_l R_b / \sigma \delta^2$. For thicker films, the radial dependence of the annular film must be retained. At times during the conduct of the CHT experiment, δ exceeded 0.1, preventing use of the simpler formulation.

The radial and circumferential velocities and velocity scales in the liquid film are represented respectively by u, U and v, V. By non-dimensionalizing the radial dimension as $r = R_i(1 - \delta r^*)$, the annular liquid film thickness is scaled from 0 at the wall to 1 at the liquid-vapor interface. Applying these scales to the continuity equation yields $U \sim \delta V$. Retaining only those terms of order δ or greater reduces the conservation of momentum equations to

$$\frac{\delta^2}{R_i}\mu_l V\left(\frac{1}{1-\delta r^*}\right)\frac{\partial P}{\partial \theta} = \frac{\partial^2 v^*}{\partial r^{*2}} - \delta\left(\frac{1}{1-\delta r^*}\right)\frac{\partial v^*}{\partial r^*}$$

Using the no-slip condition at the wall and the free shear condition at the liquid surface, the dimensionless velocity profile, v^*, after eliminating terms $o(\delta)$, can be expressed as

$$v^* = \frac{\delta^2 R \Delta P_\sigma}{\pi \mu_l V}\left\{\left(r^* - \frac{1}{2}r^{*2}\right) + \delta\left(\frac{1}{2}r^{*2} - \frac{1}{3}r^{*3}\right) + \cdots\right\}.$$

Setting r^* and v^* equal to 1 results in a velocity scale equal to

$$V \sim \frac{\delta^2 R \Delta P_\sigma}{\pi \mu_l}\left(\frac{1}{2} + \frac{1}{6}\delta\right).$$

The characteristic time for the capillary flow from the inner portion of the bend to the outer portion of the bend, t_σ, is found by dividing the distance for liquid flow, πR_i, by the velocity scale, V. Substituting the expression for the capillary pressure drop from region 2 to region 1, $\Delta P_{1|2\text{-}1}$ into the velocity scale, V, results in the following expression for the characteristic time of the capillary-driven flow:

$$t_\sigma \sim \frac{\pi^2 \mu_l R_i}{\sigma \delta^2}\frac{1-\Gamma^2}{1+1/3\delta}$$

The two time scales, t_λ and t_σ, characterize the rate of liquid accumulation in the vapor line. Liquid flow in the axial direction (scaled by t_λ) will always tend to form liquid lobes whenever the film length exceeds $2^{3/2}\pi R_i$. When there is a bend in the tube, circumferential flow (scaled by t_σ) will result in liquid collecting in the outer portion of the tubing bend. ***The bend does not eliminate the long wavelength instability, but rather, it provides a perturbation to the liquid film that augments the long wavelength instability.***

The importance of t_λ relative to t_σ can be examined by expressing the time scales as a ratio,

$$t_{\lambda\sigma} = \frac{t_\lambda}{t_\sigma} \sim \frac{1}{\pi^2}\left[\frac{1+\delta^3}{\delta(1-\delta)}\right]\left(\frac{\Gamma}{1-\Gamma^2}\right)$$

The ratio of tube radius to bend radius, Γ, varies from 0 to 1. The limits on Γ vary from 0 for a straight tube to 1 for a toroid with zero inside radius. The effect of Γ on the liquid lobe formation is illustrated in Figure 7. At $\Gamma \sim 0$ (i.e., for straight tubing), $t_{\lambda\sigma} \sim 0$ and the liquid forms axisymmetric lobes. As $\Gamma \sim 1$, and $t_{\lambda\sigma} \to \infty$, a uniform liquid film forms on the outer radius of the bend. At $0 < \Gamma < 1$, $t_{\lambda\sigma} \sim 1$ and the liquid forms into non-axisymmetric lobes on the outer region of the bend. For the CHT experiments, $t_{\lambda\sigma}$ is typically around 0.4, so the formation of non-axisymmetric lobes in the bend is expected.

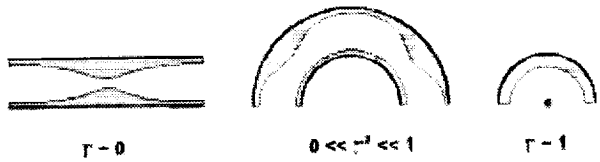

Figure 7 Types of liquid accumulation in the bend of the vapor line for various values of Γ with $\delta < 0.1$.

The ratio $t_{\lambda\sigma}$ is also a strong function of δ. The limits on $t_{\lambda\sigma}$ can be expressed in terms of the relative values of Γ and δ:

- if $\delta << \Gamma << 1$, then $t_{\lambda\sigma} \to \infty$ and the liquid film flow is characterized by t_σ;
- if $\Gamma << \delta << 1$, then $t_{\lambda\sigma} \to 0$ and the liquid film flow is characterized by t_λ.

During the CHT experiment, the liquid nearly always accumulated in the same location on the condenser side of the vapor leg. The most probable explanation for liquid accumulation in this particular location is that the radius of curvature of the bend in the glass tubing was slightly smaller at this point than at other points along the vapor leg. The non-uniform radius of curvature occurred as a result of the test loop fabrication process. The smaller radius of curvature, R_b reduces the characteristic flow time, t_λ. Therefore, liquid accumulates in the outer region of the bend more quickly at this location resulting in a larger film

thickness, δ. Since , the characteristic time for the lobe formation, t_λ, is proportional to δ^3, any small perturbation in the film thickness is greatly amplified by the long wavelength instability.

Evaporator Meniscus Oscillations

During the low-gravity CHT experiments, the evaporator meniscus did oscillate and a direct correlation of meniscus position to vapor pressure was established. Portions of two CHT rewetting experiment runs are provided which illustrate this relationship.

Figure 8 shows a small time segment (12 seconds) taken from the first rewetting experiment run,near the beginning of the test run when the system was far from steady-state. In Fig. 8 the upper graph shows the evaporator wall temperatures TC5 and TC6 against time. The major time divisions are in 30 frame (1 second) increments. TC6 is located in the center of the capillary heater and TC5 is located just beyond the capillary heater towards the vapor side of the loop. The center graph is a plot of the vapor pressure versus time. The lower graph plots the evaporator meniscus position against time. The meniscus position is referenced from thermocouple 3. The horizontal grid lines on the bottom graph are the locations of thermocouples 1 through 7.

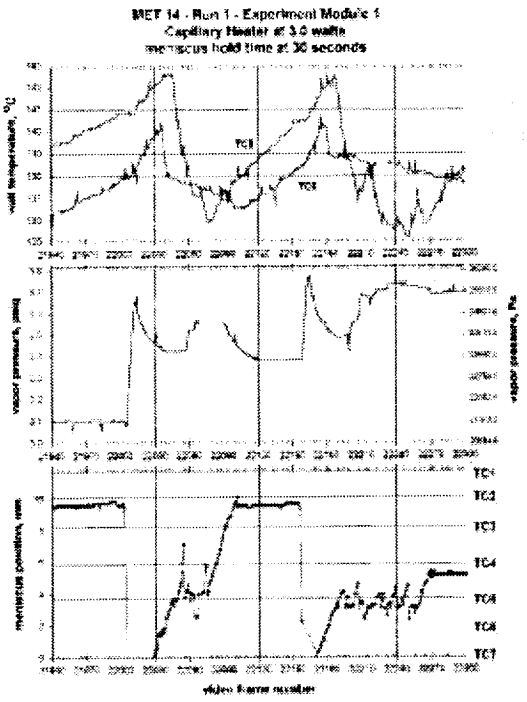

Figure 8 Time slice of evaporator wall temperatures, vapor pressure, and evaporator meniscus position from the CHT rewetting experiment - run 1.

In Figure 8 the meniscus was stable and located near TC 2 until frame 22000. Complete rewetting had occurred. Then the meniscus violently destabilized. Vapor recoil depressed the meniscus below thermocouple 7. Simultaneously, the vapor pressure jumped 4000 Pa, and after a one second time lag the wall temperatures TC6 and TC5 began to drop. These two temperatures begin to decline again once the meniscus began to move back into the evaporator.

After another 100 frames, the evaporator meniscus restabilized near TC2. Once the meniscus stabilized, the vapor pressure begins to drop, eventually leveling off, and the wall temperatures began to rise. At frame 22156, the process repeated. In all cases, the vapor pressure spikes were directly attributable to the destabilization of the evaporator meniscus (characterized by a dramatic and rapid recession).

Figure 9 shows a 12 second time slice from the second rewetting experiment run, taken near the end of the test run where quasi-steady-state operation is being approached. At the beginning of this time slice, the evaporator meniscus was oscillating with a very small amplitude (~ 500 microns) near the TC5 location. The frequency of these oscillations were about 6 to 10 Hz. The small oscillations produced vapor pressure changes that could not be resolved by the pressure transducer. At frame number 7542, the evaporator meniscus suddenly stabilized and advanced to the TC2 location. Simultaneously, the vapor pressure began to drop as the evaporation was reduced and the wall temperatures increased, especially at TC5. After 1.2 seconds (frame 7578) the meniscus violently destabilized and once again began to oscillate about the TC5 location. As the evaporation increased the vapor pressure also increased and the wall temperature at TC5 decreased dramatically. This cycle is repeated again starting at frame 7680.

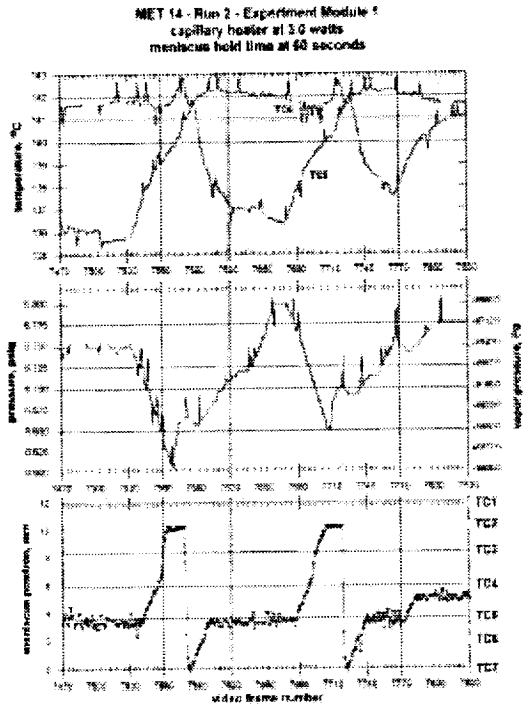

Figure 9 Time slice of evaporator wall temperatures, vapor pressure, and evaporator meniscus position from the CHT rewetting experiment - run 2.

That there is a periodic nature to these oscillations is obvious from the power spectrum analysis of the temperature data for TC7 (near the normal position of the meniscus) during run 2 for the period of time when the meniscus oscillations were present. See Figure 10. Clearly, a significant portion of the signal energy is in the 7 Hz range.

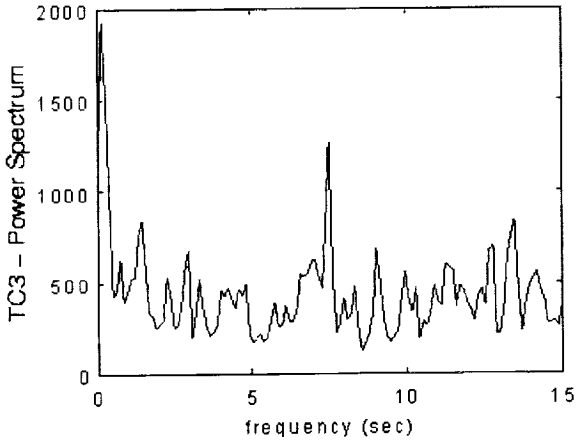

Figure 10 Power spectrum analysis of TC7 during second rewetting experiment

The previous results establish the link between vapor pressure oscillations and the meniscus destabilization and show that these oscillations are periodic. However, these do not reveal their source. One potential mechanism can be eliminated from consideration. Nucleate boiling was not observed in any of the tests.

For some of these oscillations, a liquid bridge was observed to form upstream of the intrinsic meniscus in the capillary tube. When this occurs, evaporation to the entrapped vapor bubble increases the pressure within. Eventually the liquid bridge is ejected. Given that the length in the capillary tube above the intrinsic meniscus was greater than $2^{3/2}\pi R_e$, where R_e is the internal radius of the evaporator capillary, the possibility of a long wavelength instability could not be ignored.

To see if the characteristic frequency of the observed oscillations can be explained by this mechanism, the time scale, t_λ for the formation, growth, and coalescence of lobes in the evaporator capillary is determined. To accomplish this, an estimate for the dimensionless film thickness, δ, is required. Generally, in ground tests, the initial lobe and slug formation was slowest. After the first incidence, however, the observed rate of formation increased rapidly, suggesting that much of the liquid ejected from the liquid bridge when the vapor pressure becomes sufficient to blow through the liquid bridge, finds its way to the wall of the capillary. The initial liquid film thickness after ejection of the bridge can then be estimated from the volume in the liquid bridge. Presuming the bridge volume to be roughly equal to one half of the cross-sectional area of the evaporator capillary times the critical length, ($\pi^2 R_e^3 2^{1/2}$), the dimensionless liquid film thickness after ejection of the bridge can be estimated as:

$$\delta \sim h/R_e = 2^{-1/2}\pi R_e/L$$

where L is the length of the evaporator capillary length above the bridge (~ 1 cm). This dimensionless film thickness is estimated to be 0.11, suggesting that liquid bridging is likely (Aul and Olbricht, 1990).

Now, the time scale t_λ is estimated. Evaluating the thermophysical properties at TC7, the time scale for lobe formation and bridging is on the order of 0.08s. Since this period is less than that associated with the oscillations, the possibility that the long wave instability contributes to their occurrence cannot be discounted. Further, since the time scale is very small, the absence of visual observation of liquid bridging prior to the meniscus oscillations for every occurrence may be a consequence of aliasing introduced by the 1/30 second video recording rate.

CONCLUSIONS

The CHT experiment has provided significant insight into of the fundamental operation of a capillary pumped loop heat transfer device in low-gravity. Above all, it has revealed that the present criteria used to design such systems which ignores the presence of liquid in the so-called adiabatic vapor transport region and that ignores the dynamics within the evaporator pores is inadequate for low-gravity systems. The present research has shown that the liquid film forming along the walls of the *adiabatic* region will inevitably de-stabilize due to a long wavelength instability mechanism, particularly given the long transport lines characteristic of CPL's. The present research has further shown that bends in these lines will amplify the long wavelength disturbances due to the accumulation of liquid at the outer radius of the bend due to capillary pumping. Given that CPL's rely have multi-pass heat exchangers comprising the condensers, the significance of this result is clear. In time, a liquid slug will form in each and every bend. With this conclusion, the past low gravity CPL results must be looked at with some suspicion. A majority of these tests have focused on CPL start-ups. The present results yield uncertainty about whether steady-state CPL operation is obtainable at all.

The present research has also offered a plausible explanation for the vapor pressure oscillations that have been observed in CPL's in the past. Analysis reveals that long wavelength instabilities present in the evaporator pores can lead to liquid bridging and vapor entrapment in the porous media. Subsequent evaporation to the trapped vapor increases the vapor pressure. Eventually the vapor pressure causes ejection of the bridged liquid. Recoil stresses dramatically depress the meniscus. As the meniscus attempts to rewet, the process then repeats. At high enough temperatures, wetting degradation is observed to coincide with these cyclic oscillations.

ACKNOWLDGEMENTS

We would like to acknowledge the support of NASA Microgravity Sciences Directorate under grant number UGS96-0038.

REFERENCES

Allen, J. S., Hallinan, K. P., and Lekan, J., " A Study of the Fundamental Operations of a Capillary Driven Heat Transfer Device in Both Normal and Low Gravity," presented at the 1998 STAIF Conference, Albuquerque, NM, January 27-29.

Aul, R.W. and Olbricht, W.L., 1990, "Stability of a Thin Annular Film in Pressure-Driven, Low-Reynolds Number Flow Through a Capillary," *J. of Fluid Mechanics*, 215, pp. 585-599.

Butler, D., 1986, "The Capillary Pumped Loop (CPL) GAS Experiment, G-471," Post Flight Data Report.

CAPL-2 Experiment Team, 1995, CAPL-2 Final Mission Status Report, Posted by the Goddard Space Flight Center -- Thermal Engineering Group at World Wide Web site http://sspp.gsfc.nasa.gov/capldata.html.

Douglas, D. and Ku, J. and Schlager, L., 1997, "Investigation of the Starter Pump Purge Superheat Observed in the CAPL 1 Flight," AIAA 97-3871, presented at the 1997 National Heat Transfer Conference, Baltimore, Maryland.

Gauglitz, P.A. and Radke, C.J., 1990, The Dynamics of Liquid Film Breakup in Constricted Cylindrical Capillaries,
Journal of Colloid and Interface Science, 134, No. 1, pp. 14-40.

Hu, H. H. and Joseph, D. D., 1989, "Lubricating Pipelining: Stability of Core-Annular Flow. Part 2," *Journal of Fluid Mechanics*, 205, pp. 359-396.

Kolos, K. R. and Herold, K. E., "Low Frequency Temperature and Fluid Oscillations in Capillary Pumped Loops," AIAA 97-3872, Presented at the 1997 National Heat Transfer Conference, Baltimore, Maryland.

Ku, J. and Hoang, T., 1995a, "An Experimental Study of Pressure Oscillation and Hydrodynamic Stability in a Capillary Pumped Loop," Presented at the 1995 National Heat Transfer Conference, Portland, Oregon.

Ku, J., "Start-up Issues in Capillary Pumped Loops," Presented at the 9th International Heat Pipe Conference, Albuquerque, New Mexico.

Ottenstein, L., 1997,"Two-Phase Flow Post Mission Briefing," Presentation Handout.

Stenger, F. J., "Experimental Feasibility Study of Water-Filled Capillary-Pumped Heat Transfer Loops," NASA Lewis Research Center, Cleveland, Ohio, NASA TM X-1310.

A Study of Nucleate Boiling with Forced Convection in Microgravity

Herman Merte, Jr., The University of Michigan, Department of Mechanical Engineering and Applied Mechanics,
2148 G.G. Brown, Ann Arbor, Michigan 48109-2125
e-mail: merte@umich.edu

INTRODUCTION

The ultimate objective of basic studies of flow boiling in microgravity is to improve the understanding of the processes involved, as manifested by the ability to predict its behavior. This is not yet the case for boiling heat transfer even in earth gravity, despite the considerable research activity over the past 30 years. Hahne et al [1], for example, compared 7 different correlations with their own R12 forced convection boiling data, for both up and down flow, with distinctly different results.

The elements that constitute the nucleate boiling process – nucleation, growth, motion, and collapse of the vapor bubbles (if the bulk liquid is subcooled) – are common to both pool and flow boiling. It is well known that the imposition of bulk liquid motion affects the vapor bubble behavior relative to pool boiling, but does not appear to significantly influence the heat transfer. Indeed, it has been recommended in the past that empirical correlations or experimental data of pool boiling be used for design purposes with forced convection nucleate boiling [2, 3]. It is anticipated that such will most certainly not be possible for boiling in microgravity, based on observations made with pool boiling in microgravity, to be described below. In earth gravity buoyancy will act to remove the vapor bubbles from the vicinity of the heater surface regardless of how much the imposed bulk velocity is reduced, depending, of course, on the geometry of the system. The major so-called forces governing the motion of the bubbles are buoyancy, liquid momentum and viscosity. With sufficiently high flow Reynold's Numbers, it can be intuited that the latter two forces will outweigh the first, and the process will be the same whether at earth gravity or microgravity. However, as the Reynold's Number is reduced the magnitude of the liquid momentum and viscous forces are correspondingly reduced, and in microgravity buoyancy cannot take over as a "back-up" mechanism for vapor removal, leaving only the reduced levels of liquid momentum and viscous forces. Vapor bubbles have been observed to dramatically increase in size in pool boiling in microgravity [4], and the heat flux at which dryout took place was reduced considerably below what is generally termed the critical heat flux (CHF) in earth gravity, depending on the bulk liquid subcooling. However, at heat flux levels below dryout, the nucleate pool boiling process was enhanced considerably over that in earth gravity [4,5], in spite of the large vapor bubbles formed in microgravity and perhaps as a consequence. These large vapor bubbles tended to remain in the vicinity of the heater surface, and the enhanced heat transfer appeared to be associated with the presence of what variously has been referred to as a liquid microlayer between the bubble and the heater surface. This layer serves as a boundary across which evaporation takes place, as well as a mechanism for the efficient removal of vapor bubbles from the heater surface, due to vapor pressure differences arising from surface tension.

Effects generally neglected at normal earth gravity, such as surface tension, both at the solid-liquid-vapor contact line and at the liquid-vapor surface associated with the interface temperature variation, become of consequence at microgravity conditions. The net quantitative effect of these on the vapor bubble behavior is unknown, at present, as are the related effects on the heat transfer, and provides one of the motivations for the study of the flow boiling process in microgravity.

The enhancement of the boiling process with low velocities in earth gravity for those orientations producing the formation of a liquid macrolayer described above, accompanied by "sliding" vapor bubbles, has been demonstrated. The enhancement was presented as a function of orientation and subcooling in [6, 7], and as an additional function of heated length in [8,9], while a criterion for the heat transfer for mixed natural/forced convection nucleate boiling was given in [10].

A major unknown in the prediction and application of flow boiling heat transfer in microgravity is the upper limit of the heat flux for the onset of dryout (or critical heat flux – CHF), for given conditions of fluid-heater surfaces, including geometry, system pressure and bulk liquid subcooling. As stated above, it is clearly understood that the behavior in microgravity will be no different than on earth with sufficiently high flow velocities, and would require no space experimentation. However, the boundary at which this takes place is still an unknown. Furthermore, considering the high cost of pumping power in space, in terms of the availability of power, it can be anticipated that considerable effort will be expended in optimization

of the net energy requirements. This requires a sound understanding of the fundamental processes associated with the CHF.

Some results of CHF measurements were presented in [6] for low velocity flow boiling at various orientations in earth gravity as a function of flow velocity and bulk liquid subcooling. Preliminary measurements of bubble residence times on a flat heater surface at various orientations were given in [8] which showed promise as a parameter to be used in modeling the CHF, both in earth gravity and in microgravity. The objective of the work here is to draw attention to and show results of current modeling efforts for the CHF, with low velocities in earth gravity at different orientations and subcoolings.

THE CRITICAL HEAT FLUX

Many geometrical possibilities for a heater surface exist in flowing boiling, with boiling on the inner and outer surfaces of tubes perhaps being the most common. If the vapor bubble residence time on and departure size from the heater surface bear a relationship to the CHF, as results to be given below indicate, it is important that visualization of and access to vapor bubble growth be conveniently available for research purposes. In addition, it is desirable to reduce the number of variables as much as possible in a fundamental study. These considerations dictated the use of a flat heater surface, as seen in the schematic of the test section in Figure 1.

The flat heater surface is rectangular in shape, 1.91 cm by 3.81 cm (0.75 x 1.5 inches), consisting either of a 400 Angstrom thick semi-transparent gold film sputtered on a quartz substrate which serves simultaneously as a heater and a resistance thermometer, or a copper substrate of the same size. The heater substrate is a disc which can be rotated so that the heated length in the flow direction can be changed from 1.91 to 3.81 cm (0.75 to 1.5 inches). The fluid is R-113, and the velocities can be varied between 0.5 cm/s and 60 cm/s. Details of both the experimental apparatus and model concepts to be outlined below are given in [11, 12].

For a sufficiently low velocity the CHF can be modeled reasonably well at various orientations by the correlation for pool boiling [13] corrected for the influence of bulk liquid subcooling [14], indicated by q_{eo} in Figure 2, multiplied by the square root of θ over the interval 90 to 270 deg. This arises from equating buoyancy and drag forces in the inverted positions where the vapor bubbles are held against the heater surface as they slide [15]. The angle $\theta = 0$ applies to the horizontal upward facing orientation and $\theta = 90$ to the vertical orientation with upflow.

A distortion of the measurements occurs to the right in Figure 2 as the flow velocity increases. In modeling this effect at different levels of subcooling it appeared appropriate to estimate the volumetric rate of vapor generation, using measurements of bubble frequency (or residence time), void fraction and average bubble boundary layer thickness. These were determined with the use of a platinum hot wire probe 0.025 mm in diameter by 1.3 mm long, applying a constant current to distinguish between contact with liquid or vapor. Two-dimensional spatial variations are obtained with a special mechanism to resolve displacements in increments of 0.025 mm. Figure 3 shows typical void fractions over a heater surface. From a number of such measurements it was determined that the fraction of the surface heat transfer resulting in evaporation varies inversely with the subcooling correction factor of [14] for the CHF.

The measured inverse bubble residence time $1/\tau_{res}$ is normalized relative to that predicted for an infinite horizontal flat plate at the CHF [16], and is correlated well with the CHF normalized relative to that for pool boiling, for various orientation angles and subcooling levels, as seen in Figure 4. This correspondence is then combined with a normalizing factor for the energy flux leaving the heater surface at the CHF and the computed bubble radius at departure, determined from the balance between the outward velocity of the interface due to evaporation and the buoyance induced velocity of the center of mass of the bubble. The product of the CHF and the corresponding residence time was determined to be a constant for all orientations at a given bulk flow velocity and liquid subcooling, and must be determined empirically for each velocity and subcooling at present.

It then becomes possible to predict the CHF for the different orientations, velocities, and subcoolings. These are shown in Figures 5-7 and compared with the normalized measurements for velocities ranging from 18 cm/s to 55 cm/s, over orientations $\theta = 0$ to $\theta = 360$.

A direct comparison of the experimental data with the model predictions is given in Figure 8 for $\theta = 0$ to $\theta = 360$, subcoolings from 2.8 to 22.2°K, and bulk velocities from 4 cm/s to 55 cm/s.

ACKNOWLEDGEMENTS

The work described here was supported, with appreciation, under NASA Grants NAG3-1310, NGT-50928, and NAG3-1900. The writer would like also to express his appreciation for the efforts and diligence of his former students associated with this work: L.H. Li; M.J. Brusstar; K.M. Kirk; B.J. Kirby; S.U. Nestel.

REFERENCES

1. Hahne, E., et al, "Fully Developed Nucleate Boiling in Upflow and Downflow," *Int. J. Heat Mass Transfer*, 32, 1989, 1799-1808.
2. Bergles, A.E., and Rohsenow, W.M., "The Determination of Forced-Convection Surface Boiling Heat Transfer," *J. Heat Transfer*, 86, 1964, 365-382.
3. Bartolini, R. et al, "Experimental Study on Nucleaet Boiling of Water in Vertical Upflow and Downflow," *Int. J. Multiphase Flow*, 9, 1983, 161-165.
4. Merte, H., Jr., Lee, H.S., and Keller, R.B., "Report on Pool Boiling Experiment Flown on STS-47 (PBE-IA), STS-57 (PBE-IB), and STS-60 (PBE-IC). NASA CR 198465 prepared for Lewis Research Center under Contract NAS3-25812. March, 1996.
5. Lee, H.S., Merte, H., Jr., Chiaramonte, F.P., "The Pool Boiling Curve in Microgravity," AIAA J. of Thermophysics and Heat Transfer, Vol. 11, No. 2, April-June, 1997, pp. 216-222.
6. Merte, H., Jr., "Pool and Flow Boiling in Variable and Microgravity," 2nd Microgravity Fluid Physics Conference, June 21-23, 1994, NASA-Lewis, Cleveland, OH.
7. Kirk, K.M., Merte, H., Jr., and Keller, R.B., "Low Velocity Subcooled Nucleate Flow Boiling at Various Orientations," ASME J. of Heat Transfer., Vol. 117, 2, pp. 380-386, May, 1995.
8. Merte, H., Jr., "A Study of Nucleate Boiling with Forced Convection in Microgravity", 3rd Microgravity Fluid Physics Conference, June 13-15, 1996, NASA-Lewis, Cleveland, OH.
9. Merte, H., Jr., Nestel, S.U., "Buoyancy and Heater Surface Length Effects in Forced Convection Nucleate Boiling," paper AIAA 97-0885 presented at session "Microgravity Science and Space Processing-Fundamental Fluids and Physics," AIAA 35th Aerospace Sciences Meeting and Exhibit, Reno, Nevada, Jan. 6-9, 1997. Accepted for publication in *AIAA J. of Thermo-Physics and Heat Transfer*.
10. Kirk, K.M., and Merte, H., Jr., "A Mixed Natural/Forced Convection Nucleate Boiling Heat Transfer Criteria," Heat Transfer 1994, Vol. 7, pp. 479-484. Proceedings of the 10th *International Heat Transfer Conference*, Brighton, England, August 14-18, 1994.
11. Brusstar, M.J., Merte, H., Jr., Keller, R.B., Kirby, B.J., "Effects of Heater Surface Orientation on the CHF: Part I. An experimental Evaluation of Models for Subcooled Pool Boiling," *Int. J. Heat Mass Transfer*, Vol. 40, No. 17, pp. 4007-4019, Oct., 1997.
12. Brusstar, M.J., Merte, H., Jr., "Effects of Heater Surface Orientation on the CFH: Part II. A Model for Pool and Forced Convection Subcooled Boiling," Int. J. Heat Mass Transfer, Vol. 40, No. 17, pp. 4021-4030, Oct. 1997.
13. Zuber, N., "On the Stability of Boiling Heat Transfer" Transactions of the ASME, Series C. Journal of Heat Transfer, 1958, 80 (4). 711-720.
14. Ivey, H.J., and Morris, D.J., "On the Relevance of the Vapor-Liquid Exchange Mechanism for Subcooled Boiling Heat Transfer at High Pressure," UKAEA.AEEW-R 137, 1962.
15. Brusstar, M.J., Merte, H., Jr., "Effects of Buoyancy on the Critical Heat Flux in Forced Convection," AIAA J. Thermophysics and Heat Transfer, 8, April – June, 1994, pp. 322-328.
16. Haramura, Y., and Katto, Y., "A New Hydrodynamic Model of Critical Heat Flux, Applicable to both Pool and Forced Convection on Submerged Bodies in Saturated Liquids," *Int. Journal of Heat and Mass Transfer*, 1983. 26, 389-399.

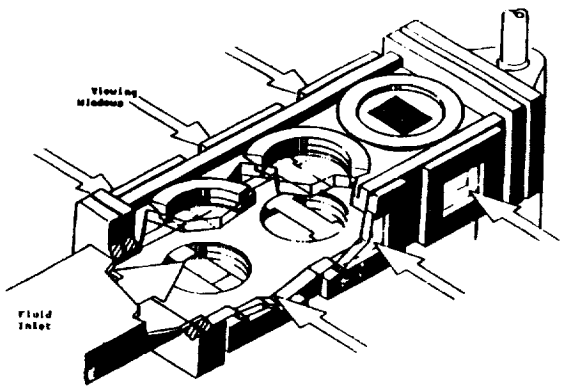

Figure 1. Test section. Flow area = 10.80 cm (4.25 in.) wide x 0.318, 1.27 or 2.54 cm (0.125, 0.50 or 1.0 in.) high.

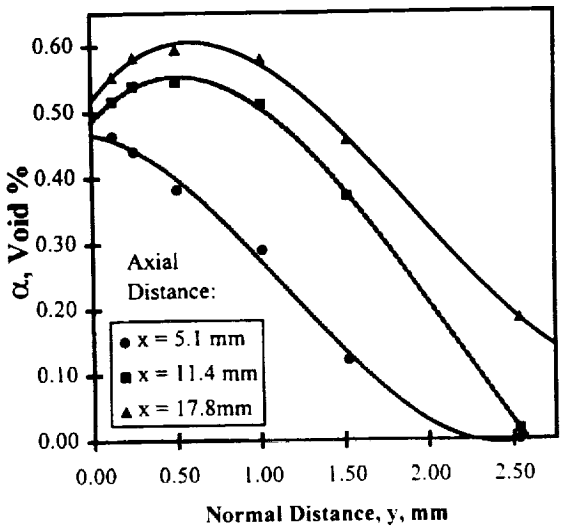

Figure 3. Void fraction profiles over the metal heater surface for θ = 150: U_{bulk} = 0.04 m s^{-1}: Re = 5400: T_{in} = 322 K: 11.1 K subcooling; $q_w^{"}$ = 175kW m^{-2}. R-113.

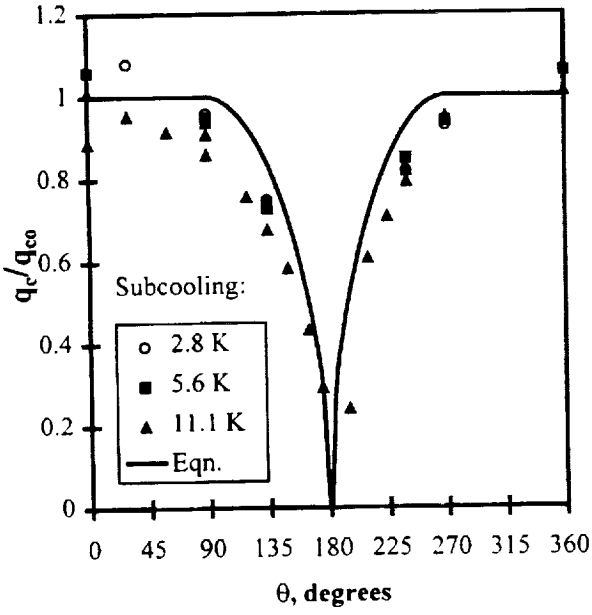

Figure 2. Measured CHF as a function of heater surface orientation compared with the CHF model: test conditions: U_{bulk} = 0.04 m s^{-1}: Re = 2700: T_{in} = 322K. R-113.

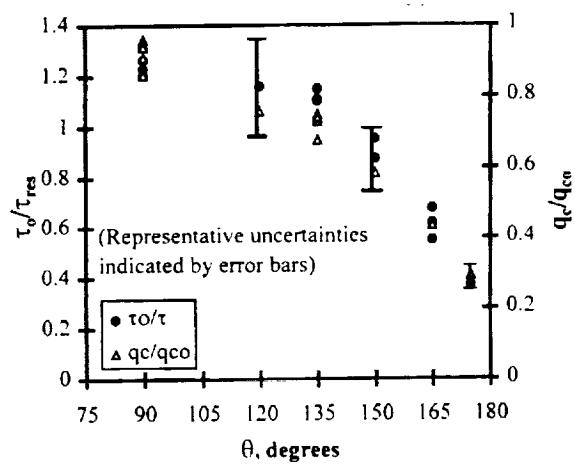

Figure 4. Reciprocal of measured bubble residence time as a function of heater surface orientation compared with corresponding CHF: test conditions: U_{bulk} = 0.04 m s^{-1}: Re = 5400: T_{in} = 332 K: test section height = 25.4 mm. R-113.

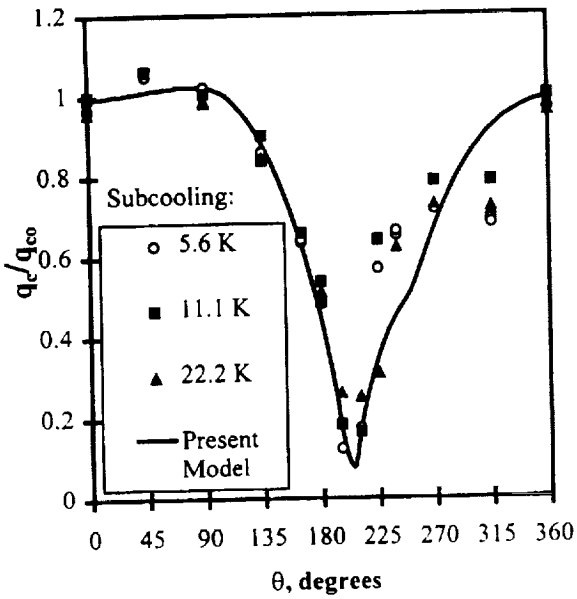

Figure 5. Comparison of measured CHF with present model prediction as a function of orientation: test conditions: U_{bulk} = 0.18 m s^{-1}; Re = 3400: test section height = 3.2 mm: T_{in} = 322 K. R-113.

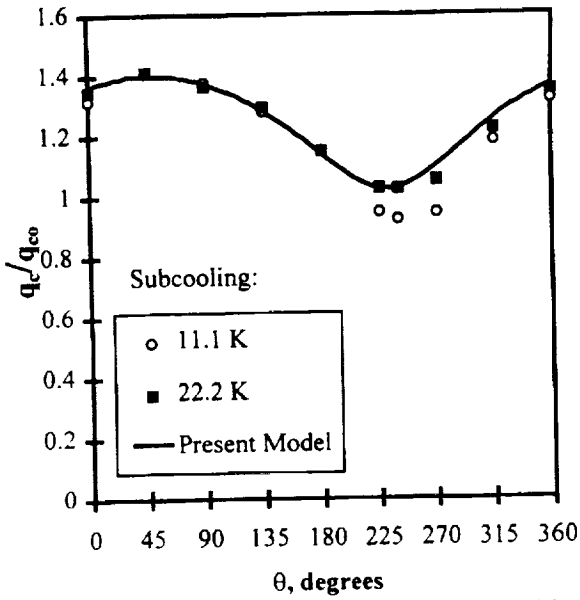

Figure 7. Comparison of measured CHF with present model prediction as a function of orientation: test conditions: U_{bulk} = 0.55 m s^{-1}; Re = 10500: test section height = 3.2 mm: T_{in} = 322 K. R-113.

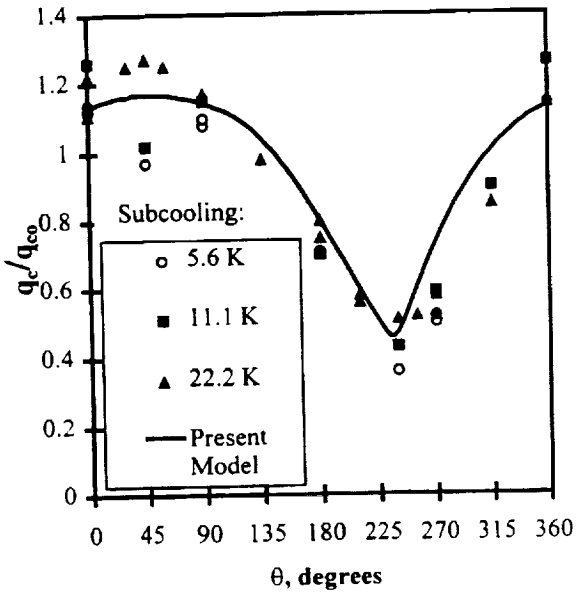

Figure 6. Comparison of measured CHF with present model prediction as a function of orientation: test conditions: U_{bulk} = 0.32 m s^{-1}; Re = 6300: test section height = 3.2 mm: T_{in} = 322 K. R-113.

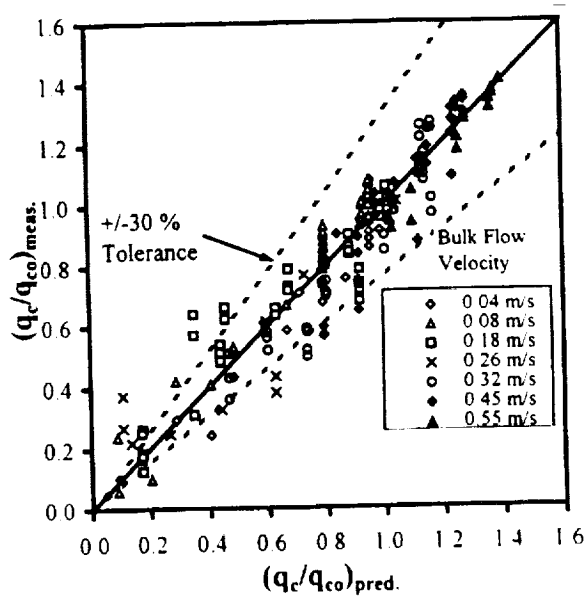

Figure 8. Comparison of measured CHF with present model predictions for bulk flow velocities ranging from 0.04 to 0.55 m s^{-1} and subcoolings ranging from 2.8 to 22.2 K. R-113.

EXPERIMENTAL INVESTIGATION OF POOL BOILING HEAT TRANSFER ENHANCEMENT IN MICROGRAVITY IN THE PRESENCE OF ELECTRIC FIELDS

Cila Herman, Department of Mechanical Engineering, The Johns Hopkins University
3400 N. Charles St., Baltimore, MD 21218, herman@titan.me.jhu.edu

INTRODUCTION

In boiling high heat flux levels are possible driven by relatively small temperature differences, which make its use increasingly attractive in aerospace applications, such as compact evaporators in the thermal control of spacecraft environments, heat pipes, and the cooling of electronic equipment. The objective of the research is to develop ways to overcome specific problems associated with boiling in the low gravity environment. One such problem is that in low gravity the critical bubble size for detachment is much larger than under terrestrial conditions, since buoyancy is a less effective means of bubble removal (*Zell (1991), Ervin et al. (1992)*). In terrestrial conditions, bubble detachment is governed by the competition between body forces (e.g. buoyancy) and surface tension forces that act to anchor the bubble along the three phase contact line. In the present study the buoyancy force is substituted by the electric force to enhance bubble removal from the heated surface. Previous studies *(Yabe et al. (1995))* indicate that in terrestrial applications nucleate boiling heat transfer can be increased by a factor of 50, as compared to values obtained for the same system without electric fields.

The discipline of electrohydrodynamics (EHD) deals with the interactions between electric, flow and temperature fields. The goal of our research is to experimentally explore the mechanisms responsible for EHD heat transfer enhancement in boiling in low gravity conditions, by visualizing the temperature distributions in the vicinity of the heated surface and around the bubble during boiling using real-time holographic interferometry (HI) combined with high-speed cinematography.

METHOD OF STUDY

In the first phase of the project the influence of the electric field on a single bubble is investigated. Pool boiling is simulated by injecting a single bubble through a nozzle into the subcooled liquid or into the thermal boundary layer developed along the flat heater surface. Injection of individual bubbles into the liquid has been used to simulate a physical situation similar to that in subcooled nucleate boiling by *Nordmann (1980), Mayinger and Chen (1986)* and *Ogata and Yabe (1993)*. The advantage of this approach is that the experimenter can control the conditions in the vicinity of the growing bubble. Conversely to the situation on the heated surface, the conditions in the vicinity of the developing bubble are generally steady. The bubble grows in a uniformly subcooled liquid. Condensation begins immediately, and it takes place over the entire perimeter of the bubble.

Since the exact location of bubble formation is known, the optical equipment can be aligned and focused accurately, which is an essential requirement for precision measurements of bubble shape, size and deformation, as well as the visualization of temperature fields by HI. The size of the bubble and the frequency of bubble departure can be controlled by suitable selection of nozzle diameter and mass flow rate of vapor. In this approach effects due to the presence of the electric field can be separated from effects caused by the temperature gradients in the thermal boundary layer. The influence of the thermal boundary layer can be investigated after activating the heater at a later stage of the research. The described experimental approach offers the advantage of yielding clear and unambiguous results depending on a limited number of controlled process parameters.

EXPERIMENTAL SETUP

Test cell. For the visualization experiments a test cell was developed. The present design incorporates most of the features required for the microgravity experiments, without the special hardware needed to operate it in the aircraft during parabolic flights. The measurement cell is rectangular. All four vertical walls of the test cell are transparent, and they allow transillumination with laser light for visualization experiments by HI. The bottom electrode is a copper cylinder, which is electrically grounded. The copper block is heated with a resistive heater and it is equipped with 6 thermocouples that provide reference temperatures for the measurements with HI. The top electrode is a mesh electrode. Bubbles are injected with a syringe into the test cell through the bottom electrode. Visualization experiments with this test cell are currently underway in the Heat Transfer Laboratory (HTL) of the Johns Hopkins University.

Working fluid. The working fluids presently used in the interferometric visualization experiments, water and PF 5052, satisfy requirements regarding thermophysical, optical and electrical properties.

Instrumentation. A 30kV power supply (Glassman MJ30) equipped with a voltmeter allows to apply the electric field to the electrodes during the experiments. The magnitude of the applied voltage can be adjusted either manually or through the LabVIEW data acquisition and control system connected to a PC. Temperatures of the heated block are recorded using type-T thermocouples, whose output is read by a data acquisition system. Images of the bubbles are recorded with 35mm photographic and 16mm high-speed cameras, scanned and analyzed using various software packages.

VISUALIZED TEMPERATURE FIELDS

HI allows the visualization of temperature fields in the vicinity of bubbles during boiling in the form of fringes. Typical visualized temperature distributions around the air bubbles injected into the thermal boundary layer in PF5052 are shown in Figure 1. The temperature of the heated surface is 35 °C. The temperature difference for a pair of fringes is approximately 0.05 °C. The heat flux applied to the bottom surface is moderate, and the fringe patterns are regular. In the image a bubble penetrating the thermal boundary layer is visible. Because of the axial symmetry of the problem, simplified reconstruction techniques can be applied to recover the temperature field.

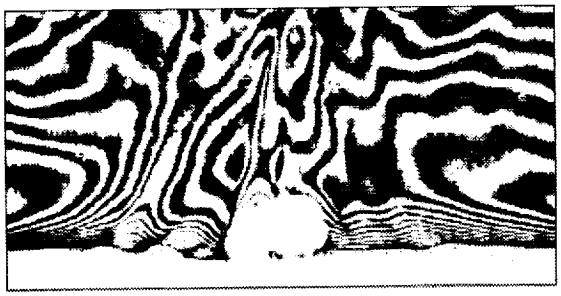

Figure 1. Temperature fields in the liquid phase in the vicinity of the bubble visualized by HI

In Figure 2 the thermal plume developing above the heated surface for more intensive heating is shown. The temperature distribution in the liquid is clearly 3D, and tomographic techniques have to be applied to recover the temperature distribution in such a physical situation. A sequence of interferometric images showing the temperature distribution around the rising bubble, recorded with a high-speed camera is shown in Figure 3. Again, the temperature distribution is 3D, and a more complex approach to evaluation, the tomographic reconstruction has to be taken.

MEASUREMENT OF THE TEMPERATURE DISTRIBUTION

From the fringe pattern temperature distributions that yield important information regarding heat transfer are determined. Two algorithms that allow the quantitative evaluation of interferometric fringe patterns and the reconstruction of temperature fields during boiling have been developed at the HTL of the Johns Hopkins University.

RECONSTRUCTION OF AXIALLY SYMMETRICAL TEMPERATURE DISTRIBUTIONS

Figure 2. Three-dimensional thermal plume above the heated surface

Data on fringe order and location, obtained by applying digital image processing to the visualization images, serves as input information for the reconstruction algorithm during the first phase of the research, when a single bubble is injected into the working fluid through a nozzle. The bubble is assumed to be axially symmetrical, which significantly reduces the computational effort for quantifying the temperature distribution around the bubble.

In an interferometric image the change of the optical path length of the light beam, caused by the phase difference between object and reference beams, is visualized. In the equation of ideal interferometry the phase change is expressed as the multiple S of the wavelength of light λ,

$$S\lambda = \int_0^L (n - n_\infty) dz . \qquad (1)$$

In Eq. (1) n is the refractive index of the measurement state, n_∞ the refractive index of the fluid during the reference exposure, S the fringe order and L is the length of the path of the light beam through the phase object. This equation is used to reconstruct the temperature distribution in the fluid when the refractive index is constant along the path of the light beam, and the temperature distribution is 2D. To be able to apply the equation of ideal interferometry, apart from these two assumptions, it is necessary to avoid the deflection of the light beam in the thermal boundary layer.

In a boiling liquid a thermal boundary layer is formed around the vapor bubble. The schematic of the physical situation and the path of the light beam in the vicinity of the bubble are illustrated in Figure 4. For the thermal boundary layer around the bubble the requirements for ideal interferometry are not satisfied, i.e. the refractive index is not constant along the path

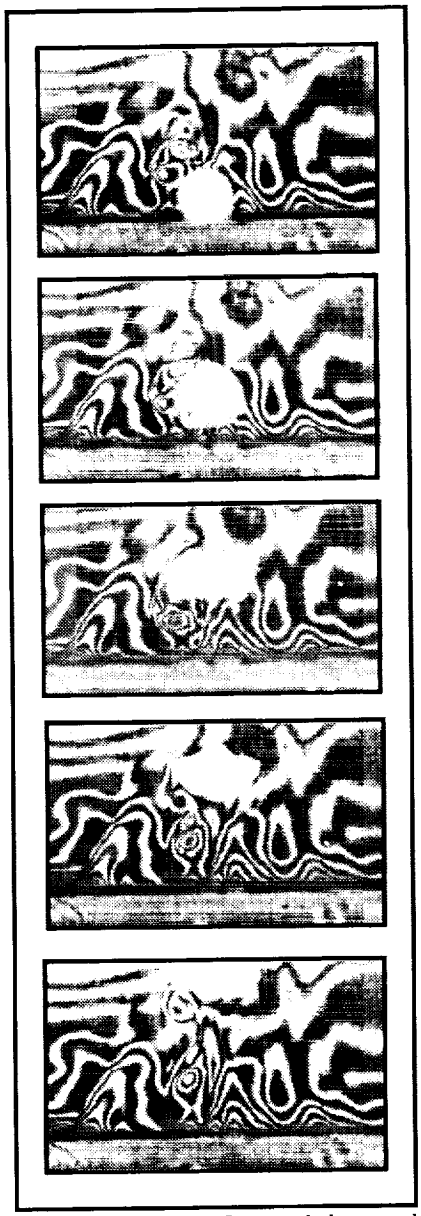

Figure 3. Sequence of 5 interferometric images showing rising bubbles injected into the thermal boundary layer through a nozzle

of the light beam in the working fluid. The refractive index n is a function of the radius r, and the integration limits are also radius dependent. For this physical situation Eq. (1) is modified as

$$S(y)\lambda = \int_{-z_0}^{+z_0} (n(r) - n_\infty) dz \ . \qquad (2)$$

In order to recover the temperature distribution $T(r)$ in the thermal boundary layer from the interference fringe pattern $S(y)$, it is necessary to integrate Equation (2) for the physical situation illustrated in Figure 4. For three dimensional refractive index fields this solution can be obtained only when images are

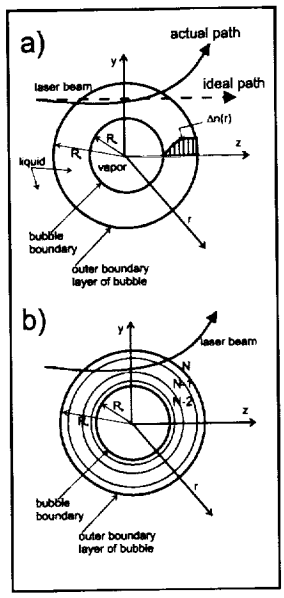

Figure 4. a) Schematic of the deflection of the light beam in the thermal boundary layer formed around a bubble and b) concentric shells introduced to approximate the refractive index variation

recorded for multiple directions of illumination. In the evaluation of temperature distributions in the vicinity of bubbles during boiling, axial symmetry of the refractive index field in the thermal boundary layer is often assumed to simplify the reconstruction process.

For this purpose the thermal boundary layer around the bubble is divided into equidistant concentric shells, and the refractive index is assumed to be constant in each of the shells. For this situation Eq. (2) can be rewritten as

$$S(y)\lambda = S_i\lambda = 2\sum_{k=i}^{N-1} \Delta n_k \left[(r_{k+1}^2 - r_i^2)^{\frac{1}{2}} - (r_k^2 - r_i^2)^{\frac{1}{2}} \right]. \qquad (3)$$

An analytical solution of Eq. (3) was described by Abel *(Hauf and Grigull, 1970)*, and the result of the inversion is

$$n(r) - n_\infty = -\frac{\lambda}{\pi} \int_r^{R_\delta} \frac{dS(y)/dy}{\sqrt{y^2 - r^2}} dy \ . \qquad (4)$$

Eq. (4) relates the measured fringe order $S(y)$, a function of the spatial coordinate y, to the change of the refractive index $n(r) - n_\infty$, which has to be determined in the evaluation procedure. For this purpose it is convenient to express the measured fringe order $S(y)$ in the form of a polynomial.

The foregoing evaluation procedure does not account for the deflection of the light beam in the thermal boundary layer around the vapor bubble. Since large temperature gradients are expected in that region, the deflection of the light beam cannot be ne-

glected in boiling experiments. In order to incorporate the deflection into the evaluation procedure, a temperature profile $T(r)$ is initially assumed. This allows to determine the path of the light beam as well as the determination of the optical path length and the phase shift $S(y)$ in the thermal boundary layer. In addition, the exit angle of the light beam is known, which allows to account for the deflections and phase shifts outside the boundary layer (in the bulk fluid and in the windows of the test cell). A computer code has been developed at the HTL that allows to vary the assumed temperature profile $T(r)$ and the boundary layer thickness δ in an iterative procedure, until the calculated values of the fringe order match the measured ones $S(y)$.

OPTICAL TOMOGRAPHY

Tomographic techniques were initially developed for medical applications, and nowadays they are becoming increasingly available in engineering measurements (*Mewes, Herman, Renz, 1994*). Medical applications are steady, as opposed to engineering problems where the "patient", the temperature field, typically cannot be maintained steady for extended periods of time. This is especially true for boiling with typical bubble frequencies up to 1 kHz. Thus tomographic reconstruction techniques developed for medical applications are not suitable for the study of high-speed, unsteady heat transfer processes.

In tomography, the measurement volume is sliced into 2D planes. In the present study these planes are parallel to the heated surface. The objective is to determine the values of the field parameter of interest in form of the field function f in these 2D planes. The field parameter is the change of the refractive index of the liquid in the measurement volume caused by temperature changes. By superimposing data for many 2D planes recorded at the same time instant, the 3D temperature distribution in the measurement volume is recovered.

Mathematical Model. The schematic in Figure 5 illustrates the basic principles of measuring the field function f in one of the 2D planes. The 2D plane is generally irradiated from multiple directions, two of which are indicated in Figure 5. A ray i irradiating the measurement volume can be uniquely described by the angle θ_i and its distance ρ_i from the origin. The directions of irradiation of the two rays shown in Figure 5 are described with the angles θ_m and θ_n. As ray i passes through the measurement volume, changes of physical properties, such as temperature of the fluid in the measurement volume, change the physical properties of the ray. These changes are then measured in form of a projection value Φ_i. In the present study this corresponds to the change of the refractive index, which causes a phase shift between the reference and measurement beams of the setup for HI. The phase

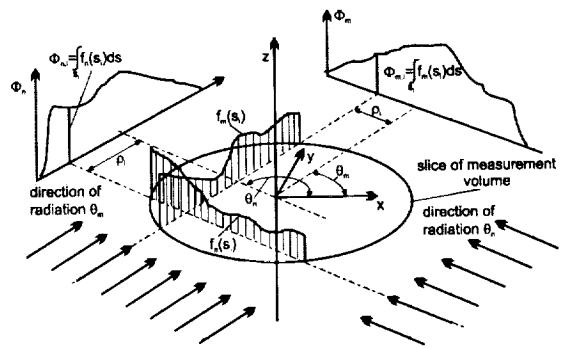

Figure 5. Principles of tomographic measurement techniques

shift is visualized through the interferometric fringe pattern and represents projection values. Mathematically, these projection values Φ_i are described as

$$\Phi_i(\rho_i, \theta_i) = \int_{s_i} f(x,y)ds \,. \qquad (5)$$

Eq. (5) describes the projection value Φ_i, that corresponds to the average value of the field function $f(x,y)$ along the ray path s_i. If the field function f is kept constant along the ray path s_i, the value of the field function f and the value of the projection value Φ_i will be identical. This is the case in the study 2D temperature fields applying HI, which requires one direction of illumination only. Consequently, in order to extend HI to three dimensions, more directions of illumination are required, and tomographic reconstruction techniques are needed to recover the field function f from the measured projection values Φ_i.

A computer code for tomographic reconstruction of unsteady 3D temperature fields from 2D projections has been developed at the HTL in the first phase of this study. The ART (**A**lgebraic **R**econstruction **T**echnique)-Sample Method *(Lübbe, 1982, Ostendorf and Mewes, 1988)* was selected for this heat transfer application based on previous positive experience with comparable physical situations. The Sample Method is based on a discrete Fourier transform, and as result an underdetermined system of equations is obtained. This system of equations can be solved in an iterative process with the ART-Algorithm.

The discrete Fourier transform is applied to the projection values Φ_i obtained for one direction of illumination. These projection values Φ_i correspond to a 1D function in the physical space, as shown in Figure 5. The result of the Fourier transform will be a 1D spectrum. The same procedure can be applied to another direction of illumination, and consequently, two spectra in the Fourier domain are obtained. These

two spectra are then connected in the Fourier domain under an angle corresponding to the angle $\Delta\theta = \theta_m - \theta_n$ between the two directions of illumination. The angle $\Delta\theta$ is also shown in Figure 5. The spectra of many directions of illumination form a 2D function in the Fourier domain. After applying the inverse 2D Fourier transform to this 2D function in the Fourier domain, the field function f is recovered. As a result of these mathematical transformations, the following system of equations is obtained

$$\Phi_i(\rho_i,\theta_i) = \sum_m \sum_n w(a_i,b_i) \cdot f(l_x m, l_y n) \,. \qquad (6)$$

The system of equations (6) has mxn unknowns corresponding to the number of grid points. In order to find a unique solution, mxn projection values Φ_i are necessary. In medical applications this requirement is satisfied by taking projection values using angle subdivisions of 1°. Apart from a sufficient number of projection values Φ_i, this method also ensures an accurate representation of the 2D function in the Fourier domain, since 180 spectra are available.

The Sample Method is a powerful tool to obtain a high spatial resolution in 3D tomographic measurements. However, to obtain high temporal resolution,

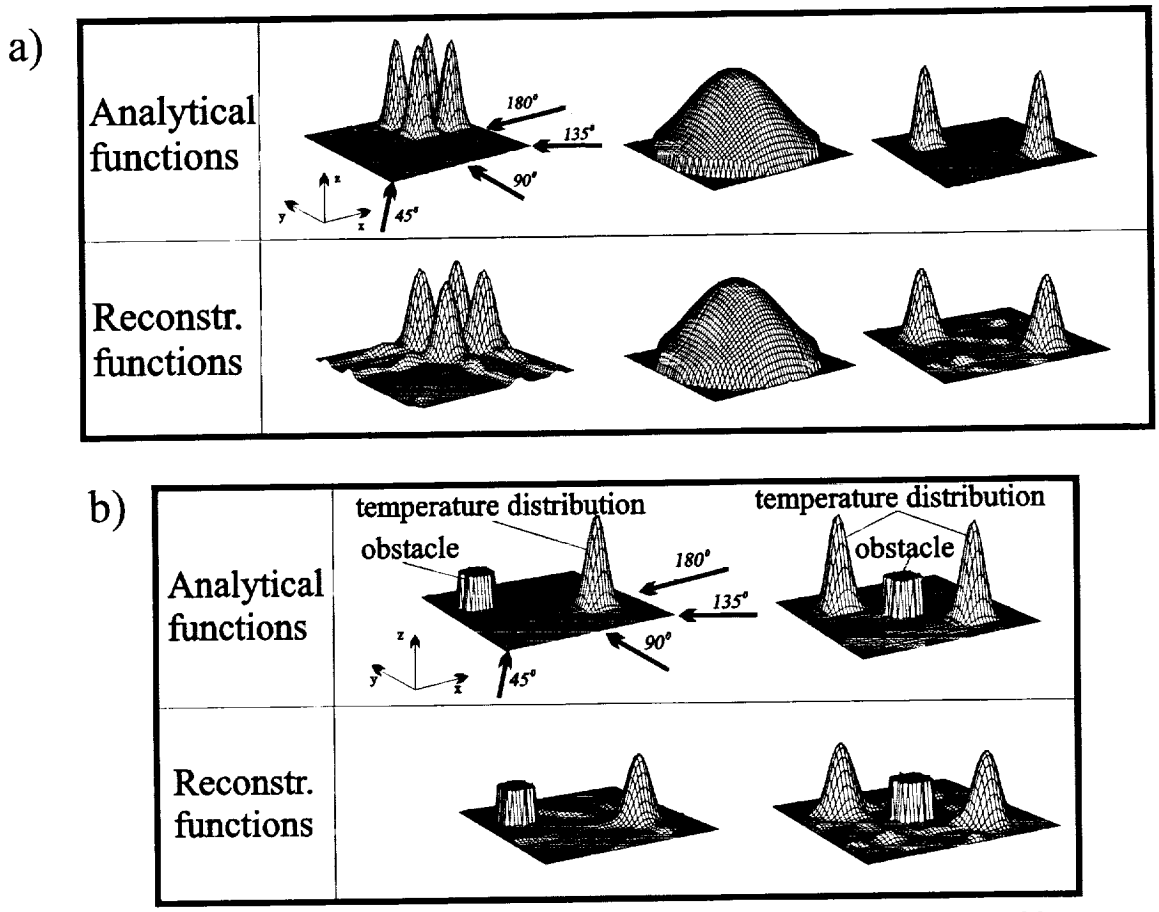

Figure 6. a) Three dimensional test functions and the corresponding reconstruction obtained by tomographic methods. b) Two analytical test functions with a cylindrical obstacle in the measurement volume and the corresponding reconstruction obtained using tomographic techniques.

In Eq. (6) l_x and l_y denote the size of one grid element, and m and n the coordinates of the grid points in the x and y directions, respectively. One should note the weight factor $w(a_i,b_i)$ that appears in Eq. (6). The weight factor is a function of the ray i, where a_i and b_i denote the slope and the intercept of the ray i. The form of the weight factor $w(a_i,b_i)$ was discussed by *Mewes, Herman and Renz (1994).*

as required in the present study, the number of projection values has to be decreased. This leaves the system of equations (6) underdetermined. The solution to this problem is the ART-Algorithm that iteratively determines the values of the field function f. In fact, the ART-Algorithm allows the reconstruction of the field function with 4 directions of illumination only, and 50 rays per direction for a grid size of 50x50 grid

points. Applying the Sample method alone would require 2500 projection values instead of 200.

The code developed at the HTL allows the reconstruction of the field function for different types of irradiation and different shapes (circular and rectangular cross section) of the measurement volume. The accuracy of reconstruction was evaluated by using analytical test functions, and the results of these tests are shown in Figure 6. The four directions of irradiation are also indicated for the first test function.

In order to apply HI to heat transfer measurements, both the investigated fluid and the vessel containing the fluid have to be transparent. Since the light beam is normally reflected at the liquid-vapor interface of the bubble, the bubble will act as an opaque obstacle in interferometric measurements. We have also applied our tomographic reconstruction algorithm to the reconstruction of the 3D field function to the situation when opaque obstacles are present in the measurement volume. The presence of an opaque obstacle prevents the probing light beams from traversing the measurement volume. As consequence, information on the average value of the field variable will be missing in regions that are in the shade of the obstacle. The reconstruction algorithm was modified to account for the presence of the obstacle and the analytical test functions used in this study as well as the corresponding tomographic reconstructions are shown in Figure 6b. Modification of illumination angles and beam numbers may be necessary to achieve the desired measurement accuracy in the study of boiling.

In order to obtain information necessary for tomographic measurements, the basic optical arrangement for in-line HI has to be modified to allow different transillumination directions. Fiber optics will be used to generate the four ray bundles needed for tomographic measurements instead of bench optics used by *Ostendorf and Mewes (1988).*

CONCLUDING REMARKS

Holographic interferometry was applied to visualize bubbles injected into the thermal boundary layer to simulate boiling. The initial experiments indicate that temperature distributions around the bubble are generally three dimensional. Two reconstruction algorithms, one assuming axially symmetrical temperature distributions and one for 3D temperature fields, were developed. Currently visualization experiments are being conducted in the heat transfer laboratory of the Johns Hopkins University.

ACKNOWLEDGMENTS

This research is supported by the NASA research grant NAG3-1815.

The author wishes to acknowledge the contribution of the graduate students Janelle Vorreiter, Eric Kang and Martin Wetzel.

REFERENCES

Ervin, J. S., Merte, H., JR., Keller, R. B., Kirk, K, 1992, *Transient Pool Boiling in Microgravity,* Int. J. Heat Mass Transfer, Vol. 35, No. 3, pp. 659-674.

Hauf, W., Grigull, U., 1970, *Optical Methods in Heat Transfer*, in Advances in Heat Transfer, Vol. 6, Academic Press Inc., New York.

Lübbe D., 1982, *Ein Meßverfahren für instationäre, dreidimensional Verteilungen und seine Anwendung auf Mischvorgänge,* Dissertation, Universität Hannover.

Mayinger, F., Chen, Y. M., 1986, *Heat Transfer at the Phase Interface of Condensing Bubbles,* Proc. 8 Int. Heat Transfer Conf., San Francisco, California, USA, pp. 1913-1918.

Mewes, D., Herman, C., Renz, R., 1994, *Tomographic measurement and reconstruction techniques,* In Optical Measurements - Techniques and Applications (F. Mayinger editor), Springer Verlag, Berlin, 371-424.8.

Nordmann, Dieter, 1980, *Temperatur, Druck und Wärmetransport in der Umgebung kondensierender Blasen, Dissertation,* Technische Universität München.

Ogata, J., Yabe, A., 1993, *Augmantation of Boiling Heat Transfer by Utilizing the EHD Effect - EHD Behaviour of Boiling Bubbles and Heat Transfer Characteristics,* Int. J. Heat Mass Transfer, Vol. 36, No. 3, pp. 783-791.

Ostendorf, W., Mewes, 1988, *Measurement of temperature fields in mixing vessels using optical tomography*, Chem. Eng. Technol., Vol. 11, pp. 148-155.

Yabe, A., Mori, Y. and Hijikata, K., 1995, *Active Heat Transfer Enhancement by Utilizing Electric Fields,* In : Annual Review of Heat Transfer, Vol. 7, Begell House Publishing.

Zell, M., 1991, *Untersuchung des Siedevorgangs unter reduzierter Schwerkraft (Investigations of boiling under reduced gravity),* Dissertation, Technische Universität München, Germany.

Session 3B

Near Critical Point Flows

CRITICAL VISCOSITY OF XENON: SURPRISES AND SCIENTIFIC RESULTS

R. F. Berg[1], M. R. Moldover[1], and G. A. Zimmerli[2]

[1]Physical and Chemical Properties Div., National Institute of Standards and Technology, Gaithersburg, MD 20899,
[2]NYMA Incorporated, 2001 Aerospace Parkway, Brook Park, Ohio 44142; present address: National Center for Microgravity Research, c/o NASA Lewis Research Center, Cleveland, OH 44135

ABSTRACT

The Critical Viscosity of Xenon (CVX) experiment, which flew on board Space Shuttle flight STS-85 in August 1997, measured the viscosity of xenon near the liquid-vapor critical point. Very close to the critical temperature (T_c = 290 K), the viscosity η of a pure fluid is expected to diverge as a power law, $\eta \propto [(T-T_c)/T_c]^{-y}$. Microgravity allowed CVX to make the first direct observation of this divergence. This talk will summarize the scientific results and the unexpected behavior of CVX in orbit.

SUMMARY

The scientific results are measurements of the viscosity at frequencies from 2 Hz to 12 Hz and at temperatures as close as 0.3 mK to T_c. We obtained these results by immersing a novel oscillator in the xenon, oscillating it with an electrostatic torque X, and measuring the resulting displacement θ . The transfer function defined by the ratio of Fourier transforms $X(f)/\theta$ (f) yielded the viscosity measured at frequency f. After calibrating the viscometer at T_c + 1 K, the sample's temperature was ramped slowly twice to just below T_c.

The second ramp spanned only 3 mK at a rate of approximately –2 K/year.

Figure 1 compares the microgravity data taken at 2 Hz with two sets of ground data.

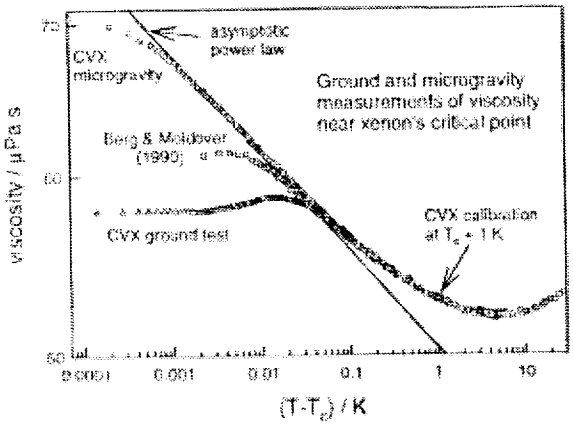

Figure 1. Xenon's viscosity near the critical point. The line has the slope y=0.0429 derived from microgravity data.

The observed divergence of viscosity is a factor of two larger than the best ground measurements [1]. It is characterized by the exponent y = 0.0429 ± 0.0003, indicated by the slope of the solid line. The exponent is in agreement with the value $y = 0.0416 \pm 0.0013$ from a recent two-loop perturbation expansion [2]. All previous measurements near liquid-vapor critical points were limited by Earth's gravity. In contrast, the microgravity measurements made by CVX were limited only by viscoelasticity.

Close to T_c, viscoelasticity caused the microgravity data to deviate from the asymptotic power law. Viscoelasticity is caused by the strong divergence of the decay time τ of the fluid's critical fluctuations, and its characterization requires generalization of viscosity to a complex quantity. Viscoelastic behavior was evident at T_c + 3 mK, further from T_c than predicted. It caused a rounding of the divergence and the appearance of an imaginary component of viscosity. Previous ground-based measurements [3,4] provided only qualitative indications of viscoelasticity. In contrast, the present experiment provided an accurate test of theory. Viscoelastic behavior scaled as $Af\tau$. The measured value of A is 1.90 ± 0.33 times the result of a one-loop calculation [5]. The uncertainty of A is dominated by the uncertainty of the correlation length amplitude measured by others.

The orbital environment affected CVX in surprising ways. These effects, which were absent in preflight and postflight tests, included spurious viscosity signals related to the Shuttle's orbit and greatly increased noise below 0.1 Hz.

Figure 2 illustrates the spurious viscosity signals by plotting the magnitude of the oscillator's transfer function measured at 1 Hz during a typical 24 hour period. The data include oscillations with a 45-minute period and three "spikes" which lasted approximately five minutes each.

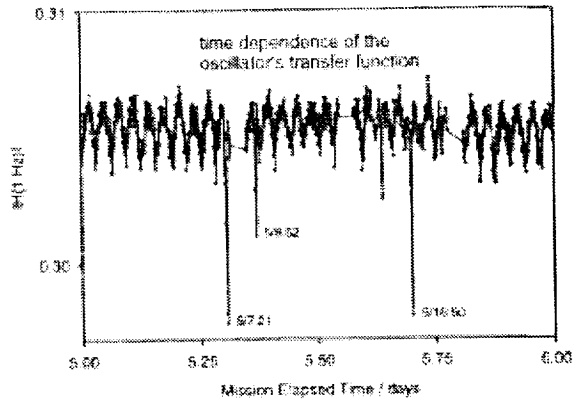

Figure 2. Typical oscillations and spikes in the magnitude data at 1 Hz. The oscillation's 45-minute period was half that of the Shuttle's orbital period.

Such oscillations and spikes occurred throughout the mission, and they affected the magnitude of the transfer function at all frequencies. (Figure 2 displays data at 1 Hz, a frequency chosen because the oscillator's motion was insensitive to viscosity changes at this frequency.) Because the oscillations and spikes were present only in the magnitude data, they represented a time-dependent effect on only the instrument and not on the sample or the oscillator. We mitigated their effects by excluding the spikes from the data and averaging the remaining data in groups of 45 minutes.

The 45-minute period was half that of the Shuttle's orbital period, which suggests that they were not driven directly by the Shuttle's exposure to the sun or by the Earth's magnetic. Ground tests of CVX revealed no susceptibility to magnetic field variations comparable to those experienced in orbit. The minima of the oscillations occurred when the Shuttle was near the equator, and the spikes usually occurred when the Shuttle was near the South Atlantic Anomaly, a region of minimum magnetic field near Argentina. For low Earth orbit, both regions are associated with larger fluxes of the charged particles trapped in the Earth's magnetic field. This timing and the phase of the 45-minute oscillations suggest that the effect could have been caused by charged particles [6].

Figure 3 is an example of the greatly increased the noise at low frequencies. In contrast to the oscillations and spikes seen at all frequencies, the noise was present in the phase as well as the magnitude, suggesting that either the sample or the oscillator was directly affected. The noise prevented our use of the low frequency measurements in the analysis.

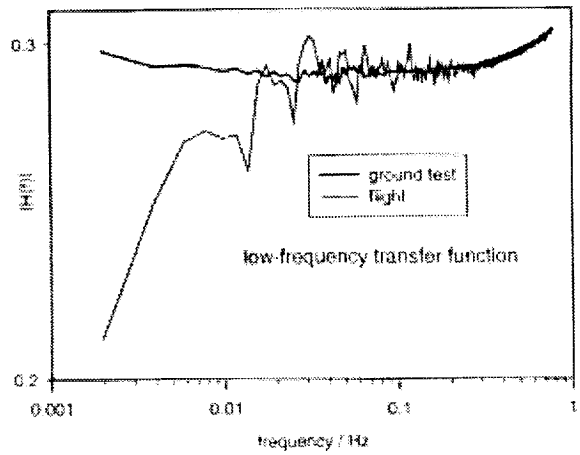

Figure 3. Frequency dependence of the transfer function's magnitude. Low frequency noise was much greater in orbit than on Earth.

REFERENCES

1. R.F. Berg and M.R. Moldover, J. Chem. Phys. **93**, 1926 (1990).
2. H. Hao, R.A. Ferrell, and J.K. Bhattacharjee, preprint (1997).
3. L. Bruschi, Il Nuovo Cimento **1D**, 362 (1982).
4. Y. Izumi, Y. Miyake, and R. Kono, Phys. Rev. A **23**, 272 (1981).
5. J.K. Bhattacharjee and R.A. Ferrell, Phys. Rev. A **27**, 1544 (1983).
6. C.K. Purvis, http://satori2.lerc.nasa.gov/DOC/sceov/sceov.html

GROWTH AND MORPHOLOGY OF PHASE SEPARATING SUPERCRITICAL FLUIDS (GMSF), BOILING IN SUBCRITICAL FLUIDS, AND CRITICAL FLUCTUATIONS

John Hegseth[1], Vadym Nikolayev [1], Daniel Beysens[2], Yves Garrabos[3], and Carole Chabot[3], [1]Department of Physics, University of New Orleans, New Orleans, Louisiana 70148, U.S.A. [2] Commissariat à l'Energie Atomique, Département de Rechereche Fondamentale sur la Matière Condensée, CEA-Grenoble, 17, Avenue des Martyrs, 38054 Grenoble Cedex 9, France. [3] Institut de Chimie de la Matière Condensée de Bordeaux, CNRS-Université Bordeaux I Château Brivazac, Avenue du Docteur A. Schweitzer, 33608 Pessac Cedex, France

INTRODUCTION

The GMSF flight experiment will study the properties of a fluid near the liquid-gas critical point. It has the following three scientific objectives related to the three areas of experimentation. The first objective is to study the relation between the morphology and the growth kinetics of domains during phase separation. Another objective is to study the gas-liquid interfacial behavior as the critical point is approached from the two-phase region. The final objective is to visualize density fluctuations in a pure fluid to study their spatial-temporal evolution and statistics.

We know from previous experiments performed near the critical point of pure fluids and binary liquids that there are two simple growth laws at late times in phase separation. The "fast" growth appears when the volumes of the phases are nearly equal and the droplet pattern is interconnected. In this case the size of the droplets grows linearly in time. The "slow" growth appears when the pattern of droplets embedded in the majority phase is disconnected. In this case the size of the droplets increases in proportion to time to the power 1/3. The volume fraction of the minority phase appears to determine this change of behavior. Recent theory predicts that a transition between these two regimes exists[1]. In the GMSF experiment we plan to look for this transition as the volume fraction and average density is changed.

Previous experiments have also shown that density fluctuations near a critical point in a transparent media can be visualized using microscopy[2]. These fluctuations are fundamental to the behavior of near critical fluids and are responsible for the rapid change with respect to temperature of their material properties (e.g., divergence of the compressibility and the thermal expansion coefficient, disappearance of the thermal diffusivity). Another objective of our flight experiment is to observe these fluctuations close to the diffraction limited optical resolution while the fluid is at the critical point - within the temperature and density precision of our instruments and methods.

In previous experiments the temperature has usually been decreased from the one-phase region into the two-phase region. More recently, however, experiments with an increase in temperature from the two-phase region into the one-phase region have been tried (i.e., boiling experiments). In these experiments a very interesting contact angle change has been seen in a large gas bubble in contact with the cell wall as the fluid was heated toward the critical point[3]. These results were obtained on the MIR space station using the ALICE II apparatus in a pure liquid-gas sample near the critical point. The third objective of our planned experiments is to repeat these previous experiments to obtain a complete set of results and test some theoretical ideas about the cause of these effects.

BACKGROUND

Phase separation in liquid mixtures and pure fluids is a common process that occurs in many areas of natural science and industry. Industrial applications are especially important in heat and mass transfer processes and materials processing. A clearer understanding of the exact physics of phase separation is desirable for improved materials, e.g., metallic alloys, polymer alloys[4], and flat panel displays. Phase separation is also an important fundamental scientific problem. A particularly important feature in the phase separation process, especially in applications, is the growth and morphology of domains (e.g., liquid droplets) after the process has been started. The connection between the morphology of the domains and the growth laws is still unclear. Only a few experimental results are available where density or concentration is systematically varied[5,6]. In the region of the critical point, it has been found relatively easy to continuously vary the physical parameters that control phase separation, as can be seen in Figure 1. In addition, the critical slowing down of dynamical processes that occurs near the critical point enables a detailed investigation of the mechanisms involved in the separation process. Results from phase separation experiments done near the critical point can be scaled by natural space and time scales (fluctuation correlation length and the fluctuation relaxation time) that result in master curves[6] that are universal, i.e., curves that are *valid for all fluids* within two factors.

Previous experiments with pure fluids under reduced gravity have shown[7] that when $M=(\rho-\rho_c)/\rho_c=0$ an interconnected pattern is formed. At M=0 the vol-

ume fraction, f, of the minority phase is f=1/2 where f = [minority phase volume]/[total volume]. At this large f value, the characteristic wavelength is found, at late times, to grow linearly with time t (*fast* growth). At late times when the volume fraction is very small (f<0.03), and the gravity effects are negligible, previous experiments[8] show that the growth follows a power law in time with exponent 1/3 (*slow* growth). Previous low gravity experiments also suggest a transition between fast growth and slow growth as the volume fractions is varied as shown in Figure 1. A recent theory has shown that the linear growth can result from hydrodynamic lubrication interactions between the droplets at high volume fractions[1]. In this theory the coalescence between two droplets will induce a flow that will cause another droplet to coalesce. The linear growth follows from the self-similarity of the resulting chain reaction. This theory also shows the existence of a fast growth to slow growth transition.

A process that is complementary to phase separation (one-phase to two-phase) is the boiling process (two-phase to one-phase). This is a very important topic in applications because many types of heat transfer technologies use this process. Although there is much applied research in this area, a survey of the literature shows that there does not appear to be many fundamental studies. This is perhaps a result of the complicated combination of fluid dynamics, heat transfer, and interfacial phenomena that constitutes this subject. Many of the complications are caused by the buoyancy from gravity that lifts the gas bubbles that nucleate on a hot surface. A competing force, surface tension, holds the bubbles on the surface so that when an expanding gas bubble become large enough, buoyancy overcomes the surface tension and the bubble goes upward. Near the critical point in microgravity both buoyancy and interfacial tension are very small, allowing this process to be observed under simplified conditions. Very recently a new theory has offered an explanation for the contact angle change previously observed in microgravity in a bubble in contact with the cell wall[9]. This theory proposes a fundamental explanation of the observations in terms of a non-equilibrium wetting transition. This theory is not limited to near critical fluids and explains the "burnout" or "boiling crisis" transition on the well known boiling curve [10].

Perhaps the most scientifically challenging part of our experiments are the direct observation of critical fluctuations. This is because there has never been, to our knowledge, a direct experimental observation of these fluctuations in space and time. Although many measurements of the critical exponents have indirectly given evidence in support of their existence, a direct visual confirmation of their existence will be much stronger evidence. In addition, a detailed study of the probability distribution of the fluctuations could lead to more interesting studies.

EXPERIMENTAL DETAILS AND RESULTS

In this set of experiments, to be performed on the MIR space station using the ALICE II apparatus, we will attempt to optimize the information that can be obtained from the liquid-gas phase transition near the critical point. This is accomplished by programming the ALICE II to continuously visualize and monitor the fluid. The three types of experiments correspond to the following three operations: 1) decreasing the temperature and density from the one-phase state to the two-phase state (phase separation experiments), 2) decreasing the temperature from the one-phase state to the critical point (fluctuation experiments), and 3) increasing the temperature from the two-phase state to the one-phase state (supercritical boiling). All of the experiments will use sample cells as shown in Figure 2, and each sample cell contains either SF_6 or CO_2. Some of these cells have slightly off-critical densities. The new cells that will be used will have the capability of changing the sample density by varying the cell volume (with the mass in the cell constant) as can be seen in Figure 3. This new degree of freedom is a significant improvement in the state of the art and allows many new experiments. We plan to use two constant density sample cells of SF_6 (0.2% off-critical and 0.7% off critical) and three variable volume sample cells. Two of the variable volume cells can be seen in Figure 4 and Figure 5. The off-critical density of the fluid is varied by either introducing a new constant density cell into ALICE II or by adjusting a variable volume cell. Corresponding to a given off-critical density will be two experimental runs that will consist of a supercritical boiling experiment followed by a phase separation experiment, each using an ALICE II computer program (ALICE II is fully automated requiring very little cosmonaut time). The temperature is first continuously increased from the two-phase state to the one-phase state (boiling). This temperature increase is followed by a series of temperature quenches into the two-phase state (phase separation). In addition, at a given temperature we will quench the density, as shown in Figure 1, using the variable volume cell and cosmonaut participation (the density will be changed by changing the volume of the cell through a rod and screw mechanism that is manually adjusted by the cosmonaut).

We also hope that we will be able to directly observe and study critical fluctuations. This critical fluctuations experiment will use a temperature quenching protocal that is similar to the phase

separation experiments, except that we will quench as close as possible to the critical temperature. This experiment will be attempted using a variable volume cell that is adjusted as close as possible to the critical density on the ground. In order to visualize critical fluctuations we have made a specially modified cell and thermostat. The sapphire plates, shown in Figure 2, have been replaced with lenses and two other lenses are placed in the thermostat. This system increases the magnification of the ALICE II's current microscope to the diffraction limited resolution.

All the data and visualizations that result from these experiments are stored on DAT digital videotapes and PCMCIA cards. The cards and tapes are later returned to earth.

High precision temperature control is performed automatically by the ALICE II apparatus. The temperature stability of ALICE II is estimated, using data from previous experiments, at 10μK per 10 hours. Previous experiments have also found that the temperature repeatability of ALICE II is 40 μK over 2 days. This is accomplished using a cylindrical thermostat with three shields and a copper SCU (Sample Cell Unit) in the center that contains the sample cell. Six Peltier elements in contact with the SCU pump heat in and out of the SCU allowing temperature quenches with 10% overshoot as small as 100μk.

We have many results that have been obtained while we have prepared the three new thermostats. Figure 4 and Figure 5 show examples of direct observation views of the samples for two of the variable volume cells. Figure 6 shows two microscopic views of boiling in a ground based experiment. In both cases a 0.2 mm thermistor is heated by laser light of the same intensity. The difference in character is due to the change in fluid characteristics as the ambient temperature in increased toward the critical temperature.

FUTURE PLANS

Hardware for the GMSF experiment will be transported to the MIR station on the Space Shuttle mission STS-91 in June 1998. The operation of the ALICE II apparatus may commence in summer 1998 depending on crew training. We are also engaged in simulating the contact angle change previously observed in ALICE II during the heating of a two-phase fluid.

REFERENCES

1. V. S. Nikolayev, D. Beysens, and P. Guenoun, Phys. Rev. Lett **76**, 3144 (1996).
2. P. Guenoun, F. Perrot, and D. Beysens, Phys. Rev. Lett. **63**, 1152 (1989).
3. J. Hegseth, D. Beysens, V. Nikolayev, Y. Garrabos, and C. Chabot, in *Proceedings of the 1997 Microgravity Fundamental Physics Workshop,* NASA Document, **D-15677**, 127 (1998).
4. J. D. Gunton, M. San Miguel and P. S. Sahni, in *Phase Transitions and Critical Phenomena*, vol 8, edited by C. Domb and J. L. Lebowitz (Academic Press, 1983), p.269 and references therein.
5. N. C. Wong and C. M. Knobler, Phys. Rev. **A 24**, 3205 (1981).
6. Y. Jayalakshmi, B. Khalil and D. Beysens, Phys. Rev. Lett. **69**, 3088 (1992).
7. Y. Garrabos, B. Le Neindre, P. Guenoun, B. Khalil and D. Beysens, Europhys. Lett. **19**, 491 (1992) and refs. therein.
8. A. Cumming, P. Wiltzius, F. S. Bates and J. H. Rosedale, Phys. Rev. **A 45**, 885 (1992); T. Baumberger, F. Perrot and D. Beysens, Phys. Rev. **A** 7636 (1992).
9. V. Nikolayev and D. Beysens, "Boiling crisis and nonequilibrium wetting transition", submitted to Phy. Rev. Lett. (1998).
10. F. P. Incropera, D. P. DeWitt, *Introduction to Heat Transfer*, (Wiley & Sons, 1996).

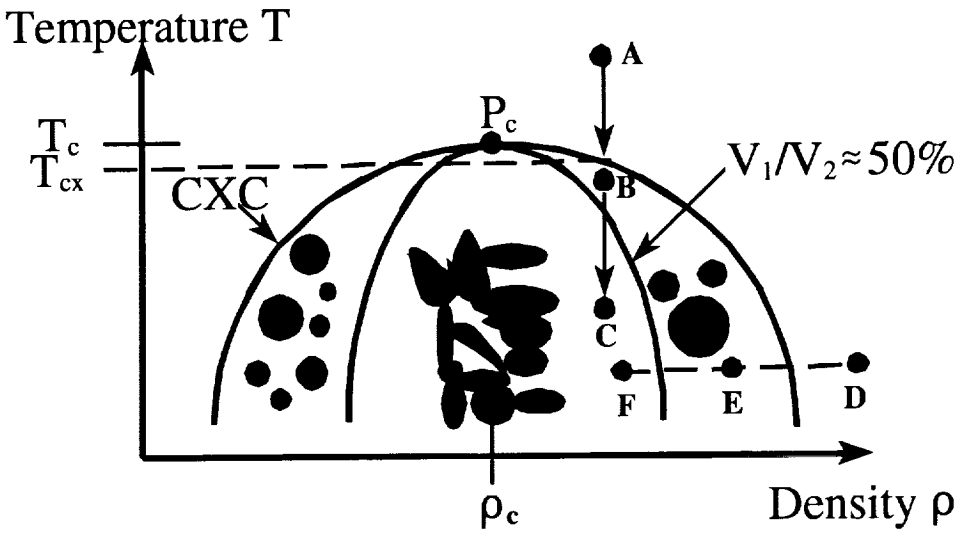

FIGURE 1. Growth and morphology phase diagram (schematic) of SF_6 that shows the volume fraction for transition from slow growth to fast growth. Also shown are the critical point P_c, the critical temperature T_c (45.55°C), the critical density ρ_c (0.737 g/cm^3), and the coexistence curve CXC. When the supercritical fluid (point A, density off critical by +0.5%) is quenched below the CXC, droplets of vapor (volume V_1) and liquid (volume V_2) nucleate and grow. Previous experiments show that the curve $V_1/V_2 \approx 0.50\%$ separates a region of slow growth (A-B, quench 50 mK below CXC) where the droplets are disconnected and grow as (time)$^{1/3}$, and a region of fast growth (A-C, quench 3 mK below CXC), where the droplets are interconnected and grow as (time)^1. Points D-E-F shows a schematic of a density quench that is possible using a variable volume cell.

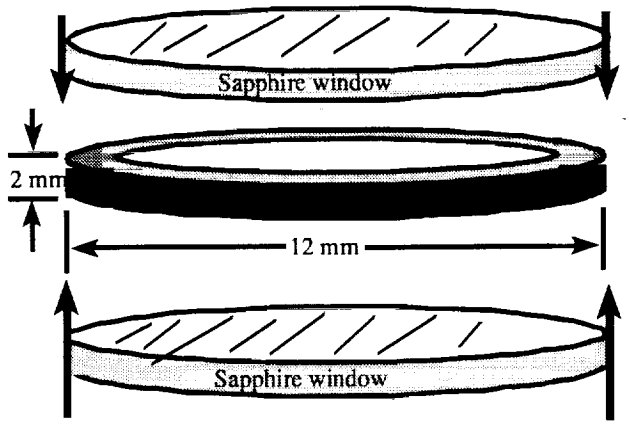

FIGURE 2. The sample cell consists of a thin copper alloy cylindrical shell (12mm I.D., although the thickness in this Figure shows 2mm, in fact the thickness varies from 2mm to 4mm depending on the sample) sandwiched between two sapphire windows. The volume enclosed by the cylindrical shell and the sapphire windows contains either an SF_6 or a CO_2 sample that has a density that is close to the critical density. Light shines through the two sapphire windows in order to study the pattern formation and fluctuations in the fluid as the temperature or density is changed.

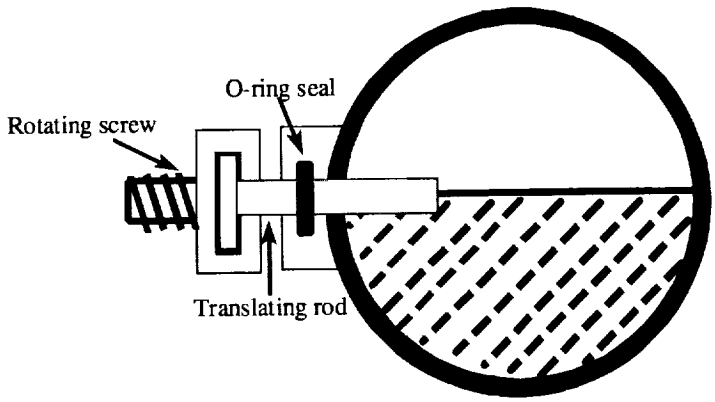

FIGURE 3. Variable volume cell. The density of the fluid in the cell is changed by increasing or decreasing the volume of the cell. When the rod is displaced further into the cell the volume decreases and when the rod is displace out from the cell the volume in increased. The o-ring seal prevents the high pressure fluid from leaking. The rod is prevented from rotating by using a coupling to the screw that slips as the screw rotates.

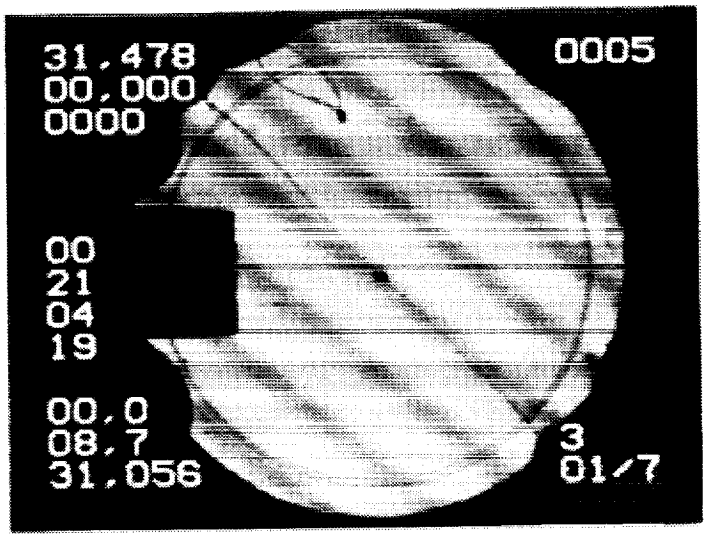

FIGURE 4. Variable volume cell filled with CO_2 in the one-phase state. Shown is the direct observation view of a new variable volume cell. The shadow of the piston can be seen on the left. Several 0.2 mm thermistors can also be seen in the middle and toward the edge. The circle at the edge is a 10.0mm diameter circle etched in the sapphire for reference. The stripes in the image are shadows from a grid projected through the fluid sample. Deviations of this grid shadow indicate density gradients. The numbers displayed on the image indicate time, temperature, computer instruction, thermostat number, experiment number, CCD gain, and other useful information.

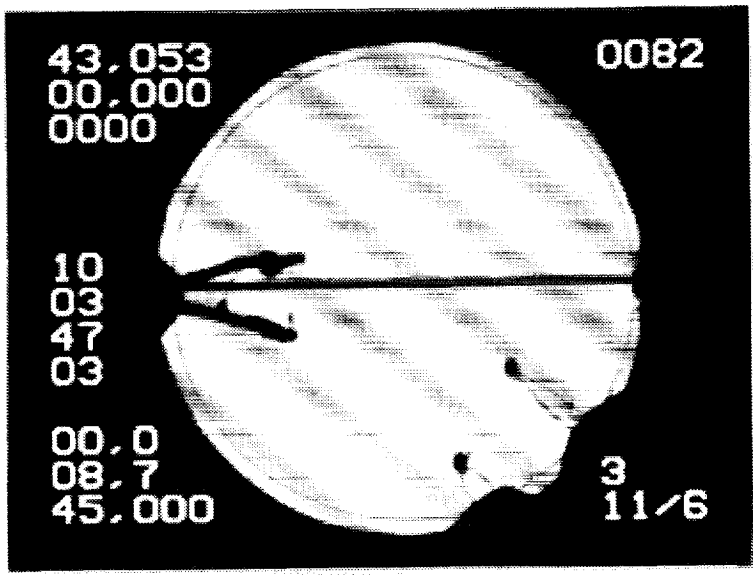

FIGURE 5. Variable volume cell filled with SF_6 in the two-phase state. Shown is the direct observation view of a new variable volume cell. The shadow of the piston can be seen on the left with several wires extending from it to support a small 0.2mm thermistor. Several other 0.2 mm thermistors can also be seen toward the edge of the cell. The circle at the edge is a 10.0mm diameter circle etched in the sapphire for reference. The stripes in the image are shadows from a grid projected through the fluid sample. The meniscus can also be seen going horizontally through the image. Because this image is inverted the liquid is above the gas.

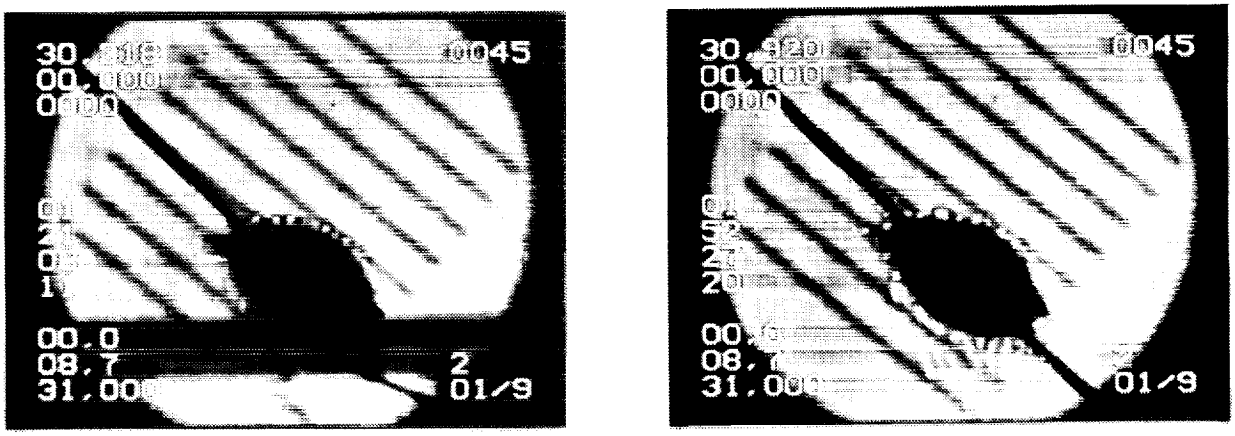

FIGURE 6. Two microscopic views of a 0.2mm thermistor in the variable volume cell filled with CO_2 in the two-phase state. In each image the thermistor is heated by laser light of the same intensity. The meniscus can be seen going horizontally through the image on the left. As the cell is heated toward the critical temperature the meniscus moves out of the field of view. The laser light heating initiates bubble nucleation and boiling in both cases. Because this image is inverted the liquid is above the gas and the bubbles appear to travel downward. Qualitative differences can be seen between the two cases. Bubble production increases as the average temperature is increased. The bubbles also appear to be more distorted when the average temperature is closer to the critical point.

A COMPRESSIBLE GEOPHYSICAL FLOW EXPERIMENT (CGFE)

John Hegseth, Laudelino Garcia, and M. Kamel Amara, Department of Physics, University of New Orleans, New Orleans, Louisiana 70148, jjhph@uno.edu

INTRODUCTION

Many important problems such as climate change, weather prediction, and mantel convection are examples of geophysical flows. Much of the information regarding geophysical flows has come from direct planetary observations and numerical models. Planetary observations are neither controlled nor repeatable. Numerical models are often limited by machine memory size, by machine speed, and by algorithmic precision. We hope to develop a prototype experimental system that will take full advantage of the microgravity environment to study large-scale planetary flows. The unique characteristic of the experiment that we envision is that we will create a system where a spherically symmetric density gradient is established in a compressible fluid. This will mimic the single most striking and obvious property of most large-scale geophysical flows, the radial density gradient. The spherical geometry and gravity have made geophysical flow experiments very difficult to perform in a terrestrial laboratory [1]. As a consequence, some previous experiments have been made in microgravity conditions [2][3]. These experiments used a high voltage AC source applied across a spherical capacitor filled with fluid to create a spherically symmetric central force. The force results from the presence of a dielectric in an electric field gradient (electrophoresis and a dielectrophoretic force). These previous efforts in microgravity have been made using incompressible fluids without density stratification. The novelty of this project is to work with a fluid near the critical point where the compressibility of the fluid is greatly increased. In this case the density is expected to have a large variation throughout the fluid when a radial force is applied. This system, using highly compressible critical fluid, is called the Compressible Geophysical Flow Experiment (CGFE).

The objective of this project is to build and demonstrate an experimental system in which a compressible fluid in spherical geometry becomes stratified in density when an AC electric field is applied. If this proves successful, our long-term plan is to make another system where flow is driven by heating, in analogy to a geophysical system, in preparation for a microgravity experiment. Our current apparatus consists of a spherical capacitor filled with fluid in a temperature controlled environment. To generate such a density gradient we use a small system (1" diameter) and we operate the system near the fluid's critical density and critical temperature. This makes the fluid highly compressible because compressibility is one of the well-known divergent properties of a fluid near its critical point. The central force will induce, in principle, a spherically symmetric density gradient that is analogous to a geophysical fluid system. To help us test our ideas we have also built another small cell of similar spherical geometry, that uses incompressible fluid, the same central force, and driving of the fluid by an imposed temperature gradient. The first steps in building the CGFE are presented here. For clarity, we also present some background information, some results showing density stratification in a compressible fluid, and the measurement techniques used.

BACKGROUND

To understand how density stratification occurs, we consider elements from the physics of critical phenomenon of liquid-gas phase transitions and electrodynamics. As is well known in critical phenomena, there exists in fluids a special point in the (p, T, ρ) phase diagram where the distinction between the gas phase and the liquid phase disappears (p is the pressure, T is the temperature, and ρ is the density of the fluid). This point in the phase diagram is called the critical point (p_c, T_c, ρ_c). Near the critical point many properties of a fluid, both thermodynamic and transport, either diverge or disappear. The compressibility is one of the most strongly divergent properties of a fluid [4]. The gravitational field induces a strong density gradient in fluids near the critical point. The microgravity environment has made detailed investigations of critical fluids possible leading to some unexpected results [5][6][7].

An electric field influences a dielectric fluid near the critical point. These influences include a mechanical body force exerted on a fluid in a non-uniform field [8]. A uniform field will exert a force on any free charge in a fluid and polarize the molecules. A non-uniform field, or an electric field *gradient*, will polarize the fluid and exert a force on the fluid [8]. In spherical geometry, as shown in Figure 1, the electric field gradient produces a central body force. This effect has been previously used in space experiments to study geophysical instabilities driven by buoyancy and rotation [2][3] in incompressible dielectric fluids. These experiments have yielded many interesting flow patterns and have shown that the change in dielectric constant caused by heating induces a "buoyancy" force in an electric field gradient. In our experiment we will induce a spherical density gradient in a compressible

critical fluid and study the resulting flow patterns when the system is driven far from equilibrium by heating.

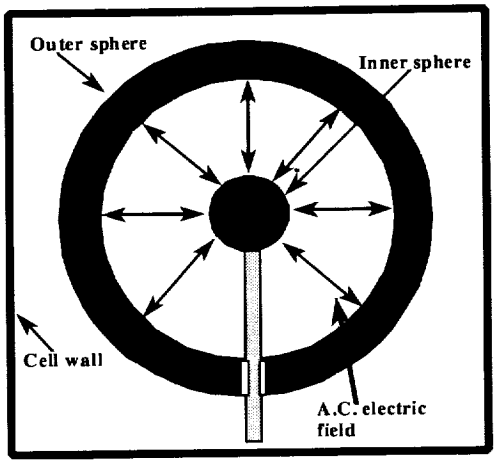

Figure 1. Above is a schematic of the compressible flow cell currently being tested. Fluid near the critical point is contained inside a larger cylindrical cell (see Figure 2). A large AC potential difference that is applied across two conducting concentric spheres induces a spherical density gradient in the fluid between the spheres.

The density stratification of a critical fluid from the earth's gravity makes it impossible to make a spherically symmetric density gradient on earth using an electric field. Doing this experiment in microgravity is necessary. In addition, near the critical point the properties of the fluid make it highly sensitive to buoyancy from gravity. The temperature difference needed to drive convection gets very small as the average temperature approaches T_c. The high pressure of a critical fluid cell also makes it difficult to develop the thermal forcing system. To better understand this system we have also developed a cell of similar geometry that uses an incompressible fluid at room temperature and pressure. Because the central force on a fluid in a spherical capacitor decreases in radius as r^{-5}, a small incompressible fluid cell can create a large effective gravity [9]. This makes it possible to make a second ground based study in parallel with the critical fluid cell development and testing. We have also tested a critical fluid cell to see if appreciable density changes can be induced through electrostriction and dielectrophoresis in a critical fluid. These results will be discussed in the next section.

RESULTS

We have tested for a density gradient by applying an electric field to a temperature controlled cell that we constructed. This cell uses a piece of cylindrical copper 3 inches long and 3 inches in diameter. A 1.5-inch diameter cylindrical hole is milled through its center along the cylinder axis. A small spherical electrode ¼-inch in diameter is placed at the center of this cylindrical hole, as can be seen in Figure 2.

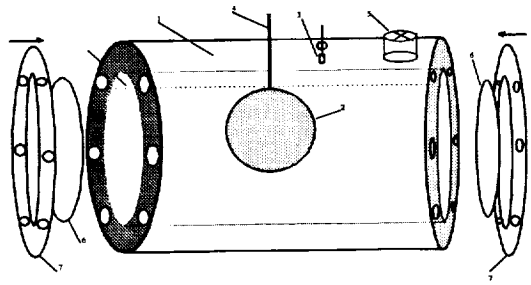

Figure 2. Shown above is a schematic of the sample cell. The cylinder is 7.62cm (3") long, 7.62cm in outer diameter and is 3.81cm in inner diameter. The inner electrode is a sphere of radius Ri=0.3175cm. The cell is filled with SF_6 and operated near the critical point. 1- Cylindrical body made of copper. 2- Spherical electrode made of copper with a diameter of 0.635cm (1/4"). 3- YSI thermistor placed 2.0 cm deep in the cylinder wall. 4- Conducting rod used to supply high voltage to the sphere. 5- Vacuum valve. 6- Sapphire windows with O-rings to seal the cell. 7- Flanges.

Two sapphire windows are placed at each end of the copper so that light may pass through the region near the spherical electrode and seal the SF_6 in the cell. This electrode is connected with an insulated conducting rod passing through the cylinder wall. The high potential is applied to this electrode and the surrounding copper is grounded. A YSI series 44000 thermistor is embedded 2 cm in the cylinder wall to measure and control the cell's temperature. The cell is then placed inside a larger cylindrical chamber that is 12 cm in length with a diameter of 9cm. A second YSI thermistor is placed in the outer chamber to monitor its temperature. A sixteen bit data acquisition board (National Instruments AT-MIO 16-X) is used to control the temperature of the SF_6 to a precision of ±2 mK using both thermistors in the system. The cell uses a valve connection, as shown in Figure 2 and a vacuum system for SF_6 filling. The cell and the vacuum system are both thoroughly cleaned prior to filling. Filling is performed by first evacuating air from the cell and then opening the cell to a high-pressure SF_6 tank. This process is repeated several times in order to insure the removal of as much air as possible. To obtain the critical density, the cell is filled to half of the internal volume of the cell, according to the law of the rectilinear diameter [10].

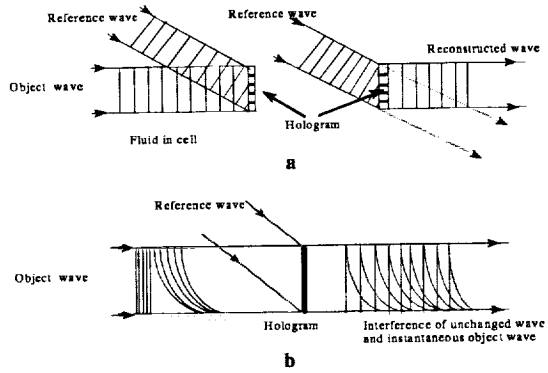

Figure 3. Holographic interferometry. a) reference hologram, b) interference from changed fluid.

Holographic interferometry is used to detect density variations in the system. In this method a reference hologram of the object of interest is first recorded. This reference hologram is capable of reproducing the optical wave that produced this reference image. A second wave, with the changes of interest present in the setup, is then superposed on the reference hologram. These two wave patterns interfere producing fringes that are caused by the differences in the two waves. A schematic of the recording and reconstruction used in holographic interferometry is shown in Figure 3. In our case the optical path length is changed between the first and second waves because the electric field has changed the fluid's density, i.e., light from the object beam passes through the fluid surrounding the center electrode. We expect that the resulting difference in fluid density will cause a phase shift of the instantaneous object wave, as shown in Figure 3. This phase shift is measured in the recorded fringe pattern. In fact, the optical path length change is less than one wavelength in our case. To detect this small change, we have placed a set of reference fringes in the first hologram by tilting one of the mirrors in the setup. The change of optical path length causes a shifting of these reference fringes. Because the interference is between two arbitrary waves, the set up does not require optical quality components, as is the case in ordinary interferometry. In addition, the second wave may be produced in real time as the object is evolving, as we have done here.

In our optical arrangement a 20mW Helium-Neon laser beam is divided into an object and reference wave with a beam splitter. Both beams are steered through a lens and mirror system so that the object wave passes through the fluid to be investigated. The hologram is made with a Newport HC-300 thermoplastic recorder and the fringe pattern is recorded in a CCD camera. The entire system was installed on a Newport VW series vibration isolated table. Figure 4 shows two holographic interferograms before and after an electric field has been applied. The top image was taken with zero voltage applied to the cell and the bottom image with 3000 volts across the cell. The shift of fringes was analyzed with the help of an EPIX frame grabber and image processor.

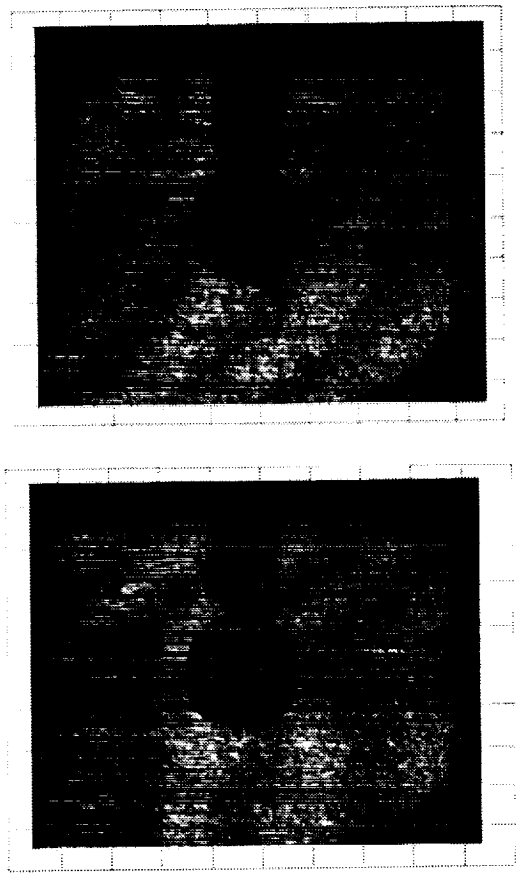

Figure 4. Two holographic interferograms showing the fringe pattern in SF_6 at $T=T_c+30mK$. The top image shows the reference fringes and the bottom image shows the fringe pattern after 3000 VAC is applied to the center sphere.

Our capacitor geometry gives an electric force distribution close to the inner sphere that in theory can be approximated by two concentric spheres. However, other asymmetries, especially the vertical density gradient induced by terrestrial gravity, produce a force field that changes the density profile from that expected in a symmetric system. Because of this, as well as other reasons discussed below, the fringe pattern shown in the hologram is not totally symmetric. The typical fringe shift observed is approximately ½ of a wavelength. This shift was observed only in a region close to the inner sphere.

Because the thermal expansion coefficient diverges at the critical point, a small temperature gradient can easily cause a large buoyancy force causing convection. One of the most difficult tasks in this experiment was to minimize the fluid convection in the cell. The fact that we used a relatively large cell made it very difficult to avoid thermal gradients and avoid gravitationally induced convection. This was especially true at the windows where the difference between the temperature in the fluid and the temperature at the windows is estimated to be approximately 20mK. This convection at the windows should cause a decrease in the density change throughout the cell as the convection mixes the fluid. However, the convection should not produce a mayor perturbation to the fringe pattern if the convection is steady. Fortunately, the convection was steady during periods of over one day where T was at T_c+30mK as was seen in a holographic fringe pattern of the fluid cell taken over one day.

DISCUSSION

The electric field appears to act as a body force that compresses the fluid in much the same way as the earth's gravity compresses the fluid. To estimate the bulk density change induced by this body force we can use the Clausius-Mossetti relation [11]:

$\delta p = \frac{\varepsilon_0}{6}(\kappa-1)(\kappa+2)E^2$, δp is the change in pressure, ε_0 is the permittivity constant, and κ is the dielectric constant. The pressure is related to the density, in an isothermal fluid, by the definition of the isothermal compressibility, K_t [12]: $\delta p = \frac{1}{K_t}\frac{\delta\rho}{\rho}$, where ρ is the density and $\delta\rho$ is the change in density. K_t of SF_6 near the critical point diverges as [4][11]:

$K_t = \frac{0.0459}{p_c}T^{*-1.24}$, the reduced temperature is $T^*=(T-T_c)/T_c$ and p_c is the fluid's critical pressure. Using the above equations the Clausius-Mossetti relationship can be written as:

$$\frac{\delta\rho}{\rho} = \frac{\varepsilon_0}{6}K_t E^2(\kappa-1)(\kappa+2).$$

To model the electric field in the cell we consider the system to be two concentric spheres. This is justified because most of the change in density in the data of Figure 4 is near the center electrode where the field is primarily radial. For example, $E_\theta/E_r < 1.5\%$ at a distance of less than 1cm from the center electrode. The electric field, E, between two concentric spheres is:

$E(r) = d(1+\beta)\beta\frac{V_0}{r^2}$, where V_o is the potential difference between the inner and outer sphere, d is the gap between the spheres, β is the aspect ratio ($\beta=R_i/d$), R_i is the radius of the inner sphere, and r is the radial distance. Using the above expression for the electric field in a spherical capacitor, we obtain the equivalent density change produced in the spherical capacitor:

$$\frac{\delta\rho}{\rho} = \frac{\varepsilon_0}{6}K_t(\kappa-1)(\kappa+2)d^2(1+\beta)^2\beta^2\frac{V_0}{r^4}$$

Figure 5 shows the density profile for the above formula for κ=1.2800 at $\rho=\rho_c$ [13].

A typical value of the applied voltage V_0 in the literature is 10,000 volts [3] [14]. Those relatively high values of voltages result in a dielectrophoteric force of magnitude of $1g$ or greater depending on the selected values for the parameters of the cell [9].

We use the Lorentz-Lorenz relation:

$\frac{n^2-1}{n^2+2} = \frac{4}{3}\pi\alpha\rho$, to analyze these fringes and compare them with the expected density differences (n is the index of refraction and α is the polarizability). By differentiating and using the above relation we get:

$$\rho\frac{dn}{d\rho} = \frac{(n^2-1)(n^2+2)}{6n}.$$

The optical path length of the light in a small length, Δz, along the optic axis of the fluid is:

$N\lambda = \Delta z n(\rho)$,

λ is the wavelength of light and N is the number of wavelengths in Δz. We take the cylinder axis and the optical axis to be the z coordinate. The observed shift in the number of fringes at a point in the image, ΔN, is the total change in the number of wavelengths along the beam's path through the cell. The local optical path length change, $\delta N\lambda$, is found by differentiating the above formula:

$$\delta N\lambda = \Delta z\frac{\delta\rho}{\rho}\frac{(n^2-1)(n^2+2)}{6n}.$$

The temperature of the fluid in the cell for the data in Figure 4 is at $T=T_c$+30mK. The light transmitted through the critical fluid is affected by the refractive index variations due to the electric field according to the above discussion. The fringe pattern results from the total optical path length change that occurs along the total path of the light through the cell. In our case we assume no refraction and take the path to be along

the z direction. A total phase shift, ΔN, can be calculated by integrating δN along z through the cell:

$$\Delta N = \int \delta N = \frac{(n^2-1)(n^2+2)}{6n\lambda}\int \frac{\delta\rho}{\rho} dz$$

Substituting the above expression for δρ/ρ we obtain:

$$\Delta N = \frac{\varepsilon_0 K_t (\kappa-1)(\kappa+2)(n^2-1)(n^2+2)}{36n\lambda} \times$$

$$d^2(1+\beta)^2\beta^2 V_0^2 \int \frac{dz}{(x_0^2+y_0^2+z)^4},$$

$(x_o^2 + y_o^2 + z^2) = r^2$. x_o and y_o are measured from the center of the inner sphere to a point in the (x, y) plane perpendicular to z. x_o and y_o are also the coordinates of the field of view shown in Figure 4, We define $R=(x_o^2 + y_o^2)^{1/2}$ to be the perpendicular distance from the z-axis with the origin at the center of the sphere. Figure 6 shows a plot of ΔN vs. R. In this plot $T = T_c + 30mK$, V_0 is 3000 volts, and the other values are given above. From Figure 6 we can see that close to the inner sphere the fringe shift is close to ΔN = 1/2. As can be seen in the data of Figure 4, after subtracting off the reference pattern at the top of Figure 4, a typical fringe shift is ΔN = 0.51. The estimated fringe shift is good despite all the approximations made in the electric field model, the presence of convection, and the density gradient induced by gravity.

CONCLUSION

A varying density profile was induced in a critical fluid using an electric field. The visualization of this profile with a total density change estimated at 0.2%, though small, is very encouraging. This is because these result correspond well to the calculated density changes and suggest that our method of calculating the density profiles is valid. Using these results we can calculate expected density profiles that will occur when our system is appropriately modified as in our new cell.

Our new critical fluid cell uses two transparent sapphire domes coated with Indium Tin Oxide that forms a one-inch diameter outer sphere. Concentric with the outer sphere is a ¼-inch diameter conducing inner sphere at the center. Figure 7 shows the expected density profiles that will be induced in weightlessness at various temperatures at 10,000 volts. From these profiles we can expect to see some significant density gradients induced in the cell. We have also improved the temperature control to <1mK. Our new test system has been designed to reduce temperature gradients and the resulting convection at the cell windows. This larger electric field gradient will also produce a large g_e [9] [14] between the two spheres. The new system will undergo laboratory tests like those described above. It will also be used on a parabolic flight test with NASA's KC-135 aircraft that is currently scheduled for August 1998. This parabolic flight will try to test if a spherically symmetric density gradient in low gravity is induced as expected.

By replacing the inner sphere, the new cell can be easily modified. Depending on the choice of Ri we could expect densities variation in the critical SF_6 between 10%-60% with an applied electrical potential of 5000 volts. With an appropriately chosen Ri, this system could easily be made to be geometrically similar to the earth's outer core [9].

REFERENCES

[1] D.E Smylie, "Thermal convection in dielectric liquids and modeling in geophysical fluid dynamics", Earth and Planetary Science Letters, **1**, 339 (1966).

[2] J. E. Hart, J. Toomre, A.E. Deane, N. E. Hurlburt, G. E. Glatzmaier, G. H. Fichtl, F. Leslie, W. W. Fowlis, P. A. Gilman, "Laboratory experiments on planetary and stellar convection performed on spacelab 3", Science, **234**, 61 (1986).

[3] C. Egbers, A. Delgado, and H. J. Rath, "First experimental investigation of density driven large-scale ocean motions under microgravity", ASME Forum on Micro. Flows, **111**, 41 (1991).

[4] M. R. Moldover, J. V. Sengers, R. W. Gammon, and R. J. Hocken, "Gravity effects in fluids near the gas-liquid critical point", Rev. Mod. Phys, **51**, 79 (1979).

[5] H. Boukari, J.N. Shumeyer, M.E. Briggs, and R. W. Gammon, ``Critical speeding up in pure fluids", Phys.Rev.A, **41**, 2260 (1990).

[6] B. Zappoli, D. Bailly, Y. Garrabos, B. LeNeindre, P. Guenoun, and D. Beysens, ``Anomalous heat transport by the piston effect in supercritical fluids under zero gravity", Phys. Rev. A **41**, 2264 (1990).

[7] J. Hegseth, D. Beysens, V. Nikolayev, Y. Garrabos and C. Chabot "Phase separation and boiling near the critical point in pure fluids", in *Proceedings of the 1997 NASA/JPL Microgravity Fundamental Physics Workshop*, NASA Document, **D-15677**, 127 (1998).

[8] L. D. Landau and E. M. Lifshitz, *Electrodynamics of Continuous Media*, (Addison- Wesley, Reading Mass., 1960).

[9] J. Hegseth and L. Garcia, "A geophysical flow experiment in a compressible critical fluid" Third Microgravity Fluid Physics Conference, NASA C.P. **3338**, 773 (1996).

[10] C. Morteau, M Salzman, Y. Garrabos, D. Beysens, "Density characterization of slightly off-

critical fluid cells using the ALICE 2 facility", in *Proceedings of the 2nd European Sympsium on Fluids in Space*, edited by A. Viviani (Jean Gilder Congressisrl, 1997) p. 327-333.
[11] G. Zimmerli., R. A. Wilkinson., R. A. Ferrel, M. R. Moldover. "Electric field effects on a near-critical fluid in microgravity" [pre-print].
[12] J.A. Stratton, *Electromagnetic Theory,* (McGraw-Hill, 1941).
[13] B. J. Thijsse, "The dielectric constant of SF_6 near the critical point, J. Chem. Phys. **74**,4678 (1981).
[14] J. E. Hart, G. A. Glatzmaier, and J. Toomre, "Space-laboratory and numerical simulations of thermal convection in a rotating hemispherical shell with radial gravity", J. Fluid Mech., **173**, 519 (1986).

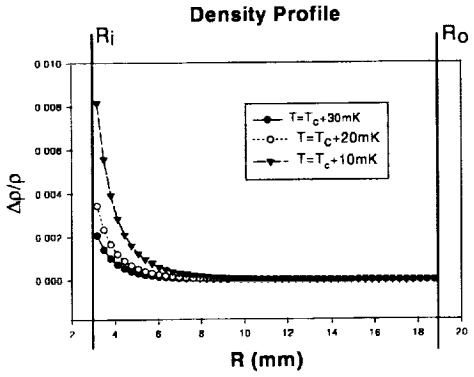

Figure 5. Three plots of the estimated density change relative to the SF_6 density at the outer cylinder for the cell in Figure 2. Plots for three different temperatures are shown. The fluid's density change due to the electric field in this cell should vary from 0.0% to 0.2% when 3000 volts are applied at $T=T_c+30mK$.

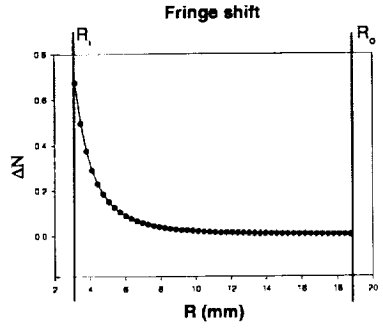

Figure 6. The calculated fringe shift for the cell in Figure 2. $T=T_c+30mK$ and $V_0=3000$ volts.

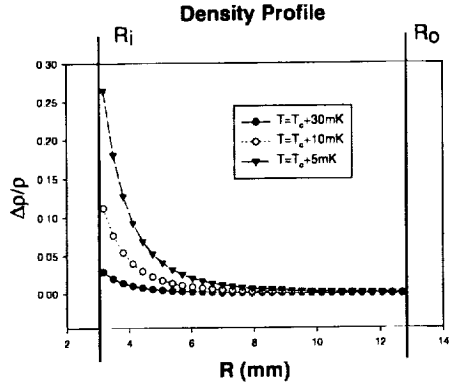

Figure 7. Density profiles for the new cell.

PHASE SEPARATION KINETICS IN ISOPYCNIC MIXTURES OF H_2O/CO_2/ETHOXYLATED ALCOHOL SURFACTANTS

Markus Lesemann[1], Michael E. Paulaitis[1], and Eric W. Kaler[2], [1]Department of Chemical Engineering Johns Hopkins University, Baltimore, MD 21218, email: michaelp@jhunix.hcf.jhu.edu, [2]Department of Chemical Engineering, University of Delaware, Newark, Delaware 19716.

Abstract

Ternary mixtures of H_2O and CO_2 with ethoxylated alcohol (C_iE_j) surfactants form three coexisting liquid phases at conditions where two of the phases have equal densities (isopycnic phases). Isopycnic phase behavior has been observed for mixtures containing C_8E_5, $C_{10}E_6$, and $C_{12}E_6$ surfactants, but not for those mixtures containing either C_4E_1 or C_8E_3 surfactants. Pressure-temperature (PT) projections for this three-phase equilibrium were determined for $H_2O/CO_2/C_8E_5$ and $H_2O/CO_2/C_{10}E_6$ mixtures at temperatures from approximately 25 to 33 °C and pressures between 90 and 350 bar. Measurements of the microstructure in $H_2O/CO_2/C_{12}E_6$ mixtures as a function of temperature (25-31 °C), pressure (63.1-90.7 bar), and CO_2 composition (0-3.9 wt%) have also been carried out to show that while micellar structure remains essentially unchanged, critical concentration fluctuations increase as the phase boundary and plait point are approached. In this report, we present our first measurements of the kinetics of isopycnic phase separation for ternary mixtures of $H_2O/CO_2/C_8E_5$.

Introduction

Surfactant solutions containing near-critical or supercritical fluids that form equilibrium phases of equal density (isopycnic phases) are uniquely suited for simulating phase separation in microgravity environments where density differences between the separating phases are irrelevant. For compressible supercritical-fluid mixtures, pressure becomes an additional operating field variable with which to adjust and control phase boundaries.[1-3] As a consequence, rapid pressure quenches can be made to access metastable or unstable regions of the phase diagram, thereby permitting the convenient study of phase separation dynamics and mechanisms. In addition, low interfacial tensions and the presence of colloidal microstructure in surfactant-containing solutions,[1,3-5] retard phase separation. A goal of this work is to study isopycnic phase behavior for three-phase, liquid-liquid-liquid (L1-L2-L3) equilibrium in ternary mixtures of H_2O and CO_2 with ethoxylated alcohol (C_iE_j) surfactants: C_4E_1, C_8E_3, C_8E_5, $C_{10}E_6$, and $C_{12}E_6$. CO_2 was selected as the near-critical or supercritical fluid because it has a readily accessible critical point (31.06 °C and 73.825 bar) and a reasonably high critical density (0.4660 g/cm^3).[6]

Surfactant self-assembly in near-critical or supercritical fluids opens the possibility that pressure or fluid density can be used to alter surfactant microstructure.[7,8] Prior studies of surfactant microstructure in solutions containing supercritical or near-critical fluids have focused on the supercritical fluid-rich region of the phase diagram where the effects of pressure on microstructure and phase behavior are expected to be large. A second goal of our work is to examine, using small angle neutron scattering, the effects of CO_2 on the interactions, critical fluctuations, and structure of ethoxylated alcohol/water micellar solutions in the water-rich region of the phase diagram. In preliminary experiments on $D_2O/CO_2/C_{12}E_6$ micellar solutions,[9] we found that the scattering spectra can be modeled using a polydisperse hard-sphere form factor to determine particle shape and size, together with an Ornstein-Zernike structure factor to quantify the critical phenomena. Our results indicate the presence of spherical micelles approximately 50 Å in diameter. Further, micelle structure does not change over the range of temperatures, pressures, and compositions studied. The increase in S(0) and ξ are consistent with increasing critical concentration fluctuations caused by the approach to the phase boundary and a plait point.

Little is known about the rate of formation and growth of new phases. A third goal of this work is to investigate the separation of an equilibrium phase into two phases after both pressure and temperature quenches. Since isopycnic surfactant solutions have intrinsically slower times for mass transfer compared to molecular solutions, temperature changes and pressure changes that equilibrate within less than a few minutes are expected to be essentially instantaneous on the time scale of the phase separation kinetics. Limited observations have been made of isopycnic phase separation.[10,11] From this previous work,[11] we anticipate observations of dissipative structures as the density difference between the phases vanishes. Elimination of convection driven by buoyancy will enable easier analysis of quasielastic light scattering data. The important role of viscosity in controlling the evolution of these phases can also be determined. Our combined small angle light and neutron scattering observations of the growth of new phases on length scales ranging from 10 Å to 10 μm or more will provide a unique base of information to guide and test emerging theories. This information will also be central to the exploitation of the microgravity environment of space to mitigate density differences in producing new alloys or other materials. In this report, we present our first measurements of the kinetics of isopycnic phase separation for ternary mixtures of $H_2O/CO_2/C_8E_5$.

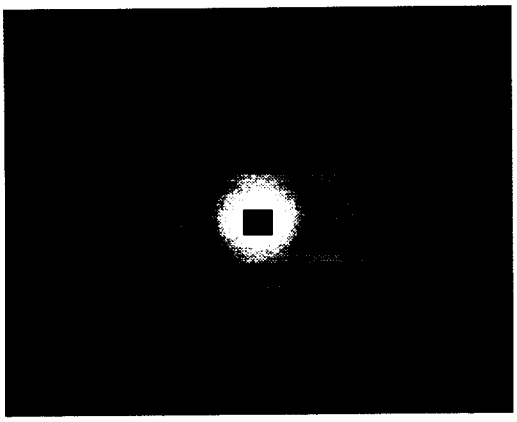

Fig. 1 Pattern of scattered light after a quench from a one-phase into a two-phase region: spinodal ring. The square in the center is a beamstop that protects the camera from the transmitted beam.

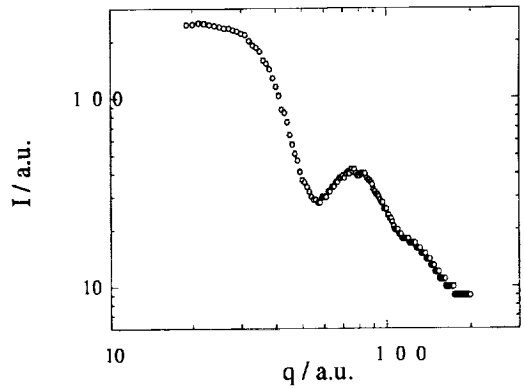

Fig. 2 Radially integrated intensity of the scattering pattern shown in Fig. 1. The relative maximum corresponds to a wave vector of 2.1×10^{-3} nm^{-1}.

Experimental Section

Pentaethylene glycol monooctyl ether (C_8E_5) (Bachem Bioscience Inc.) with a purity of 97 wt-% and research grade CO_2 (> 99.998 %, Potomac Airgas, Inc.) were used without further purification. H_2O was filtered and purified using a Millipore apparatus.

Phase separation kinetics in ternary mixtures of $H_2O/CO_2/C_8E_5$ are measured by means of time resolved small angle light scattering (SALS). The experimental setup consists of the sapphire view cell used in our phase equilibrium studies[9] and a scattering cell, designed and constructed in-house. The scattering cell has two 5 mm thick sapphire windows, placed parallel to each other and separated by a distance of 1 mm. The windows are sealed against the stainless steel body of the scattering cell by custom-made Teflon seals. The scattering cell and view cell are connected to each other through high-pressure tubing to enable the scattering cell to be filled from the view cell and to pressurize the contents of the scattering cell using the pressurizing system for the view cell. The system pressure is measured to an accuracy of 0.1 % using an Omega PX 945 pressure transducer. A Teflon coated stir bar in the scattering cell allows mixing using an external magnet. The scattering cell has been tested up to a pressure of approximately 500 bar. Temperature is controlled by placing the scattering cell in an aluminum jacket through which water from a Hart Scientific high precision bath is circulated. The view cell is immersed in this bath. The scattering cell temperature is measured by a thermistor located in the aluminum jacket. Pressure quenches from the one-phase region into the two-phase, L1-L2 region of the phase diagram are accomplished by instantaneously decreasing the pressure in the view cell. Thus, time resolved scattering data can be collected using the scattering cell, while simultaneously monitoring the phase behavior of the system at identical conditions in the view cell.

The optical system consists of a He-Ne laser (λ = 632.8 nm) that is focused to a point in the sample volume using a lens with 30 cm focal length. The scattered light is captured on a mica screen at a distance of 50 cm from the sample. The resulting scattering pattern is recorded by a CCD camera (Cohu 4910) connected to a frame grabber card (Scion LG-3) in a Macintosh G3 computer using Scion software. With this setup, up to 30 scattering patterns can be recorded per second. The data are processed using NIH Image software and data reduction software comparable to the modules used by NIST for analysis of SANS data. We plot the scattering intensity as function of the absolute of the scattering vector, q, given by

$$q = (4\pi/\lambda) \sin(\theta/2)$$

where q is the scattering angle and λ is the wavelength of the He-Ne laser.

Results and Discussion

Isothermal pressure quenches from the one-phase into the two-phase region, where surfactant-rich and surfactant-lean phases coexist (the L1 and L2 phases, respectively) were performed. Ideally, the final pressure after the quench brings the system to isopycnic L1 and L2 phases. While these phases separate, a spinodal ring is observed in the light scattering pattern, as shown in Fig. 1. This spinodal ring corresponds to a relative maximum in the plot of scattering intensity vs. q. An example of such a plot is given in Fig. 2 for a measurement after a pressure quench into the two-phase region of approximately 5 bar. The observed maximum corresponds to $q = 2.1\times10^{-3}$ nm^{-1}, which indicates the existence of scattering entities having an approximate length scale of 470 nm. However, a large scattered intensity is also found for very small q val-

ues. Therefore, we assume that even larger structures are present in the solution. We note that the apparent saturation in scattering intensity for $q \rightarrow 0$ is an experimental artifact. In order to resolve the local maximum in the spectrum, the CCD camera gain had to be increased causing the apparent saturation at very small scattering angles.

This local maximum moves to smaller values of q with time between when it is first observed 2.5 minutes after the pressure quench and completely vanishes approximately 45.0 minutes later. At longer times, light is merely scattered to very small scattering angles; i.e., large droplets or clusters of the second phase have formed. Thus, the observed spinodal ring decreases in diameter over time revealing, as expected, so-called coarsening: the length scale characterizing the domains formed immediately after the pressure quench into the two phase region increases over time.

Conclusions

The data collected so far show that isothermal pressure quenches from a one-phase region into the two-phase region corresponding approximately to isopycnic L1 and L2 equilibrium phases result in patterns of the scattered light (spinodal rings) typical of early phase separation. The time evolution of these scattering patterns show the expected coarsening of the non-equilibrium structures over time. We are currently focusing on the kinetics of this coarsening to obtained quantitative measurements of the phase separation kinetics.

Acknowledgments

This work is supported by the National Aeronautics and Space Administration 9NAG3-1424). We acknowledge the support of the National Institute of Standards and Technology, U.S. Department of Commerce, in providing the facilities used in the SANS experiments. The assistance of John Barker and Charlie Glinka during the SANS experiments is gratefully acknowledged, as are helpful discussions with Steve Kline, Y. Jayalakshmi, K.-V. Schubert, and John van Zanten.

References

1. J. M. Ritter and M. E. Paulaitis, Langmuir *6*, 934-941 (1990).

2. G. J. McFann and K. P. Johnston, Langmuir *9*, 2942-2948 (1993).

3. G. J. McFann, K. P. Johnston, and S. M. Howdle, AIChE J. 40, 543-555 (1994).

4. E. W. Kaler, J. F. Billman, J. L. Fulton and R. D. Smith, J. Phys. Chem. *95*, 458-462 (1991).

5. J. M. Tingey, J. L. Fulton, D. W. Matson and R. D. Smith, J. Phys. Chem. *95*, 1443-1448 (1991).

6. "Carbon Dioxide International Thermodynamic Properties of the Fluid State -3;" S. Angus, B. Armstrong and K. M. d. Reuk, Eds.; Pergamon Press: Oxford, 1976.

7. J. L. Fulton and R. D. Smith, J. Phys. Chem. *92*, 2903-2907 (1988).

8. R. W. Gale, J. L. Fulton and R. D. Smith, J. Am. Chem. Soc. *109*, 920-921 (1987).

9. R. G. Zielinski, E. W. Kaler and M. E. Paulaitis, J. Phys. Chem. *99*, 10354-10358 (1995).

10. C. Houessou, P. Guenoun, R. Gastaud, F. Perrot and D. Beysens, Phys. Rev. A *32*, 1818-1821 (1985).

11. G. M. Schneider, M. Dittman, U. Metz and J. Wenzel, J. Pure & Applied Chem. *59*, 79-86 (1987).

Session 3C

Interfacial Phenomena II

THE DISSOLUTION OF AN INTERFACE BETWEEN MISCIBLE LIQUIDS

D. H. Vlad[1], J. V. Maher[1], [1]Department of Physics and Astronomy, University of Pittsburgh, Pittsburgh, PA 15217

Abstract

The dissapearance of the surface tension of the interface of a binary mixture, measured using the dynamic surface light scattering technique, is slower for a binary mixture of higher density contrast. A comparison with a naive diffusion model, expected to provide a lower limit for the speed of dissolution in the absence of gravity shows that the the interfacial surface tension dissapears much slower than even by diffusion with the effect becoming much more pronounced when density contrast between the liquid phases is increased. Thus, the factor most likely to be responsible for this anomalously slow dissolution is gravity. A mechanism could be based on the competition between diffusive relaxation and sedimentation at the dissolving interface.

In a previous experiment[1] May and Maher studied the process of dissolution of liquid interfaces between miscible liquids by using dynamic surface light scattering. They observed that the interfacial surface tension decays anomalously slowly during the dissolution. They speculated that the process might be affected by gravity slowing down the dissolution. Computer simulations[2] of the process were not able to identify a significantly different rate of dissolution unless a strong restoring field was introduced into the simulations.

We have designed and performed experiments to explore the role of gravity in the interfacial dissolution process. We chose to study the well understood[3] cyclohexane and methanol (CM) binary mixture, since the densities of the components are naturally well matched. The strength of the coupling with gravity can be tuned by mixing in deuterated forms of the two components[4], which change the density contrast across the interface.

For CM the density contrast between the upper and lower phase at a temperature of 225 mK below T_c is $2x10^{-3}\ g/cm^3$. When a small amount of deuterated cyclohexane ia added, the density contrast can be considerably reduced[4]. We prepared a cyclohexane + deuterated cyclohexane + methanol mixture (CDCM) of deuterated fraction 1.65% which have a density contrast about 5 times smaller than the density contrast for CM. For such a small density difference the density contrast is obtained from the measurement of the capillary length as in Ref. [5] since the rule of additivity of volumes fails[4]. To explore an even larger range of density contrast we prepared a cyclohexane and deuterated methanol d_4 (CDM) mixture, of density contrast about 8 times larger than CM.

At a temperature below the critical temperature the mixture is in a two phase state, and the upper and lower phases are separated by a sharp interface of the order of the correlation length. After the mixture's temperature is raised above T_c the interface starts dissolving while the system evolves toward the thermodynamic equilibrium one phase state.

The dissolution process can be studied by measuring the autocorrelation function of the light scattered by the capillary waves which naturally exist on the interface. For a binary mixture near the critical temperature the capillary waves are overdamped and the dispersion relation for interfacial capillary waves allows the reduction of the surface light scattering autocorrelation function to the form[6]:

$$G(t) \sim e^{-t/\tau} \tag{1}$$

with the relaxation time

$$\tau = \frac{2(\eta_1 + \eta_2)}{\sigma q} \tag{2}$$

where η_1 and η_2 are the viscosities of the two liquids, σ is the interfacial tension and q is the wavenumber of the scattered light. Thus, the interfacial surface tension can be extracted from the autocorrelation function of the scattered light.

Having an extremely small density contast, CDCM was unstable during heating. The flow of the mixture along the walls of the cell distroyed the integrity of the interface and we had to abandon our autocorrelation function measurements on this mixture. For the other two mixtures, CM and CDM the temperature gradients were brought under control by setting the heating time to a few minutes. About 30 minutes after raising the temperature, the mixture typically reached thermal equilibrium and the interface regained its flattness lost during the heating process. Our experiments showed that, after the temperature was raised, the relaxation time of the autocorrelation function for CDM is significantly smaller than that of CM indicating a smaller reduction in the effective interfacial tension and a corresponding slower progress to the interfacial dissolution. Since the main difference between the two mixtures is the density

contrast, which is higher for CDM, we attribute this difference in dissolution to the effect of gravity.

During the dissolution, the thermodynamic state of the system is far from equilibrium and the dynamics of the process is difficult to understand. However, in the absence of gravity we might expect that the mixing process should evolve at least as fast as diffusion. Since anything other than diffusion should speed up the mixing process, diffusion should set a lower limit for the speed of dissolution.

May and Maher compared the surface tension data obtained for an isobutyric acid and water binary mixture with a naive diffusion model and found that the interface dissolves even slower than diffusion. In a naive diffusion model of the interface, the smooth density gradient inside the interface can be taken as constant. A dissolving interface contains a significant amount of free energy due to the concentration gradients. As in the case of an equilibrium interface, an effective surface tension can be defined even for a dissolving interface[7],

$$\sigma \propto \int \left(\frac{dc}{dz}\right)^2 dz \tag{3}$$

where c is the local composition and z is the direction normal to the interface.

This naive diffusion model predicts that the surface tension of the dissolving interface should be inverse proportional to the interface thickness

$$\sigma = \frac{F(T,t)}{[\xi_0 + (D_{eff}t)^{1/2}]} \tag{4}$$

In agreement with May and Maher experiments, the results of our experiments found that the interfaces of both CM and CDM mixtures dissolve even slower than predicted by the naive diffusion model, expected to set a lower limit for the speed of dissolution. Together with the results that the interface of CDM dissloves even slower than the interface of CM, this strongly suggests that gravity is indeed slowing down the dissolution process.

In order to understand how gravity can affect the dissolution process, we propose a dimensional argument for a dissolving interface based on the competition between diffusion and sedimentation. Let us consider a domain of radius R, of the order of the interface thickness. The domain is dissolved diffusively in a time of the order of

$$\tau_d = \frac{R^2}{D}. \tag{5}$$

where D is the diffusion constant. Gravity sediments the domain. A characteristic time for sedimentation can be obtained as the time in which the fluctuation travels a distance equal to its own radius. Neglecting a multiplying numerical geometrical factor which depends on the shape of the domain, the sedimentation characteristic time should be

$$\tau_s = \frac{\eta}{R\Delta\rho g} \tag{6}$$

where g is the gravitational acceleration and $\Delta\rho$ is the density difference between the liquids.

Immediately after the temperature of the mixture is raised and the interface starts dissolving, the interface thickness is small, the diffusion time is much smaller than the sedimentation time, and the dissolution process is dominated by diffusion. But as the interface thickness increases, the relative importance of the sedimentation increases. When the two characteristic times have the same order of magnitude, gravity might begin affecting the dissolution.

A length scale for the interface thickness, R^*, is selected by this competition. R^* is obtained by setting the two characteristic times equal.

$$R^{*3} = \frac{\eta D}{\Delta\rho g}. \tag{7}$$

With reasonable numbers for the systems in the present experiment, the interface thickness reaches R^* in about 2-3 minutes for CM and about 30 sec for the CDM. This is a very large time for computer simulations of the dynamics of the dissolving interfaces and this could explain the failure of the simulations to observe a dissolution process different from diffusion.

Density fluctuations of size of the order of R^* could create a high density gradient inhomogeneous layer of thickness of the order of R^*. A recent experiment by Alberto Vailati and Marzio Giglio[8] showed that "giant

Mixture	$T_{final} - T_c$ (mK)	L $(10^{-4}cm)$	R^* $(10^{-4}cm)$
CM	35	9.0 ± 5.0	4.9
CM	52	6.2 ± 3.5	5.3
CM	95	7.2 ± 3.6	6.0
CM	173	5.2 ± 4.1	6.8
CDM	35	4.0 ± 1.6	2.5
CDM	61	1.5 ± 0.7	2.8
CDM	172	1.7 ± 0.7	3.5

Table 1: The interface thickness extracted from the results obtained in the surface light scattering experiments (L) vs R^*, the thickness selected by the diffusion/sedimentation competition across the interface.

fluctuations" at the interface in binary mixtures do exist under conditions similar to our system.

Our results from the surface light scattering experiments are consistent with the dimensional argument for competition between diffusion and sedimentation. Table 1 shows the magnitude of R^* and L, the thickness of the interface obtained from the experimental data. The magnitude of the thickness of the inhomogeneous region was extracted from the surface tension by using the simplifying assumption that the concentration difference between the upper and lower plane of the inhomogeneous region does not change in time.

This work was supported by NASA under Grant No. NAG3-1833.

References

[1] S. E. May and J. V. Maher, Phys. Rev. Lett. **67**, 2013 (1991).

[2] D. Jasnow (private communication).

[3] D. C. Jones and S. Amstell, J. Chem. Soc. 1316 (1930); E. L. Eckfeld and W. W. Lucasse, J. Phys. Chem. **47**, 164 (1943).

[4] C. Houessou, P. Guenoun, R. Gastaud, F. Perrot and D. Beysens, Phys. Rev. **A**, 1818 (1985).

[5] Connie Warren and W. W. Webb, J. Chem. Phys. **50**, 3694 (1969).

[6] *e.g.* J. Meunier, in *Liquids at Interfaces*, edited by J. Charvolin, J. F. Joanny and J. Zinn-Justin (North-Holland, New York, 1988).

[7] J. W. Cahn and J. E. Holliard, J. Chem. Phys. **28**, 258 (1958); H. T. Davis, in *Numerical Simulation and Oil Recovery*, edited by M. Wheeler (Springer-Verlag, Berlin, 1988), p. 105.

[8] Alberto Vailati and Marzio Giglio, Nature **390**, 262 (1997).

INVESTIGATION OF THERMAL STRESS CONVECTION IN NONISOTHERMAL GASES UNDER MICROGRAVITY CONDITIONS

Daniel W. Mackowski, Mechanical Engineering Department
Auburn University, AL 36849, dmckwski@eng.auburn.edu

1. INTRODUCTION

The continuum description of momentum and energy transport in gases, based upon Newton–Stokes–Fourier constitutive relations, can become inaccurate in rarefied or highly nonequilbrium regimes, i.e., regimes in which the Knudsen number Kn ($= \lambda/L$, where λ is the gas mean free path and L is the characteristic system or gradient length) is no longer small. The Burnett equations, which represent the order–Kn^2 solution to the Boltzmann equation, ostensibly provide a means of extending continuum formulations into the transitional Knudsen regimes ($\sim Kn < 1$).

The accuracy and validity of the Burnett equations, however, have not been firmly established. As has been noted by several authors, the asymptotic series expansion of the molecular distribution function – from which the Burnett equations are derived – has unknown convergence properties for finite Kn.[1,2] The Burnett equations can also lead to Second–law impossibilities, such as heat flux in an isothermal gas.[3] Furthermore, the Burnett equations increase the order of the differential equations that govern momentum and heat transport in the gas. Additional boundary condition information is required to fully close the problem – yet such information is generally not available from physical principles alone.

Because of these issues, it is generally held that the Burnett equations are valid only in regimes in which the Navier-Stokes-Fourier level of approximation already provides an adequate description of transport, i.e., regimes in which the Burnett contributions represent a small perturbation to heat and momentum transport. Such conditions can be representative of high–Mach number flows, for which application of the Burnett equations appears to have been the most successful.[4–7] On the other hand, there is not a broad understanding of the accuracy of the Burnett equations when applied to slow–moving, nonisothermal flow (SNIF) conditions. As noted by Kogan, 'thermal stresses' (fluid stresses resulting from temperature gradients – which are predicted by the Burnett equations) could become a significant convection mechanism in buoyancy–free, nonisothermal gases.[8,9] Indeed, it has been recently suggested that thermal stress convection could affect the growth of crystals in microgravity physical vapor transport experiments.[10,11]

The work presented here consists of a theoretical and numerical examination of thermally–induced stresses and flows in enclosed, highly nonisothermal gases under buoyancy–free conditions. A central objective has been to identify a strategy in which stress and/or convection effects, as predicted by the Burnett equations, could be isolated and measured in microgravity–based experiments. Because of the questionable veracity of the Burnett equations, a second objective has been to test Burnett predictions of nonisothermal gas stress and convection with the exact description provided by the direct simulation Monte Carlo (DSMC) method.

2. PREDICTION OF THERMAL STRESS CONVECTION

The initial phase of the project was aimed at calculation, using continuum and DSMC methods, of gas convection in two dimensional nonuniformly heated rectangular enclosures. Typically, two adjacent surfaces of the enclosure were modeled as adiabatic, zero–stress surfaces (i.e., planes of symmetry), and the other two adjacent surfaces were maintained at specified temperature distributions with one surface transferring a net amount of heat to the gas, and the other transferring the heat from the gas.

The continuum formulations of momentum and energy transport are identical to Navier–Stokes–Fourier models, with the exception of the Burnett stress tensor in the momentum equations and the creep and jump boundary conditions. For the conditions examined here (i.e., slow–moving flow, with $Re_L \ll 1$) the only significant terms in the Burnett stress tensor relations will be those involving temperature gradients. This thermal stress component appears as[8,11]

$$\boldsymbol{\tau}_T = -\frac{\mu^2 \mathcal{R}}{P}\left[\omega_3\left(\nabla\nabla T - \frac{1}{3}(\nabla^2 T)\,\mathbf{I}\right) + \frac{\omega_5}{2T}\left((\nabla T)(\nabla T) - \frac{1}{3}(\nabla T\cdot\nabla T)\,\mathbf{I}\right)\right] \quad (1)$$

in which μ is the dynamic viscosity, R is the gas constant, and ω_3 and ω_5 are dimensionless, order–unity coefficients which depend on the interaction potential of the molecules. The creep and jump boundary conditions appear

$$\mathbf{u} = \frac{c_S \mu R}{P}\left(\nabla T - \hat{n}\,\frac{\partial T}{\partial n}\right) \quad (2)$$

$$T = T_w + \frac{c_T \lambda}{T}\,\frac{\partial T}{\partial n} \quad (3)$$

where n is the outward normal and the dimensionless coefficients c_S and c_T depend on the thermal and momentum accommodation properties of the surface.[12] Numerical solution of the governing equations was accomplished using the SIMPLER algorithm of Patankar.[13] Coefficients corresponding to hard−sphere molecules, which gives a temperature−dependent viscosity of $\mu \sim T^{1/2}$, were used in the computations.

Direct simulation Monte Carlo calculations of hard−sphere gas convection and heat transfer were accomplished using the standard procedure developed by Bird.[14,15] The cell size was nominally set to $0.1\lambda_0$, where λ_0 represents the mean−free−path at the equilibrium state of the system, and 10−20 molecules were assigned per cell. Simulations were conducted for a Knudsen range of $Kn = 0.01 - 0.2$. Because thermal creep and stress flows will be on the order of Kn times the mean molecular velocity, resolution of the flows using DSMC required simulation times on the order of $10^6 - 10^7$ time steps.

Our continuum and DSMC calculations to date indicate that it would be very difficult to create conditions in the enclosure that result in measurable thermal stress flows that are comparable to or larger than thermal creep flows, and simultaneously maintain the $Kn < 0.1$ regime required of the Burnett equations. With the exception of the pure continuum limit ($Kn \to 0$, under which thermal stress vanishes), elimination of thermal creep cannot be accomplished by maintaining the heated/cooled walls at uniform temperatures. Rather, the discontinuity (or jump) between the surface and adjacent gas temperatures − which will be proportional to Kn and the local normal temperature gradient − will lead to nonuniform gas temperatures along the nonuniformly heated surfaces. For all realistic values of Kn, thermal creep flows generated by the temperature jump effects were substantially larger than those resulting from thermal stress.

To minimize the effects of creep, we performed additional simulations in which the temperature distributions along the heated/cooled surfaces were assigned to provide, for a given Kn, nearly uniform gas temperature adjacent to the surface. Surface temperature distributions were determined from solution of the gas conduction equation with uniform gas temperature boundary conditions along the heated/cooled surfaces, and subsequent application of the solution into Eq. (3) to predict $T_w(x)$. This approach imposed a surface temperature on the heated surface which increased towards the junction with the cooled surface, with an opposite trend along the cooled wall. The effect of this strategy resulted in thermal creep flows that were confined about the hot/cold junction, and left a bulk, thermal−stress driven convection pattern in the bulk of the enclosure. However, this strategy would also lead to highly nonequilibrium conditions in the vicinity of the hot/cold surface junction, for which the Burnett equations are not expected to hold.

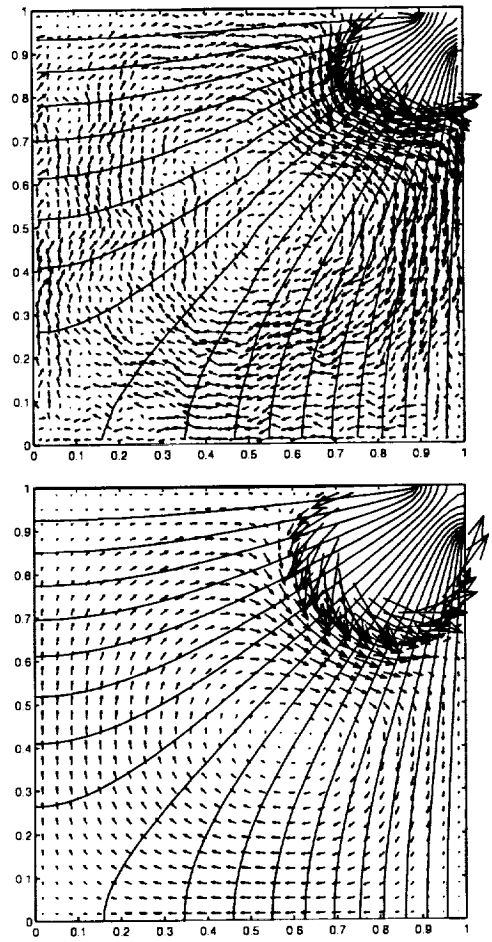

Fig. 1: DSMC (top) and continuum (bottom) results

The comparison between continuum/Burnett and DSMC predictions of convective flows in the enclosure has been inconclusive. DSMC calculations have shown convective flows that are qualitatively similar than those predicted by the continuum model. As an example, we show in Fig. 1 plots of velocity vectors and isotherms, calculated using the DSMC (top) and continuum (bottom) models, for a $Kn = 0.02$ hard−sphere gas contained in an enclosure with a relative temperature difference on the hot and cold walls of $2(T_H - T_C)/(T_H + T_C) = 1$. The heated wall is on the top, and the left and bottom walls are symmetry surfaces. A strip of the walls adjacent to the hot/cold junction, equal to 0.1 of the wall length, is held adiabatic, and the remainder of the walls have temperature distributions set to give isothermal gas conditions per the procedure discussed above. Velocity vectors corresponding to ther-

mal creep along the adiabatic surfaces (seen in the tight counterclockwise rotation in the upper right corner) have been removed from the plot to allow resolution of the thermal stress flows. The stress flow – as predicted by the continuum model – results in a clockwise rotation in the main body of the gas for the given conditions. A similar pattern is seen in the DSMC results. We cannot establish, however, whether the observed DSMC flows result from thermal stress, or are due to slip effects at the walls. As mentioned above, the veracity of the Burnett relations is also questionable for the highly nonequilibrium conditions of the simulations. On the other hand, temperature profiles calculated via DSMC and continuum models show significant agreement.

3. THERMAL STRESS IN 1–D HEAT TRANSFER

A simpler situation in which to compare continuum/Burnett and DSMC predictions of thermal stress effects is offered by 1–D heat transfer in a stationary gas. In this situation, the effects of thermal stress would be seen in the pressure distribution and normal stress in the gas.[16]

The computational domain was now taken to be a slab of gas contained between two parallel surfaces, separated by a distance L, with the surfaces at $x = 0$ and L maintained at uniform temperatures of T_{CS} and T_{HS} (with $T_{HS} > T_{CS}$), respectively. In nondimensional form (with pressure and stress normalized with the equilibrium pressure P_m and temperature by the equilibrium temperature T_m), the Burnett equation for the x–directed, normal component of the stress tensor is[7,17]

$$\tau^* = \phi + \frac{c_1 Kn^2 \theta}{\phi}\left[\omega_4 \frac{\theta'\phi'}{\phi} - \omega_2\left(\frac{\theta\phi'}{\phi}\right)' + \omega_3\theta'' + \omega_5\frac{\theta'^2}{\theta}\right] \tag{4}$$

In the above, $\phi = P/P_m$, $\tau^* = \tau/P_m$, $\theta = T/T_m$, the prime denotes differentiation with respect to $\xi = x/L$, $c_1 = (4\pi/3)(5/16)^2 = 0.4091$, and the dimensionless ω coefficients depend on the molecular interaction potential. Since the gas is stationary and buoyancy–free, the stress τ will be a constant. In the limit of $Kn \to 0$, this gives the Navier–Stokes result of $P = \tau =$ constant. For finite Kn, however, the additional source of thermal stress can act within the nonisothermal gas. The magnitude of the thermal stress will vary with position – by virtue of the dependence of temperature and temperature gradient on position – and consequently pressure will vary to maintain a constant normal stress.

The Burnett equations make no contribution to the heat flux for a stationary gas. Consequently, the gas temperature will be described by

$$q^* = \text{constant} = \theta^{1/2}\theta' \tag{5}$$

where q^* is the dimensionless heat flux ($= qL/kT_m$). Equation (5) can be used to combine the last two terms in Eq. (4), which results in

$$\tau^* = \phi + \frac{c_1 Kn^2}{\phi}\left[\theta\left(\omega_4\frac{\theta'\phi'}{\phi} - \omega_2\left(\frac{\theta\phi'}{\phi}\right)'\right) - \frac{c_2 q^{*2}}{\theta}\right] \tag{6}$$

where $c_2 = (\omega_3 - 2\omega_5)/2 = 0.9900$ for hard–sphere molecules.

Two separate effects – or regimes – on ϕ can be anticipated from inspection of Eq. (6). One effect, which is discussed by Kogan[18] and Makashev[19], derives from the fact that the derivatives of ϕ will be multiplied by the small parameter (for near–continuum conditions) of Kn^2. The solution to Eq. (6) could therefore exhibit 'boundary layers' of width $\Delta\xi \sim Kn$. It is shown below that this property, combined with appropriate boundary conditions, will allow for a limited description of the Knudsen layers adjacent to the surfaces.

A second characteristic regime, as indicated by Eq. (6), would occur outside the Knudsen layers. By expanding ϕ in a power series of Kn^2, and neglecting all terms higher than Kn^2, the pressure distribution in the bulk gas would be given approximately by

$$\phi \approx \tau^* + \frac{c_1 c_2 (Kn\, q^*)^2}{\tau^* \theta} \tag{7}$$

As is evident from inspection of Eq. (7), thermal stress would create a pressure gradient in the gas, with pressure increasing towards the cooler regions in the gas. The gradient would be proportional to the square of $Kn\, q^* \sim \sqrt{\theta}\, d\theta/d(x/\lambda)$ – which can be interpreted as a Knudsen number based on the characteristic length of the temperature gradient (note that this quantity is independent of L). It should be emphasized that the effect predicted from Eq. (7) is fundamentally different than the pressure gradient created by 'thermal transpiration' of a gas in a tube with an imposed axial temperature gradient.[20,21] The latter is a result of thermal slip at the walls of the tube, and leads to a pressure that increases in the direction of increasing temperature. Thermal stress, on the other hand, results from the effect of temperature gradients on the molecular velocity distribution function within the gas.

Although the thermal stress pressure gradient can be labeled 'hydrostatic' – since the gas is at rest – it

is distinctly different than that resulting from a gravitational acceleration in the $x-$direction. Unlike the latter, thermal stress would not result in a difference between the normal forces acting on the hot and cold surfaces. In other words, the 'pressure' measured at the surfaces – which would physically represent the normal stress τ – would be identical for both surfaces.

Thermal stress, however, will result in a different value of the normal stress than that predicted from the Navier–Stokes level of approximation. This follows from conservation of energy requirements. In particular, the average pressure in the gas represents the equilibrium pressure that would be attained if the walls were instantaneously made adiabatic. Since the equilibrium pressure is used to normalize the dimensional pressure P, this statement is equivalent to

$$\int_0^1 \phi \, d\xi = 1 \tag{8}$$

Regardless of the values of q^* and Kn, the pressure distribution in the gas must satisfy the energy conservation constraint implied by Eq. (8). Consequently, the normal stress τ^* would be obtained as the eigenvalue to Eq. (6) such that the solution (for specified boundary conditions) satisfies Eq. (8). In general, this value will be different than the Navier–Stokes result of $\tau^* = 1$.

An approximate value for τ^* can be obtained by neglecting the effects of the Knudsen layers at the surfaces, for which the pressure distribution would be given by Eq. (7). To order Kn^2, this gives[16]

$$\tau^* \approx 1 - c_1 c_2 \left(Kn\, q^*\right)^2 \tag{9}$$

This relatively–simple approximation indicates that thermal stress will lower the normal stress in a closed system relative to that predicted from the Navier–Stokes level – although we note again that the effects of Knudsen layers have been neglected in the analysis.

The final elements required to close the problem are the boundary conditions for pressure. As is the case with the Navier–Stokes approximation, the boundary conditions for the Burnett equations should represent an extrapolation of the solution across the region, adjacent to the wall, where the solution is no longer valid. Makashev[19] and Schamberg[22] have proposed boundary conditions that are consistent with the order–Kn^2 accuracy of the Burnett equations. The accuracy of these approaches, however, has not been well established.[23] Alternatively, order–Kn relations can be derived for the pressure 'slip' adjacent to a heated or cooled surface.[12,21] However, our work at this stage is primarily concerned with determining whether there are boundary conditions which, when coupled to the Burnett equations, can reproduce DSMC predictions of pressure distributions in a nonisothermal gas. Therefore, the pressures at the hot and cold surfaces were taken to be parameters, and were chosen to provide the best agreement between theory and DSMC results. The obvious choice for the pressure at the surfaces will be the values determined from DSMC predictions.

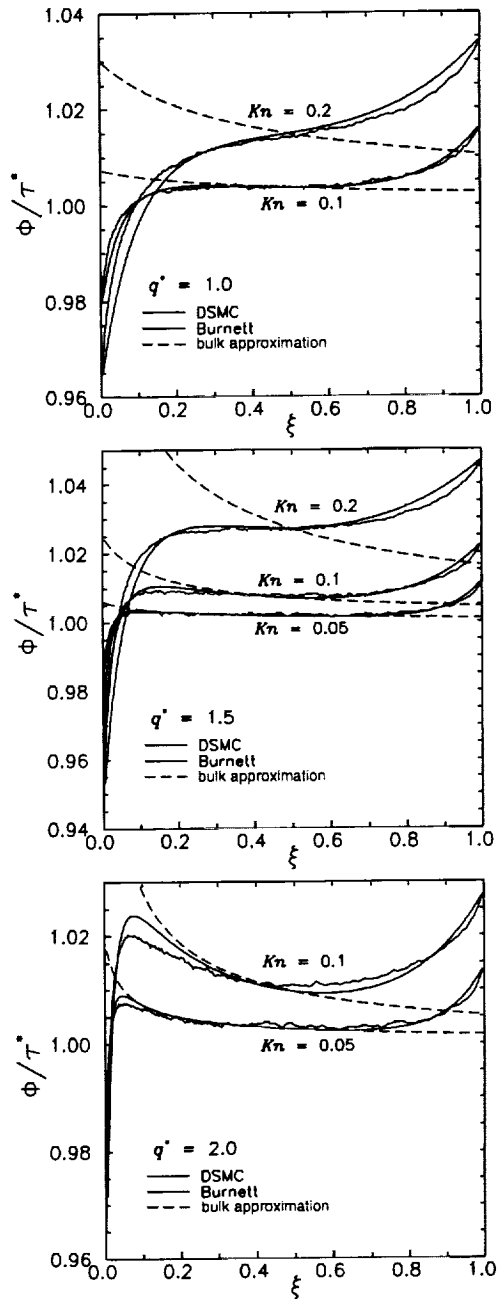

Figs. 2–4: DSMC and continuum pressure distributions

Comparisons of Burnett (via numerical solution of Eq. (6)) and DSMC predictions of pressure distribution appear in Figs. 2–4. Each plot shows $P/\tau = \phi/\tau^*$ vs.

$xi = x/L$ for a fixed value of q^*, with Kn a parameter. Two theoretical predictions of P/τ are shown for each set of DSMC results. The first corresponds to the numerical solution of Eq. (6), with boundary conditions obtained from extrapolation of the DSMC–derived pressures to the surfaces and temperatures predicted from Eq. (5). The second represents the bulk gas thermal stress pressure distribution predicted from Eq. (7), which does not account for boundary effects. This latter prediction has been shifted by a constant to match with the full–Burnett solution at $\xi = 0.5$.

As is evident from the results, the pressure profiles show distinct Knudsen layers at both the cooled and heated surfaces. The drop in pressure at the cooled surface, and the increase in pressure at the hot surface, are both consistent with the predictions of pressure slip relations.[21] The pressure drop at the cold surface can be considerable for the conditions examined here – amounting to around an 8% decrease for $Kn = 0.2$ and $q^* = 1.5$.

The solutions of the Burnett equation, with DSMC derived boundary conditions, are seen to capture the essential features of the DSMC pressure distribution. In particular, the solutions provide a good description of the width and form of the Knudsen layers and the pressure distribution outside the layers. The difference between the theoretical and DSMC results is greatest at the edge of the cold–surface Knudsen layers, for which the theoretical model tends to overpredict the pressure. This is most evident for the results corresponding to $q^* = 2.0$ in Fig. 4. Nevertheless, the fact that the Burnett equations can resolve, to a reasonable accuracy, the Knudsen layers at the surface is somewhat surprising – especially when considering that the theory is based on the order–Kn continuum temperature profile. We also examined solutions to Eq. (6) using boundary values of ϕ that were different than the DSMC results, and found that the exact, DSMC–derived boundary conditions provide the best overall agreement between Burnett equation predictions and DSMC results.

The DSMC results for $q^* = 2.0$ appear to show a pressure distribution in the bulk gas that is described by Eq. (7). On the other hand, the pressure distribution for $q^* = 1.5$ and $Kn = 0.2$ (Fig. 3) – for which Eq. (7) predicts a greater effect – is dominated by the Knudsen layers extending from the surfaces. To eliminate the effects of the Knudsen layers at the hot wall, we performed additional DSMC calculations in which the velocities of the incoming molecules at the hot boundary were sampled from the Chapman–Enskog distribution function for the fixed values of q^* and Kn. By doing so, the hot surface now approximated an open boundary. The corresponding DSMC results showed a

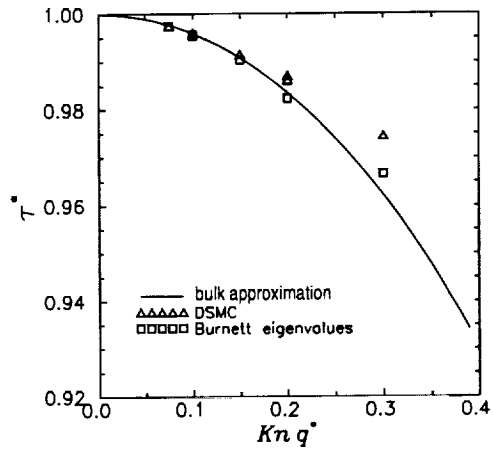

Fig. 5: DSMC and continuum normal stress

pressure distribution in the bulk gas that was accurately represented by Eq. (7).

A final comparison of theory and experiment can be obtained from the dimensionless normal stress. The simplified model of Eq. (9) indicates that τ^* should be a function primarily of $Kn\,q^*$. Accordingly, we plot in Fig. 5 the DSMC values of τ^* vs. $Kn\,q^*$ for the seven different combinations of Kn and q^* that were used in the closed system calculations (results of Figs. 2–4). Theoretical results correspond to the derived eigenvalues of Eq. (6) for the DSMC–derived boundary conditions, and to the approximation given by Eq. (9).

The first point to make is that the predictions of τ^* from full solution of the Burnett differential equation are nearly equivalent to those obtained from the bulk–gas approximation of Eq. (9). Evidently, the decrease in pressure at the cold surface is compensated by the increase at the hot, so that the Knudsen layers have a small effect on the averaged pressure in the gas. Secondly, the primary dependence of τ^* on $Kn\,q^*$ is supported in the DSMC results at $Kn\,q^* = 0.1$ and 0.2 – which each correspond to two combinations of Kn and q^*. As observed, the results are nearly identical at these points. Finally, the theoretical predictions are in excellent agreement with the DSMC results for $Kn\,q^* \leq 0.15$, beyond which the theory overpredicts the decrease in τ^*. As can be seen from the results, the relative decrease in normal stress on the surfaces is quite small, i.e., $\tau^* = 0.975$ for $q^* = 2.0$ and $Kn = 0.2$, or a 2.5% decrease in 'measured' pressure at the surface. We should emphasize, however, that this decrease is still significantly larger than the numerical precision of the DSMC simulations.

SUMMARY

The project has sought to ascertain the veracity of

the Burnett relations, as applied to slow moving, highly nonisothermal gases, by comparison of convection and stress predictions with those generated by the DSMC method. The Burnett equations were found to provide reasonable descriptions of the pressure distribution and normal stress in stationary gases with a 1−D temperature gradient. Continuum/Burnett predictions of thermal stress convection in 2−D heated enclosures, however, are not quantitatively supported by DSMC results. For such situations, it appears that thermal creep flows, generated at the boundaries of the enclosure, will be significantly larger than the flows resulting from thermal stress in the gas.

ACKNOWLEDGEMENTS

This work has been supported through NASA−MSAD contract NAG3−1882, R. Balasubramaniam, technical contract officer. The author has benefitted from helpful collaborations with Daniel Rosner and Dimitrios Papadopoulos.

REFERENCES

[1] S. Chapman, and T. G. Cowling, *The Mathematical Theory of Non Uniform Gases* (Cambridge University Press, London, 1970).

[2] C. Cergignani, *Mathematical Methods in Kinetic Theory*, Second Edition (Plenum Press, New York, 1990), ch. 5.

[3] L. A. Woods, *An Introduction to the Kinetic Theory of Gases and Magnetoplasmas*, Oxford University Press, 1993.

[4] K. A. Fisko and D. R. Chapman, "Comparison of Burnett, Super--Burnett, and Monte--Carlo solutions for hypersonic shock structure," *Rarefied Gas Dynamics: Theoretical and Computational Techniques*, E. P. Muntz, D. P. Weaver, and D. H. Campbell, Eds., Vol. 118, Progress in Astronautics and Aeronautics, 1989, pp. 374--395.

[5] G. C. Pham--Van--Diep, D. A. Erwin, and E. P. Muntz, "Testing continuum descriptions of low--Mach--number shock structures," *J. Fluid Mech.* **232**, 403 (1991).

[6] F. E. Lumpkin and D. R. Chapman, "Accuracy of the Burnett equations for hypersonic real gas flows," *J. Thermophysics Heat Transfer* **6**, 419 (1992).

[7] X. Zhong, R. W. MacCormack, and D. R. Chapman, "Stabilization of the Burnett equations and application to hypersonic flows," *AIAA J.* **31**, 1036 (1993).

[8] M. N. Kogan, "Molecular Gas Dynamics," in *Annual Review of Fluid Mechanics*, M. Van Dyke and W. G. Vincenti, Eds., Annual Review, Palo Alto, 1973, Vol. 5, pp. 383.

[9] Y. Sone, "Flow induced by thermal stress in rarefied gas," *Phys. Fluids* **15**, 1418 (1972).

[10] D. E. Rosner, "Side wall gas 'creep' and 'thermal stress convection in microgravity experiments on film growth by vapor transport," *Phys. Fluids* **A1**, 1761 (1989).

[11] A. Viviani and R. Savino, "Recent developments in vapour crystal growth fluid dynamics," *J. Crystal Growth* **133**, 217 (1993).

[12] S. K. Loyalka, "Temperature jump and thermal creep slip: rigid sphere gas," *Phys. Fluids A* **1**, 403 (1989).

[13] S. V. Patankar, *Numerical Heat Transfer and Fluid Flow*, McGraw-Hill, N.Y., 1980.

[14] G. A. Bird, *Molecular Gas Dynamics and the Direct Simulation of Gas Flows* , (Oxford, Clarendon Press, 1994).

[15] D. H. Papadopoulos and D. E. Rosner, "Enclosure gas flows driven by non--isothermal walls," *Phys. Fluids* **7**, 2535 (1995).

[16] D. W. Mackowski, D. H. Papadopoulos, and D. E. Rosner, 'Comparison of Burnett and DSMC preditions of pressure distributions and normal stress in one--dimensional, strongly nonisothermal gases," *Phys. Fluids*, in review (1998).

[17] C. J. Lee, "Unique determination of solutions to the Burnett equations," *AIAA J.* **32**, 985 (1994).

[18] M. N. Kogan, *Rarefied Gas Dynamics* (Plenum Press, New York, 1969), ch. 3.

[19] N. K. Makashev, "On the boundary conditions for the equations of gas dynamics corresponding to the higher approximations in the Chapman--Enskog method of solution of the Boltzmann equation," *Fluid Dyn.* **14**, 385 (1979).

[20] J. C. Maxwell, "On the stresses in rarefied gases arising from inequalities of temperature (appendix)," *Philos. Trans. Roy. Soc. Lond.* **170**, 231 (1979).

[21] D. C. Wadsworth, "Slip effects in a confined rarefied gas. I: temperature slip," *Phys. Fluids A* **5**, 1831 (1993).

[22] R. Schamberg, "The fundamental difference equations and the boundary conditions for high speed slip flow," Ph.D. Thesis, California Inst. Tech., Pasadena, CA, 1947.

[23] X. Zhong and K. Koura, "Comparison of solutions of the Burnett equations, Navier--Stokes equations, and DSMC for Couette flow," *Twentieth International Symposium on Rarefied Gas Dynamics*, Bejing, 1996.

PHORETIC FORCE MEASUREMENT FOR MICROPARTICLES UNDER MICROGRAVITY CONDITIONS.

E. J. Davis and R. Zheng, University of Washington, Department of Chemical Engineering, Box 351750, Seattle, WA, 98195-1750, davis@cheme.washington.edu.

INTRODUCTION

Microparticles can deposit on surfaces under the influence of a variety of forces. In the absence of gravity, forces that would otherwise be negligible become dominant. Even in a gravitational field some of these forces can be much larger than the gravitational force. Among these are the phoretic forces that arise when a small particle exists in a nonuniform gas. In the case of the thermophoretic force, molecules colliding with the particle that come from a higher temperature region exchange more momentum and kinetic energy with the particle than do molecules coming from a lower temperature region. The resulting force can cause the particle to deposit on a colder surface or move away from a higher temperature surface. Applications include particle deposition on semiconductor surfaces and on surfaces in combustion processes, containerless processing, and the production of nanophase materials, pigments and other fine particles.

Momentum and energy transfer associated with gas molecule collisions are not well understood and cannot be predicted from first principles for "engineering" surfaces. Neither of the two limiting cases of perfect accommodation or specular reflection adequately describe most collisions, so in the last century James Clerk Maxwell introduced the concept of accommodation coefficients to describe collisional processes. Experiments are needed to determine accommodation coefficients.

This research program involves theoretical and experimental studies of phoretic forces that act on micrometer-size particles. Phoretic forces are strongly dependent on the mean free path and kinetic energy of the gas molecules, and for a given microparticle monatomic, diatomic and polyatomic gases behave very differently. Li and Davis [1,2] reported measurements using helium, nitrogen and carbon dioxide for a variety of microspheres including nonvolatile liquid droplets, polystyrene latex (PSL) spheres, glass microspheres and metallic nickel spheres. These systems represent a wide range of thermal conductivities and other properties. Li and Davis compared their results with numerous theories in existence, and to make such comparisons it is necessary to know the thermal properties of the gas and microparticle. Furthermore, their work was limited to spherical particles. Many microparticles of interest have irregular shapes and unknown thermal properties, so it is necessary to measure their thermal properties to interpret and predict the thermophoretic force.

To perform thermophoretic force experiments we have built a special electrodynamic balance (EDB) equipped with heat exchangers mounted in a vacuum chamber. The chamber pressure can be varied to alter the mean free path of the gas molecules. The thermal and radiative properties of microparticles can also be measured by single particle experiments in which a charged microparticle is levitated in an EDB and illuminated with a laser beam. The principles and applications of the EDB have been surveyed by Davis [3,4]. Spjut *et al.* [5] at MIT introduced the electrodynamic thermogravimetric analyzer (EDTGA) for the study of carbonaceous particles, and the MIT group performed a variety of investigations reviewed by Bar-Ziv *et al.* [6]. These include particle temperature measurements by infrared pyrometry and transient heating experiments [7]. Bar-Ziv and Sarofim [8] provided an additional review of the literature associated with particle heating in an EDB, including the effects of microparticle properties on the electromagnetic heat source function.

Monazam *et al.* [9] and Monazam and Maloney [10] at the Morgantown Energy Technology Center (METC) adapted the techniques of Spjut and his coworkers to determine heat capacities, temperatures and absorptivities of single carbon particles by means of pulsed heating experiments. A levitated particle with a diameter of order 100 μm was illuminated from two sides using a CO_2 laser (10.6 μm wavelength) with a repetition rate of 100 Hz and a pulse duration of 3 ms. The particle temperature was determined from measurements of the radiant emissive power of the particle using Planck's distribution law for the monochromatic radiant emission intensity.

The time-dependent temperature distribution in the microsphere was modeled by assuming that the heat flux associated with the electromagnetic radiation is uniform over the surface of the sphere. That is, the heat source was treated as a boundary condition rather than as an electromagnetic heat source within the sphere. Convective and radiative heat losses were included in the surface boundary condition, but for the conditions of the experiments gas phase conduction was the dominant heat loss. They solved the governing unsteady state heat conduction equation numerically, and performed parametric studies, comparing predicted surface temperatures with measured temperatures. The authors recognized that the use of a spatially uniform energy flux at the surface is an approximation that may not be valid for other materials with physical and optical properties that differ from carbon.

It was the objective of part of our recent studies to develop a more rigorous analysis of unsteady state

heating of a sphere by electromagnetic radiation, taking into account a spatially-dependent surface energy flux based on Mie theory. The analysis of the METC group is recovered as a special case of a more general formulation.

PULSED HEATING OF MICROSPHERES

The governing conduction equation and auxiliary conditions used by Monazam and his coworkers are

$$\rho_1 C_1 \frac{\partial T}{\partial t} = \kappa_1 \frac{1}{r^2} \frac{\partial}{\partial r}\left(r^2 \frac{\partial T}{\partial r} \right), \tag{1}$$

with auxiliary conditions

$$T(r,0) = T_0, \quad \frac{\partial T}{\partial x}(0,x) = 0, \tag{2}$$

and

$$\kappa_1 \frac{\partial T}{\partial r}(a,t) = \frac{1}{2}\alpha_r I_{inc}(t) - \left\{ h_c [T(a,t) - T(\infty,t)] + \sigma \varepsilon_r \left[T^4(a,t) - T^4(\infty,t) \right] \right\} \tag{3}$$

The boundary condition at the surface of the sphere includes the time-dependent intensity, $I_{inc}(t)$, of the pulsed incident beam, the convective heat transfer coefficient, h_c, and the radiative heat loss. The absorptivity, α_r is assumed to equal the emissivity, ε_r, of the particle. Here, κ_1 is the thermal conductivity of the microparticle, and σ is the Stefan-Boltzmann constant. The incident intensity in the surface boundary condition is divided by two because the laser beam was split to heat the particle from two sides.

Monazam *et al.* solved this system of equations numerically, but for the conditions used in their experiments an approximate analytical solution can be obtained. This is accomplished by writing the linear approximation

$$T^4(a,t) - T_\infty^4 \cong h_r [T(a,t) - T_\infty], \tag{4}$$

in which h_r is a radiant energy heat transfer coefficient defined by

$$h_r = \left[T_m^2(a,\infty) + T_\infty^2 \right] \left[T_m(a,\infty) + T_\infty \right] \tag{5}$$

and $T_m(a,\infty)$ is the mean surface temperature at large times, which can be computed by solving an energy balance on the sphere under the assumption that the heat flux averaged over one cycle is zero at large times

The heat transfer coefficient, h_c, is κ_2/a for a stagnant gas and for low gas Peclet numbers. For the conditions of the METC researchers, h_r was less than 10% of h_c, so the linearization should be accurate at later times. The heat loss at early times is overestimated by this approximation because h_r is overestimated by using the asymptotic mean surface temperature. Thus, it can be anticipated that the analytical solution developed using approximation (4) will underpredict the temperature at small times but should be accurate after some transient period.

The solution of the linearized problem is

$$\frac{T(x,\tau) - T_0}{T_0} = 2\beta(1 - Bi) \sum_{n=1}^{\infty} \frac{\sin \lambda_n}{(\sin^2 \lambda_n - Bi)} \frac{\sin \lambda_n x}{x} \int_0^\tau f(\tau') \exp\left[-\lambda_n^2 (\tau - \tau') \right] d\tau', \tag{6}$$

in which β, Bi, x and τ are dimensionless parameters and variables defined by

$$\beta = a\alpha_r I_{inc}/2\kappa_1 T_0, \quad Bi = (h_c + h_r)a/\kappa_1, \quad x = r/a, \quad \tau = \kappa_1 t / a^2 \rho_1 C_{pl}. \tag{7}$$

Here the subscript 1 refers to the particle and 2 denotes the gas, β is the dimensionless electromagnetic energy flux, Bi is a composite Biot number, and $f(\tau)$ is the normalized laser pulse function, which is unity for the first 3 ms of a pulse and zero for the next 7 ms for the experimental conditions at METC.

The eigenvalues in Eq. (5) satisfy the transcendental equation

$$\tan \lambda_n = \lambda_n / (1 - Bi). \tag{8}$$

The solution represented by Eq. (6) is compared with the numerical solution of Monazam and Maloney in Figure 1. The physical parameters they used are a = 70 μm, $\alpha_r = \varepsilon_r = 0.85$, $I_{inc} = 4.50$ MW/m^2, $\kappa_1 = 1.675$ W/m-K, $\kappa_2 = 0.048$ W/m-K, $C_1 = 1466$ J/kg-K, and $\rho_1 = 1050$ kg/m^3. The Biot number corresponding to their conditions is 0.032. The agreement is excellent at later times, and during the transient period when the time-averaged temperature changes, the analytical solution predicts temperatures only slightly lower than the numerical solution.

A more detailed comparison between theory and experiment is shown in Figure 2 for one cycle in the asymptotic region. The agreement is very good, indicating that the best-fit parameters selected by Monazam and Maloney are consistent with their model of uniform surface heating.

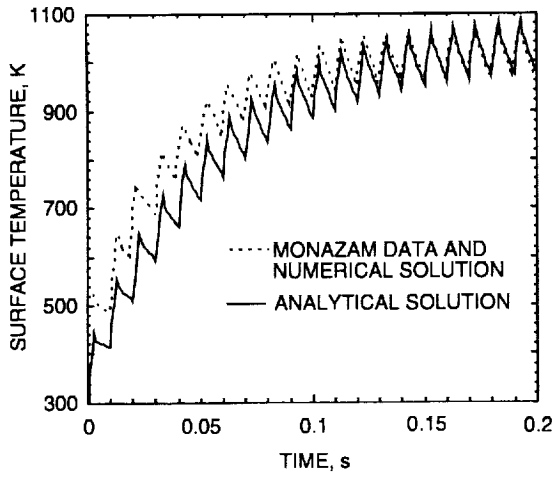

Figure 1. A comparison between theory and experiment for a carbonaceous particle.

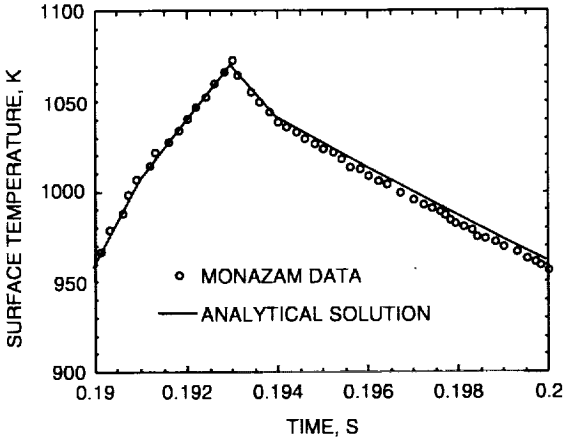

Figure 2. A comparison between theory and experiment for one cycle at later times.

SPATIALLY NONUNIFORM HEATING

The assumption of uniform surface heating is highly questionable when the thermal conductivity of the particle is not as large as that of carbon. For the 140 μm diameter sphere of Monazam and Maloney, the light scattering size is $X = 2\pi a/\lambda = 41.498$. Using a refractive index of $N = 5.0+i4.0$, we computed the source function, $\mathbf{E}\cdot\mathbf{E}^*/E^2_{inc}$, presented in Figure 3 for one-sided heating using Mie theory as outlined by Bohren and Huffman [9]. Due to the strong absorption of electromagnetic energy, the source is concentrated near the surface, as assumed by Monazam and Maloney, but the source is highly nonuniform in the θ-direction. Our computations indicate that all of the energy absorption is confined to the outer 2% of the sphere, that is, to the region $x = r/a > 0.98$, and the source function is nearly independent of azimuthal angle φ.

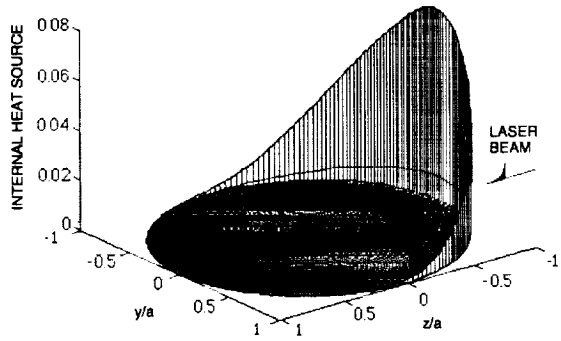

Figure 3. The internal heat source function for a carbonaceous sphere with X = 41.498 and $N = 5.0+I4.0$.

The internal heat generation function for an absorbing sphere is

$$Q(r,\theta,\phi) = \frac{4\pi I_{inc} Re[N_1]Im[N_1]}{\lambda_{inc}} \frac{\mathbf{E}\cdot\mathbf{E}^*}{E^2_{inc}}. \qquad (9)$$

The pulsed heating problem can now be solved using a source function such as that depicted in Figure 3 or, alternately, as an equivalent surface source problem. For two-sided heating, the shape of the source function, considered as the surface source shown in Figure 3, can be approximated by the intensity distribution

$$I(a,\theta) = I_{max}\cos^2\theta. \qquad (10)$$

Here I_{max} is the intensity at $\theta = 0°, 180°$, and θ is measured from the direction of propagation of one of the laser beams. This approximation is in very good agreement with the exact surface intensity distribution computed from Mie theory as demonstrated in Figure 4.

When the angular dependence of the temperature distribution is considered, the nondimensional heat conduction equation becomes

$$\frac{\partial U}{\partial \tau} = \frac{1}{x^2}\frac{\partial}{\partial x}\left(x^2\frac{\partial U}{\partial x}\right) + \frac{1}{x^2}\frac{\partial}{\partial \eta}\left[(1-\eta^2)\frac{\partial U}{\partial \eta}\right], \qquad (11)$$

in which

$$U = \frac{T - T_0}{T_0}, \quad \text{and} \quad \eta = \cos\theta. \qquad (12)$$

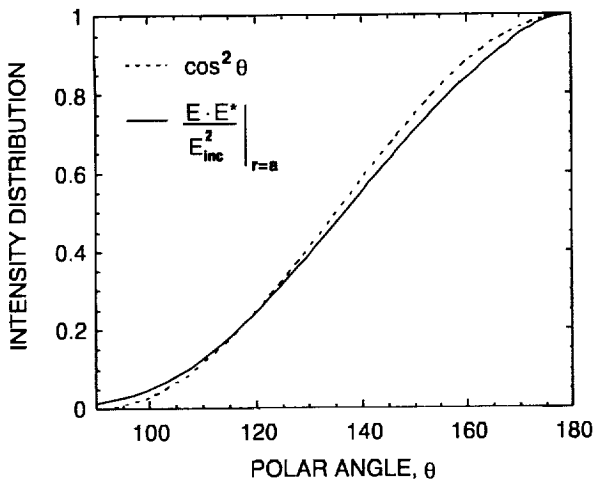

Figure 4. Comparison between the exact solution for the surface intensity distribution and Eq. (10).

The auxiliary conditions are given by

$$U(x,\eta,0)=\frac{\partial U}{\partial x}(0,\eta,\tau)=0, \tag{13}$$

and

$$\frac{\partial U}{\partial x}(1,\eta,\tau)=3\beta f(\tau)\eta^2-\mathrm{Bi}U(1,\eta,\tau). \tag{14}$$

The solution for the surface temperature is

$$U(1,\eta,\tau)=\frac{\beta}{(2+\mathrm{Bi})}\left\{[-f(\tau)]+\sum_{m=1}^{\infty}(6I_1+\gamma_{m0}^2 I_2)\frac{X_{m0}(1)}{N_{m0}^2}\int_0^\tau f(\tau')e^{-\gamma_{m0}^2(\tau-\tau')}d\tau'+(3\eta^2-1)\sum_{m=1}^{\infty}\gamma_{m2}^2 I_3\frac{X_{m2}(1)}{N_{m2}^2}\int_0^\tau f(\tau')e^{-\gamma_{m2}^2(\tau-\tau')}d\tau'\right\}. \tag{15}$$

Here N_{m0} and N_{m2} are the norms of the eigenfunctions $X_{m0}(x)$ and $X_{m2}(x)$, respectively, given by

$$N_{m0}=\sqrt{(\gamma_{m0}-\sin\gamma_{m0}\cos\gamma_{m0})/\pi\gamma_{m0}^2}, \tag{16}$$

and

$$N_{m2}=\sqrt{\frac{1}{2}\left[J_{5/2}^2(\gamma_{m2})+J_{3/2}^2(\gamma_{m2})\right]-\frac{5}{2\gamma_{m2}}J_{5/2}(\gamma_{m2})J_{3/2}(\gamma_{m2})}. \tag{17}$$

The eigenfunctions may be written in terms of Bessel functions as

$$X_{m0}(x)=\frac{1}{\sqrt{x}}J_{1/2}(\gamma_{m0}x), \tag{18}$$

and

$$X_{m2}(x)=\frac{1}{\sqrt{x}}J_{5/2}(\gamma_{m2}x). \tag{19}$$

The eigenvalues γ_{m0} satisfy Eq. (8), and the eigenvalues γ_{m2} satisfy

$$\tan\gamma_{m2}=\frac{\gamma_{m2}^3-3(3-\mathrm{Bi})\gamma_{m2}}{(4-\mathrm{Bi})\gamma_{m2}^2-3(3-\mathrm{Bi})}, \tag{20}$$

The integrals I_1, I_2 and I_3 are defined by

$$I_1=\int_0^1 x^2 X_{m0}(x)dx, \tag{21}$$

$$I_2=\int_0^1 x^4 X_{m0}(x)dx, \tag{22}$$

and

$$I_3=\int_0^1 x^4 X_{m2}(x)dx. \tag{23}$$

For Biot numbers larger than those for relatively highly conducting carbon spheres Eq. (15) predicts very large angular variation in the surface temperature. Such variations must be taken into account in the interpretation of data to determine the thermal properties. The surface temperatures at $\theta = 0°$ and $90°$ are illustrated in Figure 5 for $\kappa_1 = 0.167$ W/m-K (Bi = 0.320). The other physical properties are those used by Monazam and Maloney. Additional results have been reported in a paper by Davis and Widmann [12] that is in press.

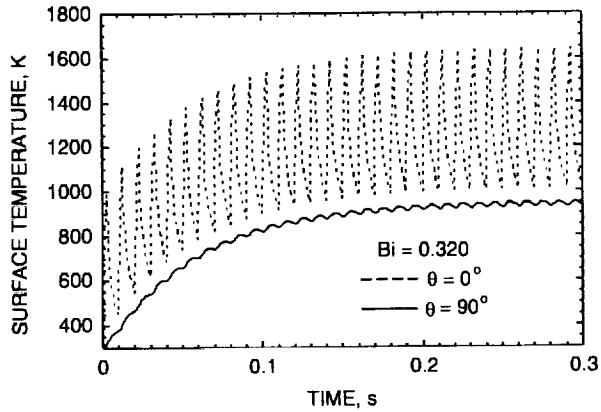

Figure 5. Surface temperature histories for a lower thermal conductivity particle.

THERMOPHORETIC FORCE

The existing apparatus used for thermophoretic force measurements, which is shown in Figure 6, has been modified to improve the data acquistion system and to facilitate the alignment of the electrodes used for particle levitation. Studies of the effects of natural convection on the thermophoretic force have been carried out over a wide range of system pressures, and Figure 7 shows the levitation voltage as a function of pressure for a polystyrene latex sphere in air.

The change in the levitation voltage (with and without a temperature gradient in the gas phase) yields the ratio of the thermophoretic force to the gravitational force. If V_0 is the dc levitation voltage required to balance the gravitational force, mg, and V is the levitation voltage required to balance the particle when gravity and other external forces, F, act on the particle, the force ratio F/mg is given by

$$F / mg = (V_0 - V)/ V_0. \qquad (24)$$

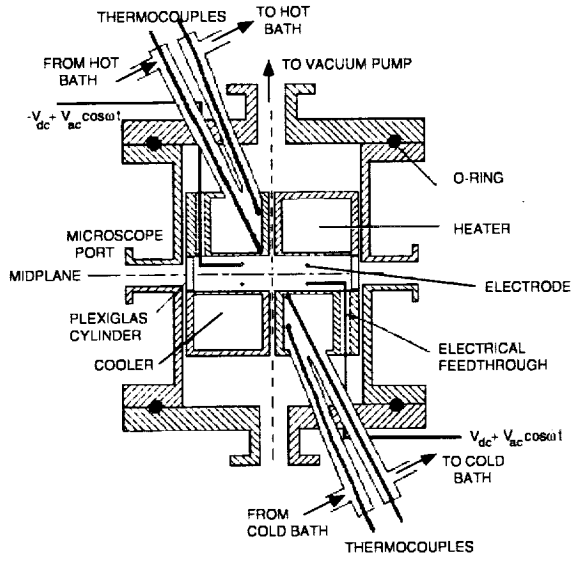

Figure 6. Cross section of the electrodynamic balance used for thermophoretic force measurement.

The external forces can include the phoretic force as well as aerodynamic drag associated with convective motion of the gas.

The data of Figure 7 indicate that for pressures greater than 20 torr natural convection occurred due to edge effects associated with temperature differences between the heat exchangers and the chamber wall, but those effects become negligible as the system pressure decreases. At low pressures the free-molecule regime is reached, and the force becomes independent of pressure.

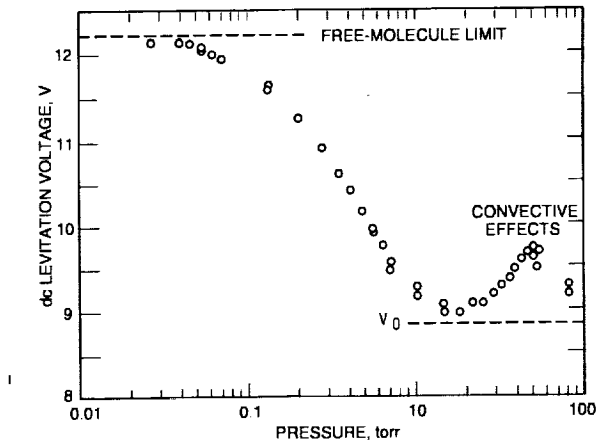

Figure 7. Levitation voltage data for a PSL sphere in air as a function of the chamber pressure.

Data for the intermediate or transition regime (between the continuum regime and the free-molecule regime) are used to determine the accommodation coefficients for momentum and energy transfer between the gas molecules and the microparticle.It is highly desirable to minimize the effects of natural convection, and modifications in the apparatus will be made to do so.

ACKNOWLEDGMENT

The authors are grateful to NASA for the support of this research through Grant NAG3-1837.

REFERENCES

1. W. Li and E. J. Davis, Measurement of the Thermophoretic Force by Electrodynamic Levitation: Microspheres in Air, *J. Aerosol Sci.* **26**:1063-1083 (1995).
2. W. Li and E. J. Davis, The Effects of Gas and Particle Properties on Thermophoresis, *J. Aerosol Sci.* **26**:1085-1099 (1995).
3. E. J. Davis, Microchemical Engineering: The Chemistry and Physics of the Microparticle, in *Advances in Chemical Engineering*, Vol. 18, J. L. Anderson, ed., Academic Press, New York, pp. 1-94, 1992.
4. E. J. Davis, A History of Single Aerosol Particle Levitation, *Aerosol Sci. Technol.* **26**, 212-254 (1997).
5. R. E. Spjut, E. Bar-Ziv, A. F. Sarofim and J. P. Longwell, Electrodynamic Thermogravimetric Analyzer, *Rev. Sci. Instrum.* **57**, 1604-1610 (1986).
6. E. Bar-Ziv, D. B. Jones, R. E. Spjut, D. R. Dudek, A. F. Sarofim and J. P. Longwell, Measurement of Combustion Kinetics of a Single Char Particle in an

Electrodynamic Thermogravimetric Analyzer, *Combust. Flame* **75**, 81-106 (1989).

7. R. E. Spjut, A. F. Sarofim and J. P. Longwell, Laser Heating and Particle Temperature Measurement in an Electrodynamic Balance, *Langmuir* **1**, 355-360 (1985).
8. E. Bar-Ziv and A. F. Sarofim, The Electrodynamic Chamber: A Tool for Studying High Temperature Kinetics Involving Liquid and Solid Particles, *Prog. Energy Combust. Sci.* **17**, 1-65 (1991).
9. E. R. Monazam, D. J. Maloney and L. O. Lawson, Measurements of Heat Capacities, Temperatures, and Absorptivities of Single Particles in an Electrodynamic Balance, *Rev. Sci. Instrum.* **60**, 3460-3465 (1989).
10. E. R. Monazam and D. J. Maloney, Temperature Transients Associated with Pulsed Heating of Single Particles, *J. Appl. Phys.* **71**, 2552-2559 (1992).
11. C. F. Bohren and D. R. Huffman, *Absorption and Scattering of Light by Small Particles*, John Wiley and Sons, New York, 1983.
12. E. J. Davis and J. F. Widmann, Pulsed Electromagnetic Heating of Microparticles, *Intl. J. Heat Mass Transfer*, in press (1998).

SURFACTANTS ON A DROPLET IN AN EXTENSIONAL FLOW: STRESSES CREATED BY MONOLAYER-FORMING SURFACTANTS

C. E. Eggleton[1] and K. J. Stebe[2], [1]Department of Mechanical Engineering , UMBC, 1000 Hilltop Circle, Baltimore, MD 21250, eggleton@umbc7.umbc.edu; [2]Department of Chemical Engineering, The Johns Hopkins University, 3400 North Charles Street, Baltimore, MD 21218, kjs@jhu.edu

INTRODUCTION

Surfactants adsorb on interfaces of moving drops or bubbles and reduce the surface tension γ. Surface convection redistributes adsorbed surfactant, creating surface tension gradients or Marangoni stresses. Through these mechanisms, surfactants alter the stress balance at the interface. Consider the example of a droplet centered in an extensional flow as shown in Figure 1.

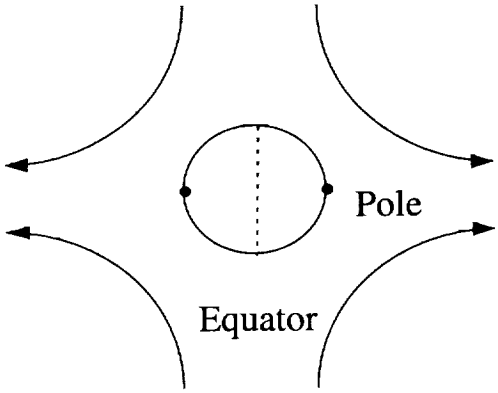

Figure 1

The surfactant adsorbed on the interface is swept by surface convection away from the equator and toward the drop poles. If surfactant mass transfer is slower than the surface convective flux, surfactant accumulates near the drop poles, and is depleted near the equator. The surface tension at the poles is reduced, causing a Marangoni stress to pull from the pole toward the equator resisting the surface velocity. The local normal stress balance is also altered; the regions of lower surface tension require higher mean curvatures to balance the normal stress jump. These stresses alter the resulting flow fields and the deformation of the droplet.

Such phenomena have been extensively studied in the context of a simple model in which γ is assumed to depend linearly on the surface concentration Γ, and Γ to be linearly related to the bulk concentration C. These assumptions are limited to trace surfactant concentrations. They are of limited utility even when dilute amounts of surfactant are present, since locally elevated surface concentrations can be created by the surface convective flux, and the assumed linear relationship between the surface tension and the local surface concentration breaks down. This linear relationship neglects the finite dimensions of the surfactant molecules at the interface. The surface pressure Π is defined:

$$\Pi = \gamma_o - \gamma(\Gamma)$$

where γ_o is the surface tension in the absence of surfactant. Let Γ_∞ denote the upper bound to the surface concentration that can be accommodated in a monolayer; or $1/\Gamma_\infty$ be the limiting area/molecule. The surface pressure is the work per unit area to compress a surfactant monolayer; Π increases strongly when $1/\Gamma_\infty$ is approached. A typical isotherm showing such behavior for an insoluble surfactant is shown in Figure 2.

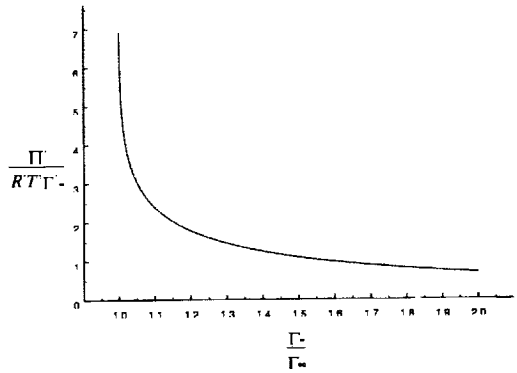

Figure 2

In this limit, contraction of the interface is strongly resisted, whereas expansion is not. That is, the interface behaves as if it were incompressible, but not inextensible. One surface tension model which accounts for this behavior is[1]:

$$\Pi = \gamma_o - \gamma(\Gamma) = -RT\Gamma_\infty \ln(1 - \Gamma/\Gamma_\infty)$$

which is commonly adopted to explain the surface tension data for a wide range of surfactants.[2] In this expression, RT is the product of the ideal gas constant and the temperature. The Marangoni stresses that occur are proportional to the derivative of this expression:

$$\nabla_s \gamma(\Gamma) = -\frac{RT}{(1-\Gamma/\Gamma_\infty)} \nabla_s \Gamma$$

Note that for Γ approaching Γ_∞, these equations are singular. The singularities prevent the surface concentration from reaching its upper bound through two effects. Suppose that surfactant is swept by surface convection toward the drop pole, forcing surfactant to collect there. Elevated Marangoni stresses develop, opposing the surface convective flux, forcing the local Γ to remain less than Γ_∞. The surface tension is also strongly reduced, allowing the interface to deform more easily and to decrease Γ. The Marangoni stress manifests first; the interface can be strongly stressed tangentially while the surface tension is still finite.

Using this model, a drop in an extensional flow is studied in the limit where the internal and external fluid viscosities μ are equal. The aim is to understand surfactant effects on strongly deforming interfaces. For example, consider a non-deforming spherical droplet with a surfactant-laden interface. It is understood that the interface can be rendered partially immobile if the surfactant is insoluble (the stagnant cap regime) or completely immobile if such surfactant is present in sufficient quantity.[3-5] This same interface can be made tangentially mobile if a surfactant is introduced with mass transfer rates that are sufficiently rapid, again at high surfactant concentration.[6] The question of how a deforming droplet interface behaves in such limits is the focus of this work.

The response of a spherical droplet of radius a to an applied flow with strain rate G is studied. Initially, the surfactant is uniformly distributed on the interface, with initial surface concentration Γ_{eq} and surface tension γ_{eq}. The ratio of the characteristic viscous stresses that deform the drop to the Laplace pressures that resist deformation defines the capillary number Ca:

$$Ca = \frac{\mu G a}{\gamma_{eq}}$$

The drop is studied as a function of the strain rate (Ca) and the fraction of interface initially covered by surfactant :

$$x = \frac{\Gamma_{eq}}{\Gamma_\infty}$$

The coverage x is varied from 0.01-0.996. (Such coverages can be realized for surfactants in experiment.)

The initially spherical drop deforms quasistatically until some steady shape is attained for the specified Ca and x; Ca is then augmented, and the evolution to a new steady shape is recorded. This proceeds until the strain rate is so large that no steady shape can be attained. The deformation DF as a function of Ca and x is found as a part of the solution, and reported here. However, the main focus of this work is to gain insights into the constitutive behavior at the interface, particularly at high surfactant concentrations.

These results are discussed in greater detail in Eggleton *et al.*[7] and Eggleton & Stebe[8], along with a thorough review of previous work on this problem. In this paper, three issues are addressed:

(i) *The physical chemical mechanism which causes stagnant regions to occur at steady state on the interface for finite Ca is described.* For insoluble surfactants, the stagnant cap limit is shown to apply to any axisymmetric fluid particle at steady state when surface diffusion is negligible. In particular, at low surface coverages ($x<<1$) stagnant tips are shown to occur at the drop poles. At elevated coverages, (e.g. x=0.99) the entire interface is rendered immobile in this limit. This is caused at finite Ca by the Marangoni stress which strongly opposes the surface velocity to prevent Γ from reaching Γ_∞ anywhere on the interface. At high initial coverages, any surface concentration gradient causes Γ to approach Γ_∞ near the poles. Therefore, a strong Marangoni stress resisting the accumulation occurs for an infinitesimal surface concentration gradient. As a result, Γ remains nearly spatially uniform, not only at steady state, but throughout the deformation process.

(ii) *A new paradigm is proposed to describe the (unsteady) mechanical behavior of surfactant-laden interfaces at elevated concentration.* The observation that Γ remains spatially uniform for x near unity for an insoluble surfactant is used to pose a new manner for describing the interface at high surfactant concentration. Throughout the deformation, Marangoni stresses regulate the tangential velocity to force Γ to remain spatially uniform. The surface mass balance is simplified assuming that no gradients in Γ develop. This balance then constrains the global area dilatation to balance local dilatation. This approach is shown to agree with the full solution.

(iii) *These results are extended to soluble surfactants with adsorption/desorption controlled mass transfer.* For soluble surfactants, the adsorption-desorption controlled limit is studied. For high initial surface concentrations in the insoluble limit, the Marangoni stress alone regulates the surface velocity to force Γ to remain everywhere less than Γ_∞. However, soluble surfactants can adsorb/desorb to enforce the limiting area/surfactant molecule constraint. Surfactants swept by surface convection can be replenished near the equator by adsorption, and removed from the pole by desorption. This allows the tangential velocity to remain finite while Γ remains everywhere less than Γ_∞. The tangential velocity increases to the clean interface limit as the adsorption-desorption rates increase relative to the surface convection rate. In the high coverage limit, Γ again remains spatially uniform, and increases with the mass transfer rate to its equilibrium

value. A simplified approach neglecting Γ gradients in the mass balance agrees with the full solution.

GOVERNING EQUATIONS

An initially spherical droplet of radius a is centered in an pure extensional flow in the creeping flow limit. Quantities associated with the internal (external) fluid are denoted with subscript 1 (2). The governing equations are stated here in dimensionless form, where the following scales have been adopted:

$$p_i = \frac{p_i' a'}{\gamma_{eq}'};\ t = \frac{t'}{G'};\ j = \frac{j'}{\Gamma_{eq}' G'}$$

$$\Gamma = \frac{\Gamma'}{\Gamma_{eq}'};\ x = \frac{x'}{a'};\ v_i = \frac{v_i'}{a' G''}$$

(In this equation only, dimensional quantities are indicated by a prime). The pressure and velocity in fluid i are denoted by p_i and v_i, respectively; the surface velocity is denoted v_s; time is denoted t, mass flux between the interface and the bulk is denoted j. The position vector with respect to the center of mass of the drop is denoted x; the interface is located at $x_s(t)$. All lengths are made dimensionless by the drop radius.

The velocities fields are subject to the following boundary conditions:

(i.) The velocities are continuous at the interface:

$$v_1 = v_2 = v_s$$

(ii.) The interface deforms according to the kinematic condition:

$$\frac{dx_s}{dt} = (n \cdot v_s)n$$

where n is the unit normal vector to the interface.

(iii.) The stress balance at the interface requires:

$$[-p]n + Ca[\, n \cdot \tau\,] = 2H\gamma n - \nabla_s \gamma$$

where τ is the rate of strain tensor; the quantities in square brackets represent jumps; $-\nabla_s\gamma$ denotes the a Marangoni stress and $2H$ is the mean curvature of the interface.

(iv.) The equations for γ and $\nabla_s\gamma$ in dimensionless form become:

$$\gamma(\Gamma) = \frac{\gamma_o}{\gamma_{eq}} + E\ln(1 - x\Gamma)$$

$$\nabla_s \gamma(\Gamma) = -\frac{Ex}{(1 - x\Gamma)}\nabla_s \Gamma$$

where E is the elasticity parameter defined:

$$E = \frac{RT\Gamma_\infty}{\gamma_{eq}}$$

(v.) The surface mass balance determines the local surface concentration Γ:

$$\frac{\partial \Gamma}{\partial t} + \nabla_s \cdot (\Gamma v_t) - \frac{1}{Ca\Lambda}\nabla_s^2 \Gamma + 2Hv_n\Gamma = j$$

where v_t is the tangential surface velocity and v_n is the normal surface velocity. The dimensionless surface diffusion coefficient, scaled with surface tension-related quantities is defined:

$$\Lambda = \frac{\gamma_{eq} a}{\mu D_s}$$

For insoluble surfactants, the flux from the bulk j is zero. (The form for j for adsorption-desorption control is discussed with the results.)

(vi.) The far field velocity is:

$$lim_{x\to\infty} v_1 = v_\infty = \begin{bmatrix} -1 & 0 & 0 \\ 0 & -1 & 0 \\ 0 & 0 & 2 \end{bmatrix} \cdot x$$

(vii.) The velocities fields in both fluids obey Stokes' equations which can be recast to give the axisymmetric boundary integral formula for the surface velocity:

$$v_s(x_s) = v_\infty(x_s) - \frac{1}{8\pi}\int_{s=0}^{s=L} M(x_s, \zeta) \cdot \{-[p]n + Ca[n \cdot \tau]\}(\zeta) d\zeta$$

where M is the axisymmetric Greens' function for Stokes' flow and ζ is the integration variable along the interface. The function M is singular when x_s approaches ζ. The manner in which these singularities are avoided and the details of the solution technique are discussed in Pawar & Stebe[9].

The two parameters related to the surfactant physical chemistry are fixed (*i.e.* E=0.2, a typical value. Λ=10^3, indicating weak surface diffusion, but not as weak as is typical in experiment). The drop is initially spherical with Γ=γ=1.0. The flow field is initiated at fixed Ca and coverage x. The stress jump for the initial shape is known and substituted into the boundary integral equation. Using v_s from this equation, the interface location x_s and curvature $2H$ are updated. Using the surface mass balance, Γ is redistributed. The stress jump and v_s are recalculated. This continues until either v_n tends to zero and the drop has attained a steady shape, or until no such steady solution can be obtained. Thus, the quasistatic evolution of the droplet from its initial state to the largest stable deformation realizable is obtained.

RESULTS

I. Insoluble Surfactants

If large surface concentration gradients develop as a result of the imposed flow, the surface tension near the poles will be strongly reduced. The normal stress jump will then generate a more highly curved tip region, causing the drop to deform more than it would in the absence of surfactant; this is termed the tip

stretching dominated regime. If only weak concentration gradients develop, the interface dilutes uniformly as the deformation proceeds, smaller deformations result when compared to the clean interface case; this is the dilution dominated regime. The deformations realized for insoluble surfactants as a function of x are presented in Figure 3. where the deformations are defined: DF=(L-B)/(L+B), L being the length and B the breadth of the droplet. The DF realized are tip stretching dominated for small x, and dilution dominated as x approaches unity.

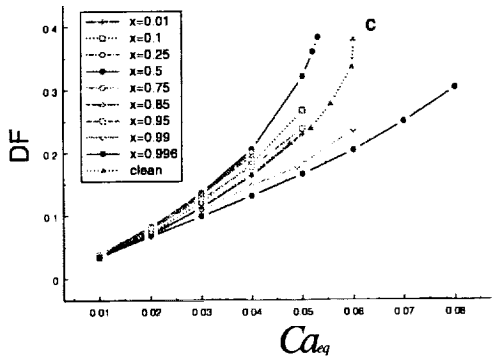

Figure 3

The corresponding (steady state) surface concentration and surface velocity profiles are shown as a function of x in Figures 4 and 5, respectively, for Ca=0.04. The governing equations are solved in terms of arclength s; the results are presented here for s normalized by the drop half-length; s=0 locates the drop pole, s=0.5 the drop equator.

First consider the results for small x ($x \leq 0.5$). The coupling between the Marangoni stress and surface concentration gradients is initially weak (e.g. for x=0.1, $\nabla_s\gamma$ is initially roughly $Ex\nabla_s\Gamma$ = $0.02\nabla_s\Gamma$.) Therefore, the surface convective flux is initially strong, sweeping surfactant toward the drop tips. This continues until the surfactant accumulation is sufficient to generate a large Marangoni stress opposing the surface velocity. At steady state, Γ is elevated in the drop tip region, depleted near the drop equator. This is indeed consistent with the occurrence of deformations in excess of the surfactant-free droplet.

As the initial coverage increases, so does the Marangoni stress resisting accumulation at the poles. The gradients in Γ diminish with x. The surface velocity is strong in the regions where Γ is low, small where Γ is large. This is the signature of stagnant cap behavior. Stagnant caps have been shown to occur on translating drops when surface diffusion is negligible. The surface mass balance reduces to the requirement that the product $v_t\Gamma$=0. For this flow, when surface diffusion is neglected, (Λ infinite), the interface is indeed divided into stagnant and mobile regions.

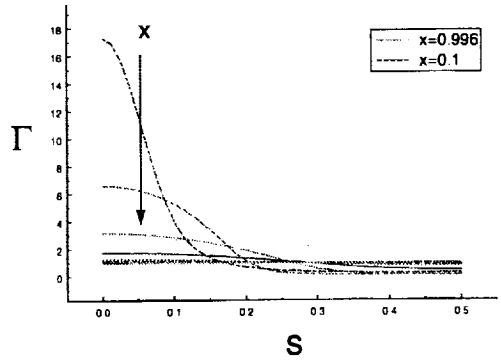

Figure 4

The occurrence of stagnant caps may be significant in the phenomenon of tip streaming, which has been observed in the experiments of de Bruin[10]. In these experiments, surfactants are present at dilute concentrations. Bubbles are subjected to flow fields which cause them to form pointed tips from which surfactant-rich drops are shed from relatively surfactant-poor parent drops. When surfactants are deliberately added in high concentration, the phenomenon is suppressed. Thus far, this phenomenon has not been described. We seek to demonstrate tip streaming in the regime of x <<1 for drop:external fluid viscosity ratios<<1.

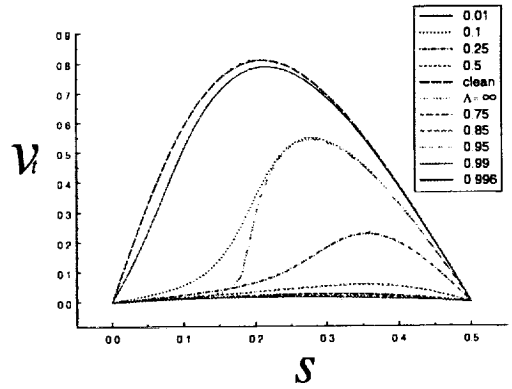

Figure 5

As the surfactant coverage increases, the initial coupling between the Marangoni stresses and the surface concentration gradients becomes large. For example, at x=0.996, $\nabla_s\gamma$ is initially $\nabla_s\Gamma Ex/(1-x) \cong 50\nabla_s\Gamma$.) Consider the results for x=0.996. Strong Marangoni stresses arise for small concentration gradi-

ents. The strongly stressed interface forces Γ to remain nearly uniform as the deformation proceeds. At high x, the drop deforms less than the surfactant-free case, consistent with a dilution dominated mechanism. At steady state, the tangential velocities are small for Λ of 10^3; for Λ infinite, they would be zero.

The observation that Γ remains uniform for elevated x is used to propose a simplified boundary condition for the drop interface throughout the deformation process that reduces to the no-slip condition at steady state. In the surface mass balance, terms associated with concentration gradients are neglected. The balance then requires the tangential mass flux to supply regions diluted by surface dilatation to keep the concentration uniform.

$$-\frac{1}{\Gamma}\frac{\partial\Gamma}{\partial t}=\frac{1}{A}\frac{dA}{dt}=\nabla_s\cdot(v_t)+2Hv_n$$

The far right hand side of this equation is the local surface dilatation. Since the surfactant is insoluble, the rate of change of Γ is related to the total area of the droplet A. This condition relates the local area dilatation to the global area dilatation. The evolution of the droplet is studied for x=0.996 using this equation instead of the full surface mass balance to calculate Γ for *Ca* up to the highest *Ca* for which a stable drop shape could be attained. The results for Γ are shown in Figure 6; the symbols are the approximate solution, the lines the full solution. The deformations agree to better than 1% for all cases.

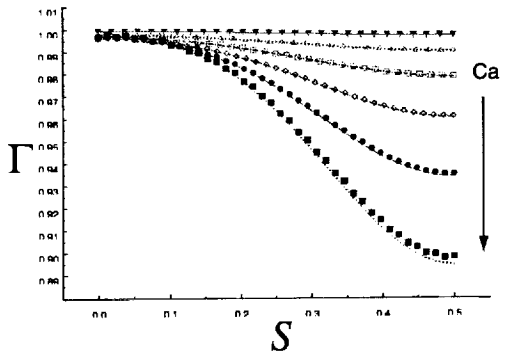

Figure 6

II. Adsorption-Desorption Controlled Surfactants

The arguments behind the kinetic expression used for an adsorption-desorption flux are presented first, followed by a discussion of the results obtained in this limit. For a monolayer forming surfactant, the rate of adsorption is proportional to the concentration of surfactant adjacent to the interface, and the space remaining on the interface, (Γ_∞-Γ). Desorption is assumed first order in Γ. In the adsorption-desorption controlled limit, the concentration in the bulk is uniform, and given by C_∞. The (dimensional) kinetic expression for adsorption-desorption is:

$$j=\beta C_s(\Gamma_\infty-\Gamma)-\alpha\Gamma$$

where α(β) are the kinetic constant for desorption (adsorption) respectively. In a quiescent system at steady state, this expression reduces to the Langmuir adsorption isotherm and is thermodynamically consistent with the equation of state adopted for the surface tension. This flux should appear on the right hand side of the surface mass balance presented in equation (v.). When recast in dimensionless form, the flux becomes:

$$j=Bi(1+k)(1-\Gamma);\ k=\frac{\beta C_\infty}{\alpha}$$

where k is a scaled concentration and *Bi* is the Biot number, the ratio of the desorption rate to the surface convective rate:

$$Bi=\frac{\alpha}{G}=\frac{B}{Ca}$$

B is defined to isolate *G* in *Ca*. For *B* of zero, the insoluble results are recovered. As *B* increases from zero, the rates of adsorption-desorption increase. The scaled concentration k is related to the fractional coverage x through the Langmuir adsorption isotherm:

$$x=\frac{k}{(1+k)}$$

In Eggleton & Stebe, the results are discussed for a range of x. Here, only the elevated concentration results (x=0.99) are discussed. The Γ and v_t profiles are shown at steady state for Ca of 0.04 in Figures 7 and 8, respectively.

Notice the scale in Figure 7, the deviations in Γ from its initial distribution are small for all cases; they are largest for the insoluble case, decreasing monotonically with *B*. For the highest *B* studied (*B*=1.0, corresponding to a *Bi* =*B/Ca* =25) the mass transfer is sufficiently rapid compared to the surface convective flux that the surface concentration is in equilibrium with the bulk fluid. The corresponding tangential velocities approach the clean interface result as *B* increases.

Simplifying the surface mass balance to neglect terms related to gradients in Γ, the mass balance becomes,

$$-\frac{1}{\Gamma}\frac{\partial\Gamma}{\partial t}+\frac{B}{Ca}(1+k)\frac{(1-\Gamma)}{\Gamma}=\nabla_s\cdot(v_t)+2Hv_n$$

The surface concentration is calculated based on this simplified balance; Γ is then used to calculate

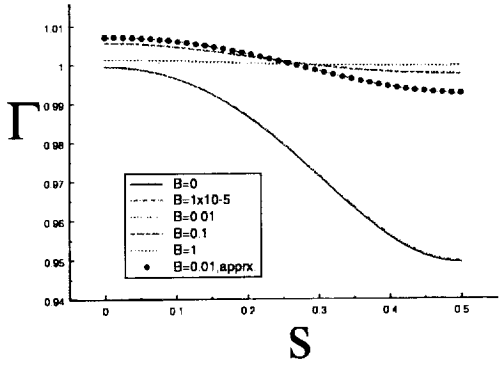

Figure 7

the stresses in the boundary integral equation. At steady state, this equation requires the tangential flux of surfactant along the interface to be balanced by the rate of adsorption-desorption exchange; the no-slip condition is recovered as B tends to zero.

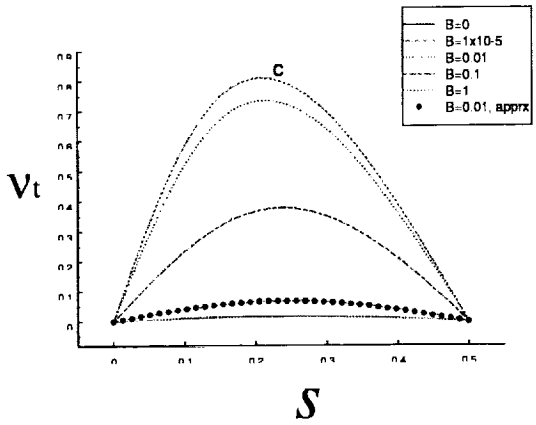

Figure 8

The results using this approximation agree well with the full solution for x=0.99 at Ca=0.04 as shown in Figures 7 and 8.

In conclusion, the three points delineated in the Introduction have been demonstrated for a strongly deforming drop interface. In the high concentration limit, Γ is nearly uniform for all cases because of the minimum area/surfactant molecule constraint. This allows simplified approaches to solving interfacial flows at finite *Ca*.

FIGURE CAPTIONS

Figure 1. A schematic of a drop centered in a pure extensional field.

Figure 2. The surface pressure Π vs. area/molecule showing the divergence in Π as the minimum area/molecule $1/\Gamma_\infty$ is approached.

Figure 3. Deformations DF vs. *Ca* realized for insoluble surfactants as a function of coverage x ranging from 0.01 to 0.996.

Figure 4. The steady state Γ profiles are shown for as a function of x for Ca=0.04.

Figure 5. The steady state v_t profiles are shown for as a function of x for Ca=0.04.

Figure 6. The approximate solution for $x=0.996$ for Γ as a function of *Ca* up to 0.06, the highest *Ca* for which a stable drop shape was attained. Symbols represent the approximate solution; the lines the full solution.

Figure 7. . The Γ profiles are shown at steady state for x=0.99 and *Ca*= 0.04 for soluble surfactant as a function of *B*.

Figure 8 The v_t profiles are shown at steady state for x=0.99 and *Ca*= 0.04 for soluble surfactant as a function of *B*.

REFERENCES

1. Defay, R. & Prigogine, I. Surface Tension and Adsorption, J.W. Arrowsmith, Ltd., Bristol, Great Britain, 1966

2. Chang, C. H. & Frances, E.I., *Colloids and Surfaces A* **100**, 1 (1995)

3. Davis, R.E. & Acrivos, A. *Chem Engng Sci.* **21**, 681 (1966)

4. He, Z., Maldarelli, C. and Dagan, Z. *J. Colloid Int. Sci. 146, 442, (1991)*

5. Sadhal, S.S. & Johnson, R.E., *J. Fluid Mech,* 126, 237 (1983)

6. Stebe, K.J , Lin, S.Y. and Maldarelli, C. *Phys. Fluids A,* **3**(1), 3 (1991)

7. Eggleton, C.D., Pawar, Y.P., & Stebe, K.J. in review, *J. Fluid Mech.*

8. Eggleton C.D. & Stebe, K.J. , in review, *J. Colloid Int. Sci.*

9. Pawar, Y.P. & Stebe, K.J., *Phys. Fluids* **8**(7), 1738 (1996)

10. deBruin, R.A. *Chem. Engng Sci.* **48**, 277 (1993)

Session 4A

Phase Change II: Solidification

INTERFACE MORPHOLOGY DURING CRYSTAL GROWTH: EFFECTS OF ANISOTROPY AND FLUID FLOW

S. R. Coriell[1], B. T. Murray [2], A. A. Chernov [3], and G. B. McFadden[4], [1] Metallurgy Division, National Institute of Standards and Technology, Gaithersburg, MD 20899, USA, coriell@nist.gov, [2]Binghamton University, Binghamton, NY 13902, USA, bmurray@binghamton.edu, [3]Universities Space Research Association and NASA Marshall Space Flight Center, 4950 Corporate Drive, Suite 100, Huntsville, AL 35806, USA, alex.chernov@msfc.nasa.gov, [4]Mathematical and Computatational Sciences Division, National Institute of Standards and Technology, Gaithersburg, MD 20899, USA, mcfadden@nist.gov

1 INTRODUCTION

During crystal growth or solidification of a binary alloy from a liquid phase, temperature and solute gradients are inherently present. In a gravitational field, these gradients can give rise to fluid flow in the melt. The interaction of fluid flow with the crystal-melt interface [1, 2] plays an important role in determining the properties of the solidified material. Convection in the melt and interface instability may both produce solute inhomogeneities. In the absence of fluid flow, the conditions for the onset of morphological instability of isotropic materials are well established. However, the coupling between morphological instability and fluid flow can be complicated; interfacial instabilities depend on temperature and solute gradients which may be strongly influenced by the flow field. The flow field, in turn, may be influenced by the morphology of the interface.

Previously, we have carried out a number of theoretical investigations relevant to the experimental studies in space by J. J. Favier and colleagues (Centre d'Etudes Nucleaires de Grenoble) and R. Abbaschian and colleagues (University of Florida) utilizing the MEPHISTO apparatus [3, 4]. In the MEPHISTO space experiments, dilute alloys of tin containing bismuth (USMP-1 & 3) and dilute alloys of bismuth containing tin (USMP-2 & 4) were directionally solidified for growth conditions in the vicinity of the planar-cellular transition. While tin is fairly isotropic, bismuth is extremely anisotropic and forms facets during growth. We first discuss recent results on the morphological stability of highly anisotropic materials.

During alloy solidification, a crystal-fluid interface may become unstable, leading to cellular or dendritic growth. Linear morphological stability theory [5, 6] describes the conditions under which the interface becomes unstable. The original treatment of morphological stability by Mullins and Sekerka assumed local equilibrium at the crystal-melt interface and isotropy of the crystal-melt surface tension; this is an excellent approximation for many metals at low growth velocities. However, many materials, including semiconductors and metals such as gallium and bismuth, grow with facets indicating strong anisotropy and deviations from local equilibrium. The stability of faceted growth has also been reviewed [7]. The effect of anisotropy of surface tension and interface kinetics on morphological stability has been treated in a quasi-static approximation to the diffusion field; kinetic anisotropy causes traveling waves along the crystal-melt interface [8]. Yuferev [9] showed that for growth in which the interface is near a singular orientation (an atomically smooth orientation), there is an enhancement of morphological stability; more detailed calculations for a binary alloy [10] and for growth into a supersaturated solution [11] and supercooled melt [12] have been carried out. The effect of shear flows and anisotropic interface kinetics on the morphological stability of a binary alloy growing from the melt [13] and a crystal growing from supersaturated solution [14, 15] have also been considered. Recently we have extended the analysis of growth from a supersaturated solution to allow for a kinetic coefficient which is a nonlinear function of supersaturation and crystallographic orientation [16]. Experimental measurements on the (100) face of ammonium dihydrogen phosphate (ADP) and potassium dihydrogen phosphate (KDP) have shown that the kinetic coefficient is strongly nonlinear in supersaturation [17, 18, 19] and that the non-linearity may cause step bunching [18]. If the kinetic coefficient depends on supersaturation, an additional mechanism affecting interface stability is present, whose physical basis has the following interpretation. If the kinetic coefficient increases with supersaturation, then a protuberance on the interface sees a higher supersaturation and will grow faster than a depression, which sees a lower supersaturation, and hence there is enhanced instability.

The motion of elementary steps is the essence of layerwise growth and decrystallization (dissolution, melting, or evaporation). If the step motion occurs by regular step trains with a constant interstep distance, homogeneous crystals are produced. However, under a wide range of conditions the elementary steps cluster into

step bunches. In other words, the interface is morphologically unstable with respect to step bunching. The step bunches trap impurities in amounts which depend on the local step densities, and therefore the impurity distribution differs from that formed by regular step trains. As a result, bands enriched or depleted in point-defects appear in the grown crystal [20]. Step bunches themselves may, in turn, lose their stability and trap inclusions of solvent.

Experiments and theory indicate that a solution flowing above a vicinal face of a crystal can either enhance or prevent the development of step bunches [7, 21, 22, 23]. For growth on a prism face of ADP, experiments by Chernov et al. [21] showed that macrosteps develop on the portion of the growth hillock where the flow was down the hillock (in the direction of step motion). On reversing the direction of flow, the original macrosteps disappeared, but new macrosteps developed on the other side of the growth hillock. This indicated that flow in the direction of step motion is destabilizing and that flow opposite to direction of step motion is stabilizing. Growth hillocks arise when growth is by a dislocation mechanism. Since a shear flow along the interface will be in the direction of step motion on one side of the hillock and opposite to the direction of step motion on the other side of the hillock, it is unclear that enhanced stability will result from the shear flow. Maximum stability might be obtained when there is no flow since the step motion provides a stabilizing influence. However, an oscillating flow of a given frequency might also provide enhanced stabilization.

In this manuscript, we treat the effect of shear flows on the morphological stability of a crystal growing from solution by a step mechanism at a given constant velocity $\bar{V}$. We carry out some calculations for a shear flow that is sinusoidal in time. For directional solidification of a binary alloy with an isotropic interface, Schulze and Davis [24, 25, 26] have studied the influence of oscillating shear flows on morphological stability.

2 THEORY

In order to treat anisotropic kinetics phenomenologically, we assume that growth is by the motion of elementary steps, which leads to a macroscopic anisotropic kinetic law. The interface kinetic coefficient $\beta(p)$, defined as the ratio of the solute flux and the deviation $(C_I - \bar{C}_e)$ of the interface concentration C_I from the equilibrium solution concentration $\bar{C}_e$, is given by $\beta(p) = \beta_{st}|p|$, $p = \tan\theta$, where θ measures the deviation of the slope of the interface from a singular orientation [7]. In general the kinetic coefficient $\beta(p)$ may be a nonlinear function of p and may depend on C_I [16], but here we will use the simple form given above. If the planar interface is a singular interface ($p = 0$), its kinetic coefficient vanishes and in this model there is no growth. In reality, a singular interface becomes macroscopically or locally vicinal due to a screw dislocation or a two-dimensional nucleation mechanism, which generates steps. A locally finite value of p at any macroscopic area of the interface results. The unidirectional step motion introduces anisotropy and we will only consider perturbations along the direction of the step motion. Further, we assume that the perturbations are sufficiently small that the quantity p does not change sign.

Our sign convention is such that positive p corresponds to step motion to the left (negative x direction). If we consider a small sinusoidal perturbation of a planar interface characterized by a constant positive value of $p = \bar{p}$, then regions of the perturbed interface with positive slopes will have larger values of p and therefore larger kinetic coefficients and larger step densities. Thus for the same supersaturation, regions of the interface with positive slopes will grow faster than regions with negative slope; this leads to a translation of the sinusoidal perturbed interface in the direction of the step motion. As previously discussed [10, 11, 22, 23], both this lateral translation of the sinusoidal interface perturbation and the lateral flow of liquid can move a depression in the interface to a solute-enriched region of solution where it can grow faster and thus provide a stabilizing mechanism.

We have carried out a linear stability analysis for growth at constant velocity $\bar{V}$ in the z–direction into a supersaturated solution. We solve the incompressible Navier-Stokes equations for the fluid velocity u and the convection-diffusion equation for solute concentration $C(x, z, t)$ in the absence of gravity. We consider a two-dimensional problem and assume all quantities are independent of the coordinate y. For simplicity, we assume that the density of crystal and melt are the same. The basic equations and boundary conditions have been given previously [16].

The fluid velocity in the solution is measured in the laboratory frame in which the crystal is at rest, so that in the undisturbed state $\bar{u} = (\bar{U}(z,t), 0, 0)$, where $\bar{U}(z,t)$ represents the imposed shear flow velocity profile. We will consider shear flows of the form

$$\bar{U}(z,t) = S_0[\nu/\bar{V}][1 - \exp(-\bar{V}z/\nu)]$$

$$+[S_1/\lambda]\exp[-\bar{V}z/(2\nu)]\sinh[\lambda z]\exp(i\omega t), \quad (1)$$

where ν is the kinematic viscosity; S_0 and S_1 are constants. The complex constant λ is given by

$$\lambda = \sqrt{[\bar{V}/(2\nu)]^2 + i\omega/\nu} \quad (2)$$

We use complex quantities with the understanding that the actual flow is given by the real part of the complex quantity. This form for the shear flow satisfies the fluid flow equations and boundary conditions at the interface ($z = 0$). The shear rate S at the interface is $S = S_0 + S_1 \exp(i\omega t)$. The unmodulated flow velocity attains a constant value far from the interface and the unmodulated shear rate decays exponentially with a characteristic decay length of $\nu/\bar{V}$. There are no pressure gradients in the undisturbed state.

For the linear stability analysis of the base state, the variables are written as the superposition of the base state component (overbars) and a perturbation (hats). The perturbed quantities are Fourier analyzed in the lateral direction, so that the variables are written as

$$\begin{pmatrix} u(x,z,t) \\ w(x,z,t) \\ P(x,z,t) \\ C(x,z,t) \\ h(x,t) \end{pmatrix} = \begin{pmatrix} \bar{U}(z,t) \\ 0 \\ 0 \\ \bar{C}(z) \\ 0 \end{pmatrix} + \begin{pmatrix} \hat{u}(z,t) \\ \hat{w}(z,t) \\ \hat{P}(z,t) \\ \hat{C}(z,t) \\ \hat{h}(t) \end{pmatrix} \exp(ik_x x), \quad (3)$$

where $\hat{h}$ is the amplitude of the perturbed interface, and k_x is the wavenumber in the x-direction. Governing equations for the perturbation quantities are obtained by substituting the above quantities into the complete set of nonlinear equations and linearizing in the perturbation quantities.

The fluid equations can be reduced to a single fourth-order equation for the perturbed vertical velocity $\hat{w}$, by applying the curl operator twice to the momentum equation and taking the z-component of the resulting equation. The linearized equations for the stability problem are then

$$\left[L\left(\nu L + \bar{V}\frac{\partial}{\partial z} - \frac{\partial}{\partial t}\right) - ik_x\left(\bar{U}L - \frac{\partial^2 \bar{U}}{\partial z^2}\right)\right]\hat{w} = 0, \quad (4)$$

$$\left[DL + \bar{V}\frac{\partial}{\partial z} - \frac{\partial}{\partial t} - ik_x\bar{U}\right]\hat{C} = \frac{\partial \bar{C}}{\partial z}\hat{w}, \quad (5)$$

where we have defined the operator $L = \partial^2/\partial z^2 - k_x^2$.

Solutions to the above set of equations which have time-periodic coefficients can be obtained using the framework of Floquet theory [27]. The solutions for the perturbation quantities are represented by the product of a periodic Fourier series and an exponential term with complex growth rate σ,

$$f(z,t) = e^{\sigma t}\sum_{|m|\le M} f_m(z)e^{im\omega t}, \quad (6)$$

where $f(z,t)$ represents any of the perturbation quantities.

3 RESULTS and DISCUSSION

We have carried out a series of calculations using the following parameters: diffusion coefficient $D = 1.0 \cdot 10^{-5}$ cm^2/s, capillary parameter , $= 5.0 \cdot 10^{-8}$ cm, $C_s/\bar{C}_e = 5$, $\beta_{st} = 0.1$ cm/s, $\nu = 0.01$ cm^2/s [22], where C_s is the concentration in the crystal; these are typical for growth from supersaturated solutions. In Fig. 1 we show results for the crystal growth rate $\bar{V}$ at the onset of instability for a shear rate of the form $S = S_0 + S_1 \exp(i\omega t)$ with $S_0 = -0.1$ s^{-1}, $\omega = 1$ s^{-1} and S_1 varying from 0 to 10 s^{-1} for three values of the wavenumber k_x of a sinusoidal perturbation. The interface is stable for velocities above the curves. For $S_1 = 0$ (no oscillation), the velocity as a function of wavenumber is shown in Fig. 2 of reference [15]. Since negative values of S_0 corresponds to flow in the direction of step motion, the interface is destabilized, e.g., by a factor of ten at a wavenumber of 100 cm^{-1}. It is interesting that by adding an oscillatory flow, one can obtain a restabilization of the interface as shown by the minimum in the $k_x = 100$ cm^{-1} in Fig. 1. However, values of S_1 above the minimum destabilize the interface. The number of temporal modes [M in Eq. (6)] needed to obtain accurate results depends on the parameters. For the lowest wavenumber in Fig. 1 we have used twelve temporal modes; a smaller number is sufficient for higher wavenumbers. We are carrying out a number of calculations of $\bar{V}$ for various values of the parameters, S_0, S_1, k_x, and ω.

References

[1] M. E. Glicksman, S. R. Coriell, and G. B. McFadden, Interaction of Flows with the Crystal-Melt Interface, Ann. Rev. Fluid Mech., Vol. 18, 1986, pp. 307-335.

[2] S. H. Davis, Effects of Flow on Morphological Stability, in *Handbook of Crystal Growth 1 Fundamentals*, Part B: Transport and Stability, Ed. D.

T. J. Hurle (North-Holland, Amsterdam, 1993) pp. 859-897.

[3] J. J. Favier, P. Lehmann, B. Drevet, J. P. Garandet, D. Camel, and S. R. Coriell, A Study of Morphological Stability during Directional Solidification of a Sn-Bi Alloy in Microgravity, in *Materials and Fluids under Low Gravity*, Lecture Notes in Physics, Vol. 464, ed. L. Ratke, H. Walter, and B. Feuerbacher (Springer-Verlag, Berlin, 1996) pp. 77-94.

[4] R. Abbaschian, A. B. Gokhale, D. B. Allen, and S. R. Coriell, A Study of Directional Solidification of Faceted Bi-Sn Alloys in Microgravity, in *Solidification Science and Processing*, ed. I. Ohnaka and D. M. Stefanescu ((The Minerals, Metals & Materials Society, Warrendale, PA, 1996) pp. 73-84.

[5] W. W. Mullins and R. F. Sekerka, Stability of a Planar Interface during Solidification of a Dilute Binary Alloy, J. Appl. Phys., Vol. 35, 1964, pp. 444-451.

[6] S. R. Coriell and G. B. McFadden, Morphological Stability, in *Handbook of Crystal Growth 1 Fundamentals*, Part B: Transport and Stability, Ed. D. T. J. Hurle (North-Holland, Amsterdam, 1993) pp. 785-857.

[7] A. A. Chernov and T. Nishinaga, Growth Shapes and Their Stability at Anisotropic Interface Kinetics: Theoretical Aspects for Solution Growth Morphology of Crystals, Ed. I. Sunagawa (Terra, Tokyo, 1987) pp. 207-267.

[8] S. R. Coriell and R. F. Sekerka, The Effect of the Anisotropy of Surface Tension and Interface Kinetics on Morphological Stability, J. Crystal Growth, Vol. 34, 1976, pp. 157-163.

[9] V. S. Yuferev, Stability of a Crystal-Melt Interface with a Lateral Growth Mechanism, Phys. Chem. Mech. of Surfaces, Vol. 2, 1983, pp. 1916-1925.

[10] S. R. Coriell, B. T. Murray, and A. A. Chernov, Kinetic Self-Stabilization of a Stepped Interface: Binary Alloy Solidification, J. Crystal Growth, Vol. 141, 1994, pp. 219-233.

[11] A. A. Chernov, S. R. Coriell, and B. T. Murray, Morphological Stability of a Vicinal Face Induced by Step Flow, J. Crystal Growth, Vol. 132, 1993, pp. 405-413.

[12] A. A. Chernov, S. R. Coriell, and B. T. Murray, Kinetic Self-Stabilization of a Stepped Interface: Growth into a Supercooled Melt, J. Crystal Growth, Vol. 149, 1995, pp. 120-130.

[13] S. R. Coriell, B. T. Murray, A. A. Chernov, and G. B. McFadden, Effects of Shear Flow and Anisotropic Kinetics on the Morphological Stability of a Binary Alloy, Metallurgical and Materials Trans., Vol. 27A, 1996, pp. 687-694.

[14] S. Yu. Potapenko, Morphological Instability of Steps during Crystal Growth from Solution Flow, J. Crystal Growth 158 (1996) 346.

[15] S. R. Coriell, B. T. Murray, A. A. Chernov, and G. B. McFadden, Step Bunching on a Vicinal Face of a Crystal in a Flowing Solution, J. Crystal Growth, Vol. 169, 1996, pp. 773-785.

[16] S. R. Coriell, A. A. Chernov, B. T. Murray, and G. B. McFadden, Step Bunching: Generalized Kinetics, J. Crystal Growth, Vol. 183, 1998, pp. 669-682.

[17] A. A. Chernov and L. N. Rashkovich, Spiral Crystal Growth with Nonlinear Dependence of Step Growth Rate on Supersaturation; The {110} Faces of KH_2PO_4 Crystals in Aqueous Solution, J. Crystal Growth, Vol. 84, 1987, pp. 389-393.

[18] L. N. Rashkovich and B. Yu. Shekunov, Morphology of Growing Vicinal Surface; Prismatic Faces of ADP and KDP Crystals in Solutions, J. Crystal Growth, Vol. 100, 1990, pp. 133-144.

[19] L. N. Rashkovich, KDP-family Single Crystals (Adam Hilger, Bristol, 1991).

[20] E. Bauser, Atomic Mechanisms in Semiconductor Liquid Phase Epitaxy, in *Handbook of Crystal Growth 3 Thin Films and Epitaxy*, Part B: Growth Mechanisms and Dynamics, Ed. D. T. J. Hurle (North-Holland, Amsterdam, 1994) pp. 879-939.

[21] A. A. Chernov, Yu. G. Kuznetsov, I. L. Smol'sky, and V. N. Rozhansky, Hydrodynamic Effect in Growth of ADP Crystals from Aqueous Solutions in the Kinetic Regime, Soviet Phys.-Cryst., Vol. 31, 1986, pp. 705-709.

[22] A. A. Chernov, How Does the Flow within the Boundary Layer Influence Morphological Stability of a Vicinal Face, J. Crystal Growth, Vol. 118, 1992, pp. 333-347.

[23] A. A. Chernov, Formation of Crystals in Solutions, Contemp. Phys., Vol. 30, 1989, pp. 251-276.

[24] T. P. Schulze and S. H. Davis, The Influence of Oscillatory and Steady Shears on Interfacial Stability during Directional Solidification, J. Crystal Growth, Vol. 143, 1994, pp. 317-333.

[25] T. P. Schulze and S. H. Davis, Shear Stabilization of Morphological Instability during Directional Solidification, J. Crystal Growth, Vol. 149, 1995, pp. 253-265.

[26] T. P. Schulze and S. H. Davis, Shear Stabilization of a Solidifying Front: Weakly Nonlinear Analysis in a Long-wave Limit, Phys. Fluids, Vol. 8, 1996, pp. 2319-2336.

[27] B. T. Murray, S. R. Coriell, G. B. McFadden, A. A. Wheeler, B. V. Saunders, Gravitational Modulation of Thermosolutal Convection during Directional Solidification, J. Crystal Growth, Vol. 129, 1993, pp. 70-80.

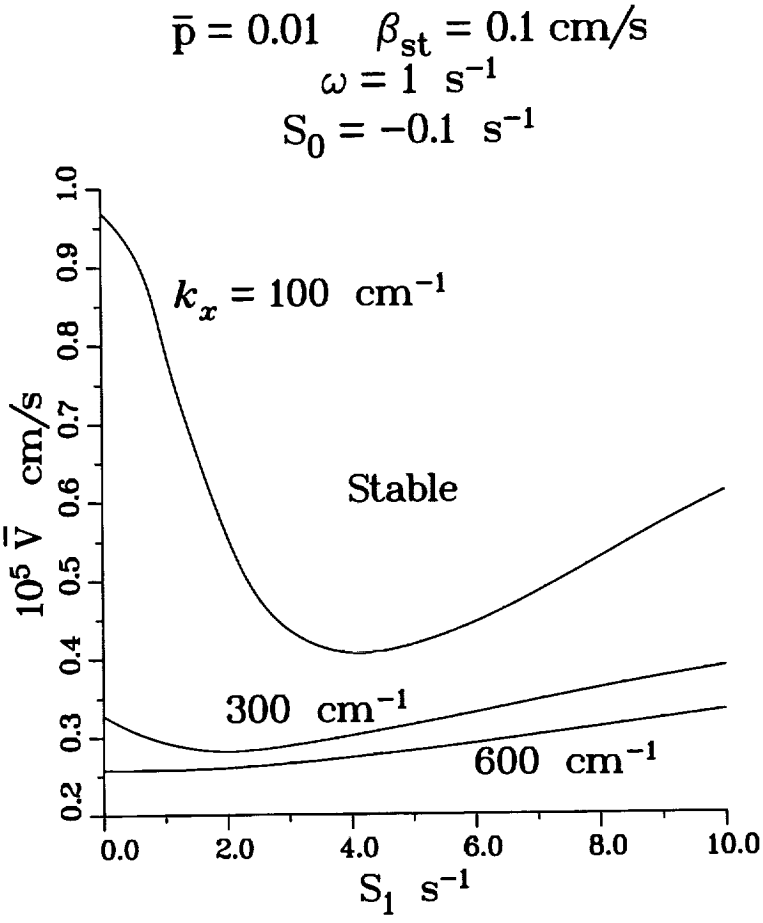

Figure 1: The crystal growth velocity above which the interface is linearly stable as a function of the magnitude S_1 of the oscillatory shear rate for sinusoidal perturbations of wavenumbers k_x of 100, 300, and 600 cm^{-1}. The shear rate at the interface is $S_0 + S_1 \exp(i\omega t)$ with $S_0 = -0.1$ s^{-1} and $\omega = 1$ s^{-1}. The non-oscillatory part of the flow is in the direction of step motion and is destabilizing.

DIRECTIONAL SOLIDIFICATION OF A BINARY ALLOY INTO A CELLULAR CONVECTIVE FLOW: LOCALIZED MORPHOLOGIES

Y.-J. Chen and S. H. Davis, Department of Engineering Sciences and Applied Mathematics, Northwestern University, Evanston, IL60208

ABSTRACT

A steady, two dimensional cellular convection modifies the morphological instability of a binary alloy that undergoes directional solidification. When the convection wavelength is far longer than that of the morphological cells, the behavior of the moving front is described by a slow, spatial-temporal dynamics obtained through a multiple-scale analysis. The resulting system has a 'parametric-excitation' structure in space, with complex parameters characterizing the interactions between flow, solute diffusion, and rejection. The convection stabilizes two dimensional disturbances oriented with the flow, but destabilizes three dimensional disturbances in general. When the flow is weak, the morphological instability behaves incommensurably to the flow wavelength, but becomes quantized and forced to fit into the flow-box as the flow gets stronger. At large flow magnitudes the instability is localized, confined in narrow envelopes with cells traveling with the flow. In this case the solutions are discrete eigenstates in an unbounded space. Their stability boundary and asymptotics are obtained by the WKB analysis.

1 INTRODUCTION

In the absence of flow, the morphological instability of a binary alloy undergoing directional solidification is driven by the adverse gradient of solute concentration at the solid-liquid interface. This instability occurs when the interface advances with a speed V greater than a critical value V_c, when cellular patterns form on the moving front. When the liquid (melt) is flowing, the solute concentration profile is altered. In general, the liquid motions may delay or promote the instability depending on the interactions between the solute and momentum transport.

Flow-modified morphological instability has been studied by many authors (e.g. see [6] for a review). Flows can be inherent in the nature of the solidifying process, such as solutal convection in a density stratified melt ([3], [4]). The motion here is due to buoyancy effects that exist even when the interface is not deformable. Flows can also be *imposed* through a far-field pressure gradient. In this case the purpose of the flows may be in the interest of material processing. The examples include plane Couette flow [5], asymptotic suction profile ([7], [8], [11]), and stagnation-point flow [1].

In the present analysis we examine the morphological instability of a pre-existing cellular convective flow (see figure 1). Such flows exist when hydrodynamic instabilities occur before the morphological instability, or when the liquid is subjected to a high-frequency vibration or acceleration (g-jitter). The flow is considered to be spatially periodic, with a wavelength $2\pi/\alpha$ typically much longer than the wavelength $2\pi/\beta$ of the morphological instability. This assumption is appropriate for metallic alloys for which typical Schmidt numbers are large, and the viscous length-scale can be ten or hundred times longer than the diffusion length-scale. The present work is related to that of Bühler & Davis [2], in which numerical calculations to the linear problem have been performed. Their study showed that in such flows the morphological instability can be confined in localized, stationary envelopes distributed periodically on the interface. Each envelope contains many morphological cells traveling in the flow direction. The stability and mechanism of the onset of this solution have yet to be revealed.

We treat the solutal-momentum transport as a perturbation of the Mullins-Serkerka problem [10]. The 'pure' (no-flow) morphological instability has its critical wavenumber β_c at a critical morphological number M_c, as shown schematically in figure 2a. For the smallness of α comparing with β_c, we evoke a multiple-scale analysis near the critical point (β_c, M_c). The resulting dynamics has a 'parametric-excitation' form in the slow, spatial variable, where the periodic coefficients are generated by the cellular flow. The linear problem is then solved by the numerical branch-tracing technique with the asymptotic structures obtained through a WKB-type analysis.

We observe that disturbances (rolls) perpendicular to the flow (figure 2b) are stabilized, since the tangential component of the flow either compresses or stretches the morphological cells along the interface. That is, a wave structure which is unstable without the flow has now been altered and pushed to the regime where the surface tension or solute diffusion help to stabilize. In contrast, rolls aligned with the flow (figure 2c) are desta-

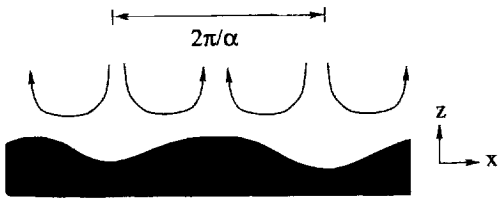

Figure 1: Schematic diagram for a spatially periodic flow impressing on the solid- liquid interface of a binary alloy.

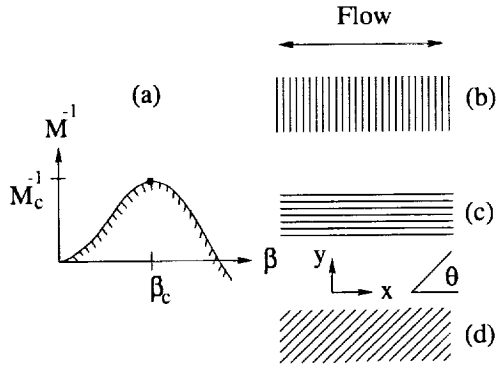

Figure 2: (a) Marginal stability diagram of the pure morphological instability. Solutions in hatched area are unstable. The morphological cell has a wave-vector (b) parallel, (c) perpendicular, and (d) an angle θ to the flow.

bilized by the normal flow component. The morphologies have incommensurate structures (aperiodic in space) when the flow is weak, and develop localized wave envelopes, as observed in [2], when the flow strength increases. The stability boundary and the onset of the traveling cells are identified.

2 Solutal Transport Equations

Consider a dilute binary alloy solidifying into a cellular flow field. The averaged solid-liquid interface moves in a constant velocity V. The solute rejected on the interface has a partition coefficient k and diffusivity D in the liquid. We invoke the 'frozen temperature approximation' [9] that gives the temperature T in the solid and liquid permanently by $T = T_0 + Gz$, where G is the imposed temperature gradient, and T_0 is a reference temperature. The coordinate variable z is fixed on the moving front with positive z-direction pointing to the liquid. The interfacial coordinates are spanned by the (x, y)-axes. The temperature will not be disturbed when the thermal boundary layer is far thicker than the momentum and concentration boundary layers.

We choose the velocity, time, length, and concentration scales to be V, D/V^2, $\ell_c = D/V$, and $\Delta c = (1/k - 1)c_\infty$, respectively. Referred to those scalings and chosen coordinates, the solutal transport equation in the liquid can be written

$$\begin{aligned} Sc^{-1}\{\partial_t \boldsymbol{v} + (\boldsymbol{v} - \hat{e}_z)\cdot\nabla\boldsymbol{v}\} &= -\nabla p + \nabla^2 \boldsymbol{v}, \\ \nabla\cdot\boldsymbol{v} = 0, \quad \partial_t c + (\boldsymbol{v} - \hat{e}_z)\cdot\nabla c &= \nabla^2 c. \end{aligned} \tag{1}$$

In the above formulation we have assumed the melt to be an incompressible, Newtonian liquid. The Schmidt number $Sc = \nu/D$ measures the strength of liquid viscosity to the solute diffusivity.

On the solid-liquid interface $z = h(x, y, t)$, the no-slip condition $\boldsymbol{v} = 0$ is applied. It is also assumed that the density change upon solidification is negligible, and the velocity $\boldsymbol{v}$ approaches the far-field distribution $\boldsymbol{v}_\infty$ as $z \to \infty$. The field $\boldsymbol{v}_\infty$ is $\frac{2\pi}{\alpha}$ periodic in x and is the driving force of the convective flow. The solute boundary conditions on the interface consist of the mass conservation law and a local thermodynamic equilibrium:

$$v_n\{(1-k)c + k\} = -\hat{n}\cdot\nabla c \tag{2}$$

$$M^{-1}h = 1 - c + 2\Gamma\kappa(h). \tag{3}$$

Here, $\hat{n}$ is the unit normal vector pointing into the liquid phase, v_n the speed of the front normal to itself, and κ the mean curvature, a functional of the interface shape function h. The mass conservation law (2) assumes that solute diffusion in the solid is negligible comparing with that in the liquid. The Gibbs-Thomson condition (3) depicts the alteration of temperature of interface from the equilibrium melting temperature of the pure solvent due to the presence of solute (constitutional undercooling) and the curvature of the interface itself (capillary undercooling). The morphological number and surface energy parameter are given by

$$M = \frac{mG_c}{G}, \qquad \Gamma = \frac{T_m\gamma}{mG_c\ell_c^2 L_v}$$

where $G_c = -\Delta c/\ell_c$ measures the concentration gradient. The liquidus slope of the phase diagram is denoted by m, and the parameters γ, T_m, L_v stand for surface tension, solvent melting temperature, and latent heat per unit volume, respectively.

3 Basic State

The given cellular flow has a spatial period $\frac{2\pi}{\alpha}$, which is considered to be much longer than the morphologi-

cal length-scale ℓ_c. The velocity field is represented by a simple sinusoidal function in the direction x, and decays to zero at the interface exponentially. We use P to denote the value of the far-field velocity. Its tangential component is written

$$u = -\{1 - \mathrm{e}^{(h-z)/s}\} P \sin \alpha x. \tag{4}$$

The parameter s distinguishes a general class of flows [2]. Its magnitude represents the thickness of the viscous boundary layer near the interface. Flow type in (4) is motivated by the 'asymptotic suction profile', in which the remote field, $P \sin \alpha x$, is replaced by a constant, and the parameter s is equivalent to the Schmidt number Sc. The asymptotic suction profile is an exact solution to the momentum equation, while the remote flow (4) serves as an approximation for $\alpha \ll 1$ and flows near the interface. This enables us to simplify the analysis and consider only the situation of large Schmidt-number, metallic alloys ($Sc \to \infty$). Consequently, the liquid inertia is neglected, and the parameter s can take any positive value ($0 < s < \infty$).

Flows with $s \leq 1$ can occur in a Hele-Shaw-like apparatus for example, where the close proximity of the sidewalls creates a thin viscous boundary layer. Boundary layers of exponential type are also observed in electrically conducting liquid with flows induced by strong magnetic fields. For those examples the spatial period $\frac{2\pi}{\alpha}$ can be introduced through solutal buoyancy or magnetohydrodynamic instability.

While the flow field is treated as an approximate solution to the momentum transport equation, the resulting solutal and interfacial profiles (c_0, h_0) can be obtained by introducing the expansions

$$\begin{aligned} c_0(\alpha x, z) &\sim \mathrm{e}^{h_0 - z} + \alpha\delta f_1(z) \cos \alpha x, \\ h_0(\alpha x) &\sim 0 + \alpha\delta f_2(z) \cos \alpha x, \end{aligned} \tag{5}$$

into the solutal transport equation and boundary conditions. Functions f_1 and f_2 can be obtained in a straightforward manner. In (5) we have rescaled the flow effects and employed a expansion parameter $\alpha\delta$ [2], where

$$\delta \equiv \frac{P}{1+s},$$

to indicate the order of magnitude of the flow perturbations. The expansion uses that fact that the solutal and interfacial shape functions are weakly perturbed off the profiles of the quiescent case as $\alpha\delta \ll 1$. The parameter δ here represents the magnitude of velocity near the interface when $s \ll 1$, and the velocity gradient when $s \gg 1$. The scaling is introduced in the expansions, since only the magnitude of the flow is important when the concentration boundary layer is subjected to an extremely thin viscous layer, while for a thick viscous layer only the velocity gradient near the interface is relevant to the convective transport.

4 Dynamics In Slow Variables

The imposed flow field breaks the rotational symmetry of the plane surface. We shall subject the basic state (4, 5) to a 'roll-like' disturbance, with an angle θ to the flow direction (figure 2d). Recall that, in the absence of flow, the most dangerous perturbation is the normal mode $\mathrm{e}^{i\vec{\beta}_c \cdot (x,y)}$ at the critical morphological number M_c. In the case with flow the motion introduces a slow, spatial change. It is thus reasonable to assume that the most dangerous disturbance now has a form $f(\epsilon x)\mathrm{e}^{i\vec{\beta}_c \cdot (x,y)}$, $\epsilon \ll 1$, where $f(\epsilon x)$ is a slowly varying function. The parameter ϵ enables us to perform a multiple-scale analysis near the point of (β_c, M_c) (see figure 2).

Formally, we assume a perturbation expansion:

$$\begin{aligned} M^{-1} \mapsto M_c^{-1} - \mu_1\epsilon^2 m, \quad \alpha \mapsto \epsilon\alpha, \quad \delta \mapsto \mu_2\epsilon^2\hat{\delta}, \\ \tau = \mu_3\epsilon^2 t, \quad \eta = \epsilon x, \quad \xi = \epsilon^2 x, \\ \boldsymbol{u} \sim \boldsymbol{u}_0 + \{\epsilon \boldsymbol{u}_1(\tau, \eta, \xi, z) + \epsilon^2 \boldsymbol{u}_2 + \\ \epsilon^3 \boldsymbol{u}_3\}\mathrm{e}^{i\vec{\beta}_c \cdot (x,y)} + \{\text{c.c.}\}, \end{aligned}$$

where $\boldsymbol{u} = (c, h)$, $\{\text{c.c.}\}$ represents complex conjugate, and μ_i are coefficients which will be determined later to renormalize the slow-variable dynamics. By substituting the above expansions into the governing transport equations, and collecting the like powers of ϵ, we arrive at a series of linear problems, which can be written as

$$\begin{aligned} \mathrm{L}\boldsymbol{u}_1 &= 0, & O(\epsilon) \\ \mathrm{L}\boldsymbol{u}_2 &= F_1(\boldsymbol{u}_1), & O(\epsilon^2) \\ \mathrm{L}\boldsymbol{u}_3 &= F_2(\boldsymbol{u}_1, \boldsymbol{u}_2), & O(\epsilon^3), \end{aligned}$$

where L is the linear operator of the no-flow case. Since the operator L is singular, the solvability condition is necessary to solve $\boldsymbol{u}_i$ at each order. The quadratic nature of the turning point at (β_c, M_c) results in the inhomogeneous term $F_1(\boldsymbol{u}_1)$ that is already in the range of L. The leading-order behavior of (c_1, h_1) is then determined by the solvability condition at $O(\epsilon^3)$. This procedure results in a dynamical system in the slow variable (dropping subscript '1'):

$$\begin{aligned} \partial_\tau h = \{m + i\hat{\delta}\cos\theta \sin \alpha\eta\}h + \{\cos\theta\partial_\eta\}^2 h - \\ ah|h|^2 + O(\epsilon\alpha\hat{\delta}\cos\alpha\eta\, h), \end{aligned} \tag{6}$$

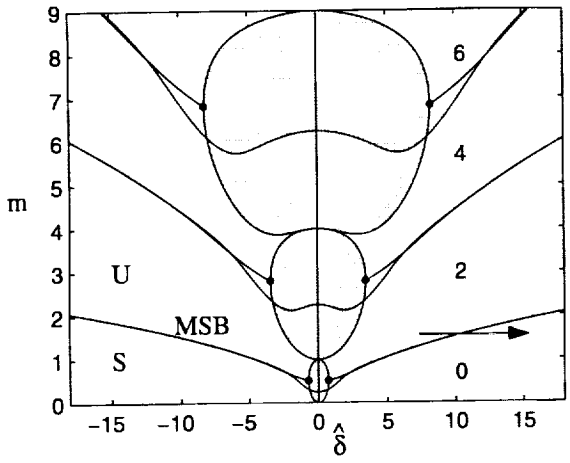

Figure 3: Characteristic curves for the 2d-roll equation. Shaded area represents solutions that are incommensurate with the flow. Solid circles are double degenerate points. The arrow indicates a path showing flow-induced *stability*. Symbol 'S' denotes stability, 'U' denotes instability, and 'MSB' denotes marginal stability boundary.

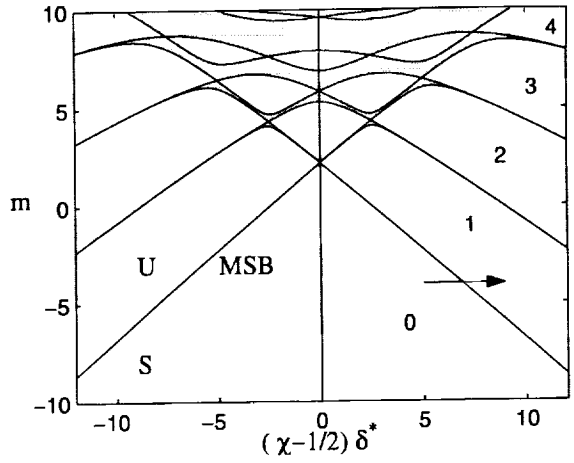

Figure 4: Characteristic curves for the longitudinal-roll equation. Shaded area represents solutions that are spatially incommensurate with the flow. The arrow indicates a path showing flow-induced *instability*. Symbol 'S' denotes stability, 'U' denotes instability, and 'MSB' denotes marginal stability boundary.

with appropriate constants μ_i. The Landau constant a determines the supercriticality ($a > 0$) or subcriticality ($a < 0$) of the system. When $\hat{\delta} \equiv 0$, equation(6) recovers the system of the pure morphological problem in [12]. Equation(6) is written in the form for which the morphological instability has an $O(1)$ wavenumber in the remote-flow direction ($\cos\theta = O(1)$, cf. figure 2b). In this case the flow component $\hat{\delta}\sin\alpha\eta$ tangential to the interface has the leading-order contribution, and the normal component $\alpha\hat{\delta}\cos\alpha\eta$ is formally $O(\epsilon)$. That is, not until very close to the stagnation points ($\eta = \frac{n\pi}{\alpha}$) does the effect of the normal component enter.

When one rotates the wave-vector of the morphological cells to be nearly perpendicular to the flow direction, ($\cos\theta = O(\epsilon)$, cf. figure 2c), the tangential and normal flow components will have the same orders of magnitude; equation(6) will then need to be modified. In this regime we rescale the flow parameter $\delta \mapsto \mu_4\epsilon\delta^*$ such that the flow interacts with the morphological instability at $O(\epsilon^3)$. The slow-variable dynamics is then rewritten

$$\partial_\tau h = \{m + \delta^* \sin\alpha\eta\partial_\eta + \chi\alpha\delta^*\cos\alpha\eta\}h + \epsilon^2\partial_\eta^2 h - ah|h|^2, \quad (7)$$

where $\chi = \chi(k,\Gamma,s)$ is an $O(1)$ parameter. Equation (7) is a singular perturbation problem with the surface-tension force $\epsilon^2\partial_\eta^2 h$ now acting as a regularization term.

5 Linear Stability Analysis

To determine the initial behavior of small disturbances we neglect the nonlinear terms in (6, 7). It is convenient in the analysis to study only the normal mode: $h(\tau,\eta) \mapsto e^{i\omega\tau}h(\eta)$, and have the disturbance wave-vector oriented either with x or y axis (cf. figure 2b, c). The deduced system are then referred to as '2d' and 'longitudinal' (3d) rolls respectively, according to their relevant morphological structures:

$$\text{2d roll: } \{m - i\omega + i\hat{\delta}\sin\alpha\eta\}h + \partial_\eta^2 h = 0, \quad (8)$$

$$\text{longitudinal roll: } \{m - i\omega + \delta^*\sin\alpha\eta\partial_\eta + \chi\alpha\delta^*\cos\alpha\eta\}h + \epsilon^2\partial_\eta^2 h = 0. \quad (9)$$

As noted, the longitudinal-roll equation is a singular perturbation problem; thus the term $\epsilon^2\partial_\eta^2 h$ must be retained. The systems have parametric-excitation form, driven by the imposed flow. In analogy to a pendulum problem, the two 'spatial pendula' here have periodic spring-constants in accordance with the flow period, controlled by complex parameters. The Floquet theory describes the complicated nature of the spatial behaviors. The coefficients have period $\frac{2\pi}{\alpha}$, and there

are solutions in the form

$$h(\eta) = e^{\mu\eta}\phi(\eta), \quad \phi(\eta + 2\pi/\alpha) = \phi(\eta).$$

Since we are concerned only with the spatially bounded solutions (eigenfunctions); this demands Re $\mu = 0$. Figures 3 & 4 plot the boundaries of those solutions, in which the lines were obtained by the numerical branch-tracing technique, and numbers labelled represent the number of unstable modes (Im $\omega < 0$) that have lengths fitted into the flow-box. The branching solutions were traced in the (δ, m, ω)-space, while only period $\frac{2\pi}{\alpha}$ and $\frac{4\pi}{\alpha}$ solutions are plotted. Solutions within the boundaries are aperiodic functions, and the interfacial perturbations are incommensurate (spatially unsynchronized) with the flow. As the flow rate $|\delta|$ increases, the 2d-roll solution (figure 3) changes from stationary ($\omega \equiv 0$) to time-dependent modes at the double degenerate points (solid circles), where branches of solutions collide and pairs of oscillatory modes ($\omega = \pm\omega^*$) bifurcate. In contrast, all solutions of the longitudinal roll are stationary (figure 4), with the 'incommensurate bands' shrinking to thin, film-like layers as $\epsilon \to 0^+$. This behavior suggests that the eigenstates are essentially quantized. That is, discrete eigenmodes exist in an unbounded state, and the induced morphology has a structure spatially synchronizing with the flow-periodicity. In the longitudinal-roll perturbation, this quantization occurs due to the regularization of the surface tension force (cf. equation 9). The morphological cells are aligned with the flow, with a secondary structure near the flow-stagnation points (figure 5). For the 2d disturbance, the quantization happens at high flow rates after the double degenerate points. The oscillatory modes are in agreement with the traveling-cell solutions observed in [2], in which cells are traveling in the flow direction, with the amplitude confined in narrow envelopes located between the stagnation points (figure 6).

Our analysis also indicates that the flow stabilizes the 2d disturbance since the marginal morphological number m_c has been delayed ($m_c > 0$), but destabilizes the 3d disturbance with the instability occurs before the pure morphological instability ($m_c < 0$). A WKB type analysis delivers the asymptotics of the stability boundaries and the local structures:

$$\text{2d-roll:} \quad m_c \propto |\alpha||\hat{\delta}|^{1/2}, \omega \propto \hat{\delta},$$
$$h \sim e^{-\mu_5|\alpha||\hat{\delta}|^{1/2}(\eta-\eta_0)^2}.$$
$$\text{longitudinal-roll:} \quad m_c \propto -|\alpha\delta^*|, \quad \omega \equiv 0,$$
$$h \sim e^{-\mu_6|\alpha\delta^*/\epsilon^2|(\eta-\eta_0)^2}.$$

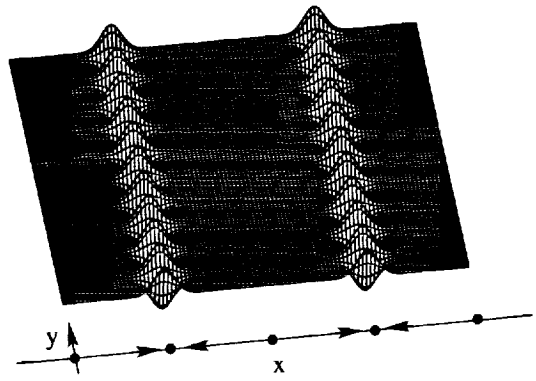

Figure 5: Longitudinal-roll morphology (perspective view) Solid circles are stagnation points, and arrows the flow direction.

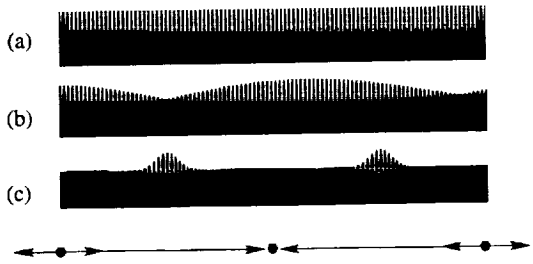

Figure 6: Two dimensional rolls (side-view) predicted by the linear stability analysis: (a) pure, (b) incommensurate, and (c) localized morphologies. Solid circles are stagnation points, and arrows the flow direction.

In agreement with the results of the branch-tracing calculation, the eigenmodes have localized structures at the positions where, for the 2d, the tangential flow component is the strongest and, for the 3d, the normal flow component dominates. The discrete modes are the 'turning-point' solutions in the WKB analysis.

6 Discussion And Summary

Linear stability analysis shows the flow stabilizes 2d but destabilizes 3d disturbances. The mechanism may be tightly bound with the structure of the marginal stability curve shown in figure 2a. A disturbance along the flow direction (figure 6) is compressed or stretched near the stagnation points by the tangential flow component. This changes its wavenumber so that the local β becomes larger or smaller than the critical value for the pure morphological instability. The surface ten-

sion force or solute diffusion help stabilize the interface locally. However, when a disturbance has 3d structure (figure 5), the normal flow component will compress the concentration boundary layer at the stagnation points and promotes the constitutional undercooling. This effectively lowers the morphological number such that the interface is locally destabilized. These two mechanisms predict that, near the onset of the instability, patterns like figure 6 may occur in a confined, 2d geometry (Hele-Shaw slot, for example). In a fully three dimensional setting one would expect to see a pattern close to figure 5, since it is the more unstable.

In summary, we investigate the effects of a cellular convective flow on the directional solidification of a dilute binary alloy. The imposed flow has spatial wavenumber α and strength parameter δ that controls the perturbation to the interfacial deformation. A multiple-scale analysis is performed near the onset of the morphological instability, which results in a weakly nonlinear equation in slow, space and time variables. The dynamics of the front is parametrically excited by the imposed flow. Its linear problem is solved by the numerical branch-tracing method. It is found that the remote, spatially periodic flow stabilizes 2d disturbances in the flow direction, yet promotes 3d instability. The localized morphological instability previously observed are identified as the quantization of the eigenstates, in which the unstable modes are discrete in an unbounded space, and the perturbed interfacial structures are forced to be spatially synchronized with the flow. The stability boundary and the asymptotic structure of the eigenmodes are obtained by the WKB method in the limit of $\alpha \to 0^+$.

ACKNOWLEDGMENT

This work was supported by NASA, Microgravity Science and Application Program.

REFERENCES

[1] Brattkus, K. & Davis, S. H. *J. Cryst. Growth*, **89**, 423, 1988.

[2] Bühler, L. & Davis, S. H. *J. Cryst. Growth*, (In press) 1998.

[3] Coriell, S. R., Cordes, M. R., Boettinger, W.S. & Serkerka, R. F. *J. Cryst. Growth*, **49**, 13, 1980.

[4] Coriell, S. R., & McFadden, G.B. *J. Cryst. Growth*, **94**, 513,1989.

[5] Coriell, S.R., McFadden, G.B. & Boisvert, R.F. *J. Cryst. Growth*, **69**, 15, 1984.

[6] Davis., S.H., in: *Handbook of Crystal Growth 1*, Hurle, D.T.J. editor, vol. 1 ch. 13, p861. Elsevier Science Publishers, 1993.

[7] Forth, S.A. & Wheeler, A. A. *J. Fluid Mech.*, **202**, 339, 1989.

[8] Hobbs, A. K. & Metzener, P. *J. Cryst. Growth*, **112**, 539, 1991.

[9] Langer, J. S. *Rev. Mod. Phys.*, **52**(1), 1, 1980.

[10] Mullins, W.W. & Serkerka, R.F. *J. Appl. Phys.*, **35**(2),444,1964.

[11] Schulze, T. P. & Davis, S. H. *J. Cryst. Growth*, **143**, 317, 1994.

[12] Wollkind, D. J. & Segel, L. A. *Philos. Trans. Roy. Soc. London A* **268**, 351, 1970.

FLUID DYNAMICS AND SOLIDIFICATION OF MOLTEN SOLDER DROPLETS IMPACTING ON A SUBSTRATE IN MICROGRAVITY

C. M. Megaridis[1], D. Poulikakos [2], G. Diversiev[1], K. Boomsma[1], B. Xiong[1] and V. Nayagam[3], [1]Department of Mechanical Engineering, University of Illinois at Chicago, Chicago IL 60607-7022, cmm@uic.edu, [2]Institute of Energy Technology, Swiss Federal Institute of Technology, ETH Center, CH-8092 Zurich, Switzerland, [3]National Center for Microgravity Research, Cleveland, Ohio 44135.

INTRODUCTION

This program investigates the fluid dynamics and simultaneous solidification of molten solder droplets impacting on a flat substrate. The problem of interest is directly relevant to the printing of microscopic solder droplets in surface mounting of microelectronic devices. The study consists of a theoretical and an experimental component. The theoretical work uses axisymmetric Navier-Stokes models based on finite element techniques. The experimental work will be ultimately performed in microgravity in order to allow for the use of larger solder droplets which make feasible the performance of accurate measurements, while maintaining similitude of the relevant fluid dynamics groups (Re, We).

A schematic of the two distinct stages (flight and impact) of the problem examined is shown in Fig. 1. The primary application of interest (solder microdroplet dispensing) employs solder droplets approximately 50 to 100 μm in diameter, which collide, spread, recoil and eventually solidify on the substrate. Due to the small size of the droplets and the relatively high surface tension coefficient of solder, gravity effects are negligible. This solder application technology has shown great promise in microelectronic packaging and assembly, therefore, the development of a good understanding of the pertinent fluid dynamics and solidification phenomena is essential for its successful commercial implementation. However, progress in this area has been hindered by the small length scales of the problem (50 to 100 μm), which have made experimental measurements of the relevant transport phenomena difficult. Alternative approaches, which employed much larger (mm-size) droplets, yielded results that were affected by the masking effects of gravity. Hence, even though mm-size droplets yield significantly improved resolution, the applicability of the obtained results for much smaller droplets remains suspect. Conducting experiments in a microgravity environment eliminates the unwanted influence of gravity and makes the experimental investigation of large droplet dispension directly relevant.

The Reynolds, Weber and Froude numbers characteristic of the process shown in Fig. 1 are defined by

$$\mathrm{Re}=\frac{V_0 d_0}{\nu},\quad We=\frac{\rho V_0^2 d_0}{\gamma},\quad Fr=\frac{V_0^2}{d_0 g} \qquad (1)$$

where V_0, d_0 denote droplet impact velocity and diameter, while ρ, ν, γ correspond to the density, kinematic viscosity and surface tension coefficient of the liquid. To exemplify the disparity in the importance of gravity in the dispension of large and small droplets, the values of Re, We and Fr were calculated for a set of parameters corresponding to the real dispension process in normal gravity (50 micron diameter solder droplet impacting on a flat surface with a velocity 1m/s). These values were Re=157, We=1.2, Fr=2038, and illustrate the importance of inertia and surface tension, as well as the insignificance of gravity effects. If a larger (1mm) drop is used in normal gravity experiments, a slower impact velocity V_0 is required for similitude based on Re. In turn, similitude in terms of the Weber number requires a smaller surface tension coefficient. To maintain similitude in this specific example, the surface tension coefficient as well as the impact velocity of the larger droplets need be reduced by twenty-fold. The resulting values of the above dimensionless groups are then Re=157, We=1.2 and Fr=0.25. Clearly, the drastic decrease in the value of the Froude number proves that gravity effects become significant for mm-size droplets, and that the presence of a microgravity environment is necessary in large solder-droplet impact experiments.

OBJECTIVE

The study aims to create a science base and identify the influence of the dominant process parameters in solder droplet dispensing. These parameters are: droplet size and velocity; droplet, substrate and ambient gas temperatures; and contact angle between solder and substrate before and after solidification. The sensitivity of the solidified-droplet (bump) shape and

size to variations in the above parameters is critical because solder bump volume, position, and height variation are key metrics for solder jet technology. Through a combination of experiments and numerical modeling, the effect of the dimensionless groups defined in Eq. (1) and the physics they represent are systematically documented.

METHODOLOGY

The research consists of a theoretical and an experimental component. The theoretical component investigates the fluid dynamics and solidification of a molten solder droplet during its impact on the substrate, in order to attain a fundamental understanding of the miniature solder deposition process. The experimental component tests the numerical predictions and provides necessary input data (such as wetting angles) for the theoretical model. Details of both components are given below.

Theoretical

The model simulates the axisymmetric impact and subsequent solidification of an initially spherical, molten solder droplet on a flat multi-layer composite substrate. When a gravitational field is present, the droplet is injected along that direction, which is orthogonal to the target surface. The Navier-Stokes equations combined with heat transfer and solidification are solved in the liquid phase using a Lagrangian approach. The heat conduction equation is solved in the solid phase, i.e., substrate and solidified sector of the droplet. It is noted that the employed axisymmetric approach is valid for situations where the solder droplet impinges on the substrate at an angle equal or approaching 90°. The mathematical model formulation has been described elsewhere in detail (see Waldvogel et al., 1996; Waldvogel and Poulikakos, 1997) and will not be repeated here for brevity. However, a brief description is given in the following for completeness.

Fluid Dynamics: Laminar flow of a constant property fluid (molten solder) is assumed. The radial and axial components of the momentum equation are considered along with the continuity equation. The artificial compressibility method is employed, thus introducing a pressure term to the mass conservation equation. The free surface deformation is tracked by the two corresponding stress balance equations (along r and z). The wetting force at the dynamic contact line between the liquid droplet and the substrate is neglected throughout the analysis. This assumption is valid during the initial stages of droplet impact where inertia forces are high with respect to the retarding forces of viscosity and surface tension. In the case of solder jetting, solidification occurs very quickly at the contact area, thus eliminating the need for a wetting condition altogether. The moving contact line is treated by allowing for slipping along the radial direction (Dussan, 1979).

Heat Transfer: The Lagrangian formulation is used for the conjugate heat transfer process in the droplet and the substrate. The energy conservation equation is solved in the droplet interior as well as in the substrate. Heat transfer from all exposed surfaces is neglected.

Thermal Contact Resistance: Thermal contact resistance between droplet and substrate is modeled by a thin layer of arbitrary thickness. This layer is assigned zero heat capacity and experiences only axial conduction. Thermal contact resistance is quantified by a dimensionless coefficient (Biot number), defined by

$$Bi = \frac{h_c d_0}{k_0} \quad (2)$$

where h_c denotes the heat transfer coefficient for the thin contact area between the droplet and the substrate, k_0 the thermal conductivity of the solder and d_0 the droplet diameter before impact. Unfortunately, no correlations published to date have been identified to determine the value of h_c in the parametric domain of solder jetting. To this end, specific attention is given to identify the thermal contact resistance in solder microdroplet dispensing and, in turn, facilitate future studies in this area.

Solidification: The following assumptions are made regarding the solidification of the molten-solder droplet. First, since a eutectic alloy is studied, a sharp boundary separating distinct liquid and solid regions is included in the model. Furthermore, it is assumed that phase change occurs at the equilibrium freezing temperature (i.e., no undercooling is considered). It is noted that the droplet solid and liquid phase densities are nearly identical since the 63% Sn–37% Pb solder material experiences only a 0.2% contraction upon freezing. The exact specific heat method proposed by Bushko and Grosse (1991) was adopted to model solidification. This approach facilitates the finite element formulation and has the added advantage that it is very accurate in conserving energy as the droplet solidifies.

Numerical Solution Procedure

The computational domain is discretized with a mesh of triangular elements, and the numerical model is solved using a Galerkin finite element method. Quadratic and linear shape functions are used for velocity and pressure, respectively. An implicit method is utilized for the numerical integration of the fluid dynamics equations in time, while a Crank-Nicholson scheme is used for the energy equation. The details of the iterative solution technique and mesh generation algorithm are given in Waldvogel and Poulikakos (1997). The spatial resolution needed to provide grid and time-step independence is ~600 nodes in the droplet and ~1,100 nodes in the substrate. A dimensionless time step of $\delta t\ V_0 / d_0 = 5\times10^{-4}$ was found adequate for time-step insensitive results.

Experimental

Two separate jetting apparati are employed in the experiments. The first is capable of jetting 50-80μm solder droplets with velocities ~1m/s, while the other generates mm-sized droplets at injection speeds of ~0.1m/s. Both devices create droplets on demand, and feature heated reservoirs, in which high-purity 63%Sn–37%Pb solder is maintained at temperatures ~210°C (melting point of solder is 183° C). The first device uses nitrogen gas to pressurize the system forming the droplets, thus hindering the formation of oxides within the reservoir. Individual droplets are generated as a voltage pulse excites a piezoelectric transducer mounted within the device. The second device (which forms larger droplets) utilizes mechanical forcing of the solder pool (via a plunger) through a round orifice at the bottom of the reservoir. The droplet flight occurs in a nitrogen atmosphere to avoid oxygen adsorption on the solder surface. The presence of oxygen is avoided because it is known to degrade the surface properties of liquid solder. The impact velocity V_0 of the small droplets is determined using a stroboscope and a steady stream of droplets generated at a known injection frequency. For the larger droplets, a high-speed video system is used to measure droplet impact velocities.

The solidified shape of the small deposited droplets is evaluated using scanning electron microscopy (SEM). The experimental results reported in the following section were all obtained in normal gravity. Small droplets impacted on a two-layer composite substrate (Ni on Si). For the larger (mm) droplets, the substrates consisted of a single-layer metal material.

RESULTS AND DISCUSSION

Thermal Contact Resistance of Microdroplets

The thermal contact resistance between a typical electronic substrate and impacting solder droplets was examined first. The chosen conditions correspond to a 63%Sn–37%Pb solder droplet with pre-impact diameter d_0=53μm, velocity V_0=1.6 m/s and temperature 210°C. The two-layered substrate (consisting of a 2μm-thick nickel layer on a 212μm layer of silicon) had an initial temperature of 35°C. The dimensionless numbers corresponding to these baseline conditions are Re=266, We=3.23 and Fr=4930. These operating conditions are characteristic of practical situations, and have been chosen primarily because of the availability of experimental data; see Waldvogel and Poulikakos (1997), as well as Xiong et al. (1998).

A series of model simulations was performed with all process parameters fixed to the baseline values stated above, while the values of *Bi* were varied over a range from 0.01 to 0.75. These values of *Bi* correspond to contact heat transfer coefficients h_c in the range 4–350 kW/m^2 K. Even though the value of *Bi* changed from run to run, it was kept constant throughout each of these simulations. The computed solder bump outline for each value of *Bi* revealed that this shape is very sensitive to the contact resistance between droplet and substrate; see Xiong et al. (1998). Figure 2 presents two geometric parameters describing the solidified-bump shape and its dependence on thermal contact resistance. Both parameters are plotted in their dimensionless form versus Biot number (likewise, heat transfer coefficient h_c). Two values of height (z/d_0) for each solidified bump appear in Fig. 2: one on the symmetry axis and another at the off-axis location of maximum elevation. It is clear that for all values of *Bi* examined, these two heights are essentially identical. Figure 2 also shows that the predicted bump height varies by up to 20% depending on thermal contact resistance; the maximum height is realized at *Bi*=0.1 (or h_c=47.2 kW/m^2 K). These variations of bump dimensions with thermal contact resistance can be critical in solder jetting, as solder bump height deviations of only a few percent can be detrimental to the successful implementation of the technique in high-precision electronic component manufacturing. The dimensionless contact area $(d_{con}/d_o)^2$ between the solidified solder droplet and the substrate is also shown in Fig. 2 and demonstrates a weaker dependence on thermal contact resistance, with an overall increasing trend towards higher values of *Bi* or h_c.

According to this trend, more efficient heat transport results in larger contact area, and, in turn, better attachment of the bump on the substrate.

A detailed comparison of several computed bump shapes with those determined experimentally was conducted, see Xiong et al. (1998), to determine the value(s) of *Bi* which provided the best match between the two shapes. Shape comparisons were conducted by means of the morphology of the ripples on the outline of the bump (see Fig. 3), and by measuring the contact area at the bump base. A phase-dependent value of *Bi* allowed best agreement between experiment and modeling. More specifically, the value Bi_l=0.5 (h_c= 235 kW/m^2 K) was identified for liquid solder/substrate contact, and the value Bi_s= 0.0275 (h_c= 13 kW/m^2 K) for solid solder/substrate contact. Figure 3a shows the bump geometry obtained in the experiments under the baseline conditions. Figure 3b displays the respective model-predicted shape when the above-mentioned values of Bi_l and Bi_s were used. It was concluded that the best agreement between experiment and modeling occurs when the thermal contact between solder and the substrate is reduced nearly by twenty-fold with the appearance of the solid phase.

Impact of Large Droplets

The results presented in this section were obtained in normal gravity and are discussed to demonstrate the capabilities of the solder-droplet generation apparatus and the high-speed visualization equipment. Both will be implemented in the pending microgravity experiments which will involve mm-sized droplets.

A 63%Sn–37%Pb solder droplet with pre-impact diameter d_0=0.9mm, velocity V_0=0.6m/s and temperature 210°C was visualized using high-speed video during its collision with a smooth stainless steel substrate at a temperature of 20°C. The dimensionless numbers corresponding to these conditions are Re=1676, We=7.4 and Fr=37. Figure 4 presents the temporal variation of two geometric parameters describing instantaneous droplet shape from impact up to complete solidification. These parameters are maximum height z_{max} and maximum splat diameter d_{max}, both of which change during the dynamic stages of the impact event. Both maximum height and diameter have been normalized in Fig. 4 with respect to d_0; time is also presented in a dimensionless form, i.e., $t^*=tV_0/d_0$. The oscillatory nature of the event is apparent in both curves of Fig. 4. The error bars drawn over selected points of the curves shown in Fig. 4a and 4b indicate the uncertainty tied to pixel size resolution. It is noted that time zero in Fig. 4 corresponds to the first acquired image where contact of the droplet and substrate was visualized. In this case, time zero does not correspond to the instant when contact between the two bodies was first established (time resolution is 1ms). The shape of the solidified bump is shown by the inset of Fig. 4b.

Figure 5 presents selected experimental images obtained via high-speed video when a 0.9mm solder droplet impacted on a smooth copper substrate of temperature 25°C. The initial droplet temperature was 210°C, and the impact velocity was 1.14m/s. The non-dimensional numbers corresponding to these conditions are Re = 3200, We = 27.7 and Fr = 147.5. In the shown sequence, time proceeds from left to right and from top to bottom. Under the above conditions, breakup of the droplet was revealed at the end of the first recoiling cycle after impact. The smaller droplet created by this breakup was subsequently reattached to the main mass, eventually creating a solid bump showing no apparent signs of the earlier separation event (see bottom right frame).

Acknowledgment

This work was supported by NASA Grant NAG3-1905.

REFERENCES

Bushko, W. and Grosse, I. R., 1991, "New Finite Element Method for Multidimensional Phase Change Heat Transfer Problems," Num. Heat Transfer, Part B, Vol. 19, pp. 31-48.

Dussan V., E. B., 1979, "On the Spreading of Liquids on Solid Surfaces: Static and Dynamic Contact Lines," *Ann. Rev. Fluid Mech.*, Vol. 11, pp. 371-400.

Waldvogel, J. M., Poulikakos, D., Wallace, D. B., and Marusak, R., 1996, "Transport Phenomena in Picoliter Size Solder Droplet Dispension," *Transactions of the ASME, J. Heat Transfer*, Vol. 118, pp. 148-156.

Waldvogel, J. M. and Poulikakos, D., 1997, "Solidification Phenomena in Picoliter Size Solder Droplet Deposition on a Composite Substrate," *Int. J. Heat Mass Transfer*, Vol. 40, pp. 295-309.

Xiong, B., Megaridis, C. M., Poulikakos, D. and Hoang, H., 1998, "An Investigation of Key Factors Affecting Solder Microdroplet Deposition," *ASME, J. Heat Transfer*, Vol. 120, pp. 259-270.

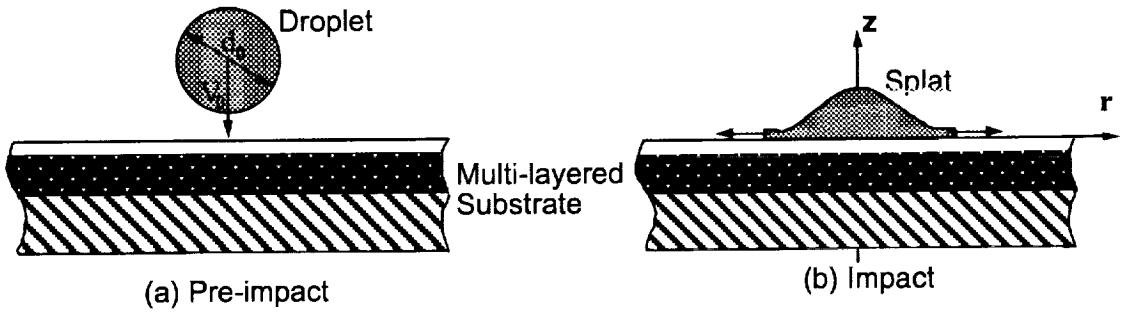

Fig. 1 Basic stages in solder microdroplet dispensing: (a) Flight, (b) Impact.

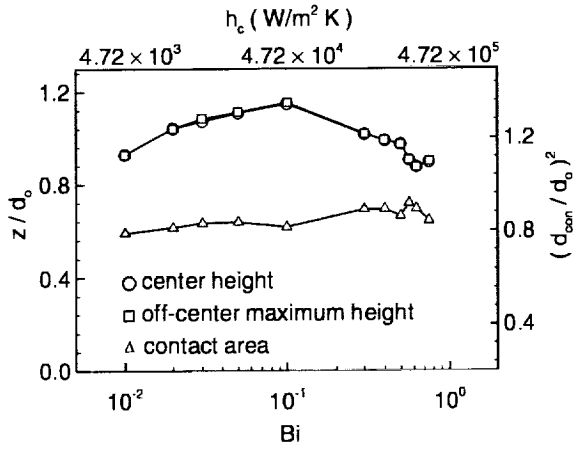

Fig. 2 Geometric parameters describing the solder bump shape and its dependence on thermal contact resistance: z/d_0 denotes the dimensionless height either on the symmetry axis (circles) or at the off-axis location of maximum elevation (squares); $(d_{con}/d_0)^2$ denotes the dimensionless contact area between the solidified solder droplet and the substrate.

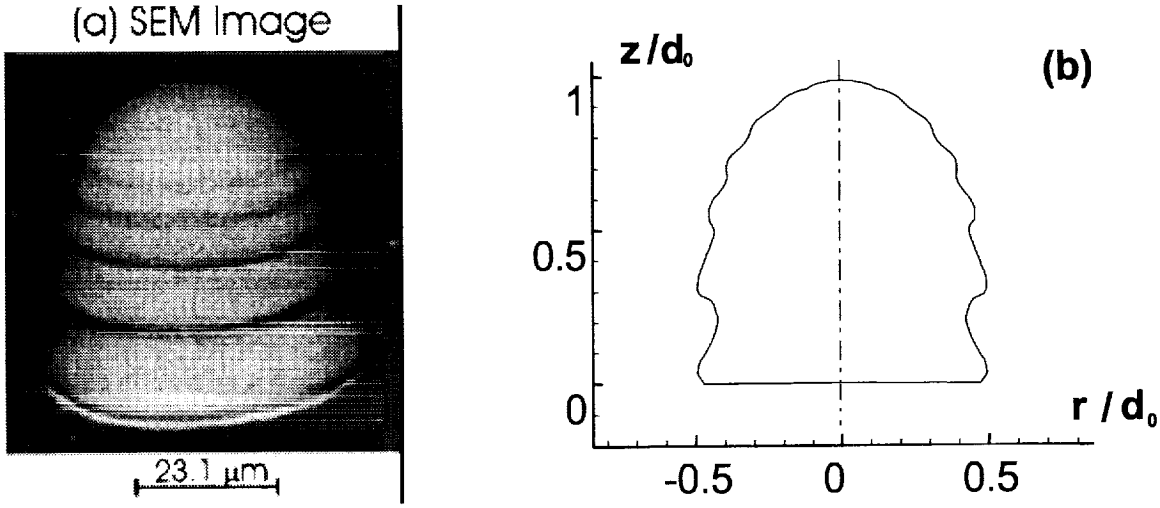

Fig. 3 (a) Solder bump geometry obtained in the microdroplet experiments for the baseline jetting conditions (Re=266, We=3.23 and Fr=4930). (b) Model-predicted shape providing best agreement between experiment and modeling. In order to achieve this agreement, a phase-dependent value of *Bi* was used: Bi_l=0.5 for liquid solder/substrate contact, Bi_s=0.0275 for solid solder/substrate contact.

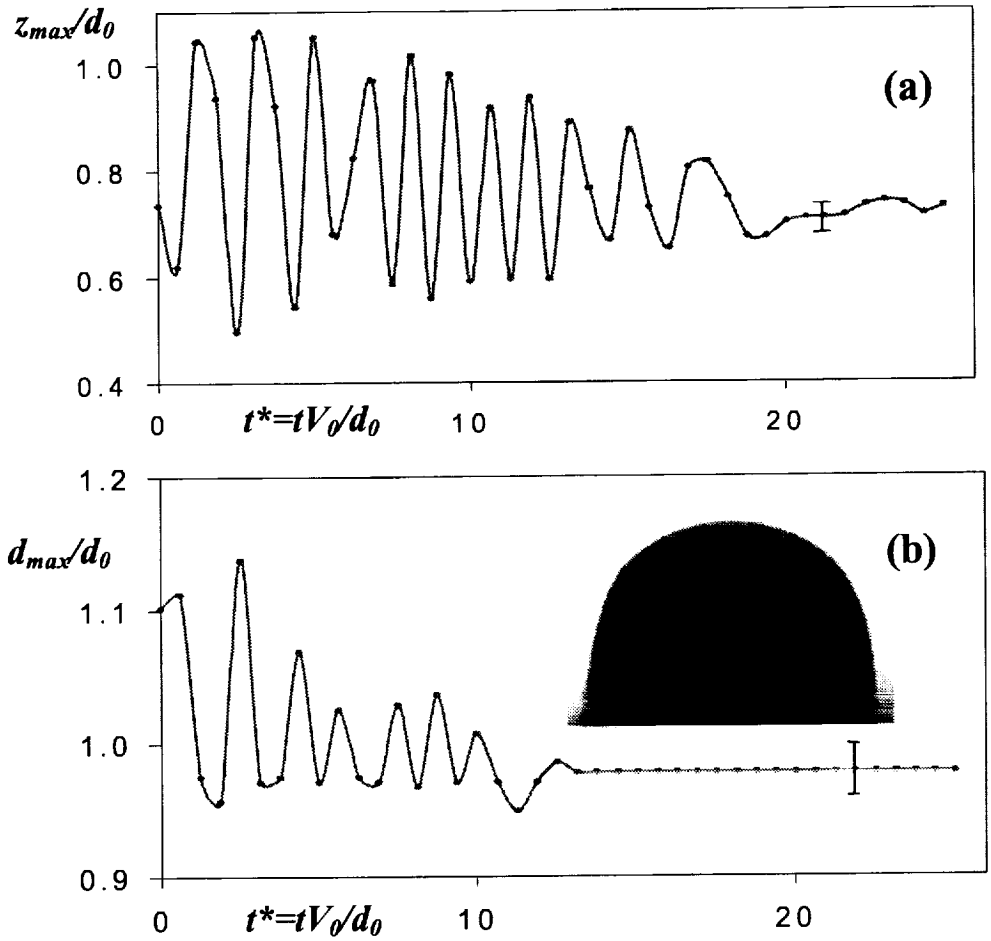

Fig. 4 Temporal variation of (a) dimensionless maximum droplet height z_{max}/d_0, and (b) maximum splat diameter d_{max}/d_0 from impact up to complete solidification of a mm-sized solder droplet impacting on a stainless steel substrate (Re=1676, We=7.4 and Fr=37). The error bars indicate the uncertainty due to pixel size resolution. The shape of the solidified bump is shown in the inset of frame (b).

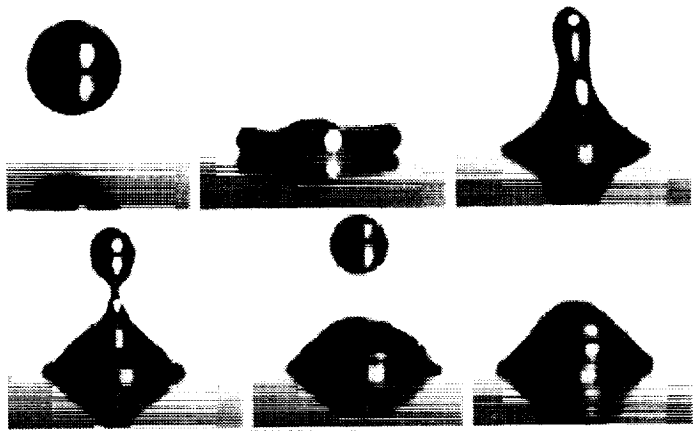

Fig. 5 Selected experimental images obtained using high-speed video when a 0.9mm solder droplet impacted on a smooth copper substrate (Re = 3200, We = 27.7 and Fr = 147.5). Time proceeds from left to right and from top to bottom. Under these conditions, breakup of the droplet was observed at the end of the first recoiling cycle after impact.

TWO DIMENSIONAL DENDRITIC CRYSTAL GROWTH FOR WEAK UNDERCOOLING

S. Tanveer, M. D. Kunka, M. R. Foster, The Ohio State University, Columbus OH 43210.
tanveer@math.ohio-state.edu

INTRODUCTION

Dendritic crystal growth has been a subject of interest to physicists, metallurgists as well as mathematicians. The most common example of such a growth is the well-known ice-crystal. From a physicist's perspective, dendrites constitute a relatively simple but important problem of pattern formation in non-equilibrium growth [3-5]. In metallurgy, dendrites are common to crystal formation in the manufacture of alloy when the growth rate exceeds some critical value. The literature on the subject is vast and reviewed in [3-6], as well as in our paper [1]. Here, we report a summary of the contents of our recent paper [2]; the reader is referred to it for more details.

APPROACH

In the first of a sequence of papers on dendritic crystal growth for weak undercooling [1], we derived asymptotic equations for weak nondimensional undercooling Δ (non-dimensionalized appropriately, through a combination of latent and specific heat) for a dendrite that was asymptotically a parabola in the far-field. A Peclet number, P was introduced in accordance to

$$\Delta = \sqrt{\pi P}\, e^P\, erfc\, (\sqrt{P}) \tag{1}$$

which is clearly small for small Δ. Based on the length scale a, associated with the far-field parabola, a velocity scale $U = 2 D P / a$ was identified, where D is the diffusion constant. a and a/U are used to nondimensionalize all lengths and times. We determined that if the initial deviations from an Ivantsov state (parabolic dendrite with a corresponding temperature profile) are limited to an $O(1)$ region near the tip, then the dynamic evolution of the dendrite for the nondimensional time $t \ll P^{-1}$ involves the $O(1)$ tip region only; in that region, the temperature is harmonic to the leading order, with appropriate boundary and far-field matching conditions. It is to be noted that the derivation does not assume that the deviation from the Ivantsov state is small; only that it does not extend all the way to the far-field $O(P^{-1})$ region. This tip-region dynamics was recast in terms of the evolution of the conformal mapping function from an upper-half ζ plane ($\zeta = \xi + i\eta$) to the exterior of the dendrite in the z-plane, where $z = x + iy$ (See Fig. 1). This function $z(\zeta, t)$ was shown to satisfy the following nonlinear integro-differential equation for real ζ (i.e. on ξ-axis):

$$z_t = (H + iR) z_\xi, \tag{2}$$

where

$$R(\xi, t) = \frac{1 - \mathcal{B}\, Im\, \omega_\xi}{|z_\xi|^2}, \tag{3}$$

$$-H(\xi, t) = \mathcal{H}\{R\}(\xi, t) \equiv -\frac{1}{\pi} \int_{-\infty}^{+\infty} \frac{d\xi'}{\xi' - \xi}\, R(\xi', t), \tag{4}$$

$$\omega(\xi, t) = K(\xi, t) + i\, \mathcal{H}\{K\}(\xi, t), \tag{5}$$

where

$$K(\xi, t) = (1 + a f(\xi, t))\, \kappa(\xi, t), \tag{6}$$

$$\kappa(\xi, t) = -\frac{1}{|z_\xi|}\, Im\, \frac{z_{\xi\xi}}{z_\xi}, \tag{7}$$

$$f(\xi, t) = 1 - cos\, 4(\theta - \theta_0) = 1 - Re\, \left(\frac{z_\xi^2}{\bar{z}_\xi^2} e^{-i\, 4\theta_0} \right). \tag{8}$$

In the above, the nondimensional surface energy parameter $\mathcal{B}$ is given by

$$\mathcal{B} = \frac{c_p\, \tilde{d}_0\, T_M}{2\, a\, L\, P} \tag{9}$$

where $\tilde{d}_0$ is the capillary length, c_p the specific heat, T_M the melting temperature of a planar interface, and L the latent heat. Further, in the above, κ is physically the nondimensional curvature and $1 + a\, f$ is a four-fold surface energy anisotropy correction. Here θ the angle between the normal to the interface (pointing towards the melt) and the y axis, while θ_0 is some fixed value denoting a direction along which surface energy is a minimum.

Through a linearization of the equation for $z(\xi, t)$ about some generally arbitrarily time dependent state, we were able to determine expression for growth rate of an initially localized disturbance in terms of the base state, through a Fourier-analysis, when the disturbance is far from the tip. In the special case of a base state that is steady and is close to an Ivantsov state, the expressions for the growth rate were in accordance to prior results [7]. Interestingly enough, it was possible to obtain the same results by analytically continuing the equations (2)-(8) to the lower-half complex ζ plane and carrying

out an asymptotic analysis for the linearized equations near singularities of z_ζ.

It is to be noted that while the lower-half ζ plane does not correspond to any part of the physical domain, singularities of $z(\zeta, t)$ approaching the real axis from below correspond to interfacial distortions. In particular, we found that according to the linearized dynamics, surface energy prevents an initially localized disturbance from remaining localized beyond a certain time. Arbitrarily small initial interfacial distortions (noise), representable by some singularity distribution in $Im\ \zeta < 0$, significantly affect the interface later in time when singularities of the associated zero-surface-energy problem approach or cross $Im\ \zeta = 0$, even though surface energy locally smooths out all singularities in the linearized dynamics. The extent to which the zero-surface-energy singularity dynamics relates to growth rate and dispersion of disturbances for small non-zero surface energy was also uncovered. Hence, zero-surface-energy singularity dynamics have both qualitative and quantitative impact on the physical predictions mentioned above.

The relation between complex singularity dynamics and the evolving physical features of a dendrite transcends the restriction posed by linearized dynamics since a singularity of the conformal map in $Im\ \zeta < 0$ can result in large interfacial distortions when that singularity approaches $Im\ \zeta = 0$. In particular, if we consider an isolated singularity $\zeta_s(t)$ of z_ζ in the lower-half plane so that

$$z_\zeta \sim E_0(t)\,(\zeta - \zeta_s)^{-\beta} \qquad (10)$$

near $\zeta = \zeta_s(t)$, then if the singularity is very close to the real axis, we can expect a corner pointed towards the crystal, with included angle $(1-\beta)\,\pi$. This is locally rounded off over a length scale determined by singularity distance from the real axis. The larger the $|E_0|$ (singularity 'strength'), the larger is the impact region on the interface. $arg\ E_0$ determines the orientation of this distortion relative to the y-axis. The physical effect of an isolated complex singularity corresponding to $\beta = 1$ (pole) is to create parallel sided indentation with width $\pi\ E_0$ and depth that scales as $-\ln\ \eta_s$, where $\eta_s = Im\ \zeta_s$.

It is to be noted that the geometrical features at the interface associated with (10), as discussed above, will remain intact for a period of time, even when the actual singularity $\zeta_s(t)$ is smoothed out or replaced by a cluster of other singularities, provided there is some intermediate range: $\mathcal{B}^\delta << |\zeta - \zeta_s(t)| << 1$ for some δ and some set of real ζ for which the behavior (10) persists.

Prior work for dendrites [1], as well as by others on the mathematically analagous Hele-Shaw problem, shows that the zero-surface-energy dynamics preserves the form of the singularity – i.e. β in (10) remains invariant with time; only its position $\zeta_s(t)$ and its strength $E_0(t)$ evolve (except for a pole where E_0 is invariant). When $\beta < 0$, the form (10) is not invariant. Generally for an initial singularity of that kind,

$$z_\zeta \sim A_0(t) + E_0(t)\,(\zeta - \zeta_s(t))^{-\beta} \qquad (11)$$

for ζ sufficiently close to ζ_s. Such singularity on the real axis does not introduce discontinuity in slope, except in non-generic cases– $A_0 = 0$ just when $Im\ \zeta_s = 0$. In this exceptional case, the corner is directed towards the melt, in contrast to $\beta > 0$ case, when it is directed towards the crystal.

All singularities, regardless of their type, were shown to continually approach the real axis with time, though for $\beta > \frac{1}{2}$, they do not impinge the real axis in finite time–indeed they slow down significantly as they come close to the real axis.

A point where $z_\zeta = 0$, but z_ζ is otherwise analytic, is referred to as a zero. A zero on the real axis corresponds to a zero-angled cusp on the interface that protrudes into the melt. Prior work, discussed in [1], shows that a zero remains invariant with time, when surface energy is neglected, i.e. the form

$$z_\zeta \sim z_{\zeta\zeta}(\zeta_0(t), t)\,(\zeta - \zeta_0(t)) \qquad (12)$$

remains invariant. The evolution equation for $\zeta_0(t)$, however, is found to be different from that of a singularity $\zeta_s(t)$. In particular $\zeta_0(t)$ may or may not approach the real axis. For some set of initial conditions, a zero does impact the real axis in finite time. The mathematical solution ceases to be physically meaningful beyond this cusp-formation time.

The connection between the dynamics in the extended domain $Im\ \zeta \leq 0$ and the physical features of an evolving dendrite, as described above, is particularly useful, since there is strong evidence that the zero-surface-energy dynamics in the extended domain is well-posed [See [8]-[9] for evidence for the mathematically similar Hele-Shaw problem], in contrast to the interfacial evolution itself. In the latter case, the domain is restricted to $Im\ \zeta = 0$. This well-posedness at the zeroth order mathematically justifies a systematic perturbation procedure in the extended complex domain to study how small but nonzero surface energy (with or without anisotropy) alters the zero-surface-energy dynamics. The viewpoint we followed in [1]-[2], following the Hele-Shaw analysis with isotropy [9]-[10], is that the interfacial dynamics comes as a byproduct of the dynamics in the extended domain.

A necessary drawback to the above mentioned procedure is that now one must specify initial conditions in the extended complex domain $Im\ \zeta \leq 0$, which obviously cannot be done in an experiment where only the initial interface shape, up to some non-zero error, can be controlled. Connection to observed statistical features of an experiment can be made only by studying the statistics of an ensemble of complex-plane initial conditions, allowing for every conceivable singularity distribution, and with each member of the ensemble consistent with the given initial shape to within experimental error. Clearly, many different singularity distribution can result in the same approximate interfacial shape. However, an essential precursor to such a statistical study is the thorough description of the dynamics of *all* possible forms for singularities in $Im\ \zeta < 0$. Once this is clarified, one can proceed with the statistical study for an ensemble of initial conditions. That such an approach may be useful is already demonstrated in [2], where we obtain dendrite coarsening results based on an ensemble of particular singularities. However, in general, the analytic continuation of $z(\zeta,0)$ into $Im\ \zeta < 0$, corresponding to a general analytic initial shape, can be expected to contain natural boundaries and perhaps other singularities that are not isolated. Further, even the class of all possible forms of isolated singularities is too broad to study; only a small subset of possible initial conditions contains the specific classes of isolated singularities and zeros, as in (10) and (12), are considered. Nonetheless, such isolated-singularity distributions do correspond to a range of interfacial distortion, when they come close to the real axis. For that reason, we believe that the statistical features of the interfacial dynamics within this limited class of initial conditions are not very different from what is observed in experiment – with the additional proviso that a two-dimensional theory is applicable, at least insofar as scaling predictions.

However, even within the class of possible initial singularities studied, there are basic mathematical issues concerning the asymptotic matching of inner and outer regions in the complex plane (as the surface-energy parameter goes to zero) that remain unresolved. In carrying out matching in the neighborhood of a singularity that is preserved by the zero-surface-energy dynamics, it is observed that the matching is necessarily sectorial–the inner solution does not match to the outer solution in every direction in the complex plane; it can be matched in a certain sector only. This is not a surprising result, since the steady dendrite problem is known to have the same features. However, unlike the steady problem where there are well defined global Stokes lines even beyond the immediate vicinity of an inner-region that determine local sectors of matching (See [11] for instance.), no basic mathematical principle exists for the time-evolving flow. Only local Stokes lines, corresponding to local similarity solutions of the partial differential equations in the inner region, can be identified. There, we invoke a matching principle based on one used in the Hele-Shaw context [9] . The only direct evidence that such a matching principle is sound is our prior finding, in [1], that there is consistency between results from a Fourier analysis in the real domain and a complex singularity approach involving inner-outer matching for the linearized problem.

Further mathematical difficulties arise with initial zeros of z_ζ, since the full investigation of the dynamics at different stages is hampered by lack, in many cases, of either analytical or numerical solutions to a set of complicated partial differential equations in the complex plane. It is to be noted that the mathematical theory of nonlinear higher order partial differential equation in the complex plane is quite undeveloped. Progress in this case has been made, as in [8], with additional ansatz on the dynamics at intermediate stage[s]. There is no direct evidence that these ansatz are correct by themselves, though the careful numerical calculations of the interfaces themselves, for a sequence of computations for decreasing surface energy, indirectly confirm the basic features of the analytic theory, both for the associated isotropic Hele-Shaw problem [10], and also for anisotropic Hele-Shaw and dendrite problems. This work will be reported in an upcoming paper.

Despite the qualifiers above and the fact that our method necessarily requires a lengthy investigation of complex dynamics involving many kinds of initial singularities with corresponding inner equations depending on their distance from the real axis as well as the relative ordering of anisotropy and surface energy, this technique is the only one known for the fully nonlinear, time-evolving dendrite in the small-surface-energy limit. This limit is precisely the most difficult to explore computationally , since resolving small capillary lengths necessarily strains the capacities of computers. Further, even for cases where $\mathcal{B}$ is not small, the small surface energy limit cannot be avoided at large distances from the dendrite tip, where the curvature of an essentially parabolic keeps decreasing.

ISSUES ADDRESSED

In [2], we continue our study of complex singularities initiated in [1] by including small but nonzero surface energy ($0 < \mathcal{B} << 1$) in the nonlinear dynamics in the extended complex domain, generally taking anisotropy into account. The purpose of this paper is to address, partly or wholly the following important issues:

1. How does a non-zero $\mathcal{B}$ alter singularities described in (10)? Do the the alterations and modifications to the singularity stay confined to a small cluster around $\zeta_s(t)$? Is there an intermediate spatial scale over which the behavior (10) is relevant as $\mathcal{B} \rightarrow 0$? If so, is there a limitation on the order of $|E_0(0)|$ and the time for which this is so such behavior persists? How does anisotropy in surface energy come into play?
2. What are the time and spatial scales over which surface energy effects become important to the real axis dynamics for a singularity corresponding to $\beta > \frac{1}{2}$? Recall that according to zero-surface-energy dynamics, such singularities do not impinge the real axis in finite time, though it continually approaches it.
3. For singularities corresponding to $0 < \beta < \frac{1}{4}$, which are known, in the absence of surface energy, to impact the real axis in finite time (leading to corners at the interface), what are the relevant space and time scales associated with a small nonzero $\mathcal{B}$, when $Im\ \zeta_s(t) \rightarrow 0$
4. What can be expected about the growth rate of interfacial distortions associated with approaching complex singularities discussed above in (1)-(3) ? How does surface energy dissipation of weak singularities, determine a cut-off in the growth rate ? How does anistropy affect the result ? It is often stated in the literature that interfacial distortions that point towards the crystal appear to remain stationary in the laboratory frame. Is there a limitation on the time scale over which this is true ?
5. What is the effect of anisotropic surface energy on an initial zero? Is there a 'daughter singularity' $\zeta_d(t)$ that emerges from an initial zero $\zeta_0(0)$, as for the isotropic Hele-Shaw problem [8]-[10] ? If so, how does anisotropy alter the structure of the cluster of actual singularities of z_ζ that are centered at $\zeta_d(t)$.
6. How does the impact of $\zeta_d(t)$ on the real axis affect the interfacial features? As with isotropic Hele-Shaw problem, can one expect the daughter singularity impact time to indicate when an actual interface will veer off from the corresponding zero-surface energy solution ?
7. How are interfacial cusps, associated with a zero $\zeta_0(t)$ impacting the real axis in finite time, prevented by small surface energy effects ? One scenario is that small surface energy becomes important only when the interface becomes close to a cusp, i.e. when curvature of the zero-surface-energy solution becomes large. The second is that the interface never comes close to cusp-formation because it necessarily veers off from the corresponding zero-surface-energy solution significantly before any $\zeta_0(t)$ can impact the real axis. In the context of complex singularity dynamics of this paper, the two scenarios are distinguished by the question: does a daughter singularity $\zeta_d(t)$ necessarily impact the real axis before the corresponding zero $\zeta_0(t)$?
8. How does a given disturbance, that may be associated with many different complex singularity distributions cause $O(1)$ localized deviation in interfacial slope from a smooth background state, evolve in time. Is there a rescaling under which the equations remain invariant in the small surface energy limit ? What does such an invariance tell us about the dynamics ?
9. How do surface energy and anisotropy modify or confirm the coarsening scenario that we proposed in [1]? The selection effect of surface energy on an ensemble of assumed singularities of different strengths is examined in [2], resulting in a prediction for the coarsening rate of $|y|^{1/2}$ for an intermediate range of distances where $|y|$ is large compared to some inverse power of $\mathcal{B}$. There is no necessary contradiction with the well known $|y|^{1/3}$ coarsening result [12], since that is valid for all sufficiently large distances from the tip.

ACKNOWLEDGEMENTS

The authors gratefully acknowledge the support of NASA Micro-Gravity Grant NAG3-1947.

References

[1] M.D. Kunka, M.R. Foster & S. Tanveer, ***Physical Review E***, 56, 3068, (1997)

[2] M.D. Kunka, M.R. Foster & S. Tanveer, Submitted to ***Physical Review E***, 1998.

[3] J.S. Langer, "Chance & Matter", ed. J. Souletie, North Holland, Amsterdam (1987).

[4] D.A. Kessler, J. Koplik & H. Levine, ***Advances in Physics***, **37**, 255 (1988).

[5] P. Pelce, "Dynamics of curved fronts", Academic (1988).

[6] M.E. Glicksman & S.P. Marsh, "The dendrite", in Handbook of Crystal Growth, Vol. 1, Edited by D.T.J. Hurle.

[7] M. Barber, A. Barbieri & J.S. Langer, ***Phys. Rev. A*** **36**, 3340 (1987).

[8] G.R. Baker, M. Siegel & S. Tanveer, ***J. Comp. Physics***, **120**, 348 (1995).

[9] S. Tanveer, ***Philosophical Transactions of the Royal Society of London A***, **343**, 155, (1993).

[10] M. Siegel, S. Tanveer & W. Dai, (1996), To appear in ***J. Fl. Mech.***

[11] S. Tanveer, ***Phys. Rev. A*** **40**, 4756 (1989).

[12] P. Voorhees & M. Glicksman, Oswald ripening and relaxation in dendritic structures, ***Met. Trans. A*** **15A**, 995 (1984).

Figure 1: Conformal map from upper-half ζ plane to the dendrite exterior

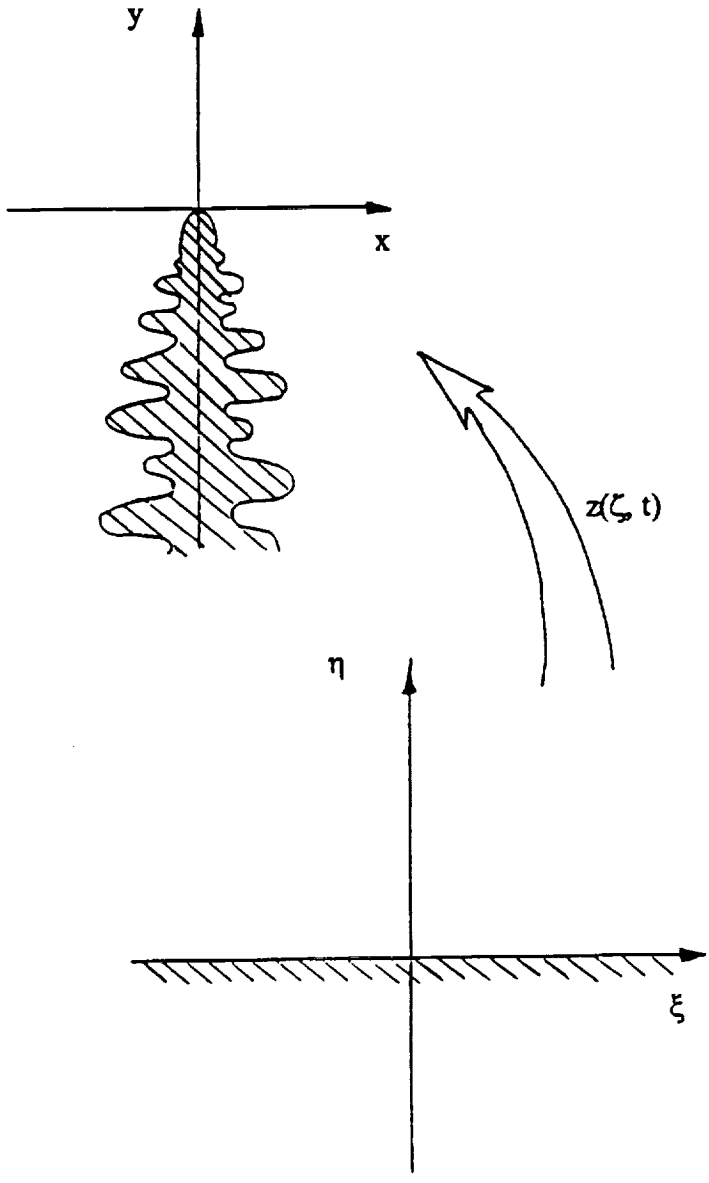

Session 4B

Granular Media

PARTICLE SEGREGATION IN COLLISIONAL SHEARING FLOWS.

J. T. Jenkins[1] and M. Y. Louge[2], [1]Department of Theoretical and Applied Mechanics, [2]Sibley School of Mechanical and Aerospace Engineering, Cornell University, Ithaca, NY 14853.

INTRODUCTION

The size segregation of flowing or shaken grains is a commonly observed phenomenon in industrial processes and in nature. In many industrial processes a homogeneous aggregate is desired; in these, size segregation is undesirable. However, in the mining industry, for example, segregation by size is exploited in some processing operations. Also, grain segregation is useful in understanding the origin of natural grain deposits; here it provides an indication of whether an aggregate of grains was deposited dry, with the larger grains above, or under water, with the larger grains below [1].

In systems that do not involve much agitation of the grains, several mechanisms that involve gravity have been identified as leading to such segregation. These include the preferential downward percolation of smaller particles in relatively slow inclined shear flows [2], the upward frictional ratchetting of large particles [3], and the preferential filling of space beneath larger particles by smaller particles in a system that is occasionally shaken [4,5].

In highly agitated flows, there is a mechanism independent of gravity that is available to drive separation of different grains. This is associated with spatial gradients in the energy of their velocity fluctuations. In steady, fully-developed flows, the balance of momentum exchanged in collisional interaction between and among different species of grains requires, in general, that spatial gradients of concentration be balanced by spatial gradients of particle fluctuation energy.

In sheared or vibrated systems of colliding grains, gravity also influences mixtures of grains of different sizes. Here, buoyant forces act to separate grains that differ in size and, consequently, in the local volume that they displace. In reduced gravity, buoyancy is suppressed and attention can be focused on the simpler balance involving the gradients in concentration and the gradients in fluctuation energy. Reduced gravity also eliminates the possibility that a collisional flow will condense into a slower, denser flow dominated by enduring contacts rather than by collisions.

Because collisions between grains inevitably dissipate energy, collisional granular shear flows are usually of limited extent in the direction transverse to the flow. One consequence of this is that shear flows are strongly influenced by their boundaries. Because grains, on average, slip relative to boundaries, a bumpy or frictional boundary can convert slip energy into fluctuation energy. However, because each collision between a grain and the boundary dissipates fluctuation energy, there is a competition between production and dissipation.

In principle, it is possible to design the geometry of the boundary - for example, the size and spacing of the bumps - so that the boundary either produces or dissipates fluctuation energy [6]. This permits the control of the component of the spatial gradient of the fluctuation energy that is normal to the boundary. The gradients in fluctuation energy established by such boundaries may be exploited to drive the separation by size or other properties in a binary mixture of spherical grains.

Microgravity makes the visual observations possible by permitting us to employ moderate rates of shear. On earth, the effects of gravity can be minimized by shearing so rapidly that the particle pressure overwhelms gravity.

However, in this event, separation takes place too rapidly for visual observation, buoyancy and/or condensation associated with the centripetal acceleration must be accounted for, and the particles can be severely damaged. Because, in the absence of gravity, the only available time scale is proportional to the speed of the moving boundary, this speed can be made arbitrarily slow to permit observations and to avoid particle damage, without altering the phenomenon under study.

The primary goal of this research is to carry out a physical experiment in which particle segregation is induced and maintained in a collisional flow of a binary mixture of two different types of spheres. The segregation will be driven in the absence of gravity by a spatial gradient in the kinetic energy of the velocity fluctuations of the mixture. The flow is to take place in a shear cell in the form of a race track in which the grains are sheared by the motion of the inner boundary relative to the outer. The gradient of the kinetic energy is to be maintained using boundaries with different geometric features that result in different rates of conversion of the mean slip velocity into fluctuation energy at their surfaces.

The planned experiments will isolate and investigate two different sub-mechanisms of collisional segregation that usually occur together: the first is associated with differences in the inertia of the spheres, the second is associated with differences in the geometry of the spheres. We will attempt to neutralize a third sub-mechanism associated with differences in collisional dissipation between the two types of spheres. Inertial segregation will be studied in a system of spheres with different masses, but

equal diameters; geometric segregation will be studied in a system with different diameters, but equal masses.

In the experiment, a steady shearing flow will be maintained in shear cell by the relative motion of parallel, bumpy boundaries. The resulting profiles of mean velocity, fluctuation velocity, and concentration will be measured in a region of fully-developed flow. They will be compared with those predicted by theory and those measured in computer simulations. We will also test simple analytical results for the mean velocity and fluctuation energy, obtained in a dense limit of the kinetic theory, against the experiment. The extent of agreement between the experiments, the theory, and the computer simulations will provide a test of the assumptions upon which the theory and the computer simulations are based.

For the theory, these include the assumptions that the collisions are instantaneous and binary, that there is no correlation in pair position and/or velocity, that terms quadratic in the gradients may be neglected, that friction may be incorporated into the flow theory and boundary conditions in relatively simple ways, that there is equipartition of energy between the two species, that the inertia associated with diffusion may be neglected, and that the species viscosity does not influence segregation. The computer simulations are based on a hybrid hard-particle overlap algorithm for collisional interactions and the implementation of a simple three parameter model of a collision.

Computer simulations play an important role in the research. They have guided the design of the shear cell shown in Fig. 1, and they have assisted us in determining the strategy for flow visualization and in establishing our requirements for microgravity.

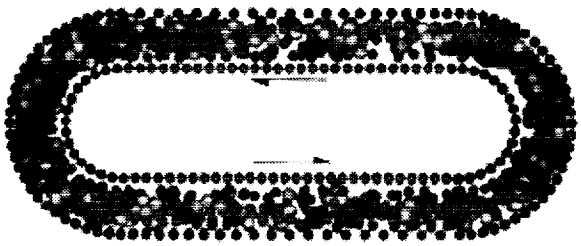

Figure 1 A shear cell of modest size. The outer boundary is fixed. The inner boundary moves with speed U in the direction shown.

The link between the computer simulations, the theory, and the physical experiments is provided by our ability to measure the collision parameters in an accurate and reproducible experiment. Our hope is to provide a demonstration of the power and utility of computer simulations and to establish them as an equal partner to theory and physical experiment. In this event, fewer physical experiments need be done, and the simulations can be used with confidence as the basis of the theoretical modeling. Also, with advances in computing power, such simulation may eventually be employed to study the behavior of complete systems of technological importance that involve collisional granular flow.

The success of experiment will indicate that the general theoretical framework provided by the kinetic theory is the appropriate one for describing collisional granular flow. It will reinforce our confidence in our modeling of the boundary conditions, the frictional interactions, and in the simplifying assumptions that were made to describe segregation. The experiments may also show that the dense limit of the kinetic theory for a single species provides an adequate description of the mixture velocity, mixture fluctuation energy, and mixture concentration. Then relatively simple analytical formula may be used to predict these, at least in steady, fully-developed flows. Similar simplifications of the theory for segregation are likely to emerge from our study of simple limiting cases.

We anticipate that the knowledge gained in this activity will contribute to our understanding of particle segregation in reduced gravity, where segregation mechanisms other than gravitational begin to dominate and collisional flows are more easily sustained. Examples of such flows are those involved in the transport of materials in Lunar and Martian environments and in manufacturing processes in space. We also anticipate that we will gain insight into the role played by collisional segregation mechanisms in grain flows in Earth gravity.

BACKGROUND

Most experimental studies of particle segregation are carried out on flows involving a free surface that are condensed by gravity into layers of grains in relative motion [2]. In each layer grains interact with at least several of their neighbors through rubbing and bumping. Phenomenological models of segregation in such flows that take into account their significant features often provide a satisfactory description [2]. Because the interactions of a single particle with its neighbors are so complicated and because the statistical characterizations of the interactions certainly involve strong correlations between the positions and velocities of particles, it is likely that a more detailed treatment is not possible.

Careful observations of particle segregation in less condensed free surface flows are less common. Such flows involve interactions between particles that are more violent than rubbing and bumping; these interactions can often be realistically modeled as binary collisions. Also, in these more agitated flows, the particle interactions are more random and, as a consequence, their statistical description is simpler.

Collisional flows can most easily be maintained in a shear cell. Typically, in such a cell, the flow takes place in a cylindrical annulus in which the bottom and sides are rotated and the top is held fixed [7]. The weight of the top is supported by collisions with the agitated grains of the shearing flow. This weight can be adjusted in order to maintain a fixed flow thickness or to vary the thickness in a controlled way. Knowledge of how the cell has been filled and the thickness of the flow permit the calculation of the average volume fraction. A measurement of the force necessary to keep the top from rotating permits the determination of the shear stress required to maintain the relative velocity of the bottom and top.

At high enough rates of shear, the weight of the grains in the cell is often a small fraction of the weight of the top of the cell. In this event, the influence of gravity on the flow may be neglected. However, the centripetal acceleration is always important; at the highest shear rates, it is typically more than five times the gravitational acceleration. Also, at the high shear rates necessary to render gravity negligible, collisions between the particles and between the particles and the boundaries may become so violent as to cause significant damage.

Theories for the prediction of particle segregation in collisional shearing flows make use of the analogy between the molecules of a dense gas and the agitated macroscopic grains that exists provided that the collisions between grains do not dissipate too much energy [8]. The most refined theory for segregation in dense molecular gases is a kinetic theory for mixtures of elastic spheres based on the assumption of molecular chaos and the correct extension to mixtures of Enskog's characterization of the influence of the finite volume of the particles on their frequency of [9, 10]. The derivation of the theory employs the Chapman-Enskog expansion to obtain the velocity distributions to sixth order. The results of the theory are consistent with irreversible thermodynamics, have been presented graphically, and are available numerically.

In our application of this theory to mixtures of inelastic grains, we have characterized the amount of permitted dissipation and we have obtained analytical results at second order in the Chapman-Enskog expansion for binary mixtures [8]. Analytical expressions permit the rational approximation of the coefficient governing transport, segregation, and dissipation over a range of mixture and species volume fractions and particle size and mass ratios.

The presence of dissipation in collisions permits collisional shearing flows of inelastic grains to achieve a steady balance in which the rate at which the kinetic energy of the velocity fluctuations increases, due to collisions driven by gradients in the mean velocity of the mixture, is equal to the rate at which it decreases, due to the energy lost in each collision, and the rate at which it is transported, due to inhomogeneities in the flow. The experimental study of special, simple types of binary mixtures of spheres in inhomogeneous steady shearing flows permits various aspects of the phenomena of segregation to be studied separately and helps in developing intuition about the behavior of more complicated mixtures.

In order to carry out the analysis of such experiments, we have extended existing theory for shearing flows of identical spheres in several ways. We have accounted for friction in collisions between particles in the flow by incorporating the additional energy loss into an effective coefficient of restitution [11]. We have extended existing boundary conditions for a single species interacting with either a bumpy or a frictional boundaries to apply to a binary mixture interacting with a boundary that is both bumpy and frictional [12]. We have generalized existing theory for a dense shearing flow of a single species slightly to apply to the prediction of the profiles of mixture mean velocity and mixture mean kinetic energy in dense shearing flows of a binary mixture between bumpy, frictional boundaries.

In order to incorporate friction into the kinetic theory, a simple but realistic model of a frictional collision must be employed. The simplest such model distinguishes between collisions in which the relative velocity of the points of contact is momentarily zero during a collision and those in which it is not. The former are called sticking collisions, the latter are called sliding collisions. The model employs three parameters: a coefficient of normal restitution for both sticking and sliding collisions, a coefficient of friction for sliding collisions, and a coefficient of tangential restitution for sticking collisions [13]. We have employed the model to interpret the results of experiments on binary collisions between identical spheres and collisions between a single sphere and a flat or a bumpy boundary. The parameters determined in this way provide an excellent fit to the data [14, 15].

Computer simulations have played important roles in the development of the field of granular mechanics [16, 17]. Such simulations of dissipative but frictionless disks and spheres have, in some instances, supported simple predictions of the kinetic theory and, in other instances, shown that collisional granular flows of frictionless, inelastic particles could behave in ways far more complicated than predicted. A corresponding contribution from computer simulations for frictional particles was not possible until a simple, physically realistic model of the frictional interaction between two colliding spheres could be verified in physical experiments. Using the simple model, numerical simulations have

contributed to an understanding of the flow of inelastic frictional spheres down frictional inclines and in the determination of boundary conditions for frictional, inelastic spheres interacting with a flat, frictional elastic wall [18, 19]. Such simulations can now be employed with confidence to interpret physical experiments and to inform the development of theory.

PRELIMINARY RESULTS

The objectives of the experiment are to control the distributions of mixture fluctuation energy across the cell using boundaries with the appropriate geometric features and collision properties; to measure profiles of mixture mean velocity, mixture number density, and mixture fluctuation energy across the cell in order to compare them with the predictions of both the dense and the full theory and to compare the flows and fields of fluctuation energy and species' number densities with those predicted in the computer simulations.

As Figs. 2 demonstrates with an image acquired on the KC 135 microgravity experimental aircraft, the vision algorithm can determine the location of the sphere centers accurately.

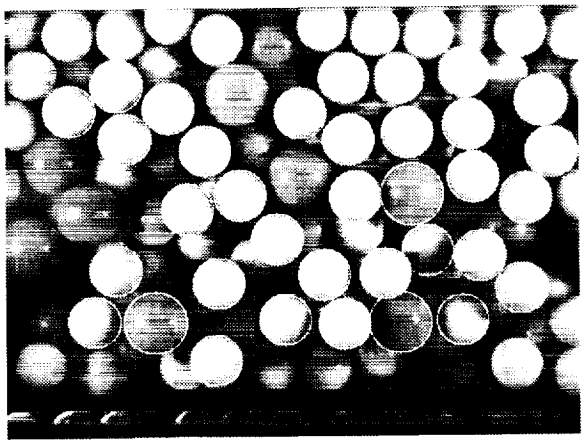

Figure 2 View of the fully-developed region of the prototype cell with ν_A = 10% and ν_B = 30%. Circles indicate detected spheres.

Figs. 3 and 4 show that the computer vision algorithm produces profiles of mean velocity and temperature that are in reasonable agreement with the computer simulations.

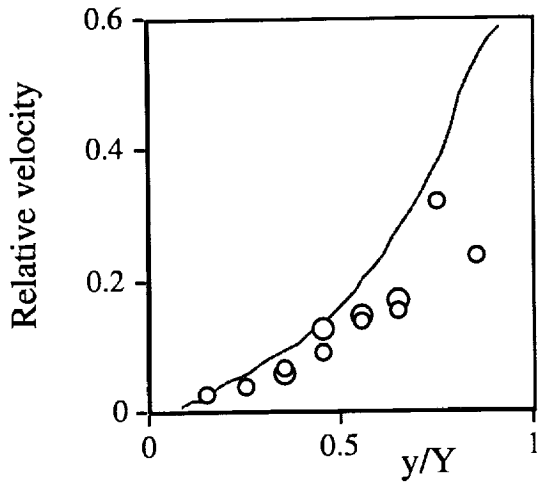

Figure 3 Mean transverse grain velocity profile relative to the speed of the boundary. The small and large circles represent data for the small and large spheres, respectively. The lines are predictions of the simulations.

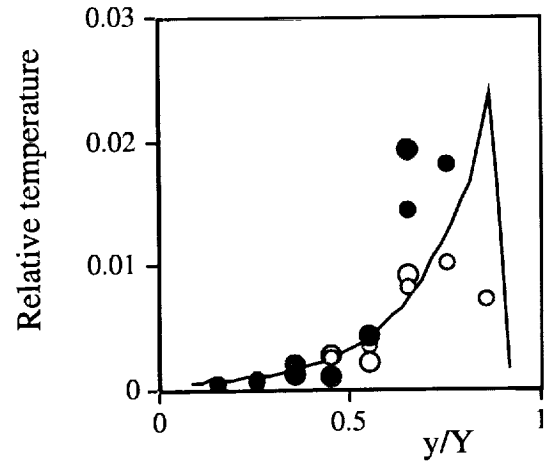

Figure 4 Temperature made dimensionless with $m_B U^2$. The filled and open circles represent temperature in the x- and y-directions, respectively.

The computer simulations were carried out in a cell that was periodic in the flow direction with a square cross-section of about eight diameters of the smaller spheres in the flow. On its inner and outer boundaries, cylinders with the diameter of the smaller spheres in the flow were spaced with their centers one and one and one-half diameters apart, respectively. The side walls were flat. The spheres in the flow were of the same material with their diameters in a ratio of four to three. The coefficient of friction and the coefficient of tangential restitution in all collisions were taken to be 0.1 and 0.4, respectively. The coefficient of normal restitution

between spheres in the flow was taken to be 0.9; that for collisions between spheres in the flow and the boundaries was taken to be 0.8. These are typical values measured in experiment [15].

Note that Figs. 3 and 4 indicate that the chain was run too fast in the KC 135 tests for the frame rate employed. As a consequence, the velocity statistics near the moving boundary were not captured as accurately as they can be.

AKNOWLEDGEMENT

This research is sponsored by the Life Sciences and Microgravity Research Program of the National Aeronautics and Space Administration.

REFERENCES

[1] S. B.Savage, Interparticle percolation and segregation in granular materials: a review. In A. P. S. Salvadurai, Ed., Developments in Engineering Mechanics, pp.347-363, Amsterdam, 1987. Elsevier Science Publishers.

[2] S. B. Savage and C. K. K. Lun,
Particle size segregation in inclined chute flow of dry cohesionless granular solids. Journal of Fluid Mechanics, 189, 311-335, 1988.

[3] P. K. Haff and B.T. Werner,
Computer simulation of the mechanical sorting of grains. Powder Technology}, 48, 239-245, 1986.

[4] A. Rosato, K. J. Strandburg, F. Prinz, and R.H. Swendsen, Monte Carlo simulation of particulate matter segregation.
Powder Technology, 49, 59-69, 1986.

[5] A. Rosato, K. J. Strandburg, F. Prinz, and R. H. Swendsen, Why the Brazil nuts are on top: size segregation of particulate matter by shaking.
Physical Review Letters, 58, 1038-1040, 1986.

[6] D. M. Hanes, J. T. Jenkins, and M. W. Richman, The thickness of steady plane shear flows of smooth, inelastic circular disks driven by identical boundaries. Journal of Applied Mechanics, 55, 969-974, 1989.

[7] K. Craig, R. H. Buckholz, and G. Domoto.
An experimental study of rapid flow of dry cohesionless metal powders. Journal of Applied Mechanics}, 53, 935-942, 1986.

[8] J. T. Jenkins and F. Mancini. Kinetic theory for smooth, nearly elastic spheres. Physics of Fluids, A1, 2050-2057, 1989.

[9] M. Lopez deHaro, E. G. D. Cohen, and J. M. Kincaid, The Enskog theory for multicomponent mixtures. I. Linear transport theory, Journal of Chemical Physics, 78, 2746-2759, 1983.

[10] J. M. Kincaid, E. G. D. Cohen, and M. L'opez de Haro, The Enskog theory for multicomponent mixtures. II. Thermal diffusion, Journal of Chemical Physics, 86, 963-975, 1987.

[11] J. T. Jenkins and C. Zhang, Kinetic theory for identical, slightly frictional, nearly elastic spheres.
Physics of Fluids}, Under review, 1997.

[12] J. T. Jenkins.Boundary conditions for collisional grain flow at a bumpy, frictional wall.In preparation, 1997.

[13] O. R. Walton. Numerical simulation of inelastic, frictional particle interactions. In M.C. Roco, ED., Particulate Two-Phase Flow, Boston, 1992. Butterworth-Heinemann.

[14] S. F. Foerster, M. Y. Louge, H. Chang, and K. Allia, Measurements of the collision properties of small spheres. Physics of Fluids, 6, 1108-1115, 1994.

[15] A. Lorenz, C. Tuozzolo, and M. Y. Louge.
Measurements of impact properties of small, nearly spherical particles. Experimental Mechanics, 37, 292-298, 1997.

[16] C. S. Campbell, The stress tensor for simple shear flow of a granular material. Journal of Fluid Mechanics, 203, 449-473, 1989.

[17] O. R. Walton and R. L. Braun, Stress calculations for assemblies of inelastic spheres in uniform shear. Acta Mechanica, 63, 73-86, 1986.

[18] O. R. Walton, R. L. Braun, R. G. Mallon, and D. M. Cervelli. Particle-dynamics calculations of gravity flow of inelastic, frictional spheres. In M. Satake and J. T. Jenkins, Eds., Micromechanics of Granular Materials - New Models and Constitutive Relations, pp. 153-162, Amsterdam, 1989. Elsevier.

[19] M. Y. Louge, Computer simulations of rapid granular flows of spheres interacting with a flat frictional boundary. Physics of Fluids, 6, 2253-2269, 1994.

MATERIAL INSTABILITIES IN PARTICULATE SYSTEMS

J.D. Goddard
Department of Applied Mechanics and Engineering Sciences
University of California – La Jolla

Please refer to the Conference Book of Abstracts or the NCMR Website at
http://www.ncmr.org

GRAVITY AND GRANULAR MATERIALS

R.P. Behringer[1], Daniel Hovell[1], Lou Kondic[1], Sarath Tennakoon[1], Christian Veje[2]
[1]*Department of Physics and Center for Nonlinear and Complex Systems, Duke University, Durham NC, 27708-0305*
bob@ phy.duke.edu
[2]*Center for Chaos and Turbulence Studies, Niels Bhor Institute, Blegdamsvej 17, DK-2100 Copenhagen ø, Denmark*

We describe experiments that probe a number of different types of granular flow where either gravity is effectively eliminated or it is modulated in time. These experiments include the shaking of granular materials both vertically and horizontally, and the shearing of a 2D granular material. For the shaken system, we identify interesting dynamical phenomena and relate them to standard simple friction models. An interesting application of this set of experiments is to the mixing of dissimilar materials. For the sheared system we identify a new kind of dynamical phase transition.

I. INTRODUCTION

Granular flows exhibit a rich phenomenology [1] that is still only partially understood. On the Earth, granular materials show dynamics that is often dominated by the effects of gravity. For instance, they are typically random densely packed at rest; if they initially have a large kinetic energy, so that they are in a gas-like state, inelastic effects quickly dissipate that energy, leading back to the dense state. In a reduced gravity environment, the dynamics of granular materials is almost certainly different. The dense packed state is much less likely to occur, and other interesting phenomena are likely to be unmasked. For instance, in the present work, we have identified a second-order-like phase transition that is always masked by gravity for ordinary materials; this transition would be accessible in low gravity. Goldhirsch and Zanetti [2] have predicted that as a granular gas cools, it will undergo another dynamical transition that will lead to spatial inhomogeneity, although gravity makes the study and interpretation of this effect on earth difficult.

Understanding these phenomena would be scientifically interesting, and quite possibly technically important. Such understanding would be crucial in any effort to mine in a reduced gravity environment, such as the Moon.

In the experiments described below we have probed the effects of gravity in two ways. In the first, we have modulated gravity through shaking. In the second kind of experiment, we studied 2D granular systems where the "grains" slid on a smooth slippery surface that is horizontal. In this case, the surface carried the weight of the grains, and gravity played no role in setting the density of the grains. In the following two sections we highlight some of the recent results for each of these two types of experiments.

II. MODULATION OF GRAVITY BY SHAKING

Shaking provides a simple way of modulating gravity. Here, we vary gravity by shaking both in the vertical direction with a displacement

$$z = A_\upsilon \cos(\omega_\upsilon t), \qquad (1)$$

and in the horizontal direction with a displacement

$$x = A_h \cos(\omega_h t + \phi). \qquad (2)$$

The most important control parameters are then the dimensionless accelerations $\Gamma_i \equiv A_i \omega_i^2 / g$, where $i = h, \upsilon$.

For these experiments, we have developed a novel apparatus, Fig. 1, that allows us to provide independent 2-axis shaking (a third axis could be added in future experiments). An additional feature of the apparatus is that it allows us to fluidize the grains by gas flow through a porous bottom plate. This fluidization is intended to reduce the contact forces between grains, and also reduces the effect of gravity.

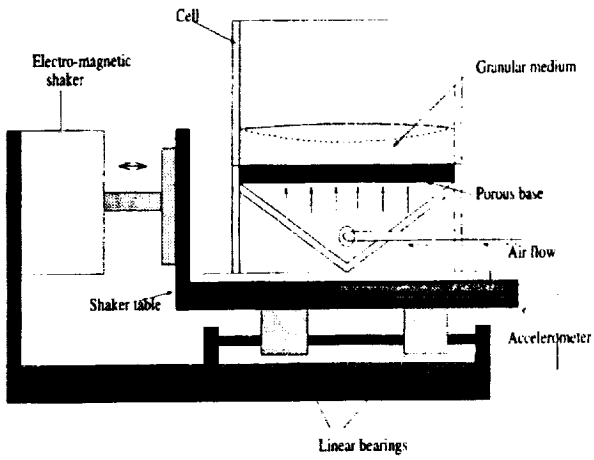

Figure 1: Schematic of the apparatus. The rectangular cell is made of Plexiglas, and is mounted on a Plexiglas base of the same cross-sectional dimensions which is attached to a small table. The table is mounted on four linear bearings running on horizontal cylindrical guidance rods rigidly attached to a fixed bottom frame. The bottom section of the cell acts as a gas distributor. An electro-mechanical actuator, driven by a sinusoidal AC signal provides the horizontal driving.

Gravity plays a crucial role in granular friction, since gravity is responsible for the compaction of virtually every earth-bound material. By modulating gravity, as in these experiments, we provide a useful probe of friction laws which date to the time of Coulomb, but are still only partially understood. The simple picture is that static friction provides a restraining shear force up to some maximum, $F_f = \mu F_N$, after which slipping, i.e. failure can occur. At failure, the friction coefficient falls to its kinetic value, μ_k.

For purely horizontal shaking, we have studied [3] the onset of flow as $\Gamma_h\Gamma$ is increased from 0. Key findings of this work are contained in Figs. 2 to Fig. 5. The initial transition to flow is hysteretic, i.e. once flow has begun at $\Gamma = \Gamma^*$, it can be sustained to lower $\Gamma = \Gamma_c$. The hysteresis is lifted, however, if the layer is dilated about 2% by gas fluidization. This amount of fluidization corresponds to an effective decrease of the weight of the grains of about 40%. We interpret this result to mean that the primary source of hysteresis comes from the friction at grain contacts, with possibly a less important contribution due to the interlocking of grains. Here, a key point is that in ordinary descriptions of granular friction, it is not possible to distinguish between the normal forces generated by the interlocking of grains, and the tangenial friction forces at grain contacts.

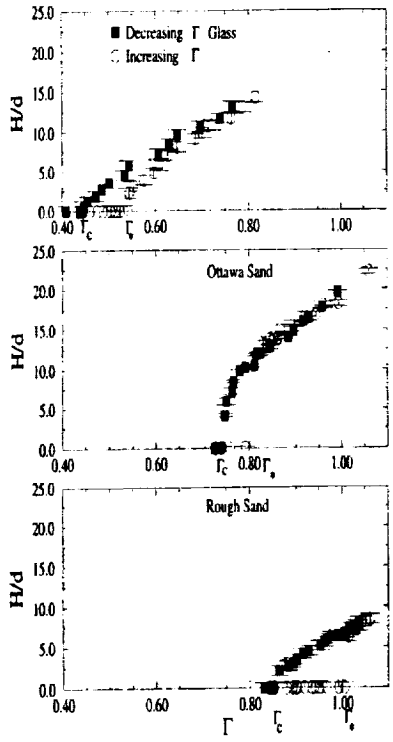

Figure 2: Height, ΓH of the fluidized layer vs. Γ_h for horizontal shaking. Data are for several materials, and show the hysteresis at onset. Flow begins at Γ^* and ceases with decreasing Γ at Γ_c.

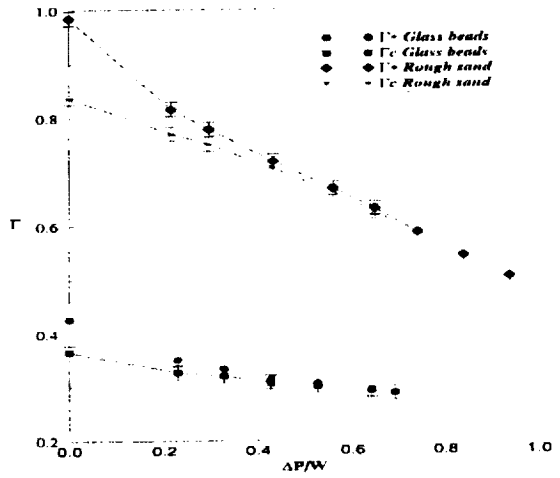

Figure 3: Data for Γ^* and Γ_c vs. gas levitation pressure in units of the weight per area of the material. For modest amounts of gas levitation, the hysteresis in the transition to flow is removed.

The overall flow pattern consists of sloshing motion which drives convection in the direction of shaking, plus a novel wall shearing effect that drives a weaker flow in the cross direction to shaking as well as downward at the sidewalls parallel to the shaking direction, Fig. 4.

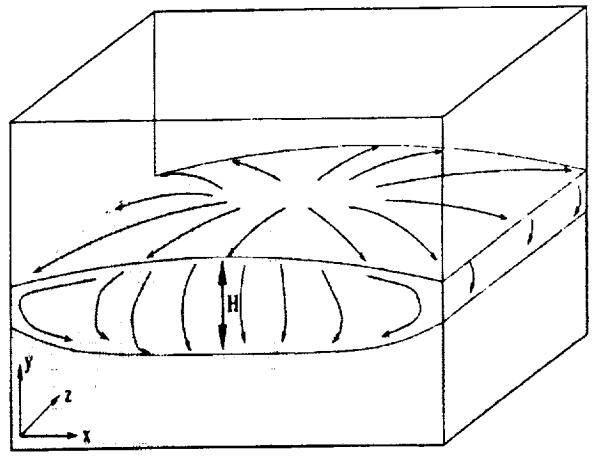

Figure 4: Sketch of time-averaged flow lines for horizontal shaking. The direction of shaking is the x-direction. H is the height of the flowing (fluidized) layer. The strongest flow consists of sloshing of the grains in the x-direction, with down flow at the endwalls, and corresponding inflow towards the center. There is also a shear-driven flow downward on average along the x-y bounding walls.

We have probed the latter effect through soft-particle MD simulations. These simulations are for 7000 particles interacting via a soft-particle simulation [5]. The downward motion at the sidewall occurs because of dilation near that wall from shearing. Hence, near this wall, grains have an enhanced mobility, and can fall under gravity. We expect that this mechanism would occur routinely when there is a shear layer plus gravity.

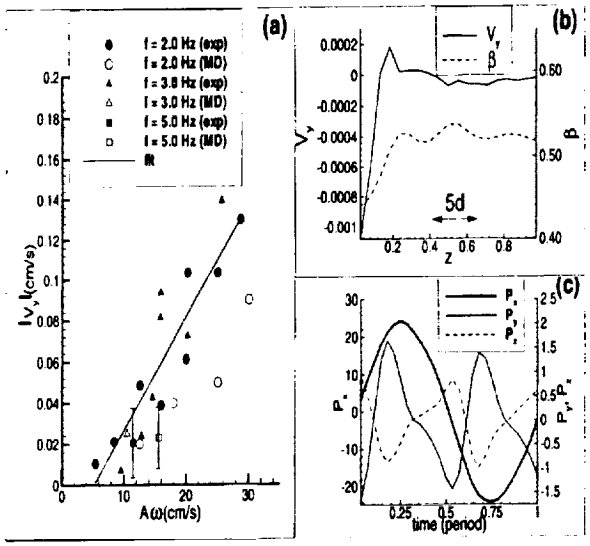

Figure 5: a) Experimental data (solid symbols) and MD simulations (open symbols) for shear-driven downward vertical velocity at the x-y walls vs. shaking velocity, $A_h\omega_h$. b) Velocity profile, V_y, obtained from MD simulations. c) MD simulations show complex structure over a shaking period for the mean value of the particle momentum.

For mixed vertical and horizontal shaking, a number of interesting effects occur [4], including the spontaneous formation of static heaps and at higher horizontal accelerations, the onset of sloshing flow. Static heaps form spontaneously at $\Gamma_h = \Gamma_{h1}$ when $\Gamma_v < 1$, and Γ_h is gradually increased from 0. Sloshing flow occurs at yet higher $\Gamma_h = \Gamma_{h2}$ when Coulomb friction can no longer sustain grains from sloshing up and down the inclined slope of the spontaneously formed heap.

Below, we describe recent results in the context of Fig. 6. We understand the formation of static heaps at the point at which grains become unstable to the horizontal acceleration under the reduced effective gravity $g(1 - \Gamma_v)$ that occurs as the shaker is accelerating downward. At the same time, if the shaker is driven horizontally in phase ($\phi = 0$) with the vertical motion, then the grains will slide until they reach the appropriate end wall. This process stops when a steep enough incline has developed, so long as Γ_h is not too large. However, if the Γ_h is large enough, slipping will occur for either direction of horizontal motion, and sloshing of the grains results. Standard Coulomb friction predicts all of these features qualitatively but not quantitatively. Specifically, we consider a simple model consisting of a block resting on an plane inclined at an angle θ and subject to uniform (i.e. non-oscillatory) accelerations of size $g\Gamma_v$ and $g\Gamma_h$ in the vertical and horizontal directions respectively. The block will first slide on a horizontal surface when $\Gamma_h = \mu(\Gamma_c - \Gamma_v)$ ($\Gamma_c = 1$), and we identify this event with the onset of static heap formation at Γ_{h1}, Fig. 7. We identify sloshing in the granular system with a Γ_{h2} such that the block would slide for either direction of horizontal shaking, Fig. 8. A comparison of the model and the experiment, even when Γ_c is allowed to be adjustable, shows that the model is only approximately correct.

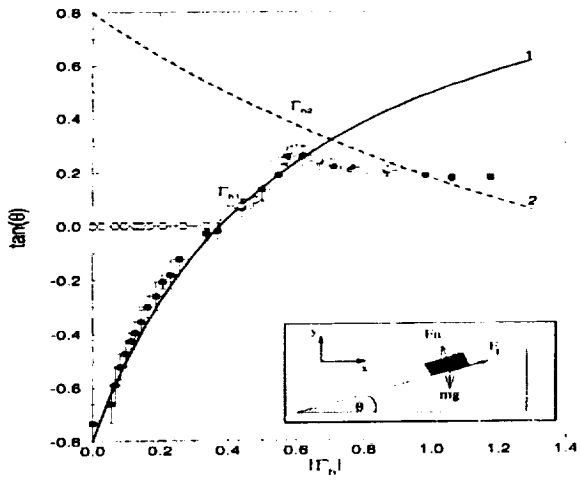

Figure 6: Data for the onset of flow under vertical and horizontal shaking. Here, Γ_v is held constant at 0.68. Open symbols are pertain to Γ_h increasing from 0, starting from a flat heap. Solid symbols pertain to a similar increase in Γ_h starting from a heap inclined at the ordinary angle of repose. Solid curves are derived from simple Coulomb friction, based on the sketch in the inset.

The shaker experiment provide several other interesting insights, although for space reasons, we do not provide extensive details here. One particularly interesting application of the shaking technique used here is for the mixing of dissimilar granular materials. Another system that we consider consists of a binary mixture of spheres that are identical except that some of the spheres have a higher coefficient of rolling friction than the other half. The spheres are then placed on a flat surface that is shaken horizontally. We find interesting segregation effects that we will describe elsewhere.

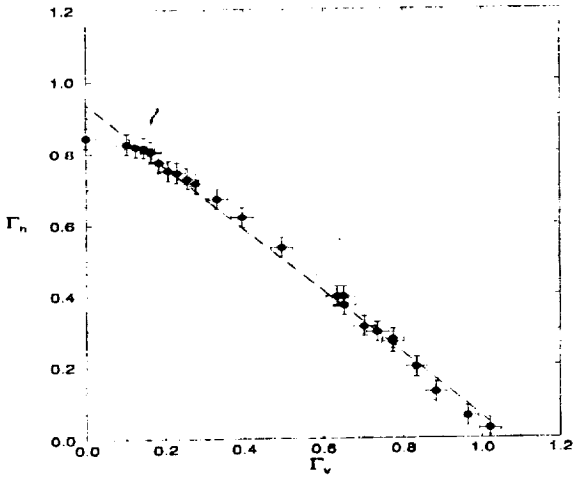

Figure 7: Comparison of data for the onset Γ_h vs. Γ_v for the spontaneous formation of a heap (Γ_1) and the simple Coulomb friction model – i.e. a straight line.

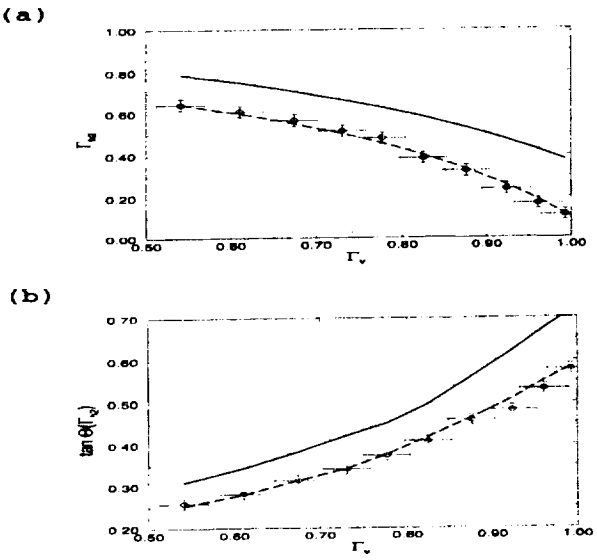

Figure 8: Data for Γ_{h2}, the onset of sloshing, and the angle of the heap at Γ_{h2} for $\Gamma_v = 0.68$. Solid curves are based on the predictions of a simple friction model.

The final experiment [6] consists of disks, a 2D granular material, that slide on a smooth slippery plane, and that are sheared in an annular geometry, Fig. 9. Specifically, the grains are sheared either by a rough inner wheel or by a surrounding rough outer ring. A key feature in these experiments is the absence of gravity, so that we can independently control the density. The disks are photoelastic, i.e. birefringent in proportion to the local deformation of the disks. We view them using a circular polariscope and use a novel technique to relate the photoelastic measurement to the applied force. In this technique, we exploit the fact that the transmitted light intensity, I depends locally on the local difference in the principle stresses with a disk. As the force at a contact increases, a series of light and dark bands appears within the disk, with the number of bands depending on the contact force. Hence, G, the gradient-square of $\Pi G = |\Delta G|^2$, integrated over a grain size gives a good measure of the number of bands, and hence of the local applied force. In addition, each disk is marked with a dark bar so that we can track individual particle positions and orientations using video. From these measurements we deduce particle velocities, V and rotation rates (spins), S. Here, we will focus on the velocity in the azimuthal direction, V_θ, where V_θ is the angular velocity of the grains. In addition, we measure the local packing fraction, γ, which is effectively the density of disks. Here, we will focus on shearing by the inner wheel only, although it is also possible to shear by the outer ring.

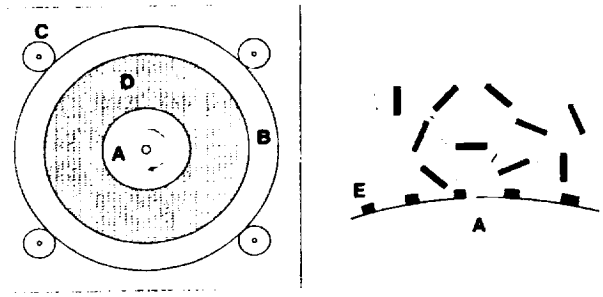

Figure 9: Sketch of 2D shear apparatus. Disks confined to a horizontal plane, and the region between wheel, A, and outer ring, B are steadily sheared by the wheel. The wheel is roughened by teeth, E, and have small dark bars for tracking purposes.

The figures below present some of the key results. Shearing by the inner wheel creates a shear band where the density (packing fraction, γ) is significantly reduced, Fig. 10, and where there is a nearly exponential variation of the mean azimuthal velocity, V_θ with distance, r/d, from the wheel, where d is the particle diameter (Fig. 11). In addition, the mean particle rotation rates, or spins, S show novel oscillations with distance from the wheel. There is a decreasing amount of dilation as γ increases. We observe approximate but not perfect rate invariance in the V_θ and S, as we change the wheel rotation rate, Ω, and we attribute the modest departures from rate invariance to small long time restructuring of the grains well away from the wheel.

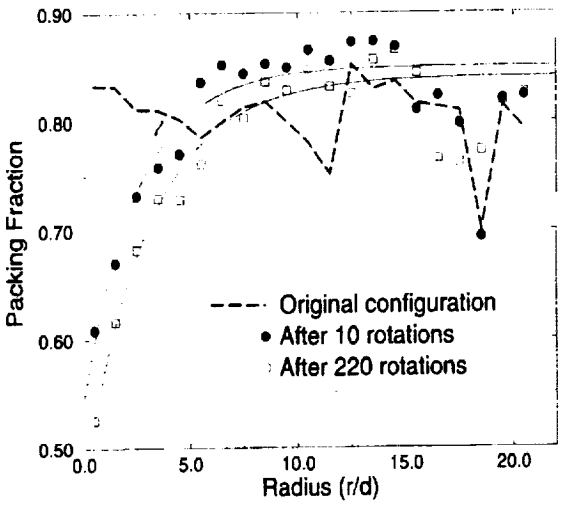

Figure 10: Packing fraction profile, γ vs. radial distance r/d (d = particle diameter) from the shearing wheel, showing the formation of a shear band.

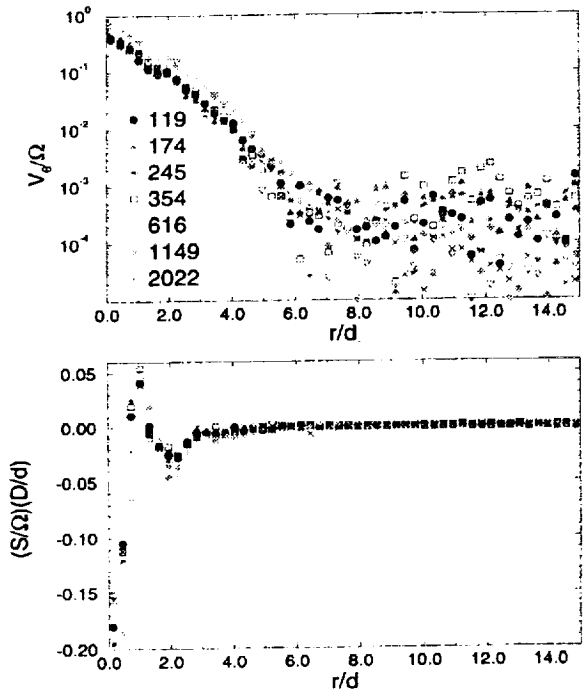

Figure 11: Mean azimuthal velocity, V_θ, and mean spin, S vs. distance r from the shearing wheel in units of a disk diameter, D. Data are for different wheel rotation rates, $\Omega = 2\tau/\tau$, where τ is the time in seconds for one wheel revolution. Data are normalized to test for rate invariance, i.e., kinematic quantities such as S or V_θ should be linearly proportion to Ω.

Distributions for V_θ and S are also quite interesting, Fig. 12. These show a combination of stick and slip motion for the particles nearest the wheel. As the packing fraction γ increase, there is transition from essentially complete slipping to nonslip with both rotation and translation of the disks.

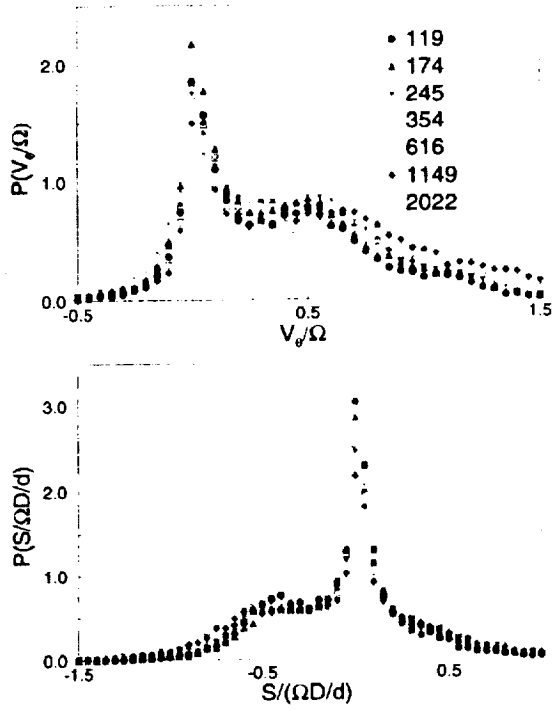

Figure 12: Examples of the distributions for azimuthal velocity and spin of particles next to the shearing wheel. The packing fraction is $\gamma = 0.788$ which is above the critical packing fraction.

A particularly interesting feature of these experiments is the observation of a transition at a critical packing fraction, γ_c, that has some of the hallmarks of a second order phase transition. Here, $\gamma - \gamma_c$ is the order parameter. At $\gamma_c \simeq 0.77$, the grains can just sustain shear, and the system is highly compressible. Also, there is critical slowing down: for instance the mean speed of the grains vanishes, Fig. 13. The distribution of forces changes qualitatively near γ_c. Well above γ_c, the distribution is qualitatively like the predictions of the q-model [7] of Coppersmith et al.: roughly exponential for large forces. Time series for the stress and the corresponding spectra are similar to these that we found for sheared 3D materials [8]. Specifically, for a give shear rate and γ, the spectrum typically varies as f^{-2} at high frequencies, f, and as a powerlaw, $P \propto f^{-\alpha}$ with $0 < \alpha < 1$. Nearer the transition, the distribution is qualitatively different, and ongoing

measurements will be characterize the distribution in that case. We observe an interesting and apparently smooth change from slip to nonslip behavior as we pass beyond γ_c.

Finally, if we define a slip event to be continuous decrease in the measured stress. Distributions of the size, M of slip events are exponentially distributed well above γ_c but appear to vary as M^{-1} for small M when γ is close to γ_c.

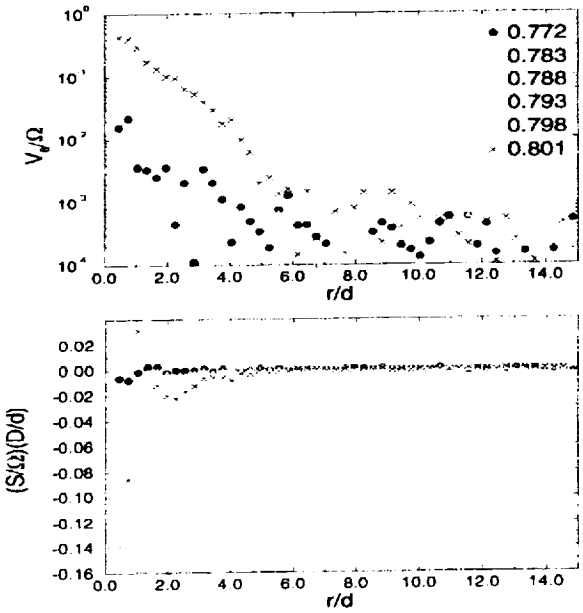

Figure 13: Mean azimuthal velocity and spin profiles for various packings fraction γ showing slowing down near as $\gamma - \gamma_c$ from above. We estimate that $\gamma_c = 0.77$ for this 2D system.

Acknowledgments. This work was supported by NASA grant NAG3-1917. We appreciate the hospitality of the P.M.M.H. of the Ecole Superieure de Physique et Chemie Industrielle de Paris, where parts of this work were carried out.

[1] For reviews see H.M. Jaeger, S.R. Nagel and R.P. Behringer, Rev. Mod. Phys. **68**, 1259 (1996); R.P. Behringer and J.T. Jenkins, ed. *Powders and Grains '97*, Balkema, Rotterdam (1997); H.J. Herrmann, S. Luding, and J.P. Hovi, eds. *Dry Granular Media*, NATO ASI series, Kluver, Amsterdam (1998).

[2] I. Goldhirsch and G. Zanetti, Phys. Rev. Lett. **70**, 1619 (1993).

[3] S. Tennakoon, L. Kondic, and R.P. Behringer, submitted to Phys. Rev. Lett. (1998).

[4] S. Tennakoon and R.P. Behringer, to appear, Phys. Rev. Lett. (1998).

[5] G.S. Grest and K. Kremer, Comp. Phys. Comm. **55**, 269 (1989); P.A. Thompson and G.S. Grest, Phys. Rev. Lett. **67**, 1751 (1991).

[6] D. Howell, B. Miller, C. O'Hern, and R.P. Behringer, in *Friction, Arching, Contact Dynamics*, p. 133-148, World Scientific (1997); C.T. Veje, D.W. Howell, and R.P. Behringer, S. Schollmann, S. Luding and H.J. Herrmann, in *Dry Granular Media*, eds. H.J. Herrmann, S. Luding, J.P. Hovi, Nato ASI series, Kluver, Amsterdam (1998).

[7] C.-h. Liu et al. *Science* **269**, 513 (1995); S.N. Coppersmith et al. Phys. Rev. E **53**, 4673 (1996).

[8] B. Miller, C. O'Hern, and R.P. Behringer, Phys. Rev. Lett. **77**, 3110 (1996).

MRI MEASUREMENTS AND GRANULAR DYNAMICS SIMULATION OF SEGREGATION OF GRANULAR MIXTURE

M. Nakagawa[1], Jamie L. Moss[1] and Stephen A. Altobelli[2]
[1] Particulate Science and Technology Group, Division of Engineering, Golden, Colorado 80401;
mnakagaw@mines.edu, jmoss@mines.edu,
[2]The New Mexico Resonance, 2425, Ridgecrest Dr. SE, Albuquerque, New Mexico 87108; salto@nmr.org.

INTRODUCTION

Rich physics of static/dynamic behavior of granular materials have promoted a great intest among researcheres in different fields. Most recently, compaction, segregation and a various types of pattern formation have captured attention of many physisists. Segregation seems to exists anytime when different species of particles are in the relative motion. Bulk materila handling plants frequently experience non-uniform products due to size, shape, and density variations among particles.

A counter-intuitive axial segregation phenomenon in a rotating horizontal cylinder has recently been under an intense scrutiny by many researchers in different disciplines [1-10], however, the first detailed observation of this phenomena was made by Oyama[11] in 1930. He conducted a series of experiments using a short cylinder made of cast iron with its diameter and length of 200mm and 400mm, respectively. After 15 minutes of rotation, he recorded patterns of axially segregated bands created by the mixtures of different sizes of limestones, different weight ratios (6.14, 2.59 and 2.37), different filling ratios (4kg, 6kg, and 8kg) and rotating speed (10, 20, 40, 60 and 100rpm).

Donald and Roseman [12], Bridgwater[13], and Roger and Clement[14] extended Oyama's work and investigated mechanisms of the axial band segregation. Donald and Roseman concluded that the axial banding only occurred if the static angle of repose was larger for the smaller particles than that for the larger particles. Bridgwater expanded the explanation given by Oyama and proposed a mechanism to allow smaller particles to accumulate near the end cap. Extra friction again the end caps brings particles right next to the caps to a higher level, and the larger particles tend to roll down the slope easier than the smaller particles do. These two effects produce a high concentration of smaller particles next to the end caps. Along the cylinder axis, statistical variations in the concentration were proposed to cause the axial band formation for the similar reason described above. Roger and Clement also observed axial segregation but the cylinder they used was probably too short compared to the length to isolate the effects due to the boundary walls. Das Gupta et al. [1] further expanded the argument by the previous authors and actually measured the dynamic angle of repose of a single component of different size of particles. They found that the dynamic angle of repose depended on the rotation speeds and it did not differ much when it was smaller than a critical value. However, when the flow was driven harder to cause the higher dynamic angle of repose, then the smaller particles started to show the higher the dynamic angle of repose.

Savage[3] reported that axial segregation occurred for the 50-50 volume mixture of spherical and rod-shaped particles of similar size. Based on the visual observation that rod-shaped particles always formed axial bands adjacent to the two end caps where the dynamic angle of repose was higher suggesting more resistance of the rod-shaped particles to rolling. He formulated a diffusion like equation which contains both a Fickian diffusion flux term and a preferential drift term. When the drift due to angle of repose exceeds the diffusion flux, then the combined terms described above gives a negative effective overall diffusion coefficient which promotes the axial segregation.

There is a growing consensus that the interplay between the particle dynamics and the evolving internal structures during the segregation process must be carefully investigated. Magnetic resonance imaging (MRI) has recently been used to non-invasively obtain much needed static/dynamic information such as concentration, velocity and fluctuations in velocity. It has proven to be capable of depicting the evolution of segregation processes in a rotating cylinder. Segregation in a straight horizontal rotating cylinder involves two processes: the first is to transport small particles in the radial direction to form a radial core, and the second is to transform the radial core into axially segregated bands. Percolation and/or "stopping" [14] have been suggested as possible mechanisms for the radial segregation. As to driving mechanisms for axial band formation, however, much less is known. It has been proposed that the dynamic angle of repose promotes this process, and Hill and Kakalios[7] have reported that particles mix or demix depending upon the competition between angle of repose. We claim that the dynamic angle of repose could be one of the causes for a particular range of solid fraction and rotation rates, however, it fails to offer reasonable explanations for certain phenomena associated with the axial migration. For example, we always observe that the radial segregation preceds the axial segregation. The radially segregated core of small particles then transforms into axially segregated bands. By definition, the effects of the dynamic angle of repose is restricted near the free surface where the flowing layer is present. However, the process of transformation from the radially segregated core to the axially segregated bands occurs by migration of small particles located in the deep radial core region.

We have designed a series of experiments so that the effects of the dynamic angle of repose can be localized in a very confined region by filling the cylinder almost completely full. Under these extreme conditions, small particles still form a radial core and also migrated to form axial bands. This can not be explained simply by the argument based on the dynamic angle of repose. We present our recent non-invasive experimental images to show a new way of forming axial bands.

As to 2D experiments we have identified in our experiments that particles located near the center of the cylinder axis behave quite differently from the ones located near the boundary. The particles near the center seem to move slower and randomly. On the contrary, the particles located far from the center are engaged in the rapid shearing motion.

EXPERIMENTAL

We have first investigated behavior of granular particles in a long horizontal cylinder. We prepare initial samples whose volume is almost completely occupied by the particles. The cylinder of length of 27cm with an inner diameter of 7cm is made of acrylic material. To achieve a maximum initial packing so that we can minimize the size of the flowing layer, premixed particles are poured into the cylinder. Near consistent tappings on the side of cylinder during the pouring provide a desired packing. Once the initial sample is prepared in this way, it is placed on a pair of rollers which were placed on the horizontal table and rotated at 20 rpm.

Particles used for this experiment are poppy seeds, mustard seeds and pharmaceutical pills which give excellent NMR signals. Poppy seeds are flat, angular and smallest with about 1mm of effective diameter. Mustard seeds are relatively round and have about 1.7 mm diameter and a bulk density of 1.3 g/cm^3. Pharmaceutical pills of 1 and 4 mm are used for the detailed investigation in conjunction with MRI presented in this article. The 4mm particles are painted black by a commercially available permanent oil based ink to help visualize for non-MRI experiments. There is no signs of alternation of the surface properties after these particles are painted. The pills contain a liquid core of medium chain triglyceroide and the gelatin outer shell weighs about 30% of the total weight of a particle of either size. Recently, Louge et al. [15] conducted a detailed binary impact experiment using these particles and estimated the normal coefficient of restitution to be around 0.89. When the cylinder is partially filled and the dynamic angle of repose seems to have significant effects on segregation processes, material properties of particles such as the coefficient of restitution and friction were important factors. In the current investigation, however, it is less known that which properties play more important roles.

Nakagawa et al.[16] first conducted non-invasive MRI of flows of mustard seeds in a horizontal rotating cylinder. MRI was also used to study shaking of granular materials [17]. Later, a similar MRI was applied first by Nakagawa et al.[6] and later by Hill and Kakalios[9] to investigate evolution of radial and axial segregation by studying internal structures during the process. A similar technique was used in this experiment. Recently, Ovryn et al [18] have proposed to develop a versatile, user-friendly and inexpensive NMR machine to promote research in Microgravity Fluid Physics discipline.

For 2D experiments, we use a very short cylinder of the gap and diameter of 5 mm and 11 cm, respectively. Pharmaceutical pills of 2mm are used. We painted some of these particles with the permanent black ink as described earlier to place a line of these painted particles going through the center of the cylinder. This line is placed to study the motion of particles located near and far from the center of the cylinder. To follow the motion of particles we use a high resolution 8mm camcorder.

RESULTS AND DISCUSSIONS

One of the main purposes of conducting a series of segregation experiments with the proposed high filling ratios is to gain more insights for the possible existence of a mechanism which is capable of producing radial and axial segregation phenomena independent of the effects of the dynamic angle of repose. Regardless the filling ratio, the cylinder rotation drives particle migration. In the event of the moderate filling rations of about 50% as have been investigated extensively, there exists a substantial flowing layer which induces particles migration in both radial and axial directions. As indicated earlier by Nakagawa et al.[16] the flowing depth increases rapidly as the rotation speed increases slightly. However, as soon as the flow is developed, the dilated flow becomes deep enough to carry small particles into the core to form a radial core.

On the contrary, in an almost completely filled cylinder there is very little room for the surface flow to develop. Initially, when the cylinder starts rotating, sparsely located small particles accumulate near the bottom of the very minute flowing layer to form streaks of different lengths. After a few rotations, a series of streaks merge to form a thin ring structure. When this is completed, there is hardly any small particles outside the ring since all the small particles have migrated in the radial direction to form the ring.

In the region outside the ring, there is hardly any small particles visible to the eyes at the ends. Inside the ring, there are still some small particles present since they did not participate in the active migratory mechanism as described earlier. The concentration of

small particles in this region, however, increases in time. It appears that the small particles are accumulated in the core through axial migratory motion. The radial ring formation and axial-filling of the core are observed at both ands of the cylinder. With this high filling ratio, the axial-filling is truly three-dimensional mechanism and has not previously been observed by any 2D rotating cylinder experiments. The radial migratory behavior of small particles in a short 2D drum may impose severe restrictions on particle drift in the axial direction. It is conceivable that even for the case with moderate filling ratios, the axial-filling could take place in the formation of the radial core. So, it might be more realistic to view that even the radial core formation process must be discussed in conjunction with the axial migration of particles as a true 3D phenomenon.

When the initial axial filling is completed at both ends, the radial core at one end starts disappearing faster than the other, indicating axial migration of small particles. The end result is shown in Fig.1 below. Well separated bands of large and small particles are formed together with a rather sharp interface region where there is a core of small particles still present. Unlike the final configuration obtained for a partially filled cylinder experiments with the odd number of bands, we have almost completely separated two bands. Since there is no surface flow influenced by the friction of the end caps, there is no reason to observe a larger concentration of smaller particles right next to the end caps. However, based on the symmetry argument, this two band configuration does not seem to be as stable as three bands. What we reported here may still be an intermediate stage of an evolving process.

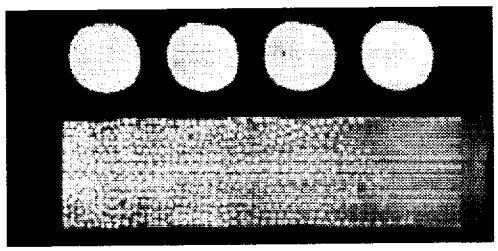

Figure 1 NMR image of axial band segregation in a nearly packed cylinder.

Figure 2 shows a series of line configurations at different times of the dispersion process. The initial straight line (Fig. 2a) soon becomes shorter through the dispersion of particles near the boundary. The shortened line then shifts downward and rotates in the direction of the cylinder (Fig. 2b). This line continues to become shorter and move around in the central region where the fast shearing is not affecting its motion (Figs. 2c and 2d), and eventually disperses to the surrounding particles to form a mixture.

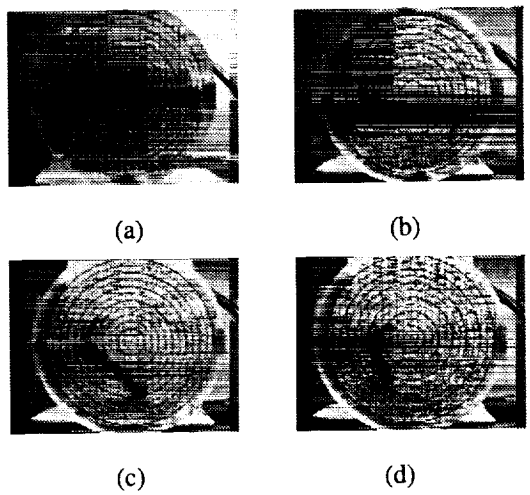

Figure 2. Motion of particles in a short cylinder.

In conclusion, a brief description of a close up observation of particle motion is given. With this high filling ratio, there is not enough room for particles to establish a surface flow, however, using little space or voids available for them they constantly rearrange themselves through a series of collapses of local structures (micro-collapses). It is observed that these micro-collapses occur everywhere in the cylinder perimeter. Keeping the same high filling ratio, we have also conducted a series of experiments where the two axially segregated initial ands transformed into a radially segregated core. A close look at the interface between the bands of large end small particles in the beginning also provides a very clear picture as to how each species diffuses through the voids created by a series of micro-collapses. This diffusive motion of particles in the central region was also observed in the 2D experiment.

ACKNOWLEDGEMENTS

MN and JLM were supported, in part, by NASA through contract NAG3-1970. MN would like to acknowledge members of the Particulate Science and Technology Group of Colorado School of Mines, in particular, Jon Eggert and David Wu for their critical discussions. We would also like to acknowledge Taiho Pharmaceutical Co. for their generous donation of pharmaceutical particles.

REFERENCES

1. Das Gupta, S., Khakhar, D.V., and Bhatia, S.K. "Axial segregation of particles in a horizontal rotating cylinder," Chem. Eng. Sci., 46, 1513, 1991.
2. Fauve, S., Laroche, C., and Douady, S., in Physics of Granular Media, edited by D. Bideau and J. Dodds, Nova Science, Commack, NY., 277, 1991.

3. Savage, S.B., in Disorder and Granular Media, edited by D. Bideau and A. Hansen, North-Holland, Amsterdam, 255, 1993.
4. Zik, O., Levin, D., Lipson, S.G., Shtrikman, S., and Stavans, J., "Totationally induced segregation of granular materials," Phys. Rev. Lett., 73, 644, 1994.
5. Nakagawa, M., "Axial migration of granular flows in a rotating cylinder," Chem. Eng. Sci., 49, 2540, 1994.
6. Nakagawa, M., Altobelli, S.A., Caprihan, S., and Fukushima, E., " NMRI study: axial migration of radially segregated core of granular mixtures in a horizontal cylinder," Chem. Eng. Sci., Vol. 52, No.23, 4423, 1997.
7. Hill, K.M. and Kakalios, J., " Reversible axial segregation of binary mixtures of granular materials," Phys. Rev. E., 49, 3610, 1994.
8. Hill, K.M. and Kakalios, J., " Reversible axial segregation of rotating granular media," Phys. Rev. E., 52, 4393, 1995.
9. Hill, K.M. and Caprihan, A., and Kakalios, J., "Bulk segregation in rotated garnular material measured by Magnetic Resonance Imgain," Phys.Re. Lett., 78, 50, 1997.
10. Chicharro, R., Peralta-Fabi, R., and Velasco, R.M., "Segregation in dry granular system.," Powders and Grains 97, Behringer and Jenkins (eds), Balkema, Roterdam.
11. Oyama, Y., Bull. Inst. Phys. Chem. Res. Japan Rep., 18, 600, 1939.
12. Donald, M.B. and Roseman, B., " Mixing and demixing of solids particulate I. Mechanics in a horizontal drum mixer," Br. Chem. Eng., 7, 749, 1962
13. Bridgwater, J., Sharpe, N.W., and Stocker D.C.,"Particle mixing by percolation," Trans. Inst. Chem. Eng. 47, T 11.
14. Cantelaube, F. and Bideau, D., "Radial segregation in a 2D drum: an experimental analysis," Europhys. Lett. 30, 133, 1995.
15. Louge, M.Y., Tuozzolo, C., and Lorenz, A., "On binary impact of small liquid-filled shell. Phys. Fluids (submitted).
16. Nakagawa, M., Altobelli, S.A., Caprihan, C., Fukushima, E., and Jeong, E.,-K., "Non-invasive measurements of garnular flows by magnertic resonance imaging," Experiments in Fluids, 16, 54-60, 1993.
17. Ehrichs, E.E., Jaeger, H.M., Karzmar, G.S., Knight, J.B., Kuperman, V.Yu., and Nagel, S.R., Science, 267, 1632, 1995.
18. Ovryn, B., Caprihan, C., Altobelli, S.A., Seymour, J.D., and Fukushima, E., "A robust magnetic resonance imager for ground and flight based measurements of fluid physics phenomena," Proceedings for the fourth microgravity fluid physics and transport phenomena conference, August 12-14, Cleveland, Ohio, 1998.

Session 4C

Thermocapillary Flows I

SURFACE TENSION DRIVEN CONVECTION EXPERIMENT-2 (STDCE-2)

Y. Kamotani[1], S. Ostrach[2] and J. Masud[3] [1,2,3] Department of Mechanical and Aerospace Engineering
Case Western Reserve University, Cleveland, Ohio 44106

INTRODUCTION

Thermocapillary flows are known to become oscillatory (time-periodic), but how and when they become oscillatory in containers of unit-order aspect ratio are not yet fully understood. The present work is a part of our continuous effort to obtain a better understanding of the phenomenon. Thermocapillary flow experiments in normal gravity are limited to a narrow parametric range in order to minimize gravity and buoyancy effects, which is an important reason for our lack of full understanding of the oscillation phenomenon. One important unanswered question is what role, if any, free surface deformation plays in the oscillation mechanism. For that reason we performed thermocapillary flow experiments, called the Surface Tension Driven Convection Experiment-2 (STDCE-2), aboard the USML-2 Spacelab in 1995. The main objectives of the experiments were to investigate oscillatory thermocapillary flows in microgravity and to clarify the importance of free surface deformation in such flows.

Steady and oscillatory thermocapillary flows were generated in cylindrical containers by employing two heating modes. A CO_2 laser with adjustable power and beam diameter was used in the Constant Flux (CF) configuration to heat the free surface. The other configuration investigated in STDCE-2 was the Constant Temperature (CT) configuration in which a submerged cylindrical cartridge heater placed at the symmetry (axial) axis of the test container heated the fluid. Both heating modes cause non-uniform temperature distributions on the free surface, which generates thermocapillary flow. The flow field was investigated by flow visualization, and the temperature field was measured by thermistors and an infrared imager. The free surface shape and motion were measured by a Ronchi system. The hardware performed well and we were able to conduct more tests than originally planned. From the successful experiments a large amount of data was acquired. The analysis of the data is now nearly complete. Some important results are presented and discussed herein.

DESCRIPTION OF EXPERIMENT

Experimental Apparatus

The experimental arrangement for STDCE-2 is sketched in Fig. 1. The objective of STDCE-2 was to investigate the onset conditions and nature of oscillatory flows under a variety of test conditions and

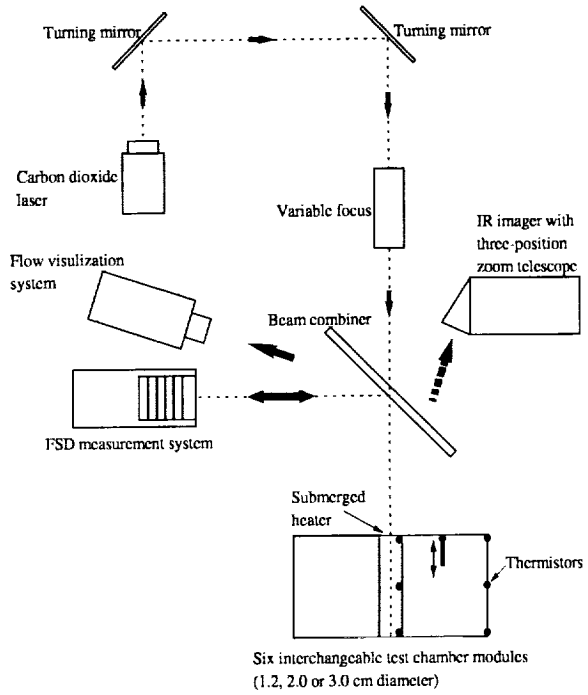

Figure 1. Schematic layout of STDCE-2.

configurations, including a study of the effect of heating mode, heating rate, surface heat flux distribution, container size and static free surface shape on the oscillations. Cylindrical test cells of various sizes (1.2, 2.0 and 3.0 cm diameter test cells), each with a nominal aspect ratio of one (radius=depth), were used. Silicone oil with kinematic viscosity of two centistokes was selected for use in STDCE-2. In the CF heating mode the laser power level and laser spot size could be varied to study the effects of heat input and surface heat flux distribution on the flow field. In the CT mode the cartridge heater power could be varied to study the effect of internal heat input and heater-to-external wall temperature gradients on the flow field. The static free surface shape of the test fluid was a variable in the STDCE-2 test matrix. Each test module contained an oil delivery system, which allowed the oil in the module's test cell to be filled to various levels. The free surface shapes in the STDCE-2 tests are shown in Fig. 2.

Each test chamber module consisted of an upper housing, a test section, a lower housing and an oil reservoir. The test section of each module consisted of

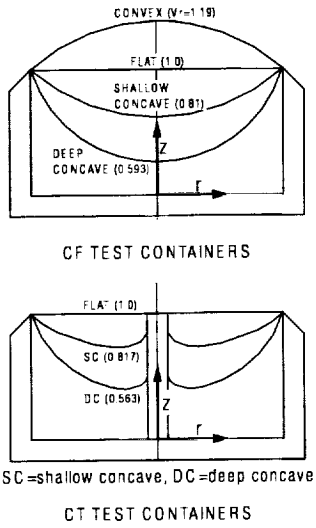

Figure 2. Free surface shapes in STDCE-2.

a high thermal conductivity, cylindrical, water-cooled copper test chamber wall with water cooled channels, a Teflon bottom, a movable thermistor, a central cartridge heater (for CT modules), an oil fill port, and a floor thermistor all held in place by an aluminum backing plate and bolts and sealed with an O-ring. The side walls were maintained at a nearly uniform temperature by circulating water. Each test chamber module included a reservoir containing a mixture of oil and tracer particles.

Temperatures were measured using thermistors positioned at various locations within and at the boundaries of the test cell (see Fig. 1). Side wall temperature was monitored at three locations. Bulk fluid temperature was measured using a movable thermistor which was translated by a thermistor crank external to the module. The movable thermistor could be precisely positioned parallel (± 0.1 mm) to the axis of the test cell. All temperature measurements in the STDCE-2 tests were accurate within ±0.1 C with a response time of 0.1 seconds.

For the CT modules, a submerged, cylindrical electrical resistance heater (centered in the test cell) was used to heat the oil. These cartridge heaters were one-tenth the diameter (1.2, 2.0 and 3.0 mm) of the test chamber and extended the depth of the test cell from the pinning edge plane. Three thermistors were embedded in the heater's shell. The RF-excited CO_2 laser was used to heat the fluid surface during the CF tests at powers from 0.2 to 5.0 Watts, in 0.01 Watt increments, with all the energy absorbed within 0.2 mm of the surface. The optics were designed to produce heating zone sizes between 0.6-6 mm at the free surface for both curved and flat surface shapes.

A flow visualization system illuminated suspended 70 micrometer tracer particles (Pliolite) in the test fluid to provide a qualitative record of the bulk flow. In addition, this system was used extensively to monitor the flow for the onset of oscillations and the fluid behavior while filling the test cell. Laser diode was used for illumination for both flow visualization and free surface deformation measurement.

A scanning IR imaging system operating in the 8-14 micrometer wavelength range was used to detect radiated emissions to determine the thermal signature along the fluid free surface. The imager was identical to that used in the STDCE-1 experiments. A zoom telescope was fitted externally to the imager to properly focus to the three test cell sizes. New to STDCE-2 was a Ronchi interferometer, designed to measure the dynamic surface deformation during the experiment.

Ranges of Parameters

The important dimensionless parameters for steady thermocapillary flows in the present experimental configuration with a flat free surface are: Marangoni number $Ma = \sigma_T \Delta T R/\mu\alpha$, Prandtl number $Pr = \nu/\alpha$, aspect ratio $Ar = H/R$, and heater ratio $Hr = R_h/R$, where ΔT is the temperature difference between the heater and the side wall, R is the container radius, H is the depth, R_h is the heater radius, μ is the fluid dynamic viscosity, ν is the kinematic viscosity, α is the fluid thermal diffusivity, and σ_T is the temperature coefficient of surface tension. The Reynods number of the flow, $R\sigma$, can be computed as Ma/Pr. In addition, the relative fluid volume (Vr) is important in the curved surface tests and its value for each shape is given in Fig. 2. Based on numerical analysis, the heat loss from the free surface relative to the total heat transfer rate is estimated to be about 3 % so that it is not a major factor in the present experiments.

Forty two tests were performed in the CF mode. The parametric ranges of those CF tests were: $Ma < 6\times10^4$, Pr = 22-32, and Hr = 0.05, 0.1, and 0.2. 32 tests were conducted with Ar = 1. In the other 10 tests a cylindrical plastic disc was inserted at the bottom of each test chamber to reduce its aspect ratio to 0.5. The fluid viscosity in the above Pr is evaluated at the mean temperature, $(T_H + T_C)/2$, where T_H is the free surface temperature at the center. The above Ma is based on ΔT, which is convenient because Ma is defined similarly in other configurations. Later, a Ma based on Q will also be introduced. Ar and Hr in the thirteen CT tests were fixed at 1.0 and 0.1, respectively. The values of Pr and Ma in the CT tests were Pr=26-31 and $Ma \leq 1.7\times10^5$.

RESULTS AND DISCUSSION

Oscillatory Flow in CT Configuration

It is known from our previous studies[1,2] in the CT configuration that once ΔT is increased beyond a certain value (called the ΔT_{cr} herein), the flow field becomes oscillatory with corresponding time periodic variations in the temperature field. The onset of oscillatory flow disturbs the axial symmetry of the flow and temperature fields which then become three dimensional and periodic in time. The observed oscillatory motion in all the tests in STDCE-2 was similar in nature. In oscillatory flow, the fluid particles moved back and forth in the azimuthal direction with the frequency of oscillations as they circulated in the flow cell. In addition to the oscillatory motion in the azimuthal direction, a very slow rotation of the whole flow field was also observed. The time period of this rotation was much larger than the time period of the oscillatory motion in the azimuthal direction. In a fixed radial (r-z) plane (see Fig. 2), the flow was observed to go through periods of strong and weak motion during one oscillatory cycle. The observed oscillatory flow field is similar to that described by Kamotani et al.[1,2] in 1-g tests

The onset of oscillatory flow is signified by ΔT_{cr} which is shown in Fig. 3 for various test containers with flat free surface. 1-g data from Kamotani et

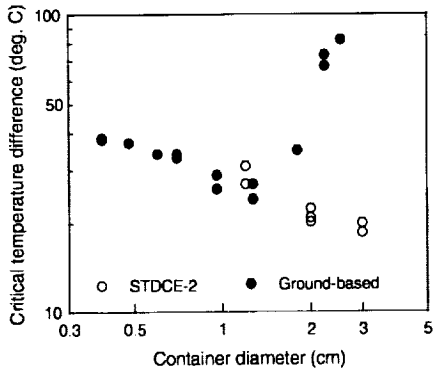

Figure 3. Critical temperature differences for CT tests.

al. [1] for the CT configuration (same fluid and Hr as in the STDCE-2 tests) are also included to increase the range so as to make the trend clear. It can be seen that the data taken in normal gravity exhibit two different trends: ΔT_{cr} decreases gradually with increasing container diameter (D) up to about D=1.2 cm and then increases sharply beyond that. For the test containers with diameter around 1.2 cm, the onset of oscillations in 1-g and microgravity occur at a similar ΔT_{cr}. The small difference in ΔT_{cr} noticeable from Fig. 3 is due to a somewhat different cold wall temperature in the 1-g (~25 °C) and microgravity (~15 °C) experiments, which results in slightly higher viscosity in the microgravity tests for the same fluid. For the test containers with 1.2 cm diameter, in addition to the similarity in the observed oscillatory flow field , the oscillation frequency and the IR image of the free surface were also similar in the 1-g and microgravity tests. This clearly shows that for the 1.2 cm diameter test container, buoyancy does not influence the onset of oscillations. Therefore, one can conclude that the onset of oscillations in test containers with diameter smaller than 1.2 cm is not affected by buoyancy in normal gravity as the influence of buoyancy is reduced with decreasing test container dimensions. Then, in the absence of buoyancy it can be seen from Fig. 3 that ΔT_{cr} decreases with increasing test section size.

In order to determine the criteria for the onset of oscillations, it is appropriate to look at the problem in a nondimensional manner. The important factors which could influence the onset of oscillations in the absence of buoyancy are: Ma, Pr, Hr, Ar, heat loss from the free surface and the deformability of the free surface. In the present experiments, the heat loss from the free surface is estimated numerically and is found to be insignificant for the conditions near the onset of oscillations. Therefore, if the free surface is assumed to be nondeformable, then the conditions of the experiment are determined by Pr, Ar, Hr and Ma. In the present experiments Ar and Hr are fixed and Pr is nearly constant in all the tests, therefore, the only variable parameter is Ma. Consequently, the onset of oscillations should be characterized by a critical Marangoni number (Ma_{cr}). In order to see the behavior of Ma_{cr} in the present and in our 1-g experiments, the data in Fig. 3 (1-g data for D≤1.2 cm) are nondimensionalized in terms of Ma_{cr} and plotted in Fig. 4 against the test container diameter to differentiate among various tests. From Fig. 4 it is clearly seen

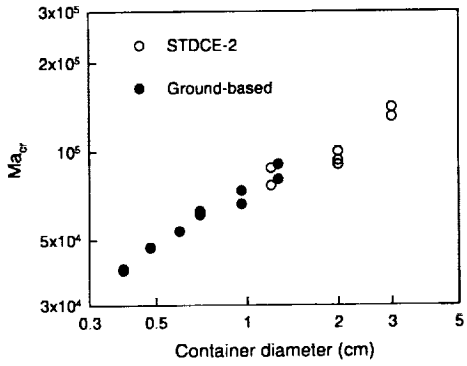

Figure 4. Critical Marangoni numbers for CT tests.

that for different tests with similar Pr, Ar and Hr, the value of Ma_{cr} changes almost fourfold over the range of the experiments. This shows that Ma_{cr} is not a sufficient parameter to characterize the onset of oscillations in the CT configuration. The same conclusion was obtained in our previous work in other configurations.

It is clear then that some other factor needs to be included in the analysis. Since buoyancy and heat loss from the free surface are insignificant, the only important factor is the deformability of the free surface. Based on our extensive experimental and theoretical work on the oscillation phenomenon, we believe that the additional aspect is free surface deformation. The detailed theoretical basis for oscillatory thermocapillary flows in the so-called half-zone configuration is given by Kamotani et al.[3] The same concept is applied to the present configuration. It is convenient to divide the flow field into two: surface flow along the free surface toward the cold wall and return flow in the interior toward the heated region. The surface flow is driven by thermocapillarity and the return flow is due to the pressure field caused by the surface flow. Consider a transient situation where the surface flow is somewhat changed for some reason. The return flow does not respond to that change immediately, because the surface flow must deform the free surface shape first to modify the pressure field. Such a small delay could cause a large change in the flow field, if the free surface deformation alters the thermal boundary layer thickness along the free surface significantly.

It can be shown that the amount of transient free surface deformation relative to the thermal boundary layer thickness in the hot corner (the region next to the heater where the surface temperature gradient is large) can be expressed as

$$\left(\frac{\rho\alpha^2}{R\sigma}\right)^{1/2} Ma \equiv S \qquad (1)$$

where σ is the surface tension. The above parameter is called a surface deformation parameter or S-parameter. According to our oscillation model, the oscillation process could start when the S-parameter becomes larger than a certain finite number. The critical conditions are plotted in terms of Ma and S in Fig. 5 As the figure shows, all the data can be correlated well by S: The flow becomes oscillatory when S is larger than about 15.

According to our oscillation model, the oscillation period (1/f) scales with the time of convection along the heater surface. Based on that, the dimensionless oscillation frequency (f*) is defined as

$$f^* \equiv \left(\frac{fR^2}{\alpha}\right) Ma^{-2/5} \qquad (2)$$

The dimensionless frequencies measured in STDCE-2 and in our ground-based tests with small containers are plotted against

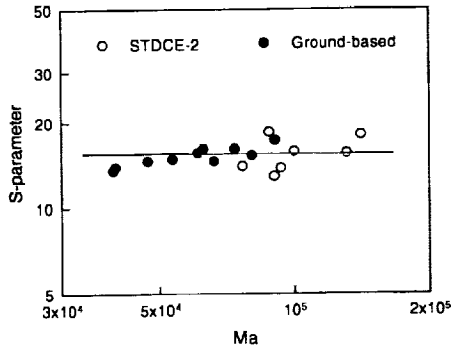

Figure 5. Critical S-parameter for CT tests.

Ma in Fig. 6. The dimensionless frequency is nearly constant, equal to about 1.8, in all the tests, consistent with the scaling law of Eq. (2).

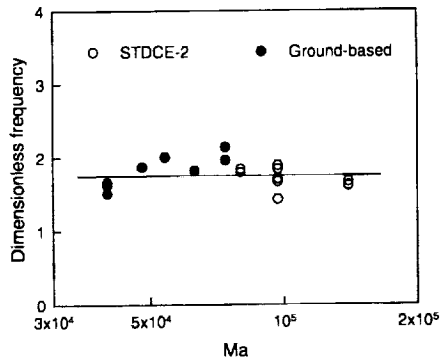

Figure 6. Dimensionless oscillation frequencies for CT tests.

Oscillatory Flow in CF Configuration

The oscillatory flow structure in the CF configuration was similar to that in the CT configuration. The heat input at the onset of oscillations is called critical heat flux (Q_{cr}). The critical heat fluxes measured in the flat surface tests with Ar = 1 are presented in Fig. 7, together with data taken in our ground-based tests with smaller containers filled with the same fluid (Lee et al.[4]). The flow was found to be already oscillating at the minimum power of the CO_2 laser for the 1.2 cm container, so that the critical heat flux could not be determined for that container. As seen in Fig. 7, trend of the space data is consistent with that of the ground data: Q_{cr} increases with increasing D. According to Fig. 7, Q_{cr} seems to depend slightly on Hr but the effect of Hr is within the experimental error.

It can be shown from scaling and numerical analyses (Kamotani et al.[5]) that the steady flow in the CF

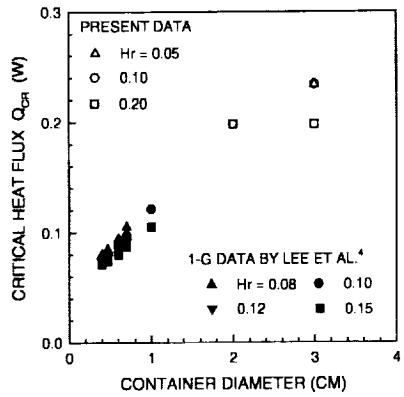

Figure 7. Critical heat fluxes in CF tests.

configuration is driven mainly in the bulk region outside the heated region. Then, it is appropriate to use the following Marangoni number based on Q,

$$Ma_Q = \left(\frac{\sigma_T Q}{k\mu\alpha}\right)^{2/3} \qquad (3)$$

Based on the critical heat flux for onset of oscillations, we compute $(Ma_Q)_{cr}$ according to Eq. (3). The result is given in Fig. 8, where we plot $(Ma_Q)_{cr}$ against D, since D is the only main quantity varied in those tests. If $(Ma_Q)_{cr}$ is the only parameter to specify onset of oscillations, it should not vary with D. Figure 8 shows that, as we have found also in various other experiments under different conditions, including the CT tests in STDCE-2, the critical Marangoni number varies with container size. Clearly, Ma alone cannot specify the onset.

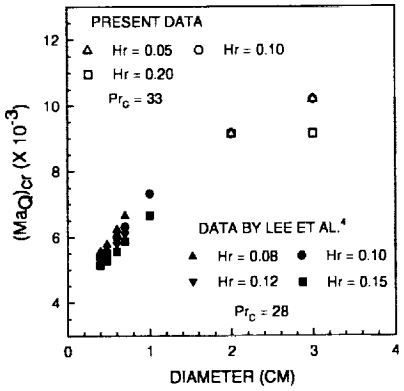

Figure 8. Critical Marangoni numbers for CF tests.

As in the case of CT configuration, free surface deformation plays an important role in the oscillation mechanism, as explained in Kamotani et al.[5] The ratio of free surface deformation in the heated region to the thermal boundary layer thickness is called S-parameter as before, and it can be shown that the S-parameter in the CF configuration can be expressed as (Kamotani et al.[5])

$$S = \left(\frac{\rho\alpha^2}{\sigma R}\right)^{1/2} Ma_Q^{1/8}\, Pr^{1/8} \qquad (4)$$

The data in Fig. 8 are replotted in Fig. 9 where S is

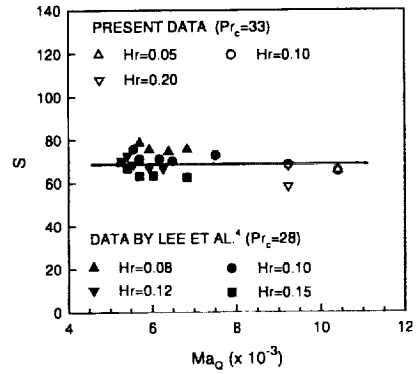

Figure 9. Critical S-parameter for CF tests.

computed according to equation (4). As seen in the figure, all the data are correlated very well with the S-parameter: all the data lie within S = 69 ± 14%. The data scatter is largely due to the effect of absorption length. Therefore, one can say that the flow becomes oscillatory when S is larger than about 70. It is clear that Ma_Q is an important parameter, because the oscillations are a convection phenomenon, but in the parametric ranges of STDCE-2 and our ground tests the S-parameter is the limiting parameter.

The frequency of oscillations are shown in Fig. 10. Only a few data are available from our ground-based tests. Except for the data for D = 1.2 cm, the oscillations frequencies were obtained near the onset of oscillations. The frequency decreases with increasing D. The frequency is not a strong function of Hr. As in the CT configuration, the oscillation period scales with the time of convection, based on which the oscillation frequency is non-dimensionalized herein as (Kamotani et al.[5])

$$f^* = \left(\frac{fR^2}{\alpha}\right) / Ma_Q \qquad (5)$$

The dimensionless frequencies are presented in Fig. 10. The figure shows that f* is nearly constant (about 0.018) in agreement with Eq. (5). The values for D = 1.2 cm are generally smaller than those for other containers, which is due to the fact that the oscillatory flow was not close to the onset.

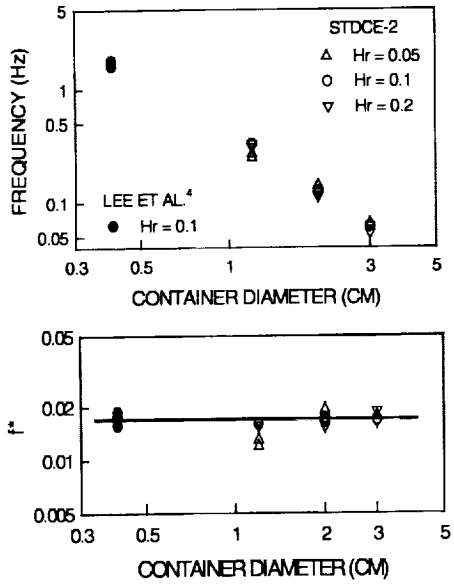

Figure 10. Dimensional and dimensionless oscillation frequencies for CF tests.

SUMMARY

The Surface Tension Driven Convection Experiment-2 (STDCE-2) was conducted aboard the USML-2 Spacelab in 1995 to study oscillatory thermocapillary flows. The STDCE-2 completed all of its defined tests for the mission, several re-run tests to check data reproducibility, and additional tests with shallow test chambers. In all, 42 constant flux tests and 13 constant temperature tests were conducted and completed successfully, and oscillations were found in most of the tests. The hardware performed very well, and the quality of the video and digital data was excellent. Only some important data taken in the STDCE-2 tests are presented and discussed herein. The most important finding is that the Marangoni number cannot specify the onset of oscillations, which suggests that free surface deformation plays an important role. Based on the physical model of oscillations, we introduce a surface deformation parameter, which represents the ratio of transient free surface deformation to thermal boundary layer thickness in the heated region. The parameter correlates the STDCE-2 and our ground-based data well.

ACKNOWLEDGMENTS

The authors would like to thank many people, especially the NASA Lewis Research Center engineering and operations teams, who worked hard to make STDCE-2 a successful project. Special thanks to the payload crew of USML-2, Drs. Fred Leslie, Kathy Thornton, Cady Coleman,and Al Sacco, who conducted the tests expertly to obtain excellent data. We would like to thank Dr. H. Philip Stahl and Mr. Kevin Sturtz for designing the Ronchi system and analyzing the data. The work done at Case Western Reserve University is supported by NASA under grant NAG3-1568.

REFERENCES

[1]Kamotani, Y., Masud, J., and Pline, A., "Oscillatory Convection Due to Combined Buoyancy and Thermocapillarity" J. Thermophysics & Heat Transfer, Vol.10, No.1, pp.102-108, (1996).

[2]Kamotani, Y., Lee J. H., Ostrach, S., and Pline, A., "An Experimental Study of Oscillatory Thermocapillary Convection in Cylindrical Containers" Physics of Fluids A, Vol.4, No.5, pp.955-962, (1992).

[3]Kamotani, Y. and Ostrach, S., "Theoretical Analysis of Thermocapillary Flow in Cylindrical Columns of High Prandtl Number Fluids," accepted for publication in Journal of Heat Transfer, 1998.

[4]Lee, J. H., Ostrach, S., and Kamotani, Y., "A Study of Oscillatory Thermocapillary Convection in Circular Containers with CO_2 Laser Heating," Report EMAE/TR-94-213, Department of Mechanical and Aerospace Engineering, Case Western Reserve University, Cleveland, OH. (1994).

[5]Kamotani, Y., Ostrach, S., and Masud, J., "Oscillatory Thermocapillary Flows in Open Cylindrical Containers Induced by CO_2 Laser Heating," accepted for publication in International Journal of Heat and Mass Transfer, 1998.

H. Haj-Hariri[1], [1]Mechanical and Aerospace Enginering, University of Virginia, Charlottesville VA 22903, USA, hh2b@virginia.edu, A. Borhan[2], [2]Chemical Engineering, The Pennsylvania State University, University Park PA 16801, borhan@psu.edu

Abstract

Thermocapillary flows are of considerable technological importance in materials processing applications such as crystal growth from the melt, particularly under microgravity conditions where the influence of buoyancy is minimized. The structure and stability of thermocapillary convection has been a subject of active research during the past decade in an effort to better understand, and eventually control, thermally-induced motions in the melt and optimize the quality of the resulting product. In this study, thermally-driven convection within a differentially-heated rectangular box containing two immiscible liquid layers is considered in the absence of gravity. The effects of fluid-fluid interface deformations on the structure of the basic flow state in these systems is examined. Such deformations are shown to be small when the contact line of the interface is pinned on the solid boundaries. Results comparing two-layer thermocapillary flow with a single-layer one are presented and discussed.

1 Introduction

Space-based processing of electronic materials has received much attention during the past decade because a number of undesireable features of semiconductor crystals grown on earth have been attributed to the effect of gravity [6, 9]. Production of III-V semiconductor crystals, such as GaAs and InP, involves additional complications which are not present in the growth of single element crystals like silicon or germanium, namely the existence of volatile components such as arsenic (in GaAs) and phosphorous (in InP). In growing crystals from a melt containing volatile components, stringent control of the stoichiometry is crucial in order to avoid crystallographic defects and degradation of electronic properties of the resulting product. One approach to minimize evaporation of the volatile component from the melt during processing of these materials has been the encapsulation of the melt in a low melting point amorphous molten glass phase, such as boron oxide or pyrolitic boron nitride. The main distinction between the unencapsulated and the liquid-encapsulated crystal (LEC) growth techniques is the presence of the additional liquid-liquid interface between the melt and the encapsulant in LEC growth. The addition of this new interface in a highly nonisothermal environment can be a source of new and complex dynamics that may significantly influence crystal quality.

In comparison with the unencapsulated process, modeling of LEC growth has received considerably less attention. One of the most widely studied model problems associated with the crystal growth process has been thermocapillary convection in a single fluid layer confined within a differentially-heated rectangular cavity, representing an idealization of the open-boat crystal growth technique (cf. review by Kuhlmann [5]). These studies have been recently extended to the case of immiscible double liquid layers with the imposed temperature gradient parallel to the free surface [1, 2, 4, 7, 12, 15]. Villers and Platten [15] performed a one-dimensional analysis assuming a constant temperature gradient across the open cavity, while others obtained solutions of the two-dimensional problem for small aspect-ratio liquid layers. The results of these studies show that under microgravity conditions, the strength of the thermocapillary convection in the layer in contact with the solid boundary can be significantly reduced, suggesting that liquid encapsulation can be used as a means of suppressing thermocapillary convection in the melt. Since the encapsulant in LEC growth is typically very viscous (e.g., boron oxide), a reduction in the strength of the thermocapillary convection in the melt by the encapsulant may be expected based on the experimental results of Eyer and Leiste [3], who showed that a solid encapsulation technique can eliminate striations in silicon crystals. Although the results of these studies suggest that encapsulation may be used to reduce the strength of steady thermocapillary convection, the effect of encapsulation on the stability of this flow remains an open question.

Most recently, Prakash and Koster [10, 11] extended the above analyses to include a third immiscible liquid layer. They performed both a one-dimensional analysis similar to that of Villers and Platten [15] and an asymptotic analysis for shallow rectangular cavities similar to

results of their analysis indicate that for equal layer heights and encapsulant viscosities, the flow in the middle (encapsulated) layer is qualitatively the same, but weaker than that obtained by Sen and Davis for a single layer. However, when the middle layer is much thicker than the encapsulant, then the interface deformations can be quite different from those for a single layer. Hence, for small aspect-ratio cavities, the flow pattern in the encapsulated layer seems to be strongly dependent on the encapsulation thickness. We will show that it is a *combination* of the viscosity and thickness of the encapsulant layer which determines the flow pattern and interfacial deformations of the encapsulated layer. This insight allows for the effective single-layer modeling of the pinned-interface multi-layer system; we will elaborate on this simplification later in this article.

All of these studies have focused on steady thermocapillary convection in small aspect-ratio liquid layers and, aside from the asymptotic analysis of Prakash and Koster [11], previous studies have neglected deformations of the fluid-fluid interfaces in order to avoid the complexity associated with the determination of the unknown interface shapes. The recent flight experiment of Koster [13] underscores the need for a more detailed investigation of thermocapillary convection in multi-layered systems accounting for finite interface deformations in conjunction with a suitable dynamic contact line condition. In this paper, we perform a numerical study of thermocapillary convection in a rectangular box containing two horizontal immiscible fluid layers differentially heated from the side in the absence of gravity. We use domain mapping in conjunction with a finite difference scheme on a staggered grid to solve for the flow field while allowing the interface to deform. We examine the effect of a (highly viscous) top liquid layer on the strength of thermocapillary convection in the (less viscous) bottom layer for different aspect ratios of the bottom layer. In the present study the two layers have the same aspect ratio.

2 Governing Equations

In this section, the dimensionless equations and boundary conditions governing the momentum and energy transport processes in a differentially-heated rectangular box of height H and length L are presented. The two-dimensional box contains two horizontal immiscible liquid layers that are differentially heated from the side in the absence of gravity. The liquid phase below $\mathcal{D}$, while the top phase is represented by $\hat{\mathcal{D}}$ with its properties distinguished by a caret. The subscript 's' will be used to represent an interface-specific property. In the following presentation, all lengths are made dimensionless with the box height H, velocities with a characteristic velocity U obtained through a tangential stress balance at the interface (cf. Ostrach [8]), stresses with $\mu U/H$ (where μ denotes the viscosity of the bottom phase), time with H/U, and temperature with the characteristic temperature difference ΔT imposed across the box. For thermally-driven flows under consideration $U \equiv (\Delta T/\mu)\sigma_{,T}$, where $\sigma_{,T}$ is a physicochemical parameter representing the sensitivity of the interfacial tension to temperature. The dimensionless parameters resulting from this nondimensionalization are presented below.

Material:	
Prandtl number	$Pr = \nu/\alpha$
Viscosity ratio	$\lambda = \hat{\mu}/\mu$
Density ratio	$\gamma = \hat{\rho}/\rho$
Thermal conductivity ratio	$\kappa = \hat{k}/k$
Thermal diffusivity ratio	$\beta = \hat{\alpha}/\alpha$
Dynamic and Thermal:	
Reynolds number	$Re = UH/\nu$
Capillary number	$Ca = \mu U/\sigma$
Geometric:	
Aspect ratio	$A = H/L$
Thickness ratio	φ

In the above expressions, σ represents the interfacial tension between the two phases, and ν and α denote the kinematic viscosity and thermal diffusivity, respectively.

The vector invariant form of the equations governing the flow field in the two incompressible Newtonian fluid phases are given by

$$u_{,t} + \nabla \cdot (uu) = \frac{1}{Re}\nabla \cdot \Pi \quad , \quad \nabla \cdot u = 0 \qquad in\ \mathcal{D}$$

$$\hat{u}_{,t} + \nabla \cdot (\hat{u}\hat{u}) = \frac{1}{\gamma Re}\nabla \cdot \hat{\Pi} \quad , \quad \nabla \cdot \hat{u} = 0 \qquad in\ \hat{\mathcal{D}}$$

where $\Pi = -pI + [\nabla u + (\nabla u)^{\dagger}]$ and $\hat{\Pi} = -\hat{p}I + \lambda[\nabla \hat{u} + (\nabla \hat{u})^{\dagger}]$ represent the Newtonian stress tensors in the two phases. The boundary conditions on the interface $x = x_s(t)$ ---having surface normal $\hat{n}$ pointing into the bottom phase $\mathcal{D}$--- are comprised of the dynamic and

$$\hat{n}\cdot(\Pi-\hat{\Pi})=\nabla_s T+\frac{1}{Ca}(\nabla_s\cdot\hat{n})\hat{n},$$

$$u=\hat{u}\qquad,\qquad dx_s/dt=u\,,$$

where the surface-gradient operator, ∇_s, is defined as $(I-nn)\cdot\nabla$. The no-slip condition is imposed on the solid walls, with the contact line of the interface with the side walls assumed to be pinned in this paper. In a follow-up study, we will incorporate a boundary condition of the Navier type which would allow for some slip in the presence of excessive shear stresses, namely

$$\hat{b}\cdot\Pi\cdot\hat{c}=\tau u\cdot\hat{c}\qquad(\tau\ll 1)\,,$$

where $\hat{b}$ and $\hat{c}$ represent the unit vector normal to the wall and the in-plane unit vector normal to the contact line, respectively. This condition will help regularize the non-integrable singularity that would exist at the location of a contact line if the no-slip condition were maintained.

There is direct coupling between the momentum and energy equations primarily as a result of the temperature-dependence of the interfacial tension, σ, though other fluid properties such as viscosity, μ, and thermal conductivity, k, could also vary with temperature. The temperature dependencies of all fluid properties, except for that of the interfacial tension, are neglected in this study. To accomodate the temperature-dependence of the interfacial tension, σ, the dimensionless energy equations in the two phases are written as:

$$T_{,t}+\nabla\cdot(uT)=\frac{1}{Ma}\nabla^2 T\qquad in\ \mathcal{D}$$

$$\hat{T}_{,t}+\nabla\cdot(\hat{u}\hat{T})=\frac{\beta}{Ma}\nabla^2\hat{T}\qquad in\ \hat{\mathcal{D}},$$

where the Marangoni number is defined as $Ma=PrRe=UH/\alpha$. The no-flux condition is imposed on all insulated solid boundaries, while the boundary conditions at the interface, $x=x_s(t)$, consist of the continuity of temperature and heat flux, i.e.

$$T=\hat{T}\qquad,\qquad\hat{n}\cdot\nabla T=\kappa\hat{n}\cdot\nabla\hat{T}\,.$$

These equations are solved using a finite-difference scheme on a staggered grid in conjunction with domain mapping in order to account for interface deformations.

3 Results and Discussion

We present a comparison of the numerical results for the single-layer thermocapillary flow with $Re=Ma=10$ characterized by $\lambda=10$, $\kappa=0.1$, $\beta=0.1$, and $\gamma=1$. Computational results are presented for three different aspect ratios (2, 1, and 1/2) of the bottom layer.

Figures 1(a)--(c) contain the midplane horizontal-velocity profiles of the single and double-layer problem for each of the aspect ratios considered. Figures 2(a)--(c) contain a comparison of the surface (interface) velocities. All figures clearly demonstrate a reduction in the intensity of the thermocapillary flow upon the introduction of a more viscous 'encapsulant'. This is quite well known by now.

However, some other interesting conclusions are possible. First, it is not a coincidence that for $A=1/2$ the seemingly disparate mid-plane velocity profiles of the single and double-layer flows share a common zero crossing. Moreover, the velocity profiles in the two layers are symmetric despite their vastly disparate viscosities. These observations are explained by noting the return-flow nature of the profiles in both problems, and realizing that the position of the zero crossing of the profile ---in a one-dimensional flow--- is at two-thirds of the thickness from the no-slip boundary. Moreover, the top-down symmetry of the two-layer problem is a consequence of both layers supporting a return-flow profile which for equal layer thicknesses results in equal magnitudes for the velocity gradient just above and below the interface. The higher viscosity of the encapsulant layer gives rise to a higher pressure gradient in that layer in order to satisfy the no-net flux condition through cross sections. As an aside, this pressure distribution causes the surface deformation to have the reverse sense to what it would be in the absence of the encapsulant layer. The symmetry of the velocity gradients motivates one to consider the (effective) tangential stress condition at the interface:

$$\frac{\partial\hat{u}}{\partial y}=-\frac{\partial u}{\partial y}\quad\Rightarrow$$

$$\left(-\frac{\partial T}{\partial x}=\frac{\partial u}{\partial y}-\lambda\frac{\partial\hat{u}}{\partial y}\right)\quad\rightarrow\quad\left(-\frac{\partial T}{\partial x}=(1+\lambda)\frac{\partial u}{\partial y}\right).$$

In other words, the flow within the encapsulated layer may be closely approximated by simply considering the single-layer problem, but with a modified shear-stress condition. While these observations are based on the small-aspect-ratio problem, they apply serendipitously well even in the case with $A=4$ ($\phi=0.5$), which is not a small aspect ratio anymore. Figure 3 shows the surface velocity for the effectively encapsulated single layer with $A=2$. The double-layer results from Figure 2(a) are also included in this figure so as to show the

of the streamfunction, as well as a plot of the surface deformation, for the two-layer problem with $A = 2$ and $\phi = 0.5$ are provided in Figures 4 and 5, respectively.

Finally, Prakash & Koster [10] remarked about the nature of the deformation of the middle layer of a three-layer system depending on the thickness of the encapsulant layers. From the tangential-stress balance at the interface it can be seen that a reduction in the thickness of the encapsulant layer is equivalent to an increase in its viscosity, i.e. both effects result in an increase in the interfacial shear stress carried by the encapsulant. Whereas the above authors conjectured the existence of some relation based on their numerical results, we have shown the explicit form of the relationship based on fundamental observations.

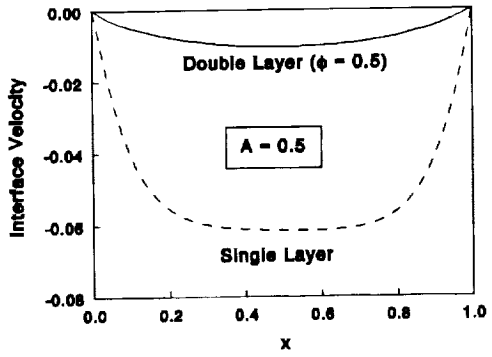

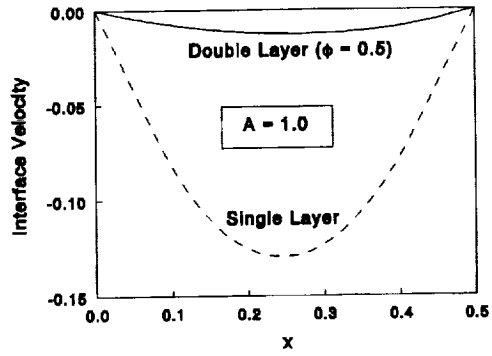

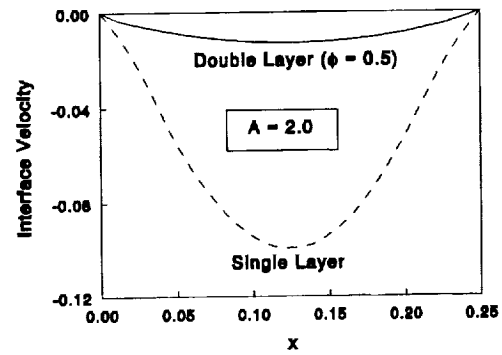

Figure 1: (a)-(c) Surface velocity comparison of the single and double-layer thermocapillary flow for various aspect ratios.

References

[1] E. Crespo del Arco, G. P. Extremet, and R. L. Sani. Thermocapillary convection in a two-layer fluid system with a flat interface. *Adv. Space Res.*, 11(7):129--132, 1991.

[2] T. Doi and J. N. Koster. Thermocapillary convection in two immiscible liquid layers with free surface *Phys. Fluids A*, 5(8):1914--1927, 1993.

[3] A. Eyer and H. Leiste. Striation-free silicon crystals by float-zoning with surface-coated melt. *J. Crystal Growth*, 71:249--252, 1985.

[4] J. P. Fontaine and R. L. Sani. Thermocapillary effects in a multilayered fluid system. paper 92--0689, AIAA aerosapce sciences meeting, Reno, NV, 1992.

[5] H. C. Kuhlmann. Thermocapillary flows in finite-size systems. *Math. and Computer Modelling*, 20(10--1):145--173, 1994.

[6] W. E. Langlois. Buoyancy-driven flows in crystal-growth melts. *Ann. Rev. Fluid Mech.*, 17:191--216, 1985.

[7] Q. S. Liu, G. Chen, and B. Roux. Thermogravitational and thermocapillary convection in a cavity containing two superposed immiscible liquid layers. *Int. J. Heat Mass Transfer*, 36(1):101--117, 1993.

[8] S. Ostrach. Low--gravity fluid flows. *Ann. Rev. Fluid Mech.*, 14:313--345, 1982.

[9] S. M. Pimputkar and S. Ostrach. Convective effects in crystals grown from melt. *J. Crystal Growth*, 55:614--646, 1981.

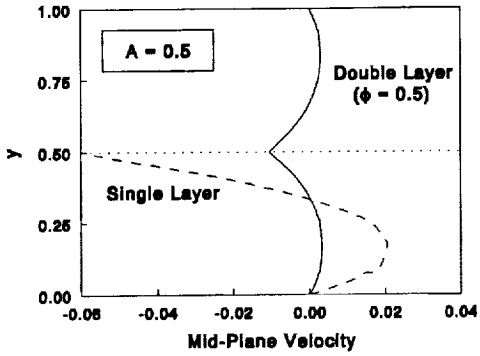

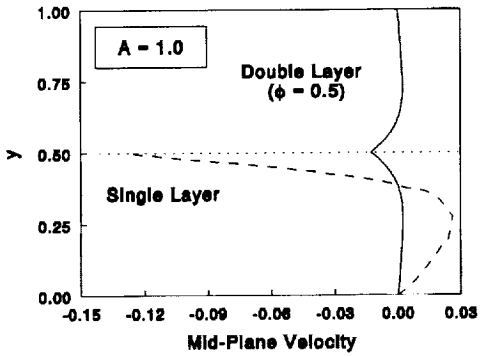

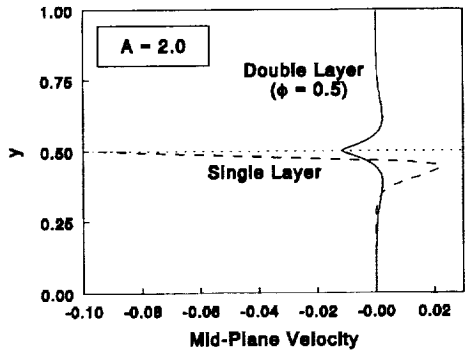

Figure 2: (a)-(c) Mid-plane velocity profile comparison of the single and double-layer thermocapillary flow for various aspect ratios.

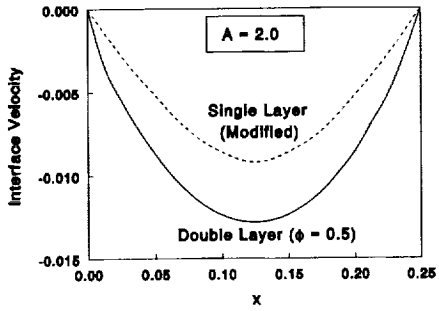

Figure 3: Surface velocity of the modified single-layer problem compared with that of the equivalent two-layer system

[10] A. Prakash and J. N. Koster. Natural and thermocapillary convection in three layers. *Eur. J. Mech., B/Fluids*, 12(5):635--655, 1993.

[11] A. Prakash and J. N. Koster. Convection in multiple layers of immiscible liquids in a shallow cavity. 2. steady thermocapillary-convection. *Int. J. Multiphase Flow*, 20(2):397--414, 1994.

[12] N. Ramachandran. Thermal buoyancy and Marangoni convection in a two fluid layered system--a numerical study. Paper 90--0254, AIAA aerospace sciences meeting, Reno, NV, 1990.

[13] G. Seibert. Early mission report on the four ESA facilities: Biorack; Bubble, Drop and Particle Unit; Critical Point Facility and Advanced Protein Crystallization Facility flown on the IML-2 Spacelab Mission. *Microgravity News from ESA*, 7(3):2--7, 1994.

[14] A. S. Sen and S. H. Davis. Steady thermocapillary flows in two-dimensional slots. *J. Fluid Mech.*, 121:163--186, 1982.

[15] D. Villers and J. K. Platten. Influence of interfacial tension gradients on thermal convection in two superposed immiscible liquid layers. *Appl. Sci. Res.*, 47:177--191, 1990.

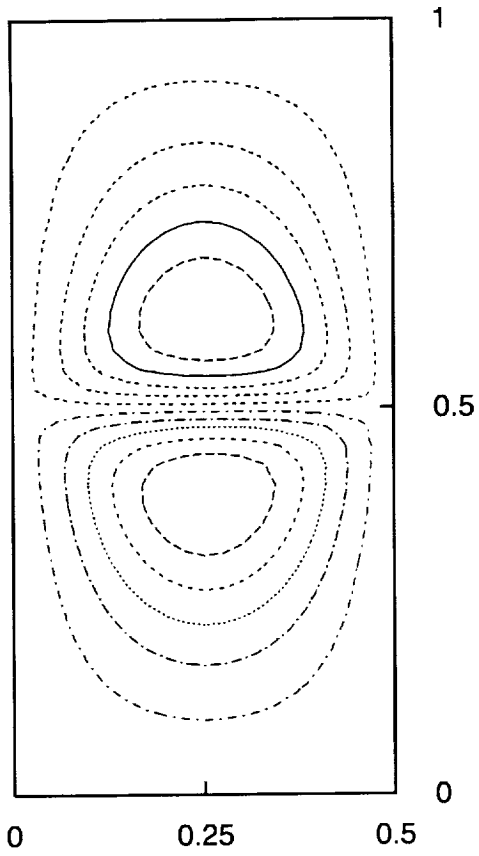

Figure 4: Streamfunction for the two-layer case with $A = 2$, $\phi = 0.5$. $\phi_{\min} = -0.00047$ in the upper layer, and $\phi_{\max} = 0.00049$ in the lower layer

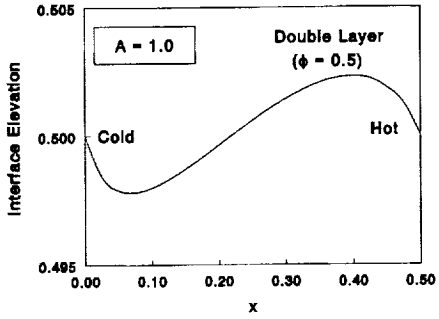

Figure 5: Surface deformation for the two-layer case with $A = 2$, $\phi = 0.5$

STUDIES IN THERMOCAPILLARY CONVECTION OF THE MARANGONI-BENARD TYPE

R.E. Kelly[1] and A.C. Or[1]
[1]Mechanical & Aerospace Engineering, University of California, Los Angeles, CA 90095-1597, USA,
rekelly@seas.ucla.edu

INTRODUCTION

Previous research by the authors [1-3] has shown that either oscillatory, nonplanar shear or temporal modulation of a boundary temperature can stabilize significantly the onset of thermocapillary convection in a fluid layer originally at rest and heated from below. Within the context of control theory, both methods are forms of open loop control. We now extend our investigation of the control of Marangoni-Benard convection by considering the effects of closed loop control using feedback. The basic model for the linearized problem is similar to one employed by Tang and Bau [4] who showed that Rayleigh-Benard convection can be stabilized by the use of linear feedback control. We also use the temperature of the lower boundary as an actuator but, instead of sensing the temperature within the layer, we assume that the depth of the layer can be measured in order to input information to the actuator.

Marangoni-Benard convection can occur in one of two distinct ways. One mode of instability, typical of situations involving moderate Bond numbers, was studied first by Pearson [5]. I occurs for a critical wavelength of the order of the depth of the layer and typically involves negligible surface deformation. The preferred pattern of convection is one of hexagons. A quite different mode of instability occurs at the very small Bond numbers typical of a microgravity situation. It was studied first by Scriven and Sternling [6] and by Smith [7]. The critical wavelength for this mode is much larger than the depth and considerable surface deformation occurs. A recent experimental investigation [8] has shown that the onset of this long wavelength mode can often lead to rupture of the fluid layer. We therefore felt that control of this mode of instability would be a worthy test of the use of feedback control because rupture of the layer is usually detrimental to any application where thermocapillary convection is possible.

The long wavelength mode of Marangoni Benard convection differs from Rayleigh-Benard convection not only by its length-scale but also by the fact that a sub-critical instability is dominant rather than the supercritical bifurcation characteristic of Rayleigh-Benard convection (which gives rise to convective rolls). Due to this difference, a control strategy considerably more complicated than that used by Tang and Bau [4] must be employed. In fact, we show that a nonlinear control strategy is essential in order to eliminate the subcritical instability and to stabilize the layer. Another major difference between our analysis and that of Tang and Bau, who considered the control of an individual normal mode, is that we can consider direct control of arbitrary disturbances as long as they are composed of large wavelength components.

ANALYSIS

Only a brief review of the problem formulation and analysis will be given here because a detailed presentation [9] has recently been submitted for journal publication. We consider a gas-liquid layer model contained between two parallel walls contained at constant but unequal temperatures, with the wall bounding the liquid having the higher temperature. In particular, the simplified two-layer model of VanHook et al. [8] is used, in which the effects of heat transfer in the gas layer are modeled but dynamical effects of the gas are ignored. Because we restrict the analysis to large wavelength disturbances, both linear and nonlinear effects can be investigated by means of a small wavenumber expansion [8,10]. We further restrict the analysis to values of the Marangoni number (M) close to the critical value (M_c). This restriction allows us to explore the problem on a weakly nonlinear basis for arbitrary values of the surface tension, which is usually assumed to be large for nonlinear studies where M is well above M_c. For the large wavelength case, it is convenient to define and use the parameter $D = M/G$, where G is the Galileo number. VanHook et al. [8] refer to D^{-1} as being the dynamic Bond number. At lowest order in an expansion involving the nondimensional wavenumber $q(<<1)$, the critical condition for the case without control is determined to be $\frac{3}{2}D(1|F) = 1$, where F is the two-layer Biot number as defined in [8]. We can then define $\epsilon \frac{3}{2}D(1|F) - 1$ as a measure of sub- or supercriticality. If η represents the deflection of the interface relative to the undisturbed level of the interface, the weakly nonlinear regime is explored by means of the scalings $c = q^2R$ and $\eta = q^2A$, where R and A are $O(1)$. After defining a suitable nondimensional

time τ, an amplitude equation arises at $O(q^2)$ in which nonlinear quadratic terms appear, namely,

$$\frac{\partial A}{\partial \tau} + \nabla \cdot \left(R + \frac{1}{B}\nabla^2 + (2F-1)A \right) \nabla A = 0 \qquad (1)$$

where B is the ordinary Bond number. Because the amplitude equation involves quadratic terms, subcritical instability with $R<0$ of the transcritical type occurs. Although subcritical equilibrium solutions are possible, they turn out to be unstable. Equilibrium solutions are not possible for $R>0$. We then have a picture of a very unstable situation, with instability occurring for $R<0$ as well as $R>0$ and growth being possibly limited only by higher-order nonlinear terms. The above scaling fails if $F = 1/2$, in which case cubic terms in A must be considered. For that case, it can be shown that the cubic term augments the instability instead of limiting growth.

We now seek to stabilize this very unstable situation by utilizing feedback control. The interfacial deflection is assumed to be measured, and a control temperature T_c at the lower wall is assumed of the form

$$T_c = K_1\eta + K_2\eta^2 + K_3\eta^3. \qquad (2)$$

Higher-order terms could be included in the control law but would not appear in our weakly nonlinear analysis. The lower boundary now has an inhomogeneous temperature, which is assumed to vary smoothly along the wall. For the linear problem, the critical condition for disturbances with $q \to 0$ is found to be $c = K_1$ where $K_j = 3DK_j/2(1 + H)$, $j = 1,2,3$, and where H is the one-layer Biot number [9]. Thus, linear feedback control has a stabilizing effect, obtained basically by heating or cooling the fluid in such a way that the thermocapillary effect at the interface is in part cancelled. In terms of the ratio of the critical Marangoni number with control to that without, we obtain

$$M_c\frac{(K_1 \neq 0)}{(K_1 = 0)} = \frac{1}{1 - K_{1,eff}}. \qquad (3)$$

where $K_{1,eff} = K_1/(1+F)(1+H)$. As $K_{1,eff}$ increases from zero, the ratio (3) increases in magnitude and approaches infinity as $K_{1,eff} \to 1$. In this limit, the thermocapillary effect arising at the interface is exactly cancelled by the control. However, stabilization by linear control does not affect the fact that subcritical instability can occur. Because this instability is associated with the quadratic terms in (1), we must have $K_2 \neq 0$ in (2) in order to eliminate the possibility of subcritical instability. With control, the coefficient of the quadratic term turns out to be

$$2F - 1 - a_1\hat{K}_1 - 2\hat{K}_2 \qquad (4)$$

where $a_1 = 2(1 - (1 + F)H)$. We want to make this term small by suitable selection of $\hat{K}_2$. However, exact cancellation might not occur, and so we let

$$2F - 1 - a_1\hat{K}_1 - 2\hat{K}_2 = \alpha q \qquad (5)$$

where α is an $O(1)$ parameter. With the quadratic term in (1) almost eliminated, we can then balance the linear terms with the next order nonlinear (cubic) term by defining $c - \hat{K}_1 = q^2R$ and $\eta = qA$ to obtain the following cubic amplitude equation:

$$\frac{\partial A}{\partial \tau} + \nabla \cdot \left(R + \frac{1}{B}\nabla^2 + \alpha A + \beta A^2 \right) \nabla A = 0 \qquad (6)$$

which can be compared to (1). The cubic term can now control the growth of the instability for $R > 0$ if $\beta < 0$ where $\beta = \beta(H, F, \hat{K}_1, \hat{K}_3)$ is a function defined by the analysis. When this is achieved, the original subcritical instability has been converted into a supercritical bifurcation.

Values of K_1, K_2 and K_3 required to achieve a supercritical bifurcation at $\epsilon > 0$(i.e., $M_c(K_1, K_2, K_3) > M_c(0)$) are given in Table 1. As is clear, the values of K_1, K_2 and K_3 and all $O(1)$ even for an increase of 100% in the critical Marangoni number.

F	r	β	D_c	K_1	K_2	K_3
0.33	0.50	0.00	0.75	0.49	–0.59	0.54
0.67	0.50	0.00	0.60	0.61	–0.30	1.18
0.33	0.50	–0.50	0.75	0.49	–0.59	0.70
0.67	0.50	–0.50	0.60	0.61	–0.30	1.38
0.33	1.00	–0.50	1.00	0.73	–0.76	0.86
0.67	1.00	–0.50	0.80	0.92	–0.61	1.49

Table 1: Values of Control Gains Computed from Selected Parameters

CONCLUSIONS

We conclude that feedback control can be used to postpone the onset of Marangoni-Benard long-wavelength convection and even to convert the subcritical bifurcation characteristic of the case without control into a supercritical bifurcation. In order to achieve this goal, however, a nonlinear control strategy of the type given by (2) is required. The gain K_1 is selected to give the desired increase in M_c, K_2 is chosen so as to eliminate the possibility of a transcritical bifurcation, and K_3 is then selected to give a forward pitchfork (supercritical) bifurcation. With K_2 and $K_3 = 0$, convection could start for M well below M_c due to finite amplitude disturbances even though $M_c(K_1) > M_c(0)$.

ACKNOWLEDGMENT

Besides being supported by the NASA Microgravity Fluid Physics Program under Grant no. NAG 3-1819, A.O. received partial support from the USAF under Grant no. F49620-93-1-0332, awarded to Professor J.L. Speyer of UCLA. The authors are grateful to Professor Speyer for his interest in this research.

REFERENCES

1. Or, A.C. and Kelly, R.E., 1995 Onset of Marangoni convection in a layer of fluid modulated by a weak nonplanar oscillatory shear, *Int. J. Heat Mass Transfer*, **38**, 2269-2279.
2. Or, A.C. and Kelly, R.E., 1998 Thermocapillary and oscillatory-shear instabilities in a layer of liquid with a deformable surface, *J. Fluid Mech.*, **360**, 21-39.
3. Kelly, R.E. 1997 The effects of thermal modulation upon the onset of Marangoni convection, *Bull. Amer. Phys. Soc.*, **42**, 2182 (abstract).
4. Tang, J. and Bau, H.H., 1994 Stabilization of the no-motion state in the Rayleigh-Benard problem, *Proc. R. Soc. Lond. A*, **447**, 587-607
5. Pearson, J.R.A. 1958 On convection cells induced by surface tension, *J. Fluid Mech.*, **4**, 489-500.
6. Scriven, L.E. and Sternling, C.V. 1964 On cellular convection driven by surface tension gradients: effects of mean surface tension and surface viscosity, *J. Fluid Mech.*, **19**, 321-340.
7. Smith, K.A., 1966 On convective instability induced by surface tension, *J. Fluid Mech.*, **24**, 401-414.
8. VanHook, S.J., Schatz, M.F., Swift, J.B., McCormick, W.D. & Swinney, H.L., 1997 Long-wavelength surface-tension-driven Benard convection: experiment and theory, *J. Fluid Mech.*, **345**, 45-78.
9. Or, A.C. and Kelly, R.E., Cortelezzi, L. and Speyer, J.L., 1998 Control of long-wavelength Marangoni-Benard convection, submitted for publication.
10. Oron, A., Davis, S.H., and Bankoff, S.G. 1997 Long-scale evolution of thin liquid films, *Revs. Mod. Phys.*, **69**, 931-980.
11. Bau, H.H. 1998 Control of Marangoni Benard convection, submitted for publication.

Thermocapillary Convection in a Low-Pr Material under Simulated Reduced Gravity

Mingtao Cheng and Sindo Kou
Department of Materials Science and Engineering
University of Wisconsin
Madison, WI 53706

Abstract

A liquid bridge of molten Si (Pr = 0.027) was established by having the bottom of a Si rod in contact with the top of a resistance heated BN rod, both rods being 13 mm in diameter. The height of the liquid bridge was 10 mm and the temperature difference was 50 °C, corresponding to a high Marangoni number of 6200. Temperature oscillations were detected on the free surface with an optical pyrometer. Oscillation about 0.07 Hz in frequency and 4 °C in amplitude was observed. The rapid response of the optical pyrometer helped revealed the faster and weaker waves superimposed on the oscillation, e.g., about 1.5 Hz and 1.5 °C, and 10 Hz and 0.5 °C.

Introduction

Thermocapillary convection becomes significantly more important as gravity and hence gravity-induced buoyancy convection are reduced. The vast majority of experimental studies on thermocapillary convection have been on high Pr materials, typically silicone oil. In microgravity floating-zone crystal growth of Si thermocapillary convection is often strong and oscillatory, causing composition fluctuations in the resultant crystal called dopant striations. Dopant striations due to oscillatory thermocapillary convection have been reported in floating-zone crystals of several low Pr materials, Si (1-10), GaAs(11), Mo (12-13), Nb (14) and Ti_3Pt (15).

Croll et al. (2, 3) determined the Marangoni number corresponding to the onset of dopant striations in floating-zone growth from a 10 mm diameter P-doped Si rod heated with a focused halogen lamp. The rod was coated with an oxide film of SiO_2 except for an annular opening 0.5 to 3 mm high, which served as the free surface during crystal growth. The temperature difference across the annular opening was measured with a vertical thermocouple in contact with the melt surface. The critical Marangoni number was reported to be about 150 –200 (based on a thermal diffusivity $\alpha = 1.3 \times 10^{-5}$ m^2/s and a temperature coefficient of surface tension $\partial\gamma/\partial T = -2.8 \times 10^{-3}$ N/m/°C). No temperature fluctuations were picked up by the thermocouple. Kaiser et al. (16) found by numerical simulation that the critical Marangoni number for the onset of time-dependent flow in a P-doped Si floating zone is about 80. No temperature oscillations were shown.

Levenstam et al. (17) determined the critical Reynolds number for the onset of temperature fluctuation in a noncylindrical molten Si zone between a 8 mm diameter Si rod at the top and a 10 mm diameter quartz tube at the bottom. The lower half of the melt was contained in the quartz tube and only the upper half had a free surface. The melt was heated with focused halogen lamps, and the melt temperature was measured with a thermocouple positioned

at the top of the inner wall of the quartz tube. The critical Reynolds number was reported to be in the range of 8000 – 64000, which corresponds to a Marangoni number of 200 – 1700 (based on $\alpha = 1.3 \times 10^{-5}$ m^2/s and $\partial\gamma/\partial T = -2.8 \times 10^{-3}$ N/m/°C).

Nakamura et al. (18) observed free-surface temperature fluctuations in a 10 mm high Si liquid bridge, which was held between two graphite rods of 10 mm diameter and which was heated with a focused halogen lamp to150°C hotter at the top than at the bottom. The Marangoni number 14600 reported is based on $\alpha = 2.28 \times 10^{-5}$ m^2/s and $\partial\gamma/\partial T = -2.0 \times 10^{-3}$N/m/°C. Temperature fluctuations were measured both on the ground and in a rocket, with four vertical SiO_2-shielded thermocouples in contact with the free surface at 2 mm from the bottom and 90° from each other in the circumferential direction. The amplitude of oscillation was higher in the rocket (about 5 °C) than on the ground (about 2 °C), and no characteristic frequencies were identified in either case after complete melting of Si. With a "slender" bridge of 20 % less volume on the ground, however, a larger amplitude of oscillation of about 5 °C, a characteristic frequency of about 0.2 Hz and a phase difference between nonadjacent thermocouples were observed. Significant contamination of molten Si by carbon from graphite and oxygen from SiO_2 was reported.

In the present study an optical pyrometer, which responds to temperature fluctuations much faster than thermocouples, is used. Since BN and Al_2O_3 are chemically compatible with molten Si, a BN rod and Al_2O_3 thermocouple shield were used.

Experimental Procedure

Melting Si with a focused halogen lamp, though available in our laboratory, was not used in view of interference with temperature measurements by optical pyrometry. Induction melting, though also available, was not used either in view of interference of electromagnetic stirring with thermocapillary convection. Melting by resistance heating was, therefore, chosen.

The furnace is shown schematically in Fig. 1. It consisted of a graphite heater, the insulation surrounding the heater, and a BN rod going through and heated by the heater. The insulation had one round port on the top for loading the Si rod, one rectangular port on the side for viewing and one rectangular port at the front for temperature measurements. The Si and BN rods were both 13 mm in diameter. The Si rod was of 99.999 % purity. A R-type thermocouple was used to measure the temperature at the bottom of the liquid bridge. It was protected by a thin Al_2O_3 shield of 0.1 mm wall and 1 mm OD, which was positioned horizontally such that its top was even with the top surface of the BN rod and its tip at the center. The furnace was contained in a vacuum chamber to prevent oxidation from air at high temperatures. The chamber was pumped down to 3×10^{-6} torr before heating was started.

The optical pyrometer system had a response of 10 kHz, a spot diameter of 0.8 mm at the target, a resolution of 0.01 °C and a maximum sampling rate of 80 readings per second. The pyrometer system was connected to a personal computer both for data acquisition and analysis by Fourier transformation.

Results and Discussion

Because of the high surface tension and low density of molten Si, the 10 mm high liquid bridge was very stable and the free surface was essentially cylindrical. Due to limited wetting of BN by molten Si, the molten Si did not creep down the BN rod and escape. For the same reason, however, the molten Si often missed a small portion of the edge of the BN rod, as illustrated in Fig. 2a. It is well known in crystal growth that the free surface has to expand as much as 11° at the growth front if Si is to grow into a perfect cylindrical shape (19). For this reason, even a perfectly cylindrical liquid bridge always solidified with necking on the top and bulging and even extrusion at the bottom, as illustrated in Fig. 2b. This necking after solidification does not imply necking in the liquid bridge. The surface of the solidified Si was mirror-like, clean and free of oxide films or scum.

The physical properties of molten Si are listed in Table1. The dynamic Bond number is defined as follows:

$$Bo = \beta\rho g L^2/(-\partial\gamma/\partial T) \qquad [1]$$

where L is the height of the liquid bridge and g is gravitational acceleration. From L = 10 mm and Table 1, Bo is about one. In view of the relatively small Bo thermocapillary convection is expected to dominate in the liquid bridge in ground-base experiments. Numerical computation of heat transfer and fluid flow shows clearly that thermocapillary convection dominates in a Si floating zone 10 mm in height and diameter (20). The Marangoni number is defined as follows:

$$Ma = (-\partial\gamma/\partial T)L\Delta T/(\rho\nu\alpha) \qquad [2]$$

The liquid bridge was 10 mm high, and the temperature indicated by the thermocouple at the bottom of the liquid bridge was 1463 °C. Since the temperature at the top of the liquid bridge is the melting point of Si, 1412 °C, the temperature difference across the liquid bridge is about 50 °C. From Table 1 the Marangoni number is about 6200. The evidence of flow oscillation at this high level of the Marangoni number is clear from the result shown in Fig. 3, where temperature fluctuation was measured near (0.5 mm) the bottom of the liquid bridge.

The oscillation has a characteristic frequency of about 0.07 Hz, as shown in Fig. 4, and an amplitude of roughly 4 °C. This is different from the cylindrical liquid bridge of 10 mm height and 150 °C temperature difference in the ground-base experiment of Nakamura et al. (18), where no characteristic frequency was observed. On the contrary, it is more like the oscillation of 0.2 Hz and 5 °C observed in the "slender" bridge in the ground-base experiment. It is not clear if the difference is caused by the carbon (and oxygen) dissolution in their molten Si, or the use of different heating methods in the two studies, or something else.

As already pointed out the pyrometer used in the present study responded to temperature fluctuations much faster than thermocouples in previous studies (2, 3, 17, 18). As a result, the detail of oscillation can be brought out, e.g., as shown in a 5-second section of the oscillation in Fig. 5. There appears to be sharper and more widely separated spikes of about 1.5 °C as well as

smaller and more closely packed cycles of about 0.5 °C. From Fig. 6 the frequencies are about 1.5 Hz for the spikes and, for example, 10 Hz for some of the smaller cycles.

Conclusions

A stable liquid bridge of molten Si has been established between a Si rod on the top and a BN rod at the bottom by resistance heating. At a high Marangoni number of 6200, several levels of characteristic frequency and amplitude of oscillation have been observed, e.g., 0.07 Hz and 4 °C, 1.5 Hz and 1.5 °C, and 10 Hz and 0.5 °C.

References

1. A. Croll, W. Mueller and R. Nitsche, Proc. 6th European Symposium on Material Sciences under Microgravity Conditions, Bordeaux, France, 2-5 December 1986, ESA SP-256 (February 1987) 87.
2. A. Croll, W. Muller-Sebert and R. Nitsche, Proc. 7th European Symposium on Materials and Fluid Sciences in Microgravity, Oxford, UK, 10- 15 September 1989, ESA SP-295 (January 1990) 263.
3. A. Croll, W. Muller-Sebert, K. W. Benz and R. Nitsche, Microgravity Sci. Technol., 111/4 (Feb. 1991), Hanser Publishers, Munich, p. 204.
4. A. Eyer and R. Nitsche, Proc. 3rd European Symposium on Material Science in Space, Grenoble 24-27 April 1979, ESA SP-142 (June 1979) 75.
5. A. Eyer, H. Leiste and R. Nitsche, Proc. 5th European Symposium on Materials Sciences under Microgravity, Schloss Elman, 5-7 November 1984, ESA SP-222, p. 173.
6. A. Eyer, B. 0. Kolbesen and R. Nitsche, Journal of Crystal Growth 57 (1982) 145.
7. A. Eyer and H. Leiste, Journal of Crystal Growth 71 (1985) 249.
8. A. Eyer, H. Lesite and R. Nitsche, Journal of Crystal Growth 71 (1985) 173.
9. A. Croll, W. Muller and R. Nitsche, Journal of Crystal Growth 79 (1986) 65.
10. A. Croll, P. Dold and K. W. Benz, Journal of Crystal Growth 137 (1994) 95.
11. R. Rupp, S. Auerochs, G. Muller, C. Weyrich and S. Leibenzeder, Adv. Space Res. I 1 (1991) 297.
12. 1. V. Barmin, A. V. Egorov and A. S. Senchenkov, Oral presentation at 8th European Symposium on Materials and Fluids Sciences in Microgravity, Brussels, Belgium, 12-14 April, 1992.
13. M. Jurisch and W. Loser, Journal of Crystal Growth 102 (1990) 214.
14. M. Jurisch, Journal of Crystal Growth 102 (1990) 223.
15. Y. K. Chang, Journal of Crystal Growth 62 (1983) 627.
16. Th. Kaiser and K. W. Benz, Journal of Crystal Growth 183 (1998) 564.
17. M. Levenstam, G. Amberg, T. Carlberg and M. Anderson, Journal of Crystal Growth 158 (1996) 224.
18. S. Nakamura, T. Hibiya, K. Kakimoto. N. Imaishi, S. Nishizawa, A. Hirata, K. Mukai, S. Yoda and T. Morita, Journal of Crystal Growth 186 (1998) 85.
19. T. Surek and B. Chalmers, Journal of Crystal Growth 29 (1975) 1.
20. C. W. Lan and S. Kou, Journal of Crystal Growth 108(1991) 351-366.

Table 1 Physical properties of molten Si

Melting point	Density	Kinematic viscosity	Thermal Diffusivity	Prandtl Number	Thermal expansion coefficient	Temperature coefficient of surface tension
T_m, °C	ρ, kg/m^3	ν, m^2/s	α, m^2/s	Pr=ν/α	β, 1/°C	$\partial\gamma/\partial T$, N/m/°C
1412	2.53×10^3	3.5×10^{-7}	2.55×10^{-5} or 1.3×10^{-5}	1.37×10^{-2}	1.43×10^{-4}	-0.28×10^{-3}

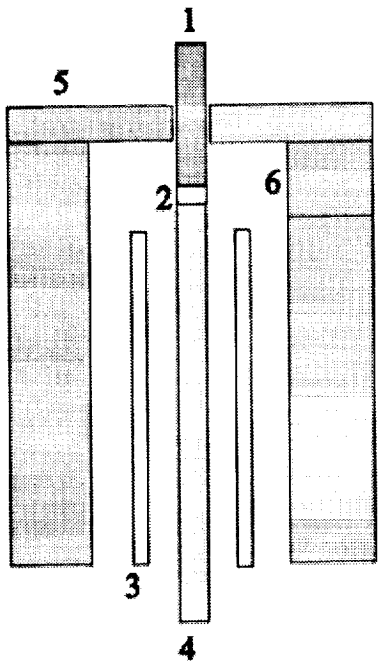

Fig. 1 Apparatus: 1.Si rod, 2. Si molten zone, 3. heater, 4. BN rod, 5. thermal insulation, 6. port.

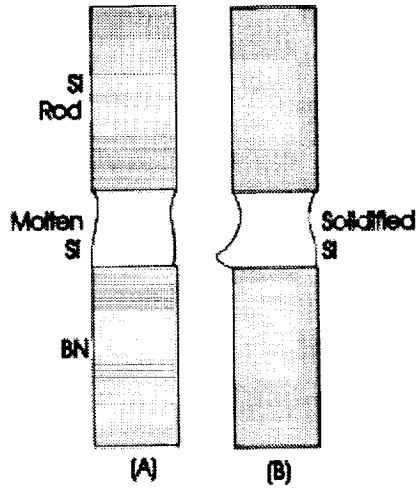

Fig. 2 The liquid bridge: (A) during experiment; (B) after experiment.

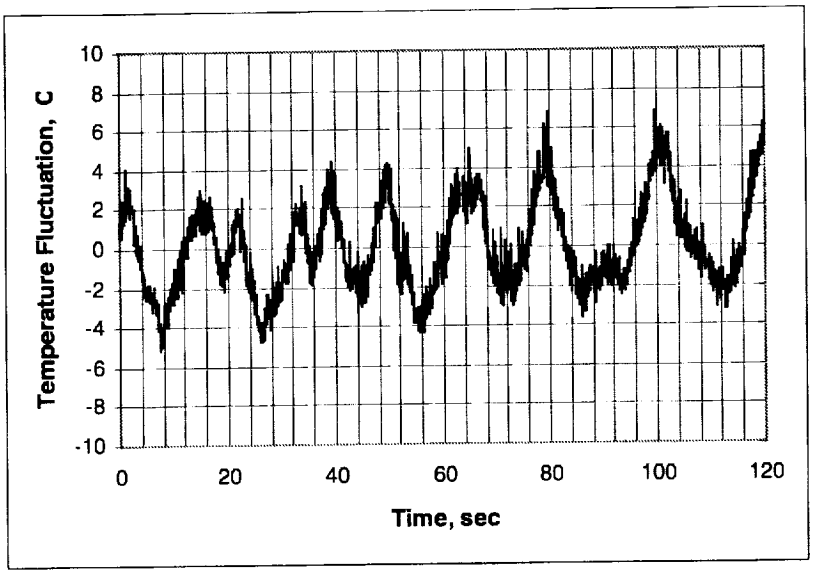

Fig. 3 Overview of temperature fluctuation.

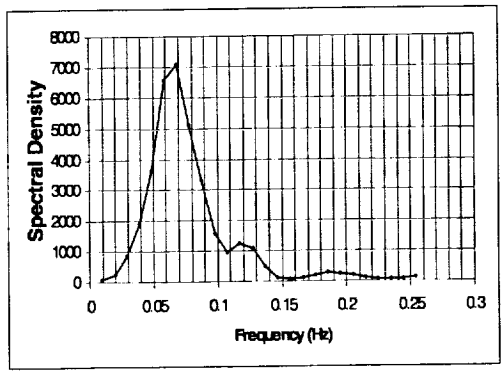

Fig. 4 Spectral analysis of the oscillation shown in Fig. 3.

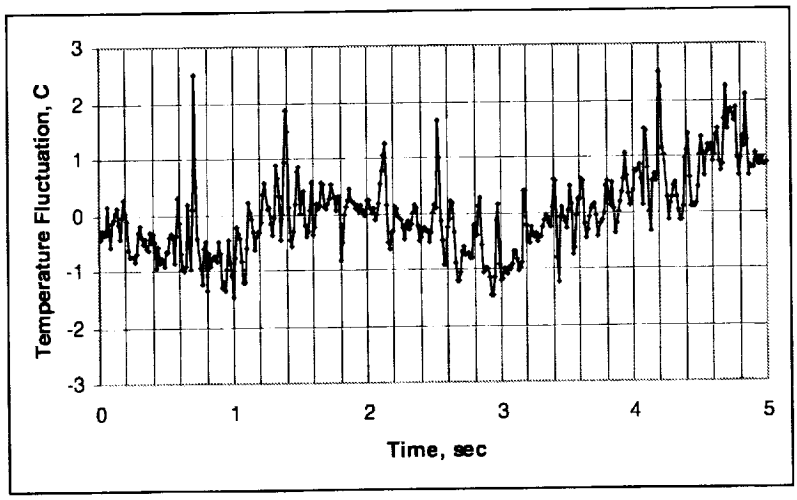

Fig. 5 Enlarged view of a 5-second section of the oscillation shown in Fig. 3.

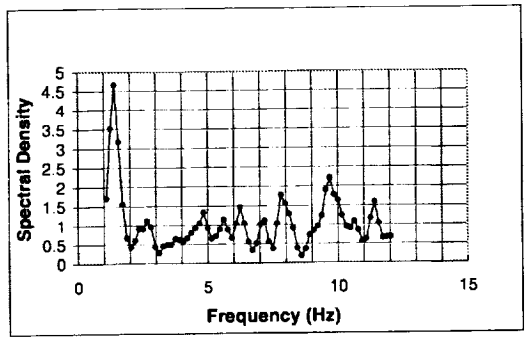

Fig. 6 Spectral analysis of the Oscillation shown in Fig. 5.

Exposition

PHASE DIAGRAMS OF ELECTRIC-FIELD-INDUCED AGGREGATION IN CONDUCTING COLLOIDS.

B. Khusid[1] and A. Acrivos[2], The Levich Institute, City College of the City University of New York, Steinman Hall T-1M, 140th Street and Convent Avenue, New York, NY 10031,
[1]boris@levdec.engr.ccny.cuny.edu, [2]acrivos@scisun.sci.ccny.cuny.edu.

1. INTRODUCTION

Under the application of a sufficiently strong electric field, a suspension may undergo reversible phase transitions from a homogeneous random arrangement of particles into a variety of ordered aggregation patterns. The surprising fact about electric-field driven phase transitions is that the aggregation patterns, that are observed in very diverse systems of colloids, display a number of common structural features and modes of evolution thereby implying that a universal mechanism may exist to account for these phenomena. It is now generally believed that this mechanism emanates from the presence of the long-range anisotropic interactions between colloidal particles due to their polarization in an applied field. But, in spite of numerous applications of the electric-field-driven phenomena in biotechnology, separation, electrorheology, materials engineering, micro-devices for chemical analysis, etc. which have expanded rapidly over the last decade, our understanding of these phenomena is far from complete. Thus, it is the purpose of the proposed research to develop a theory and then test experimentally, under normal- and low-gravity conditions, the accuracy of the theoretical predictions regarding the effect of the synergism of the interparticle electric and hydrodynamic interactions on the phase diagram of a suspension.

The main results from our theoretical studies performed to-date enable one to trace how the variations of the electrical properties of the constituent materials influence the topology of the suspension phase diagram and then, by using an appropriate phase diagram, to evaluate how the electric-field-induced transformations will depend on the frequency and the strength of the applied field and the particle concentration.

2. ELECTRIC-FIELD-INDUCED PHASE TRANSITIONS

The first step in the development of a theory for the electric-field-induced phase transitions in a suspension of electrically uncharged conducting particles dispersed in a conducting fluid was taken in Refs. [1, 2]. To begin with, the density of the free energy of a suspension containing randomly arranged hard spheres subject to an electric field was written [1] as

$$F = k_B T f_0(c)/v_p - W \qquad (1)$$

where the first term in Eq. (1) refers to the free energy of a suspension in the absence of the electric field, as a function of the temperature T with k_B being Boltzmann's constant, and the volume concentration of the particles c with v_p being the particle volume; the second term in Eq. (1) refers to the electric energy of a suspension caused by the interaction of the particles with the applied electric field and by the electric-field-induced long-range interparticle interactions. The concentration dependence of the function $f_0(c)$ in Eq. (1) is well understood [3, 4].

The main obstacle which had to be overcome in constructing a theory of electric-field-induced phase transitions was that, for materials such as conducting suspensions whose complex dielectric permittivity $\varepsilon_s^* = \varepsilon_s' - i\varepsilon_s''$ varies strongly with the frequency of the applied electric field, the electric energy density W in Eq. (1) cannot be constructed using macroscopic electrodynamics [5]. The reason for this difficulty is that the frequency dependence of the dielectric permittivity implies that such a material contains mobile charges and electric dipoles capable of orientation, so that the stored electric energy will depend on the time-history of how the electric field was established [6].

To be sure, an expression for the electric energy density W of a conducting material, namely, Brillouin's formula (see Eq. (2) below), can be derived from macroscopic electrodynamics [5, 6], but only when the energy dissipation in this material is negligibly small and the time-variations of the applied electric field are very slow compared to the rate of relaxation phenomena, i.e.

$$W = \frac{1}{2}\frac{d}{d\omega}\left[\omega\varepsilon_s'(\omega)\right]\left\langle E^2(\omega)\right\rangle_T \qquad (2)$$

only if $\left|\varepsilon_s''(\omega)\right| << \varepsilon_s'(\omega)$ and $\omega t_s << 1$ where ω and $E(\omega)$ are the frequency and the Fourier amplitude of the applied electric field, respectively; the value of t_s determines the relaxation time of dielectric phenomena; and $\langle\ \rangle_T$ denotes the time average. Recall, that the real component ε_s' gives the dielectric constant of a material whereas the imaginary

component ε_s'' determines the power dissipation (loss) in this material due to its conductivity. As can be seen from Eq. (2), Brillouin's formula is applicable only under the severe limitations that effects of conductivity are negligibly small so as not to cause losses in the stored electric energy. That is why Brillouin's formula cannot be utilized in Eq. (1) to describe electric-field-driven phase transformations in conducting colloids which strongly depend on conductivity effects.

To overcome the limitations of Brillouin's formula, we developed [1] a microscopic theory for the electric energy density W of conducting spheres dispersed in a conducting fluid when the particles were arranged randomly and provided that the particles and the suspending fluid can be described by the model of a leaky dielectric; i.e. when their dielectric constants, ε_p and ε_f, and conductivities, σ_p and σ_f, are frequency independent. This model corresponds to the classical mechanism of the so-called Maxwell-Wagner interfacial polarization typical of colloids [4, 7]. In this case, the short-term polarization of the particles and of the fluid is determined solely by their instantaneous polarization whereas their long-term polarization arises from the build-up of charge at the interface between the particles and the surrounding fluid. We exploited two microstructure-based techniques for solving the problem. One of them is based on a mean-field approximation (a cell model) where the average field acting on each particle is considered to be the well-known Lorentz-Lorenz local field [5, 6] rather than the applied field, while the second made use of statistical methods and a renormalization technique for calculating the $O(c^2)$ term in the expansion for the electric energy density W in powers of the particle concentration. But, as we found [1], the main contribution to the electric energy of a suspension as well as to its complex permittivity is given by multiparticle interactions leading to a change in the local electric field acting on a particle. That is the reason why, for example, the cell model, which accounts only for this effect, yields the well-known Maxwell-Wagner expression for the complex permittivity of a suspension which correlates well with experimental data.

The theory of Ref. [1] relates the electric energy density of a conducting suspension to the dielectric constants and conductivities of the particles and of the suspending fluid, the particle concentration, and the frequency and the strength of the applied electric field. To illustrate the advantages of this theory, the first two terms in the expansion of the electric energy density W in powers of the particle concentration were substituted in Eq. (1) which was then used to study the phase separation of a dilute conducting suspension subject to strong electric fields [1]. On this basis, we then calculated in Refs. [1, 2] the critical conditions beyond which the random arrangement of the particles becomes unstable in the presence of spatially uniform and non-uniform electric fields.

The main objective of the present work is to extend our previous studies [1, 2] beyond the dilute regime and to develop a microscopic theory for phase diagrams of concentrated conducting suspensions subject to strong dc and ac electric fields. To this end, we employ in Eq. (1) the full expression for the free energy density of a conducting suspension, as a function of a concentration, which we derived in Ref. [1] using the mean field approximation, and then investigate the topology of the suspension phase diagram, i.e. "the particle concentration-the electric field strength", and relate it to the electrical properties of the constituent materials.

As was shown in Ref. [1], the expression for the electric energy density W of a conducting suspension being subjected to a dc electric field E for short ($t \ll t_s$) and for long ($t \gg t_s$) times, is given by Eqs. (3) and (4), respectively, while, for an ac electric field $E_0 \cos\omega t$ and for the long-term $t \gg t_s$ regime, the equation for the time average of the electric energy of a suspension is given by Eq. (5)

$$W = \frac{\varepsilon_f}{2}\frac{1+2c\beta_\varepsilon}{1-c\beta_\varepsilon}E^2 \tag{3}$$

$$W = \left[\frac{\varepsilon_f}{2}\frac{1+2c\beta_\varepsilon}{1-c\beta_\varepsilon} + \frac{9c(1-c)\left(\varepsilon_f\sigma_p - \varepsilon_p\sigma_f\right)^2}{2\left(\varepsilon_p+2\varepsilon_f\right)\left(1-c\beta_\varepsilon\right)\left(\sigma_p+2\sigma_f\right)^2\left(1-c\beta_\sigma\right)^2}\right]E^2 \tag{4}$$

$$W = \left[\frac{\varepsilon_f}{4}\frac{1+2c\beta_\varepsilon}{1-c\beta_\varepsilon} + \frac{9c(1-c)\left(\varepsilon_f\sigma_p - \varepsilon_p\sigma_f\right)^2}{4\left(1+\omega^2 t_s^2\right)\left(\varepsilon_p+2\varepsilon_f\right)\left(1-c\beta_\varepsilon\right)\left(\sigma_p+2\sigma_f\right)^2\left(1-c\beta_\sigma\right)^2}\right]E_0^2 \tag{5}$$

with $t_s = \dfrac{(\varepsilon_p + 2\varepsilon_f)(1 - c\beta_\varepsilon)}{(\sigma_p + 2\sigma_f)(1 - c\beta_\sigma)}$, $\beta_\varepsilon = \dfrac{\varepsilon_p - \varepsilon_f}{\varepsilon_p + 2\varepsilon_f}$, $\beta_\sigma = \dfrac{\sigma_p - \sigma_f}{\sigma_p + 2\sigma_f}$.

For brevity, we included the vacuum permittivity ε_0 as a multiplier in the definition of dielectric constants ε_p and ε_f in Eqs. (4)-(5).

Equation (3) and the first terms in Eqs. (4) and (5), which are determined solely by the instantaneous polarization of the particles and the fluid, are consistent with the relationship for the electric energy of a non-conducting suspension $W = \frac{1}{2}\varepsilon_s(c)E^2$ given by macroscopic electrodynamics [5] with $\varepsilon_s(c)$ given by Maxwell's equation [7]. The second terms in Eqs. (4) and (5) correspond to the energy required to build the charge at the particle surface and to redistribute the electric field inside the particles and the suspending fluid when the time constants of the particles and of the fluid are different; that is when $\varepsilon_f/\sigma_f \neq \varepsilon_p/\sigma_p$ [1]. But since the second term in Eq. (5) approaches zero as $\omega t_s \to \infty$ the electric energy of the suspension for high frequencies becomes the same as that for a non-conducting material. On the other hand, for a slowly varying electric field, $\omega t_s << 1$, Eq. (5) yields the expression for the time average of the electric energy which is consistent with the expression given by the substitution of the Maxwell-Wagner relation for $\varepsilon_s'(\omega)$ into Brillouin's formula, Eq. (2), [1].

Now, the osmotic pressure of a suspension Π (equal to $-(\partial F/\partial V)_{N,T,E}$ [8]) and the chemical potential of a particle μ (equal to $(F + \Pi V)/N$ [8]) can be evaluated from the equation of the free energy, Eq. (1). On calculating these expressions, $f_0(c)$ is conveniently expressed in the terms of the suspension compressibility factor $Z(c)$ where a good approximation for $Z(c)$ of a suspension in the disordered state is given, for example [3, 4], by the Carnahan-Starling equation and the asymptotics $Z \to \infty$ as $c \to c_m$ where $c_m \sim 0.63 - 0.64$ corresponds to random close packing of spheres.

The random arrangement of the particles in a suspension is stable as long as the osmotic pressure increases with concentration, which can be written as

$$\frac{\partial}{\partial c}\left(\frac{\Pi v_p}{k_B T}\right) = Z + c\frac{dZ}{dc} - c\frac{\partial^2}{\partial c^2}\left(\frac{W v_p}{k_B T}\right) > 0 \quad (6)$$

Consequently, as seen from Eq. (6), as long as the third term on the right-side is positive, in the other words as long as the interparticle interactions increase the suspension energy, an increase in the strength of the electric field decreases the value of $\partial\Pi/\partial c$ and finally renders the random arrangement of the particles unstable when

$$\frac{\partial \Pi}{\partial c} = 0 \quad (7)$$

Now, Eq. (7) represents the spinodal curve in an equilibrium phase diagram of particle concentration vs. the electric field strength of a conducting suspension subject to an electric field. Specifically, this curve is the locus of points for which the curvature of the suspension free energy changes from convex to concave [8].

For the case when $\partial^2 W/\partial c^2 > 0$ over the entire range $0 \le c < c_m$, the spinodal points exist over the entire concentration range as well, so that increasing the strength of an electric field applied to this suspension will eventually cause the electric-field-induced transition. Thus, the phase diagram of such a suspension consists of the low-field one-phase region which includes the random spatial arrangement of the particles in the absence of an electric field and the high-field two-phase region corresponding to the appearance of aggregates caused by the action of an applied field. This phase diagram appears to be similar to the phase diagram concentration vs. temperature of a binary fluid or a binary alloy with a miscibility gap [8], so that these species exist in solution at high temperature but their mixture eventually separates into coexisting phases below the critical point of miscibility. In this regard, the application of an electric field to a conducting suspension is equivalent to a quench of an atomic system from its high-temperature one-phase state. Although such a similarity between the structural ordering in colloids and the structural behavior in conventional atomic systems- gas, liquid, crystal, and glasses- under suitable conditions has already been well recorded [3, 4], electric-field driven phase transitions in colloids have not been treated from this point of view thus far.

The critical point on the spinodal curve of the suspension, namely, c_{cr} and E_{cr}^2, coincides with the inflection point of Π as a function of c, so that Eq. (7) has a multiple root. In a two-phase region (at

$E^2 \geq E_{cr}^2$), the value of the osmotic pressure and of the chemical potential of the particles in the coexisting phases are equal. The latter leads to the following relations [8] between the particle concentrations in the both phases, c_1 and c_2, respectively:

$$\mu(c_1) = \mu(c_2) \quad \text{and} \quad \Pi(c_1) = \Pi(c_2) \tag{8}$$

Now, Eqs. (8) represents the coexistence curve in the phase diagram of a suspension. This curve is located to the left of the spinodal curve in the low-concentration part of the phase diagram and to the right of the spinodal curve in the high-concentration part of this diagram. Moreover, $c_1 \to c_{cr}$ and $c_2 \to c_{cr}$ as $E \to E_{cr}$.

On the other hand, if the third term on the right-side of Eq. (6) is negative, in other words when the long-range interparticle interactions lower the suspension energy (i.e. when $\partial^2 W/\partial c^2 < 0$ over the entire range $0 \leq c < c_m$), an increase in the strength of the applied electric field increases the value of $\partial\Pi/\partial c$. In this case, the random arrangement of the particles appears to be stable, so that the phase diagram of such a suspension reduces to the one-phase domain.

As can be seen from Eqs (4)-(5), the sign of $\partial^2 W/\partial c^2$ depends on the particle-to-fluid ratios of the conductivities and of the dielectric constants, the frequency of the applied electric field, and the particle concentration. For a high-frequency electric field when $\omega t_s \to \infty$, Eq. (5) yields

$$\frac{\partial^2 W}{\partial c^2} = \frac{3\varepsilon_f \beta_\varepsilon^2 E_0^2}{2(1-\beta_\varepsilon c)^3} > 0 \tag{9}$$

Thus, the sign of $\partial^2 W/\partial c^2$ at $\beta_\varepsilon \neq 0$ always becomes positive over $0 \leq c < c_m$ when the frequency of the applied electric field becomes sufficiently high. Hence it follows that there always exists a threshold value of the frequency, above which the particles having a dielectric constant different from that of the suspending fluid (regardless of the mismatch of their conductivities, σ_p/σ_f) will aggregate as the strength of an applied electric field becomes sufficiently large. However, as we shall see, the sign of $\partial^2 W/\partial c^2$ may become negative for low frequencies. If this happens over the entire concentration range, $0 \leq c < c_m$, the electric-field-induced aggregation of the particles will not occur at all. A peculiarity of concentrated suspensions is that the sign of the electric energy density of the interparticle interactions, i.e. $\partial^2 W/\partial c^2$, may change at some value of the concentration. As a result of this feature, which is absent in the theory for a dilute case [1], the ability or inabilty of the particles to aggregate in the presence of applied electric fields depends on the particle concentration as well.

As in the case of conventional atomic systems [8], the use of a spinodal curve provides a convenient way to distinguish "metastable" and "unstable" states of a suspension subject to an electric field, where we refer to the domain between the coexistence curve and the spinodal curve in its phase diagram as metastable, and the domain beyond the spinodal line as unstable. The free energy of a suspension, being considered as a function of the particle concentration, is convex in the metastable region of the phase diagram "the particle concentration-the electric field strength", so that the free energy will increase with a spontaneous concentration fluctuation, giving rise to an energetic barrier that will stabilize the suspension. The free energy, however, turns into a concave function of the particle concentration in the unstable region of the phase diagram, so that no energetic barrier to phase separation will exist in this state. This distinction can correspond to two different mechanisms of electric-field-induced transformations in a suspension: spinodal decomposition and nucleation, as occurs in atomic systems. For atomic systems, the former (in the unstable domain) corresponds to the growth of long-wavelength spontaneous concentration fluctuations with time whereas the nucleation of microdomains of the other phase starts the transformation for the latter (in the metastable domain). However, as recent research demonstrates (see review in Ref. [9]), there is no sharp dividing line between nucleation and spinodal transformations in atomic systems. Rather there exists a gradual transition in the dynamic behavior of a quenched system as the quench point on its phase diagram varies from one domain to the other in the vicinity of the spinodal curve.

In any event, we can expect that there exists some similarity between how spinodal and nucleation transformations operate in a suspension subject to an electric field and how they operate in quenched atomic systems, even though the electric-field-induced interparticle interactions are anisotropic. In this connection, we proceed in Sec. 3 to construct, based on Eqs. (7) and (8), a classification scheme which shall predict how the topology of the suspension phase diagram "the particle concentration-the electric field strength" depends on the particle and fluid dielectric constants and conductivities and the frequency of applied field. This will make it possible to exploit the great body of experimental data and theoretical

predictions available for the quenching of atomic systems and use it as a framework for interpreting the morphology and kinetics of aggregation patterns in colloidal suspensions generated by the application of electric fields.

3. CLASSIFICATION SCHEME OF DC- AND AC-FIELD PHASE DIAGRAMS

A thorough analysis of Eqs. (7) and (8) which yields a complete set of phase diagrams of suspensions subject to electric fields as a function of the mismatch of the dielectric constants and of conductivities of the particles to those of the fluid will be published elsewhere. Due to the limitations on the length of the paper, we consider only the main features of these diagrams shown in Fig. 1 where $\lambda = \varepsilon_f E^2 v_p / k_B T$ is the electric-to-thermal energy ratio, 1 and 2 are the spinodal and coexistence curves, and M and U denote the metastable and unstable domains.

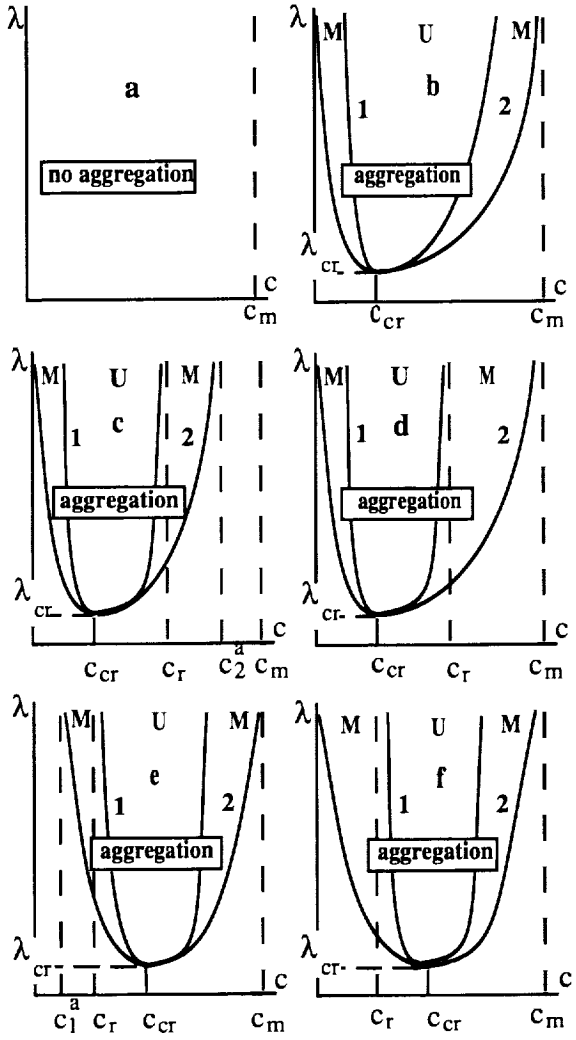

Figure 1.

The simplest phase diagram shown in Figs. 1a corresponds to the case when $\partial^2 W/\partial c^2$ is negative over the entire concentration range, $0 \le c < c_m$, so that no aggregation at all is predicted to occur in the presence of an electric field. In contrast, the phase diagram sketched in Figs. 1b shows the predicted behavior when $\partial^2 W/\partial c^2$ is positive over $0 \le c < c_m$ so that, regardless of the particle concentration, the suspension will start aggregating as long as the applied dc field becomes sufficiently large.

The diagrams depicted in Figs. 1c and 1d are encountered when $\partial^2 W/\partial c^2$ changes its sign with increasing concentration from positive at $c = 0$ to negative at $c = c_m$, so that it equals zero at some concentration c_r. The phase diagrams given in Figs. 1e and 1f represent the case when $\partial^2 W/\partial c^2$ changes its sign with decreasing concentration from positive at $c = c_m$ to negative at $c = 0$, so that it equals zero at some concentration c_r. The separation between the spinodal and coexistence curves along the vertical lines of constant concentrations on the phase diagram in Fig. 1 increases indefinitely with increasing strength of the electric field.

As seen from Fig. 1, a metastable domain in the high-concentration parts of the phase diagrams in Fig. 1c (at $c_r < c < c_2^a$) and Fig. 1d (at $c_r < c < c_m$) as well as in the low-concentration parts of the phase diagrams in Fig. 1e (at $c_1^a < c < c_r$) and in Fig. 1f (for $0 < c < c_r$) is retained regardless of the strength of the applied dc field. Hence, only the nucleation mechanisms of electric-field-induced transformations will operate in such suspensions under these conditions. However, for the phase diagram in Fig. 1b, an increase in the electric field strength along the vertical line of constant concentration will inevitably lead to the transition from a metastable to an unstable domain at any concentration. Thus for such suspensions, the nucleation mechanism will operate in weak fields (below the spinodal curve) whereas the spinodal decomposition will inevitably operate in strong fields (above the spinodal curve). This qualitative distinction between the transformation mechanisms should manifest itself by the dependence of the morphology of the aggregation patterns to be formed on the strength of the applied field.

The map plotted in Fig. 2 demonstrates how the topology of the phase diagram of a suspension subject to dc fields relates to the mismatch of the dielectric constants and the conductivities of the particles and

those of the suspending fluid. The domains in Fig. 2 are lettered to correspond to the phase diagrams in Fig. 1 whereas the numbers 1, 2, 3, and 4 denote the curves

$$\partial^2 W/\partial c^2\big|_{c=c_m} = 0, \quad \partial^2 W/\partial c^2\big|_{c=0} = 0,$$

$$\int_0^{c_m} c\left(\partial^2 W/\partial c^2\right) dc = 0, \text{ and}$$

$$\int_0^{c_m} (c_m - c)\left(\partial^2 W/\partial c^2\right) dc = 0, \text{ respectively.}$$

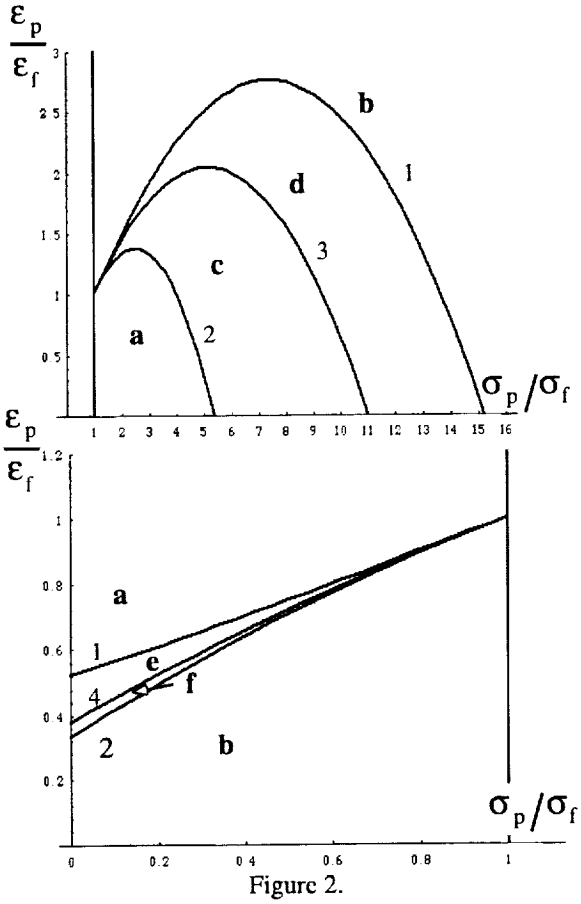

Figure 2.

An increase in the frequency of an ac electric field affects the shape and the size of sub-domains in Fig. 2. For example, as ωt_s increases, the domain "a" located in the region $\sigma_p < \sigma_f$ shrinks to the line $\varepsilon_p = \varepsilon_f$, so that it disappears gradually as $\omega t_s \to \infty$. On the other hand, the domain "a" located in the region $\sigma_p > \sigma_f$ is retained while its boundaries move indefinitely to the right as $\omega t_s \to \infty$ and, moreover, the separation between them along the lines $\varepsilon_p/\varepsilon_f = \text{const}$ increases. In particular, this demonstrates why $\partial^2 W/\partial c^2$ should always become positive at any fixed values of the σ_p/σ_f and $\varepsilon_p/\varepsilon_f$ ratios as the field frequency is made sufficiently high.

It should be pointed out that the particle content, c_2, of the high-concentration phase of a suspension in the phase diagrams in Fig. 1 increases dramatically with the strength of the applied field. Thus, it is quite realistic to suppose that a high-concentration phase in the diagrams in Fig. 1 should undergo subsequent disorder-to-order transitions in the presence of sufficiently strong electric fields as occurs in the absence of an electric field [3, 4]. In this connection, we also mention recent studies of non-conducting suspensions subject to strong electric fields [10] which demonstrate that a high-concentrated phase in such colloids eventually form a crystalline body-centered tetragonal solid. Unfortunately, a description of these transformations cannot be included in the diagrams in Fig. 1 because of the absence of an equation for the free energy of conducting anisotropic aggregates, which is required for this analysis.

4. ACKNOWLEDGEMENT

This work was supported in part by grants from NASA (NCC3-607) and the NSF (CTS-9318820).

5. REFERENCES

1. B. Khusid and A. Acrivos, Phys. Rev. E, **52**, 1669 (1995)
2. B. Khusid and A. Acrivos, Phys. Rev. E, **54**, 5428 (1996)
3. A. K. Sood, in *Solid State Physics*, v.45, edited by H. Ehrenreich and D. Turnbull, pp. 2-73 (Academic Press, San Diego, CA, 1991)
4. W.B. Russel, D.A. Saville, and W.R. Schowalter, *Colloidal Dispersions*, (Cambridge University Press, Cambridge, 1989)
5. L.D. Landau, L.P. Lifshitz, and L.P. Pitaevskii, *Electrodynamics of Continuous Media*, (Pergamon Press Oxford, 1984)
6. L. Brillouin, *Wave Propagation and Group Velocity*, (Academic Press, New York 1960)
7. T.B. Jones, *Electromechanics of Particles* (Cambridge University Press, Cambridge, 1995)
8. L.D. Landau and L.P. Lifshitz, *Statistical Physics, Pt. 1* (Pergamon Press Oxford, 1980)
9. K.F. Kelton, in *Solid State Physics*, v.45, edited by H. Ehrenreich and D. Turnbull, pp. 75-177 (Academic Press, San Diego, CA, 1991)
10. J.E. Martin, J. Odinek, T.C. Halsey, and R. Kamien, Phys. Rev. E, **57**, 756 (1998)

Ultrasound Thermal Field Imaging of Opaque Fluids [1]

C. David Andereck
Department of Physics
The Ohio State University
174 W. 18th Ave.
Columbus, Ohio 43210
E-mail: andereck@mps.ohio-state.edu

[1] Work supported by NASA Grant NAG3-2138.

Introduction

- Buoyancy driven flows of transparent fluids in systems with rigid boundaries at the top and bottom (Rayleigh-Bénard convection) have been extensively studied, both for their potential applications and as examples of pattern formation in non-equilibrium systems (Cross and Hohenberg (1993), Ahlers (1991), and Koschmieder (1993)).
- It is much more difficult to study the flows of opaque fluids such as liquid metals and certain semiconductors and polymer melts, owing to the lack of optical access to the interior of the fluid. The thermal properties of liquid metals are quite different from typically used transparent fluids, which means that an attempt to model with a transparent fluid the detailed flow properties of a liquid metal under thermal stress is doomed to failure (see Carpenter and Homsy (1989), who discuss the effect of the Prandtl number on surface tension gradients).
- Likewise, polymer melts and solutions, being viscoelastic materials, are also impossible to model with typical transparent Newtonian fluids. Nevertheless there are numerous situations in which it is important to understand the behavior of the flow of these fluids and therefore new diagnostic methods are needed.
- In this presentation we will briefly discuss optical techniques for transparent fluids, review the basic approaches that have been tried in opaque fluids, and then will discuss the use of ultrasound as a tool for measuring the thermal field, and *hence the flow pattern*, in opaque fluid flows. Such a tool will find its ultimate payoff in materials processing applications in microgravity where thermal gradients may be large although velocities may be very low.

Diagnostic Tools for Studying Flows of Transparent Fluids

- **Particle Seeding:**
  - **Isotropic particles:** By tracking small isotropic particles the 2D or 3D flow field can be mapped. This is the basis for particle image velocimetry (PIV) and particle tracking velocimetry (Guezennec, et al. (1994)). The necessary ingredient is a particle that is small compared with expected flow features and that is nearly neutrally buoyant. There is typically a large investment in software to analyze the data, but the outcome is a flow field map with only a minimum invasion of the fluid.
  - **Non-isotropic particles:** The particles used can be anything from aluminum powder to Kalliroscope (Matisse and Gorman (1984)), the latter being polymeric flakes that are

somewhat more dense than water, and of the order of a few microns in size. These particles attempt to align with the flow (Savas (1985)). Their reflectance depends on their orientation to the viewing direction, so the flow field is revealed by the presence of higher and lower levels of reflected light in different regions of the flow. They have proved useful for extracting qualitative, and some quantitative, information about flow patterns (Gorman and Swinney (1982), Shaw, et al. (1982), Hegseth, et al. (1996)).

- **Other Velocimetry Approaches:**

  - **Laser Doppler velocimetry (LDV)** (Somerscales (1981), Jacobs, et al. (1988)): The essence of the technique is that laser light is focused into a small volume of the fluid. As seed particles pass through this volume they scatter Doppler shifted light. This light is detected, and the resulting signal yields the velocity of the particle. Using the multiple wavelengths from an Ar laser it is possible to measure more than one velocity component at once. This system is capable of very high precision measurements of velocity, but requires scanning of the scattering volume to map the velocity field.

  - **Hot-wire probes** (Blackwelder (1981)): These probes rely on the flowing fluid to carry away thermal energy from a small wire of circular or planar cross section. Seeding of the flow is not needed and the technique works with opaque fluids, but the probes are quite invasive. Furthermore it is difficult to scan the flow field.

- **Thermal field imaging:**

  There are several non-invasive methods of visualizing the thermal field in a transparent fluid that take advantage of the variation of the optical index of refraction of the fluid with temperature. In each case the result is a map related to the average of the temperature field along the line of observation. This is particularly effective if the flow field is essentially 2D, however, the averaging may be useful in other, 3D, flows as well.

  - **Optical interferometry** (Goldstein (1983): This is an extremely sensitive technique. In a typical situation, a test chamber is placed in one of the two arms of a Mach-Zehnder interferometer. If the fluid temperature is uniform there will be a uniform phase shift of the light across the wavefront as it passes through the fluid. In the presence of temperature (index of refraction) variations there will be differing phase shifts across the chamber. When the light recombines with the light from the other arm unequal phase shifts result in a distortion of the fringe pattern (Prakash and Koster (1996)).

  - **Schlieren and shadowgraph** (Goldstein (1983)): These techniques rely on refraction of the light passing through the cell. Variation of the temperature in a plane perpendicular to the direction of light propagation results in regions in which the light emerging from the cell is either diverging or converging. This effect can be used to produce an image of the flow that reveals the pattern of rolls or cells in the flow. Contrast in a Schlieren (shadowgraph) image is proportional to the integral along the optical path through the test cell of the *first derivative (second derivative)* of the index of refraction in the direction perpendicular to the direction of propagation. Attempts to extract quantitative

information about the temperature field and nonlinear modes have been made (Dong and Ebadian (1992), Schöpf, Patterson and Brooker (1996), Kolodner and Williams (1990), Winkler and Kolodner (1992)). This approach has been used for many experiments in pattern formation in both liquids and gasses (Wu, et al. (1995)).

Diagnostic Tools for Studying Flows of Opaque Fluids

- **Velocimeters:**

  - **Invasive probes**: Hot-wire probes may be used, as already described above. A second approach is to use an incorporated magnet probe, which works only in conducting fluids such as liquid metals (Hung and Andereck (1988)). In this system a small high-field magnet is placed at the surface of the fluid or just inside. On either side of the magnet are placed small electrodes. As the fluid flows through the magnetic field the conduction electrons move perpendicular to the flow in response to the Lorentz force, giving rise to a potential difference between the electrodes. The potential difference depends on the field strength and fluid properties, but the probe can be quite sensitive; we have used such a probe to measure velocities as small as 0.1 cm/s. This type of probe, though very sensitive, suffers from being invasive and difficult to scan.

  - **Ultrasound Doppler velocimetry:** This technique has been used in both transparent and opaque fluids (Takeda (1986) and (1991)). The fluid is seeded with small particles that serve as scattering sites for ultrasound pulses introduced from a transducer in contact with the fluid. As the pulse propagates sound is scattered from the seed particles, and is Doppler shifted. When the scattered sound is received two measurements are made: The first is the time the signal was received, and the second is the shift of the ultrasound signal frequency. From the former the electronics extracts the distance of the scatterer from the transducer/detector. From the latter the velocity of the scatterer, and hence of the fluid, is determined. The result is a map of one component of the velocity field along the line of sight. This is an improvement over LDV, which provides only a velocity at one point at a time, and it is also usable in opaque fluids such as mercury (Takeda (1987)). Of course, a difficulty is finding appropriate seed particles, an important consideration for liquid metals. A second drawback is that the velocity resolution is not as high as for LDV, the lowest detectable velocity being a few cm/s. This places severe limits on its usefulness in weak flows such as might be found near convective onset.

- **Temperature probes:**

  - **Thermistors and thermocouples**: These probes offer very high precision at a point, but suffer from invasive characteristics. It is possible to embed several probes in the test cell walls to obtain a crude map of the field at the boundary, or to detect fluctuations in temperature (Busse and Sommermann (1996)). It is more problematic to measure temperatures in the interior of the fluid. The thermistor also introduces a small amount of heating. One is faced with either constructing a grid of a very large number of these probes to obtain enough spatial resolution (Pfeffer, Buzyna and Kung (1980)), or providing a traversing system for the probe so that different points may be reached (Hung

and Andereck (1988)). Neither approach is particularly satisfactory.

- **X-ray imaging**: It is possible to use x-rays in a manner similar to the use of visible light in the optical techniques described previously. Signal attenuation variations due to sample density discontinuities is the basis for medical imaging and non-destructive testing of solids. This approach is now being used for imaging density variations in solidification (Campbell and Koster (1994), Pool and Koster (1994), Campbell and Koster (1995a) and (1995b), Derebail and Koster (1997), and Koster, Derebail and Groetzbach (1997)) This has proven quite successful in a limited range of operating conditions. The drawbacks are not trivial. Obviously there is a safety aspect to it. This is not an insurmountable problem, although it is an inconvenience. To achieve energetic x-rays requires considerable power input, possibly a problem in space-based experiments. More importantly there are limitations on the depth of the fluid that may be probed, at least for liquid metals: The penetration depth for x-rays is a fraction of a cm for energies up to 1 Mev for mercury. As a result, the experiments referenced above were for test cells of only 2 mm thickness. At higher energies one might also expect considerable sample heating to occur as well. Although in principle x-rays might be useful diagnostics for certain situations involving opaque fluids, in practice there are severe limitations.

Proposed Investigations

- **Introduction:** The imaging of velocity and thermal fields in opaque fluids is in a very unsatisfactory state. Current techniques require invasive probes or seed particles or only yield the temperature or velocity at a point in the flow. There are no elegant approaches for liquid metals in particular, even though a knowledge of the velocity and temperature fields in such fluids is of great importance for materials processing. *We propose the use of ultrasound imaging of the thermal field as a partial solution to this problem.* Why use ultrasound? It is non-invasive and no seeding is required. Just as the index of refraction for light varies with the temperature of the material, so sound speed varies with the temperature of the medium through which the sound propagates. So ultrasound may be used in a way analogous to the non-invasive optical techniques, even with fluids that are opaque to visible light. Spatial resolution of a few millimeters or less is achievable with moderate frequencies (the wavelength is 0.015 cm at 10 MHz). Temperature resolution of a fraction of a degree is possible. Sensor arrays allow for rapid scanning of entire cross-sections of a test cell with no moving parts, a dramatic improvement over single point temperature measurements. Ultrasound thermal field imaging offers a very significant improvement potential over current techniques, while not being technologically beyond the state-of-the-art (see Shung and Zipparo (1996).

- **Proof of concept**: To begin we propose an ultrasound analog of optical interferometry, but *since we know precisely the phase of the emitted pulse there is no need for a reference beam.* Suppose there is a variation in the temperature of the fluid across the test cell. If a pulse of ultrasound traverses the fluid along a line at temperature T_1 it will take a time determined by both the distance across the chamber and the speed of sound at that temperature. If in some other region of the system the temperature is $T_2 \neq T_1$, then the traversal time will be different owing to the sound velocity difference. By moving the transducers along the chamber we will map out the sound speed as a function of

position, and thereby indirectly measure the fluid temperature field. We will begin with a simple rectangular cell with transparent sidewalls, probably containing water as the convecting fluid, and with an externally imposed vertical temperature gradient. This allows both optical shadowgraph and ultrasound imaging for confirmation that the ultrasound imaging is faithful to the pattern. Molten gallium would be a particularly interesting first opaque fluid to study in view of its relation to semiconductor processing. Braunsfurth and Mullin (1996) studied molten gallium in a long, square cross section chamber, with an imposed horizontal temperature difference along the channel, a model version of the Bridgman system. Their probe was a set of two thermocouples just slightly below the surface. They found numerous interesting oscillatory states, but the only characterization was in terms of time dependence at one or two points. Lacking was an indication of the spatial nature of the flow. Both spatial and temporal information is needed to model these flows, a possibility with the proposed system.

- **Further instrumentation development**: A more sophisticated approach would involve an array of transmitters and detectors, eliminating the traversing of the probe, but the principle is the same. Also, with a large rectangular transmitter and an array of receivers an analog to the shadowgraph technique could be constructed. The temperature variations across the fluid would lead to focusing and defocusing of the sound pulses, and simple intensity measurements would yield a picture of the flow pattern.

- **Future Directions:** The future possibilities for this diagnostic tool are varied. One important direction would be to study the thermal field of a liquid metal in contact with another liquid, so that thermocapillary effects at the interface would be important (Géoris, et al.(1993), Géoris, P. and Legros, J. C. (1993) and (1996), Prakash and Koster (1993), (1994a) and (1994b)). It will be possible to investigate solidification of pure metals and binary alloys. One can imagine extending the technique to tomography by using phased arrays of transducers. Imaging the thermal field of polymer melts would be of interest to the materials processing community. Another exciting possibility is the study of magnetohydrodynamic (MHD) systems. The influence of magnetic fields on convective liquid metals is of interest in solidification, and the general MHD problem shows up in a variety of contexts (Takeshita et al. (1996), Segawa et al. (1996)). The ability to observe the patterns deep in the interior of such flows would be very valuable.

Bibliography

Ahlers, G., *Physica D* **51**, 421 (1991).

Blackwelder, R. F., in *Methods of Experimental Physics: Volume 18, Fluid Dynamics, Part A*, R. J. Emrich, ed. (Academic, New York, 1981), p.259.

Braunsfurth, M. G. and Mullin, T., *J. Fluid Mech.* **327, 199** (1996).

Busse, F. H., and Sommermann, G., in *Advances in Multi-Fluid Flows*, eds. Y.Y. Renardy, A.V. Coward, D.T. Papageorgiou, S.-M. Sun (SIAM, Philadelphia, 1996), p. 33

Campbell, T. A., and Koster, J. N., *J. Crystal Growth* **140**, 414 (1994).

Campbell, T. A., and Koster, J. N., *J. Crystal Growth* **147**, 408 (1995a).

Campbell, T. A., and Koster, J. N., *Meas. Sci. Tech.* **6**, 472 (1995).

Carpenter, B. M., and Homsy, G. M., *J. Fluid Mech.* **207**, 121 (1989).

Cross, M. C., and Hohenberg, P. C., *Rev. Mod. Phys.* **65**, 851 (1993).

Derebail, R., and Koster, J. N., *Int. J. Heat Mass Transfer* **40**, 1169 (1997).
Dong, Z. F., and Ebadian, M. A., *Int. J. Heat Mass Transfer* **35**, 1833 (1992).
Géoris, P., Hennenberg, M., Simanovskii, I. B., Nepomniaschy, A. , Wertgeim, I. I., Legros, J. C., *Phys Fluids A* **5**, 1575 (1993).
Géoris, P. and Legros, J. C., in Proceedings of the 44th Congress of the International Astronautical Federation, Oct 16-22, 1993, Graz, Austria.
Géoris, P. and Legros, J. C., in *Materials and Fluids Under Low Gravity*, L. Ratke, H. Walter, B. Feuerbacher, Eds. (Springer, Berlin, 1996), p. 299.
Goldstein, R. J. *Fluid Mechanics Measurements* (Hemisphere, Springer, Washington, 1983).
Gorman, M. A., and Swinney, H. L., *J. Fluid Mech.* **117**, 123 (1982).
Guezennec, Y. G., Brodkey, R. S., Trigui, N., and Kent, J. C., *Exp. Fluids* **17**, 209 (1994).
Hegseth, J. J., Baxter, G. W., and Andereck, C. D., *Phys. Rev. E* **53**, 507 (1996).
Hung, M-C., and Andereck, C. D., *Phys. Lett. A* **132**, 253 (1988).
Jacobs, D. A., Jacobs, C. W., and Andereck, C. D., *Phys. Fluids* **31**, 3457 (1988).
Kolodner, P., and Williams, H., in *Proceedings of the NATO Advanced Research Workshop on Nonlinear Evolution of Spatio-Temporal Structures in Dissipative Continuous Systems*, F. H. Busse and L. Kramer, eds. (Plenum, New York, 1990), p. 73.
Koschmieder, E. L. *Bénard Cells and Taylor Vortices* (Cambridge, New York, 1993).
Koster, J. N., Derebail, R., and Groetzbach, A., *Appl. Phys. A* **64**, 45 (1997).
Matisse, P. and Gorman, M., *Phys. Fluids*, **27**, 759 (1984).
Pfeffer, R. L., Buzyna, G., and Kung, R., *J. Atmos. Sci.* **37**, 2129 (1980).
Pool, R. E., and Koster, J. N., *Int. J. Heat Mass Transfer* **37**, 2583 (1994).
Prakash, A., and Koster, J. N., *Int. J. Multiphase Flow* **20**, 383 (1994a).
Prakash, A., and Koster, J. N., *Int. J. Multiphase Flow* **20**, 397 (1994b).
Prakash, A., and Koster, J. N., *Eur. J. Mech. B/Fluids* **12**, 635 1993).
Prakash, A., and Koster, J. N., *Trans. ASME* **118**, 366 (1996).
Savas, O., *J. Fluid Mech.* **152**, 235 (1985).
Schöpf, W., Patterson, J. C., and Brooker, A. M. H., *Exp. Fluids* **21**, 331 (1996).
Segawa, T., Sano, M., Naest, A., and Glazier, J. A., preprint (1996).
Shaw, R. S., Andereck, C. D., Reith, L. A., and Swinney, H. L., *Phys. Rev. Lett.* **48**, 1172 (1982).
Shung, K. K., and Zipparo, M., *IEEE Eng. in Medicine and Biol.* **15**, 20 (1996).
Somerscales, E. F. C., in *Methods of Experimental Physics: Volume 18, Fluid Dynamics, Part A*, R. J. Emrich, ed. (Academic, New York, 1981), p. 93.
Takeda, Y., *Int. J. Heat Fluid Flow* **7**, 313 (1986).
Takeda, Y., *Nucl. Tech.* **79**, (1987).
Takeda, Y., *Nucl. Eng. and Design* **126**, 277 (1991).
Takeshita, T., Segawa, T., Glazier, J. A., and Sano, M., *Phys. Rev. Lett.* **76**, 1465 (1996).
Winkler, B. L., and Kolodner, P., *J. Fluid Mech.* **240**, 31 (1992).
Wu, M., Ahlers, G., and Cannell, D. C., *Phys. Rev. Lett.* **75**, 1743(1995).

A NOVEL ACOUSTO-ELECTRIC LEVITATOR FOR STUDIES OF DROP AND PARTICLE CLUSTERS AND ARRAYS

Robert E. Apfel, Yibing Zheng, and Yuren Tian, Department of Mechanical Engineering, Yale University, New Haven, CT 0511, robert.apfel@yale.edu

ABSTRACT

A novel and compact instrumentation for studying the behavior of drop sprays and of clusters of drops now permits fundamental research into the behavior of reacting and non-reacting fluid and solid species. The new capability is made possible by simultaneous acousto-electric levitation and charging of "seed" droplets (10-30 μm in diameter) which come together in 2-D clusters (with up to 300 droplets). These clusters are interesting in their own right because of their crystalline and quasi-crystalline forms, which depend on the acoustic and electric field parameters. By varying the electric and acoustic field intensities, one can cause a cluster of droplets to condense into larger drops (e.g. 50-300 μm) which, because of their charge, form uniformly spaced 2-D arrays of monodispersed drops (e.g. 30-40 array drops in preliminary experiments). One or more layers of these 2-D arrays can form in the acoustic standing wave. Such a configuration permits a wide range of fundamental studies of drop evaporation, combustion, and nucleation. The drops can be single or multicomponent. Therefore, fundamental materials studies can also be performed. Using this same Cluster and Array Generation (CAG) instrumentation, it has been also possible in preliminary experiments to demonstrate the clustering and arraying of solid particles, both coated with an electrically conducting layer and uncoated, and both charged and uncharged.

INTRODUCTION

The generation, control, and applications of sprays and aerosols cover a vast subject of relevance to the energy, environmental, and materials sciences. Fuels, soot and other environmental by-products, coatings, and intermediaries in particle synthesis all begin as sprays and aerosols. Understanding the behavior of multi-drop and particle systems and controlling the processes that created them require a good correspondence between theoretical modeling and benchmark experiments. The results of this characterization will provide benchmark data for comparison with theoretical analyses and numerical modeling, with the goal of developing an ability to predict changes in the process as we vary acoustical, electrical, and material parameters.

The literature on clusters and arrays of particles or drops (sprays) is very considerable and therefore is only selectively reviewed. Single drop evaporation and/or combustion has been studied with a wide variety of techniques, a few of which are reviewed here. Models of evaporation have been validated, for example, by levitating a drop either electrodynamically[1] or acoustically.[2] These techniques are also appropriate for multicomponent drops.[3] High temperature liquid structure has been investigated using aeroacoustic levitation techniques which permit the handling of heavy particles or drops.[4] Yet for many processes involving dense sprays, evaporation, ignition, and combustion processes are controlled by the interaction of droplets[5]; therefore, single drop evaporation models are entirely inadequate.

The study of the combustion of drops and sprays has advanced both experimentally and theoretically, as reviewed recently in the volume edited by Chiu and Chigier.[6] Some of the important advances illustrate how the evaporation, ignition and combustion of sprays are controlled by different parameters for dense vs. dilute clusters because of droplet interactions. Bellan, for example, has shown theoretically that for multicomponent drops, when the volatility of the solute is much greater than the solvent, liquid mass diffusion is important for dilute sprays, but not for dense sprays.[7]

"The allure of small controlled groups of droplets," according to Dunn-Rankin et al. "is that they provide an opportunity to isolate the effects of neighboring droplets on drop aerodynamics, drop vaporization, and drop combustion" which is not possible in spatially and temporally unsteady fields characteristic of a full spray or flame.[8] Their studies with streams has been one way to control the environment so that modeling and experimentation can be compared.

Annamalai has extensively surveyed the literature on the evaporation and combustion of arrays and clouds and has presented the PSI cell model as a way of determining relationships between group and spray combustion results.[9,10] Annamalai concludes that "no detailed theory is available on flame spread involving an array of drops," and that cloud ignition and combustion data in an unconfined environment is lacking.[11] In his review, Chiu reviews the research accomplishments in droplet and spray combustion over a 40 year period. He concludes: "Needless to say, extensive experimental studies must be initiated to validate theoretical and numerical results."[12] In his report, Tambour considers the influence of multisize sprays on flame properties, spanning the range from small drops (20-25 μm), which are comparable to the "seed drops" we discuss below, to large drops (80-100 μm) which are of the same order as the array drops we produced with our apparatus.[13]

Need for a benchmark system

These studies barely begin to scratch the surface of the broad amount of theoretical, experimental, and numerical work being done to understand drop and particle clusters and arrays, and their many applications. Just as the single drop became the central focus of very dilute evaporating or combusting systems, we need equivalent controllable

benchmark multi-drop systems to validate dense spray evaporation and combustion models.

Control of arrays of drops and/or particles has recently improved with further development of the original work on multi-particle levitation using an electrodynamic balance by Wuerker et al.[14] The group of E. J. Davis, for example, used a double-ring electrodynamic balance apparatus to levitate $NaNO_3$ particles with particle size nominally of 3.5 μm. (These were generated by producing solution drops of about 30 μm with a vibrating orifice generator and passing them through a drying tube.) [15] They were able to achieve improved control of particle size and charge, as well as to manipulate the relative spacing of the particles. This novel approach permits a wide variety of experiments where the interaction of the particles or drops is crucial to the observed phenomena.

CURRENT DEVELOPMENTS WITH CAG APPARATUS

Compact apparatus for levitating small drops is shown in Figure 1. It is an acoustic levitation cell driven by a composite transducer consisting of back-to-back piezoelectric discs, an aluminum horn, and a suitable reflector required for establishing an acoustic standing wave at approximately 28.2 kHz. If several drops of liquid are simultaneously levitated in this apparatus, acoustic radiation forces will normally drive them to a position just below a pressure node along the axis of the system. There they will aggregate and coalesce.

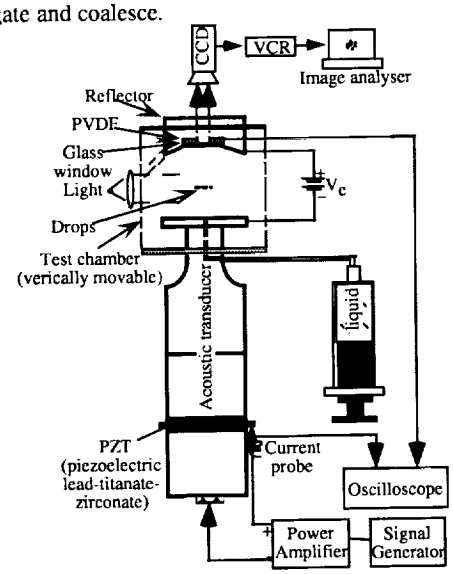

Figure 1: Levitation Apparatus

The top and bottom reflectors in the acoustic standing wave cell are plates of a capacitor that can be held at a potential varying from a few hundred to three thousand volts. The result of this new capability[16] is that a liquid placed on the lower plate can be atomized and charged by the vibrations of the electrodes. As the "seed" droplets are drawn toward the levitation plane, we note that they aggregate into two dimensional clusters (which we define to be groups of drops that are virtually touching). As seed drops are added to the cluster, there comes a point when the drops suddenly coalesce into a single drop (with perhaps a few "petals" of seed drops on the exterior of the drop). This coalesced drop becomes part of a two dimensional array of drops, as the process is repeated with new seed drops and clusters. An array, for the purposes of this discussion, is characterized by drops spaced by more than one drop diameter. We are left with a number of important questions:

- What defines the size of a seed drop?
- What defines the size of the cluster of seed drops?
- What triggers the cluster to coalesce?
- How uniform in size are the array drops arising from cluster coalescence?
- What determines the spacing of the array drops and how uniform is this spacing?
- What determines the degree of stability of the array?
- If cluster size, array drop size, and array drop spacing could be controlled, as well as drop material and host gas, what applications would suggest themselves, both in terms of validating theoretical models and in terms of technological significance?
- Can solid particles be similarly clustered and arrayed, and if so, what are the controlling parameters and potential applications?

Initial observations and interpretation with the new apparatus

The fluid dynamical processes by which seed drops become clusters, and clusters become arrays have transient phases which are difficult to capture in still figures. We have put short video sequences of these processes on the World Wide Web at URL: **www.yale.edu/bubble/array**

Seed droplet formation

It is observed that if a few drops of ethanol are placed on the bottom plate of the 28 KHz resonator, then at a threshold level of vibration atomization, clustering, and arraying processes commence, leading to two or more planes of collected drops near the pressure nodes of the sound field (Fig. 2a, next page). These collected clusters and arrays have originated from a mist of fine droplets rising from the bottom plate of the cell (Fig. 2b). These drops, which we call "seed" drops, are approximately 25-40 μm in diameter and fairly uniform in size. The mechanism of generation is quite clear. The capillary wavelength of the ethanol surface is given by $\lambda_c = (2\pi\gamma/\rho f^2)^{1/3}$; here γ is the surface tension, ρ is ethanol's density, and f is the acoustic frequency. According to Lang et al.[17], the drop diameter from the surface instability ~ 0.67 λ_c. In the present case, the observed size is somewhat smaller than the predictions. The discrepancy may be attributed to the state agitation of the surface or the small electric charge on each seed drop.

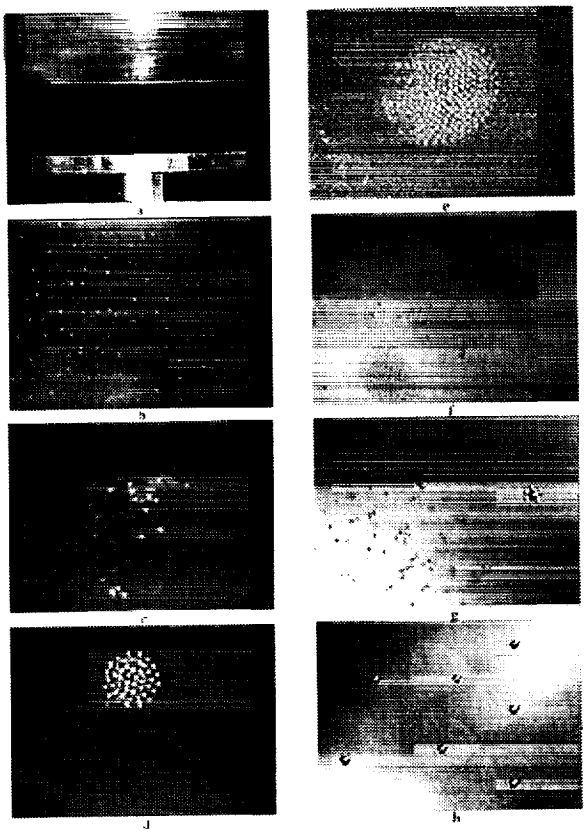

Figure 2: Droplet Cluster and Array Examples.

Cluster formation

Each seed drop is attracted toward the center of the cell by acoustic radiation forces as described in ref. 16. They aggregate together into a two dimensional cluster, as shown in the two-figure sequence 2c and 2d, but because of the small electrical charge on each drop, they do not immediately coalesce. The size of these clusters is determined by the balance of acoustic attraction and electrical repulsion. The acoustic attraction comes from two sources, as described in our lab's earlier work[18]: 1) the primary acoustic radiation force draws all drops to the same position in the sound field, and 2) a secondary, attractive interparticle force draws the drops toward each other. The repulsive force is simply coulombic in nature. The maximum size is determined when a new seed drop feels sufficient repulsion as to be expelled from the periphery of the flat cluster.

By increasing the acoustic field or decreasing the charge on the seeds, the cluster size can grow. Figure 2e shows a remarkable 2-D cluster consisting of 242 seed drops! Note also in Fig. 2f that under the right circumstances these clusters may undergo a fissioning process.

Cluster coalescence

The interparticle forces between drops plus the gentle agitation of the acoustic field increase the probability that two of the seed drops in the cluster will touch and coalesce, as shown in Fig. 2g. In the left part of the figure it is clear that the seed drops are beginning to form dimers and trimers as a precursor to the rapid (10-50 msec) formation of a cluster, which then coalesces to an array drop, as shown on the right side of the figure. The initial coalescence starts a chain reaction, because the secondary interparticle force goes as the diameter of the drop to the sixth power. As soon as two drops coalesce, increasing their effective diameter, the forces of attraction become stronger, and the process promotes more and more coalescence, until almost all of the drops have formed into a single drop, which we call an "array" drop for reasons to be made clear shortly. A "before"and "after" coalescence sequence is shown in Fig. 3; here 85 seed drops of about 45 μm diameter have coalesced into a single drop of approximately 200 μm in approximately 50 ms (which is determined primarily by the strength of the secondary interparticle acoustic forces.

Fig. 2g also shows the array drop with a few "petals," which are seed drops that haven't coalesced, perhaps because the smaller total drop area of the array drop (compared to the sum of the areas of the seed drops) increases the surface charge density, and thus produces greater coulombic repulsion.

Array formation, and array drop charge

As each array drop forms, it is repelled from the center of the levitation cell by the newly generated seed drops which are aggregating and then coalescing. Each array drop remains in the potential well of the acoustic field but finds a new position with a minimum total energy of the system. This is a dynamic equilibrium, with the array of drops moving, and sometimes rotating around the central position. Fig. 2h shows a 2-D array of drops formed in the combined acoustical and electrical fields. The figure also shows a background pattern which look like triangles. This is just another plane of a drop array (out of focus), as the acoustic levitation cell can support two or three layers of drop arrays.

One can control the motion of the drop array by altering the acoustic and electric fields. For example, by lowering the acoustic field and raising the electric field, the primary force for levitation against gravity becomes electrical. In fact, this is precisely how the charge of the array drops can be measured. If the electric field is reduced too much, the drops will fall out. This is just the "Millikan oil drop experiment." In this way, we have observed that the drop charge density is approximately 1/1000 of the critical charge density — $q^* = 8\pi (\varepsilon\gamma a^3)^{1/2}$, which is referred to as the Rayleigh limit.

Figures 4 and 5 show the results of varying acoustic and electric field parameters. We see that as the electric field goes up for a constant acoustic field, the charge per seed drop goes up, and therefore the cluster size at which coalescence occurs decreases. Increased acoustic field strength for a constant electric field tends reduces drop spacing without having a major effect on drop size.

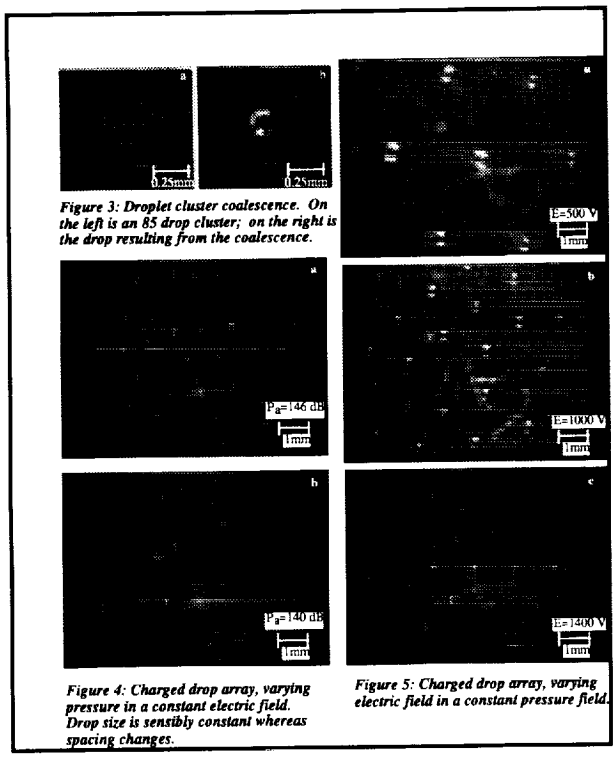

Figure 3: Droplet cluster coalescence. On the left is an 85 drop cluster; on the right is the drop resulting from the coalescence.

Figure 4: Charged drop array, varying pressure in a constant electric field. Drop size is sensibly constant whereas spacing changes.

Figure 5: Charged drop array, varying electric field in a constant pressure field.

From these figures we note a few remarkable features

- The drop spacing appears uniform and controllable with electric and acoustic field adjustments.
- The array drop size seems reasonably uniform. We illustrate this uniformity by simply measuring the size of each drop using a CCD camera, frame capture, and a drop-size analysis system developed for the analysis of our space shuttle data.[19] Figure 6 gives two size distributions for two different sets of conditions, illustrating that at higher electric fields, the drop distribution is narrower and the mean drop size is smaller.

Benchmark capability for drop clusters and array

The initial investigations reported above suggest that this new "Cluster and Array Generation," or CAG apparatus, can provide benchmark conditions for testing a significant set of questions related to evaporation and combustion studies. Moreover, the proper engineering of this capability may provide opportunities for new technologies in energy, pollution, and materials processing studies.

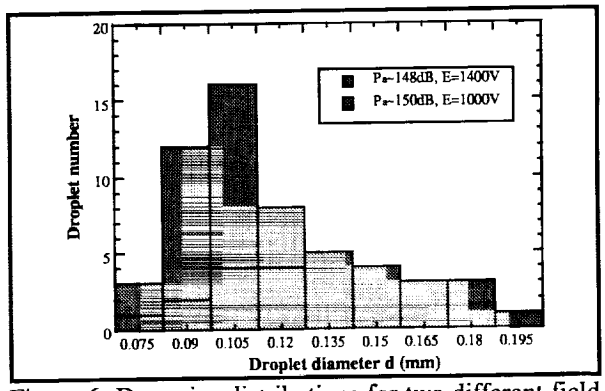

Figure 6: Drop size distributions for two different field conditions

Important unanswered questions

The initial work focused primarily on one liquid, ethanol. Clearly, the liquid properties that will be important for single component liquids include: surface tension and density. For multiple component drops, we can consider a number of cases:

- The second component is a surfactant, which primarily affects the surface tension and the surface viscosity. Additionally, surfactants may provide a barrier to seed drop coalescence.
- The second component may be a dissolved species.
- The second component might be small solid particles.

The physical characteristics that will be important are: seed drop size and drop charge. Size is affected by surface tension, density, and more strongly by acoustic frequency. Charge is affected by the electric field. But after seed drop formation, the electric field and acoustic fields can be altered, taking on important roles in influencing final array drop size and spacing.

ACKNOWLEDGMENTS

This work has been supported by a grant from NASA through a contract with the Jet Propulsion Laboratory, # 958722 and NASA Grant NAG3-2147.

REFERENCES

[1] W. Li and E. James Davis, Aerosol Sci. and Tech. **25**, 11 (1996).
[2] Y. Tian and R. Apfel, J. Aerosol Sci. (1996).
[3] See, for example, C. L Aardahl, W.R. Foss, and E.J. Davis, Ind. Eng. Chem. Res.**35**, 2834 (1996).
[4] See, for example, S. Ansell, S. Krishnan, J.K. Richard Weber, J. J. Felten, P.C. Nordine, M. A. Beno, D.L. Price, and M.-L. Saboungi, Phys. Rev. Lett., in press.
[5] G. Chen and A. Gomez, Combustion and Flame, **110**, 392 (1997).

[6] Mechanics and Combustion of Droplets and Sprays, Eds. H.H. Chiu and N. Chigier, Begell House, New York, 1995.
[7] J. Bellan, "Dyanamics and Thermodynamics of Dense and Dilute Clusters of Drops," Ref. 5, p.60
[8] D. Dunn-Rankin, W. A. Sirignano, R. H. Rangel, and M.E. Orme, "Drop Arrays and Streams," Ref. 5, p.76.
[9] K. Annamalai and W. Ryan, Prog. Energy Combust. Sci., **18**, 221 (1992).
[10] K. Annamalai, "Interactive processes in evaporation and combustion of liquid drop arrays and clouds,"Ref. 5, 116 ff.
[11] ibid, p. 154.
[12] H.H. Chiu, "Modern developments in mechanics and combustion of many droplet systems," Ref. 5, p. 183.
[13] Y. Tambour, "Structure of multisize sprays and its effect on spray flame properties," Ref. 5, pp. 210 ff.
[14] R.F. Wuerker, H. Shelton, and R.V. Langmuir, J. Appl. Phys. **30,** 342 (1959).
[15] e.g., R. Vehring, C.L. Aardahl, E.J. Davis, G. Schweiger, and D.S. Covert, Rev. Sci. Instrum. **68**, 70(1997).
[16] Y. Tian and R.E. Apfel, J. Aerosol Sci. **27**, 721 (1996).
[17] J. Lang, J. Acoust. Soc. Am. **34**, 6 (1962).
[18] M.A. H. Weiser, R.E. Apfel and E.A. Neppiras, Acustica, **56**, 114 (1984).
[19] R. G. Holt, Y. Tian, J. Jankovsky, and R. E. Apfel, "Surface-controlled drop oscillations in space," J. Acoust. Soc. Am., in press.

Fluid Physics of Foam Evolution and Flow: Objectives

H. Aref, S. Thoroddsen, J. Sullivan: Univ. of Illinois

- Use 2D foam code, which incorporates known geometry of dry foam (fluid surfaces are circular arcs) and known dynamics (von Neumann's law), to compare to 2D simulations using Surface Evolver.

- Extend 2D code to foam flow situations with simple boundaries, such as foam evolution in contracting or expanding nozzles, foam flow around a moving object, and so on.

- Extend 2D foam flow code to allow ideal gas within the bubbles in which case novel bubble differentiation phenomena take place.

- Extend 2D flow code to the case of small but finite liquid content in the films.

- Construct a new 3D foam flow and evolution code package, based on the Surface Evolver package of Brakke. Use this code to explore a range of phenomena, including those already explored in the 2D case, and all those listed above as extensions.

- Perform a series of physical experiments closely related to the numerical simulations, and develop the experimental methodology for automatic monitoring of dynamic change in an evolving foam.

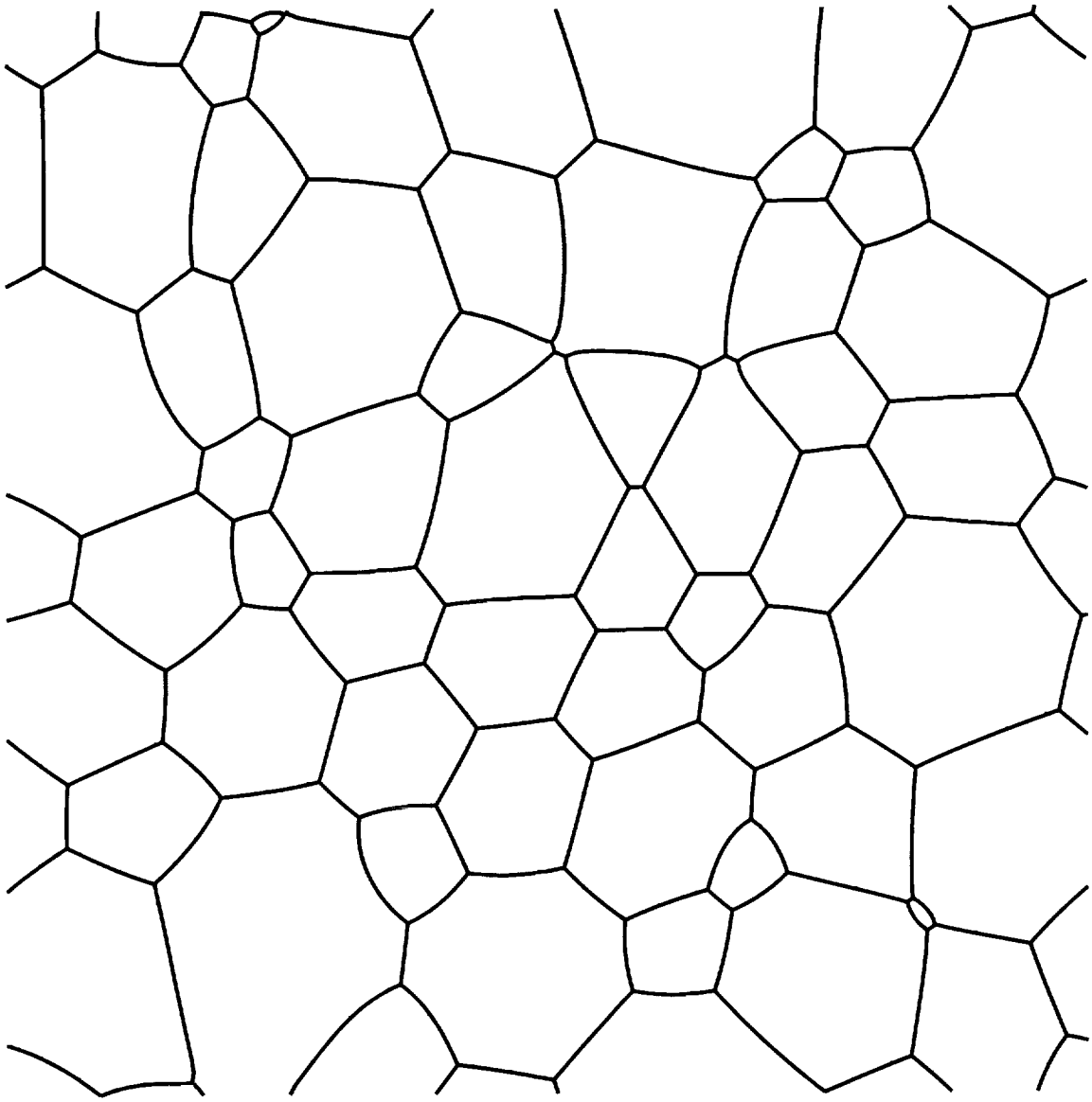

2D foam configuration (periodic boundary conditions; incompressible fluid) computed with the Surface Evolver. In the 2D foam code of Herdtle/Aref (1992) one makes use of the known geometry that each interface is a circular arc. In the Surface Evolver each interface is discretized by a number of points; this figures shows an example where diffusion between bubbles is fast enough that not all arcs are exactly circular.

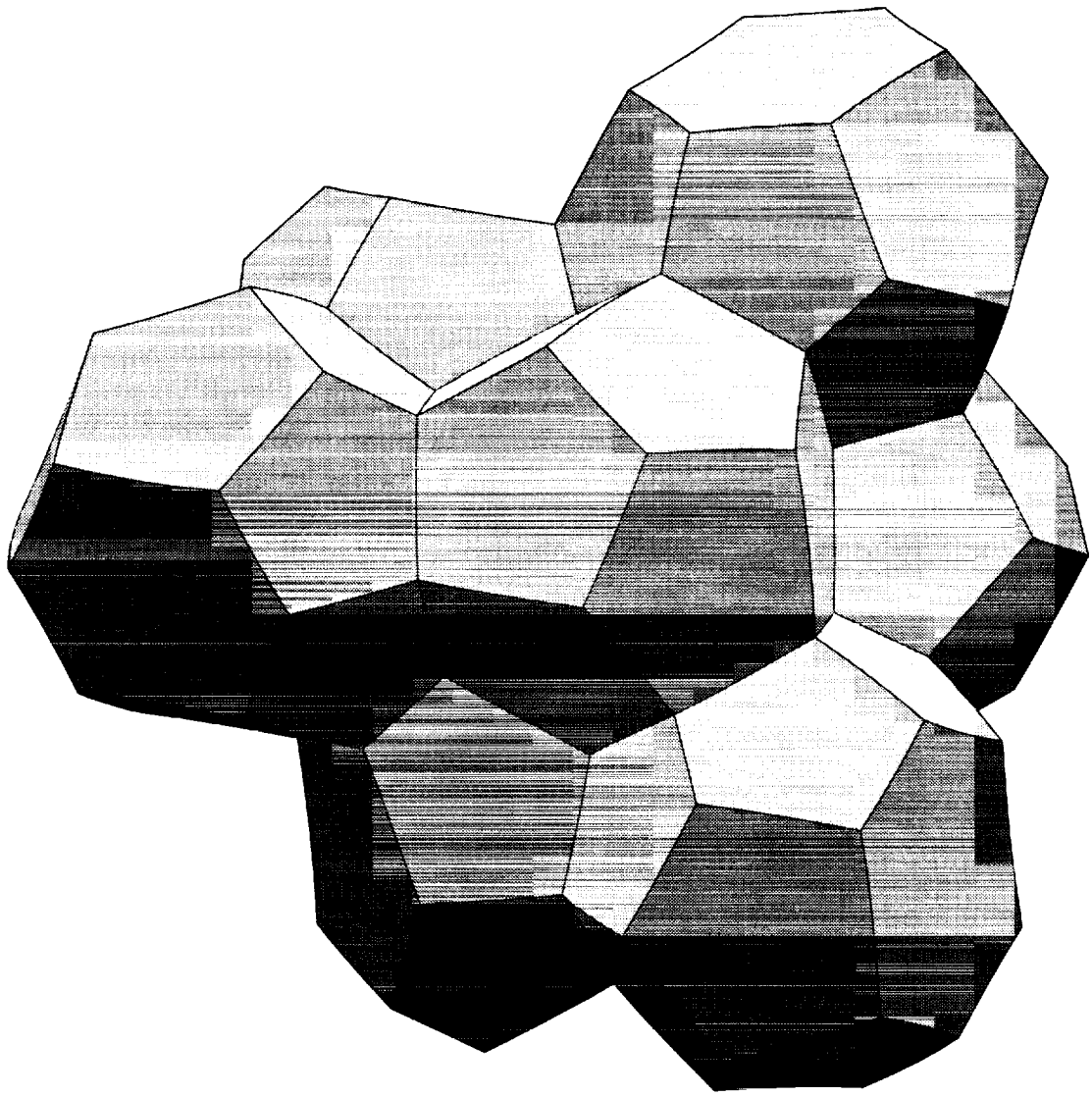

3D equilibrium foam configuration (with periodic boundary conditions and incompressible gas) computed with the Surface Evolver. This example is the equal-volume foam discovered by Weaire and Phelan.

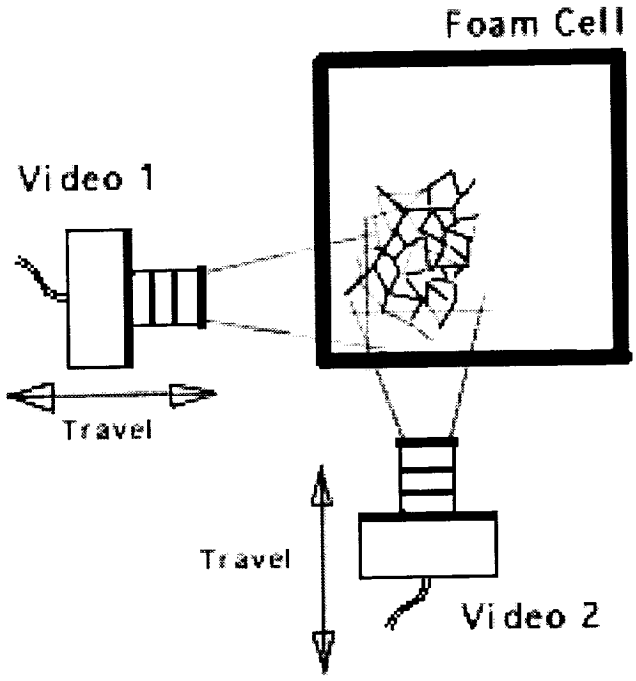

The relative location of the video cameras and the foam cell (not to scale).

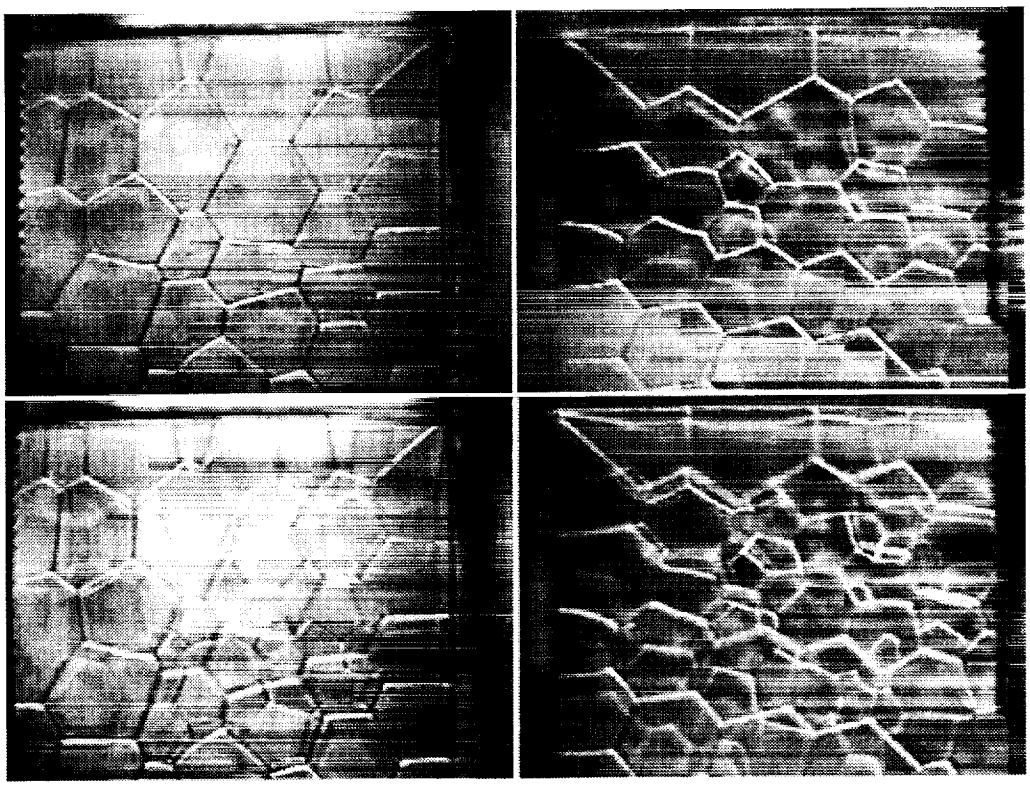

Video images of the foam-cells closest to the walls of the container, the left and right panels showing two perpendicular views. The lower images are focused on a plane 2mm inside the container. The horizontal span of each image is approximately 2.5cm.

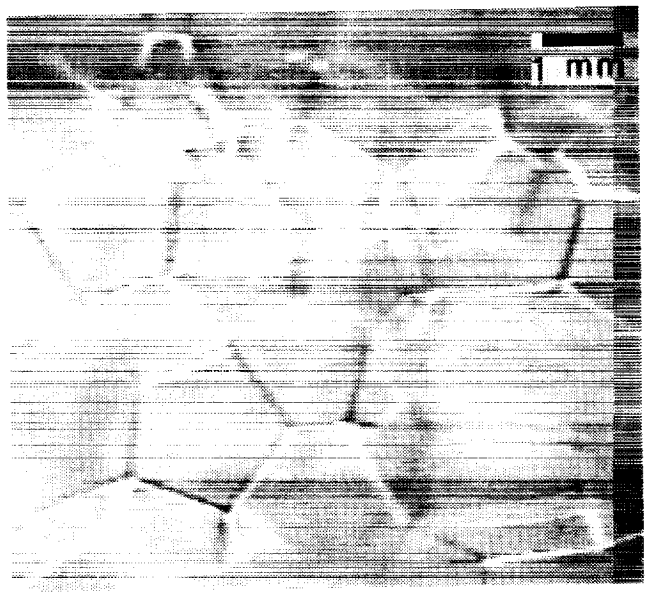

Section of a video-image whose focal plane is centered 1 cm inside the foam.

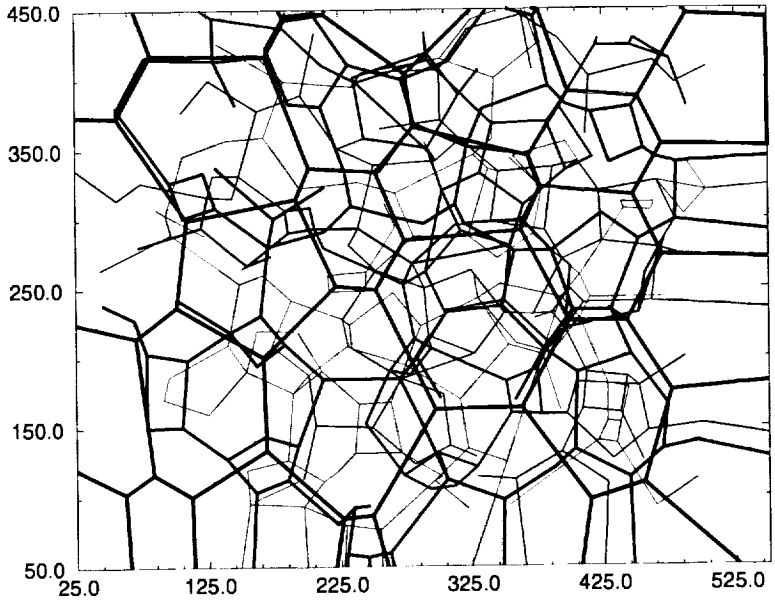

Manually reconstructed Plateau borders. Decreasing line thickness gives an indication of the depth into the foam. The axes are in pixel units.

INERTIAL EFFECTS IN SUSPENSION DYNAMICS

J.F. Brady
Division of Chemistry and Chemical Engineering, 210-41
California Institute of Technology

Please refer to the Conference Book of Abstracts or the NCMR Website at
http://www.ncmr.org

MARANGONI EFFECTS ON NEAR-BUBBLE TRANSPORT DURING BOILING OF BINARY MIXTURES

Van P. Carey, Mechanical Engineering Department, University of California at Berkeley,
6123 Etcheverry Hall, Berkeley, CA 94720, vcarey@,me.berkeley.edu

ABSTRACT

Results of our recently-completed reduced gravity experimental studies indicate that Marangoni effects in some systems tend to draw liquid toward the surface during binary mixture boiling, resisting the tendency to create a blanketing vapor film over the heated surface. These experiments demonstrated that Marangoni effects can sustain nucleate boiling at reduced gravity (< O.Olg) in some systems, resulting in heat transfer coefficients that are virtually the same as those observed for the same conditions at lg. They also demonstrated that the resulting pool boiling critical heat flux condition was only slightly lower than that observed at 1 g for the same conditions. The results clearly indicate that Marangoni effects in these systems are at least equal in importance to gravity buoyancy under lg conditions, and they are the dominant mechanism at reduced gravity. These results suggest that it is possible to achieve enhanced boiling heat transfer and high critical heat flux even under reduced gravity conditions by properly selecting a binary mixture working fluid.

Work under this project will experimentally obtain more detailed information on how Marangoni forces affect microscale transport near bubbles growing at the heated surface during binary mixture boiling. To accomplish this objective, novel experiments will be conducted which will generate a stable bubble in a temperature gradient near the heated surface. The temperature field created in the liquid around the bubble will result in vaporization over the portion of its interface near the heated surface and condensation over portions of its interface away from the heated surface. This type of simultaneous vaporization and condensation scenario is characteristic of bubbles during boiling of binary mixtures. In the experiments we propose to document the shape of the bubble and the density field in the adjacent liquid by using schlieren and/or interferometer optical methods. We will simultaneously determine the surface temperature and heat flow transported by the bubble. A computational model of the microscale transport in the liquid near the bubble will be developed concurrently. The experimental data will be compared with the computational predictions of the temperature and concentration fields near the bubble and the overall transport. The proposed experiments will span conditions ranging from those that help move liquid toward the heated surface to those that tend to move liquid away from the heated surface. The proposed studies will be done using a modified version of the experimental system fabricated for our recently-completed study of Marangoni effects. By conducting the experiments under low gravity conditions, we will be able to directly observe the effect of the Marangoni forces on transport without the presence of buoyancy which tends to obscure the effects of these forces. These investigations will provide information vital to the more effective use of binary mixture working fluids in a variety of applications, including terrestrial heat pump systems, power cycles or spacecraft thermal control.

OVERVIEW OF EXPOSITION DISPLAY

The boiling data of Ahmed and Carey (1997) shown in Fig. 1 is typical of the results obtained in the studies described above when Marangoni effects are strong. At comparable conditions, the nucleate boiling heat transfer data obtained under reduced gravity are only slightly different from data obtained at 2g. For low concentrations of propanol in water, the critical heat flux for reduced gravity conditions is somewhat lower than that for the same mixture and conditions at 2g, but it is well above the critical heat flux for pure water under 1 g at the same pressure. These data, which reflect the global effects of gravity and Marangoni forces on heat transfer, clearly indicate that Marangoni effects in these systems are at least equal in importance to gravity buoyancy under Ig conditions, and they are the dominant mechanism at reduced gravity. These results suggest that it is possible to achieve enhanced boiling heat transfer and high critical heat flux even under reduced gravity conditions by properly selecting a binary mixture working fluid.

The heated surface element shown in Fig. 2 is energized by a cartridge heater installed in the outside end of the element. The element is made of oxygen-free pure copper which has a well known thermal conductivity. Thermocouple instrumentation in the element will make it possible to detennine the heat transfer from the heated surface (from the axial temperature gradient and known conductivity). A single artifticial cavity will be created at the center of the heated surface to enhance the probability of bubble nucleation at the center of the heater surface. Experiments will be conducted using dilute aqueous binary mixture solutions at subatmospheric pressure. For such conditions, our previous experiments have shown that large diameter bubbles form at the heated surface, as indicated schematically in Fig. 2. We will position the cold plate heat exchanger at a distance of about 1-2 cm from the heated element. A bubble that forms by nucleation on the heated surface will grow large enough that the end away from the heated surface will come into close proximity to the cold plate surface. The cold plate will be cooled by an internal flow of cold water from an ice water reservoir. The binary liquid will vary in temperature near the bubble from the lower cold plate temperature at one end to the heated surface temperature at the other. Condensation of vapor will occur at the interface of the bubble near the cold plate while vaporization occurs at the interface of the bubble near the heated surface. By carefully adjusting the heat input to the heated surface and the temperature of the cold plate, we will stabilize the bubble at a fixed size, as indicated in Fig 2.

Although the bubble generated in the test section will be stationary, fluid within and outside the bubble will be in motion. As indicated schematically in Fig. 3, vapor generated at the interface near the heated surface will flow across the bubble and condense on the portion of the interface near the cold plate surface. Also, for water-alcohol mixtures, the interface near the heated surface will have a lower concentration of alcohol than the portion of the interface near the cold-plate surface. Consequently, the surface tension will be higher at the hot end of the bubble. The surface tension imbalance along the interface will induce a flow of liquid along the interface towards the heated surface. This flow is also indicated schematically in Fig. 3. At lg this Marangoni flow interacts with gravity buoyancy to dictate the transport between the interface and the surrounding liquid. Under reduced gravity. Marangoni effects alone will dictate the transport in the liquid.

For gravity levels at or above Ig, the vapor in the bubble will experience an upward buoyancy force. If the heated surface is facing upwards, this will skew the bubble shape in the manner shown in Fig. 4a. Note that this tends to thicken the liquid film between the bubble interface and the heated surface and thin the liquid film between the bubble interface and the coldplate surface. This will significantly alter the transport of heat and mass to the interface at these locations. In contrast, at reduced gravity the bubble will be very nearly spherical, as depicted in Fig. 4b.

The research objectives for this study are:

(1) To obtain a more complete understanding of how gravity buoyancy and Marangoni effects drive microscale transport during bubble growth in binary mixture nucleate boiling.

The fluid motion near the stationary bubble is a good model of Marangoni and buoyancy driven fluid motion near bubbles in boiling processes and the results of this study will provide much needed insight into how they contribute to the bubble growth **process.**

(2) To obtain a database documenting the temperature and density conditions in the liquid and the bubble interface shape that accompanies the microscale transport adjacent to the vaporizing/condensing bubble in our experiments.

This database will be of tremendous value to investigators who want to test computational models of transport near growing bubbles during boiling of binary mixtures.

(3) To assess treatments of interface transport boundary conditions in computational models of bubble growth in binary mixture boiling.

While several treatments have bee proposed and discussed in the literature, none have been validated against experimental data.

(4) To explore parametric effects on microscale transport.

Once we have established consistency of our computational model of microscale transport with our experimental results, we will use it to examine parametric effects of imposed temperature and pressure conditions and fluid properties on microscale transport near bubbles during bubble growth in binary mixture boiling. This will further expand our understanding of how these factors affect the boiling process, and thus further contribute to efforts to make more optimal use of binary mixture coolants in thermal control systems for ground-based and space applications.

The open square boiling curve is the 9.5 kPa curve corrected to a pressure of 5.5 kPa using the pressure correction from the correlation of Schlünder (1982).

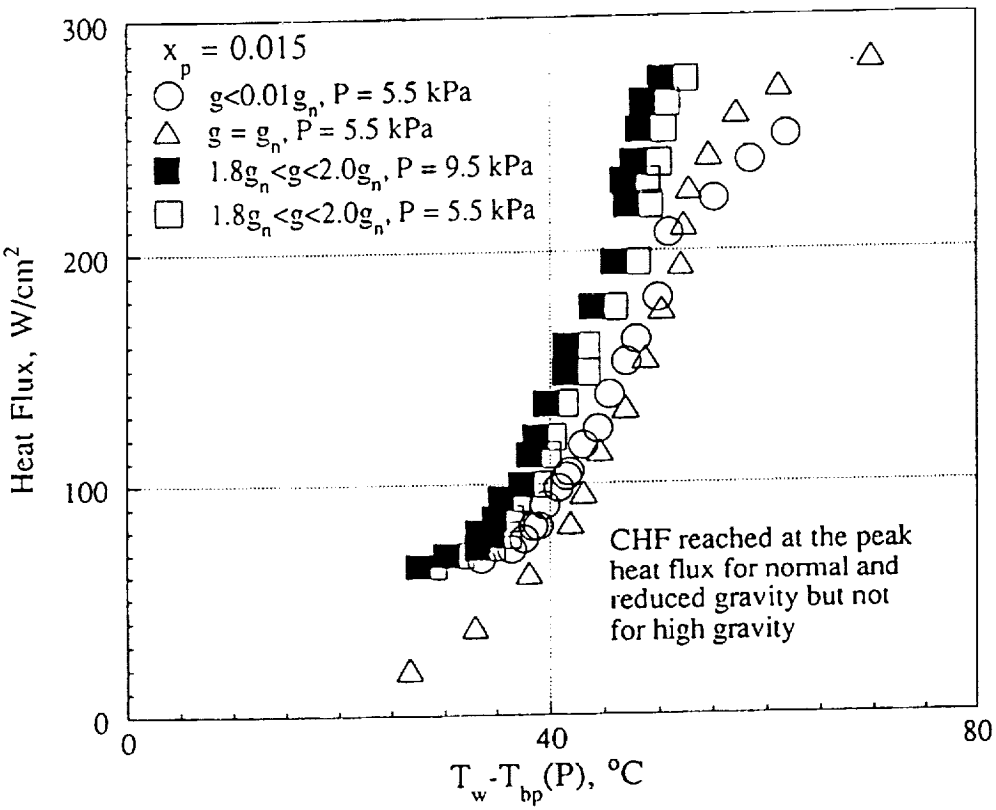

Fig. 1. Boiling curve for water-propanol mixture at a propanol mole fraction of 0.015.

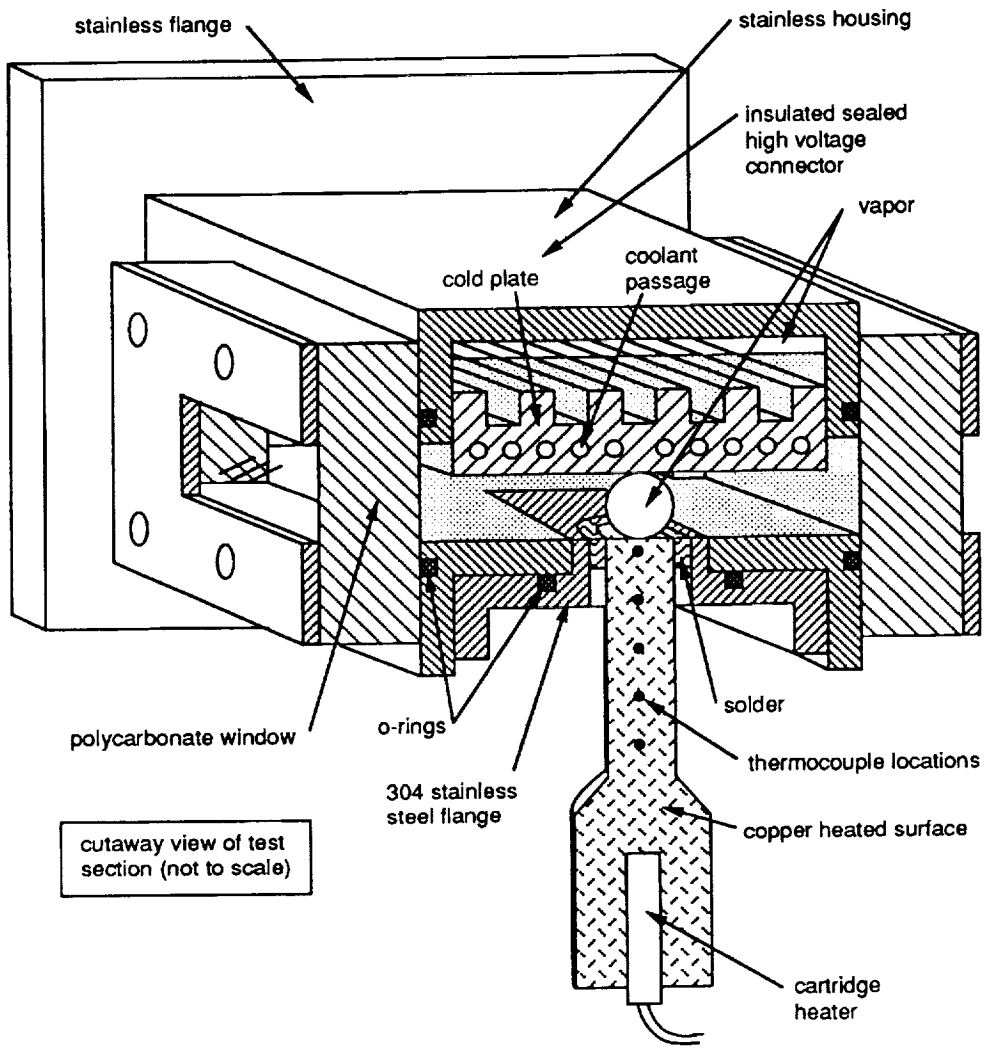

Fig. 2. Schematic of test section for stable bubble experiments.

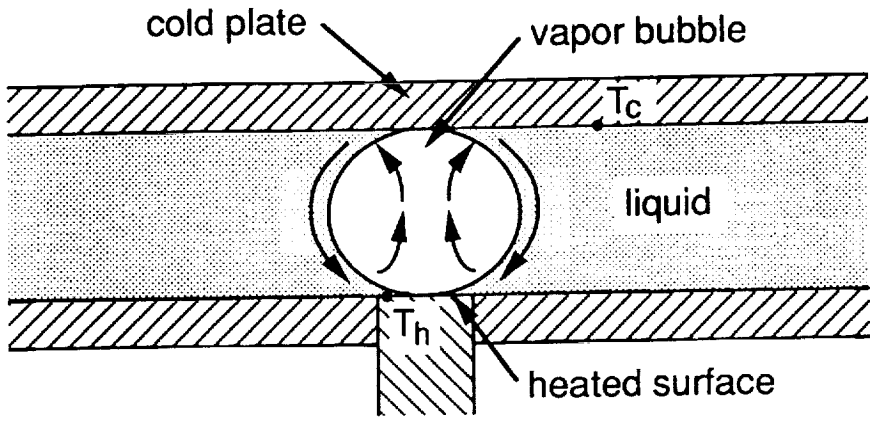

Fig. 3. Fluid motions near stable bubble interface.

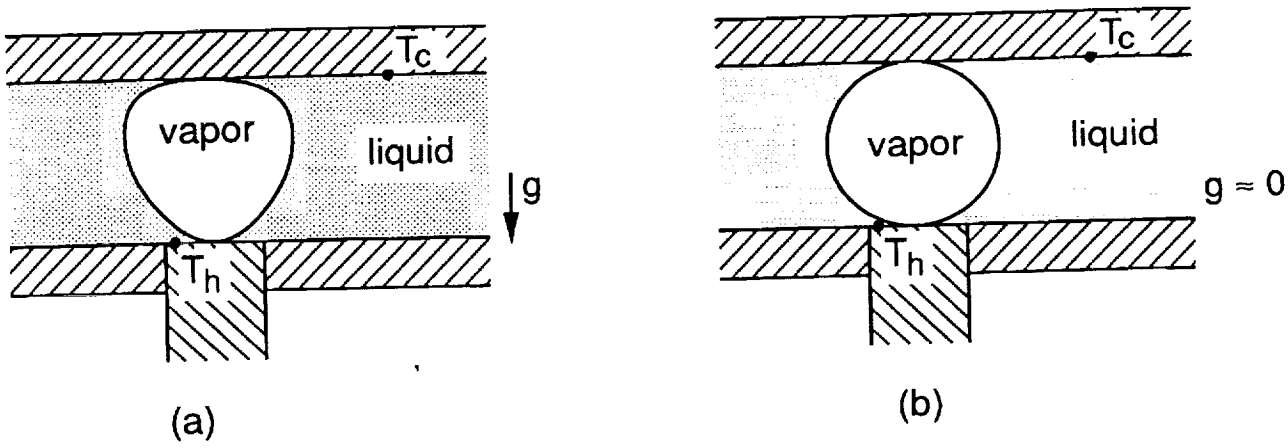

Fig. 4. Profile shapes for stable bubble.

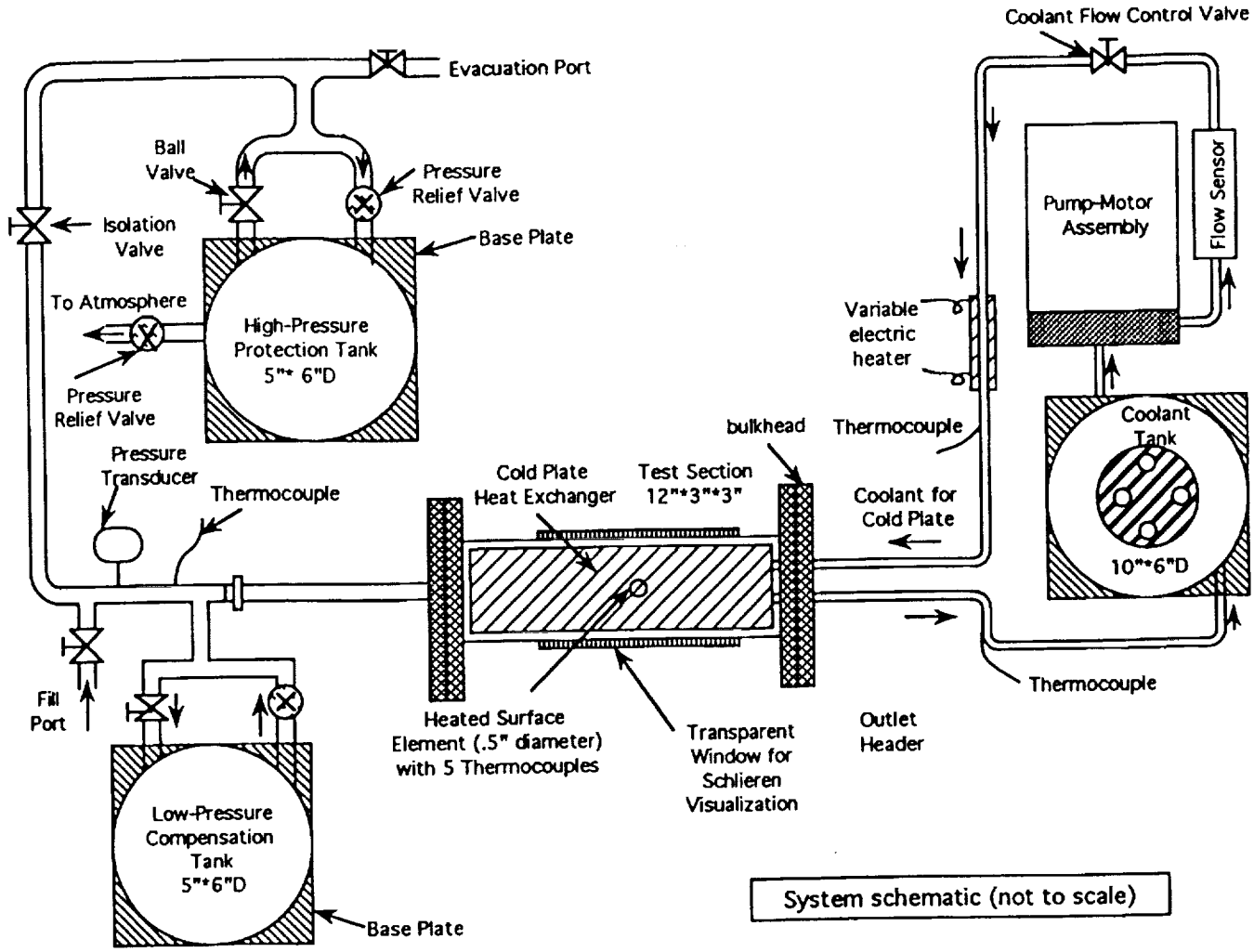

Fig. 5. Schematic of test system used in experiments.

DYNAMICS OF DUST IN PHOTOELECTRON LAYERS NEAR SURFACES IN SPACE

J.E. Colwell, M. Horanyi, A. Sickafoose
Laboratory for Atmospheric and Space Physics
University of Colorado

S. Robertson
Department of Physics
University of Colorado

R. Walch
University of Northern Colorado

Please refer to the Conference Book of Abstracts or the NCMR Website at http://www.ncmr.org

SCALING OF MULTIPHASE FLOW REGIMES AND INTERFACIAL BEHAVIOR AT MICROGRAVITY

C.J. Crowley
Creare Incorporated

Please refer to the Conference Book of Abstracts or the NCMR Website at http://www.ncmr.org

THERMOCAPILLARY-INDUCED PHASE SEPARATION WITH COALESCENCE

Robert H. Davis, Michael A. Rother and Alexander Z. Zinchenko
Department of Chemical Engineering, University of Colorado, Boulder, Colorado 80309-0424

ABSTRACT

Research has been initiated on interactions of two or more deformable drops (or bubbles) in a viscous fluid and subject to a temperature and/or gravitational field. An asymptotic theory for nearly spherical drops shows that small deformations reduce the coalescence and phase separation rates. Boundary-integral simulations for large deformations show that bubbles experience alignment and enhanced coalescence, whereas more viscous drops may break as a result of hydrodynamic interactions. Preliminary experiments for buoyancy motion confirm these observations. Simulations of many drops show clustering phenomena which lead to enhanced phase separation rates.

INTRODUCTION

Thermocapillary motion of drops and bubbles in a temperature gradient often leads to undesirable coalescence and phase separation, both on earth and in low-gravity environments. If properly understood, however, thermocapillary effects may be used in a positive way to control multiphase fluid transport and phase separation. Unfortunately, current understanding is primarily limited to the motion of single drops and bubbles, or at most two interacting drops and bubbles, which are often assumed to remain spherical. An outstanding need is for new scientific approaches for the study of thermocapillary and gravitational motion of drops and bubbles in concentrated dispersions which exhibit significant distortions of drop and bubble shapes from spherical.

We seek to meet the outstanding need by employing asymptotic and boundary-integral methods to predict drop interactions and deformations in temperature gradients, with or without gravity present. These methods have only recently been made sufficiently powerful to meet the objectives of the proposed work, including fully three-dimensional simulations of multiple drops. The theoretical work is complemented by ground-based experiments with transparent systems, for which drop deformation, coalescence, and phase separation may be directly observed and quantified. This research is undertaken in two subtasks:

(i) *Deformation Effects on Coalescence* - An asymptotic analysis is performed for drops or bubbles having small deformations (due to their small size and/or large interfacial tensions), based on a combination of lubrication theory and boundary-integral theory for close approach and film drainage. This is complemented by full three-dimensional boundary-integral numerical calculations for large deformations. Theoretical predictions of the conditions which yield coalescence, noncoalescence, or breakup will be tested with microvideo experiments for both buoyancy-driven and thermocapillary interactions of deformable drops.

(ii) *Migration and Phase Separation in Concentrated Emulsions* - The spatially-inhomogeneous population dynamics equations may be solved to predict phase separation rates in the presence of a temperature gradient for dispersions of drops or bubbles at moderate concentrations, at which both migration and coalescence are important. For concentrated emulsions of large, deformable drops, calculation of the separation rate will be possible for the first time (for either gravitational or thermocapillary motion), using three-dimensional boundary-integral simulations. A thermocapillary cell will be constructed to measure phase separation rates and to test the provocative hypothesis that undesirable coalescence and phase separation can be controlled by proper combination of gravitational and thermocapillary effects.

This research will provide fundamental understanding of how drop or bubble migration due to residual gravity and/or thermocapillary effects interacts cooperatively with coalescence to promote macroscopic phase separation of an immiscible dispersion. It is anticipated that this research will help resolve some critical issues, such as the roles of concentration, viscosity, interfacial tension, and other parameters on the coalescence process. The planned experiments and theory are also expected to provide a basis for predicting and controlling the rate of phase separation in space science applications such as processing of liquid-phase-miscibility-gap materials, gassing and degassing molten materials and cell cultures, and aqueous biphase partitioning systems. In addition, the results may be relevant to more traditional applications involving coalescence and phase separation in liquid-liquid and gas-liquid dispersions, including extraction, raindrop growth, flotation, emulsification, and creaming.

PRELIMINARY RESULTS

The asymptotic theory for the effects of small deformations on drop and bubble coalescence in gravitational motion was completed previously (Rother *et al.*, 1997), and it has now been extended to the interaction of two nearly spherical drops or bubbles in a tempera-

ture field. The results show that the collision efficiency (a dimensionless coalescence rate) decreases sharply with increasing drop size when deformation becomes important (Figure 1).

A boundary-integral code described previously (Zinchenko *et al.*, 1997) has been improved with a new, curvatureless formulation (Zinchenko and Davis, 1997) and with mesh adaptation and stabilization (Zinchenko and Davis, 1998) to study the interaction and shape evolution of deformable drops and bubbles in a gravitational field at higher Bond number (where the Bond number is the ratio of gravitational forces and interfacial-tension forces on the larger drop). Bubbles and drops with low viscosity tend to become aligned and coalesce due to their shape deformations (Figure 2), as observed and described previously by Manga and Stone (1993, 1995), whereas drops with modest viscosity become stretched and may break (Figure 3). We have also observed these phenomena in preliminary experiments with glycerol/water drops in caster oil (Figure 4).

Initial progress on the simulation of many deformable drops (c.f. Zinchenko and Davis, 1998) has been made by combining boundary-integral methods for neighboring drops with economical multipole techniques previously used in multiparticle conductivity (Zinchenko, 1994, 1998). These simulations indicate that deformation-induced drift and clustering occur (Figure 5). As a result, the average sedimentation or phase separation rate in an emulsion increases with time, even in the absence of coalescence (Figure 6).

PLANNED RESEARCH

Boundary-integral simulations of the interaction of two deformable drops or bubbles will be performed for thermocapillary migration, extending previous work for axisymmetric motion (Zhou and Davis, 1996). Systematic calculations of the system parameter and initial offsets which demarcate coalescence, breakup, and separation will be completed. Population dynamics calculations will be performed to study the evolution of drop sizes and phase separation rates in dilute systems, and considerable effort will be devoted to multidrop simulations of concentrated emulsions. Experimental work will include both microscopic observations of the interactions of two or more drops, and macroscopic measurements of phase separation.

REFERENCES

Manga, M. H. and Stone, H. A. (1993) Buoyancy-driven interactions between two deformable viscous drops, *J. Fluid Mech.* **256**, 647-683.

Manga, M. H. and Stone, H. A. (1995) Collective hydrodynamics of deformable drops and bubbles in dilute low Reynolds number suspensions, *J. Fluid Mech.* **300**, 231-263.

Rother, M. A., Zinchenko, A. Z., and Davis, R. H. (1997) Buoyancy-driven coalescence of slightly deformable drops, *J. Fluid Mech.* **346**, 117-148.

Zhou, H. and Davis, R. H. (1996) Axisymmetric thermocapillary migration of two deformable viscous drops, *J. Colloid Interf. Sci.* **181**, 60-72.

Zinchenko, A. Z. (1994) An efficient algorithm for calculating multiparticle thermal interaction in a concentrated dispersion of spheres, *J. Comput. Phys.* **111**, 120-134.

Zinchenko, A. Z. (1998) Effective conductivity of loaded granular materials by numerical simulation. *Phil. Trans. Roy. Soc. Lond. A* **356** (to appear).

Zinchenko, A. Z. and Davis, R. H. (1997) A curvatureless boundary-integral algorithm for viscous interactions of deformable drops, *Proc. 5th Conf. CFD Soc. Canada*, 11.27-11.32.

Zinchenko, A. Z. and Davis, R. H. (1998) Passive mesh stabilization and its applications in boundary-integral calculations, *Proc. 6th Int. Conf. on Num. Grid Generation in Comp. Field Sim.*, London.

Zinchenko, A Z., Rother, M. A., and Davis, R. H. (1997) A novel boundary-integral algorithm for viscous interactions of deformable drops, *Phys. Fluids* **9**, 1493-15.

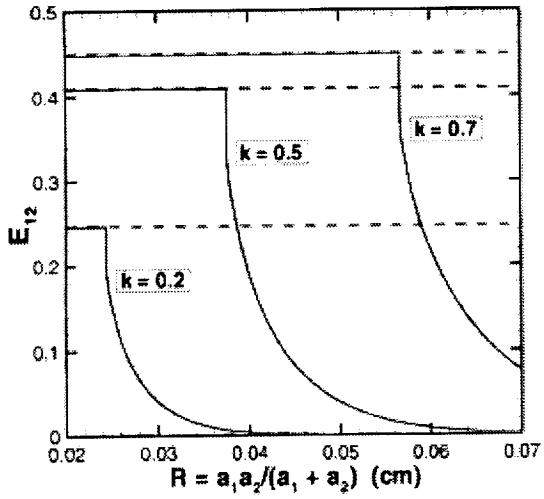

Figure 1 - The collision efficiency of two slightly deformable ethyl salicylate drops undergoing thermocapillary motion in diethylene glycol with a temperature gradient of 44°C/cm. Results are shown for drop size ratios of k = 0.2, 0.5, and 0.7.

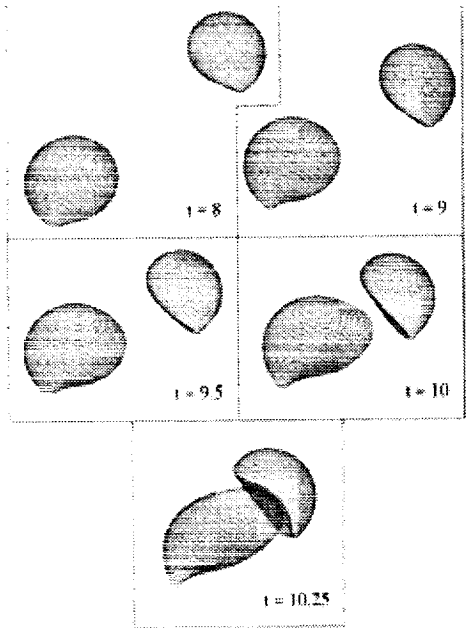

Figure 2 - Boundary-integral simulation of the deformation-induced alignment and capture of a larger bubble by a smaller one for drop-to-medium viscosity ratio $\hat{\mu} = 10^{-3}$, size ratio a_2/a_1 = 0.7, and Bond number Bo = 14.3 (from Zinchenko and Davis, 1997).

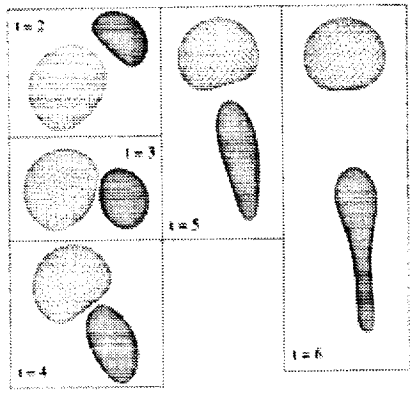

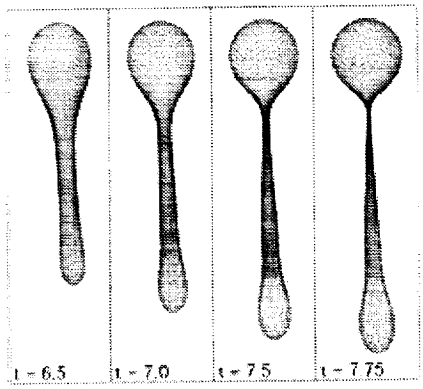

Figure 3 - Boundary-integral simulation of the stretching and impending breaking of a smaller drop interacting with a larger one with size ratio a_2/a_1 = 0.7, drop-to-medium viscosity ratio unity, and Bond number Bo = 5.3. Only the smaller drop is shown in the final four frames.

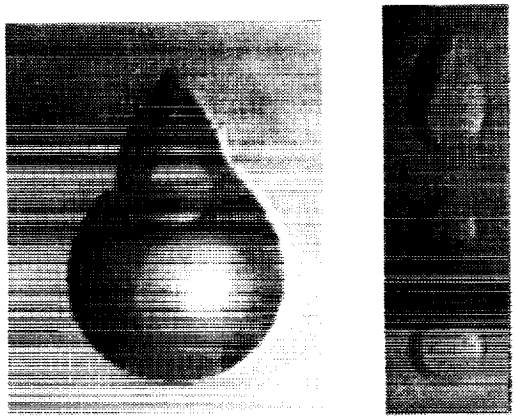

Figure 4 - Experiments on the interaction of two rising glycerol/water drops in castor oil showing (left) capture of the smaller drop for drop-to-medium viscosity ratio $\mu = 0.003$, and Bond number $Bo = 3.5$, and (right) breakup of the smaller drop for $\mu = 0.4$ and $Bo = 3.8$.

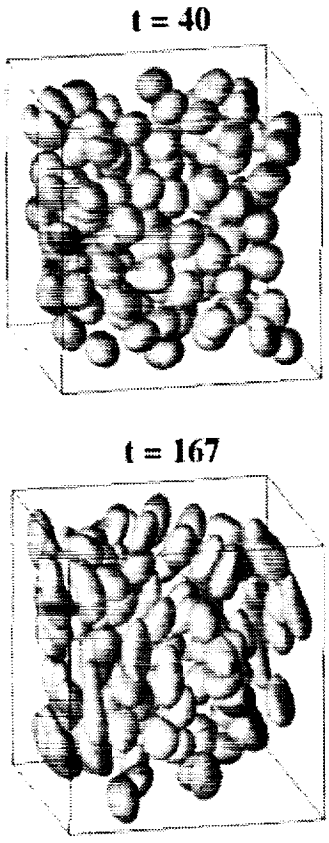

Figure 5 - Boundary-integral simulation of gravity sedimentation of a monodisperse emulsion with $N = 125$ drops in a cubic cell continued triple-periodically into the whole space at drop-to-medium viscosity ratio $\mu = 1$, Bond number $Bo = 1.75$, and drop volume fraction $c = 0.25$.

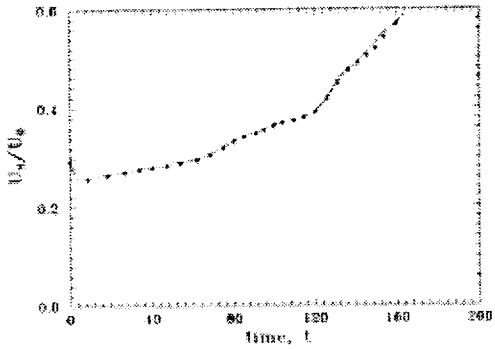

Figure 6 - Volume-averaged sedimentation rate (divided by that of a single spherical drop) versus time for a monodisperse emulsion with drop-to-medium viscosity ratio $\mu = 1$, Bond number $Bo = 1.75$, drop volume fraction $c = 0.25$, and number of drops in the periodic cell $N = 125$. The solid line is for 1280 boundary elements per drop, and the symbols are for 720 elements per drop.

Simulation of Rotating Thermal Convection and Comparison with Space-Laboratory Experiments

Anil E. Deane
Institute for Physical Science and Technology
University of Maryland, College Park
deane@morphy.umd.edu

The deep atmospheres of the planets such as Jupiter and Saturn and rotating stars such as our Sun are strongly influenced by buoyancy and Coriolis forces. In addition the giant planets also feel the effects of differential heating (North-South temperature gradients). The latitudinal variation of Coriolis forces is crucial to understanding large-scale motions (scales comparable to the curvature of the body) that are manifested in diverse phenomena such as the differential rotation of the Sun, and the cloud bands on Jupiter.

While important results have been obtained in terrestrial laboratory experiments, in an ambitious and novel experiment, Prof. John Hart has led an effort at the University of Colorado to move from a terrestrial laboratory situation to a space laboratory platform in order to study the effects of these forces on deep atmospheres. In the terrestrial laboratory gravity is aligned with the rotation vector unlike the geophysical case where these vectors move from being (anti-)parallel at the poles to orthogonal at the equator. In the Geophysical Fluid Flow Cell (GFFC) experiment which has been run twice in a microgravity environment (in 1985 and in 1995) radial gravity was achieved by charging a dielectric liquid with an ac voltage on the inner sphere (the outer sphere is ground). The inner and outer spheres were held at different temperatures and the whole apparatus rotated. Thus an analog of the geophysical environments was made. During its missions the GFFC obtained large quantities of data in a wide variety of parameter ranges. This data has shown many interesting flow features that are poorly understood.

The Spectral Element Method combines the geometric flexibility of finite element method with the exponential accuracy of spectral methods. The solution domain is broken up into quadrilateral elements each of which contains a representation as N^{th} order polynomials.

Using the Spectral-Element Method we are able to obtain highly accurate solutions corresponding to the geometry and parameter regime of the GFFC experiment. We present some preliminary results of surveys in Rayleigh number (corresponding to thermal driving) and Taylor number (corresponding to rotational driving). Also, in the GFFC experimental arrangement of obtaining radial gravity the force law is proportional to $1/r^5$ as opposed to the desired $1/r^2$. In our numerical simulations we are able to study the effects of this difference in the force laws and some results have been obtained.

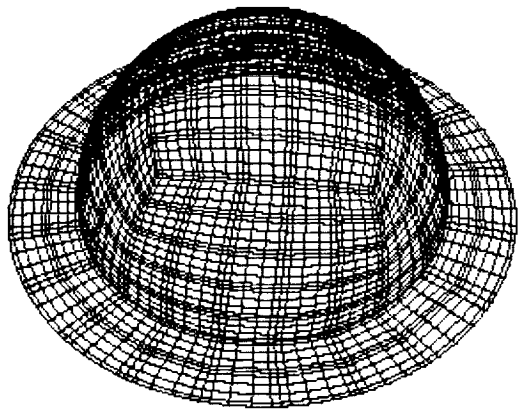

This is a typical spectral element grid we use. Shown is the inner hemisphere and the equatorial plane. Each element has a N=7 order polynomial representation in each of the three dimensions. This grid has 250 elements and was used in the simulations corresponding to Figures 4&5.

Figure 1

References:

J.E. Hart, J. Toomre, A.E. Deane, N.E. Hurlburt, G.A. Glatzmaier, G.H. Fichtl, F.Leslie, W.W. Fowlis and P.A. Gilman *Laboratory experiments on planetary and stellar convection performed on SpaceLab 3,* Science 234, pp 61-64 (1986).

J.E. Hart, G.A. Glatzmaier and J. Toomre *Space-laboratory and numerical simulations of thermal convection in a rotating hemispherical shell with radial gravity,* J. Fluid Mech. 173, pp. 519-544 (1986).

This 2D calculation has 64 elements with 9^{th} order polynomial representation in each element.

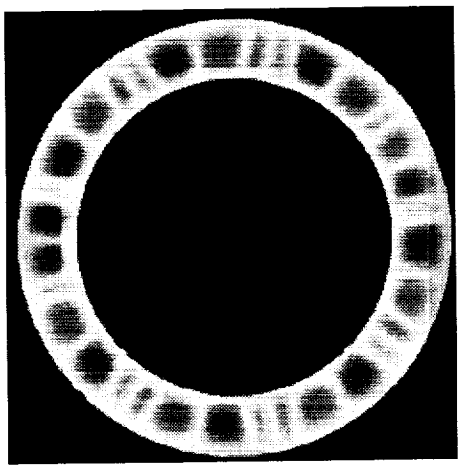

Figure 2(a)

At $Ra=10^4$, Ta=0, Pr=8.4 we find steady convection

Shown on the left is the streamfunction

Shown on the right is the temperature

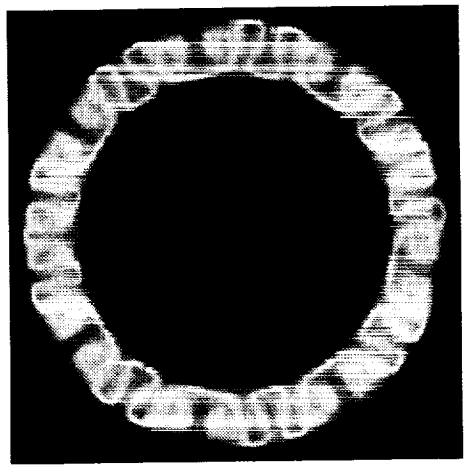

Figure 2(b)

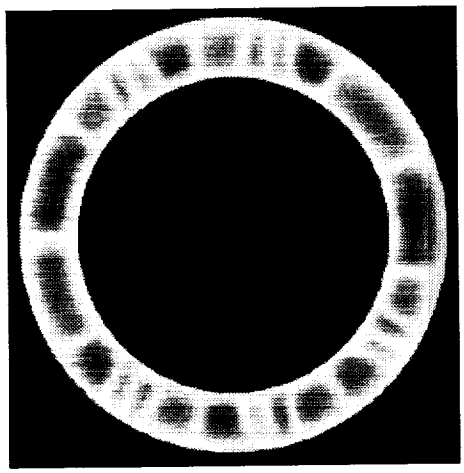

Figure 3(a)

At $Ra=1.5x10^4$, Ta=0, Pr=8.4 we find unsteady convection

Shown on the left is the streamfunction

Shown on the right is the temperature

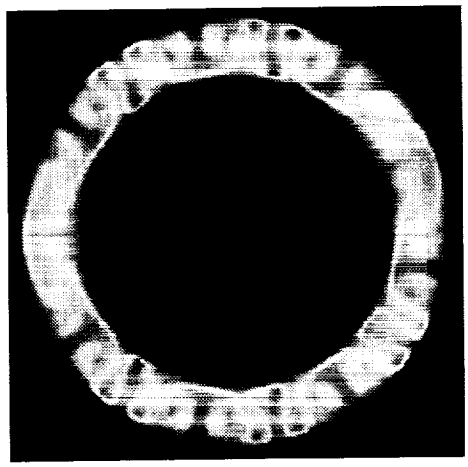

Figure 3(b)

We see that at the higher Rayleigh number the steady convection pattern has become unsteady with cells merging near the equator (although since this is a non-rotating case the "equator" is only one for reference, there being no preferred axis).

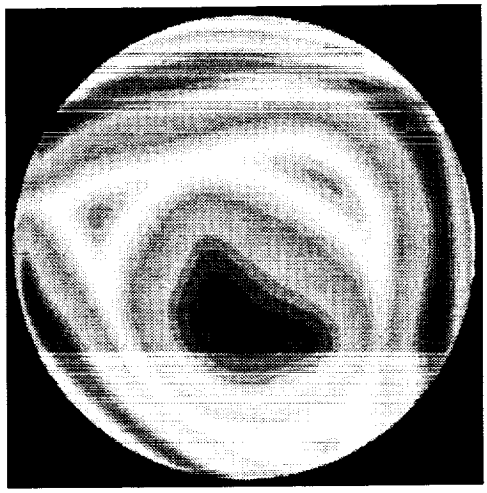

On the left is a view of the temperature field at radius corresponding to 50% of gap. We are looking down from the pole so that the pole is at the center and the equator forms the perimeter. The flow is at $Ra=6.9x10^3$, Ta=0, Pr=1. Gravity is constant but does point radially inwards as in the GFFC experiment.

Figure 4

On the right is a similar view of the temperature field as in figure 4, but with $Ra=6.9x10^3$, $Ta=2.6x10^4$, Pr=1. Gravity varies as $1/r^5$ and points radially inwards as in the GFFC experiment.

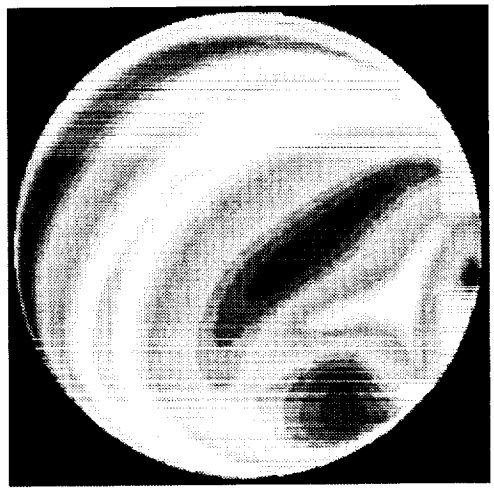

Figure 5

For the non-rotating case of Figure 4 we see that fairly regular convection is evident as compared to the rotating case of Figure 5 where the convection obtains strong directional components and is strongest in the equatorial belt.

Attenuation of Gas Turbulence by a Nearly Stationary Dispersion of Fine Particles

J. K. Eaton, W. Hwang, A. D. Paris

Department of Mechanical Engineering

Stanford University

Sponsor: NASA; Microgravity Fluid Physics Program

Background

- Fine particles with a mass loading ratio as low as 5% can attenuate turbulence
- Existing models do not correctly explain the attenuation, which is a function of $St_{particle}$, $Re_{particle}$, Re_{flow}, mass loading ratio, and flow structure

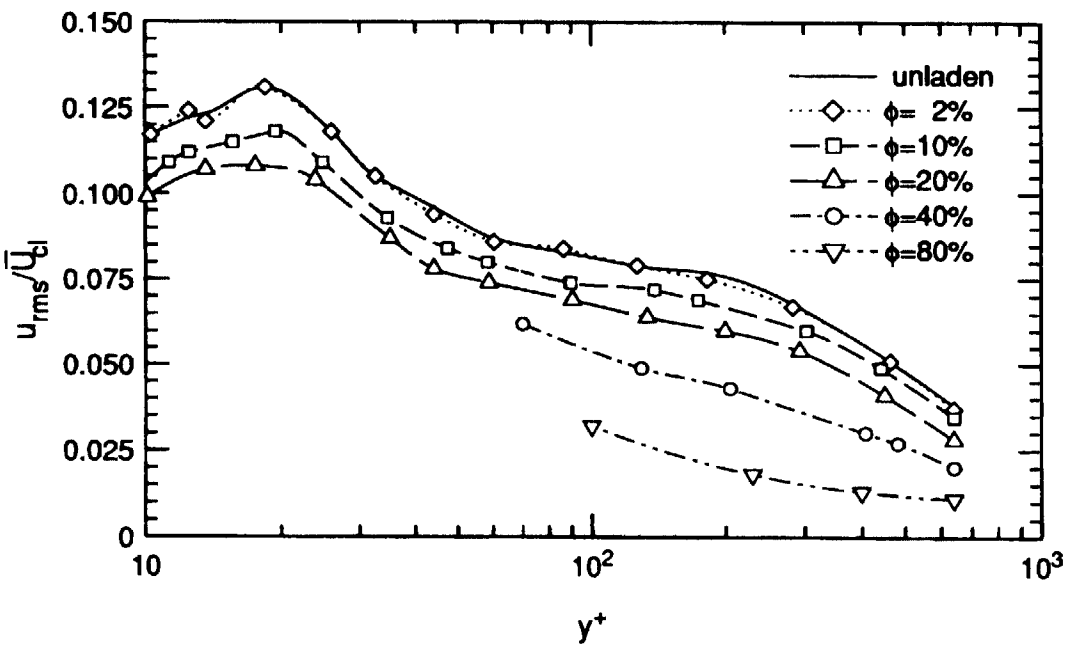

Streamwise turbulence intensity with various loadings of 70 μm copper particles.
From Kulick et al. (1994)

Transport Equation for TKE in Homogeneous Flow

$$\frac{Dk}{Dt} = -\overline{u_i' u_k'}\partial_k U_i - \nu\overline{\partial_k u_i' \partial_k u_i'} - \frac{1}{\rho_f \tau_p}\left[C(\overline{u_i' u_i'} - \overline{u_i' v_i'}) + (\overline{c' u_i' u_i'} - \overline{c' u_i' v_i'}) + (U_i - V_i)\overline{c' u_i'}\right]$$

production from mean gradient

dissipation by viscosity

Represents the drag on turbulent eddies by particles. Incorporated in current models, but does not capture full turbulence modification.

Possible Cause

The gravitational potential energy of particles is converted to turbulent velocity fluctuations which distort the turbulent eddies, leading to higher dissipation rate.

Objectives

- Investigate the direct effects of particles on homogeneous turbulence by using a microgravity environment to eliminate the mean velocity of the particles
- Observe distortion of individual eddies by particles and also examine the details of the flow around single particles

Current Status

- The current emphasis is to create isotropic homogeneous turbulence in the chamber. Testing several different methods including ejectors, grids, various configurations of the synthetic jets.
- Two-phase PIV system development nearly complete

Facility

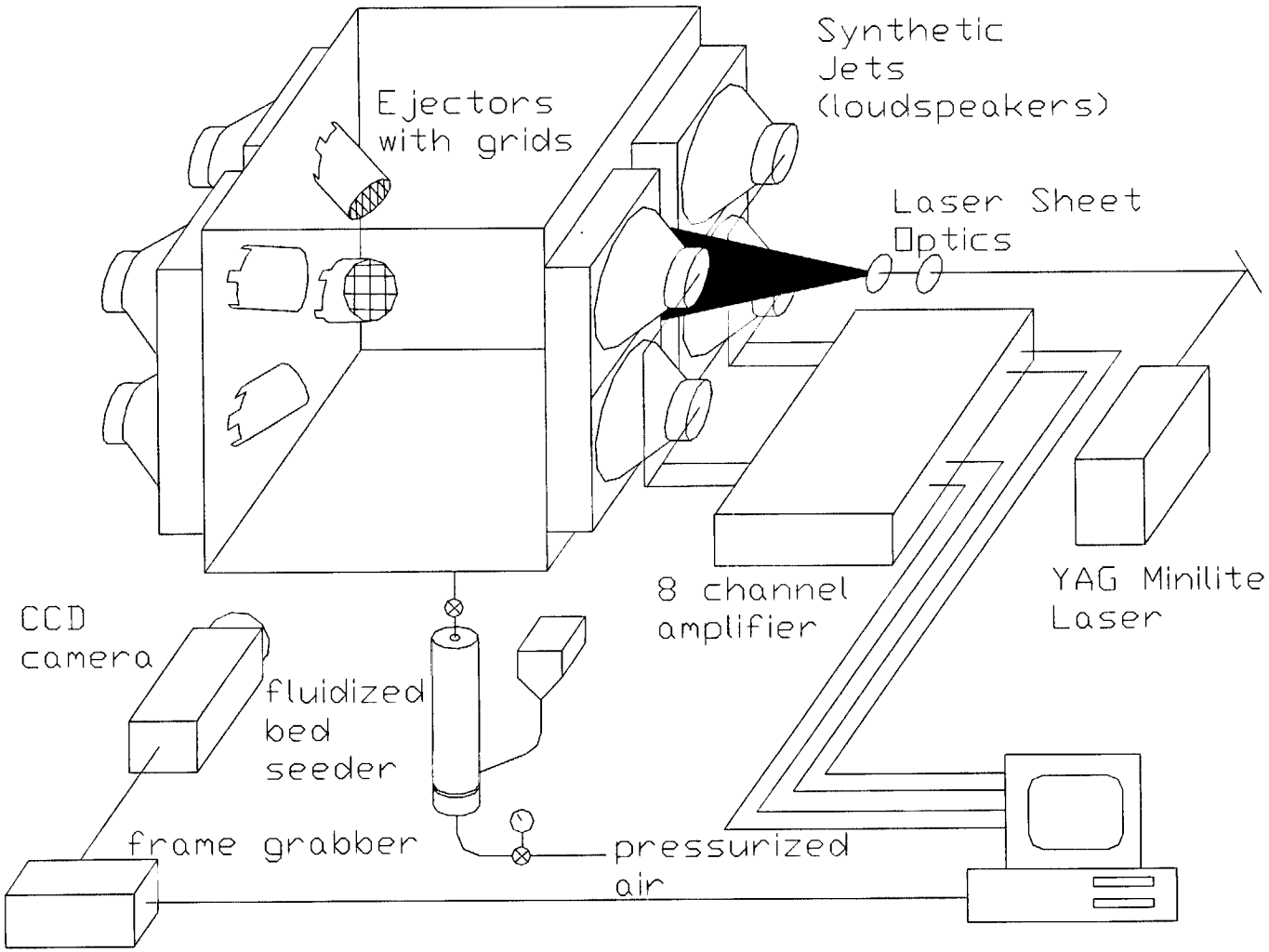
Synthetic
Jets
(loudspeakers)
Ejectors
with grids
Laser Sheet
Optics
8 channel
amplifier
YAG Minilite
Laser
CCD
camera
fluidized
bed
seeder
frame grabber
pressurized
air

Synthetic Jet

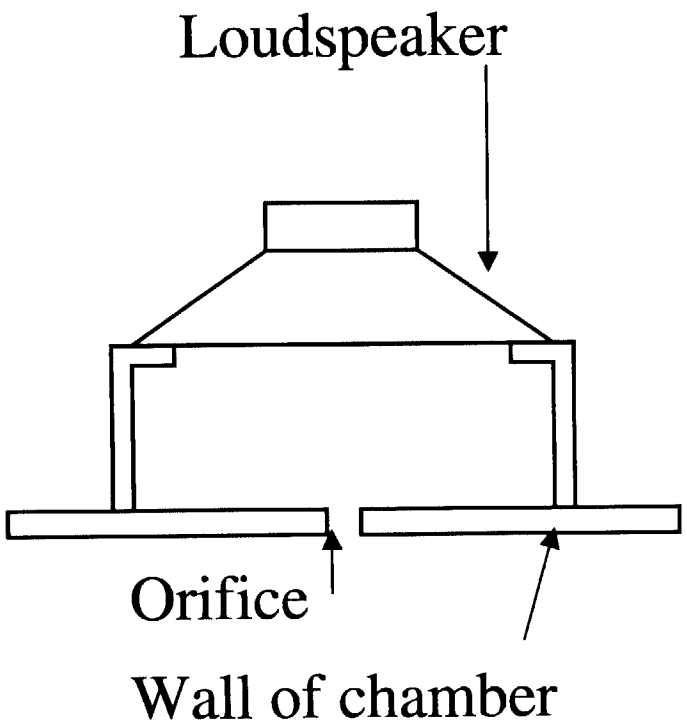

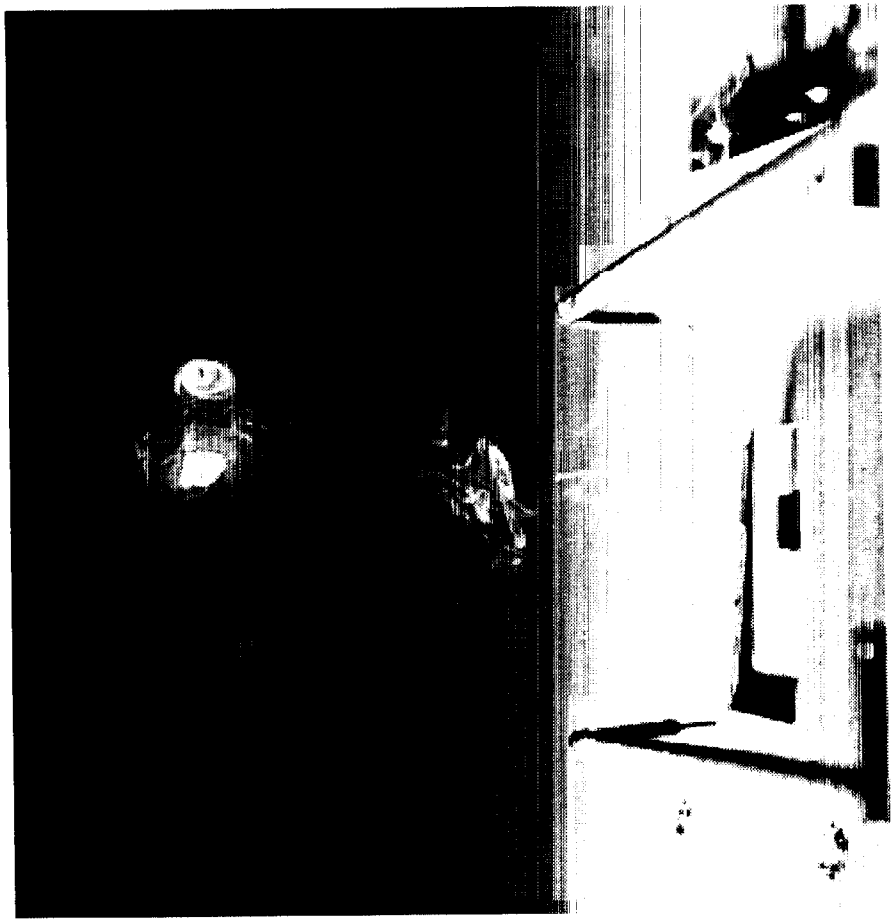

Vortex ring ejected from a square orifice

Digitized PIV photograph

(single laser pulse)

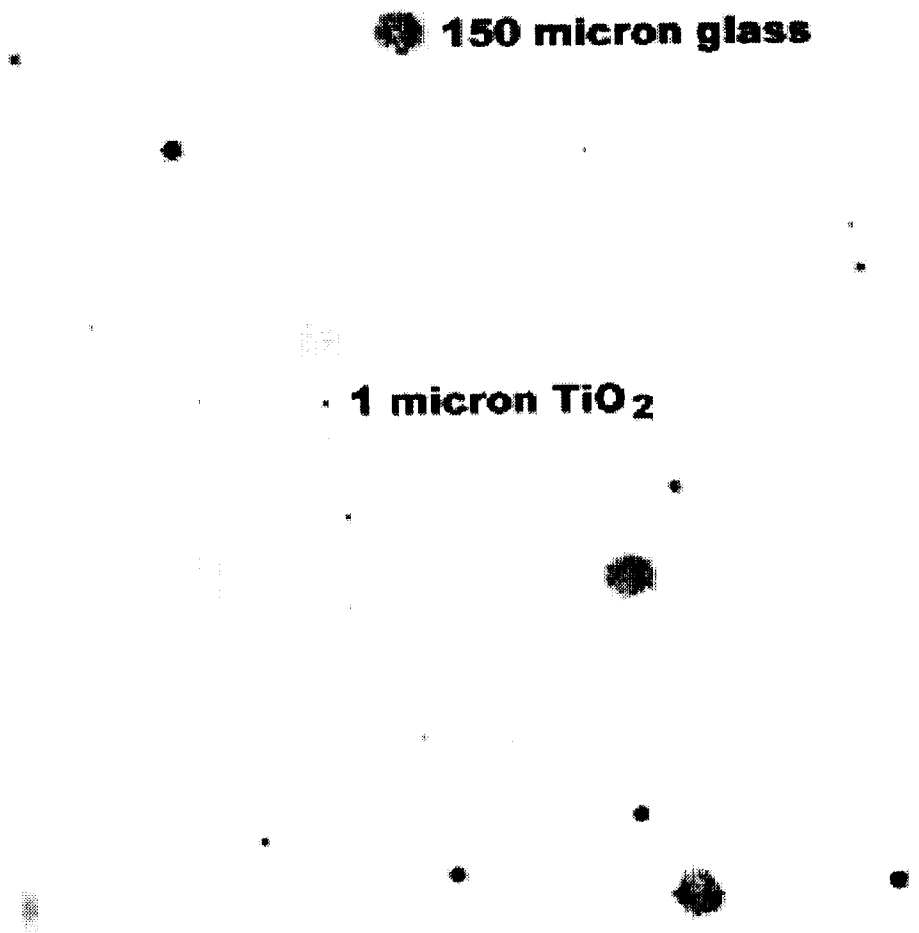

A DUST AGGREGATION AND CONCENTRATION SYSTEM (DACS) FOR THE MICROGRAVITY SPACE ENVIRONMENT

F.J. Giovane, Space Science Division, Naval Research Laboratory, Washington, DC 20375-5320,
giovane@nrl.navy.mil
J. Blum, Astrophysical Institute and University Observatory, University of Jena, Jena, Germany
blum@astro.uni-jena.de

INTRODUCTION

The formation of planetary systems is a multi-stage process that has fundamental importance to astrophysics and the understanding about origins of life. In the early stages of the proto-solar nebula fine dispersed dust grains accumulate into larger and larger bodies through frequent collisions between the dust grains due to Brownian motion, differential drift velocities, and decoupling from gas turbulence until their internal gravity becomes the dominant source for their further growth. An understanding of the changing morphologies and light scattering characteristics of aggregated dust under various growth conditions is needed to better interpret astronomical observations of dust in star forming regions. However, the direct simulation of the long-term behavior of a cloud of dust grains under thermal motion, as in the very early stages of the proto-solar nebula, is not possible in a terrestrial laboratory. Even in levitation-compensated experimental setups the relative velocity is determined by the Earth's gravity field, and a velocity field, which simulates the motion of astronomical dust grains, is not feasible.

It was with the goal of developing a system for observing the self-interaction of a cloud of dust grains that the present international team of investigators joined together in the Cosmic Dust Aggregation, (CODAG) Microgravity Experiment. CODAG, when it flies later this year, will for the first time undertake the study of light scattering from a cloud of astrophysical relevant dust aggregating under controlled conditions. Its observation time is however limited by the diffusion time of dust to the walls of the stationary chamber. A solution was therefore sort to overcome this deficiency, that is to dramatically extend the duration with which dust particles can be suspended and concentrated. It was felt that if the duration could be extended the formation of larger aggregates will result, and essential information on one of the fundamental steps in planetary formation obtained.

Based on the lessons learned from the CODAG, and from experience gained in drop tower tests, parabolic flights, and ground experiments conducted at the University of Jena (UJena), Germany, the concept for the Dust Aggregation and Concentration System (DACS) for the microgravity space environment was developed.

The DACS concept will allow the morphology of a dust cloud to be studied as the individual particles aggregate and concentrate. The system represents a unique opportunity to study in situ astrophysical conditions similar to those experienced in the formation and evolution of the proto-solar nebula. The DACS project team, whose principal interests are in astrophysics will naturally pursue this interesting area. However, it is expected that the unique opportunity afforded by the DACS to hold dust particles and aerosols in suspension for extended periods, and the instruments ability to concentrate these particles during suspension will be of interest to scientist in other fields such as fluid dynamics, material and biological science, etc.

1.1 Objectives

The following are the principal objectives of the Dust Aggregation and Concentration System, DACS definition project. These goals are fully within the context of NASA's Human Exploration and Development of Space Enterprise, and they are directly responsive to the objectives of NASA's "Origins" theme and to the President's new Civilian Space Policy.

The following objectives relate to an optically thin particle cloud in a low gas pressure and microgravity environment, and obviously can not be achieved until the proposed investigation is completed, and a flight unit built and flown. The following objectives therefore represent the end goals of the DACS development effort.

a. Grow larger aggregates than is presently possible in a stationary chamber.
b. Make precise light scattering measurement of the evolving dust aggregate cloud.
c. Acquire greater understanding of the dust concentration mechanism and the maximum concentration achievable.
d. Explore the instabilities at the interface of gas to dust dominated regions.

During the course of the project we seek to define the physical parameters that control the behavior of the suspended dust cloud and define the require-

ments for those instruments best suited to gather data during the aggregation process

At the completion of this definition study it is expected that we will have obtained:

A. A practical understanding of the optical induced thermo-phoresis effect for both single and aggregated particles.
B. Computer simulation tools, validated by laboratory tests, to better predict the behavior of dust and low pressure gas in a microgravity environment.
C. A sufficiently detailed design of the DACS and its science requirements to expeditiously develop a flight instrument.

1.2 Dust Aggregation in Astrophysics

There are four major points that distinguish terrestrial dust and dust aggregation from the process occurring in a pre-solar nebula. It is generally believed that under the conditions of the preplanetary nebula that:

1. Planetesimals agglomerate from dust whose initial grain size is typically believed to be less than 1 mm in radius.
2. Dust grains are principally restricted to 4 groups of uncharged and un-magnetized particles: (1) silicates, (2) carbonaceous matter, (3) organics, and (4) ices (mainly water).
3. Dust is embedded in a thin gas environment; the gas flow around the particles is molecular and not viscous.
4. Aggregation in space is always ballistic and not diffusive - i.e. particles are on linear trajectories when colliding. This yields different fractal structures of the aggregates as compared to the diffusive case.

Under these conditions our ability to use terrestrial models for the dust aggregation process is very limited. As a consequence, there have been only three dust experiments known to us that deal with astrophysically relevant environments:

I. Praburam & Coree (1995) have investigated the growth of carbon particles in a plasma environment which is not representative of the young solar system (see 2 above);
II. Higuchi & Sugiura (1993) investigated the distribution of fluffy aggregates floating in the air under relatively uncontrolled and unregulated environmental conditions.
III. Nuth et al. (1994) have observed the magnetically enhanced coagulation of metal particles. Although this is a useful study to see how such particles might come together, it is a very unlikely mechanism for dust aggregation in the early solar system.

The characteristics of these dust experiments, however, do not resemble the conditions that are believed to exist in the early solar system.

Consequently, until recently dust aggregation work remained mainly the subject of theoretical and computational studies. Four years ago one of us, Blum, began a movement towards solving the astrophysics questions. He initiated a laboratory at the University of Jena (UJena), dedicated to dust aggregation experiments that fulfill the conditions 1 through 4 given above. Giovane and B.A.Gustafson (U of Florida) joined him three years ago to expand the CODAG experiment to include the study of light scattering from the aggregated particle cloud. Over the years Blum's team at UJena have acquired extensive experience in the microgravity area, in particle generation, and in particle suspension. Several auxiliary devices were specifically invented there for this purpose. Much of the auxiliary equipment that is envisioned to be part of DACS derives from these developmental efforts. Among these successes was a de-agglomeration device for the production of monodispersed, high number density aerosols under low vacuum and microgravity conditions, Blum et al. (1996a) and the laboratory prototype of the DACS chamber.

The work at UJena led to the detailed study of Brownian motion of micron sized dust gains and aggregates in microgravity, Blum et al (1996b), in conditions approximating those of the very early presolar nebular. Dust aggregation in a turbulent gas environment and in a levitation tube were observed and aggregate size distributions were measured for large dust aggregates composed of up to one thousand particles each, Wurm & Blum, (submitted 1997)). Such aggregated particles are illustrated in Figure 1. In another laboratory experiment, the critical velocity below which sticking occurs and above which particles rebound was determined. Poppe & Blum (1996) showed that the critical sticking velocity is a factor of 6 greater than theory. Recent results of laboratory experiments are summarized in Blum (1997). These ground based experiments, including parabolic and drop tower tests have contributed to the technique and understanding of what is required to achieve large aggregate particles. However they are in themselves incapable of providing the environment required to meet the DAC Experiments objectives.

Figure 1. Examples of aggregated 1.95•m particles generated in the UJena Rotating Chamber. Bar at bottom of the figure is 100 microns in length.

Long period suspension of dust is needed for deeper insight into the astrophysical questions. The CODAG Experiment, which allows the Brownian motion driven dust to aggregate, is inadequate to provide the suspension time needed. The diffusion and drift time of the dust in a stationary chamber, even in a microgravity environment, severely limits the duration that particles can remain suspended. However, it is from the CODAG experience and the work done at UJena that a new approach involving a rotating chamber has emerged. We will adapt this approach in the DACS, and perfect it to the degree needed to achieve a space experiment that will meet the proposed objectives. The approach that we will take will allow extended periods of particle suspension, and thereby very greatly increase the duration of the dust aggregation. It is believed that the process can be continued right through to macroscopic agglomerates.

1.3 The Rotating Chamber Concept

In order to overcome some of the limitations in the duration over which the aerosols can be sustained in a 1 g laboratory environment, a rotating chamber was developed at UJena to take advantage of the angular velocity effect on the motion of the dust. This chamber is illustrated in Figure 2.

With this apparatus it has been shown that a dust cloud can be suspended for several minutes in an earth gravity field. The resulting observations corresponds very well with the time predicted by calculations which take into account the centrifugal forces driving the particles to the chamber walls. In the earth's gravitation field, the relative motion of the dust particles in the chamber is due to residual sedimentation and leads to rapid aggregation of the dust particles. This rapid aggregation and the limited time that the dust can be suspended make it necessary to bring a rotating chamber into space and the microgravity environment in order to achieve our goals.

Figure 2. The rotating chamber at the University of Jena with associated apparatus. A microscope and fast CCD Camera are illustrated at left looking into the chamber.

DISCUSSION

2.1 The Dust Aggregation and Concentration System

The CODAG microgravity experiment, as we have noted, is limited by the grain diffusion and drift to the chamber walls. Therefore the growth of very large aggregates over a long period of time, requires an alternate approach. The fundamental success of the UJena laboratory rotating chamber in supporting a cloud for several minutes led us to believe that it can be modified for the microgravity environment to achieve the required very long period suspension that will allow the aggregation of a very large number of dust grains. The most prominent change required in the microgravity environment is in the introduction of a one dimensional external force field with an associated field gradient. The field gradient is required to allow particles moving under the influence of the gas in the rotating chamber to move faster in one half of the drum chamber than in the other half. If the resulting force moving the particles towards concentration is stronger than the dispersive centrifugal forces due to the rotation induced by the gas, then the particles will be concentrated in an effective way. The

concentration effect will be strongest in a large chamber with slow rotational velocities. In other words, for the right combination of forces, those created by the rotating gas on the particles in the drum and another force acting in part counter to this motion, there will be a net motion of particles towards an equilibrium point removed from the center of rotation. If this force is greater than the centrifugal force, which tends to drive the particles outward, the particles will concentrate.

We have been studying potential candidates for the simulation of the vertical component of the pre-planetary gravitational field. As we excluded for astrophysical reasons charged and magnetic particles, and thus electrical or magnetic fields, the only remaining and practical externally applicable acceleration field for the rotating chamber experiments seems to be the light induced phoresis force.

One might argue that in order to simulate the concentration effect in pre-solar turbulent eddies, the use of tidal forces or any other inertial force would be preferred. However, any tidal force outside the Earth's surface acts in just the wrong direction: in general, such forces become stronger in the direction in which the forces act. The same holds for centrifugal forces as an example of an inertial force. Only inside the Earth are the gravitational field and its gradient anti-parallel. Unfortunately, the gravitational gradient is almost infinitely small. Thus, the light-induced phoresis force appears to be the only solution available to us to create the kind of force needed, that is if the conditions to exclude charged and magnetic particles and, therefore electrical or magnetic fields, are adhered to.

This phoresis force is created by illuminating a cloud of dust particles, which are embedded in a rarefied gas environment. The light interaction with the particle results in the gas surrounding the particle being differentially heated. This results in the molecules with slightly greater temperature, and therefore higher velocities, creating a differential force on the dust grain. The phenomena was originally observed by Ehrenhaft in the early part of this century (ca. 1910). Since that time several investigators have studied it. F. Deguillon (1950) suspended particles by electrical fields while illuminated. He observed that the particles move both towards and away from the light source depending on their optical characteristics. Orr and Keng (1964) measured both these photophoresis effects in a chamber where the light controlled the rate of fall of the particle. When the particle moves towards the light source the phoresis was termed negative: when it move away it was termed positive. Kerker and Cooke (1982) provided a realistic model of the force on particles in the free-molecular regime.

One of us (Blum) has observed such a motion in a cloud of optically thin transparent particles during microgravity parabolic flight experiments. In the case of the transparent particles, which were observed to travel towards the illumination source, we could properly term this an optically induced negative thermo-phoresis effect. However, both for simplicity and to maintain the more traditional terminology we will refer to the effect as the "photophoresis" effect and the force that causes the effect the "photophoresis force" or "photophoretic" force. It should be kept in mind that the motion is due to a differential heating of the gas and not directly to the photons of the light source impacting the particles.

Since the direction of the force is not directly material to its application in DACS (either positive or negative photophoretic force are suitable) we will not differentiate between the two in the following discussion except when necessary. What is important is the light's wavelength and how it is focused, as these determine the strength of the photophoretic force field for a particular dust particle.

Let us now look with greater detail into the process that might be created in a microgravity environment and its relationship to the conditions that exist in the pre-solar nebula. Dust grains in the pre-solar nebula may be incorporated into turbulent gas eddies. A dust particle within such an eddy is not only subject to gas drag (friction) forces but also to centrifugal forces which tend to drive the grains out of the eddy. However, an additional vertical (perpendicular to the solar nebula's midplane) gravitational field is present which results in a sedimentation of the grains towards the midplane of the solar nebula. Due to the large extent of the eddies (typically of the order of the half-thickness of the disk), the particles are sedimenting faster in the upper half of the turbulent eddy than in the lower half (closer to the midplane of the nebula). It has been shown by Klahr & Henning (1997) that for typical eddy sizes and gas densities in the solar nebula, a net concentration by factors exceeding 100 can be reached for grain sizes of mm and below.

The effect of particle concentration in a rotating cylindrical chamber depends strongly on the gradient of the one dimensional photophoretic force field which is superimposed on the centrifugal force field due to the rotation of the chamber. A force field of the form given in Equation. 2 (below) can be deconvolved into a constant mean acceleration -g and into a harmonic component $-\Omega^2 z$ which acts like a spring and drives the particles towards the equilibrium point

x_s (see Equation. 3). If the gradient of the harmonic acceleration $-\Omega^2$ is larger than the centrifugal acceleration gradient ω^2, the net concentration effect is stronger than the dispersion of the grains and particles are concentrated in an effective way. This, in some measure, mimics the sedimenting process in the presolar nebula.

2.2 Numerical Modeling

In order to effectively model the rotating chamber system numerically, a particle tracking scheme fully coupled to the gas phase of the system will be employed. In this scheme, the motion of each dust particle is determined by a governing equation of motion which directly takes into account the local forces, such as particle inertia and drag, as well as external forces such as the photophoretic force. Thus no generalizations concerning particle-particle and gas-particle interactions need to be made and individual particle trajectories at any given instant are known. Similarly, the fluid phase is modeled in such a manner to account for flow modulations through the disturbance flow generated by the dispersed particle phase. This characteristic is quite desirable as little is known about the gas phase as the dust particles congregate at the equilibrium point and the flow is modified.

In a similar manner the photophoresis effect will be modeled. Here we will introduce theoretical and laboratory determined light scattering models to better explain the effect and its changes with particle characteristic. Laboratory tests will be very closely linked with the fluid dynamic models, so that the result of one will determine the direction of study of the other.

2.3 Conditions for Aggregation and Concentration.

Consider a cylindrical vacuum chamber, rotating at an angular velocity w in a gradient field. The cylinder is rotated about its horizontal symmetry axis (as illustrated in Figure 3), into which a cloud of particles and gas are injected. The injected gas quickly assumes the rotational motion of the chamber. The gas rotation is stiff, with a constant angular velocity tied to that of the chamber. On the side, where the rotating gas moves against the gradient field, there is an equilibrium point at which the motion induced by the gas equals the velocity of the dust due to the gradient field. The particles are levitated near this equilibrium point, with the particles orbiting about that point.

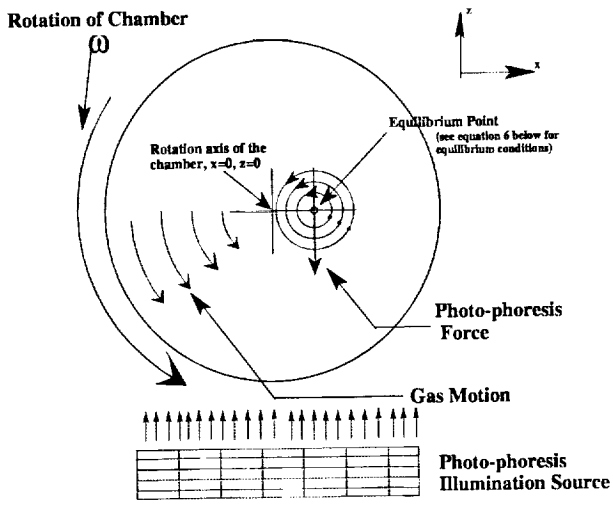

Figure 3. Cylindrical Vacuum Chamber rotating with angular velocity ω.

The response time of the dust particles to the gas motion is

$$\tau_f = s\,\rho_d / v_t\,\rho_g \qquad \text{(equation 1.0)}$$

where s is the particle radius, ρ_d & ρ_g are the densities of the dust and gas respectively, and v_t is the mean thermal velocity of the gas molecules. A one dimensional external force field (the photophoresis field) is added resulting in an acceleration g_z,

$$g_z = -g - \Omega^2 z \qquad \text{(equation 2.0)}$$

where g is the mean acceleration and Ω^2 is the acceleration gradient applied in the z direction. Following the mathematics of Klahr & Henning (1997) we have the dust particles orbital radii a at time t,

$$a = a_o\, e^{(\tau_f^{ct})} \qquad \text{(equation 3.0)}$$

where a_o is the initial orbital radius at time $t = 0$ and

$$c = \omega^2 - {}^1/_2\,\Omega^2 \qquad \text{(equation 4.0)}$$

There is a net orbital drift towards the stability point at

$$x_s = \tau_f\, g\, /\omega \;,\; z=0. \qquad \text{(equation 5.0)}$$

where the net forces balance if the condition

$$\omega^2 < {}^1/_2\,\Omega^2 \qquad \text{(equation 6.0)}$$

is met. The time scale for the orbital decay τ_c is

$$\tau_c = {}^1/(\tau_f\, c) = {}^1/\{\tau_f\ (\omega^2 - {}^1/_2\, \Omega^2)\}$$

(equation 7.0)

Let us consider a candidate DACS rotating chamber and the parameters that might exist or be imposed:

Chamber Radius, L = 5 cm
Chamber Temperature, T = 300°K
Gas Pressure, P = 1 mbar
SiO_2 Particles of size, S = 1 μm radius
Rotation period = 63 s., or ω=0.1 radians/s.

we obtain from equation 1.0, the response time of the dust to gas $\tau_f \simeq 3$ milliseconds. The mean acceleration has been observed in parabolic flight experiments to be $g \sim 0.1$ m/s^2, and the acceleration gradient due to the photophoresis effect will be chosen to be $\Omega^2 \sim 1$ sec^2, which indicates that the force field at z = L will be 50% greater than the field at z = 0, and 50 % less at z = -L than at z=0. Equation 7.0 provides the time scale of the decay, τ_c = 680 seconds, and equation 5.0 gives the orbital stability point at x_s = 3 mm.

Under these conditions the stability point will be located a short distance from the cylinder's rotational axis and the decay of the dust orbits will result in a significant concentration of dust at the equilibrium point in a relatively short time. The particles and gas balance changes in the equilibrium region as the particle cloud is concentrated around the equilibrium point a region will be formed having more dust than gas. The behavior of this fluid is not well understood and will require further work during the study phase. The photophoresis effect observed in parabolic flights also became less predicable as the dust aggregates and concentrates. This issue will also be a topic of modeling and study during the course of this investigation.

ACKNOWLEGEMENT

This research is supported by National Aeronautics and Space Administration DPI C-32055-G. Facilities and equipment to carry out this project have also been provided by the Naval Research Laboratory, the German Space Agency (DLR), the University of Jena, the University of Florida, and the Max Planck Society, to whom we are most grateful. We would also like to acknowledge our fellow investigators on this project: K. Kailasanth, E. Chang, and L. Marlin (NRL), G. Wurm and L.-O. Heim (Univ. Jena), B.A. Gustafson and Y.L. Xu (U of Florida), S. Tehranian (George Mason U.), H.U. Keller (MPI fur Aeronomic).

REFERENCES

1. J. Blum, Coagulation experiments, ASP Conference Series, in press.
2. J. Blum, M. Schnaiter, G. Wurm, M, Rott, The deagglomeration and dispersion of small dust particles - principles and applications, Rev. Sci. Instrum. 67, 589, 1996a.
3. J. Blum, G. Wurm, S. Kempf, Th. Henning, The Brownian motion of dust particles in the solar nebula - an experimental approach to the problem of pre-planetesimal dust aggregation, Icarus 124, 441, 1996b.
4. F. Deguillon, Photophoresis of suspensions of colored solutions in air and their coefficients of absorption, Comp . Ren. 231, 274, 1950
5. B.A.S. Gustafson, Optical properties of dust from laboratory scattering measurements; Physics, Chemistry, and Dynamics of Interplanetary Dust, ed. Bo A.S.Gustafson and Martha S. Hanner, Astro. Society of the Pacific Press, 1996,
6. Y. Higuchi, N. Sugiura, Determination of size distribution of fluffy aggregates floating in the air, Proc. 3rd Int. Congress on Optical Particle Sizing, 217, 1993.
7. M. Kerker and D.D. Cooke, Photophoretic force on aerosol particles in the free-molecule regime, J. Opt. Soc. Am. 72, 1267, 1982
8. J.A. Nuth, O. Berg, J. Faris, P. Wasilewski, Magnetically enhanced coagulation of very small iron grains, Icarus 107, 155, 1994.
9. Orr, Jr. and E.Y.H.Keng, Photophoretic effects in the stratosphere, J. Atmos. Sci. 21, 475, 1964
10. T. Poppe, J. Blum, Experiments on preplanetary grain growth, Adv. Space Res, in press.
11. G. Praburam and J. Goree, Cosmic dust synthesis by accretion and coagulation, Astrophysical Journal 441, 830, 1995.
12. G. Wurm, J. Blum, Experiments on preplanetary dust coagulation and aggregation, Icarus, submitted.
13. Y. Xu, electromagnetic scattering by an aggrregate of spheres, Appl. Opt. 34, 4573., 1995
14. Y. Xu, Calculation of the addition coefficients in electromagnetic multi-sphere scattering theory, J.Comput. Phys., in press

PLASMA DUST CRYSTALLIZATION

J. Goree, R.A. Quinn
Dept. of Physics and Astronomy
The University of Iowa

G. Morfill, H. Thomas, T. Hagl, U. Kopoka, H. Rothermel, M. Zuzic
Max-Planck-Institut fuer extraterrestrische Physik, Germany

Please refer to the Conference Book of Abstracts or the NCMR Website at
http://www.ncmr.org

Determination of the Accommodation Coefficient Using Vapor/Gas Bubble Dynamics in an Acoustic Field

Nail A. Gumerov

Hertz-Knudsen-Langmuir Formula (1882) for Kinetics of Phase Transitions:

$$\xi = \frac{\beta(T_a)}{\sqrt{2\pi R_v T_a}}\left[p_s(T_a) - p_v\right]$$

ξ the rate of evaporation (condensation),

β the accommodation (condensation) coefficient,

T_a the temperature of the interface,

p_s the saturation pressure,

p_v the vapor pressure,

R_v the gas constant of the vapor.

Non-Equilibrium Evaporation/Condensation:

- Vacuum Evaporation;
- Processing of Molten Metals;
- Vapor Explosions;
- High Velocity Jets;
- Atmospheric Small Droplet Clouds;
- Sound Propagation in Vapor/Droplet Mixtures;
- Bubbles/Droplets in Acoustic Fields;
- Laser Vaporization;
- Other High-Speed Processes.

Rectified Heat and Mass Transfer To a Vapor Bubble

Rectified heat and mass transfer to vapor bubbles can strongly depend on the value of the accommodation coefficient

Dependence of the growth rate of a water vapor bubble in 10 kHz acoustic field on the bubble size (p=1 bar, T=373 K).

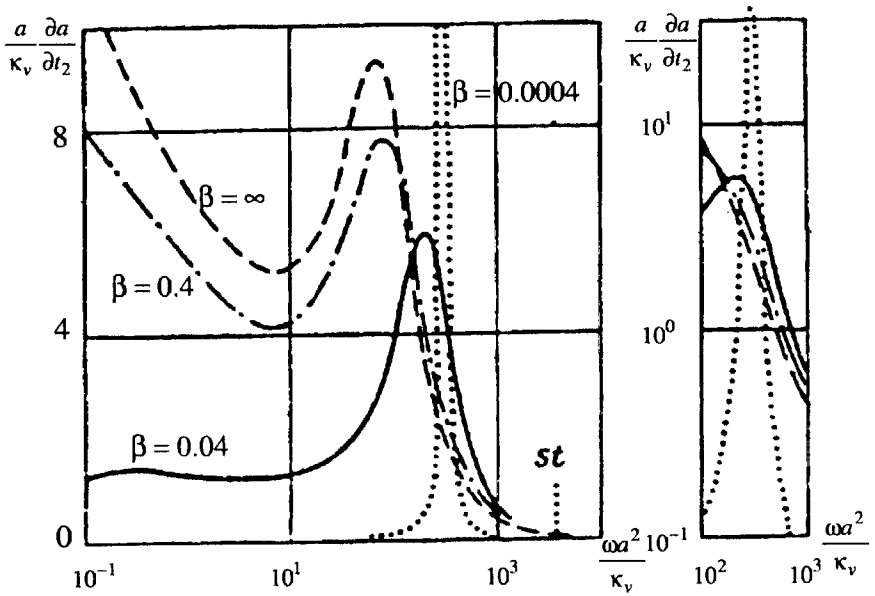

Stable time-averaged radius of a water vapor bubble at various values of the accommodation coefficient (p=1 bar, T=373 K).

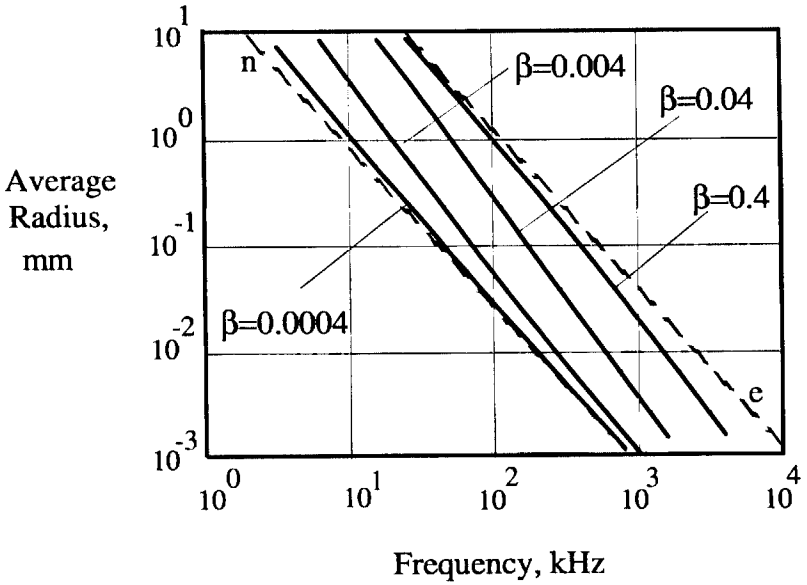

N.A. Gumerov, Weakly non-linear oscillations of the radius of a vapour bubble in an acoustic field. *J. Appl. Maths Mechs* 55 (2), 205-211, 1991.

Bubble Motion in Standing Acoustic Waves

Standing wave:

$$p_\infty = p_{\infty 0}\left[1+\varepsilon\cos\omega t\sin kx\right],\quad \rho\frac{dU_\infty}{dt} = -\nabla p_\infty,\quad \omega = Ck.$$

Bubble motion ($ka \ll 1$):

$$F = F_b + F_m + F_\mu = 0,$$

$$F_b = \frac{4}{3}\pi a^3\rho\frac{dU_\infty}{dt},\quad F_m = \frac{2}{3}\pi a^3\rho\frac{d\left[a^3(U_\infty - U_b)\right]}{dt},\quad F_\mu = 4\pi K_\mu a(U_\infty - U_b),$$

$$\frac{dx_b}{dt} = U_b.$$

Equations of Bubble Radial Pulsation

- Modified Keller-Miksis Equation:

$$\left(1-\frac{w_a}{C}\right)a\dot{w}_a+2\left(1-\frac{w_a}{4C}\right)\dot{a}w_a-\frac{1}{2}w_a^2=\frac{1}{\rho}\left(1+\frac{\dot{a}}{C}+\frac{a}{C}\frac{d}{dt}\right)\left[p_g-p_\infty(t)-\frac{2\sigma}{a}-\frac{4\mu}{a}w_a+\left(\frac{1}{\rho_{ga}}-\frac{1}{\rho}\right)\xi^2\right].$$

- Mass, Momentum, and Energy Conservation at the Interface:

$$\rho(\dot{a}-w_a)=\rho_{ga}(\dot{a}-w_{ga})=\xi,$$

$$-p_a+\tau_a^{rr}+\xi w_a=-p_g+\xi w_{ga}+2\frac{\sigma}{a},$$

$$\left(-p_a+\tau_a^{rr}\right)w_a-q_a+\frac{1}{2}\xi w_a^2=-p_g-q_{ga}+\frac{1}{2}\xi w_{ga}^2+\xi_v l_v+\xi_i l_i+\dot{\sigma}+\frac{2\sigma\dot{a}}{a},$$

$$\xi=\xi_v+\xi_i,\quad \xi_i=c_i\xi,\quad j_a=c_a\xi-\xi_i.$$

- Kinetics of Phase Transitions:

$$\xi_v=\frac{\beta_v(c_a,T_a)}{\sqrt{2\pi R_v T_a}}\left[p_s(T_a)-p_v\right],\quad \xi_i=\frac{\beta_i(c_a,T_a)}{\sqrt{2\pi R_v T_a}}\left[H(T_a)c_a-p_i\right]$$

- Heat and Mass Diffusion Fluxes:

$$q_{ga}=-\lambda_g\left.\frac{\partial T_g}{\partial r}\right|_{r=a(t)},\quad q_a=-\lambda\left.\frac{\partial T}{\partial r}\right|_{r=a(t)},\qquad j_a=-\rho D\left.\frac{\partial c}{\partial r}\right|_{r=a(t)}.$$

Heat and Mass Transfer in Gas and Liquid

- Model of Gas

$$p_g = p_i(t) + p_v(t),$$

$$p_g(t) = \rho_g(r,t) R_g(t) T_g(r,t), \quad R_g(t) = c_i(t) R_i + c_v(t) R_v,$$

$$\frac{\partial \rho_g}{\partial t} + \frac{1}{r^2}\frac{\partial (r^2 \rho_g w_g)}{\partial r} = 0, \quad \rho_g c_{pg}\left(\frac{\partial T_g}{\partial t} + w_g \frac{\partial T_g}{\partial r}\right) + \dot{p}_g = \frac{1}{r^2}\frac{\partial}{\partial r}\left(r^2 \lambda_g \frac{\partial T_g}{\partial r}\right),$$

$$\text{at } r = a: \quad w_g = w_{ga}, \quad T_g = T_a.$$

- Model of Liquid

$$\rho c_l\left(\frac{\partial T}{\partial t} + \frac{a^2 w_a}{r^2}\frac{\partial T}{\partial r}\right) = \frac{1}{r^2}\frac{\partial}{\partial r}\left(r^2 \lambda \frac{\partial T}{\partial r}\right) + \frac{12 \mu w_a^2 a^4}{r^6},$$

$$\frac{\partial c}{\partial t} + \frac{a^2 w_a}{r^2}\frac{\partial c}{\partial r} = \frac{1}{r^2}\frac{\partial}{\partial r}\left(r^2 D \frac{\partial T}{\partial r}\right),$$

$$\text{at } r = a: \quad T = T_a, \quad c = c_a, \quad \text{at } r = \infty: \quad T = T_\infty, \quad c = c_\infty.$$

Methods of Solution

- Asymptotic Multiscale Technique
- Direct Numerical Simulations

Multiscale Technnique:

1. Space - time transformation : $(r,t) \rightarrow (\eta, t), \quad \eta = r/a(t);$
2. Introduce mutiple scales : $t \rightarrow \{t_0, t_1, \ldots\}, \quad t_n = \varepsilon^n t;$
3. Expand derivatives : $\frac{d}{dt} \rightarrow \frac{\partial}{\partial t_0} + \varepsilon \frac{\partial}{\partial t_1} + \varepsilon^2 \frac{\partial}{\partial t_2} \ldots;$
4. Expand unknowns : $a(t) \rightarrow \langle a \rangle (t_1, t_2, \ldots)[1 + \varepsilon a_1 + \ldots];$
5. Search for periodic solutions with respect to the 'fast' time, t_0;
6. Solve diffusion problems for complex amplitudes and find complex amplitudes of the fluxes;
7. Obtain right hand side vector in the matrix equation for complex amplitudes at the m – th order of approximation :

$$\mathbf{L}_n \mathbf{X}^0_{mn} = \mathbf{F}^0_{mn}, \quad n = 0,1,2, \quad m = 1,2,$$

8. Derive equations for the average bubble size/position from the solvability conditions :

$$\frac{\partial \langle a \rangle}{\partial t_2} = F(\langle a \rangle) \sin^2 k \langle x_b \rangle - G(\langle a \rangle), \quad \frac{\partial^2 \langle x_b \rangle}{\partial t_2^2} = E\left(\langle a \rangle, \langle x_b \rangle, \frac{\partial \langle x_b \rangle}{\partial t_2} \right)$$

9. Investigate the influence of β on solution of these equation.

ENGINEERING OF NOVEL BIOCOLLOID SUSPENSIONS

D.A. Hammer, S. Rodgers, A. Hiddessen
Department of Chemical Engineering
University of Pennsylvania

D.A. Weitz
Department of Physics
University of Pennsylvania

Please refer to the Conference Book of Abstracts or the NCMR Website at
http://www.ncmr.org

SONOLUMINESCENCE IN SPACE: THE CRITICAL ROLE OF BUOYANCY IN STABILITY AND EMISSION MECHANISMS

R. Glynn Holt (rgholt@bu.edu) and Ronald A. Roy (ronroy@bu.edu), Boston University, Dept. of Aerospace and Mechanical Engineering, 110 Cummington St, Boston, MA 02215

INTRODUCTION

Sonoluminescence ("light from sound") is the result of extremely nonlinear pulsations of gas/vapor bubbles in liquids when subject to sufficiently high amplitude acoustic pressures. In a single collapse, a bubble's volume can be compressed more than a thousand-fold in the span of less than a microsecond. Even the simplest consideration of the thermodynamics yields pressures on the order of 10,000 ATM. and temperatures of at least 10,000K. On the face of things, it is not surprising that light should be emitted from such an extreme process. For a general review of some of the remarkable experimental results issuing from the study of sonoluminescence in acoustically levitated bubbles we refer to a number of articles [Roy 1994; Crum 1994; Crum & Roy 1994; Putterman 1995] The phenomenon has achieved prominence in the public eye [Browne, 1996; Glanz, 1996; Knight, 1996]. The increase in scientific interest can be gauged by noting that, while as recently as 1990 (the year after Gaitan discovered light from a single bubble) there were 4 SL-related articles in refereed journals, this number increased to 13 in 1995, 24 in 1996, 31 in 1997, and 14 refereed journal articles have already appeared in 1998!

Experiments [Gaitan et al. 1992a,b, 1997; Barber et al. 1991, 1992, 1994; Hiller et al. 1992, 1994; Holt et al. 1994, 1996; Löfstedt et al. 1995; Matula et al. 1995, 1996, 1997a,b,c,d; Lepoint et al. 1997, among others] have uncovered the existence of many unexplained features surrounding the observation of sonoluminescence. Of these, we have identified four which are fundamental, and in which gravity plays (or is predicted by theory to play) a critical role. These are:

- the light emission mechanism itself,
- the mechanism for anomalous mass flux stability,
- the disappearance of the bubble at some critical acoustic pressure, and
- the appearance of quasiperiodic and chaotic oscillations in the flash timing.

Gravity, in the context of buoyancy, is implicated in all four of these unexplained phenomena.

PROBLEM STATEMENT

The scientific objectives of the planned research are:

(1) To test the predictions of the fractoluminescence light emission theory of single bubble sonoluminescence [Prosperetti 1997] which relies on the asymmetry induced by buoyancy-induced translatory oscillations to postulate that a jet forms during the final stages of bubble collapse. This hypothesized jet shoots through the bubble interior and makes contact with opposite bubble wall at near Mach speeds and 'fractures' the water, with resultant light emission. Vortices in the liquid carry off excess linear momentum [Longuet-Higgins 1996], so that the process can repeat the next acoustic cycle. This theory has many specific predictions, which can be summarized here by noting that, if gravity is reduced to the ambient orbital level of 10^{-5} g, then this theory would predict a completely different picture of the parameter space and its regions of stability and light emission than the one which has recently been uncovered in 1g experimentation [Holt and Gaitan, 1996, 1996a; Gaitan and Holt, 1997]. Simply by making careful measurements of the details of light emission and mechanical oscillations of bubbles in μg, where buoyancy-induced coupling of translation and oscillation motions is absent, we can definitively establish the viability of this theory.

(2) To measure the mass flux and mechanical stability boundaries which constrain the appearance of light emission in the parameter space of acoustic pressure, dissolved gas concentration and equilibrium radius. These measurements will test both the fractoluminescence and the chemical reaction/diffusion theories that model the non-diffusive anomalous mass flux observed in 1g experiments [Löfstedt et al. 1995; Holt & Gaitan 1996a]. The latter theory [Lohse et al. 1996a,b] relies on the assumption that gravitational effects are not important in the convective-diffusion treatment of mass transfer.

(3) To measure the precise values of acoustic pressure and equilibrium radius where a light-emitting bubble disappears, an unexplained phenomenon which is a ubiquitous feature of 1g experiments. The disappearance represents an upper bound on the acoustic pressure (and hence energy input to the system) which can be employed to drive the bubble oscillations. These measurements will directly test a theory [Cordry 1996; Matula et al. 1997c] which postulates that the variation in buoyant force with each acoustic cycle's expansion and contraction of the bubble leads to a loss of levitation above some critical acoustic pressure.

(4) To test whether chaotic and quasiperiodic timing of the flashes observed in 1g [Holt et al. 1994] is

due to buoyancy-induced effects or germane to the phenomenon of light emission itself. The nonlinear coupling of translational and radial motion via the buoyant force is postulated to result in quasiperiodic and chaotic modulation of the volume oscillations, but this would not occur in μg. Simultaneous monitoring of the timing of individual flashes during detuning of the system will allow us to determine the presence or absence of the nonlinear effects, and thus to prove or disprove the conjecture.

BACKGROUND

Rather than giving a comprehensive review of light emission and nonlinear bubble dynamics in general, we will use the four above features to both motivate and organize our background section. Reviews of nonlinear bubble dynamics are numerous; a compilation is available in Leighton [1994]. Since the research is so topical, no comprehensive review of competing theories for the light emission mechanism can be written. We briefly list some of the top contenders, which include electron conduction-quenched plasma [Moss et al., 1997], shock-wave mediated Bremmstrahlung [Wu & Roberts 1994], plasma discharge [Lepoint et al. 1997], superradiance [Trentalange & Pandey 1995], acoustic superresonance [Brenner et al. 1996], quantum vacuum fluctuations [Eberlein 1995], confinement of post-ionization electrons [Bernstein and Zakin 1995] and collision-induced dipole emission [Frommhold & Atchley 1994]. Other than the fractoluminescence theory discussed above, only one of these various theories for the light emission mechanism would be directly influenced by gravity, and that is the plasma discharge theory, which relies on a shape instability (Rayleigh-Taylor mechanism) to concentrate electric charge on the surface of a critical microjet that penetrates the collapsing bubble interior. The net result is "lightning" inside the bubble due to plasma discharge associated with spray electrification of the jet as it breaks up into droplets. While this theory has not gained widespread acceptance, it nevertheless has been able to explain some features of the light emission. Except to say that it remains a contender and falls under the heading of "affected by gravity", we will not discuss this theory further. In the next section, we concentrate on one theory in particular which has the potential to explain in a unified fashion many of the experimental observations.

Time-varying buoyancy: the direct effect of gravity

Consider the situation of a single air bubble in water, subject to a harmonic acoustic field which is also a standing wave. The acoustic wavelength is much larger than the bubble radius R_0 (kR_0 is small, where k is the acoustic wavenumber). On the acoustic time scale (typical acoustic periods are 50 microseconds), the bubble will contract during the compression phase of the field. The pressure and temperature will increase. During the expansion phase of the external field, the bubble expands. Thus the bubble volume, $V(t)$, can change significantly during an acoustic cycle.

An oscillating bubble in a standing pressure wave experiences a nonlinear body force dominated by the large relative compressibility between the bubble and the host fluid. The force depends on the time-average of the product of the bubble volume and the pressure gradient, known as the primary Bjerknes force [Rayleigh 1894; Bjerknes 1906; Yosioka & Kawasima 1955; Doinikov 1994]. Its functional form is $F_a \propto < V(t) \bullet \nabla P_a(r,t) >$, where <...> denotes a time-average over one acoustic cycle, and $P_a(r,t)$ is the acoustic pressure field. F_a acts in the direction of the pressure gradient of the standing wave, and thus it can balance the buoyant force and cause stable trapping of a bubble.

Finally, the bubble experiences a buoyant force $F_b = \rho g V(t)$ directed opposite the acceleration due to gravity. In practice, the fact that this force varies in time with the bubble volume is usually ignored, due to the small change in volume coupled with the inertia and drag resistance to translational motion in the liquid. Thus, one normally considers an acoustically levitated bubble to have a fixed vertical position at constant acoustic pressure which will depend on the ratio of the magnitudes of the forces F_b/F_a. However, in the parameter regimes where sonoluminescence occurs, the ratio of V_{max}/V_0 can reach 10^3 and greater, as shown in Fig. 1.

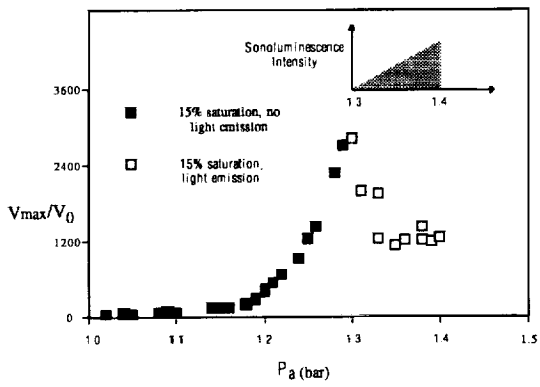

Figure 1. The measured ratio of V_{max} / V_0 for a bubble as a function of pressure. Light emission begins very near the peak value of the normalized response. The dissolved air concentration in the water was 15% of the saturation concentration at 1 atmosphere ambient pressure. The equilibrium or ambient radius varies with pressure in a complicated fashion, and is implicit in these measurements. Derived from Gaitan and Holt (1998).

The resulting ratio of F_b/F_a can vary by a factor $O(10^3)$ during a single acoustic cycle -- thus the bubble must undergo translatory oscillations driven by the time-

varying buoyant force F_b! This is a fundamental result, independent of any proposed theory for sonoluminescence. It is the basis for the fact that gravity plays a tremendously important role in these nonlinear bubble oscillations (despite that fact that a straightforward calculation of a static Bond number for earth-based levitation yields $\rho\ g(R_0)^2 / 2\sigma \sim O(10^{-7})$ for a 10 micron bubble!). The effect of gravity lies in the magnitude of the changes in F_b. The ratio F_b/F_a can be considered a coupling strength between the radius of the bubble and the position of the bubble's center of mass. Because of this nonlinear coupling, volume oscillations can drive translatory oscillations. If gravity is effectively removed, this coupling constant will become much smaller than unity, and thus its effects will virtually disappear.

INVESTIGATIVE APPROACH

Our short-term plan is to perform 1g laboratory, drop tower, and parabolic flight experiments. Certain basic questions can be answered scientifically by drop tower and parabolic flight tests. But going beyond a "light or no light" level of sophistication will require the experimentation time to change key parameters. Significant experimentation, as we have documented, has been performed in 1g leading to a rationale for an experimental design in which the critical measurables are already identified and the relevant parameters are well characterized. Since 0g experimentation time is limited, the scope of our plan is finely focused: this investigation is mainly concerned with probing mechanisms for the light emission and related mechanical stability, not with a parameter study. In the section that follows we detail the experimental plan; here, we present the plan's essential features for rapid consideration. The crucial host fluid is water. The important dissolved gases are air and argon. Controlled dissolved gas concentration must be achieved in preparation and/or storage. The acoustic system must be capable of generating controlled acoustic pressures ranging from 1/10 ATM to 3 ATM. The dissolved gas concentration must be varied, either by pre-flight preparation, in-flight preparation, or variation of the test cell's ambient pressure. Temperature must be controlled. The critical measurables and their associated method are:

- acoustic pressure versus time, $P_a(t)$
  (in situ hydrophone)
- instantaneous radius versus time, $R(t)$
  (laser light scattering)
- maximum and equilibrium radius, R_{max} & R_0
  (imaging)
- flash timing, intensity and duration
  (time-resolved photometry)
- flash spatial distribution
  (multiple coincidence detectors)

We emphasize that these are all techniques with which we have extensive experience from ground-based laboratory experimental work. This is not to say that the experiments have all been done, but that the measurements we propose are eminently feasible.

Method and Diagnostics

The experimental techniques will build on an optical scattering/acoustic levitation/imaging system used in Holt and Gaitan [1996, 1996a, 1997] and a photometric system used by Holt et al. [1994], and by Matula & Roy et al. [1997a,b]. This section will simply highlight features of the apparatus and method, as well as discuss calibration and procedures.

Figure 2. Schematic of the experimental setup.

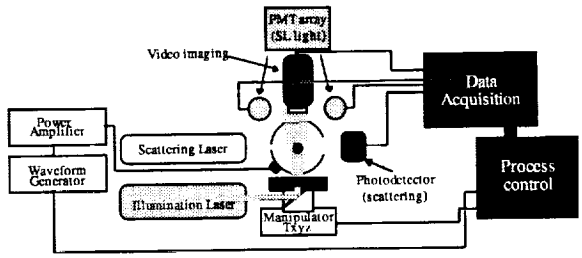

To monitor the oscillations of the bubble wall, it is illuminated by a linearly-polarized laser beam, and the scattered intensity as a function of time at a specific angle from the forward is recorded. The voltage output of a photodetector (typically a fast photodiode, but PMT's are useful for low intensity work) positioned at the aforementioned angle is the time signal of interest. For purely spherical volume oscillations, a monotonic transfer function can be theoretically derived and experimentally calibrated [Holt & Crum 1990] relating the voltage and the bubble radius R(t).

To determine the presence and nature of shape oscillations, a variety of techniques will be utilized in the manner of Holt & Gaitan [1996]. First, to detect the onset and frequency of shape oscillations, the scattered light intensity $V_{exp}(t)$ can be monitored for either a period-doubling or a rapid amplitude change [Gaitan & Holt, 1996]. Time-gating techniques can be used to provide a trigger criterion for shape oscillations coupled to the ringing oscillation after the main bubble maximum expansion. The values of acoustic pressure P_a and equilibrium radius R_0 at the onset of shape oscillations will be measured. Secondly, to determine the mode of oscillation, high-resolution, short-illumination-pulse video will be used.

High-resolution video imaging with short (<1μsec) pulse illumination will be employed to obtain mechanical response information, R_0, R_{max}, shape mode, and translational motion can all be obtained via this technique by improving on the system used by Holt

and Gaitan [1996]. Digital image processing techniques will be utilized to derive statistics from individual images.

Calibration

1. Cell pressure:

The method used to calibrate the cell pressure is outlined in Crum [1983]. A small hydro-phone will be permanently mounted inside the cell. The pressure gradient in the gravitational direction will be measured. While levitating a bubble in the cell in 1g we measure its equilibrium position with respect to the measured pressure gradient in the cell, its equilibrium radius, and the hydrophone voltage as the pressure is varied. Using the equation expressing the balance of the acoustic force and the buoyant force for small oscillations to solve for the pressure, a calibration constant can be determined from fitting techniques. It is a null method, and is very sensitive to small changes in pressure. As a check, numerical fitting of the equations of motion for small-amplitude oscillations will be performed with the calibrated photodetector output as the data to be fit by varying the acoustic pressure amplitude in the model. Gaitan & Holt [1998] have verified that, while the Rayleigh-Plesset equation cannot predict where in the P_a, R space the asymptotic equilibria exist, it can accurately predict one of the triple (P_a, R_0, R_{max}) given the other two. Thus we can calibrate in situ in 0g as well.

2. Bubble radius

The quantity $I_{exp}(R,t)$, the incident scattered light intensity falling on the photodetector, is equal to $I_0 \int\int I_{rel}(R(t))\, d\theta\, d\phi$, where the limits on the spherical angle variables θ and ϕ in the integral are determined by the particular photodetection scheme used. I_0 is the intensity incident on the bubble. I_{rel} is the normalized component of the intensity (with linear polarization parallel to the scattering plane) scattered into an angle θ from the forward. I_{rel} is calculable from Mie theory. Thus, the photodetector output $V_{exp}(R,t) = F \int\int I_{rel}(R(t))\, d\theta\, d\phi$, where F is an apparatus-dependent constant to be determined empirically.

First, a stably oscillating bubble is obtained in the cell and moved into the beam. The output voltage is monitored on an oscilloscope, and the time average is recorded. During calibration, only linearly oscillating bubbles are used, since $R_0 = \langle R(t) \rangle$ only for linear oscillations, and hence $\langle I_{exp}(R,t) \rangle = I_{exp}(R_0)$ only for linear oscillations. As soon as $V_{exp}(R_0)$ has been recorded, an independent measurement of R_0 is made by instantaneously turning the sound field off while acquiring video images [Holt & Gaitan, 1996a]. The video image can be calibrated by a known scale. The calibration constant F is then determined by taking the ratio of the experimental voltage to the relative intensity Dividing the photodiode output by F gives the experimental relative intensity, which can then be used to find the radius. In this fashion, bubble radii can be obtained to within about 4% [Holt 1989].

An alternate technique has recently been introduced [Lentz et al. 1995]. This technique relies on the angular variation in the Mie scattering, where the number and location of intensity maxima are unique for a given bubble radius (at fixed laser wavelength). Thus, an absolute determination of R is possible. While the technique is very accurate, it is much slower than the previous technique. Nevertheless, it will be a valuable independent check on the fixed-angle method, and is able to provide in situ calibration without accessing the interior of the acoustic test cell.

Procedure

We present here the generic procedures for obtaining data by varying the accessible para-meters of the system. These can be divided into two classes:

1. Mechanical parameters

P_a will be varied between 0.5 and 1.5 ATM, depending on the dissolved gas concentration, and increasing to higher pressures if the pressure for disappearance is not the same as in 1g. The practical problem this introduces in 1g, i.e. changing the position of levitation, can be addressed with feedback control on the vertical translational stage via a PC-controlled stepper mike motor. Pressure control itself will be accomplished via a PC-controlled step sequence, increasing and decreasing the pressure in a controlled fashion with operator intervention possible at every step.

R_0 will be implicitly varied via the constraints of mass flux equilibrium and shape instability. From our experience in 1g, the approximate range should be 1 - 25 microns in equilibrium radius, and 20 to 70 microns in maximum radius. This may, of course, change dramatically with the removal of buoyancy-induced translatory oscillations.

The acoustic frequency $f_d$will be fixed at the resonance of the acoustic cell; with temperature control this should remain constant. When investigating variations in flash timing, f_d will be varied no more than a few hundred Hz from the resonance frequency.

2. Material parameters

The host liquid for all experiments will be water, distilled, micro-filtered and de-ionized to 17Mohm resistivity at 20°C. Two gases will be used, air and argon. They will be dissolved in water at varying percentages of saturation with respect to 100% saturation at 760 mm-Hg ambient pressure at 20°C for air over water. Air as a mixture of gases in the proportions found at sea level will be dissolved in equilibration at ambient pressures from 400 mm Hg down to

the vapor pressure. Argon will be prepared in the same way, only the absolute pressure of the argon will reflect its partial pressure in air at sea level. Thus, argon will be dissolved in equilibration at ambient pressures from 8mm down to 3mm Hg.

Data Acquisition

The optical Mie scattering data will be the primary source for both information and triggering purposes for the other data acquisition methods. A photodiode or photomultiplier tube with a scattering laser-line bandpass filter will detect the scattered light. A calibrated system will yield both equilibrium and time-varying radius values. This signal will be digitized at 2 GS/s, and minimum 10 bit resolution, with record lengths up to 1Mb.

The Mie signal will be used to trigger a short light pulse (diode laser, superbright LED or short halogen strobe light) backlighting the bubble for obtaining high resolution video/CCD images Appropriate optical filters will be used to block out the Mie signal.

Matched photomultiplier tubes (or a mini-array) will be used to detect the sonoluminescence flashes. Flash timing circuitry will include a Constant Fraction Discriminator and Time-Amplitude Converter. Relative intensity measurements will be made using pulse height analysis with appropriate coincidence criteria, both to yield intensity as a function of parameter variation, and to detect spatial anisotropies in the emitted light.

MICROGRAVITY RATIONALE

The aspect of gravity which affects the proposed measurements is the buoyant force on the gas bubble. This is unavoidable in a material sense, since the density and compressibility contrast are required to obtain volume oscillations in an isotropic pressure field. In addition to the transla-tional oscillations discussed in the previous sections, the presence of the buoyant force (and the need to overcome it) results in: 1) a perturbation from the ideal spherical symmetry in which one would like to perform experiments; 2) a requirement of a minimum pressure below which experi-ments cannot be performed simply because the bubbles will rise to the container surface; 3) non-linear acoustic streaming, which will affect measurements of mass flux and mechanical stability.

We can quantify our discussion in the background section by considering the difference in the nonlinear coupling constant F_b/F_a in 1g and μg. To obtain simple order-of-magnitude results in this section we ignore the dependence on the relative phase of the bubble oscillation with respect to the acoustic field. The time-average ratio F_b/F_a is exactly unity on earth when the bubble is displaced above the central antinode of the standing wave acoustic field to a point where the gradient of the field is strong enough so that the forces balance -- this is the definition of acoustic levitation. As long as the volume oscillations of the bubble remain on the order of 25% or so, then the volume in the force equations $V(t)$ can be replaced by V_0, the equilibrium volume of the bubble. As is borne out in laboratory results, for these mild oscillations the bubble remains at the location given by $F_b/F_a = 1 \approx \rho\ g\ /\ K(P_a k)^2 z$, given suitable low-amplitude approximations, where K is a material constant, P is the acoustic pressure amplitude, k is the acoustic wavenumber and z is the vertical height above the antinode. Thus $z \approx \rho\ g\ /\ K(P_a k)^2$ has no time dependence and depends only on P_a for low amplitudes.

However, as Fig. 1 shows, the ratio V_{max}/V_0 for the high-amplitude oscillations during sonoluminescence can exceed 10^3. Thus in 1g the ratio of F_b/F_a can vary roughly by a factor $V_{max} / \langle V(t) \rangle \approx 10^3$ during a single acoustic cycle. This means that the gravity-induced nonlinear coupling to the translational mode will be a maximum precisely when sonoluminescence occurs!

If, however, gravity is reduced to orbital ambient levels of $< 10^{-4}$ g, this means that F_b/F_a is also reduced to $O(10^{-4})$ or less, since F_b is linear in g. Thus even in the sonoluminescence regime, the coupling strength is only of order 10^{-2}. A bubble in microgravity will thus be located almost precisely at the acoustic pressure antinode, where the field gradient is zero. The nonlinear coupling between the volume mode and translation mode is removed.

The time scales in the problem dictate the need for extended periods of low acceleration. There are, of course, very short time scales involved in the problem, such as the picosecond scale for individual sonoluminescence flash widths. However, beginning with the diffusive time scale for the growth, dissolution or equilibration of bubbles (on the order of seconds), the need for long time experiments become clear. For a given dissolved gas concentration, both mechanical and photometric data must be gathered as phenomena develop on the diffusive time scale at a constant acoustic pressure. Then the pressure must be incremented and measurements repeated while still at the same dissolved gas concentration, until the critical pressure and radius where the bubble disappears. Such a sequence, even if fully automated, could require tens of minutes.

ACKNOWLEDGEMENTS

Work supported by NASA.

REFERENCES

Barber, B.P. and Putterman, S.J., Nature 352, 318 (1991)

Barber, B.P., Hiller, R., Katshushi, A., Fetterman, H. and Putterman, S., J. Acoust. Soc. Am. 91, 3061 (1992)

Barber, B.P., C.C. Wu, R. Löfstedt, P.H. Roberts and S.J. Putterman, Phys. Rev. Lett. 72, 1380 (1994)

Bjerknes, V.F.K., Fields of Force, (Columbia, New York, 1906)

Browne, M., New York Times, 12/31 edition, C1 (1996)

Cordry, S., Ph.D. Thesis, University of Mississippi (1995)

Crum, L.A., J. Acoust. Soc. Am. 73, 116 (1983)

Crum, L.A., Physics Today 47 (9), 22 (1994)

*Crum, L.A. and Roy, R.A, Science 265, 233-234 (1994)

Doinikov, A.A., J. Fluid Mech. 267, 1 (1994)

Frommhold, L. and A.A. Atchley, Phys. Rev. Lett. 73, 2883 (1994)

Gaitan, D.F., Crum, L.A., Church, C.C. and Roy, R.A. J. Acoust. Soc. Am. 91, 3166 (1992a)

Gaitan, D.F., R.G. Holt and A.A. Atchley, J. Acoust. Soc. Am. 92 4(2), 5aPAa1, (1992b)

Gaitan, D.F. and R.G. Holt, J. Acoust. Soc. Am. 100, 4(2), 3280 (1996)

Gaitan, D.F. and R.G. Holt (in preparation, 1998)

Glanz, J., Science 274, 718 (1996)

Greenspan, H. P. and A. Nadim, Phys. Fluids 5A, 1065 (1993)

Hiller, R., S.J. Putterman and B.P. Barber, Phys. Rev. Lett. 69, 1182 (1992)

Holt, R.G., Proceedings of the 13th International Congress on Acoustics, Belgrade, P. Pravica and G. Drakulic, eds., Sava Centar, Belgrade, Volume 1, p. 131 (1989)

Holt, R. G. and L. A. Crum, Appl. Opt. 29, 4182 (1990)

Holt, R.G. and L.A. Crum, J. Acoust. Soc. Am. 91, 1924 (1992)

Holt, R.G., D.F. Gaitan, A.A. Atchley and J. Holzfuss, Phys. Rev. Lett. 72, 1376 (1994)

Holt, R.G. and D.F. Gaitan, Proceedings of the 3rd Microgravity Fluid Physics Conference, Cleveland, OH, NASA CP 3338, p. 591 (1996)

Holt, R.G. and D.F. Gaitan, Phys. Rev. Lett. 77, 3791 (1996a)

Holt, R.G., J. Holzfuss, A. Judt, A. Phillip, and S. Horsburgh, Proceedings of the 12th International Symposium on Nonlinear Acoustics, M.F. Hamilton and D.T. Blackstock, eds., Elsevier, New York, p. 497 (1990)

Knight, P., Nature 381, 736 (1996)

Leighton, T.G. The Acoustic Bubble, Academic Press, London, Chapters 4 & 5 (1994)

Löfstedt, R. et al., Phys. Rev. E 51, 4400 (1995)

Lepoint, T., De Pauw, D., Lepoint-Muillie, F., Goldman, M., Goldman, A., J. Acoust. Soc. Am. (in press 1997).

Marinesco, N. and J.J. Trillat, Proc. R. Acad. Sci. 196, 858 (1933)

Matula, T.J., R.A. Roy, P.D. Mourad, W.B. McNamara and K.S. Suslick, Phys. Rev. Lett. 75, 2602-2605 (1995)

Matula, T.J., R.A. Roy, L.A. Crum and D.L. Kuhns, J. Acoust. Soc. Am. 100, 4(2), 2717 (1996)

Matula, T.J., S.M. Cordry, R.A. Roy and L.A. Crum, J. Acoust. Soc. Am., (submitted 1997c)

Matula, T.J., Hallaj, I.M., Cleveland, R.O., Crum, L.A., Moss, W.C., Roy, R.A., J. Acoust. Soc. Am. 103, 1377 (1998)

Prosperetti, A., J. Acoust. Soc. Am. 101, 2003 (1997)

Putterman, S.J., Scientific American 272 (2), 46 (1995)

Rayleigh (J.W. Strutt), The Theory of Sound, (Dover, New York, 1945)

Roy, R.A., Ultrasonics Sonochemistry 1, 5-8 (1994)

Yosioka, K. and Y. Kawasima, Acustica 5, 167 (1955)

RHEOLOGY OF FOAM NEAR THE ORDER-DISORDER PHASE TRANSITION.

R. Glynn Holt (rgholt@bu.edu) and J. Gregory McDaniel (jgm@bu.edu), Boston University, Dept. of Aerospace and Mechanical Engineering, 110 Cummington St, Boston, MA 02215

INTRODUCTION

Foams are extremely important in a variety of industrial applications. They are widely used in fire-fighting applications, including the Fire Suppression Systems aboard the Space Shuttle and Spacelab module. The petroleum industry utilizes foams in flow applications such as enhanced oil recovery and as drilling fluids. They are used in various industries as trapping, transport and separation agents. Arguably the most important quality of a foam in many of these industrial processes is its response to imposed strain, or its rheological behavior. Yet there exists almost no experimental data on the rheological properties of real 3D foams. This is due in large part to the earth-based requirements for contact containment, and to the fact that gravity-induced drainage quickly destroys all but the "driest" foams, those with a very high gas volume fraction ϕ . We will develop a unique method to provide non-contact control and manipulation of foam samples. The development of this technique, together with experimentation in 0g, will provide the ability to carry out a set of benchmark experiments which will allow determination of a foam's yield stress, bulk modulus and viscosity as a continuous function of gas volume fraction from the dry limit ($\phi \approx 1$) through the order-disorder phase transition to the wet limit ($\phi \approx 0$) of a bubbly liquid. In addition to providing the first measurements of such quantities as functions of f to compare with theory, the knowledge gained will have practical application to the myriad actual uses of foams on the earth, and to space-based systems.

PROBLEM STATEMENT

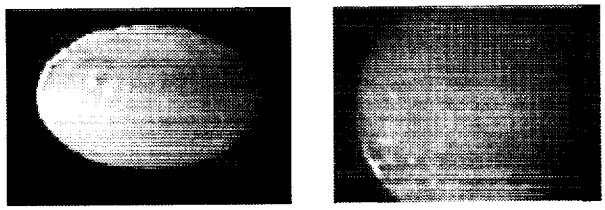

Figure 1. A side (left) and top (right) view of a foam drop approximately 0.75 cm in diameter. The drop is levitated in a 23 kHz acoustic standing wave field. Note that, while the drop is almost spherical from the top view, the high acoustic pressure required to levitate in 1g has caused significant deformation shown in the side view. Gravity acts in the vertical direction in the side view. This is a dry, fine foam.

Before we define the problem, we present the target of our investigation: a "foam drop". By this we mean a sample of foam which is not in contact with any solid boundaries. Figure 1 presents a video image of an example foam drop which is levitated in 1g in the laboratory.

The scientific objectives of the research are:

1) To develop a novel acoustic technique for measuring static and dynamic stress-response properties of foams. Foam drops (where the number of individual bubbles is very large) will be levitated in 1g in an acoustic field, and then manipulated via the acoustic and hydrostatic forces acting on the drop. In this way, both extensional shear strain and pure dilatational strain can be applied in a controlled fashion. Both stress/strain behavior (elastic modulus, yield stress) and effective bulk shear viscosity for foams as a function of gas volume fraction, foam coarseness, and material composition will be measured. The 1g limit of volume fraction for useful experimentation will be determined, and microgravity experiments will be designed to enable these measurements to be made down to and through the order-disorder phase transition (where a foam loses its rigidity) in volume fraction.

2) To model the response of foam drops to static and time-varying modulation of the acoustic field and the ambient pressure. The purpose of the modelling will be to relate three fundamentally important rheological properties, the yield stress, the bulk elastic modulus, and the effective bulk shear viscosity, to physical observables under the two strain conditions encountered in experiments. We will treat the foam as a lumped-element continuum with a known imposed average velocity field. The quasi-static response will allow direct determination of the yield stress. By developing expressions for frequency and damping of modal oscillations of foam drops, we can infer bulk modulus and viscosity. A variety of algorithms, such as the matrix pencil method [Sarkar and Pereira, 1995] and the total least swuares Prony method [Golub and Van Loan, 1980] will be assessed to extract lumped parameters from the transient data.

3) To define experiments which can be performed in the extended μg environment, where the effects of drainage and high acoustic fields can be avoided. The ultimate goal of this project is to determine physical properties as functions of the volume fraction. Theory predicts (at least for 2D) that several phenomena become apparent only near the order-disorder phase transition, where the individual bubbles in the foam can be considered to become weakly interacting. The technique developed in objective 1 above, coupled with the lack of 1g drainage, could provide definitive measurements of elasticity and viscosity as functions of the volume fraction for 3D foams, and

confirm some predictions of 2D theoretical work, while providing motivation for 3D theoretical work.

BACKGROUND

A foam is a very complex entity to study. At the outset, the would-be researcher is presented with the problem of multiple spatial scales. It is a two-phase composition, and the liquid phase is also a multicomponent material, which immediately suggests that any study of dynamical response properties will have to take into account multiple time scales. Such a problem might at first suggest that a detailed microscopic analysis would be in order. And yet, a foam's practical and physical importance depends on its macrosopic properties. Engineers would like to know how a foam responds to an applied strain. What are the regimes of elastic vs plastic response, and how do they vary with compositional parameters? Physicists would like to know the scaling properties in the asymptotic limits of large cell number and large times. Is the evolution of such a non-equilibrium system robust with respect to perturbations in either compositional parameters or external forces? Answering these questions entails measurements of a foam's gross properties, both topological (cell size distribution, average area, etc.) and physicochemical (bulk shear viscosity, bulk modulus, and so on). It is this crucial gap in current rheological knowledge which we seek to fill.

Foams on earth are notoriously difficult to work with. In fact, two fundamental processes, diffusion-driven coarsening ("aging") and gravity-driven drainage, ensure that a sufficient time (on the order of minutes) after the creation of a typical fresh foam, one is no longer dealing with the same substance either topologically or rheologically. Apart from some measurements of 2D rheology which are complicated by the effects of method-dependent wall-slip, the 3D rheology of foams remains largely unknown.

However, as Kraynik (1988) understatedly points out, despite the gaps in our understanding of foams, their practical uses in industrial processes "...have not been completely inhibited by unresolved fundamental issues." Foams are of tremendous economical importance in industry. Foams are widely used in firefighting applications, and are especially effective in fighting flammable liquid fires. In fact the Fire Suppression System aboard the Space Shuttle utilizes cylinders of Halon foam, which, when fired, force a rapidly expanding foam into the convoluted spaces behind instrument panels. Foams are critical in the process of enhanced oil recovery (Edwards et al. 1991; Stebe and Maldarelli, 1994), due to their surface-active and highly viscous nature. They are also used as drilling fluids in underpressurized geologic formations. They are used as transport agents, and as trapping agents. They are also used as separation agents, where ore refinement is accomplished by froth flotation of the typically lighter and hydrophobic contaminants. See Aubert et al. (1986) for a review of some popular applications.

Foams also serve as model disordered systems far from equilibrium (Berge et al., 1990; Bak, et al. 1987; Stine, et al. 1990; Weaire and Rivier, 1984). The statistics of such systems, where thermodynamic equilibrium arguments do not apply, is thought to be governed by a "self-organized criticality", which can often be characterized by some multifractal scaling analysis. Whether or not this is the case for foams seems to depend upon both the volume fraction, the material, and the strain history (Weaire and Kermode, 1984). The macroscopic rheological properties which are of interest in this study will, in general, depend on the structure: a fractal foam will possess a different elastic modulus from one possessing a unimodal size distribution (Herdtle and Aref, 1992).

BASICS

We must briefly introduce some basics (a comprehensive review of fundamental ideas can be found in the textbook by Edwards, et al., 1991; and, see Kraynik, 1988 for a technical overview). The fundamental unit of a foam is a gas pocket contained by a thin liquid shell. The close proximity of many such gas "cells" or "bubbles" connected by their liquid shells constitutes an elementary foam. The thin interbubble films meet at fluid vertices known as Plateau borders. The capillary pressure in the borders is balanced by the so-called disjoining pressure in the thin film region. The liquid shell is quasi-stabilized against rapid dissolution and coalescence of the bubbles by the presence of one or more surfactant species, which hinder gas diffusion and thinning flows at the interbubble boundaries. Thus the surface rheology peculiar to surfactants (especially soluble ones) will be intimately involved in both the static and dynamic mechanical properties of the macroscopic foam.

The fundamental descriptive parameter of a macroscopic foam is the gas volume fraction ϕ . A "dry" foam is approached in the limit as $\phi \rightarrow 1.0$. A "wet" foam, thus, is the descriptor of decreasing volume fraction. A critical transition occurs as ϕ is decreased to the order-disorder phase transition (or rigidity-loss transition). As the term implies, the foam will cease to be rigid and ordered structurally, and will flow freely, becoming a bubbly liquid, as ϕ approaches and passes this value. This critical value, ϕ_c, which will differ slightly for different compositions (and should also be a strain-rate dependent quantity), is related (although as yet only informally) to the value for crystal/random close-packing of hard sphere models ($\phi_c = 0.74$ or 0.63, respectively, for 2D and 3D). Just as the order-disorder transition for hard-sphere models engenders changes (and sometimes discontinuities) in the mechanical and thermodynamical properties of the

matter, so the rigidity-loss transition is the boundary of qualitative and quantitative changes in macroscopic foam properties.

The most obvious of these physical and rheological properties is the yield stress, τ_0, which classically represents the transition from elastic to plastic response to applied strain in solids. The yield stress for a foam does not even exist until the volume fraction exceeds ϕ_c, and is an increasing function of ϕ thereafter. Likewise, the shear elastic modulus G, does not exist for a fluid, and only starts to exist and increase as ϕ is increased beyond ϕ_c. The dilatational elastic modulus Gd will depend on both the topology of the foam and the surface elasticity (both intrinsic and Gibb's (see Edwards et al., 1991)), which will be material dependent. The bulk shear viscosity at gas volume fractions below ϕ_c is dominated by the bulk shear viscosity of the host liquid, with only minor perturbations due to the presence of surfactants and bubbles in the bulk. But the effective bulk shear viscosity, μ_e, of a foam beyond ϕ_c is dominated by the effects of surfactant-induced surface viscosities, and topological structure and processes. The effective foam dilatational viscosity κ, which will be a measure of purely dilatational flow dissipation, will be an important quantity with which to quantify the effects of different surfactant materials, since in pure dilatational motion, no topological processes will occur.

INVESTIGATIVE APPROACH

Experimental Methods

For 1g and mg (parabolic aircraft flights) experiments, we will use acoustic levitation techniques for positioning and induction of extensional shear strain (the techniques will have to be modified somewhat for mg, since only small positioning forces will be required). The basic method is one which has been developed by Trinh and coworkers (Trinh, 1986; Trinh and Hsu, (1986a and 1986b)) and extended by Tian et al., 1995 and Holt et al. 1997. Pure dilatational strain will be applied to a levitated sample by varying (as a step function and periodically) the ambient (hydrostatic) pressure. Sample deformation will be measured via an optical extinction technique and via video techniques (Trinh, Holt and Thiessen, 1996). This section will highlight features of the apparatus and method. We will also discuss diagnostic measurements necessary to characterize our foam samples.

Figure 2 presents the salient features of an acoustic levitation apparatus. This technique has been successfully used to perform liquid drop experiments in air (Marston and Apfel, 1979; Tian et al., 1993). A single foam 'drop' will be levitated in air. The foam drop is acoustically levitated in a doubly resonant standing wave pressure field in the air gap between the horn and the reflector. The acoustic pressure is varied sinusoidally at approximately 20 kHz. Nonlinear radiation pressure serves to hold the foam in a fixed position slightly above a pressure node, where the buoyant force is balanced (Doinikov, 1994). In practice, this limits the upper range of foam drop radii to 1 cm at an operating frequency around 20 kHz, and correspondingly larger at lower frequencies.

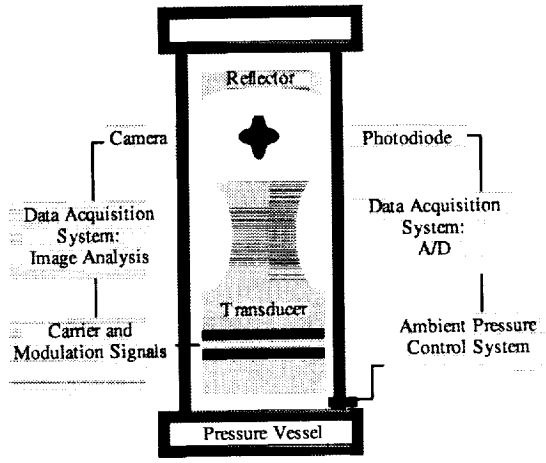

Figure 2. Schematic of a foam drop levitator enclosed in a pressure vessel.

The foam drops we will levitate will be comparable in size to the acoustic wavelength. If k is the acoustic wavenumber in air, and R_0 is the foam drop radius, then the size parameter kR_0 will be of order 10^{-1}. For these values of kR_0, the time-average acoustic radiation pressure (which is responsible for balancing the gravitational force) is distributed non-uniformly over the bubble surface (Marston (1980); Marston et al. (1981); Tian et al. (1993)). By varying the acoustic pressure amplitude P_a, we can vary the magnitude of the imposed strain, which is axisymmetric and approximately extensional shear (Weaire and Kermode, 1984). The amplitude can be varied as a step function, quasi-statically, or be periodically modulated, without affecting stable levitation of the drop. The frequency of the modulation will be swept to find the fundamental resonance of the quadrupole eigenmode (with respect to the velocity field, where there exist 4 velocity nodes) This fundamental, lowest energy shape oscillation mode can be described spatially by the order 2 axisymmetric spherical harmonic function $Y_{mn} = Y_{02}(\theta,\phi)$ with a time-varying amplitude coefficient. Figure 3 shows a levitated foam drop in 1g undergoing quadrupole modal oscillations. The foam was created by bubbling air into a solution of water and Kodak Photoflo. The resonance frequency of the quadrupole mode was approximately 150 Hz.

The imposition of pure dilatational strain will be accomplished by varying the ambient pressure of a containment chamber surrounding the acoustic levitation apparatus. This can be effected because the foam will possess a capillary overpressure $P_c = 2\sigma\ S/V$ due to surface tension. By varying the ambient pressure P_0

the equilibrium ratio S/V will change, and the foam drop will either expand or contract in response. P_0 can be varied as a step function, quasi-statically, or be periodically modulated, although this will affect the levitation conditions somewhat.

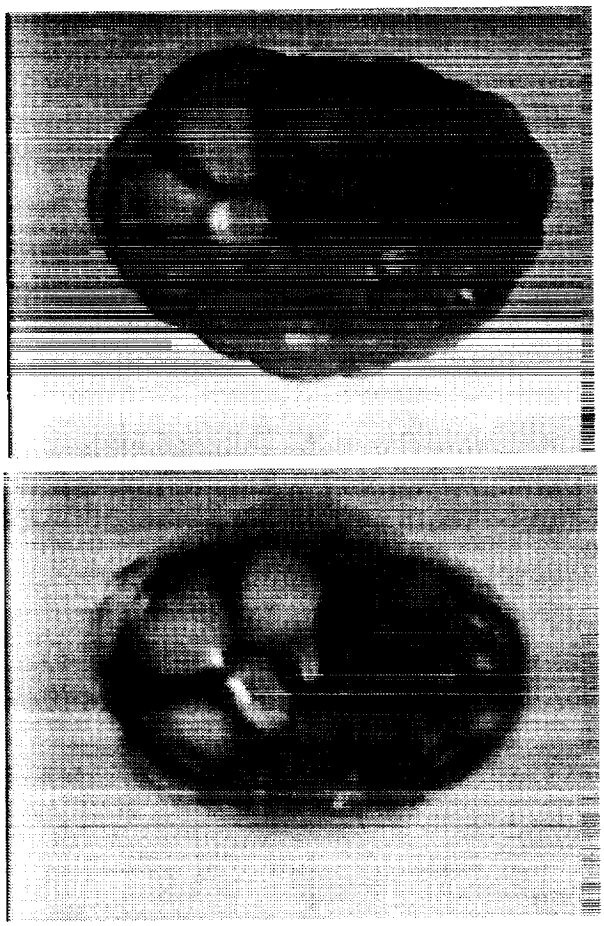

Figure 3. A coarse foam drop levitated in an apparatus similar to Fig. 2. On the top, the drop is levitated but not modulated. The modulation frequency was swept until a resonant maximum in the response was observed at approximately 150 Hz for this drop. The drop on the bottom depicts the time-averaged (the shutter speed was 1/60 sec) quadrupole (n = 2) oscillations of the drop.

Our primary observables for the experiments will be the drop shape (and its deformation) and volume as a function of time. These will yield relaxation, frequency and damping quantities, depending on the temporal nature of the applied strain. Regardless of the type of strain imposed, deformation information can be obtained in two complementary ways. Time and space resolved video images will yield the full surface outline of the drop. Thus, absolute spatial deformation can be measured, and temporally resolved up to a Nyquist frequency of 15 Hz. Digital image processing techniques will be used (Trinh et al., 1994) to automatically acquire and obtain geometrical measurements on sequences of images, typically with 100 micron resolution. For the oscillatory measurements, an optical extinction method (Tian et al., 1995) can be used to obtain frequency and amplitude information which requires much less digital storage space and post-processing. The Nyquist frequency will be upwards of 100 kHz for this type of data collection, which will be easily enough dynamic range.

Diagnostics

Several characterization measurements must be made in order to tie rheological behavior to both topological and material parameters. These are not as straightforward as one might hope, and so we must explore, modify and customize existing techniques, as well as perhaps invent new ones. In this sub-section, therefore, we will present viable candidates for such measurements, but note at the outset that these may not be the only ones we will ultimately use.

The most important topological parameter which must be reliably measured and controlled is the volume fraction ϕ . A direct measurement in a 3D configuration is only possible in the small component limit, where a video tomography measurement could be used (Thomas et al., 1995). A direct measurement in a 2D configuration is possible. The foam sample could be confined between two transparent plates, and the 2D image could thus be analyzed directly (Glazier et al., 1987; Khan et al., 1988). Capillary wetting could be minimized in order to avoid an underestimate of the liquid present.

Several indirect methods also suggest themselves. ϕ is related to the surface/volume ratio S/V, which is related to the capillary pressure via the surface tension. Thus, a measurement of the capillary pressure via either the monopole (dilatational) oscillation mode frequency, or directly by monitoring decomposition in a closed cell (Stamenovic and Wilson, 1984).

The distribution of cell radii or area $P(a)$ is also important: from such a measurement, the order parameter m_2 could also be determined. $P(a)$ could be measured directly using the above mentioned methods of tomography or spreading between plates. The temporal variation of $P(a)$, and hence also of $\langle a \rangle$ (and thus the scaling, if it is present) could be determined using an optical scattering technique developed by Durian et al. (1991).

The fluid material composition and surface rheology must also be determined. Compositional concentration of surfactants will be controlled in production, but relevant surface rheological parameters must be measured. The time-dependent surface tension can be measured via digital pendant-drop tensiometry (Lin, McKeigue and Maldarelli, 1990), which we currently employ as a fluid diagnostic in our lab. Surface (Gibbs') elasticity and viscosity can be inferred via a liquid drop oscillational method (Tian et al. 1995)

which can utilize the same levitation apparatus as the foams.

Our current plans call for the host fluid to be water. Candidates for surfactant materials which have well-studied surface properties include non-ionic polethoxy types (Triton-X-100, for example, Brij series, Tween series), proteins (BSA), and certain ionic types (SDS, anionic; DTAB, CTAB, cationic). Alcohols such as decanol and pentanol are often used, although an alcohol in water alone will not produce a stable foam. In order to compare to some previous measurements, some complicated formulae will also be used: glycerine/water and sodium oleate (Sun et al., 1994); decanol, butyl alcohol, water, polyethylene oxide, and Witconate AOK (Khan et al., 1988). It will be important to establish a connection to these earlier results.

Procedure

Foam production

There exist many ways to obtain foams of varying size distribution, material composition, and volume fraction. Bubbling (whether active or passive) a gas through the liquid phase is a way to obtain a relatively coarse foam. Forcing flow through a cellular lattice or packed column is a popular method to obtain fairly fine foams. Air-aspirated generation, where the liquid phase is sprayed onto a more or less fine mechanical grid, is a good technique for producing very dry foams. Forced pipe flow in small diameter tubes (Khan et al., 1988) is a good way to vary the volume fraction by varying the tube diameter. Ultrasonic agitation of the liquid phase is a final way to obtain a fairly polydisperse size distribution foam. For our purposes, many of these methods will be employed in order to obtain the characteristics we need. Once obtained, the foam sample must be shaped in a nearly spherical form. The sample must then be successfully transferred to the trapping region of the acoustic field.

Variation of parameters

The levitating pressure will be varied between approximately 150 dB and 170 dB. Suppressed carrier modulation will be used to periodically modulate the levitation field, thus minimizing the oscillation (present in simple AM) of levitation position. Modulation frequencies will range from 1 to 500 Hz. After initial location of modal frequencies, computer-controlled pressure-frequency schedules will be initiated to obtain response curves as the frequency is swept. The ambient or hydrostatic pressure will be varied from 0.5 atm to 1.5 atm (the lower limit is determined by levitation stability in the reduced pressure).

For each of the above experiments, the effect of varying the concentration of one surfactant component will be investigated. Since these will be well-characterized surfactants, we will be able to infer the dependences of the foam rheological properties on the surface rheological properties which will change as the concentration changes.

Finally, for all of these experiments, the volume fraction will be varied from the dry limit ($\phi = 1$) down to the minimum attainable in 1g (about 0.9 for our measurements). The increments will be fine enough to enable preliminary assessment of the functional dependence of rheological properties on ϕ .

The deformation data obtained will be analyzed digitally, as will the optical extinction data. The yield stress will be measured directly from the relaxation after a quasistatic strain variation. Elastic moduli will be obtained from step-function pressure (acoustic and ambient) variation. Elastic moduli and viscosities will be obtained from periodic pressure oscillations.

MICROGRAVITY RATIONALE

All but the driest foams drain in gravity. The liquid component will flow downward, and the bubbles will rise until a pool of liquid with a dry foam cap will form. Gravity will thus prevent the measurement of any properties as the gas volume fraction is decreased towards the order-disorder transition, because the foam will be destroyed. Even a dry foam has a finite weight. Thus, it must be supported against gravity, but preferably without container contact, whose forces can dominate. Thus, experimentation is frustrated by gravity. Acoustics in 1g can alleviate the contact problem, but at the expense of requiring intense acoustic fields causing undesirable nonlinear acoustic effects. The first of these is the resulting static deformation even at minimum trapping pressure -- a spherical equilibrium drop cannot be obtained, nor can the limit of zero strain be achieved. Secondly, at such high pressures, acoustic streaming flow occurs, which can cause uncontrolled sample rotation. This will not only hamper attempts to obtain known strain, but will have the undesirable effect of drying out the foam prematurely.

The most important control parameter for rheological experiments is the volume fraction ϕ . Yet the useful range for 1g experimentation is $\phi > 0.92$, which is well above the rigidity loss transition. The unavoidable fluid drainage destroys the essentially isotropic nature of a foam for wet foams. Imposition of slow rotation about a horizontal axis (a clinostat, see Cengel and Lemlich, 1989) can minimize drainage effects, but has only proven effective for $\phi > 0.89$, which is again well above ϕ_c. Thus, in 1g we are limited to experimentation with very dry foams.

Certainly 1g measurements are important in their own right, and indeed have already proven feasible, as shown in Fig. 2. As Kraynik has pointed out, experimental measurements, especially systematic measurements such as we envision, are sorely lacking in the literature. Thus the reporting of parameter dependences for foam rheological properties will be a valuable contribution to the knowledge of foams. In addition to their intrinsic importance, 1g measurements will set limits for parameters to be investigated in μg,

and provide bounding values for the foam rheological properties under study.

But the 1g measurements can only probe the dry foam limit. Thus, measurements of important physical phenomena near the critical volume fraction cannot be performed in 1g. The experiments require more than just a few seconds of low gravity. The time scales involved for a single frequency sweep are on the order of several minutes, and that would be just one data point! Performing rheology experiments on aging foams to study the effects of the scaling/non-scaling behavior would require times on the order of an hour or so. Thus, extended low gravity, such as aboard the Spacelab module or aboard the space station, is absolutely necessary to carry out the full range of experiments.

Thus, for all these reasons, it is desirable to perform foam rheology experiments in microgravity. The dominance of surface tension forces and the lack of a buoyant/weight force would a) guarantee an external-stress-free equilibrium condition; b) eliminate fluid drainage from the interbubble regions; and c) eliminate nonlinear effects of intense acoustic fields. A smooth variation of the volume fraction from 1.0 down through 0.63 and into the bubbly liquid limit would enable the determination of quantities which are continuous (viscosity) and discontinuous (modulus, yield stress) at ϕ_c.

ACKNOWLEDGEMENTS

RGH gratefully acknowledges discussions and assistance from EH Trinh. Work supported by NASA.

REFERENCES

Aubert, J.H., A.M. Kraynik and P.B. Rand, Sci. Am. 254, 74 (1986)

Bak, P., C. Tang and K. Wiesenfield, Phys. Rev. Lett. 59, 381 (1987)

Berge, B., A.J. Simon and A. Libchaber, Phys. Rev. A 41, 6893 (1990)

Cengel, J.D. and R. Lemlich, J. Colloid Interface Sci. 128, 608 (1989)

Derjaguin, B. and E. Obuchov, Kolloid Z. 68, 16 (1934)

Derjaguin, B. Kolloid Z. 64, 1 (1933)

Doinikov, A.A., J. Fluid Mech. 267, 1 (1994)

Durian, D.J., D.A. Weitz and D.J. Pine, Phys. Rev. A 44, R7902 (1991)

Durian, D.J., D.A. Weitz and D.J. Pine, Science 252, 686 (1991)

Edwards, D.A., H. Brenner and D.T. Wasan, J. Colloid Interface Sci. 130, 266 (1989)

Glazier, J.A., S.P. Gross and J. Stavans, Phys. Rev. A 36, 306 (1987)

Golub, G.H. and C.F. Van Loan, SIAM J. 17, 883 (1983)

Holt, RG. and E.H. Trinh, Phys. Rev. Lett. 77, 1274 (1996)

Holt, R.G., Y. Tian, J. Jankovsky and R.E. Apfel, J. Acoust. Soc. Am. 102, 3802 (1997).

Herdtle, T. and H. Aref, J. Fluid. Mech. 241, 233 (1992)

Khan, S.A., C.A. Schnepper and R.C. Armstrong, J. Rheol. 32, 69 (1988)

Kraynik, A.M., Ann. Rev. Fluid Mech. 20, 325 (1988)

Lin, S.Y., K. McKeigue and C. Maldarelli, AIChE Journal 36, 1785 (1990)

Marston, P.L. and R.E. Apfel, J. Colloid Interface Sci. 68, 280 (1979)

Marston, P.L., J. Acoust. Soc. Am. 67, 15 (1980)

Marston, P.L., S.E. LoPorto-Arione and G.L. Pullen, J. Acoust. Soc. Am. 69, 1499 (1981)

Sarkar, T.K. and O. Pereira, IEEE Antennas and Propagation Mag., 37, 48 (1995)

Stamenovic´, D. and T.A. Wilson, J. Appl. Mech. 51, 229 (1984)

Stebe, K.J. and C. Maldarelli, J. Colloid Interface Sci. 163, 177 (1994)

Stine, K.J., S.A. Rausco, B.G. Moore, J.A. Wise and C.M. Knobler, Phys. Rev. A 41, 6884 (1990)

Sun, Q., J.P. Butler, B. Suki and D. Stamenovic´, J. Colloid Interface Sci. 163, 269 (1994)

Tian, Y., R.G. Holt and R.E. Apfel, Phys. Fluids 7, 2938 (1995).

Tian, Y., R.G. Holt and R.E. Apfel, Rev. Sci. Inst. 66, 3349 (1995)

Tian, Yuren, R. Glynn Holt, and Robert E. Apfel, J. Acoust. Soc. Am. 93, 3096 (1993).

Trinh, E.H., R.G. Holt and D.B. Thiessen, Phys. Fluids 8, 43 (1996).

Trinh, E.H. and C.J. Hsu, J Acoust. Soc. Am. 79, 1335 (1986a)

Trinh, E.H. and C.J. Hsu, J Acoust. Soc. Am. 80, 1757 (1986b)

Trinh, E.H., L.G. Leal, Z.C. Feng and R.G. Holt, Proc. 2nd Microgravity Fluid Physics Conference, p. 1-1 (1994)

Trinh, E.H., P.L. Marston and J.L. Robey, J. Colloid Interface Sci. 124, 95 (1988)

Trinh, E.H., Rev. Sci. Instrum. 56, 2059 (1986)

Weaire, D. and J.P. Kermode, Phil. Mag. B 48, 245 (1983)

Weaire, D. and J.P. Kermode, Phil. Mag. B 50, 379 (1984)

Fluid Flow in An Evaporating Droplet

H. Hu and R. Larson, Department of Chem. Eng., University of Michigan,
2300 Hayward St., Ann Arbor, MI 48109.

ABSTRACT

Droplet evaporation is a common phenomenon in everyday life. For example, when a droplet of coffee or salt solution is dropped onto a surface and the droplet dries out, a ring of coffee or salt particles is left on the surface(Deegan, et al., 1997). This phenomenon exists not only in everyday life, but also in many practical industrial processes and scientific research and could also be used to assist in DNA sequence analysis, if the flow field in the droplet produced by the evaporation could be understood and predicted in detail.

In order to measure the fluid flow in a droplet, small particles can be suspended into the fluid as tracers. From the ratio of gravitational force to Brownian force $a^4 \Delta\rho g / k_B T$, we find that particle's tendency to settle is proportional to a^4(a is particle radius). So, to keep the particles from settling, the droplet size should be chosen to be in a range 0.1 -1.0μm in experiments. For such small particles, the Brownian force will affect the motion of the particle preventing accurate measurement of the flow field. This problem could be overcome by using larger particles as tracers to measure fluid flow under microgravity since the gravitational acceleration g is then very small. For larger particles, Brownian force would hardly affect the motion of the particles. Therefore, an accurate flow field could be determined from experiments in microgravity.

Deegan et al.(1997) measured the radial, height-averaged velocity distribution in an evaporating droplet and observed the formation of a ring. Their experimental results agreed well with the results of the theoretical analysis which they also carried out. Kantor(1997) also derived a velocity field using a different expression for the evaporation rate than that used by Deegan et al. Both expressions predict a height-averaged outward radial flow in an evaporating droplet. But both theories give only an expression for the radial height-averaged velocity.

In this paper, we will investigate the fluid flow in an evaporating droplet under normal gravity, and compare experiments to theories. Then, we will present our ideas about the experimental measurement of fluid flow in an evaporating droplet under microgravity.

THEORY

Let us consider a droplet on the surface, as shown in fig.1. The process of its evaporation is often divided into two phases. In the first phase, the contact angle decreases while the contact line holds its original position. In an evaporating droplet with a fixed, or pinned, contact line, the liquid must flow radially outward for the contact line to maintain its position, and the contact angle decreases with time as the droplet volume

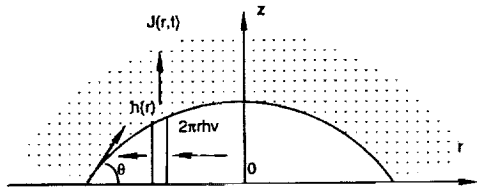

Fig. 1 A droplet on the surface

decreases. When the contact angle decreases to a critical angle, the second phase of evaporation starts. In this second phase, the contact line recedes while the contact angle remains constant(D. M. Anderson et al., 1995). The rate of decrease of the contact angle in the first phase depends on the evaporation rate of the droplet. Therefore, the evaporation of liquid induces the fluid flow in a droplet. From the theory of diffusion and a mass balance in the droplet, the relationship between the height-averaged velocity and local evaporation rate was obtained:

$$\rho\frac{\partial h}{\partial t} + \rho\frac{1}{r}\frac{\partial(rvh)}{\partial r} = -J(r,t) \qquad (1)$$

Here, the boundary condition is r=0, rvh=0. v is the height averaged velocity, $J(r,t)$ is the local evaporation rate. Deegan et al. and Kantor respectively developed their own expressions for the local evaporation rate. From the theory of Deegan et al., the local evaporation rate is:

$$J = J_o(1-r^2)^{-\lambda} \qquad (2)$$

where J_o is the evaporation rate when $\lambda = 0$, and λ controls the heterogeneity of droplet evaporation.

From the theory of Kantor, the local evaporation rate is:

$$(\hat{n} \bullet J) = \frac{A}{R}\left[2\arctan\left(e^{-\lambda'}\right)\sqrt{\sinh^2(\lambda') + \sin^2(\mu)}\right]^{-1} \qquad (3)$$

where $A = 17.28(1-H)\sqrt{T}\exp\left(\frac{-5283}{T}\right)$, H is the ambient humidity, $\delta \equiv \tan\left(\frac{\theta}{2}\right) \equiv \tanh(\lambda')$, θ is the contact angle, $\hat{n}$ is an outward-pointing normal vector at some point on the oblate surface, and λ' and μ are the parameters of the oblate spheroid, defined such that at the surface of the droplet, the r and z coordinates satisfy:

$$\frac{r^2}{(\cosh\lambda\cos\mu)^2}+\frac{z^2}{(\sinh\lambda\sin\mu)^2}=1$$

Combining (1),(2) and (3), the radial height-averaged velocity v for different theories were derived. From the theory of Deegan et al., it is:

$$v=\frac{1}{4}\frac{R}{t_f}\left[\frac{M(0)}{M(t)}\right]\tilde{r}^{-1}\left(\left(1-\tilde{r}^2\right)^{-\lambda}-\left(1-\tilde{r}^2\right)\right) \quad (4)$$

where $M(0), M(t)$ are the mass of the droplet at time 0 and time t, $\tilde{r}=r/R$ is the dimensionless radial position of a particle.

From the theory of Kantor, the radial height-averaged velocity is:

$$v=\frac{A\sqrt{1-\delta^2}}{2R\alpha\delta}\frac{1}{\tilde{r}(1-\tilde{r}^2)}\left[\frac{1+\delta^2}{1-\delta^2}\left(\sqrt{1-\tilde{r}^2(1-\delta^2)}-1\right)+\frac{1}{6\delta^4}\left(\left(\left(1-\delta^2\right)^2-2\delta^2\left(1-\tilde{r}^2\right)\right)\sqrt{\left(1+\delta^2\right)^2-4\delta^2\tilde{r}^2}-\left(1+\delta^2\right)\left(\left(1-\delta^2\right)^2-2\delta^2\right)\right)\right] \quad (5)$$

where $\alpha=\arctan\left(\sqrt{\frac{1-\delta}{1+\delta}}\right)$ and the variable δ is calculated by integrating the following equation:

$$\frac{\partial\theta}{\partial t}=-4\frac{A}{R^2}\left[\arctan\left(\sqrt{\frac{1-\delta}{1+\delta}}\right)\sqrt{1+\delta^2}\,(1+\delta^2)^2\right]^{-1}$$

$$\delta=\tan\left(\frac{\theta}{2}\right)$$

The local radial and vertical velocity v_r and v_z must satisfy the continuity equation:

$$\frac{\partial(rv_r)}{\partial r}+\frac{\partial(rv_z)}{\partial z}=0 \quad (6)$$

For the solvent with low surface tension, the droplet on the surface is flat, so the lubrication theory can be applied. This implies that the radial velocity profile is parabolic. We also take the shear stress at the droplet surface to be zero; hence $\frac{\partial v_r}{\partial z}=0$ at z=h(r). Thus,

$$v_r=A'(z-2h)z \quad (7)$$

The relation between v_r and v is therefore:

$$v_r=\frac{3}{2}v\left(\frac{2z}{h}-\frac{z^2}{h^2}\right) \quad (8)$$

Once the evaporation rate is specified, v_r and v_z are obtained by combining eqns.(4),(5),(6) and(8). From the theory of Deegan et al., they are:

$$v_r=\frac{3}{8}\frac{R}{t_f-t}\frac{1}{\tilde{r}}\left[\left(1-\tilde{r}^2\right)^{-\lambda}-\left(1-\tilde{r}^2\right)\right]\left[2\left(\frac{z}{h}\right)-\left(\frac{z}{h}\right)^2\right] \quad (9)$$

$$v_z=\frac{3}{8}\frac{R}{t_f-t}\frac{1}{\tilde{r}}\left[\lambda\left(1-\tilde{r}^2\right)^{-\lambda-1}+1\right]\left[3\left(\frac{z}{h}\right)^2-\left(\frac{z}{h}\right)^3\right] \quad (10)$$

Likewise, from Kantor's theory, the local radial and vertical velocity v_r and v_z are:

$$v_r=\frac{3A\sqrt{1-\delta^2}}{4R^2\alpha\delta}\frac{1}{\tilde{r}(1-\tilde{r}^2)}\left[\frac{1+\delta^2}{1-\delta^2}\left(\sqrt{1-\tilde{r}^2(1-\delta^2)}-1\right)+\frac{1}{6\delta^4}\left(\left(\left(1-\delta^2\right)^2-2\delta^2\left(1-\tilde{r}^2\right)\right)\sqrt{\left(1+\delta^2\right)^2-4\delta^2\tilde{r}^2}-\left(1+\delta^2\right)\left(\left(1-\delta^2\right)^2-2\delta^2\right)\right)\right]\left(\frac{2z}{h}-\frac{z^2}{h^2}\right) \quad (11)$$

$$v_z=-\frac{3A\sqrt{1-\delta^2}}{4R^2\alpha\delta}\frac{1}{(1-\tilde{r}^2)^2}\left[\frac{1+\delta^2}{1-\delta^2}\left(\frac{2-(1-\delta^2)(1+\tilde{r}^2)}{\sqrt{1-\tilde{r}^2(1-\delta^2)}}-2\right)+\frac{1}{6\delta^4}\left(2(1-\delta^2)^2\sqrt{(1+\delta^2)^2-4\delta^2\tilde{r}^2}-\frac{4\delta^2\left((1-\delta^2)^2-2\delta^2(1-\tilde{r}^2)\right)(1-\tilde{r}^2)}{\sqrt{(1+\delta^2)^2-4\delta^2\tilde{r}^2}}-2(1+\delta^2)\left((1-\delta^2)^2-2\delta^2\right)\right)\right]\left(\frac{z^2}{h}-\frac{z^3}{3h^2}\right) \quad (12)$$

EXPERIMENTS

To determine which of the above two theories more closely approximates the real behavior, we measure the velocity field in an evaporating droplet. In these experiments, fluorescent particles of diameter around 0.74μm are used as tracers to obtain the flow path lines in the droplet.

An inverted fluorescent microscope(Nikon eclipse TE 200, 40x Power objective)is used to observe particle motion in the droplet. Droplets of radius 800-1000μm are spotted onto a glass substrate using an Eppendorf pipette (adjustable volume:0.5-10μl).

In order to measure the velocity field in the droplet we constructed the simple apparatus shown in fig. 2. It is a small cell covered by a millipore membrane to slow down the evaporation rate and keep the droplet from being disturbed by air currents. The millioprc filters used contain 6×10^8 holes per cm^2 of diameter=0.15μm. Using these filters, the droplet evaporation could be slowed down enough that the droplet evaporation time t_f could be made as long as 2 to 3 hours. Such long times are needed to allow time for measuring the initial droplet position and size and to track carefully a particle position as a function of time.

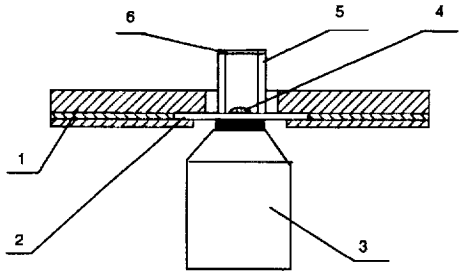

1. Support 2. Glass coverslip 3. Inverted microscope objective
4. Droplet 5. Seal Cylinder 6. Porous Membrane

Fig. 2 Experimental Apparatus

The suspension of fluorescent particles obtained from Polysciences was diluted 2000-fold to obtain a solution with a particle concentration of 125ppm. After spotting a droplet onto the coverslip and confining it in the geometry shown in fig. 2, we first measure the position of the contact line along the edge of the droplet. We then measure the air-water surface profile of the droplet at different times so that the volume vs. time can be determined. Finally, we choose a particle in the droplet and follow its motion with time, recording the particle's coordinates in the droplet at various times, yielding a three dimensional path line.

RESULTS AND ANALYSIS

1. The shape of droplet and droplet evaporation rate

Since the rate of decrease in droplet volume with time is a key parameter in the droplet evaporation models, a series of droplet profiles are measured at different times. In fig. 3, the symbols are the measured droplet surface profiles determined form the maximum vertical heights at which particles could be found at each radial position r at time t. Data could not be obtained near the center of the droplet because of the limited working distance of the objective, which did not permit viewing of the very top of the droplet. Nevertheless, enough of the profile is obtained to permit a fit by the profile expected for the droplet, namely that of a spherical cap.

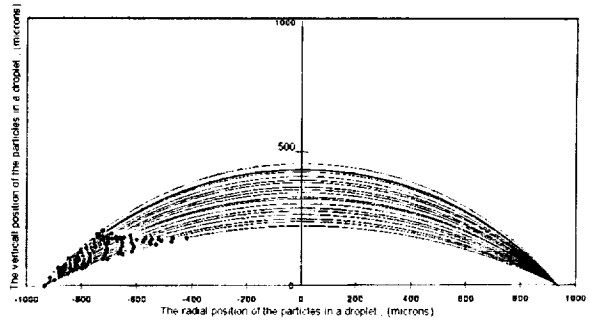

Fig. 3 The surface profiles of the droplet at different times

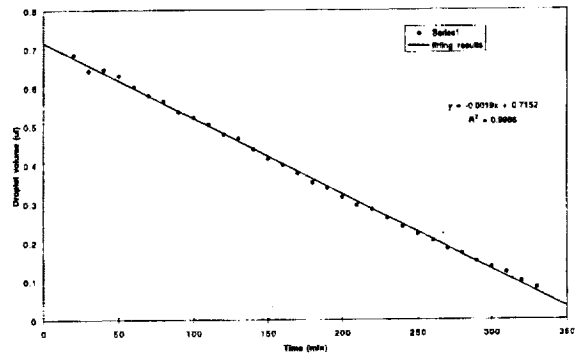

Fig. 4 The droplet volume as a function of time

The droplet volume at each time is calculated using the spherical-cap model and plotted in fig. 4. The volume of the droplet decreases linearly with time. This implies that the overall evaporation rate of the droplet is almost constant, which agrees with the theory of Deegan, et al. and the experimental results of Rowan, et al.(1995). From theory of Deegan et al., the overall evaporation rate $\dot{m}$ is:

$$\dot{m} = \frac{M(0) - M(t)}{t} = \frac{V(0) - V(t)}{t} \rho \quad (13)$$

where V(t) is the volume of the droplet at time t and ρ is the density of the solvent. So, from the experimental data of droplet volume vs. time, we can obtain the drying time, overall evaporation rate, and initial volume of the droplet by fitting experimental data with a straight line, as shown in fig.4(solid line).

The theory of Kantor predicts an overall evaporation rate that depends on contact angle as:

$$\frac{\partial V}{\partial t} = \frac{-\pi R A \sqrt{1-\delta^2}}{\alpha}, \delta \equiv \tan\left(\frac{\theta}{2}\right) \quad (14)$$

If the initial contact angle is small, eqn. (14) becomes:

$$\frac{\partial V}{\partial t} \approx -4RA\left[1 + \frac{2}{\pi}\delta + O(\delta^2)\right] \quad (15)$$

From eqn. (15), we can see that when the initial contact angle is small, Kantor's theory predicts that the overall evaporation rate will be almost constant.

2. Particle's path in the droplet.

Two typical experimental results are plotted in figs 5 and 6. The filled and open symbols are the experimental radial and vertical positions of a particle as a function of time. The radial position(open symbols) increases and the vertical position(filled symbols) decreases, showing that the particle moves toward the edge of droplet and toward the substrate as drying progresses.

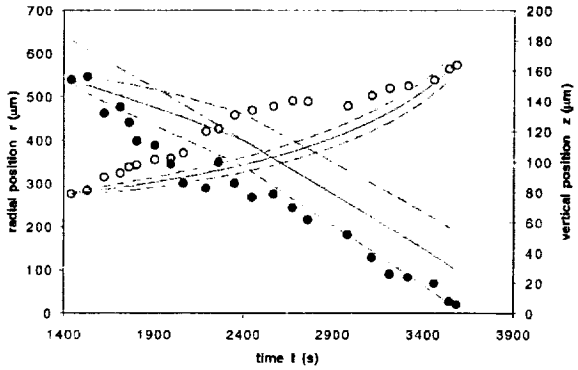

Fig. 5a The position of particle vs. time for λ=0.5 according to the theory of Deegan, et al.

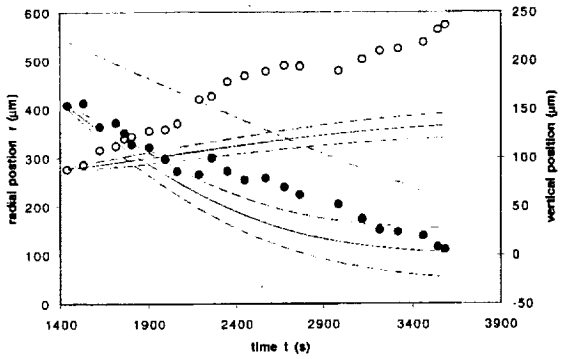

Fig. 5b The position of particle vs. time for H=0.975 according to the theory of Kantor

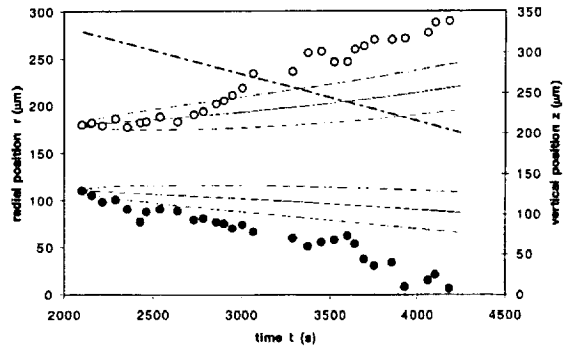

Fig. 6a The position of particle vs. time for λ=0.5 according to the theory of Deegan, et al.

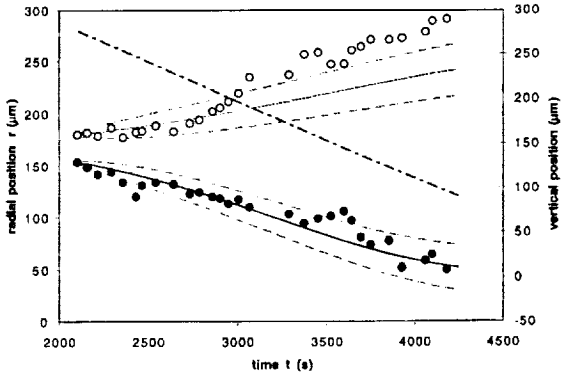

Fig. 6b The position of particle vs. time for H=0.975 according to the theory of Kantor

We also compare the experimental data with the theory of Deegan, et al. and of Kantor. Before we calculate the radial and vertical position of a particle in the droplet using the evaporation models, we must to find the parameter λ in the model of Deegan,et al. (equations 9 and 10) and the humidity H in the Kantor's model(equations 11 and 12). In order to find λ and H, we adjust λ and H so that the time for a particle in the center of the droplet, which is supposed to be fixed on the surface of the droplet, to reach the glass substrate is equal to the drying time of the droplet.

Using the fitted λ and H, we calculate the radial and vertical position of a particle in the droplet predicted by the two theories; these predictions are plotted in fig. 5 and 6. In each figure the solid line is that calculated from the theory without Brownian motion, while the dashed lines show the range of deviations expected to be produced by Brownian motion, using the theoretical diffusivity value. In general, the vertical position of the particle agrees with the prediction of both theories to within the experimental error due to Brownian motion. In one case(fig. 5), the predictions of the model of Deegan at al. are somewhat better than those of Kantor's model, while the reverse is true in fig. 6. The predictions of the radial velocity do not

agree as well with the experiments as do the predictions of the vertical velocity.

3. Additional predictions

3.1 The fluid velocity in the droplet.

From eqns. (9) to (12), we calculate the vertical and radial velocities respectively, which are plotted in figs 7 and 8 for the theory of Deegan et al. and Kantor at times 4400 sec. Here we have taken the droplet radius R to be 797μm, its height h(0) to be 365μm and the drying time t_f to be 4480 sec.. We can see the velocity fields for the two theories differ significantly. In the theory of Deegan, et al., the radial velocity is higher than in the theory of Kantor, especially near the edge of the droplet. Kantor's theory shows a higher vertical velocity than does the theory of Deegan et al., so that when the droplet is nearly dry the velocity vectors point almost completely downward; see fig. 8.

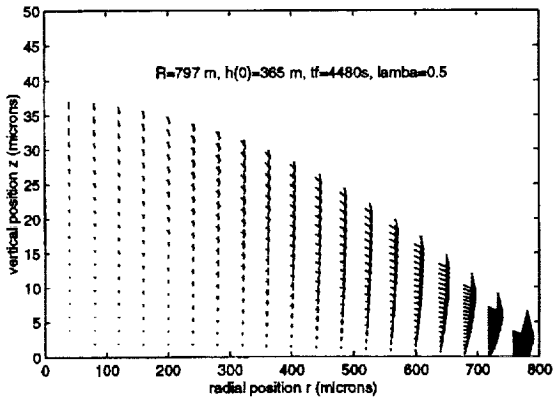

Fig. 7 The velocity field at t=4400s according to the theory of Deegan, et al.

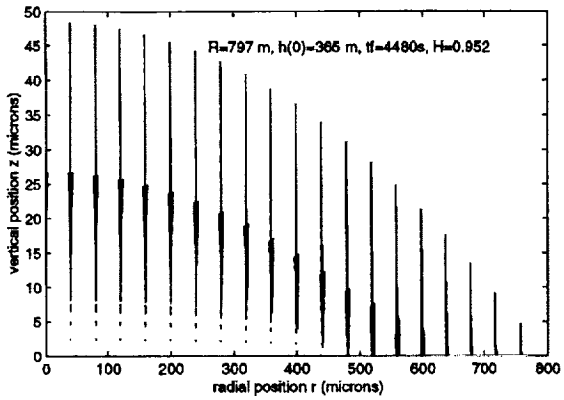

Fig. 8 The velocity field at t=4400s according to the theory of Kantor

3.2 Different evaporation conditions

By changing λ in the theory of Deegan, et al. and changing the H humidity in Kantor's theory, we can determine how the evaporation rate affects the calculated results. The results are plotted in figs. 9 to 12. In figs 9 and 10, we can see that the variation in r and z becomes larger with increasing λ. This implies that the more nonuniform the evaporation rate is, the stronger the flow is. In figs. 11 and 12, a decrease in the humidity produces an increase in the driving force for mass transfer during evaporation, and so the variations in z and r also become larger.

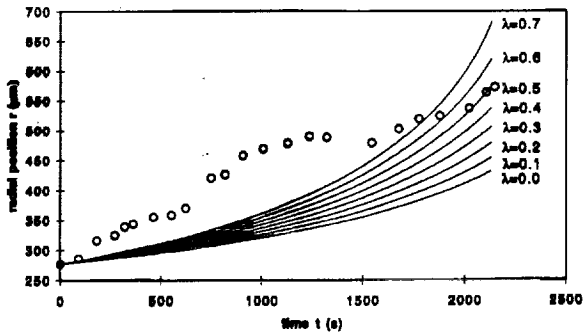

Fig. 9 The effect of λ on the time-dependent radial position of a particle

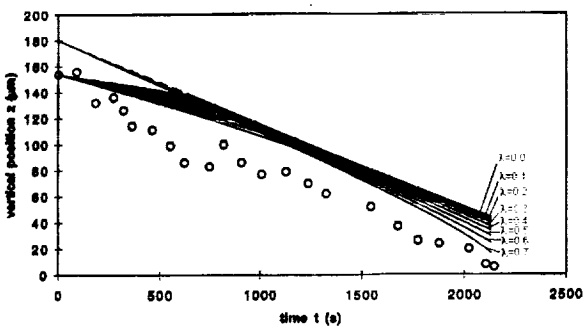

Fig. 10 The effect of λ on the time-dependent vertical(solid lines) position of a particle and the local height(dashed lines) of the droplet

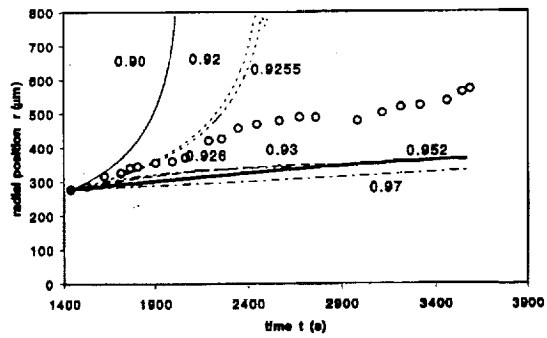

Fig. 11 The effect of humidity H on the time-dependent radial position of a particle from Kantor's theory

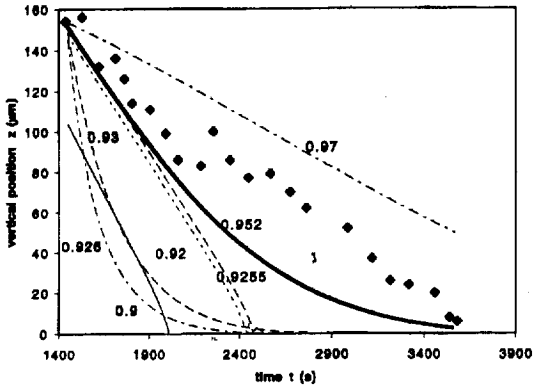

Fig. 12 The effect of humidity H on the time-dependent vertical position of a particle from Kantor's theory

CONCLUSION

1. Experimentally, the overall evaporation rate of an evaporating droplet is almost constant. This result agrees perfectly with the theory of Deegan, et al., and approximately with Kantor's theory.
2. The surface shape of droplet is that of a spherical cap.
3. The theory of Deegan et al. and that of Kantor give predictions of radial and vertical velocity that are in reasonable agreement with measured velocities, especially for the vertical velocity. A precise comparison is not yet possible, because of experimental error due to Brownian motion.
4. Near the end of the drying process, the theory of Deegan et al. predicts a much higher radial velocity than vertical velocity. For Kantor's theory, the vertical velocity is larger than the radial velocity near the end of drying.

ACKNOWLEDGE

We appreciate that NASA funds this project.

REFERENCE

1. D. M. Anderson and S. H. Davis, Phys. Fluids, 2:248(1995).

2. R. D. Deegan, O. Bakajin, T. F. Dupont, G. Huber, S. R. Nagel, T. A. Witten, Contact line deposits in an evaporation drop(to be published, 1996).

3. R. Kantor, A model of DNA Stretching in spots,(to be published, 1997).

4. S. M. Rowan, M. I. Newton, and G. McHale, J. Phys. Chem., 99:13268-13271(1995).

Gas-Particle Interactions in a Microgravity Flow Cell

Michel Louge and James Jenkins
Cornell University

NASA microgravity conference, Cleveland, OH, August 1998

Motivation:

Employ μgravity to study the essential physics of pneumatic transport without inertial fluid forces

Under Earth gravity:

- Particle entrainment requires large drag:

$$Re = \frac{u\rho d}{\mu} \sim 1.5 \left(\frac{\rho_s \rho g d^3}{\mu^2}\right)^{0.5} ;$$

for 200μm plastic spheres in air, Re ~ 30.

- The suspending gas stream is inertial:

$$Re_{pipe} \bullet 100\ Re \sim 3000.$$

- Grain agitation is not set independently.

Instead, we seek:

Random viscous fluid flow with random inertial granular flow.

Apparatus

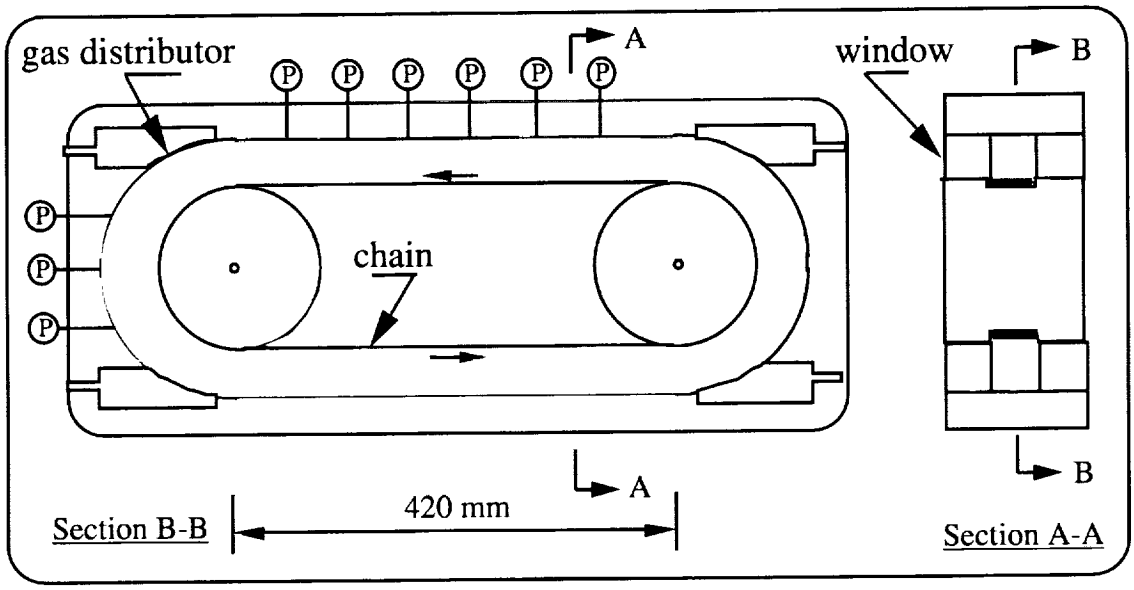

- use metal spheres to avoid electrostatics;
- closely-spaced bumps on both boundaries to energize the grains;
- measure •p to balance gas introduction;
- grains observed through windows.
- modify the existing μgSEG design;
- use smaller 1mm spheres.

Study the role of the gas

Simulations of Sangani, Mo, Tsao and Koch, *JFM* (1996).

Simple shear, no mean relative velocity, low particle Reynolds number = $\rho \gamma d^2 / \mu$.

Effects of the gas/Stokes number $St \sim \gamma \tau$ with particle relaxation time $\tau = \rho_s d^2 / 18\mu$. In our tests, the shear rate is $\gamma \sim U/Y$.

The gas affects the grains for $St < St_c \sim 23$ to 45.

For steel beads of 1mm:

U (cm/sec)	Re	St
1	0.03	10
10	0.3	90

The apparatus permits us to create values of St across the critical value St_c predicted by Sangani, Mo, Tsao and Koch.

Benefits of microgravity

- Low velocities ∅ viscous fluid flow;
- control of granular agitation;
- forces ~ ρ/ρ_s in liquid suspensions are negligible in the gas (lift, added mass, history, contact lubrication).
- use of relatively large spheres.

Applications

- mining in reduced gravity;
- flows of gas-solid processes on Earth.

Microgravity Experiments to Evaluate Electrostatic Forces in Controlling Cohesion and Adhesion of Granular Materials

J. Marshall
SETI Institute, NASA Ames Research Center, MS 239-12, Moffett Field, CA 94035; jmarshall@mail.arc.nasa.gov

M. Weislogel and **T. Jacobson**
NASA Lewis Research Center, MS 500/102, Cleveland, OH 44135

Background

- Previous microgravity experiments aboard USML-1 and -2 led to the current plan to test a fundamental hypothesis that the electrostatic behavior of dielectric grains may be strongly influenced by previously unrecognized (long-range Coulombic) dipole-dipole interactions

- In USML experiments, it was determined that a cloud of untreated dielectric sand grains always aggregates (virtually spontaneously) into filamentary structures of single-grain width, but up to tens of grains in length. Conversion from monodispersion to aggregation is driven by ***Coulombic viscosity***, and constitutes an ***electrostructural phase change*** of granular matter. Results strongly implied that grains had natural electrostatic ***dipolarity***, even though they had only random surface charges from triboelectrification.

- Electrostatic grain interactions (of long-range) are generally perceived to result only from net charge. Our current hypothesis suggests that there is another long-range electrostatic force at work.

Applications of Research

- Electrostatic **aggregation** (particularly dipole-mediated), might be pervasive and affect many types of granular systems:

  - Astrophysical-scale systems such as interstellar nebulae, protoplanetary dust and debris disks, and planetary rings

  - Planetary-scale systems such as debris palls from meteorite impact, volcanic eruptions, and aeolian dust storms

  - Industrial-scale systems in mining, powder and grain processing, pharmaceuticals, and smoke-stack technologies.

- Electrostatic **adhesion** of dust and sand on Mars is of concern because of its potentially critical importance to human exploration. Adhesion of martian surface materials will affect design and performance of spacesuits, habitats, processing plants, solar panels, and externally exposed equipment such as surface rovers or communication and weather stations.

Hypothesis

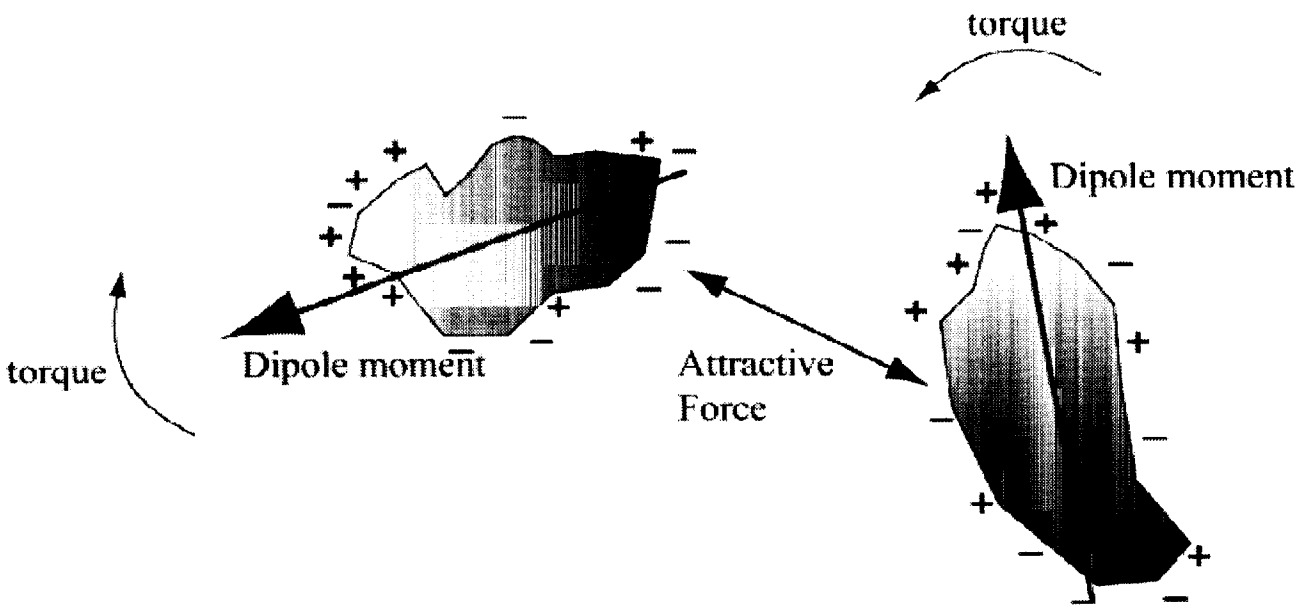

- Non-uniform distribution of charge carriers on a grain surface creates a dipole moment on the grain.
- Interaction of these dipole moments creates both a torque and an attractive force between the grains.
- No net surplus of charge carriers is required.

Microgravity Approach

How can the electrostatic character of a single grain be interrogated in a way that does not alter the parameters being measured ?

- Allow grains and aggregates to express their interactions through unconstrained motions (acceleration/drift rates, repulsions, attractions) while they are freely suspended under microgravity conditions as part of a dispersed cloud

- Induce grain/aggregate motions by controlled electrical (homogeneous & inhomogeneous) fields and variable electrical neutralization of the grain cloud

- Rotational & translational motions of filamentary aggregates are diagnostic expressions of the forces at work. Different electrostatic forces (inductive, monopole, dipole) cause different types of motion, thus enabling each force to be isolated for study

- Merit of microgravity experimentation is borne out by the fact that the dipolarity of grains was discovered in previous Space Shuttle experiments

Design Concept For Experimental Cells

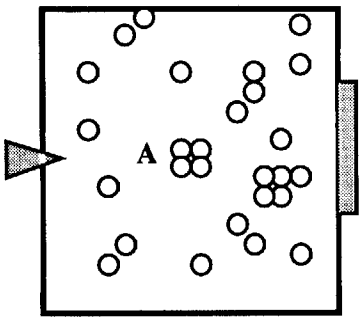

Grains neutralized

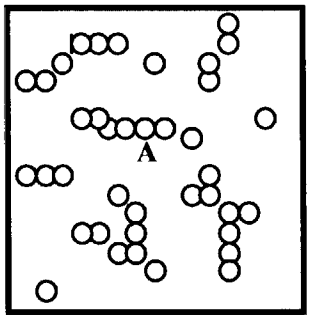

CONFIGURATION A

Van der Waal effects:

Modules fitted with AC corona only

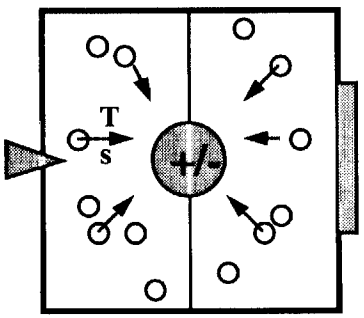

Grains neutralized

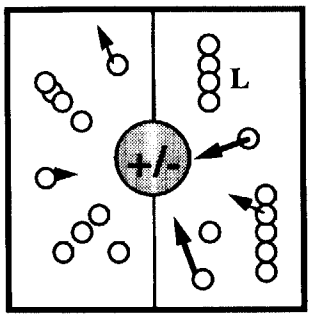

CONFIGURATION B

Dielectric induction:

Modules fitted with chargeable metal spheres (coated and uncoated) for inhomogeneous field

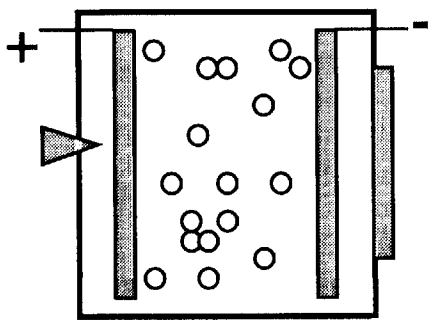

Grains neutralized

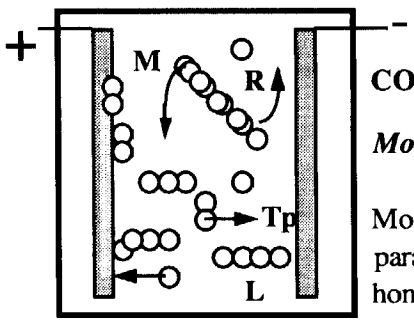

CONFIGURATION C

Monopole/dipole:

Modules fitted with parallel plates for homogeneous field

Dipole model tested by separating dipole forces from Van der Waals, dielectric polarization and monopole (net charge) effects on aggregation, and by studying charged versus neutralized grains. Electrostatic aggregates manipulated by charged surfaces to determine dipole moments reflected by induced aggregate orientations.

Experiments conducted in series of small (150 cubic cm) cells used previously in USML flights. Grains and aggregates observed by 3-D video imagery –the primary data source.

Some quantifiable parameters
R = rotation rate between plates gives dipole moment. Tp = translation rates to plates gives monopole (net charge) and charge randomness. Ts = translation rates to spheres; sigma values give randomness of charge distribution.
L = length of aggregate vs. degree of applied neutralization. A = aspect ratio (shape of aggregates) vs. degree of neutralization.
M = mass attached to a plate as function of neutralization/voltage

Investigation Strategy

Investigating the dipole model, aggregation, and related electrostatic phenomena, involves two investigative levels. The first seeks to PROVE the dipole concept and develop fundamental understanding of electrostatic processes. The second seeks to define the IMPLICATIONS of dipole effects and other aggregation phenomena through analytical and computational modeling. Both strategies currently involve activities in the following areas:

- Engineering design concepts for a microgravity experiment
- Definition of science requirements and experimental methods
- Computer modeling to explore grain behavior, and as a tool for calibration of engineering designs
- Analytical modeling to explore scientific applications of the dipole/aggregation concepts
- Corroborative laboratory experiments on grain charging as a test of dipole manifestations

Progress: Development of Analytical, Computational and Experimental Tools

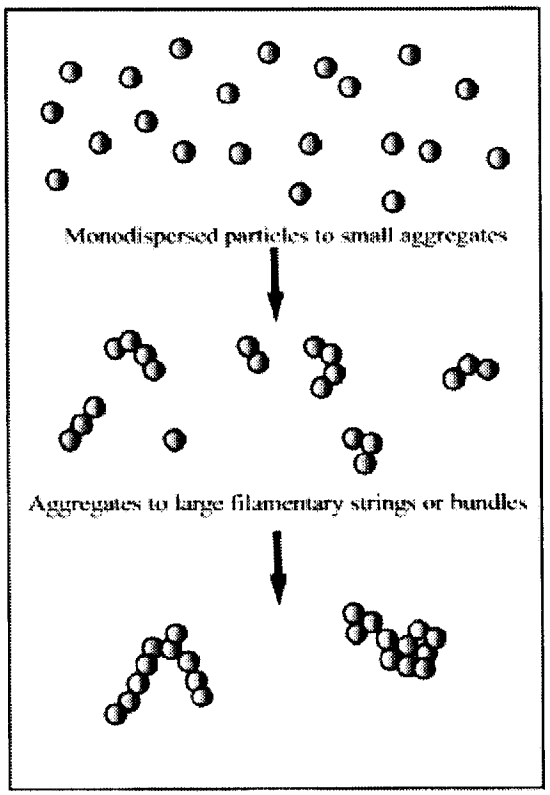

Analytical models developed for Coulombic viscosity, electro-structural phase changes, and aeolian transport.

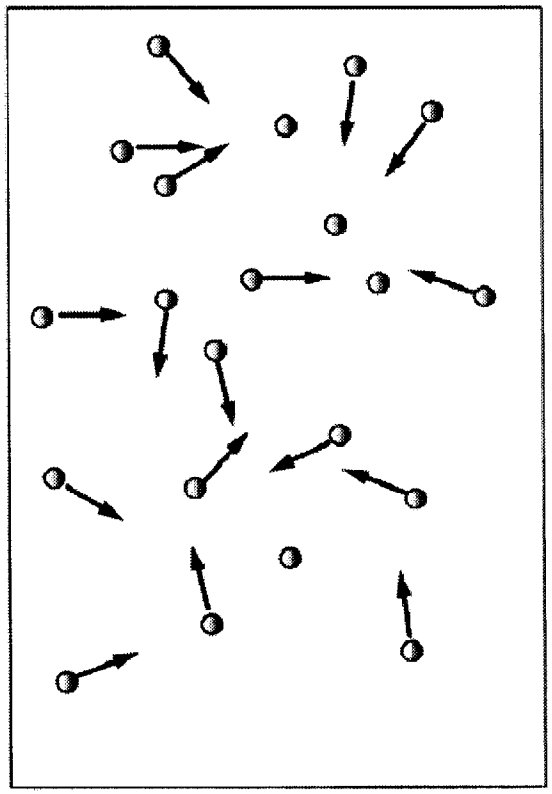

Computer models being developed for aggregation and fluidized granular flow.

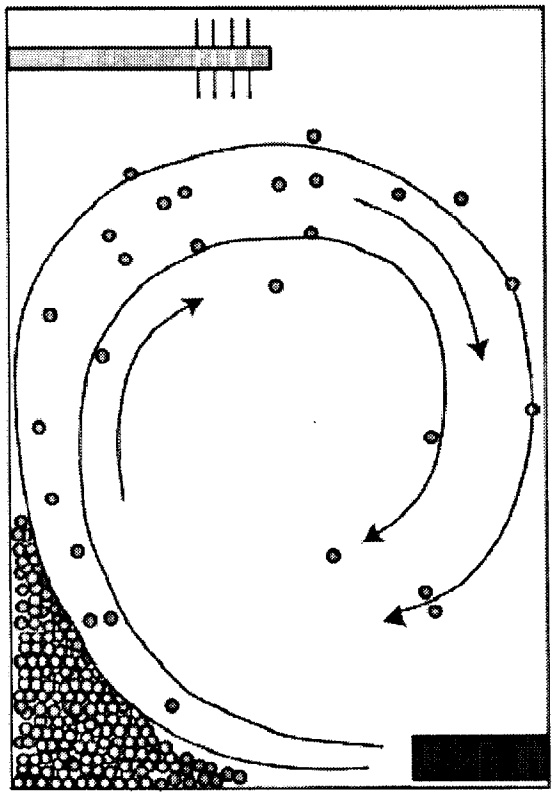

Lab experiments to measure effects of triboelectric charge saturation on grains using RF and eletrometer methods.

Progress: Science Requirements and Engineering Concepts

- At LeRC, an experiment development team has been formed to identify "tall poles" in the experiment design. In concert with the PI, the team has quantified science requirements, and will conduct proof-of-concept tests as necessary. The team will establish carrier options based on these science requirements. Several concepts have already been proposed and are being reviewed regarding automated verses crew-interactive test apparatus.

- Science data are obtained from rates of formation, drift, and rotation of aggregates which form during the experiment. The challenge for these measurements is to provide a well-characterized "electrostatically clean" test cell in which an imaging system records 3-D grain behavior. Other issues concern initial dispersion of grains, control of local cloud density, variable voltage for the aggregate "manipulators", and ability to neutralize charged grains. These issues need to be addressed in proof tests in the low-g environments of the KC-135 aircraft and drop tower experiments.

SINGLE BUBBLE SONOLUMINESCENCE IN LOW GRAVITY AND OPTICAL RADIATION PRESSURE POSITIONING OF THE BUBBLE

D. B. Thiessen, J. E. Young, M. J. Marr-Lyon, S. L. Richardson, C. D. Breckon, S. G. Douthit, P. S. Jian, W. E. Torruellas, P. L. Marston, Department of Physics, Washington State University, Pullman, WA 99164-2814; marston@wsu.edu

Principal investigator: Professor Philip L. Marston.

Co-investigator: Professor William Torruellas.

Background: Several groups of researchers have demonstrated that high frequency sound in water may be used to cause the regular repeated compression and luminescence of a small bubble of gas in a flask. The phenomena is known as single bubble sonoluminescence (SBSL). It is potentially important because light emitted by the bubble appears to be associated with a significant concentration of energy within the volume of the bubble. Unfortunately, the detailed physical mechanisms causing the radiation of light by oscillating bubbles are poorly understood and there is some evidence that carrying out experiments in a weightless environment may provide helpful clues. In addition, the radiation pressure of laser beams on the bubble may provide a way of simulating weightless experiments in the laboratory.

Goals and expected outcome: We hope to be able to distinguish between different models for the SBSL light emission process or to be able to extend the range over which stable SBSL is achievable.

Status: The investigation is being carried out in stages. In the first stage, measurements of the intensity of SBSL flashes from small bubbles in water are being carried out in the simulated weightlessness of NASA's KC-135 aircraft. A set of such measurements were recently completed by a team of WSU physics majors operating out of one of NASA's facilities in Houston Texas. The measured intensity in simulated weightlessness differ from measurements taken in ordinary and enhanced effective gravity of the accelerating aircraft. The causes of the shifts in intensity are currently being investigated. Other work is intended to partially simulate a weightlessness environment in the laboratory by using the radiation pressure of laser beams.

Timeline: This grant is for 1998-2000

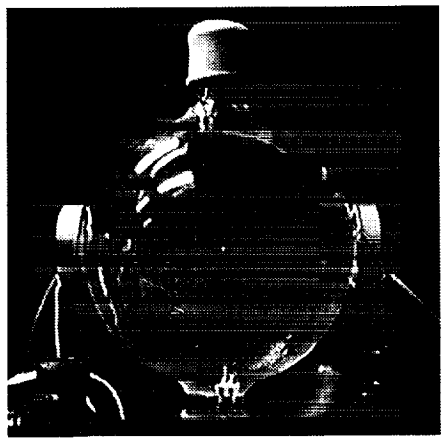

Part 1: Measurements of SBSL intensity in reduced gravity and hyper-gravity

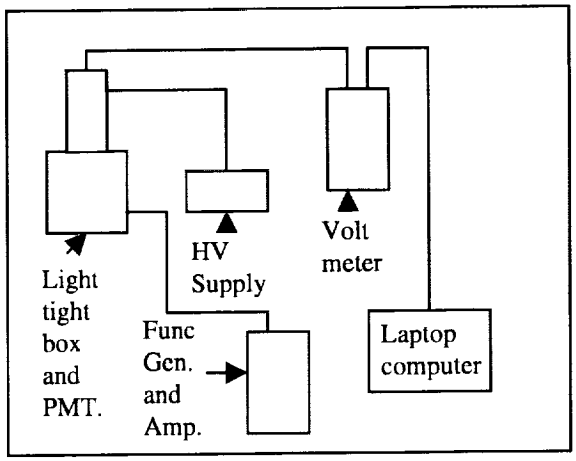

Figure 1: Diagram of SBSL apparatus flown in March 1998 on the KC-135 by WSU undergraduate physics majors J. Young, S. Richardson, C. Breckon, and S. Douthit. The effective gravitational acceleration is also recorded at the same time as the relative SBSL light intensity. Partially degassed water was used and the acoustic frequency was 34 kHz.

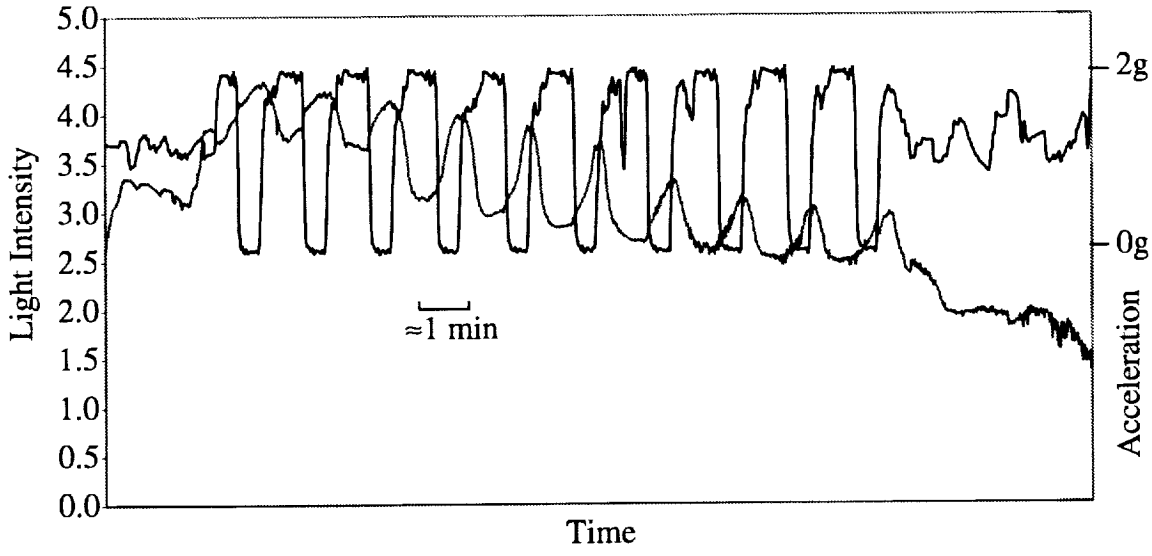

Figure 2: This figure shows the correlation between the light intensity (arbitrary units) and the effective vertical gravitational acceleration of the KC-135 aircraft.

Part 2: Optical positioning of the bubble in normal gravity

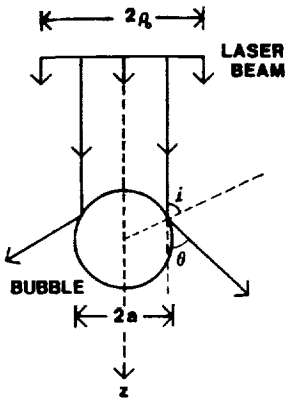

Figure 3: Idealized interaction of an optical plane wave with a bubble. Reflections are shown for two rays, each characterized by local angle of incidence i and scattering angle θ.

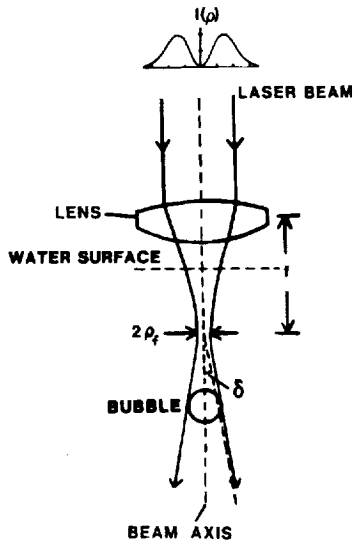

Figure 4: Optical trapping of a bubble in a focused beam with the divergence greatly exaggerated. The irradiance profile $I(\rho)$ at top is that for a pure TEM_{01}^{*} mode while, for the actual mode, the minimum in center was less pronounced.

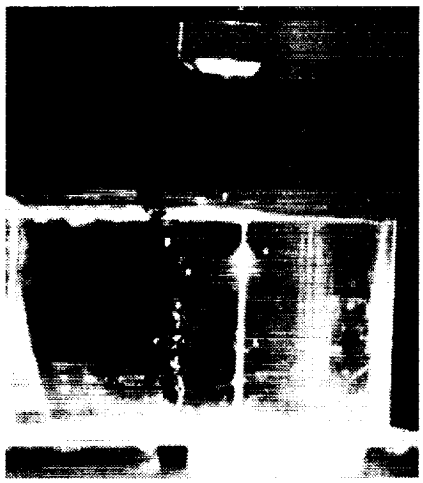

Figure 5: Photograph of a trapped bubble with $a = 15\mu m$. The beam path in the water is visible due to fluorescing and scattering in the water. The bubble is located at the top of the bright spot caused by reflection off the bubble's surface.

Bubble radius a (μm)	Beam power P (W)
10	0.11
20	0.87
30	2.93
40	6.95

Table 1: Estimated optical beam power required to levitate a bubble in water for a fixed beam radius to bubble ratio of 1.5.

Figures 3–5 and Table 1 from Unger and Marston, J. Acoust. Soc. Am. **83**, 970–975 (1988).

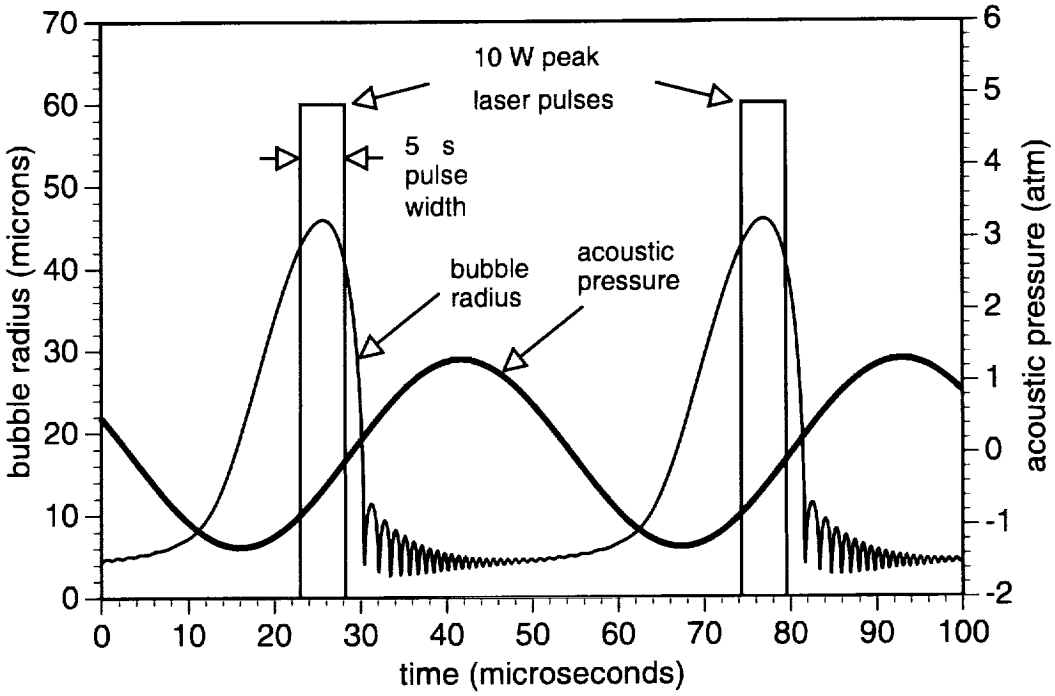

Figure 6: One of the curves shows the bubble radius as a function of time used to calculate the buoyancy and optical radiation force on an SBSL bubble. The radius-time curve is given by integrating a modified Rayleigh-Plesset equation for the indicated acoustic pressure oscillations. The power as a function of time is also shown for a laser pulse timed to coincide with the maximum bubble radius.

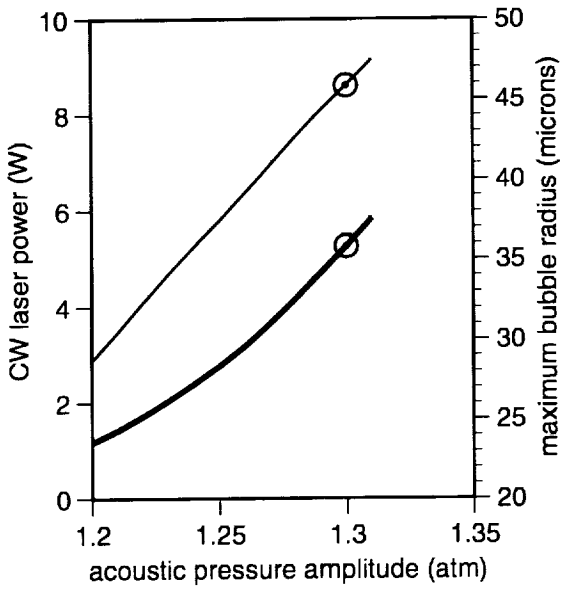

Figure 7: The upper (lighter) curve shows the maximum bubble radius calculated as a function of peak acoustic pressure where the points show the example given in Figure 6. The lower (darker) curve shows the approximate CW laser power required to counteract the average buoyancy entirely with the average optical radiation force.

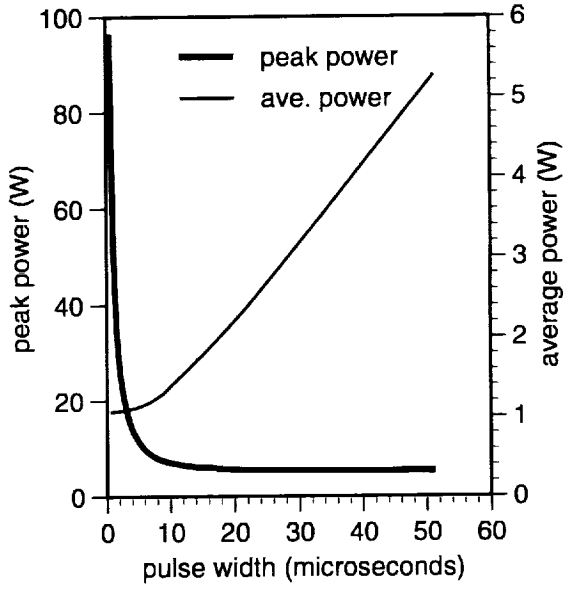

Figure 8: For the situation shown in Figure 6 the laser is pulsed as indicated. With the average optical radiation force matching the bubble buoyancy (as in Figure 7), the estimated peak and average laser powers are shown as a function of the pulse width.

AN INTERFEROMETRIC INVESTIGATION OF CONTACT LINE DYNAMICS IN SPREADING POLYMER MELTS AND SOLUTIONS

G. H. McKinley[1] and B. Ovryn[2] ,[1]Mechanical Engineering, M.I.T. Room 3 -250, 77 Massachusetts Avenue, Cambridge, MA 02139 (gareth@mit.edu) [2]Mechanical and Aerospace Engineering, Case Western Reserve University and NCMR, NASA Lewis, MS-110-3, 21000 Brookpark Road, Cleveland, Ohio, 44135 (ovryn@wave.lerc.nasa.gov)

INTRODUCTION

Moving contact-line problems in polymeric materials are encountered in many coating flows, gravity-driven drainage and in spin-coating operations where spreading arises from the combined action of gravitational and/or centrifugal body forces on a deposited droplet. Examples of industrial processes where spreading of a viscous liquid over a flat dry substrate is important include: dip-coating of sheet metal; gravity drainage of paints; spin-coating of surface layers on silicon substrates and coating of inks on paper. Typically, the polymeric material is dissolved in a low-vapor pressure solvent that evaporates increasingly rapidly as the surface area of the film increases. Achieving a spatially uniform coating requires careful control and understanding of the mechanisms that influence the radial spreading dynamics of a fluid droplet. As the mass fraction of solvent progressively decreases, the viscoelastic properties become increasingly important. The interface profile is therefore governed by an ever-changing balance between surface tension, viscous stresses and elastic stresses, and pronounced differences in the shape of the interface between Newtonian and non-Newtonian droplets have been predicted and observed experimentally.

The theoretical and experimental literature associated with the dynamics and stability of the slow {~*O*(seconds)} spreading of a viscous liquid over a flat dry substrate is extremely extensive and several excellent reviews are available (Padday, 1978; Dussan V, 1979, de Gennes, 1985). These reviews show that in addition to the bulk properties of the coating fluid (the viscosity μ and density ρ) and the equilibrium surface properties (the surface tension σ and the equilibrium contact angle θ_e) it is also important to understand the local dynamics of the motion of the contact line (or 'common line') between the liquid, the vapor and the solid substrate, typically characterized by a dynamic advancing contact angle θ_a. Application of the no-slip boundary condition of continuum fluid mechanics at the advancing contact line leads to a well-known singularity in the fluid stresses (cf. Dussan V, 1979) and it is necessary to relax this condition. Numerous methods have been proposed to deal with this singularity including (but not limited to) the possibility of local fluid slip in a microscopic region at the contact line or the existence of a thin 'precursor film' in advance of the macroscopically observable contact line (de Gennes 1985). Theoretical studies have shown how it is possible to systematically decompose the full spreading and wetting problem into a number of simpler sub-problems that are connected by matched asymptotic expansions (e.g. Goodwin & Homsy, 1991).

- In the bulk of the fluid (denoted *Region I* by Homsy & coworkers), on length scales of (typically) greater than a few microns, the slow motion of the spreading fluid film is described globally by a lubrication analysis appropriate to the geometry of interest and capillary effects are, in general, negligible since the surface is almost flat.
- In a smaller 'inner region;' (*Region II*) capillary effects become important and, in conjunction with the viscous stresses in the film, balance the imposed body force driving the spreading (e.g. the gravitational body force or angular rotation) and govern the shape of this region.
- In *Region III*, (on length scales of 100 Å and smaller) 'long range' forces (in a molecular sense) become important in the wetting of the substrate and there exists the possibility of the formation of a precursor film or local slip between the fluid and solid molecules.

We have begun the preliminary phase of a four year investigation to systematically measure the spatial and temporal evolution of surface profiles of Newtonian liquids, weakly elastic dilute polymer solutions, inelastic shear thinning fluids and oligomeric polymer melts that develop in the inner and outer regions (I, II) of the flow down an inclined plane using a recently developed phase shifted laser feedback interference microscope (Ovryn & Andrews,1998). This instrument is capable of measuring changes in the optical path–length (film thickness) with high axial precision {~*O*(nm)}, high transverse spatial resolution {~*O*(300μm)} and short temporal resolution {~*O*(ms)}. An important attribute of this interferometer is that the previous operating parameters can be achieved with minimal power deposited on a thermally sensitive liquid film {~*O*(μW/cm^2)}.

To elucidate the possible rheological behavior near the contact line, experiments will focus on a single solid substrate (polished silicon wafers) and four distinct classes of fluids; a simple viscous Newtonian reference standard, a dilute polymer solution, an inelastic shear-thinning fluid and a weakly entangled oligomeric melt. Access to a microgravity environment will ultimately be important for two reasons: (1) in the absence of centrifugal forces arising from droplet rotation, the experimental spreading rate can be systematically controlled by varying the gravitational body force imposed on the drop and (2) the 'inner scale' region over which elastic, viscous and capillary effects are all important will be physically enlarged as the gravitational driving force is reduced. The dynamics in this region governs

the feasibility and stability of possible future microgravity materials processing operations that might involve spin coating or dip-coating of barrier materials or etch resists.

NON-NEWTONIAN RHEOLOGY

In many commercially important operations (indicated in Figure 1) the rheology of the fluid coating may be non-Newtonian (*i.e.* it may exhibit shear-thinning in the viscosity or the presence of additional viscoelastic normal stresses; Bird *et al.* 1987) which can have a very important effect in the region of high shear rate and on the complex two-dimensional flow near the advancing contact line. Until recently, however, few studies have focused on this challenging problem. The global dynamical evolution of a viscoelastic film (*i.e.* the gradual thinning of region I in Figure 1) draining down a vertical plate has been studied experimentally and numerically by Pennington *et al.* (1994) and the leveling of a viscoelastic film on a horizontal substrate has been considered by Bousfield (1991). In spin-coating operations, dilute polymer solutions are typically employed and recently Fraysse & Homsy (1994) and Borkar *et al.* (1994) have numerically and experimentally studied the effects of fluid elasticity on the global evolution (*i.e.* Region I dynamics) and stability of the radially-spreading fluid film. In both studies, for the typical operating conditions and fluid formulations used industrially, the authors found no qualitative differences (beyond an initial transient associated with the linear viscoelasticity of the fluid) between the long term dynamical response of the Newtonian and viscoelastic films. This is partly because the fluids studied were dilute polymer solutions and elastic effects are relatively unimportant. In many spin-coating operations, the solvent is volatile and as the experiment proceeds and the area of the coated film increases, the solvent evaporates and the film becomes increasingly elastic in nature as the concentration increases. These evaporative losses can dominate the convective spreading at long times and significantly affect the final thickness profile of the coated film (Lawrence and Zhou, 1991).

More recently, Spaid & Homsy (1994 & 1996) have examined in closer detail the inner region (region II) response and shown that, in fact, elastic effects in the fluid coupled with the form of the boundary condition applied in region III can dramatically affect the local evolution in the shape of the free surface near the contact line and also affect the stability of this motion; however no experimental measurements of the surface profiles for viscoelastic fluids in this region exist.

For more concentrated polymeric systems such as polymer melts, Brochard & de Gennes (1984) discuss the possibility of a new 'foot region' (entirely separate from Region II) that can be significantly expanded in spatial extent (and as large as several μm) in which slip of the entangled polymer molecules is important and

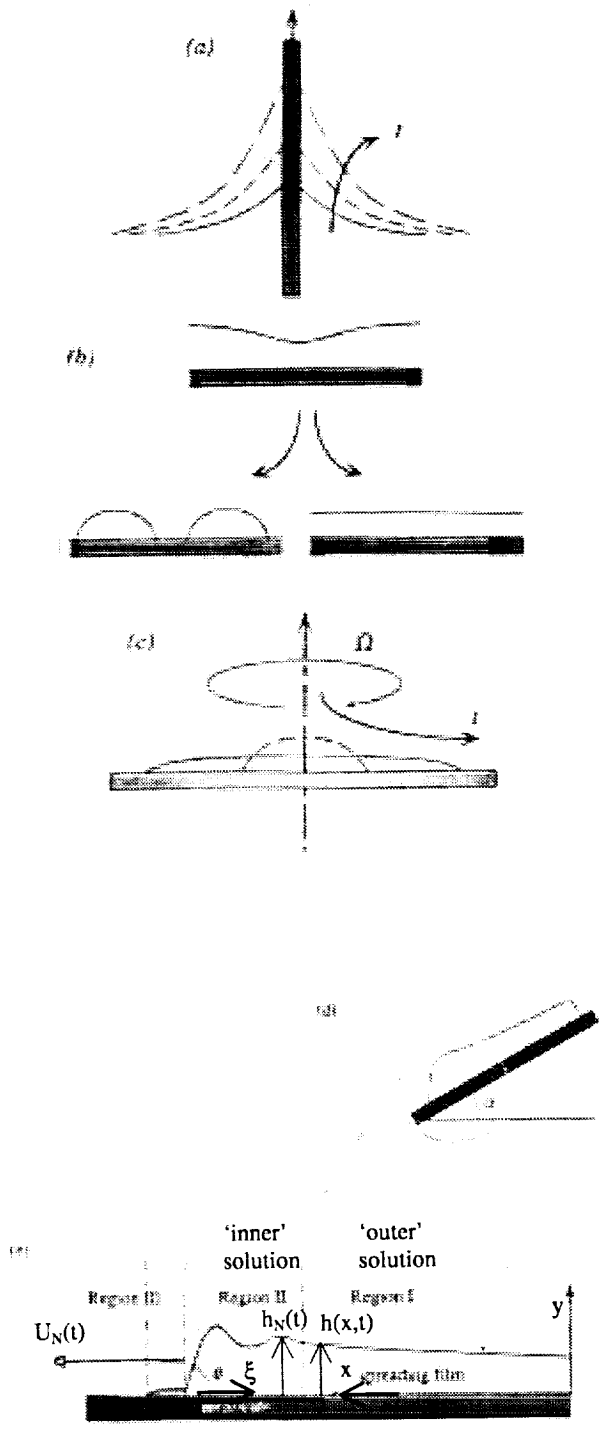

Figure 1. Examples of coating flows in which the motion of the dynamic contact line and the non-Newtonian rheology of the fluid are important: (a) dip-coating; (b) level and stability of fluid films; (c) spin-coating and (d) drainage of a sheet down an inclined plane. The nomenclature used to describe the various regions is indicated in (e).

the contact angle is almost zero. de Gennes (1995) has concluded that viscoelastic polymeric melts represent a separate dynamical class of wetting phenomena.

Experimental results by Lewandowski and Dupuis (1994) demonstrate the pronounced difference between the wetting response of melts and other polymer solutions. A cleaned platinum plate is lowered into a low molecular weight melt of polybutene at a slow fixed speed to a maximum depth and then withdrawn at an equal rate. Despite the slow rate of immersion, extremely large hysteresis were observed in the measured force as a consequence of the dynamic wetting of the polymer melt onto the Pt. substrate. By contrast, no hysteresis was observed with a dilute polymer solution. The observed wetting hysteresis may be associated with the extremely long time scale required to develop an equilibrium surface conformation in the film due to both the high viscosity of the fluid and to the dramatically lowered advancing contact angle in the polymeric 'foot' region. The 'static' (equilibrium) surface tension is obtained at infinitesimally slow immersion rates.

This extended time scale for the approach to steady state has also been observed in preliminary experiments by McKinley (1997) using a similar oligomeric polybutene melt. Figure 2 (a) shows that the transient response in the bulk shear stress during imposition of steady shear flow is extremely rapid (the stress is fully developed within 50 ms). By contrast, when a cleaned platinum plate, attached to a Wilhelmy balance (Krüss K-12), is lowered until it just touches the surface of the fluid and subsequently held stationary, the dynamical response is many orders of magnitude slower. The capillary length of the fluid can be estimated as $L \approx \sqrt{(\sigma/\rho g)} = 1.6$ mm; however, the fluid meniscus takes over 20 minutes to evolve to its equilibrium configuration and approach the final 'static' surface tension of $\sigma = 29.8 \times 10^{-3}$ N/m.

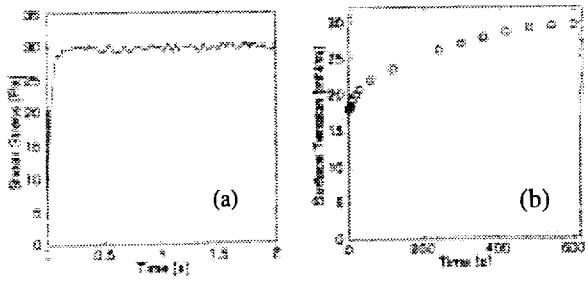

Figure 2. Evolution of shear stress (a) and surface tension (b) in a oligomeric polybutene melt. (a) Transient response in the bulk shear stress after steady shear flow ($\dot{\gamma}_0 = 1 s^{-1}$) is extremely rapid. (b) Response in the nominal surface tension in a Wilhelmy plate apparatus is considerably slower.

LUBRICATION ANALYSIS

We briefly review the fluid mechanics associated with the physics of spreading and wetting which is most clearly understood through the use of matched asymptotic expansions in the regions denoted I and II in Figure 1; this notation closely follows that of Hornsy and co-workers (1991, 1994, 1996).

Region I

In this 'outer region' the characteristic thickness of the film $h_N(t)$ is small compared to the lateral extent ($h_N(t) << x_N(t)$) and the viscous fluid spreads slowly; lubrication analysis can therefore be used to describe the rate of spreading. Huppert (1982) and others have shown that it is possible to construct similarity solutions of power-law type to the non-linear diffusion equation describing the long-time evolution in the film thickness $h(x,t)$. These solutions are typically of the form:

$$h(x,t) = C\, t^m\, f(\eta) \text{ where } \eta = A\, x/\, t^p \qquad (1)$$

Here C and A are dimensional constants and m, p are (fractional) exponents that depend on the form of the body force driving the spreading (e.g. coriolis forces in spin-coating, gravitational body forces in drainage problems or gravity currents) and on the geometry of the problem (i.e. radial spreading of a puddle or rectilinear flow down a plane).

For gravitational spreading of a sheet of Newtonian fluid down a plane inclined at an angle α (the geometry of principal interest in the present proposal), the characteristic velocity is $U_N = \rho\, g\, \sin(\alpha)\, h_N^2/(3\, \eta_o)$. The exponents in eq. (1) are determined to be $m = -1/3$, and $p = 1$; other details of the self similar solution can be found in Huppert (1982) and Goodwin & Homsy (1991). The corrections to the exponents and for the rate of spreading for inelastic non-Newtonian fluid with a power-law viscosity have also been recently evaluated (Pascal, 1994).

Numerous experimental measurements and analyses for spin-coating geometries (see *e.g.* Stillwagon & Larson; 1987, Borkar *et al.* 1994, Fraysse & Homsy 1994) have shown that the analogous self-similar solutions obtained in this geometry are in good agreement with observations for both Newtonian and weakly elastic constant-viscosity fluid films. The corrections to the profiles for shear-thinning inelastic liquids have also been computed (Acrivos *et al.* 1960).

These lubrication solutions, however, neglect the curvature of the free-surface and hence fail to capture the shape of the leading edge in the vicinity of the contact line region ($x \approx x_N$) where surface tension effects become increasingly important. They thus constitute the leading order term in an asymptotic expansion for an 'outer region' which must be matched to an 'inner region' expansion near the contact line.

Region II

In this 'inner region' capillary forces balance the viscous stresses in the fluid and the driving body force. This leads to a new characteristic length scale $l = (3Ca)^{-1/3} h_N$ and a rescaling of the characteristic lateral distance from the contact line of the form

$$\xi = (3Ca)^{1/3} (x_N - x)/h_N \qquad (2)$$

It is now recognized (Goodwin & Homsy 1991) that in this inner region both global curvature effects (arising from a radial geometry) and the form of the forcing are unimportant (once the characteristic velocity U_N arising from the forcing is incorporated into the definition of Ca). The solution to the lubrication equations is in effect 'quasi-static' and applies to spin-coating, gravitational spreading and other similar problems.

To compute the profile from the resulting nonlinear equations, it is necessary to impose a boundary condition at the contact line itself ($\xi = 0$). Applying the no-slip boundary condition leads to the well-known singularity in the solution field, and the appropriate boundary condition relies on a knowledge of the physics on even smaller length scales in the local region III or 'core region' (de Gennes, 1985). The solution for a viscous Newtonian fluid with a Navier slip boundary condition predicts the formation of a distinctive *'capillary ridge'*; the shape of the ridge and associated stability analyses of the advancing planar profile show that, in fact, *for Newtonian fluids* the global spreading of the film and the onset of fingering is insensitive to the choice of boundary condition applied (Troian *et al.* 1989, Spaid & Homsy 1996). Goodwin & Homsy (1991) have also extended the analysis beyond the lubrication limit to consider the full 2D steady Stokes equations. Although the quantitative features of the capillary ridges change, they always remain present over all parameter space considered.

Spaid & Homsy (1994) considered the first corrections to this local profile arising from weak elasticity using the Oldroyd-B model (Bird *et al.* 1987) and showed that the correction scales with the parameter $(1-\eta_s/\eta_o)(3Ca)^{1/3}(Wi)(h_N/x_N)$ where n_S is the solvent contribution to the total viscosity (η_O) and $Wi = \lambda_1 U_N/h_N$ is the Weissenberg number characterizing viscoelastic effects in the fluid film. They also showed that the spatial form of this macroscopic correction to the film profile near the contact line is very sensitive to the form of the chosen microscopic boundary condition and can increase or decrease the amplitude of the capillary ridges. More recent analysis has additionally shown that, since the driving force for fingering instability is the gravitational body force acting on the capillary ridges (Troian *et al.* 1989), this viscoelastic correction can significantly affect the stability of the advancing front (Spaid & Homsy 1996). It is clear that for viscoelastic fluids the molecular physics in the core region III can indeed affect the observable macroscopic dynamics of the spreading material.

In more concentrated solutions and in polymer melts, perturbation approaches using the Oldroyd-B constitutive model (which is only applicable for dilute solutions) are inappropriate and Brochard & de Gennes (1984) have shown that an entirely new 'foot region' can develop from the microscopic response of the polymer chains to the fluid stresses near the contact line and this can dramatically affect the dynamical spreading and profile of the film in region II. The shape of the 'foot region' is discussed in detail by Brochard & de Gennes (1984) and is especially important at short times and small drop volumes. The capillary ridges in Region II are eliminated in favor of a 'foot' that may be several microns in height, and smoothly blends at large distances from the contact line into a 'cap' region similar to that in a Newtonian fluid.

Region III

Since the microscopic physics of in Region III can have a pronounced impact on the dynamics of the contact line motion, significant theoretical effort has been expended in understanding the nature of the fluid-solid interaction in this 'core region'. The early work is reviewed by Dussan V (1979) and De Gennes (1985). More recent theoretical work has shown that there are at least four ways of relieving the singular stress at the contact line:

- Local slip between the fluid and the wall (see e.g. Kalliadasis & Chang) leads to a Navier slip boundary condition of the form $V_{slip}\ (\xi=0) = \alpha\tau_{\xi\zeta}$ (i.e. proportional to the shear stress near the contact line) and a slip length or 'extrapolation length' ~ $\alpha^{1/2}$. This extrapolation length is expected to be anomalously large in polymer melts and leads to the formation of the foot region as discussed by Brochard & de Gennes (1984).
- Existence of a precursor film of thickness $b \sim O(100\ \text{Å})$ formed through continuous evaporation and deposition of vapor on the dry substrate ahead of the macroscopically observable contact line.
- A shear-rate-dependent viscosity in the fluid which lowers the shear stress near the contact line. Weidner & Schwartz (1994) have recently shown that for the gravity-driven drainage of the Ellis model (Bird et al. 1987), this shear-thinning completely relieves the singularity and eliminates the core region III entirely!
- Surface tension gradients which arise near the contact line as a result of evaporation and the accumulation of impurities due to the recirculating flow in the capillary ridge region can also affect the motion. Shikhmurzaev (1993) has shown that incorporating such Marangoni effects can also relieve the singular stress and give accurate predictions of the velocity field and dynamic contact angle.

Observations of the Dynamics in Region I & II

The four mechanisms discussed above for relieving the contact line singularity may each be appropriate, depending on the particular fluid and substrate of inter-

est. The review by de Gennes (1985) discusses the few quantitative measurements of the film profiles in Region II, and the connection to the first two suggested boundary conditions in Region III, however he points out that because of the experimental difficulties involved *"we do not yet have a quantitative experimental law for the simplest (steady state) film profile"* as the rate of spreading is varied (e.g. by changing the bulk viscosity, the temperature or the angle of the inclined plane) even in a simple liquid.

The vast majority of experimental observations in non-Newtonian fluids have focused on the macroscopic dynamical evolution of the thinning film in Region I using contact methods such as profilometry on the cured film after the experiment is completed (e.g. Stillwagon & Larson, 1987) or measurement of the radial extent of spreading as a function of time (e.g. Fraysse & Homsy, 1994). This is sufficient for many engineering applications since observations in spin-coating operations have shown that for dilute polymer solutions, any modifications in Region II have little affect on the overall rate of spreading (Borkar *et al.* 1994). However, almost no quantitative information on the fundamental fluid physics of the inner structure near the advancing contact line is available. As de Gennes (1985) points out, even apparently simple silicone oils (which behave essentially as Newtonian fluids in the bulk with very little viscoelasticity) can show extremely anomalous wetting and spreading responses, due to the dynamics of the entangled chains near the advancing contact line.

As a result of the lubrication approximations commonly used to theoretically describe Region II and the self-similar solutions that ensue, the kinematics of the fluid motion in the inner region near the contact line can be inferred if *a sufficiently accurate measurement of the spatially - and temporally-varying height profile h(x,t) can be obtained.* Each of the postulated mechanisms for relieving the singular contact line result in a distinctively different predicted capillary ridge profile for a non-Newtonian fluid (although the variations are non-monotonic in the relevant parameter (e.g. α, *b)* characterizing the boundary condition). Recently, non-contact in-situ measurements of the dynamical evolution of film thickness (in the 'outer' Region I) have been made using various laser interferometry configurations (Tong *et al.* 1989; Borkar *et al.* 1994) and a pulsed or stroboscopic laser interferometry system has been used to monitor evaporation effects in a drying film (Peurrung & Graves, 1991). These experiments have not had sufficient spatial or temporal resolution to permit the study of the 'inner' Region II. Melo *et al.* (1989) obtained elegant photographic images of the formation of the capillary ridge in a silicone oil spreading over a spinning disk and showed that its development lead to onset of a fingering instability consistent with lubrication theory predictions. However, these observations are qualitative in nature and there is an absence of quantitative measurements of the development of the capillary ridge and its connection to the microscopic physics in the core region III.

EXPERIMENTAL PLAN

In order to focus on the wide range of possible rheological behavior near the contact line, the proposed experiments focus on a single solid substrate (polished silicon wafers) and four distinct classes of fluids; a simple viscous Newtonian reference standard, a dilute polymer solution, an inelastic shear-thinning fluid and a weakly entangled oligomeric melt. A phase shifted laser feedback interference microscope will be used to probe *both* the outer and inner (Regions I & II) fluid dynamics of an advancing sheet of fluid.

An inclined plane geometry will be employed with individual polished silicon wafers (surface roughness typically $\leq$ 10 nm) and which can be coated to vary the surface wetting characteristics. The wafers will be mounted on Peltier heating elements providing both an isothermal boundary condition and allowing uniform elevation of the experimental test temperature; the latter will be especially useful when highly entangled high molecular weight polymer melts are employed.

The measured profiles of surface height will be compared with the predictions of the similarity solutions. As the fluid flows down the plane, there are two possible ways of experimentally reconstructing the anticipated similarity forms: *(a)* the dimensionless function $f(\eta)$ can be constructed at one instant in time t_1 by obtaining a 'snapshot' of the spatial variations in the surface profile and plotting them in terms of the similarity variable $\eta_1 = x/t_1$ and *(b)* the gradual variation in the surface profile can be monitored at a fixed position x_1 and the similarity profile $f(\eta)$ constructed from the measurements of $h(x_1,t) = f(\eta_1 \equiv x_1/t)\, t^{-1/3}$.

To explore the influence of fluid rheology on the possible 'core region' mechanisms that might relieve the stress singularity at the contact line, four distinct classes of fluid will be examined:

(i) A Newtonian fluid of moderate viscosity and low molecular weight (e.g. glycerol, oligomeric melts of PIB, PS or polydimethylsiloxane (PDMS)) will first be examined as a control. More viscous PDMS oils with higher molecular weights are deliberately excluded from consideration here, because of their possibly anomalous melt-like behavior (de Gennes, 1985);

(ii) A high-viscosity dilute polymer solution (referred to generically as a 'Boger fluid'; Boger 1977/78) will be studied to investigate the first effects of elasticity. A Boger fluid consisting of 0.05 wt% monodisperse polystyrene dissolved in a Newtonian oligomeric styrene can readily be prepared (Spiegelberg & McKinley, 1997). Studies of the spreading characteristics of such fluids in Region I have shown that at least macroscopically (in length scales x > 1mm) the fluids behave similarly to Newtonian fluids (Fraysse & Homsy 1994)

after initial viscoelastic transients have decayed, however, the local surface profile in region II is unknown.
(iii) An inelastic shear-thinning fluid will be studied in order to investigate if shear-thinning near the contact line can eliminate the singular stresses and obviate the need for a core region. Aqueous solutions prepared from moderate concentrations (2 wt% – 5 wt%) of Xanthan gum exhibit almost immeasurable elasticity and shear-thinning across a wide range of shear rates.
(iv) The effects of polymeric entanglements will be examined by focusing on a homologous series of progressively higher molecular weight PDMS oils and 'gums'. To facilitate the flow of these materials, the spreading experiments will be performed at elevated temperatures using the Peltier hot stage.

CONCLUSIONS

We have begun a four-year investigation to measure the dynamics in a small inner region of a fluid near an advancing contact line. For non-Newtonian fluids, the resulting film profile is predicted to be markedly different to that expected in simple Newtonian liquids and this leads to changes in the stability of the advancing fluid film. When the gravitational body force on the film is lowered the extent of the 'inner' region near the contact line singularity is expanded, and can be imaged using interferometry. Phase shifted laser feedback interferometry has both sufficient lateral and vertical spatial resolution to accurately resolve systematic variations in the film profiles as the bulk rheology of the fluid is modified.

REFERENCES

Acrivos, A., Shah, M.J. and Petersen, E.E., On the Flow of a Non-Newtonian Liquid on a Rotating Disk, *J. Appl. Phys.*, **31**, (1960), 963-971.

Bird, R.B., Armstrong, R.C. and Hassager, O., Dynamics of Polymeric Liquids. Volume 1: Fluid Mechanics, Vol. 1, 2nd Edition, Wiley Interscience, New York, 1987.

Boger, D.V., A Highly Elastic Constant-Viscosity Fluid, *J. Non-Newtonian Fluid Mech.*, **3**, (1977/78), 87-91.

Borkar, A.V., Tsamopoulos, J.A., Gupta, S.A. and Gupta, R.K., Spin coating of viscoelastic and nonvolatile fluids over a planar disk, *Phys. Fluids*, **6**(11), (1994), 3539-3553.

Brochard, F. and deGennes, P.G., Spreading laws for liquid polymer droplets: interpretation of the "foot", *J. Physique Lett.*, **45**, (1984), L-597 -- L-602.

de Gennes, P.-G., Wetting: Statics and Dynamics, *Rev. Mod. Phys.*, **57**, (1985), 827.

de Gennes, P.-G., Introduction to Polymer Dynamics, Lezioni Lincee, Cambridge University Press, Cambridge, 1990.

Dussan V, E.B., On the Spreading of Liquids on Solid Surfaces: Static and Dynamic Contact Lines, *Ann. Rev. Fluid Mech.*, **11**, (1979), 371.

Fraysse, N. and Homsy, G.M., An experimental Study of Rivulet Instabilities in Centrifugal Spin-Coating of Viscous Newtonian and non-Newtonian Fluids, *Phys. Fluids*, **6**(4), (1994), 1491-1504.

Goodwin, R. and Homsy, G.M., Viscous flow down a slope in the vicinity of a contact line, *Phys. Fluids A*, **3**(4), (1991), 515-528.

Huppert, H.E., Flow and Instability of a Viscous Current Down a Slope, *Nature*, **300**, (1982), 427-428.

Huppert, H.E., The Propagation of Two-Dimensional and Axisymmetric Viscous Gravity Currents over a Rigid Horizontal Surface, *J. Fluid Mech.*, **121**, (1982), 43-58.

Kalliadasis, S. and Chang, H.-C., Apparent dynamic contact angle of an advancing gas-liquid meniscus, *Phys. Fluids*, **6**(1), (1994), 12-23.

Lawrence, C.J. and Zhou, W.,Spin-Coating of Non-Newtonian Fluids, *J. Non-Newt. Fluid Mech.*, **39**, (1991), 137-151.

Lewandowski, F.Y. and Dupuis, D., Dynamic Measurements of Surface Tension of Solutions of Polyisobutylene in Mixtures of Polybutene Oil and Decalin, *J. Non-Newtonian Fluid Mech.*, **52**, (1994), 233-248.

McKinley, G.H., (1997) Unpublished.

Melo, F., Joanny, J.F. and Fauve, S., Fingering Instability of Spinning Drops, *Phys. Rev. Lett.*, **63**(18), (1989), 1958-1961.

Ovryn, B. and Andrews, J.H., Phase-Shifted Laser Feedback Interferometry, *Opt. Let.*, **23(14)**, (1998), In press.

Padday, J.F., *Wetting, Spreading & Adhesion*, Academic Press, New York, 1978.

Padday, J.F., Spreading, Wetting and Contact Angles, *J. Adhesion Sci. & Tech.*, **6**(12), (1996), 1347-1358.

Pennington, S.V., Waters, N.D., Rennie, G.K. and Staples, E.J., Draining Non-Newtonian Films Part 2. Measurement of the Rate of Change of Film Thickness by Laser Interferometry., *J. Non-Newtonian Fluid Mech.*, **37**, (1990), 209-231.

Peurrung, L.M. and Graves, D.B., Film Thickness Profiles over Topography in Spin Coating, *J. Electrochem. Soc.*, **138**(7), (1991), 2115-2124.

Sawicki, C., *in* Wetting, Spreading & Adhesion, J. F. Padday (ed.), Academic Press, New York, 1996.

Shikhmurzaev, Y.D., The moving contact line on a smooth solid surface, *Int. J. Multiphase Flow*, **19**(4), (1993), 589-610.

Spaid, M.A. and Homsy, G.M., Viscoelastic Free Surface Flows: Spin-Coating and Dynamic Contact Lines, *J. Non-Newt. Fluid Mech.*, **55**, (1994), 249-281.

Spaid, M.A. and Homsy, G.M., Stability of Newtonian and Viscoelastic Dynamic Contact lines, *Phys. Fluids*, **8**(2), (1996), 460-478.

Spiegelberg, S.H. and McKinley, G.H., Stress Relaxation and Elastic Decohesion of Viscoelastic Polymer Solutions in Extensional Flow, *J. Non-Newtonian Fluid Mech.*, **67**, (1997), 49-76.

Stillwagon, L.E., Larson, R.G. and Taylor, G.N., Planarization of Substrate Topography by Spin-Coating, *J. Electrochem. Soc.*, **134**(8), (1987), 2030-2037.

Tong, H.M., Saenger, K.L. and Durning, C.J., A Study of Solvent Diffusion in Thin Polyimide Films using Laser Interferometry, *J. Polym. Sci. Polym. Phys. Ed.*, **27**, (1989), 689-712.

Troian, S.M., Herbolzheimer, E., Safran, S.A. and Joanny, J.F., Fingering Instabilities of Driven Spreading Films, *Europhys. Lett.*, **10**, (1989), 25-30.

Weidner, D.E. and Schwartz, L.W., Contact-Line Motion of Shear-Thinning Liquids, *Phys. Fluids*, **6**(11), (1994), 3535-3538.

NUMERICAL SIMULATION OF PARAMETRIC INSTABILITY IN TWO AND THREE-DIMENSIONAL FLUID INTERFACES.

C. Pozrikidis[1] and S. A. Yon[1], [1]Dept. of Applied Mechanics and Engineering Sciences,
University of California, La Jolla, California 92093 syon@ames.ucsd.edu

INTRODUCTION

The behavior of the interface between two fluids in unsteady motion has been the subject of extensive experimental and theoretical studies dating back to Faraday's observations in 1831. It is now well known that, when subjected to a harmonic oscillation perpendicular to the plane of the undisturbed surface, the interface between two liquids may develop standing waves whose precise form and temporal evolution depend on the geometry of the container, the viscosity of the fluids, and the properties of the contact line between the fluids and container. Under most circumstances, the standing waves on a three-dimensional interface have a square unit cell, as shown in Figure 1, and oscillate with half the frequency of the external acceleration, while the amplitude exhibits a more general type of sub-harmonic behavior.

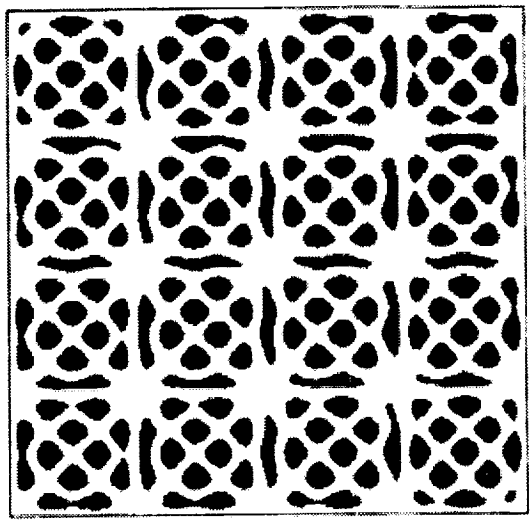

Figure 1. Schematic of level lines in a three-dimensional doubly-periodic standing wave on a water-air interface forced at 64 Hz (Douady, 1990).

More complicated patterns have been observed, however, especially when the forcing vibration is not monochromatic.

A large number of experimental studies following Faraday's observations have shown that a harmonically forced interface may sustain large but finite amplitude waves over a broad range of frequencies and amplitudes of the forcing vibration (e.g. Edwards and Fauve 1994, Kudrolli and Gollub 1997). One striking feature of the motion is that, as the amplitude of the oscillation is increased, spatially periodic patterns with square, hexagonal, or triangular cells yield disordered and fluctuating states (e.g. Crawford, Gollub and Lane 1993). The occurrence of disordered states has a profound effect on the rate of mixing at the interface, drifting of fluid parcels and suspended particles, gas entrainment, bubble generation and entrainment by interfacial structures (e.g. Mesquita, Kane and Gollub 1992). It has been shown that as the fluids become more viscous, the doubly-periodic three-dimensional waves are replaced by linear two-dimensional waves. Furthermore, under certain conditions, an oscillating interface may develop soliton-like deformations which serve to demonstrate the richness of the non-linear motion (Wu, Keolian and Rudnick 1984, Miles 1984).

To explain Faraday's observations, Benjamin and Ursell (1954) considered the harmonic oscillations of the free surface of a liquid of finite depth in a cylindrical container, assuming that the interface remains horizontal at the contact line. Linearization of the governing equations yields a Mathieu equation, whose study reveals the existence of regimes in which the amplitude of the standing interfacial waves is periodic or non-periodic but bounded, and other regimes in which amplitude grows exponentially and the flow is unstable.

More recently, Kumar and Tuckerman (1994) presented a Floquet analysis taking full account of fluid viscosity on both sides of the interface (a similar study was carried out by the present P.I. in an unpublished research report). When viscous forces are included, the linearized evolution equation can no longer be reduced to a single ordinary differential equation, and an eigen-value problem involving partial differential equations must be solved. In earlier studies, the effect of viscosity had been emulated by inclusion of a damping term in the Mathieu equation or a dissipation term in the boundary integral formulation.

The highly nonlinear motion of an interface with finite and large amplitude deformations has not proven receptive to numerical simulation. An exception is the recent work of Jiang et al. (1997) who performed boundary integral computations for two-dimensional potential flow. Analogous investigations of the nonlinear behavior of unforced progressive waves, in the absence of externally imposed accelerations, have revealed a host of behaviors (e.g. Zufiria 1988, Mercer and Roberts 1992).

RESEARCH AND OBJECTIVES

We study the fully nonlinear behavior of forced standing waves at the interface between two

generally viscous fluids with different densities, in the presence of surface tension, considering both two-dimensional and three-dimensional doubly-periodic wave patterns. We concentrate on large amplitude waves with steep interfacial deformations, identify the occurrence and study the characteristics of non-periodic and disordered states, and establish conditions for interfacial breakup. One of the more important objectives is the exhaustive investigation of the effects of viscosity and surface tension on the limiting form of steep waves.

For each type of interfacial wave, including two-dimensional and three-dimensional doubly periodic patterns, we study the response of the system to excitations with varying frequency and amplitude. For bounded flows, we examine the significance of the contact line expressed by a proper contact angle boundary condition. Interrogating the results of the numerical simulation, we study particle paths and fluid mixing in the vicinity of the interface. We anticipate that, under certain conditions, large amplitude oscillations will lead to the formation of cusps in the interface and the subsequent formation of separated drops. Establishing such conditions and resolving the underlying physics of the flow will be given special attention.

The investigation relies on numerical solutions of selected families of initial value problems using four complementary classes of computational techniques described in the next section.

MATHEMATICAL FORMULATION AND NUMERICAL METHODS

Inviscid Flow

Consider the interface between two stably stratified, effectively inviscid fluid layers of finite depth, with non-vanishing interfacial tension, placed within a container consisting of flat boundaries parallel to the undisturbed interface as shown in Figure 2, and subjected to harmonic vertical acceleration.

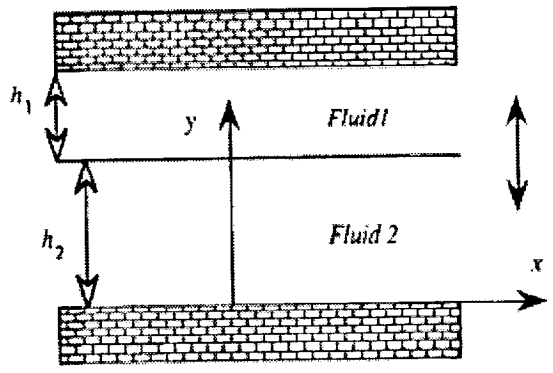

Figure 2. Schematic of interface and boundaries employed in two and three-dimensional potential simulations.

In the undeformed state, the fluids move like rigid bodies with acceleration $a\exp(-i\Omega t)$. In the deformed state, the behavior of the interface depends on the depth ratio h_1/h_2, the density ratio ρ_1/ρ_2, two reduced waves numbers $k_1 h_2$ and $k_2 h_2$, the reduced amplitude of the oscillation d/h_2, the inverse Bond number and the effective Froude number.

When the density of the upper fluid is negligible, we obtain, through the application of standard boundary integral techniques for potential flow, an integral equation relating the potential along the interface to the normal component of interfacial velocity

$$\phi(x_0) = -2\int_{fs} G(x, x_0)\nabla\phi(x)\cdot n(x)dl(x) + 2\int_{fs}^{PV} \nabla G(x, x_0)\cdot n(x)\phi(x)dl(x) \quad (1)$$

where fs is the interface, and G is the Green's function of Laplace's equation representing the flow due to a periodic array of point sources on the interface. Careful selection of G, accounting for the periodic nature of the interface and the presence (or absence) of vertical and lateral boundaries greatly simplifies the domain of the integral operators. Given the distribution of ϕ on the interface at some initial time, equation (1) becomes a Fredholm integral equation of the first kind for the normal velocity on the interface. The iterated numerical procedure for solution of the potential on the interface involves the following steps: (a) Given the position and potential at a finite number of marker points defining the interface, solve equation (1) for the interfacial velocity. (b) Update the marker point locations using the interfacial velocity, and update the potential using the unsteady Bernoulli equation

$$\frac{\partial\phi}{\partial t} = -\frac{(p_0 + \gamma k)}{\rho} - \frac{u^2}{2} - y(g + a\cos(\omega t)) \quad (2)$$

where p_0 is the pressure in the upper fluid, k is the mean curvature of the interface, γ is the surface tension, and ω is the frequency of the imposed acceleration.

For two-dimensional problems, we may employ a complex transformation to map one period of the interface onto a closed contour, thereby allowing the use of the free-space Green's function and simplifying the domain of integration. To describe the motion of the interface when complex interfacial

structures develop, we employ an adaptive marker point re-distribution method based on interfacial curvature. The anticipated occurrence of small scale instabilities may require occasional smoothing of the interface.

For a three-dimensional disturbance, the integral equation (1) must be solved in physical space, and we employ a Green's function exploiting the doubly periodic nature of the standing wave, as shown in Figure 3 (Pozrikidis 1995).

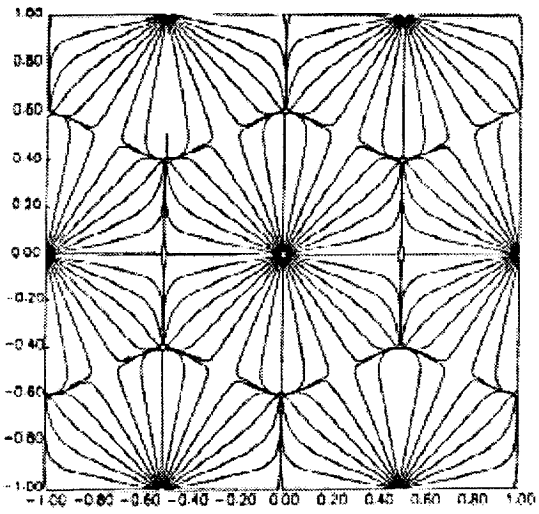

Figure 3. Streamlines in the plane of a hexagonal doubly-periodic array of three-dimensional point sources.

We describe one period of the interface in terms of global curvilinear coordinates and solve the integral equation using a high order spectral method, or alternately, divide one period of the interface into a set of triangular elements and solve the integral equation using a triangle spectral method. With either method, redistribution of interfacial marker points using the advancing front method will be required when complex interfacial structures develop.

When the density of the upper fluid is not negligible, we may regard the flow as being induced by vortices distributed along the interface, the strength of the vortex sheet evolving in time according to the motion of the fluid. Note that this technique is restricted to two-dimensional disturbances. Describing the interface in terms of the Lagrangian variable a, we express the position of an interfacial marker point in terms of the Biot-Savart law

$$\frac{dX(a)}{dt} = \frac{1}{2\pi} \int_C^{PV} \begin{bmatrix} -Y(a)+y(a') \\ X(a)-x(a') \end{bmatrix} \frac{\gamma}{r^2} \frac{\partial l}{\partial a'} da' + v(a) \tag{3}$$

where c is the trace of the vortex sheet, γ is the strength of the vortex sheet, and v is the velocity induced by the image system. The strength of the vortex sheet is governed by the evolution equation

$$\left(\frac{\partial \gamma}{\partial t}\right)_a + \gamma t \cdot \frac{\partial v}{\partial l} = 2At \cdot \left(\frac{\partial v}{\partial t}\right)_a + \frac{A\gamma}{2} \frac{\partial \gamma}{\partial l} + \frac{2}{(\rho_1+\rho_2)} \frac{\partial(\Delta p)}{\partial l} - 2Ag \cdot t + 2A\frac{dU}{dt} \cdot t \tag{4}$$

where A is the Atwood ratio and $\mathbf{t}$ is the unit tangent vector on the interface. The numerical procedure employs an advanced implementation of the well established point-vortex method (Mercer and Roberts 1992, Pozrikidis 1997).

Viscous Flow

The effects of viscosity on the morphology of forced interfacial waves have been studied only in the context of Floquet theory for small disturbances. We plan to carry out an extensive numerical study of the viscous problem using two classes of numerical techniques: (a) The immersed boundary method for flows with non-vanishing Reynolds number, and (b) the boundary integral method for Stokes flow when the effects of inertia are negligible. In both cases, we will restrict ourselves to two-dimensional disturbances.

In the limit of vanishing Reynolds number, the governing equations become linear with respect to velocity and pressure, and the oscillations of the interface are in phase with the forcing vibration. As the Reynolds number increases, discrepancies arise; in the limit as Reynolds number increases without bound, we obtain behavior similar to that described by Mathieu's equation for small disturbances. Three important objectives of this research are: 1) Describe changes in the frequency of oscillation as the effects of inertia become more important; 2) Describe the associated changes in the shapes of the standing waves; 3) Describe the mechanisms of unsteady vorticity generation at the interface.

In the immersed boundary method, the effect of the interface is modeled in terms of a generalized distribution of point forces on the interface, with strength equal to the discontinuity in hydrodynamic traction due to surface tension. The physical properties of the fluids undergo a step discontinuity across the interface, and the corresponding gradients are expressed in terms of delta functions. Smoothing these representations allows the computation of the motion by solution of a generalized Navier-Stokes equation using standard finite-difference techniques without explicitly treating the interface (Pozrikidis 1997, Sheth and Pozrikidis 1995).

The theory and application of the boundary integral method for two-dimensional Stokes flow are

well established, (e.g. Pozrikidis 1992) but the anticipated geometric complexity of the deforming interface, including the presence of cusps and corners, will still require careful application of sophisticated numerical techniques.

REFERENCES

Benjamin, T. N. and F. Ursell, 1954. The stability of the plane free surface of a liquid in vertical periodic motion. *Proc. Roy. Soc. London A* **225**, 505-515.

Crawford, J. D., J. P. Gollub and D. Lane, 1993. Hidden symmetries of parametrically forced waves. *Nonlinearity* **6**, 119-164.

Douady, S. 1990. Experimental study of the Faraday instability. *J. Fluid Mech.* **221**, 383-409.

Edwards, W. S. and S. Fauve 1994. Patterns and quasi-patterns in the Faraday experiment. *J. Fluid Mech.* **278**, 123-148.

Jiang, L., C. L. Ting, M. Perlin, and W. W. Schultz 1996. Moderate and steep Faraday waves: instabilities, modulation and temporal assymetries. *J. Fluid Mech.* **329**, 275-307.

Kudrolli, A. and J. P. Gollub 1997. Patterns and spatiotemporal chaos in parametrically forced surface waves: A systematic survey at large aspect ratio. *Physica D.* (in press).

Kumar, K. and L. S. Tuckerman 1994. Parametric instability of the interface between two fluids. *J. Fluid Mech.* **279**, 49-68.

Mercer, G. N. and A. J. Roberts 1992. Standing waves in deep water: Their stability and extreme form. *Phys. Fluids A* **4**, 259-269.

Mesquita, O. N., S. Kane and J. P. Gollub 1992. Transport by capillary waves: Fluctuating Stokes drift. *Phys. Rev.* **45**, 3700-3705.

Miles, J. 1984. Parametrically excited solitary waves. *J. Fluid Mech.* **148**, 451-460.

Pozrikidis, C. 1992. *Boundary Integral and Singularity Methods for Linearized Viscous Flow.* Cambridge University Press.

Pozrikidis, C. 1996. Computation of periodic Green's functions of Stokes flow. *J. Eng. Math.* **30**, 79-96.

Pozrikidis, C. 1997. *Introduction to Theoritical and Computational Fluid Dynamics.* Oxford University Press.

Sheth, K. and C. Pozrikidis 1995. Effects of inertia on the deformation of liquid drops in simple shear flow. *Computers & Fluids* **24**, 101-119.

Wu, J., R. Keolian and I. Rudnick 1984. Observation of a nonpropagating hydrodynamic soliton. *Phys. Rev. Lett.* **52**, 1421-1424.

Zufiria, J. A. 1988. Vortex-in-cell simulation of bubble competition in a Rayliegh-Taylor instability. *Phys. Fluids* **31**, 3199-3212.

COMPLEX DYNAMICS IN MARANGONI CONVECTION WITH ROTATION

H. Riecke, F. Sain, Engineering Sciences and Applied Mathematics, Northwestern University, Evanston, IL 60208,
h-riecke@nwu.edu

1 INTRODUCTION

Under conditions of reduced gravity surface-tension gradients become increasingly important in driving convection with free surfaces. In contrast to Boussinesq buoyancy-driven convection the typical planform of the convection pattern is hexagonal. While complex dynamics have been studied in great detail in systems that lead to roll- or stripe-like patterns, this is not the case for hexagonal structures. Due to their increased bending rigidity spatio-temporal chaos in hexagonal structures may be qualitatively different from that observed in Rayleigh-Bénard convection. The goal of this project is to investigate various instabilities of hexagonal structures, focussing on those that are due to the effect of a rotation of the system around an axis perpendicular to the fluid layer. Based on the complex behavior found for roll convection in the presence of rotation, complex dynamics are also expected to arise for hexagonal structures. The results may be relevant, for instance, to crystal growth from the melt which is often performed in the presence of rotation.

2 ROTATION IN BUOYANCY-DRIVEN CONVECTION

In the presence of rotation, the convection rolls of Rayleigh-Bénard convection are known to become unstable immediately at the onset of convection to rolls of a different orientation if the rotation rate is large enough [1]. This Küppers-Lortz instability leads to a persistent switching of the roll orientation. Since the change in orientation is about 60° a simple description of the switching is given by three coupled equations for the amplitudes A, B, and C of the three sets of rolls participating in the switching,

$$\partial_t A = \lambda A - A\left(g|A|^2 + (h+\rho)|B|^2 + (h-\rho)|C|^2\right) \quad (1)$$

and cyclic permutations thereof. The bifurcation parameter λ is proportional to the heating. The instability sets in when ρ, which is proportional to the rotation, is large enough. Within (1) the switching corresponds to a heteroclinic cycle connecting the three roll modes [2]. Thus, within this model the period of the switching diverges in time and the pattern remains longer and longer near one of the (unstable) roll states.

In systems with large aspect ratio the switching need not occur coherently across the whole system. Instead domains with different orientation arise (see fig.1) and the switching occurs *via* the propagation of the fronts separating the domains. For instance, in the sequence of panels (3-5) in fig.1 a domain of rolls oriented diagonally top-right to bottom-left invades the domain of rolls that are oriented essentially horizontally. Since this state of spatio-temporal chaos arises at very small convection amplitudes it is accessible to weakly nonlinear theories.

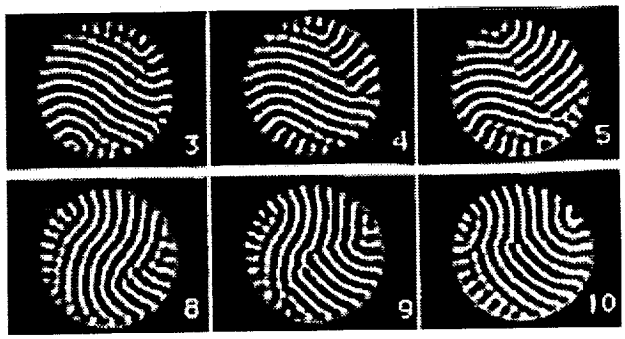

Figure 1: Snapshots of experimentally observed Küppers-Lortz state in buoyancy-driven convection (top view) [3].

3 HEXAGONS WITH ROTATION: SWIFT'S HOPF BIFURCATION

The effect of rotation on hexagonal structures in general has been studied in detail within the coupled amplitude equations describing hexagons that are strictly periodic. These equations are given by in space

$$\begin{aligned}\partial_t A &= \lambda A + kB^*C^* - \\ &\quad A\left(g|A|^2 + (h+\rho)|B|^2 + (h-\rho)|C|^2\right) \quad (2)\end{aligned}$$

and cyclic permutations [4]. It is found that the rotation affects in particular the stability of the hexagons with respect to rolls. While in the absence of rotation the hexagons become unstable to rolls in a steady, hysteretic bifurcation, the instability becomes oscillatory in the presence of rotation and non-hysteretic. Thus, periodic oscillations with finite period are expected. The oscillations are phase-shifted such that at different times a different set of rolls dominates. Within a simple order-parameter model these oscillations have been confirmed in small systems [5] as shown in fig.2.

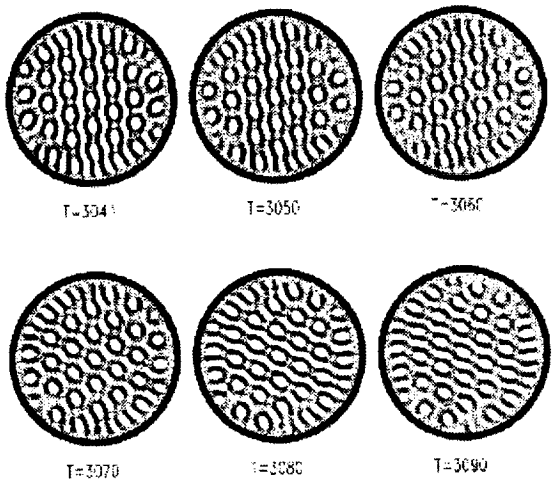

Figure 2: Snapshot of numerically obtained oscillating hexagon pattern [5].

4 HEXAGONS WITH ROTATION: LARGE ASPECT RATIO

The goal of this project is to study the effect of rotation on hexagonal structures as they arise in surface-tension driven convection. In addition to the derivation of reduced equations describing the system in suitable cases the research will investigate the behavior of the hexagons in larger systems in which the pattern cannot be described adequately by ordinary differential equations, i.e. in regimes in which the dynamics cease to be low-dimensional.

4.1 THE BASIC EQUATIONS

In this project a single fluid layer will be considered that is bounded on one side by a plate and has a free surface on the other side. A small amount of residual gravity will be included which will affect the layer mainly *via* the hydrostatic pressure. For other choices of the parameters weak buoyancy effects could be included as well. The plate will be heated and the free surface will be cooled. The rotation will be assumed to be small enough to ignore the centrifugal force, and the surface tension will for now be assumed to be large enough to keep the surface flat. The heat transport across the air layer above the fluid will be modelled with a Biot number. The dimensionless Navier-Stokes and heat equations together with the incompressibility condition are then given by [6]

$$\frac{1}{\mathcal{P}}(\partial_t + \mathbf{v}\cdot\nabla)\mathbf{v} = -\nabla p + 2\Omega\times\mathbf{v} + \Delta\mathbf{v} - \mathcal{G}\mathbf{e}_z, \quad (3)$$

$$\nabla\cdot\mathbf{v} = 0, \quad (4)$$

$$(\partial_t + \mathbf{v}\cdot\nabla)\theta = \Delta\theta, \quad (5)$$

and the boundary conditions at top and bottom read

$$\mathbf{v} = 0, \qquad \theta = 1, \qquad \text{at } z = 0, \quad (6)$$

$$\mathbf{n}\cdot\mathbf{\Pi}\cdot\mathbf{t}_i = \mathcal{M}\mathbf{t}_i\cdot\nabla\theta, \qquad \text{at } z = d, \quad (7)$$

$$\mathbf{n}\cdot\nabla\theta = -\mathcal{B}_i\theta \qquad \text{at } z = d. \quad (8)$$

The linear stability of the motionless layer in the presence of rotation has been studied in a number of different situations [7, 8, 9, 10]. The rotation is found to have a stabilizing effect on the layer and tends to increase the wavenumber at onset.

4.2 GINZBURG-LANDAU AND PHASE EQUATIONS

Within the coupled amplitude equations (2) Swift's Hopf bifurcation leads to stable oscillations and the pattern is spatially coherent over the whole system, just as was found in the Küppers-Lortz case. Again, this need not be the case in large systems. We will therefore study the stability of the hexagonal pattern with respect to long-wave perturbations below and above the Hopf bifurcation. To do so, we plan to derive three coupled Ginzburg-Landau equations for the amplitudes of the three roll modes,

$$\partial_t A = (\mathbf{n}_A\cdot\nabla)^2 A + \lambda A + kB^*C^* - A\left(g|A|^2 + (h+\rho)|B|^2 + (h-\rho)|C|^2\right), \quad (9)$$

(and cyclic permutations) where $\mathbf{n}_A$ is the unit vector perpendicular to the rolls corresponding to mode A. In general also quadratic gradient terms will arise, which have not been displayed in (9). From (9) the stability of hexagons can then be determined. Such a weakly nonlinear analysis has been performed in the absence of rotation in [11]. The effect of rotation has been studied to some extent in [12].

Below the Hopf bifurcation ($\lambda < \lambda_H$), i.e. for the steady hexagonal structure, the analysis of long-wave side-band instabilities leads to two coupled phase equations that capture slow deformations of the pattern in the plane. In the absence of rotation these equations have been derived previously [13]. They can be combined into a single vector equation for the two phases of the form

$$\partial_t\mathbf{\Phi} = D_\perp\nabla^2\mathbf{\Phi} + (D_{||} - D_\perp)\nabla(\nabla\cdot\mathbf{\Phi}). \quad (10)$$

In the presence of rotation also terms involving $\mathbf{e}_z\cdot(\nabla\times\mathbf{\Phi})$ will arise, which will modify the stability limits.

Above the Hopf bifurcation one obtains a complex Ginzburg-Landau equation for the complex amplitude associated with the oscillations. Since the Hopf bifurcation is a secondary bifurcation this equation has to be coupled to the phase Φ of the underlying hexagonal pattern. Of particular interest is the question whether the hexagon pattern can become unstable at all wavenumbers and whether this leads to complex dynamics (similar to the Benjamin-Feir instability of traveling waves) or to localized patterns. The latter scenario has been found in the transition to drift waves in various systems [14, 15, 16] and at a secondary transition from square patterns in electroconvection [17]. The fate of the pattern beyond the onset of the instabilities will be investigated in detailed numerical simulations of (9).

4.3 LONG-WAVE EQUATION

The main draw-back of Ginzburg-Landau equations is that they break the isotropy of the system. This is due to the fact that they are obtained in an expansion around the regular hexagon pattern that allows only small and slow variations of the wave vector. The orientation of the underlying hexagon pattern is fixed at leading order and the slowly varying perturbations allow only a slight modification of that orientation. For the description of regular hexagon patterns this is sufficient. However, if these patterns become unstable and develop into spatially complex patterns the dynamics most likely also include modes of a quite different orientation. To treat such a situation Ginzburg-Landau equations are not suitable. For the complex patterns and dynamics of interest in this project the computational effort to solve the full fluid equations is exceedingly large. For a first investigation into this regime it is therefore suitable to consider cases that are more accessible. The air layer above the fluid is typically a poor conductor compared to the fluid. If one considers a bottom plate that is also poorly conducting convection sets in first with a long wavelength. In this regime it is therefore possible to derive long-wave equations. Compared to the full equations they constitute a considerable reduction of computational effort since the number of equations has been reduced and, moreover, the problem has been reduced from a three-dimensional problem to one in two dimensions. Importantly, they preserve the isotropy. In addition, they are strongly nonlinear and not restricted to small convection amplitudes. In the absence of rotation long-wave equations have been derived for surface-tension driven convection in a number of different situations: for infinite Prandtl number [18], for finite Prandtl number including the effect of a mean flow [19], as well as for the more complicated case of a deformable interface [20].

Equations of the same form as the long-wave equations have also been used extensively to study important qualitative features of pattern-forming systems. If the wavelength of the pattern at onset is finite they are obtained in an approximate way from the basic equations in a weakly nonlinear theory by expanding the full equations in Fourier modes and adiabatically eliminating the damped (non-active) modes. This leads to integro-differential equations in Fourier space. In order to obtain local equations in real space the integral kernels are then expanded in the wavenumber. This is a systematic expansion for long-wave instabilities. For short-wave instabilities it is an approximation that is not well controlled. In Rayleigh-Bénard convection with free-slip boundary conditions it has been shown, however, that it can lead to quite good agreement with the full equations (e.g. [21, 22]).

In this project the effect of rotation on the hexagonal patterns will be investigated using long-wave equations. We will derive them from the fluid equations. We will first perform a linear stability analysis to establish the parameter range over which the assumption of small wavenumber is justified. Based on similar calculations on buoyancy-driven convection [23] and on Marangoni convection [7] it is expected that the critical wavenumber increases with rotation rate. In that case the long-wave equation would be asymptotically valid only for sufficiently small rotation rates. The linear analysis will indicate how small these rates have to be. As mentioned before, however, it is expected that even somewhat outside that regime the equations will provide a good model for the dynamics of the system. For infinite Prandtl number a single equation will be obtained. It will be of the form

$$\begin{aligned}\partial_t \psi &= R\psi - (\nabla^2+1)^2\psi - \psi^3 + g_3(\nabla\cdot(\nabla\psi)^2\nabla\psi) \\ &\quad + \mathbf{e}_z\cdot\left(\Gamma(\nabla\psi\times\nabla(\nabla^2\psi)) + g_2(\nabla\times(\nabla\psi)^2\nabla\psi)\right) \\ &\quad + \alpha\psi^2 + \beta(\nabla\psi)^2 + \ldots \qquad (11)\end{aligned}$$

where the ellipses denote additional terms. For small Prandtl numbers an additional equation for the mean flow would be obtained [19]. As in the vector-phase equation the terms involving a cross-product arise due to the rotation. We therefore focus on their influence on the system.

In preliminary work we have investigated (11) in order to see whether interesting results are to be expected. Within a weakly nonlinear calculation we have addressed the stability of the hexagonal pattern. The main motivation for considering (11) rather than the amplitude equations (9) is that it allows to consider perturbations of the hexagon by modes that are rotated with respect to the hexagon pattern. A straightforward ansatz for such a perturbation is of the form

$$\begin{aligned}\psi &= \epsilon A\left(e^{ix} + e^{i(-x/2+y\sqrt{3}/2)} + e^{i(-x/2-y\sqrt{3}/2)}\right) + \\ &\quad \epsilon\delta P_0 e^{\sigma t + ix\cos\theta + iy\sin\theta} + c.c., \qquad (12)\end{aligned}$$

where A denotes the amplitude of the hexagon and P that of a perturbation with the same wavelength but rotated with respect

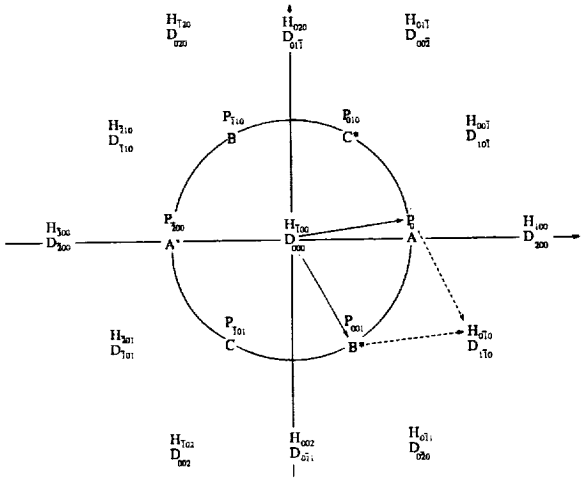

Figure 3: Wavevectors of modes that have to be kept in the perturbation expansion in order to avoid singularities in the growth rate at $\theta = 0$. The modes A, B, and C correspond to the basic hexagon. The circle denotes the circle of critical wavenumbers.

to the hexagon by an angle θ ($\epsilon \ll 1$ and $\delta \ll 1$). It turns out that this ansatz leads to singularities in the growth rate σ for $\theta = 0$ and $\theta = \pi/3$ due to resonances involving the quadratic terms that couple the three modes of the hexagon pattern. In order to get meaningful results over the range of angles that is of interest, $-\pi/6 < \theta < \pi/6$, it is therefore necessary to include the resonantly excited modes in the perturbation ansatz. This leads to a large number of perturbation modes. The wave vectors of the modes that have to be kept in this calculation are sketched in fig.3. In order to remove the singularity at $\theta = 0$ all the modes of type P have to be treated on the same footing.

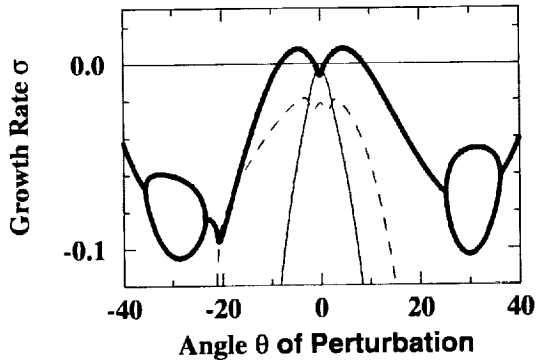

Figure 4: Growth rate of perturbations with wavelength 2π of the hexagonal pattern for $R = 0.125$, $\alpha = 0 = g_2$, $\beta = 0.2$, $\gamma = 10$, $g_3 = 10$.

In preliminary calculations we find, as expected, that the hexagonal pattern becomes unstable with respect to Swift's Hopf bifurcation (i.e. for $\theta = 0$) with increasing control parameter (Marangoni number) R. However, this Hopf bifurcation can be preempted by a Hopf bifurcation at a finite angle θ. This is shown in fig.4. The thick solid line denotes the branch of perturbations that destabilize the hexagon. It is connected with that of Swift's Hopf bifurcation ($\theta = 0$). However, for $\theta = 0$ the instability sets in only for larger values of R. For lower values of R the instability is characterized by modes that are rotated with respect to the hexagon pattern. The thin solid line corresponds to the two branches of modes that are associated with the two translation symmetries of the system, as can be seen from the fact that their growth rate vanishes for $\theta = 0$. For wavenumbers closer to the neutral curve (i.e. q noticeably larger or smaller than $q_c \equiv 1$) they will also lead to instabilities. They will presumably also be affected by the rotation.

Detailed analyses will show under which conditions which of the instabilities dominates. Subsequently, we will perform detailed numerical simulations of the long-wave equations (11) to investigate the nonlinear evolution ensuing from the instabilities. The dynamics could include periodic solutions as well as spatially and temporally chaotic ones. For the chaotic solutions we plan a detailed characterization of the resulting patterns using correlation functions, local coordination numbers, analysis of front motion and other tools as found appropriate.

5 CONCLUSION

Preliminary investigations of a qualitative model for the effect of rotation on hexagonal patterns as they arise in surface-tension driven convection have shown promising new instabilities. They are anticipated to lead to complex patterns of types that differ from those investigated in the context of buoyancy-driven convection. From an applied point of view, these complex flow patterns may, for instance, be relevant for the distribution of impurities in crystal growth from the melt in the presence of rotation.

Further extensions within this project may address instabilities of Marangoni convection with free-slip boundary conditions, as they may be realizable in freely suspended films (in strongly reduced gravity) [24]. In buoyancy-driven roll convection it has been found that for free-slip boundary conditions rotation leads to an additional instability, which arises at small angles θ [25]. Whether this instability also arises for hexagonal patterns and in surface-tension driven convection is not known.

REFERENCES

1. G. Küppers and D. Lortz. Transition from laminar convection to thermal turbulence in a rotating fluid layer. *J. Fluid Mech.*, 35:609, 1969.

2. F.H. Busse and K.E. Heikes. Convection in a rotating layer: a simple case of turbulence. *Science*, 208:173, 1980.

3. F. Zhong and R.E. Ecke. Pattern dynamics and heat transport in rotating Rayleigh-Bénard convection. *Chaos*, 2:163, 1992.

4. J.W. Swift. Convection in a rotating fluid layer. In *Contemporary Mathematics Vol. 28*, page 435, 1984.

5. J. Millàn-Rodriguez, C. Perez-Garcia, M. Bestehorn, M. Fantz, and R. Friedrich. Pattern formation in convection of rotating fluids with broken vertical symmetry. *Phys. Rev. A*, 46:4729, 1992.

6. A.A. Golovin, A.A. Nepomnyashchy, and L.M. Pismen. Non-linear evolution and secondary instabilities of Marangoni convection in a liquid-gas system with deformable interface. *J. Fluid Mech.*, 341:317, 1997.

7. A. Vidal and A. Acrivos. The influence of Coriolis force on surface-tension-driven convection. *J. Fluid Mech.*, 26:807, 1966.

8. G.A. McConaghy and B.A. Finlayson. Surface tension driven oscillatory instability in a rotating fluid layer. *J. Fluid Mech.*, 39:49, 1969.

9. T. Namikawa, M. Takashima, and S. Matsushita. The effect of rotation on convective instability induced by surface tension and buoyancy. *J. Phys. Soc. Japan*, 28:1340, 1970.

10. A. Kaddame and G. Lebon. Bénard-Marangoni convection in a rotating fluid with and without surface deformation. *Appl. Sci. Res.*, 52:295, 1994.

11. M. Bestehorn. Phase and amplitude instabilities for Bénard-Marangoni convection in fluid layers with large aspect ratio. *Phys. Rev. E*, 48:3622, 1993.

12. D.N. Riahi. Nonlinear Bénard-Marangoni convection in a rotating layer. *Int. J. Eng. Sci.*, 32:877, 1994.

13. J. Lauzeral, S. Metens, and D. Walgraef. On the phase dynamics of hexagonal patterns. *Europhys. Lett.*, 24:707, 1993.

14. G. Faivre, S. de Cheveigne, C. Guthmann, and P. Kurowski. Solitary tilt waves in thin lamellar eutectics. *Europhys. Lett.*, 9:779, 1989.

15. H. Riecke and H.-G. Paap. Parity-breaking and Hopf bifurcation in axisymmetric Taylor vortex flow. *Phys. Rev. A*, 45:8605, 1992.

16. A. Bayliss, B.J. Matkowsky, and H. Riecke. Structure and dynamics of modulated traveling waves in cellular flames. *Physica D*, 74:1–23, 1994.

17. B. Janiaud, H. Kokubo, and M. Sano. Coupled phase instability of a cellular pattern. *Phys. Rev. E*, 47:2237, 1993.

18. E. Knobloch. Pattern selection in long-wavelength convection. *Physica D*, 41:450, 1990.

19. L. Shtilman and G. Sivashinsky. Hexagonal structure of large-scale Marangoni convection. *Physica D*, 52:477, 1991.

20. A.A. Golovin, A.A. Nepomnyashchy, and L.M. Pismen. Pattern formation in large-scale Marangoni convection with deformable interface. *Physica D*, 81:117–147, 1995.

21. M. Fantz, R. Friedrich, M. Bestehorn, and H. Haken. Pattern-formation in rotating Bénard convection. *Physica D*, 61:147, 1992.

22. M. Neufeld, R. Friedrich, and H. Haken. Order-parameter equation and model equation for high Prandtl number Rayleigh-Bénard convection in a rotating large aspect ratio system. *Z. Phys. B*, 92:243, 1993.

23. D.N. Riahi. Nonlinear convection in a rotating layer with finite conducting boundaries. *Phys. Fluids A*, 2:353, 1990.

24. A. Oron, R.J. Deissler, and J.C. Duh. Marangoni instability in a liquid layer with 2 free surfaces. *Eur. J. Mech. B*, 14:737, 1995.

25. T. Clune and E. Knobloch. Pattern selection in rotating convection with experimental boundary-conditions. *Phys. Rev. E*, 47:2536, 1993.

The Effect of Surface Induced Flows on Bubble and Particle Aggregation

Scott A. Guelcher, Yuri E. Solomentsev, Marcel Böhmer*, John L. Anderson, and Paul J. Sides**

Department of Chemical Engineering
Carnegie Mellon University
Pittsburgh, PA 15213

*Philips Research Laboratories
Eindhoven, Prof. Holstlaan 4
5656 AA Eindhoven, The Netherlands

**Corresponding author: ps7r@andrew.cmu.edu

ABSTRACT

Almost 20 years have elapsed since a phenomenon called "radial specific coalescence" was identified. During studies of electrolytic oxygen evolution from the back side of a vertically oriented, transparent tin oxide electrode in alkaline electrolyte, one of the authors (Sides) observed that large "collector" bubbles appeared to attract smaller bubbles. The bubbles moved parallel to the surface of the electrode, while the electric field was normal to the electrode surface. The phenomenon was reported but not explained. More recently self ordering of latex particles was observed during electrophoretic deposition at low DC voltages likewise on a transparent tin oxide electrode. As in the bubble work, the field was normal to the electrode while the particles moved parallel to it. Fluid convection caused by surface induced flows (SIF) can explain these two apparently different experimental observations: the aggregation of particles on an electrode during electrophoretic deposition, and a radial bubble coalescence pattern on an electrode during electrolytic gas evolution. An externally imposed driving force (the gradient of electrical potential or temperature), interacting with the surface of particles or bubbles very near a planar conducting surface, drives the convection of fluid that causes particles and bubbles to approach each other on the electrode.

Phenomena. Two seemingly different phenomena, the aggregation of colloidal particles deposited on an electrode and the coalescence of gas bubbles generated near an electrode, can be explained from a unified point of view based on considering fluid convection. Sides and Tobias[1,2] studied the electrolytic evolution of oxygen bubbles from the back side of a vertically oriented, transparent tin oxide electrode in alkaline electrolyte. The authors discovered a phenomenon they termed "specific radial coalescence," whereby central "collector" bubbles appeared to attract smaller bubbles. A sequence of images from these experiments, appearing in Figure 1, demonstrates the effect.[2] The first frame shows a large bubble in the lower left quadrant with six smaller bubbles arranged around it in a near hexagonal array. As time elapses, each smaller bubble moves toward the large bubble until it eventually coalesces with it. The bubbles move as if "attracted" to the larger bubble from all points surrounding it; the effect was therefore independent of gravity since buoyancy would have moved the bubbles unidirectionally. Most of the bubbles in the experiment were mobile, which indicates the presence of a small but finite film of liquid between the bubbles and the electrode. Janssen and van Stralen[3] reported similar observations of lateral bubble motion on a transparent electrode during electrolytic gas evolution. The interactions between the bubbles appeared to be significant over distances over several bubble diameters (tens of microns) and could not be attributed to conventional colloidal/surface forces.

Colloidal particles can form ordered layers in both direct and alternating electric fields during electrophoretic deposition (EPD) on conducting surfaces.[5,6,7,8] Conditions under which the self-ordering occurs vary widely. Böhmer[4], studying field-induced lateral motion of 4 and 10 μm polystyrene spheres on a transparent indium-doped tin oxide (ITO) electrode, observed *in situ* clustering under direct current field strengths less than 20 V/m. The particles on the surface of the electrode aggregated to form clusters even though the particles were initially several radii apart. A time series of photographs, appearing in Figure 2, demonstrates this field-induced cluster formation. The first

doublets formed after 60 s. (Figure 2b). Subsequently, these doublets formed triplets and higher-order aggregates (Figure 2b, 2c). Particle-cluster and cluster-cluster aggregation continued until, as seen in the last picture of the series taken after 12 minutes, only one particle was left and several large ordered clusters were formed (Figure 2f). This series of photographs shows both the long-range nature of the interactions and cluster-cluster aggregation. The clusters separated into single particles when the electric field was reversed. Also, the particles exhibited Brownian motion even when they appeared to be on the surface of the electrode, which again indicated the presence of a small but finite gap of liquid between the particles and the electrode.

We propose a unified explanation for self-aggregation of particles and bubbles near surfaces. The mechanism is based on convection induced by the surfaces of particles or bubbles as they interact with an electric field or temperature gradient normal to the surface. Gradients perpendicular to fluid/fluid interfaces are known to produce convection[9,10,11], but these flows originate from perturbations in the interfacial tension caused by the coupling of electrical, thermal and composition gradients with deformation of the interface. The foundation of this model, however, is *steady* convection resulting from flows about particles and bubbles held stationary at a solid surface. The analysis for particle clustering is an elaboration of the mechanism first proposed by Böhmer[4].

Analysis. We attribute the long-range interactions (of order several radii) between particles and bubbles near a conducting solid-liquid interface to fluid convection induced by interactions between the applied field (electrical or thermal) and the surface of the particles and bubbles. These phoretic interactions[12] create a recirculating fluid flow pattern in the vicinity of the bodies. For a particle near an electrode, the electrical stresses resulting from the action of the electric field on the ions within the electrical double layer about the particle's surface produce an electroosmotic "slip velocity" at the outer edge of the double layer that drives the flow about the particle as shown in Figure 3a. The slip velocity is given by the Helmholtz expression, $\mathbf{v}^s = (-\varepsilon \zeta/\eta)\mathbf{E}$, where ε is the permittivity of the fluid (water), η is the viscosity[13], ζ is the zeta potential of the particle's surface, and $\mathbf{E}$ is the electric field tangent to the particle's surface.

For a bubble near a heated wall, an interfacial tension gradient over the bubble's surface results from an overall temperature gradient perpendicular to the wall. Fluid flow must balance the resulting interfacial stress at the interface, $\sigma^s = \gamma' \nabla T$ where γ' is the derivative of interfacial tension with temperature and ∇T is the temperature gradient at the interface.[14,15] Calculated fluid streamlines for this type of "Marangoni" flow appear in Figure 3b.

The phoretic velocity fields about a particle or bubble held stationary very near a planar electrode must be calculated in order to compare our hydrodynamic theory quantitatively with experimental observations of aggregation. For the case of a non-conducting, charged, spherical particle that is large relative to the thickness of the double layer, we first determined the spatial variation of the electrical potential by solving Laplace's equation which follows from charge (ion) conservation in the electrolyte solution. The potential on the electrode was assumed uniform. From this solution we calculated the electric field $\mathbf{E}$ at each point on the surface of the particle, from which the slip velocity was determined. Then the steady Stokes-flow equations were solved using the slip velocity boundary condition ($\mathbf{v} = \mathbf{v}^s$) at the particle's surface (*i.e.*, at the outer edge of the double layer). Details are given by Solomentsev *et al.*[16] The streamlines of Figure 3a are essentially the same for any gap distance h less than 10% of the radius of the particle. The calculation of the Marangoni flow field in the vicinity of a bubble very near a heated plane wall at uniform temperature proceeded similarly except that the Stokes equations were solved by balancing the hydrodynamic stress with the interfacial stress ($\sigma = \sigma^s$) at the surface of the bubble. The overall thermal gradient, used as the boundary condition far from the bubble, was calculated from the heat dissipation on the electrode's surface due to electrochemical reaction on the electrode and ohmic heat production in the antimony-doped tin oxide film, as described later. Again, the streamlines of Figure 3b are independent of the gap between the bubble and the surface when it is less than 10% of the particle's radius.

The calculated streamlines for either electroosmotic or Marangoni flows, Figure 3, indicate that the effect of convection could be to either attract two particles or repel them. A "test" body adjacent to the electrode will be convected toward the first body. The flow field about the test body will have a similar effect on the first body if they are of equal

size, so that the two particles or bubbles approach each other. A test body far from the electrode will be convected away from the first body as it approaches the electrode but then will be convected toward the first body when it is near the electrode. Since the flow is linear with the applied electric or temperature field, the direction of the fluid velocity changes if the direction of the field is reversed, which resulted in the de-clustering of particles observed experimentally[5] in the case of electrophoretic deposition.

In the case of EPD of particles, we have analyzed the clustering of groups of particles by neglecting the effects of multiple particles on the local electrical potential and fluid velocity. The velocity of a test particle toward the central particle, v_r, is assumed equal to the fluid velocity in the absence of the test particle, v_{r0}, multiplied by a correction factor q to account for the hydrodynamic hindrance due to the electrode surface.[17] Multiple simulations of triplets of different initial configurations accounted for the random nature of the aggregation process. The initial configuration of the three particles was chosen randomly except that no overlap was allowed. The position versus time of each particle was computed by integrating its velocity over time, where the particle's velocity was given by the sum of v_r caused by the other two particles. The parameter q was considered a single adjustable parameter independent of the relative positions of the three particles. Details of the calculations are reported elsewhere.[16]

The de-clustering time of a triplet (T^E), defined as the time required for the three initially contiguous particles to disaggregate, was calculated as a function of the final mean center-to-center separation distance ($d = [d_{12} + d_{13} + d_{32}]/3$) between the particles for random initial configurations. The following expression approximates the calculated values of $T^E(d)$ in the range $2<d<7$ very well:

$$T^E(d) = 2.19\frac{(d-2)}{q}\exp(0.277\,d) \qquad (1)$$

This theoretical result is compared to the experimental data of Böhmer[5] in Figure 4. The experimental data are for de-clustering of triplets upon reversal of the field; thus, d represents the mean spacing at each time. In this plot, the separation distance was normalized by the particle's radius (a), and the de-clustering time by a/v^s with |E| equal to the applied electric field perpendicular to the electrode. The best-fit value of the hydrodynamic correction factor (q) is 0.5, which is expected for gaps between the particle and electrode of 1-10% of the particle's radius.[17]

Symbols of different shapes in Figure 4 represent different triplets in the experiments. The applied voltage was different for each triplet, either -1 V or -1.5 V. The data as plotted in Figure 4, with time normalized by the slip velocity v^s (which is itself proportional to the applied electric field), indicate that the relative motion among the three particles was linear with the electric field, as predicted by the theory.

Although the liquid-gas interface might be charged, the motion of bubbles at electrodes leading to specific radial coalescence cannot be attributed to electroosmosis because the velocities observed by Sides and Tobias[7] were two to three orders of magnitude higher than the estimated magnitude of the electroosmotic slip velocity v^s. On the other hand, the observed lateral motion of equal-size bubbles toward each other can be explained in terms of Marangoni convection around each bubble near the electrode, where the velocity scale is given by $v^m = g'$—Ta/2h with g' being the derivative of surface tension with respect to temperature and a the bubble's radius.[15] The theory for this case resembles the theory developed for deposited particles; that is, a test bubble is entrained in the convective flow about the other bubble (v_{r0}) and moves toward it at velocity $v_r = qv_{r0}$ where q is the hindrance factor of the electrode. These calculations for the change in center-to-center distance (d) between the bubbles as a function of time (t) are fit by the following empirical equation (h=0.05):

$$d(t) = q(3.336 - 0.185t)\exp(0.030t) \qquad (2)$$

The distance is normalized by a and the time by a/v^m.

The temperature gradient at the surface of the bubble must be determined in order to calculate the magnitude of the Marangoni flow field about a deposited bubble. We solved Laplace's equation for the temperature field around a bubble subject to a constant uniform temperature at the electrode and a specified gradient of temperature far from the bubble and the electrode. In the experiments of Sides and Tobias, no temperature measurements were made, so the far-field gradient was estimated from the irreversibilities of the electrochemical reaction and

the ohmic losses in the thin tin oxide electrode used in the experiments. The homogeneous ohmic heating of the electrolyte was neglected in these calculations because it raised the overall temperature but did not affect the gradients on the time scale of the experiments. We used film theory[18] in the aqueous phase to express this gradient $(-\nabla T)_s = Q/k$, where Q is the heat flux dissipated from the electrode, and k is the thermal conductivity of the electrolyte. This quotient is a reasonable approximation of the average gradient for bubbles having diameters smaller than the thermal boundary layer thickness. Estimating the thickness of the thermal boundary layer by analogy from mass transfer correlations developed for electrolytic gas evolution[19], one obtains approximately 140 mm, which is between three and four times the diameter of the largest bubble considered in this analysis. Prior analysis has shown that this distance from the electrode is sufficient for disturbances in the potential or the temperature to relax.[20] The heat flux Q from the anode to the electrolyte can be approximated by the sum of the irreversible heat flux Q_{rxn} generated at the anode surface by the electrode reaction, and the ohmic heat flux from the tin oxide film Q_{film}. The flux Q_{rxn} is calculated by

$$Q_{rxn} = i\eta_{rxn} \tag{3}$$

where i is the current density and h_{rxn} is the electrochemical overpotential for oxygen evolution. The ohmic heat flux is calculated by

$$Q_{film} = i^2 R_{sq} L^2 \tag{4}$$

where L is the effective current path length taken as half the cell width (1.5×10^{-3} m). The electrode had an electrical resistivity R_{sq} = 100 ohms per square. For a current density of 5,000 A m^{-2} and an overpotential of 1 V, the above equations yield a total heat flux Q = 10,600 W m^{-2} and a temperature gradient $(-\nabla T)_s$ = 17,700 K m^{-1}; for a current density of 1,000 A m^{-2}, the temperature gradient was 2,070 K m^{-1}. The bubbles ranged in radius from 13 to 22 mm. Therefore, we estimate that the temperature difference between the bottom (hot region) and top (cold region) of the bubbles varied from about 0.05 K to 0.8 K. The corresponding difference in interfacial tension varied from about 0.007 10^{-3} N m^{-1} to 0.12 10^{-3} N m^{-1}.

Using the above estimates of the temperature gradient, the theory expressed by equation (2) is compared to the experimental values of d versus t for four different pairs of bubbles in Figure 5. The data were obtained by analyzing movies of the radial coalescence.[6] As in the case of particles, there is good agreement between the theory and the experiment, and the data scale as predicted with two different parameters, bubble radius and current density (*i.e.*, temperature gradient). The value of the hydrodynamic correction factor (q) was assumed to be 1.0.

Discussion Aggregation of particles near an electrode and coalescence of bubbles near a heated wall are physically different phenomena but can be explained by a similar hydrodynamic mechanism resulting from convection induced by interfacial forces. For bodies of approximately the same size, the phoretic flow theory is in reasonable agreement with the experimental data when the hydrodynamic correction factor q is of order unity. The analysis described above accounts for the aggregation of equal-size particles or bubbles (Figure 1), but modification of the theory is necessary when the primary particle is much larger than the test particle (Figure 2). In this case the velocity of the test particle (bubble) toward the primary particle (bubble) is a superposition of the mutual entrainment mechanism described in this paper and the additional electrophoretic (thermocapillary) velocity caused by perturbation of the electrical potential (temperature) around the primary particle (bubble). For a size ratio of about 0.2, the attractive velocity due to the perturbed electrical potential is comparable to the convective velocity; thus, the velocity of a small particle in close proximity of a large collector particle on an electrode can be significantly greater than the entrainment velocity of a particle of the same size as the collector particle.

Yeh *et al.*[6] observed clustering under conditions of alternating current (1 kHz) and a field strength of 25,000 V/m. These authors offered a qualitative explanation based on electrohydrodynamic interaction of lateral electric field gradients with the double layer of the electrode rather than the particle. Their model does not predict sufficient flow velocities at the field strengths used by Böhmer to explain his observations. Furthermore, Yeh *et al.*'s model cannot explain the motion of bubbles on electrodes mentioned above. To compare the expected flow velocities predicted by the model of Yeh *et al.* and the results reported herein under Böhmer's conditions, we calculated the ratio of the lateral fluid velocities predicted by the two models. Assuming that within the electrode double layer current is carried by a single ionic species of

concentration n_0, Yeh *et al.* presented the following equation for the transverse fluid velocity v_t:

$$v_t \approx \frac{k_B T}{\eta D_o} l_d^3 \frac{J_o}{eR} \qquad (5)$$

where k_B is the Boltzmann constant, e is electron charge, D_0 is the diffusion coefficient of the ion, l_d is the double layer thickness, J_0 is the current density, and R is the length scale of the feature on the electrode surface. Since the feature on the electrode in the present case is a particle, R is the particle radius. The fluid velocity due to electroosmosis v_{eo} about a deposited charged particle, according to our model, is:

$$v_{eo} = f(r)\frac{\varepsilon\zeta}{\eta} E_\infty \qquad (6)$$

where E_∞ is the magnitude of the applied electric field and f(r) is a factor less than unity that gives the correct estimation of the transverse flow as a function of center-to-center distance "r". The ratio v_{eo}/v_t is calculated from the following equation:

$$\frac{v_{eo}}{v_t} = f(r)\frac{e}{k_B T}\frac{\varepsilon\zeta a D_o}{\kappa l_d^3} \qquad (7)$$

where k is the specific conductivity of the electrolyte. Values of v_{eo}/v_t as a function of the center-to-center distance r between two particles on the surface of the electrode are presented in Table 1. The data 1 indicate that the electroosmotic phenomenon described in this work is 1 to 2 orders of magnitude stronger than the effect described by Yeh *et al.* for the conditions of Böhmer's experiments.

Our conclusion is that a purely hydrodynamic model for self-aggregation of nearly equal-size particles deposited on an electrode and for bubbles formed on a hot surface (which here is an electrode) can quantitatively explain the observed rates of clustering and coalescence. The concept is that the fluid convection driving aggregation derives from direct interactions between the field (electrical or thermal) and the deposited species (particle or bubble).

Acknowledgments This work was partially supported under NSF Grant CTS-9420780. S.G. acknowledges support from the NASA Graduate Student Researchers Program under Grant NGT5-50054.

References

1. Sides, P. J. Bubble Dynamics at Gas Evolving Electrodes, Ph.D. Thesis, University of California, Berkeley, 1981.
2. Sides, P.J. & Tobias, C.W. *J. Electrochem. Soc.* **132**, 583 (1985).
3. Janssen, L.J.J. & van Stralen, S.J.D. *Electrochimica Acta* **26**, 1011 (1981).
4. Böhmer, M. *Langmuir* **12**, 5747 (1996).
5. Trau, M., Saville, D.A. & Aksay, I.A. *Science* **272**, 706 (1996).
6. Yeh, S.-R., Seul, M. & Shraiman, B.I. *Nature* **386**, 57 (1997).
7. Giersig, M. & Mulvaney, P. *J. Phys. Chem.* **97**, 6334 (1993).
8. Giersig, M. & Mulvaney, P. *Langmuir* **9**, 3408 (1993).
9. Taylor, G.I. & McEwan, A.D. *J. Fluid Mech* **22**, 1 (1965).
10. Sternling, C.V. & Scriven, L.E. *AIChE J.* **5**, 514 (1959).
11. Scriven, L.E. & Sternling, C.V. *Nature* **187**, 186 (1960).
12. Anderson, J.L. *Annual. Rev. Fluid Mech.* **21**, 61 (1989).
13. Hunter R.J., Zeta potential in colloid science : principles and applications. London: Academic Press, 386 (1981).
14. Levich, V.G. & Krylov, V.S. *Annual Rev. Fluid Mech.* **1**, 293 (1969).
15. Young, N.O., Goldstein, J.S & Block, M.J. *J. Fluid Mech.* **6**, 350 (1959).
16. Solomentsev, Yu., Böhmer, M. & Anderson, J.L. submitted to *Langmuir* (1997).
17. Goldman, A.J., Cox, R.G. & Brenner, H. *Chem. Eng. Sci.* **22**, 653 (1967).
18. Bird, R.B., Stewart, W.E. & Lightfoot, E.N., Transport Phenomena. New York: John Wiley & Sons, 659 (1960).
19. Sides, P. J., "Phenomena and Effects of Electrolytic Gas Evolution" *Modern Aspects of Electrochemistry* **V. 18** R. E. White, B. E. Conway, J. O'M. Bockris, eds., Plenum, New York (1986).
20. Sides, P. J. and C.W. Tobias, *Journal of the Electrochemical Society* **127**, 288 (1980).

Figure Captions

Figure 1. Frames from the movie of Sides and Tobias showing electrolytic gas evolution (oxygen) from the back side of a tin oxide electrode in KOH. The bubbles grow away from the viewer as if on the far side of a pane of glass. The frames represent a square about 150 mm on a side and approximately 0.4 ms elapses between frames. One can particularly see the phenomenon of specific radial coalescence by following the fates of bubbles 1 - 6 as they seem to be attracted to the larger bubble they surround. Bubbles 7 and 8 will coalesce with the bubble on the right edge of the viewing area.
Frame 4: Bubble 1 has arrived at its "collector" bubble and coalesces with it in frame 5. Bubbles 2-5 are approaching their collector bubble. Bubble 8 reaches the bubble on the right edge of the frame (left) and coalesces with it in frme 5. Bubble 7 is moving toward the bubble on the right edge.
Frame 7: Bubbles 2 - 5 have all reached the collector. Bubble 8 has reached its collector.
Frame 9: All bubbles have coalesced with their respective collectors..

Figure 2. Time series for the formation of clusters of 10 μm PS particles starting from a semi-regular array at 1.5 V.

Figure 3. a) Fluid convection induced by electroosomosis about a stationary particle near an electrode whose surface is the horizontal axis at the bottom. In this example the particle could be negative and the electrode positive, so the electroosmotic slip velocity draws fluid upward near the particle. If the particle and electrode have the same sign of charge, then the arrows on the streamlines are reversed. The fluid velocity is zero along the electrode's surface. b) Convection induced by thermocapillary motion about a stationary bubble near a surface where a uniform gradient of temperature exists perpendicular to the surface, such that the surface is hotter than the fluid. If the temperature gradient is reversed, then the arrows on the streamlines are reversed.

Figure 4. De-clustering time as a function of the mean center-to-center distance d for three particles. Time is normalized by a/v^s where a is the particle's radius and v^s is the magnitude of the electroosmotic slip velocity (= $(\varepsilon z/h)E_\bullet$), while the separation distance is normalized by a. The symbols are the data from the experiments by Böhmer[5] in which three particles initially in contact separated (de-clustered) when the electric field was reversed; in this case, d is the mean separation among the three particles at the designated time. Each symbol represents a different triplet, and the horizontal error bars correspond to the standard deviations of the distance measurements. The solid line is the prediction from the hydrodynamic theory (equation (1)) with the hydrodynamic hindrance factor q = 0.50. For the theoretical predictions, d is the initial mean separation and the vertical bars are the standard deviations of simulations for the range $2<d<5$ (10-15 trials at each separation), with random but non-overlapping initial placement of the three particles.

Figure 5. Dimensionless center-to-center distance d as a function of dimensionless time t for 8 pairs of bubbles of approximately equal size. The parameter t is normalized by a/v^m where v^m is the magnitude of the Marangoni velocity ($v^m = g'—Ta/2h$), and d is normalized by the particle's radius a. Filled symbols correspond to a current density of 1000 A m^{-2}, while the open symbols correspond to a current density of 5000 A m^{-2}. Symbols of different shapes represent different pairs of bubbles. The solid line is calculated from the theory (equation (2)) with q= 1.0.

Table 1

Center-to-center distance (radii)	f(r)	v_{eo}/v_t
4	0.06	31
3	0.12	63
2	0.18	94

Ratio of the expected electroosmotic velocity v_{eo} to the transverse electrohydrodynamic velocity v_t of Yeh *et al.* calculated from eq (7). The calculations were performed based on the experimental conditions of Böhmer: ion concentration $n_0 = 10^{-4}$ M (corresponding to $l_d = 30\ 10^{-9}$ m and $\kappa = 15\ 10^{-4}$ ohm^{-1} m^{-1}), ionic diffusion coefficient $D_0 = 2\ 10^{-9}$ m^2 s^{-1}, particle zeta potential $\zeta = 0.08$ V, and particle radius $a = 5\ 10^{-6}$ m.

Figures

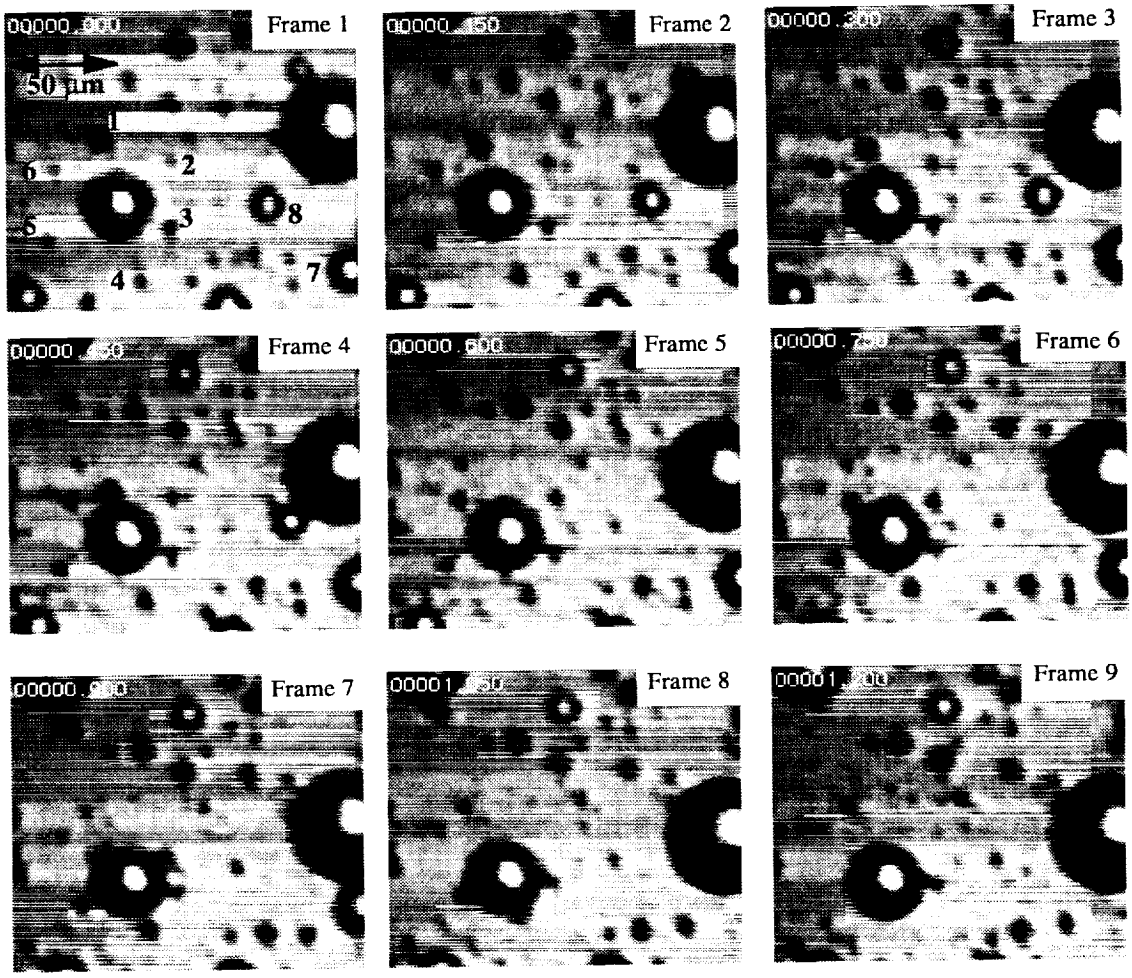

Figure 1.

a.

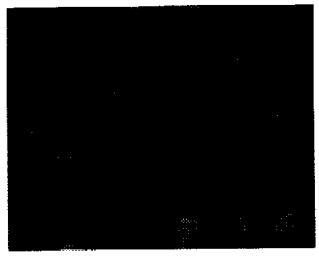

b.

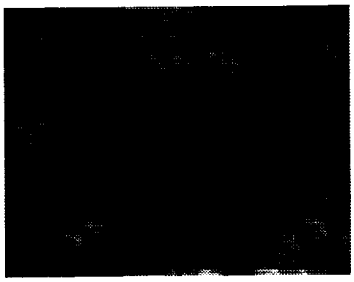

c.

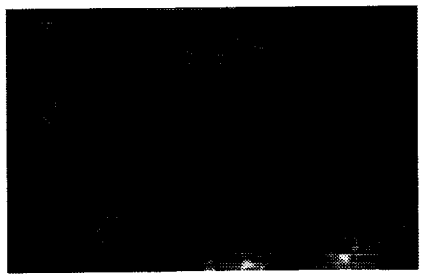

d.

Figure 2.

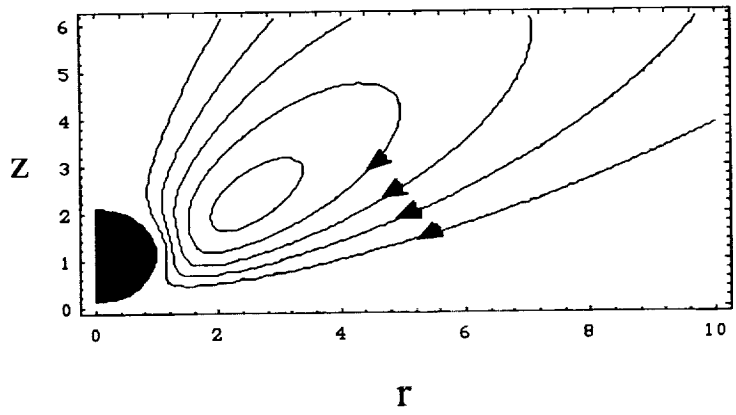

a.

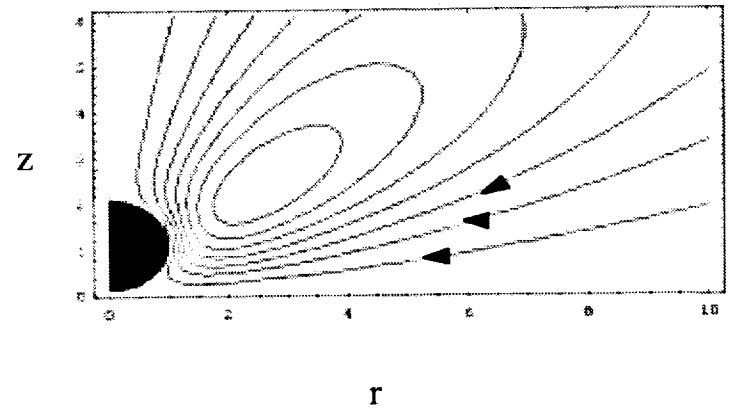

b.

Figure 3.

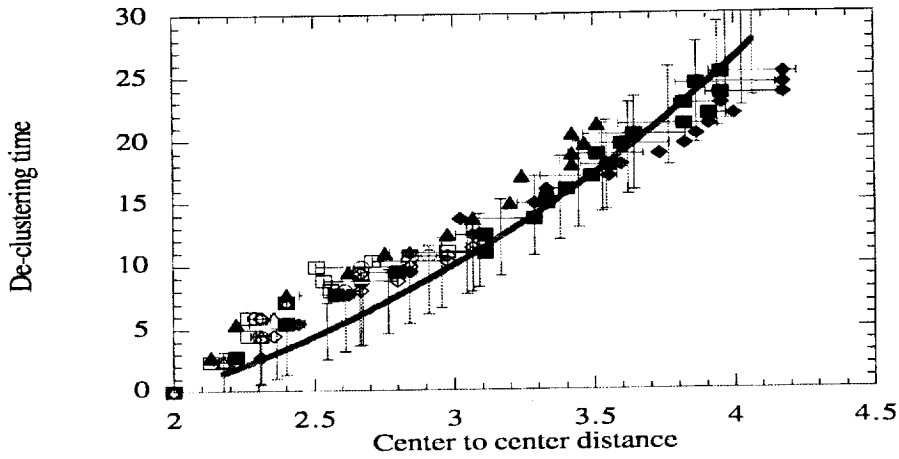
De-clustering time
30
25
20
15
10
5
0
2
2.5
3
3.5
4
4.5
Center to center distance

Figure 4.

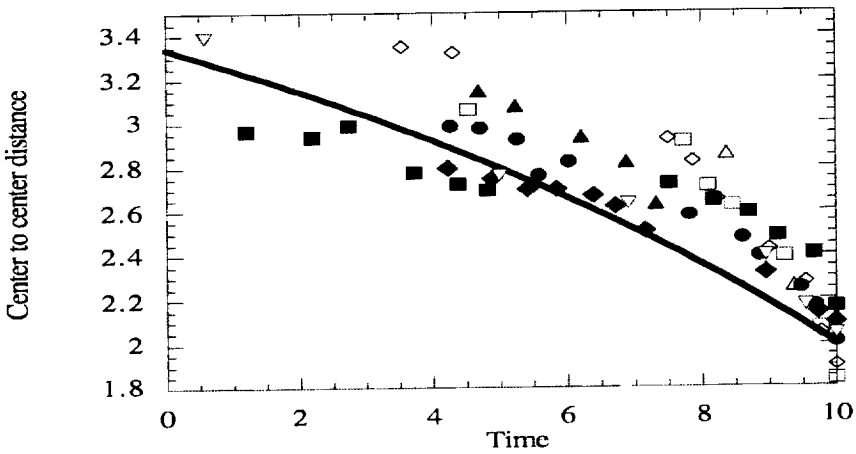

Figure 5.

Modeling of Transport Processes in a Solid Oxide Electrolyzer Generating Oxygen on Mars

K. R. Sridhar
The University of Arizona
Tucson, Arizona

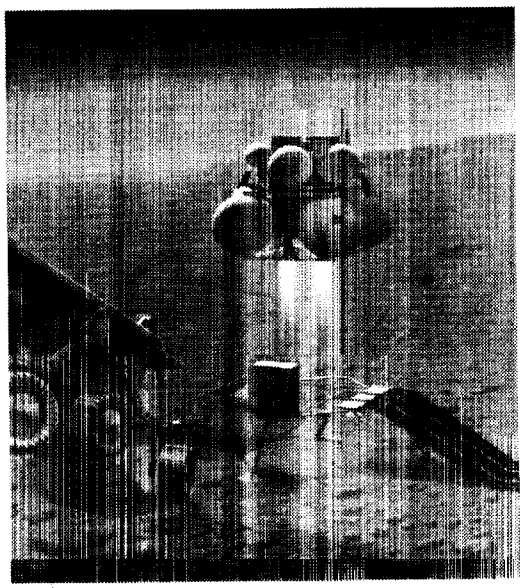

K.R. Sridhar, (520) 621-6111

In-Situ Resource Utilization (ISRU) is Living off the Land
An Early Example!

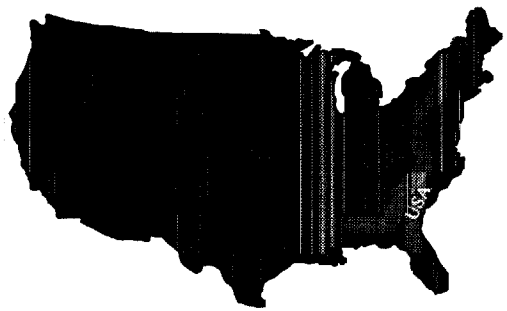

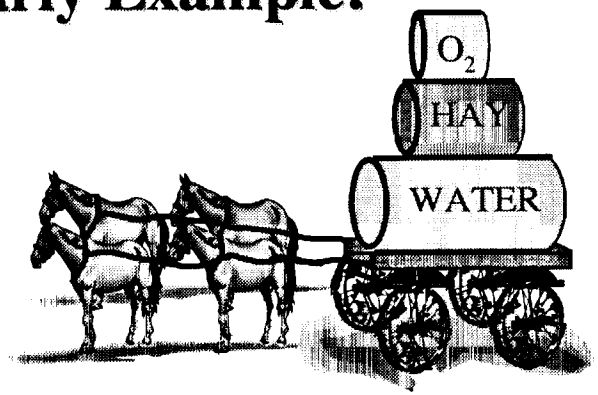

280 lb
350 lb
1370 lb
2000 lb

Mules Consumables / day

Oxygen	12 lb
Hay	15 lb
Water	58 lb
Total	85 lb

Six mules can pull a light wagon with 2000 lb max load for 25 miles/ day
MAX RANGE = 100 MILES

ISRU can:
- **Increase range of missions**
- **Increase duration of missions**
- **Reduce mass carried from source**
- **Provide self sufficiency**
- **Relax closure requirements for consumables regeneration**
- **Lower risk**

Oxygen Generation on Mars

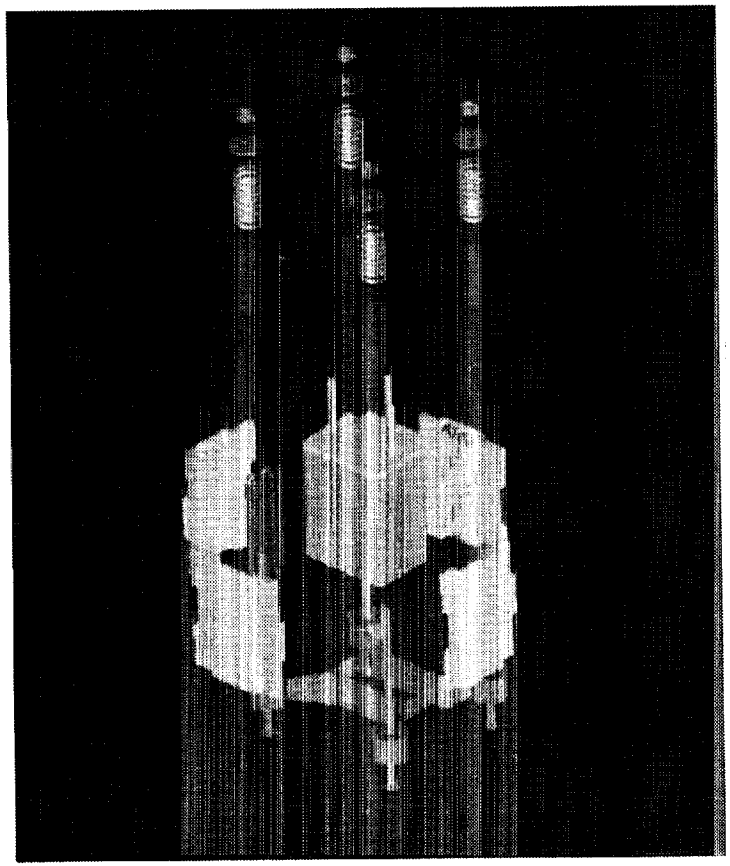

- Oxygen can be generated from the predominantly CO_2 atmosphere of Mars using the solid oxide electrolysis (SOE) process. The SOE process can be used to:
  - produce oxidant for the return vehicle propellant on sample return and human missions, and planetary mobility systems (rovers, hoppers,...)
  - make-up oxygen for closed loop life support systems on human missions
  - provide nighttime power in a regenerative fuel cell mode
  - compress oxygen for storage and/or liquefaction

OXYGEN GENERATION PRINCIPLE

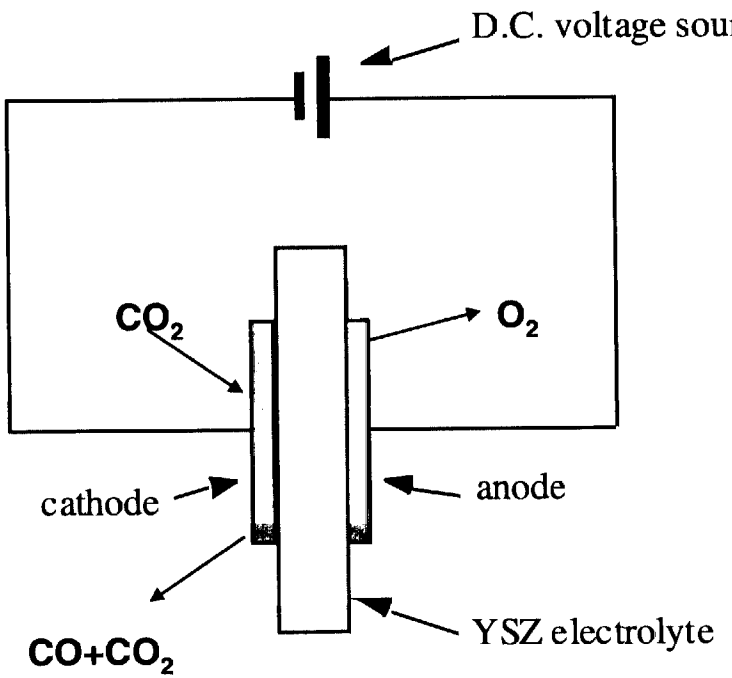

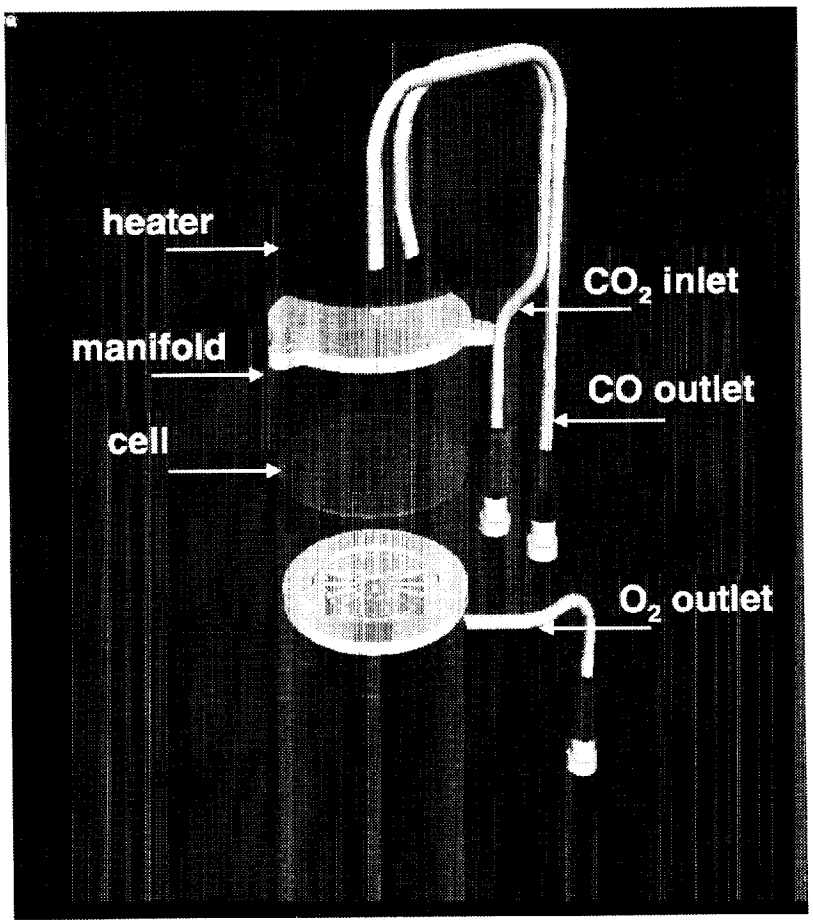

ZIRCONIA CELL PROCESS

DEPT. OF AEROSPACE AND MECHANICAL ENGINEERING
K.R. Sridhar, (520) 621-6111

Oxygen Generator System on 2001 Mars Lander

- **Landmark experiment: first ever demonstration of materials manufactured using resources from other planets, uses SOE process**

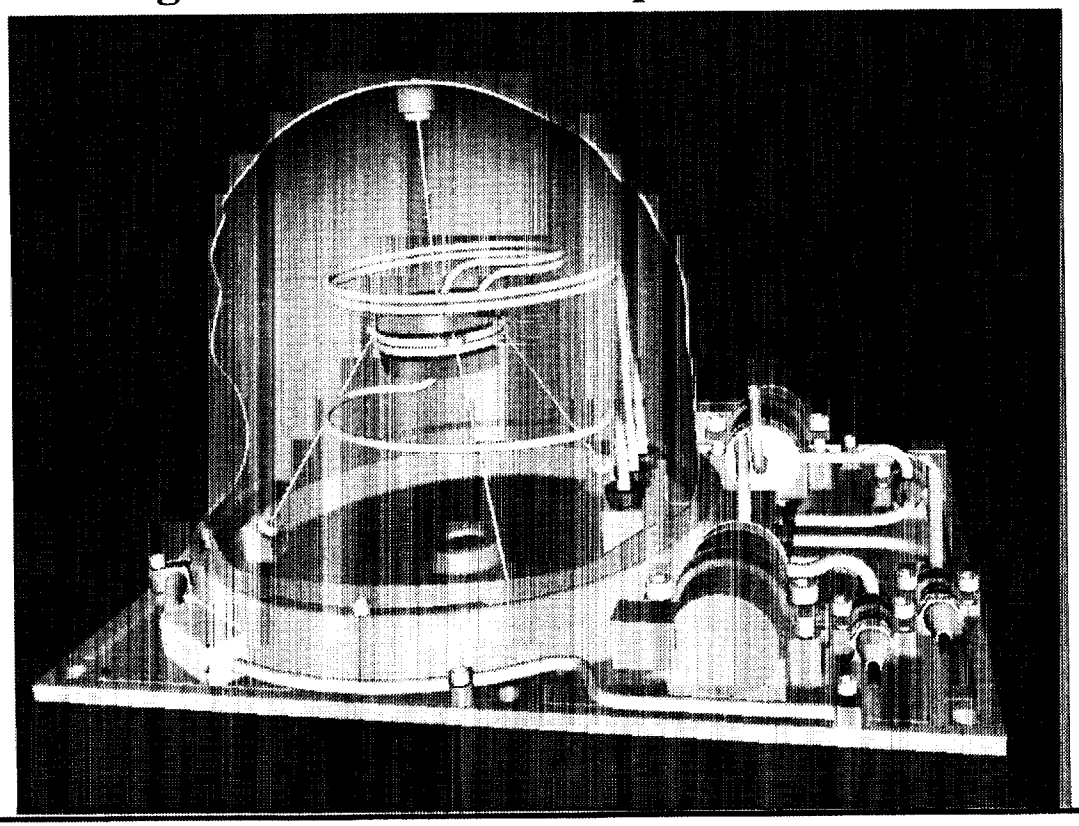

DEPT. OF AEROSPACE AND MECHANICAL ENGINEERING
K.R. Sridhar, (520) 621-6111

Transport Processes

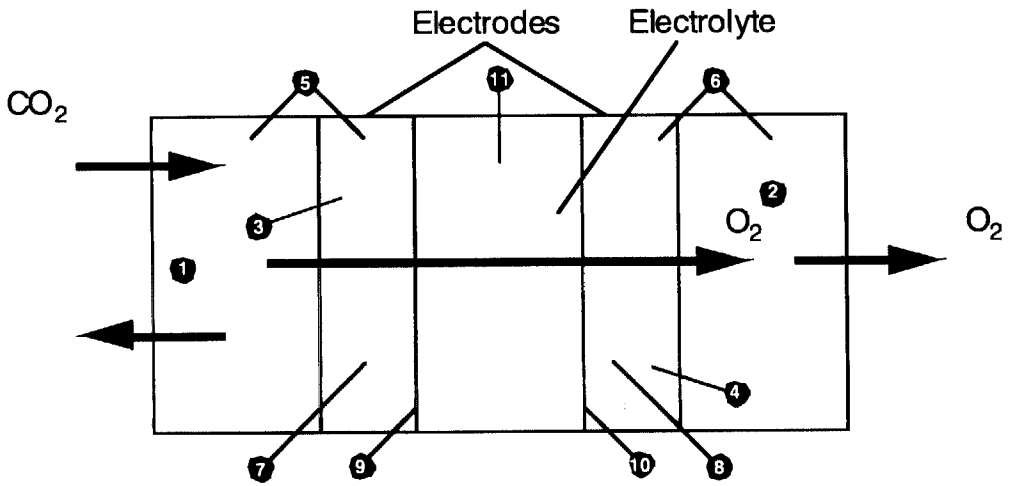

1 2 bulk transport of gases to gas/electrode interface

3 4 diffusion of gases in the porous electrode

5 6 pre-electrochemical homogenous chemical reaction

$$O + O \rightleftharpoons O_2$$

$$CO_2 \rightleftharpoons CO + O$$

7 8 migration of electroactive species (O) to/from the electrode/electrolyte interface

9 10 electrochemical reaction at the three phase boundary

11 ionic transport in solid electrolyte

DEPT. OF AEROSPACE AND MECHANICAL ENGINEERING
K.R. Sridhar, (520) 621-6111

Research Approach

- Laboratory experiments to characterize the performance of the electrolyzer
  - measurements of overpotentials
  - determination of activation and concentration overpotential components
  - determination of contact and material resistances
- Modeling of transport processes
  - transport equations
  - material properties from lab data
  - constants from experiments
- Validation experiments
- Improved electrolyzer design

K.R. Sridhar, (520) 621-6111

Work in Progress

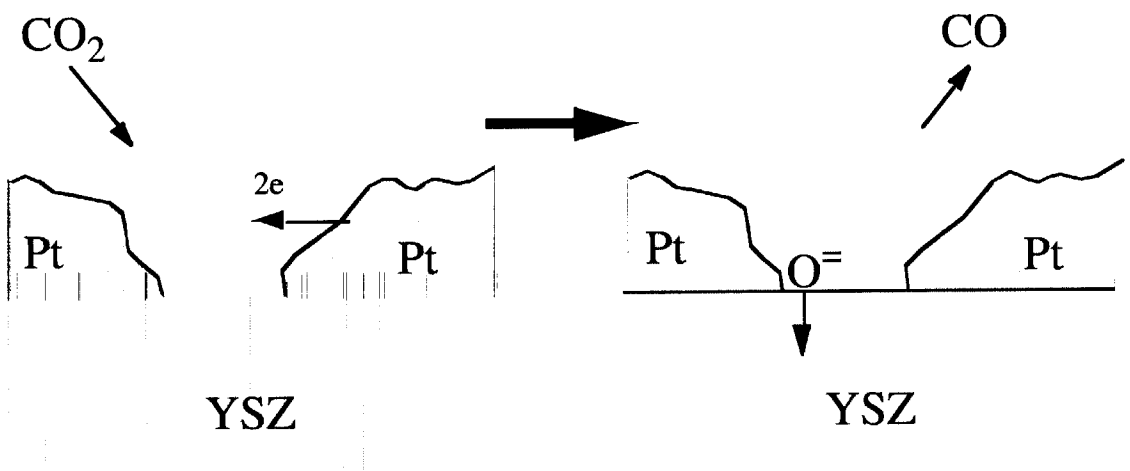

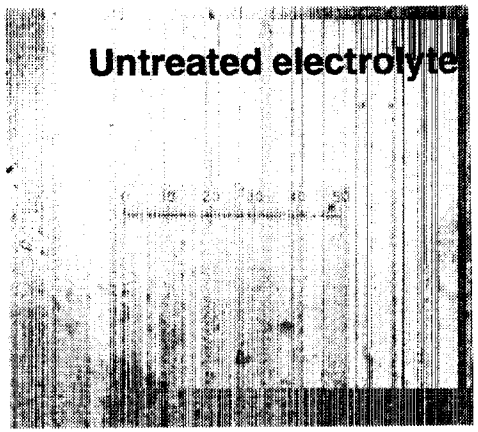

Three phase boundaries (between electrode, electrolyte and gas phase) are where oxygen ion transport occur

Laser treatment of the electrolyte (right) to cause controlled pitting increases the effective three phase area for a given projected area of the electrolyte

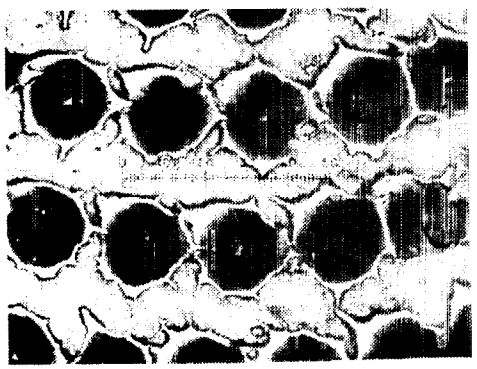

DEPT. OF AEROSPACE AND MECHANICAL ENGINEERING

K.R. Sridhar, (520) 621-6111

Work in Progress

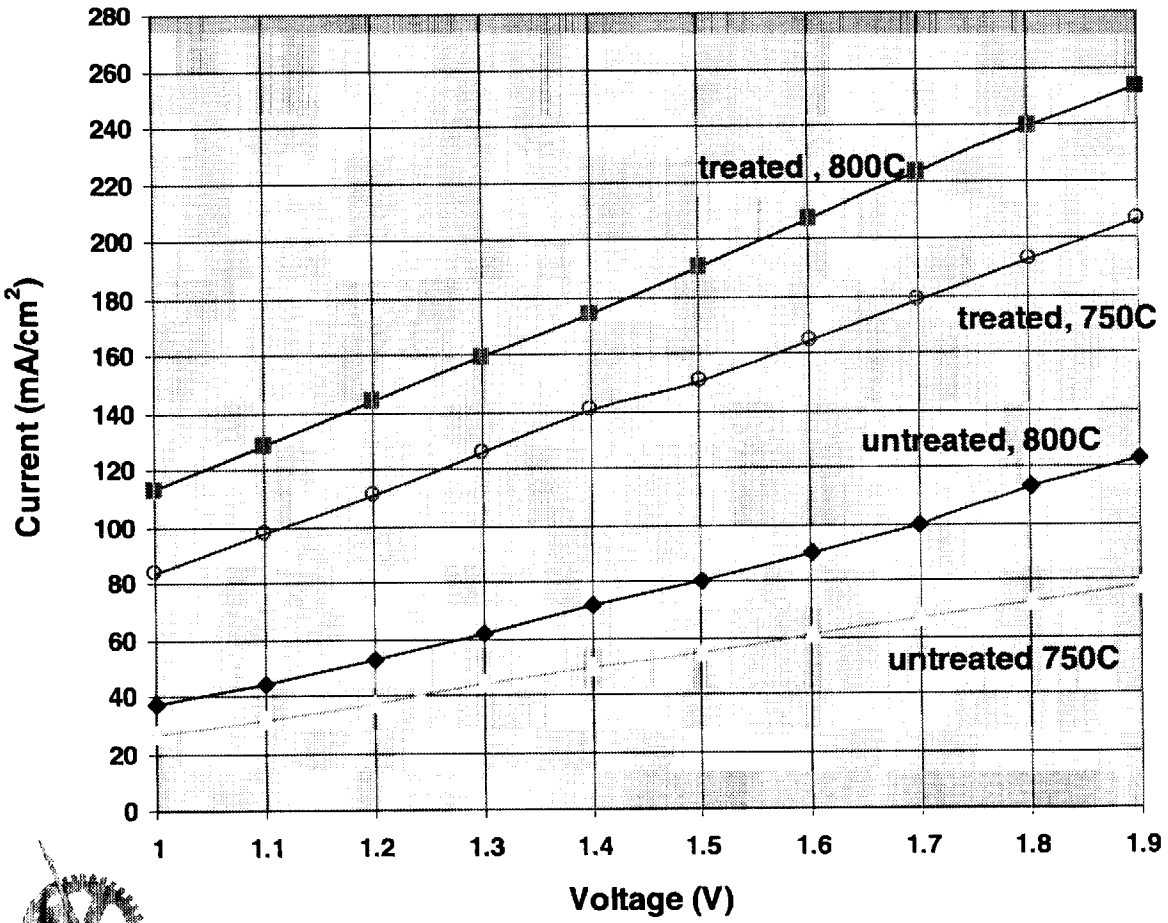

The treated electrolyte with the enhanced three phase boundary offers significant improvement in performance

Further evaluation is underway

DEPT. OF AEROSPACE AND MECHANICAL ENGINEERING
K.R. Sridhar, (520) 621-6111

COMPUTATIONS OF BOILING IN MICROGRAVITY

Grétar Tryggvason
Department of Mechanical Engineering
University of Michigan
and
David Jacqmin
NASA Lewis Research Center

Proposed Research

- Development of a three-dimensional, grid adaptive, fully parallel numerical method and a code to simulate boiling in microgravity. The method is based on an already existing two-dimensional code and techniques used for three-dimensional flows with no phase change
- The applications of the method to study the growth of bubbles in boiling heat transfer under both flow and no-flow conditions as well as the resulting heat transfer

Numerical Method

Finite Difference/Front Tracking discretization of the "one-field" formulation.
Source terms are added at the interface to satisfy boundary conditions there.

$$\frac{\partial \rho \bar{u}}{\partial t} + \nabla \cdot \rho \bar{u}\bar{u} = -\nabla p + \bar{f} + \nabla \cdot \mu\left(\nabla \bar{u} + \nabla^T \bar{u}\right) + \int_F \sigma \kappa \bar{n} \delta\left(\bar{x} - \bar{x}_f\right) da$$

$$\nabla \cdot \bar{u} = 0$$

$$\frac{D\rho}{Dt} = 0$$

$$\frac{D\mu}{Dt} = 0$$

Second order time and space discretization on a staggered grid

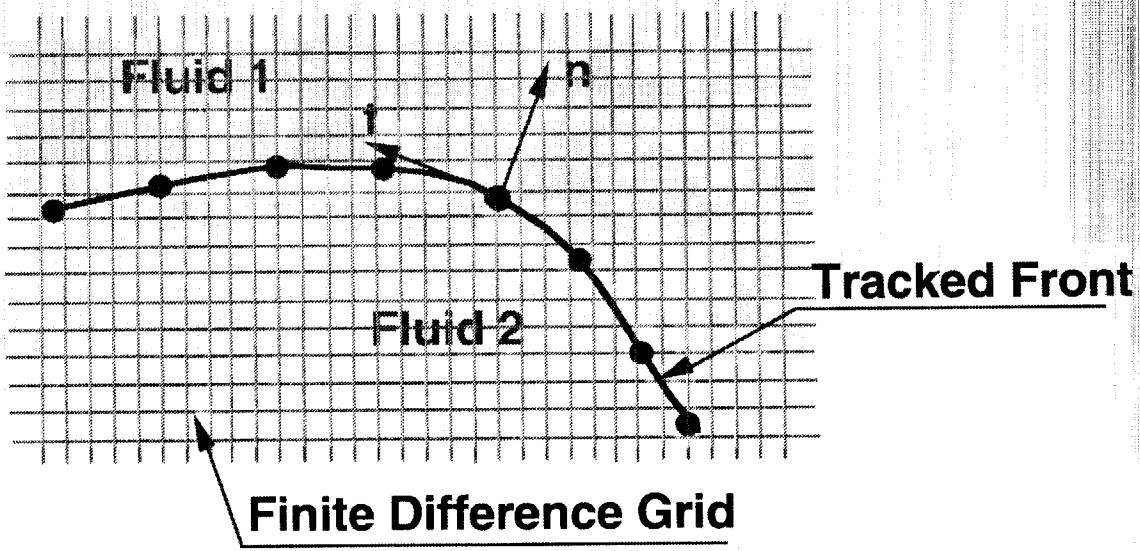

References:

S.O. Unverdi and G. Tryggvason. A front-tracking method for viscous, incompressible, multi-fluid flows, J. Comput Phys. 100 (1992), 25-37

D. Juric and G. Tryggvason. Computations of Boiling Flows. To appear in Int'l. J. Multiphase Flow.

Preliminary Results-Boiling

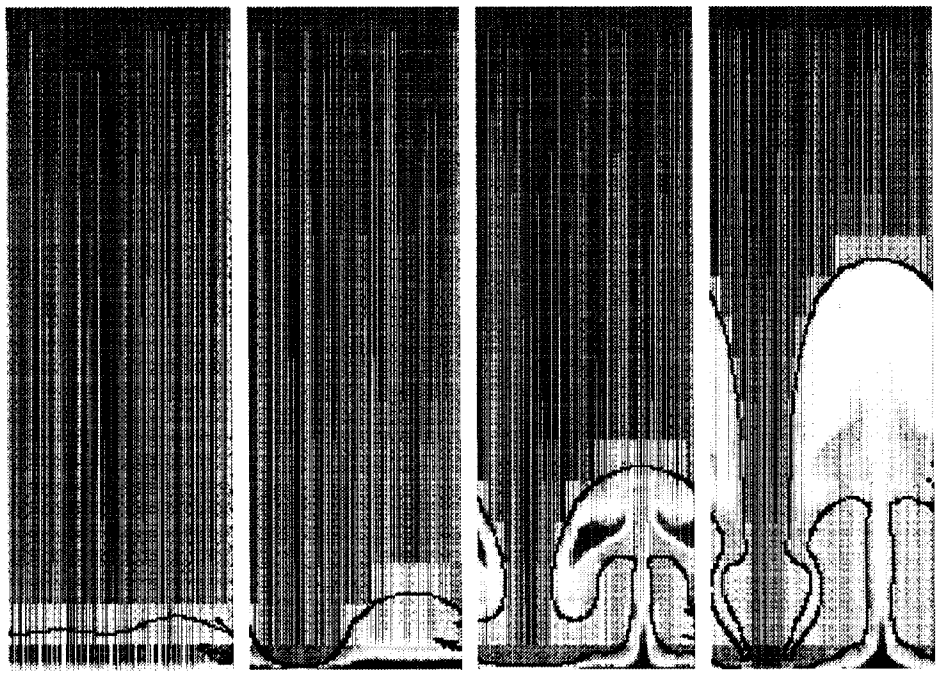

Two-dimensional results

Reference: D. Juric and G. Tryggvason. Computations of Boiling Flows. To appear in Int'l. J. Multiphase Flow.

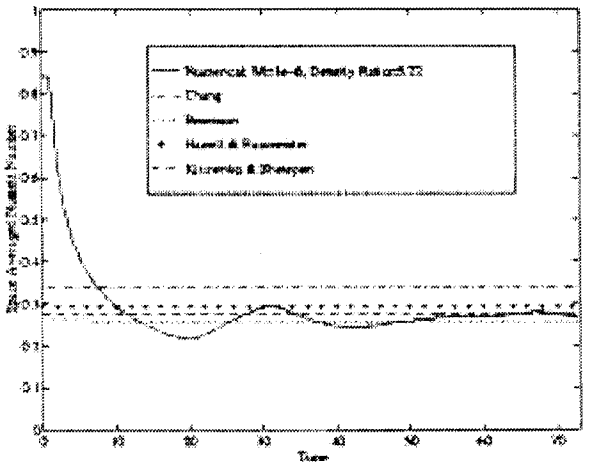

The boiling of hydrogen at high pressure is shown in the figure above, at four different times. The color represents the temperature, with red hot and blue cold. The bottom wall has a constant heat flux. The average heat flux is shown versus time in the figure to the right. Prediction by various experimental correlations are shown by horizontal lines.

Other Relevant Results

Dendritic Solidification

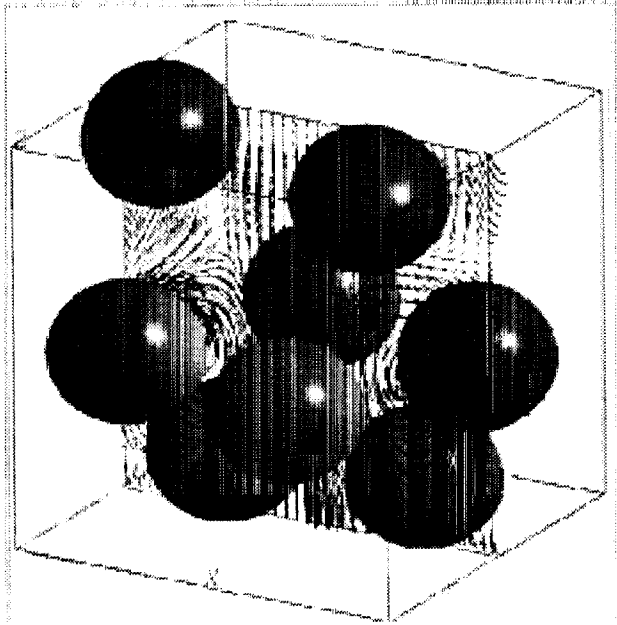

Motion of bubbles

Other Applications—A few examples:

M.R. Nobari, Y.-J. Jan and G. Tryggvason. "Head-on Collision of Drops--A Numerical Investigation." Phys. Fluids 8, 29-42 (1996).

M.R.H. Nobari, and G. Tryggvason, "Numerical Simulations of Three-Dimensional Drop Collisions." AIAA Journal 34 (1996), 750-755.

A. Esmaeeli and G. Tryggvason, "An Inverse Energy Cascade in Two-Dimensional, Low Reynolds Number Bubbly Flows." J. Fluid Mech. 314 (1996), 315-330.

G. Agresar, J.J. Linderman, G. Tryggvason, and K.G. Powell. An Adaptive, Cartesian, Front-Tracking Method for the Motion, Deformation and Adhesion of Circulating Cells. To appear in J. Comput. Phys.

Conclusion

The physical problem addressed in this study is of fundamental importance for thermal/fluid management in microgravity. Since flow regimes are usually very different than on earth, design data obtained on earth is generally not applicable to microgravity conditions. This study will result in both a greatly improved understanding of boiling multiphase flows as well as tools that can be used to address other situations. This should greatly reduce the need for experiments for relatively simple situations and help plan experiments for more complex flows.

ENTROPIC SURFACE CRYSTALS AND CRYSTAL GROWTH IN BINARY HARD-SPHERE COLLOIDS

A.G. Yodh
Department of Physics and Astronomy
University of Pennsylvania

Please refer to the Conference Book of Abstracts or the NCMR Website at http://www.ncmr.org

ENHANCED BOILING ON MICRO-CONFIGURED COMPOSITE SURFACES UNDER MICROGRAVITY CONDITIONS

Nengli Zhang and An-Ti Chai, NASA/Lewis Research Center, Cleveland, OH 44135

INTRODUCTION

As an efficient heat transfer mode, boiling has been considered in various aspects of space missions, such as in thermal management, in thermal power generation, in cooling devices and in other heat exchangers. It is self-evident that both economy and reliability are the crucial factors for any space mission. Nucleate boiling near the critical heat flux (CHF) can provide excellent economy along with high efficiency of heat transfer. However, nucleate boiling performance can deteriorate in a reduced gravity environment and nucleate boiling usually has a potentially dangerous characteristic in the CHF regime.

The performance of pool boiling heat transfer on a composite surface was studied experimentally and numerically by Blagojevic et al.[1]. They found a plateau in the boiling curve in the CHF regime accompanied by a reduction in the peak heat flux. Yang and Zhang [2] divided composite enhanced surfaces into two categories: discrete insert/matrix type composites and micro-configured insert into matrix types. They presented a hypothesis to explain the formation of the plateau of the boiling curve in the CHF region. This explanation may provide a guideline to search for the proper construction of enhanced boiling surfaces with a wider safety margin in the CHF regime.

New materials, such as micro-configured metal-graphite composites, could be an idea boiling surface for boiling enhancement. The pool boiling experimental results show that the average boiling heat transfer coefficient of Freon-113 in the nucleate boiling regime on the copper - graphite (Cu-Gr) composite surfaces, with up to 35°C wall superheat, is 3.0 to 4.6 times that for the pure copper heater surface [3]. Compared to other enhanced boiling surfaces these types of composite surfaces have unique attributes as they do not incur extra pressure drop, have no fouling and offer low primary and maintenance costs. The composite fabricated by SPARTA Inc. consists of a certain volume fraction of graphite fibers having diameters of 10 to15 μm embedded uniaxially within a copper matrix, as shown in Fig. 1. The metal-graphite micro-configured composite surfaces were found, through a numerical simulation, to have nonisothermal surfaces under boiling conditions [3, 4]. Based on the non-isothermal surface result, a reduced sensitivity of the CHF to superheat variation for the surfaces was predicted by Yang and Zhang [2].

Due to the nonisothermal conditions of the surfaces, the thermocapillary forces along the micro bubble base would benefit the bubble detachment and may play the main role in a microgravity environment. Because the bubble detachment manifests

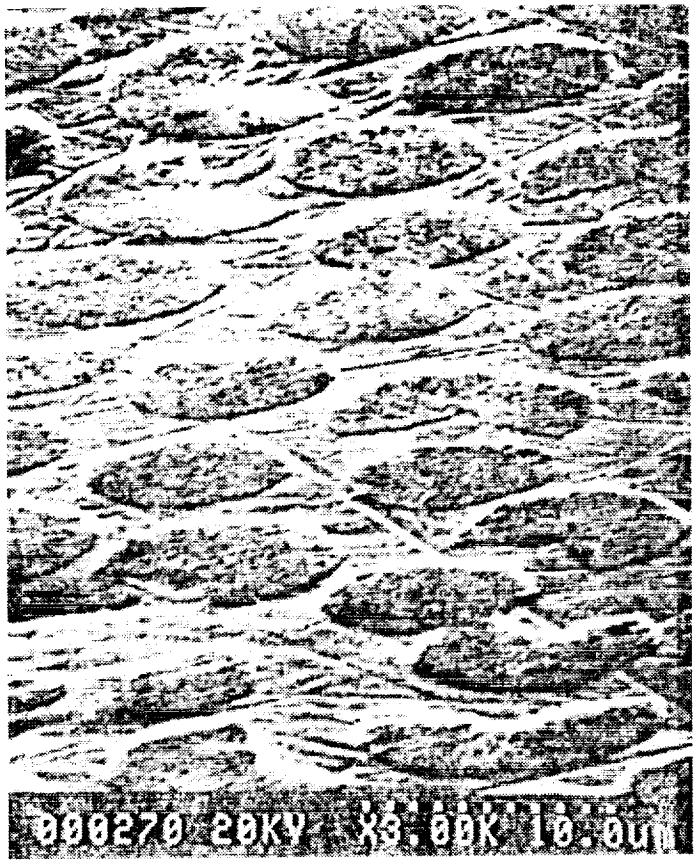

Fig. 1 A Photo of Magnified Cu-Gr Composite Surface

itself by a necking process, the thermocapillary forces formed by the temperature difference between the fiber tips and the copper matrix would neck the bubble and play a more important role in bubble detachment than buoyancy. Figure 2 shows the forces acting on a micro bubble on a composite surface. Therefore, it is reasonable to predict that the nucleate boiling performance of the surfaces, including that in the CHF regime, will not be reduced significantly when buoyancy vanishes under microgravity.

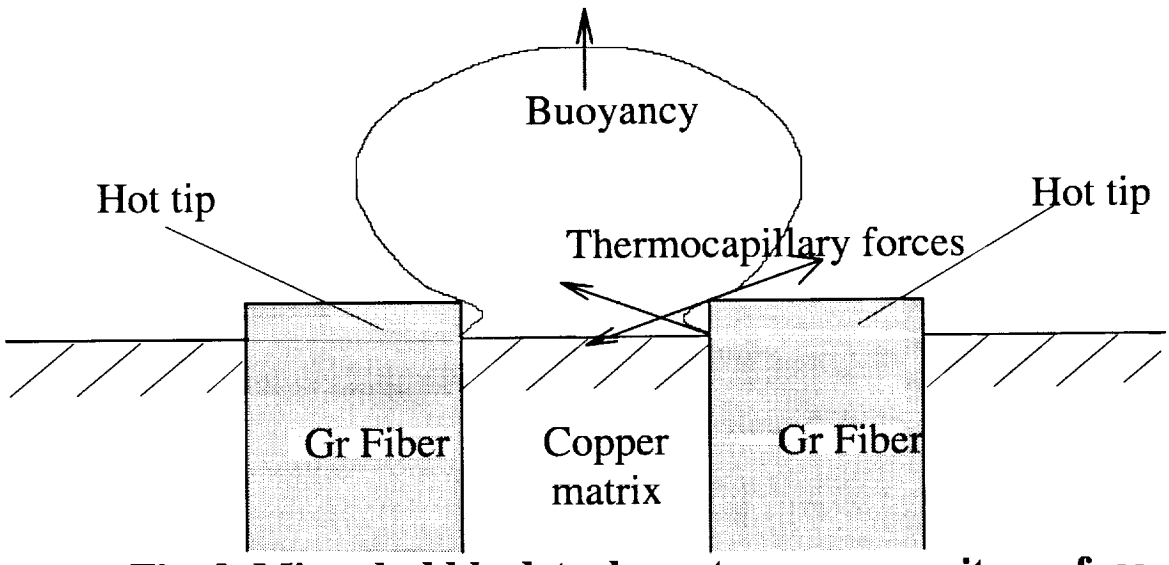

Fig. 2 Micro bubble detachment on a composite surface

EXPERIMENTAL SETUP

A schematic of the experimental setup is shown in Fig. 3.

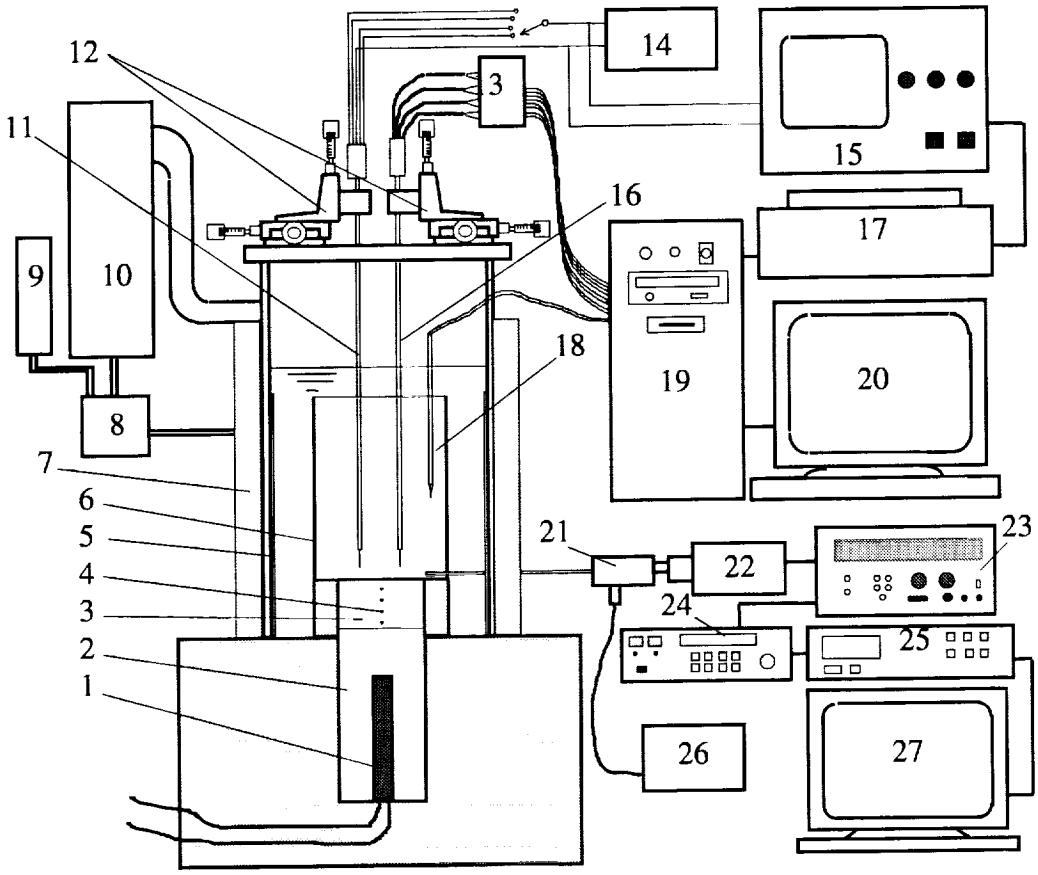

Fig. 3 Schematic of the Experimental Setup

It will be slightly modified to meet the constraints for the experiments in the space shuttle. A micro-configured composite test sample *3*, serving as the boiling surface and insulated on its side wall, is glued to the heat conducting copper block *2* by using high temperature epoxy with high thermal conductivity. As the main heater, a cartridge heater *1*, whose power is supplied and varied by an adjustable voltage controller, is inserted into the copper block surrounded by an insulator. Four thermocouples *4* are embedded on the centerline of the test sample to measure the temperatures along the heat transfer path, and the temperature of the boiling surface can be determined by extrapolation. A strip heater *5* is placed on the wall of the boiling vessel as the auxiliary heater to maintain the working liquid at a saturated temperature. To prevent the heating effect of the strip heater on the boiling surface, the glass sleeve *6* is placed on the extension plate of the boiling surface. Insulating material *7* is used to protect the heat loss from the boiling vessel. A condensation system used to recover the evaporating working fluid, consists of the condensate preheater *8*, condenser 9, and main

condenser *10*. The micro electrical resistance probe set *11* and the micro-thermocouple set *16* are held, respectively, by three-dimensional micrometer stages *12* which can sense movements to 0.1 μm in the vertical direction and 1 μm in the two horizontal directions. The temperature data measured by the micro-thermocouple set are recorded by the computer data acquisition system consisting of the terminator connector *13*, the computer data acquisition *19* and the monitor *20*. The Oscillator *14* and the oscilloscope *15* constitute the frequency measurement system to detect and count the micro bubbles emitted from the boiling surface. A printer *17* is shared by the temperature and the frequency measurement systems. A thermocouple *18* is used to monitor the working fluid temperature. The high magnification borescope probe *21* is inserted into the boiling vessel and immersed in the working liquid to capture the motion of embryonic bubbles which are illuminated by light source *26* through a glass fiber light guide cable. A high speed motion recorder system consists of a high speed video camera *22* and the motion analyzer *23* which provides immediate, slow-motion playback through the regular video recorder *24* and the monitor *27*. Any interesting details can be printed out instantly by the color video printer *25*. Before using the high speed recorder system a regular video camera can be utilized to replace *22* and *23* in preliminary tests the system.

MATHEMATICAL MODEL

An analytical model will be developed to help provide fundamental understanding of the coupled heat transfer and bubble formation mechanisms. According to the two-tier model for nucleate boiling on micro-configured composite surfaces, the micro bubbles coalesce at their maximum cross section, as shown in Fig. 4, and their diameter, D, is related to the fiber diameter, d, and the volume fraction of the fiber, α, by

$$D = (d/2)\sqrt{(\pi/\alpha)} \tag{1}$$

The plane of coalescence of the micro bubbles is regarded as the maximum thickness of the liquid film entrapped between the micro bubbles, δ_m which can be determined as

$$\delta_m = (d/2)\sqrt{[(\pi/4\alpha) - (\sqrt{(\pi/2\alpha)} - 1)^2]} \tag{2}$$

The volume of liquid trapped between the micro bubbles, then, is

$$V_l = (3\pi/4)\, D^2\, \delta_m + (\pi/3)\, \delta_m^3 \tag{3}$$

Idealizing the liquid volume as a column of constant cross-section, the microlayer thickness can be derived as

$$\delta = [(3/4)\, D^2\, \delta_m + (1/3)\, \delta_m^3] / [(3/4)\, D^2 + \delta_m^2] \tag{4}$$

Assuming the bubbles that have coalesced to form a vapor mass (mushroom) are of same diameter, D_m, the liquid volume being entrapped between the bubbles is

$$V_{l,m} = D_m^3 [\cos\theta/2 - (\pi/8)(\cos\theta - \cos^3\theta/3)] \quad (5)$$

The macrolayer thickness can be shown to be

$$\Delta = (D_m \cos\theta / 2) [1 - \pi (1 - \cos^2\theta / 3) / 4] / (1 - \pi \sin^2\theta / 4) \quad (6)$$

where, θ is the contact angle. According to the two tier model the primary contributors of the boiling heat transfer in the low heat flux boiling region are micro bubbles. Therefore, the boiling heat flux, q_l, can be expressed as

$$q_l = f\, n\, \rho_v\, h_{fg}\, \pi\, D^3 / 6 \quad (7)$$

where f is the frequency of the micro bubbles emitted from the surface, n, the active

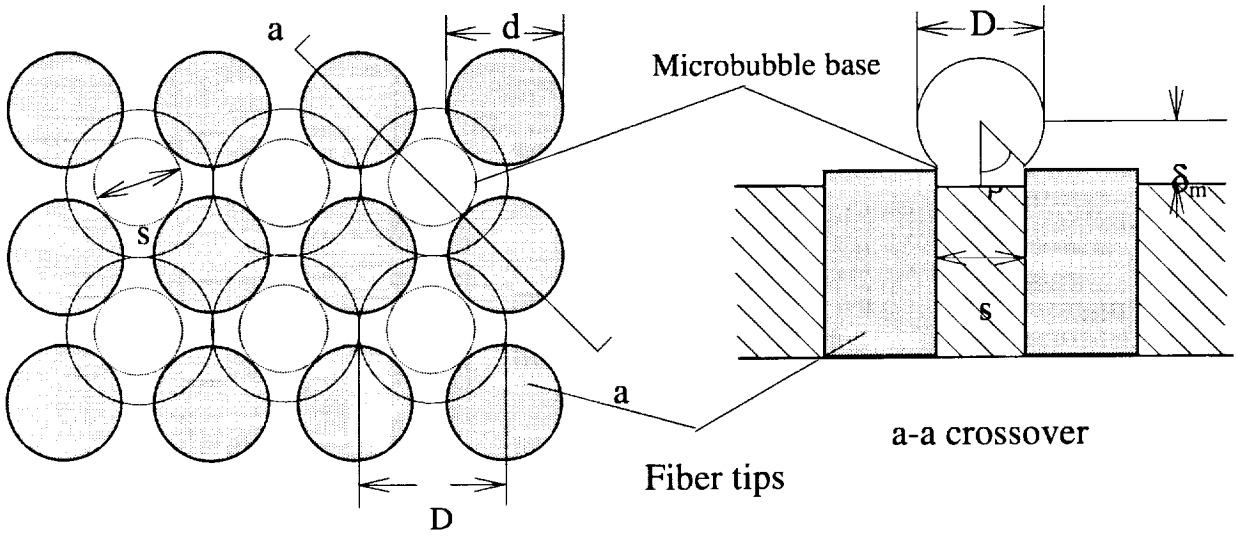

(a) top view of multiple microbubbles and fiber tips

(b) side view of a single micro-bubble on the composite surface

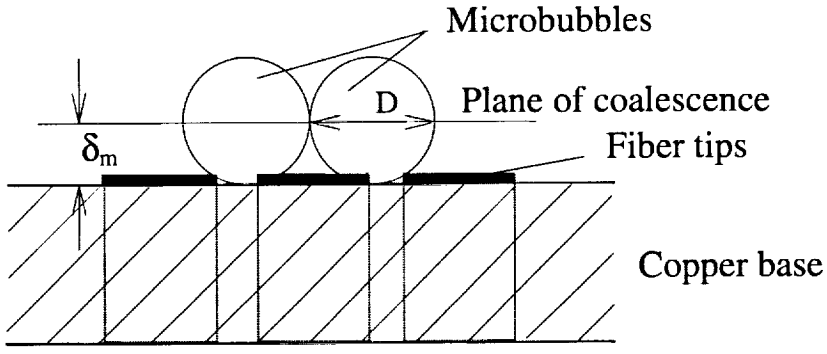

(c) side view of cross section

Fig. 4 Mechanism of Microlayer Formation on a Composite Surface

site density, ρ_v, the density of vapor and, h_{fg}, the latent heat of vaporization. In the high heat flux boiling region, the boiling heat flux consists of two parts: latent heat transport by the micro bubbles under the vapor stems and evaporation on the interface along the macrolayer which equals the heat conduction across the macrolayer (refer to Fig. 4). The total heat flux, q_h, is

$$q_h = f\, n\, \rho_v\, h_{fg}\, \pi\, D^3 / 6 + N\, V_{l.m}\, k_l\, \Delta t_w / \Delta^2 \qquad (8)$$

where N is density of the vapor stem, k_l, thermal conductivity of the working fluid, Δt_w, wall superheat. The CHF, q_{cr}, can be evaluated as the macrolayer evaporates to dryness before the mushroom departs, and can be expressed as

$$q_{cr} = (n\, V_l + N\, V_{l.m})\, \rho_l\, h_{fg} / \tau_d \qquad (9)$$

where τ_d is the vapor mushroom hovering time.

To predict the heat fluxes the parameters f, n, D, N, D_m and τ_d have to be determined. All of the parameters can be directly measured through the experiments except for n and N. The relationships between n, N and q_l, q_h will be determined through the experimental data processing. Solving a two dimensional conduction equation coupled with the evaporation boundary condition for the macrolayer to refine the second term in Eq. 8, allows further improvement of the model. The effects of microgravity on the heat fluxes should be reflected in changes of the frequency f and the diameter D_m. Definite mathematical expressions of these quantities will be developed based on the results of the ground-based low gravity experiments. The puzzle as to why a smooth and continuous transition of the boiling mechanism occurs across the isolated and coalesced bubble regimes will hopefully be resolved from the evaluation of Eqs. 7 and 8.

REFERENCES

1. B. D. Blagojevvic, D. M. Novakovic, G. S. Ilic, (1990): Pool Boiling Heat Transfer from Composite Solid Wall, *Proceedings of 9th International Heat Transfer Conference, Jerusalem, Israel*, Vol.4, 307-310
2. W-J. Yang, N. Zhang, (1992): Boiling Performance on Nonisothermal Surfaces, *Proceedings of Engineering Foundation Conference on Pool and External Flow Boiling, March 22 -27, 1992 / Senta Barbara, California*, 119-124
3. G. W. Yang, (1995): Micro- and Macro-Phenomena in Nucleate Pool Boiling on Graphite-Cooper Composite Materials, *PhD. Thesis, The University of Michigan, Ann Arbor, Michigan*
4. G. W. Yang, W. J. Yang, N. Zhang, (1992): Mechanisms of Nucleate Pool Boiling on Composite Surfaces, *International Communication Journal of Heat and Mass Transfer,* Vol. 19, No. 6, 781-79

THE SMALL-SCALE STRUCTURE OF TURBULENCE

G. Zimmerli
The National Center for Microgravity Research
NASA Lewis Research Center

W.I. Goldburg
Department of Physics and Astronomy
University of Pittsburgh

Please refer to the Conference Book of Abstracts or the NCMR Website at
http://www.ncmr.org

Session 5A

Phase Change III: Boiling

INVESTIGATION OF NUCLEATE BOILING MECHANISMS UNDER MICROGRAVITY CONDITIONS *

V.K. Dhir[1], D.M. Qiu[1], N. Ramanujapu[1] and M.M. Hasan[2], [1]Mechanical and Aerospace Engineering Department, University of California, Los Angeles, CA 90095, U.S.A, [2]NASA Lewis Research Center, 2100 Brookpark Road, Cleveland, OH 44135, U.S.A., e-mail: Vdhir@seas.ucla.edu

ABSTRACT

The present work is aimed at the experimental studies and numerical modeling of the bubble growth mechanisms of a single bubble attached to a heating surface and of a bubble sliding along an inclined heated plate. Single artificial cavity of 10 μm in diameter was made on the polished Silicon wafer which was electrically heated at the back side in order to control the surface nucleation superheat. Experiments with a sliding bubble were conducted at different inclination angles of the downward facing heated surface for the purpose of studying the effect of magnitude of components of gravity acting parallel to and normal to the heat transfer surface. Information on the bubble shape and size, the bubble induced liquid velocities as well as the surface temperature were obtained using the high speed imaging and hydrogen bubble techniques. Analytical/numerical models were developed to describe the heat transfer through the micro-macro layer underneath and around a bubble formed at a nucleation site. In the micro layer model the capillary and disjoining pressures were included. Evolution of the bubble-liquid interface along with induced liquid motion was modeled. As a follow-up to the studies at normal gravity, experiments are being conducted in the KC-135 aircraft to understand the bubble growth/detachment under low gravity conditions. Experiments have been defined to be performed under long duration of microgravity conditions in the space shuttle. The experiment in the space shuttle will provide bubble growth and detachment data at microgravity and will lead to validation of the nucleate boiling heat transfer model developed from the preceding studies conducted at normal and low gravity (KC-135) conditions.

INTRODUCTION

Boiling is known as a highly efficient mode of heat transfer. It is employed in component cooling and in various energy conversion systems. For space applications boiling is the heat transfer mode of choice since the size of the components can be significantly reduced for a given power rating. For any space mission the size, and in turn the weight of the components plays an important role in the economics of the mission.

*This work received support from NASA under Microgravity Fluid Physics Program.

Applications of boiling heat transfer in space can be found in such areas as thermal management, fluid handling and control, and power systems. For space power systems based on the Rankine cycle (a representative power cycle), the key issues that need to be addressed are the magnitude of boiling heat transfer coefficient and the critical heat flux under low gravity conditions.

The investigations of boiling heat transfer for space applications impose unique constraints in terms of the number of experiments that can be conducted under microgravity conditions, the duration of the experiments, the expense and the difficulties involved in performing the experiments. Thus, for space applications, it is even more important that a better understanding of the boiling mechanism be developed so that experiments are needed only for confirmation of the predictions.

The objectives of the present work are to delineate through experiments and analysis, the contributions of some of the key mechanisms to total heat transfer rate during nucleate boiling under microgravity conditions. This includes the contribution of micro/macro layer evaporation on single and merged bubbles attached to a heated wall, heat transfer during sliding motion of a bubble along the heater wall and heat transfer due to fluid motion resulting from bubble growth and Marangoni effect. The effect of fluid motion induced by a growing sliding bubble is also considered.

Under microgravity conditions the early data of *Keshock and Siegel*[1] and *Siegel and Keshock*[2] on bubble growth and heat transfer show that the effect of reduced gravity is to reduce the buoyancy and inertia forces acting on a bubble. As a result, under reduced gravity bubbles grow larger and stay longer on the heater surface. This in turn leads to merger of bubbles on the heater surface and existence of conditions similar to fully developed nucleate boiling. Thus, under microgravity conditions partial nucleate boiling region may be very short or non-existent.

Erwin et al[3] and *Erwin and Merte*[4] have studied transient nucleate boiling on a gold film sputtered on a quartz plate by using a 5-second drop tower (10^{-5} g_e) at NASA Lewis Research Center. R-113 was used as the test liquid in the experiments. It was found that the time or temperature for initiation of nucleate boiling was greater for pool at near saturation temperature than that for a subcooled pool. They also noted the occurrence of energetic boiling at relatively low heat fluxes. The

energetic boiling in which vapor mass rapidly covered the heater was postulated to be associated with an instability at the wrinkled vapor-liquid interface. Recently, *Merte et al*[5] have reported results of pool boiling experiments conducted in the space shuttle for the same surface that was used in the drop tower tests. Subcooled boiling during long periods of microgravity was found to be unstable. The surface was found to dryout and rewet. Average heat transfer coefficients during the dryout and rewetting periods were, however, found to be about the same. The nucleate boiling heat fluxes were higher than those obtained on a similar surface at earth normal gravity conditions.

Experimental studies of flow boiling under low gravity conditions are far fewer and limited than those for pool boiling. The earliest study of flow boiling under reduced gravity conditions is that of *Cochran*[6] . The experiments were conducted in the drop tower with flow velocities varying from 4.2 to 11.5 cm/s . These short-duration (2.2 second) low gravity tests were focused on the boiling process near inception. In comparison to normal gravity tests, it was found that in microgravity, bubbles tended to stay on the heating surface, become large enough to coalesce with neighboring bubbles and acquired irregular shapes. The size of bubbles along the heating surface was found to correlate with thickness of the thermal layer. More recently, *Saito et al*[7] have studied flow boiling of water on a heater rod placed in a square channel. The experiments were conducted in Japanese low gravity experimental aircraft (MU-300) at 0.01 g_e for 20 seconds. In the experiments, subcooled nucleate boiling heat transfer data for water were taken at velocities varying from 3.7-22.9 cm/s and pressure in the range of 0.9 to 2.4 bars. Nucleate boiling heat transfer coefficients were found to increase slightly in the direction of flow and the magnitudes of the heat transfer coefficients were about the same as at normal gravity.

Finally, it appears that recent studies of nucleate boiling under microgravity have shed light on this complex phenomena, however, the studies are non-conclusive. Questions remain on the stability of nucleate boiling, the reasons for equivalence of magnitudes of heat transfer coefficients at normal gravity and low gravity conditions and on the physics that underlies the phenomena. As such, there is no mechanistic model that describes the observed physical behavior and the dependence of nucleate boiling heat flux on wall superheat.

DESCRIPTION OF THE RESEARCH

In view of the above discussion, the natural question that arises: how does microgravity affect nucleate boiling heat transfer? Thus, the main objective of present work is to develop a physical understanding of the key phenomena and to advance mechanistic models so that development of a global model for nucleate boiling under microgravity conditions is facilitated. The work is both experimental and analytical/numerical in nature and is first focused on a single bubble, i.e. without interaction of neighboring bubbles. To be able to predict nucleate boiling heat transfer under microgravity conditions, a quantitative understanding of several mechanisms during nucleate boiling at normal gravity is needed which includes 1) Heat transfer to a single bubble as well as that associated with micro/macro layer evaporation; 2) Heat transfer and flow field for a bubble sliding along a heated wall. For item 1) the numerical results and the experimental data have been compared.

THEORETICAL/NUMERICAL STUDIES

Complete numerical simulation of the flow and temperature field during the bubble growth cycle on a horizontal surface was conducted. The computational domain is divided into micro and macro regions as shown in Fig.1. The micro-region contains the thin film that forms underneath the bubble whereas the macro region consists of the bubble and the liquid surrounding the bubble. Finite difference scheme along with a level set method was used to solve the equations governing the conservation of mass, momentum and energy. The disjoining pressure effect is included in the numerical simulation to account for heat transfer through the liquid micro-layer. The pressure gradients in the vapor and liquid are related through the drag experienced by the liquid in the microlayer, the capillary force resulting from the change in the shape of the interface, the disjoining pressure and the recoil pressure.

Figure 2 shows the calculated bubble growth patterns at 1 atm pressure and saturated water. Table 1 gives the calculated bubble diameter at departure and the time for bubble growth for different g levels. In obtaining the results water at one at atmosphere was used as the test liquid and the contact angle was assumed to be 38°. The wall superheat was 6.7 °C. It is found that the bubble diameter at departure approximately scales as $g^{-1/2}$ and the bubble growth time scales as $g^{-0.9}$. High heat flux was observed to exist in the micro layer. (for details, see *Son and Dhir* [8])

Table 1 Prediction of Bubble Growth Period and Departure Diameter for Saturation Water

Gravity	Bubble departure diameter (mm)	Bubble growth Period (sec.)
1 g	2.3	0.0034
0.126 g	6.2	0.25
0.01 g	21.5	2.7
0.0001 g	209	135

EXPERIMENTS AT NORMAL GRAVITY

The ongoing experiments have the objective to provide, in a very clean manner, the basic information to

validate a mechanistic model for prediction of nucleate boiling heat flux as a function of wall superheat. With the presumption that dependence of cavity site density on wall superheat is known (true for designed surface with artificial cavities) the prediction of heat flux requires a knowledge of interfacial area per cavity, interfacial heat flux, and heat transfer on the unpopulated area of the heater. Size of bubbles at breakoff, bubble release frequency and the number of bubble release sites influence the time and area averaged heat transfer and also determine the vapor generation rate.

Experiments at normal gravity were conducted on the set-up using a polished Silicon wafer (4" in diameter) as heat transfer surface. 10μm diameter cavity was formed in the center of the wafer. The schematic is shown at Fig.3. The processes of nucleation, the bubble growth and merger (in vertical direction) were recorded with a high speed video camera using saturated and subcooled PF-5060 and water as test liquid at one atmosphere pressure.

Fig.4 compares the bubble shape and size just prior to departure predicted from the numerical simulations and that observed in the experiments. The contact angle was 50°. A good agreement between predicted and observed bubble shapes and sizes is seen.

Experiments of bubbles sliding along a downward-facing rectangular heating surface have also been conducted. The micro gage heaters were bonded on the back side of the Silicon wafer on which miniature thermocouples were also attached. Each of the micro heaters was separately connected to the power supply so that the heater surface superheat profile could be controlled. Single vapor bubbles were generated upstream of the heat transfer surface and were allowed to slide over the surface. Fig.5 shows the schematic of the set-up. Three glass windows are used for the purpose of optical measurements including interferometry for the temperature field around the sliding bubble. A provision was made to hold and orient on a standard optical table the set-up at different angles to the gravitational acceleration vector.

The bubble shapes and size, and in turn the bubble growth rate along the surface were recorded using high speed video camera in two directions simultaneously. The wall superheat priori to the sliding of bubble and the transient temperature variation due to the sliding bubble were measured at different subcoolings, heating rate and inclination angles of the surface. A large wake region was observed behind the sliding bubble. This region became smaller with increase in the inclination angle. Preliminary information has been obtained on the temperature field around a sliding bubble (using interferometry) and the local velocity field around a sliding bubble (using silvered glass particle as tracers for PF-5060 and hydrogen bubbles for water).

Figure 6 shows the changes in typical shape and size of a bubble sliding along the surface at a small inclination angle. It is found that bubbles change shape from a initially shape of a sphere to a long ellipsoid or deformed long ellipsoid at the downstream end of the inclined plate. Between the sliding bubble and the heat transfer surface wedge-like liquid gap was observed. The angle of the wedge is found to be a function of plate angle of inclination and bubble size.

Figure 7 shows the sliding bubble volume along the surface at three inclination angles. Larger inclination angle, i.e. smaller gravitational acceleration component normal to the surface, leads to lower bubble growth rate, indicating lower heat transfer rate between the bubble and the surface. The effective bubble diameter has been found to increase at a rate higher than $\sqrt{t}$ for a thermally controlled growth.

EXPERIMENTS IN THE KC-135 AND IN THE SPACE SHUTTLE

Since at normal gravity, there is always a gravitational component parallel to and normal to an inclined surface, the bubble shape and detachment, which are sensitive to magnitude of gravitational acceleration, must be studied under low gravity conditions. As such, experiments are being conducted in KC135 and are proposed to be performed in space shuttle to further quantify the effect of significantly reduced gravity (10^{-5} g_e) on the bubble detachment process in particular, and on the heat transfer in general. It is necessary that boiling experiments be carried out on "designed" surface. These experiments will not only provide data on the scaling effect of gravity on various processes, including bubble growth and departure, but will also be valuable in validating the predictive model for nucleate boiling heat transfer under microgravity conditions.

The data of the ongoing experiments in KC-135 will be very helpful in assessment of the overall heat transfer model, and in the design of the experiment for the space shuttle.

CONCLUDING REAMARKS

Complete numerical simulations and experiments for bubble growth, detachment and merger (vertically) at an artificial cavity formed on a polished Silicon wafer for PF5060 and water have been carried out. The bubble departure diameter and release frequency have been analyzed for different wall superheats, subcoolings and contact angles. The scaling of these parameters with magnitude of gravitational acceleration has been carried out. For sliding bubble experiments, the results for bubble growth rate, surface temperature, and the liquid motion were obtained. The effects of subcooling and component of gravitational acceleration normal to the surface was studied. During their sliding

motion, the bubbles are formed to elongate into an elliptical shape and a liquid wedge is formed between the heater surface and the vapor liquid interface.

Reference

1. Keshock, E.G., and Siegel, R., (1964). Focus Acting on Bubble in Nucleate Boiling under Normal and Reduced Gravity Conditions, NASA TN-D-2999.
2. Siegel, R. and Keshock, E.G., (1964). Effect of Reduced Gravity on Nucleate Bubble Dynamics in Water, *AIChE J.*, Vol. 10. 4, pp.509-516.
3. Ervin, J.S., Merte, H., Kellers, R.B., and Kirk, K., (1992). Transient Boiling in Microgravity, *Intl. J. heat mass Transfer*, Vol. 35, No.3, pp.659-674.
4. Ervin, J.S. and Merte, H., (1993)Boiling Nucleation and Propagation in Microgravity, *Heat transfer in Microgravity*, ASME-HTD Vol.269,pp.659-674.
5. Merte, H., (1994). Pool and Flow Boiling in Variable and Microgravity, *2nd Microgravity Fluid Physics Conference*, Paper No.33, Cleveland, OH, June 21-23.
6. Cochran, T.H., (1970). Forced-Covection Boiling Near Inception in Zero Gravity, *NASA TN D-5612*.
7. Saito, M., Yamaoka, N., Miyazaki, K., Kinoshita, M., and Abe, Y., (1994). Boiling Two-Phase Flow under Microgravity, *Nuclear Engineering Design*, Vol.146, pp.451-461.
8. Son, G., and Dhir, V.K.,(1998). Numerical simulation of a single Bubble During Partial Nucleate Boiling on a Horizontal Surface, submitted for publication in *J. Heat Mass Transfer* .

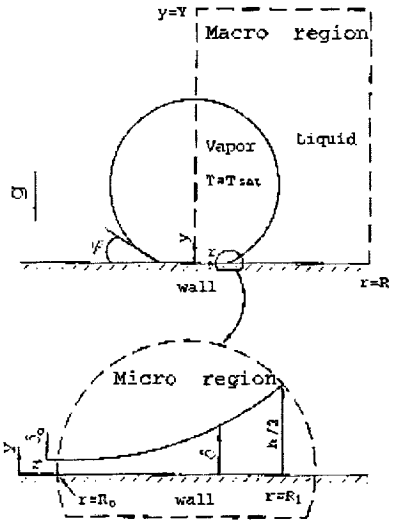

Fig. 1 Micro and macro-regions in numerical simulation

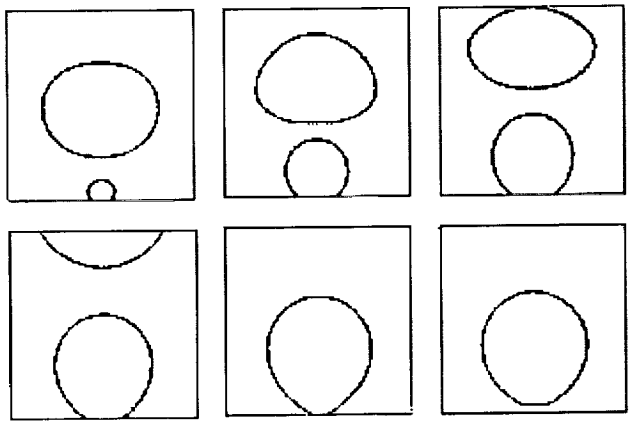

Fig. 2 Bubble growth patterns from numerical simulation and the images from the experiments on the micro-machined Silicon wafer

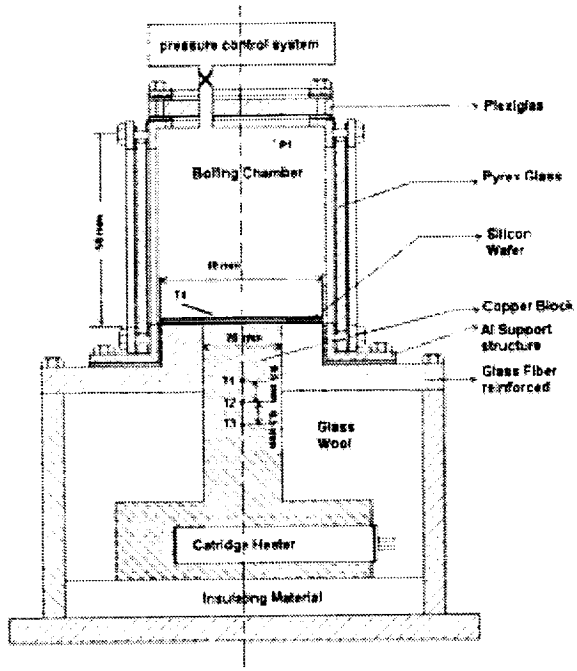

Fig. 3 Schematic of the set-up for nucleate boiling experiments with the micro-machined Silicon wafer

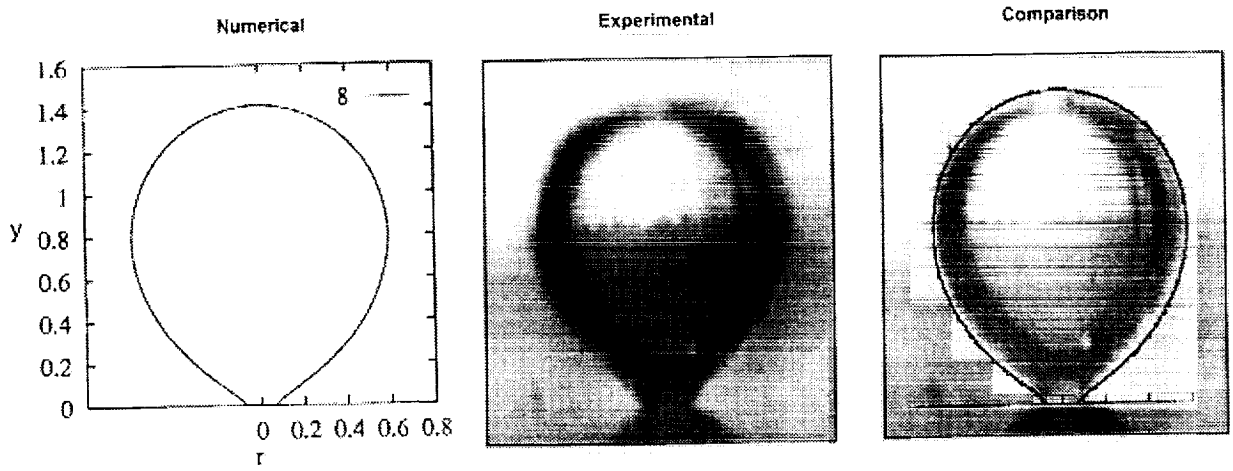

Fig. 4 Bubble shapes from numerical simulation and experiments for saturated water at contact angle 50° and wall superheat 8.5 K

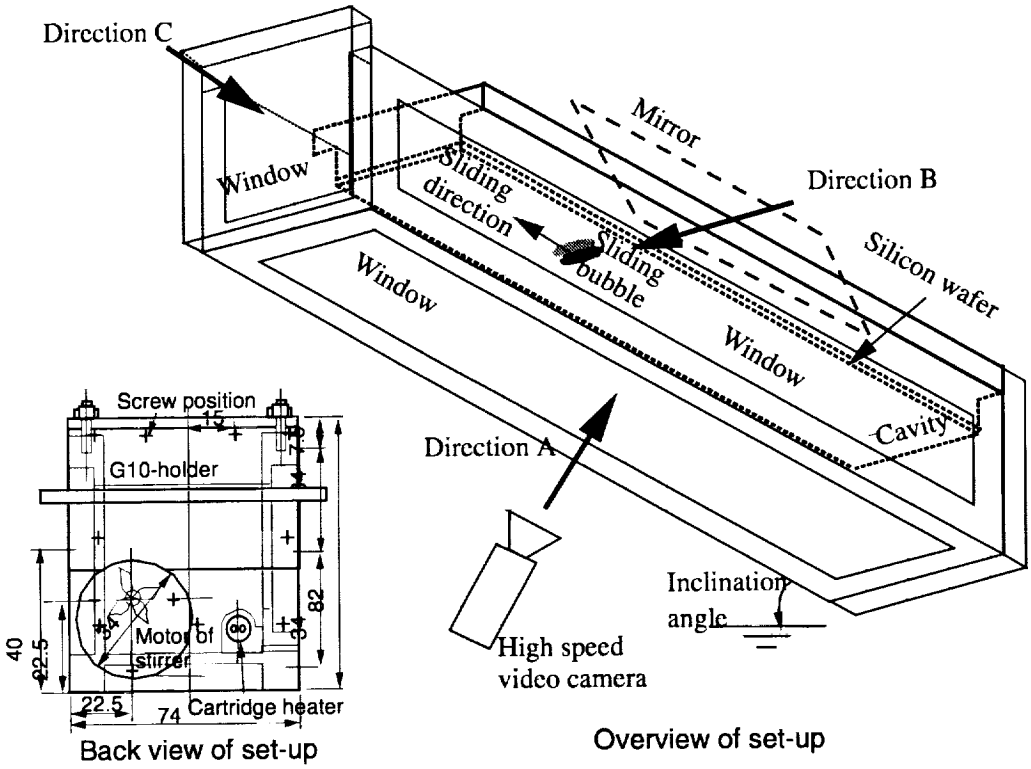

(a) Overview of set-up

Fig. 5 Schematic of the set-up for sliding bubble experiments (to be continued)

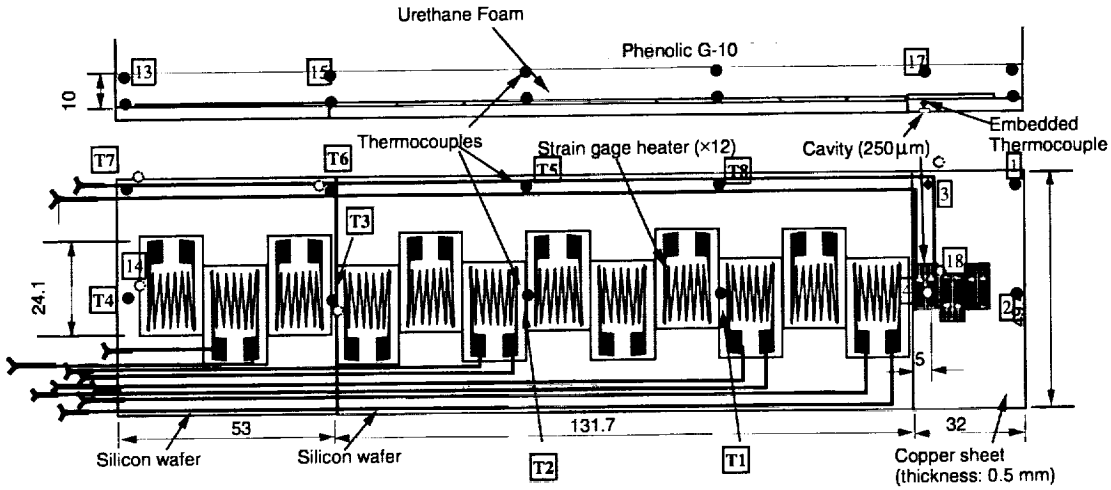

(b) Configuration of heating plate

Fig. 5 Schematic of the set-up for sliding bubble experiments (continued)

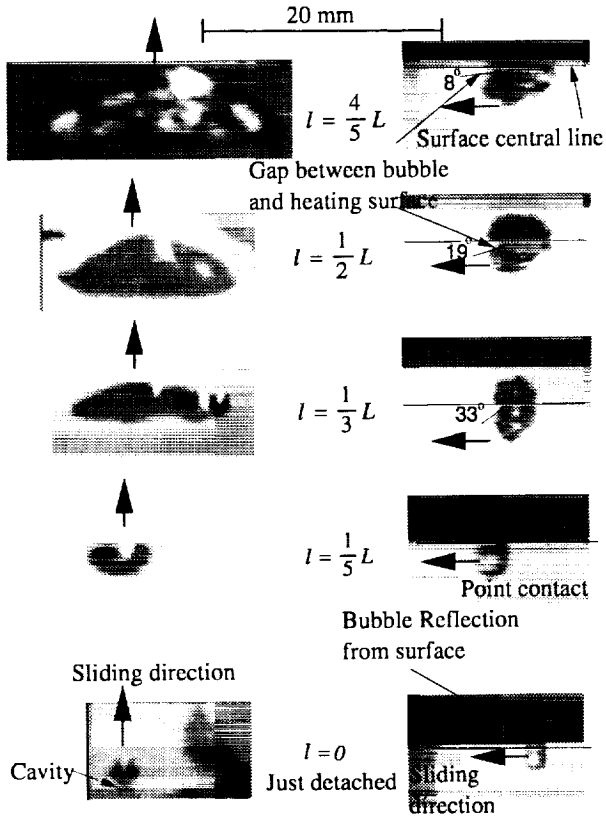

Fig. 6 Change of sliding bubble shape at surface inclination angle 15°, subcooling 1 K and wall superheat 7.3 K (l: distance from cavity; L: distance from cavity to upper end of plate)

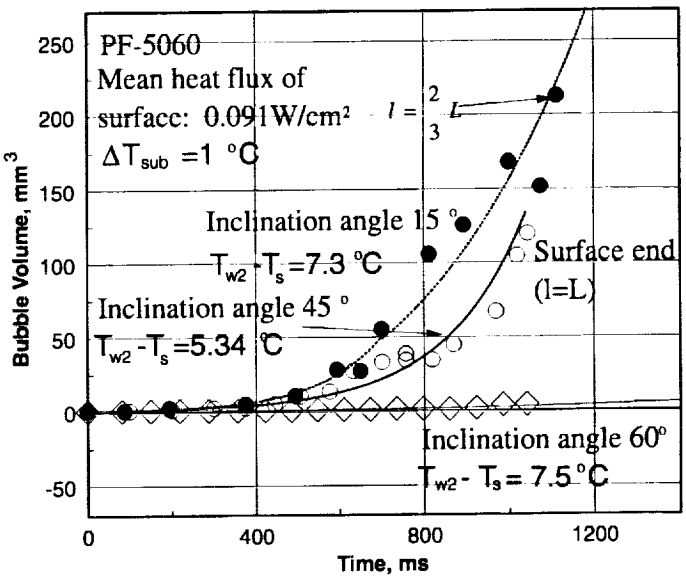

Fig. 7 Influence of inclination angle on sliding bubble growth rate

BOILING HEAT TRANSFER MEASUREMENTS ON HIGHLY CONDUCTIVE SURFACES USING MICROSCALE HEATER AND TEMPERATURE ARRAYS

J. Kim[1], S.W. Bae[2], M.W. Whitten[1], J.D. Mullen[1], R.W. Quine[1], and T.S. Kalkur[3]
[1]University of Denver, Department of Engineering, Denver, CO 80208, jkim@du..edu, [2]Pohang University of Science and Technology, Department of Mechanical Engineering, Pohang, Kyungbuk, 790-784, Korea, bswon@postech.ac.kr, [3]University of Colorado, Department of Electrical Engineering, Colorado Springs, CO 80933, kalkur@vlsie.uccs.edu.

ABSTRACT

Two systems have been developed to study boiling heat transfer on the microscale. The first system utilizes a 32 x 32 array of diodes to measure the local temperature fluctuations during boiling on a silicon wafer heated from below. The second system utilizes an array of 96 microscale heaters each maintained at constant surface temperature using electronic feedback loops. The power required to keep each heater at constant temperature is measured, enabling the local heat transfer coefficient to be determined. Both of these systems as well as some preliminary results are discussed.

INTRODUCTION

The vast majority of experimental work performed to date regarding boiling has utilized single heaters that were large compared to individual bubble sizes, making it difficult to look at details of the boiling process. These experiments usually used a heating element operated in a constant heat flux mode, making it difficult to study transition boiling effects beyond critical heat flux (CHF). Other experiments have utilized surfaces held at constant temperature, but the *local* heat flux and temperature were not measurable and can vary significantly across the heater. Even when local measurements were obtained (e.g., Cooper and Lloyd--1969, Hohl, et al.--1997), this was done at only a few locations on the heater surface. The pioneering work of Kenning (1992) and Watwe and Hollingsworth (1994) using liquid crystals on thin, electrically heated stainless steel plates did much to elucidate the heat transfer mechanisms associated with large scale phenomenon because information regarding temperature fluctuations were available with high resolution across the heater surface. The work described in this paper complements the liquid crystal work in that boiling on a comparatively small heated area is investigated in detail with high spatial and temporal resolution.

It must be remembered that boiling behavior on small heated areas can differ from that on large heated areas. First, the total number of nucleation sites is much smaller, and can result in heaters smaller than the corresponding average distance between nucleation sites on large heaters. Boiling can be delayed to higher wall superheats as a result, or the number of nucleation sites may not be statistically representative. Second, the Taylor wavelength, which is significant at CHF and transition and film boiling, can be larger than the heater size. Third, edge-effects can become significant.

DIODE ARRAY

This technique uses a 32 x 32 array of silicon diodes constructed on a silicon substrate to obtain the surface temperature distribution by measuring the forward voltage drop across each diode. Silicon diodes typically have a forward voltage drop of 0.7 V that decreases by 2 mV for every 1 °C increase in temperature near room temperature. The voltage drop across a diode is approximately proportional to the inverse of the absolute temperature of the diode for a wide range of temperatures.

Use of silicon diodes to measure temperature is not new. Diodes and the associated electronics specifically designed to measure temperature are commercially available (two suppliers are Validyne Engineering and Lake Shore Cryotronics). The main application of silicon diode temperature sensors is in measuring cryogenic temperatures since the forward voltage drop changes rapidly with temperature at low temperatures, although commercially available units cite useful temperature ranges from 1.4 K to 475 K.

The advantages of using a diode array to measure temperature rather than microthermocouples or liquid crystals are that 1). the temperature can be measured at many more points than is possible using microthermocouples, 2). temperature fluctuations over a much wider range can be measured compared to liquid crystals, 3). the resolution of the temperature measurements is much better than is possible using liquid crystals. The main limitation on the current technique is that the measurements are confined to relatively small areas.

The ultimate goal of this work is to determine local heat transfer coefficients by measuring the local temperatures vs. time, then numerically determining the local heat flux. One difficulty with using a silicon substrate is that the high thermal conductivity of silicon tends to smear out temperature gradients, making the determination of local heat flux difficult. An option is to build the diode array on a 0.2 μm layer of single crystal silicon-on-quartz substrate. Because quartz has a much lower thermal conductivity than silicon (k_{Si}=135 W/m-K, k_{qtz}=1.5 W/m-K), small

changes in heat transfer from the surface result in relatively large changes in temperature, greatly increasing the accuracy of the numerically determined heat flux. This technology has the added advantage that the silicon layer is transparent, allowing visual observations from beneath the heater to be made while measuring heat flux distributions. Work is currently progressing on building such a diode array.

In the current configuration, a chip containing the diodes is heated from below using a cartridge heater embedded in an aluminum rod. Thermocouples along the rod measure the temperature gradient along the rod enabling the heat flux to be determined.

Description of the diode array. An example of how the diodes would be connected together is shown on Figure 1 for a 3 x 3 array of diodes. If the voltage drop across diode A-2 is desired, a current (typically 1 mA) is sent into row A while the other rows are grounded. Simultaneously, column 2 is grounded while the other columns are set to 5 V. All of the diodes in the array with the exception of A-2 are now either reverse biased or have no voltage drop across them. The voltage at A is then measured to obtain the forward voltage drop across diode A-2. The voltage drop across the other diodes in the array are obtained by scanning across the array. A 32 x 32 p-n junction isolated diode array was built on a p-type wafer using VLSI techniques-a photograph of a diode in the array is shown on Figure 2.

Up to eight arrays can be made on a single wafer. Once a wafer has been processed, the wafer is diced to obtain the individual chips. These chips are epoxied to a Pin Grid Array (PGA), and connections from the chips to the PGA are made using wire-bonds.

The current used to sense the voltage drop across the diode must not influence the temperature measurement by heating the diode significantly. The energy dissipated by a typical diode with a 1 mA sensing current is 7 W/cm^2. While this may seem like a large heat flux, it must be remembered that the sensing current is only applied for a very short time (typically 1 μs if scanning occurs at 1 MHz for a 32 x 32 array). An upper bound on the temperature rise of the surface can be obtained by assuming that the silicon substrate acts as a semi-infinite solid subjected to a step change in wall heat flux (Incropera and Dewitt–1996):

$$T(0,t) - T_i = \frac{2q_0''(\alpha t/\pi)^{1/2}}{k}$$

For the conditions described above, the surface temperature rise is just 0.005 °C, which is well within the uncertainty of the measurement. The actual temperature rise is much lower since only a small portion of the surface is heated.

Description of circuitry and data acquisition unit. An electronic circuit is used to scan the diodes in the array and provide signal conditioning. The circuit receives two external signals: a start pulse and a signal from an external clock, both of which enter a counter. The start pulse tells the counter to begin counting, while the external clock is used to set the frequency at which counting occurs. The actual counting frequency is half the clock frequency. Counting frequencies of up to 2.5 MHz are possible with the current circuitry. The signal exiting the counter enters two Erasable Programmable Read Only Memories (EPROM), one for choosing the row and one for choosing the column. Every time a pulse from the clock enters the EPROMs, they output two 5-bit digital signals corresponding to row and column numbers. In the present configuration, all of the diodes in a particular row are scanned before going on to the next row. The entire array is scanned once every time the circuit receives an external start pulse.

The measured voltage drops across the diodes are multiplexed into one continuous signal that is typically between 0.8–0.6 V. To take advantage of the resolution of the A/D converter (12 bit, 0-5V), this signal is sent through a signal conditioning unit that offsets, inverts, and amplifies the signal to match a 0-5 V range.

Calculations indicate that the A/D converter should be able to resolve temperature changes in the diodes as small as 0.05 °C. This is based on 12 bits of resolution, an assumed range in voltage drop of 0.8-0.6 V, and the measured change in voltage drop with temperature.

Calibration. Calibration of the diode array is performed by placing the array in an oil bath at known temperature and measuring the voltage output from the circuit vs. the bath temperature. An accurate value of the thermal conductivity of the aluminum rod is needed in order to compute the heat flux through the silicon. A bar of aluminum from the same stock used to heat the chip was machined so that it could be heated from one end using the same type of cartridge heater used to heat the chip. Thermocouples along the rod were used to measure the temperature gradient along the rod. Numerical simulation of the temperatures in the rod and surrounding insulation showed that the heat transfer through the insulation was negligible compared to the heat transferred along the rod. The thermal conductivity of the aluminum was computed from the data to be 243 W/m-K.

Preliminary results. The concept was tested on a 3 x 3 array of commercially available diodes connected to the circuit. The output was observed on an oscilloscope as each diode was heated in turn using a hot-air gun. As expected, the output voltage from the circuit was observed to increase with increasing temperature.

Once the concept was verified, a 32 x 32 diode array was constructed. It was found, however, that the interconnects between diodes in the vertical direction were faulty. Only half of the bottom row of diodes (a total of 16 diodes) could therefore be addressed. The problem with the interconnects is currently being fixed, and a new diode array is being constructed.

Calibration of the 16 working diodes in the current array was performed–a plot of voltage drop vs. temperature for these diodes is shown on Figure 3. The change in voltage drop across the diodes is nominally -1.1 mV/°C. The difference between the measured value and the ideal value of -2 mV/°C is thought to be due to the use of a recycled silicon wafer. The new diode array is being built on a prime grade wafer.

CONSTANT TEMPERATURE HEATER ARRAY

The local wall heat flux variations in boiling of FC-72 on a small heated area was examined using an array of microscale heaters each maintained at constant surface temperature. The scale of the individual heaters was approximately the same as that of the departing bubbles in nucleate boiling. The information contained in this paper is unique in that data was taken at many points simultaneously instead of at a single point, enabling a much more detailed picture of the heat transfer process to be obtained. An additional advantage of this work is that the heat flux was measured directly, instead of being inferred from average heat flux data and void fraction measurements.

Experimental apparatus. Much of the experimental apparatus has been discussed elsewhere (Rule, et al.–1997, Rule and Kim–1997, Rule–1998), so only a brief summary of the experimental apparatus will be given here. Local surface heat flux and temperature measurements are provided by an array of platinum resistance heater elements deposited on a quartz wafer in a serpentine pattern. Each of these elements is 0.26 mm x 0.26 mm in size, and have a nominal resistance of 1000 Ω and a nominal temperature coefficient of resistance of 0.002 $°C^{-1}$. Ninety six individual heaters are arranged in a square array about 2.7 mm on a side, as shown in Figure 4.

The temperature of each heater in the array is kept constant by a feedback circuit similar to that used in constant temperature hot-wire anemometry (Figure 5). The control resistor in the circuit is a digital potentiometer from Dallas Semiconductor. The instantaneous power required to keep each heater at a constant temperature is measured and used to determine the heat flux from each heater element. Because all the heaters in the array are at the same temperature, heat conduction between adjacent heaters is negligible. There is conduction from each heater element to the surrounding quartz substrate, but this can be measured and subtracted from the total power supplied to the heater element, enabling the power supplied to the fluid to be determined.

Shown on Figure 6 is a schematic of an experimental apparatus provided by NASA and used in these studies. The bellows and the surrounding housing allowed the test section pressure to be controlled. A stirrer was used to break up stratification within the test chamber, while a temperature controller and a series of Kapton heaters attached to the boiling chamber were used to control the bulk fluid temperature. The fluid was degassed by pulling a vacuum on the fluid. The final dissolved gas concentration in the liquid, determined using the chamber temperature and pressure and the properties of FC-72 (3M Fluorinert Manual--1995), was less than 1.5×10^{-3} moles/mole.

Heater calibration. The heater array was calibrated in an insulated, circulating constant temperature oil bath which was held within 0.2 °C of the calibration temperature. An impinging jet of oil onto the heater provided a high heat transfer coefficient. Calibration consisted of finding the value of the control resistor ($R_{control}$ in Figure 5) that causes the feedback loop to just begin regulating.

Results from previous work. Detailed results of saturated, pool boiling of FC-72 with this heater facing upward were presented in Rule and Kim (1997) and Rule (1998). The results presented include spatially-averaged time-averaged data, spatially-averaged time-resolved data, time-resolved data from individual heaters in the array, as well as spatially-resolved time-averaged data. Other results included data that was conditionally sampled on boiling, as well as the heat flux during liquid contact in the transition boiling regime. Some of the main conclusions resulting from this work were:

1). The inner heaters reach CHF at lower wall superheats than that for the array averaged heat flux.

2). Significant variations in boiling fraction occur over the surface of small heaters during nucleate and transition boiling, indicating that point measurements of heat flux, temperature, or void fraction may not be representative of average boiling behavior.

3). Vapor patches at CHF and during transition boiling were observed to move with time, and were related to the bubble dynamics above the heater.

4). Heat transfer during liquid contact in transition boiling was constant for a given wall superheat for the inner heaters, and was observed to decrease with increasing wall superheat.

Recent results. Visualization of the bubble behavior on the surface along with heat transfer measurements has recently been performed. The semi-transparent nature of the heater array enabled high speed digital videos (SpeedCam, monochrome, 1000

fps, 512 x 512 resolution with an Infinity Optical KC microscope lens with IF-4 objective) to be made of the bubbles from below.

Some preliminary data taken under saturated, pool boiling conditions is discussed. A snapshot of boiling in the isolated bubble regime (ΔT_{sat}=29 °C, T_{sat}=51 °C in Denver, CO) was shown on Figure 4. Heat flux data was obtained at 2500 Hz, while videos were taken at 1000 Hz with 512 x 512 resolution. Shown on Figure 7 is the time varying evolution of the bubble on the upper left corner of the heater array (the bubble growing on heaters 44 and 72-74). The corresponding heat flux traces on selected heaters is shown on Figure 8. Between 14 and 15 ms, the shadow from the bubble that departed previously is seen. Nucleation of a new bubble occurs between 16 ms and 18 ms–this corresponds to a sharp increase in the wall heat flux. The formation of what appears to be a dry spot underneath the growing bubble occurs soon after nucleation. This dry spot shrinks in size starting from 18 ms and seems to disappear around 21 ms, which corresponds to a sharp drop in wall heat transfer. The detached bubble moves away from the surface between 21 ms and 28 ms. It is interesting to note that there is a large amount of heat transfer associated with nucleation, but also a large amount of heat transfer as the dry spot shrinks and liquid re-wets the wall.. The magnitude of heat transfer during re-wetting of the wall is smaller than during nucleation, but is of longer duration, resulting in comparable overall heat transfer rates. The heat transfer after bubble departure is very low in comparison.

The large heat transfer associated with nucleation could be due to evaporation of the microlayer, as postulated. The numerical models, however, do not seem to predict the large amounts of heat that are transferred just before the bubble departs the surface. The heat transfer mechanism seen is different from the widely accepted view that microlayer evaporation is the dominant heat transfer mechanism in saturated pool boiling. It is important to note that this data is preliminary–data from other bubbles on the surface suggest different heat transfer mechanisms.

CONCLUSIONS

Two techniques for making local measurements in boiling heat transfer have been developed. One technique measures wall temperature on a wall with constant heat flux, while the other measures wall heat flux on a wall held at constant temperature. Both methods promise to help clarify boiling heat transfer mechanisms.

ACKNOWLEDGEMENTS

The funding for this work was provided by NASA MSAD, and is gratefully acknowledged. The grant monitor is Mr. John McQuillen.

REFERENCES

3M Corporation, 1995, *3M Fluorinert Liquids Product and Contact Guide.*

Cooper, M.G. and Lloyd, A.J.P., 1969, "The microlayer in nucleate boiling", *International Journal of Heat and Mass Transfer*, Vol. 12, pp. 895-913.

Hohl, R., Auracher, H., Blum, J., and Marquardt, W. (1997), "Identification of Liquid-Vapor Fluctuations Between Nucleate and Film Boiling in Natural Convection", Proceedings of the 1997 Engineering Foundation Conference on Convective Flow and Pool Boiling, Irsee, Germany.

Incropera, F.P. and Dewitt, D.P, 1996, Fundamentals of Heat and Mass Transfer, Fourth Edition, John Wiley and Sons.

Kenning, D.B.R., 1992, "Wall Temperature Patterns in Nucleate Boiling", *International Journal of Heat and Mass Transfer*, Vol. 35, pp. 73-86.

Rule, T.D., Kim, J., Quine, R.W., Kalkur, T.S., and Chung, J.N., 1997, "Measurements of Spatially and Temporally Resolved Heat Transfer Coefficients in Subcooled Pool Boiling", Proceedings of the 1997 Engineering Foundation Conference on Convective Flow and Pool Boiling, Irsee, Germany.

Rule, T.D. and Kim, J., 1997, "Wall Heat Transfer Measurements in Saturated Pool Boiling of FC-72 on a Small Heated Area", proceedings of the ASME IMECE conference, Dallas, TX.

Rule, T.D., 1998, "Design, Construction and Qualification of a Microscale Heater Array for Use in Boiling Heat Transfer", Master's Thesis, School of Mechanical and Materials Engineering, Washington State University, Pullman, WA.

Watwe, A.A. and Hollingsworth, D.K., 1994, "Liquid Crystal Images of Surface Temperature During Incipient Pool Boiling", *Experimental Thermal and Fluid Science*, Vol. 9, pp. 22-33.

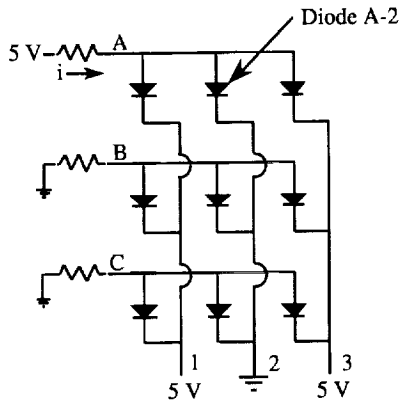

Figure 1: Example of a 3 x 3 diode array.

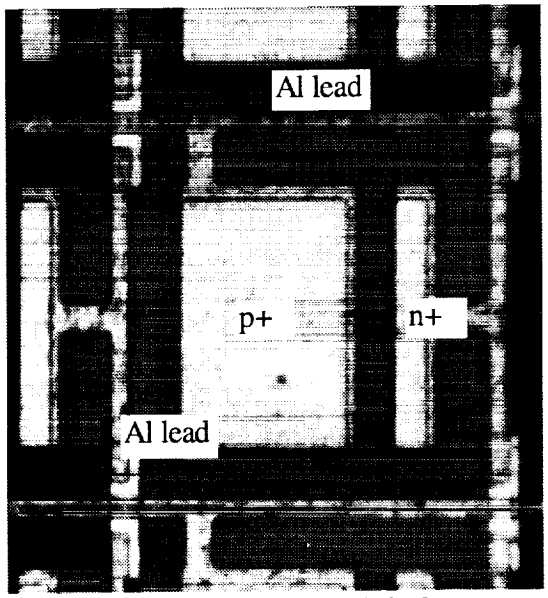

Figure 2: Photograph of a diode in the array.

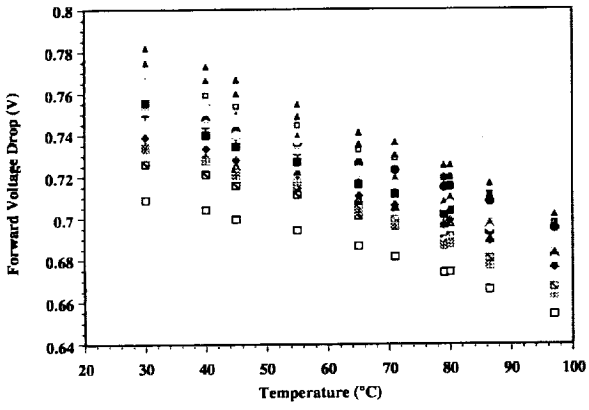

Figure 3: Calibration of diode array.

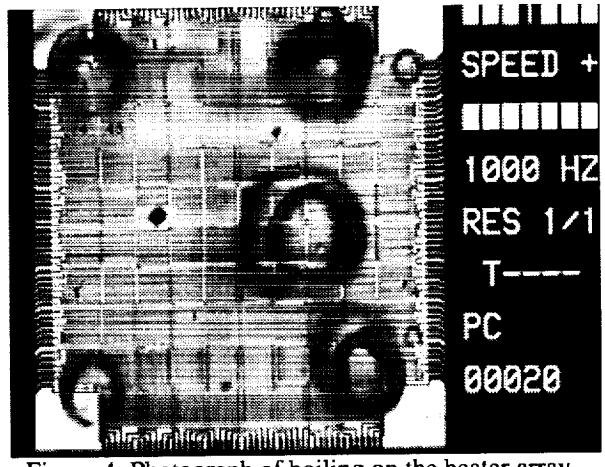

Figure 4: Photograph of boiling on the heater array– isolated bubble regime. Each heater in the array is 0.27 mm x 0.27 mm in size.

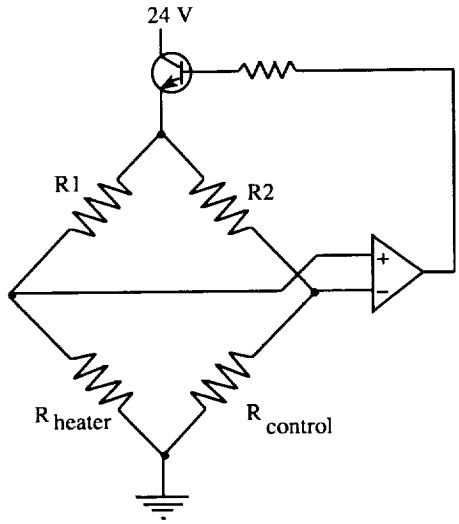

Figure 5: Schematic of feedback loop.

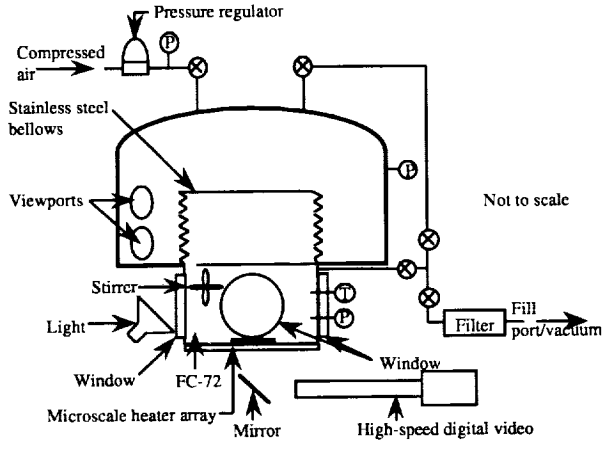

Figure 6: Schematic of experimental apparatus.

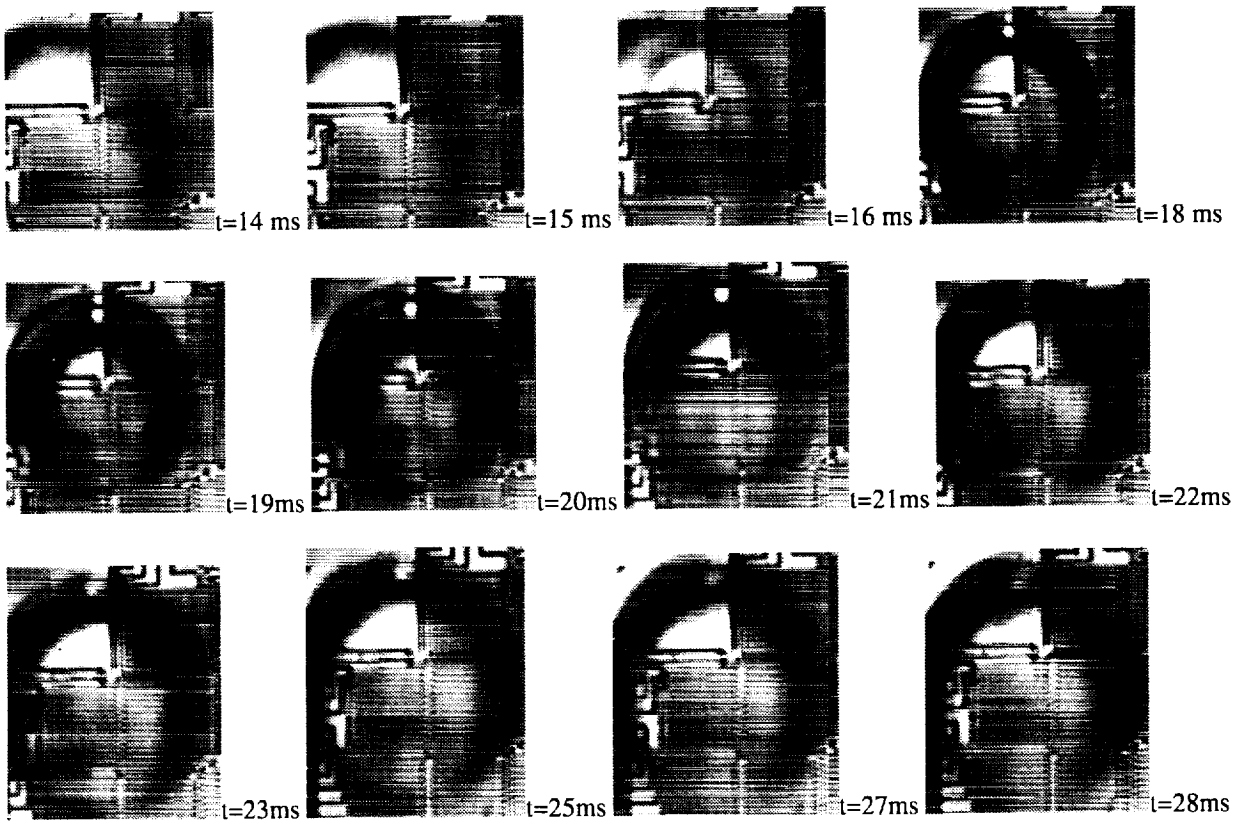

Figure 7: Evolution of one bubble on the surface.

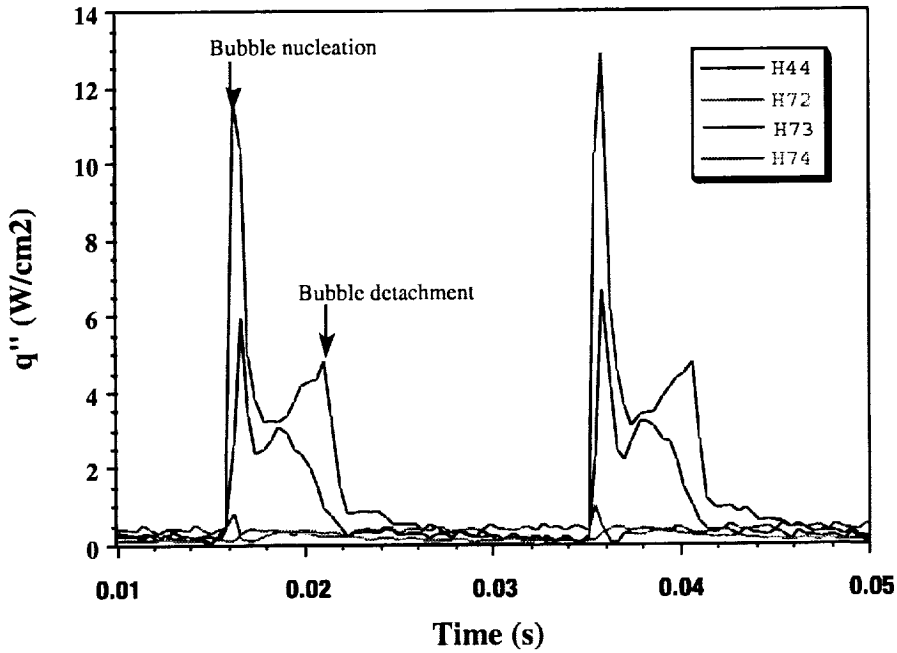

Figure 8: Wall heat flux vs. time for selected heaters. The times correspond to those on Figure 7.

VIBRATION-INDUCED DROPLET ATOMIZATION

M. K. Smith, A. James, B. Vukasinovic, and A. Glezer
The George W. Woodruff School of Mechanical Engineering
Georgia Institute of Technology, Atlanta, GA 30332-0405
marc.smith@me.gatech

INTRODUCTION

Thermal management is critical to a number of technologies used in a microgravity environment and in Earth-based systems. Examples include electronic cooling, power generation systems, metal forming and extrusion, and HVAC (heating, venting, and air conditioning) systems. One technique that can deliver the large heat fluxes required for many of these technologies is two-phase heat transfer. This type of heat transfer is seen in the boiling or evaporation of a liquid and in the condensation of a vapor. Such processes provide very large heat fluxes with small temperature differences. A heat pipe is an example of a device that exploits such two-phase heat transfer to provide high heat fluxes in a simple passive device. However, one of the limitations of the heat pipe is that the heat flux is limited by the rate at which the liquid phase is transported along the pipe by the capillary wicking material.

The purpose of our work is to improve on the passive heat pipe by using a more active means of transporting the liquid phase in a similar heat transfer cell. The process we are considering is called vibration-induced droplet atomization. In this process, a small liquid droplet is place on a thin metal diaphragm that is made to vibrate by an attached piezoelectric transducer. The vibration induces capillary waves on the free surface of the droplet that grow in amplitude and then begin to eject small secondary droplets from the wave crests. In some situations, this ejection process can develop so rapidly that the entire droplet seems to burst into a small cloud of atomized droplets that move away from the diaphragm at speeds of up to 50 cm/s. If such a process could be incorporated into a heat transfer cell, the active atomization and transport of the small liquid droplets could provide a much larger heat flux capability for the device.

The first step in exploiting this bursting process for use in heat transfer cells or in any other technology is to understand the basic atomization process itself. In the sections that follow, we present some of our work on the nature and character of this phenomenon. First, we discuss in more detail the nature of a typical bursting event. Then, we describe the experimental apparatus and protocols used in this research and present data that characterizes the bursting process in this system. The response of the system can be explained in terms of a simple interaction between the droplet ejection process and the nonlinear dynamics of the vibrating diaphragm. This interaction is embodied in a simple mathematical model that is described next. Finally, we discuss the results, present our conclusions, and describe our future work with this process.

DROPLET BURSTING

The overall phenomenon of droplet bursting is shown in Figure 1. A liquid droplet with a volume of approximately 200 μl and a diameter of approximately 5 mm was placed at the center of a horizontal, circular metal diaphragm. The diaphragm was clamped at its periphery and was driven by a piezoelectric ceramic disk centrally-mounted on its bottom side. Excitation of the piezoelectric disk caused the diaphragm to

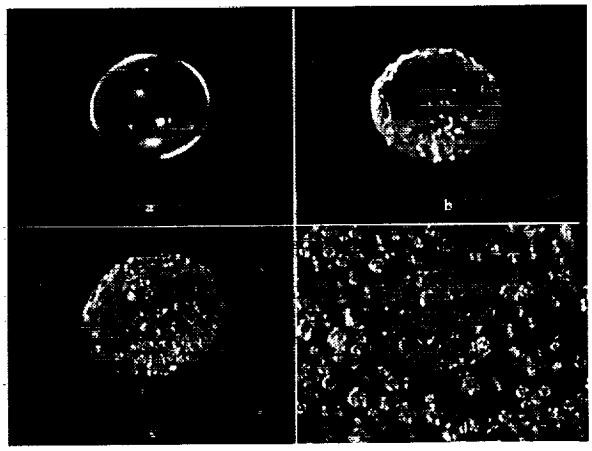

Figure 1: A sequence of video frames showing perspective views of a liquid droplet on a vibrating diaphragm. The excitation frequency is held fixed. The excitation amplitude is increased from image a) to c) and then fixed after that. a) The undisturbed droplet, b) non-axisymmetric wave motion on the surface, c) intense wave motions over the entire droplet surface and the ejection of a few small secondary droplets, and d) the small secondary droplets that have fallen on the diaphragm after the bursting event.

vibrate in the vertical direction in its fundamental axisymmetric mode. Figure 1 shows a sequence of video frames of this system as the excitation amplitude is increased, but with the frequency fixed at about 1000 Hz. Figure 1a shows the unforced droplet for reference. For small values of the excitation amplitude, axisymmetric standing waves appeared on the surface of the droplet. At slightly higher excitation amplitudes, the droplet underwent a transition to a non-axisymmetric wave form as shown in Figure 1b. The excitation amplitude was increased once again and in Figure 1c, we see that the surface waves have increased in magnitude and complexity and that a few small secondary droplets have already been ejected from some of the wave crests. At this point, we held the excitation amplitude fixed and observed a slow intensification of the droplet ejection process until suddenly, within a half a second or so, the entire droplet seemed to explode into a spray of much smaller secondary droplets. The spray was directed away from the surface of the diaphragm with initial droplet ejection speeds of up to 50 cm/s. The ejected droplets reached a maximum height above the diaphragm of about 5 cm. The end result of this bursting process is shown in Figure 1d, where we see that most of the ejected secondary droplets have landed back on the surface of the diaphragm under gravity.

The bursting process displayed in Figure 1 has several interesting fluid dynamical events. The first is the appearance of the standing axisymmetric waves on the free surface of the droplet. These waves are classical Faraday waves with some edge modifications due the contact line of the droplet. The instability of these waves produces the non-axisymmetric motions that were observed. Such instabilities have been reviewed by Miles and Henderson (1990).

The Faraday waves grow in amplitude and complexity as the driving amplitude is increased until we begin to see the ejection of a few small secondary droplets from the wave crests of the primary droplet. This kind of droplet ejection has been studied by several other researchers in related geometries (see Goodridge, et al., 1996 for example). While the rate of droplet ejection depends on the excitation amplitude, the more interesting fact is that for a fixed excitation amplitude the rate of ejection slowly increases with time. At this point in the process, the wave motion seems to have become more evenly distributed across the free surface of the primary droplet and the droplet ejection sites seem to occur evenly throughout the center portion of the droplet.

The most interesting event is the burst. It occurs after the first appearance of droplet ejection and the length of time needed to burst depends on the excitation amplitude. When a large excitation signal is applied to the diaphragm, bursting can occur immediately. For smaller excitation amplitudes (but still large enough), bursting may be delayed on the order of seconds to maybe a minute or more after the forcing is applied.

The purpose of this paper is to describe and characterize this dramatic bursting event. In the sections that follow, we describe our experiments and mathematical modeling of the bursting process and present some results.

EXPERIMENTAL SETUP

The experimental apparatus used in this work is shown in Figure 2. The transducer used to vibrate the liquid droplet was a circular steel diaphragm 29 mm in diameter and 0.2 mm thick. A piezoelectric ceramic was plated onto a small circular area centered on the lower surface of the diaphragm. The diaphragm was mounted in an aluminum ring holder by clamping the outer edge with a retaining ring. The inside diameter of this ring and thus the active diameter of the vibrating diaphragm was 27 mm. The diaphragm was excited using a signal generator coupled to an amplifier that applied a constant sinusoidal voltage to the ceramic. This causes the ceramic to expand and contract, which in turn induces the diaphragm to vibrate in its fundamental axisymmetric mode. The frequency and voltage applied to the ceramic were monitored and controlled.

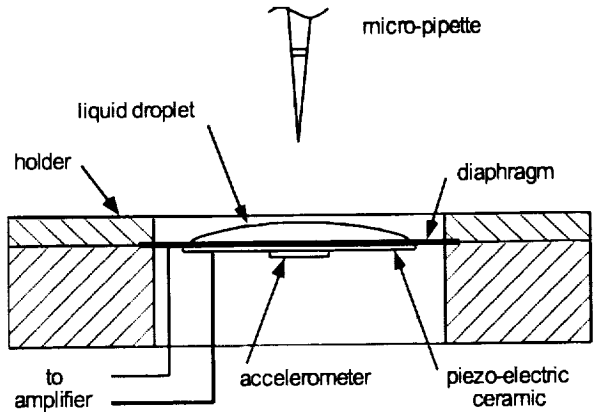

Figure 2: A sketch of the experimental setup.

The acceleration of the diaphragm was measured with a small accelerometer glued to the center of the piezoelectric ceramic on the lower surface of the diaphragm. The accelerometer has a range of 350 g

and a precision of about ± 0.01 g. Given a nominal forcing frequency of 1000 Hz, we only recorded the oscillation amplitude of the output from the accelerometer. This amplitude was obtained with a small circuit that squared the voltage signal from the accelerometer and then passed it through a 40 Hz low-pass filter. The resulting signal was sampled at a rate of 100 Hz. A square root was taken once the signal was discretized by the data acquisition computer.

Finally, the temperature of the aluminum retaining ring was monitored by an embedded thermocouple in order to correct the final results for variations in the temperature of the diaphragm due to the small but normal variations in the ambient temperature of the room.

The upper surface of the diaphragm was cleaned prior to each run using a strict protocol. This was done in order to reduce any possible contamination of the free surface of the droplet so as to promote the repeatability of the results. At the very beginning of each set of runs, an air duster was used to remove any microscopic dust that might have been present on the diaphragm. The cleaning procedure before each run consisted of the following steps: removal of the secondary droplets from the previous run using a small pipette, drying of the surface by tissue, surface cleaning by acetone, and finally, cleaning by distilled water.

We used distilled water in these experiments. Varying volumes of water ranging from 100 μl to 400 μl were placed at the center of the upper surface of the diaphragm using a micro-pipette with a precision of about 1 μl. The free surface motion on the droplet and the evolution of the bursting event were recorded using a video camera with a 1/10,000 sec shutter speed.

A typical response plot of the acceleration amplitude of a dry diaphragm versus frequency for various values of the applied voltage is shown in Figure 3. The symbols are the experimental data points and the solid curves are the results of the mathematical model that we shall describe later. The behavior of this system is typical of a slightly nonlinear structural system forced near its resonance frequency. The influence of a small droplet of water (without any droplet ejection) on this behavior is shown in Figure 4. For these data, we set the driving amplitude well below the amplitude needed for any droplet ejection to occur. We see that the additional mass of the water droplet lowers the resonance frequency of the system as expected. In addition, the peak acceleration amplitude at resonance decreases slightly as the frequency decreases. This behavior is typical of the structural damping that occurs as a result of the flexing of the steel diaphragm.

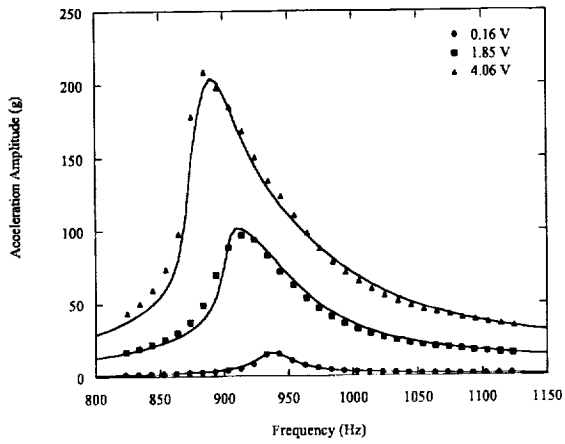

Figure 3: The frequency response of a dry diaphragm for various values of the applied voltage (measured in volts). The acceleration is measured in units of one gravity.

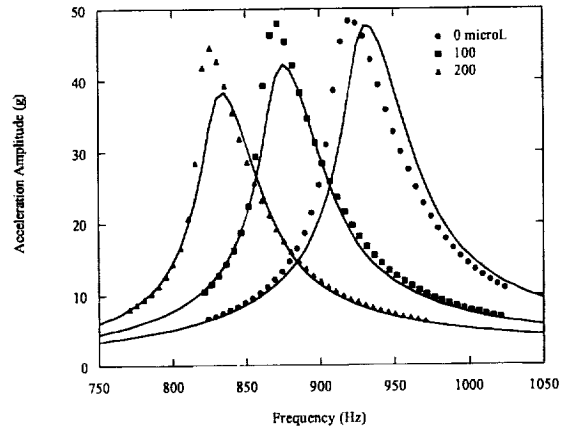

Figure 4: The effect of the droplet mass on the frequency response of the diaphragm for two different droplet volumes (measured in microliters). The acceleration is measured in units of one gravity.

Figure 5 shows the acceleration amplitude of a typical bursting event in our experiment. For these experiments, a constant voltage is applied to the diaphragm at time zero. Initially, the acceleration of the diaphragm jumps to a value corresponding to the imposed voltage. It then slowly increases from this initial value. During this time we observed a few

small droplets being ejected from the large droplet and land back on the diaphragm. Then suddenly, the acceleration rapidly rises to a maximum and decreases to a new, but lower constant level. The rapid change in acceleration occurred when the droplet was observed to burst. For a driving frequency closer to the initial resonance frequency of the system or for a higher driving voltage the bursting signature can be made to occur almost immediately. We shall discuss this event in more detail in the following section.

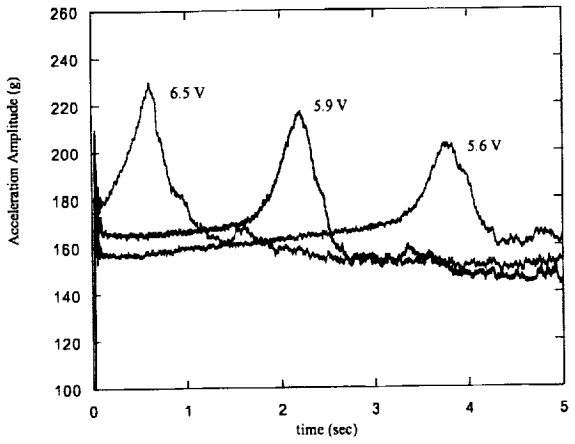

Figure 5: The acceleration signature of a bursting droplet for various driving voltages and at a driving frequency of 750 Hz.

MATHEMATICAL MODEL

Our mathematical model of the diaphragm-droplet system is shown in Figure 6. The diaphragm is modeled as a lumped mass connected to a nonlinear spring, a nonlinear structural damper, and a piezoelectric driving element. We account for the axisymmetric motion of the diaphragm by using the generalized mass of the diaphragm and the piezoelectric ceramic based on the measured mode shape in this frequency range. The stiffness of the diaphragm is included using a nonlinear spring function fitted to the observed behavior of the diaphragm without any water droplets present. Also based on our observations, a small amount of structural damping is included. The piezoelectric element is simply a linear spring that can vary its own length x when a voltage is applied. The droplet is also modeled as a lumped mass. We account for the initial spreading of the droplet by computing a generalized mass for a droplet with a given volume, a given contact angle, and a spherical-cap shape using the same mode shape of the diaphragm as before. We account for droplet ejection by allowing the droplet mass to decrease at a linear rate if the acceleration of the diaphragm is large enough.

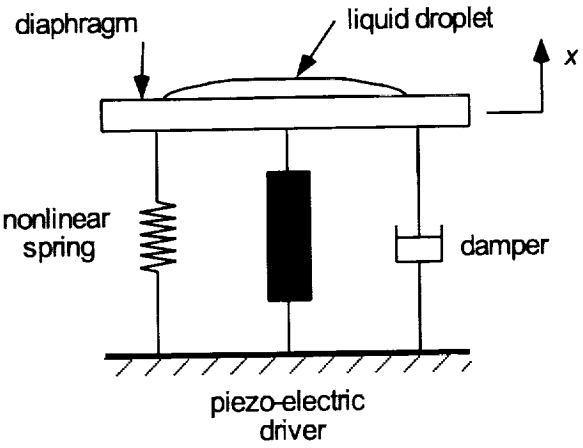

Figure 6: The mathematical model of the diaphragm and liquid droplet system.

In this one-degree-of-freedom model, the motion of the diaphragm is described by the following pair of differential equation in time:

$$m\ddot{x} + \frac{c(x)}{\omega}\dot{x} + k(x)x = A\cos(\omega t) \quad (1)$$

$$m = f(m_l, m_d, m_r) \quad (2)$$

$$\dot{m}_d = \begin{cases} 0, & \ddot{x} < a_c \\ -r(\ddot{x} - a_c), & \ddot{x} > a_c \end{cases} \quad (3)$$

Here, x is the displacement at the center of the diaphragm and m is the total generalized mass of the system. It is composed of m_l the generalized mass of the diaphragm, m_d the generalized mass of the droplet, and m_r the residual mass of the droplets that have fallen back on the diaphragm. The structural damping of the system is $c(x)$, $k(x)$ is the nonlinear spring function for the system, A is the driving coefficient derived from the piezoelectric element, and ω is the frequency of the oscillations. Finally, r is the rate of droplet ejection from the large primary droplet and a_c is the critical acceleration above which droplet ejection occurs.

These two equations were integrated in time using the fourth-order Runge-Kutta integrator in MATLAB (ode45). To compare the numerical results to the experimental data, the acceleration time response was squared and digitally low-pass-filtered with the same

cutoff frequency of 40 Hz as in the experiments. The results were then square-rooted and plotted. To give the best comparison to the experimental data, the nonlinear functions for the stiffness and the structural damping of the diaphragm were fitted to the data for a dry diaphragm. The two parameters characterizing the bursting process, r and α_c were fitted to the data in order to produce the best overall agreement between the model and the experiments.

RESULTS

The first results of our simulations, plotted in Figure 3, show good agreement between the model and the experiment. This simple model does a good job of predicting the behavior of the dry diaphragm over a range of driving voltages because the model parameters were optimized for these conditions. Nevertheless, the results show that this simple model of a lumped spring-mass-damper system is a good one for this apparatus.

The effect of adding a droplet to the diaphragm is shown in Figure 4. As mentioned earlier, the droplet mass lowers the resonance frequency and amplitude of the system. We track the drop in the resonance frequency quite well, but over-predict the drop in the peak resonance amplitude. We are about 14% lower than the experimental peak at the largest droplet volume considered. The discrepancy is primarily due to the fact that the structural parameters for the model were optimized for a system acceleration response of about 100 g. The experimental data in Figure 4 have a peak acceleration no larger than 50 g.

A simulation of droplet bursting is shown in Figure 7. This is a plot of the acceleration of the diaphragm versus time for several different driving voltages. The 5.9 V level is the threshold voltage. Below this value, no secondary droplets are ejected from the primary droplet. For larger driving voltages, we see a relatively slow increase in the acceleration amplitude on the plate until suddenly the voltage rises and falls to a slightly lower level.

While the quantitative agreement between the bursting results of the experiment and the simulations shown in Figure 5 and Figure 7 are not very good, at least the general trends are predicted. We see that as the driving voltage increases, the ejection time peak is shifted to smaller times, the peak response increases slightly, and the final response is slightly reduced. The differences are primarily due to the simplicity of the mathematical model used for both the droplet ejection process and the vibration of the diaphragm.

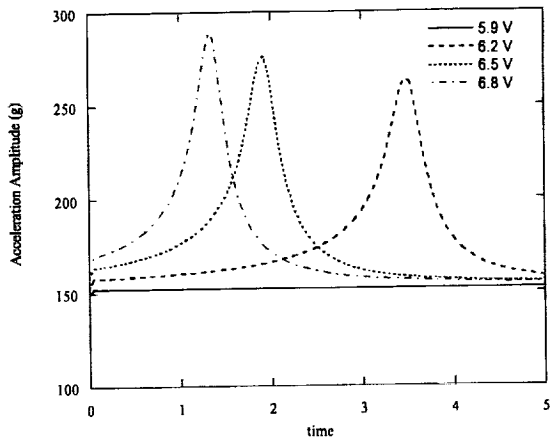

Figure 7: The numerical simulation of the acceleration signature of a bursting droplet driven at 825 Hz. The acceleration is measured in units of one gravity.

CONCLUSIONS

An analysis of the experiments and simulations presented above show that a droplet bursting event occurs when the system passes through a resonance condition. To explain this process, assume the fact that small secondary droplets are ejected from the crests of free surface waves on the larger droplet when the acceleration amplitude of the diaphragm is larger than a critical value. Also, assume that the rate of droplet ejection depends on the magnitude of this acceleration. Bursting occurs when the initial acceleration of the diaphragm is higher than the critical acceleration and the driving frequency is larger than the initial resonance frequency of the diaphragm-droplet system. Under these conditions, some droplet ejection occurs immediately after the driving voltage is applied. If the initial diaphragm acceleration is too high, the rate of droplet ejection will be very large and the droplet will appear to burst immediately.

If the initial diaphragm acceleration is just above the critical acceleration, the rate of droplet ejection from the larger droplet will be very small. As the secondary droplets are ejected, the effective mass of the diaphragm-droplet system is reduced, which increases the resonance frequency of the system and brings it closer to the driving frequency. When this occurs, the vibration amplitude of the system increases, leading to even more droplet ejection. In this way, the droplet ejection process allows the system to pass through its resonance frequency and to experience the very large peak acceleration associated

with this event. If this peak acceleration is large enough, it will drive the droplet ejection rate to the large values needed to produce a bursting event.

The time delay for the bursting event depends on the difference between the initial diaphragm acceleration and the critical acceleration. The smaller this difference, the larger the time delay for bursting to occur. Also, if the initial driving frequency is below the resonance frequency of the system, bursting may not occur at all. If the initial driving acceleration is just large enough to cause a low rate of droplet ejection, the system will then move away from resonance, the acceleration of the diaphragm will decrease, and droplet ejection will slow down and it may stop completely.

The key to the droplet atomization process we have investigated is the piezoelectric vibrating diaphragm. This simple device gives us an easy and consistent way to achieve accelerations above 200 g, which are needed to atomize and eject the small secondary droplets from larger droplets or films. The device is inexpensive and its power requirement is very small. In contrast, traditional shakers that attain these levels of acceleration are very large, expensive, and difficult to use.

We have incorporated this device into a design for a new heat transfer cell for use in a micro-gravity environment. The cell is essentially a cylindrical container with a hot surface on one end and a cold surface on the other. The vibrating diaphragm is mounted in the center of the cold surface. Water droplets condense on the cold surface and collect on the vibrating diaphragm. Here, they are atomized and propelled against the hot surface, where they evaporate. The water vapor travels back across the cell and condenses on the cold surface, where the cycle is repeated. A prototype of this heat transfer cell has been built and tested. It can operate continuously and provides a modest level of heat transfer, about 20 W/cm^2. Our work during the next few years will be to optimize the design of this cell to see if we can produce a device that has significantly better performance than conventional heat exchangers and heat pipes.

Finally, we have begun a series of experiments and numerical studies that will give us a detailed understanding of the process through which droplets are ejected from a free surface wave crest. We need this information in order to determine the critical acceleration and the rate of droplet ejection used in our simple vibration system model described above. This level of understanding of the droplet ejection process will allow us to optimize the vibration induced droplet atomization technology for use in such things as our heat transfer cell in a microgravity environment. In addition, it will allow us to adapt the technology for use in other processes or systems, such as spray coating, emulsification, encapsulation, etc. In addition, we may be able to devise new ways to do things that are now done by other, possibly less efficient methods.

ACKNOWLEDGMENTS

This work was supported by the NASA Microgravity Research Division though grant number NAG3-1949.

REFERENCES

Goodridge, C. L., Shi, W. T., and Lathrop, D. P. (1996) "Threshold Dynamics of Singular Gravity-Capillary Waves," *Phys. Rev. Let.* **76**, pp. 1824-27.

Miles, J. & Henderson, D. (1990) "Parametrically Forced Surface Waves," *Ann. Rev. Fluid Mech.* **22**, pp. 143-65.

Session 5B

Suspensions

EFFECTS OF GRAVITY ON SHEARED TURBULENCE LADEN WITH BUBBLES OR DROPLETS

Said Elghobashi[1], [1]Mechanical and Aerospace Engineering Department, University of California, Irvine, California 92697, USA, selghoba@uci.edu, Juan Lasheras[2], [2] Applied Mechanics and Engineering Sciences Department, University of California, La Jolla, California 92093, USA, lasheras@ames.ucsd.edu

1 INTRODUCTION

The objective of this numerical/experimental study is to improve the understanding of the effects of gravity on the two-way interaction between dispersed particles (bubbles or liquid droplets) and the carrier turbulent flow. Due to the imposed page limit, only a condensed description of the results will be presented. Reference is made to other publications for the details.

The experiments reported here are concerned with the dispersion of liquid droplets by homogeneous turbulence under various gravitational conditions and the effect of these droplets on the evolution of the turbulence of the carrier fluid (air).

The numerical results presented here are obtained from direct numerical simulations (DNS) of bubble - laden turbulent flow to examine the effects of small bubbles on the behavior of decaying turbulence. All published DNS studies of turbulent flows laden with particles, except [7], adopt the Lagrangian-Eulerian approach. In this approach the carrier flow velocity field is obtained by solving the Navier-Stokes and continuity equations at fixed mesh points whereas the trajectories of the dispersed particles are computed by solving the Lagrangian equation of particle motion [1],[2]. Using this method to simulate turbulent flows with two-way coupling between the particles and the carrier flow is limited at present and in the foreseeable future by the memory and speed of available supercomputers, including the latest parallel supercomputers. This limitation forces all DNS of particle - laden turbulent flows (with two-way coupling) to compute the trajectories of *only* a fraction of the *actual number* of particles. The accuracy of DNS results is directly proportional to the magnitude of this fraction, being highest when the fraction equals unity [2].

The alternative approach for predicting particle-laden flows is known as the 'two-fluid' (TF), or 'Eulerian-Eulerian', approach [3], and has been used only with the Reynolds - averaged equations of motion, not with DNS. In the TF approach, the governing equations are obtained by volume - averaging the equations of motion of both phases (the carrier flow and particles) based on the assumption that the dispersed particles behave as a "continuum" under certain conditions.

The objective of the numerical part of this paper is to describe briefly how DNS can be performed using the two-fluid approach for bubble - laden homogeneous isotropic turbulence without forcing. More details are given in [7]. Turbulent homogeneous shear flows laden with droplets/bubbles will be studied in the next phase of the project.

2 NUMERICAL STUDY

2.1 Governing Equations

We consider spherical bubbles with diameter d much smaller than the characteristic length scale of the flow, L_f, and average the equations of motion of the fluid and bubble over a length scale scale λ which is much smaller than L_f but much larger than the bubble diameter, $d \ll \lambda \ll L_f$. Thus the bubble phase can be treated as a continuum characterized by the velocity $V_i(\mathbf{r},t)$ and concentration (or, volume fraction) $C(\mathbf{r},t)= \pi d^3 n(\mathbf{r},t)/6$, where $n(\mathbf{r},t)$ is the bubble number density.

We assume that the density of the gas and, consequently, the mass of the bubble are negligible compared to those of the surrounding fluid, $\rho_f \gg \rho_b = 0$. We also assume that the bubble concentration, C, is small enough (i.e. $C \leq 10^{-3}$) and thus neglect its contribution to the fluid inertia and continuity, i.e. we retain C only in the buoyancy term in the momentum equation of the carrier flow. This is analogous to the Boussinesq approximation in a stratified fluid with effective density $(1 - C)\rho_f$.

The resulting equations of the conservation of the fluid and bubble phase momentum and mass are [7]:

$$\frac{DU_i}{Dt} = -\frac{1}{\rho_f}\partial_i \tilde{P} + \nu \, \Delta U_i + (C - < C >) \, g \, \delta_{iz} \, , \quad (1)$$

$$\partial_j U_j = 0 \, , \quad (2)$$

$$\frac{dV_i}{dt} = 3\frac{DU_i}{Dt} + \frac{1}{\tau_b}(U_i - V_i + W\delta_{iz}) \, , \quad (3)$$

$$\frac{\partial C}{\partial t} + \partial_j C V_j = 0 \, , \quad (4)$$

where U_i is the fluid velocity, and V_i is the velocity of the bubble phase. The Lagrangian derivatives $D/Dt = \partial/\partial t + U_j\partial_j$ and $d/dt = \partial/\partial t + V_j\partial_j$ are taken along the trajectories of the fluid point and bubble, respectively, and g is the projection of the gravity acceleration on the $z-$ axis, $g_i = -g\delta_{iz}$. The modified hydrostatic part $\tilde{P}$ of the pressure field in eq.(1) is defined as:

$$\tilde{P} = P + \rho_f g \int_0^z (1 - < C >) dz \,, \tag{5}$$

where $< C >$ is the ensemble-averaged bubble concentration. We evaluate $< C >$ as an average over a horizontal (z) plane. The bubble response time τ_b and terminal velocity W are defined as

$$\tau_b = \frac{d^2}{36\nu} \,, \tag{6}$$

$$W = 2\tau_b g \,. \tag{7}$$

The momentum conservation and continuity equations (1)-(4) for both phases are solved in a cubical domain with periodic boundary conditions. The equations are discretized in an Eulerian framework using a second-order finite-difference technique on a staggered grid containing 96^3 points equispaced within unit length in each of three coordinate directions (x,y,z). The Adams - Bashforth scheme is used to integrate the equations in time. Pressure is obtained by solving the Poisson equation using Fast Fourier Transform. More details about the numerical method and its accuracy are discussed by Elghobashi and Truesdell [6].

2.2 Results

In this section we present the DNS results for bubble dispersion in isotropic decaying turbulence with both one-way and two-way coupling.

2.2.1 Dispersion of bubbles in isotropic decaying turbulence (with one-way coupling)

DNS of bubble dispersion in isotropic decaying turbulence is performed with the initial condition: $Re_{\lambda 0} = 25$. The initial bubble velocity and concentration are prescribed as:

$$V_i = \delta_{iz} W, \;\; C_0 = \alpha_0 \,, \tag{8}$$

where the bubble terminal velocity W is given by (7).

The ability of the simulation to resolve the motion at the smallest turbulence scales is assured by the criterion $\eta\, k_{max} > 1$, where k_{max} is the highest resolved wavenumber, and η is the Kolmogorov length scale $\eta = (\nu^3/\epsilon)^{1/4}$. The bubble response time is restricted by the two conditions :

$$d_b < \eta \,, \tag{9}$$

$$Re_b = \frac{W\, d_b}{\nu} < 1, \tag{10}$$

which are necessary for the derivation of (3) [7]. Substituting the terminal velocity (7) and the bubble diameter ($d_b = (36\nu\tau_b)^{1/2}$) in (9) and (10), and using the equality $\eta^2 = \nu\tau_k$, we rewrite the conditions (9) and (10) respectively as

$$\frac{\tau_b}{\tau_k} < \frac{1}{36} \simeq 0.028, \tag{11}$$

$$\tau_b < \left(\frac{\nu}{144 g^2}\right)^{1/3} = \tau_* \,. \tag{12}$$

Both conditions (11) and (12) are satisfied throughout our simulations.

Figure 1 shows the time evolution of the concentration spectrum. It is evident that no numerical instability occurs. The spectrum $E_C(k)$ at high wave numbers approaches an asymptotic form at t=10. The high wavenumber range in the spectrum (i.e. $k \geq 40$) would detect any numerical instability if it existed. The reason for the absence of the instability is that the fluctuations of the bubble concentration, caused by the preferential accumulation, are proportional to the ratio τ_b/τ_k which decreases with time (approximately as $\sim 1/t$) in decaying turbulence.

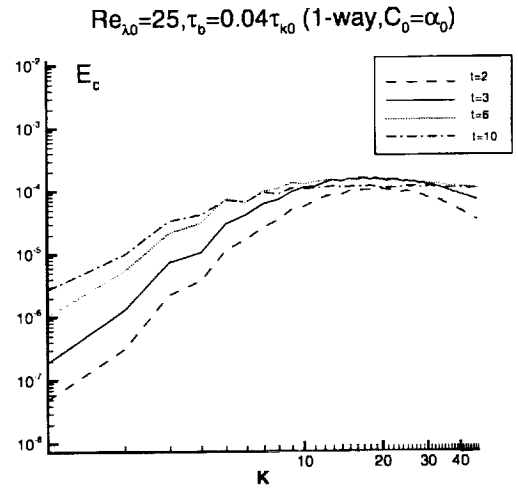

Figure 1: Time evolution of spectrum of bubble concentration fluctuation

It should be noted that both the accumulation of bubbles and the absence of the diffusivity in the transport equation for the bubble concentration (4) may lead to instabilities in the numerical solution due to the development of steep gradients in the concentration field. The occurrence of this numerical instability depends on the initial distribution of the bubble concentration, the flow Reynolds number and the bubble response time. In our DNS we chose the initial microscale Reynolds number $Re_{\lambda 0} = 25$, so that at time of the injection of bubbles (t=1) the small-scale motions are resolved, i.e. $k_{max}\eta \geq 1$ where $k_{max} = N_g\pi$ is the maximum wave number for the given grid resolution $N_g = 96$. The numerical instability may occur for higher-inertia bubbles, i.e. for τ_b of the order of the Kolmogorov time scale τ_k. However, prescribing $\tau_b \simeq \tau_k$ would violate the condition $d_b < \eta$, which is necessary for deriving equation (3) of bubble motion.

2.3 Two-way coupling effects on decaying turbulence

Here we examine the effects of the dispersed bubbles on the temporal development of decaying isotropic turbulence. We consider three cases with different initial bubble concentration profiles in z-direction, but with the same bubble response time as in the one-way coupling case.

The first case is for a uniform initial bubble concentration, $C_0 = \alpha_0$, where α_0 is a reference concentration set equal to 0.005 to allow neglecting bubble-bubble interactions. The second case is for stable linear stratification, with a constant concentration gradient in the vertical (z) coordinate, $C_0 = \alpha_0(1+z)$, while the third case is for unstable linear stratification, $C_0 = \alpha_0(2-z)$. In the cases of stable and unstable stratification, periodic boundary conditions in the z-direction are imposed on the instantaneous concentration fluctuation $C' = C - < C >$. We first consider the modification of the turbulence energy spectrum $E(k)$, which is governed by

$$\partial_t E(k) = T(k) - \epsilon(k) + \Psi_b(k), \qquad (13)$$

where $\epsilon(k)$ is the dissipation rate of $E(k)$, and $T(k)$ is the rate of energy transfer between the wave numbers (i.e. between the different scales). The source of the modification of the energy spectrum and spectral transfer process is $\Psi_b(k)$ which can be regarded as a spectral buoyancy flux, analogous to that in a stratified fluid with density C', and is defined as

$$\Psi_b(\boldsymbol{k}) = g\, Re\, \{C'(\boldsymbol{k})U_z^*(\boldsymbol{k})\}\,. \qquad (14)$$

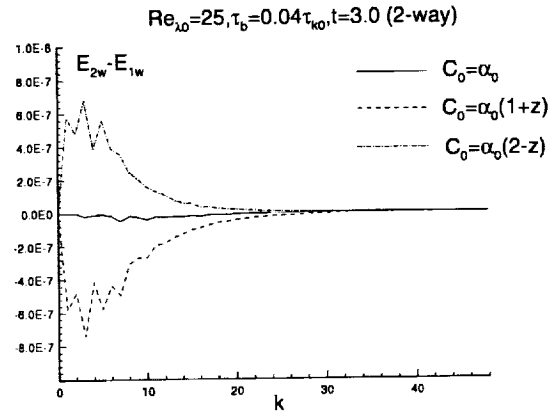

Figure 2: Modification of the turbulence energy spectrum in a bubble-laden decaying turbulence

Figure 2 shows the difference between the energy spectra in two-way and one-way coupling cases computed at time t=3. As expected, the turbulence energy increases in the case of unstable stratification and is reduced in the case of stable stratification. In the non-stratified two-way coupling case, the spectrum remains practically unchanged compared to the one-way coupling case.

3 EXPERIMENTAL STUDY

The objectives of the experiments reported here are measuring the dispersion of the droplets by homogeneous turbulence under various gravitational conditions and determining the effects of the presence of the droplets on the evolution of the turbulence of the carrier fluid (air).

Experimental facility and initial conditions

The experimental facility (Fig. 3) consists of a blow-down wind tunnel made up of two sections. The first section serves as the two-phase flow generation system, while the second is a 2 meter long test section of $20 \times 20\,cm$ square cross section. The air flow, which is supplied by a blower, passes through a slight contraction duct followed by a honeycomb and a grid which damp out the fluctuations generated by the blower. The air stream then flows through the spray generation system. This system consists of two arrays of 33 airblast atomizers each arranged so that the air flow is uniformly laden with droplets. Each atomizer is made of a pressurized

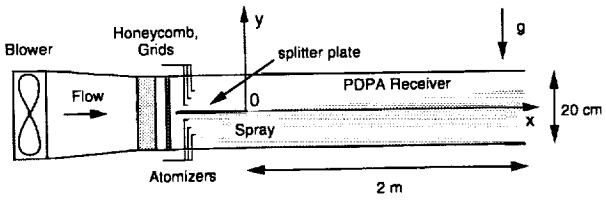

Figure 3: Experimental facility.

air jet impinging normally onto a water jet, thus creating a spray whose main characteristics are given by the pressure of the air and the water flowrate supplying the liquid jet [10],[11]. In the experiments reported here, only one of the two arrays was supplied with water, thus only half of the cross section of the channel flow was loaded with droplets. A splitter plate is placed horizontally at the mid-plane of the channel, separating the droplet-laden flow from the non laden air flow (see Fig. 3). The length of the splitter plate is long enough to ensure that the size distribution of the droplets is uniform across the cross section of the channel before entering the test section. Note that x, y, z correspond respectively to the longitudinal, normal and spanwise coordinates. Due to the spanwise uniformity of the flow, all measurements reported here were made at the $z = 0$ plane.

Preliminary measurements have been carried out to determine the characteristics of both the turbulent air flow and the spray. Velocity measurements were made using hot-wire anemometry. Measurements of mean longitudinal velocity profiles show that the small wake resulting from the presence of the splitter plate follows the common decay law $\frac{\Delta U}{U} \propto x^{-1/2}$, where ΔU is the velocity deficit in the wake. Since for $x > 35\,cm$, $\frac{\Delta U}{U} < 10\%$, most of the measurements reported here have been done beyond this downstream location where it is then considered that the wake has no longer influence on the flow. As we are interested in the interaction between the particules and a homogeneous turbulent flow, we restricted our investigation to the region $-40\,mm < y < 40\,mm$ in order to avoid any effect of the boundary layers forming at the top and bottom surfaces of the test section. The mean velocity in the free stream selected for these experiments, U, is $14\,m/s$, while the longitudinal turbulent intensity , u'/U is measured to be 2%. This corresponds to mean and turbulent Reynolds numbers, $Re = \frac{UH}{\nu}$ and $Re_t = \frac{u'L}{\nu}$, of $1.9\,10^5$ and 1900 respectively. H is the height of the channel, and L is the integral scale of the flow, calculated from the turbulent spectrum measured in the free

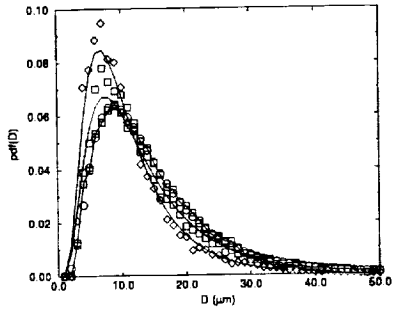

Figure 4: Probality density function for ○, $y = -30$; □, 0; ◇, 30 mm, — respective log-normal fits, x=19 cm, stable stratified case.

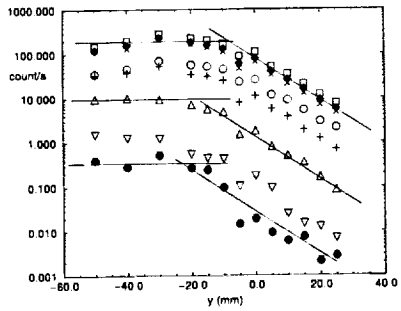

Figure 5: Flux of particles profiles, x=107 cm. ○, $D <$ 5; □, 10; ◇, 15; ×, 25; +, 35; △, 50; ▽, 65; •, 80 μm.

stream. It is approximately $10\,cm$. The droplet void fraction in the free stream is $\alpha = 1.8\,10^{-5}$. The spray size distribution and the velocity of the droplets were measured with a Phase Doppler Particle sizer (Aerometrics PDPA). This instrument has already been tested successfully on a similar experiment [9]. The initial size distribution is shown in Fig. 4 by the open circles. The corresponding mean size is $D_{10} = 15\,\mu m$ and the Sauter Mean Diameter is $D_{32} = 33\,\mu m$. As can be seen, the initial probability density function for the droplet sizes is well described by a log-normal distribution. As we are interested in determining the turbulent diffusivity of the droplets of various sizes, velocity measurements and concentration of droplets have been done for different sizes of particles. For this purpose, PDF have been discretized into 8 bins corresponding respectively to diameters, D, less than 5, 10, 15, 25, 35, 50, 65 and 80 μm.

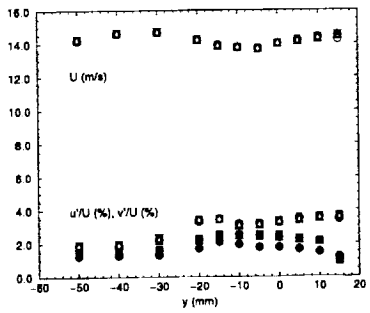

Figure 6: Mean and fluctuations velocity profiles, x=67 cm. Open symbols, longitudinal velocity; closed symbols, normal velocity. ○, $D < 5$; □, 15; ◇, 35; △, 80 μm

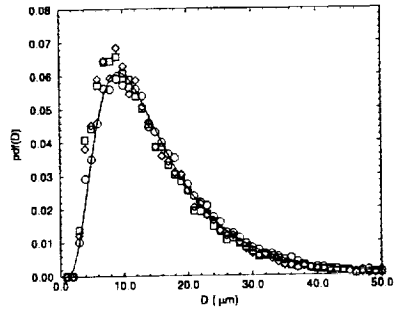

Figure 7: Probality density function for ○, $y = -30$; □, 0; ◇, 30 mm, — log-normal fit for y=-30mm. x=156 cm, stable stratified case.

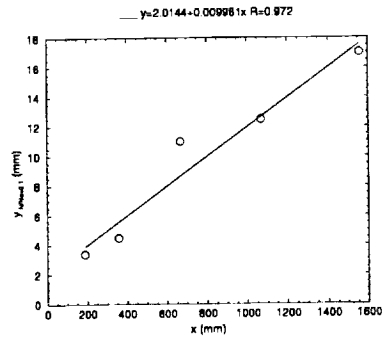

Figure 8: Upper limit of the diffusion zone for droplets of size, $10 < D < 15\,\mu m$.

3.1 Results

Two sets of experiments were conducted to systematically study the role of gravity. In all the experiments, only half of the wind tunnel entrance cross section was laden with uniform-concentration spray of droplets of a given polydispersed size distribution shown by the open circles in Fig. 4. In the first set, the uniform-concentration droplet spray initially occupied the lower half portion of the entrance cross section (stable stratified case), while in the second set the spray initially occupied the upper half portion of the wind tunnel cross section (unstable stratified case).

Stably-stratified case

The mean and fluctuations of the longitudinal and normal velocities are shown in Fig. 6; for clarity, only four bins are shown. One observes that, at $x = 67\,cm$ there is still a slight influence of the splitter wake. Indeed, around the position $y = 0\,mm$, there is a slight effect in the mean velocity and an increase in both fluctuating components of the velocity. Nevertheless, one can conclude that the flow is almost homogeneous turbulence with the value of u'/U and v'/U being close to those of the free stream, that is 2 and 1.4 respectively, giving a ratio u'/v' of 1.4, close to the well known value of 1.2 reported for turbulent channel flow by Comte-Bellot and Corrsin [8]. The main point to note is the fact that no influence of the particles' sizes is observed on the fluctuations of the velocity, but for the smallest ones ($D < 5\mu m$) whose value is constant and equal to the value in the free stream. This fact is more clearly shown in Fig. 5 where profiles of the flux of particles across the probe volume (an indicator of the concentration of the droplets) are plotted according to their size. These profiles show two very distinct regions. The first one, where the flux is constant, corresponds to the free stream, and the second one where the particle turbulent diffusion has already carried the droplets from the droplet-laden free stream to the upper part of the channel with no droplets. One observes that the decrease of the mass flux is almost exponential, and more importantly that it is, to a first order approximation, the same for all droplets whatever their size (note that the three straight lines are parallel to each other). This is further confirmed in Fig. 7 where we show the size PDF of the droplets measured at three different vertical positions. All three distributions are seen to be almost identical, but for a small decrease in the number of big droplets resulting in a small increase of the PDF for small diameters when y increases.

As one can see in Fig. 4, this was not the case at downstream distances closer to the splitter plate where a difference in PDFs is observed. Indeed, one clearly

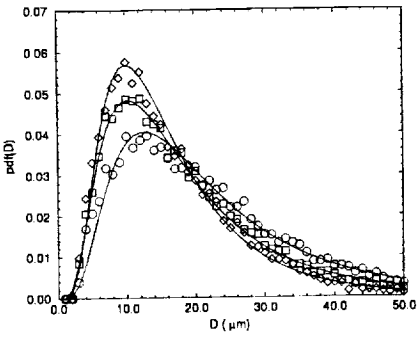

Figure 9: Probality density function for $\circ$, $y = -30$; $\square$, 0; $\diamond$, 30 mm, — log-normal fit for y=30 mm. x=156 cm, unstable stratified case.

notes that small droplets are diffused in the upper part of the channel much faster than big ones resulting in an important increase of the PDF for small diameters when y increases. The large scale eddies structure of the wake is responsible for this effect. The rate of diffusion of droplets in the upper half of the channel can be measured from the data shown in Fig. 5. The upper limit can indeed be defined as the location where the data rate has fallen below a certain threshold. Normalizing these curves by the data rate in the free stream, N_o, and using a definition similar to that used in boundary layers, the upper limit of the diffusion zone has been chosen to be the location where the normalized data rate, N/N_o, is 0.1. The result obtained for particles of size $10 < D < 15\,\mu m$, representative of the spray, is shown in Fig. 8. One observes that this evolution is almost linear with a growth rate of 1%, a value very close to the measured normal turbulent intensity, v'/U, of 1.4%.

Unstably-stratified case

Similar measurements have been carried out where the injection of droplets was done in the upper half of the channel. In this second case the diffusion process is in the same direction as the gravity. Figure 9 shows three PDF taken across the test section. One clearly observes that big droplets are diffused in the lower part at a much larger rate than small ones. This can be seen from the widening of the distribution when descending from $y = 30\,mm$ to $y = -30\,mm$. Measurements are currently in progress to obtain a better understanding of the difference that exists between the stable and unstable, the marked difference observed in the PDFs cannot be explained with the simple linear addition of the settling velocity of the droplets which is less than $0.1\,m/s$ in all cases. Additionnal similar measurements are underway with a vertical splitter plate in order to separate diffusion effects from gravity effects.

Acknowledgements This research has been supported by NASA grant NAG3-1831.

References

[1] C.T.Crowe, T.R.Troutt and J.N.Chung, "Numerical models for two-phase turbulent flows", Ann. Rev. Fluid Mech. **28**, 11 (1996).

[2] S.E.Elghobashi, "On predicting particle-laden turbulent flows", App. Sci. Res. **52**, 309 (1994).

[3] S.E.Elghobashi and T.W.Abou-Arab, "A two-equation turbulence model for two-phase flows", Phys. Fluids **26**, 931 (1983).

[4] J.K.Eaton and J.R.Fessler, "Preferential concentration of particles by turbulence", Int. J. Multiphase Flow **20**, Suppl., 169 (1994).

[5] L.-P.Wang and M.R.Maxey, "Settling velocity and concentration distribution of heavy particles in homogeneous isotropic turbulence", J. Fluid Mech. **256**, 27 (1993).

[6] S.E.Elghobashi and G.C.Truesdell, "On the two-way interaction between homogeneous turbulence and dispersed solid particles. I: Turbulence modification", Phys. Fluids A**5**, 1790 (1993).

[7] O.A.Druzhinin and S. Elghobashi, "Direct numerical simulations of bubble-laden turbulent flows using the two-fluid formulation", Phys. Fluids **10**, 685-697 (1998).

[8] G. Comte-Bellot and S. Corrsin, "Isotropy of grid generated turbulence" J. Fluid Mech.**25**, 657-682 (1966).

[9] K. T. Kiger, "Particle Dispersion and Inter-Phase Kinetic Enery Transfer in a Turbulent Two-Phase Shear Layer" PhD. Dissertation, University of California San Diego (1995).

[10] B.J. Lazaro and J.C. Lasheras, "Particle Dispersion in the developing Shears Layer. Part I" J. Fluid Mech. **235**, 143-178 (1992).

[11] B.J. Lazaro and J.C. Lasheras, 1992 "Particle Dispersion in the developing Shears Layer. Part II" J. Fluid Mech. **235** 143-178 (1992).

BUOYANCY DRIVEN SHEAR FLOWS OF BUBBLE SUSPENSIONS

D.L. Koch, R.J. Hill, T. Chellppannair, R. Zenit
Chemical Engineering
Cornell University

A. Sangani, P.D.M. Spelt
Chemical Engineering and Materials Science
Syracuse University

Please refer to the Conference Book of Abstracts or the NCMR Website at
http://www.ncmr.org

DIRECT NUMERICAL SIMULATION OF THREE-DIMENSIONAL DROP BREAKUP IN ISOTROPIC TURBULENCE

Jerzy Blawzdziewicz, Department of Chemical Engineering, Yale University, New Haven, CT 06520-8286
jerzy@taylor.eng.yale.edu
Vittorio Cristini, Department of Chemical Engineering, Yale University, New Haven, CT 06520-8286
vittorio.cristini@yale.edu
Michael Loewenberg, Department of Chemical Engineering, Yale University, New Haven, CT 06520-8286
michael.loewenberg@yale.edu
Lance R. Collins, Department of Chemical Engineering, Pennsylvania State University,
University Park, PA 16802-4400
lxc12@psu.edu

ABSTRACT

Deformation and breakup of a three-dimensional viscous drop in isotropic turbulence has been modeled by direct numerical simulation. A pseudospectral representation of the turbulent outer flow field is rigorously connected to a detailed three-dimensional description of the drop microphysics using boundary integral calculations. The drop is assumed to be smaller than the Kolmogorov scale. Drop dynamics depend on the drop viscosity and a capillary number. In weaker flows, our simulations indicate that drops break at modest length into two large daughter drops with only a small volume of satellite drops. In stronger flows, drops become highly elongated before breaking and produce many smaller drops. Drops with higher viscosity are stabilized against breakup. Under the same conditions, our simulations show that on some trajectories drops may become highly elongated and recover to modest length without breaking while drops on other trajectories may break at only modest length. Our results indicate that simplified models are unreliable predictors of drop breakup.

1. INTRODUCTION

Drop breakup in turbulent flows is important for a wide range of engineering applications including spraying, emulsifying, and homogenizing operations. Recently, there is considerable interest in drop breakup dynamics because of its impact on the performance of two-phase chemical reactors for the chemical and pharmaceutical industries. For most of these applications, process design is expensive and unreliable because drop breakup in turbulent flows is poorly understood. Two basic questions remain: (1) How do drop breakup rates depend on turbulence and microphysical parameters? and (2) To what extent can the drop size distribution in a turbulent flow be controlled or predicted? These questions are addressed herein.

There have been several experimental investigations of drop breakup in viscous flows (Rallison, 1984; Stone, 1994). Simulations of deformable drops in viscous flows have relied almost exclusively on boundary integral methods which allows higher resolution than with finite element methods because discretization is needed only on the drop interface (Pozrikidis, 1992). However, comprehensive numerical results are available only for drop breakup in axisymmetric flows (Rallison & Acrivos, 1978; Stone & Leal, 1989; Kennedy, Pozrikidis & Skalak, 1994); breakup was inferred by the nonexistence of a steady shape. The difficulty of describing a highly-deformed drop interface has prevented more detailed simulations of three-dimensional drop breakup. Recently, we developed a new algorithm that overcomes this obstacle and provides the capability for detailed 3-D drop breakup simulations which are required for computations of drop breakup rates and drop size distributions (Cristini, Blawzdziewicz & Loewenberg, 1998).

Due to the increased complexity of the problem, the current understanding of drop breakup in turbulent flows is at a much earlier stage than breakup in viscous flows. Phenomenological models of drop breakup, based largely on the classical scaling argument of Kolmogorov and Hinze are widely used (Kolmogorov, 1949; Hinze, 1955). Accordingly, the maximum stable drop size (critical Weber number) is obtained from a balance between turbulent pressure fluctuations and capillary pressure; the resulting estimate applies for drop sizes in the inertial range.

Only recently has a detailed numerical simulation of drop breakup in turbulence been developed. Shreekumar *et al.* (Shreekumar, Kumar & Gandhi, 1996) developed a boundary integral description for the response of an inviscid drop to a single pressure fluctuation. For drop sizes in the inertial range, the maximum stable size was predicted. Their simulations rely on a statistical model of the outer flow field (Batchelor, 1953); Shreekumar *et al.* were unable to establish a rigorous connection between the macroscopic turbulent flow field and the microphysical drop dynamics.

In this article, we present the first direct numerical simulation of drop breakup in isotropic turbulence. No ad hoc assumptions are needed. Our simulations

involve detailed boundary integral calculations of microphysical drop dynamics and breakup rigorously coupled to a pseudo-spectral representation of the turbulent outer flow field. Sub-Kolmogorov size drops are assumed. The problem formulation is described in §2, the numerical method is described in §2, and numerical results are presented in §3. Concluding remarks and extensions of this work are given in §4.

2. PROBLEM FORMULATION

In general, drop dynamics in turbulent flow are too complex for rigorous numerical simulation. The problem that we investigate here is made tractable by the restriction that the drops are smaller than the Kolmogorov length: $a/\eta << 1$, where a is the undeformed drop radius and $\eta = \nu^{3/4}\epsilon^{-1/4}$ is the Kolmogorov length (ν is the continuous-phase kinematic viscosity and ϵ is the specific dissipation rate). The Kolmogorov time is $\tau_\eta = \eta^2/\nu$. The local Reynolds number based on the drop size and local shear-rate is τ_η^{-1} is

$$Re_{loc} = (a/\eta)^2 << 1. \qquad (1)$$

Thus, drop dynamics are governed by the Stokes equations embedded in the external velocity field linearized about the center of mass of a drop.

The behavior of the system depends on the viscosity ratio and the capillary number:

$$\lambda = \mu/\mu, \qquad (2)$$

$$Ca = \sqrt{\rho\mu\epsilon}\, a/\sigma = \tau_d/\tau_\eta \qquad (3)$$

where μ and ρ are the viscosity and density of the continuous-phase fluid, μ is the dispersed-phase viscosity, and σ is the interfacial tension. The drop relaxation time is $\mu a/\sigma$.

We assume that the density contrast is moderate $\Delta\rho/\rho \le O(1)$ and that the acceleration of a fluid element the turbulent outer flow field $b = \eta/\tau_\eta$ is at least as large as the acceleration of gravity $g/b \le O(1)$. Thus, the sedimentation velocity $v_g = \Delta\rho g a^2/\mu$ is smaller than the Kolmogorov velocity $v_g = \eta/\tau_\eta$:

$$v_g/v_\eta = (\Delta\rho/\rho)(g/b)(a/\eta)^2 << 1, \qquad (4)$$

and inertial stresses $\Delta\rho ba$ are smaller than viscous stresses μ/τ_η:

$$\frac{\Delta\rho ba}{\mu/\tau_\eta} = (\Delta\rho/\rho)(a/\eta) << 1. \qquad (5)$$

By assumption (4), it follows that drop trajectories closely coincide with streaklines of the turbulent flow field; drop dynamics can be computed using precalculated streaklines from the turbulent outer flow field. Gravity sedimentation will have only a small $O(v_g/v_\eta)$ effect because the outer flow field is statistically isotropic. The acceleration of a drop moving along a streakline of the turbulent flow field has little effect on its dynamics according to Eq. (5). The foregoing assumptions are satisfied for viscous liquid-liquid dispersions; an example system is given in Table 1.

Drop dynamics may also depend on the macroscopic Reynolds number (i.e. system size) (Meneveau & Sreenivasan, 1991; Lam, Sathyagal, Kumar & Ramkrishna, 1996) but this is not explored here. Surfactant effects are also omitted. A small mass loading of drops is assumed thus, turbulence modulation induced by the suspended drops is negligible (Sundaram & Collins, 1998b).

Table 1: Example System

μ(Pa s)	.1	a/η	.1
ρ(Kg/m^3)	10^3	g/b	1
$\hat{\mu}$(Pa s)	.1	Ca	.25
$\Delta\rho/\rho$	.1	λ	1
σ(N/m)	.04	Re_{loc}	.01
a(mm)	.1	v_g/v_η	.001
ϵ(W/Kg)	1	$\frac{\Delta\rho ba}{\mu/\tau_\eta}$	.01
η(mm)	1		

3. NUMERICAL METHOD

3.1 Direct Numerical Simulation of Isotropic Turbulence

In our simulations, homogeneous isotropic turbulence is described by direct numerical simulation (DNS) of the full Navier-Stokes equations:

$$\frac{\partial \mathbf{u}\infty}{\partial t} + \mathbf{u}\infty \cdot \nabla\mathbf{u}\infty = -\frac{\nabla p}{\rho} + \nu\nabla^2\mathbf{u}\infty + \mathbf{F}_s, \qquad (6)$$

$$\nabla \cdot \mathbf{u}\infty = 0, \qquad (7)$$

where $\mathbf{u}\infty$ and p are the fluid velocity and pressure that satisfy periodic boundary conditions. The stochastic forcing function $\mathbf{F}_s$ maintains stationary isotropic turbulence by continuously adding energy to the system through the lowest wavenumbers ($\kappa \le \sqrt{2}$) (Eswaran & Pope, 1988). Eqs. (6)-(7) were solved on a three-dimensional 128^3 lattice which corresponds to Reynolds number for the outer flow of 100 based on the Taylor microscale. A pseudospectral algorithm (Canuto, Hussaini, Quarteroni & Zang, 1988) with partial dealiasing accomplished by zeroing wavenumbers beyond $\frac{8}{9}\kappa_{max}$ (Patterson & Orszag, 1971). Fourth-order Runge-Kutta integration was used for time-integration. Further details of our DNS algorithm are available elsewhere (Sundaram & Collins, 1996; Sundaram & Collins, 1997; Sundaram & Collins, 1998a).

3.2 Direct Numerical Simulation of Isotropic Turbulence

3.2.1 Boundary Integral Formulation. The evolution of a deformable drop is described by time-integrating the fluid velocity on a set of N interfacial marker points in a reference frame moving on a streakline of turbulent outer flow field. Microscale drop dynamics are characterized by quasisteady Stokes flow (inside and outside the drop) by assumption (1). Boundary conditions on the deformable drop interface are obtained by imposing continuity of the velocity, a normal stress jump equal to the capillary pressure $\sigma\kappa$, and continuity of the tangential stresses on the assumption that surface tension gradients associated with adsorbed surfactant are absent. Here, κ is the local mean curvature.

It is convenient to recast the Stokes equations as an integral equation over the drop interface S. Thus, marker point velocities are obtained by solving the second-kind integral equation (Pozrikidis, 1992; Rallison & Acrivos, 1978)

$$\mathbf{u}(\mathbf{x}_0) = \frac{2}{\lambda+1} Ca\,\mathbf{u}^{\infty}(\mathbf{x}_0) - \frac{2}{\lambda+1}\frac{1}{8\pi}\int_S \mathbf{G}\cdot f d(S + \frac{\lambda-1}{\lambda+1}\frac{3}{2\pi}\int_S [\mathbf{T}\cdot\mathbf{u}]\cdot\mathbf{n}\,dS, \qquad (8)$$

which has been made dimensionless using the drop size for characteristic length and the capillary velocity σ/μ for the characteristic velocity.

$$\mathbf{G} = \frac{\mathbf{I}}{r} + \frac{\hat{\mathbf{x}}\hat{\mathbf{x}}}{r^3}, \quad \mathbf{T} = \frac{\hat{\mathbf{x}}\hat{\mathbf{x}}\hat{\mathbf{x}}}{r^5} \qquad (9)$$

are the Stokeslet and stresslet kernel functions, $\mathbf{x}_0$ is a marker point on the drop interface, $\hat{\mathbf{x}} = \mathbf{x} - \mathbf{x}_0$ and $r = |\hat{\mathbf{x}}|$.

Viscous stresses dominate the buoyancy stresses induced by acceleration of the drop on a turbulent streakline according to (5) and surface tension gradients (associated with adsorbed surfactant) are omitted. Thus, the surface traction is

$$\mathbf{f} = 2\kappa\mathbf{n}, \qquad (10)$$

where κ and $\mathbf{n}$ are the mean curvature and outward normal.

The local velocity field in the streakline reference frame is:

$$\mathbf{u}^{\infty}(\mathbf{x}_0) = \nabla\mathbf{u}^{\infty}(\mathbf{x}_c)\cdot(\mathbf{x}_0 - \mathbf{x}_c) + O(Re_{loc}), \qquad (11)$$

where $\mathbf{x}_c$ is the instantaneous center-of-mass of the drop and a point on the turbulent streakline. The error term results from small $O(a/\eta)^2$ quadratic variations. The time-dependent velocity gradient $\nabla\mathbf{u}^{\infty}$ is obtained at lattice points by direct numerical simulation of the outer flow field (c.f. §2.1) and interpolated to the center of the drop using Hermite cubic spline interpolation to obtain $\nabla\mathbf{u}^{\infty}(\mathbf{x}_c)$ (Sundaram & Collins, 1996). The microscale drop dynamics are thereby rigorously connected to the turbulent outer flow.

Eq. (8) is recast into a singularity-subtracted form for efficient trapezoid-rule integration on the drop interface (Loewenberg & Hinch, 1996) and solved by simple iterations which is made possible by purging the eigensolutions (Pozrikidis, 1992). The normal vector and curvature on the drop interfaces are calculated by a local surface-fitting algorithm (Zinchenko, Rother & Davis, 1997). The resulting accuracy of the marker-point velocities is $O(1/N)$. Stability for time-integration of Eq. (8) requires $\Delta t \le N^{-1/2}$. Thus, consistent $O(1/N)$ accuracy is obtained by advancing the marker-points with a second-order Runge-Kutta integration of marker-point velocities.

3.2.2 Adaptive Interface Discretization. Our simulations rely on a recently-developed surface discretization algorithm (Cristini, Blawzdziewicz & Loewenberg, 1998). The resulting discretization is fully adaptive and independent of the drop deformation history. It maintains nearly equilateral triangulation and optimal marker-point density needed to uniformly resolve the interface and calculate the evolution of a highly distorted drop with prescribed accuracy.

Grid equilibration is a robust $O(N)$ calculation; the $O(N^2)$ fluid-velocity calculation is time-controlling. Thus, by keeping minimizing the number of marker points, the efficiency of our simulations is greatly increased. Equilateral triangulation maximizes the time-step for the fluid velocity calculation and thereby further enhances computational efficiency. More importantly, however, adaptive surface discretization is essential for detailed drop breakup simulations and breakup rate calculations.

3.2.3 Breakup Times. Drop pinch-off occurs with nearly constant neck-thinning velocity $\sim\sigma/\mu$ (Blawzdziewicz, Cristini & Loewenberg, 1997). Thus, drop breakup times can be accurately obtained by extrapolation from small necks at the onset of breakup. Thus, our simulations can be used to obtain drop breakup rates.

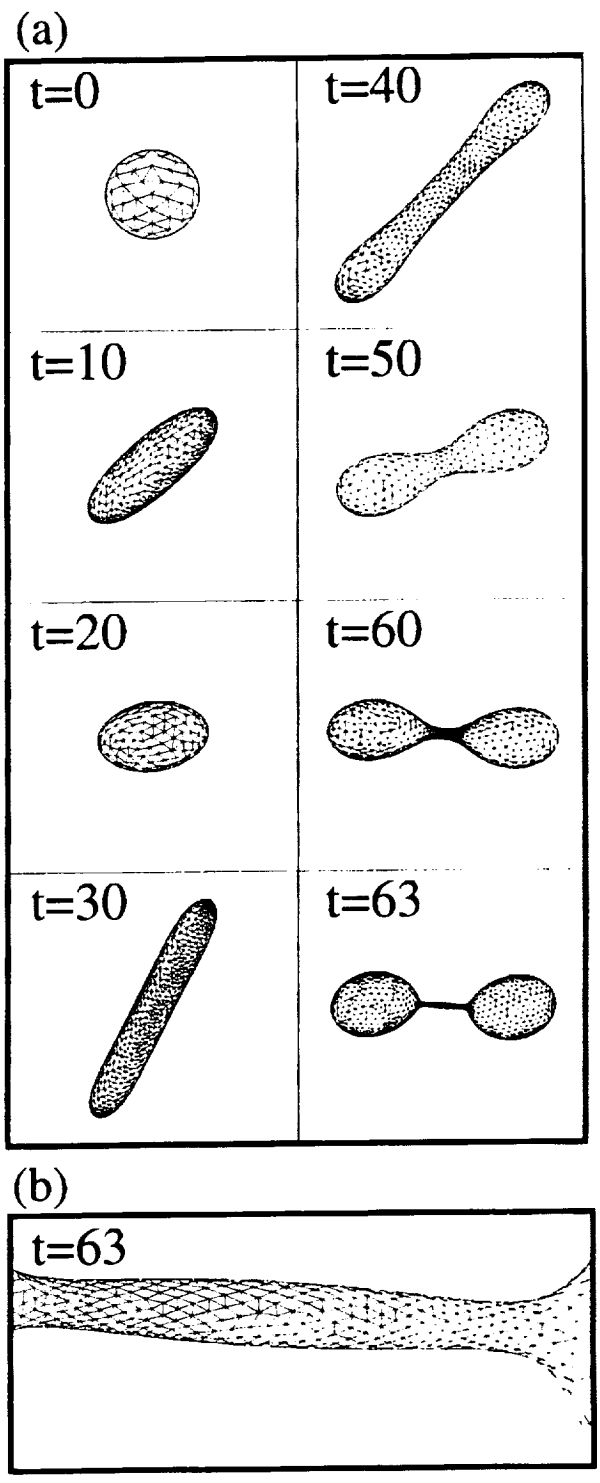

Figure 1: DROP BREAKING IN ISOTROPIC TURBULENCE: Ca = 0.27, λ = 1. (a) SEQUENCE; (b) CLOSE-UP OF NECK CORRESPONDING TO t = 63. TIME NORMALIZED BY THE DROP RELAXATION TIME $\mu a/\sigma$.

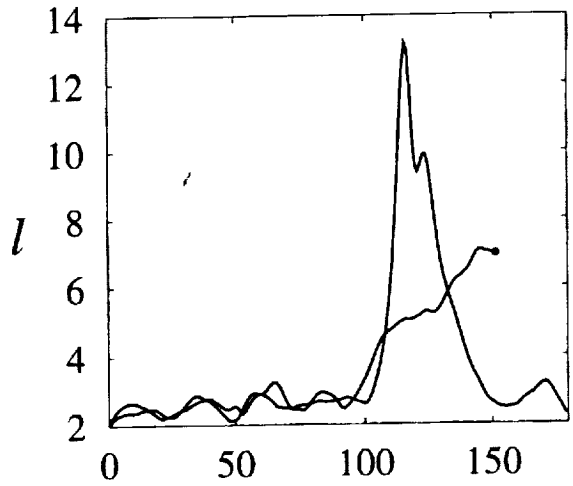

Figure 2: DROP-LENGTH HISTORY FOR TWO TRAJECTORIES: Ca = 0.3, λ = 1. TIME NORMALIZED BY THE DROP RELAXATION TIME $\mu a/\sigma$.

4. NUMERICAL RESULTS

The results depicted in figures 1-2, indicate that our new algorithm provides a detailed description of drop breakup in turbulence. Figure 1 depicts the breakup of a drop along a particular trajectory. The close-up shown in figure 1b demonstrates that our algorithm maintains resolution of the interface up to the instant of pinch-off. This calculation requires 2 CPU hours on a workstation which supports the feasibility of calculating statistical properties, such as breakup rates, using a large number of trajectories.

Figure 2 depicts the drop-length history for two different trajectories under identical conditions (same Ca and λ) in isotropic turbulence: on one trajectory, the drop attains a length of 13 drop radii but does not break; on the other trajectory the drop slowly stretches and eventually breaks at a modest length of 7 radii. Recently, it was proposed that breakup rates of drops in turbulence can be computed using simplified small-deformation models. Unfortunately however, small-deformation models of drop dynamics are known to be unreliable predictors of drop breakup (Barthes-Biesel & Acrivos, 1973; Rallison, 1980). Our results support this conclusion: small deformation models cannot be expected to reliably predict drop breakup under the conditions depicted in figure 2.

4.1 Work-in-Progress

Several more drop trajectories will be presented that demonstrate the dependence of drop dynamics the drop viscosity and capillary number. For a given viscosity ratio, our calculations show that drop breakup at lower capillary numbers occurs by a deterministic end-pinching mechanism that produces two large daughter drops

and only a very small volume of satellite drops. At higher capillary numbers, drops get stretched into a highly elongated thread before breaking is initiated by end-pinching. "Dispersion breakup" (Tjahjadi & Ottino, 1991) resulting from the growth of a capillary-wave instability grows and eventually dominates the end-pinching mechanism for thread-like drops. Dispersion breakup produces a large number of smaller drops comparable to the thread diameter and still smaller satellite drops in between. High viscosity drops are stabilized against breakup; higher capillary numbers are needed to break drops with high viscosities.

5. CONCLUSIONS

A direct numerical simulation of 3-D drop breakup in isotropic turbulence has been developed. Our algorithm provides a powerful new tool for exploring detailed drop dynamics in isotropic turbulence.

Our calculations show that drop deformation dynamics and the mode of drop breakup have a complex dependence on the system parameters: capillary number and viscosity ratio. Drops with viscosity ratios close to unity break most easily. Higher capillary numbers are needed to break drops with higher and lower viscosities. At low capillary numbers, drop breakup produces two large daughter drops with only a very small volume partitioned into satellite drops; at high capillary numbers, many smaller drops result from breakup. This qualitative finding suggests that the drop size distribution may be manipulated by varying the capillary number (energy dissipation rate).

Diverse drop dynamics are possible. On different trajectories, under identical conditions, our results show that drops may become highly distorted without breaking or may break without large deformation. This finding casts considerable doubt on the use of small-deformation models for describing drop dynamics in turbulent flows.

The efficiency of our algorithm makes feasible reliable statistical calculations such as drop breakup rates. Using the known asymptotic behavior of drop pinch-off (Blawzdziewicz, Cristini & Loewenberg, 1997), it should be possible to continue our simulations beyond the breakup event and compute the evolving drop size distribution in a turbulent flow. In principle, our simulations may be adapted to larger inertial-range drops by interpolating DNS velocities onto the drop interface and incorporating capillary stresses into the equations governing the outer flow field by reverse coupling (Sundaram & Collins, 1998b).

REFERENCES

J. Blawzdziewicz, V. Cristini, and M. Loewenberg. Analysis of drop breakup in creeping flows. *Bull. Am. Phys. Soc.*, 42:2125, 1997.

G.K. Batchelor. *The Theory of Homogeneous Turbulence.* Cambridge University Press, 1953.

D. Barthés-Biesel and A. Acrivos. Deformation and burst of a liquid droplet freely suspended in a linear shear field. *J. Fluid Mech.*, 61:1-21, 1973.

V. Cristini, J. Blawzdziewicz, and M. Loewenberg. Drop breakup in three-dimensional viscous flows. *Phys. Fluids*, 1998 in review.

C. Canuto, M.Y. Hussaini, A. Quarteroni, and T.A. Zang. *Spectral methods in fluid dynamics.* Springer-Verlag, New York, 1988.

R.A. de Bruijn. *Deformation and Breakup of drops in simple shear flows.* PhD thesis, Tech. Univ. Eindhoven, 1989.

V. Eswaran and S.B. Pope. An examination of forcing in direct numerical simulations of turbulence. *Comput. Fluids*, 16:257, 1988.

O. Hinze. Fundamentals of the hydrodynamic mechanism of splitting in dispersion processes. *AICHE J.*, 1:289-295, 1955.

A.N. Kolmogorov. On the disintegration of drops in turbulent flow. *Dokl. Akad. Nauk.*, 66:825-828, 1949.

M.R. Kennedy, C. Pozrikidis, and R. Skalak. Motion and deformation of liquid drops and the rheology of dilute emulsions in simple shear flow. *Comput. Fluids*, 23:251-278, 1994.

M. Loewenberg and E.J. Hinch. Numerical simulation of a concentrated emulsion in shear flows. *J. Fluid Mech.*, 321:395-419, 1996.

A. Lam, A. Sathyagal, S. Kumar, and D. Ramkrishna. Maximum stable drop diameter in stirred dispersions. *AICHE J.*, 42:1547-1552, 1996.

C. Meneveau and K.R. Sreenivasan. Multifractal nature of turbulent energy dissipation. *J. Fluid Mech.*, 224:429-484, 1991.

G.S. Patterson and S.A. Orszag. Spectral calculation of isotropic turbulence: efficient removal of aliasing interactions. *Phys. Fluids*, 14:2538-2541, 1971.

C. Pozrikidis. *Boundary Integral and Singularity Methods for Linearized Viscous Flow.* Cambridge University Press, 1992.

J.M. Rallison and A. Acrivos. A numerical study of the deformation and burst of a drop in an extensional flow. *J. Fluid Mech.*, 89:191-209, 1978.

J.M. Rallison. Note on the time-dependent deformation of a viscous drop which is almost spherical. *J. Fluid Mech.*, 98:625-633, 1980.

J.M. Rallison. A numerical study of the deformation and burst of a viscous drop in general linear shear flows. *J. Fluid Mech.*, 109:465-482, 1981.

J.M. Rallison. The deformation of small viscous drops and bubbles in shear. *Ann. Rev. Fluid Mech.*, 16:45-66, 1984.

S. Sundaram and L.R. Collins. Numerical considerations in simulating a turbulent suspension of finite-volume particles. *J. Comput. Phys.*, 124:337-350, 1996.

S. Sundaram and L.R. Collins. Collision statistics in an isotropic, particle-laden turbulent suspension i. direct numerical simulations. *J. Fluid Mech.*, 335:75-109, 1997.

S. Sundaram and L.R. Collins. Collision statistics in an isotropic, particle-laden turbulent suspension ii. theory. *J. Fluid Mech.*, 1998a in preparation.

S. Sundaram and L.R. Collins. A numerical study of turbulence modulation of isotropic turbulence by suspended particles. *J. Fluid Mech.*, 1998b in review.

Shreekumar, R, Kumar, and K.S. Gandhi. Breakage of a drop of inviscid fluid due to a pressure fluctuation at its surface. *J. Fluid Mech.*, 328:1-17, 1996.

H.A. Stone and L.G. Leal. Relaxation and breakup of an initially extended drop in an otherwise quiescent fluid. *J. Fluid Mech.*, 198:399-427, 1989.

H.A. Stone. Dynamics of drop deformation and breakup in viscous fluids. *Ann. Rev. Fluid Mech.*, 26:65-102, 1994.

M. Tjahjadi and J.M. Ottino. Stretching and breakup of droplets in chaotic flows. *J. Fluid Mech.*, 232:191-219, 1991.

A.Z. Zinchenko and M.A. Rother, R.H. Davis. A novel boundary-integral algorithm for viscous interaction of deformable drops. *Phys. Fluids A*, 9:1493-1511, 1997.

Session 5C

Special Topics I

NON-COALESCENCE EFFECTS IN MICROGRAVITY

G. P. Neitzel[1], P. Dell'Aversana [2] and D. Castagnolo[2]

[1]School of Mechanical Engineering, Georgia Institute of Technology, Atlanta, GA 30332-0405 USA
paul.neitzel@me.gatech.edu
[2]Microgravity Advanced Research and Support Center, Via Communale Tavernola, 80144 Napoli, ITALY.

ABSTRACT

Forced non-coalescence between two bodies of the same liquid may be achieved by a variety of means, all of which provide relative tangential motion of the adjacent free-surfaces. This motion serves to provide a lubricating film of the surrounding gas to the gap which prevents the liquid surfaces from coming into contact. One means of forcing non-coalescence is to use thermocapillarity to drive the lubricating film by having the liquids at different temperatures. This paper will examine a number of scenarios of non-coalescence behavior, both qualitatively and quantitatively, and describe some envisioned applications of the phenomenon which may have relevance in both microgravity and terrestrial environments.

INTRODUCTION

Forced non-coalescence between two bodies of the same liquid was noted a century ago by Lord Rayleigh (1899), who commented on streams of water which bounce off one another. Nearly eighty years later, Walker (1978) described experiments in which droplets could be made to "float" on the surface of the same liquid using vibration. Recent investigations of this topic were motivated by difficulties experienced in re-connecting a broken liquid bridge during a laboratory experiment on thermocapillary convection; a similar experience was reported as occurring during a space-flight experiment (Napolitano, Monti & Russo 1986). A paper by Dell'Aversana, Banavar & Koplik (1996) describes the influence of relative motion and the establishment of a lubricating film as the non-coalescence mechanism.

Thermocapillarity is easily used to prevent a pair of drops of liquid from coalescing. Consider the photograph shown in Figure 1. Here, two drops of 5 cS silicone oil are attached to copper rods and subjected to a temperature difference as they are pressed together. Glass beads and smoke are used to visualize the flows both within and exterior to the droplets, respectively. The upper drop is hotter than the lower one, resulting in a region near the point of apparent contact which is either colder (upper drop) or hotter (lower drop) than the bulk liquid in the drop, and hence, the majority of the free-surface. The existence of a surface-temperature gradient and the temperature dependence of surface tension provide a liquid flow toward the contact region in the upper drop and away from it on the lower one, as illustrated in the sketch provided as Figure 2.

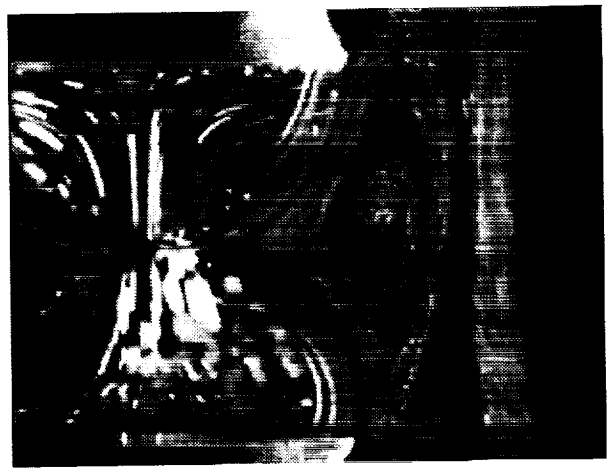

Figure 1: Two non-coalescing drops of silicone oil subjected to a temperature difference. Flows within the drops and in the air are visualized by hollow glass beads and smoke, respectively.

Since the air must migrate from the periphery of the geometry to the center and out again, the pressure

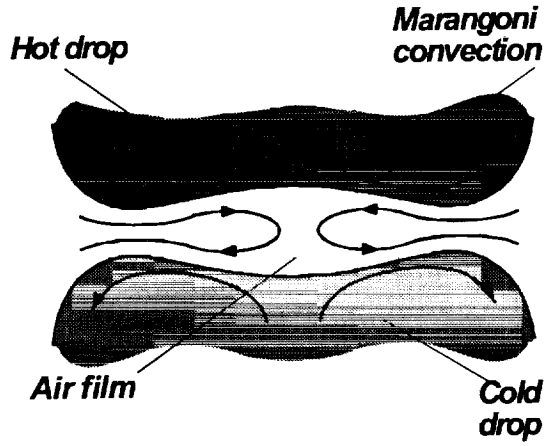

Figure 2: Expanded view of the air film separating two non-coalescing droplets.

at $r = 0$ is a maximum for the film, resulting in the dimpled appearance of the liquid surfaces, as sketched. This dimpling is confirmed through interferometry measurements made in a different, but related, geometry, as described next.

This same mechanism of using thermocapillary convection to suppress coalescence can be employed to suppress the wetting of a solid surface by a normally wetting liquid. In this case, the lower, cold drop of Figs. 1 and 2 is replaced by a cold, solid surface. In the event that this surface is a transparent one such as glass, the gap between the drop and the surface can be interrogated using interferometry from below. Dell'Aversana, Tontodonato & Carotenuto (1997), under sponsorship of this project, have used this technique to quantify the film shape and thickness. This film obviously changes in both size and shape as the droplet is pressed more firmly against the glass, the area of near-contact increasing to accommodate the increased load.

In addition to the droplet-droplet and droplet-solid examples above, a hot droplet may also be pressed against a cold bath with similar results. Such a configuration is shown in Figure 3 with a small satellite droplet nestled against the main drop. In the case of the satellite droplet, it resists coalescing with either

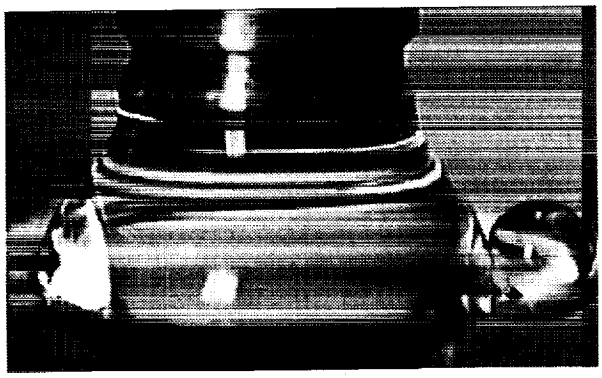

Figure 3: Non-coalescing drop, bath and satellite drop

the bulk liquid or the main drop due to surface motion driven by the rapidly moving surface of the main drop. This is determined through the use of flow visualization showing that the circulation in the satellite drop is of a single sense. Interestingly, in this drop-bath configuration, as the drop is grown larger through the addition of more liquid through the supporting heater, it reaches a size beyond which the flow within it is no longer steady (Dell'Aversana *et al.* 1997). In this case, the oscillatory flow which ensues is, not surprisingly, reminiscent of that seen for unstable thermocapillary convection within liquid bridges.

An additional discussion of the general features of the non-coalescence and non-wetting scenarios described above may be found in a paper by Dell'Aversana & Neitzel (1998). The remainder of this paper will describe some additional quantitative measurements and numerical simulations which have been undertaken and the potential application of such systems.

PRESSURE EFFECTS

Since the phenomena described in the previous section arise because of the existence of a thin, lubricating film of gas separating two free surfaces or a liquid and a solid, a natural question arises as to the minimum pressure necessary in the surrounding gas to sustain the effect. To address this question, we have installed a device for creating a pair of non-coalescing drops within a chamber capable of being evacuated to precisely controlled pressures. The lower drop remains on a fixed pedestal and the upper drop is moved toward it, its vertical position controlled to within 1 μm. The temperatures of the two heaters may be controlled to within 0.01 K and the pressure held constant to within 0.2 mbar.

For these experiments, a fixed volume of silicone oil is deposited on the flat surfaces of the 3 mm diameter copper rods using a micropipette. Allowing the volume to be continuously adjusted by injection of liquid through the top rod (as is done in the tests shown in Figure 1) creates problems with the volume changing as the pressure is decreased.

Droplets were formed using 5 cS silicone oil on each of the copper rods and these were placed in the pressure chamber. With a given temperature difference ΔT between the droplets and a fixed amount of relative displacement (beyond the point of first apparent contact), the pressure was then systematically decreased within the chamber in discrete steps, holding at each pressure level for an adequate time to assure the absence of transient behavior. The pressure at which coalescence occurred was noted and is termed

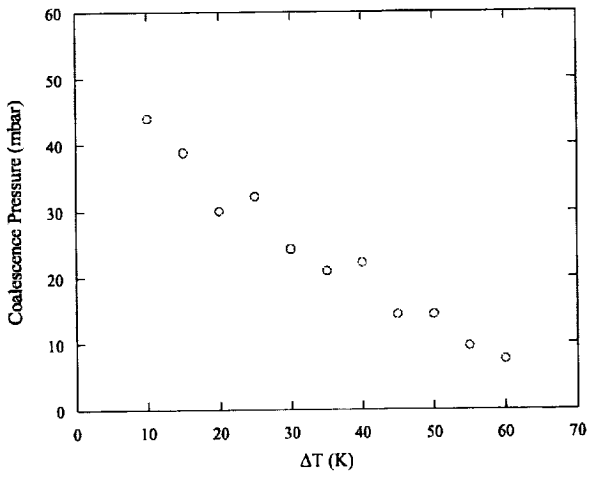

Figure 4: Coalescence pressure versus ΔT for a fixed relative displacement of 150 μm.

the coalescence pressure in the following figures.

The strength of the driving thermocapillary convection in the bulk is clearly a function of the temperature difference between the drops. Consequently, one would intuitively expect that, as ΔT is increased, less surrounding air is necessary to sustain coalescence or, in terms of the pressure, the pressure necessary to prevent coalescence decreases. This expectation is confirmed through the measurements leading to the graph in Figure 4.

Similarly, one's intuition would suggest that the greater the amount of relative displacement (i.e., squeezing) between the drops, the more difficult it would be to prevent coalescence. In terms of coalescence pressure, therefore, this should increase as the relative displacement increases. Figure 5 shows data from experiments for a fixed temperature difference between the drops of 25 K. Similar behavior is observed for other temperature differences.

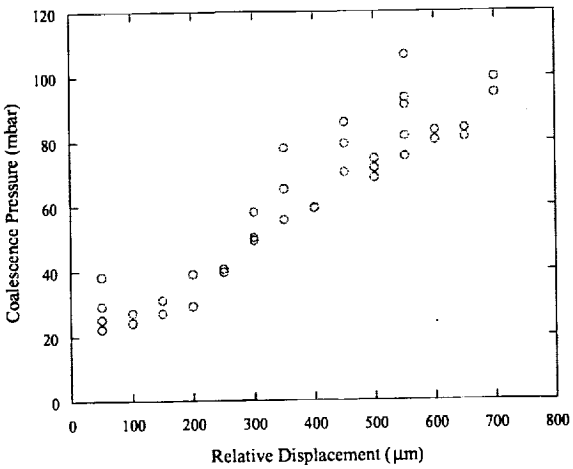

Figure 5: Dependence of coalescence pressure on droplet relative displacement for ΔT = 25 K.

The results of these sealed-chamber experiments confirm the existence of the lubricating air film demonstrated convincingly by experiments employing interferometry. What is perhaps most surprising about these results is the magnitude (or lack thereof) of the ambient pressure needed to suppress coalescence. From Figure 4, we see that if the droplets are differentially heated to a rather large ΔT of 60 K, a surrounding-gas pressure of less than 10 mbar is required to keep them apart.

At these pressures, the mechanism responsible for coalescence of the droplets is no doubt related to the failure of the gas film due to rarefaction effects. While it is the pressure within the film and not in the surrounding atmosphere which supports the load placed on the system, one might begin to estimate the validity of the continuum hypothesis by examining the Knudsen number calculated on the basis of this ambient pressure and a length scale associated with the film itself. From a crude chart of a standard atmosphere, one may estimate that the mean-free path corresponding to an atmospheric pressure of 10 mbar is roughly 3 μm. From the interferometry data of Dell'Aversana *et al.* (1997), one can see that the thickness of the film at the edge of a droplet (pressed against glass) with a relative displacement of 100 μm is roughly 5 μm. Since the ratio of these yields a Knudsen number of $O(1)$, the hypothesis is indeed worthy of further investigation.

NUMERICAL SIMULATIONS

Preliminary numerical simulations of the flow in the lubricating layer between a two-dimensional droplet and a solid surface have been performed under the assumption of a specified free-surface deformation (as determined from interferometry results from the axisymmetric experiments) and an imposed velocity distribution along the free surface.

Figure 6 shows a streamline pattern and isotherms from one such simulation, indicating a maximum pressure attained at the symmetry plane as stated earlier. Current simulation efforts are directed at the solution of the coupled droplet/film problem. This problem is exacerbated by the three-order-of-magnitude (μm → mm) disparity in relevant length scales for the film and the droplet.

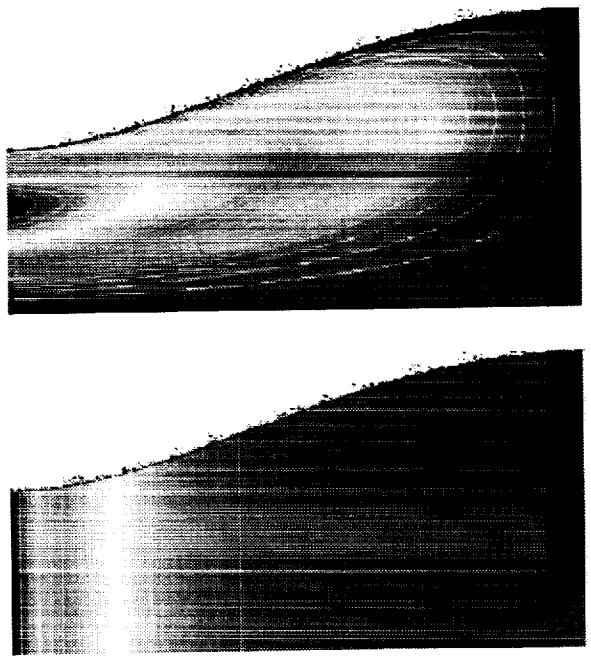

Figure 6: Streamlines (upper) and isobars (lower) for the flow within the lubricating gas film between a liquid drop and a solid wall below it. The right-hand boundary marks the symmetry plane of the calculation.

POTENTIAL APPLICATIONS

The non-coalescence and non-wetting phenomena described above offer some interesting possibilities for applications in either microgravity or terrestrial environments. First, one might think of utilizing such a system to provide a very low-friction bearing in an application in which the loads to be supported are small. We have made measurements of the load that a thermocapillary-driven film can support with a droplet attached to a 3 mm heater pressed against either glass or a cold bath) of the same liquid (roughly 30 K cooler in both cases. The measurements were performed employing a modified platinum-ring tensiometer normally used to conduct surface-tension measurements.

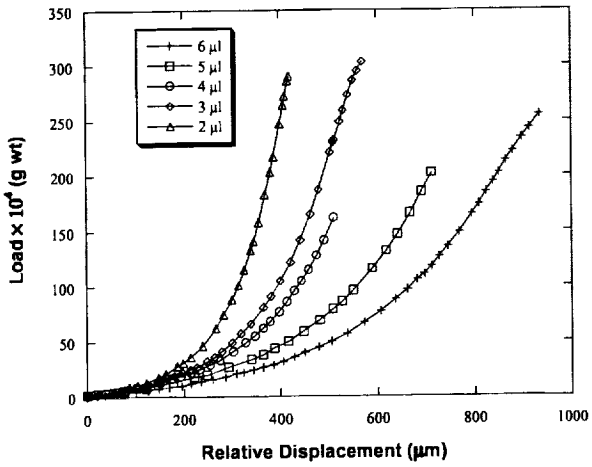

Figure 7: Load versus relative displacement for droplet/glass systems.

Figure 7 above shows some of the results measured for droplets of different volumes when pressed against glass. The results are not scaled, so that a given relative displacement represents a larger fraction of droplet size for smaller droplets. Figure 8 below compares the results for 5 µl droplets pressed against both glass and a cold bath. The load measured for the droplet-bath system is less than that for the droplet-glass with the same relative displacement due to the deformation of the bath surface.

Hence, in a microgravity environment, it may be possible to tailor a non-coalescing bearing system to support a small load or perhaps to position a rotating system precisely. With regard to the latter application, the "bearings" themselves are nearly frictionless and self-centering, so such a system is very desirable. We have also had success (Nalevanko 1997) in achieving non-coalescence with "threads" of liquid rather than discrete drops, so a large range of geometric designs is possible.

As an exercise in the use of non-coalescing liquids to support a load, a small device has been manufactured which is easily floated on a cold bath of liquid.

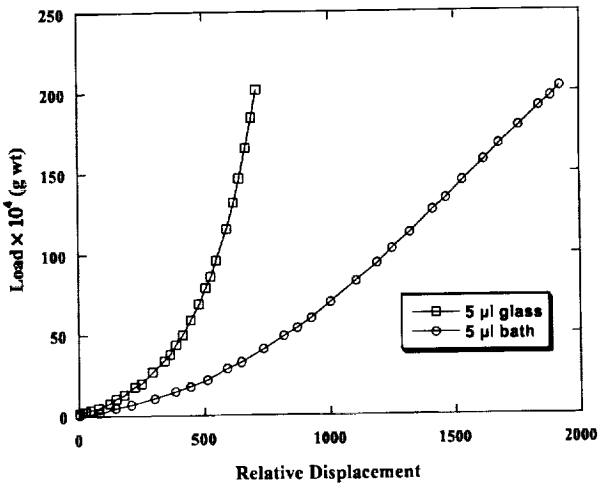

Figure 8: Comparison of loads for droplet-glass and droplet-bath systems.

The device itself is a thin metallic plate containing a number of circular discs to which droplets may be affixed. The total mass of the device with droplets included is approximately 0.2 g. Once the droplets are attached to the discs, the device is inverted, suspended above the cold bath and heated radiantly using a high-intensity light source. When lowered into position, the droplets do not coalesce with the bath but float on thin air films. Placing a magnetized needle on top of this device while it is floating results in a compass which is very sensitive to nearby magnetic fields.

As mentioned in the Introduction, Walker (1978) has made water droplets "float" on the surface of a bath of water through the use of vibration. We have succeeded in repeating these experiments using silicone oils and it is likely that the technique would also be successful with other liquids. The non-coalescence mechanism at work here is the existence of a lubricating film driven by the imposed oscillations. We shall be examining the extension of this work to the use of acoustic forcing to suppress coalescence within a cloud of droplets. The successful demonstration of this could be of benefit in applications in which it is desirable to maintain small droplet size for more efficient droplet combustion.

ACKNOWLEDGMENT

This work was supported by the NASA Microgravity Research Division under grant NAG3-1894.

REFERENCES

Dell'Aversana, P., Banavar, J. R. & Koplik, J. 1996 Suppression of coalescence by shear and temperature gradients. *Phys. Fluids* **8**, 15-28.

Dell'Aversana, P. & Neitzel, G. P. 1998 When liquids stay dry. *Phys. Today* **51**, 38-41.

Dell'Aversana, P., Tontodonato, V. & Carotenuto, L. 1997 Suppression of coalescence and wetting: the shape of the interstitial film. *Phys. Fluids* **9**, 2475-2485.

Nalevanko, J. C. 1997 Design of an apparatus for investigation of 2-D liquid drop non-coalescence. M.S. Thesis, Georgia Institute of Technology.

Napolitano, L., Monti, R. & Russo, G. 1986 Marangoni convection in one- and two-liquids floating zones. *Naturwissenschaft* **73**, 352.

Rayleigh, L. 1899 Investigations in capillarity. *Philos. Mag* **36**, 321.

Walker, J. 1978 Drops of liquid can be made to float on the liquid. What enables them to do so? *Sci. Amer.* **238**, 151-158.

COLLISIONS INTO DUST EXPERIMENT: SCIENCE GOALS AND IMPLEMENTATION

J. E. Colwell[1], M. Taylor[2], L. Lininger[3], B. Arbetter[1],and A. Sikorski[1], [1]Laboratory for Atmospheric and Space Physics, University of Colorado, Boulder CO 80309-0392, USA, [2]STScI, 3700 San Martin Dr., Baltimore MD 21218, USA, [3]Lockheed Martin Missiles and Space, 1111 Lockheed Martin Way, Sunnyvale CA 94089, USA.

ABSTRACT

The Collisions Into Dust Experiment (COLLIDE), is a microgravity experiment flown in a Get Away Special Canister (GASCAN) on board the orbiter Columbia in STS-90, launched April 17, 1998. The experiment is designed to provide the first data on the release of dust from the surfaces of small solar system bodies, such as planetary ring particles, in low-energy collisions. Here we discuss the scientific issues that are addressed by COLLIDE, its implementation, and expected results.

BACKGROUND

Dust is ubiquitous in the solar system. Surfaces of asteroids, planetary satellites and planetary ring particles are coated with dust generated by the hypervelocity bombardment of micrometeoroids. In planetary rings and in the early stages of planetesimal accretion in the protoplanetary nebula, interparticle collisions occur at low relative velocities. Planetary ring particles are on nearly circular orbits with low inclinations, and collision velocities are set by Keplerian shear and small perturbations in orbits induced by nearby moons. This results in collision velocities on the order of 1 cm/s.

The dust released by these interparticle collisions has been observed by the Voyager 1 and 2 spacecrafts in the ring systems of each of the giant planets. In some planetary ring systems, and in some circumstellar disks, only the dust component of the particle size distribution is observable. High phase angle Voyager 2 images of the Uranian and Neptunian ring systems revealed both broad and narrow dust rings with lifetimes less than 100 years (Smith et al. 1986, 1989, Broadfoot et al. 1986). To sustain the dust rings to the present epoch, there must be a continuous supply of dust from micrometeoroid bombardment of so-called "parent bodies" - larger ring particles which are not observable due to their low optical depth. These parent bodies also release dust in mutual collisions which typically occur at speeds much less than 1 m/s (Colwell and Esposito 1990a). The dust thus acts as a tracer of the more massive particles in the disk. Understanding the collisional release of dust in low energy collisions is therefore necessary to link dust observations to the large particle dynamics. The partitioning of energy in low energy collisions between dust-covered low-surface-gravity particles will influence the dynamical evolution of these collisionally evolved systems, and whether collisions are accretional or erosional. This has important implications for the early stages of planetesimal accretion.

Planetary ring particles range in size from submicron to several km. The bulk of the mass and surface area of Saturn's optically thick rings is made up of particles smaller than a few meters in radius (e.g. Esposito et al. 1984). The particles in these rings suffer collisions on the short orbital time scale of several hours. The amount of dust released in these collisions and the velocity distribution of the dust is unknown, however. These parameters are crucial to our understanding of planetary rings (e.g. Weidenschilling 1984). The size and velocity distributions of the macroscopic ring particles have been inferred from the dust optical depth (Colwell and Esposito 1990a, 1990b). However, these inferences were based on extrapolations of impact experiments from the km/sec velocity range to the cm/sec velocity range, and further data is needed to determine the validity of these extrapolations.

The accretion of the planets proceeded from coagulation of dust grains in the solar nebula to the binary collisional accretion of km-sized planetesimals. Van der Waals forces between dust grains are sufficient to account for growth of cm-sized aggregates in a nebula with up to a moderate level of turbulence (Weidenschilling 1980). Bodies meter-sized and larger decouple from the nebular gas, and consequently have relative velocities low enough to allow for further collisional growth. The details of the growth process in the critical centimeter-to-meter range are not known, and depend greatly on the efficiency of mass loss during collisions. These collisions likely occurred at relative velocities of 1-100 cm/sec for either a laminar or turbulent nebula (Weidenschilling 1993). Velocities in this range are significantly higher than escape velocities for centimeter-to-meter size particles, and so collisions must have been highly inelastic in order for growth to proceed. Dusty regoliths covering particles may have helped to dissipate collisional energy, reducing the rate of mass loss during collisions and promoting accretional growth of larger bodies. If not, collisional growth alone may be insufficient to account for the formation of km-sized planetresimals, and a disk layer dense and quiescent enough to allow for gravitational instability might have been required.

The Collisions Into Dust Experiment (COLLIDE) is the first microgravity experiment to study the partitioning of energy into dust ejecta in very low velocity impacts. Although not exactly duplicating the conditions that exist in a collision between planetary ring particles or planetesimals, COLLIDE will provide the

first experimental information on the amount, speed, and direction of dust particles ejected from a deep regolith when impacted at low velocities. This data will make a natural extension of the existing set of ground-based laboratory data on high velocity impacts into powders (e.g. Stoffler et al. 1975, Hartmann 1985, Yamamoto and Nakamura 1997).

EXPERIMENTAL APPROACH

The data obtained by COLLIDE can only be obtained in a microgravity environment. The energy imparted to the target regolith in the low-velocity impacts studied here is insufficient to overcome Earth's gravity and allow ejecta properties such as velocity distributions to be measured. Because of the relatively long time scale for the slowest impacts, extended periods of microgravity are necessary. The time for each impact experiment in COLLIDE ranges from 30 s to 180 s, and the total duration of the experiment is 27 minutes. The Get Away Special program provides extended periods of microgravity for completely self-contained payloads in the Space Shuttle Orbiter payload bay. COLLIDE is a Get Away Special payload for the Space Shuttle (STS) and had its first flight on STS-90, launched April 17, 1998, landed May 3, 1998.

The experiment consists of six independent impactor box systems (IBS, Figure 1) to allow six different sets of impact parameters to be used during one flight (Table 1). Each IBS is self-contained, with a target tray of simulated planetary regolith (JSC-1, a powdered basalt, passed through a #60 sieve). Because the ejecta is dispersed by the impact, each IBS can be used only once per flight.

Table 1. COLLIDE Impact Parameters

IBS	Velocity (cm/s)	Impactor Radius (cm)	Dust Depth (cm)
1	100.0	.95	1.9
2	1.05	.48	0.95
3	1.05	.48	1.9
4	21.5	.48	1.9
5	4.64	.48	1.9
6	100.0	.48	1.9

COLLIDE was designed and built primarily by students at the Laboratory for Atmospheric and Space Physics at the University of Colorado. The time from initial design to flight was less than 2 years. The experiment is powered by 18 alkaline D cells. Each impact takes place in sequence to minimize power draw and prevent vibrations from one experiment interfering with another. The Get Away Special canister was evacuated and sealed prior to launch at a pressure of approximately 0.1 torr to minimize gas-particle interactions between the ejecta and the ambient atmosphere. Two camcorders were in separate, sealed containers with air to pevent outgassing of lubricants. Each camcorder views three IBS's with a line of sight parallel to the plane of the target surface. Each IBS has a transparent top made of two layers of polycarbonate to allow data recording by the video camcorder at the opposite end of the experiment. Each IBS also includes a planar mirror mounted on the bottom to provide the camcorder a normal view of the impact on the surface of the JSC-1. This will allow a measurement of the crater diameter and the duration of crater formation (Figure 2).

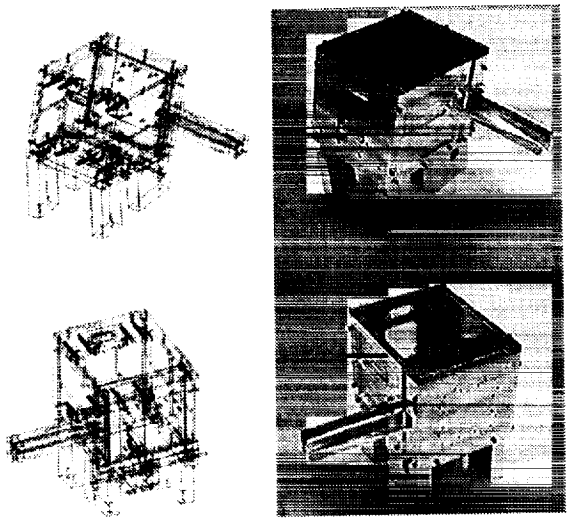

Figure 1. CAD drawings and prototype models of a COLLIDE IBS, showing the door guide, target tray, and polycarbonate top for video recording of the impact experiment.

The target JSC-1 powder is held in place by a door until the experiment runs, and the door slides open under operation by a digital linear stepper motor. The teflon sphere projectiles are launched by springs designed to provide impact speeds between 1 and 100 cm/s. The projectiles are held in place by a spring-loaded door which is released by actuating a shape memory alloy circuit to fire the projectile (Figure 3). The operation of each IBS, including the stepper motors, LEDs, and launcher is controlled by an Intel 80C51GB microcontroller. The microcontroller also turns on the camcorders and signals them to start and stop recording. The flight-ready experiment is shown in Figure 4.

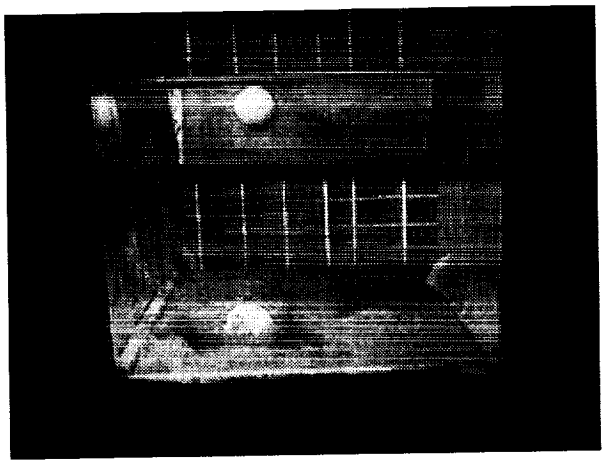

Figure 2. A ground-based test illustrating the type of view that the COLLIDE camcorders will have of each impact. The projectile is seen twice – once directly and once in an angled mirror to provide a view of the impact parallel to the projectile direction of motion. Illumination is from the top with red high-intensity LEDs.

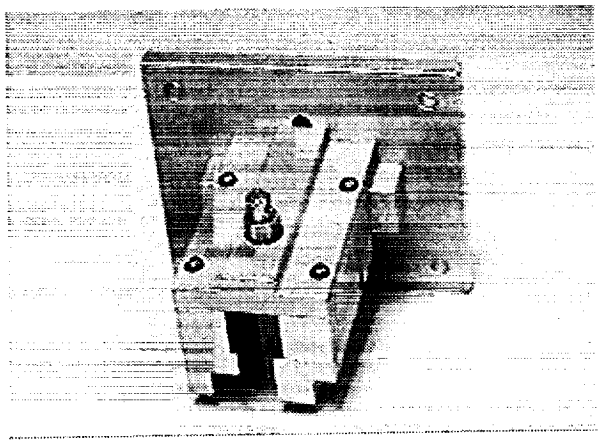

Figure 3. The launcher mechanism. The spring-loaded plunger visible on top of the launcher holds a spring-loaded plastic lever in place which in turn holds the projectile in place against a spring designed to provide the desired impact velocity. The launcher is designed to allow multiple projectile sizes with a minimum of changes to the parts. The plunger is pulled by a shape memory alloy circuit which contracts when heated by an electrical current.

The ensemble of many impact experiments will allow us to express fundamental quantities, such as ejecta mass, as a function of non-dimensional scaling parameters. These will then be compared to the existing set of data on high-energy impacts from ground-based experiments.

A baroswitch which activated on ascent of STS-90 through 50,000 feet closed the COLLIDE power circuit. This began a 24 hour timing circuit in COLLIDE, and the first impact was scheduled to occur 24 hours after launch. Astronaut initiation of the experiment occurred at 27.9 hours after launch, after the nominal end of the built-in timer.

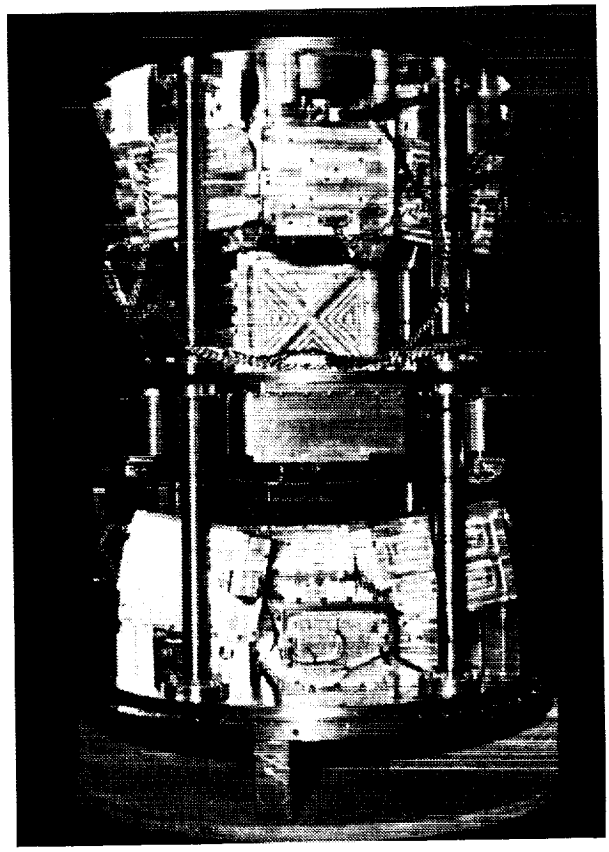

Figure 4. COLLIDE just prior to integration in the flight canister at the Kennedy Space Center for flight on STS-90.

EXPECTED RESULTS

The data consist of videotape records of each impact taken by consumer grade digital video camcorders. Illumination is provided by 20 high-intensity light emitting diodes in each IBS, mounted on the wall opposite the target tray, and fiduciary marks on the bottom of each IBS provide reference for later data analysis of ejecta trajectories. Because each camcorder simultaneously images three IBS's, the resolution is too low to track individual dust particles. The CCDs on each camcorder have a total of 570,000 pixels. Each IBS will fill approximately one sixth of the total camera field of view and the projected dimension of a pixel at the distance of impact is approximately 0.05

cm. The frame rate of the camcorder is 30 frames per second. The fastest projectile in COLLIDE (1 m/s) was chosen to allow an accurate speed determination from analysis of the tape at that frame rate.

The camcorder makes digital videotape recordings which will be loaded directly onto a computer for frame by frame analysis. The basic quantities that will be determined from analysis of the videotapes will include: (1) exact speed of the projectile, (2) mean speed of the ejecta, (3) spatial and angular distribution of ejecta trajectories, (4) transient crater diameter and time of crater formation, and (5) total ejected mass. These results will guide further experimental studies of low energy impacts into dust, and also numerical simulations of granular media. COLLIDE will provide points of calibration for both numerical simulations of low velocity impacts in a low gravity environment, and also analytical models of the partitioning of energy in such impacts.

REFERENCES

Broadfoot, A. L., et al., Ultraviolet Spectrometer Observations of Uranus, Science, 233, 74-79 (1986).

Colwell, J. E., and L. W. Esposito, A Numerical Model of the Uranian Dust Rings, Icarus, 86, 530-560 (1990a).

Colwell, J. E., and L. W. Esposito, A Model of Dust Production in the Neptune Ring System, Geophys. Res. Lett., 17, 1741-1744 (1990b).

Esposito, L. W., J. N. Cuzzi, J. B. Holberg, E. A. Marouf, G. L. Tyler, and C. C. Porco, Saturn's Rings: Structure, Dynamics, and Particle Properties, in Saturn, (T. Gehrels and M. S. Matthews, eds.), pp. 463-545, Univ. of Arizona Press, Tucson (1984).

Hartmann, W. K. Impact Experiments, Icarus, 63, 69-98 (1985).

Stoffler, D., D. E. Gault, J. Wedekind, and G. Polkowski, Experimental Hypervelocity Impact into Quartz Sand: Distribution and Shock Metamorphism of Ejecta, J. Geophys. Res., 80, 4062-4077 (1975).

Smith, B. A., et al., Voyager 2 in the Uranian System: Imaging Science Results, Science, 233, 43-64 (1986).

Smith, B. A., et al., Voyager 2 at Neptune: Imaging Science Results, Science, 246, 1422-1449 (1989).

Weidenschilling, S. J., Dust to planetesimals: Settling and coagulation in the solar nebula, Icarus 44, 172-189 (1980).

Weidenschilling, S. J., C. R. Chapman, D. R. Davis, and R. Greenberg, Ring Particles: Collisional Interactions and Physical Nature, in Planetary Rings (R. Greenberg and A. Brahic, eds.), pp. 367-416, University of Arizona Press, Tucson (1984).

Weidenschilling, S. J., and J.N. Cuzzi, Formation of Planetesimals in the Solar Nebula, in Protostars and Planets III, (E. H. Levy and J. I. Lunine, eds.), pp. 1031-1060, University of Arizona Press, Tucson (1993).

Yamamoto, S., and A. M. Nakamura, Velocity Measurements of Impact Ejecta from Regolith Targets, Icarus, 128, 160-170 (1997).

WEAKLY NONLINEAR DESCRIPTION OF PARAMETRIC INSTABILITIES IN VIBRATING FLOWS

E. Knobloch, Department of Physics, University of California, Berkeley CA 94720, USA, knobloch@physics.berkeley.edu, J. M. Vega, E.T.S.I. Aeronauticos, Universidad Politecnica de Madrid, 28040 Madrid, Spain, vega@fmetsia.upm.es

Introduction

This project focuses on the effects of weak dissipation on vibrational flows in migrogravity and in particular on (a) the generation of mean flows through viscous effects and their reaction on the flows themselves, and (b) the effects of finite group velocity and dispersion on the resulting dynamics in large domains. The basic mechanism responsible for the generation of such flows is nonlinear and was identified by Schlichting [21] and Longuet-Higgins [14]. However, only recently has it become possible to describe such flows self-consistently in terms of amplitude equations for the parametrically excited waves coupled to a mean flow equation. The derivation of these equations is nontrivial because the limit of zero viscosity is singular. This project focuses on various aspects of this singular problem (i.e., the limit $C \equiv \nu(gh^3)^{-1/2} \ll 1$, where ν is the kinematic viscosity and h is the liquid depth) in the weakly nonlinear regime. A number of distinct cases is identified depending on the values of the Bond number, the size of the nonlinear terms, distance above threshold and the length scales of interest. The theory provides a *quantitative* explanation of a number of experiments on the vibration modes of liquid bridges and related experiments on parametric excitation of capillary waves in containers of both small and large aspect ratio. The following is a summary of results obtained thus far.

Surface-wave damping in a brimful circular cylinder [19]

Henderson and Miles [6] discovered a substantial discrepancy between the measured decay rate of free oscillations of a brimful circular cylinder and theoretical predictions based on leading order asymptotics in powers of $C^{1/2}, C = \nu(gR^3)^{-1/2}$, where R is the radius of the cylinder. At the same time they found good agreement between the measured and predicted frequencies. The resolution of this discrepancy follows from the observation by Higuera et al [7] and Martel and Knobloch [17] that under typical conditions the $\mathcal{O}(C)$ term in the expansion of the damping rates $\mathrm{Re}(s)$ of capillary and gravity-capillary waves is comparable to the leading order term.

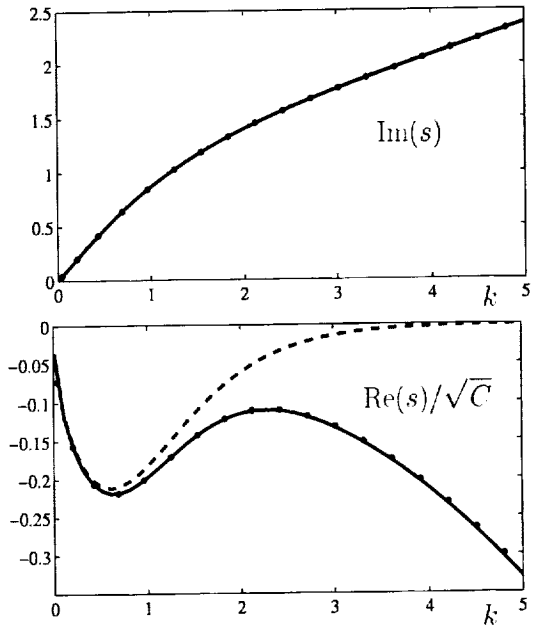

Figure 1: The gravity-capillary modes for $k = \mathcal{O}(1)$. The dots indicate the exact solution; asymptotic results through $\mathcal{O}(C^{1/2})$ and $\mathcal{O}(C)$ are indicated by dashed and solid lines, respectively.

This is so despite the fact that C is typically small, $C \approx 10^{-4}$. Fig. 1 shows what happens in a horizontally infinite layer of depth h [17]. The figure shows the decay rate $\mathrm{Re}(s)$ and frequency $\mathrm{Im}(s)$ as a function of the wavenumber k, nondimensionalized using h^{-1}, for the parameter values used in [6] : $B \equiv \rho g h^2/\sigma = 1.96\ 10^2$ and $C \equiv \nu(gh^3)^{-1/2} = 0.43\ 10^{-4}$. Here σ is the surface tension.

In a cylinder the corresponding calculations are more involved because of viscous boundary layers at the sidewall and the presence of a contact line. We find

$$\mathrm{Re}(s) = C^{1/2}\omega_1 + C\omega_2 + \mathcal{O}(C^{3/2}), \quad (1)$$

$$\mathrm{Im}(s) = \omega_0 - C^{1/2}\omega_1 + \mathcal{O}(C^{3/2}), \quad (2)$$

where the $\mathcal{O}(C^{1/2})$ terms come from viscous dissipation in the oscillatory Stokes boundary layers near the solid wall and bottom of the cylinder, and the $\mathcal{O}(C)$

terms come from (a) viscous disipation in the bulk and (b) a first correction to the viscous dissipation in the Stokes boundary layers. The neglected $\mathcal{O}(C^{3/2})$ includes viscous dissipation in the oscillatory boundary layer at the free surface. We find that ω_2/ω_1 for typical Bond numbers $B = \rho g R^2/\sigma$ and aspect ratios $\Lambda = h/R$ is quite large even for the fundamental mode and increases with the mode number. As a result the $\mathcal{O}(C)$ term in s is important and its omission leads to errors that increase with the mode number, as found in [6]. The absence of this term in ω implies that the leading order approximation for the frequencies is much better than the corresponding approximation for the damping rates. The computation of the $\mathcal{O}(C)$ terms requires care because of a singularity in the expansion at the (pinned) contact line. The theoretical damping rates (1) are compared with measured rates in Table 1, and demonstrate a substantial improvement over the $\mathcal{O}(C^{1/2})$ results of [6].

The brimful cylinder is ideal for understanding the effects of dissipation in boundary layers because the meniscus is pinned to the brim, thereby eliminating unknown effects arising from the dynamics of the meniscus. In addition the absence of corners in the container makes the boundary layer structure uniform and relatively simple. The damping rate calculation lends us confidence that we have correctly identified the major source of discrepancy between existing theory and experiment and that we know how to correct the theory, at least in cases in which surface contamination and contact angle dynamics can be ignored. It follows that (the bulk of the) dissipation in clean-surface experiments is accounted for by the classical Navier-Stokes formulation and is not due to unknown dissipation mechanisms in the meniscus or air-water interface. In particular any residual discrepancy between theory and experiment can now be used as a diagnostic for the presence of contamination. This fact has triggered a new experimental effort to measure damping rates of gravity-capillary waves in finite domains by M. Schatz (private communication). In addition the calculation forms the basis for future nonlinear studies of gravity-capillary waves in cylinders and their interactions.

	Experiment		Approximation		Theory	
(m,q)	f	Δ	f_1	Δ_1	f_2	Δ_2
$(1,0)$	4.65	1.4	4.66	1.13	4.67	1.37
$(2,0)$	6.32	1.8	6.32	1.24	6.34	1.75
$(0,1)$	6.84	1.2	6.73	0.44	6.85	0.95
$(3,0)$	7.80	2.2	7.79	1.29	7.82	2.11
$(1,1)$	8.57	1.5	8.57	0.48	8.59	1.45
$(4,0)$	9.26	2.4	9.24	1.32	9.27	2.47

Table 1: Comparison between theory and the experiment [6]. Here f_j is the dimensional frequency (in Hz) to $\mathcal{O}(C^{1/2})$ $(j = 1)$, to $\mathcal{O}(C)$ $(j = 2)$, with Δ_j the corresponding nondimensional damping rates. m and q are the azimuthal and radial wavenumbers, respectively. After [19].

Chaotic oscillations in a nearly inviscid axisymmetric capillary bridge at $2:1$ resonance [16]

This paper considers a liquid bridge in microgravity supported between two disks vibrating at two frequencies close to $2:1$ resonance. Under appropriate conditions this vibration excites the corresponding natural vibration modes (assumed axisymmetric) and these interact nonlinearly. In the nearly inviscid limit $C \ll 1$ this interaction is described by a pair of amplitude equations whose structure depends on the parity of the excited modes. Specifically, if the displacement of the disks follows $z = \pm\Lambda + h_\pm(t)$, where

$$h_\pm(t) = \mu[\beta_1^\pm \exp(i(\Omega_1+\delta\omega_1)t) + \beta_2^\pm \exp(i(\Omega_2+\delta\omega_2)t)],$$

$\mu \ll 1$, $\Omega_2 = 2\Omega_1$, then the equations for the evolution of the amplitudes of the two competing modes take the form $(k = 1, 2)$

$$\begin{aligned} \epsilon\delta A_{k\tau} &= -[(1+i)\alpha_{4k}\sqrt{C} + \alpha_{5k}C - i\alpha_{3k}\ell\delta]\epsilon A_k \\ &+ i\alpha_{2k}\epsilon^2 N_k + i\mu(\alpha_{1k}^+\beta_k^+ - \alpha_{1k}^-\beta_k^-) + \cdots (3) \end{aligned}$$

Here $\tau = \delta t$, $\Lambda = \Lambda_0 + \delta\ell$, $\delta \ll 1$, $\beta_k^\pm, \omega_k, \ell = \mathcal{O}(1)$ and if the mode A_2 is even in z, $N_1 = A_2\bar{A}_1$, $N_2 = A_1^2$. This occurs at $\Lambda_0 \approx 0.249$ and $\Lambda_0 \approx 2.23$. At each of these values two natural oscillation modes with frequencies in $2:1$ ratio are present; it is these modes that are driven by the vibration of the two disks. Finally ϵ measures the amplitude of the two modes. On the other hand, if A_2 is odd in z the nonlinearities are of third order, and $N_k = i\epsilon(\alpha_{2k1}|A_1|^2 + \alpha_{2k2}|A_2|^2)A_k$, $k = 1, 2$.

All the coefficients appearing in Eqs. (3) have been computed from the equations of motion, including the important (but formally subdominant) terms α_{5k}. These calculations require the computation of the contributions from the Stokes boundary layers at the disks, the interface boundary layer, the two corner tori near the edge of the disks and from the bulk. Because of the assumption $C \ll 1$ all nonlinear terms are purely imaginary. The presence of the inhomogeneous terms in

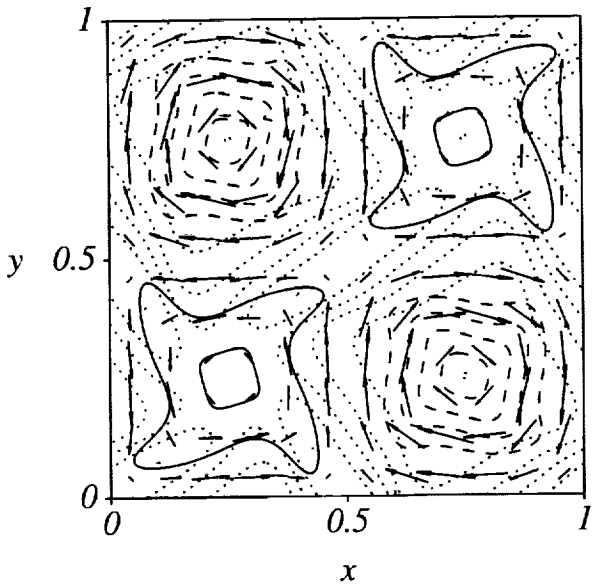

Figure 2: Contour plot of the non-oscillatory components of the film thickness (dotted), vorticity Ω (solid for $\Omega > 0$, dashed for $\Omega < 0$) and velocity arrows for an ordered state. From [25].

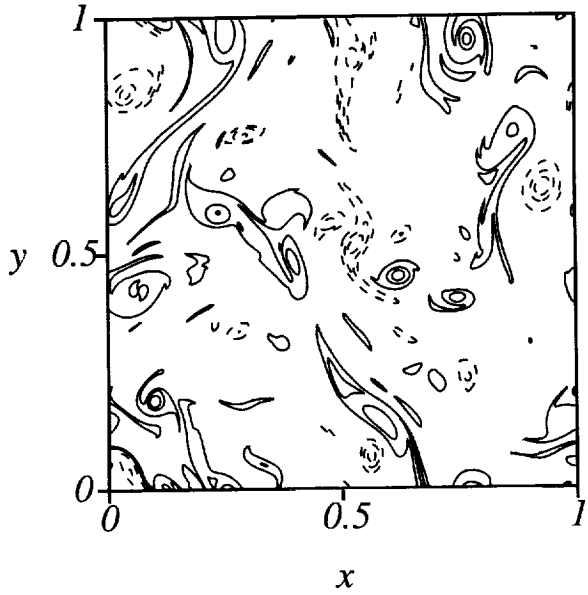

Figure 3: Vorticity contours for a spatially disordered state. From [25].

Eqs. (3) implies that new phenomena are present that are not captured by standard treatments of the $2:1$ resonance [12, 9]. Both cases have been analysed, and the results used to make a number of predictions about the sub- and superharmonic response of a liquid bridge subjected to this type of excitation under experimentally relevant conditions. The ensuing chaotic oscillations have beed studied numerically and characterized using numerically determined Liapunov exponents.

Quasi-steady vortical structures in vertically vibrating soap films [25]

In a recent paper Afenchenko et al [1] describe the results of an experimental study of flows in vertically vibrated soap films; in this experiment the frame holding the film was rigidly and symmetrically attached to the lateral wall of a closed cavity, which was vibrated vertically. These vortical structures (first reported by Taylor [24]) are similar to ones described by Airiau [2], who excited the film using a loudspeaker fitted to the bottom of the cavity, which was otherwise open. We have examined in detail the possible mechanisms that could lead to the generation of such flows, with special emphasis on those effects that are independent of the shape of the frame supporting the film, of the attachment mode (i.e., the size of the meniscus), and of the excitation process. Thus we focus on those effects that are present in any experiment, e.g., in [1, 2]. In this theory the observed vortical structures are a consequence of the oscillatory tangential and normal stresses on the film due to the surrounding air. The air also damps out Marangoni waves. Because of nonlinearities these stresses (and the inertia of the film) produce non-oscillatory deflection of the the film, variation in its thickness, and forcing terms that combine to produce a streaming flow in the film. Coupled evolution equations for these quantities are derived. When the excitation frequency is close to an eigenfrequency of a Marangoni mode of the soap film, the dominant forcing in these equations arises from the nonlinear hydrodynamics within the film volume, while both volume forcing and surface forcing by air are important when there is no resonance with a Marangoni mode. The computed vortex patterns (see Figs. 2,3) agree qualitatively with the experiments.

Compressional modes in parametrically driven Faraday waves in an annulus [18]

Experiments by Douady et al [4] on parametrically driven water waves in an annulus ($C = 4.4\ 10^{-4}$, $B = 8.9$) reveal the presence of a secondary instability of a uniform pattern of standing waves (SW) in the form of an oscillatory *compression* mode (CM). We develop a theory describing this observation based on

(suitably modified) nonlocal amplitude equations for the subharmonic response of the system of the type derived by Knobloch and De Luca [10] for traveling wave convection and Alvarez-Pereira and Vega [3] for pulsating flames, with the nonlinear coefficients deduced from Hansen and Alstrom [5]:

$$A_t = (-1+i\nu)A + \mu\langle\bar{B}\rangle + iA(\beta|A|^2 + \gamma\langle|B|^2\rangle) + i\alpha A_{xx} \tag{4}$$

$$B_t = (-1+i\nu)B + \mu\langle\bar{A}\rangle + iB(\beta|B|^2 + \gamma\langle|A|^2\rangle) + i\alpha B_{xx}, \tag{5}$$

subject to the periodic boundary conditions $A(x+1,t) = A(x,t)$, $B(x+1,t) = B(x,t)$. Here $\langle\cdots\rangle$ represents a spatial average over $0 \le x < 1$. These equations describe the slow temporal evolution of the amplitudes of left-(A) and right-traveling (B) waves in their comoving frames, and provide an asymptotic description of the system sufficiently close to threshold of the Faraday instability that the envelope dynamics are dominated by advection at the group velocity of the waves. A description of this type is appropriate in the weak dissipation limit in which the natural modes of the unforced system, left and right-traveling waves, decay slowly. For this reason the coefficients of the cubic terms are purely imaginary. In the first instance we ignore the presence of viscosity-generated mean flows and study the resulting nonlocal equations. Within this description the onset of the compression mode is described as a secondary pitchfork bifurcation from SW with eigenvector that breaks the SW reflection symmetry. We show that such CM are described by steady but nonuniform solutions of the nonlocal equations with periodic boundary conditions (appropriate to an annular cell) and are present for experimental parameter values. We explore the transition from this mode and identify consecutive bifurcations to nonsteady but uniform states, and to states with complex spatio-temporal dynamics (Fig. 4), some of which are strongly hysteretic. Future work will include viscosity-driven mean flows with self-consistent coupling to the amplitude equations and explore the dynamics of the resulting system of equations. Such mean flows are present not only in large aspect ratio annuli but also in smaller systems, and hence are relevant to the experiments.

A related investigation of the corresponding problem with exact or broken D_4 symmetry is under way, motivated by the Faraday problem in a square or nearly square container. In a container with exact square symmetry two modes related by a 90° rotation are exactly degenerate; this degeneracy is broken if the container is slightly rectangular. Simonelli and Gollub [22] found

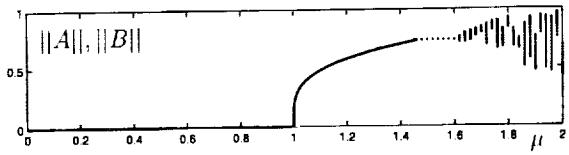

Figure 4: Stable solutions of Eqs. (4,5) for $\nu = 0$, $\beta = 3$, $\gamma = -1$, $\alpha = 0.1$, showing SW ($0 < \mu < 1.46$), CM ($1.46 < \mu < 1.62$) and complex states ($\mu > 1.62$).

no time-dependent dynamics associated with the resulting mode interaction in a square domain. However in a slightly rectangular container they observed periodic and chaotic bursts very close to onset. The real parts of the necessary cubic coefficients are being calculated to leading order in $\mathcal{O}(C)$ together with the mean flows generated in these two geometries. A self-consistent inclusion of such flows offers the possibility of providing the first quantitative description of this interesting behavior. An explanation along the lines described in the next section for the presence of bursts is anticipated.

Bursts [15]

Under appropriate conditions the competition between nearly degenerate Hopf modes with odd and even parity results in dramatic bursting behavior very near the onset of primary instability. This behavior arises in two-dimensional systems of large but finite aspect ratio undergoing an oscillatory instability, or in systems with nearly square symmetry, as discussed by Landsberg and Knobloch [13]. In both cases it is due to the same mechanism.

In a slender system with left-right reflection symmetry (such as a narrow rectangular convection cell) undergoing an oscillatory instability from the trivial state the first two unstable modes typically have opposite parity under reflection. Moreover, because the neutral stability curve for the unbounded system has a parabolic minimum these set in in close succession as the control parameter is increased. We write the perturbation from the trivial state as

$$\Psi(x,y,t) = \epsilon^{\frac{1}{2}}\,\mathrm{Re}\,\{z_+ f_+(x,y) + z_- f_-(x,y)\} + \mathcal{O}(\epsilon),$$

where $\epsilon \ll 1$, $f_\pm(-x,y) = \pm f_\pm(x,y)$, and y denotes the transverse variables. The complex amplitudes $z_\pm(t)$ then satisfy the equations [13]

$$\begin{aligned} \dot{z}_\pm &= [\lambda \pm \Delta\lambda + i(\omega \pm \Delta\omega)]z_\pm + A(|z_+|^2 + |z_-|^2)z_\pm \\ &\quad + B|z_\pm|^2 z_\pm + C\bar{z}_\pm z_\mp^2. \end{aligned} \tag{6}$$

In these equations the nonlinear terms have identical (complex) coefficients because of an approximate *interchange* symmetry between the odd and even modes. The resulting D_4 symmetry [13] is weakly broken whenever $\Delta\lambda \neq 0$ and/or $\Delta\omega \neq 0$, a consequence of the finite aspect ratio of the system. The dynamics in systems with exact D_4 symmetry ($\Delta\lambda = \Delta\omega = 0$) can be shown to take place on a two-dimensional manifold [23] and hence are necessarily simple although the solutions can become unbounded. This is no longer so when the D_4 symmetry is broken. In this case the solutions can experience repeated episodes of dramatic growth followed by collapse but do not become unbounded. The resulting bursts can be periodic or chaotic and set in at a secondary instability very close to onset. To identify such bursts we write

$$z_\pm = \rho^{-\frac{1}{2}} \sin(\frac{\theta}{2} + \frac{\pi}{4} \pm \frac{\pi}{4})\, e^{i(\pm\phi+\psi)/2}$$

and introduce a new time-like variable τ defined by $d\tau/dt = \rho^{-1}$. In terms of these variables Eqs. (6) become

$$\frac{d\rho}{d\tau} = -\rho[2A_R + B_R(1+\cos^2\theta) + C_R \sin^2\theta \cos 2\phi] - 2(\lambda + \Delta\lambda\cos\theta)\rho^2 \quad (7)$$

$$\frac{d\theta}{d\tau} = \sin\theta[\cos\theta(-B_R + C_R\cos 2\phi) - C_I \sin 2\phi] - 2\Delta\lambda\,\rho\sin\theta \quad (8)$$

$$\frac{d\phi}{d\tau} = \cos\theta(B_I - C_I\cos 2\phi) - C_R \sin 2\phi + 2\Delta\omega\,\rho, \quad (9)$$

where $A = A_R + iA_I$, etc., together with a decoupled equation for $\psi(t)$. The amplitude of the disturbance is measured by $r \equiv |z_+|^2 + |z_-|^2 = \rho^{-1}$; thus $\rho = 0$ corresponds to infinite amplitude states. Eqs (7-9) show that the restriction to the invariant subspace $\Sigma \equiv \{\rho = 0\}$ is equivalent to taking $\Delta\lambda = \Delta\omega = 0$ in (8,9). The fixed points of the resulting D_4-symmetric problem correspond to (infinite amplitude) periodic oscillations in time because of the decoupled phase $\psi(t)$. Depending on A, B and C the subspace Σ may contain additional fixed points and/or limit cycles [23]. In our scenario, a burst occurs for $\lambda > 0$ when a trajectory follows the stable manifold of a fixed point (or a limit cycle) $P_1 \in \Sigma$ that is *unstable* within Σ. The instability within Σ then kicks the trajectory towards another fixed point (or limit cycle) $P_2 \in \Sigma$. If this point has an unstable ρ eigenvalue the trajectory escapes from Σ towards a $\rho > 0$ fixed point (or limit cycle), forming a burst. If $\Delta\lambda$ and/or $\Delta\omega \neq 0$ this fixed point may itself be unstable to perturbations of type P_1 and the process then repeats. The scenario thus requires that at least one of the branches in the D_4-symmetric system be subcritical (P_1) and one supercritical (P_2).

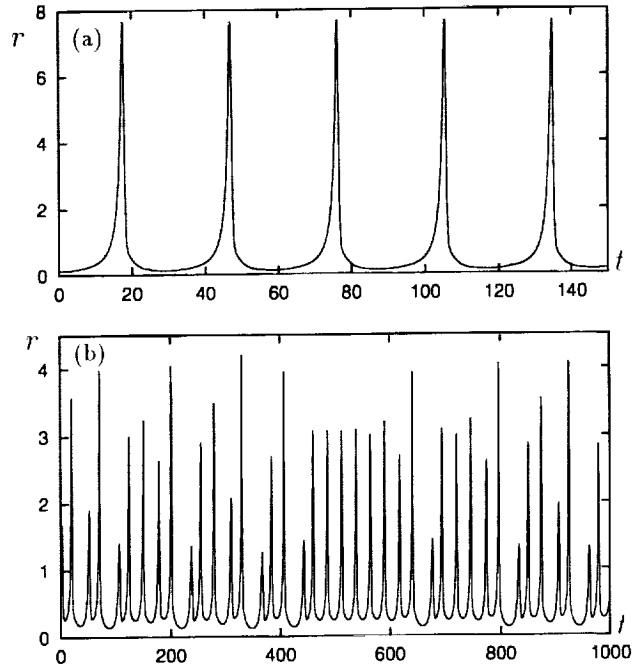

Figure 5: Bursts arising from periodic and chaotic rotations. (a) $\lambda = 0.1$ and (b) $\lambda = 0.072$. The coefficients are $\Delta\lambda = 0.03$, $\Delta\omega = 0.02$, $A = 1 - 1.5i$, $B = -2.8 + 5i$, $C = 1 + i$.

When $\Delta\lambda$ and/or $\Delta\omega \neq 0$ two types of oscillations in (θ, ϕ) are possible: rotations and librations. These oscillations are coupled to excursions in amplitude. Fig. 5 shows a typical sequence of large amplitude bursts arising from repeated excursions towards the infinite amplitude ($\rho = 0$) solutions. The amplitude of these events decreases with increasing $\Delta\lambda$ and their frequency increases, much as found in several experiments. The mechanism outlined here arises naturally in systems with reflection symmetry and appears to be responsible for the regular and irregular bursting exhibited by such systems very close to onset of a primary oscillatory instability.

Dynamics of parametrically modulated dissipative systems in an annulus [11]

Dynamics of parametrically modulated dissipative systems undergoing a symmetry-breaking Hopf bifurcation on a line are explored in full generality, with particular emphasis on the case in which either standing waves or travelling waves are subcritical [20]. The spatially uni-

form states satisfy equations of the form (cf. Eqs. (4,5))

$$\dot{A} = aA + b\bar{B} + c|A|^2A + d|B|^2A \quad (10)$$

$$\dot{B} = aB + b\bar{A} + c|B|^2B + d|A|^2B. \quad (11)$$

Here a, c and d are complex while b may be taken to be positive. In contrast to Eqs. (4,5) we assume that $\mathrm{Re}(a)$ can pass through zero leading to a spontaneous oscillatory instability, and study the effect of parametric modulation ($b > 0$) on these oscillations. In closely related equations (see Eqs. (6)) bursts occur when one of the branches is subcritical (cf. [8]). We have identified the possible dynamical regimes involving spatially uniform states. These include standing waves and non-symmetric mixed modes phase-locked to the drive and interactions between them. The effects of group velocity and dispersion on the stability properties of the spatially uniform states identified above are being analyzed. As a result a number of new instabilities leading, for example, to compression-like states have been described and these lead to various novel spatially inhomogeneous states.

Acknowledgements

This work was supported by NASA under grant UGS97-0308 and by NSF under grant DMS-9703684. We are grateful to F. Higuera, M. Higuera, F. Mancebo, C. Martel, J. Mochlis and J. Nicolas for their assistance in developing the projects described above, and to P. Weidman for making his experimental results available prior to publication.

References

[1] V.O. Afenchenko, A.B. Ezersky, S.V. Kiyashko, M.I. Rabinovich and P.D. Weidman, Phys. Fluids, in press.

[2] M. Airiau, DEA Report, Ecole Normale Superieure, Paris (1986).

[3] C. Alvarez-Pereira and J.M. Vega, Euro. Jnl. of Appl. Math. 3, 55 (1992).

[4] S. Douady, S. Fauve and O. Thual, Europhys. Lett. 10, 309 (1989).

[5] P.L. Hansen and P. Alstrom, J. Fluid Mech. 351, 301 (1997).

[6] D.M. Henderson and J.W. Miles, J. Fluid Mech. 275, 285 (1994).

[7] M. Higuera, J.A. Nicolas and J.M. Vega, Phys. Fluids 6, 438 (1994).

[8] P.C. Hirschberg and E. Knobloch, Physica D 90, 56 (1996).

[9] D.W. Hughes and M.R.E. Proctor, J. Fluid Mech. 244, 583 (1992).

[10] E. Knobloch and J. DeLuca, Nonlinearity 3, 575 (1990).

[11] E. Knobloch, C. Martel, J. Moehlis and J.M. Vega, in preparation.

[12] E. Knobloch and M.R.E. Proctor, Proc. R. Soc. London A 415, 61 (1988).

[13] A.S. Landsberg and E. Knobloch, Phys. Rev. E 53, 3579 (1996).

[14] M.S. Longuet-Higgins, Phil. Trans. R. Soc. London A 245, 535 (1953).

[15] J. Moehlis and E. Knobloch, Phys. Rev. Lett., in press.

[16] F.J. Mancebo, J.A. Nicolas and J.M. Vega, Phys. Fluids, in press.

[17] C. Martel and E. Knobloch, Phys. Rev. E 56, 5544 (1997).

[18] C. Martel, E. Knobloch and J.M. Vega, in preparation.

[19] C. Martel, J.A. Nicolas and J.M. Vega, J. Fluid Mech. 360, 213 (1998).

[20] H. Riecke, J.D. Crawford and E. Knobloch, in NATO ASI Series B 237, 61 (1991).

[21] H. Schlichting, Z. Phys. 33, 327 (1932).

[22] F. Simonelli and J.P. Gollub, J. Fluid Mech. 199, 471 (1989).

[23] J.W. Swift, Nonlinearity 1, 333 (1988).

[24] S. Taylor, Proc. R. Soc. London 27, 71 (1878).

[25] J.M. Vega, F.J. Higuera and P.D. Weidman, J. Fluid Mech., in press.

Session 6A

Phase Change IV: Boiling

PRESSURE-RADIATION FORCES ON VAPOR BUBBLES

V. Harik, Y. Hao, H.N. Oğuz, A. Prosperetti, Department of Mechanical Engineering, The Johns Hopkins University, Baltimore MD 21218, prosperetti@jhu.edu

Abstract

In a microgravity environment the absence of buoyancy prevents vapor bubbles from moving away from a boiling surface. This circumstance negatively affects boiling heat transfer and promotes an early transition to the highly inefficient film boiling regime. Acoustic pressure radiation (or Bjerknes) forces provide a possible alternative to buoyancy as a means for bubble removal. After summarizing the results of a study of vapor bubbles in sound fields, the paper describes the action of acoustic pressure gradients on vapor bubbles.

1 Introduction

At normal gravity, the effectiveness of boiling as a heat transfer mechanism relies in no small measure on the rapid removal of vapor bubbles from the heated surface. This process has a two-fold benefit, as it both aids in removing latent heat and in promoting microconvective motion near the surface. On the basis of this remark, one would be led to believe that boiling at reduced gravity would be very inefficient. Somewhat surprisingly, at small to moderate heat fluxes, this statement is only partly true as shown by several experiments (Siegel 1967; Clark 1968; Zell et al. 1989; Oka et al. 1992, and others). Two major differences between micro- and normal-gravity boiling are however evident: (*i*) The bubble shape, size, and general dynamics is radically different; (*ii*) The critical heat flux is reduced severalfold at low gravity. As first shown by Siegel and Keshock (1964), a major heat removal mechanism in low gravity is the fact that a detaching bubble does not go far from the heated surface so that subsequent bubbles feed into it until the bubble leaves. At this point another bubble grows, detaches, is fed by smaller ones, and the cycle repeats. This process compounds with vigorous surface instabilities (Ervin et al. 1992) to produce a substantial heat transfer.

While the hovering of large bubbles near the nucleation site is beneficial at low to moderate heat fluxes, it is also at the root of the observed reduction in critical heat flux, where the heating surface is surrounded by a vapor blanket (Oka et al. 1992; Chung 1994). In order to increase the critical heat flux at low gravity it is therefore desirable to remove bubbles from the heated surface providing a substitute for buoyancy. In this paper we consider the action of acoustic pressure forces on vapor bubbles as a means to achieving this end.

The action of acoustic radiation forces on gas – rather than vapor – bubbles is well known (see e.g. Crum and Eller 1970; Crum and Nordling 1972; Crum 1971, 1975; Agrest and Kuznetsov 1972, 1973; Weiser and Apfel 1982; Barmatz and Collas 1985; Trinh and Hsu 1986; Holt and Crum 1992; Lee and Wang 1993a, Matula et al. 1997). For example, radiation forces are a major factor in acoustic cavitation where they promote violent translational motion and spatial reorganization of the gas that evolves from the liquid in an intense sound field. These and other aspects of pressure radiation forces have been extensively studied both experimentally and theoretically (see e.g. Yosioka and Kawasima 1955; Eller 1968; Foster et al. 1968; Löfsted and Putterman 1991; Lee and Wang 1993). In particular, Dr. E. Trinh (JPL) has carried out experiments on the Space Shuttle USML-1 demonstrating the action of these forces on drops and gas bubbles (Marston et al. 1993).

Gas bubbles are attracted or repelled by the pressure antinodes according as to whether they are driven below or above their resonance frequency. Furthermore, in the linear regime, neighboring bubbles repel each other when one is driven above and one below the natural frequency while they attract otherwise.

The resonance frequencies of bubbles thus play a major role for gas bubbles. While the situation may be expected to be similar for vapor bubbles, comparatively less work has been carried out on these systems (Finch and Neppiras 1973; Alekseev 1976a, 1976b; Khabeev 1976; Akulichev et al. 1979; Hsieh 1979; Marston and Greene 1978; Marston 1979; Nagiev and Khabeev 1979). After reviewing the results of our recent analysis of the forced oscillations of vapor bubbles in a sound field (Hao and Prosperetti 1998), we study the action of sound field gradients on oscillating vapor bubbles.

2 Vapor bubble oscillations

Even with the assumption of sphericity, the complete problem of a vapor bubble undergoing non-linear radial pulsations in a sound field is a complex problem as its exact solution requires a consideration of the equations

of conservation of mass, momentum, and energy in the liquid and in the vapor coupled by suitable interface conditions. It is however possible to considerably simplify the problem with the aid of reasonable approximations. We begin by reviewing the mathematical model and then present some typical results.

2.1 Mathematical model

We neglect the liquid thermal expansion and assume that the ratio of the vapor to the liquid density is very small, which enables us to equate the velocity $\dot{R}$ of the bubble interface to the liquid velocity. With these assumptions the continuity and momentum equations in the liquid can be combined in the usual way to give the well-known Keller equation for the radial motion (Keller and Kolodner 1956; Keller and Miksis 1980; Prosperetti and Lezzi 1986). This equation differs from the Rayleigh-Plesset equation as it includes first-order liquid compressibility corrections and is

$$\left(1-\frac{\dot{R}}{c}\right) R\ddot{R}+\frac{3}{2}\left(1-\frac{1}{3}\frac{\dot{R}}{c}\right)\dot{R}^2 = \frac{1}{\rho_L}\left(1+\frac{\dot{R}}{c}+\frac{R}{c}\frac{d}{dt}\right)\left[p_B-P(t)\right]. \quad (1)$$

In this equation dots denote time derivatives, c is the speed of sound in the liquid, $P=P(t)$ denotes the sum of the static ambient pressure and the time-dependent pressure field driving the bubble into oscillation, and p_B is the pressure on the liquid side of the interface related to the bubble internal pressure p by the balance of normal stresses across the interface, namely

$$p = p_B+\frac{2\sigma}{R}+4\mu\frac{\dot{R}}{R}, \quad (2)$$

in which σ is the surface tension coefficient and μ the liquid viscosity. In the present study we consider ambient pressures of the form

$$P(t) = p_\infty - P_A(x_B)\sin\omega t, \quad (3)$$

where p_∞ is the static pressure, P_A is the acoustic pressure amplitude at the position x_B of the bubble, and ω is the sound angular frequency.

While we include liquid compressibility effects in the radial equation (1) to account for energy losses by acoustic radiation, we can neglect such effects in the liquid energy equation in view of the fact that the liquid temperature field is affected by the bubble only over regions that are much smaller than the wavelength of sound. We thus write

$$\frac{\partial T_L}{\partial t}+\frac{R^2\dot{R}}{r^2}\frac{\partial T_L}{\partial r} = \frac{D_L}{r^2}\frac{\partial}{\partial r}\left(r^2\frac{\partial T_L}{\partial r}\right), \quad (4)$$

where T_L is the liquid temperature, $(R^2/r^2)\dot{R}$ is the incompressible velocity field at a distance r from the bubble center, and D_L denotes the thermal diffusivity of the liquid. The boundary conditions are $T_L \to T_\infty$ at large distances from the bubble and, at the bubble surface $r=R(t)$, $T_L = T_s(p)$, where $T_s(p)$ is the saturation temperature corresponding to the bubble internal pressure p,

A standard simplification in the dynamics of gas bubbles in sound fields of moderate amplitude is to treat the bubble internal pressure as spatially uniform (Prosperetti 1991). This approximation, that hinges on the smallness of the Mach number of the vapor flow, holds also in the case of vapor bubbles, and actually even more so in view of the fact that the acoustic pressures of interest are usually smaller than in acoustic cavitation. It can be shown that, from this approximation and from the assumption of perfect-gas behavior of the vapor, one can derive the following expression for the vapor velocity (Nigmatulin and Khabeev 1975; Nigmatulin et al. 1981; Prosperetti et al. 1988; Prosperetti 1991)

$$v = \frac{1}{\gamma p}\left[(\gamma-1)k_V\frac{\partial T_V}{\partial r}-\frac{1}{3}r\dot{p}\right], \quad (5)$$

where γ is the ratio of the specific heats and k_V the thermal conductivity. The unknown vapor temperature field can then be found from the energy equation in the form

$$\rho_V c_{pV}\left(\frac{\partial T_V}{\partial t}+v\frac{\partial T_V}{\partial r}\right)-\dot{p} = \frac{1}{r^2}\frac{\partial}{\partial r}\left(k_V r^2\frac{\partial T_V}{\partial r}\right), \quad (6)$$

where c_{pV} is the vapor specific heat at constant pressure.

The conservation of energy at the interface requires that

$$k_L\left.\frac{\partial T_L}{\partial r}\right|_{r=R}-k_V\left.\frac{\partial T_V}{\partial r}\right|_{r=R} = L\dot{m} = L\rho_V\left(\dot{R}-v\right), \quad (7)$$

where L is the latent heat. Upon using (5) to express v, this relation gives

$$k_L\left.\frac{\partial T_L}{\partial r}\right|_{r=R} = L\rho_V R\left(\frac{\dot{R}}{R}+\frac{\dot{p}}{3\gamma p}\right)+\frac{c_s}{c_{pV}}k_V\left.\frac{\partial T_V}{\partial r}\right|_{r=R} \quad (8)$$

where $c_s = c_{pV}-(L/T_s)$ is the specific heat along the saturation line. For water at 100 ° $c_s/c_{pV} \simeq$ -1.45.

It is well known that, due to kinetic effects, strict thermodynamic equilibrium does not prevail at an interface during phase change (see e.g. Labuntsov and

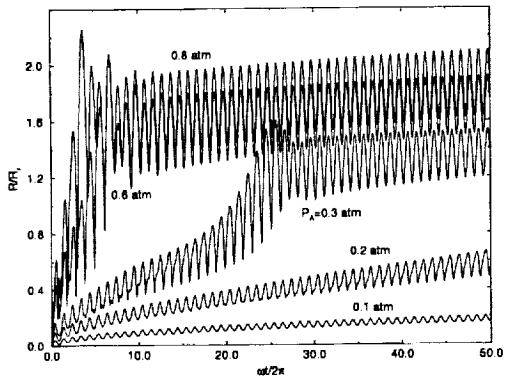

Figure 1: Radius versus time for vapor bubbles in saturated water at 1 atm and 1 kHz for various acoustic pressure amplitudes. The radius is normalized by the linear resonant radius $R_{res} = 2.71$ mm.

Kryukov 1979). When the accommodation coefficient is not too small, these effects become appreciable only when the vapor Mach number approaches 1, which is far from the conditions that may reasonably be expected in the problem considered here. Therefore we assume thermodynamic equilibrium, as a consequence of which the liquid and vapor temperature at the interface have the same value T_S, and the vapor pressure is given by the saturation relation

$$p = p_{sat}(T_S)\,, \tag{9}$$

with its derivative along the saturation line expressed by the Clausius-Clapeyron relation

$$\left.\frac{dp}{dT_s}\right|_{sat} = \frac{L\rho_V}{T_s}\,. \tag{10}$$

In view of the approximation of spatially uniform pressure, (9) gives the pressure everywhere in the bubble once the surface temperature is known. The local value of the temperature, however, varies from place to place according to the energy equation (6). The local value of the vapor density is given by the perfect-gas equation of state:

$$\rho_V = \frac{\gamma}{\gamma - 1}\frac{p}{c_{pV}T_V}\,. \tag{11}$$

2.2 Results

The partial differential equations constituting the previous mathematical model are turned into ordinary differential equations in time by using a collocation method based on Chebyshev polynomials (Kamath and Prosperetti 1989; Hao and Prosperetti 1998). Figure 1 shows some examples of the radius versus time for vapor bubbles in saturated water at 1 atm. The radius is normalized by the linear resonant radius that has the value 2.71 mm in the conditions of this example. The driving frequency is 1 kHz and results are given for different pressure amplitudes.

The first feature that stands out from these results is the relatively rapid growth of the average radius of the bubble. This is a manifestation of the phenomenon of rectified heat transfer, which is the analogue of rectified diffusion of mass for gas bubbles. The sound field "pumps" heat into the bubble due to the alternating stretching and compressing of the thermal boundary layer and of the bubble surface. The growth is relatively rapid up to the resonant radius, after which it slows down considerably although it is never zero. Thus, in contrast to the results of quasi-linear theory (Alekseev 1976a, 1976b), no true dynamic equilibrium radius exists when nonlinearities are fully taken into account. The response in the vicinity of the resonant radius is particularly strong, but clear traces of the nonlinear resonances at lower radii can also be detected in the figure.

As for the so-called "second resonance" of vapor bubbles (Finch and Neppiras 1973; Alekseev 1976a, 1976b; Khabeev 1976; Hsieh 1979; Marston and Greene 1978; Marston 1979; Nagiev and Khabeev 1979), it actually turns out that this is not a resonance at all, but a condition of linearly unstable equilibrium. Nonlinear effects can promote the growth of the bubble beyond this value of the radius which therefore does not play a significant role in the bubble response.

3 Pressure-radiation forces

The net pressure force on a body in a fluid is given by

$$F = -\oint_S p\,\mathbf{n}\,dS\,, \tag{12}$$

where the integration is over the surface of the body and $\mathbf{n}$ is the outwardly directed normal. If the pressure field is slowly varying over the region occupied by the body, we may set $p \simeq p(x_B,t) + (x - x_B)\cdot\nabla p + \ldots$. Upon substituting into (12) we find

$$F \simeq -V\nabla p(x_B,t)\,, \tag{13}$$

where V is the volume of the body. In the case of the bubble considered in the previous section, the pressure field acting on its surface consists of the incident sound field P_A, of the pressure field due to the motion of other bubbles in its neighborhood, if any, and of the pressure

field due to the bubble itself. In the acoustic approximation all these fields combine additively and the last one, being spherically symmetric, contributes nothing to the integral (12). The primary acoustic field has usually a wavelength much greater than the bubble radius, and therefore its contribution is adequately represented by (13):

$$F_1 = V \sin \omega t \, \nabla P_A(x_B) . \qquad (14)$$

The pressure field p_2 due to another bubble is negligibly small unless the distance r from the given bubble is at most a few tens of times the radius. In typical conditions, this distance is much smaller than the wavelength and therefore this pressure field can be approximated by its expression in an incompressible liquid which is (see e.g. Plesset and Prosperetti 1977)

$$p_2(r,t) = P_2(t) + \frac{R_2}{r}\,[p_{B2} - P_2(t)] + \frac{1}{2}\frac{R_2}{r}\,\dot{R}_2^2 \left[1 - \left(\frac{R}{r}\right)^3\right], \qquad (15)$$

where the symbols have the same meaning as in Eq. (1) with the subscript 2 consistently used to denote quantities pertaining to the second bubble. Equation (15) shows that the scale of variation of p_2 is r and therefore, if the two bubbles are separated by at least a few times R, the approximation (13) is again applicable with the result

$$F_2 = V \frac{R_2}{r^2}\,[p_{B2} - P_2(t)] + \frac{1}{2} V \frac{R_2}{r^2}\,\dot{R}_2^2 \left[1 - 4\left(\frac{R}{r}\right)^3\right]. \qquad (16)$$

The direction of this force is along the line joining the centers of the two bubbles. The time averages of F_1 and F_2 are called the primary and secondary Bjerknes forces, respectively. For example

$$F_{B1} = < V \sin \omega t > \nabla P_A(x_B) \equiv \nabla P_A(x_B) \left(\frac{\omega}{2\pi}\int_0^{2\pi/\omega} \frac{4}{3}\,\pi R^3(t) \sin \omega t \, dt\right). \qquad (17)$$

The principal reason to consider a second bubble here is the fact that the vapor bubbles of present concern grow near solid boundaries the effect of which, to a first approximation, can be represented by an "image" bubble that pulsates in phase with the real bubble.

Figure 2 shows the instantaneous primary force (14) (dashed line, right vertical scale) superimposed on the normalized bubble radius (solid line, left vertical scale) as a function of time for the case with P_A = 0.3 atm of

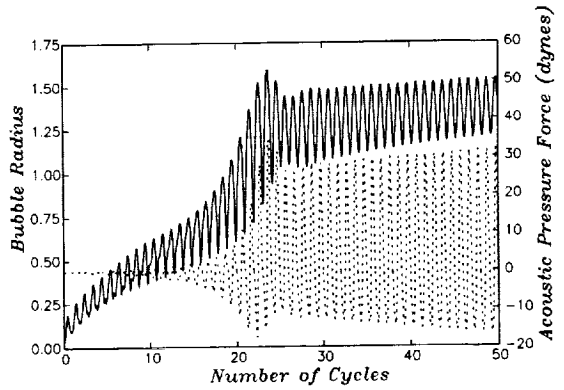

Figure 2: The solid line (left vertical scale) is the radius versus time for a vapor bubble in saturated water at 1 atm and 1 kHz for an acoustic pressure amplitude of 0.3 atm. The radius is normalized by the linear resonant radius R_{res} = 2.71 mm. The dashed line (right vertical scale) shows the corresponding instantaneous force (14).

Fig. 1. To generate this figure we have assumed a spatial distribution of the pressure given by

$$P_A(x) = P_S \cos kx , \qquad (18)$$

where P_S is amplitude of the wave and k the wave number. The bubble is positioned at z = 2 mm, so that kx = 0.0084 rad. The amplitude of oscillation of the force is proportional to the instantaneous volume and therefore it grows with the bubble mean radius. The time average value of the force, shown in Fig. 3 (dashed line, right vertical scale; the solid line to be read on the other scale is the mean radius), behaves however in a very different manner. It starts out negative, since the bubble is driven below its natural frequency, becomes more negative as the amplitude of oscillation grows with the bubble radius, and then abruptly changes sign as the radius goes through the resonant value. After a brief transient, one observes a steady decline in spite of the fact that, as shown by the solid line, the mean bubble radius keeps increasing. This behavior is a consequence of the fact that, as the radius moves further and further away from resonance, the oscillation amplitude of the bubble decreases. To have an intuitive feeling for the magnitude of the effect, note that the buoyancy force on a bubble with a radius equal to the resonant value, 2.71 mm, is about 82 dynes. Thus the acoustic effect is small, although it can be increased by placing the bubble at a greater distance from the pressure antinode where the pressure gradient is stronger.

Corresponding results for different parameter values are shown in Figs. 4 and 5. Here P_S = 0.6 atm and $\omega/2\pi$

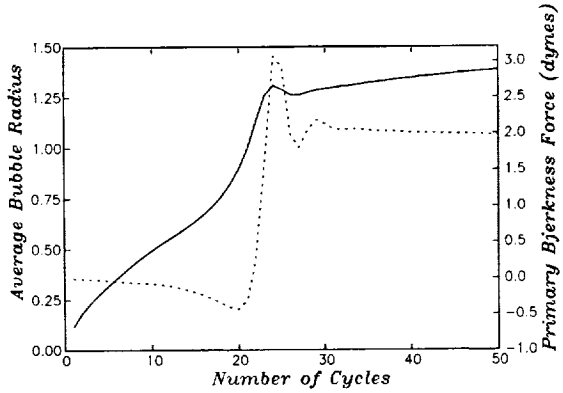

Figure 3: Bubble radius (solid line) and pressure-radiation force (dashed line) averaged over each cycle for the case of Fig. 2.

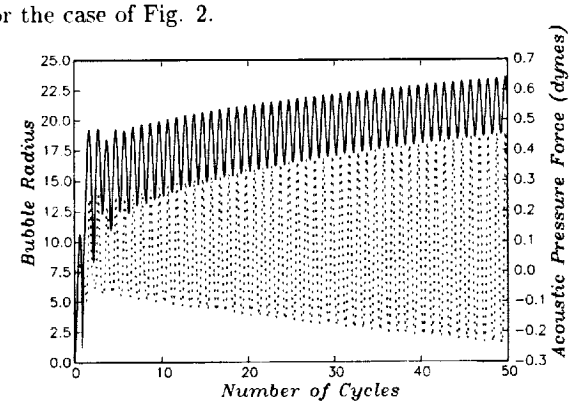

Figure 4: The solid line (left vertical scale) is the radius versus time for a vapor bubble in saturated water at 1 atm and 20 kHz for an acoustic pressure amplitude of 0.6 atm. The radius is normalized by the linear resonant radius $R_{res} = 10$ μm. The dashed line (right vertical scale) shows the corresponding instantaneous force (14).

= 20 kHz. The liquid is saturated water at 1 atm and R_{res} = 10 μm. The pressure field is again given by (18) and the bubble is at 0.2 mm from the antinode. In this case the initial bubble radius is equal to the resonant value. As a consequence the amplitude of oscillation is large and the bubble grows very quickly. The Bjerknes force is always positive, i.e., directed away from the pressure antinode.

4 Conclusions

We have found that the action of acoustic pressure gradients on oscillating vapor bubbles is similar to that on gas bubbles. As shown in Hao and Prosperetti (1998) the

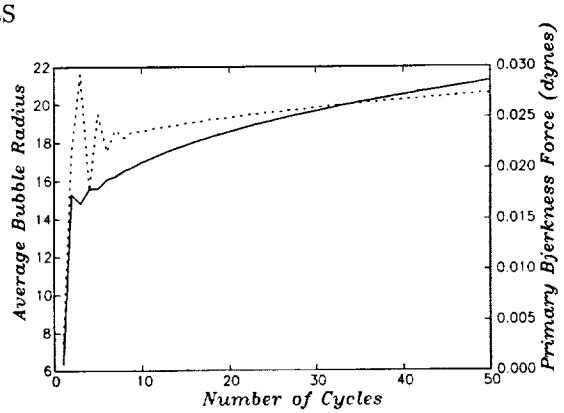

Figure 5: Bubble radius (solid line) and pressure-radiation force (dased line) averaged over each cycle for the case of Fig. 4.

so-called second resonance of vapor bubble is really not a resonance at all and has no effect on acoustic forces.

A potential difficulty in the practical application of Bjerknes forces in boiling is the fact that they vanish exactly when the bubble is placed at a pressure antinode. If the boiling surface is rigid, it will be an antinode and no appreciable acoustic force can exist. This difficulty could be remedied by endowing the surface with a limited compliance. Another possibility would be to have the acoustic force act tangentially to a suitably shaped surface.

References

[1] E.M. Agrest and G.N. Kuznetsov. Migration of gas-filled cavities in an inhomogeneous sound field. *Sov. Phys. Acoust.*, 18:143–147, 1972.

[2] E.M. Agrest and G.N. Kuznetsov. Instantaneous parameters of the motion of a cavitation bubble in an inhomogeneous sound field. *Sov. Phys. Acoust.*, 19:212–215, 1973.

[3] Akulichev, V.A., Alekseev, V.N., & Yushin, V.P., 1979, Growth of vapor bubbles in an ultrasonic field, *Sov. Phys. Acoust.*, **25**, 453–457.

[4] Alekseev, V.N., 1976, Nonsteady behavior of a vapor bubble in an ultrasonic field, *Sov. Phys. Acoust.*, **22**, 104–107.

[5] Alekseev, V.N., 1976, Steady-state behavior of a vapor bubble in an ultrasonic field, *Sov. Phys. Acoust.*, **21**, 311–313.

[6] M. Barmatz and P. Collas. Acoustic radiation potential on a sphere in plane, cylindrical, and spherical standing wave fields. *J. Acoust.Soc. Am.*, 77:928–945, 1985.

[7] J.A. Clark. Gravic and agravic effects in cryogenic heat transfer. In K.J. Bell, editor, *Advances in Cryogenic Heat Transfer - Chemical Engineering Progress Symposium Series Vol. 64, No. 87*, pages 93–102. American Institute of Chemical Engineers, 1968.

[8] L.A. Crum. Acoustic force on a liquid droplet in an acoustic stationary wave. *J. Acoust.Soc. Am.*, 50:157–163, 1971.

[9] L.A. Crum. Bjerknes forces on bubbles in a stationary sound field. *J. Acoust.Soc. Am.*, 57:1363–1370, 1975.

[10] L.A. Crum and A.I. Eller. Motion of bubbles in a stationary sound field. *J. Acoust.Soc. Am.*, 48:181–189, 1970.

[11] L.A. Crum and D.A. Nordling. Velocity of transient cavities in an acoustic stationary wave. *J. Acoust.Soc. Am.*, 52:294–301, 1972.

[12] A.I. Eller. Force on a bubble in a standing acoustic wave. *J. Acous. Soc. Am.*, 43:170–171, 1986.

[13] J.S. Ervin, Merte H. Jr., R.B. Keller, and K. Kirk. Transient pool boiling in microgravity. *Int. J. Heat Mass Trans.*, 35:659–674, 1992.

[14] R.D. Finch and E.A. Neppiras. Vapor bubble dynamics. *J. Acoust. Soc. Am.*, 53:1402–1410, 1973.

[15] J.M. Foster, J.A. Botts, A.R. Barbin, and R.T. Vachon. Bubble trajectories and equilibrium levels in vibrated liquid columns. *J. Basic Eng.*, 90:125–132, 1968.

[16] L.P. Gor'kov. On the forces acting on a small particle in an acoustic field in an ideal fluid. *Sov. Phys. Acoust.*, 6:773–775, 1962.

[17] R.G. Holt and L.A. Crum. Acoustically forced oscillations of air bubbles in water: Experimental results. *J. Acoust. Soc. Am.*, 91:1924–1932, 1992.

[18] D.Y. Hsieh. On oscillation of vapor bubbles. *J. Acoust. Soc. Am.*, 66:1514–1515, 1979.

[19] Chung. J.N. Bubble dynamics, two-phase flow, and boiling heat transfer in a microgravity environment. In B.S. Singh, editor, *Second Microgravity Fluid Physics Conference*, pages 259–264. NASA No. 3276, 1994.

[20] N.S. Khabeev. Heat transfer and phase-transition effects in the oscillation of vapor bubbles. *Sov. Phys. Acoust.*, 21:501–505, 1976.

[21] C.P. Lee and T.G. Wang. Acoustic radiation force on a bubble. *J. Acoust.Soc. Am.*, 93:1637–1640, 1993.

[22] R. Löfsted and S. Putterman. Theory of long wavelength acoustic radiation pressure. *J. Acous. Soc. Am.*, 90:2027–2033, 1991.

[23] P.L. Marston. Evaporation-condensation resonance frequency of oscillating vapor bubbles. *J. Acoust. Soc. Am.*, 66:1516–1521, 1979.

[24] P.L. Marston and D.B. Greene. Stable microscopic bubbles in helium i and evaporation-condensation resonance. *J. Acoust. Soc. Am.*, 64:319–321, 1978.

[25] T. J. Matula, S. M. Cordry, R. A. Roy, and L. A. Crum. Bjerknes force and bubble levitation under single-bubble sonoluminescence conditions. *J. Acoust. Soc. Am.*, 102:1522–1527.

[26] H. Jr. Merte. Pool and flow boiling in variable and microgravity. In B.S. Singh, editor, *Second Microgravity Fluid Physics Conference*, pages 265–272. NASA No. 3276, 1994.

[27] F.B. Nagiev and N.S. Khabeev. Heat-transfer and phase-transition effects associated with oscillations of vapor-gas bubbles. *Sov. Phys. Acoust.*, 25:148–152, 1979.

[28] T. Oka, Y. Abe, K. Tanaka, Y.H. Mori, and A. Nagashima. Observational study of pool boiling under microgravity. *JSME Int. J.*, II-35:280–286, 1992.

[29] Y. Hao and A. Prosperetti. The dynamics of vapor bubbles in acoustic pressure fields. *J. Fluid Mech.*, submitted, 1998.

[30] R. Siegel. Effects of reduced gravity on heat transfer. In J.P. Hartnett and T.F. Jr. Irvine, editors, *Advances in Heat Transfer - Vol. 4*, pages 143–228. Academic Press, 1967.

[31] R. Siegel and E.G. Keshock. Effects of reduced gravity on nucleate boiling bubble dynamics in saturated water. *A.I.Ch.E. J.*, 10:509–517, 1964.

[32] E.H. Trinh and C.J. Hsu. Acoustic levitation methods for density measurements. *J. Acoust.Soc. Am.*, 80:1757–1761, 1986.

[33] M.A.H. Weiser and R.E. Apfel. Extension of acoustic levitation to include the study of micron-size particles in a more compressible host liquid. *J. Acoust.Soc. Am.*, 71:1261–1268, 1982.

[34] K. Yosioka and Y. Kawasima. Acoustic radiation pressure on a compressible sphere. *Acustica*, 5:167–178, 1955.

[35] M. Zell, J. Straub, and B. Vogel. Pool boiling under microgravity. *PCH*, 11:813–823, 1989.

Condensation of Forced Convection Two-Phase Flow in a Miniature Tube

E. BEGG[1], A. FAGHRI[1], 1 *Department of Mechanical Engineering, University of Connecticut, Storrs, CT 06269,* D. KRUSTALEV [2], 2 *Thermocore, Inc.Lancaster, PA 17601*

Nomenclature

c_p	specific heat at constant pressure, J/(kg-K)
f_v	vapor friction factor
h_{fg}	latent heat of vaporization, J/kg
h_o	outer surface convective heat transfer coefficient, W/(m^2 K)
k	thermal conductivity, W/(m-K)
L_δ	length of the liquid film to the point of complete condensation (Fig. 1), m
K	curvature, m^{-1}
Ma	$\overline{w}_v/\sqrt{\gamma_0 R_g T_v}$, Mach number
$\dot{m}_{\ell,in}$	liquid mass flow rate at z = 0, kg/s
$\dot{m}_\ell$	total mass flow rate at z = 0, kg/s
$\dot{m}$	mass flow rate, kg/s
p	pressure, Pa
Q	$Q = 2\pi R \int_0^z q_w dz - \left(c_{p,\ell}, \dot{m}_\ell, \overline{T}_\ell - c_{p,\ell,in}, \dot{m}_{\ell,in}, \overline{T}_{\ell,in}\right)$, axial heat flow due to phase change, W
q	heat flux, W/m^2
r	radial coordinate, m
R	inner radius of the channel, m
R_g	gas constant, J/(kg-K)
Re	$2\overline{w}_v(R-\delta)\rho_v/\mu_v$, axial vapor Reynolds number
Re$_r$	$2v_{v,\delta}(R-\delta)\rho_v/\mu_v$, radial vapor Reynolds number
T	temperature, K
v	radial velocity, m/s
w	axial velocity, m/s
$\overline{w}$	area-averaged axial velocity m/s
z	axial coordinate, m

Greek Symbols

α	accommodation coefficient
β	momentum flux coefficient
γ_0	c_p/c_v, ratio of specific heats
Δ	$d\delta/dz$
δ	liquid film thickness, m
μ	dynamic viscosity, Pa-s
ρ	density, kg/m^3
σ	surface tension, N/m
φ	inclination angle

Subscripts

ent	entrance
in	at z = 0
ℓ	liquid
men	meniscus
sat	saturation
v	vapor
w	wall
δ	liquid film free surface
$crit$	at critical complete condensation

Introduction

Electronic cooling and other high heat flux applications require a fundamental understanding of the condensation process in small diameter channels in order to optimize design configurations of devices used in these applications. Unlike conventional size passages in which surface tension effects are limited, surface tension in miniature size channels can have a significant role on the overall hydrodynamics and in particular on the thin films that are believed to be the dominant mechanisms controlling the heat transfer characteristics.

For forced convection condensation in miniature circular tubes the two phase flow regime maps for conventional sized tubes may not be relevant because of the role of surface tension in the hydrodynamics. Srinivasan and Shah (1997) point out that very limited data is available concerning the basic flow patterns for two phase flow with or without heat transfer in miniature circular tubes.

Condensation in conventional size circular tubes comprise a well-defined body of work. Collier and Thome (1994) present a generally accepted description of the two phase flow patterns during forced convection condensation in conventional size horizontal tubes with co-current flow. The range of flow patterns present depend on the total energy convected into the tube. In order of increasing velocity, the flow is found to be stratified, slug, plug or wavy, and annular.

The objective of this work is to model annular film condensation in miniature circular cylinder tubes where capillary phenomena can conceivably result in blocking of the tube cross section with liquid at some distance from the condenser entrance. A physical description is illustrated in Fig. 1 (a). This phenomenon is referred to as complete condensation. An experiment with visualization was conducted and a mathematical

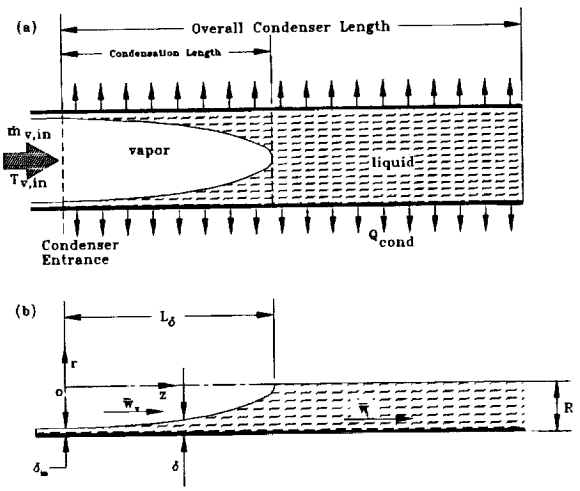

Figure 1: Description of the physical model for annular film condensation in a miniature tube. (a) Structure of two phase flow for complete condensation. (b)Coordinate system and conventions for film condensation model.

model was developed on this subject in this work.

Flow Visualization in Miniature Tubes

A circular Pyrex tube of 3.25 mm inside diameter and 5.00 mm outside diameter was used in a loop thermosyphon for flow visualization. The overall length of the horizontal test section was 302 mm with an insulated inlet section of 97 mm and a condenser length of 205 mm. Experiments were conducted over a range of heat loads from 4.9 to 10 W.

Figure 2 is a photograph of the complete condensation phenomenon for the operating conditions of $Q_{in} = 7.7W$, $T_v = 59.0°C$. A liquid film on the lower wall is obvious closer to the location of complete condensation. A dramatic thinning of the film on the lower wall is also apparent. Immediately after the decrease in film thickness at the bottom wall, the liquid is seen to completely span the tube cross section. The closing off of the channel to vapor flow appears similar to a capillary tube meniscus. Note the slight inclination of the meniscus due to the effect of gravity.

Mathematical Formulation

A summary of the analysis is given below. For the complete development of the mathematical model see Begg et al. (1998).

A steady state mathematical model of condensation which leads to complete condensation is presented and includes coupled vapor and liquid flows with shear stresses at the liquid free surface due to the vapor-liquid frictional interaction and surface tension gradient. The model is based on the following simplifying assumptions:

1. The vapor is saturated and there is no temperature gradient in vapor in radial direction.

2. Heat transport in the thin liquid films is only due to conduction in the radial direction.

3. Inertia terms can be neglected for the viscous flow in the liquid films with low Reynolds numbers.

4. Force on liquid due to surface tension is much greater than the gravitational force and therefore the liquid is distributed onto the walls in a film of locally uniform thickness.

5. The solid tube wall is infinitely thin so that its thermal resistance in the radial direction can be neglected as well as the axial heat conduction.

The cylindrical coordinate system used is shown in Fig. 1(b). Both the vapor and liquid flow along the z-coordinate. The physical situation should be described taking into consideration the vapor compressibility and the vapor temperature variation along the channel. Also the second principal radius of curvature of the liquid-vapor interface should be accounted for (in the equation relating vapor and liquid pressures) while it is usually neglected in modeling of film flows in tubes of larger diameters. The mass and energy balances for the liquid film shown in Fig. 2(a) yield:

$$\frac{dQ}{dz} = 2\pi k_\ell \frac{T_w - T_\delta}{\ln[R/(R-\delta)]} - \frac{d}{dz}\left(c_{p,\ell} \dot{m}_\ell \overline{T}_\ell\right) \quad (1)$$

where $\overline{T}_\ell$ is the area-averaged liquid temperature for a given z location. For consideration of subcooling in the condensed liquid, $\overline{T}_\ell$ is found from an average area given by

$$\overline{T}_\ell = \frac{2\int_{R-\delta}^{R} r T_\ell(r) dr}{[R^2 - (R-\delta)^2]} \quad (2)$$

where $T_\ell(r)$ is the assumed liquid film temperature profile given by the temperature distribution in a cylindrical wall.

$$T_\ell(r) = T_\delta + \frac{T_w - T_\delta}{ln\frac{R}{R-\delta}} ln\frac{r}{R-\delta} \quad (3)$$

The derivative of $\overline{T}_\ell$ is approximated by

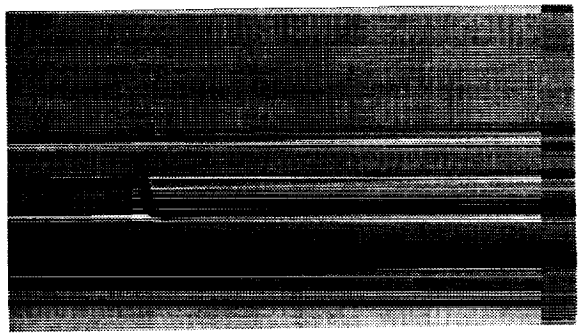

Figure 2: Photograph of annular film condensation resulting in complete condensation in a 3.25 mm inside diameter tube. $Q_{in} = 7.7W$, $T_v = 59.0^oC$

$$\frac{d\overline{T}_\ell}{dz} = \frac{dT_\delta}{dz} + \left(\frac{dT_w}{dz} - \frac{dT_\delta}{dz}\right) \times \ln\left(\frac{R-\delta}{R}\right) \frac{2}{[R^2-(R-\delta)^2]} \left[\left(\ln\frac{R}{R-\delta} - \frac{1}{2}\right)\frac{R^2}{2} + \frac{(R-\delta)^2}{4}\right] \quad (4)$$

The momentum conservation for viscous flow in a liquid film in which the inertia terms are assumed to be negligible is

$$\frac{1}{r}\frac{\partial}{\partial r}\left(r\frac{\partial w_\ell}{\partial r}\right) = \frac{1}{\mu_\ell}\left(\frac{dp_\ell}{dz} + \rho_\ell g sin\varphi\right) \quad (5)$$

The boundary conditions for the last equation are the non-slip condition at $r = R$ and specified shear stresses at the liquid-vapor interface due to the frictional liquid-vapor interaction, $\tau_{\ell,v}$, and the surface tension gradient related to the interfacial temperature gradient along the channel.

$$w_\ell|_{r=R} = 0 \quad (6)$$

$$\frac{\partial w_\ell}{\partial r}|_{(r=R-\delta)} = \frac{1}{\mu_\ell}\left[-\tau_{\ell,v} - \frac{d\sigma}{dT}\frac{dT_\delta}{dz}\right] \equiv E \quad (7)$$

where T_δ is the local liquid-vapor interface temperature and $\frac{d\sigma}{dT}$ is the Marangoni effect.

Taking into account the effect of the condensation process on the shear stress term, an expression from the Munoz-Cobol et al. (1996) analysis is used for $\tau_{\ell,v}$. The equation for the axial pressure gradient in the liquid is

$$\frac{dp_\ell}{dz} = \rho_\ell g \sin\varphi + \mu_\ell\left[\frac{1}{2\pi\rho_\ell}\left(\frac{Q}{h_{fg}} - \dot{m}_{\ell,in}\right) + E(R-\delta)F\right] \left[\frac{R^4}{16} + \frac{(R-\delta)^2}{2}\left(F + \frac{(R-\delta)^2}{8} - \frac{R^2}{4}\right)\right]^{-1} \quad (8)$$

where

$$F = \frac{(R-\delta)^2}{2}\left(\ln\frac{R}{R-\delta} + \frac{1}{2}\right) - \frac{R^2}{4} \quad (9)$$

The pressure difference between the vapor and liquid phases is due to capillary effects (Faghri, 1995).

$$p_v - p_\ell = \sigma\left\{\frac{d^2\delta}{dz^2}\left[1 + \left(\frac{d\delta}{dz}\right)^2\right]^{-3/2} + \frac{1}{R-\delta}\cos\left(\text{atan}\frac{d\delta}{dz}\right)\right\} - p_d \quad (10)$$

The term with cosine in the right-hand side of this equation is due to the second principal radius of the interfacial curvature for a cylindrical film. Introducing an additional variable

$$d\delta/dz = \Delta \quad (11)$$

eq. (10) can be rewritten as follows.

$$\frac{d\Delta}{dz} = \left[1 + (\Delta)^2\right]^{3/2}\left(\frac{p_v - p_\ell + p_d}{\sigma} - \frac{\cos(\text{atan}\Delta)}{R-\delta}\right) \quad (12)$$

The compressible quasi-one-dimensional momentum equation for the vapor flow in the form suggested by Bankston and Smith (1973) is modified to account for non-uniformity of the vapor cross-sectional area of the liquid-vapor interface following Faghri (1995).

$$\frac{dp_v}{dz} = \rho_v g\sin\varphi + \frac{1}{A_v}\left[\frac{d}{dz}\left(-\beta_v\rho_v\overline{w}_v^2 A_v\right) - f_v\rho_v\overline{w}_v^2\pi(R-\delta) + 2\pi(R-\delta)\rho_v v_{v,\delta}^2 \sin(\text{atan}\Delta)\right] \quad (13)$$

with $\beta_v = 1.33$ for small radial Reynolds numbers.

The perfect gas law is employed to account for the compressibility of the vapor

$$\rho_v = \frac{p_v}{R_g T_v} \quad (14)$$

Therefore

$$\frac{d\rho_v}{dz} = \frac{1}{R_g}\left(\frac{dp_v}{dz}\frac{1}{T_v} - \frac{p_v}{T_v^2}\frac{dT_v}{dz}\right) \quad (15)$$

The saturated vapor temperature and pressure are related by the Clausius-Clapeyron equation which can be written in the following form.

$$\frac{dT_v}{dz} = \frac{dp_v}{dz}\frac{R_g T_v^2}{p_v h_{fg}} \tag{16}$$

The seven first order differential equations Eqs. (1), (8), (11), (12), (13), (15), and (16) include the following seven variables: δ, Δ, p_ℓ, Q, p_v, ρ_v, and T_v. Therefore, seven boundary conditions are set forth at $z = 0$

$$\delta = \delta_{in} \tag{17}$$

$$\Delta = 0 \tag{18}$$

$$p_\ell = p_{v,in} - \frac{2\sigma}{R - \delta_{in}} + p_d \tag{19}$$

$$Q = 0 \tag{20}$$

$$p_v \equiv p_{v,in} = p_{v,\mathrm{sat}}(T_{v,in}) \tag{21}$$

$$\rho_{v,in} = \frac{p_{v,in}}{R_g T_{v,in}} \tag{22}$$

$$T_v = T_{v,in} \tag{23}$$

In boundary condition (17), δ_{in} is defined from the condition in the adiabatic zone at the entrance to the condenser where the liquid and vapor pressure gradients are equal. This condition is satisfied by solving equations (8) and (13) for δ_{in} for the case of Q =0, $v_{v,\delta}$ =0, dA_v/dz =0 and dT_δ/dz =0. There are also parameters $\dot{m}_{\ell,in}$ and $\overline{w}_{v,in}$ and an additional variable T_δ involved in this problem. They will be considered using additional algebraic equations. The parameter $\dot{m}_{\ell,in}$ should be found using a constitutive condition at the entrance of the condenser.

$$\dot{m}_{\ell,in} = \dot{m}_l - Q_t/h_{fg} \tag{24}$$

where Q_t is the total heat load of the condenser. Also $\overline{w}_{v,in} = Q_t/(h_{fg}\rho_v A_{v,in})$.

The liquid-vapor interface temperature, T_δ, differs from the saturated bulk vapor temperature because of the interfacial resistance and effects of curvature on saturation pressure over liquid films. The interfacial resistance, is defined as (Faghri, 1995):

$$q_\delta = -\left(\frac{2\alpha}{2-\alpha}\right)\frac{h_{fg}}{\sqrt{2\pi R_g}}\left[\frac{p_v}{\sqrt{T_v}} - \frac{(p_{\mathrm{sat}})_\delta}{\sqrt{T_\delta}}\right] \tag{25}$$

where p_v and $(p_{\mathrm{sat}})_\delta$ are the saturation pressures corresponding to T_v and at the thin liquid film interface, respectively. The following two algebraic equations should be solved to determine T_δ for every point along the z-direction. The relation between the saturation vapor pressure over the thin evaporating film, $(p_{\mathrm{sat}})_\delta$, affected by the surface tension, and the normal saturation pressure corresponding to T_δ, $p_{\mathrm{sat}}(T_\delta)$, is given by the extended Kelvin equation (Faghri, 1995):

$$(p_{\mathrm{sat}})_\delta = p_{\mathrm{sat}}(T_\delta) \exp\left[\frac{(p_{\mathrm{sat}})_\delta - p_{\mathrm{sat}}(T_\delta) - \sigma K + p_d}{\rho_\ell R_g T_\delta}\right] \tag{26}$$

where K is the local curvature of the liquid-vapor interface defined by the term in outer brackets in eq. (10). Noticing that under steady state conditions, q_δ is due to heat conduction through the liquid film, it follows from this condition and eq. (25):

$$T_\delta = T_w + \frac{(R-\delta)}{k_l}\ln\frac{R}{R-\delta}\left(\frac{2\alpha}{2-\alpha}\right)\frac{h_{fg}}{\sqrt{2\pi R_g}}\left[\frac{p_v}{\sqrt{T_v}} - \frac{(p_{\mathrm{sat}})_\delta}{\sqrt{T_\delta}}\right] \tag{27}$$

Equations (26) and (27) determine the interfacial temperature, T_δ, and pressure, $(p_{\mathrm{sat}})_\delta$, for a given vapor pressure, $p_v = p_{v,\mathrm{sat}}(T_v)$, temperature of the solid-liquid interface, T_w, and the liquid film thickness, δ.

For the case of variable wall temperature, an additional variable, T_w, and first order ordinary differential equation must be added to the seven previously specified.

T_w is local wall temperature and can vary along the condenser length. If the convective heat transfer coefficient at the outer tube wall, h_o and the cooling liquid temperature, T_∞, are known, the local wall temperature can be defined using an energy balance.

$$h_o(T_w - T_\infty) = \frac{1}{2\pi R}\frac{dQ}{dz} \tag{28}$$

Another boundary condition is also required and that is given by

$$z = 0, T_w = T_{w,in} \tag{29}$$

Numerical Procedure

Equations (1), (8), (13), (15), and (16) with corresponding boundary conditions have been solved using the standard Runge-Kutta procedure. Algebraic equations (26) and (27) with two unknowns, $(p_{sat})_\delta$ and T_δ, have been solved numerically for every point on z using a standard numerical procedure

(Wegstein's iteration method). All the unknown variables were found with the accuracy of 0.0005%. During the numerical procedure the interval $0 \leq z \leq L_\delta$ was divided into at least 500 parts, and the thermophysical properties of the saturated vapor and liquid were recalculated for each of the parts at the corresponding vapor temperature $T_v(z)$.

Results and Discussion

Figure 3 (a) shows variation of the liquid film thickness along the condenser with a constant wall temperature of 340 K. The vapor ($T_{v,in}$ = 363 K) pressure drop over the condensation length is insignificant compared to the liquid pressure drop as shown in Figs. 3 (b, c). Condensation is more intensive in the region where the film thickness is at the minimum. For the cases of Q_{in}= 8 W and Q_{in} = 10 W, representing complete condensation and critical complete condensation, respectively, the incoming vapor is totally condensed. This is not true for Q_{in}= 12 W, the incomplete condensation case. Figure 3 (d) shows the cumulative sum of the heat removed from the vapor by condensation. For Q_{in} = 12 W, not all of the heat load coming into the condenser is rejected at the termination of the calculation.

Results are obtained for the convective cooling boundary condition shown in Fig. 4. The wall temperature is non-uniform with a significant increase just prior to the point of complete condensation, coincident with the thinning of the liquid film, as shown in Fig. 4 (d). Decrease of the convective heat transfer coefficient, h_o, from 20,000 to 15,000 W/m^{2}K resulted in an increase of the wall temperature that shortened the condensation length, as shown in Fig. 4 (a, d).

Summary of the Complete Condensation Phenomenon
Features of complete condensation in the annular film regime include the segregation of liquid and vapor into distinct regions within the tube. Initially, the annular film thickness increases gradually in the downstream direction. After reaching the local maximum value, it suddenly decreases to its minimum thickness and then dramatically increases to the radius of the tube. The region at the convergence of the liquid film is similar to the classic capillary meniscus in appearance. This forms a well defined location marking the transition to single-phase liquid flow. Downstream of the location of the meniscus-like surface, the entire cross section of the tube is occupied by liquid. Any additional heat removal downstream of this location only results in subcooling of the liquid. The axial distance from the inlet of the condenser tube at z = 0 to the location at which the entire cross section is filled with liquid is defined as L_δ, the condensation length.

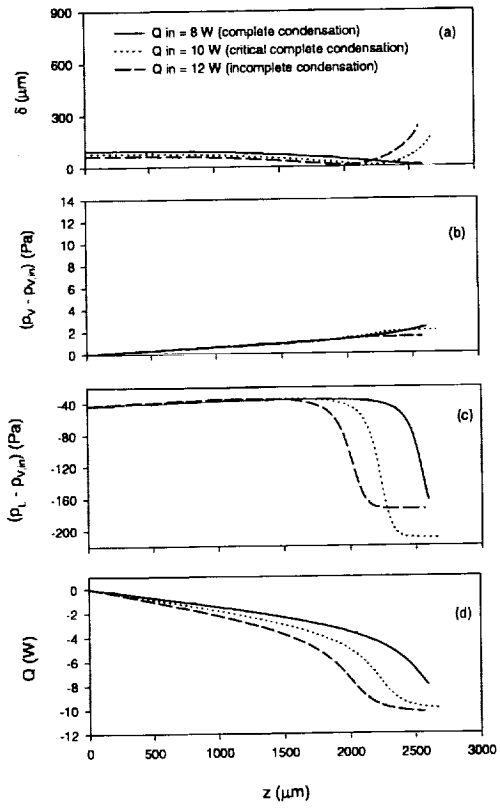

Figure 3: Annular film condensation in circular tube with constant wall temperature. $R = 1.5mm$, $m_t = 0.01g/s$, $T_w = 340K$, $T_v = 363K$ (a) film thickness (b) vapor pressure (c) liquid pressure (d) cumulative heat rate rejected

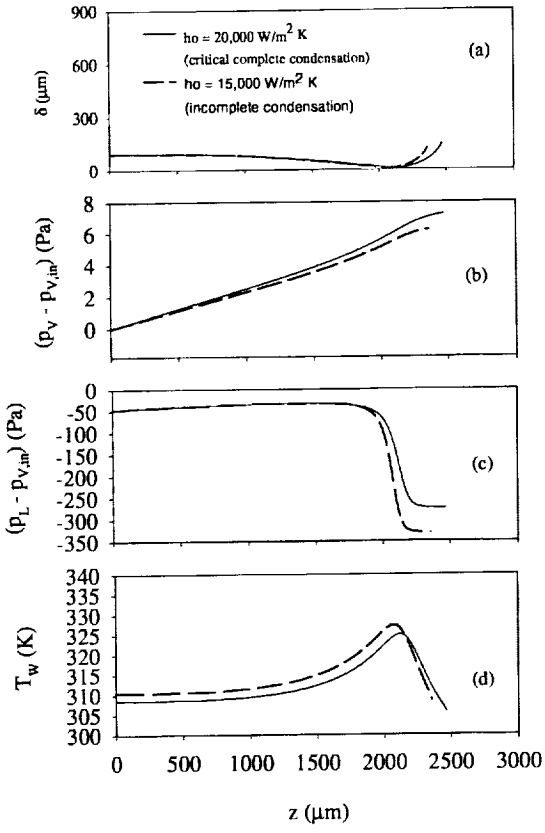

Figure 4: Annular film condensation in circular tube with convective boundary condition. $R = 1.5mm$, $m_l = 0.01g/s$, $T_{v,in} = 323K$, $T_{\inf} = 300K$, $Q_{in} = 5.83W$ (a) film thickness (b) vapor pressure (c) liquid pressure (d) wall temperature

Conclusions

Based on the numerical results and visual observations, the following conclusions have been made.

1. Length of film condensation in miniature tubes is very restricted due to surface tension effects that result in complete condensation a short distance from the condenser inlet.

2. The complete condensation length is a non-linear function of the vapor-wall temperature difference, increasing with the temperature difference approaching zero.

3. Pressure drop in the vapor phase was usually insignificant compared to the pressure drop in liquid. Consequently, the vapor temperature variation along the condenser was infinitesimal.

4. Variation of the wall temperature can be significant for convective cooling boundary condition.

5. Complete condensation in small diameter tubes is a truly steady phenomenon.

A very distinct transition is anticipated between the steady phenomenon of complete condensation and the next two-phase flow regime, which is referred to here as incomplete condensation. It is anticipated that incomplete condensation will be characterized by fluctuations of the liquid-vapor interface in the annular film which result in bubbles of vapor passing downstream of confluence of the liquid film. The meniscus-like feature will no longer be stationary and an unsteady two-phase flow bubbly-type flow will exist in the tube.

Acknowledgments

Funding for this work was provided by NASA Grant NAG3-1870 and NSF Grant CTS-941458.

References

Begg, E., Khrustalev, D., and Faghri, A., "Complete Condensation of Forced Convection Two Phase Flow in a Miniature Tube," to be presented at ASME International Conference, Anaheim, CA. Nov. 1998.

Bankston, C.A. and Smith, H.J., 1973, "Vapor Flow in Cylindrical Heat Pipes," ASME J. Heat Transfer, Vol.95, pp. 371-376.

Collier, J. G. and Thome, J. R., 1994, Convective Boiling and Condensation, Third Edition, Oxford University Press, New York.

Faghri, A., 1995 Heat Pipe Science and Technology, Taylor and Francis, Washington, D.C.

Munoz-Cobo, J.L., Herranz, L., Sancho, J., Tkachenko, I., and Verdu, G., 1996, "Turbulent Vapor Condensation With Noncondensible Gases in Vertical Tubes," Int. J. Heat Mass Transfer, Vol. 39, No. 15, pp. 3249 - 3260,.

Srinivasan, V. and Shah, R. K., 1997, "Condensation in Compact Heat Exchangers," Enhanced Heat Transfer, vol. 4, pp. 237-256.

ACOUSTIC STREAMING IN MICROGRAVITY: FLOW STABILITY AND HEAT TRANSFER ENHANCEMENT

E.H. Trinh , Jet Propulsion Laboratory, California Institute of Technology, MS 183-401, 4800 Oak Grove Drive, Pasadena CA 91109, Eugene.H.Trinh@jpl.nasa.gov

INTRODUCTION

The virtual elimination of natural buoyancy in microgravity significantly impacts the rates of heat and mass transport between solid structures or between phases in disperse fluid systems. Artificially induced flows must therefore be introduced in order to provide the required enhancement and to avoid the shutdown of needed heat and mass exchanges. We are developing an acoustic method based on streaming flows to provide the additional circulation in systems where standard mechanical flow actuators are not easily implemented, or practical. This approach is well suited for small-scale or even miniature structures and for multiphase systems such as multi-bubble or droplet suspensions in a fluid host medium. In addition to providing a precise control on the global streaming flow characteristics, this method also the direct modification of the local single particle environment by inducing oscillatory motion of the fluid particle surface. The application of acoustic streaming to heat and mass transport enhancement is not novel, and it has been investigated in the past [**1-4**]. We believe, however, that the results we present in this paper on the interaction between single fluid particles and streaming flows are new, and they have the potential to impact the technology developed for use in microgravity.

In this paper, we will first briefly discuss the experimental approach, and we will present results for drops and bubbles levitated in a liquid host and the effects of shape oscillations and capillary waves on the local flow fields. We will also report some preliminary results on the use of streaming flows for the control of the evaporation rate and rotation of electrostatically levitated droplets in 1-G. The purpose of this paper is not to discuss technical issues in detail, but to present an overview of the various aspects of this research task.

EXPERIMENTAL APPROACH

The work described in this paper has been carried out using single particle levitation based on ultrasonic and electrostatic methods in liquid as well as gaseous host media. A typical system consists of one or a few single droplets or bubbles levitated or trapped in a resonant cavity. Acoustic streaming flows are generated, and the flow fields are characterized both in the absence as well as in the presence of the particles. Detailed observation of the dynamics of the fluid particle motion and of the local flow environment is carried out through optical observation and visualization through suspended tracer particles. Three-dimensional imaging is implemented through a multi-camera setup, and quantitative flow measurements will be carried out using a pulsed Particle Image Velocimetry system.

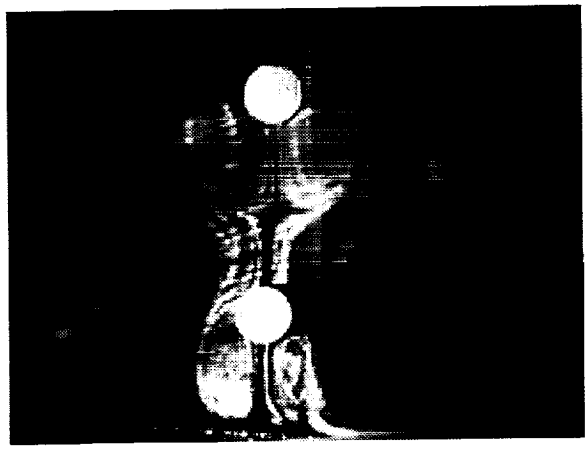

Figure 1 is a photograph showing a chamber enclosing an ultrasonic device and two solid spherical particles levitated in the standing wave. The streaming flow field is visualized using incense smoke, which mostly composed of droplets about 0.5 μm in diameter. Shown are vortices attached to the lower hemisphere of each levitated sample. The ultrasonic standing wave has a frequency of 23 kHz and the host fluid is air.

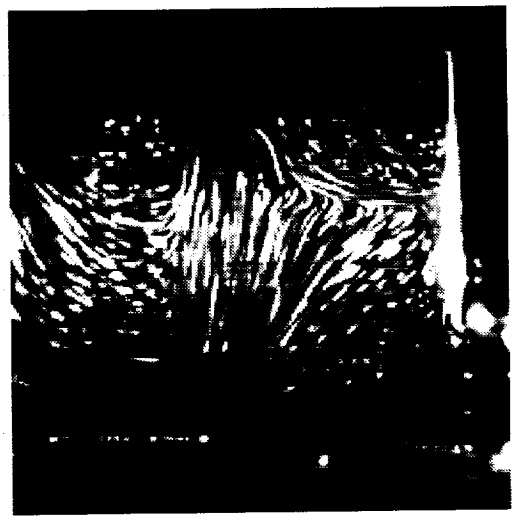

Figure 2 is a time-exposure photograph showing a water-filled ultrasonic resonant cell and the streaming flow generated by a transducer placed at the chamber bottom. The flow has been made visible using suspended polymer particles in the liquid and illuminated by a laser sheet. The water-filled cell resonates at 22 kHz and at 66 kHz.

In some experiments, we have used electrostatic levitated charged droplets in order to investigate the streaming flow fields at low ultrasonic power. This combination of electric and ultrasonic fields allows a quasi simulation of microgravity conditions that might require only low to moderate forced convection.

INDUCED STREAMING FLOW and BUBBLES and DROPLETS in LIQUIDS

The acoustic parameters and the geometry of the cell determine the morphology of the streaming flow fields within closed cavities. The transducer generating the primary sound wave generates a steady outward flow that is redirected by the walls of the container. The presence of a strong primary standing wave also contributes to the detailed distribution of the induced circulation, although the classic results of Andrade [**5**] showing vortices distributed between nodes and antinodes of a standing wave are not often found in our experimental results. In general, for moderate acoustic pressure and in both the cases of gas and liquid host fluids, we have found that the streaming flow pattern in a resonant chamber with a multi-wavelength standing wave is invariably in the form of a single toroidal vortex having its main axis coincident with the chamber symmetry axis. The levitated fluid particles are thus immersed in this primary circulation, and the rate at which they transfer energy and matter to the environment is significantly affected by this outer streaming flow. In the cases where the inner to outer fluid viscosity ratio is low, one would also expect the appearance of internal circulation. This was experimentally confirmed by examining levitated silicone oil drops in distilled water.

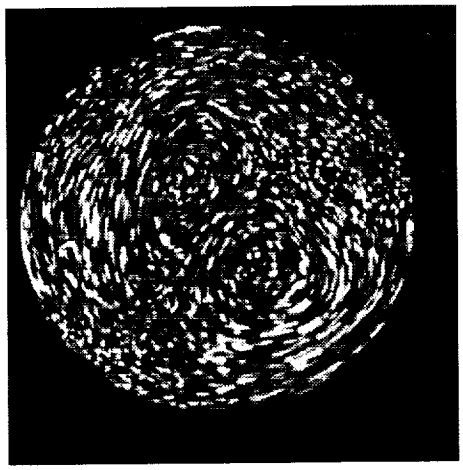

Figure 3 shows a time-exposed photograph of a drop containing undissolved dye particles and trapped at a pressure antinode of a 22 kHz ultrasonic standing wave. The drop is 0.8 cm in diameter and the exposure time is 5 seconds. Although this drop displays a characteristic dipole flow pattern, more typical internal flows do not show such high degree of symmetry.

Figure 4 shows photographs of internal flows observed inside air bubbles trapped at the pressure nodal plane of a 23 kHz ultrasonic standing wave. The bubble diameter is 0.4 cm and contains incense smoke. The photographs are actually prints of a single frame video image taken at a shutter speed of 1/50 s. Although only one lobe is clearly visible on the prints; the flow pattern is that of a symmetrical toroidal vortex. It is thus apparent that streaming will alter both the external and internal flow environments of isolated drops and bubbles immersed in a liquid harboring an ultrasonic standing wave.

In addition to the technical issue of implementing a method for enhancing heat and mass transfer in a low-gravity environment, the quantitative characterization of the induced internal flows in droplets and bubbles must be resolved in the absence of natural buoyancy. A complete isothermal experimental system is extremely difficult to achieve due to the ultrasonic energy input from the sound generator. The resulting slight thermal gradient in the gravitational field invariably drives buoyant convection.

Direct interaction between the ultrasonic field and the fluid particles also contributes to the generation of forced convection in the immediate particle vicinity. Due to parametric coupling, capillary waves with frequency equal to half the acoustic frequency are induced on the upper surface of trapped bubbles. We had previously observed the existence of these waves [**6**(Asaki et al.)], but only recent flow visualization of the flow field external to the bubble has shown that these waves also induce substantial steady fluid flow in the liquid around the bubble surface. A detailed study of the flow inside the bubble also shows a sig-

nificant enhancement when capillary waves are present. This increase in both internal and external circulation is reflected in a faster rate of air dissolution into the host water: this rate has been measured to be up to a factor of three greater for a bubble with capillary waves than for one with a smooth interface.

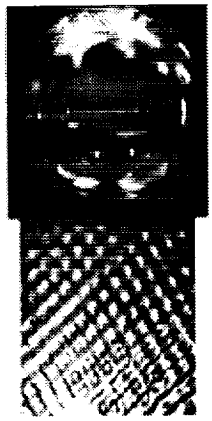

Figure 5 shows a video still frame of the capillary

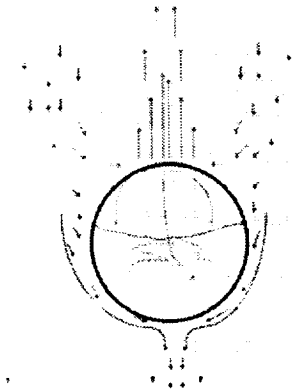

waves as recorded under stroboscopic illumination. Also shown is a schematic description of the asymmetric forced convection associated with these waves.

Another approach to the generation of local circulation is derived from the effects of driven drop and bubble *shape* oscillations. An examination of the flow field external to the oscillating fluid particles reveals significant symmetrical forced convection spatially extending to a distance equal to several particle diameters.

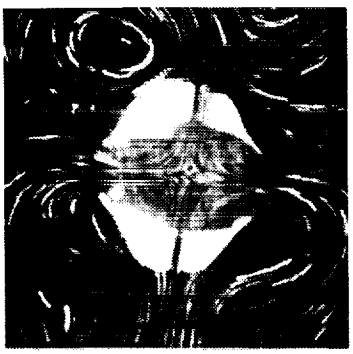

Figure 6 is a time-exposure of a levitated drop driven into the fundamental mode of shape oscillations. The recorded motion of tracer particles illuminated by a laser sheet shows the vortical steady flow generated by the shape oscillations in addition to the time varying oscillatory motion.

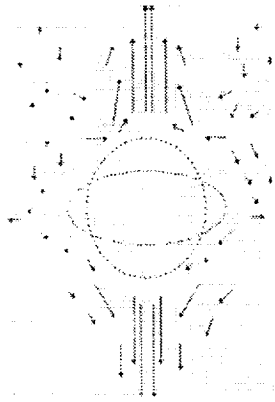

Also shown is a schematic description of the induced flow around an oscillating bubble.

STREAMING FLOW in RESONANT CHAMBERS in AIR and AROUND LEVITATED or SUSPENDED SAMPLES

The advantages of the acoustic streaming method in the generation of forced flows arise from the avoidance of major equipment requiring mechanical moving parts, and in the direct interaction between the acoustic field and the objects immersed in it. This is vividly illustrated by the generation of attached vortices on any solid or liquid samples (see figure 1). In a typical application requiring a closed chamber, the only requirement is an acoustic device generating a one dimensional high intensity standing wave to be used as the source of the steady flow. Regular three-dimensional vortical motion will naturally establish itself within the enclosed volume. The length scale of applicable experimental systems can be as large as 10 cm or as small as 0.01 cm. **Figure 7** is a photograph of a steady streaming flow field in a near cubical chamber with a standing wave at 23 kHz. This is a two-dimensional image of a three-dimensional flow field: in addition to the velocity component in the plane of the image, a perpendicular component also exists in the direction normal to the plane of the picture. A thorough mixing of the air within the chamber is therefore carried out by the acoustically-forced convective flow.

A streaming velocity as high as several meters per second has been observed in high amplitude ultrasonic standing waves in closed chambers, thus leading to the generation of turbulent flow fields. Low-gravity applications, however, will probably require a more moder-

ate range of flow parameters as a primary requirement appears to be the need to compensate for the absence of natural buoyancy or free convection.

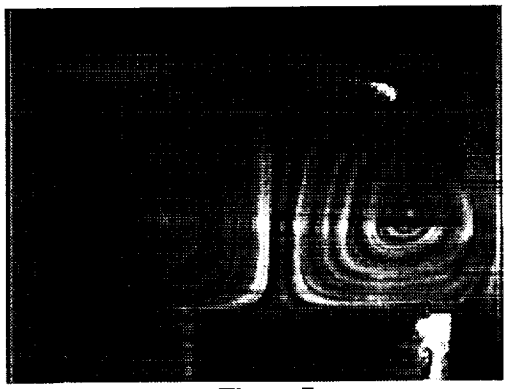

Figure 7

The streaming velocity observed in this study ranges from 0.1 to over 100 cm/s in air and from 0.1 to 5 cm/s in water.

A fundamental scientific issue in fluid dynamics is the stability of vortical flow. We believe that the streaming flows around a heated spherical samples in a high intensity sound wave can be used as a simple experimental system to investigate this problem. In this instance of coupled fluid dynamical and heat transport interaction, a transition to instability of attached vortices is observed as the streaming Reynolds number (based on the streaming flow velocity and the diameter of the spherical sample) is slowly increased. Vortex stretching, instability, and finally shedding can be observed in detail. Experimentation of microgravity would allow the elimination of the natural convection contribution, and would therefore drastically simplify the analysis.

Figure 8 shows the stretching and detaching of toroidal vortex initially attached to the upstream side of a heated sample positioned near the velocity antinode of an ultrasonic standing wave.

Although the results presented in this paper are mostly for isothermal systems, we have also carried out measurements of laser-heated levitated samples and the effects of streaming flow velocity on the hot sample temperature [**7,8**]. The results indicate that for the same radiant input power in air at atmospheric pressure, a moderate streaming flow velocity reduces the temperature of a levitated sample by over 30%.

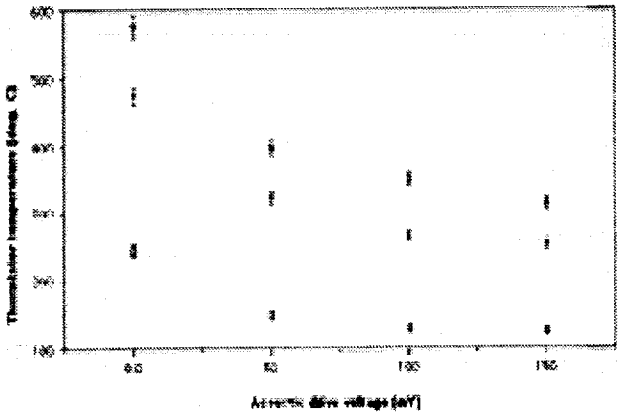

Figure 9 is a plot of the temperature of a spot-heated thermistor positioned at the velocity antinode of an ultrasonic standing wave as a function of the acoustic drive amplitude. The streaming Reynolds number is roughly proportional to the square of the drive voltage. At the highest acoustic level used in this test, the initial temperature of the 2 mm diameter, 5 mm long cylindrical thermistor is lowered from 580 to about 325 °C. The streaming flow and the acoustic motion effectively remove heat from the local heat source into the surrounding gas.

As a final topic, we will address the effects of streaming flows on the rotational stability of freely levitated single particle. Previous flight experiments using acoustic positioning have shown that high intensity sound fields used to position drops in microgravity also induce an uncontrolled sample rotation along a well determined axis whose direction varies with the acoustic parameters settings. Since rotation of a particle also affects its heat and mass transport characteristics, such an issue is relevant to our current studies. We have speculated that the steady streaming flow fields are responsible for this unexpected additional torque. In order to validate this supposition, we have studied the rotational behavior of an electrostatically levitated droplet carrying a surface charge using an ultrasonic-electrostatic hybrid apparatus. This device allows the independent levitation of droplets through either ultrasonic or electrostatic means, but more importantly, it allows the study of the effects of very low acoustic field on a levitated droplet. We have found that sample rotation can be effectively controlled

through acoustic parameter adjustments: Both the orientation of the rotation axis and the rotation rate can be varied by changing the frequency and the amplitude of the ultrasonic standing wave. The effects of these parameter changes on the streaming flow field have been observed using flow visualization and PIV methods.

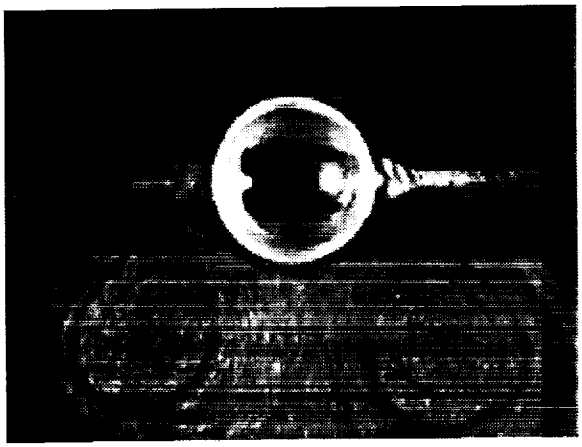

Figure 10a shows a levitated water drop in a stationary, non-rotating state, together with the flow pattern obtained from the scattering from suspended incense smoke illuminated by a laser sheet. A nearly symmetrical toroidal vortex is shown attached to the levitated drop.

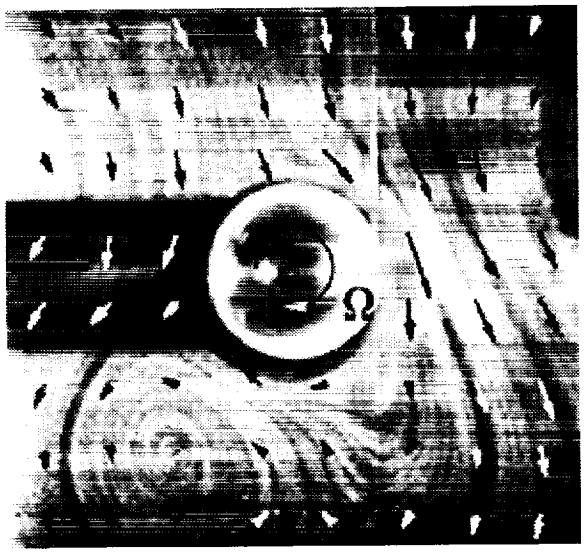

Figure 10b shows the same drop after appropriate changes have been made to the acoustic settings. Upon altering the acoustic parameters, the characteristics of the flow field start to change, breaking the initial symmetrical pattern. Rotation sets in after a threshold is reached, and a steady flow pattern results from the motion of both the air and the levitated drop.

SUMMARY

The objective of above summarized description of this research task is to illustrate the potential for the technological application of acoustic methods to active control of forced convection in microgravity. We believe that the versatility and simplicity of these techniques are a definite improvement over standard mechanical flow generation systems. We have seen that one has the ability to generate substantial forced circulation in both liquids and gases, from a macroscopic to a very small scale, as well as the capability to control the dynamics of individual fluid particles in a multiphase suspension. Significant enhancement of the heat transfer has been demonstrated, and the possibility of fine-tuning experimental parameters to control sample rotation has been validated. In addition to these issues dealing with practical applications, we have discovered a wealth of new physical phenomena of relevance to current interest in fundamental fluid dynamics.

ACKNOWLEDGMENTS

The research described in this paper was carried out at the Jet Propulsion Laboratory, California Institute of Technology, under funding from the Microgravity Research Division of the National Aeronautics and Space Administration.

REFERENCES

B.J. Davidson, "Heat transfer from a vibrating circular cylinder". Int. J. Heat Mass transfer, **16**, 1703 (1973)

Y.Y. Borisov and N.M. Gynkiva, "Acoustic Drying", in *Physical Principles of Ultrasonic Technology*, L.D. Rosenberg Editor, Vol. 2, Plenum, N.Y. (1973)

R.M. Fand and J. Kaye, "the influence of sound on free convection from a horizontal cylinder", J. Heat Transfer **83**, 2 (1961) and **83**, 133 (1961)

P.D. Richardson, "Heat transfer from a circular cylinder by acoustic streaming", J. Fluid Mech. **30**, 337 (1967), J. Acoust. Soc. Am. **36**,2323 (1964), *Proceedings of the Third International Heat Transfer Conference*, **3**, 71 (1966)

E.N. da C. Andrade," On the circulation caused by the vibration of air in a tube", Proc. Roy. Soc. London **A 134**, 445 (1931)

T. J. Asaki, P.L. Marston. and E.H. Trinh "Shape oscillations of bubbles in water driven by modulated ultrasonic radiation pressure: observation and detection

with scattered laser light", , J. Acoust. Soc. Am. **93**, 706 (1993)

E.H. Trinh and J.L. Robey, " Experimental study of streaming flows associated with ultrasonic levitators ", Phys. Fluids **6,** 3567 (1994)

E.H. Trinh and S.S. Sadhal "Acoustic streaming and processing of low melting point materials", , Heat Transfer in Microgravity Systems, S.S. Sadhal and A. Gopinath Eds. HTD-vol 290, 46-52, ASME, NY 1994.

Session 6B

Special Topics II

EXTENSIONAL RHEOMETRY OF POLYMER SOLUTIONS AND THE UNIAXIAL ELONGATION OF VISCOELASTIC FILAMENTS

G.H. McKinley[1], Stephen H. Spiegelberg[1], Shelley L. Anna[1] and Minwu Yao[2],
[1]Department of Mechanical Engineering, M.I.T., Cambridge MA 02139, USA,
[2]Ohio Aerospace Institute, Brookpark, OH 44132, USA

1. INTRODUCTION

In a recent review [1] for the National Research Council on the future research trends in non-Newtonian fluid mechanics, Denn remarks that "There are two major outstanding problems in rheological measurement. One is the measurement of extensional stresses of mobile fluids such as polymer solutions, ... This measurement is essential for determining the predictive power of constitutive equations and the flow is closely related to many important processing situations." Pioneered by Matta & Tytus [2] and Sridhar *et al.* [3], the filament stretching device is one of the most promising experimental techniques that has been developed for providing accurate measurements of the transient extensional viscosity for polymer solutions. In the filament stretching apparatus, a cylindrical liquid bridge of aspect ratio $\Lambda_0 \equiv L_0/R_0$ is first generated between two concentric circular plates and then elongated by pulling one or both of the end-plate fixtures at an exponentially-increasing rate as indicated schematically in Fig.1. It is hoped that the resulting flow kinematics in the liquid column approximate an ideal uniaxial elongational flow and the extensional viscosity function is then determined from the axial force at the end-plate a which is measured as a function of time, whilst the total Hencky strain applied to the material is computed from the total stretch imposed on the sample.

For very small fluid samples, gravitational body forces can be neglected, however it becomes increasingly difficult to quantitatively measure the very small and rapidly-varying tensile forces generated in the fluid filament. Conversely, for large samples in which dynamical evolution of the tensile force can readily be measured, gravitational sagging in a $1g$ environment makes analysis of the kinematics and dynamics impossible without *a priori* choice of a constitutive model for the fluid. This defeats the initial design object of using the device as a rheometer for deducing the constitutive response of the fluid. Both effects can be overcome in a μg environment; however, even in reduced gravity, the deformable nature of the free-surface of the test fluid and the no-slip boundary conditions pinning the liquid bridge to the rigid endplates preclude generation of truly homogeneous kinematics in a filament stretching device, and it is essential to combine experimental measurements with computational rheometry in order to understand the dynamical characteristics of the apparatus.

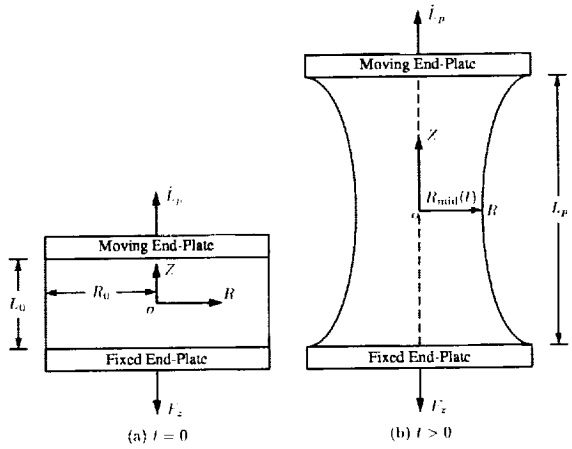

Figure. 1 Schematic Diagram of the filament Stretching Device.

2. NUMERICAL SIMULATIONS & CONSTITUTIVE EQUATIONS

Simulation of fluid motion in a filament stretching device constitutes a transient two-dimensional free-surface problem in non-Newtonian fluid dynamics. Details of the finite element method, remeshing algorithms and time-stepping used to solve this problem are provided elsewhere [4,5]. Here we focus primarily on the form of constitutive model chosen to characterize the experimental test fluids. In the present work we focus on single relaxation mode formulations of two common nonlinear differential constitutive equations which can accurately capture the viscoelastic characteristics of polymer solutions; (a) the Finitely Extensible Nonlinear Elastic FENE dumbbell model and (b) the Giesekus model [6].

These constitutive equations can be written compactly in the following form:

$$A_{(1)} = -\frac{1}{\lambda_1}\left[I + \alpha(A - I)\right]\cdot\left[f(trA)A - I\right] \quad (1)$$

Where the subscript (1) indicates the upper-convected derivative

$$A_{(1)} = \frac{\partial A}{\partial t} + \boldsymbol{v}\cdot\nabla A - \left\{\nabla \boldsymbol{v}^{T}\cdot A + A\cdot\nabla \boldsymbol{v}\right\} \quad (2)$$

Here $A \equiv \langle QQ \rangle$ is the ensemble average of the second moment of the end-to-end vector (Q) characterizing the overall conformation of the individual polymer chains, λ_1 is the fluid relaxation time and $f(trA) = L^2/(L^2 - trA)$. The parameter L characterizes the finite extensibility of the dumbbells and α is a measure of the anisotropic drag that acts on an elongated polymer chain. The total stress arising from the polymer and the Newtonian solvent is then given by

$$\tau = \eta_s \dot{\gamma} + G f(trA) A \quad (3)$$

where η_s is the solvent viscosity, G is the elastic modulus of the polymer and $\eta_p \equiv G\lambda_1$ is the polymeric contribution to the total zero-shear rate viscosity, $\eta_0 \equiv \eta_s + \eta_p$. The retardation parameter is denoted $\beta \equiv \eta_s/\eta_0$. A Newtonian fluid corresponds to $G = 0$; the FENE-P model is given by $\alpha = 0$, and the Giesekus model is given by $L^2 \to \infty$, $\alpha > 0$.

For a uniaxial extensional flow with imposed stretch rate $\dot{E}$, the dimensionless rate of deformation is characterized by the Deborah number $De \equiv \lambda_1 \dot{E}$ and the total stretch imparted to a fluid element is characterized by the Hencky (or 'true') strain measure $\varepsilon = \dot{E}t$. Both the FENE-P and Giesekus viscoelastic models predict a finite extensional viscosity at large strains, and it is thus possible to choose values of α or L^2 that give *identical* steady state extensional viscosities and simply focus on the role of the *transient uniaxial extensional viscosity*. As we show below, this material function plays a key role in the evolution of the filament. In the limit $L^2 = 1/\alpha \to \infty$ the two models reduce to the quasi-linear Oldroyd-B model [6] and the transient extensional viscosity grows without bound for all strains.

In the numerical results presented below we retain elastic effects (De) and surface tension effects (as characterized by the Capillary number, $Ca \equiv \eta_0 \dot{E} R_0/\sigma$) but ignore gravitational and inertial effects.

3. OVERVIEW OF RESULTS

We have extensively investigated the dynamical evolution of elongating viscoelastic fluid columns in filament stretching rheometers both numerically and experimentally, and detailed results can be found elsewhere [4-5,7-9]. Here we first provide a broad overview of the important non-Newtonian phenomena that can be observed in such devices and then focus more closely on mechanisms for filament rupture at long times (high strains).

In this research, two distinct classes of polymeric fluids have been investigated: *(i)* dilute polymer solutions which exhibit pronounced strain-hardening (e.g. polystyrene (PS) or polyisobutylene (PIB)-based 'Boger fluids' [7,8]), and *(ii)* concentrated polymer solutions which are strongly shear-thinning in simple steady shear flow and only show weakly strain-hardening behavior in extension. It is found from both experimental and numerical studies that, under the same stretching conditions, the dynamical response of these two classes of viscoelastic fluids is dramatically different.

For a Boger fluid exhibiting a constant shear viscosity and a pronounced strain-hardening in uniaxial extension, the overall evolutionary dynamic behavior of an elongating liquid in a filament stretching device is now fairly well understood. A more detailed summary of the key observations for this type of fluid has been given elsewhere [9]. Due to the very large (exponential) increase in the transient extensional viscosity, the filament radius becomes progressively more axially uniform at large strains and hence leads to an increasingly homogeneous extensional deformation. As a result of this strain-hardening, the failure mechanism for the slender fluid columns is dramatically different from the capillary-driven breakup observed in Newtonian fluid jets which exhibit no strain-hardening [10,11]. In a filament stretching device, the large axial tensile stresses developed at large strains inhibit further elongation in the mid-region of the liquid bridge. Instead, the fluid reservoirs near either rigid end-plate are rapidly drained of fluid. The increasing curvature of the free surface in this region and the resulting gradients in the normal stresses lead to the onset of a local elastic instability [8]. Consequently, the stretching capability of the device (as characterized

by the maximum achievable Hencky strain) is limited by the onset of a viscoelastic failure mechanism originating near the end-plates.

It is clear from Figure 2 (shown below), that varying the extensional rheology can significantly change the evolution of the filament profile. Semi-dilute or concentrated polymer solutions (which can be well-modeled by the Giesekus model) typically exhibit shear-thinning viscometric rheological properties and significantly less pronounced strain-hardening in extension. The current understanding of their extensional rheological behavior is still very limited. device never become spatially or temporally homogeneous.

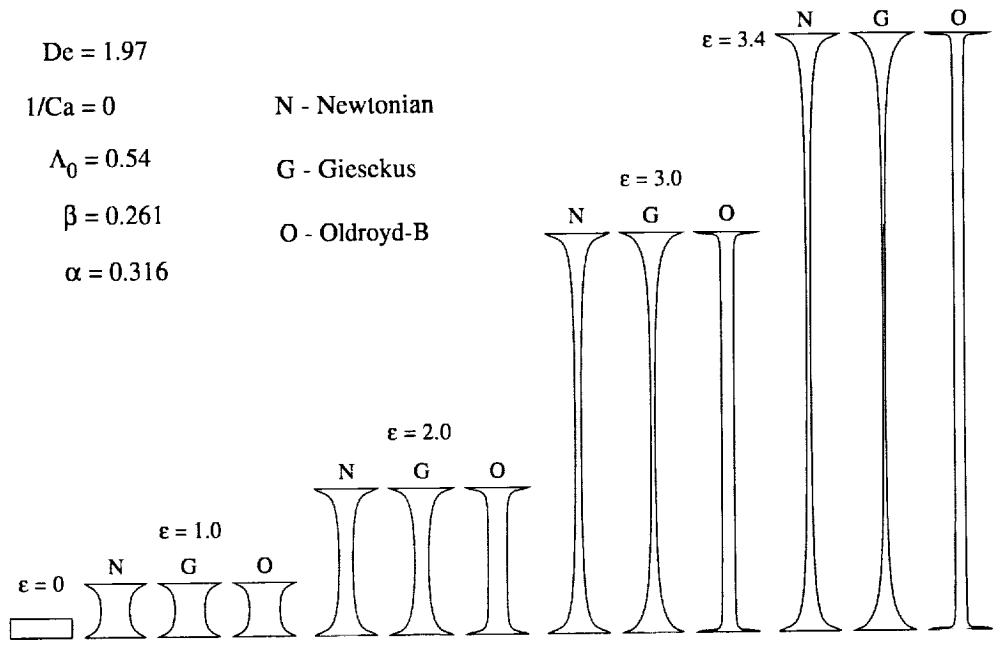

Figure 2 Comparison of the predicted profiles for viscous and viscoelastic filaments described by the Newtonian (N), Oldroyd-B (O) and Giesekus (G) constitutive equations during uniaxial elongation at De = 1.97.

In a recent study, Hassager *et al.* [22] show that as the parameter controlling the level of strain-hardening in the fluid is varied and the ultimate steady-state extensional viscosity is gradually decreased then the filament can undergo a ductile failure in which the radius of the filament rapidly decreases to zero at the axial mid-plane. This *unstable necking* phenomenon may be expected to severely compromise the ability of the filament stretching device to measure the extensional viscosity of weakly strain-hardening fluids such as polymer melts and concentrated polymer solutions. Little experimental data for such materials has been available to date; however recently we have used filament stretching rheometry to investigate a range of concentrated polymeric fluids from concentrated solutions to pressure-sensitive adhesives [9,13], and we now proceed to describe some selected observations in further detail.

4. Results for Weakly Strain-Hardening Materials

Here we focus on a combined experimental and numerical study of the dynamical behavior of shear-thinning and weakly strain-hardening concen-

trated polymer solutions. Further details are reported by Yao *et al.* [5, 9]. The numerical simulations are coupled with experimental measurements using a 5.0 wt.% solution of monodisperse polystyrene and show that even for such concentrated polymeric fluids it is possible to quantitatively measure the transient uniaxial extensional viscosity over a range of strain rates. Although the deformation in the elongating fluid filament is neither spatially nor temporally homogeneous, when a single uniaxial stretching profile is applied to the end-plates of the device, accurate measurements of the tensile force and the rate of deformation of fluid elements near the mid-plane of the filament are sufficient to extract the transient extensional viscosity function. One important characteristic predicted by the simulations with the Giesekus model is that after an initial period of linear viscoelastic stress growth, the rate of necking in the fluid filament increases much more rapidly than is observed in either a corresponding Newtonian fluid or in an ideal elastic fluid (modeled by the Oldroyd-B or FENE-P constitutive equation). Consequently, this leads to the onset of unstable necking and the simulations suggest that the filament will eventually fail, or *rupture* in a finite time. The evolution in the radius $R_{mid}(t)$ measured at the midplane of the filament is shown in Figure 3. The dashed lines with slopes –0.5 and –0.75 indicate theoretical estimates of the evolution in $R_{mid}(t)$ assuming homogeneous elongation or a lubrication-like squeeze flow at short times, respectively.

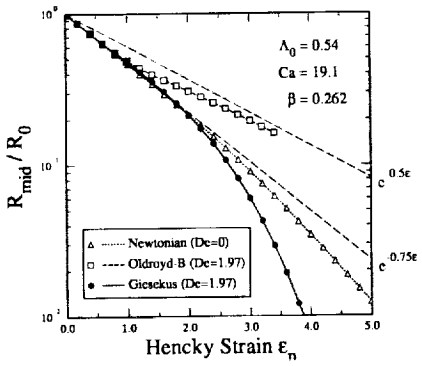

Figure 3. Evolution in the filament radius at the midplane as a function of strain for Newtonian, Oldroyd-B and Giesekus fluids at same imposed stretching rate.

A generalized Considère criterion [9,12,13] can be used to help understand this unstable necking in the filament profile. This criterion can be obtained from energetic considerations of the static stability of an elastic column and it shows that homogeneous elongation of a viscoelastic filament is unstable when the tensile force in the column passes through a maximum. However, the rate of evolution in the necking is found to be a sensitive function of the dynamics of the chosen constitutive model [9, 12].

The primary function of the filament stretching rheometer is to measure the extensional viscosity, $\bar{\eta}^+(\dot{\varepsilon}_0, t)$ as a function of Hencky strain and Deborah number. It is known from theoretical analysis that the extensional viscosity of the weakly strain-hardening fluid (simulated by the Giesekus model) differs significantly from that of the pronounced strain-hardening fluid (represented by the Oldroyd-B model). The Oldroyd-B model predicts an unbounded polymer stress growth, whereas in the Giesekus model the transient stress growth function approaches a steady state at large strains. We can use observations of the midpoint radius of the filament and the tensile force exerted on the endplate to compare measured values of the transient extensional viscosity for the weakly strain-hardening test fluid with numerical simulations of the filament stretching device and with theoretical predictions for homogeneous uniaxial elongation.

A typical set of experimental data at an imposed dimensionless stretch rate of $De = 1.89$ is shown in Figure 4 below.

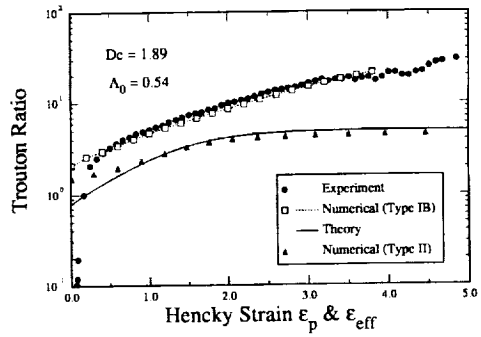

Figure 4. Evolution in transient Trouton ratio as a function of strain for 5 wt% PS/DOP fluid (•) and comparison with numerical simulations and 1D homogeneous theory.

The extensional viscosity function in a filament stretching device represents the extensional stress growth of the fluid elements in the vicinity of the mid-plane between the two end-plates. Consequently, an accurate estimate of the *local* extensional strain

rate at the mid-plane is necessary. Using the imposed axial extension rate $\dot{E}$ in the standard analysis provides an excellent comparison between the experiments (●) and the numerical calculations (denoted by 'type I' analysis and indicated by □ in Fig.4) but poor agreement with the ideal predicted response of the Giesekus model in homogeneous shear free flow (shown by the solid line). In particular, $\dot{E}$ underestimates the effective *local* extensional strain rate $\dot{\varepsilon}_{eff} \equiv -2\,d\ln(R_{mid})/dt$ at the mid-plane, especially at large strains. As a result, the Trouton ratio presented in Fig. 4 does not approach a steady state, instead it increases monotonically with strain (time). The results of numerical simulations, can also be post-processed using the actual extension rate computed from $R_{mid}(t)$ and the predicted Trouton ratio, using this 'Type II' analysis is plotted in Fig. 4 as a function of the effective strain

$$\varepsilon_{eff} = \int \dot{\varepsilon}_{eff}(t')\,dt' \qquad (4)$$

accumulated at the mid-plane. The use of $\dot{\varepsilon}_{eff}$ in the type II analysis provides a far superior approximation of the local extensional strain rate at the mid-plane. As a result, the numerical prediction shown in Fig. 4 approaches a steady state value that agrees well with the theoretical value expected for the Giesekus model with an anisotropic network parameter of $\alpha = 0.32$ deduced from the shear rheology.

5. Filament Failure Following Cessation of Stretching

Following the cessation of uniaxial elongation, the numerical simulations predict an interesting and complex evolution in the kinematics of the fluid filament. Initially the elastic tensile stresses in the column relax in the nonlinear form predicted theoretically, indicating that filament stretching devices can be used to monitor transient extensional stress relaxation, provided that the evolution history of the tensile force at the end-plate and the filament radius at the mid-plane are carefully measured. However, at longer times after cessation of stretching, the local extension rate at the axial mid-plane begins to increase rapidly, leading to a 'necking failure' that is greatly accelerated compared to that expected in a corresponding Newtonian filament. The calculations show that this unstable necking is not driven by the surface tension but by the viscoelasticity of the fluid, and is coupled with significant 'elastic recoil' of the previously elongated material near the end-plates.

The rate of necking in the column is a sensitive function of the extensional viscosity predicted by the constitutive model; in particular the *magnitude* and the *rate* of strain-hardening that occurs during uniaxial elongation. This phenomena can also be simply and accurately described by an appropriate set of coupled one-dimensional thin filament equations that use the finite element computations to provide a suitable initial condition for the distribution of the polymeric stresses in the filament.

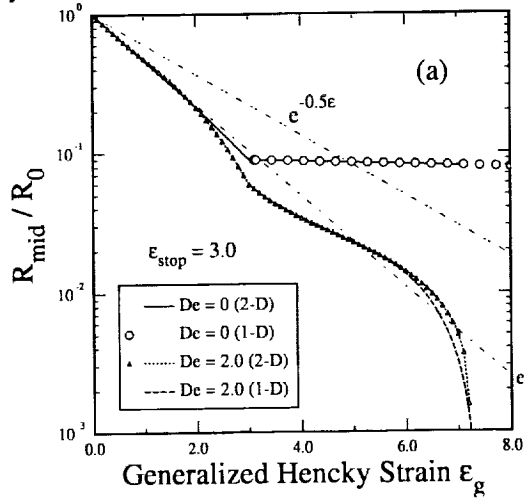

Figure 5. Evolution in the midpoint radius for a Newtonian and Giesekus filament following cessation of stretching at a final Hencky strain of $\varepsilon_{stop} = 3.0$

In Fig. 5, we show the evolution in the fluid kinematics as characterized by the mid-plane radius. For the weakly strain-hardening test fluid, the initial radial deformation is very similar to the Newtonian filament within the small strain range $\varepsilon \le 2$. Beyond that range, the necking in the test fluid filament starts to accelerate. At $\varepsilon = 3$, the necking rate of the viscoelastic test fluid is about twice that in the Newtonian fluid and is increasing monotonically with time. For the Newtonian fluid, the two-stage deformation history can be easily recognized from the sudden change in the slope of the $R_{mid}(t)$ curve shown in Fig. 5(a). Also shown in Fig.~11 are the predictions of a one-dimensional theory for the filament breakup. Previous work [10] has shown how a set of one-dimensional 'thin filament' equations can be used to model the evolution of a viscoelastic jet from an initial perturbed configuration, and accurately capture

both the initial linear viscoelastic amplification in disturbance growth rate and the subsequent nonlinear stabilization computed in more expensive finite element calculations. Asymptotic analysis of the one-dimensional equation set by Renardy [11] has further shown that the dynamical evolution of the necked jet is a sensitive function of the constitutive model chosen to describe the viscoelastic fluid.

We have adapted these ideas to explore the role of extensional fluid rheology on evolution of the long slender fluid column generated in a filament stretching apparatus following cessation of elongation. In Fig. 6 below, the initial condition is taken to be the necked configuration of a Newtonian filament at a strain of $\varepsilon_{stop} = 3$ (as shown in Fig 2 and 5). The relaxation time, viscosity and surface tension are held fixed and only the nonlinear parameter describing the degree of strain-hardening is varied.

The pronounced differences in the rate of thinning and the longevity of the thin filament predicted by this analysis is manifested in everyday concepts such as 'stringiness' and 'tackiness'. The numerical calculations suggest that measuring the time to failure is a simple and rapid probe of the magnitude of the extensional viscosity of a viscoelastic fluid. Current experiments in our laboratory are aimed at reproducing these observations experimentally.

References

[1] Denn, M.M., Research Trends in Fluid Dynamics, J. L. Lumley, A. Acrivos, L. G. Leal and S. Leibovich (ed.), AIP Press, New York, 1993.

[2] Matta, J.E. and Tytus, R.P, *J. Non-Newtonian Fluid Mech.*, **35**, (1990), 215-229.

[3] Tirtaatmadja, V. and Sridhar, T., *J. Rheol.*, **37**(6), (1993), 1081-1102.

[4] Yao, M. and McKinley, G.H., *J. Non-Newtonian Fluid Mech.*, **74**((1-3)), (1998), 47-88.

[5] Yao, M. and McKinley, G.H, *J. Non-Newtonian Fluid Mech.*, (1998), In press.

[6] Bird, R.B., Armstrong, R.C. and Hassager, O., Dynamics of Polymeric Liquids. Volume 1: Fluid Mechanics, 2nd Edition, Wiley Interscience, New York, 1987.

[7] Spiegelberg, S.H., Ables, D.C. and McKinley, G.H., *J. Non-Newtonian Fluid Mech.*, **64**(2-3), (1996), 229-267.

[8] Spiegelberg, S.H. and McKinley, G.H., *J. Non-Newtonian Fluid Mech.*, **67**, (1996), 49-76.

[9] Yao, M., Spiegelberg, S.H. and McKinley, G.H., *J. Non-Newtonian Fluids*, (1998), submitted.

[10] Bousfield, D.W., Keunings, R., Marrucci, G. and Denn, M.M., *J. Non-Newt. Fluid Mech.*, **21**, (1986), 79-97.

[11] Renardy, M., *J. Non-Newt. Fluid Mech.*, **59**, (1995), 267-282.

[12] Hassager, O., Kolte, M.I. and Renardy, M., *J. Non-Newt. Fluid Mech.*, **78** (1997),.

[13] Christensen, S.F. and McKinley, G.H., *Int. J. Adhesion & Adhesives*, (1998), in press.

[14] Malkin, A.Y. and Petrie, C.J.S., *J. Rheol.*, **41**(1), (1997), 1-25.

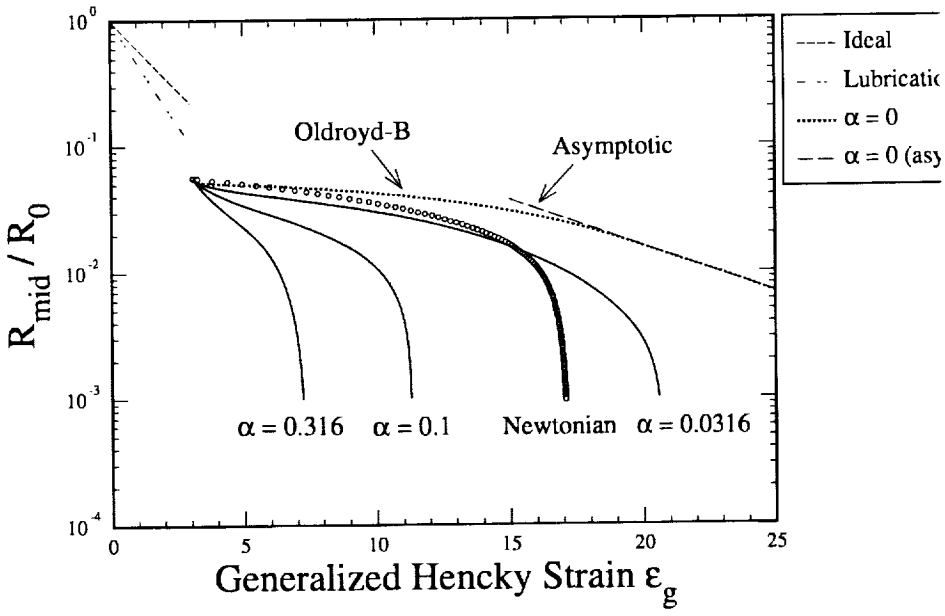

Figure 6 Necking and Breakup in a viscoelastic filament as a function of the nonlinear network parameter characterizing the degree of strain-hardening in the filament.

FLOW-INDUCED BIREFRINGENCE MEASUREMENT SYSTEM USING DUAL-CRYSTAL TRANSVERSE ELECTRO-OPTIC MODULATOR FOR MICROGRAVITY FLUID PHYSICS APPLICATIONS

Jeffrey R. Mackey, NYMA, Inc. NASA Lewis Group
2001 Aerospace Parkway, Brook Park, Ohio 44142 , jmackey@lerc.nasa.gov

ABSTRACT

We have developed a new instrument that can measure fast transient birefringence and polymer chain orientation angle in complex fluids. The instrument uses a dual-crystal transverse electro-optic modulator with the second crystal's modulation voltage applied 180° out of phase from that of the first crystal. In this manner, the second crystal compensates for the intrinsic static birefringence of the first crystal, *and* it doubles the modulation depth. By incorporating a transverse electro-optic modulator with two lithium-niobate ($LiNbO_3$) crystals oriented orthogonal to each other with a custom-designed optical system, we have produced a very small, robust instrument capable of fast transient retardation measurements. By measuring the sample thickness or optical path length through the sample, we can calculate the transient birefringence. This system can also measure dichroism.

We have compared the calibration results and retardation and orientation angle measurements of this instrument with those of a photoelastic modulator (PEM) based system using a quarter wave plate and a high-precision 1/16-wave plate to simulate a birefringent sample. Transient birefringence measurements on the order of 10^{-9} can be measured using either modulator.

INTRODUCTION

Existing polarimeters traditionally incorporate either a single-crystal PEM or a rotating retardation plate as the modulator element. Although these systems are capable of very sensitive birefringence and dichroism measurements, they are either too large or too fragile to survive the forces encountered by space-based experiments during launch and landing on board the STS or sounding rockets. For example, sounding rocket launch loads are typically on the order of 17g. In order to obtain the desired sensitivity while maintaining a stable and rugged configuration, we suggest using a dual-crystal transverse electro-optic modulator (EOM) geometry. The modulator crystals must be oriented with their principal axes orthogonal to each other and at ±45° with respect to the polarization state of the incident light. The drive voltage applied to the second crystal must be 180° from that of the first crystal. The suggested optical configuration is shown in figure 1.

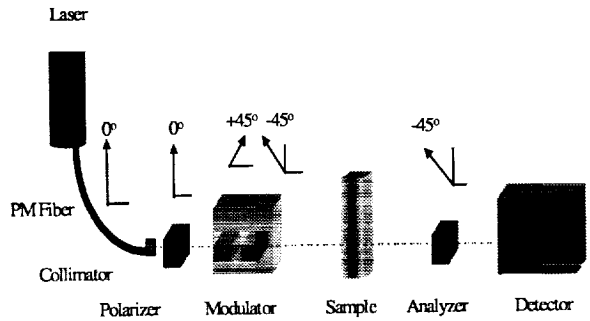

Figure 1. Birefringence Measurement System showing polarization and dual-crystal modulator geometry.

Transverse electro-optic modulators can be made very small, rugged and lightweight. $LiNbO_3$ crystals are non-hygroscopic, and they can be mounted in a resonant circuit to reduce electrical power needed to drive the modulator. These are all highly desirable qualities when designing an experiment suitable for space flight.

We have demonstrated through the Mueller matrix calculations and by experimentation how to design a flight-worthy electro-optically modulated birefringence measurement system. We show that the retardation and thus the birefringence of an optically transparent fluid polymer can be measured accurately using this novel technique.

OVERVIEW OF BIREFRINGENCE

Birefringence ($\Delta n'$) is the difference in a material's refractive index with respect to the polarization state of light propagating through it. In an optically transparent stressed polymer material, the orientation and degree of deformation of the molecular polymer chains cause an anisotropic polarization. If the light propagates through a birefringent material along the z-direction, the x and y components of its electric field vector will be different from one another. This results in a phase difference or retardation (δ) as the light traverses the sample material. If the material is not dichroic, then the retardation is related directly to its birefringence. This can be expressed as

$$\Delta n' = n_o - n_e = -\frac{\delta\lambda}{2\pi d} \qquad (1)$$

where n_o and n_e are the refractive indices for ordinary and extraordinary light rays respectively, λ is the vacuum wavelength of the light, and d is the sample material thickness.

One can apply this knowledge using the stress optic law, which provides a simple relationship between the material stress and the refractive index tensor. In terms of shear stress (τ_{xy}), the stress optic law can be expressed as

$$\tau_{xy} = \frac{1}{2} C\Delta n' \sin(2\chi(t)) \qquad (2)$$

where C is the materials stress optic coefficient and $\chi(t)$ is the time-variant orientation angle of the molecular polymer chains with respect to the flow or stress direction. Thus, in order to measure a material's shear stress, we must measure the birefringence and average molecular chain orientation angle simultaneously.

THEORY OF DUAL CRYSTAL TRANSVERSE ELECTRO-OPTIC MODULATION

We developed a dual-crystal modulation technique using the Stokes parameters and Mueller matrix representations of the optical elements. We implemented the theory using the transverse electro-optic effect or Pockel's effect and its application to the $LiNbO_3$ crystals as two separate Mueller matrices.

A birefringent crystal possesses two distinct indices of refraction. These indices are represented by n_o and n_e, which are the ordinary and extraordinary index of refraction, respectively. When a voltage is applied across the crystal in a direction normal to the direction of light propagation, the difference between polarization-sensitive refractive indices changes. This change results in a voltage-sensitive phase retardation between the ordinary and extraordinary light rays, which can be mathematically expressed as

$$\Delta\phi = \frac{2\pi}{\lambda}(n_o - n_e)L - \frac{2\pi}{\lambda} r_{33} n_o^{\,3} \frac{VL}{D} \qquad (3)$$

where r_{33} is the appropriate electro-optic coefficient, L is the crystal length, D is the distance between electrodes and V is the voltage applied across the crystal. If V is an alternating voltage, we can modulate the electric field vector or polarization state of the light passing through the crystal. For pure $LiNbO_3$, n_o= 2.2866 and n_e= 2.2028 at 20°C*. A transverse electro-optic crystal configuration is shown in figure 2.

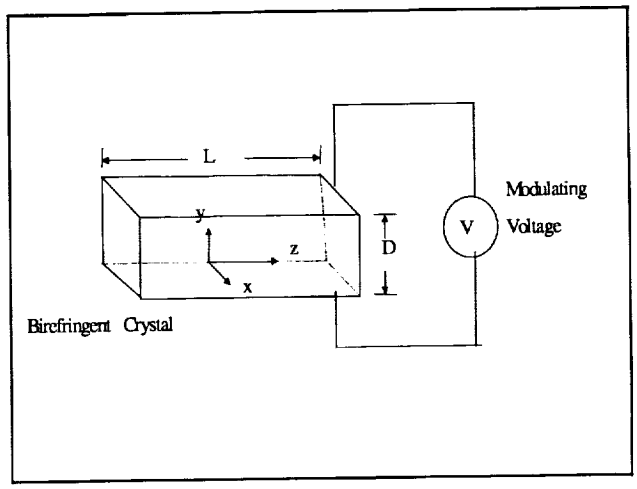

Figure 2. Transverse electro-optic modulator geometry. Light propagates in the z-direction. We apply modulation voltage in the ±y-direction.

From equation (3), we can see that the electro-optic effect is maximized when the electric field vector of plane-polarized light is incident on the left crystal face at a 45° angle with respect to the z-axis. We can also observe that there is static birefringence that depends largely on crystal length L. In many crystals, including $LiNbO_3$, this static birefringence is highly temperature dependent[2,4]. We have experimented with single-crystal $LiNbO_3$ modulators and have measured the effective static retardation to be 2.24×10^{-2} radians in a 40mm length crystal at 20°C. We see that this retardation corresponds to a static birefringence of 5.69×10^{-8} radians. Although the crystal's static birefringence is quite small, it is not thermally stable[2]. One may use a single-crystal transverse electro-optic modulator in this type of instrument, but the instrument must be operated in a temperature-stabilized environment. The temperature-dependent static birefringence is an undesirable property since it reduces the instrument's sensitivity and stability when measuring very small birefringence levels in a sample material. Fortunately, by using the dual-crystal configuration shown in the preceding figure 1, we can compensate for both the residual static birefringence and the thermal instability while doubling the modulation depth.

In order to derive how this geometry works, we need to describe how polarized light interacts with the optical elements. Since light is an electromagnetic wave,

* From Manufacturer's data sheet.

the Stokes vector, S that consists of four parameters, can characterize its polarization state. These parameters are I, Q, U, and V, which are based on the electric field vector.

$$S = \begin{bmatrix} I \\ Q \\ U \\ V \end{bmatrix} = \begin{bmatrix} (Ex(t))^2 + (Ey(t))^2 \\ (Ex(t))^2 - (Ey(t))^2 \\ 2Ex(t)Ey(t)\cos(\delta) \\ 2Ex(t)Ey(t)\sin(\delta) \end{bmatrix} \quad (4)$$

In equation (4), Ex(t) and Ey(t) are the time-dependent x and y electric field vector components, and δ is the instantaneous phase retardation between $-\pi$ and $+\pi$. The parameter I, represents the intensity of the light while the parameters Q, U, and V specify its state of polarization.

The polarization state of an optical system can be modeled using the Stokes vector of the incident light multiplied by the Mueller matrices of the individual optical elements. The multiplications are done in reverse order to generate the output Stokes vector that yields information about the subject material under study. That is, if we represent the incident light with the Stokes vector $[S_i]$ and have polarization optical elements represented by their 4x4 Mueller matrices [Analyzer], [Sample] and [Modulator] as shown in figure 3, the output Stokes vector is computed as

$$[S_{out}] = [\text{Analyzer}][\text{Sample}][\text{Modulator}][S_i]. \quad (5)$$

For the dual-crystal polarimeter in our experiment, we have the following polarization state configuration shown in figure 3. All angles are referenced looking into the laser. We define the input polarization at zero degrees. The dual-crystal transverse electro-optic modulator crystals are at ±45° and the analyzer is at -45° with respect to the input polarization state.

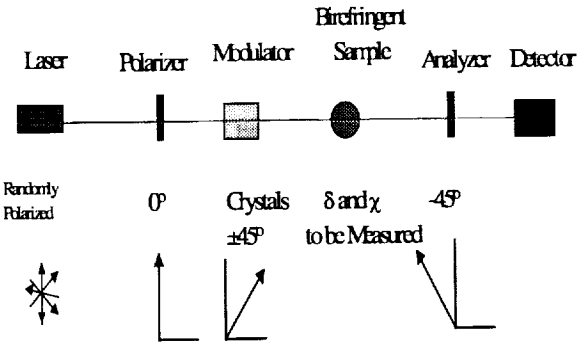

Figure 3. Polarization state representation of optical elements.

We multiplied the representative Mueller matrices in reverse order to calculate an equivalent system matrix that was then multiplied by the input Stokes vector. The resulting Stokes vector describes the intensity and polarization of the light emerging from the last element in the system matrix. Once equation (5) is computed using the matrix elements, it is Fourier-Bessel expanded so that I(t) can be written in terms of quantities measurable by two heterodyning lock-in amplifiers The time-variant intensity, I(t), is given by the first element of the resultant Stokes vector and is given below.

$$I(t) = Idc[1 + 2J_1(A_0)\sin(\omega t)\sin(\delta(t))\cos(2\chi(t)) + 2J_2(A_0)\cos(2\omega t)\{1 - \cos(\delta(t))\}\sin(2\chi(t))\cos(2\chi(t)) + \ldots] \quad (6)$$

where $A_0 = 2.4048$. Equation (6) gives us I(t) in terms of the in-phase and in-quadrature signal components.

INSTRUMENT STABILITY

Since thermal stability is a major problem for a single-crystal $LiNbO_3$ transverse electro-optic modulator, we performed stability tests. We configured the system with the input polarizer at 0°, the single-crystal modulator at +45°, and the analyzer at –45°. We placed a quarter wave plate in the sample space and rotated it to give approximately 1/16 wave retardation. This is where the I_ω and $I_{2\omega}$ signals are equal. We then separated these signals slightly by rotating the quarter wave plate a few degrees. We increased the laboratory temperature by 10°F over a period of 16 hours. We recorded data over this period to observe the signal variance. The stability of the single-crystal modulator is very poor due to the temperature dependence of the intrinsic birefringence of lithium niobate [4]. We then repeated this test using a dual-crystal $LiNbO_3$ modulator. Figure 4 shows the results of both tests.

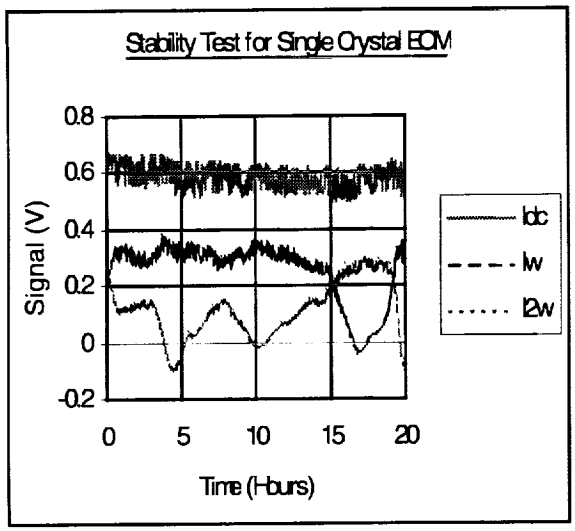

Figure 4a. Long term stability test results for a single-crystal EOM. The plots show the photodetector and lock-in amplifier signal outputs. Idc is the dc signal plus the detector bias voltage while $I\omega$ and $I2\omega$ are the first and second harmonic signals respectively.

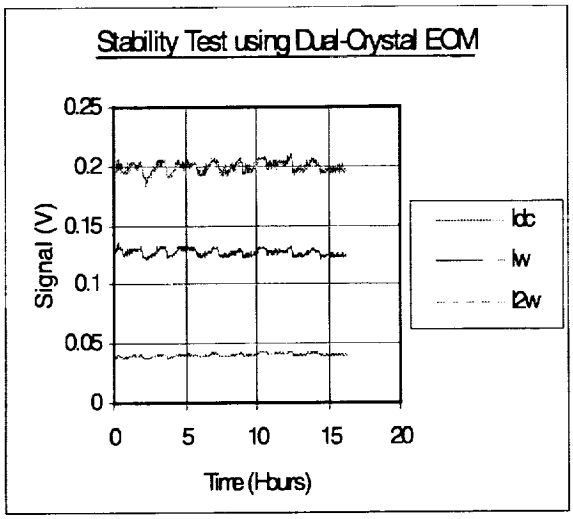

Figure 4b. Long term stability test results for a dual-crystal EOM. The plots show the photodetector and lock-in amplifier signal outputs. Idc is the dc signal plus the detector bias voltage while $I\omega$ and $I2\omega$ are the first and second harmonic signals respectively.

INSTRUMENT CALIBRATION

Since we wanted to set the instrument where $J_0(A)=0$, we performed a standard "zero-Bessel calibration" as described in reference 6. This method involves the measurement of the dc signal while incrementing the modulation voltage for three different retardation values in the sample space. The results are shown in figure 5a.

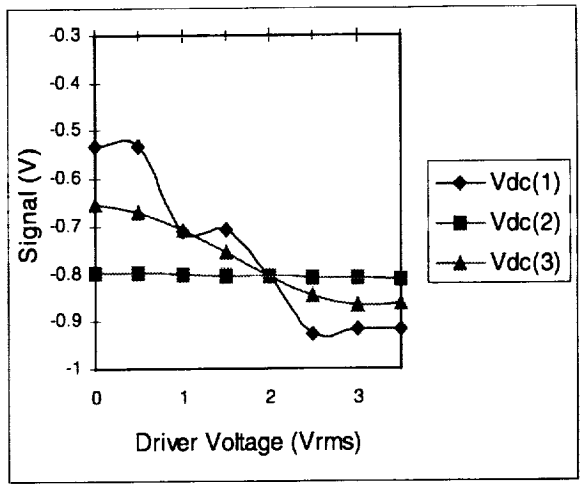

Figure 5a. "Zero-Bessel" plot to calibrate for $J_0(A)=0$. In this case, the dc signal is plotted against modulation voltage for three different retardation values in the sample space.

We observe that the approximate modulation voltage setting is 2V. This calibration method is subject to noise in the dc signal and is not as accurate as we would want.

There are several other ways to calibrate this system, but perhaps the most useful method is one that maps out the Bessel functions $J_1(A)$ and $J_2(A)$ simultaneously, yielding a full calibration sweep instead of just a single-point calibration measurement. With the instrument configured so that the input polarizer is at 0°, the electro-optic modulator crystals are at ±45°, and the analyzer is at –45°, we place a retardation plate in the sample space. As long as the retarder is oriented such that the first and second harmonic signals are present, we may increment the modulation voltage, record the in-phase and in-quadrature lock-in amplifier output signals, and scale these accordingly to observe their correlation with $J_1(A)$ and $J_2(A)$. The parameter A is proportional to the modulation voltage. The calibration plot then gives us our modulation voltage at any desired Bessel function value. We plotted the correlation between our electro-optic modulator and the theoretical Bessel function values in figure 5b.

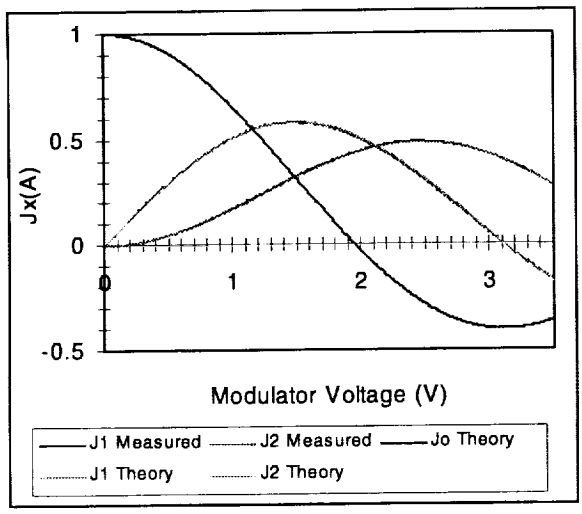

Figure 5b. Calibration curves generated using a dual-crystal transverse electro-optic modulator. Modulation voltage was incremented from 0 to 3.5V rms with the modulation frequency held constant at 42KHz.

From the figure 5b calibration plot, we may more accurately observe that $J_0(A)=0$ when our modulation voltage is approximately 1.95V rms. The calibration plots determine the correct modulation voltage where $J_0(A)=0$.

By setting the modulation voltage such that $J_0(A)=0$, we can easily obtain the sample retardation, $\delta(t)$ and sample orientation angle, $\chi(t)$. In this case, the value of A is 2.4048. The Bessel function calibration values are given as $J_0(A)=0$, $J_1(A)=0.5191$ and $J_2(A)=0.4317$.

MEASUREMENT RESULTS

We took measurements of the retardation and orientation angle of a rotating quarter wave plate using the electro-optically modulated system and the same optical system incorporating a photoelastic modulator (PEM) in place of the EOM. The intrinsic static strain retardation of the dual-crystal EOM was 3.85×10^{-4} while that of the PEM was an order of magnitude greater. We placed a quarter wave retardation plate in the sample space. We altered the retardation and orientation angle using a piezo-driven rotary mount to rotate the retardation plate at constant angular velocity. The dc signal component as well as the first two harmonics were recorded to calculate retardation and orientation angle simultaneously. These measurement results are shown in figure 6. We generated these plots using the Extensional Rheology Experiment flight prototype optical assembly. The optical assembly consists of a diode laser head, laser-to-fiber coupler, polarization-maintaining optical fiber, collimating microlens, beam splitter polarizer cube, polarizer/collimator mounting assembly with rotational adjustment capability, beam splitter analyzer cube, analyzer housing with rotational adjustment capability, analyzer-to-detector mounting fixture, and a high-speed silicone pin-diode based photodetector. All of these components were used in the optical configuration to compare performance between the PEM and EOM systems. The only component that we changed for this comparison was the modulator itself.

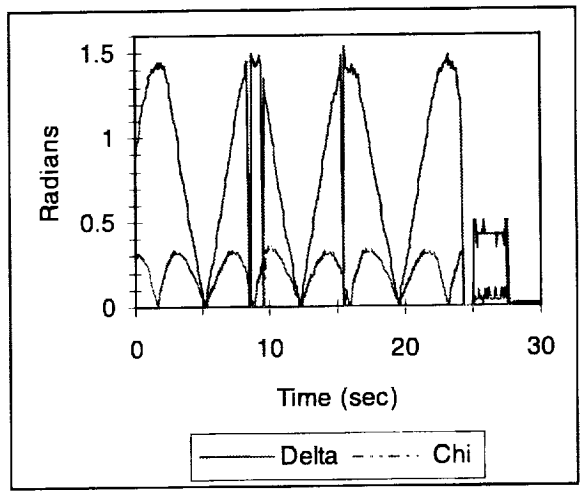

Figure 6a. Retardation (Delta) and Orientation Angle (Chi) vs. Time for a rotating quarter wave plate in the PEM-based system.

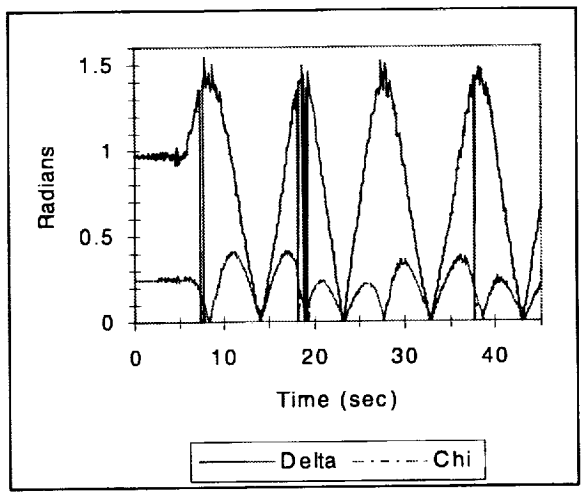

Figure 6b. Retardation (Delta) and Orientation Angle (Chi) vs. Time for a rotating quarter wave plate in the EOM-based system.

The figure 6 plots give the retardation ranging from zero to $\pi/2$ and the orientation angle ranging from zero

to $\pi/8$. The slight variation in the orientation angle on the figure 6b plot is due to the inability to rotate the EOM to the correct angle on our breadboard system. A very slight deviation leads to many other terms in the output Stokes vector. The orientation angle calculation is very sensitive to these terms. The final flight system design will correct this problem by enabling rotational alignment of the EOM.

To get a more accurate measurement of the retardation, we placed a precision $\pi/8$ (0.3927 radians) plate in the sample space. This retardation plate has a tolerance of ± 0.001 waves or ± 0.0063 radians according to the manufacturer. The PEM-based system measured the retardation at 0.401 radians while the EOM-based system measured it at 0.396 radians.

DISCUSSION AND CONCLUSIONS

We have developed a stable transverse electro-optically modulated birefringence measurement system suitable for microgravity fluid physics applications. The experimental results from the dual-crystal EOM compare favorably with those of the PEM. They also agree within the accepted tolerances of the retardation plates used. This type of modulation scheme has many advantages over existing modulation schemes. Advantages include variable modulation frequency from 0 to 100MHz, low power consumption, low mass, small size, and an extremely rugged package. The only potential disadvantage is that $LiNbO_3$ may experience photorefractive damage with high-powered lasers.

Due to its small size, this type of system may be useful in many types of terrestrial and microgravity applications where experiment space is very limited.

ACKNOWLEDGEMENTS

This work was funded as part of the Extensional Rheology Experiment (ERE). We thank Dr. Charles Hultgren of New Focus, Inc. for loaning us the electro-optic modulator while our units were being fabricated. We also thank Dr. Steve Spiegelberg of MIT for the loan of his photoelastic modulator and Dr. Ben Ovryn of the National Center for Microgravity Research for his calibration method. We also thank Efrain Patino of NYMA, Inc., for machining the custom optical mounts, Eric Anderson of ADF, Inc., for the modulator drive circuit design and Ed Selent of ADF, Inc., for the lock-in amplifier serial communications programming.

REFERENCES

1. Frattini, Paul L, Galante, Stephen R. and Chilcote, Steven M, "Practical Aspects of Polarization Modulated Flow Birefringence: A Technique-Oriented Review", Carnegie Mellon University, (1990).
2. "Practical Uses and Applications of Electro-Optic Modulators", New Focus, Inc, *Application Note # 2*.
3. Walker, M. J., "Matrix Calculus and the Stokes Parameters of Polarized Radiation", *J. Optical. Soc. Am.*, pp. 170-174, (1954).
4. Denton, R. T., Chen, F. S. and Ballman, A. A., "Lithium Tantalate Light Modulators", *Journal of Applied Physics*, Vol. 38, Number 4, pp. 1611-1617, March, (1967).
5. McKinley, G. H. and Spiegelberg, S. H., "The Extensional Rheology of Non-Newtonian Materials", Third Annual Microgravity Fluid Physics Conference, *NASA Conference Publication 3338*, pp. 377- 382, (1996.)
6. Oakberg, T., "PEM-90™ Photoelastic Modulator Systems User Manual", Hinds™ Instruments, Inc., (1994).

PHASE SHIFTED LASER FEEDBACK INTERFERENCE MICROSCOPY: APPLICATIONS TO FLUID PHYSICS PHENOMENA

B. Ovryn[1]and J. H. Andrews[2] ,[1]Mechanical and Aerospace Engineering, NCMR, Case Western Reserve University, NASA Lewis, MS 110-3, 21000 Brookpark Road, Cleveland, Ohio 44135 (ovryn@wave.lerc.nasa.gov) [2] Center for Photon Induced Processes, Physics and Astronomy, Youngstown State University,Youngstown, Ohio 44555

INTRODUCTION

We have combined the techniques of phase-shifting interferometry (PSI) and laser feedback interferometry (LFI) to produce a confocal interference microscope.[1] This new instrument can be used to measure changes in the optical path length (OPL) and discern variations in sample reflectivity. The PSI-LFI microscope has high dynamic range. Changes in OPL can be measured with subnanometer precision at dc. As with other applications of PSI, phase unwrapping can be employed to measure large changes in OPL. After a brief discussion of the basis of LFI, we demonstrate some of the characteristics of this instrument and its application to measuring the interface of a static drop on a coated silicon surface.

Since the invention of gas and semiconductor lasers, many investigators have shown that optical feedback can lead to a variety of complex changes in the operating characteristics of a laser, including, polarization changes, power fluctuations, lasing threshold and mode hopping, and chaos.[2-8] In spite of this complexity, several investigators have been able to measure changes in the optical path length (OPL) and to discern variations in sample reflectivity with a laser feedback interferometer (LFI); applications to atomic force and optical microscopy have been particularly fruitful. To produce accurate height profiles of a variety of objects, previous LFI microscopes have either used calibrated feedback loops to maintain an extremum of the LFI response (usually a minimum) as the topology varied or used modulation of the OPL (based upon either oscillation of the sample or the OPL through the electro-optic effect) combined with lock-in detection.[3,7,8]

Because phase measurements based upon lock-in detection require a trade-off between the increased signal-to-noise ratio and the complexity of the electronics and measurement, we have combined the principles of phase shifting interferometry (PSI) with laser feedback interferometry. The pixel sampling rate of the new instrument is not limited by the time constant associated with lock-in techniques, nor does it rely on a well calibrated feedback loop to yield a measurement of the OPL. As in other applications of PSI,[9] experimentally controlled phase changes are introduced and the phase and visibility are determined independently using an over-determined set of measurements of the intensity; both the phase and visibility are unaffected by the bias intensity.

A further attribute of this approach is that the effect of multiple reflections between the cavity and the sample surface can be determined and therefore it is not necessary (as has been done previously) to assume that they are negligible. The manifestations of the multiple reflections, are systematic oscillations in the LFI response as a function of the change in OPL between the laser's output mirror and the sample.

Provided that the time rate of change of the phase due to changes of the OPL is small compared to the inverse of the photon lifetime,[11,12] and that the laser's frequency is unperturbed by the laser feedback,[4,5,8] then there will not be any phase distortion in the response of the interferometer and the change in steady-state intensity due to feedback from the sample is given by:

$$I(m,b,\delta,\psi) = Io\{1 + m\cos(2k\delta + \psi)\sum_{j=0}^{\infty}(-b)^{j}\cos[j(2k\delta + \psi)]\} \quad (1)$$

where δ is the optical path length, k is the wave number, Ψ represents an experimentally controlled phase shift and m and b are given by:

$$m = K\frac{(1-R_2)\sqrt{R_2}\sqrt{R_{e\,ff}}}{1-R_1+1-R_2} \qquad b = \sqrt{R_2}\sqrt{R_{e\,ff}}$$

With the exception of the sum over multiple reflections between the output mirror of the laser and the sample, the measured intensity, I, given by Equation 1 is equivalent to the interference of two wavefronts and m can be interpreted as the fringe visibility.[3,14] In LFI, however, the fringe visibility depends upon the laser operating parameters which are included in K, as well as the reflectivities of the back and front laser mirrors, R_1 and R_2 and the effective sample reflectivity, R_{eff}, for coupling back into the laser cavity. Because the fringe visibility is directly proportional to the amplitude reflectivity of the object, a measurement of its spatial variation over a sample's surface, with constant laser parameters, can be used to map topology;, the visibility also depends upon the scalar product of the polarizations between the incident and reflected wavefronts.

In previous applications of PSI, the fringe visibility has been used to determine if the phase shift has produced adequate modulation of the intensity (for example, at individual pixels in an array detector); for modulation lower than the signal-to-noise ratio, the pixel is usually flagged as bad.[9,15,16] In an LFI microscope, however, a spatially varying visibility presents a direct measure of the change in sample reflectivity. By combining PSI with LFI, we have produced measurements of both the phase and fringe visibility and have

characterized the effect of multiple reflections on the measured quantities.

Phase shifting techniques can be applied to any realization of LFI. We first present an experiment to demonstrate measurements of phase and visibility in the presence of multiple reflections and then present an application to interference microscopy. The light from a Helium-Neon laser (Uniphase, Model 1107P, $\lambda = 632.8$ nm) passes through a neutral density (ND) filter (New Focus, Model 5514,5), modulated with an electro-optic modulator (New Focus, Model 4002) and then passes through a polarizer. After illuminating a single crystal silicon wafer held stationary at the focus of a microscope objective (Mitutoyo, Model G Plan NIR), the wavefront was then reflected and re-entered the laser cavity. The laser power was measured using a photodetector (New Focus, 1201) after transmission through the rear mirror. A triangular wave was applied to the modulator such that a change in the OPL of approximately $\lambda/8$ nm was acheived. Five discrete voltages were sequentially superimposed upon the modulator and the OPL and visibility were determined for various settings of the neutral density filter.[17] Figure 1 shows the visibility and OPL determined for two particular settings of the ND filter. For each of the OPL data sets, a linear least squares fit was subtracted. The standard deviation of the difference is used to produce a measure of the phase error. Figure 1 demonstrates that high signal-to-noise ratios can be achieved at extremely low fringe modulation. Unlike a Michelson interferometer, the fringe visibility in our PSI-LFI microscope does not exceed 50%.

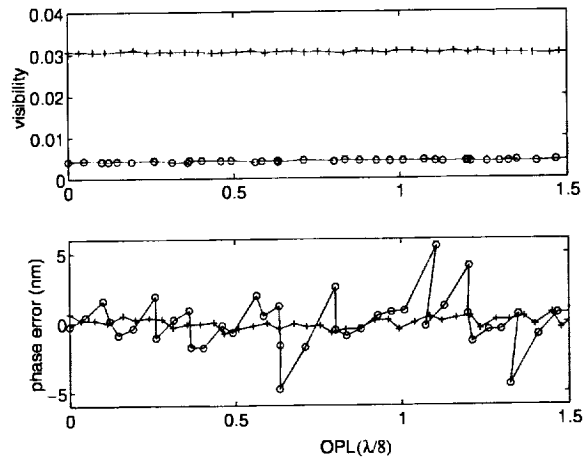

Figure 1. Visibility and phase measurements for two settings of the neutral density filter. Neither of these data sets indicate systematic oscillations, so only j = 1 in Eq. 1. The slope was removed from the linear ramp change in the OPL by subtracting a least squares line.

As the amount of light fed back into the laser increases, the light can take more than a single pass between laser and sample. The manifestation of the multiple reflections are the systematic oscillations in the OPL and visibility shown in Figure 2. Superposed on the visibility and OPL data is a fit based upon several additional terms in Eq. 1.[1] The bottom plot in Figure 2 shows the error in the OPL obtained from the standard deviation of the difference between the data and the prediction based upon the model. Figure 3 shows the error in the OPL as a function of the change in visibility obtained for several positions of the OD filter. The errors shown in Figure 3 were calculated from differences between the data and least squares lines at low visibility and from differences based upon the model at higher visibility (circles).

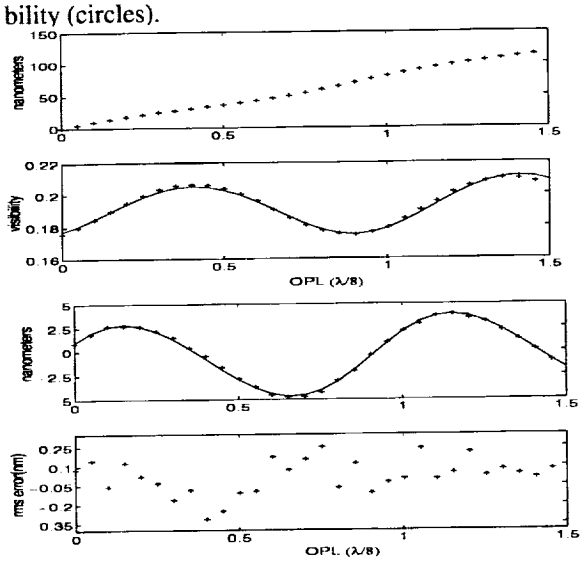

Figure 2. Visibility and OPL measurements obtained with moderately high visibility. Once the linear slope has been removed from the OPL oscillations become apparent. The solid lines represent predictions using several terms in Eq. 1. The bottom plot represents the difference between the data and the model.

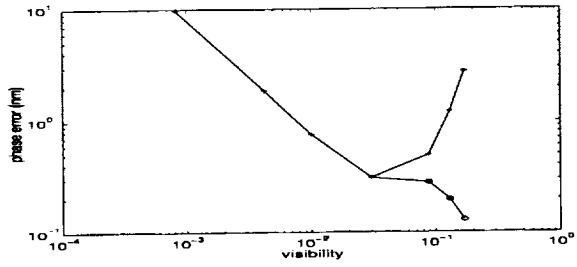

Figure 3: OPL error at different fringe visibilities. Errors were obtained by subtracting least squares lines from the measured OPL. At high visibility, fits based upon Eq. 1. were used as well (o).

Figure 3 demonstrates that the phase error is inversely proportional to the visibility. At higher visibilities, however, it is essential that the data are corrected for the effect of systematic oscillations. Figure 4 represents the amount of power reflected back through the OD filter as a function of the visibility. On the basis of Figures 3 and 4, it can be observed that small errors in the OPL may be obtained even when only a fraction of the power is reflected back to the laser.

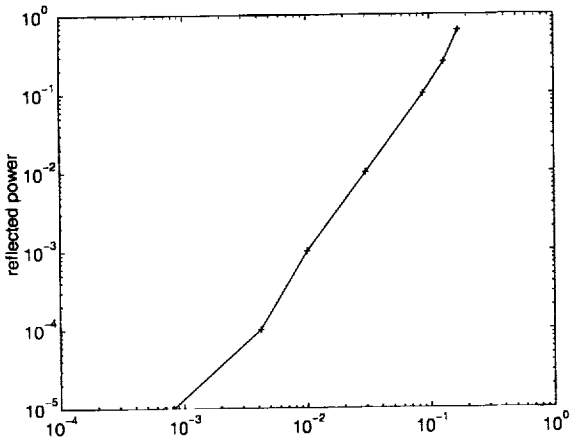

Figure 4. Amount of power that is reflected back through the OD filters as a function of the measured visibility.

If required, it is possible to increase the signal-to-noise ratio obtained at low reflected powers by averaging repeatedly acquired data sets. Due to both environmental disturbances (which may appear systematic) and changes in the sample, however, temporal averaging may be of limited utility in increasing the S/N. Figure 5 shows that averaging 10 individual phase measurements increases the S/N by approximately $\sqrt{10}$; the phase error has been reduced from 6.9 nm to about 2.2 nm.

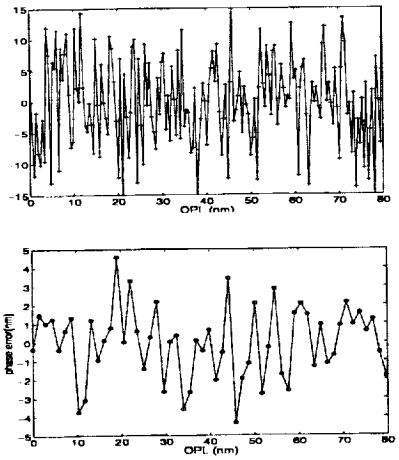

Figure 5. Reduction in phase error due to temporal averaging of the phase measurements. The error base been reduced from 6.9 nm to 2.2 nm by averaging 10 phase measurements.

Phase shifted laser feedback microscopy

We have combined PSI-LFI with a high numerical aperture, reflecting light microscope. While this instrument is not yet optimally designed (further immunity from environmental disturbances is still possible), we have obtained data which demonstrate the utility of the instrument. Figures 6 shows data obtained from an optical reference standard (Geller Microanalytical, Inc, Model MRS-3). The reference standard consists of 1000 angstroms of chromium (300 angstroms of chromium oxide on top of 700 angstroms of chromium) on top of approximately 1000 angstroms of indium tin oxide on top of a quartz substrate. The pitch of the patterns and height of the chromium layer are NIST traceable; the height of the chromium layer is 100 nm. The reference standard has several patterns of varying spatial frequency. The sample was mounted on a piezoelectric stage which translated along two axes under closed-loop control (Queensgate, Inc., Model S221). Both scanning and data acquisition were accomplished with Labview which operated the stage via the parallel port.

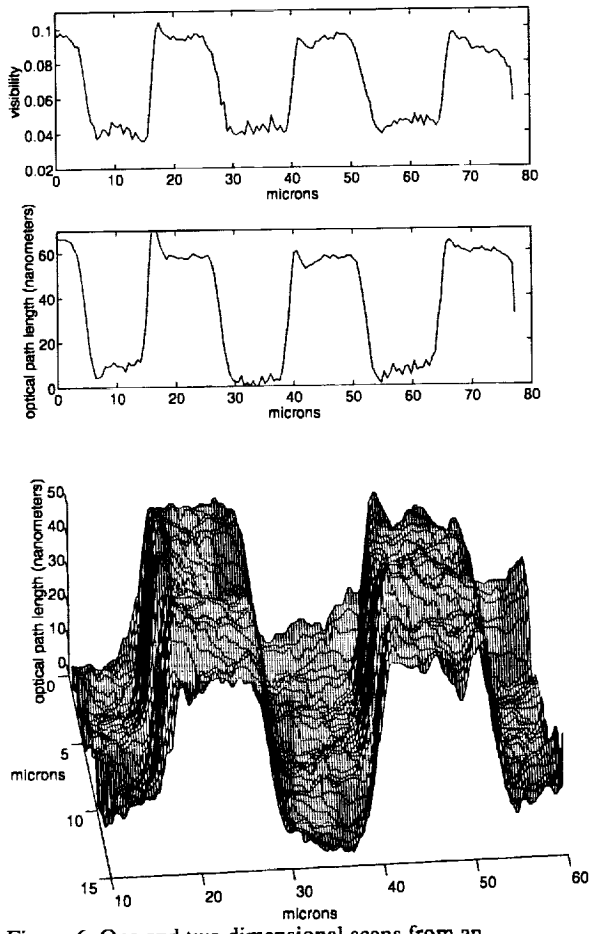

Figure 6. One and two dimensional scans from an area on the reference standard. The two scan corresponds to the region from 10 to 60 microns in the 1D scan.

Figure 7 shows a visibility image obtained by raster scanning an etched silicon sample. Figure 9, shows the visibility (top) and OPL (bottom) obtained from a single 16 μm line scan across the bottom-most solid bar of Fig. 7. Both the visibility and phase measurements reveal the step changes. Although this image was acquired without moving the sample along the optical axis, it is possible to use the measured parameters to control a feedback loop which adjusts the sample position at every pixel.

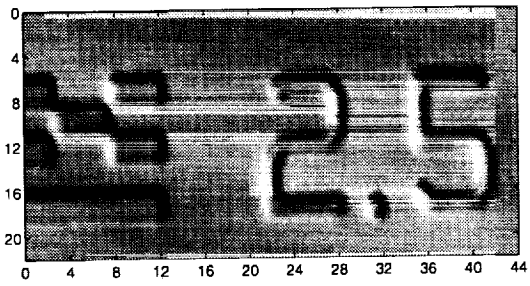

Figure 7. Visibility image obtained when an etched silicon sample was raster scanned in a phase- shifted, laser feedback microscope using a 50/0.8 NA objective.

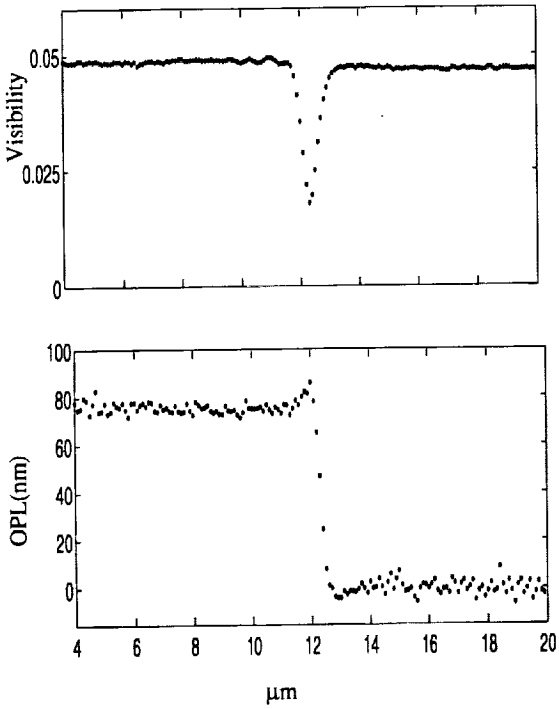

Figure 8. Visibility and OPL obtained from a single line scan across the bottom-most 2.5 μm pitch bar shown in Figure 8. Both the visibility and phase indicate the steps in the silicon. A linear slope of 7.6 nm/μm was subtracted from the OPL data.

MEASUREMENT OF INTERFACES

Figures 9 and 10 show the visibility and OPL measured across the edge of a 60,000 cS PDMS (silicone oil) drop deposited on a piece of fluorinated coated single crystal silicon wafer; the surface was wiped with toluene and dipped in the barrier coat. Images were obtained with a 50x/0.8 NA objective. There are systematic oscillations in both the visibility and the OPL due to multiple reflections.

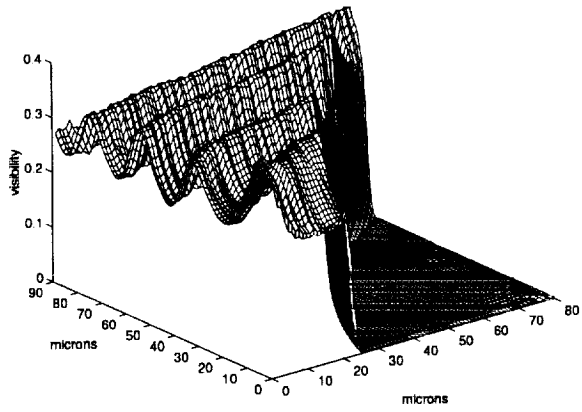

Figure 9. Visibility across the edge of a silicone oil drop on a coated piece of silicon wafer. The ripples are due to multiple reflections obtained at high visibility.

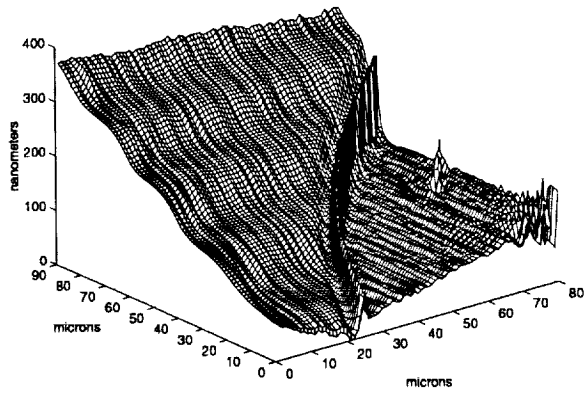

Figure 10. OPL across the edge of a silicone oil drop on a coated piece of silicon wafer. The ripples are due to multiple reflections obtained at high visibility. The slope of the silicon wafer can be observed.

RESPONSE TIME

The response time of the interferometer is limited by how quickly the photodetector can responds to the phase shifts applied to the electro-optic modulator. Figure 11 shows the output voltage applied electro-optic modulator and the response of the photodetector for two sets of five sequential phases required for a single phase measurement. Each of the phase shifts to the electro-optic modulator was briefly maintained so that averaging of the raw intensity from the photodetector could be obtained.

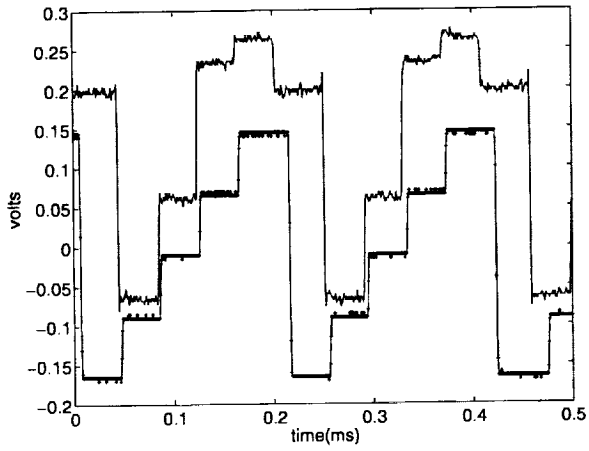

Figure 12. Response of the photodetector (top trace) to two sets of five sequential phase shifts (voltages) to the electro-optic modulator. Each set of five phase shifts is required for a single phase measurement. The brief intervals at each phase shift were used to average the raw intensity measurement.

CONCLUSIONS

We have designed a laser feedback interferometer which can be used to measure oscillatory and d.c. changes in the OPL. This interferometer can be combined with a.c. detection techniques or it can be used with d.c. phase shift methods. Changes in the OPL can be determined sub-nanometer accuracy at d.c. We have also verified the predicted oscillatory behavior of the interferometer at higher visibility. When combined with a high numerical aperture microscope, the method offers excellent edge detection. A further attribute of the method is that high signal-to-noise ratios may be achieved with low power deposition on the sample. Response times are limited by photon lifetime, detector electronics and modulator rise time rather than lock-in detection and feedback loop parameters.

REFERENCES

1. B. Ovryn and J. H. Andrews, Opt. Lett. 23(14) In press.
2. G. Stephan and D. Hugon, Phys. Rev. Lett. 55, 703 (1985).
3. A. Bearden, M. P. O'Neill, L. C. Osborne, and T. L .Wong, Optics Lett. 18, 238 (1993).
4. Th. H. Peek, P.T. Bolwijn, and C. Th. Alkemade, Am. J. Phys. 35, 820 (1967).
5. G. A. Acket, D. Lenstra, A.J. Den Boef, and B. H. Verbeek, IEEE J. Quant. Elect. QE20, 1163 (1984).
6. J. Mork, B. Tromberg, and J. Mark, IEEE J. Quant. Elect. 28, (1992).
7. R. Juskaitis, T. Wilson, and N.P. Rea, Opt. Comm. 109, 167 (1994).
8. D. Sarid, V. Weissenberger, D. A. Iams, and J. T. Ingle, IEEE J. Quant. Elect. 25, 1968 (1989).
9. K. Creath, in Progress in Optics XXVI, E. Wolf ed. (North-Holland, Amsterdam, 1988), pp. 349-393.
10. R. Lang and K. Kobayashi, J. Quant. Electr. QE-16, 347 (1980).
11. E. B. Hooper, Jr. and G. Bekefi, J. Appl. Phys. 37, 4083-4094 (1966), erratum, 38, 1998 (1967).
12. A. Yariv, Quantum Electronics (Wiley, New York, 1989), p. 192ff.
13. D. Lenstra, M. van Vaalen, and B. Jaskorzynska, Physica 125C, 255 (1984).
14. B. Ovryn, J. H. Andrews and S. Eppell, SPIE 2655, 153-162 (1996).
15. J. E. Greivenkamp and J. H. Bruning, "Phase shifting interferometry" in Optical Shop Testing, D. Malacara, Ed. (Wiley, New York, 1992). B. Ovryn and E. M. Haacke, Appl. Opt., 32,147 (1993).
16. In the absence of systematic errors, the signal-to-noise ratio of a phase measurement depends upon environmental perturbations, errors in the phase shifts and the error in the intensity measurements and is inversely proportional to the fringe visibility. See J. Schwider in Progress in Optics XXVIII, E. Wolf ed. (North-Holland, Amsterdam, 1990), pp. 272-343.
17. P. Hariharan, B. F. Oreb, and T. Eiju, Appl. Opt. 26, 2504 (1987); P. Hariharan, Appl. Opt. 26, 2506 (1987).

Session 6C

Convective Instability

Long-Wavelength Rupturing Instability in Surface-Tension-Driven Benard Convection

J. B. Swift[1], Stephen J. Van Hook[1], Ricardo Becerril[1], W. D. McCormick[1], H. L. Swinney[1], [1] Center for Nonlinear Dynamics and Dept. of Physics, The University of Texas, Austin TX 78712, USA, svanhook@chaos.ph.utexas.edu., Michael F. Schatz[2], [2] Georgia Institute of Technology, Atlanta, Georgia 30332. schatz@ranch.physics.gatech.edu.

1 INTRODUCTION

A liquid layer with a free upper surface and heated from below is subject to instabilities due to both thermocapillary and buoyancy forces. While buoyancy is usually dominant in terrestrial convection experiments, thermocapillarity is dominant in microgravity. Using thin liquid layers (< 0.05 cm), one can also achieve thermocapillary-dominated convection in terrestrial experiments. The criterion for determining that an experiment is thermocapillary-dominanted is that $M/R > 1$, where the Marangoni number $M = \sigma_T \Delta T d/\rho\nu\kappa$ characterizes the thermocapillary driving and the Rayleigh number $R = \alpha g \Delta T d^3/\nu\kappa$ characterizes the buoyancy driving (see figure 1 for definitions). In the experiments described in this paper, $M/R \geq 100$.

In the thermocapillary-driven regime, two qualitatively different instabilities can appear --- short-wavelength hexagonal Benard convection cells [1, 2] and a long-wavelength deformational mode[3, 4, 5]. The hexagonal and long-wavelength instabilities differ in the stabilizing mechanisms that compete with destabilizing thermocapillary effects due to different types of fluctuations[6]. The short-wavelength hexagonal instability originates from temperature fluctuations on the free surface, which initiate thermocapillary flow along the interface; the imposed vertical temperature difference across the liquid layer sustains the flow. Thermal and viscous diffusion, however, dampen the temperature fluctuations and associated fluid flow. Alternatively, the long-wavelength mode originates from fluctuations of the free surface height $h(x, y)$, which cause a temperature variation on the interface because of the imposed temperature gradient. By thermocapillarity, the cool elevated region pulls liquid from the warm depressed region and, if allowed to continue, thermocapillarity would pile all the liquid from one region of the layer into an adjacent region. Gravity, though, attempts to flatten the interface and thus to stabilize these deformational perturbations. In addition, surface tension selects a long-wavelength for this deformational instability since surface tension resists *curvature* of the interface and thus stabilizes long wavelength modes least.

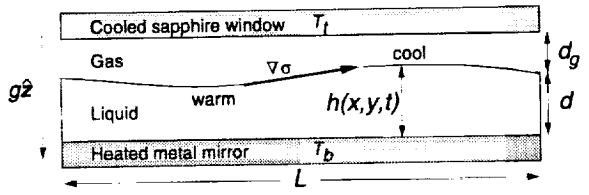

Figure 1: Sketch of surface-tension-driven Bénard (Marangoni) convection cell of horizontal extent $L = 3.81$ cm, mean liquid depth $d \sim 0.01$ cm, mean gas depth $d_g \sim 0.03$ cm, and local interface position $h(x, y, t)$. There is a mean temperature different ΔT across the liquid layer. The liquid has surface tension σ, temperature coefficient of surface tension σ_T, kinematic viscosity ν, thermal diffusivity κ, and thermal expansion coefficient α.

2 LINEAR THEORY

The linear stability analysis for the short-wavelength mode was first published by Pearson [1] and the stability analysis for the full problem, including the long-wavelength mode, was first published by Smith [4]. The hexagonal mode appears at wavenumber $q = 2$ (nondimensionalized by d) when

$$M_c \approx 80 \left(1 + \frac{k_g}{k}\right), \tag{1}$$

where k and k_g are, respectively, the liquid and gas thermal conductivities. The long-wavelength mode appears at wavenumber $q = 0$ at $M_c = 2G/3(1 + F)$, where

$$F \equiv \frac{d}{d_g} \left(\frac{1 - \frac{k_g}{k}}{1 + \frac{dk_g}{kd_g}} \right) \tag{2}$$

characterizes heat transport at the interface. In a real experiment of horizontal extent L, the long-wavelength mode occurs at $q_c = 2\pi d/L$ and

$$M_c = \frac{2G}{3(1 + F)} + \frac{q_c^2}{C}, \tag{3}$$

where $C = \rho\nu\kappa/\sigma d$ is the capillary number. The instability seen in a given experiment corresponds to the smaller of the M_c in equations (1) and (3). While $G \to 0$

in microgravity, and thus the long-wavelength mode would be the primary instability in an experiment of very large aspect ratio ($q_o \to 0$), the Benard hexagons can still be the primary instability in a finite-aspect ratio system. For example, experiments on Benard convection aboard Apollo 14 [7] and Apollo 17 [8] yielded short-wavelength Benard convection cells and not the long-wavelength instability, even though $G < 1$. In the Apollo experiments, the aspect-ratio correction (q_o^2/C) shifted the onset of the long-wavelength mode to $M \sim 280$, above the onset of hexagons.

3 NONLINEAR THEORY

To examine the nonlinear stability and behavior of the long-wavelength instability, we have derived an evolution equation for the interface height $h(x, y, t)$ from the Navier-Stokes equations in the limit of long wavelength disturbances[6]:

$$\frac{\partial h}{\partial t} + \nabla \cdot \left\{ \frac{3D}{2} \frac{h^2 \nabla h}{f(F,h)} - h^3 \nabla h + \frac{h^3}{B} \nabla^2 \nabla h \right\} = 0, \quad (4)$$

where the domain of both x and y is $[0,2\pi]$, $f(F,h) \equiv (1+F-Fh)^2/(1+F)$, $D \equiv M/G$ is the inverse dynamic Bond number, and $B = GC/q_o^2$ is the static Bond number. The first term in curly brackets describes the effect of thermocapillarity; the second, gravity; and the third, surface tension. Equation (4) reduces to the evolution equations of Davis[9, 10] and Oron & Rosenau[11] in the limit of $F = 0$ ($d_g/d \to \infty$, or $k = k_g$). The linear stability analysis of this equation agrees with Smith [4] for $q_o \ll 1$.

To determine the nature of the bifurcation, we perform a weakly nonlinear analysis of the evolution equation (4) by considering just the two lowest order wavenumbers in the deformation $\eta \equiv h - 1$; we assume that the lowest order $\eta_1 \approx |\epsilon|^{\frac{1}{2}}$, where $\epsilon \equiv (M - M_c)/M_c$, the second lowest order $\eta_2 \approx |\epsilon|$, and all higher orders of η go as the 3/2 or higher power of $|\epsilon|$. The bifurcation is found to be subcritical (a backwards pitchfork) for all parameters. In addition, the signs of the second and higher order modes (η_2, etc.) change at $F = 1/2$, hinting at the qualitative difference in solutions that we will describe later for $F < 1/2$ and $F > 1/2$.

Equation (4) can also be solved to find all the one-dimensional steady states $h(x)$; The solutions we find agree with the weakly nonlinear analysis for small $|\epsilon|$; the bifurcation curve continues backwards in ϵ until it terminates because the solutions represented cease

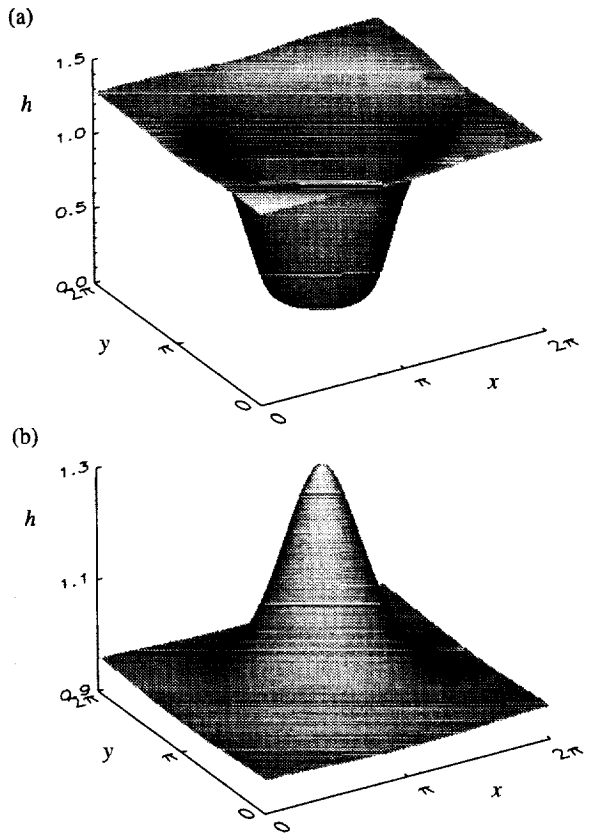

Figure 2: Two-dimensional profile of long-wavelength mode just before rupture for 5% above linear instability. (a) Dry spot with $F = 1/3$ and $B = 30$, (b) High spot with $F = 2/3$ and $B = 30$.

to become physical. Nowhere does the bifurcation curve turn over in a saddle-node bifurcation and form a stable branch. The unstable solutions on the bifurcation curve appear differently for $F < 1/2$ and $F > 1/2$; for $F < 1/2$, the solutions are localized depressions and for $F > 1/2$ the solutions are localized elevations. Oron and Rosenau [11] performed a similar analysis for $F = 0$ and also found no stable solutions.

We numerically simulate (4) with both one- and two-dimensional interfaces. We use a spectral method in order to enforce the continuity condition, which in one dimension is $\int_0^{2\pi} (h - 1)\, dx = 0$. Fourier series are the natural basis function since we use periodic boundary conditions, and Fourier series automatically satisfy continuity. The simulation employs a pseudospectral method to handle the nonlinear terms. Because of the fourth-order nonlinearity, a 2/5 rule (equivalent to the 2/3 rule for quadratic nonlinearities) is required to prevent aliasing --- e.g., for 128 spatial locations, only 51 spectral modes q from -25 to +25 are used. At each time-step, the power in the remaining 3/5 of modes is set to zero.

A dry spot forms for $F < 1/2$ (figure 2 a), while for $F > 1/2$ a high spot forms, which physically would pop up to the top plate (figure 2 b). Thus, the prediction of weakly nonlinear and potential theory of a change at $F = 1/2$ is observed in the simulations. The structure of the dry or high spot does not depend strongly on F far from $F = 1/2$, though the size depends on the static Bond number B, which gives the relative strengths of gravity and surface tension. High surface tension (B small) prevents sharp structures from forming, while a low surface tension (B large) allows the formation of sharp structures. As predicted by the nonlinear analyses, no stable, deformed states before rupture are seen in either one or two dimensions. After rupture, the dry spot eventually saturates, though this phenomenon is not not captured by the evolution equation since as $h_{min} \to 0$, the power in the higher order modes begins to dominate, spectral convergence is lost, and the simulation breaks down.

4 EXPERIMENTAL DESIGN

The liquid lies on a 3.81-cm-diameter, gold-plated aluminum mirror (see figure 3). The mirror is attached to an aluminum plate whose bottom is heated by a 14 Ω thin-film resistance heater. A thermistor in the center of the aluminum plate measures T_b. A cooled, 3-mm-thick sapphire window bounds the gas from above. Chloroform is employed as the cooling fluid to allow imaging with an infrared (3-5 μm) camera. Cooled chloroform is pumped between two sapphire windows and then through a heat exchanger that maintains the temperature of the chloroform at 21.3 $\pm$ 0.1 °C.

The total gap ($d + d_g$) between the lower sapphire window and the mirror bottom is uniform to 10 fringes (3.2 μm), as verified interferometrically. The size of the gap is determined by introducing indium shims of various sizes and observing the change in the interference fringes between the window and the mirror. We consider the gap to have the same thickness as the shim when the shim does not perturb the fringes, but a slightly thicker shim (by 5 μm) does.

An aluminum sidewall laterally constrains the liquid. The liquid depth is uniform to a fringe (0.32 μm) in the central 75% of the cell at $\Delta T = 0$. The depth is measured using a stylus attached to a micrometer. The position of the upper interface is determined when the liquid suddenly wets the sharp tip of the stylus as the stylus is lowered. The stylus is then lowered further until contact with the mirror is signaled by an ohmmeter connected to the stylus and the metal mirror. The liquid depths can be measured to ± 5 μm.

For most experiments we use a ν = 0.102 Stoke (at 50° C) silicone oil that has been distilled once to remove low vapor pressure components, which can condense on the cool, upper plate [12]. Infrared images are made using an infrared-absorbing (at 4.61 μm with an extinction length of order a few microns) polymethylhydrosiloxane silicone oil with $\nu \approx 0.25$ Stoke at 50 °C.

Liquid depths range from 0.007 to 0.027 cm. Gas layer thicknesses range from 0.02 to 0.10 cm. The gas in the upper layer is typically air, although a few experiments employ helium gas. We used helium since it has a much larger thermal conductivity than that of air and thus allows varying F without varying d or d_g.

We use an optical system that serves as both an interferometer and a shadowgraph. When the deformation is small, we use the optical system as an interferometer to give an indication of the deformation of the interface. The mirror-window fringes are much stronger than the mirror-liquid fringes, so it is difficult to count the mirror-liquid fringes to get a quantitative measure of the deformation. When the deformation is large, we use the optical system as shadowgraph, where deformation acts as a lens to focus the incident light. The initial formation of a localized depression is signaled by a bright spot on the shadowgraph image. Once the interface is significantly deformed (as the liquid is in the process of forming a dry or high spot), the deformation can be seen

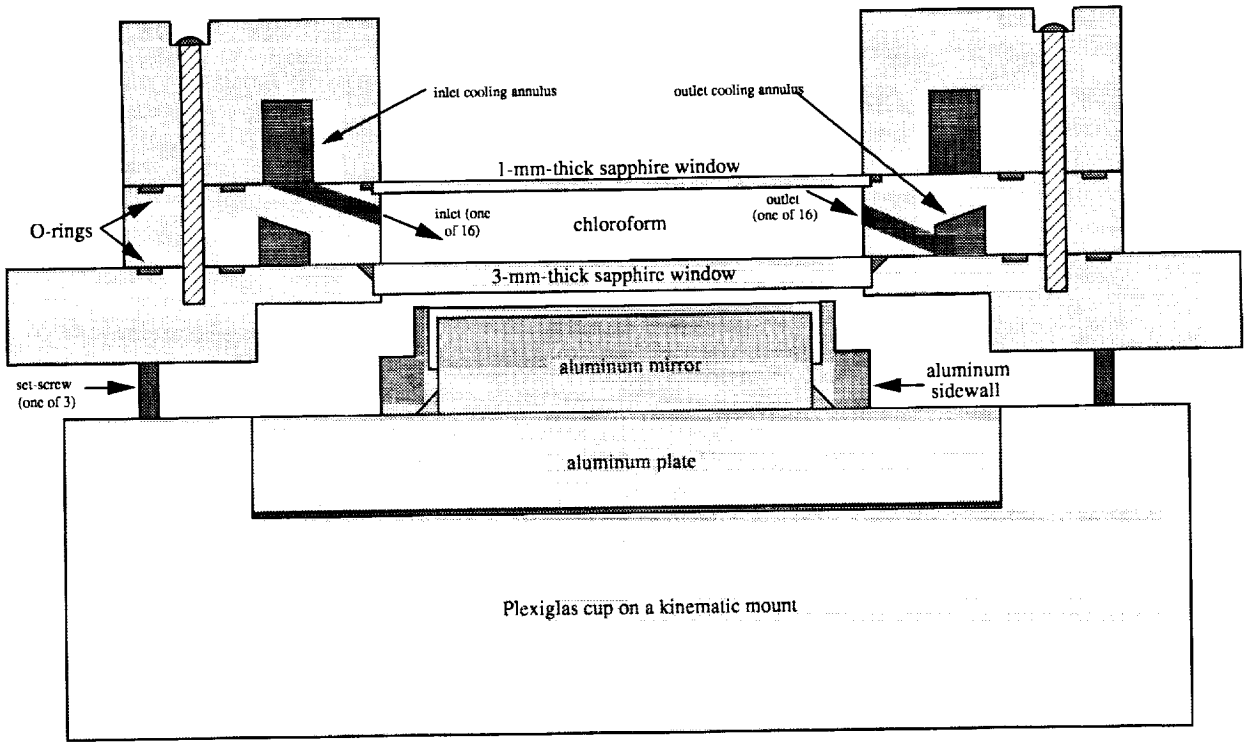

Figure 3: Cross-section of experimental apparatus. Both top and bottom plates are thermally conducting relative to the liquid and gas.

by eye. For making images used in this paper, we employed a 256 256 pixel Amber Engineering Proview 5256 LN_2-cooled InSb infrared staring array sensitive in a 0.08 μm band centered around 4.61 μm.

5 EXPERIMENTAL RESULTS

We see four distinct states at onset of instability: the two long-wavelength modes of dry spots (figure 4a) and high spots (figure 4b), a mixed long-wavelength and hexagonal state (figure 4c), and hexagons (figure 4d).

We observe three of these states at the onset of instability for $F < 1/2$. For large G (independent of F), Benard hexagons form (figure 4d). For small G, the long-wavelength dry spot forms (figure 4a). For intermediate G, both the long-wavelength (dry spot) and hexagonal modes appear together (figure 4c). In this case, the long-wavelength deformational mode is linearly unstable and its formation induces the formation of the hexagonal mode by increasing the local depth in the region surrounding the dry spot. The horizontal extent of the dry spot is $\sim 100d$ and the area of the dry spot is typically $1/4 - 1/3$ the area of the entire cell. Once the dry spot forms, fluid flow consists of steady-state convection concentrated at the edge of the dry spot.

As predicted by nonlinear theory, for $F > 1/2$ the liquid layer forms a high spot (figure 4d), where the liquid pops-up to the top plate (sapphire window).

Since the time-scale of formation of the hexagons is the vertical diffusion time ($d^2/\kappa \approx 0.1$ s), while the time-scale for the long-wavelength mode is the horizontal diffusion time ($L^2/\kappa \approx 3$ hours), quickly ramping the temperature above $M = 80$ allows formation of the hexagons as the primary instability even when the long-wavelength instability would be primary if ΔT were increased quasistatically, as assumed by linear theory. If ΔT is then decreased slowly below onset of hexagons, a dry spot can form once the hexagons have disappeared.

A comparison of the experimental measurements of onset to linear stability theory is given in figure 5. The linear stability theory assuming periodic boundary conditions (the dotted line in figure 5) gives good agreement with the experiments for deep liquid depths ($d > \approx 0.015$ cm), but poor agreement for shallow liquid depths. Much of the deviation of theory from experiment is due to sidewall effects, both the pinning of the liquid at the sidewalls and under- or over-filling of the liquid. The experiments used a fixed sidewall height of 0.02 cm, so experiments with thinner depths were underfilled

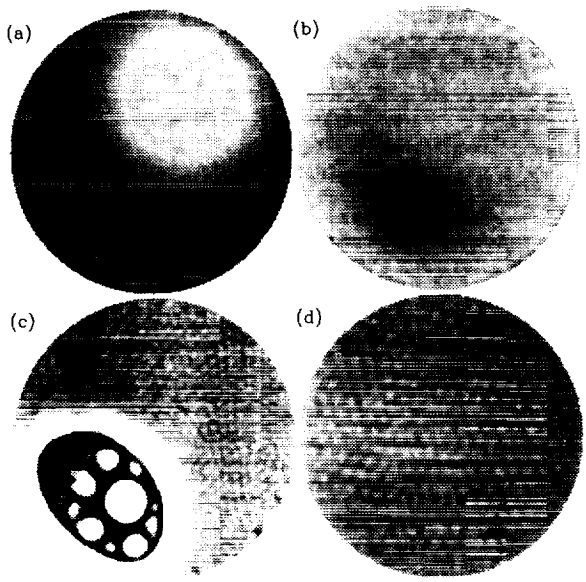

Figure 4: Infrared images of states seen in the experiment. (a) a dry spot (d = 0.025 cm, F = -0.06). (b) a high spot (d = 0.037 cm, F = 0.91). (c) dry spot with hexagons in the surrounding region (d = 0.025 cm). (the dry spot looks cold the camera sees through the infrared-absorbing liquid to the mirror, which appears cold in the infrared); (d) hexagons (d = 0.045 cm, G = 370).

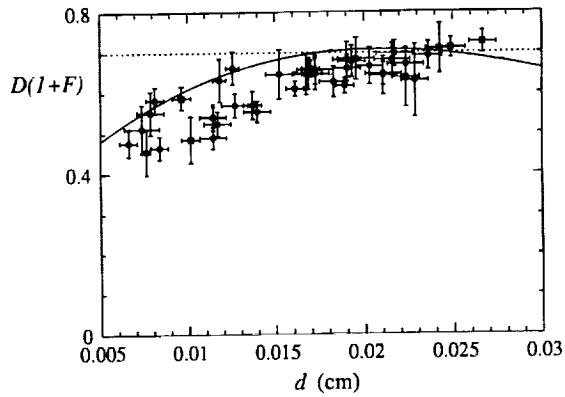

Figure 5: Comparison of instability onset with the predictions of linear stability theory. The prediction of linear stability theory assuming periodic boundary conditions is given by the dashed line at 0.70. This theory gives good agreement with the experiments for thick liquid depths, but there is a significant departure for thin depths. The prediction of linear stability theory including the sidewall effects is given by the curved solid line.

and experiments in thicker depths were overfilled. The presence of sidewalls of height different from the mean liquid depth led to an initially deformed interface, even for no imposed temperature gradient. To examine the effects of the sidewalls, we solved equation (4) using non-periodic boundary conditions with Chebyshev polynomials as our basis functions. The boundary conditions used corresponded to pinning of the liquid surface at the sidewall and no net liquid flux through the sidewalls; these boundary conditions automatically satisfied the conservation of liquid condition. The curved, solid line in figure 5 shows the comparison of the experiments with the new theoretical prediction [13]. The quantitative agreement is much better than with periodic boundary conditions, though the agreement is still not exact.

6 CONCLUSION

Two modes of instability exist in surface-tension-driven Benard-Marangoni convection where the liquid is heated from below and cooled from above. The short-wavelength hexagonal mode ($q = 2$) occurs for large G, when diffusion is the important (slow) stabilizing mechanism. The long-wavelength deformational mode ($q = 2\pi d/L \ll 1$) occurs for small G, when gravity is the important (slow) stabilizing mechanism. This long-wavelength instability can take the form of either a localized depression that evolves to a dry spot, or a localized elevation (high spot) that accelerates upwards and causes the liquid to pop up to the top plate. The relative thicknesses and thermal conductivities of the liquid and gas layers determine whether the dry spot or high spot forms; a high spot forms where the liquid thermal conductivity is much larger than the gas thermal conductivity and the liquid depth is nearly equal to or greater than the gas depth. The deformation due to the long-wavelength mode can cause the formation of the hexagonal mode by increasing the local value of M above the critical value for the hexagons.

The long-wavelength instability is be described by an evolution equation for the height of the interface. Analysis of the evolution equation predicts that the instability is subcritical and that the unstable, backwards branch of the bifurcation curve never turns over to a stable branch. Numerical simulations of the evolution equation reveal dry spot and high spot states that agree qualitatively with what is seen in the experiment. Linear stability theory using periodic boundary conditions works well when the interface is initially flat; however,

when the interface is deformed, the deformation much be included in the theory to predict the correct onset.

This research is supported by the NASA Microgravity Science and Applications Division (Grant No. NAG3-1839), the Office of Naval Research (Grant No. N00014-89-J-1495), and a NASA ESS Cooperative Agreement (NCCS5-154).

References

[1] J. R. A. Pearson, J. Fluid Mech. **4**, 489 (1958).

[2] M. F. Schatz, S. J. VanHook, W. D. McCormick, J. B. Swift and H. L. Swinney, Phys. Rev. Lett. **75**, 1938 (1995).

[3] L. E. Scriven and C. V. Sternling, J. Fluid Mech. **19**, 321 (1964).

[4] K. A. Smith, J. Fluid Mech. **24**, 401 (1966).

[5] S. J. Van Hook, M. F. Schatz, W. D. McCormick, J. B. Swift, and H. L. Swinney, Phys. Rev. Lett. **75**, 4397 (1995).

[6] S. J. Van Hook, M. F. Schatz, J. B. Swift, W. D. McCormick, and H. L. Swinney, J. Fluid Mech. **345**, 45 (1997).

[7] P. G. Grodzka and T. C. Bannister, Science **176**, 506--508 (1972).

[8] P. G. Grodzka and T. C. Bannister, Science **187**, 165 (1975).

[9] S. H. Davis, in *Waves on Fluid Interfaces*, edited by R. E. Meyer (Academic Press, New York, NY, 1983), p. 291.

[10] S. H. Davis, Annu. Rev. Fluid Mech. **19**, 403 (1987).

[11] A. Oron and P. Rosenau, J. Phys. II (France) **2**, 131 (1992).

[12] M. F. Schatz and K. Howden, Exp. Fluids **19**, 359 (1995).

[13] R. Becerril, S. J. Van Hook, and J. B. Swift, submitted to Phys. Fluids (1998).

PLIF Flow Visualization of Incompressible Richtmyer-Meshkov Instability

C.E. Niederhaus[1] and J.W. Jacobs[2],
Department of Aerospace and Mechanical Engineering
University of Arizona
Tucson, AZ 85721
[1]email: niederha@u.arizona.edu
[2]email: jacobs@ame.arizona.edu

ABSTRACT

Richtmyer-Meshkov (RM) instability occurs when two fluids of different densities are impulsively accelerated normal to their nearly planar interface. It is one of the most fundamental of fluid instabilities and is of importance in fields ranging from astrophysics to material processing. Because RM instabilities are normally carried out in shock tubes using gases, where the generation of a sharp well controlled interface is difficult, there is a scarcity of well visualized experimental results. The experiments presented here utilize a novel technique which avoids many of the experimental difficulties that have previously limited the study of RM instability. In this system, the instability is generated by bouncing a thin rectangular tank containing two liquids off of a fixed spring. Planar Laser Induced Fluorescence (PLIF) is utilized to visualize the instability, providing very clear views of the interface far into the nonlinear regime.

INTRODUCTION

Richtmyer-Meshkov (RM) instability is the instability of an impulsively accelerated planar interface separating two fluids of different densities. For example, RM instability causes small perturbations on a flat interface, accelerated by a passing shock wave, to grow in amplitude and eventually become a turbulent flow. It is closely related to Rayleigh-Taylor instability, which is the instability of a planar interface undergoing constant acceleration, such as caused by the suspension of a heavy fluid over a lighter one in the earth's gravitational field. Like the well known Kelvin-Helmholtz instability, RM instability is a fundamental hydrodynamic instability which exhibits many of the nonlinear complexities that transform simple initial conditions into a complex turbulent flow. Furthermore, the simplicity of RM instability (in that it requires few defining parameters), and the fact that it can be generated in a closed container, makes it an excellent testbed to study nonlinear stability theory as well as turbulent transport in a heterogeneous system.

Richtmyer-Meshkov instability is of importance in fields ranging from astrophysics to materials processing. For example, RM instability is believed to occur when the outward propagating shock wave generated by the collapsing core of a dying star passes over the helium-hydrogen interface[1]. RM instability is of critical importance to inertial confinement fusion. In this case, the spherical shell which encapsulates the deuterium-tritium fuel becomes RM and RT unstable as it is accelerated inward by the ablation of its outer surface by laser or secondary X-ray radiation. Thus, these instabilities represent the single most significant barrier to attaining positive-net-yield fusion reactions in laser fusion facilities[2]. RM instability is also of importance to high speed combustion applications, where, for example, the interaction of a shock wave with a flame front can be unstable, thereby greatly enhancing mixing and significantly altering the burning rate[3]. In addition, RM instability has been identified as one of the phenomena which allows dissimilar metal alloys to be bonded together in explosive welding processes[4].

The evolution of Rayleigh-Taylor instability from small amplitude perturbations to fully turbulent flow has been well documented by numerous experimental investigations[5,6]. However, similar experimental verification from RM instability is noticeably lacking. In particular, there is a scarcity of well visualized experimental results. RM instability experiments have traditionally been carried out in shock tubes. The major difficulty in these experiments is in maintaining a well controlled, sharp boundary between two gases. One solution to this problem has been to initially separate the two gases with a thin membrane which is then broken by the passing shock wave[7,8]. However, membrane fragments can disturb the growth of the initial perturbation and generate uncontrolled small scale disturbances which can seed turbulence. Other shock tube experiments have attempted to avoid membrane effects by initially separating the two gases by a solid barrier which is removed immediately prior to firing the shock tube[9,10]. Because the diffusion coefficients of gases are large, this technique generates diffuse interfaces (typically 1 cm thick).and the initial perturbation is nonuniform and difficult to characterize, thus severely limiting the usefulness of the experimental results.

The use of liquids instead of gases eliminates the problems with generating a sharp, well defined interface because of the low diffusion coefficients of liquids. However, in low liquid speed experiments the earth's gravitational influence is much more dominant and can stabilize (or destabilize) the developing RM instability. Furthermore, it can strongly effect the turbulent flow development, thus these types of experiments must be carried out in a low gravity environment.

Recently, we have developed a novel experimental technique to study the RM instability of a liquid system[11]. In these experiments, a tank containing two stably stratified liquids is impulsively accelerated by bouncing it off of a stationary spring. These experiments represent a significant advancement in the study of RM instability because: (1) a sharp liquid/liquid interface is easy to form and visualize, and (2) the relatively low speed of the flow allows for the use of standard video imaging. The problems with gravity in liquid phase RM instability experiments are solved by keeping the fluids essentially in freefall during the evolution of the instability.

EXPERIMENTAL DESCRIPTION

The experimental apparatus (figure 1) consists of a thin rectangular tank with inside dimensions of 2.54 cm x 11.75 cm x 25.4 cm which is mounted to a sled on a linear rail system. The rails are oriented so that the sled is free to move in the vertical direction with approximately 1 m of travel. At the bottom of the rails is a fixed coil spring which is secured at one end. The bottom half of the tank is initially filled with a dyed salt solution ($Ca(NO_3)_2 + H_2O$) and the top half with a water/alcohol mixture yielding an Atwood number (the difference in densities divided by their sum) of approximately 0.15.

The tank is mounted on crossed roller bearings which allow it to move horizontally relative to the sled. A computer controlled linear stepper motor is used to oscillate the tank from side to side in an arbitrary motion. A sinusoidal motion of the correct frequency produces oscillating standing waves of specified wavelengths (corresponding to n + 1/2 waves across the tank). The amplitude of the waves can be controlled by varying the amplitude of the shaking motion. The bottom solution is dyed with disodium flourescein, which is illuminated by using a sheet of laser light (argon ion) passing through the top of the tank. A video camera is mounted to the sled which views the interface separating the two liquids. An accelerometer mounted to the tank records the acceleration history of the system.

The sled is raised to an initial height and held in place with an electromagnet. The stepper motor controller is used to oscillate the tank, trigger the data acquisition, and to trigger the release of the sled at the desired time. When the sled is released, it travels down the rails, bounces off the spring at the bottom, then travels up and down the rails until it hits the spring a second time (and so on until stopping). Because the tank is nearly in freefall before and after the bouncing, the only body forces the fluids experience is during the bouncing event, which lasts for approximately 30 msec. The experiment therefore generates an impulsive acceleration without using a shock wave. The RM instability is generated on the first bounce and evolves until the second bounce. The total time for the evolution of the instability is approximately 0.7 seconds, which yields 40 fields from a standard CCD video camera operating at 30 frames per second in interlaced mode (which yields 60 noninterlaced fields per second). The second bounce generates a second RM instability. However, the more complicated and larger amplitude initial perturbations promotes a rapid transition to turbulence.

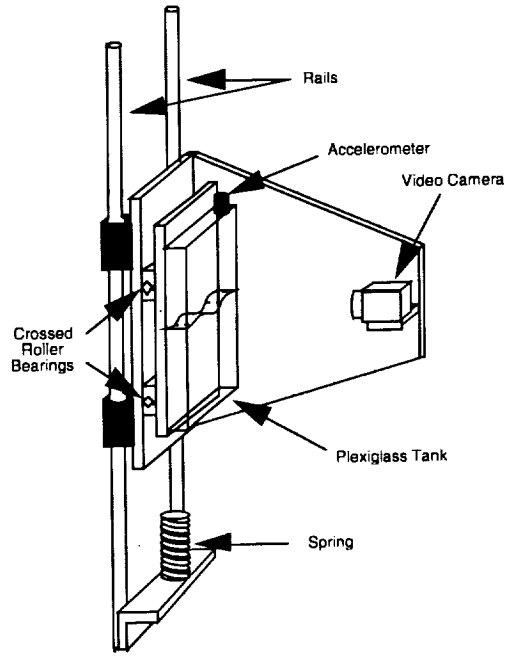

Figure 1. The experimental apparatus

EXPERIMENTAL RESULTS

Figure 2 is a sequence of PLIF images showing the evolution of the instability generated from a sinusoidal initial perturbation as viewed by the video camera. Each image is marked with a frame number (corresponding to a 1/60 sec time increment). Note that this and the following sequences are not uniformly spaced in time. Frame 0 was taken immediately before the sled contacts the spring and thus shows the initial interface shape. The impulsive acceleration in these experiments is directed from the heavier fluid into the lighter fluid, causing the initial perturbation to invert before growing. Immediately after inversion, the instability retains a sinusoidal shape. However, with time, vortices begin to form at points midway between crests and troughs, yielding the symmetric mushroom pattern typical of RT and RM instability of fluids with small density differences. As time advances, these vortices grow in size as they roll the interface around their centers to form a spiral pattern. This large amplitude interfacial pattern is reminiscent of that observed in Kelvin-Helmholtz experiments, with alternating rather than same sign vorticity. Note that, characteristic of the instability with small density

differences, the interface shape retains its top-to-bottom symmetry well into the nonlinear regime. The container bounces a second time, and thus receives a second acceleration beginning at a point between frames 40 and 41. In frames 42 and 43, one can see a dramatic change in the interfacial pattern in which the mushroom features rapidly collapse and erupt into turbulence. Close examination of these images reveals the classical patterns exhibited by Kelvin-Helmholtz instability at the points where the interface is vertical, thus suggesting that this mechanism is the cause of the rapid transition to turbulence.

As was mentioned above, the apparatus has the capability of generating arbitrary lateral tank motion. Multi-mode perturbations are generated by oscillating the tank with a combination of two different sinusoidal frequencies. Figure 3 is a PLIF sequence showing the results of an experiment with a combination of 1 1/2 and 2 1/2 wavelengths as the initial perturbation. Frame 0 was taken slightly before the impulsive acceleration and shows the initial interface shape resulting from the combination of the two modes. Because the initial amplitudes are small, the two modes evolve independently of each other early in their evolution. Furthermore, the mode with the shorter wavelength grows more rapidly. Therefore, in frame 1 the amplitude of the shorter wavelength mode has decreased to nearly zero, showing clearly the longer wavelength mode. A short time later, in frame 2, the short wavelength mode has inverted, while the longer wavelength mode has now decreased to nearly zero, thus the shorter wavelength mode is clearly shown. In frames 5-40, this multi-mode instability evolves, exhibiting the formation of a more complex structure than that observed in the single-mode experiments.

Figure 4 shows the results from another multi-mode experiment, in which a combination of the modes with 1 1/2 and 3 1/2 wavelengths is used. Again, frame 0 shows the initial perturbation and frames 1 and 2 show isolated views of the individual modes. This multi-mode instability develops into a vortex pattern that is more complex than its single-mode counterpart. However, this combination of modes develops into a pattern that is much more similar to that of the single mode instability in that it is dominated by three large vortices. Note, however, that these vortices are much further developed, i.e. there are many more coils in the final multi-mode patterns than exist in the single-mode experiments. This is a result of the fact that the multi-mode initial interface shape produces a more concentrated vorticity distribution than does the single-mode interface. Thus the vortices form much more quickly than in the single-mode experiments.

CONCLUSIONS

The experiment described above represents a significant advancement in the study of RM instability in that extremely well visualized results are obtained. However, the run times achievable in the present experimental apparatus are obviously limited. Previous shock tube experiments and computational studies have shown that turbulent flows can be obtained with a single impulsive acceleration. It appears that the limited run time of the present apparatus might not allow the turbulent flow to be obtained in this setup. The low gravity environment of space allows a unique opportunity to develop an experiment of this type which could be carried out in earth orbit. If achievable, this would provide effectively unlimited run times, and as a result yield valuable information about this fundamental and important fluid instability.

REFERENCES

[1]Arnett, W.D., Bahcall, J.N., Kirshner, R.P., and Woosley, S.E., "Supernova 1987A," *Annu. Rev. Astron. Astophys.*, **27**, 629-700 (1989).

[2]Lindl, J.D., McCrory, R.L., and Campbell, E.M., "Progress Toward Ignition and Burn Propagation in Inertial Confinement Fusion," *Physics Today*, **45** (9), 32-50 (1992).

[3]Markstein, G.H., "A Shock Tube Study of Flame Front-Pressure Wave Interaction," Sixth Symp. (Int) on Combustion, Reinhold, 387-398 (1957).

[4]Shaner, J.W., "Pattern Formation by Shock Processes," *Physica D*, **12**, 154-162 (1984).

[5]Emmons, H.W., Chang, C.T., and Watson, B.C., "Taylor Instability of Finite Surface Waves," *J. Fluid Mech.*, **7**, 177-193 (1960).

[6]Read, K.I., "Experimental Investigation of Turbulent Mixing by Rayleigh-Taylor Instability," *Physica D*, **12**, 45-58 (1984).

[7]Meshkov, E.E., "Instability of the Interface of Two Gases Accelerated by a Shock Wave," *Izv. Akad. Nauk. SSSR Mekh. Zhidk. Gaza*, **4**, 151-157 (1969). [Russian: *Izv. Acad. Sci. USSR Fluid Dyn.*, **4**, 101-104]

[8]Benjamin, R.F., "Experimental observations of shock stability and shock-induced turbulence," in *Advances in Compressible Turbulent Mixing, Proceedings of the First International Workshop on the Physics of Compressible Turbulent Mixing*, Edited by W.P. Dannevik, A.C. Buckingham, C.E. Leith, Published by Lawrence Livermore National Laboratory, Conf-8810234, pp. 341-348 (1992).

[9]Brouillette, M., and Sturtevant, B. "Experiments on the Richtmyer-Meshkov instability: single scale perturbations on a continuous interface," ***J. Fluid Mech.***, **263**, 271-292 (1994).

[10]Cavaller, C., Mercier, P., Rodriguez, G., and Haas, J.F., "A new vertical shock tube for Rayleigh-Taylor instability measurements," Proceedings of the 17th ISSWST at Bethlehem, PA; *Current Topics in Shock Waves*, Y. Kim editor, 564 (1990).

[11]Jacobs, J.W., and Sheeley, J.M. "Experimental Study of Incompressible Richtmyer-Meshkov Instability," *Phys. Fluids*, **8**, 405-415 (1996).

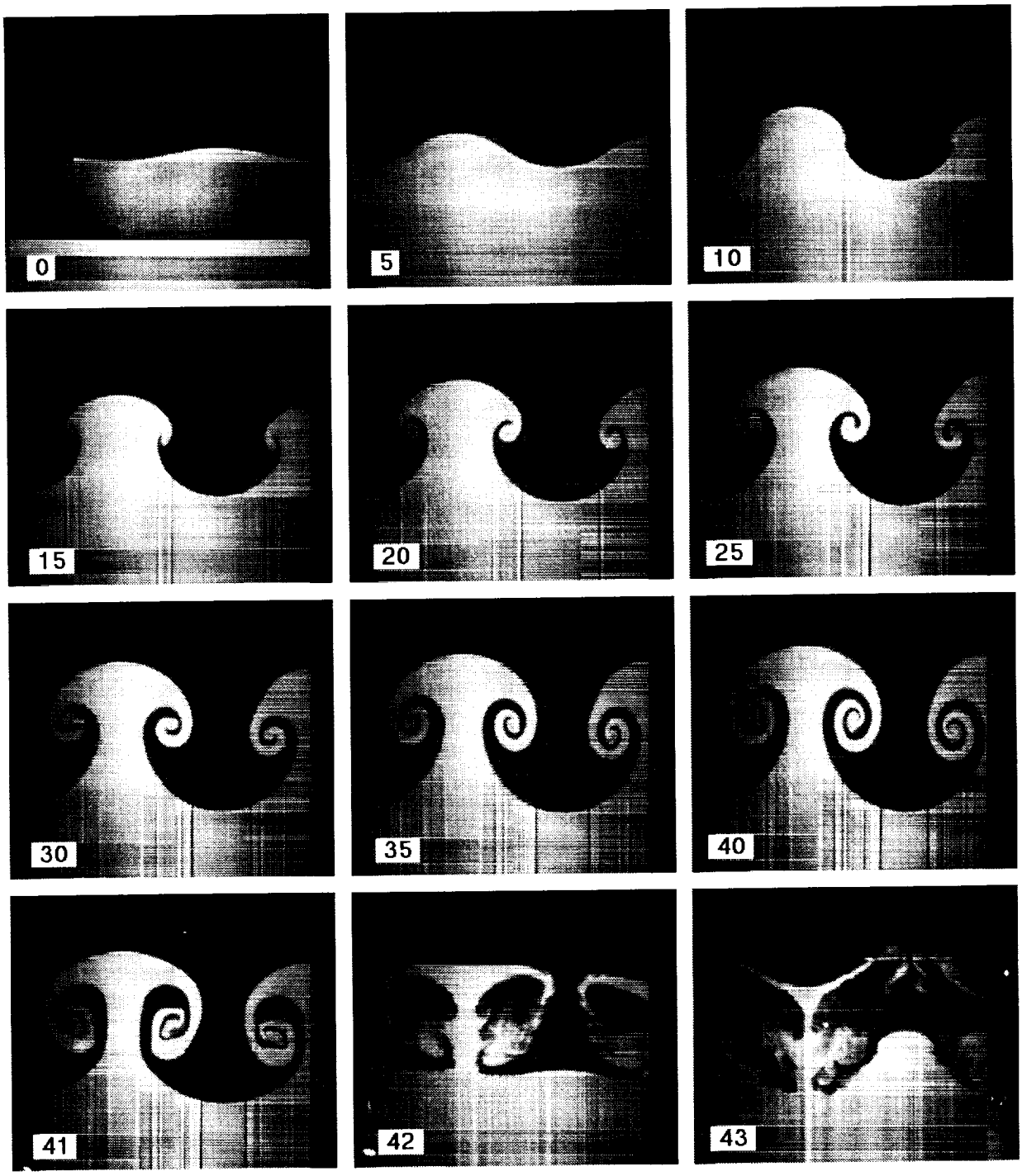

Figure 2. A sequence of PLIF images from an experiment initiated with a single-mode initial perturbation. Each image is marked with a frame number (each frame increment corresponds to a 1/60 s time increment). Note that this and the following sequences are not uniformly spaced in time.

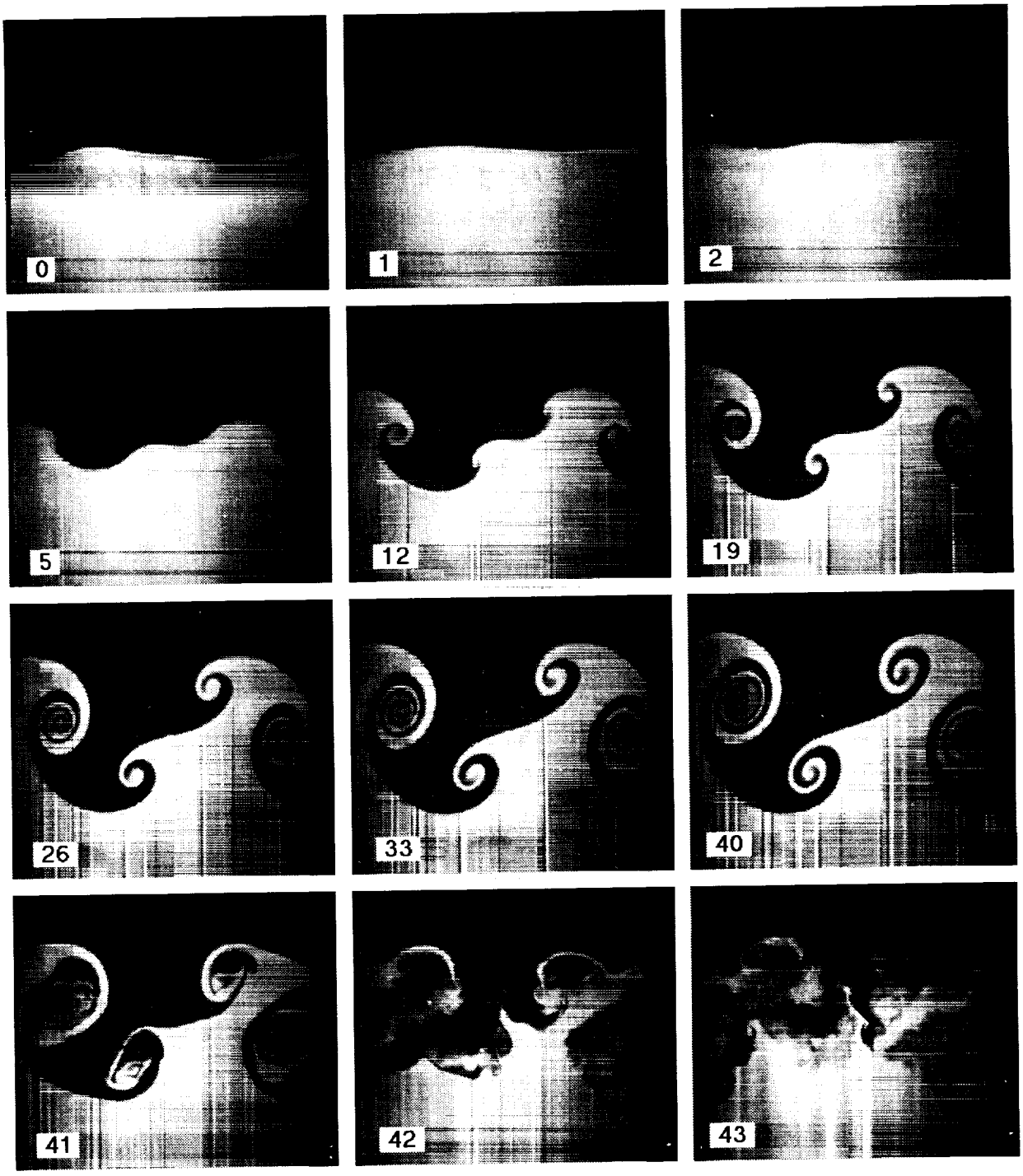

Figure 3. A sequence of PLIF images from an experiment initiated with a multi-mode initial perturbation consisting of a combination of the 1 1/2 wavelengths and 2 1/2 wavelengths modes.

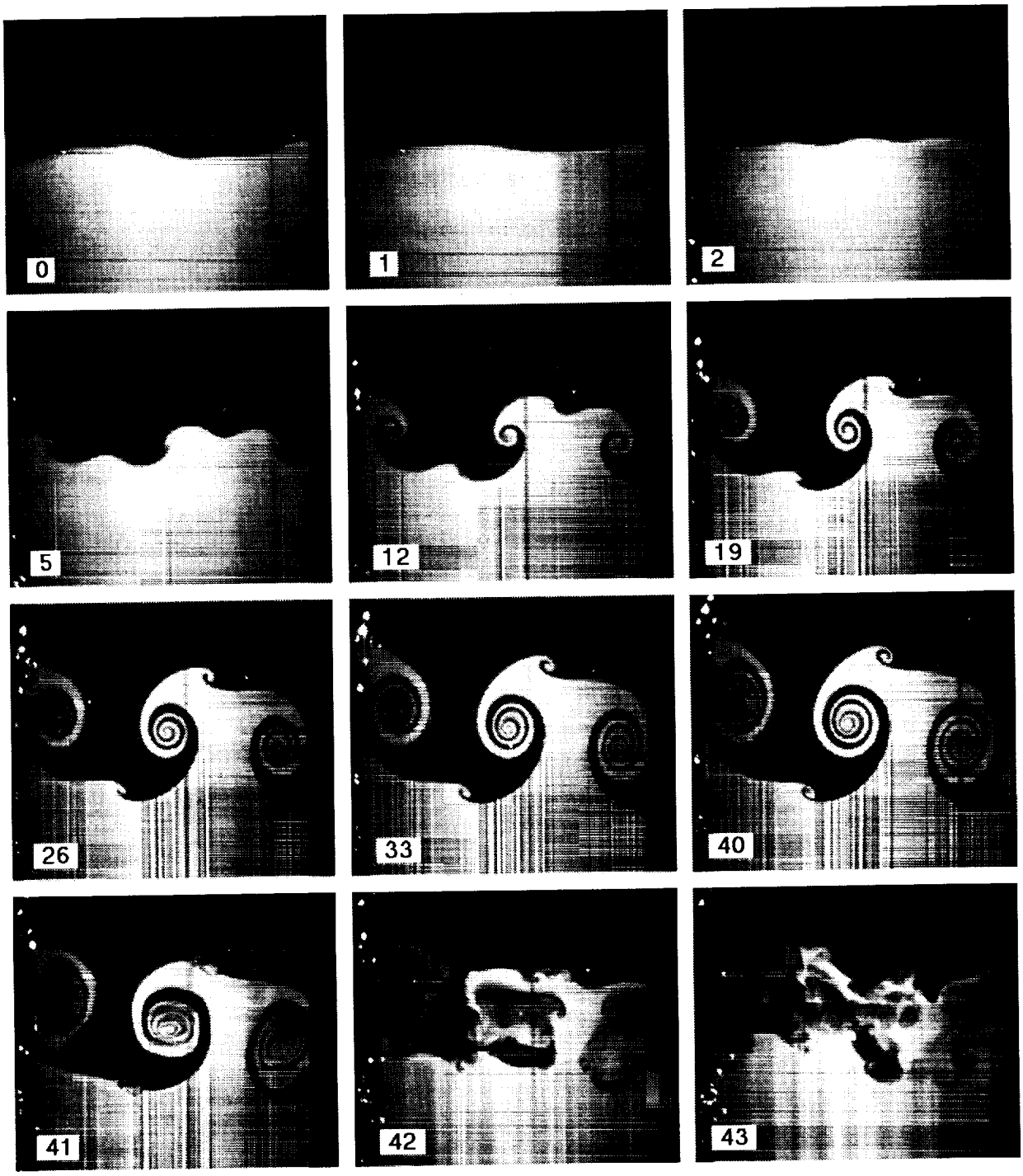

Figure 4. A sequence of PLIF images from an experiment initiated with a multi-mode initial perturbation consisting of a combination of the 1 1/2 wavelengths and 3 1/2 wavelengths modes.

ABSOLUTE AND CONVECTIVE INSTABILITY OF A LIQUID JET

S. P. Lin,[1] M. Hudman[2] and J. N. Chen[3], [1,2,3]Clarkson University, Potsdam, NY 13699.

ABSTRACT

The existence of absolute instability in a liquid jet has been predicted for some time (ref. 1-5). The disturbance grows in time and propagates both upstream and downstream in an absolutely unstable liquid jet. The image of absolute instability is captured in the NASA 2.2 sec drop tower, and is reported here. The transition from convective to absolute instability is observed experimentally. The experimental results are compared with the theoretical predictions on the transition Weber number as functions of the Reynolds number. The role of interfacial shear relative to all other relevant forces which cause the onset of jet breakup had not been quantitatively elucidated before (ref. 6), and is explained here.

IMAGE OF ABSOLUTE INSTABILITY

The commonly observed manifestation of the onset of instability in a liquid jet with a sufficiently large velocity is the amplification of disturbances which are convected downstream to break up the jet into drops. The observed instability belongs to a general class of instability called convective instability which allows the disturbance to be convected only in the downstream direction. The literature on convective instability is very rich, and is reviewed in many articles including the most recent ones by Chieger and Reitz (ref. 7), Lin (ref. 8), Lin and Reitz (ref. 6). There exists another class of instability called absolute instability which permits the disturbance to propagate in both the downstream and upstream directions. This class of instability is less well studied. Leib and Goldstein (refs. 1-2) were the first to demonstrate that, in absence of gravity and ambient gas, a liquid jet with a relatively small velocity may become absolutely unstable due to surface tension force. Even in the presence of gas, with (ref. 4) or without gas viscosity (ref. 3) or compressibility (ref. 5), absolute instability still occurs. However the physical appearance of a liquid jet which suffers the consequence of absolute instability without the interference of gravity has been obtained only recently (ref. 9). The fact that the photographs indeed give evidence of absolute instability is substantiated by the delineation of transition from convective to absolute instability observed in the NASA Lewis 2.2 second drop tower.

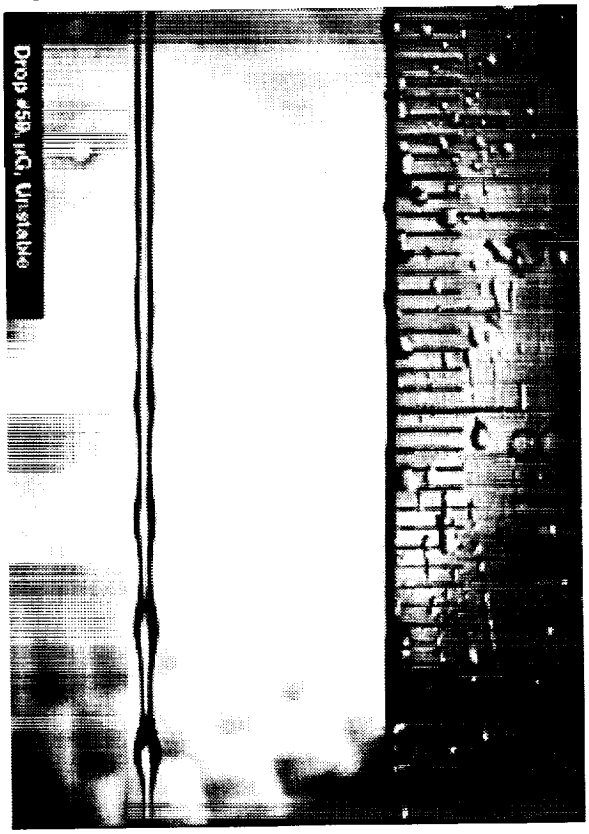

Figure 1: A Convectively Unstable Jet. *We* = 100, *Re* = 160

The detailed description of the equipment and procedure used for the experiments are available (ref. 9-10), and will not be reproduced here. The entire system was housed in a drop rig of dimension 41.4 cm x 40.6 cm x 81.2 cm, and of weight 152.4kg. The rig attained 10^{-4} g in the NASA 2.2 second drop tower, and survived 30 g impacts for more than 100 drops. Glycerin and water mixtures, SAE 10 oil, and silicon oil were used as test fluids.

Figure 1 is a photograph (ref. 9, 10) of a convectively unstable glycerin and water jet in air at *We* = 100, *Re* = 160. *Re* and *We* are the Reynolds and Weber numbers respectively defined by

$$Re = \frac{Ua}{\nu}, \; We = \frac{\rho U^2 a}{S}$$

where U is the average jet velocity, a is the nozzle radius, ν is the liquid kinematic viscosity, S is the surface tension, and ρ is the liquid density. The dimensionless wave number, defined as the ratio of $2\pi a$ and the wavelength, is 0.66 ± 0.025 based on the

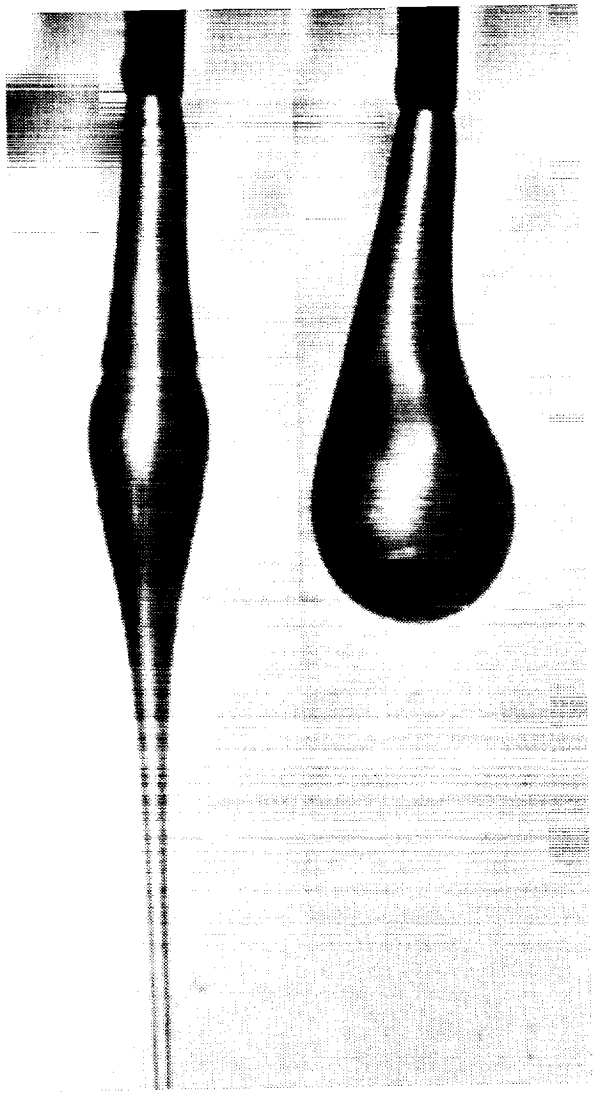

(a) 0.2 sec. after drop **(b) 0.4 sec. after drop**

Figure 2: An Absolutely Unstable Liquid Jet. (*We*=0.349, *Re*=0.082)

wavelength appearing in this figure. The observed wave number is close to 0.697 corresponding to the most amplified waves according to the Rayleigh theory. It will be shown presently that as the Weber number is decreased to lie below a critical number which is a function of other flow parameters, the convectively unstable jet suddenly becomes absolutely unstable. The onset of absolute instability has a totally different consequence. In contrast to the case of a convectively unstable jet, the disturbance in an absolutely unstable jet was observed to propagate not only in the downstream direction but also in the upstream direction, as predicted by theory.

Figures 2(a) and 2(b) are the photographs (ref. 9, 11) of a glycerin jet which give an example of absolute instability. They were taken at 0.2 sec and 0.4 sec after the test rig was dropped in the drop tower. Right after the onset of absolute instability, the upstream propagating disturbance suddenly rushed toward the nozzle tip to form a pendant while the downstream propagating disturbance grows slowly along the thin thread of liquid downstream of the forming pendant. Between 0.2 sec and 0.4 sec after the rig was dropped the liquid thread is pinched off by the pendant and washed out of the view of the camera. It appears that the physical mechanism of absolute instability remains capillary pinching as predicted by theory (ref. 12). Note also that the disturbance amplitude grows temporally everywhere along the jet after the onset of absolute instability. Thus the observed mode of instability appears to be the global absolute instability in the sense of Huerre and Monkewitz (ref. 13). The nonlinear evolution of absolute instability in a liquid jet was conjectured earlier (refs. 3, 14) to lead to a dripping jet. A dripping jet was not observed during the 2.2 seconds in the drop tower. Instead the pendant near the nozzle tip grew in volume and became more spherical in shape as the flow through the nozzle was kept constant at microgravity. It is not known if a dripping jet observed (ref. 14) on earth will also be encountered if the duration of the free fall of the test rig is much longer than 2.2 sec.

The transition from convective instability to absolute instability at different Reynolds numbers were observed. The results of the observation are given in Fig. 3. The experimental points obtained with glycerin are shown in circles, and that obtained with silicone oil are shown in squares. The uncertainties associated with *Re* and *We* are indicated respectively with horizontal and vertical error bars. For the experimental points without error bars, the length of the error bars are shorter than the diameter of the circles or the diagonal of the squares. The open circles and squares represent convective instability and the filled ones represent absolute instability. It is seen in Fig. 3 that as the velocity of a silicone oil jet corresponding to the open square with the largest values of *Re* and *We* is reduced in the successive 5 drop tower tests represented by the 5 open squares, the appearance of the jet remains that depicted in Fig. 1. Thus the jet with the values of *Re* and *We* indicated by the open squares remains convectively unstable. Further reduction in the jet velocity in the subsequent ten drop tower tests represented by the filled squares changes the appearance of the jet to that depicted in Fig. 2. Thus the jet becomes absolutely unstable at the critical set (Re_c, We_c) in the *Re* - *We* parameter space between the nearest open and filled squares, and remains

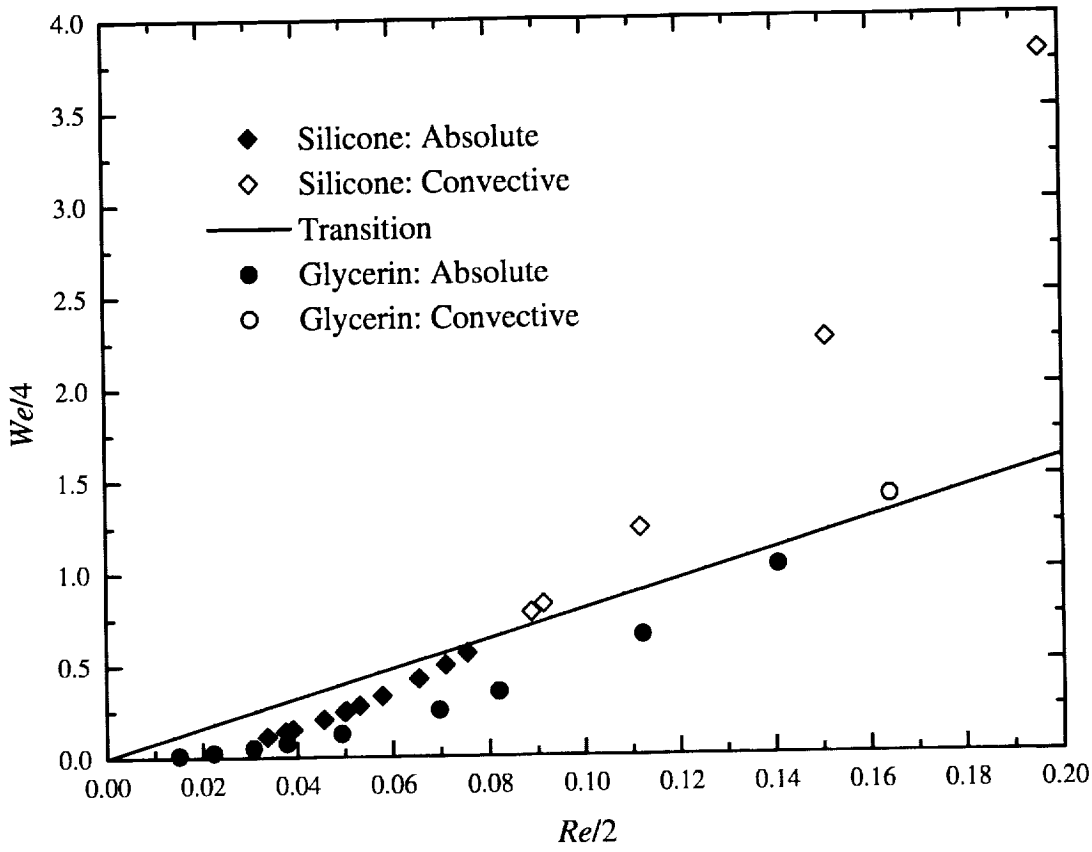

Figure 3: Transition from absolute to convective instability

absolutely unstable in the ten tests with the values of (Re, We) smaller than (Re_c, We_c). Similar results are shown in circles for a glycerin jet. The transition occurs between the nearest open and filled circles at larger values of Re and We for the glycerin jet. When the nearest open and filled circles are connected with a straight line, it happens to pass through the nearest open and filled squares and also through the origin. This is quite reasonable, since in the theoretical prediction (refs. 1-5) the transition curve in the region of small (Re, We) is almost a straight line. However, the known theoretical predictions have not been able to extend the transition curve all way to the origin due to the difficulty involved in attaining a sufficient numerical accuracy. In fact the values of Re in Fig. 3 are already so small that no accurate numerical results are available for direct comparisons on the transition curve depicted in the figure. Although a quantitative comparison between theory and experiment is not yet possible (ref. 9), the observed qualitative trends that the critical Weber numbers of transition decrease with Reynolds numbers and that the jet is convectively or absolutely unstable respectively in the region above or below the transition line appear to agree with theories.

For larger Re accurate numerical results are available. Unfortunately, for larger Reynolds numbers the transition has to be observed so far downstream from the nozzle tip that the small dimensions of the drop rig does not permit us to achieve our goal. More accurate theoretical predictions and experiments over a wider range of flow parameters including small values of (Re, We) near the origin are currently being carried out for a complete delineation of the transition between convective and absolute instabilities.

ROLE OF INTERFACIAL SHEAR

The precise roles of interfacial shear force relative to all other forces in the jet breakup has not

been elucidated (ref. 6). To fill in this information gap, we calculate the power inputs due to all forces which participate in causing the kinetic energy of the disturbance to grow in a volume of the liquid jet. The jet is enclosed by a coaxial circular cylinder. The annular region between the cylinder and the jet is filled with a viscous gas. The relative importance of each force is identified by comparing it with all other forces in the energy budget. The energy budget is obtained by forming the dot product of the linearized Navier-Stokes equations with the velocity perturbation, and then integrating over a given control volume of the liquid jet. The energy budget can be written as

$$KE = PRG + SUT + SHG + SHB + NVG + SHL + NVL + PRL + REY + DIS, \quad (1)$$

Each term in (1) represents the phase averaged time rate of change of physically distinctive factor per unit length of the liquid control volume enclosed by the interface of length λ on the side and by the two circular lids at $z=0$ and $-\lambda$. KE is the time rate of change of the disturbance kinetic energy. The last term DIS is the rate of mechanical energy dissipation through viscosity in the volume, which tends to reduce KE as it is always negative. The energy transfer between the disturbance and the basic flow through the Reynolds stress is represented by REY, the sign of which depends on the flow parameters. The rest of the surface integrals in (1) represent various rates of work done on the control surface. PRG represents the rate of work done by the gas pressure fluctuation on the liquid jet, if it is positive. If it is negative, the work is done by the liquid jet on the surrounding gas at the expense of the disturbance kinetic energy. The same sign convention is followed by the rest of the work terms. SUT is the rate of work done by the surface tension. SHG is the rate of work done by the shear stress exerted by the fluctuating gas at the interface. SHB is the rate of work done by the shear stress associated with the basic flow distortion caused by the interfacial displacement. NVG represents the rate of work done by the normal viscous stress exerted by the fluctuating gas at the interface. NVL and SHL represent respectively the rates of work done by the normal and tangential components of the viscous stress at the top and bottom ends of the control volume. The rate of the pressure work at the top and bottom ends of the control volume is given by PRL. Each term on the right side of (1) represents a different physical factor which affects the instability of the liquid jet. Therefore the relative magnitude as well as the sign of each term must be evaluated. To achieve this, we must carry out the stability analysis which provides the functions appearing in the integrands of (1). An accurate eigenvector solution is obtained by use of the Chebyshev-collocation method (ref. 15).

Table 1 gives the energy budget of a liquid jet at Re=1000, We=400, Q=0.0013, N=0.018, l=10, where Q is the gas to liquid density ratio, N is the gas to liquid viscosity ratio, and l is the ratio of the cylinder radius to the jet radius. The wave numbers k_r cover both stable and unstable disturbances. All items are normalized with the energy term of the most amplified disturbance occurring at k_{rm} = 0.684. It is seen from this table that the positive rates of change of the disturbance kinetic energy are mainly due to

k_r	KE	REY	SUT	PRL	PRG	NVG	DIS	SHL	NVL	SHG
0.140	0.127	-1.20E-05	0.129	1.59E-05	3.35E-05	9.39E-06	-0.00128	-7.91E-08	2.45E-06	-1.15E-03
0.200	0.248	-2.34E-05	0.254	7.34E-05	-2.06E-04	2.52E-05	-0.00362	-2.25E-07	6.74E-06	-1.78E-03
0.300	0.503	-4.74E-05	0.520	1.81E-04	-3.23E-04	7.95E-05	-0.01130	-6.76E-07	1.97E-05	-2.87E-03
0.400	0.771	-7.21E-05	0.804	4.20E-04	-5.06E-04	1.69E-04	-0.02410	-1.34E-06	3.80E-05	-3.84E-03
0.500	0.980	-9.10E-05	1.030	7.36E-04	-9.49E-04	2.80E-04	-0.04070	-2.10E-06	5.58E-05	-4.52E-03
0.600	1.060	-9.84E-05	1.140	6.50E-04	-1.28E-03	3.89E-04	-0.05920	-2.92E-06	6.54E-05	-4.73E-03
0.684	1.000	-9.31E-05	1.090	1.19E-03	-1.43E-03	4.52E-04	-0.06800	-3.66E-06	6.22E-05	-4.45E-03
0.700	0.973	-9.08E-05	1.060	2.15E-03	-1.45E-03	4.58E-04	-0.07160	-3.80E-06	6.03E-05	-4.34E-03
0.800	0.697	-6.81E-05	0.781	8.82E-04	-1.31E-03	4.33E-04	-0.06810	-4.51E-06	3.98E-05	-3.27E-03
0.900	0.296	-3.47E-05	0.353	4.96E-04	-7.18E-04	2.64E-04	-0.04570	-3.88E-06	1.31E-05	-1.59E-03
1.100	-0.058	3.00E-04	0.067	1.47E-03	-2.71E-03	1.47E-03	-0.12000	-1.09E-05	3.18E-07	-4.76E-03
1.200	-0.160	7.71E-04	0.182	5.79E-03	-6.71E-03	3.36E-03	-0.33400	-3.70E-05	1.05E-06	-1.08E-02

Table 1: Energy budget for Rayleigh mode.
Re=1000, Fr^{-1}=0.0, We=400, Q=0.0013, N=0.018, l=10.

the work done by the surface tension on the control liquid volume. Although the viscous normal stress exerted by gas represented by NVG as well as the normal stress work represented by PRL and NVL at the top and bottom of the cylindrical liquid column also contribute to the growth of the unstable disturbance, they are several orders of magnitude smaller than the surface tension term SUT. The major factor which resists disturbance growth is viscous dissipation. The pressure and the shear stress exerted by the gas at the liquid-gas interface are also significant factors against instability. Although the liquid tangential viscous stress represented by SHL and the bulk Reynolds stress represented by REY also contributed to drain the kinetic energy from the disturbance, they are many order of magnitudes smaller than DIS. However the sum of all negative terms are not sufficiently large in magnitude to counter the destabilizing effect of the surface tension. Thus the mechanism of the instability of a viscous liquid jet in a viscous gas by the Rayleigh mode remains capillary pinching which was demonstrated by Chandrasekhar (ref. 16) who considered an inviscid liquid jet in vacuum. An inviscid Rayleigh jet is neutral with respect to disturbances of wave number larger than the cut off wave number $k_{rc} = 1$. Thanks to viscous dissipation these disturbances are actually damped according to table 1. The stabilizing and destabilizing factors retain their signs in the range of k_r given in table 1, except for the Reynolds stress term. Although some energy is transferred from the mean flow to the disturbances of wavelength shorter than $2\pi R_1$ the growth of these disturbances are nevertheless suppressed by viscous dissipation. Note that the change of SUT with k_r is not monotonic, and its maximum does not occur at k_{rm}. In fact all of the other terms also do not change monotonically, and their maxima do not occur at the same k_r. This indicates the significance of interplay among all items in determining the maximum growth rate.

ACKNOWLEDGMENTS

This work was supported by Grant. No. NAG3-1891 of NASA.

REFERENCES

1. Leib, S.J. and Goldstein, M.E., "The generation of capillary instability on liquid jet," J. Fluid Mech. 168, 479-500 (1986).
2. Leib, S.J. and Goldstein, M.E., "Convective and absolute instability of a viscous liquid jet," Phys. Fluids, 29, 952-954 (1986).
3. Lin, S.P. and Lian, Z.W., "Absolute instability of a liquid jet in a gas," Phys. Fluids A, 1, 490-493 (1989).
4. Lin, S.P. and Lian, Z.W. "Absolute and convective instability of a viscous liquid jet surrounded by a viscous gas in a vertical pipe," Phys. Fluids. A, 5, 771-773 (1993).
5. Zhou, Z.W. and Lin, S.P., "Effects of compressibility on the atomization of liquid jets," J. Propulsion and Power, 8, 736-740 (1992).
6. Lin, S.P. and Reitz, R.D., "Drop and spray formation from a liquid jet," Annual Review of Fluid Mechanics 30, 85-105 (Annual Rev. Inc. Palo Alto, 1998).
7. Chieger, N. and Reitz, R.D., "Regimes of jet breakup and breakup mechanisms (physical aspects)," in Recent Advances in Spray Combustion: Spray Atomization and Drop Burning Phenomena, Vol. 1, ed. K.K. Kuo (AIAA Inc. Reston, 1996), pp. 109-135.
8. Lin, S.P., "Regimes of jet breakup and breakup mechanisms (mathematical aspects)," in Recent Advances in Spray Combustion: Spray Atomization and Drop Burning Phenomena, Vol. 1, ed. K.K. Kuo (AIAA Inc. Reston, 1996), pp. 137-160.
9. Vihinen, I, Honohan, A.M. and Lin, S.P., "Image of absolute instability in a liquid jet," Phys. Fluids. 9, 3117-3119 (1997).
10. Honohan, A.M., "Experimental measurements of the spatial instability of viscous liquid jet at Microgravity," M.S. thesis, Clarkson University, Potsdam, NY 1995.
11. Vihinen, I., "Absolute and convective instability of a liquid jet in microgravity," M.S. thesis, Clarkson University, Potsdam, NY 1996.
12. Lin, S.P. and Creighton, B., "Energy budget in atomization," J. of Aerosol Sci. And Tech., 12, 630-636 (1990).
13. Huerre, P. and Monkewitz, P.A., "Local and global instabilities in spatially developing flows," Annu. Rev. Fluid Mech. 22, 473-537 (1990).
14. Monkewitz, P.A., Davis, J., Bojorquez, B. and Yu, M.H., "The breakup of a liquid jet at high Weber number, Bull. Am. Phys. Soc. 33, 2273 (1988).
15. Boyd, J.P., Chebyshev and Fouier Spectral Methods, Springer Verlag, New York (1989).
16. Chandreskhar, S., Hydrodynamic and Hydromagnetic Stability, Oxford University Press (1961).

Session 7A

Bubbles and Drops

DROP EJECTION FROM AN OSCILLATING ROD

E.D. Wilkes, O.A. Basaran, School of Chemical Engineering, Purdue University, West Lafayette IN 47906, USA, obasaran@ecn.purdue.edu

ABSTRACT

The dynamics of a drop of a Newtonian liquid that is pendant from or sessile on a solid rod that is forced to undergo time-periodic oscillations along its axis is studied theoretically. The free boundary problem governing the time evolution of the shape of the drop and the flow field inside it is solved by a method of lines using a finite element algorithm incorporating an adaptive mesh. When the forcing amplitude is small, the drop approaches a limit cycle at large times and undergoes steady oscillations thereafter. However, drop breakup is the consequence if the forcing amplitude exceeds a critical value. Over a wide range of amplitudes above this critical value, drop ejection from the rod occurs during the second oscillation period from the commencement of rod motion. Remarkably, the shape of the interface at breakup and the volume of the primary drop formed are insensitive to changes in forcing amplitude. The interface shape at times close to and at breakup is a multi-valued function of distance measured along the rod axis and hence cannot be described by recently popularized one-dimensional approximations. The computations show that drop ejection occurs without the formation of a long neck. Therefore, this method of drop formation holds promise of preventing formation of undesirable satellite droplets.

1. INTRODUCTION

Formation of small drops of one phase into another phase by flowing the former phase through a suitable nozzle is of great scientific interest because of widespread use of the phenomenon in practical applications. Some well known applications include mass transfer operations in solvent extraction,[1,2] ink-jet printing,[3,4] and measurement of dynamic surface tension,[5,6] among others.

When a liquid is fed continuously through a capillary tube at a low flow rate, a portion of the drop liquid hanging from the tip of the capillary breaks off it when the force of gravity acting on the drop becomes large enough to overcome the force of surface tension.[7,8] Unfortunately, the gravitationally induced mechanism of drop breakup is not available in zero-g. One way to form drops under low-g conditions would be to vibrate the substrate supporting the drop liquid. This paper presents a theoretical analysis of the situation in which a vertical rod which supports an initially quiescent pendant drop is impulsively set into oscillations of sufficiently large amplitude along its axis so that a portion of it detaches or is ejected from the rest of the liquid that is left behind on the rod.

Forced oscillations of pendant and sessile drops sans breakup have been studied extensively because they exhibit rich non-linear behavior and also are important in applications. For example, oscillations of pendant drops[9] and also of liquid bridges[10] can be used to infer the surface tension and viscosity of the drop liquid.

Formation of drops from fine capillaries through which liquid is forced at a constant flow rate has also been extensively studied experimentally,[7,8,11] by means of one-dimensional approximations,[7,12] and computationally in the inviscid, irrotational flow limit,[13] in the Stokes flow limit,[14] and at arbitrary Reynolds numbers.[15] These studies have shown that as the drop is nearing breakup, a long thread or neck of liquid connects the about to form primary drop from the rest of the liquid hanging from the capillary. The thread first breaks at its downstream end and its tip is accelerated toward the drop that remains hanging from the tube. However, before the thread can recoil entirely and become absorbed by the liquid hanging from the tube, it breaks at its upstream end and gives rise to one or more satellite droplets. The satellite droplets are undesirable in virtually all applications. In ink-jet printing, for example, they can lead to stray marks on the paper and reduce print quality. Therefore, it is desirable to come up with ways to suppress the formation of satellite droplets.[16]

When a drop that is hanging from or sitting on the tip of a solid rod is forced to undergo time periodic oscillations along its axis and sufficient time is allowed for the drop to reach a steady oscillatory state, the drop deformation is maximized at a number of values of the forcing frequency known as the resonance frequencies for a fixed value of the forcing amplitude. When the forcing amplitude is sufficiently large, the drop should no longer oscillate and instead should undergo breakup. The equations governing the physics of drop oscillations and breakup are summarized in section 2. A powerful finite element algorithm that can go behind earlier works[9,10] and follow drops all the way to breakup is presented in section 3. Results and conclusions are taken up in sections 4 and 5.

2. PROBLEM STATEMENT

The system, shown in Figure 1, is an axisymmetric drop of an incompressible Newtonian liquid of constant volume V_0, density ρ and viscosity μ which is pendant from a solid circular rod of radius R and surrounded by a dynamically inactive ambient gas. The drop/ambient gas interface has constant surface tension σ. As in Wilkes and Basaran,[9] the rod is impulsively set into motion along its symmetry axis and sinusoidally in time with forcing amplitude AR and frequency $\Omega\sqrt{\sigma/\rho R^3}$. The three-phase drop/rod/ambient gas contact line is constrained to remain at the outer sharp edge of the rod face as the drop deforms. As time advances, the response of the drop surface $S(t)$ will be either (a) attainment of a steady oscillatory state, or limit cycle, once the initial transients decay, or (b) ejection of a primary drop from the rest of the liquid which will remain on the rod surface.

To cast the problem in dimensionless form, the rod radius R is chosen as a characteristic length scale and the capillary time $t_c \equiv \sqrt{\rho R^3/\sigma}$ is chosen as a time scale.[17,18] The corresponding velocity and pressure/stress scales are then $\sqrt{\sigma/\rho R}$ and $\sqrt{\sigma\mu^2/\rho R^3}$, respectively. The dimensionless groups governing the motion of the liquid are the Reynolds number $Re \equiv \sqrt{\sigma\rho R/\mu}$, the gravitational Bond number $G \equiv \rho g R^2/\sigma$, dimensionless forcing amplitude A, dimensionless forcing frequency Ω, and dimensionless volume V_0/R^3. Therefore, the instantaneous position of the rod relative to its initial position is given by $z'(t)\ A \sin \Omega t$. The equations are solved in a noninertial frame of reference, in which the origin of the cylindrical coordinate system (r, z, θ) moves with the rod as it oscillates. The motion of fluid within the drop is governed by the Navier-Stokes system,

$$\nabla \cdot \underline{\mathbf{v}} = 0 \qquad (1)$$

$$Re\left(\frac{D\underline{\mathbf{v}}}{Dt} + \underline{\mathbf{F}}\right) = \nabla \cdot \underline{\mathbf{T}} + ReG\underline{\mathbf{e}}_z \qquad (2)$$

In Equation (2), $\underline{\mathbf{F}} \equiv -A\Omega^2 \sin \Omega t\, \underline{\mathbf{e}}_z$ is the fictitious acceleration term which arises because of the use of a noninertial frame of reference, $\underline{\mathbf{e}}_z$ is a unit vector in the downward z-direction, and the dimensionless stress tensor for a Newtonian fluid is given by $\underline{\mathbf{T}} = -p\underline{\mathbf{I}} + [\nabla\underline{\mathbf{v}} + \nabla\underline{\mathbf{v}}^T]$. The drop shape, which is unknown *a priori*, is determined by using the kinematic condition as an additional governing equation,

$$\underline{\mathbf{n}} \cdot (\underline{\mathbf{v}} - \underline{\mathbf{v}}_s) = 0 \text{ on } S(t) \qquad (3)$$

where $\underline{\mathbf{n}}$ is the outward unit normal vector to the surface and $\underline{\mathbf{v}}$ and $\underline{\mathbf{v}}_s$ are velocities of points just inside and on the free surface $S(t)$, respectively. The other boundary conditions are axisymmetry about the z-axis, no slip and no penetration along the rod surface, the balancing of the normal stress by the capillary pressure and the vanishing of the shear stress along the free surface, and the fixed contact line.

Initially, the drop shape is a hemisphere and the fluid is quiescent; rod motion is impulsively commenced at $t = 0$.

3. COMPUTATIONAL METHOD

The transient system of governing equations (1)-(3) subject to the boundary and initial conditions stated above are solved numerically by a method of lines using the Galerkin/Finite Element Method (G/FEM) for spatial discretization and an adaptive, implicit finite difference method for time discretization. The Galerkin weighted residuals of these equations are solved for the velocity, pressure, and free surface shape by Newton iteration at each time step. Time integration is achieved using a backward-difference predictor for the first four time steps and for four time steps following each remeshing (see below), and a trapezoid-rule integrator and second-order Adams-Bashforth predictor at all other time steps. In the latter case, time step sizes are chosen adaptively such that the time truncation error does not exceed 10^{-3}.

The problem domain is divided into elements using one of three methods15. Method 1, Figure 2(a), consists of a central fixed cylindrical region of radius ~r extending from the rod to a distance ~z below it along the centerline, which is surrounded by outer regions which deform with the drop surface. The outer regions' elements are separated by fixed spines and by curves which deform in proportion to the moving surface. Method 2, Figure 2(b), consists of the same regions and a neck region between the rod and the drop regions of Method 1. The spines in this new region are horizontal and spaced at intervals which become smaller as the surface curvature increases. Method 3, Figure 2(c), is identical to Method 2 except that the spine angles in the neck region are varied so as to enable discretization of a portion of the interface which is about to overturn. Method 1 is used for the initial stages of drop oscillation until the minimum neck radius R_m reaches a specified value; at that point, Method 2 is used until the slope of the interface near the point of breakup becomes so high that Method 3 is required. Once Method 3 is invoked, no further remeshing occurs. The accuracy of this computational algorithm was confirmed by comparison of results obtained to those reported by Wilkes and Basaran[9].

Periodically, the mesh structure is reconstructed so as to conform to the present drop shape: this is referred to as remeshing. At various increments of the drop length L or when the minimum neck radius R_m approaches the present fixed region boundary δ_r, new values of δ_r and δ_z are chosen based on the present drop

shape. When Method 2 is used, the neck region length δ_y and the number of spines in this region are also recalculated. Once the new elements are located, all unknowns are interpolated from the old mesh onto the new mesh using the relevant basis functions, and time integration is resumed. When R_m falls below 0.003, the primary drop is considered to have detached.

4. RESULTS AND DISCUSSION

Figure 3 illustrates the response of a drop for a typical situation in which drop ejection occurs. In this case, $Re = 20$, $G = 0$, $\Omega = 3.5$, and $A = 0.50$. When the forcing amplitude is lower but the other parameters are the Figure 3 illustrates the response of a drop for a typical situation in which drop ejection occurs. In this case, $Re = 20$, $G = 0$, $\Omega = 3.5$, and $A = 0.50$. When the forcing amplitude is lower but the other parameters are the same, the primary resonance frequency is known to be about 3.5.[9] Figure 3 shows that during the first oscillation period after rod motion begins, the maximum elongation of the drop is considerably lower than that for each subsequent period, in accord with the results of Wilkes and Basaran.[9] During the second period, however, the drop tip nearly touches the rod and then moves farther away from it than in the first period. As the tip recedes once more, the interface necks rapidly and the drop starts breaking into two distinct fluid masses. In contrast to drop formation from a tube,[13,15] the primary drop is now moving upward toward the neck while the rod is accelerating the liquid in its vicinity toward the neck. As shown in Figure 4 at a time step near ejection, the down moving fluid near the rod and the up moving fluid in the bulk of the primary drop work in unison to prevent drop breakup. However, by this time the capillary pressure in the thin neck is so high that evacuation of the neck prevails over the former mechanism. Moreover, on account of the receding primary drop and the down moving rod, the interface above the neck overturns and becomes a multi-valued function of z. The manner in which the interface breaks is thus quite different from that observed for drop formation from a tube: Because a long thread does not form, the likelihood of satellite drop formation is minimized.

A similar series of computations was performed using the same parameters as in Figure 3 except for A, which was varied from 0.2 to 0.3. These computations showed that the critical forcing amplitude A_c for ejection under these conditions was 0.274 ± 0.001. For cases in which $A < A_c$, the drops oscillated without ejection, whereas when $A > A_c$, ejection was observed and the final drop shapes (not shown) were remarkably similar – the most notable variation in drop shape over this range of amplitudes was the extent of interface overturning, which increases with A. In each of these cases, the time of drop ejection, when it occurred, was near the end of the second rod oscillation period, except for the case with $A = 0.274$ when it occurred during the fifth period. Because the drop is at rest at the start of the oscillations, a considerably higher forcing amplitude is necessary to effect ejection in a single period. By contrast, ejection after two or more periods appears to occur only when A is equal to or slightly higher than A_c.

5. CONCLUSIONS AND OUTLOOK

The computational method used in this paper can accurately account for the fluid dynamics of drop ejection from an oscillating rod. According to the foregoing results, the interface develops an infinite slope before the radius of the thread or the neck vanishes. Therefore, recently popularized one-dimensional slender-jet equations that represent interface shape as a function of axial distance alone[7,12,14] cannot be used to model the dynamics of drop ejection.

Suppression of neck formation, in contrast to situations when a liquid is made to flow at a constant flow rate through a capillary, is an unexpected but highly desirable outcome of the technique of drop production considered here. Exploitation of this finding in practical applications such as ink-jet printing is pending.

ACKNOWLEDGMENTS

This research was sponsored by the NASA Microgravity Fluid Physics Program. EDW was also supported in part by a Shell Doctoral Dissertation Fellowship.

REFERENCES

[1] P.J. Bailes and A. Winward, "Progress in liquid-liquid extraction," Trans. Instr. Chem. Engrs. **50**, 240 (1972).

[2] W.J. Heideger and M.W. Wright, "Liquid extraction during drop formation: effect of formation time," AIChE J. **32**, 1372 (1986).

[3] T.W. Shield, D.B. Bogy, and F.E. Talke, "Drop formation by DOD ink-jet nozzles: A comparison of experiment and numerical simulation," IBM J. Res. Dev. **31**, 96 (1987).

[4] I. Rezanka and R. Eschbach, "Recent Progress in Ink Jet Technologies," (IST Press, Springfield, VA, 1996).

[5] C.A. Macleod and C.J. Radke, "A growing drop technique for measuring dynamic interfacial tension," J. Colloid Interface Sci. **160**, 435 (1993).

[6] X. Zhang, M.T. Harris, and O.A. Basaran, "Measurement of dynamic surface tension by a growing drop technique," J. Colloid Interface Sci. **168**, 47 (1994).

[7] X.D. Shi, M.P. Brenner, and S.R. Nagel, "A cascade of structure in a drop falling from a faucet," Science **265**, 219 (1994).

[8] X. Zhang and O.A. Basaran, "An experimental study of dynamics of drop formation," Phys. Fluids **7**, 1184 (1995).

[9] E.D. Wilkes and O.A. Basaran, "Forced oscillations of pendant (sessile) drops," Phys. Fluids **9** (6), 1512 (1997).

[10]T-Y. Chen and J.A. Tsamopoulos, "Non-linear dynamics of capillary bridges: theory," J. Fluid Mech. **255**, 373 (19).

[11]D.H. Peregrine, G. Shoker, and A. Symon, "The bifurcation of liquid bridges," J. Fluid Mech. **212**, 25 (1990).

[12]J. Eggers and T.F. Dupont, "Drop formation in a one-dimensional approximation of the Navier-Stokes equation," J. Fluid Mech. **262**, 205 (1994).

[13]R.M.S.M. Schulkes, "The evolution and bifurcation of a pendant drop," J. Fluid Mech. **278**, 83 (1994).

[14]M.P. Brenner, J. Eggers, K. Joseph, S.R. Nagel, and X.D. Shi, "Breakdown of scaling in droplet fission at high Reynolds numbers," Phys. Fluids **9**, 1573 (1997).

[15]E.D. Wilkes, S.D. Phillips, and O.A. Basaran, "Computational and experimental analysis of dynamics of drop formation," Phys. Fluids (1998, submitted).

[16]X. Zhang and O.A. Basaran, "Dynamics of drop formation from a capillary in the presence of an electric field," J. Fluid Mech. **326**, 239 (1996).

[17]O.A. Basaran, "Nonlinear oscillations of viscous liquid drops," J. Fluid Mech. **241**, 169 (1992).

[18]O.A. Basaran and D.W. DePaoli, "Non-linear oscillations of pendant drops," Phys. Fluids **6** (9), 2923 (1994).

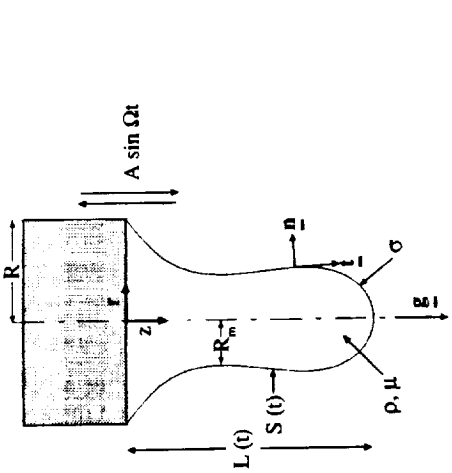

FIGURE 1. A liquid drop supported on an oscillating solid rod: definition sketch. All variables except ρ, μ, σ, and g are dimensionless.

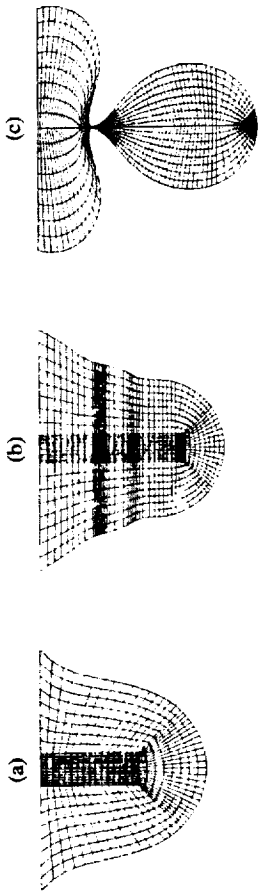

FIGURE 2. Tesselation methods used for studying drop ejection. (a) Method 1, (b) Method 2, and (c) Method 3.

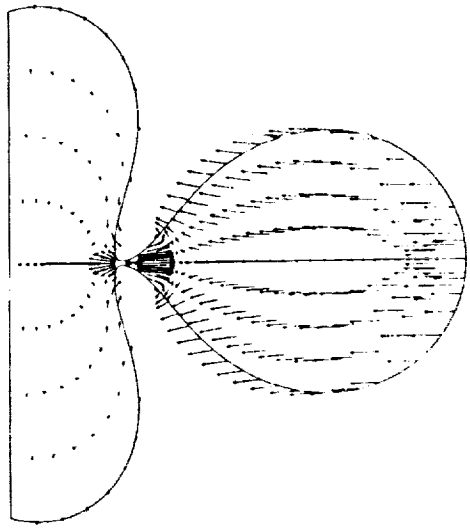

FIGURE 4. Velocity field in an oscillating drop just before ejection. Re=20, G=0, A=0.5, Ω=3.5.

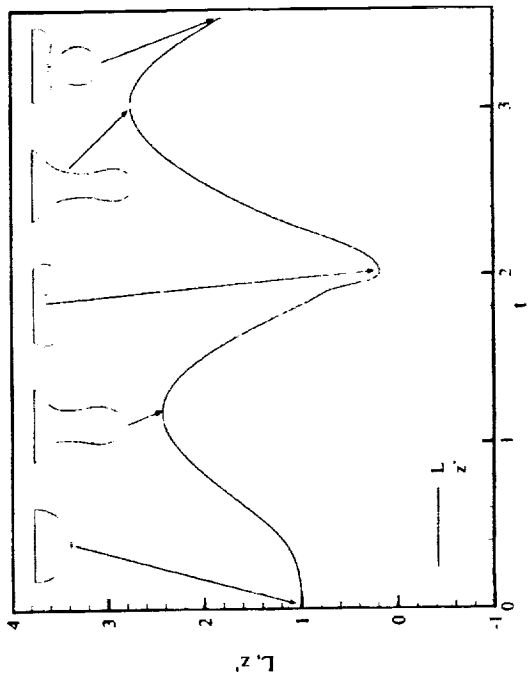

FIGURE 3. Time evolution of drop length and shape. Re=20, G=0, A=0.5, Ω=3.5.

NUMERICAL MODELING OF THREE-DIMENSIONAL FLUID FLOW WITH PHASE CHANGE

Asghar Esmaeeli, Vedat Arpacı, Department of Mechanical Engineering and Applied Mechanics, The University of Michigan, Ann Arbor, Michigan

INTRODUCTION

Bubbles are essential particles in many industrial as well as natural processes. Heat transfer through boiling, fluid cavitation, bubble driven circulation systems in metal processing, and bubble/free surface interactions in oceans are just a few examples of the many roles that bubbles play in the physical systems. One of the key questions in phase change dynamics is the prediction of mass transfer rate and its effects on the fluid flow and heat transfer of the system. There has been extensive investigations about bubble growth rate in the last few decades. The early work was concerned about solving separately the momentum and heat conduction equation and can be divided into two main categories: growth rate controlled by inertia and growth rate controlled by heat diffusion. In the inertially-controlled growth the temperature difference between bubble and liquid is negligible and the growth is controlled by the pressure difference inside and outside the bubble and inertia of the liquid. Rayleigh (1917) made such assumption to solve for the collapse of an empty cavity in a large mass of liquid. Rayleigh's solution was confined to spherically symmetric, isothermal, and inviscid flow. He also neglected the surface tension. Later on, his analysis was extended to include liquid viscosity and surface tension. In the heat diffusion controlled growth the pressure difference inside and outside bubble is negligible and the growth is controlled by heat transfer from the liquid to the bubble. The investigations of Bosnjakovic (1930), Plesset & Zwick (1952), and Skinner & Bankoff (1965) are a few examples of analyses based on the heat diffusion controlled growth. Subsequent analyses to solve the coupled equations have produced several asymptotic solutions applicable to long time only and a number of complete but approximate solutions involving simplifying assumptions about the heat conduction equation. See, for example, Plesset & Zwick (1954), Scriven (1959), and Bankoff (1958) for the former and Kosky (1968), Mikic *et al.* (1970), and Theofanous & Patel (1975) for the latter.

The use of numerical modeling in solving fluid flow with phase change is relatively new. One of the earliest of such studies is the potential flow solution of Plesset & Chapman (1971) for the collapse of an isothermal spherical vapor bubble in the neighborhood of a solid wall. A number of authors have tried to solve the boiling bubble problem by coupling the momentum equation with a simplified form of the energy equation. See Theofanous *et al.* (1969) and Prosperetti & Plesset (1977), for example. Dalle Donne & Ferranti (1975) were among the first to solve the complete equations of motion and energy. More recent numerical studies about boiling bubbles include boundary fitted/finite element method of Schunk & Rao (1994), finite volume/moving mesh method of Welch (1995), level set method of Son & Dhir (1997), and front tracking/finite difference technique of Juric & Tryggvason (1995).

So far, the last two studies present the most comprehensive numerical modeling of the phase change problem leaving aside their two-dimensionality. While it is possible to predict some of the qualitative features of the phase change phenomena by two-dimensional simulations, it is generally believed that these computations fail to provide an accurate account of the quantitative features. Therefore, it is necessary to relax this restriction in order to obtain a more realistic picture of the problem. Our aim is to present a numerical technique for modeling three-dimensional fluid flow with phase change. To the best of our knowledge, this is the first numerical study that addresses this issue. In an earlier study (i.e. Esmaeeli & Arpacı, 1998), we used a similar methodology to simulate phase change without fluid flow.

FORMULATION AND NUMERICAL METHOD

Consider a domain consisting of a liquid and its vapor undergoing phase change. The material properties of the fluids are different but constant within each phase. The governing equations for this problem are conservation of mass, momentum, and energy equations within each phase, and the jump conditions across the interface. Rather than writing the governing equations separately for each of the fluids, a single set of equations are used which are valid for the entire flow field and take the jump in properties across the interface into account. The momentum equation in conservative form for such a flow is:

$$\frac{\partial \rho \overline{u}}{\partial t} + \nabla \cdot \rho \overline{u}\,\overline{u} = -\nabla p + \nabla \cdot \mu(\nabla \overline{u} + \nabla \overline{u}^T) - \rho \overline{g} + \oint \sigma \kappa \overline{n} \delta(\overline{x} - \overline{x}^f) dA. \quad (1)$$

In the above equation $\overline{u}$ is the velocity, p is the pressure, ρ is the density, μ is the viscosity, $\overline{g}$ is the gravity, σ is the surface tension coefficient, κ is twice the mean curvature, and $\overline{n}$ is the unit vector normal to the interface. $\delta(\overline{x} - \overline{x}^f)$ is a delta function which is zero everywhere except at the interface where $\overline{x} = \overline{x}^f$ and dA is differential area of the interface.

The energy equation in conservative form is:

$$\frac{\partial \rho c T}{\partial t} + \nabla \cdot \rho c \overline{u} T = \nabla \cdot k \nabla T + \oint \overline{h} \rho_f (\overline{u}_i - \overline{u}_f).\overline{n} \delta(\overline{x} - \overline{x}^f) dA, \quad (2)$$

where T is the temperature, c is the heat capacity, and k is the heat conductivity. The last term in the above equation acts as a heat source (sink) which is zero away from the interface and its inclusion enforces the conventional energy jump condition across the front. Here, ρ_f and $\overline{u}_f$ are the fluid density and velocity at the liquid or vapor side of the interface, and $\overline{u}_i$ is the interface velocity. $\overline{h}$ is a measure of difference in the enthalpies of the liquid and the vapor and is derived using thermodynamics consideration:

$$\overline{h} = h_{fg} + T_{eq}(c_l - c_v). \quad (3)$$

Here, h_{fg} is the latent heat of evaporation, T_{eq} is the equilibrium temperature, and c_l and c_v are the heat capacities of the liquid and the vapor, respectively.

The mass conservation is:

$$\nabla \cdot \rho \overline{u} = \oint (\rho_v - \rho_l) u_n \delta(\overline{x} - \overline{x}^f) dA, \quad (4)$$

where, $u_n = \overline{u}_i.\overline{n}$. The above equation is equivalent to the conventional mass conservation equation but is better suited for numerical formulation.

The introduction of the interface velocity $\overline{u}_i$ adds an additional unknown to the problem. This new unknown is being taken care of by implementation of the modified Gibbs-Thomson relation at the interface:

$$T_f = T_{eq} + \frac{\sigma \kappa T_{eq}}{\rho_f h_{fg}} + \frac{(c_l - c_v)}{h_{fg}}(T_f - T_{eq})^2 - \frac{\rho_f (\overline{u}_i - \overline{u}_f) \cdot \overline{n}}{\phi}, \quad (5)$$

where ϕ is the kinetic mobility. The above equation was first derived by Alexiades & Solomon (1993) and then modified by Juric & Tryggvason (1996) to include the kinetic mobility effect.

The above equations are supplemented by the equations of state for the material properties:

$$\frac{\mathcal{D}\rho}{\mathcal{D}t} = 0; \quad \frac{\mathcal{D}\mu}{\mathcal{D}t} = 0; \quad \frac{\mathcal{D}k}{\mathcal{D}t} = 0; \quad \frac{\mathcal{D}c}{\mathcal{D}t} = 0, \quad (6)$$

where

$$\frac{\mathcal{D}}{\mathcal{D}t} = \frac{\partial}{\partial t} + \overline{u}_i \cdot \nabla. \quad (7)$$

Our numerical technique is an extension to the two-dimensional model developed by Juric & Tryggvason (1995). Extension of the method to three dimensions involves a number of complications in the operations on the front which will be addressed in a future publication. We use a fixed (i.e. Eulerian), regular, and staggered grid to discretize the governing equation and an unstructured (i.e. Lagrangian) grid to represent the front and to construct the material property fields. This unstructured grid is also used to distribute the source terms in the right hand side of mass conservation, momentum, and energy equations to the Eulerian grid and to interpolate the velocity, temperature, and density at the front points from the grid.

The computations start with construction of the initial temperature field T^n and the material property fields ρ^n, μ^n, c^n, k^n using known position of the front at $t = 0$, where $n = 1$. The front is then moved to a new position using the interface velocity at the current time $\overline{u}_i{}^n$. The surface tension is distributed to the grid as a body force using Peskin distribution function (see Peskin 1977) and the density ρ^{n+1} and heat capacity c^{n+1} fields are constructed at the new position. A modified projection algorithm which is first order in time and second order in spatial dimensions is used to solve the momentum equation. In the absence of pressure term, the momentum equation is solved and a provisional (i.e. unprojected) velocity field $\overline{u^*}$ is computed. The iterative part starts by guessing the front velocity at the next time step and construction of the mass source at the new position of the front. An elliptic pressure equation is then solved and the provisional velocity is corrected for the pressure to obtain the projected velocity $\overline{u}^{n+1}$. The velocity of the fluid at the front position $\overline{u}_f{}^{n+1}$ is interpolated using a Peskin interpolation function (see Peskin 1977) and the heat source is constructed. The energy equation is then solved for T^{n+1} and the Gibbs-Thomson relation is checked at the front points. If this equation is satisfied for all the front points within a predetermined tolerance, the heat conduction coefficient k^{n+1} and viscosity fields μ^{n+1} are updated for the next time step and the calculation proceeds. Otherwise, a new guess is proposed for the front velocity and the computations are repeated.

The individual parameters that control the problem are ρ_l, ρ_v, μ_l, μ_v, k_l, k_v, c_l, c_v, h_{fg}, g, ϕ, σ, $T_\infty - T_{eq}$, and initial diameter of the bubble, d_0. Here, T_∞ is the initial temperature of the fluid outside the bubble. Nondimensionalization results the following parameters: ρ_v/ρ_l, μ_v/μ_l, k_v/k_l, c_v/c_l, $Ja = c_l(T_\infty - T_{eq})/h_{fg}$, $Pr = \mu_l c_l/k_l$, $Gr = \rho_l g(\rho_l - \rho_v)d_0{}^3/\mu_l{}^2$, $Ca = c_l(T_\infty - T_{eq})\sigma/\rho_l h_{fg}{}^2 d_0$, and $\vartheta = k_l/\phi\rho_l h_{fg} d_0$. Ja is the Jacob number which is ratio of the sensible to the latent heat, Pr is the Prandtl number which is a measure of diffusion of momentum with respect to thermal energy, Gr has a strong resemblance to the Grashof number, Ca is a capillary number which is ratio of surface tension to viscous force, and ϑ is nondimensional kinetic mobility. When we present our results, $l_s = d_0$, $u_s = \mu_l/\rho_l d_0$, and $t_s = l_s/u_s$ are used as length, velocity, and time scales.

RESULTS

Here, we present some preliminary results using our numerical technique. We are interested in growth of a bubble in a superheated liquid. The growth of a vapor bubble in a superheated liquid is controlled by three factors: liquid inertia, surface tension, and heat diffusion. These factors determine what is called "the critical radius" which is the minimum radius that a nucleus should start with in order to grow. In the current study, we choose the initial bubble radius considerably larger than the critical radius. Therefore, we expect the bubble to grow.

We start our analysis by considering the behavior of a single bubble in zero gravity. The first frame of figure (1) shows the initial position of the bubble in a domain. The domain size (nondimensionalized by dividing by bubble diameter) is $2.5 \times 2.5 \times 5$ and the grid resolution is $48 \times 48 \times 96$. The initial front consists of 5832 triangular elements. Initially the liquid is superheated, the vapor is at the equilibrium temperature, and the flow is quiescent. The nondimensional variables are $Ja = 0.1$, $Pr = 0.25$, $Ca = 0.02$, and $\vartheta = 0.01$. The ratio of material properties are $\rho_v/\rho_l = 0.1$, $\mu_v/\mu_l = 0.05$, $k_v/k_l = 0.025$, and $c_v/c_l = 1.0$. The domain is periodic in the horizontal direction, wall-bounded (and insulated) at the bottom, and open at the top. At the top boundary, the pressure and normal gradient of velocity and temperature are set to zero. The second frame shows the bubble and a normal section of velocity field at the middle of the domain at time $t = 0.053$. The bubble elongates in the vertical direction. Since the gravity is zero, there is no vortical structure inside the bubble. The velocity field in the vicinity of the bubble is relatively disturbed but it is uniform in the rest of the domain. The liquid exits from the top boundary due to fluid expansion at the interface. The fluid velocity is higher around the top of the bubble compared to its side. This is due to the constrain imposed on the flow by periodicity in the horizontal direction and the existence of the wall at the bottom. This results in a higher evaporation rate around the top portion of the bubble and consequently the bubble deforms to an egg-like shape (third frame, $t = 0.106$). The ratio of final volume of the bubble to its initial volume is about fifteen. At the end of the simulation, the bubble consists of 45704 triangular elements.

In the next simulation we study growth of a bubble under high gravity. The initial setup is the same as the previous simulation. The nondimensional numbers for this run are $Ja = 0.1$, $Pr = 0.25$, $Gr = 0.32 \times 10^3$, $Ca = 0.004$, and $\vartheta = 0.05$. With the exception of density ratio which is increased to $\rho_v/\rho_l = 0.5$, all the other material property ratios are the same as the corresponding ones in the first simulation. The grid resolution is the same as the previous run. Lower density difference results in a smaller front velocity which compensates for the higher resolution that may be needed to accurately resolve this case. The first frame of figure 2 shows the bubble and the velocity field at $t = 0.0875$. The velocity is higher inside the bubble due to buoyancy. Two counter rotating vortices appear on the side of bubble which pump hot fluid from the top to the rear. Since the bubble grows, we expect the rise velocity to increase as a result of enhanced buoyancy. This is indeed the case as is seen from the scale of the velocities in the second frame at $t = 0.22$. The evaporation rate is more uniform compared to the previous case. This is due to the fact that the side of the bubble now has a chance to receive hot fluid as the bubble moves upward. As a result, the elongation in the vertical direction is much smaller compared to the first case. Moreover, unlike the previous run, an indentation appears at the rear of the bubble. This is a hydrodynamic effect and is formed as a result of local competition between the surface tension, pressure, and viscous forces. This indentation is increased as the bubble rises (third frame, $t = 0.268$). Although the high curvature developed at the rim of the bubble is a challenge to accurate computation of surface tension, comparison of our results with curvatures of analytical surfaces showed that our method successfully resolves this issue.

Inspection of the temperature field for both cases (not shown in the text) showed the gradual depletion of the superheat. The initial sharp temperature gradient at the interface was replaced with a less steep temperature gradient as a result of heat diffusion. This did not have a pronounced effect at the early period of growth. However, it decreased the growth rate at the later time.

CONCLUSIONS

We have used direct numerical simulation to study phase change phenomena. Numerical simulation of a three-dimensional boiling bubble in zero gravity showed the deformation of the bubble to an egg-like shape as a result of nonuniform evaporation at the phase boundary. Similar computations for a bubble under high gravity showed the formation of a "dimpled" bubble. For both cases, the growth rate started to halt as a result of depletion of the superheat.

ACKNOWLEDGMENT

This work was supported by NASA Microgravity program under contract number NAG3-1952 with Dr. An-Ti Chai as principal investigator. We would like to acknowledge helpful discussions with Dr. Chai during the course of this study and assistance of Dr. Amadi Nwankpa in using visualization software.

REFERENCES

Alexiades, V., and Solomon, A. D., 1993, "Mathematical

modeling of melting and freezing processes," Hemisphere, Washington, D. C., pp. 92-94.

Bankoff, S. G., 1963, "Asymptotic growth of a bubble in a liquid with uniform initial superheat," Appl. Sci. Res. sect. A, Vol. 12, pp. 267-281.

Bosnjakovic, F., 1930, Tech. Mech. Thermodynamics, Vol. 1, 358.

Dalle Donne, M., and Ferranti, M. P., 1975, "The growth of vapor bubble in superheated sodium," Int. J. Heat Mass Transfer, Vol. 18, pp. 477-493.

Esmaeeli, A., and Arpacı, V., 1998, "Numerical modeling of three-dimensional dendritic solidification," paper number FEDSM98-4983, ASME proceedings of the 1998 ASME-FED summer meeting, June 21-25, 1998, Washington, D.C., Editor: D. O. Davis.

Florschuetz, L. W., Henry, C. L., and Rashid Khan, A., 1969, "Growth rates of free vapor bubbles in liquids at uniform superheats under normal and zero gravity conditions," Int. J. Heat Mass Transfer, Vol. 12, pp. 1465-1489.

Forster, H. K., and Zuber, N., 1954, "Growth of a vapor bubble in a superheated liquid," J. Appl. Phys., Vol. 25, pp. 474-478.

Forster, H. K., and Zuber, N., 1955, "Dynamics of vapor bubble and boiling heat transfer," A.I.Ch.E. Journal, Vol. 1, pp. 531-535.

Juric, D., and Tryggvason, G., 1995, "A front-tracking method for liquid-vapor phase change," FED-Vol. 234, pp. 141-148. ASME Winter Annual Meeting, San Francisco, CA, Nov. 12-17, 1995.

Juric, D., and Tryggvason, G., 1996, "Direct numerical simulations of flows with phase change," AIAA 96- 0857, 34th AIAA Aerospace Sciences Meeting, Reno, NV, Jan. 15-18, 1996.

Kosky, P. G., 1968, "Bubble growth measurements in uniformly superheated liquids," Chem. Engng. Sci., Vol. 23, pp. 695-703.

Mikic, B. B., Rohsenow, W. M., and Griffith, P., 1970, "On bubble growth rates," Int. J. Heat Mass Transfer, Vol. 13, pp. 657-666.

Peskin, C. S., 1977, "Numerical analysis of blood flow in the heart," J. Comput. Phys., Vol. 25, pp. 220-252.

Plesset, M. S., and Chapman, R. B., 1971, "Collapse of an initially spherical vapor cavity in the neighborhood of a solid boundary," J. Fluid Mech., Vol. 47, pp. 283-290.

Plesset, M. S., and Zwick, S. A., 1952, "A nonsteady heat diffusion problem with spherical symmetry," J. Appl. Phys., Vol. 23, pp. 95-98.

Plesset, M. S., and Zwick, S. A., 1954, "The growth of vapor bubbles in superheated liquids," J. Appl. Phys., Vol. 25, pp. 493-500.

Plesset, M. S., and Prosperetti, A., 1977, "Bubble dynamics and cavitation," Ann. Rev. Fluid Mech., Vol. 9, pp. 145-181.

Prosperetti, A., and Plesset, M., 1978, "Vapor-bubble growth in a superheated liquid," J. Fluid Mech., Vol. 85, pp. 349-368.

Rayleigh, L., 1917, "On the pressure developed in a liquid during the collapse of a spherical cavity," phil. Mag., Vol. 34, pp. 94-98.

Schunk, P. R., and Rao, R. R., 1994, "Finite element analysis of multicomponent two-phase flows with interphase mass and momentum transport," Int. J. Num. Meth. Fluids, Vol. 18, pp. 821-842.

Scriven, L. E., 1959, "On the dynamics of phase growth," Chem. Engng. Sci., Vol. 10., pp. 1-13.

Skinner, L. A. and Bankoff, S. G. Dynamics of vapor bubbles in general temperature fields. Physics of Fluids Vol. 8, pp. 1417-1420.

Son, G., and Dhir, V. K., 1997, "Numerical simulation of saturated film boiling on a horizontal surface," J. Heat Transfer, pp. 525-533.

Theofanous, T. G., and Patel, P. D., 1975, "Universal relations for bubble growth," Int. J. Heat Mass Transfer, Vol. 199, pp. 425-429.

Theofanous, T. G., Biasi, L., and Isbin, H. S., 1969, "A theoretical study on bubble growth in constant and time-dependent pressure fields," Chem. Engng. Sci., Vol. 26, pp. 263-274.

Welch, S. W. J., 1995, "Local simulation of two-phase flows including interface tracking with mass transfer," J. Comp. Phys., Vol. 121, pp. 142-154.

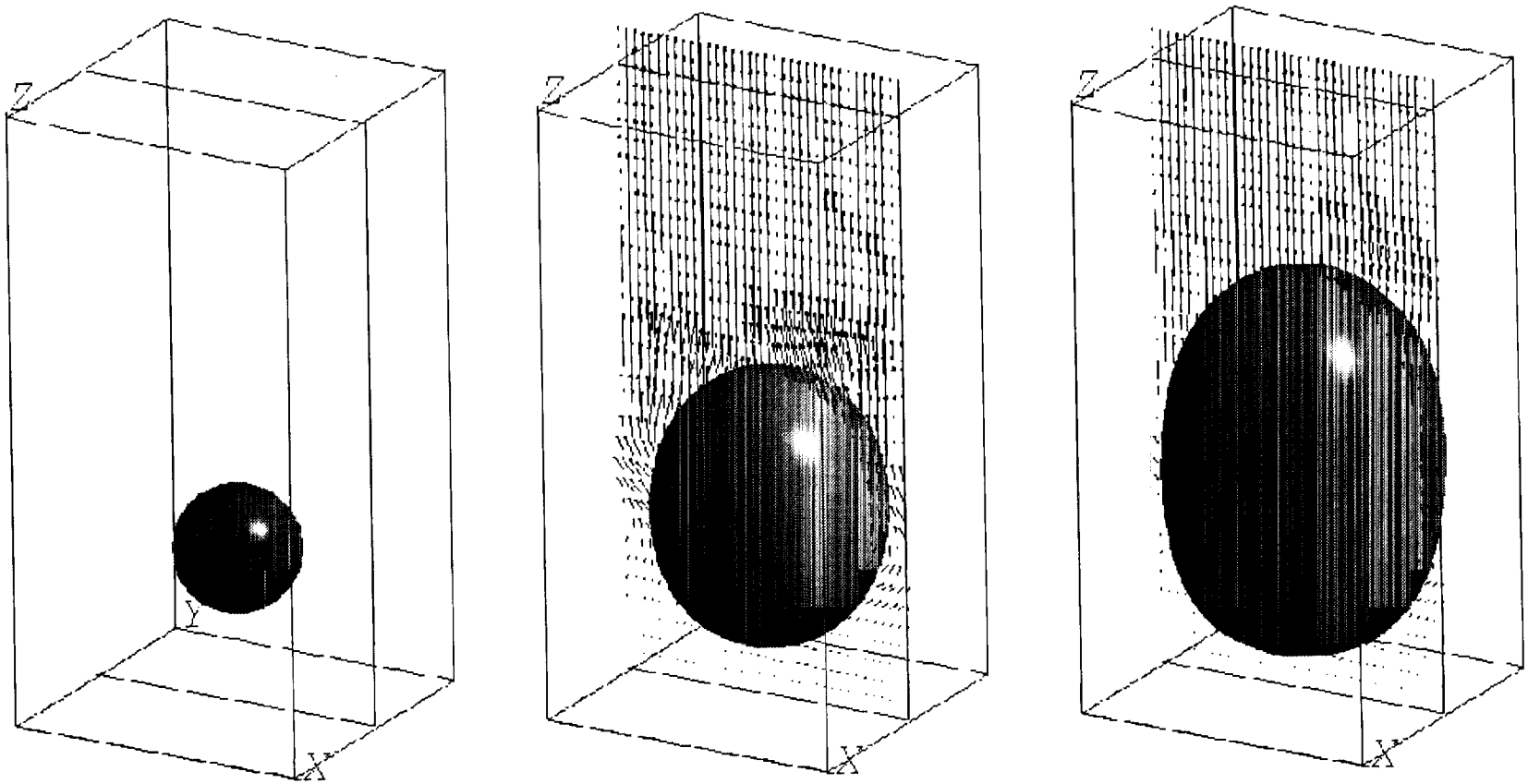

Figure 1. Growth of a vapor bubble in a superheated liquid under zero gravity. Here, $Ja = 0.1$, $Pr = 0.25$, $Ca = 0.02$, and $\vartheta = 0.01$. The ratio of material properties are $\rho_v/\rho_l = 0.1$, $\mu_v/\mu_l = 0.05$, $k_v/k_l = 0.025$, and $c_v/c_l = 1.0$.

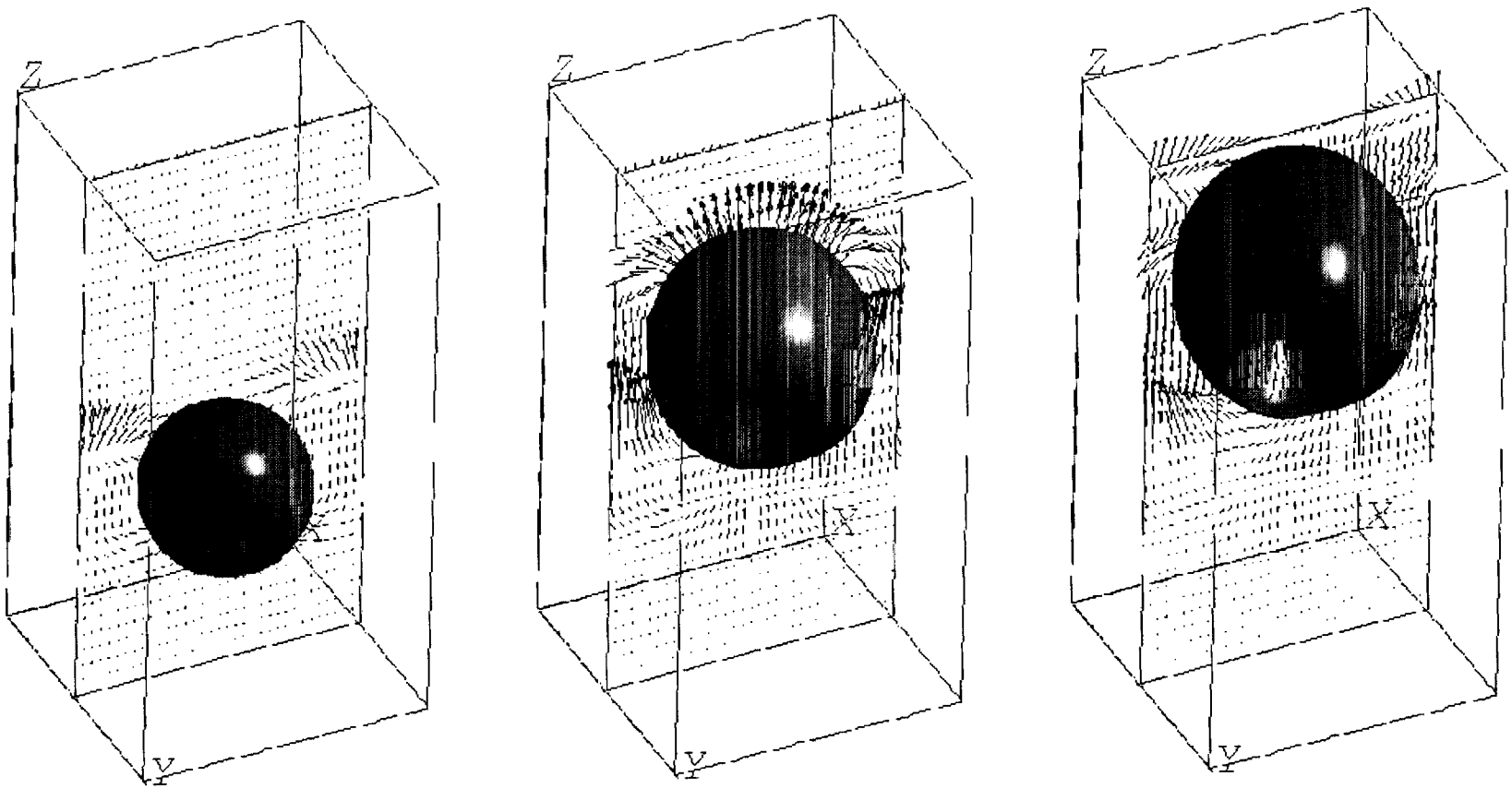

Figure 2. Growth of a vapor bubble in a superheated liquid under high gravity. Here, $Ja = 0.1$, $Pr = 0.25$, $Gr = 0.32 \times 10^3$, $Ca = 0.004$, and $\vartheta = 0.05$. The ratio of material properties are $\rho_v/\rho_l = 0.5$, $\mu_v/\mu_l = 0.05$, $k_v/k_l = 0.025$, and $c_v/c_l = 1.0$.

EXPERIMENTAL TRAJECTORIES OF TWO DROPS IN PLANAR EXTENSIONAL FLOW

D.C. Tretheway, L.G. Leal
Department of Chemical Engineering
University of California – Santa Barbara

Please refer to the Conference Book of Abstracts or the NCMR Website at
http://www.ncmr.org

GROUND-BASED STUDIES OF THERMOCAPILLARY FLOWS IN LEVITATED LASER-HEATED DROPS

S.S. Sadhal[1], H. Zhao[1], and Eugene H. Trinh[2]
[1]Department of Mechanical and Aerospace Engineering, University of Southern California, Los Angeles, CA 90089–1453, USA, sadhal@usc.edu
[2]Jet Propulsion Laboratory 183–401, 4800 Oak Grove, Pasadena, CA 91109, USA, Eugene.H.Trinh@jpl.nasa.gov

1 Introduction

The broad objectives of this investigation are to study the fluid flow phenomena together with the thermal effects on drops levitated in acoustic and/or electrostatic fields. To a large extent, experimentation in 1-G requires a strong acoustic field and therefore, there is significant interference with other thermal-fluid effects. While most of the work has been directed towards particles in strong acoustic fields to overcome gravity, some results for microgravity have been obtained. Also included in the objectives is the analysis and experimentation of the thermocapillary flow in a spot-heated drop.

A Glovebox experiment for the MSL-1 Mission has also been tied in with this investigation. One of the primary objectives of the space experiment is to evaluate the acoustic stability criteria in microgravity. In addition, an understanding of the residual internal flows within a quasi-isothermal drop, induced by a positioning ultrasonic field at various power levels, is required.

2 Analytical Results

The analytical developments have led to several new and interesting results pertaining to fluid mechanics. For the past year, much of the analytical work has been on acoustic levitation of particles. For a particle levitated in an acoustic field, its position is determined, to some extent, by the compressibility properties of the particle phase relative to the surrounding medium. For example, liquid particles in a gas tend to position themselves at the velocity antinode, while small gas bubbles in a liquid equilibrate at the velocity node. The effect of a gravity-type body force may offset the equilibrium position to a point somewhere between the node and the antinode. Investigations have been carried out for a liquid drop at the velocity antinode, a solid particle at the velocity node, and a particle in an intermediate position.

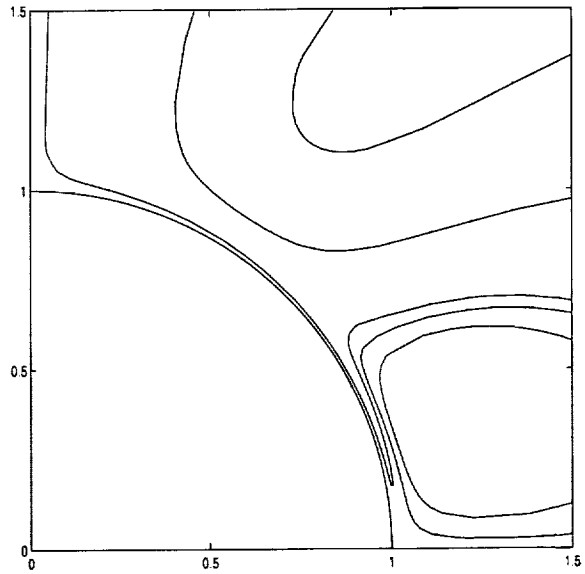

Figure 1: Flow streamlines near the surface of a solid sphere at the velocity node.

2.1 Sphere at the Velocity Node of an Acoustic Field

The flow description for the case of a particle positioned at the velocity antinode can be derived directly from Riley's [1] work which was intended for a vibrating sphere in an otherwise quiescent fluid. The flow field about the velocity node, however, has not been available and a detailed analysis for that situation has been carried out. The perturbation procedure of Riley [1] has been applied to obtain the flow field for the situation when a spherical particle is positioned at the velocity node. As in Riley's [1] solution which applies to a sphere at the velocity antinode, it is found that there is a thin shear-wave region adjacent to the spherical boundary. However, for this thin Stokes layer, the streamlines are not closed but merge with the outer flow, as shown in Figure 1. Therefore, the shear-wave layer does not cover the entire sphere as in Riley's [1] case, but lies mostly around the equatorial region of the sphere. The equatorial belt covers the region

$55^\circ < \theta < 125^\circ$, corresponding to $\cos^2\theta = \frac{1}{2}$. The details are given in a forthcoming publication [4].

Besides providing detailed knowledge about the flow field around the particle at the velocity node, the present analysis has been found to be useful for developing the solution when the particle lies between the node and the antinode.

2.2 Internal Circulation in a Drop in an Acoustic Field

An investigation of the internal flow in a drop at the antinode of a standing wave has been carried out. The main difference from the solid sphere was the inclusion of the shear stress and velocity continuity conditions at the liquid-gas interface. To the leading order of calculation, the internal flow field was found to be quite weak. Furthermore, this order being fully time-dependent has a zero mean flow. At the next higher order, steady internal flows are predicted and there is an important effect on the recirculating Stokes layer. This layer ceases to have recirculation when

$$|M| > \left(\tfrac{5}{2}\right)\sqrt{2}\,[2 + 5(\hat{\mu}/\mu)],$$

where $\hat{\mu}$ is the liquid viscosity, μ is the exterior gas-phase viscosity, and M is the dimensionless frequency parameter for the gas phase, defined by

$$M = \frac{i\omega a^2 \rho}{\mu}.$$

The detailed calculations will be presented in [3]. Experimental confirmation of this interesting new development needs to be thoroughly conducted. Although it agrees with many experiments with levitated drops where no recirculating layer has been found, a new set of experiments for specifically testing the theory need to be carried out. One possible explanation lies in the basic behavior of acoustic waves interacting with interfaces. Based on Schlichting's [2] analysis of a wave in the presence of a solid surface causes the generation of vorticity and this is manifested in the form of recirculating regions adjacent to the interface. This is also seen on a solid sphere as calculated by Riley [1]. In the case of a fluid interface, the effect of interaction is weaker in magnitude depending on the liquid viscosity. Therefore, the recirculation is weaker, and for sufficiently low viscosity there may be no recirculation at all.

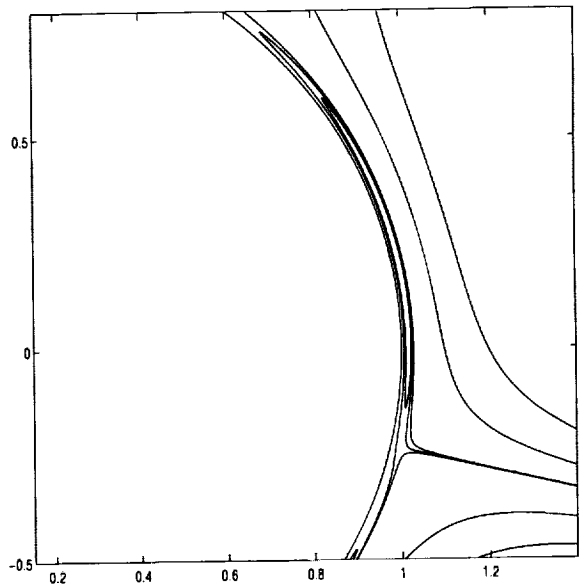

Figure 2: Flow streamlines near the particle – upper region.

2.3 Spherical Particle between the Velocity Node and the Antinode

2.3.1 Solid Particle

The previously-developed solution for a solid particle at the velocity node together with Riley's [1] solution which applies to the antinode, have been integrated to yield a complete solution. Several additional nonlinear terms have been included together with some modification of the node solution. The steady streaming part of the solution is exactly proportional to that obtained be Lee & Wang (1990) by a factor of $\frac{3}{2}$. This is a very important result, in that it verifies the extent of validity of Lee & Wang's method which allows for slip velocity to account for the Stokes layer. The present calculations have also led to the detailed flow field in the Stokes layer which exhibits some interesting patterns. The detailed flow field in the gas phase near the interface are shown in Figures 2 and 3.

In the Stokes layer, there are two axisymmetric vortices. Some of the streamlines on the outer side (gas side) of one vortex cross into the inner side, towards the interface, of the other vortex, as shown in Figure 4.

2.3.2 Liquid Drop

By allowing the continuity of tangential velocity and shear stress at the interface, the flow field for a liquid

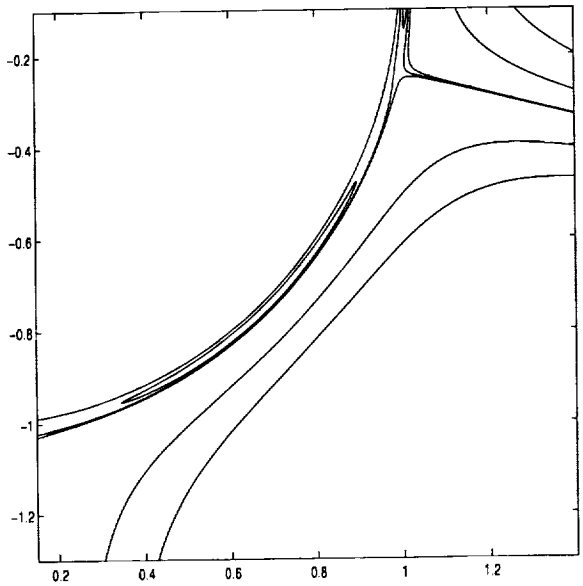

Figure 3: Flow streamlines near the particle – lower quadrant.

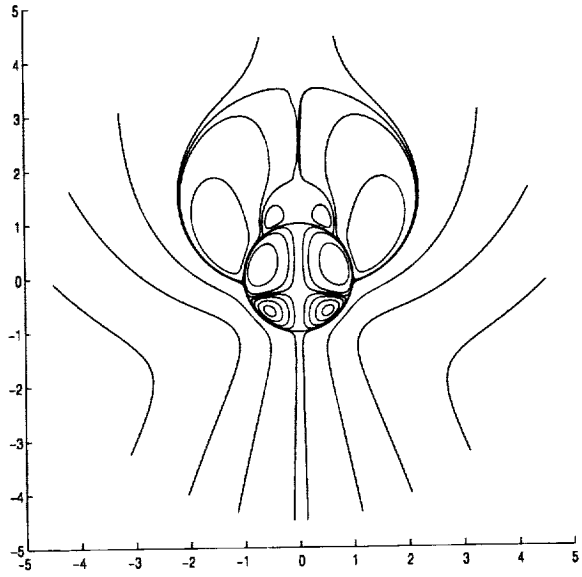

Figure 5: Theoretical prediction of streaming flow past a liquid drop between the node and the antinode. The outer streaming is in the downward direction.

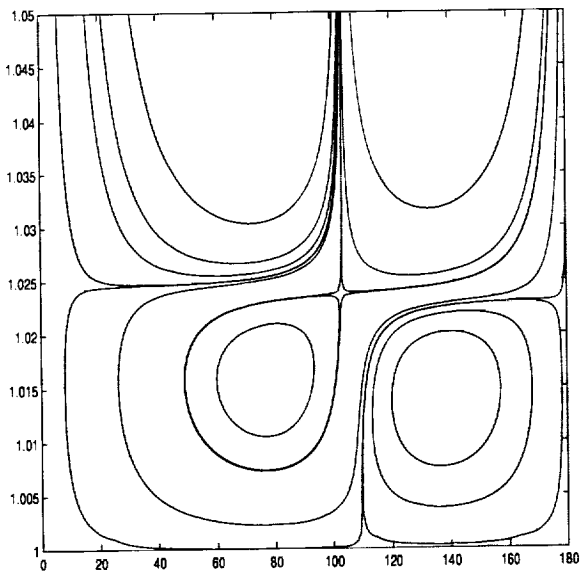

Figure 4: Detailed flow field in the Stokes layer.

drop placed between the node and the antinode has been found. As in the case of the drop at the velocity antinode, the reciculation is predicted to cease when the drop viscosity is low enough. The exact magnitudes of the parameters when this happens have not been established yet.

The exterior and interior flow fields exhibit interesting streaming-flow patterns. For the case when the recirculation in the Stokes layer does not exist (see Figure 5), there are two toroidal vortices in the drop. The exterior also has two larger vortices adjacent to the drop. The interesting feature here is that the exterior vortices are at the front of the drop with respect to the streaming flow. This is quite the opposite of what one observes for simple flow past a sphere for which the recirculating wake is at the rear. Experimental observations have exhibited the presently described phenomenon (i.e., the front-side 'wake') as shown in Figure 6. Here the striking similarity with the theoretical prediction is quite clear. A plausible physical explanation is still being sought, and detailed examination of the theoretical flow field is being conducted. Pressure calculations around the drop show the existence of a low-pressure region on the upstream side. For levitation to be possible in a gravity field, there

Figure 6: Visualization of flow around an acoustically levitated particle showing an upstream-side vortex.

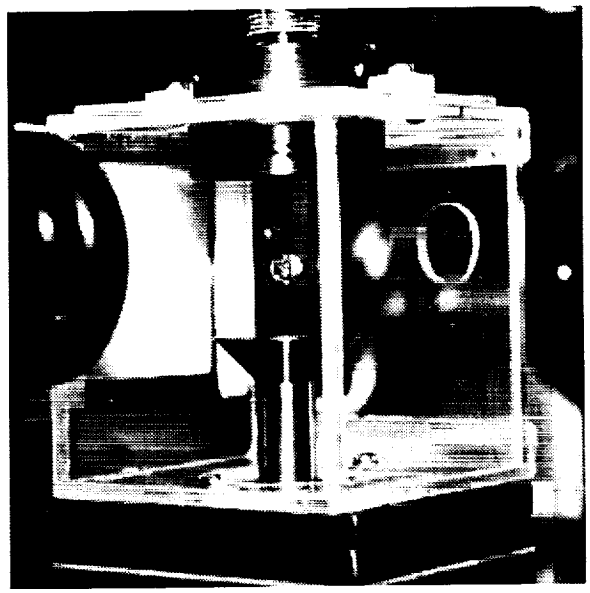

Figure 7: Photograph of an ultrasonically positioned drop during an experimental run of the Glovebox Investigation.

has to be a high-pressure region on the underside of the drop and a correspondingly low-pressure region at the top. This is consistent with the presence of the vortex at the front which can come about due to the low pressure.

3 Experimental Results

3.1 Glovebox Flight Investigation Development

An experiment for the Glovebox flight investigation took place during the MSL-1 Mission in early July 1997. This work was initiated to assess the capability for ultrasonic positioning in microgravity, and for drop internal flow measurement. A compact ultrasonic positioner (see Figure 7) was designed and integrated with laser diode illumination in order to experimentally demonstrate the rotation control of freely suspended drops in low gravity and to obtain preliminary flow field measurements for isothermal droplets. The initial goal of performing preliminary measurement on spot-heated droplets was not realized due to a combination of safety and Glovebox facility constraints.

The important findings from the flight investigations are summarized below.

1. The controlling parameters of a single axis ultrasonic system operating in air at ambient temperature which affect the ability to quiescently position a liquid drop were identified in a microgravity environment.

2. Rotation control of a drop in microgravity was investigated. The ultimate capability of the single axis levitator will be determined from the acquired information. Preliminary observations indicate a residual steady rotation of about 0.1 rps with the acoustic power required to counteract the Shuttle attitude control firings. High rotation rates necessary for drop bifurcation and fission have also been measured.

3. Tracer particles within the deployed drops have allowed the measurement of the rotation rate, and they will yield quantitative information on the dependence of acoustic torque on pressure, as well as the assessment of the internal flow within a quasi-isothermal drop in the Spacelab environment.

4. The first accurate data for drop deformation as a function of acoustic pressure were obtained for a sample located at the pressure minimum plane in the ultrasonic standing wave. All ground-based data are for a drop away from the pressure nodal plane because of gravity.

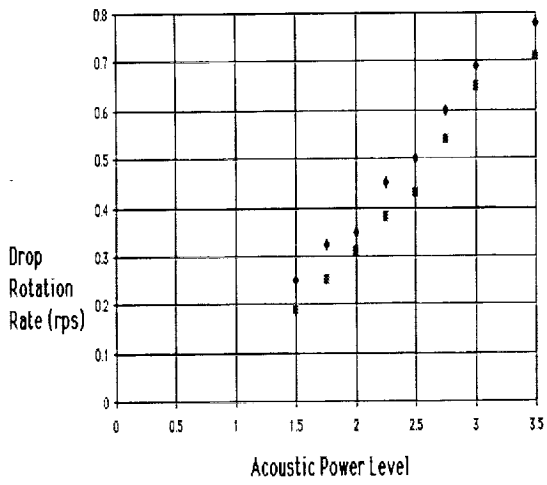

Figure 8: A plot of the measured rotation rate as a function of the acoustic power setting.

Based on these preliminary assessments, the current apparatus is deemed effective for the accurate positioning of drops in air in an actual microgravity environment. The spinning of the drop can be reduced to a very low state of residual rotation, and internal flow measurement can be achieved. Spot heating experiments, planned for a future flight, are thus deemed to be feasible.

Typical drop rotation rates as a function of the acoustic power setting are given in Figure 8. The drops were ultrasonically positioned in low gravity. As the rotation rate becomes very low, damping of residual rotation weakens and longer observation times are required to view the slowing down of residual rotation.

The development of the apparatus for the reflight of the IFFD (Internal Flow in a Free Drop) investigation is well under way. A sting heater consisting of a thermistor mounted on a stainless steel rod and held on a micropositioner stage will be used to provide local heating for a free drop with a maximum temperature rise of 20 C. The tip of the heater will be placed in the proximity of a drop in order to provide differential heating. The internal flows recorded through the motion of suspended tracer particles within the drop will be compared with those generated when the drop is in direct contact with the heater tip. Ground-based tests have shown that the heater tip can be safely moved to within 2 mm of a 4-mm diameter levitated drop without perturbing it. The effects of acoustic streaming will also be investigated for a sting-held drop by comparing the internal flows for different acoustic power levels.

3.2 Ground-Based Experimental Activities

A previously described apparatus has been used to record the motion of fluorescent tracer particles suspended in the drop liquid. The scattered light is gathered along two orthogonal views using holographic notch filters to block the elastically scattered light from the drop surface. The liquid used was an aqueous mixture of glycerin and silicone oil (Polydimethylsiloxanes) and a focused CO_2 laser was used to spot-heat the levitated drop. The results show that although it was possible to accurately measure the internal flows of isothermal drops, the combination of Earth-based ultrasonic levitation and spot heating induces an uncontrolled torque which drives a random rotational motion of the drops. The digital image processing required in the deconvolution of this rotational motion in order to extract the thermocapillary and buoyancy-driven flows requires substantial computational power, and will be pursued by this experimental effort. Control of drop evaporation has been implemented by maintaining the drop environment at a high humidity, and the Marangoni convection contribution due to evaporation can thus be neglected. Ongoing and future studies will include the measurement of flows within drastically flattened drops to constrain the flows in a two dimensional plane, the implementation of total electrostatic levitation of charged droplets, and an automated digital data reduction and analysis.

Electrostatic levitation has been useful in eliminating residual rotation of the drop. Preliminary observations have been carried out with electrostatically levitated charged drops in 1-G with focused CO_2 laser heating from the side. The quantitative characterization of the resulting complicated buoyancy and thermocapillary-induced flows require a three-dimensional analysis of the flow field. The immediate future plan is to develop the required software for the digitized video recordings of these flows using suspended tracer particles.

Thermocapillary flows coupled to natural buoyancy-driven convection have been observed for electrostatically levitated droplets using spot heating from a focused CO_2 laser directed to the right side of the drop. The current spot size is about 300 μm and the levitated drops have diameters between 3 and 5 mm. Using two overlapping views from two different video cameras, three dimensional imaging of the flow fields could be obtained and recorded on videotapes. The predicted

vertical motion could be observed, although the flow pattern is very asymmetric due to the gravitational bias. Radiant input power is controlled by varying the duty cycle of the laser. Further measurements will be taken using a smaller (100 μm laser spot size).

Acknowledgements

The investigators are very grateful for the support of this work under Grant No.: NAG3-1842 from the Microgravity Fluid Physics Program of the National Aeronautics and Space Administration.

REFERENCES

[1] N. Riley. On a sphere oscillating in a viscous liquid. *Quart. J. Mech. Appl. Math.*, **19**:461–472, 1966.

[2] H. Schlichting. Berechnung ebener periodischer Grenzchichtströmungen. *Physik Zeitschr.*, **23**:327–335, 1932.

[3] H. Zhao, S.S. Sadhal, & E.H. Trinh. Internal circulation in a drop in an acoustic field. submitted, *J. Acous. Soc. Am.*, 1998.

[4] H. Zhao, S.S. Sadhal, & E.H. Trinh. Singular perturbation analysis of an acoustically levitated sphere: Flow about the velocity node. accepted, *J. Acous. Soc. Am.*, 1998.

THERMOCAPILLARY MIGRATION AND INTERACTIONS OF BUBBLES AND DROPS

R. Shankar Subramanian, Clarkson University, Potsdam, New York 13699-5705,
R. Balasubramaniam, NCMR, NASA Lewis Research Center, Cleveland, Ohio 44135,
G. Wozniak, Freiberg University of Mining and Technology, D-09596 Freiberg, Germany and
P.H. Hadland, Aker Offshore Partner AS, P.O. Box 589, 4001 Stavanger, Norway

1. INTRODUCTION

When a drop or bubble is introduced into a second fluid in which there exists a temperature gradient, the drop (or bubble is implied from hereon) will move (1). Such motion is a consequence of the variation of the interfacial tension along the interface between the drop and the continuous phase. Reviews of the literature on this subject may be found in Wozniak *et al.* (2) and Subramanian (3). This movement is termed thermocapillary migration, and can be important in materials processing in space, and in separation processes used in long duration space excursions for recycling and on the surface of the moon.

The speed at which a drop migrates can be obtained by solving the governing continuity, Navier-Stokes, and energy equations along with the associated boundary conditions. When convective transport effects are important, the problems are nonlinear. The relative importance of convective transport of energy when compared to conduction can be judged from the magnitude of the Péclet number whereas a similar ratio for momentum transport is described by the Reynolds number, Re. When a velocity scale characteristic of thermocapillary migration is used, the Pèclet number is known as the Marangoni number, Ma. The Capillary number also is another parameter that influences the shape of the drop. Definitions of these quantities may be found in (4).

In the linear limit when the Reynolds and Marangoni numbers are negligible, the contribution of thermocapillarity can be extracted from experiments on the ground. Therefore, experiments designed to explore thermocapillary migration on the ground are subject to this important limitation; some of this experimental work is discussed in references (2,3). To better explore the parameter space in the Reynolds and Marangoni numbers than is possible on the ground, investigators have attempted to carry out experiments in reduced gravity conditions. The previous studies, as discussed by us in Balasubramaniam *et al.* (4), were subject to many limitations which raise questions regarding the utility of the data. Therefore, in summer 1994, we performed thermocapillary migration experiments in reduced gravity under conditions closer to those assumed in theoretical models. We used air bubbles and Fluorinert FC-75 drops migrating in a Dow-Corning DC-200 series silicone oil of nominal viscosity 50 centistokes. The apparatus in which the experiments were performed was the Bubble, Drop, and Particle Unit (BDPU) built under the auspices of the European Space Agency. Our experiments, carried out aboard the IML-2 mission of the Space Shuttle, yielded good data on isolated drops up to a Reynolds number of 0.85 and a Marangoni number of 280, and on isolated bubbles up to a Reynolds number of 2.2 and a Marangoni number of 810. In the case of air bubbles, the data were found to be generally consistent with our predictions from a numerical solution of the governing equations as well as an asymptotic theoretical result obtained by Balasubramaniam and Subramanian (5). Also, some preliminary results on interacting drops were obtained and reported in (4).

In an attempt to explore further the interactions between pairs of drops and pairs of bubbles and to extend the range of values of Marangoni and Reynolds numbers, we performed follow-on flight experiments aboard the LMS mission of the Space Shuttle in summer 1996. The same fluids, air and Fluorinert FC-75, were used for the bubble and drop phases, respectively, and a silicone oil of nominal viscosity 10 centistokes was employed for the continuous phase. This choice was made so as to be able to extend the maximum Marangoni number by approximately a factor of 6, and the corresponding maximum Reynolds number by a factor of approximately 30. Also, tracer particles dispersed in the silicone oil were used in the air bubble migration experiments in order to track the flow in the continuous phase during the migration process. In addition, the Point Diffraction Interferometry (PDI) system used in IML-2 was refined by the European Space Agency to incorporate a Wollaston Prism with a divergence angle of 10 degrees, so that interferometry was able to provide quantitative information on tem-

perature fields in the LMS experiments involving gentle temperature gradients. Except for these modifications, the procedures and the experiments were similar to those in IML-2.

2. EXPERIMENTAL APPARATUS AND PROCEDURE

The experiments were performed in the BDPU which was provided by the European Space Agency through a cooperative arrangement with the National Aeronautics and Space Administration. The apparatus consists of a "facility" which provided power, optical diagnostics and illumination, imaging facilities including a video camera and a motion picture camera, and other sundry support services. Within this facility, a test cell that was specific to the experiment was inserted by the payload specialist on the Shuttle when needed.

Conceptually, the experiments were simple. Within a test cell mounted in the facility and filled with a suitable liquid, a temperature gradient was established, followed by the introduction of a bubble or a drop as desired. The subsequent motion of the object, in the direction of the applied temperature gradient, was recorded for later analysis on videotape on the ground as well as on cine film on board the Shuttle in selected experiments. When a bubble or drop reached the hot wall, it was extracted and another was introduced after a small waiting period.

The heart of the experimental apparatus is the test cell. Two rectangular test cells were available. Both were of identical dimensions, measuring 60 x 45 x 45 mm in the interior. This cavity was filled with a Dow-Corning DC-200 series silicone oil of nominal viscosity 10 centistokes in both cells. As mentioned earlier, the silicone oil in the bubble cell contained a small concentration of tracer particles provided by Dornier GmbH from Germany. It was possible to maintain the two end walls (made of aluminum) in the long dimension of the cell at fixed known temperatures so that a temperature gradient could be established in the z-direction. Within the cavity, an injection needle was available when needed. When not in use, the tip was flush with the cold aluminum surface at its center. It was possible to introduce air bubbles in one test cell, and Fluorinert FC-75 drops in the other cell. The diameters of the bubbles varied from approximately 1.3 to 14.4 mm, and those of drops ranged from 2.1 to 14.3 mm. After a bubble or drop completed its traverse, it was extracted from the hot wall using an extraction tube mounted at the center of a net.

The equipment provided red background illumination and the opportunity to capture images of the interior of the test cell on videotape on the ground. Also, a limited amount of cine film was available, and was used to capture images during selected runs at suitable framing rates.

In any given run, the procedure was first to establish the desired temperature gradient over a period of 2 hours. This period included approximately 30 minutes in which the liquid in the cell was stirred by back and forth movement of the net, followed by a quiescent period lasting approximately 90 minutes. This was followed by the injection, traverse, and subsequent extraction of bubbles or drops. At low temperature gradients, interferometry images received on the ground were used as a diagnostic tool to determine when the temperature field became steady.

At the end of the heating period, when real time TV and commanding capability were available, the experiment was initiated by sending a command to inject a bubble or drop of a specified size at a specified position along the long axis of the cell. The traverse of the object was followed on the ground while recording it. When the bubble reached the opposite wall, it was usually extracted using a small tube at the center of that wall. After the passage of a sufficient amount of time, judged from interferometry images where available, the next injection was initiated. This waiting period was usually of the order of 3 minutes. For a pair of bubbles or a pair of drops, suitable commands were packaged and sent up to the apparatus to perform the sequential double injection automatically. When a sufficient number of runs were made with one temperature gradient, another gradient was employed. The bubble cell and the drop cell were each used twice. Temperature gradients of 0.33 and 1 K/mm were used with bubbles, and 0.25 and 1 K/mm with the drops. A run with a temperature gradient of 0.067 K/mm with the bubble cell yielded no usable data due to poor communications between the orbiter and ground caused by the "safe" attitude of the orbiter.

A total of 64 bubble runs and 74 drop runs were recorded on videotape, and 35 bubble runs and 38 drop runs on cine film. Of these, 53 bubble runs and 67 drop runs were analyzed. The rest either contained objects too small to be measured precisely or presented other problems that precluded analysis. A sufficient number of runs were made on isolated drops and bubbles to extend the range of Reynolds and Marangoni numbers beyond those encountered in the IML-2 experiments. The remaining experiments focused on interacting drops and bubbles. While we

introduced pairs of bubbles and pairs of drops deliberately in selected runs, sometimes a collection of two or more objects was introduced by the injection system even when the objective was to inject a single object.

3. RESULTS AND DISCUSSION

Isolated Bubbles and Drops

The video and cine images were analyzed using an automated computerized system developed by NASA Lewis Research Center. This worked by selecting single frames and tracking the boundary of the object involved. It was found that even the largest drops displayed no detectable deformation in shape while the largest bubbles in the temperature gradient of 1 K/mm were slightly oblate.

Since the position of the objects was followed throughout the traverse it was possible to calculate the velocity at various locations in the cell. The velocity changed during the traverse because of the initial acceleration of the bubble or drop upon release from the injector as well as due to the change of physical properties (principally viscosity) with temperature. Therefore, the velocity was never truly steady for any given bubble or drop. In the isolated bubble runs, the Reynolds number varied from 0.8 to 87 while the corresponding Marangoni number ranged from 51 to 5800. In the case of the drops, the range of Reynolds number was 0.14 to approximately 10 and the corresponding range of Marangoni number was 14.6 to approximately 600.

We have reported the results pertaining to isolated bubbles and drops in Hadland et al. (6). A detailed presentation and discussion can be found there. The main points are briefly summarized here. It was found that the data from LMS were generally consistent with those obtained in the earlier IML-2 experiments where there was overlap. However, as mentioned earlier, the range of Marangoni numbers was extended both in the case of bubbles and in the case of drops. Data on air bubbles were in agreement with predictions from a numerical solution except at very large values of the Marangoni number where the observed velocities were not as large as those predicted. However, at large values of the Marangoni number, the data from bubbles appeared to approach an asymptotic result good in this limit which is reported in (5). The scaled velocity of Fluorinert drops was consistent with predictions from a numerical solution reported by Ma (7) at low to moderate values of the Marangoni number. However, at large values of the Marangoni number, both an asymptotic analysis and the numerical solution predict that the scaled velocity should increase with increasing Marangoni numbers while the data did not display this behavior. The motion of the drops was unsteady due to the variation of viscosity with temperature and due to the significant amount of time it would take to achieve a steady temperature gradient distribution within a drop. This may explain the observed discrepancies at large values of the Marangoni number.

Interacting Bubbles and Drops

In some experiments on pairs of drops involving a small leading drop and a large trailing drop, the trailing drop moved slower than it would if it were isolated. This was consistent with similar behavior noted in IML-2 experiments. However, some other interesting patterns of behavior were noted in LMS experiments. In several runs a leading bubble or drop moved straight along the axis of the cell while a trailing object released a small distance behind the leader moved away from the axis in a transverse direction. This movement was typically only by a few mm in that direction but was clearly measurable. We observed the same behavior on the part of bubbles as well as drops. In some cases the trailing drop passed the leading drop when its transverse movement brought it sufficiently away from the axis. Finally, in a few experiments involving multiple drops, the drops were seen to execute three-dimensional trajectories across the cell.

Explaining the behavior of interacting drops is not trivial. It is likely that the wake of the first object plays a role in causing the observed behavior. One can envision a thermal wake behind the leading object in the case of both the bubble and drop experiments. This is a relatively thin region in which the temperature field is presumably axisymmetric and the temperature gradient is weaker than that in the undisturbed fluid. Whereas in IML-2, the trailing drop moved straight along the axis when influenced by this wake, in some LMS experiments, it appears that slight asymmetries in the positioning of the second object with respect to the wake caused the fluid in the wake to wrap around this object asymmetrically; in turn, this must have led to an asymmetry in the temperature gradient distribution on its surface which may have caused the resulting movement away from the axis of the cell.

4. CONCLUSIONS

The results for the migration velocity of isolated air bubbles extend the range of values of the Marangoni number investigated in earlier IML-2 flight experiments. The data are consistent with those from IML-2 and with theoretical predictions. The data on isolated drops display similar trends even though agreement with predictions from a numerical solution is only noted at small to moderate values of the Marangoni number. Experiments on multiple drops and bubbles show evidence of wake effects from a leading object. In some cases, the trailing bubble or drop moves off the axis of the cell; large trailing drops pass the leading drop in this way. In other experiments, trailing drops exhibit a three-dimensional trajectory. The shapes of even the largest drops in the largest temperature gradient used were spherical to within the uncertainty of the measurements while large bubbles moving in the same temperature gradient were found to be slightly oblate.

5. ACKNOWLEDGMENTS

The work described herein was supported by NASA's Microgravity Sciences and Application Division through NASA Grant NAG3-1122 from the Lewis Research Center to Clarkson University. Also, support by the German Space Agency (DARA) through DARA Grant 50WM9582-0 to G. Wozniak is gratefully acknowledged.

6. REFERENCES

1. N. O . Young, J. S. Goldstein, and M. J. Block: The motion of bubbles in a vertical temperature gradient, J. Fluid Mech., Vol. 6, 1959, pp. 350-356.

2. G. Wozniak, J. Siekmann, and J. Srulijes: Thermocapillary Bubble and Drop Dynamics Under Reduced Gravity --- Survey and Prospects, Z. Flugwiss. Weltraumforsch, Vol. 12, 1988, pp. 137-144.

3. R. S. Subramanian: The Motion of Bubbles and Drops in Reduced Gravity, in Transport Processes in Bubbles, Drops, and Particles, edited by R. Chhabra and D. De Kee, Hemisphere, New York, 1992, pp. 1-41.

4. R. Balasubramaniam, C.E. Lacy, G. Wozniak, and R.S. Subramanian: Thermocapillary Migration of Bubbles and Drops at Moderate Values of the Marangoni Number in Reduced Gravity, Phys. Fluids, Vol 8, No. 4, 1996, pp. 872-880.

5. R. Balasubramaniam and R.S. Subramanian: Thermocapillary Bubble Migration --Thermal Boundary Layers for Large Marangoni Numbers, Int. J. Multiphase Flow, Vol. 22, 1996, pp. 593-612.

6. P.H. Hadland, R. Balasubramaniam, G. Wozniak, and R.S. Subramanian: Thermocapillary Migration of Isolated Bubbles and Drops at Moderate to Large Marangoni number and Moderate Reynolds Number in Reduced Gravity, Experiments in Fluids, 1998, in press.

7. X. Ma, Numerical Simulation and Experiments on Liquid Drops in a Vertical Temperature Gradient in a Liquid of Nearly the Same Density, Ph.D. Thesis in Chemical Engineering, Clarkson University, 1998.

Session 7B

Liquid Bridges

STABILITY LIMITS AND DYNAMICS OF NONAXISYMMETRIC LIQUID BRIDGES.

J. Iwan D. Alexander[1], Lev A. Slobozhanin[2], Andrew H. Resnick[2], Jean-Francois Ramus[2] and Sylvie. Delafontaine[2]

[1]National Center for Microgravity Research and Department of Mechanical and Aerospace Engineering, Case Western Reserve University, Cleveland, OH 441106; [2]Center for Microgravity and Materials Research, University of Alabama in Huntsville, Huntsville, AL 35899

Abstract

Liquid bridges have been the focus of numerous theoretical and experimental investigations since the early work by Plateau more than a century ago. More recently, motivated by interest in their physical behavior and their occurrence in a variety of technological situations, there has been a resurgence of interest in the static and dynamic behavior of liquid bridges. Furthermore, opportunities to carry out experiments in the near weightless environment of a low-earth-orbit spacecraft have also led to a number of low-gravity experiments involving large liquid bridges. In this paper we present selected results from our work concerning the stability of nonaxisymmetric liquid bridges, the bifurcation of weightless bridges in the neighborhood of the maximum volume stability limit, isorotating axisymmetric bridges contained between equidimensional disks and bridges contained between unequal disks. For the latter, we discuss both theoretical and experimental results. Finally, we present results concerning the stability of axisymmetric equilibrium configurations for a capillary liquid partly contained in a closed circular cylinder.

1. Introduction

Liquid bridges occur in a number of different situations of physical and technological interest. The study of axisymmetric equilibria has received much attention and the stability of static bridges has been examined for various disk configurations, aspect ratios, gravity levels and rotation rates (see, for example, [1-7] and references therein.). There have also been numerous investigations of liquid bridge dynamics (e.g., [8,9]). Such investigations have been motivated by both practical considerations and basic scientific interest. The behavior of liquid bridges and drops are important considerations in propellant management problems and other fluid management problems in space [10, 11]. Pendular liquid bridges occur widely in the powder technology industry and are a major influence on powder flow processes and mechanical properties [12-13]. In porous media flow, liquid-liquid displacement can lead to evolution of pendant and sessile lobes or a lenticular bridge [13]. The formation of liquid bridges from the gel that coats lung micro-airways is a precursor in lung collapse [14]. The results for unequal diameter supports presented here are particularly relevant to floating zone crystal growth [7,15,16], since this is a common configuration [15, 16].

2. Nonaxisymmetric Bridge Stability

The stability of two types of static nonaxisymmetric bridge configurations was considered. In both cases, the bridge was held between equidimensional coaxial disks. In the first example, the stability of bridges subject to gravity oriented perpendicular to the axis through the supporting disks was examined. The second example dealt with nonaxisymmetric bridges subject to axial acceleration. Both problems were solved numerically using the *Surface Evolver code* [17].

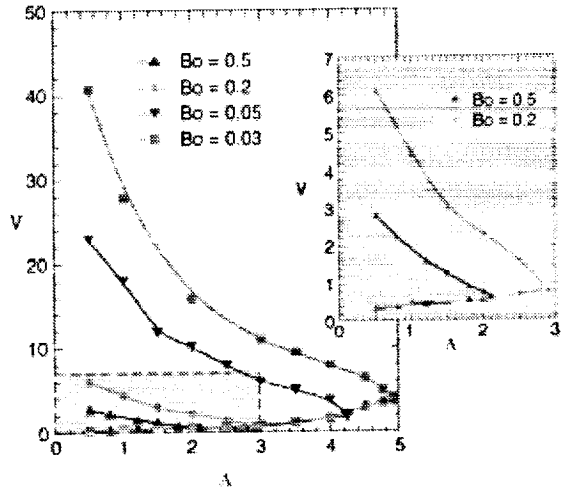

Fig. 1 Computed stability limits for lateral acceleration with Bo = 0.5, 0.2, 0.05 and 0.03.

The stability of bridges subject to lateral gravity was examined as a function of slenderness, Λ (ratio of the disk separation to the mean diameter, $2r_0$, of the two support disks), and the relative volume, V (ratio of the actual liquid volume to the volume of a cylinder with a radius r_0). The location of the stability boundary for a given Bond number, B, was determined by fixing the slenderness, Λ , and minimizing the energy for some value of V. Outside the stability boundary, the bridges break before the energy is minimized. Inside the stability boundary, bridges maintain their integrity and reach a minimum energy configuration. Thus, we employed a simple iterative search technique to find the approximate location of the boundary. For a given B and a fixed value of Λ that is less than the maximum stable slenderness, Λ_{max}, there exists a maximum and minimum stable relative volume. The maximum volume stability limit tends to infinity as $\Lambda \rightarrow 0$.

For any given (lateral) B, the minimum volume stability limit becomes indistinguishable from the zero B limit when Λ becomes sufficiently small. A more detailed description of these results is given in Ref. [18]

In related work carried out in collaboration with Prof. J. Meseguer and Dr. F. Zayas of the Universidad Politecnica de Madrid, we examined the results of an asymptotic analysis of the stability limits of liquid bridges. Here the maximum stable slenderness, Λ_{max}, of a liquid bridge between equal disks, and a nearly cylindrical volume, when subjected to both axial (B_a) and lateral (B_l) Bond numbers becomes

$$b_l = (1 - (b_a)^{2/3})^{1/2}, \qquad (1)$$

where

$$b_a = (3/2)^2 \lambda^{-3/2} B_a, \text{ and } b_l = (\pi/2)\lambda^{-1/2} B_l, \qquad (2)$$

are the reduced axial and lateral Bond numbers and $\lambda = 1 - \Lambda_{max}/\pi + v/2$, where $v = V - 1$. This suggests that, at least close to the reference configuration ($\Lambda \sim \pi$, $v \sim 0$, $B_a \sim 0$, $B_l \sim 0$), there is a self-similar solution for the stability limits, the behavior being the same regardless of the slenderness or volume. Numerical results obtained using *Surface Evolver* [17] were found to be in good agreement with Eq. (1) for a limited parameter range.

For axisymmetric bridges subject to axial gravity, it is known that along most of the maximum volume stability limit axisymmetric bridges are unstable to nonaxisymmetric perturbations. We examined the bifurcation of solutions for a weightless liquid bridge in the neighborhood of this stability boundary. Depending on the system parameters, loss of stability with respect to nonaxisymmetric perturbations resulted in either a jump or a continuous transition to stable nonaxisymmetric shapes. The value of the slenderness at which a change in the type of transition occurred was found to be $\Lambda_s = 0.4946$. Results of experiments using a neutral buoyancy technique agree with this prediction. A liquid bridge of a set slenderness was formed between coaxial disks. High precision stepping motors were used to control the disk separation while simultaneously injecting silicone oil. Oil was injected until the bridge was near the upper stability limit for the slenderness under consideration. Then precisely controlled amounts of oil were added incrementally using a calibrated microsyringe. The shape was monitored as the bridge expanded and stability limit was approached. The bridge was imaged using a coherent high magnification Fourier optical arrangement together with a high pass optical filter. This permits visualization of edges of projections of the liquid bridge surface at approximately 100x magnification. From this image, the minimum distance l (shown schematically in the photographs in Fig. 2) from the bridge surface to a stationary reticule was measured on a computer screen. Typically, the distance decreases slightly with each addition of oil until the stability limit is exceeded. When this occurs, the bridge forms a bulge. After loss of stability, the critical axisymmetric shape changes to a stable nonaxisymmetric shape. However, the nature of this transition was quite different for $\Lambda \leq 0.4$ and $\Lambda \geq 0.6$.

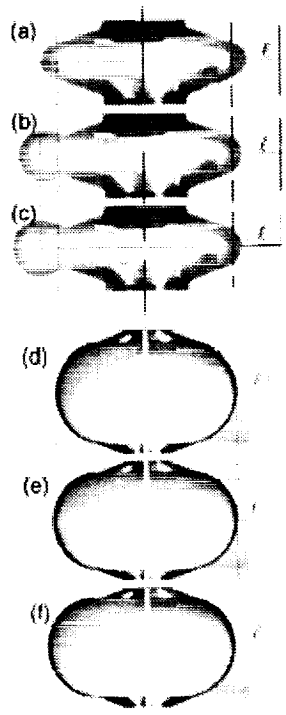

Fig. 2 Bridge images for $\Lambda = 0.225$ (*a* - *c*) and $\Lambda = 1.02$ (*d* - *f*). States (*a*) and (*d*) are stable and axisymmetric with $V_1 = 1.31$ and $V_2 = 2.82$ that are, respectively, slightly smaller than the critical (experimental) volumes for the given Λ. The nonaxisymmetric bridges (*b*) and (*c*) have $V = V_1 + 0.025$ and $V_1 + 0.05$, (*e*) and (*f*) have $V = V_2 + 0.095$ and $V_2 + 0.19$.

Figure 2 shows a sequence of images of a $\Lambda = 0.225$ bridge near the critical V value. The theoretically predicted critical volume is 1.36, the critical volume obtained experimentally was 1.33. For $\Lambda = 0.225$, a large shape deformation occurs after the addition of only a small volume increment (compare Figs. 2(a) and 2(b)). Further volume increases lead to continuous incremental shape changes (Figs. 2(b) and 2(c)). In contrast, for $\Lambda = 1.02$ (Figs. 2(d)-2(f)), we observed a continuous transition from critical axisymmetric shape to a sequence of the stable nonaxisymmetric shapes as the volume was increased. Here the theoretical critical volume is 2.96 and our experimental critical volume was between 2.83 and 2.85. In both cases, our experimental critical volumes were within 5% of the theoretical values and the nonaxisymmetric bridges were stable at volumes far beyond the maximum volume stability limit for axisymmetric bridges.

This work is described in detail in Refs. [19,20].

For bridges between coaxial disks and subject to axial gravity, little is known about the stability of nonaxisymmetric configurations beyond the maximum (axisymmetric) volume limit. We examined the stability of these bridges numerically (using *Surface Evolver*) for $B = 0.1$ and 2. We found that the maximum volume segment of the stability limit follows the same trend as for lateral gravity. That is, V tends to infinity as the slenderness, Λ , tends to zero.

3. Stability of Isorotating Liquid Bridges

The stability of axisymmetric equilibrium states of an isorotating liquid bridge between equidimensional circular disks in a constant axial gravity field was also considered [21]. Emphasis was given to the stability of bridges satisfying two types of constraint that are typical for the floating zone method used for materials purification and single crystal growth. First, we considered the constraint that the relative volume of the bridge, V, is equal to 1. For this case, the critical values of the slenderness (Λ) and of the surface slopes (β_1, β_2) at both disks have been determined for a wide range of the Bond and Weber (W) numbers. Figure 3 shows the level lines of the slope angle at the top and bottom disks ($\beta_1 = \beta_2$) for the critical surfaces of a cylindrical volume bridge. These curves lie in the region of the (, Λ)-plane enclosed by the $B = 0$ and $B = 5$ (dot-dash line) stability boundaries.

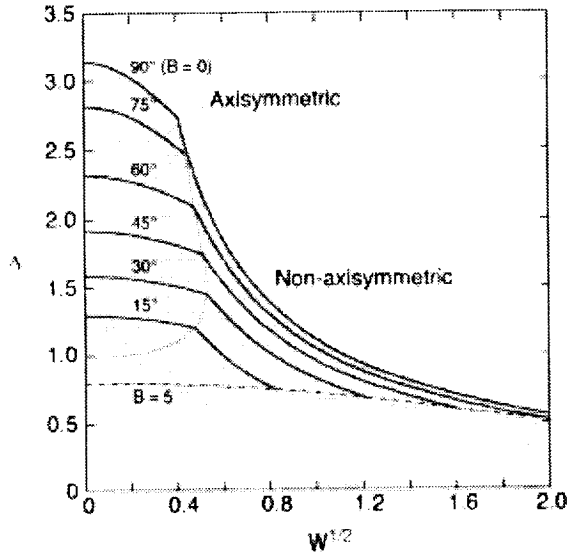

Fig. 3 Level lines of the slope angle at the top and bottom disks ($\beta_1 = \beta_2$) for the critical surfaces of a cylindrical volume bridge. The regions of critical axisymmetric and nonaxisymmetric perturbations are shaded green and yellow, respectively.

The second constraint considered is that the surface slope β_1 at one of the disks is prescribed. The chosen values were 90° and 75°. These values correspond to extremes in growth angle values encountered in floating zone crystal growth. For this case, the dependencies of critical Λ and V values on B and W were calculated. In addition, both axial gravity directions (i.e., up and down) were considered separately and the values of the slope angle, β_2, at the other disk were also analyzed for critical states.

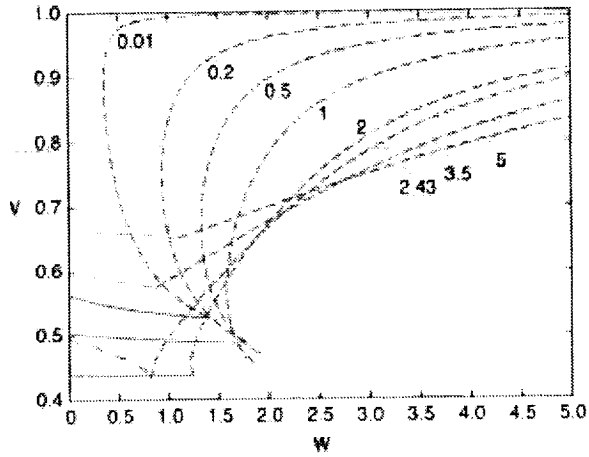

Fig. 4 Stability diagrams for bridges with $\beta_1 = 90°$ in the (W, V)-plane. Numbers on curves denote values of the positive Bond number (i.e. gravity acts such that β_1 is the surface slope at the lower disk, B. Solid (dashed) lines represent segments that correspond to states with critical axisymmetric (nonaxisymmetric) perturbations. Dot-dash lines represent states with limiting surfaces [21].

The solution of the stability problem for any axisymmetric isorotating liquid bridge between equal disks is discussed in detail using the case for $B = W = 0.1$ as an example. In particular, the relationship between the general boundary of the stability region and the stability of bridges subject to the constraints outlined above is examined. The stability region in the (Λ , V)-plane can also be constructed for any fixed pair of values of B and W. Examples of such regions are shown in Fig. 5.

The curves *1*, *2*, *3* and *4* represent the stability region boundaries for the cases of $B = W = 0$; $B = 0.1$, $W = 0$; $B = 0$, $W = 0.1$ and $B = W = 0.1$. Curves 2 and 3 illustrate the independent effects of gravity and centrifugal force. Each of these forces narrows the stability region as compared to the case $B = W = 0$. However, the shapes of the stability regions are different due to the different nature of the gravitational and centrifugal forces. Curve *4* illustrates the combined effect of these forces. As expected, the stability region for their combined action belongs to the intersection of the stability regions for their independent action.

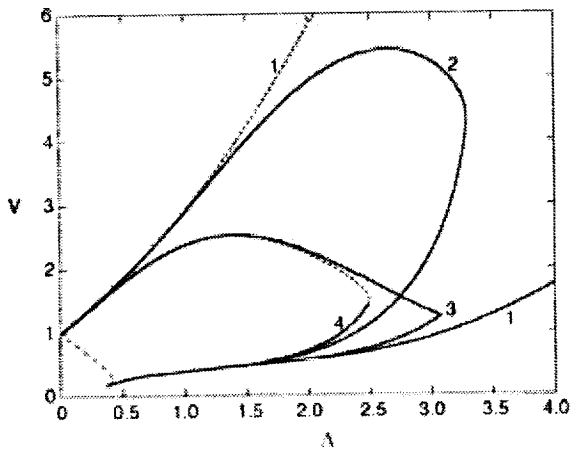

Fig. 5 General boundaries of the stability region for the cases: (1) $B = W = 0$; (2) $B = 0.1$, $W = 0$; (3) $B = 0$, $W = 0.1$; (4) $B = W = 0.1$. States critical to axisymmetric (nonaxisymmetric) perturbations are denoted by solid (dashed) lines.

The shapes of the boundaries *2*, *3* and *4* are typical for moderate values of B and W. Along the upper parts of all boundaries *1* - *4*, stability is lost to nonaxisymmetric perturbations. The lower part of each boundary consists of two segments separated by a cusp-point. On the right-hand segment, loss of stability occurs with respect to axisymmetric perturbations. The left-hand segments of these boundaries merge. However, the nature of the related critical states may be different. The entire left-hand segments of the curves *1* and *2* are determined by states with limiting surfaces. For curve *1*, these limiting surfaces are also the critical ones with respect to nonaxisymmetric perturbations. For an isorotating bridge (the curves *3* and *4*), only a part of this segment closer to the point (0, 1) is determined by states with limiting surfaces. The other part corresponds to states that are critical to nonaxisymmetric perturbations. If at least one of the parameters B and W is reasonably large, there is no neutrally stable state that is critical with respect to axisymmetric perturbations. Here the boundary points correspond either to neutrally stable surfaces that are critical with respect to nonaxisymmetric perturbations or to limiting surfaces.

Figure 6 shows the values of Λ and V for families of stable states, and for some unstable states, that have fixed values of β_1 or β_2. The stability boundary is curve *4* of Fig. 5. For stable states with $\beta_2 = 90°$ or $\beta_2 = 105°$ the Λ values lie between 0 and the critical value $\Lambda = \Lambda^*$. Values of V are bounded by 1 and the critical value $V = V^*$. Λ^* and V^* are determined by the point of intersection of $\beta_2 = const.$ and the general stability boundary. This point corresponds to the state that is neutrally stable to nonaxisymmetric perturbations and represents a "pitch-fork" bifurcation point. The construction of a level line $\beta_1 = const.$ or $\beta_2 = const.$ in the (Λ, V)-plane is important for determining the values of Λ and V for a stable bridge with a prescribed slope angle at one of disks. Finally, we note that the critical slenderness for a cylindrical volume bridge is determined by the point of intersection of the (dot-dash) line $V = 1$ and the general boundary.

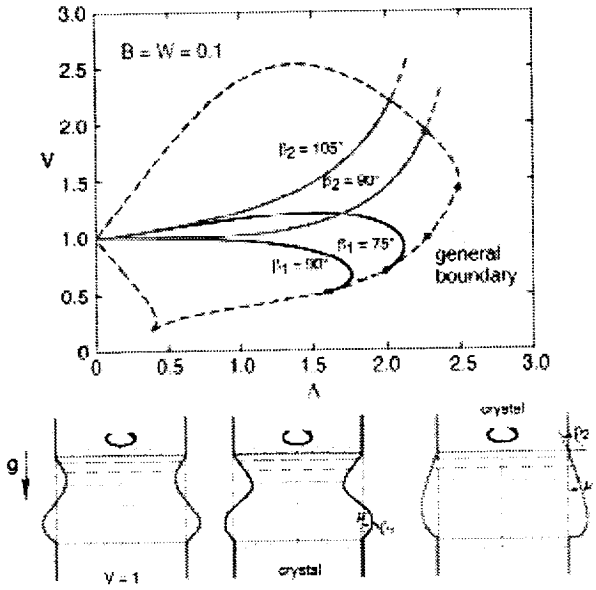

Fig. 6 Values of the slenderness, Λ, and the relative volume, V, for the stable (solid lines) and unstable (dotted lines) bridges with prescribed values of β_1 or β_2. The dashed line is the general boundary of the stability region for $B = W = 0.1$. The critical points are denoted by "open circles" and the transition point between axisymmetric and nonaxisymmetric dangerous perturbations by "closed circles".

4. Effect of Unequal Disk Radii on Stability

The stability of an axisymmetric liquid bridge between unequal circular disks in an axial gravity field was examined for all possible values of the liquid volume and disk separation. The parameter defining the disk inequality is K, the ratio between the radii of the smaller and larger disks. Both axisymmetric and nonaxisymmetric perturbations were considered.

The Λ -V plane was chosen as the appropriate parameter space to delimit the stability regions. Wide ranges of the B and K were considered. Emphasis was given to previously unexplored parts of the stability boundaries. In particular, we examined the maximum volume stability limit for bridges of arbitrary Λ and the minimum volume stability limit for small Λ bridges. The maximum volume stability limit was found to have two distinct properties: large values of the critical relative volume at small Λ, and the possibility that stability is lost to axisymmetric perturbations

at small K. For a given set of K, we determined the maximum Bond number beyond which stability is no longer possible for any combination of V and Λ. We also obtained the maximum value of the actual liquid volume of a stable bridge that can be held between given disks for all possible disk separations for fixed B. It was found that this volume decreases as K decreases and (depending on the sign of B) tends to the critical volume of a sessile or pendant drop attached to the larger disk.

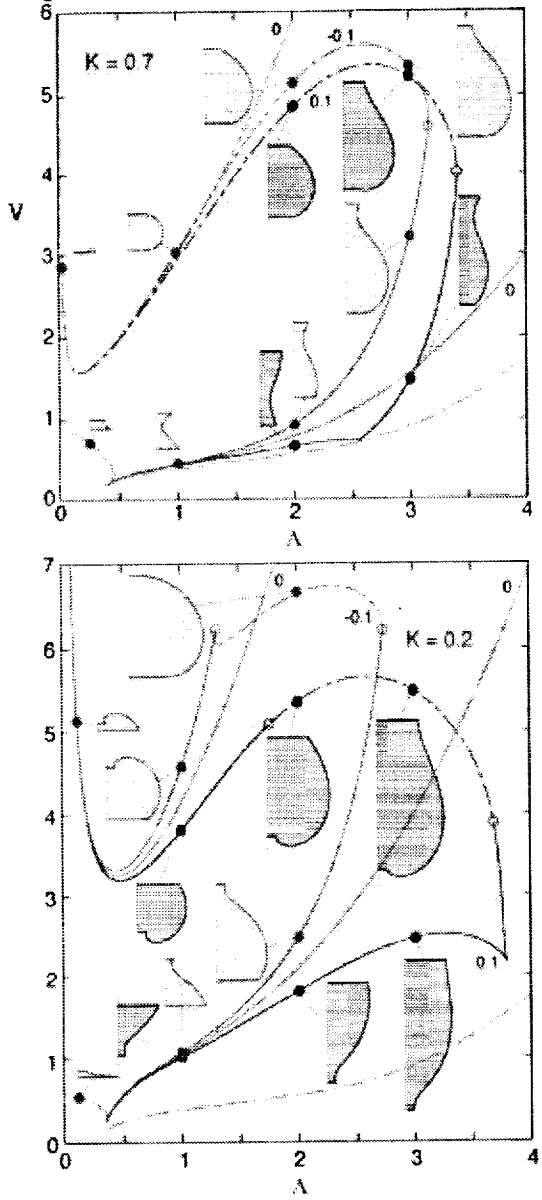

Fig. 7 Shapes of critical liquid bridge surfaces under a downward-directed axial gravity.

Figure 7. shows selected results for K =0.2 and 0.7. The Bond number is positive (negative) when the smaller disk is above (below). The corresponding states are marked by filled circles on the general stability boundaries for: (a) K = 0.7, B = ±0.1; (b) K = 0.2, B = ±0.1. Numbers on curves denote values of B. Solid (dashed) lines correspond to states critical to axisymmetric (nonaxisymmetric) perturbations. Dotted lines represent states with limiting surfaces, and the dot-dash line is the minimum volume stability limit for zero-gravity bridges between equal disks (K = 1, B = 0). A filled circle corresponds to the state with $\Lambda = \Lambda_{max}$ for a given stability boundary. Open circles represent transition points between different types of boundary segments (e.g., when states critical to axisymmetric perturbations become critical to nonaxisymmetric perturbations or change to states with limiting surfaces). Experimental results [20] are in good agreement with the results predicted by this analysis.

Finally, we present results concerning the stability of axisymmetric equilibrium configurations of a capillary liquid in a circular cylindrical container with planar ends that are orthogonal to a cylindrical wall. The liquid either is subject to an axial gravity field or is under zero-gravity conditions. We consider *doubly connected* free surfaces (i.e., they do not cross the cylinder's axis of symmetry) that bound an annular region occupied by the gas. This study was motivated by the problem of partly contained melts in low gravity solidification experiments. Preliminary results prove that a free surface with one of contact lines on one of the cylinder's planar ends and the other on a lateral wall is always unstable if the wetting angle, α, lies in the range $0 \le \alpha \le 90°$. The stability regions for this configuration have been constructed in the plane "α - V" (here $V = v_g/r_0^3$ is the relative gas volume) for set values of the B in the interval $-10 \le B \le 60$. It has been established that the stability region is connected if $B > B_0$ or $B < B_1$ ($-1.69 > B_0 > -1.70$ and $-1.79 > B_1 > -1.80$). If $B_1 < B < B_0$, the stability region consists of two disconnected parts. It was also found that a doubly connected free surface with both contact lines on a cylindrical wall may exist only under zero-gravity conditions (see Fig. 8). Further analysis revealed that only unduloidal free surfaces with profiles that contain inflection points may be stable to nonaxisymmetric perturbations. Such a free surface may be stable to arbitrary perturbations if $\alpha > 121°$. For a given $121° < \alpha < 180°$, the minimum and maximum stability limits of the relative gas volume have been determined.

Two special liquid bridge type configurations were also analyzed. One with a free surface pinned to edges of both end plates of a cylinder and the other with one part of the free surface pinned to edges of a cylinder's planar end and the other to a solid rod contained within the cylinder. This problem is connected with a new technique for "contactless" directional crystallization in low gravity. We analyzed stability conditions for the first configuration at B = 0 and B = 0.05, and arbitrary

values of other parameters (wetting angles, aspect ratio and the liquid relative volume). Similar results have been obtained for the second configuration for rod/cylinder radius ratios equal to 0.8 and 0.6.

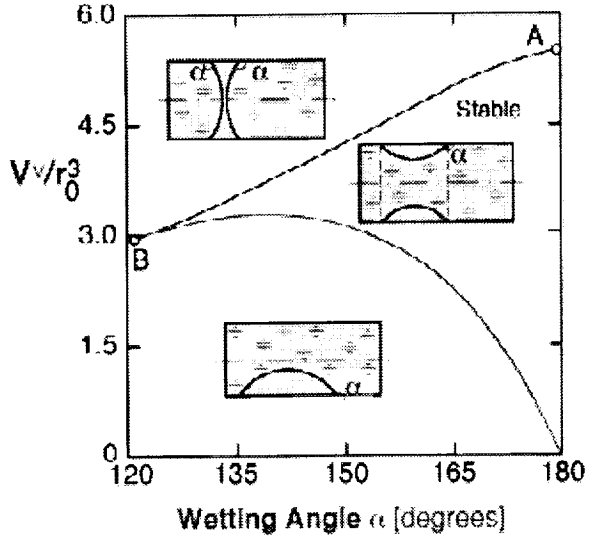

Fig. 8 Dependence of the vapor relative volume, $V^v = V^v/r_0^3$, on the wetting angle, α, for critical states of configurations with contact lines on the lateral wall of the cylinder.

Acknowledgments

This work was supported by the National Aeronautics and Space Administration through grant NAG3-1384.

References

1. L. A. Slobozhanin and J. M. Perales, "Stability of liquid bridges between equal disks in an axial gravity field," Phys. Fluids A **5**, 1305-1314 (1993).
2. D. Myshkis, V. G. Babskii, N. D. Kopachevskii, L. A. Slobozhanin and A. D. Tyuptsov, *Low-Gravity Fluid Mechanics* (Springer-Verlag, Berlin, 1987).
3. S. R. Coriell, S. C. Hardy and M. R. Cordes, "Stability of liquid zones", J. Colloid Interface Sci. **60**, 126 (1977).
4. L. H. Ungar and R. A. Brown, "The dependence of the shape and stability of captive rotating drops on multiple parameters", Philos. Trans. R. Soc. London Ser. A **306**, 347 (1982).
5. R. A. Brown and L. E. Scriven, "The shapes and stability of captive rotating drops", Philos. Trans. R. Soc. London Ser. A **297**, 51 (1980).
6. J. Lowry and P. H. Steen, "Capillary surfaces: stability from families of equilibria with application to the liquid bridge," Proc. R. Soc. London A **449**, 411-439 (1995).
7. Langbein, Crystal growth from liquid columns, J. Crys. Growth **104**, 47-59 (1990).
8. Tsamopolous, T. Chen, T. and A.Borkar, Viscous oscillations of capillary bridges, J. Fluid Mechanics, **235**, 579-609 (1992).
9. Mollot, J. Tsamopolous, T. Chen, and A. Ashgriz, Non-linear dynamics of capillary bridges: Experiments, J. Fluid Mech. **255**, 411-435 (1993).
10. G. Seebold, M. P. Hollister and H. M. Satterlee, "Capillary hydrostatics in annular tanks," J. Spacecraft **4**, No. 1, 101-105 (1967).
11. Salzman, Fluids management in space-based systems, Engineering, Construction and Operations in Space, 5th International Conference on Space, **1**, .521-526 (1966).
12. B. J. Ennis, J. Li, G. Tardos, and R. Pfeiffer, The influence of viscosity on the strength of an axially strained pendular bridge, Chem. Eng. Sci., **45**, 3071-3088 (1990).
13. V. P. Mehrota, and K.V.S. Sastry, Pendular bond strength between unequal-sized spherical particles, Powder tech., **25** 203-214 (1980).
14. L. A. Newhouse, and C. Pozrikidis, The capillary instability of annular layers and thin liquid threads, J. Fluid Mech., **242**, 193-209 (1992).
15. W. Keller and A. Mühlbauer, Floating Zone Silicon, in Preparation and Properties of Solid State Materials Vol. 5, W. R. Wilcox, ed. (Marcel Dekker, New York, 1981).
16. Mühlbauer, A. Muiznieks and J. Virbulis, Analysis of the dopant segregation effects at the floating zone growth of large silicon crystals, J. Crystal Growth, **180**, 372-380 (1997).
17. K. Brakke, Experimental Math. **1** 141- (1992).
18. J. I. D. Alexander, S. Delafontaine, A. Resnick and W. C. Carter, "Stability of non-axisymmetric liquid bridges," Microgravity Sci. Technol. **9**, 193-200 (1996).
19. L. A. Slobozhanin, J. I. D. Alexander and A. H. Resnick, "Bifurcation of the equilibrium states of a weightless liquid bridge," Phys. Fluids **9**, 1893-1905 (1997).
20. H. Resnick, "Experimental study of the dynamics and statics of nonaxisymmetric liquid bridges," Ph.D. Thesis, The University of Alabama in Huntsville, 1997.
21. L. A. Slobozhanin and J. I. D. Alexander, Stability of an isorotating liquid bridge in an axial gravity, Phys. Fluids **9**, 1880-1892 (1997).

RADIATION AND MAXWELL STRESS STABILIZATION OF LIQUID BRIDGES

M. J. Marr-Lyon, D. B. Thiessen, F. J. Blonigen, P. L. Marston, Department of Physics, Washington State University, Pullman, WA 99164-2814; marston@wsu.edu

1 Introduction

A unique and potentially useful fluid configuration which is possible in zero gravity is the liquid cylinder. One example is floating-zone crystal growth which, in zero gravity, involves a cylindrical melt bridging two solid cylinders. In low gravity, when the length of a cylindrical liquid bridge exceeds it's circumference, the bridge becomes unstable and breaks. A liquid bridge of length L and radius R is thus characterized by the ratio $S = L/2R$, where S is termed the slenderness of the bridge. The stability limit of $S = \pi$ is known as the Rayleigh-Plateau (RP) limit. For floating-zone crystal growth one might wish to have a longer liquid bridge in order to reduce the temperature gradient at the growth front since thermal stress can lead to defects in the growing crystal. A number of groups have studied stabilization methods which rely on the electrical properties of the liquid column. For example, an axial electric field has been shown to stabilize a dielectric bridge beyond the RP limit. The stabilization methods explored in this work are of a fundamentally different nature.

The modes of oscillation for a liquid bridge in zero gravity are associated with volume-conservative surface deformations which can be characterized in terms of an axial index N and azimuthal index m. The index N is the number of half-wavelengths in the axial direction and the index m is the number of wavelengths in the azimuthal direction. Axisymmetric modes of oscillation have $m = 0$ and the $(N, m) = (2, 0)$ mode is the first mode to become unstable as S is increased beyond π in the absence of stabilization. The breaking process thus involves one end of the bridge becoming fat while the other end becomes increasingly thin, leading to rupture. Stabilization is accomplished by applying a stress to the surface of the bridge to counteract the growth of the $(2, 0)$ mode. The coupling of modulated acoustic radiation stress to both axisymmetric and non-axisymmetric modes of a cylindrical liquid bridge in a Plateau tank has been demonstrated [1]. Both acoustic radiation stress [2] and the Maxwell stress [3] have been used to stabilize liquid bridges in this work. Acoustic radiation stress arises from the time-averaged acoustic pressure at the surface of an object immersed in a sound field. Both passive and active acoustic stabilization schemes as well as an active electrostatic method have been explored.

2 Experimental results

Ground based testing of stabilization past the RP limit requires simulating low gravity. This was accomplished in a Plateau tank. The bridge was deployed in a liquid bath, where the bridge liquid and the bath were of the same density and immiscible in each other. In the Plateau tank, two methods of stabilization were explored: one using acoustic radiation stresses and the other using Maxwell stresses. Acoustic transducers for use on a liquid bridge in air were also developed, and tested both in normal gravity and in reduced gravity on NASA's low-gravity KC-135 aircraft.

2.1 Active acoustic stabilization in a Plateau tank

For these experiments, the Plateau tank had an ultrasonic transducer incorporated to produce an acoustic standing wave inside the tank. The acoustic transducer has a step machined into its surface so as to create a different liquid depth between the halves of the tank. This difference in depth causes a difference in resonance frequencies between the halves, so by adjusting the drive frequency, the acoustic energy can be shifted from side to side. In the system of interest, the bridge liquid is attracted to a pressure antinode, so by spatially shifting the pressure antinode, different areas of the bridge can be affected. To detect the shape of the bridge, a two-segment photodiode is used. The bridge is illuminated with an expanded laser beam, and the image is projected onto the photodiode. The difference between the photodiode signals provides information about the shape of the bridge. This error signal is used to adjust the drive frequency of the transducer in order to keep the bridge shape cylindrical [2].

In figure 1, images of a capillary bridge that is stabilized using active feedback in a Plateau tank are shown. In figure 1 (a), the bridge is stabilized to a length of $S = 4.1$. Shortly before (b), the acoustic drive is turned off, and the $(2, 0)$ mode subsequently grows and causes the bridge to break as shown in (c).

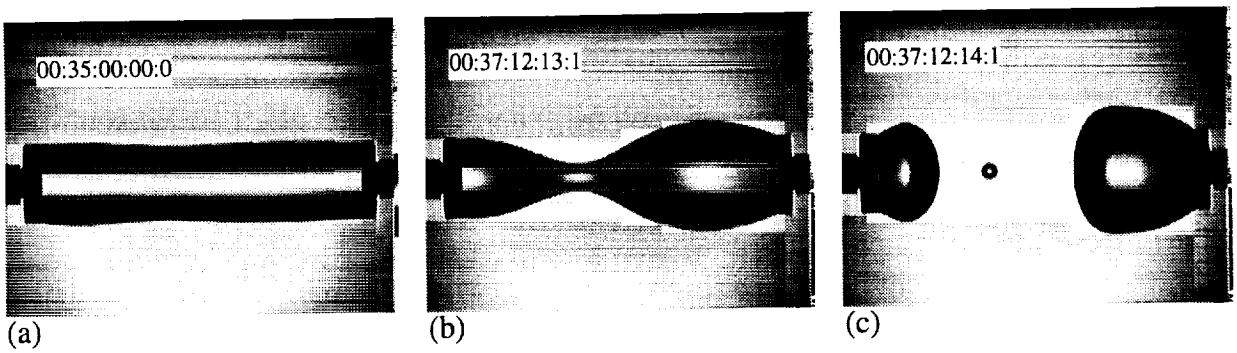

Figure 1: A capillary bridge stabilized to $S = 4.1$ using active feedback and acoustic radiation pressure. The time code shown is in the format "hours : minutes : seconds : frame : field", where there are 30 frames per second, and 2 fields per frame. In (a), the bridge has been stabilized beyond the RP limit for approximately 2.5 minutes. About 2 minutes later the acoustic drive is shut off. 470 ms after the sound is shut off, (b) shows the growth of the $(2,0)$ mode, and the bridge is shown to be completely broken in (c), which was taken 33 ms after (b).

2.2 Active stabilization in a Plateau tank using electric fields

This case is similar to that described in § 2.1. The bridge is deployed in a Plateau tank; however, here the bridge liquid is electrically conducting, and the outer bath is electrically insulating. The detection system is as previously described, except that now the control uses Maxwell electrostatic stresses instead of radiation stresses [3]. Two ring electrodes placed coaxial with the bridge may be seen in figure 2. The error signal from the photodiode now controls the potential applied to each electrode via high-voltage amplifiers. Since the conducting liquid is attracted to the ring with a high voltage, when the photodiode detects one side thinning, a potential is applied to that ring, pulling the liquid back. The electrodes were designed to optimize the coupling to the $(2,0)$ mode.

In figure 2 (a), the bridge is stabilized using active feedback and Maxwell stresses to $S = 4.1$. Just before (b) the control is turned off, and in (b) and (c) the $(2,0)$ mode grows and breaks.

2.3 Soap-film tests in normal gravity

To extend the active feedback scheme to a liquid bridge in air, a transducer needed to be developed that could rapidly spatially redistribute the acoustic energy. Testing such a transducer in normal gravity is somewhat difficult using a liquid bridge, because the maximum slenderness of a liquid bridge in normal gravity is much shorter than that in low-gravity. Using a gas-filled soap-film bridge, the effect of the transducer on the bridge can be tested with a longer bridge. The soap-film bridge also remains cylindrical, while a liquid bridge sags in normal gravity. However, the sound field does not couple well into a soap-film bridge filled with air, so a gas with different sound speed and density was needed to produce sufficient acoustic contrast to allow the sound field to couple into the bridge mode of interest. Sulfur hexafluoride (SF_6) was chosen because the speed of sound in SF_6 is about 1/3 that in air, and the density of SF_6 is about 5 times that of air.

Two transducer configurations have been designed and initial tests performed with the soap-film bridge. In one design, a standing wave is established between a dual-horn aluminum bar transducer and a cylindrical reflector. The two horns have a slightly different resonance so that a small change in the driving frequency can cause one horn or the other to radiate more intensely [4]. The spatial redistribution of radiation pressure on the bridge can then be accomplished by simply changing the drive frequency. The second design involves two tweeters which face each other with a lateral offset. Spatial redistribution of sound intensity in this case is accomplished simply by adjusting the relative drive amplitude of the two tweeters. Each of these designs was shown to be capable of exciting the $(2,0)$ mode of the soap-film bridge filled with SF_6. Figure 3 shows the $(2,0)$ mode oscillation for the soap-film bridge driven by the dual-horn transducer.

A linear model of bridge dynamics with active feedback (§ 3) suggests that a delay in applying the feedback force to the bridge can seriously limit the effectiveness of the feedback. Feedback delay is expected to be signif-

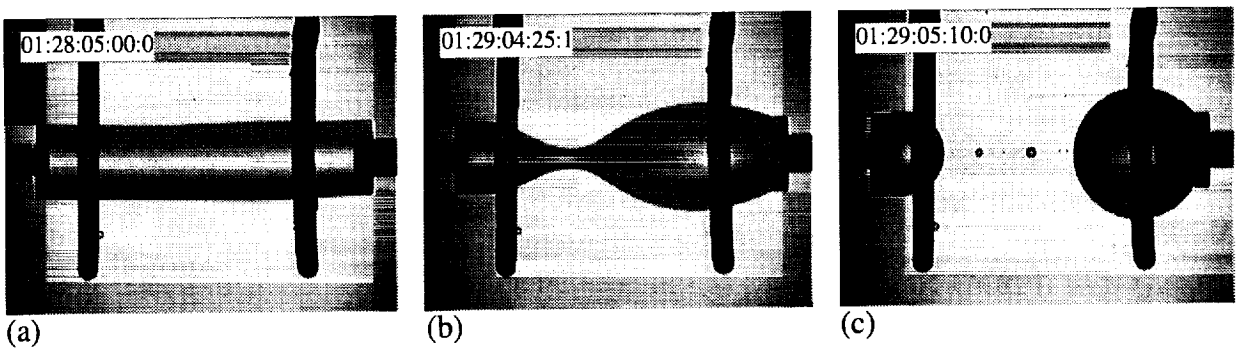

Figure 2: A capillary bridge stabilized to $S = 4.1$ using active feedback and Maxwell stresses. About 1 minute after (a), the feedback control is turned off. 520 ms after the control is turned off, (b) shows the growth of the $(2,0)$ mode, and the bridge is shown to be completely broken in (c), which was taken 480 ms after (b).

icantly less for the dual-tweeter configuration than for the dual-horn system because the lower Q of the dual-tweeter design allows for more rapid shifting of acoustic energy from one end of the bridge to the other. A clean test of active feedback stabilization for a liquid bridge in air under low-gravity conditions has not yet been made.

2.4 Passive acoustic stabilization in low gravity

A liquid bridge in air is predicted to be stabilized when positioned at a pressure node in an acoustic standing wave with the bridge axis perpendicular to the sound propagation direction [5]. In this case, the bridge is not actively controlled as in §§ 2.1 and 2.2; the stabilization is a passive result of the interaction of the sound field with the bridge. The radius of the bridge supports and the frequency of the sound field are chosen such that the radiation stresses cause the regions of smaller local radius to be expanded, and the regions of larger local radius to be squeezed, thus stabilizing the bridge against breakup of the $(2,0)$ mode.

Passive stabilization was demonstrated in low gravity for a liquid bridge in air during parabolic flights aboard NASA's KC-135 aircraft. In figure 4 (a), a liquid bridge composed of a 20 cS water and glycerol mixture is extended in a 21 kHz acoustic standing wave to $S = 3.5$. The bridge support radius is 2.16 mm. Shortly before (b), the sound field is turned off, and in (b) and (c), the $(2,0)$ mode grows and breaks. It can be seen in figure 4 (a) that the sound field also causes a static deformation in shape. The bridge contains precisely enough liquid to form a circular cylinder, but the sound field causes the bridge to be flattened. This effect is also seen when acoustically levitating liquid drops.

Since each KC-135 parabolic maneuver results in only about 20–30 seconds of low gravity, an automated bridge deployment system was developed to facilitate drawing the bridge in such a short time. The system uses synchronized stepper motors to position the supports and inject the proper volume of liquid.

3 A linear model of bridge dynamics with feedback

A linear model of the bridge dynamics including the effects of a feedback force, which is applied with some delay and gain, has been developed [2, 6]. The model accounts for viscous dissipation both in the bridge liquid and in the surrounding fluid. The boundary conditions on the end of the bridge are only approximately satisfied. The response of the bridge is analogous to that of a driven, damped, harmonic oscillator where the $(2,0)$ mode amplitude corresponds to the oscillator's displacement. The $(2,0)$ mode surface deformation has an associated change in surface area which provides a restoring force which is linearly related to the $(2,0)$ mode amplitude. The effective spring constant for this restoring force is proportional to $[(\pi/S)^2 - 1]$. Thus the natural spring constant becomes negative when $S > \pi$ which results in instability. By adding an external force proportional to the $(2,0)$ mode amplitude with the appropriate gain, the effective spring constant can be made positive even when $S > \pi$.

A delay in applying the feedback force to the bridge arises because of the finite time required to sense the bridge deformation and adjust the stress distribution on the bridge. The model predicts that this delay has the effect of reducing the effective damping of bridge os-

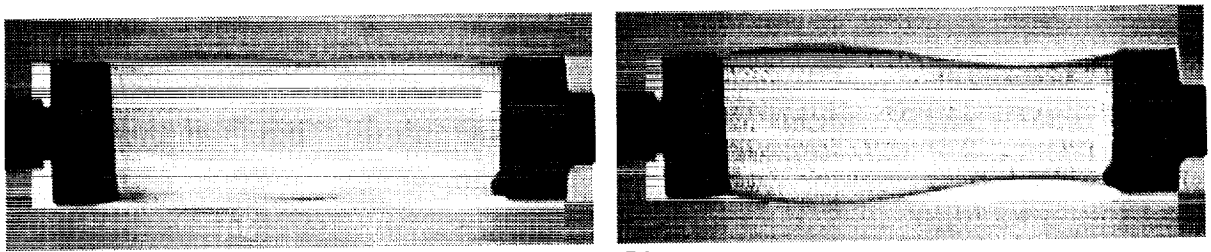

Figure 3: Images of a SF_6 filled soap-film bridge being driven in the $(2,0)$ mode. In (a), an average of several frames was taken, and (b) is a single frame.

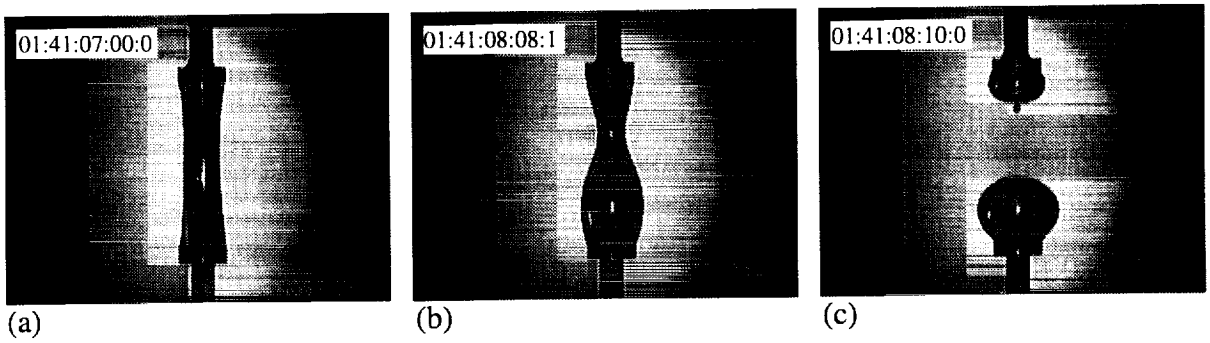

Figure 4: A liquid capillary bridge in air stabilized to $S = 3.5$ in low gravity using acoustic radiation pressure. About 1 second after (a), the sound is turned off. In (b), the growth of the $(2,0)$ mode is shown 330 ms after the sound is turned off. 50 ms after (b), the bridge has broken as shown in (c).

cillations, therefore making the bridge less stable. The model indicates that for a bridge beyond the RP limit, stability is expected for a range of gain which depends on the feedback delay. As feedback delay increases, the range of gain for stability decreases until stabilization becomes impossible. Thus the feedback delay must be less than a critical value in order for stabilization to be possible. The critical feedback delay decreases for increasing values of slenderness. Critical feedback delay also decreases for decreasing fluid viscosities.

Acknowledgment

This research was supported by NASA grant NAG3-1918.

References

[1] S. F. Morse, D. B. Thiessen, and P. L. Marston "Capillary bridge modes driven with modulated ultrasonic radiation pressure." *Phys. Fluids* **8** (1), 3-5 (1996).

[2] M. J. Marr-Lyon, D. B. Thiessen, and P. L. Marston, "Stabilization of a cylindrical capillary bridge far beyond the Rayleigh-Plateau limit using acoustic radiation pressure and active feedback," *J. Fluid Mech.* **351**, 345-357 (1997).

[3] P. L. Marston, D. B. Thiessen, M. J. Marr-Lyon, and F. J. Blonigen, "Stabilization of an electrically conducting capillary bridge beyond the Rayleigh-Plateau limit using feedback control of electrostatic stresses (abstract)," *Bull. Am. Phys. Soc.* **42**, 2122 (1997).

[4] M. J. Marr-Lyon, D. B. Thiessen, and P. L. Marston, "Stabilization of a Capillary Bridge Far Beyond the Rayleigh-Plateau Limit Using Active Feedback and Acoustic Radiation Pressure," Proceedings of the 16^{th} International Conference on Acoustics, (at press).

[5] P. L. Marston, "Capillary bridge stability in an acoustic standing wave: Linearized analysis of passive stabilization with radiation pressure (abstract)," *J. Acoust. Soc. Am.* **97**, 3377 (1995).

[6] D. B. Thiessen, M. J. Marr-Lyon, and P. L. Marston, "Linear models of capillary bridge dynamics with stabilization and approximations for the boundary layer damping (abstract)," *Bull. Am. Phys. Soc.* **42**, 2122 (1997).

STABILITY OF SHAPES HELD BY SURFACE TENSION AND SUBJECTED TO FLOW

Yi-Ju Chen, ESAM, Northwestern University, Evanston, IL 60208, USA, chen@arnold.esam.nwu.edu, Nathaniel D. Robinson and Paul H. Steen, Chemical Engineering, Cornell University, Ithaca, NY, USA, steen@cheme.cornell.edu

Abstract

Results of three problems are summarized in this contribution. Each involves the fundamental capillary instability of an interfacial bridge and is an extension of previous work. The first two problems concern equilibrium shapes of liquid bridges near the stability boundary corresponding to maximum length (Plateau-Rayleigh limit). For the first, a previously formulated nonlinear theory to account for imposed gravity and interfacial shear disturbances in an isothermal environment [1,2] is quantitatively tested in experiment. For the second problem, the liquid bridge is subjected to a shear that models the effect of a thermocapillary flow generated by a ring heater in a liquid encapsulated float-zone configuration[3]. In the absence of gravity, this symmetric perturbation can stabilize the bridge to lengths on the order of 30% beyond the Plateau-Rayleigh (PR) limit, which is on the order of heretofore unexplained shuttle observations. The third problem considers the dynamics of collapse and pinchoff of a film bridge (no gravity) --- what happens in the absence of stabilization. Here we summarize experimental efforts to measure the self-similar cone-and-crater structure predicted by a previous theory[4].

Introduction

A liquid/gas or liquid/liquid interface is shaped by surface tension whenever surface area is large relative to volume (small physical length) or when gravity is reduced relative to the surface force (small capillary length). The stability of such an interface is important to a variety of earth-based applications, to float-zone experiments in a space shuttle and to successful liquid management in a space laboratory, more generally.

Overview

Deformable interfaces of finite extent are of interest. Attention is restricted to axisymmetric shapes and pinned contact lines. Axisymmetric disturbances are the most dangerous for the axisymmetric shapes considered. These may be classified according to number of relevant length scales.

With only surface tension acting, an incompressible fluid mass of prescribed volume V takes the shape of a sphere. The sphere is characterized by a single length-scale, say $V^{1/3}$. If the fluid mass contacts a solid circular disk of radius R, then its equilibrium shapes (pieces of spheres) are characterized by length scales R and $V^{1/3}$. If, in addition, gravity acts on the mass (force/volume ρg) then the shapes depend on capillary length $(\sigma/\rho g)^{1/2}$ as well as on R and $V^{1/3}$. These figures are known as the sessile drop, bubble or pendant drop, depending on the orientation of gravity and density contrast. Three lengths are relevant, alternatively, if, in the absence of gravity, the mass contacts two solid disks, arranged coaxially and separated by length ℓ. This is known as the liquid bridge. Droplets and bridges can also be exposed to a flow. Suppose p_z represents a typical pressure gradient. Then, an additional relevant length scale enters, $\sigma/p_z R$, say. And so forth. Ratios of relevant lengths form the dimensionless control parameters of the problem. Interfacial bridges are characterized by two contact lines and at least two control parameters.

The number of contact lines is related to potential instabilities of the shapes. The sphere is always stable. Shapes with a single contact line (spherical bubbles and pendant or sessile droplets) suffer only turning point instabilities (codimension 0 bifurcations). On increasing ℓ, liquid bridges, on the other hand, undergo pitchfork bifurcations that can be unfolded with two control parameters (codimension 2). Singularity theory [5] provides the mathematical framework for the experimental results presented in the first liquid bridge problem. The interacting symmetries of pitchfork and imposed disturbance provide the framework for the second liquid bridge problem. The thin film bridge is a liquid bridge with zero net curvature ($\kappa_1 + \kappa_2 = 0$). In that problem, the dynamics of interest start at the instability occurring at a turning point bifurcation.

The influence of flow on capillary instability can be understood through the normal stress balance across the interface. In the absence of motion and body force and in an isothermal environment, this reduces to the Young-Laplace equation,

$$[p] = \sigma(\kappa_1 + \kappa_2) \tag{1}$$

where $[p]$ is the jump in pressure across the interface and κ_1 and κ_2 are the principal curvatures of the math-

ematical surface. Thus, the axial pressure gradient $[p_z]$ can be viewed as having two contributions, each from a curvature gradient. If gravity acts coaxially, there is an additional constant contribution proportional to ρg. Suppose motion arises from an imposed interfacial shear. Although the motion is driven through the tangential stress balance, it influences the shape as an axial pressure gradient in the normal stress balance. Therefore, the free boundary problem for the interface can be solved with the following strategy. Guess an interface shape, solve for the flow field to obtain the flow contribution to the pressure gradient, solve the normal stress balance for a corrected shape, and so forth. This approach also works for the nonisothermal case provided the coupling between thermal and velocity fields occurs only at the interface (ie. small Peclet number). Our analyses of liquid bridges follows this approach. A bifurcation equation is derived from a functional equation representing the normal stress balance. The steady states of this equation are studied.

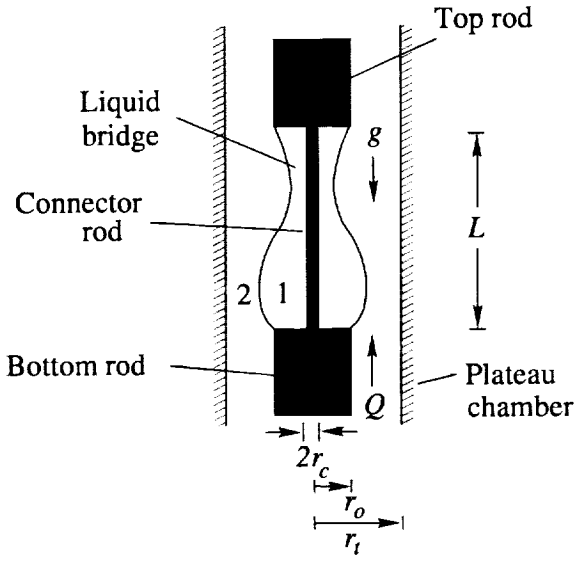

Figure 1: Sketch of a two-fluid system.

Liquid bridge: shear and gravity effects

The bridge is subject to gravity and is immersed in a pipe flow, with both perturbations acting coaxially, as sketched in figure 1. We have previously established that although each perturbation on its own is destabilizing, they can stabilize by acting in concert[6]. This is the fingerprint of a nonlinear effect. Here we summarize experimental results that probe the neighborhood of the PR limit. Figure 2 plots the deflection ϵ of the interface from cylindrical against the flow rate Q. The solid lines are the predictions of the bifurcation equation derived from a normal stress balance that takes account of motion of liquids on both sides of the interface[7]. The symbols represent measurements taken over a range of strengths of gravity and flow rate, lengths and volumes. Here Bond number is defined as $B \equiv {r_o}^2 \rho g/\sigma$, scaled length $L \equiv \ell/r_o$ and volume imperfection v is the deviation of the volume from cylindrical, scaled by the cylindrical volume.

The lengths can be ordered from 10% to 3% short of the PR limit. Several trends are discernible. For equal lengths, the slopes are comparable and the magnitude of slope increases with increasing length. The position of the intercepts depend on volume and Bond number. The region between the turning points gives the window of stable states. This is a true window (upper and lower limits) for quiescent shapes that bulge down ($B > 0$). The window narrows as the length increases. The the-

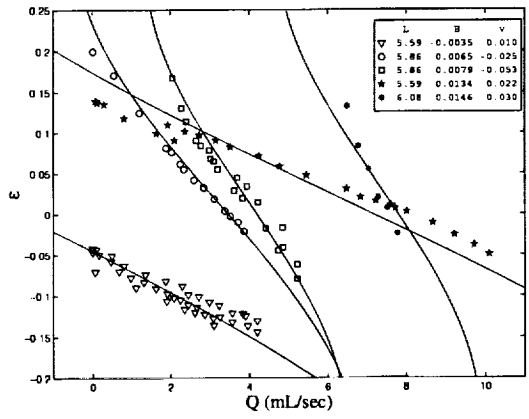

Figure 2: Surface deflection as a function of flow rate. Symbols represent experiment and solid lines are two-fluid theory [7].

ory is not only able to account for trends in the data, but it is capable of quantitative prediction. Figure 2 further suggests that the regime of validity of theory is considerable, especially as regards to length. Theory and experiment are in tight agreement except closest to the stability limit where experimental limitations of temperature control seem to preclude reliable measurements [7]. This explains the absence of data beyond the PR limit ($L = 2\pi$).

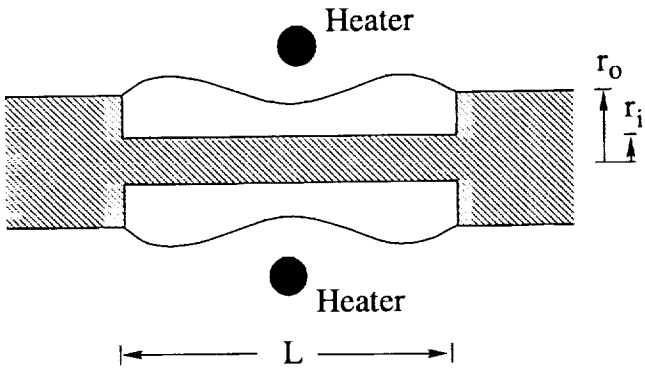

Figure 3: Sketch of a liquid float-zone in zero gravity.

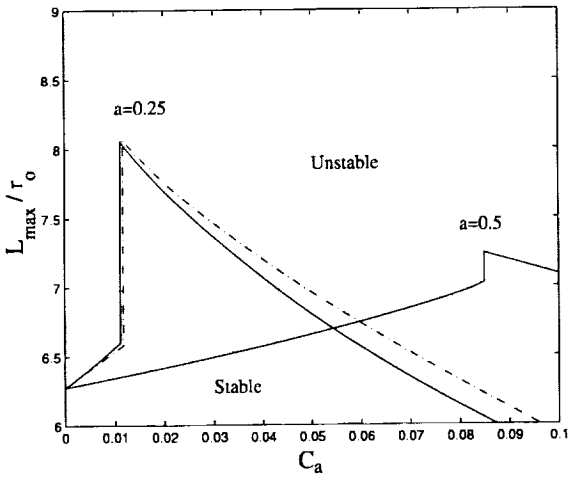

Figure 4: Maximum bridge length versus capillary number at a=0.25 and a=0.5 where $a \equiv 1 - r_t/r_o$. Dashed line represents results from perturbation method and solid lines are from computation.

Liquid bridge: encapsulated float-zone model

The second problem is motivated by observations of extra-long float zones in the Liquid Encapsulated Melt Zone (LEMZ) materials science experiment on STS57[8]. The float zone is modeled as a liquid bridge (no gravity) whose normal stress balance is influenced by pressure gradients induced by thermocapillarity. In contrast to the isothermal problem where the imposed shear is unidirectional, symmetry of the full float zone (ring heater) generates a shear symmetric about the midplane. In figure 3, the solid center rod that makes the bridge an annulus models an unmelted core or a viscosity that varies with temperature. The symmetric pressure disturbances can interact significantly with the PR pitchfork. Figure 4 plots stability limit against strength of thermocapillary flow where $Ca \equiv -\alpha\Delta T/\overline{\sigma}$ and $\sigma \equiv \overline{\sigma} + \alpha(T - \overline{T})$ and T is temperature. Figure 4 predicts stabilizations of 30-40%, depending on the extent of the solid core, offering an explanation for observations (largely qualitative in nature).

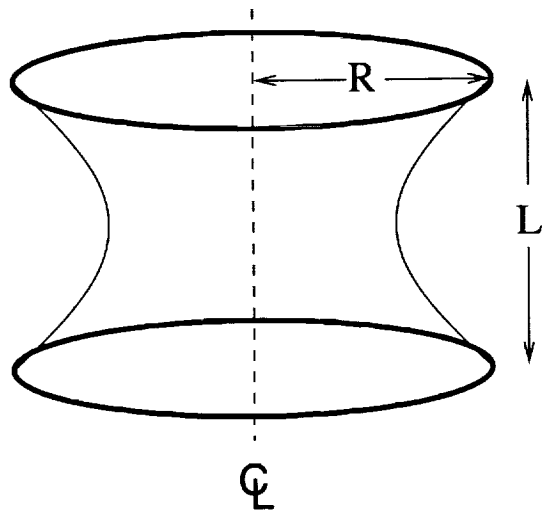

Figure 5: Schematic of soap film experiment.

Film Bridge: collapse and pinchoff

Figure 5 shows a sketch of the thin film stretched between two circular contact lines. The collapse is driven by capillary instability and resisted by the inertia of the surrounding fluid (air). Of interest is the prediction i) that both principal curvatures κ_1 and κ_2 diverge by a $t^{-2/3}$ scaling law as time t approaches the instant of

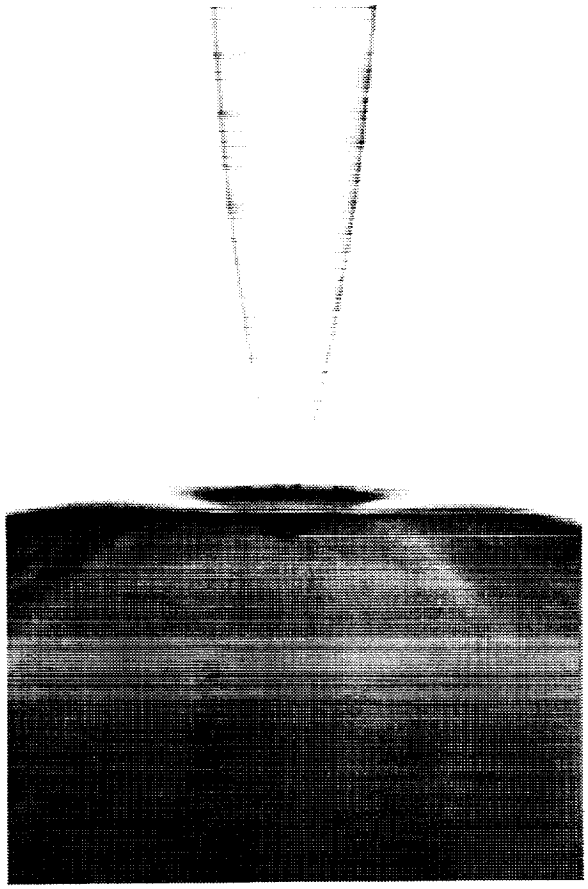

Figure 6: Photograph of cone-and-crater structure (shortly after detachment).

topological change and ii) that a cone-and-crater pinchoff structure with unique angles appears[4]. Figure 6 shows a close-up photograph of the cone-and-crater structure, just after detachment of the cone from the crater. The key prediction that the crater forms before detachment has been verified in experiment. Experiments to accurately determine the angles are underway. This prototype problem is important since aspects of the inertially-dominated film pinchoff are likely to be common to inertial pinchoff in liquid systems.

Acknowledgements

This work is supported by NASA NAG3-1854. NDR thanks NASA GSRP NGT3-52318 for fellowship and Jody Herndon for her laboratory assistance. PHS thanks Dr. Olus Boratav for useful discussions.

References

1. CHEN, Y-J & STEEN, PH 1994 Influence of flow on Interface Shape Stability *Proc. 14th IMACS World Conf.*, Atlanta, GA, July, pp.629-32.

2. CHEN, Y-J 1997 Stability and breakup of capillary surfaces of revolution: liquid and film bridges. PhD dissertation, Cornell University.

3. CHEN, Y-J & STEEN, PH 1996 Influence of thermocapillary flow on capillary stability: Long float-zones in low gravity. *Proc. 3rd Microgravity Fluid Physics Conf.*, Cleveland OH, 13-15 June, pp.481-3.

4. CHEN, Y-J & STEEN, PH 1997 Dynamics of inviscid capillary breakup:collapse and pinchoff of a film bridge. *J. Fluid Mech.* **341**, pp. 245-267.

5. GOLUBITSKY M & SCHAEFFER, DG 1985 *Singularities and Groups in Bifurcation Theory.* Vol.1, Springer-Verlag, New York.

6. LOWRY, BJ & STEEN, PH 1997 Stability of slender liquid bridges subjected to axial flows. *J. Fluid Mech.* **330**, pp. 189-213.

7. CHEN, YJ, ROBINSON, ND, HERNDON, J & STEEN, PH 1998 Liquid bridge stabilization: theory guides a codimension-two experiment, *Computer Methods in Applied Mechanics and Engineering*, in press.

8. ABBASCHIAN, R 1996, private communication.

ELECTROHYDRODYNAMIC STABILITY OF A LIQUID BRIDGE - THE 'ALEX' EXPERIMENT

C. L. Burcham[1], S. Sankaran[2], & D. A. Saville[3] [1,3]Department of Chemical Engineering, Princeton University, Princeton, NJ, [2]NASA Lewis Research Center, Cleveland OH, [3]dsaville@morticia.princeton.edu

I. RESEARCH OBJECTIVES

G. I. Taylor's[2] leaky dielectric model describes electrohydrodynamic fluid motion driven by strong electric fields. We carried out microgravity experiments aboard the space shuttle Columbia during the LMS Mission in the summer of 1996 to test that theory. Our experiments dealt with the electrohydrodynamic stability of liquid bridges.

II. BACKGROUND

Electrical forces can be used to manipulate fluids by controlling the shape of an interface or exerting a body force on bulk liquid. For example, liquids can be pumped or sprayed by an appropriately shaped electric field. For apolar liquids (such as organic compounds) where the conductivity is low, relatively high field strengths (1000 V/cm) are needed. Controlling the flow of liquids in micron-scale devices is also a rapidly emerging technology*. Here, the design of small scale fluid circuits depends, in part, on understanding the electrical forces and their relation to fluid motion; there are many other applications of electrohydrodynamics. Hence the need for a reliable, well-tested theory for designing apparatus. The current theory, the leaky dielectric model, was invented by G. I. Taylor[2] in the 1960's, but very few quantitative tests have been carried out[3]. We used a liquid bridge as a venue for our experiments. One reason for choosing the bridge configuration is it's simple geometry. In addition, studying the electrohydrodynamic stability enabled us to probe aspects of the theory which had not been previously accessible.

A liquid bridge is a column of liquid pinned to a flat plate at each end (figure 1). Over a century ago, Plateau found that a neutrally buoyant bridge is stable to small perturbations as long as its length, L, is less than it's circumference, πd ($2a = d$, the diameter). Thus, for stability $L/d < \pi$. Interfacial tension plays a dual role. With short bridges, small perturbations are smoothed by the action of interfacial tension. Longer bridges become unstable, also due to interfacial tension. All this derives from the amount of new surface created by a perturbation relative to that in the base configuration. Electrical forces have profound effects. Charging the bridge to bring it to a high potential makes it more unstable since the radially directed electric field opposes surface tension. Conversely, a field aligned with axis of the bridge may stabilize it. The mechanism depends on the presence or absence of free electrical charge.

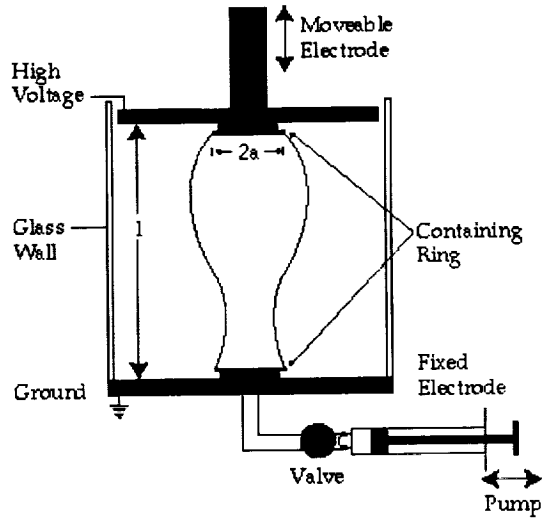

Figure 1. Schematic diagram of a liquid bridge, including features for altering the volume and imposing an electric field.

Fluid bodies composed of perfect dielectric liquids can be maintained in deformed states without motion. A perfect dielectric drop deforms into a prolate spheroid in an applied field and electrical stresses balance interfacial tension on the (static) deformed interface. Non-cylindrical equilibrium bridge configurations are possible, e.g., bridges stressed by an axial field. Bridges with $L/d > \pi$ can be stabilized, up to a point; stability derives from the arrangement of polarization charge induced on the interface.

A leaky dielectric material[1,2] behaves like a dielectric with a small conductivity. In such materials, free charge is transported by ion migration and these liquids behave as Ohmic conductors. The behavior of leaky dielectrics is quite different from perfect dielectrics because free charge congregates at interfaces due to the steep gradients in electrical properties. Thus, in contrast to the situation with a perfect dielectric, the deformation of droplet placed a steady field depends

* A recent newspaper article [*U. S. 1*, January 29,1997] reports work at Orchid Biocomputer, a company founded by the Stanford Research Institute and SmithKline Beecham on a technology for carrying out a multitude of chemical reactions on a microchip. Fluid management is by electrohydrodynamic pumping.

on the delicate balance of electrical, interfacial tension *and* hydrodynamic forces. A droplet of one fluid suspended in another may deform into a prolate spheroid whereas an oblate deformation ensues upon reversing the arrangement of fluids. Here the deformation and shape are dynamic.

A liquid bridge offers an excellent venue for studying electrohydrodynamic stability since its location is fixed by the pinned contact lines (c.f., figure 1). Following the motion of a droplet is more difficult due to translation in the applied field[4]. Buoyancy plays a major role in studying phenomena with free surfaces and, in terrestrial environments, often necessitates the use of an isopycnic system with a matrix fluid surrounding the fluid body of interest. Since interfaces play major roles in electrohydrodynamics this complicates matters greatly. For example, the influence of the electrical properties of both fluids and the interface must be understood, especially processes whereby charge crosses the interface. In our LMS experiment we avoided such problems by using a gas, sulfur hexafluoride - SF_6, as the matrix fluid. At the conditions of the experiment SF_6 behaves as a (very low viscosity) perfect dielectric gas. Neutrally buoyant liquid bridges may take on any one of three configurations: cylindrical, amphora (vase-like), or separated into two drops. In this experiment, the transitions between these three configurations were studied.

In our experiments the behavior of a given bridge is governed by two dimensionless groups: These are: the aspect ratio, $\beta = L/d$ and $\Delta = ae\varepsilon_o E^2/\gamma$ which is the ratio of stabilizing electrical forces to destabilizing interfacial tension forces. The new symbols are: ε, the dielectric constant of the bridge fluid; ε_o, the permittivity of free space; E, the field strength; and γ, the interfacial tension. The other parameters are ratios of mechanical and electrical properties which are fixed for a given fluid pair.

III. APPARATUS

The LMS experiment ALEX, an acronym for **A** Liquid **E**lectrohydrodynamics e**X**periment, was sponsored by NASA and the European Space Agency (ESA) with Daimler-Benz Aerospace as the prime contractor. Two Italian companies, Ferrari Engineering and Laben, were responsible, respectively, for the mechanical design and fabrication and electrical design, fabrication and integration. Trek Engineering (USA) built the high voltage power supply. Two test containers - TC4A & TC4B were manufactured and used in the Bubble, Drop & Particle Unit (BDPU), under the overall supervision of ESTEC, the scientific and technological arm of ESA. An especially noteworthy aspect of the experiment is that only 18 months elapsed between the science concept review and the flight aboard the space shuttle Columbia. During the LMS Mission, ALEX was operated by remote control from the Marshall Space Flight Center, Huntsville, Alabama. The success of the experiment demonstrates it is possible to carry out meaningful experiments within a short time span.

Test Container Configurations

Each test container was equipped with a carousel apparatus housing three test cells. One test cell in each container contained a 2-phase mixture, similar to that used in terrestrial experiments to serve as a tie-in to ground-based work. The other two cells contained a single liquid to be suspended as a bridge in SF_6, a high field strength dielectric gas. Five of the six cells were operated successfully. In the other cell, a 2-phase cell, the bridge spilled from the retainer rings intended to hold the column in place. Nevertheless, useful video data were obtained. Overall, nearly 20,000 video images were acquired to depict various stages of the behavior of bridges in both dc and ac fields. Analysis of the images was carried out using image analysis software developed by MARS, an ESA subcontractor. Following the mission, the hardware was recalibrated to verify the data. None of the important calibrations changed, indicating that data collected during the mission are reliable.

Experiment Sequence

The liquid bridge electrohydrodynamic experiments were conducted in a dynamic mode. For the two-phase experiments, experience with previous ground studies provided an estimate of the electric fields necessary for stability. However, since there was no theory or experimental data for single-phase configurations, the electric fields necessary for stability were determined via trial and error in flight. Thus, changes in the configuration were not pre-programmed, but determined based upon the progress of the experiment.

Before a stability experiment was performed, it was necessary to form a liquid bridge. In the two-phase experiments, a short bridge (~1 mm) was created when the TC was filled prior to the launch. For the single-phase experiments, the bridge was built in orbit to avoid spilling fluid from the containing rings during the launch. The first step was to inject a drop of fluid into the containing ring on the fixed electrode. Then the movable electrode was positioned 1.5 cm above the fixed electrode and 12 kV applied. At this field strength (8 kV/cm), the drop is pulled into a shape known as a Taylor cone. Electrical forces cause fluid to be ejected from the tip of the cone towards the movable electrode where it collects inside the containing ring on the electrode. As fluid was transferred from the fixed electrode containing ring, additional fluid was added until the movable electrode containing ring was filled and a drop of fluid visible. Then the voltage was removed and the electrodes brought together until the drops on the containing ring touched and coalesced. From this point, the single- and two-phase experiments proceeded in essentially the same

fashion. The aspect ratio of the bridge was changed by moving the electrode and injecting or withdrawing fluid into the bridge at the appropriate volumetric rate so that a perfect cylinder was formed. At the outset, the aspect ratio was increased until it was close to the Plateau limit, π, and the bridge volume checked to ensure that the configuration was cylindrical. Fluid was added or withdrawn as necessary. Then the stability of the bridge at an aspect ratio just below π was investigated.

Next, the aspect ratio was increased using an electric field to maintain a stable configuration. Commands were sent in real time to increase the field since the field needed for stability was not known *a priori*. Once the desired aspect ratio was achieved, the electric field could be raised or lowered in small steps to examine the transitions from cylinder to amphora and the pinch-off point. Between voltage steps, the bridge was allowed to assume a steady state configuration. After the pinch-off point was identified, the voltage could be increased to re-establish the bridge. Then, further increases in the field allowed the sequence of configurations leading to a perfect cylinder to be re-studied. Configurations were analyzed in real time using the image analysis program developed by MARS.

The image analysis algorithm produced digitized images and, from the edge coordinates, a trace of the bridge could be reconstructed. The edge coordinates were also used to calculate the Fast Fourier Transform (FFT) of the shape and minimum and maximum diameters. The processes of digitization and edge detection proceeded at a rate of 2 to 10 images per second.

It was important to observe a sequence of "equilibrium" bridge shapes to identify the various configurations (cf. Figure 2). Once a steady state configuration was established, the voltage was changed and shape changes monitored by following the evolution of the FFT coefficients and maximum or minimum diameter. A steady state configuration was defined as one which did not change during a certain period. Once steady state is achieved, the voltage was changed again and the process repeated.

Following the mission, all the image analysis was repeated in a more deliberate fashion. First, the telemetry data recorded in the ECIO data file was examined to determine when "events" occurred during the experiment. Events include changes in voltage, frequency, aspect ration, cell rotation, or pumping. The ECIO file was use instead of the MMI files saved during the mission since they include all of the LOS data. Next, the HRM data was reformatted and saved as a series of TIFF images which were then analyzed with a modified version of the MARS Image Analysis Software. The HRM data was used over the live video recordings since it has an accompanying time stamp allowing for the synchronization of the images with the MMI data. Over 17,000 images from the HRM data were analyzed in the previously described fashion.

The experiments conducted during the LMS mission examined the stability of six different liquid bridges for AC and DC fields. A total of 41 different experiments were conducted in two test containers, TC 4A and TC 4B, during two separate on-line periods. The experiments involved the effects of DC and AC field levels and frequencies on the stability of bridge with different aspect ratios. Sixteen experiments were conducted the first night, and 25 the next. Each test container had two single-phase and one two-phase liquid bridge experiment. Selected results are described in the following sections.

Other than an accidental camera dislocation and a minor problem with a limit switch, the test containers and BDPU hardware performed flawlessly. Also the support teams performed magnificently. Support in the POCC by Dornier, MARS, Alenia, Teledyne Brown, NASA, and ESA was invaluable to the success of our experiment. An additional support team made up of engineers from Laben and Ferrari were on hand in Italy but were not utilized extensively during the mission -- a testament to the job done prior to the

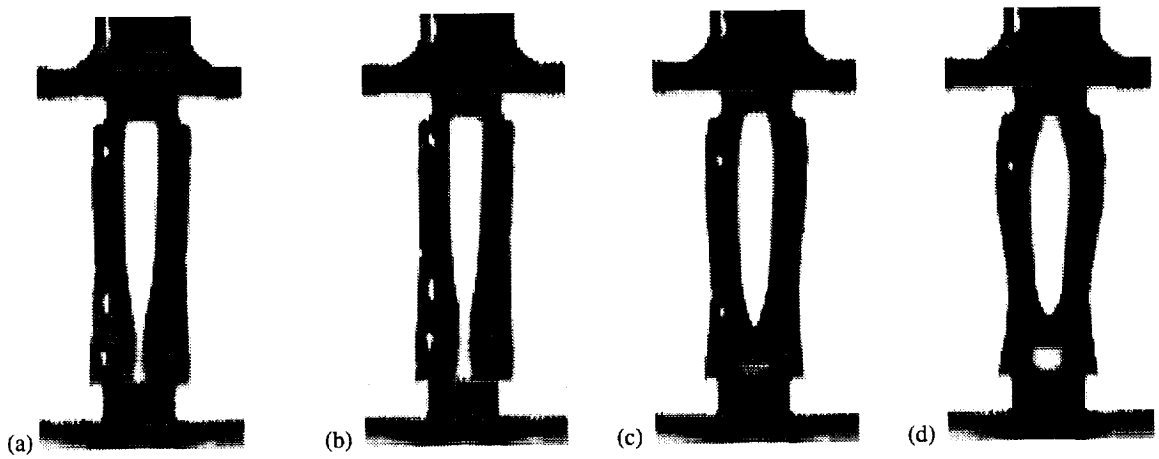

Figure 2: Deformation of a castor oil bridge in SF_6 with a decreasing electric field.
Electric field parameter: (a) = .4, b = .25, = .24, = ..

launch in fabricating and filling the test containers.

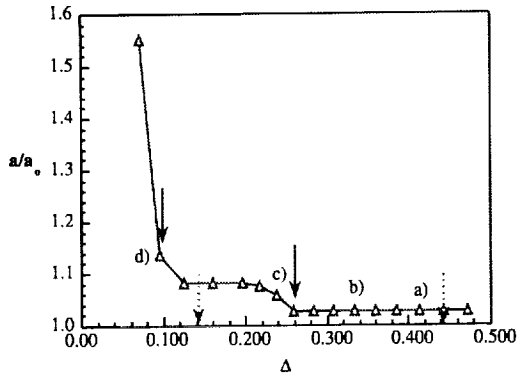

Figure 3: Maximum bridge radius - electric field parameter relation for a decreasing field. Points correspond to configurations noted in figure 2.

IV. COMPARISON OF FLIGHT AND GROUND-BASED RESULTS

With the two-phase system, transitions from cylinder to amphora and the pinch-off point were found to agree closely with the results of Sankaran and Saville[4] after taking account of the difference between the properties of the two system. The transition from cylinder to amphora occurred at $\Delta = 0.195$, and pinch-off at $\Delta = 0.057$ at $\beta = 3.36$. This compares to the values of $\Delta = 0.18$ and 0.03 reported by Sankaran and Saville[4] for the transition and pinch-off points respectively. This agreement between μ-g and 1-g experiments validates the performance of the flight system for steady fields.

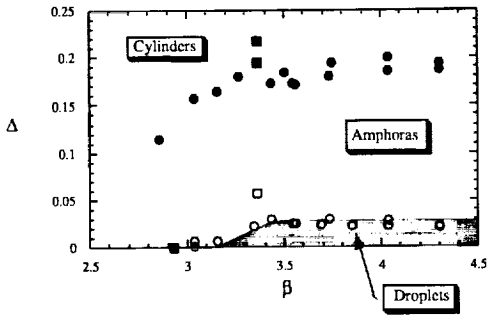

Figure 4: A comparison of flight and ground-based results in a two-phase system. ● & ○ - terrestrial experiments; ■ & ❑ - μg experiments.

V. COMPARISON BETWEEN THEORY AND EXPERIMENT

At the time of the experiment the leaky dielectric model had not been used to predict the behavior of a pinned bridge. Since that time, C. L. Burcham has completed calculations[5] to predict the stability of a liquid, leaky dielectric bridge in a dielectric gas. Some results are shown in figure 5.

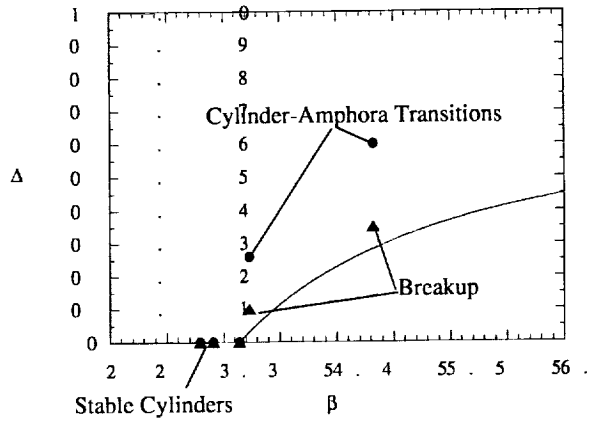

Figure 5: Comparison between theory and experiment The solid line is the theoretical demarcation between stable and unstable cylindrical bridges.

As the figure indicates, theory and experiment disagree. The reasons for this are not yet understood. One possible mechanism is surface conduction, which is not part of the theory presented here. A liquid-gas interface would amplify effects of this sort.

VI. SUMMARY & CONCLUSIONS

The ALEX apparatus performed as designed and produced a considerable amount of useful data. The primary goal, to provide data to test the leaky dielectric model in the liquid bridge configuration, was achieved.

VII. ACKNOWLEDGMENTS

The work reported here was supported in part by NASA Grants NAG8-969 and NGT-51343. The efforts of Dr. Robert Snyder and Dr. Myron Hill, both of NASA, were indispensable in the successful execution of the experiment.

VIII. BIBLIOGRAPHY

[1] D. A. Saville 1997 Electrohydrodynamics: The Taylor-Melcher leaky dielectric model *Annual Review of Fluid Mechanics* **29** 27-64.

[2] G. I. Taylor. 1966 Studies in electrohydrodynamics I. The circulation produced in a drop by an electric field. *Proc. Roy. Soc.* A291:159-66.

[3] O. Vizika & D. A. Saville 1992 The Electrohydrodynamic Deformation of Drops Suspended in Liquids in Steady and Oscillatory Electric Fields. *Journal of Fluid Mechanics* **239** 1-21.

[4] S. Sankaran & D. A. Saville 1993 Experiments on the stability of a liquid bridge in axial electric field. *The Physics of Fluids A* **5** 1081-1083.

[5] C. L. Burcham 1998 "The Electrohydrodynamic Stability of a Leaky Dielectric Liquid Bridge in an Axial Electric Field with Zero Bond Number," Ph.D. Thesis, Department of Chemical Engineering, Princeton University.

DYNAMIC MODELING OF MICROGRAVITY FLOW

J. U. Brackbill[1], Damir Juric[1], David Torres[1], Elizabeth Kallman[2], [1]Theoretical Division, Los Alamos National Laboratory, Los Alamos, NM 87545, jub@lanl.gov, [2]Mechanical Engineering, UC Berkeley, Berkeley CA 94720, USA.

1. Introduction

The absence of gravity and buoyancy in microgravity flow imposes new requirements on numerical models of fluid flow. Forces that are small in terrestrial flow, such as surface tension, are dominant in the absence of gravity, even on large spatial scales. Forces that are large in terrestrial flows, such as buoyancy, are absent in the absence of gravity. Thus, surface tension is important under almost all circumstances in microgravity flow, and must be done accurately and economically. The lack of buoyancy changes the physics of boiling and combustion, and requires the development of new approaches to modeling such flows.

Here we consider the numerical aspects of modeling microgravity flows. We revisit the continuum surface force model for use in interface capturing methods, with special emphasis on how one can compute accurately equilibrium or near equilibrium flows. We also review recent work on film boiling and solidification, using an interface tracking method.

2. Interface Capturing

The continuum surface force (CSF) model was developed to model surface pressures occurring at transient fluid interfaces with arbitrary and time-dependent topology [1]. Surface tension occurs when fluid properties change discontinuously across an interface. In numerical calculations, a transition region replaces the discontinuity, and CSF replaces surface tension by a volume force that acts throughout the transition region. Thus, a boundary-value problem at the interface is replaced by an approximate, but continuous model that mimics the problem specification in a numerical problem, where one specifies the data at grid points and interpolates between. An approximate surface delta function is introduced that allows one to solve the same equations everywhere, but which causes surface tension to contribute only in the interface region.

The CSF method differs from the diffuse interface method, which also represents an interface as a transition zone of rapid but smooth variation in the model and surface tension as a volume force [2]. Unlike CSF, diffuse interface methods resolve the transition region, and are applied most successfully to situations in which the physical phenomena of interest have a length scale commensurable with the thickness of the interfacial region (e.g. near-critical interfacial phenomena or small-scale flows such as those occurring near contact lines) and fluid flows involving large interface deformations and/or topological changes (e.g. breakup or coalescence events associated with fluid jets, droplets, and large deformation waves) [2].

However, it is difficult to model both large-scale flows and the small scales associated with the interface dynamics. Eggers notes that surface tension becomes singular near breakup, and that "resolution has not been possible anywhere near the experimentally attainable limit, even with present day computers." [3]

Thus, CSF confines the contributions of the surface tension force to a small portion of the computation mesh in the neighborhood of the interface. This poses a challenge in formulating sufficiently accurate finite difference expressions [1]. The error appears as a so-called 'parasitic' flow. The problem is not limited to CSF, but also occurs in SURFER, which formulates the surface tension in momentum conservative form [4]. As the authors of SURFER note, "Part of the price we have to pay for the locality of our method is the presence of what, we suspect, are unavoidable 'parasite' currents." " ... the parasite currents scale with the surface tension and viscosity. Dimensional analysis shows that the maximum velocity around the bubble of radius R is given by $u_{max} = K\sigma/\eta$, where K is some constant. Numerical experiments verify this law with $K \approx 10^{-2}$." [4]

As a remedy, we present a projection method in which equilibrium corresponds to achievement of constant values of a pressure like variable. The numerical errors are much reduced, and the only added complexity is the need to solve an additional elliptic equation.

Consider the incompressible Navier-Stokes equations

$$\frac{\partial \vec{u}}{\partial t} + \vec{u} \cdot \nabla \vec{u} = -\frac{\nabla p}{\rho} + \frac{1}{\rho}\nabla \cdot \vec{\tau} + \vec{g} + \frac{\vec{F}_s}{\rho}, \qquad (1)$$

$$\nabla \cdot \vec{u} = 0, \qquad (2)$$

where $\vec{u}$ is the velocity, p is the pressure, $\vec{\tau}$ is the viscous stress tensor, $\vec{g}$ is the gravity vector and $\vec{F}_s$ accounts for surface tension forces.

The volume force $\vec{F}_s$ is formulated so that it gives the correct surface tension force per unit interfacial area as the interface thickness, h, decreases to zero

$$lim_{h\to 0}\int_{\triangle V}\vec{F}_s d^3x = \int_{\triangle A}\vec{F}_a dA,$$

where

$$\vec{F}_a = \sigma\kappa\hat{n},$$

on the interface, where σ is the fluid surface tension coefficient, κ is the curvature, $\hat{n}$ is the unit normal to the interface, and $\vec{F}_a$ is the surface force per unit interfacial area.

One can decompose $\vec{F}_s/\rho$ into a solenoidal part ($\nabla \times \vec{\lambda}$) and an irrotational part divided by density

$$\frac{1}{\rho}\vec{F}_s = \nabla \times \vec{\lambda} + \frac{\nabla\phi}{\rho}. \tag{3}$$

Such a decomposition is admissible if one considers an arbitrary interface between two inviscid, incompressible fluids initially at rest. A similar decomposition was used by Bell and Marcus [5] and Sussman *et al* [6].

Substituting (3) into (1) yields

$$\frac{\partial\vec{u}}{\partial t} + \vec{u}\cdot\nabla\vec{u} = -\frac{\nabla\tilde{p}}{\rho} + \frac{1}{\rho}\nabla\cdot\vec{\tau} + \vec{g} + \nabla\times\vec{\lambda}, \tag{4}$$

where

$$\tilde{p} = p - \phi.$$

Since $\tilde{p}$ in (4) combines the pressure p and the $\nabla\phi$ component of $\vec{F}_s$ to enforce incompressibility, it is the solenoidal term, $\nabla\times\vec{\lambda}$, that accelerates the fluid. One notes that both $\tilde{p}$ and λ are constant or zero at equilibrium.

The two-step projection method will be used to advance the fluid equations (4) and (2) in time,

$$\frac{\vec{\tilde{u}} - \vec{u}^n}{\delta t} = \frac{1}{\rho^n}\nabla\cdot\vec{\tau}^n + \vec{g} + \nabla\times\vec{\lambda}^n - \vec{u}^n\cdot\nabla\vec{u}^n, \tag{5}$$

$$\frac{\vec{u}^{n+1} - \vec{\tilde{u}}}{\delta t} = -\frac{\nabla\tilde{p}^{n+1}}{\rho^n}. \tag{6}$$

The pressure term in (6) is derived by taking the divergence of (6) and enforcing incompressibility, $\nabla\cdot\vec{u}^{n+1} = 0$. This yields the pressure Poisson equation,

$$\nabla\cdot\left(\frac{1}{\rho^n}\nabla\tilde{p}^{n+1}\right) = \frac{1}{\delta t}\nabla\cdot\vec{\tilde{u}} \tag{7}$$

The decomposition (3) at time step n is performed by multiplying by ρ^n and taking the curl

$$\nabla\times\left(\rho^n\nabla\times\vec{\lambda}^n\right) = \nabla\times\vec{F}_s^n. \tag{8}$$

Let us compare the new scheme with a two-step projection method without a surface force decomposition. Denote the the pressure Poisson operator (7) by $\mathcal{L}$,

$$\mathcal{L} = \nabla\cdot\left(\frac{1}{\rho^n}\nabla\right).$$

Likewise let $\mathcal{L}^*$ denote the operator in (8),

$$\mathcal{L}^* = \nabla\times(\rho^n\nabla\times).$$

The net effect on $\vec{u}^n$ without the decomposition is

$$\vec{u}^{n+1} = \vec{u}^n + \delta t\left(\vec{a}^n - \frac{1}{\rho^n}\nabla(\mathcal{L})^{-1}\nabla\cdot\vec{a}^n\right) + \vec{g}\delta t + \delta t\left(\frac{\vec{F}_s^n}{\rho^n} - \frac{1}{\rho^n}\nabla(\mathcal{L})^{-1}\nabla\cdot\left(\frac{\vec{F}_s^n}{\rho^n}\right)\right). \tag{9}$$

The net effect on $\vec{u}^n$ with the decomposition is

$$\vec{u}^{n+1} = \vec{u}^n + \delta t\left(\vec{a}^n - \frac{1}{\rho^n}\nabla(\mathcal{L})^{-1}\nabla\cdot\vec{a}^n\right) + \vec{g}\delta t + \delta t\nabla\times(\mathcal{L}^*)^{-1}\nabla\times\vec{F}_s, \tag{10}$$

where $\vec{a}^n$ has been used to denote

$$\vec{a}^n = \frac{\nabla\cdot\vec{\tau}^n}{\rho^n} - \vec{u}^n\cdot\nabla\vec{u}^n.$$

Now the divergence of $\vec{u}^{n+1}$ will be zero analytically in both cases. However the zero divergence of $\vec{u}^{n+1}$ may not be enforced discretely. In order to enforce the zero divergence of $\vec{u}^{n+1}$ in (9) with regards to the surface tension force,

$$\nabla\cdot\frac{1}{\rho^n}\nabla(\mathcal{L})^{-1} = 1$$

must be enforced on the discrete level. This requires that the pressure Poisson equation be solved with infinite precision. In order to enforce the zero divergence of $\vec{u}^{n+1}$ in (10) with regards to the surface tension force,

$$\nabla\cdot\nabla\times = 0$$

must be enforced on the discrete level. This can be enforced on a rectilinear grid with many discretizations.

The new method with the decomposition differs from the original method by allowing one to achieve a force balance between surface tension and pressure on the discrete level. For this reason, we choose to implement the decomposition for advancing the dependent variables in

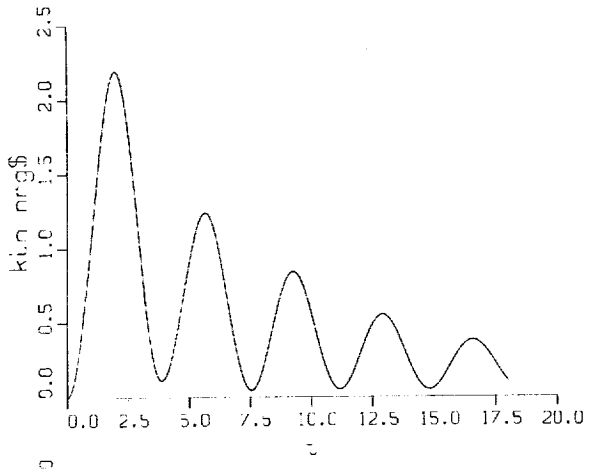

Figure 1: The relaxation of an initially square element of fluid to a circle due to surface tension corresponds to the decaying kinetic energy plotted here.

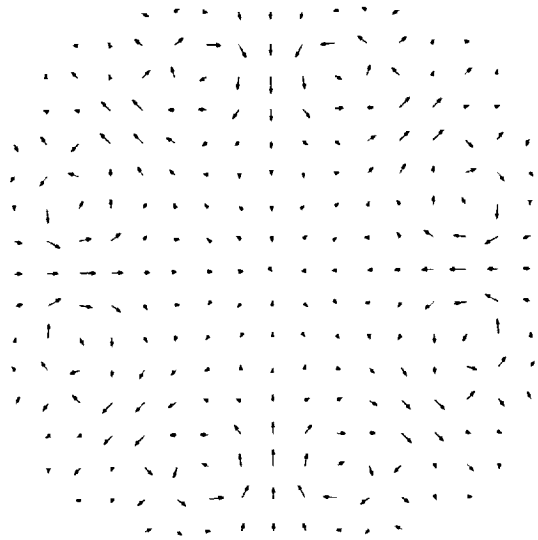

Figure 2: The parasitic flow that is observed near equilibrium in calculations using the CSF model is illustrated in a plot of the velocity vectors. The magnitude of the flow is reduced by the projection method, but not eliminated.

time for surface tension calculations. FLIP, a particle-in-cell code [7], implements (5)- (7) with the exception that in (5), the Lagrangian derivative d/dt replaces $\partial/\partial t + \vec{u} \cdot \nabla$,

$$\frac{\vec{u} - \vec{u}^n}{\delta t} = \frac{1}{\rho^n} \nabla \cdot \vec{\tau}^n + \vec{g} + \nabla \times \vec{\lambda}^n. \qquad (11)$$

Here $\vec{u}$ and $\vec{u}^n$ are assumed to be tagged to or moving with the particle.

We demonstrate the improved CSF formulation in FLIP with three standard problems.

The first problem concerns the relaxation of an initially square fluid element to a circle under the action of surface tension. The calculation of the dynamics is performed with FLIP on a 40 X 40 mesh. The interior density is 0.8, the exterior density is 0.0, and $\sigma = 2.361$. The kinetic energy, shown in Figure (1), decays to a small fraction of its initial value after several oscillations, indicating the degree of force balance that is achieved between the surface tension forces and pressure. The period of oscillation agrees closely with an identical calculation performed with a MAC code on a 100 X 100 mesh [8].

In the second problem, we compare the theoretical capillary wave speed on the interface between two fluids of different densities using the MAC scheme. On a 50 X 400 mesh, the calculated wave speed is 0.185 compared with the theoretical value, 0.222.

In the third problem we investigate the reduction in parasitic flow with the projection method. In Figure (2) velocity vectors are plotted from a calculation with FLIP on a 40 X 40 mesh of an initially circular cylinder. For this problem, any flow is an error. The magnitude of the flow corresponds to $K \approx 6. \times 10^{-4}$, compared with $K \approx 10^{-2}$ reported by Lafaurie et al. [4].

3. Interface Tracking

Our theoretical and numerical studies of interfacial flows in microgravity have also focused on exploring some of the more poorly understood physical phenomena that arise in single and multicomponent systems when fluid flow, interface dynamics and phase change are fully coupled. To accomplish this coupling we have continued to extend the capabilities of a finite difference/front tracking method developed in [9]. In its most general form the method uses a single set of conservation equations for all the phases involved. The phase boundary is treated as an imbedded interface by adding to these transport equations the appropriate source terms for surface tension, interphase mass transfer, jumps in material properties and rejection/absorption of latent heat and solute. These source terms are in the form of delta functions local-

ized at the interface and are selected in such a way as to satisfy the correct jump conditions across the phase boundary.

We begin by specifying the material properties which are considered to be constant but not generally equal for each phase. As a consequence, the bulk phases are incompressible but we allow for volume expansion or shrinkage at the phase interface due to the density change upon phase transition. Equations for the material property fields can be written for the entire domain using an indicator function, $I(\vec{x},t)$, which , for example, has the value 1 in the solid phase and 0 in the liquid phase. I is similar to the color function used in the CSF method or the phase-field variable in the phase field method. However here, as will be shown below, we determine I from the known position of the tracked interface rather than use it to determine the position of the interface. The values of the material property fields at every location are given by $b(\vec{x},t) = b_1 + (b_2 - b_1)\, I(\vec{x},t)$, where the subscripts 1 and 2 refer to the two phases. b represents density, ρ, viscosity, μ, specific heat, c, thermal conductivity, K, or chemical diffusivity, D.

Since I is constant except in a local region near the interface, we can express the gradient of I as a local surface integral

$$\nabla I = \int_{\Gamma(t)} \hat{n}\, \delta\left(\vec{x} - \vec{x}_i\right) ds\,, \tag{12}$$

where $\vec{x}_i = \vec{x}(s,t)$ is a parameterization of the phase interface, $\Gamma(t)$. $\delta\left(\vec{x} - \vec{x}_i\right)$ is a three-dimensional delta function that is non-zero only where $\vec{x} = \vec{x}_i$. Taking the divergence of Eq. (12) results in

$$\nabla^2 I = \nabla \cdot \int_{\Gamma(t)} \hat{n}\, \delta\left(\vec{x} - \vec{x}_i\right) ds\,. \tag{13}$$

Thus we find $I(\vec{x},t)$ by solving the above Poisson equation where the right hand side is a function only of the known interface position at time t. The interface is advected in a Lagrangian fashion by integrating

$$\left(d\vec{x}_i/dt\right) \cdot \hat{n} = \vec{V} \cdot \hat{n} \tag{14}$$

where $\vec{V}$ is the interface velocity vector. We assume that the tangential components of the interface velocity, $\vec{V}$, and material velocity, $\vec{u}$, at the interface are equal, *i.e.* no slip at the interface.

With the aid of Eq. (12) and the definition of ρ, the conservation of mass for the entire domain can be expressed as

$$\nabla \cdot \rho\vec{u} = -\frac{\partial \rho}{\partial t} = \vec{V} \cdot \nabla\rho = \int_{\Gamma(t)} (\rho_2 - \rho_1)\, \vec{V} \cdot \hat{n}\, \delta\left(\vec{x} - \vec{x}_i\right) ds. \tag{15}$$

By adding and subtracting the quantity $\vec{u} \cdot \nabla\rho$ to the right side of Eq. (15), we can write the equivalent statement

$$\nabla \cdot \rho\vec{u} = \vec{u} \cdot \nabla\rho + \int_{\Gamma(t)} (\rho_2 - \rho_1)\left(\vec{V} - \vec{u}\right) \cdot \hat{n}\, \delta\left(\vec{x} - \vec{x}_i\right) ds. \tag{16}$$

The integral term in the above equation can now be more intuitively viewed as a local interfacial mass transfer source/sink due to expansion/shrinkage upon phase change. If $\rho_2 = \rho_1$ or if there is locally no phase change ($\vec{V} \cdot \hat{n} = \vec{u} \cdot \hat{n}$) then Eq. (16) reduces to the customary incompressible constraint, $\nabla \cdot \vec{u} = 0$. We further note that the numerical implementation of Eq. (16) is also more robust since the surface integral represents a delta function *perturbation* to an existing smooth field ($\vec{u} \cdot \nabla\rho$) whereas the surface integral in Eq. (15) attempts to satisfy mass conservation with delta functions *directly*.

The momentum equation, in conservative form, is

$$\frac{\partial \rho\vec{u}}{\partial t} + \nabla \cdot \rho\vec{u}u = -\nabla p - \rho\vec{g} + \nabla \cdot \vec{\tau} + \int_{\Gamma(t)} \sigma\kappa\hat{n}\, \delta\left(\vec{x} - \vec{x}_i\right) ds\,, \tag{17}$$

where $\vec{\tau}$ is the deviatoric stress tensor for a Newtonian fluid $\vec{\tau} = \mu\left(\nabla\vec{u} + \nabla\vec{u}^T\right)$.

The thermal energy equation with an interfacial source term to account for liberation or absorption of latent heat, L, is

$$\frac{\partial \rho c T}{\partial t} + \nabla \cdot \rho\vec{u}cT = \nabla \cdot K\nabla T + \int_{\Gamma(t)} \dot{m}L\delta\left(\vec{x} - \vec{x}_i\right) ds \tag{18}$$

where we have neglected the viscous dissipation and for ease of discussion assume that the specific heats of both phases are identical. T is the temperature and $\dot{m}$ is the interfacial mass flux, $\dot{m} = \rho_1\left(\vec{V} - \vec{u}_1\right) \cdot \hat{n} = \rho_2\left(\vec{V} - \vec{u}_2\right) \cdot \hat{n}$.

The equation for solute transport is

$$\frac{\partial \rho\tilde{C}}{\partial t} + \nabla \cdot \rho\vec{u}\tilde{C} = \nabla \cdot \rho\tilde{D}\nabla\tilde{C} + \int_{\Gamma(t)} (1-k)\dot{m}\tilde{C}_i\delta\left(\vec{x} - \vec{x}_i\right) ds \tag{19}$$

where $\tilde{C}$ and $\tilde{D}$ are defined by the simple transformation for the solute concentration, C, and diffusivity, D,

$$\left(\tilde{C}, \tilde{D}\right) = \begin{cases} \left(C_2/k, kD_2\right), & \text{in phase 2,} \\ \left(C_1, D_1\right), & \text{in phase 1 .} \end{cases} \tag{20}$$

Similar formulations of the species equation are also used in [10] and [11]. The integral on the right hand side of Eq. (19) accounts for rejection or absorption of solute at the interface due to the difference in miscibility of the alloy components in the two phases. $\tilde{C}_i = \tilde{C}(\vec{x}_i)$

is the value of the transformed concentration at the interface. Note that the transformed concentration is continuous at the interface which makes $\tilde{C}_i$ easier to calculate numerically. In using this transformation the partition coefficient, $k = C_2(\vec{x}_i)/C_1(\vec{x}_i)$, is assumed to be constant which, for dilute mixtures, is usually a reasonable assumption. Since the interface is explicitly tracked and thus I is known we can regain the original concentration field from $C = \tilde{C} + \left(k\tilde{C} - \tilde{C}\right) I(\vec{x}, t)$.

It is important to recognize that away from the interface the single field formulation, Eqs. (16), (17), (18) and (19) reduces to the customary mass, momentum, thermal energy and solute transport equations for each of the bulk phases while integration of these equations across the interface reveals that the formulation naturally incorporates the correct mass, momentum and energy balances across the interface.

To complete our formulation, a thermodynamic constraint on the interface temperature, $T_i = T(\vec{x}_i)$, must be satisfied at the phase boundary. The simplest choice is to assume that $T_i = T_{sat}$ or if considering a dilute multicomponent solution $T_i = T_{sat} - m\tilde{C}_i$, where m is the slope of the liquid or vapor line in a phase equilibrium diagram and T_{sat} is the pure fluid saturation temperature. In reality the interface temperature is a much more complicated function and we use a more complete form derived in [9].

Equations (13), (14), (16), (17), (18), and (19) along with the interface temperature constraint are solved iteratively for the correct normal interface velocity, $\vec{V} \cdot \hat{n}$, that will satisfy the interface temperature constraint. For the spatial discretization, we use the MAC method of Harlow and Welch [8] with a staggered grid. A first order, phase change projection algorithm, similar to that of Chorin's [12], is used for the time integration. In explicit front tracking, the phase interface is represented discretely by Lagrangian markers connected to form a front which lies within and moves through the stationary Eulerian grid. As the front moves and deforms, interface points are added, deleted and reconnected as necessary throughout the calculation. Thus the interface can exhibit arbitrarily complex interface deformations and topology changes. Information from the integral source terms in Eqs. (13), (16), (17), (18) and (19) are passed between the moving Lagrangian interface and the stationary Eulerian mesh using Peskin's [13] Immersed Boundary Technique. With this technique, the sharp interface is approximated by a smooth distribution function that is used to distribute the sources at the interface over mesh points nearest the interface. Thus the front is given a finite thickness on the order of the mesh size to provide stability and smoothness with no numerical diffusion since this thickness remains constant for all time.

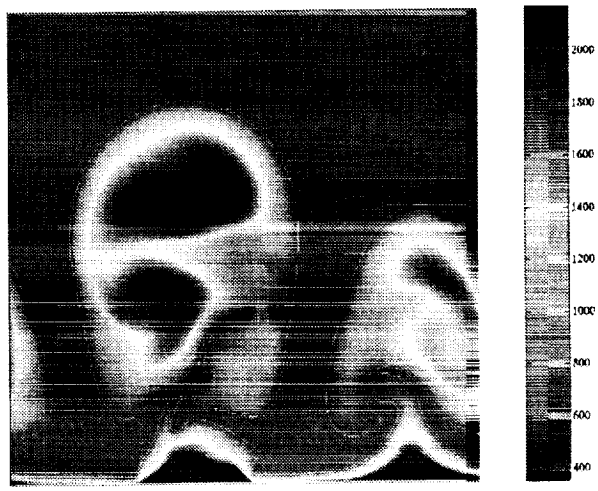

Figure 3: A simulation of film boiling of FC-72, a dielectric refrigerant used in microelectronics cooling applications. The color scale indicates temperature in K.

We demonstrate the capabilities of front-tracking for phase change problems with two-dimensional calculations of film boiling and alloy solidification.

Figure (3) shows a simulation of film boiling of FC-72, a dielectric refrigerant used in microelectronics cooling applications. In this calculation the vapor layer adjacent to the heated wall exhibits a Rayleigh-Taylor instability with hot vapor being pushed up into mushroom shaped bubbles. These bubbles then pinch off and rise. The vortical structures developing within the bubble act to mix the hot and cold vapor. Some of the thin interface filaments are artifacts of the two-dimensionality. Obviously in 3-D the radial component of surface tension would provide more realistic pinch off. The upward motion of the initial bubbles causes a downward flow of liquid pushing the interface toward the wall and additional vapor to be pulled away from the wall to form a second bubble directly underneath the first. This so-called parent-son behavior has been observed in experiments [14]. The color scale indicates the temperature in degrees Kelvin.

In figure (4) we simulate the microscale solidification of globulitic grains of an Aluminum-Silicon alloy from an initially uniform 1 wt% Silicon liquid. The color scale indicates Silicon concentration. The calculation begins with an initial distribution of six small circular

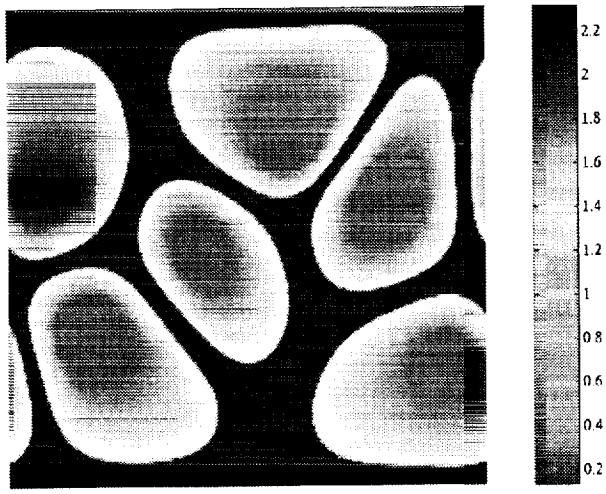

Figure 4: The solidification of six grains of an Aluminum-Silicon alloy from an initially uniform 1 wt% Silicon liquid. This simulation predicts the variation in Silicon concentration across the solid grains, a phenomenon known as "coring". The color scale indicates Silicon concentration.

grains. As the grains grow, Silicon is rejected into the liquid at the grain interfaces. These solute boundary layers interact resulting in the growth of globulitic or potato shaped grains at later times. The simulation predicts the variation in Silicon concentration across the solid grains, a phenomenon known as "coring". Knowledge of this microstructure and the coring profiles is important for determining the necessary homogenization time for heat treatment.

References

[1] J. U. Brackbill, D. B. Kothe, and C. Zemach, "A Continuum Method for Modeling Surface Tension, *J. Comput. Phys.*, Vol. 100, 335 (1992).

[2] D. M. Anderson, G. B. McFadden and A. A. Wheeler, "Diffuse-Interface Methods in Fluid Mechanics," *Ann. Rev. Fluid Mech.*, Vol. 30, 139, (1998).

[3] J. Eggers, "Nonlinear dynamics and Breakup of Free-Surface Flows," *Rev. Mod. Phys.*, Vol. 69, 865 (1997).

[4] B. Lafaurie, V. Nardone, R. Scardovelli, S. Zaleski and G. Zanetti, "Modeling Merging and Fragmentation in Multiphase Flows with SURFER," *J. Comput. Phys.*, Vol. 113, 134 (1994).

[5] J. B. Bell and D. Marcus, "A Second-Order Projection Method for Variable-Density Flows," *J. Comput. Phys.*, Vol. 101, 334 (1992).

[6] M. Sussman, P. Smereka, and S. Osher, "A Level Set Approach for Computing Solutions to Incompressible Two-Phase Flow," *J. Comput. Phys.*, Vol. 114, 146 (1994).

[7] J. U. Brackbill and H. M. Ruppel, "FLIP: A method for adaptively zoned, particle-in-cell calculations of fluid flows in 2 dimensions," *J. Comput. Phys.*, Vol. 65, 314 (1986).

[8] F. H. Harlow and J. E. Welch, "Numerical Calculation of Time-Dependent Viscous Incompressible Flow of Fluid with Free Surface," *Physics of Fluids*, Vol. 8, 2182 (1965).

[9] D. Juric and G. Tryggvason, "Computations of Boiling Flows," *Int. J. Multiphase Flow*, in press.

[10] L. H. Ungar, N. Ramprasad, and R. A. Brown, "Finite Element Methods for Unsteady Solidification Problems Arising in Prediction of Morphological Structure," *J. Sci. Comput.*,, Vol. 3, 77 (1988).

[11] H. J. Diepers, C. Beckermann and I. Steinbach, "A Phase-Field Method for Alloy Solidification with Convection," in *Solidification Processing 1997*, 426.

[12] A. J. Chorin, "Numerical Solution of the Navier-Stokes Equations", *Mathematics of Computation*, Vol. 22, 745 (1968).

[13] C. S. Peskin, "Numerical Analysis of Blood Flow in the Heart," *J. Comput. Phys.*,, Vol. 25, 220 (1977).

[14] M. Shoji, L. C. Witte and S. Sankaran, "The Influence of Surface Conditions and Subcooling on Film-Transition Boiling," *Experimental Thermal and Fluid Science*, Vol. 3, 280 (1990).

Session 7C

Interfacial Phenomena III

Fluid/Solid Boundary Conditions in Non-Isothermal Systems

PI: DANIEL E. ROSNER
NASA Grant No. NAG 3-1951
Yale University, Department of Chemical Engineering
High Temperature Chemical Reaction Engineering (HTCRE-) Laboratory
New Haven, CT 06520-8286 USA

1. Introduction, background and objectives

In a short paper (*Phys. Fluids A* **1** (11) 1761-1763 (1989)) the PI pointed out for the first time that vapor-filled nonisothermal ampoules operating in micro-gravity will experience convection *driven* by both "wall-induced thermal creep"* as well as thermal stresses (in the bulk vapor). But, as emphasized in our subsequent review of thermally-induced *particle phoresis* (Rosner *et.al.*, 1992) these "thermal creep" boundary condition (BC-) phenomena also determine the readily observed migration rates ("phoresis") of suspended "small" solid particles in suspension. This led us to the idea that careful phoresis measurements in a suitably designed microgravity environment (to preclude complications such as 'sedimentation' for particles large enough both to sustain large temperature differences and avoid appreciable Brownian motion) could be used to obtain unambiguous information about the nature of the tangential momentum transfer boundary condition over a broad range of Newtonian fluid densities. This would be especially interesting since present *theoretical* methods are really valid only in the low density ("ideal"-) gas limit. As noted below, we recently carried out numerical simulations of the "low-density" Boltzmann equation which not only clarified the wall ("creep") BC, but also thermal stress (non-Newton-Stokes-) effects within such crystal-growth ampoule flows. However, to clarify the nature of the BC transition from the Enskog-Chapman regime to the technologically important but theoretically less tractable case of *liquid-like densities* (including supercritical polyatomic vapors) it is inevitable that high-quality *experimental* data for carefully selected fluid/solid interfaces will be required. The best environment for obtaining these data appears to be the *microgravity* environment, as spelled out in Section 2 below.

Previous theoretical work on "thermal creep" at fluid/solid interfaces (going back to J.C. Maxwell[1879]) has been understandably focused on "structureless", single component *low density gas* motion adjacent to a non-isothermal smooth flat solid surface, usually exploiting an approximate (*eg.* linearized) model of the Boltzmann equation and a "diffuse reflection" molecule/surface interaction model. However, since many applications are multi-dimensional and involve non-dilute mixtures of disparate mass polyatomic molecules, frequently well outside of the domain of "ideal" gas behavior, many generalizations are urgently needed to understand and ultimately predict such flows, whether in micro-gravity or in ground-based laboratories. Progress will be slow in the absence of reliable *experimental data* on the

dimensionless thermal creep (or wall *'slip') coefficient* , C_{tc} , appearing in the relevant tangential momentum BC:

$$(v_{t,w})_{tc} = C_{tc} \bullet n \bullet (\bullet \ln T_{fluid,w} / \bullet x) \qquad (1)$$

Here $(v_{t,w})_{tc}$ is the thermal creep contribution to the *tangential* component (x-direction) of the

*It is rather remarkable that, despite the small Knudsen numbers typically associated with these flows, one cannot apply "no-slip" boundary conditions along the non-isothermal ampoule walls-*ie.* the walls *drive* a significant amount of convection!

fluid *velocity* relative to the solid surface, n is the momentum diffusivity ("kinematic viscosity", m/r) of the fluid, and $T_{fluid,w}$ is the *fluid* temperature evaluated at the fluid/solid interface. One sees from Eq.(1) that such wall-induced creep flow is subtle since for solids in gases, if C_{tc} =O(1) (as appears to be the case from the limited available experiments) then the Mach number associated with the wall creep flow is of the same order of magnitude as the fractional change of gas temperature over one mean-free-path.

In our view, the ultimate goal of this line of research is a rational molecular level theory which predicts the dependence of C_{tc} on relevant dimensionless parameters describing the way fluid molecules interact with the solid surface, and how they interact among themselves (see, *eg.*, Rosner and Papadopoulos,1996). Accordingly, microgravity-based experimental data (Section 2 below) will be an important step forward.

2. Photophoretic "space race" experiments

It might be thought that the best way to experimentally obtain this rather important dimensionless coefficient would be the "direct" one of measuring fluid velocities near non-isothermal solid surfaces using, say, laser velocimetry on very small (negligible inertia) particles immersed in the local fluid. However, even if the microgravity environment were used to preclude any confusion from bouyancy-driven convection, the phenomenon of *thermophoresis* (*eg.*, Rosner *et.al.*, 1992, Gomez and Rosner,1993) would inevitably cause the local motion of small "tracer" particles to depart systematically from that of the non-isothermal host fluid!

To avoid this dilemma we suggest exploiting the closely related phenomenon of *photophoresis* under *microgravity* conditions. This phenomenon (in which the intraparticle temperature nonuniformity which causes the thermal creep in the surrounding fluid is induced by the absorption of incident radiation) is quite sensitive to the momentum transfer boundary condition of interest (Eq.(1)) and becomes rather important at particle sizes at which sedimentation phenomena would normally set in for ground-based experiments (Castillo *et.al.*,1990, Mackowski 1989,1990). Thus, microgravity experiments involving deliberately suspended *supermicron* spherical solid particles of low thermal conductivity but with known "optical" properties (over a wide range of transparent fluid densities) could prove to be

extremely valuable in defining the nature of the momentum transfer boundary condition "transition" (*ie.*, C_{tc}-trends) from the low density (ideal gas-) limit to the *bona-fide* "liquid" limit.

One simple realization of this basic idea, would, in effect, be a "space-race" of illuminated, absorbing spheres, each immersed and simultaneously released in a different pure, transparent Newtonian fluid (including dense as well as low density polyatomic gases, and certain transparent Newtonian liquids). These low thermal conductivity spheres would be illuminated by a common non-polarized , omni-directional radiation source, and each would be large enough to sustain a significant temperature difference across its diameter (despite the isothermal environment far from each sphere). Moreover, as mentioned above, in the microgravity environment 'sedimentation' or 'bouyant rise' would be eliminated as a complication, broadening considerably the choice of informative fluid/solid combinations. Therefore, from the "photo-phoretic" drift velocity of these spheres, (recorded "from above" *via* a TV camera) and the relevant theory (see, *eg.*, Rosner *et.al.*,1992, and Mackowski, 1989), it should be possible to extract the tangential momentum thermal creep coefficient , C_{tc} , operative at each fluid/solid interface.

We have already identified most of the basic requirements for such experiments t(o extract the *dimensionless thermal creep coefficient,* C_{tc}, from measurements of photophoretic drift velocities in different Newtonian fluids). Indeed, we are currently evaluating the possible construction/use of *composite* test spheres to amplify the effects sought---*ie.*, opaque thin shells containing a thermally insulating rigid "core" of small mass. As a part of this research program we are currently working out the (asymptotic) theory of photophoresis for such test-spheres .

3. Thermophoresis of isolated solid spheres and aggregates in gases

A little-noticed but potentially very important feature (see below) of the existing theory of solid sphere thermophoresis in ideal gases is that for sphere thermal conductivities less than about 2.3 times that of the background gas, the sphere thermophoretic diffusivity can actually exceed that in the free-molecule limit! This remarkable feature, which translates to larger spheres moving faster than their smaller counterparts, may be partially 'rationalized' by noticing that, whereas the (Waldmann-) free-molecule limit calculation (see,*eg.*, Rosner,1980, Garcia-Ybarra and Rosner,1989, or Loyalka,1992) does not involve either the abovementioned creep coefficient, or the sphere thermal conductivity, the near-continuum value *does* contain both C_{tc}, and sphere thermal conductivity. We mention this behavior here because, in related studies, we have been clarifiying the effects of intrinsic thermal conductivity, particle morphology, and Knudsen number on the thermophoretic properties of suspended particles (in ideal gases), and 'coagulation-aged' populations thereof (Rosner and Khalil, 1998). While a comprehensive theory for *aggregate* thermophoresis as a function of Knudsen number is not yet available (see,*eg.*, Rosner *et.al.*,1991), and outside the scope of the present program, we have proposed that a rational estimate can be obtained by imagining that an aggregate behaves like a homogeneous sphere with an effective mobility diameter about equal to the gyration diameter but with an *effective thermal conductivity* equal to that expected for the 'granular medium' (of spherules) existing at the gyration radius (for some details, see Tandon and Rosner, 1995). Results of this plausible model indicate that the thermophoretic transport rates of aggregates of even intrinsically conductive materials (like carbonaceous soot, for which $k_p/k_g \bullet 1000$ in *ca.* 1200K

combustion products) will remain high at *all* Knudsen numbers due to the poor *effective thermal conductivity* of such aggregates. We have shown (Rosner *et al.*,1998) that this leads to the following interesting conclusions about soot thermophoretic transport rates at very high pressures: 1. Actual soot *aggregate* transport rates at very high pressures are now expected be perceptibly (but not appreciably) different from the rates formally expected using the *free-molecule* isolated sphere thermophoretic diffusivity; and: 2. If soot aggregates could be prevented from forming, or broken up prior to thermophoretic deposition, then appreciable transport rate *reductions* could be realized at very high pressures due to their high intrinsic thermal conductivity. The implications for soot *deposition* to cooled surfaces (Rosner,1986, Garcia-Ybarra and Castillo, 1997, Rosner and Khalil,1998) are immediate and potentially important.

4. Solid sphere thermophoresis in liquids and dense vapors

Dr. J. Walz and the PI have initiated a critical evaluation of the "thermal field-flow fractionation" (ThFFF-) data on apparent thermophoretic diffusivity coefficients for colloidal particles in liquids (see Shiundu *et.al.*. (1995), and one ancillary theoretical treatment (Giddings, *et.al.*,1995)). We suspect these ThFFF *data* are 'falsified' by electrostatic interactions between the colder channel wall and the suspended particles whose retention behavior is reported. Moreover, the abovementioned "theory",which attributes the apparent thermophoresis to distorted double layers in an ionically conducting liquid rather than to the fluid/solid *thermal creep boundary condition* of primary interest to this program, cannot be general since (contrary to available experiments (McNab and Meisen,1973) it would predict *no* thermophoresis in the *absence* of mobile ions in solution---*ie.*, in *electrically non-conducting* fluids. Nevertheless, some variant of the ThFFF technique *could* prove to be a fruitful source of particle or macro-molecule thermophoretic coefficient data and thereby shed light on the fluid/solid thermal creep boundary condition) but *only if such electrostatic artifacts are eliminated or systematically corrected for.*

Particle *thermal* conductivity appears to play a role in the thermophoretic properties of suspended particles in non-(electrically) conducting liquids, but there is no current *theory* to predict such thermophoretic behavior. These considerations are expected to have important implications for the abovementioned photophoretic "space-race" experiment on macroscopic ("non-colloidal") suspended spheres in dense vapors and true liquids. One route to a theoretical understanding of in such systems may be hard-sphere vapor DSMC Knudsen layer simulations (see Part 6) in which the molecular volume fraction $f = (p/6)\bullet n s^3$ is non-negligible.

5. Thermophoresis of small immiscible *liquid* droplets

It doesnot seem to be generally appreciated that thermal creep should also influence (and ultimately dominate) the phoresis of immiscible *liquid* droplets if they are sufficiently small yet much larger than the mean-free-path in the prevailing Newtonian fluid. As *is* well known, the phoresis of large droplets is often adequately described exclusively in terms of Marangoni-drven flow associated with a temperature-dependent surface tension (with negligible interfacial 'slip'). (In contrast to ordinary thermophoresis this usually leads to droplet migration towards *hotter* regions of the host fluid). However, we find (Castillo *et.al.*,1998) that,

contrary to the statement of Ruckenstein (1981), the droplet phoretic velocity is *not* simply the (algebraic) sum of the abovementioned two effects reckoned separately. Moreover, the thermophoresis of sufficiently small droplets (*eg.*, organic fuel droplets in a "spray flame", or alkali sulfate "mist" nucleated in a thermal boundary layer (Liang, *et.al.*,1989) may be appreciable for the reasons mentioned above (*ie.*, small effective thermal conductivity ratio, $k_{p,eff}/k_g$). Not surprisingly, there is little available information on the magnitude of the thermal creep coefficient, C_{tc}, for such fluid/fluid (or vitreous 'solid') interfaces.

6. Applications of Direct Simulation Monte Carlo (DSMC)

In the low density ("ideal gas"-) limit many interesting "Knudsen sublayer" questions are now being answered with the help of a *Direct Simulation Monte Carlo* (DSMC-) method of the type originally developed for rarefied external gas flows (Bird,1994)) . A preliminary account of our results was contained in the paper by Papadopoulos and Rosner, 1996, and is updated here.

The DSMC code originally written by D. Papadopoulos as part of his NASA-MSAD-supported PhD dissertation research (see, *eg.*, Papadopoulos, 1996) is being used to provide predictions against which Burnett(-level) continuum predictions can be tested. In collaboration with Prof. D.W. Mackowski (Auburn U.) we have begun to critically assess the ability of Burnett-type ("higher-order") *continuum* methods to simulate gas flows within non-isothermal enclosures. In such cases, the 'meter-stick' for accuracy is the flow-field predicted by our DSMC (ideal gas) code. Whether it would be attractive to generalize such (near-) continuum methods to apply to the dense vapor regime remains to be seen.

DSMC has now also been adapted/used to study how well the Fuchs' 2-layer model can predict variable property† Knudsen transition regime *energy transfer* from a highly overheated spherical particle (Filippov and Rosner (1998)). Variable thermophysical property corrections will

---

†Of the available 'semi-theoretical interpolation methods, the Fuchs' 2-layer model appears to be the only one able to adequately capture the observed *non-monotonic* variable properties correction at intermediate Knusden numbers.

be one (of many) correction(s) which will have to be understood to properly interpret solid particle thermophoretic and photophoretic velocities in terms of the more fundamental *thermal creep fluid/solid boundary condition* . Another motivation for this particular exercise of DSMC is the interpretation of signals produced using the promising soot diagnostic technique called "laser-induced incandescence"(LII) (Filippov *et.al.*(1998)) for both ground-based and micro-gravity combustion experiments .

Extensions of DSMC to provide solutions of the Enskog-Boltzmann equation for *dense* hard-sphere (HS-) vapors far from solid surfaces have recently been reported by Santos *et.al.*. (1996). We have now taken steps to apply this extended (dense gas) methodology to examine the behavior of such a fluid in the immediate vicinity of a solid with a *tangential* temperature

gradient. In this way we hope to gain a better theoretical understanding of tangential momentum transfer between non-isothermal solids and *dense* fluids---- both *supercritical vapors* and true *liquids*, albeit restricted to the 'hard-sphere' case. This will have an immediate bearing on the expected phoretic velocities of solid particles or small immiscible viscous droplets suspended in such fluids (*cf.* Section 2, above).

7. References cited

Bird, G.A.(1994), **Molecular Gas Dynamics and the Direct Simulation of Gas Flows**, Clarendon Press, Oxford UK (2d ed. of 1976 treatise).

Castillo, J.L., Mackowski, D.W. and Rosner, D.E.(1990), "Photophoretic Contribution to Transport of Absorbing Particles Across Combustion Gas Boundary Layers", *Prog. Energy Comb. Sci.* (ACS Symposium Special Issue: **Deposition**) **16**, 253-260

Castillo, J.L., Rosner, D.E. and Kumar, M.(1998), "Thermophoresis of Small Liquid Droplets in Gases", (in prep)

Filippov, A.V. and D.E. Rosner,(1998) "Energy Transfer Between Aerosol Particles and Gas at High Temperature Ratios in the Transition Regime"; Submitted for Edinburgh *International Aerosol Conference*, September, 1998; Prepared for submission to *Int. J. Heat Mass Transfer* May

Filippov, A.V. , D.E. Rosner, Xing, Y., McEnally, C.S., Long, M.B. and Schaeffer, A.M.(1998) "Comparison Between Detailed LII Method and TEM Analysis for Ultrafine Soot Particles in Flames", *27th Comb. Symposium*, Boulder CO; Poster# W5G05

Garcia-Ybarra, P., and Rosner, D.E., (1989), "Thermophoretic Properties of Non-spherical Particles and Large Molecules", *AIChE J.*, **35**(5) 139-147

Garcia-Ybarra, P., and Castillo, J.L.(1997), " Mass Transfer Dominated by Thermal Diffusion in Laminar Boundary Layers", *J. Fluid Mechs.* **336**, 379-409

Giddings, J.C., Shiundu, P.M. and Semenov, S.N. (1995), "Thermophoresis of Metal Particles in a Liquid", *J. Colloid Int. Sci.* **176**, 454-458

Gomez, A. and Rosner, D.E.(1993),"Thermophoretic Effects on Particles in Counterflow Laminar Diffusion Flames", *Comb. Sci. Tech.* **89**, 335-362

Liang, B., Gomez, A. Castillo, J.L. and Rosner, D.E.,(1989), "Experimental Studies of Nucleation Phenomena Within Thermal Boundary Layers", *Chem. Engrg. Communic.* **85**, 113-133

Loyalka, S.K.(1992),"Thermophoretic Force on a Single Particle-Numerical Solution of the Boltzmann Equation", *J. Aerosol Sci.* **23**(3) 291-300

Mackowski , D.W. (1989), "Photophoresis of Aerosol Particles in the Free-molecular and Slip-Flow Regimes" *Int. J. Heat Mass Transfer* **32** (5) 843-854

Mackowski , D.W. and Papadopoulos, D.W.(1997), " Comparison of Burnett and DSMC Predictions of Pressure Distributions and Normal Stress in One-Dimensional Non-isothermal Gases", *Phys. Fluids A (Fluid Dynamics)* (submitted)

McNab, G.S. and Meisen, A. (1973), "Thermophoresis in Liquids", *J. Coll. Int. Sci.* **44** (2) 339-

Papadopoulos, D.H. and Rosner, D.E., (1995), "Enlclosure Gas Flows Driven by Non-isothermal Walls" *Physics Fluids A (Fluid Dynamics)* , **7** (11) 2535-2537

Papadopoulos, D.H. and Rosner, D.E.(1996), "Direct Simulation of Concentration Creep in a Binary Gas-Filled Enclosure", *Phys Fluids* **8** (11) 3179-3193

Papadopoulos, D.H. and Rosner, D.E.(1996), "Internal Flows Driven by Kinetic Boundary Layers", Paper B3, *20th Int. Sympos. on Rarefied Gas Dynamics* , C. Shen, ed., Beijing, China, August; pp. 143-148.

Papadopoulos, D.H. (1996), **Internal Flows Induced by Kinetic Boundary Layer Phenomena** , PhD Dissertation, Yale University Graduate School, Department of Chemical Engineering, November

Rosner, D.E.(1980)," Thermal (Soret-) Diffusion Effects on Interfacial Mass Transfer Rates", *PCH*(Pergamon) **1**, 159-185

Rosner, DE.,(1986), **Transport Processes in Chemically Reacting Flow Systems**, Butterworth-Heinemann (Stoneham MA) (3d Printing, 1990; 2d ed. in preparation)

Rosner, D.E. (1989), "Side-wall Gas 'Creep' and 'Thermal Stress Convection' in Microgravity Experiments on Film Growth by Vapor Transport ", *Physics Fluids A (Fluid Dynamics)* , **1** (11) 1761-1763

Rosner, D.E., Garcia-Ybarra , P. and Mackowski, D.W.(1991), "Size and Structure-Insensitivity of the Thermophoretic Transport of Aggregated 'Soot' Particles in Gases", *Comb. Sci. Tech.* **80** 87-101

Rosner, D.E., Mackowski, D.W., Tassopoulos, M., Castillo, J.L., and Garcia-Ybarra, P. (1992)," Effects of Heat Transfer on the Dynamics and Transport of Small Particles Suspended in Gases", *I/EC-Research* (ACS), **31** (3) 760-769(1992))

Rosner, D.E., *et.al.*(1998), "Soot Morphology- and High Pressure Effects on Thermophoretically-Dominated Deposition Rates", *27th Comb. Symposium*, Boulder CO; Poster # W5G-11

Rosner, D.E. and Khalil, Y.(1998) " Particle Morphology and Knudsen Transition Effects on Thermophoretically-Dominated Total Mass Deposition Rates From 'Coagulation-Aged' Aerosol Populations", *J. Aerosol Sci.* (submitted)

Rosner, D.E. and Papadopoulos, D.(1996), "Jump, Creep and Slip Boundary Conditions at Non-Equilibrium Gas/Solid Interfaces" (Invited paper, E. Ruckenstein Birthday Issue) *I/EC-Research* (ACS), **35** (9) 3210-3222)

Ruckenstein, E.,(1981)," Can Phoretic Motions be Treated as Interfacial Tension Gradient-Driven Phenomena"?, *J. Coll. Int. Sci.*, **83**, 77-81

Santos, A. *et. al.*(1996),"Monte-Carlo Simulation Method for the Enskog Equation", *Physical Review E*, **54**(1) 438-444 ; see, also, "Simulation of the Enskog Equation *a la* Bird", *Physics of Fluids* (in press, 1997) and Paper B2, Proc. *20th Int. Sympos. on Rarefied Gas Dynamics* , Beijing, China, August 1996; pp. 137-142.

Shiundu, P.M., Liu, G. and Giddings, J.C. (1995), "Separation of Particles in Non-aqueous Suspensions by Thermal Field Flow Fractionation", *Anal. Chem.* **67**, 2705-2713

Tandon, P., and Rosner, D.E.(1995), "Translational Brownian Diffusion Coefficient of Large (Multi-particle) Suspended Aggregates", *Ind Eng Chem-Res* (ACS) **34** 3265-3277 ; see, also, *AIChE J.*, **40**(7) 1167-1182 (1994)

The two documents above correspond to Prof. Rosner's 2 page Abstract, and 6 page (Paper) contributions t
4th NASA Microgravity Fluid Physics & Transport Phenom. Conf. Aug.12-14,1998; Cleveland OH

A SYMMETRY BREAKING EXPERIMENT ABOARD MIR AND THE STABILITY OF ROTATING LIQUID FILMS

P. Concus, University of California, Berkeley CA 94720-3840, USA, concus@math.berkeley.edu,
R. Finn, Stanford University, Stanford, CA 94305-2125, USA, finn@gauss.stanford.edu,
D. Gomes, Instituto Superior Técnico, Lisbon, Portugal and University of California, Berkeley CA 94720-3840, USA, dgomes@math.berkeley.edu,
J. McCuan, Mathematical Sciences Research Institute, Berkeley, CA 94720-5070, USA, john@msri.org,
M. Weislogel, NASA Lewis Research Center, Cleveland, OH 44135, USA, mark.weislogel@lerc.nasa.gov

Abstract

We discuss results from two parts of our study on the behavior of liquids under low-gravity conditions. The first concerns the Interface Configuration Experiment (ICE) aboard the Space Station Mir on the Mir-21/NASA-2 mission; for a certain "exotic" container, distinct asymmetric liquid configurations are found as locally stable ones, even though the container itself is rotationally symmetric, in confirmation of mathematical results and numerical computations. The second investigation concerns the behavior of slowly rotating liquids; it is found that a rotating film instability observed previously in a physical experiment in 1-g, scaled to render gravity effects small, does not correspond to mathematical and computational results obtained for low-gravity. These latter results are based on the classical equilibrium theory, enhanced with a van der Waals potential of adhesion.

1 Introduction

It is essential, when planning space-based operations, to be able to predict the configurations that fluids will assume in their containers under low-gravity conditions. In such an environment surface wettability and container geometry predominate in governing equilibrium behavior. As formulated in the classical Young-Laplace-Gauss (Y-L-G) theory of capillarity, the wetting characteristics of a particular system are embodied in a well-defined equilibrium macroscopic contact angle depending only on the materials (see, e.g., [10, Chap. 1]).

According to the Y-L-G formulation, the mechanical energy E of a partly filled container, when gravity is absent or can be neglected, the situation we discuss primarily, is

$$E = \sigma(\mathcal{S} - \mathcal{S}^* \cos\gamma). \tag{1}$$

Here σ is the liquid-gas interfacial tension and $\cos\gamma$ is the liquid-solid-gas relative adhesion coefficient, γ being the contact angle between the liquid and the container; $\mathcal{S}$ denotes the area of the liquid-gas free surface and $\mathcal{S}^*$ the area of the portion of the container in contact with the liquid. Configurations of the liquid that yield a stationary value for E subject to the constraint of fixed liquid volume are, according to the classical theory, equilibrium configurations. They will be stable, as well, if E is locally minimized

Even under the simplifications of zero gravity or low-gravity conditions for which gravitational energy can be neglected, the strongly nonlinear governing equations from the classical theory are difficult to solve. Closed-form solutions for this case have been obtained for only a few simple configurations, such as in right circular cylindrical or spherical containers. Departures from these container geometries can lead to dramatic changes in fluid behavior [6], [10].

We discuss here results from two parts of our study on behavior of liquids under low-gravity conditions. The first concerns a space experiment that investigates actual physical behavior for a situation in which symmetry-breaking type of mathematical results were obtained for equilibrium behavior based on the classical Y-L-G formulation. The second concerns computational results for uniformly rotating highly wetting liquids, based on the Y-L-G formulation enhanced with a van der Waals potential of adhesion.

We are interested especially in observing the extent to which some of the striking predictions of the fully nonlinear Y-L-G theory will be observed experimentally in the presence of factors not reflected in that theory, such as contact angle hysteresis and dynamic contact line phenomena. In coordination with this effort, we seek indications as to the effects these factors will have on fluid behavior. We are guided in our procedures to some extent by the previous experiments recorded in [9], in which a discontinuous behavior predicted by the Y-L-G theory was in fact observed. The mathematical, computational, and pre-flight drop tower experiment background for those experiments can be found in [4]; other examples of such experiments can be found in the references of [4] and also in [6].

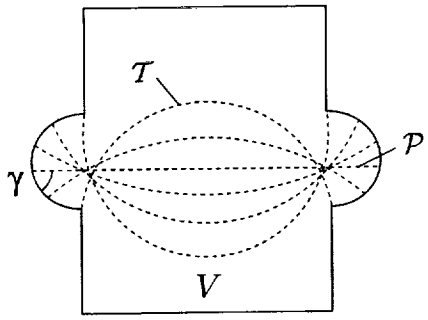

Figure 1: Axial section of exotic container, with members (dashed curves) of continuum of rotationally symmetric equilibrium interfaces, all of which meet the container with the same contact angle γ and enclose the same volume V of liquid with the container.

2 Exotic containers

2.1 Background

Of interest here are the "exotic" containers discussed in [7] from a theoretical point of view (based on the Y-L-G theory). These containers are rotationally symmetric with the remarkable property that for given contact angle and liquid volume, an infinity (in fact, an entire continuum) of distinct rotationally symmetric equilibrium configurations can appear, all of which have the same mechanical energy. Such container shapes, first studied in [12] for the special case of zero gravity and $\gamma = 90°$, are possible for any gravity level, but only for low-gravity conditions can the phenomena be expected to appear on an adequately large size scale to be readily measurable. For zero gravity the size scale can be arbitrary. Additionally, these containers exhibit marked symmetry-breaking properties, as discussed below.

The axial section of an exotic container for zero gravity and contact angle 80° is depicted in Fig. 1. The mathematically derived "exotic-bulge" portion is joined to circular cylindrical extensions and disc ends to form a closed container. The dashed curves depict members of the continuum of rotationally symmetric equilibrium interfaces, all of which enclose the same volume V of liquid with the bottom and walls of the container. The horizontal planar free surface $\mathcal{P}$ making the specified contact angle with the container is of necessity a member of the family. The topmost curved interface, which is discussed below, is denoted by $\mathcal{T}$.

It turns out that the rotationally symmetric equilibrium configurations are unstable; as is shown in [11] and [5], particular deformations that are not rotationally symmetric yield configurations with lower energy. Thus, it is possible to demonstrate a symmetric container that admits infinitely many symmetric equilibrium interfaces, but for which no interface that minimizes energy can be symmetric. This is in notable contrast with what happens in the familiar case of the right circular cylinder, for which the symmetric interface (unique for prescribed liquid volume) is stable, and no asymmetric ones can appear.

There is presently no known way to determine mathematically the surfaces that minimize energy in the exotic containers. However, numerical computations have suggested a number of particular non-rotationally-symmetric surfaces as local minima. Shown in Fig. 2 are three distinct non-rotationally-symmetric local energy minimizing surfaces for an exotic container, as obtained numerically in [3] using a modification of an early version of the Surface Evolver software package [1]. These surfaces, all of whose energies are less than that of the symmetric equilibrium family's, are depicted in order of increasing energy from left to right. We refer to the surface configurations as the "spoon", the "potato chip", and the "lichen". The contact lines of these surfaces with the container undergo respectively one, two, and three excursions from upper to lower extremities and back as they circumnavigate the bulge.

2.2 Space experiment

Depicted in Fig. 3 is the vessel for the Interface Configuration Experiment (ICE) carried out during the Mir-21/NASA-2 mission on board the Mir Space Station. Space flight experiments of such vessels on the earlier USML-1 Spacelab mission confirmed that the spoon shape (Fig. 2) is a strongly stable configuration, apparently a global energy minimizer. However, the other two nonaxisymmetric locally energy minimizing interfaces of Fig. 2 did not appear in that mission. Specific goals on Mir include an attempt to observe one of those configurations, the potato chip, and to test its stability.

To begin the experiment, which was carried out in the Mir glovebox module, a crew member attaches the ICE vessel on its side (the configuration in Fig. 3) to a labjack that is held to the glovebox floor with magnets. The reservoir valve is then opened, and the control dial is turned to displace the entire contents of the reservoir into the exotic container portion of the vessel. After a sufficient time, disturbances are imparted to the vessel and the resulting interfaces are observed, generally until they

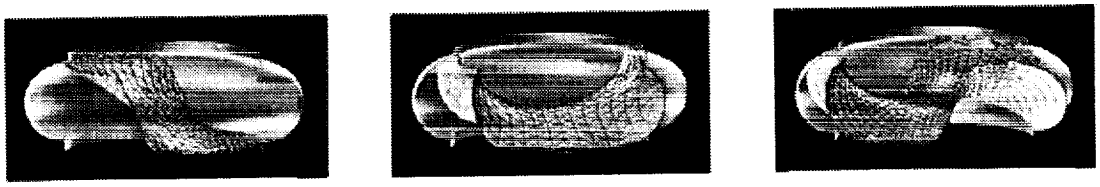

Figure 2: Computed locally stable configurations in an exotic container for zero gravity and $\gamma = 80°$. From left to right, in order of increasing energy, "spoon", "potato chip", and "lichen". All have smaller energy than the symmetric equilibrium family.

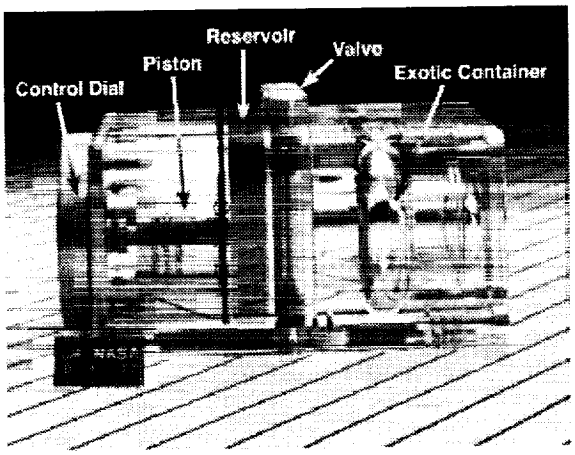

Figure 3: Experiment vessel.

become quiescent again. The disturbances are increased in amplitude until the interface either consistently returns to a particular configuration or breaks up. The two video cameras recording the process are mounted for orthogonal views, and audio is recorded simultaneously.

After the fluid was carefully dispensed into an exotic container in a manner that encouraged establishment of a configuration like that for the topmost member of the family of equipotential rotationally symmetric surfaces ($\mathcal{T}$ in Fig. 1), the crew member would then impart a perturbing impulse to the liquid by tapping the outside of the vessel with her finger. The solitary taps began as light disturbances, allowing for complete stabilization of the interface between each tap. These lighter taps were intended to dislodge a surface that might otherwise be unstable, but was "sticking" in its configuration because of resistance at the contact line (hysteresis). Subsequently, intensity of the taps was increased to test the stability of any configuration that might have formed. To induce larger amplitude axial disturbances, the crew member could slide the vessel-labjack assembly back and forth along the glovebox floor. These larger disturbances were intended to induce the liquid to leave a locally stable configuration and to settle into some different one.

Two distinct locally stable nonaxisymmetric interfaces were observed in the experiment, a spoon and a potato chip. Four equilibrium interfaces in all were formed, as shown in Fig. 4. The first was a rotationally symmetric interface (cf., $\mathcal{T}$ in Fig. 1) when the fill procedure was close to complete. It soon destabilized after completion of the fill, as a result of small disturbances imparted by the crew member in removing her hands from the vessel. Then an apparent global energy minimizer formed, a spoon like that found computationally and on USML-1, which configuration was stable to additional perturbing disturbances. Following further carefully applied moderately large disturbances another local minimizer formed, a potato chip like that in Fig. 2. This too was stable to additional perturbing disturbances. Finally, a further sizable disturbance led once more to the spoon, this time in reflected configuration.

It is important to remark that in the experiment the mathematical requirements for an exotic container are not perfectly met. There is of necessity a deviation of parameters (contact angle, liquid volume, gravity level) from their exact exotic values. Nevertheless, the asymmetry of the local minimizers did occur. This is in accord with computational evidence that the asymmetric configuration phenomenon generally is robust with respect to discretization errors from numerical approximations and to inaccuracies inherent in container fabrication. Additionally, it was observed in the experiment that even with moderately large departures from the exotic requirements (70° liquid in a 55° exotic container) the asymmetric local-minimizer property persists.

Even if conditions for an exotic container are closely satisfied, once the fluid becomes asymmetric the presence of symmetric equilibria nearby the initial one probably has little bearing on the fluid's subsequent behavior. In the experiment, the presence of the continuum of distinct symmetric equilibria apparently has its main effect

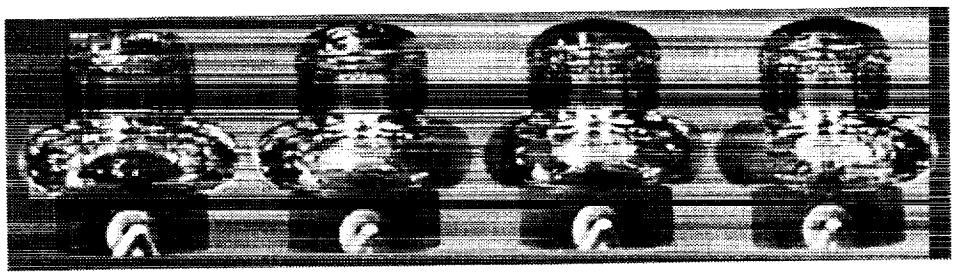

Figure 4: Configurations from Mir experiment. From left to right: (pinned) rotationally symmetric interface, spoon-right, potato chip, spoon-left

just in rendering the initial symmetric configuration unstable. It is of interest to note that in the mathematical proof of instability of the exotic continuum family only the local boundary curvature enters; if the curvature is greater than a certain lower bound, then the interface can be shown to be mathematically unstable, whether or not the container is exotic. (See [5], [11]; a proof of instability that extends to all gravity levels will appear in [15].)

2.3 Discussion

What began for us as a study of nonuniqueness and of exotic containers has led to our encountering the striking phenomenon of the asymmetry of energy minimizing liquid configurations in containers that are rotationally symmetric and for which the prescribed boundary data (contact angles) are also symmetric.

The accumulated evidence of this experiment and of its predecessors suggests strongly that in many cases of interest the Y-L-G theory reliably predicts fluid behavior in low gravity environments, or otherwise when surface forces predominate. Although in some cases considerable time (perhaps on the order of hours) may be required to overcome the effects of contact angle hysteresis, the fluid configurations finally adopted do appear to conform to predictions of the theory. The evidence suggests additionally that only in particular, perhaps rare, circumstances will capillary surfaces be uniquely determined by the data. Nor can it be expected that symmetric data will lead to symmetric configurations. In fact, as discussed above, even though the specifications for the exotic containers cannot be met exactly in practice, locally stable asymmetric surfaces will appear in them and will appear even for configurations that are distant from being exotic. These results can be important to designers of fluid management systems in low-gravity. The experimental results lend support to use of the classical Y-L-G theory in such design procedures, and it must be noted that striking and unexpected behavior predicted by that theory will actually be observed in practice. Full details of the experimental results for ICE, including data on time-dependent dynamic behavior, are given in [8].

3 Highly wetting, slowly rotating liquids

The results discussed above apply to equilibrium configurations and to contact angles within the range of applicability of classical versions of the Y-L-G theory. In this section we discuss a special configuration for which straightforward formal use of the basic premises of that theory may be insufficient.

As an example, consider a circular cylindrical rod that is dipped into a reservoir of wetting liquid. According to the classical Y-L-G theory, the liquid will move part way along the rod to a distance that is bounded for all contact angles, even 0°. For a "super-wetting" liquid, the type we wish to consider here, liquid will move over an additional portion, typically all, of the rod's surface coating it with a film. If the entire configuration is rotated about the rod's axis, the difference between the classical and highly wetting cases could give rise to very different behavior. In the first case the fluid will simply shift toward the outer portion of the reservoir, retreating somewhat along the rod, reaching a new quasi-steady equilibrium configuration. In the highly wetting case, however, it may happen that the film on the rod becomes unstable. Which case occurs can be crucial in certain applications, such as for slowly rotating liquid helium cryogenic cooling devices for orbiting satellites.

A coaxial cylindrical configuration has been proposed for such a cooling device for use in conjunction with the STEP and Gravity Probe-B Relativity Mission studies. A central rod, which contains experiment apparatus, is coaxial with a surrounding circular cylindrical

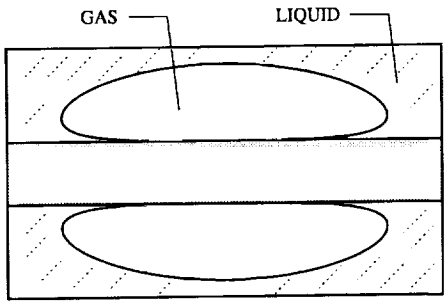

Figure 5: Axial section of rotating fluid configuration.

container. The region between the rod and the outer cylinder is partially full of liquid, and the entire configuration is to rotate with uniform speed ω such that any gas bubble is wrapped symmetrically about the rod, thereby keeping the center of mass on the axis, as desired for the experiments (Fig. 5). Using the Surface Evolver software [1], Brakke calculated configurations that a single bubble would have, based on the classical Y-L-G formulation for zero gravity for a liquid with zero degree contact angle [2]. He found that if ω is not too small, then a gas bubble will assume the desired axisymmetric shape wrapped around the rod, as depicted in Fig. 5. The liquid makes a zero degree contact angle with the rod and does not wet the rod's central portion.

In a subsequent 1-g experimental study, which attempted to minimize the relative effects of gravity (by using small physical dimensions and large rotation speeds), it was found that for the highly wetting liquid used (silicon oil) a configuration similar to that of Fig. 5 developed, except that a liquid film formed over the rod covering the otherwise exposed central portion. The film became unstable; liquid was "pumped" continually from the bulk of the liquid into the film, with blobs of liquid departing from the film sporadically. A steady configuration never was achieved [14].

In a subsequent mathematical study with the purpose of providing a theoretical framework for the experimental results, a Y-L-G formulation was used, modified to allow for the presence of a film on the rod [13]. In this modified formulation one replaces the term $-\sigma S^* cos\gamma$ in (1), corresponding to the contact energy of the wetted and dry portions of the rod, with a van der Waals potential of adhesion $-\alpha/(r-r_0)^3$ integrated over the liquid volume, with $\alpha > 0$, α small, an adhesion coefficient. The rod, of radius r_0, is covered by the film, and r is the radial coordinate of a point on the gas-liquid interface. Additionally, a rotational potential energy $-(\rho\omega^2/2)r^2$ integrated over the liquid volume is added to the right of (1).

For a model problem of a rotating cylindrical rod covered with a film of uniform thickness, the analysis led to the interesting result that there is a critical value, depending on the radius of the rod, the liquid parameters, and the rotation rate, such that any film of thickness less than the critical value is stable, no matter how long the rod. On the other hand, if the film is thicker than the critical value, then there is a critical length l depending on the above parameters and the film thickness, such that all cylindrical films shorter than l are stable while all longer films are unstable (see Fig. 6). By comparison, for the classical Plateau-Rayleigh instability for a cylindrical column composed entirely of liquid, there is a critical length for any prescribed volume of liquid; a column is unstable for lengths longer than the critical, while it is stable for shorter lengths.

Numerical experiments based on the enhanced formulation were carried out for the actual container geometry using the Surface Evolver. It was found, over a broad range of parameters that include those of practical physical interest, that the liquid films that form on the central rod were always sufficiently thin so as to remain stable, never becoming thick enough to satisfy the mathematical criteria for instability. In fact, one can show analytically that an energy minimum occurs for film thickness $O(\alpha^{1/3})$ asymptotically for small α; this result can be used with other asymptotic estimates to underpin the numerically found film stability. The numerical results indicate additionally that the ratio of the critical film thickness to $\alpha^{1/3}$ is nearly constant for a large range of α, lending additional support to the stability conclusion. Complete details are to be presented in a paper currently in preparation.

We conclude from the numerical study that the experimentally observed liquid film instability must derive from factors other than the above Plateau-Rayleigh type one. It is not known presently if an experiment conducted in low-gravity, free of the scaling and complications inherent in a 1-g experiment simulation, would exhibit the instability.

Acknowledgments

We are indebted to astronaut Shannon Lucid for the expert manner in which she conducted the ICE experiment on board the Mir Space Station. We wish to thank also the National Aeronautics and Space Administration and the Russian Space Agency for the opportunity to use Mir under their cooperative program. Additionally, we wish to thank Victor Brady for carefully carrying

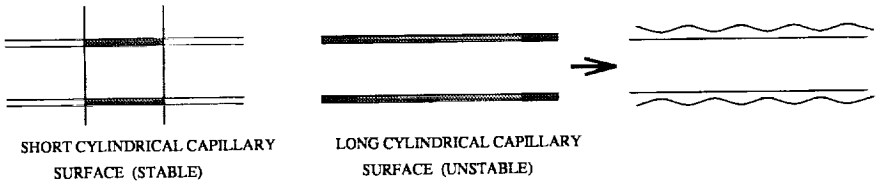

Figure 6: Stable and unstable films for film thickness greater than critical value.

out numerous computational experiments, in connection with the exotic container study. This work was supported in part by the National Aeronautics and Space Administration under Grant NAG3-1941, by the National Science Foundation under Grants DMS-9401167 and DMS-97029817, and by the Mathematical Sciences Subprogram of the Office of Energy Research, U. S. Department of Energy, under Contract Number DE-AC03-76SF00098.

References

[1] Brakke, K., *Surface Evolver*, Susquehanna Univ., Selinsgrove, PA, USA, 1996; available from `http://www.geom.umn.edu/software/evolver`.

[2] Brakke, K., *Stability of torus bubble in rotating tank*, unpublished report.

[3] Callahan, M., Concus, P., and Finn, R., *Energy minimizing capillary surfaces for exotic containers*, in Computing Optimal Geometries (with accompanying video tape), Taylor, J. E., ed., AMS Selected Lectures in Mathematics, Amer. Math. Soc., Providence, RI, 1991, pp. 13–15.

[4] Chen, A., Concus, P., Finn, R., and Weislogel, M., *On cylindrical container sections for a capillary free-surface experiment*, Microgravity Sci. Technol., 9 (1997), pp. 169–174.

[5] Concus, P. and Finn, R., *Instability of Certain Capillary Surfaces*, Manuscr. Math., 63 (1989), pp. 209–213.

[6] Concus, P. and Finn, R., *Capillary surfaces in microgravity*, in Low-Gravity Fluid Dynamics and Transport Phenomena, Koster, J. N. and Sani, R. L., eds., Progress in Astronautics and Aeronautics, Vol. 130, AIAA, Washington, DC, 1990, pp. 183–205.

[7] Concus, P. and Finn, R., *Exotic containers for capillary surfaces*, J. Fluid Mech., 224 (1991), pp. 383–394; Corrigendum, J. Fluid Mech., 232 (1991), pp. 689–690.

[8] Concus, P., Finn, R., and Weislogel, M., *Capillary surfaces in an exotic container: results from space experiments*, Preprint PAM-737, Center for Pure and Applied Mathematics, Univ. of California, Berkeley, CA, 1998.

[9] Concus, P., Finn, R., and Weislogel, M., *Measurement of critical contact angle in a microgravity space experiment*, Experiments in Fluids, submitted.

[10] Finn, R., Equilibrium Capillary Surfaces, Springer-Verlag, New York, 1986.

[11] Finn, R., *Non uniqueness and uniqueness of capillary surfaces*, Manuscr. Math., 61 (1988), pp. 347–372.

[12] Gulliver, R. and Hildebrandt, S., *Boundary configurations spanning continua of minimal surfaces*, Manuscr. Math., 54 (1986), pp. 323–347.

[13] McCuan, J., *Retardation of Rayleigh instability: a distinguishing characteristic among perfectly wetting fluids*, Preprint MSRI 1997-011, Math. Sci. Res. Inst., Berkeley, CA, 1997 (available online at `http://www.msri.org/MSRI-preprints/online/1997-011.html`).

[14] McCuan, J., Neshleba, P., and Torii, R., *Scaling laws for rotating fluid shapes*, in Proc. 7th Marcel Grossmann Meeting, Jantzen, R. and Keiser, M., eds., World Scientific, 1997.

[15] Wente, H., *Stability analysis for exotic containers*, Dynam. Contin. Discrete Impuls. Systems, 5 (1999), to appear.

CRITICAL VELOCITIES IN OPEN CAPILLARY FLOWS

Michael E. Dreyer, Uwe Rosendahl, Hans J. Rath
Center of Applied Space Technology and Microgravity (ZARM)
University of Bremen, D-28354 Bremen, Germany

INTRODUCTION

Within the compensated or reduced gravity environment of an orbiting spacecraft, the hydrostatic pressure vanishes and surface tension forces become dominant. This leads to a different design of all fluid containing devices due to the fact that a preferential orientation of the bulk liquid ceases to exist. So called surface tension tanks (STT) are used since several decades in a spacecrafts and satellites to transport and position propellant and to ensure bubble free supply of the engines. Capillary vanes are an important part of the propellant management device (PMD) of a STT. Capillary vanes consist of a more or less complicated metal sheet located near the tank wall to induce small radii of curvature of the free surface to produce a concave shape which leads to a lower pressure in the liquid than the ambient pressure. Presently the vanes create an open flow path from the bulk of the propellant to a reservoir. The reservoir supplies gas free propellant to the thrusters, whenever outflow is demanded. The detailed knowledge of stability limits and flow rates in open capillary vanes is an important criterion for an efficient design of propellant management devices (PMD) in surface tension tanks. For future surface tension tanks the reservoir shall be omitted and the thrusters supplied directly by the vanes. To guarantee gas free propellant supply the limits of flow rates in capillary vanes have to be known. Since the only work on this field are model computations by Jaekle[1] we developed a drop tower experiment to investigate the limits of flow rates in vanes experimentally.

THEORETICAL APPROACH

We consider the flow of liquid along a capillary vane as shown in Fig. 1. The vane consists of two parallel plates of distance a, breadth b and length l, and a

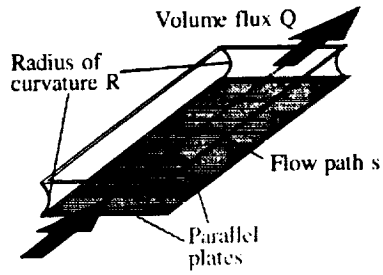

Figure 1: Model of a capillary vane consisting of two parallel plates. The flow through the vane along the vane axis s leads to a decreasing radius of curvature.

flow in direction of the vane axis s is assumed. The flow path is bounded at the sides by free surfaces. If a constant volume flux Q is applied, the inner pressure of the liquid p and the radius of curvature R of the free surface change in flow direction.

For the analysis we follow the steady state approach given by Jaekle[1] with a refinement for the pressure loss term dw_f in the BERNOULLI equation

$$\frac{1}{\rho}dp + \upsilon d\upsilon + gdz + dw_f = 0. \qquad (1)$$

The pressure p in the liquid is related to the curvature of the free surface and can be written with the GAUSS-LAPLACE equation:

$$p - p_a = \sigma\left(\frac{1}{R_1} + \frac{1}{R_2}\right). \qquad (2)$$

Surface tension is denoted with σ. We assume that the free surface in the plane perpendicular to the flow direction s is a surface of constant curvature and we consider only the radius of curvature in this plane

neglecting the curvature in flow direction, therefore with $R_1 = -R$ and $R_2 = \infty$ the pressure drop reads

$$p - p_a = -\frac{\sigma}{R}, \tag{3}$$

and the pressure gradient becomes

$$dp = \frac{\sigma}{R^2} dR. \tag{4}$$

With the conservation of mass (the mean velocity is denoted with υ)

$$A\upsilon = Q, \text{ and } d\upsilon = -\frac{Q}{A^2} dA, \tag{5}$$

the second term of Eq. (1) yields

$$\upsilon d\upsilon = -\frac{Q^2}{A^3} dA.$$

In the gravity compensated environment of the free falling capsule in the drop tower we can neglect the hydrostatic pressure.

The loss of energy per unit mass dw_f due to friction consists of two parts, the laminar viscous pressure loss and the additional entrance pressure loss which is a result of the change of the velocity profile from the entrance profile to the parabolic velocity distribution (POISEUILLE flow). The laminar pressure loss for two infinite parallel plates is obtained from an analytical solution of the NAVIER-STOKES equation

$$\frac{dp_l}{ds} = -\frac{k_{pf}}{D_h \mathrm{Re}_{D_h}} \frac{\rho}{2} \upsilon^2, \tag{6}$$

with the friction factor $k_{pf} = 96$ for parallel plates, the hydraulic diameter $D_h = 2a$ and the REYNOLDS number

$$\mathrm{Re}_{D_h} = \frac{D_h \upsilon}{\nu}. \tag{7}$$

The kinematic viscosity is denoted with ν, the density with ρ. For the additional pressure loss due to the transformation of the entrance velocity profile to the laminar parabolic velocity distribution, no analytical solution is known. We performed numerical calculations for the infinite parallel plate problem with the finite element code FIDAP and fitted the additional pressure loss to get the empirical correlation in differentiated form

$$\frac{dp_e}{ds} = \frac{k_{pe}}{D_h \mathrm{Re}_{D_h}} \frac{\rho}{2} \upsilon^2 e^{-\frac{s}{s_0}} \tag{8}$$

with $s_0 = 0.002\, D_h \mathrm{Re}_{D_h}$, and $k_{pe} = 268$.

The fourth term of the lhs of Eq. (1) can be written now

$$dw_f = \frac{1}{D_h \mathrm{Re}_{D_h}} \frac{\upsilon^2}{2} \left[k_{pf} = k_{pe} e^{-\frac{s}{s_0}} \right] ds, \tag{9}$$

and the following relation for the curvature R along the flow path s is obtained:

$$\frac{dR}{ds} = \frac{\frac{A}{2D_h^2 \mathrm{Re}_{D_h}} \left\{ k_{pf} + k_{pe} e^{-\frac{s}{s_0}} \right\}}{\frac{dA}{dR} - \frac{\sigma}{\rho} \frac{A^3}{Q^2 R^2}}. \tag{10}$$

Since dR/ds is negative the radius of curvature R decreases along the flow path. The minimal radius is reached if R equals half the plate distance: $R_{min} = a/2$. With the cross-section.

$$A = ab - 2\left[R^2 \arcsin\frac{a}{2R} - \frac{a}{2} \sqrt{R^2 - \frac{a^2}{4}} \right], \tag{11}$$

Eq. (10) can be solved numerically using a Runge-Kutta algorithm of fourth order.

Eq. (10) must be solved with the initial condition $R_0 = R(s = 0)$. Relating the pressure drop at the inlet due to losses in the reservoir of the experiment container (see Fig. 2) to the radius of curvature at $s = 0$, the initial condition reads

$$R_0 = \frac{\sigma}{\frac{\rho}{2} \upsilon^2 \left[\frac{k_{ef}}{\mathrm{Re}_e} + k_{ec} \right]}, \tag{12}$$

with $\mathrm{Re}_e = 2 r_e \upsilon / \nu$ and the area equivalent radius $r_e = \sqrt{ab/\pi}$. The constants $k_{ef} = 8$ and $k_{ec} = 2.314$ can be derived from the analysis for the capillary rise between parallel plates given by Dreyer et al.[2]. The entrance radius R_0 depends strongly on the flow condition before the inlet and must be calculated for each flow geometry separately.

Integrating Eq. (10) from $R(s = l) = R_{min}$ yields a critical volume flux Q_{crit}^{theo} which denotes the maximum volume flux that can be withdrawn through the vane. The non-dimensional form of Eq. (10) reads

$$\frac{dR^*}{ds^*} = \frac{\frac{Oh A^{*2}}{8} \frac{A^*}{Q^*} \left\{ k_{pf} + k_{pe} e^{-\frac{s}{s_0^*}} \right\}}{\frac{dA^*}{dR^*} - \frac{A^{*3}}{Q^{*2} R^{*2}}} \tag{13}$$

with $R^* = 2R/a$, $s^* = s/a$, $A^* = A/ab$, $s_0^* = Q^*/125$ OhA^*, $Q^* = Q/\sqrt{2\sigma ab^2/\rho}$. The dimensionless parameters are the OHNESORGE number $Oh = \mu/\sqrt{2a\rho\sigma}$, and the gap ratio $\Lambda = a/b$ in the non-dimensional form of $A = f(R)$

$$A^* = 1 - \frac{\Lambda}{2}\left[R^{*2}\arcsin\frac{1}{R^*} - \sqrt{R^{*2}-1}\right], \quad (14)$$

As a solution of Eq. (13) we expect a relation $Q^* = f(\mathrm{Oh}, \Lambda, l^*)$ with the non-dimensional length $l^* = \mathrm{Oh}\, l/a$ which is an appropriate form of the capillary rise height discussed in Dreyer et al.[3].

Since the result of this work shall be useful for surface tension tanks, the experimental parameter are chosen with respect to propellant data (N_2O_4 and MMH) and tank geometries. This leads to the parameter field given by the combination $Oh = 0.427 \cdot 10^{-3} \ldots 5.881 \cdot 10^{-3}$, and $\Lambda = 0.1 \ldots 0.3$.

The experiment parameter are given in Tab. 1. All fluids show perfectly wetting behavior at the capillary walls. The minimal REYNOLDS number was calculated with $Re_{min} = 2Q/\nu b$, and laminar flow conditions are expected for all experiments.

Table 1: Dimensionless parameter for the drop tower experiments.

#	Λ [–]	Oh [–]	l^* [–]	Re_{min} [–]
1	0.167	0.00238	0.045	534
29	0.1	0.0047	0.177	156
32	0.3	0.00197	0.062	578
33	0.2	0.00197	0.063	600
34	0.1	0.00197	0062	625
35	0.2	0.00152	0.029	909
35a	0.2	0.00152	0.015	977
36	0.2	0.00472	0.177	151

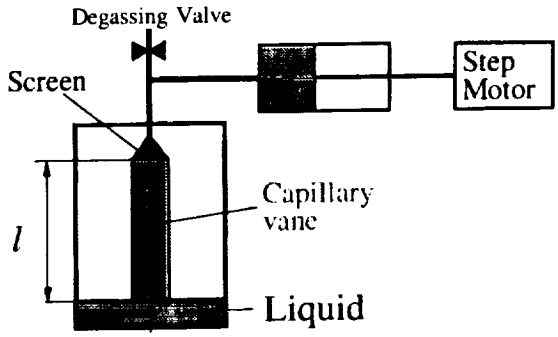

Figure 2: Schematic drawing of the experiment setup. The piston device is filled with liquid up to the screen before the drop (1g). During the microgravity period the capillary vanes fills itself and pumping starts when the meniscus reaches the screen.

EXPERIMENTS

The aim of the experiments was to determine the critical volume flux through a capillary vane, consisting of two parallel plates. To eliminate the gravity effects and to establish a liquid path between the parallel plates by means of the surface tension only, the experiments were performed under microgravity conditions using the Drop Tower Bremen (4.74 s experiment time, residual acceleration less than 10^{-5} g_0, with g_0 gravity acceleration on earth).

The experimental setup was designed to operate within a drop capsule of the Drop Tower Bremen system. The capillary vane is mounted in the experiment container. The axis of the capillary vane is perpendicular to the free surface of the test liquid under normal gravity conditions.

The withdrawal device is mounted on the top of the vane. A schematic drawing of the experiment setup is shown in Fig. 2. Before the drop the withdrawal system can be filled up to the screen with the test liquid by means of the piston and stepper motor. Via the degassing valve gas bubbles can be removed from the tube system. After the release of the capsule the meniscus rises to the top of the vane and pumping with a defined volume flux begins.

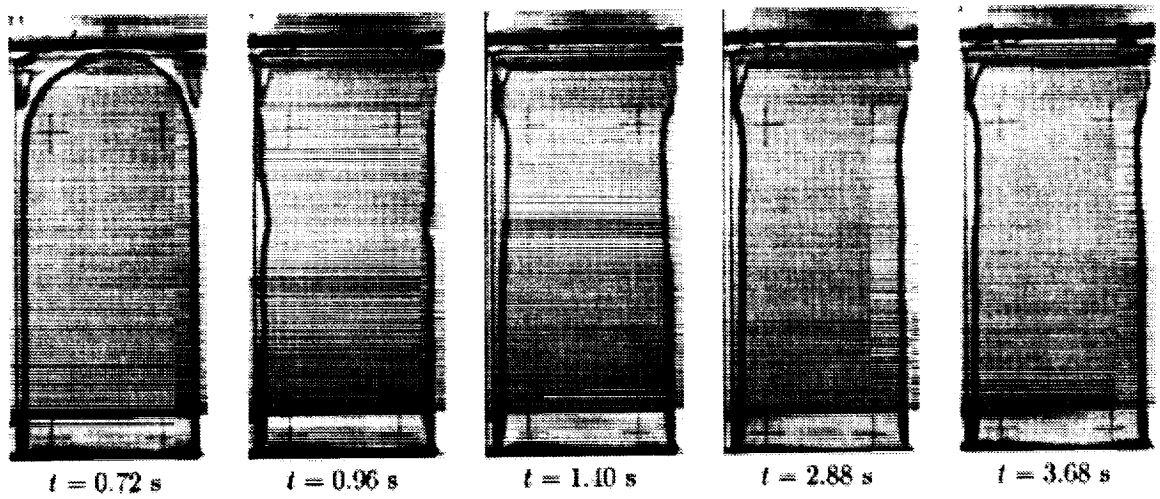

Figure 3: Subcritical volume flux (no gas ingestion): Q = 8.75 ml/s, a = 0.5 cm, b = 2.5 mm, l = 4.8 cm, SF 0.65. The liquid rises between the plates due to capillary forces (t = 0.72 s), then the withdrawal device starts sucking a defined volume flux. Disturbance waves initiated by the suction start travel along the free surface (t = 0.96 s), then the flow remains stable, no gas is ingested.

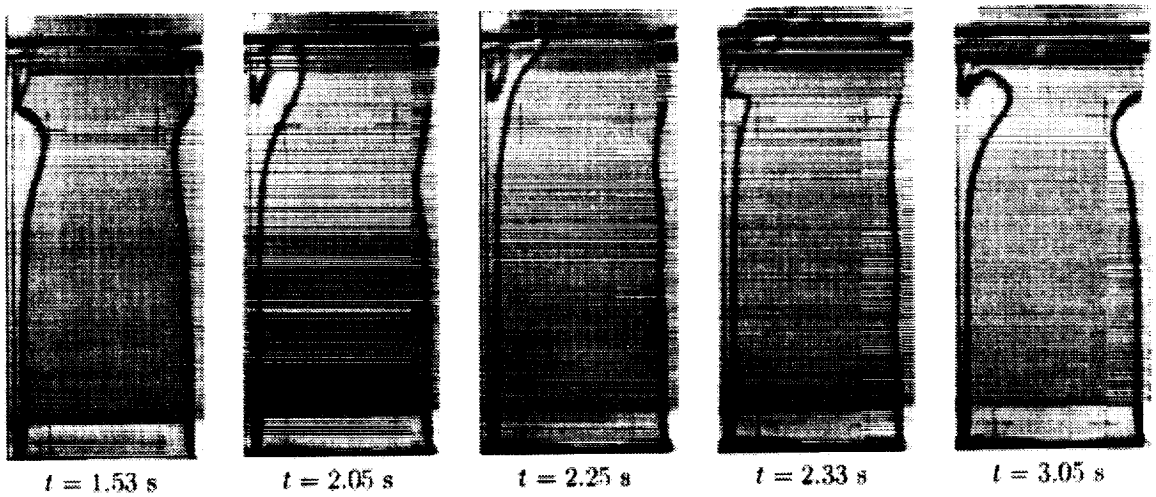

Figure 4: Subcritical volume flux (as ingestion): Q = 9.04 ml/s, a = 0.5 cm, b = 2.5 cm, l = 4.8 cm, SF 0.65. The free surface becomes unstable (t = 2.05 s), a gas bubble is ingested. The surface stabilizes (t = 2.33 s) and the cycle starts again (t = 3.05 s).

A total amount of 40 experiment were performed with an average of 5 drops for each parameter. The first drop serves to determine the exact start time for the withdrawal device. This time has to be estimated exactly within a limit of ±0.05 s. The following experiments for one parameter set were aimed to determine the critical volume flux. Due to the good agreement of the theory with the experiment the critical volume flux could be predicted with good accuracy saving drops with Q far away from the critical value. Except for the parameter set #36 at least one subcritical and one supercritical volume flux could be achieved. If possible, the highest subcritical volume flux was reproduced to eliminate experiment errors. The experiment was observed by CCD cameras and recorded on high-8 VCR. Figs. 3 and 4 show typical series of snapshots of the capillary flow. Since the plates are transparent, the video prints show the contour of the meniscus, i.e. the projection of the curved surface into a plane. By the projection the surface appears as the dark line.

The volume flux Q = 8.75 ml/s in Fig. 3 is subcritical. The meniscus rises (t = 0.72 s) and reaches the top. Then the withdrawal device starts with the predefined volume flux. This initiates surface waves traveling along the free surface upstream. After t = 1.4 s the surface remains stable for the rest of the experiment.

Increasing the volume flux about 3% to Q = 9.04 ml/s yields a supercritical flow (Fig. 4). The free surface becomes instable at one side (t = 2.05 s) and a gas bubble is ingested into the withdrawal device (t = 2.25 s). The free surface stabilizes (t = 2.33 s) and the procedure starts from the beginning (t = 3.05 s). Unsymmetrical gas ingestion occurred for all weak supercritical flows. Further increase of the volume flux leads to oscillating gas ingestion on both sides.

RESULTS

We performed experiments with different volume fluxes for each parameter set to evaluate the critical volume flux. All other parameters but the volume flux were kept constant. The critical volume flux is defined as

$$Q_{crit}^{exp} = \frac{1}{2}(Q_{max}^{sub} + Q_{min}^{super}), \qquad (15)$$

where Q_{max}^{sub} is the maximum subcritical volume flux and Q_{min}^{super} is the minimum supercritical volume flux.

Eq. (10) was solved to get the maximum volume flux Q_{crit}^{theo}. The error bars for the predicted maximum velocity result from the uncertainty of the flow length of the capillary and from temperature changes between different experiment runs Q_{crit}^{theo}/A_{mean} is normalized using the characteristic velocity $v_c = \sqrt{2\sigma/\rho a}$, thus

$$v^*_{suc\_theo} = Q_{crit}^{theo}/A_{mean} v_c \sqrt{1-\Lambda}, \qquad (16)$$

as well as

$$v^*_{suc\_exp} = Q_{crit}^{exp}/A_{mean} v_c \sqrt{1-\Lambda}. \qquad (17)$$

To compute the mean velocity of the flow the mean area $A_{mean} = 0.5\,(A_{min} + A_{max})$ is used with the definitions for the maximum area $A_{max} = ab$, and the minimum area $A_{min} = A_{max} - \pi\alpha^2/4$.

It is known from investigations by Dreyer et al.[3] for the self induced capillary flow of liquid into a vane that the maximum velocity $v_c\sqrt{1-\Lambda}$ cannot be exceeded. Therefore, we assume that $v_c\sqrt{1-\Lambda}$ is an appropriate velocity to scale the forced flow. We expect that this maximum velocity can neither be exceeded by other means such as a suction device.

The results of the computation compared with the experimental data are depicted in Fig. 5. The dotted lines mark the ±10% deviation from the identity, all data points are located within this interval. The labels at the data points refer to the data set number, the dimensionless length of the capillary, and the gap ratio, respectively. It is obvious that the dimensionless maximum possible velocity in the vane increases with decreasing dimensionless length of the capillary. For the longest flow length (#29 and #36) the laminar viscous head loss is the dominating force, the flow is fully developed and the entrance length is short compared to the capillary length. The capillary rise in these capillaries shows the well known Lucas Washburn behavior, i.e. the rise height is proportional to the square root of time. In addition the parameter point #29 and #36 have the highest Oh numbers which indicates the dominance of the viscous friction term.

The shortest flow lengths (#35 and 35a) have the highest dimensionless velocities near to the maximum v^* = 1. The entrance length is much larger than the flow length and the flow field is characterized by a core

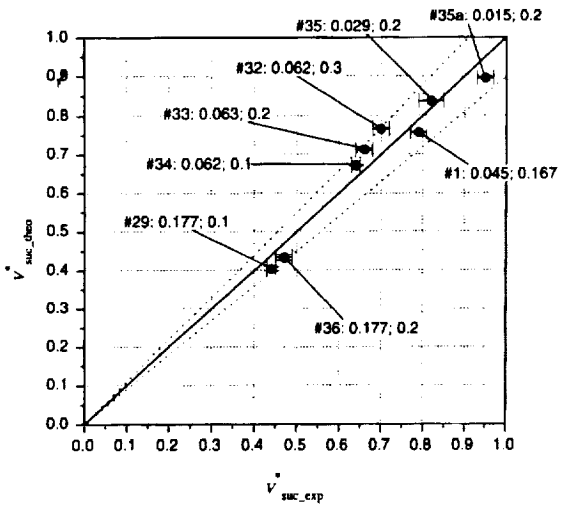

Figure 5: Comparison of experimental and theoretical predicted data for the maximum dimensionless velocity between parallel plates. The labels refer to the data set number, the dimensionless length of the capillary l^*, and the gap ratio Λ, respectively. The dotted lines mark the ±10% deviation from the identity.

flow with constant velocity and a boundary layer at the walls. For this case the convective forces at the entrance to the capillary as well as within the capillary itself play the dominant role. The capillary rise in this case shows a linear behavior if the rise height is plotted against time which is also an evidence for the dominance of the convective terms.

As mentioned before, the parameters cover a wide range of influencing forces and the theory is not valid only for viscous dominated range. The Re numbers range from Re_{min} = 150 to Re_{min} = 980. We can state that the presented theory gives a good agreement with the experimental data in spite of some assumption such as the neglect of the second radius of curvature. This leads to the fact that the order of the differential equation is not high enough to fit the solution for the radius of curvature to the boundary condition at the entrance and the outlet.

CONCLUSION AND OUTLOOK

We showed that the presented theory is able to predict the maximum forced flow velocities in capillary vanes with a good accuracy of ±10%. Experiments were performed for a wide range of the corresponding dimensionless numbers Ohnesorge, Oh, gap ratio Λ, and capillary length l^*. Both regions were covered where viscous friction force as well as convective forces are dominating the flow.

Furthermore the drop tower experiment time of t = 4.74 s is to short to reach stationary flow conditions for the shorter dimensionless flow lengths $l^* < 0.1$. The unavoidable acceleration of the liquid in the capillary gap at the beginning of the withdrawal causes disturbances of the free surface which are not damped away during the remainder of the experiment time. A sounding rocket experiment within the German TEXUS project (Technologische Experimente unter Schwerelosigkeit) is in preparation which will enable the quasi-stationary increase of the volume flux up to the critical one. The data set #35a was investigated as a precursor for the sounding rock experiment.

ACKNOWLEDGMENT

The funding of the drop tower flights and the sounding rocket flight by the European Space Agency (ESA) and support of the work by the German Aerospace Center (DLR) is gratefully acknowledged. Thanks are due to Mr. Prengel for the experimental setup and the performance of the drop tower flights.

REFERENCES

1. Jaekle, D.E., AIAA-91-2172, 27th Joint Propulsion Conference, June 24-26, Sacramento, CA, USA (1991).
2. Dreyer, M., Delgado, A., Rath, H.-J., Microgravity Science and Technology V/4, 203 (1993).
3. Dreyer, M., Delgado, A., Rath, H.-J., J. Colloid Interf. Sci. 163, 158-168 (1994).

Thermoacoustic Effects at a Solid-Fluid Boundary

A. Gopinath, Department of Mechanical Engineering, Naval Postgraduate School, Monterey CA 93943, USA,
gopinath@nps.navy.mil

1 STUDY I: Background & Introduction

Thermoacoustics can be simplistically defined as the physics of the interaction of thermal and acoustic fields, especially in the form in which one gives rise to a significant component of the other. A more careful description may be found in the general review article by Rott [1] from which it becomes clear that the field of thermoacoustics can be broadly classified into essentially two main branches on the basis of cause and effect, namely:
(a) time-averaged heat/temperature-gradient *driven* fluid oscillations, and
(b) time-averaged heat/temperature gradients *induced by* fluid oscillations.

The former topic includes, among other issues, the vast body of work on Rijke (and related) tubes and has received considerably far more attention than the latter. It is however only the latter topic with which this study is concerned, and has been most aptly named *thermoacoustic streaming* by Rott [1], by analogy with *acoustic streaming*, to describe the significant second-order time--averaged heat transfer effects produced by the interaction of strong acoustic fields with rigid boundaries. In the context of commonly used terminology in the thermoacoustic engine literature, this study deals primarily with the thermoacoustic streaming effects associated with the "refrigerator" mode (vice the "prime-mover" mode) of operation of a thermoacoustic engine. Notable early contributions to this area of thermoacoustic streaming were made by Rott [2] and Merkli & Thomann [3] (see also references in the paper by Rott [1] to a series of studies with his co-workers), and more recently by Jeong & Smith [4]. This topic has gained particular prominence in the past decade or so, due to its applicability to the fundamental processes of interest in the *stack* region of a thermoacoustic engine. Wheatley *et al.* [5] and Hofler [6] have provided some preliminary discussions of the theory of such engines and obtained experimental data using a ThermoAcoustic Couple (TAC) model of the stack, confirming the basic nature of the heat--generating mechanism underlying thermoacoustic streaming. An account of related developments with relevance to thermoacoustic engines, along with a more detailed review of both the principles of operation and the references in the literature, may be found in a fine tutorial article by Swift [7].

This study re-examines some of the above noted basic aspects of thermaocoustic streaming theory responsible for explaining the manner in which such significant time--averaged thermal effects may be created by the interaction of strong acoustic fields with rigid boundaries. The model problem chosen comprises the plane--parallel geometry of a channel in a resonant duct supporting a plane standing sound wave (as shown in Fig. 1). The focus in this study is on explaining the origin of the time-averaged temperature distribution induced in the walls and fluid gap of such a channel due to the presence of the acoustic field, and thereby attempting to predict optimum parameters that would maximize this thermal stratification. It is shown that a systematic framework based on a *dimensionless* formulation of the governing equations, which also accounts for conjugate effects due to the fluid--wall coupling, yields a self--consistent description of the scales involved and provides a clear indication of the source of the large time--averaged axial thermal stratification that can be induced in a resonant channel, for both *gaseous and non-gaseous* working fluids. The predictions from this theory are found to be in very good agreement with available experimental data in the literature. A more detailed report of this work may be found in the full-length paper by Gopinath *et al.* [8].

2 Problem Formulation

The Navier-Stokes equations are used to describe the effects of a plane standing acoustic field whose direction of oscillation is aligned with the axis of the plane-parallel geometry of a channel as shown in Fig. 1. The single channel, also shown magnified in Fig. 1, represents a "unit-cell" in a multitude of channels, all of which are enclosed in an outer larger resonant duct supporting the standing acoustic field. This collection of channels is the typical configuration representative of the *stack* of a thermoacoustic engine. The focus here is on the time-averaged temperature distribution induced in the fluid gap and walls of one such channel, due to its interactions with the resonant acoustic field.

The equations are developed with the disturbance variables defined around their quiescent undisturbed states, and suitably nondimensionalized. For the closely

spaced channels being treated, the narrow acoustic waveguide approximation is applied to develop the boundary layer form of the governing equations. The important dimensionless parameters in these equations are the Mach number, M, the gap width parameter, $\eta_0 \equiv y_0/\delta_\nu$ (or its counterpart y_0/δ_κ related through the Prandtl number). As for boundary conditions, the velocity field in the fluid is made to satisfy no--slip conditions along the channel walls ($y = 1$), and symmetry conditions about the centerplane of the fluid gap ($y = 0$). The thermal field in the fluid is suitably coupled with that of the wall *via* continuity requirements on the temperature, and the heat flux, at the wall-fluid interface ($y = 1$). In the solid material of the wall itself, heat is assumed to be transferred by simple isotropic conduction subject to the appropriate temperature and heat-flux continuity boundary conditions at the wall-fluid interface ($y_s = 1$), and symmetry about the wall centerplane ($y_s = 0$).

Only with such a formulation can one seek a self--consistent series expansion solution in powers of the parameter, $M \ll 1$, which clearly emerges as the proper perturbation parameter in the governing equations. In general, the solution to the above equations may now be developed with the remaining dimensionless parameters treated as arbitrary $O(1)$ numbers, although for the bulk of this study emphasis will be on cases for which the gap width η_0 is sufficiently large. Cases of smaller gap widths ($\eta_0 = O(1)$), which are practically more relevant in thermoacoustic engines are also dealt with in Appendix A of Ref. 1, and help establish a procedure for predicting optimum gap widths in stack design.

3 The Time-Averaged Temperature Distribution

The leading-order solution to the problem is well known and provides a description of the variation of the first harmonic quantities of the imposed standing wave, as a result of their interaction with the channel walls. The pressure distribution in the channels has to be developed with some care in a manner that is consistent with the nature of the acoustic waveform in the remainder of the resonant duct. Having determined the leading order first harmonic quantities, attention is then turned to determine the primary quantity of interest in this study, i. e. the time--averaged temperature distribution induced by the acoustic field. A search for higher order effects in the energy equation reveals that the leading order first harmonic terms interact in a nonlinear manner to generate an $O(1)$ temperature field, comprising a time--independent component, in addition to the second harmonic contribution. Since all the time--harmonic quantities have a zero temporal mean, it is the experimentally observeable, time--independent component of the $O(1)$ temperature distribution which is of key interest.

In particular, the time-averaged temperature gradient predicted at the wall-fluid interface clearly reveals the role of a second-order thermal expansion coefficient that surprisingly emerges from this analysis. It is found that for the case of an ideal gas, contrary to common expectation, viscous dissipation effects *do not* have a net thermal effect *at the wall-fluid interface*, and are instead completely balanced by compressibility work effects. Furthermore, the effects of the second-order coefficient are also negated by time-averaged expansion work effects attributable to temporal changes in the pressure and thus make no contribution to the thermoacoustic streaming phenomenon for an ideal gas. So it may be concluded that for the common case of an ideal gas working fluid in a thermoacoustic engine, it is only the time-averaged energy convective effects which make a nonzero contribution to the thermoacoustic streaming effect, thus supporting the simple "bucket-brigade" model. This is especially noteworthy since this model is based on the mechanics of gas parcel oscillation from standard *inviscid* linear acoustic theory and would not be expected to provide an explanation of viscous effects at the wall. Fortuitously though, the model does work for the particular case of an ideal gas, only due to the energy balances noted above. The issue is however far more involved for the general case of a non-gaseous working fluid, such as water or liquid--sodium which have been studied as possible thermoacoustic working fluids, wherein the neglected terms for an ideal gas are also fully capable of giving rise to significant nonzero contributions to the thermoacoustic heating/cooling effect. Due to the dissipative origin of these additional contributions the simple "bucket-brigade" model would be incapable of providing a complete description of the complete mechanics of the process.

4 Results & Conclusions

Results from the present theory have been compared with available experimental data wherever relevant. Most of the available experimental data in the literature for this problem has been obtained using a short stack of narrow gap channels (called a ThermoAcoustic Couple or TAC) with walls made from sandwiched fibre--glass

or metal in the form of sheets/plates or screens. Data from such experiments has been typically gathered in the form of temperature measurements at various axial locations along the channel wall, and/or, in the form of a net temperature difference induced across the ends of the channel (ΔT_s). All comparisons have been made only with data obtained from solid-walled channels (such as plates, and *not* screens or meshes), for which this theory has been developed. In particular detailed comparisons have been made with the data of Wheatley et al. and have showed very encouraging agreement of the measured and predicted temperature variation along the length of the stack. The deviations in the predictions are largest for larger pressure ratios which is probably due to the higher order effects that are not accounted for by the present theory.

In an effort to determine optimal stack spacing in thermoacoustic engine design, the nature of the axial thermal gradient in the stack was investigated for various stack channel spacings and gases in the engine. As per earlier predictions it was first confirmed that low-Prandtl number gases are desirable due to their ability to establish the steepest gradients in the stack. In addition it has for the first time been quantitatively determined that the crucial channel spacing in the stack which maximizes the desired thermal stratification *should optimally be about three times the thermal penetration depth*. This is an important finding since the temperature gradient in the stack falls off rapidly for spacings smaller or larger than this optimal value. So, although it's an attractive feature that the predictability of thermal performance in the stack becomes analytically considerably easier in the wide gap limit (gaps greater than about eight times the thermal penetration depth), the thermal gradient that may be induced in these cases however can be as little as a half to a third of the optimal value.

The importance of the role of the transport behavior at the ends of the stack is pointed out as being crucial in determining the thermal startification that can be established in the stack. It is found that this behaviour is intimately coupled with the requirement for continuity of temperature and heat flux at the wall--fluid interface, and this coupling is crucial in determining the nature of the large axial temperature stratification that can be induced in the channels of the stack.

5 STUDY II

A parallel experimental investigation has also been carried out with the goal of quantifying the heat transfer rates in oscillatory flows. A survey of the literature shows limited information in the regime of interest which may be characterized by a strong convective mechanism induced by the acoustic field (which dominates the buoyancy field) in the absence of any net mean flow. The flow is low-amplitude in nature, i. e. acoustic particle displacement amplitudes are small on the scale of the characteristic body dimension. The geometry under consideration is a cylinder which is representative of a heat exchanger tube. For the low amplitude cases treated, acoustic streaming is the dominant heat transport mechanism and is replaced by small scale vortex shedding when this flow becomes unstable. Relatively higher amplitude cases where strong vortex shedding and separated flow behavior are essential features will be treated elsewhere. The primary motivation here is to develop correlations which could be of utility in the design of heat exchangers for thermoacoustic engines [7]. Just as standard heat transfer handbooks abound with correlations for mean through-flows over a plethora of geometries which are applicable to conventional heat exchanger design, a modest start has been made here to develop correlations for a zero-mean oscillatory flow over a simple but vital geometry, namely the cylinder, from the viewpoint of applicability to thermoacoustic engine heat exchanger design. A more detailed report of this work may be found in the full-length paper by Gopinath & Harder [9].

6 Some Preliminaries

As noted above, this work is the report of a detailed experimental study of heat transfer from a cylinder in a low-amplitude zero-mean oscillatory flow. Despite the zero-mean nature of the flow, the convective action of the oscillatory flow can result in significant heat transport to/from a body immersed in such a flow. One of the mechanisms for heat transport in this low-amplitude regime is the strong time-averaged fluid motion (acoustic streaming) generated by the interaction of the acoustic field with the rigid boundaries. Unlike the well known dependence on only the Reynolds number, and the Prandtl number in conventional mean flows over isolated bluff bodies, the issue of heat transfer in an oscillatory flow is significantly more complicated due to the presence of a multitude of competing length scales. The ways in which these length scales can be ordered are many and lead to numerous distinct parameter regimes with quite drastically different flow, and hence heat transfer behavior [10]. In order to perform a systematic

study, it is essential to first identify the key controlling dimensionless parameters so as to be able to develop proper correlations in terms of the relevant parameters.

The flows being treated here are such that the cylinder size is small compared to the radian wavelength of the acoustic field, and yet large compared to the Stokes layer thickness so that the flow has a boundary layer nature. Under these conditions the nature of the acoustic streaming flow is governed by the streaming Reynolds number, R_s. Of interest here are cases for which $R_s \gg 1$ whereby acoustic streaming convection (vice diffusion or natural convection) is the dominant mode of steady transport. This also requires that buoyancy forces are negligible relative to forced convection effects and the appropriate criterion for this is $Gr/R_s^2 \ll 1$ (as verified later).

7 Experimental Method

An experimental setup was devised consisting of an enclosing cylindrical resonant chamber 76 mm in diameter and 2000 mm long. A heated test cylinder of diameter 5 mm, which is an electric cartridge heater, was positioned across the diameter of the resonant chamber at a suitable axial location. An acoustic driver at one end of the chamber, connected to a signal generator through an amplifier provided the necessary excitation, while the other end of the chamber had a rigid termination with an embedded microphone to measure the strength of the acoustic field. In short, once the working resonant frequencies were identified, the cartridge heater was powered and at steady state when its heat dissipation was balanced by the acoustically forced convective cooling action, readings were taken of the power disipation rate, and of the temperature of the cylinder by means of an embedded thermocouple. More details of the calibration procedure leading to the experiment, the steps in the data collection and reduction, the associated random error analysis, may all be found in the paper by Gopinath & Harder [9].

8 Results & Discussion

Nearly 800 experimental runs were carried out in the course of this study to generate over 200 distinct data points for analysis. The data was gathered for five different acoustic frequencies at pressure ratios ranging from 0.8 % to 3.2 %. The resulting values of R_s ranged from about 40 to 1070, while the corresponding values of Nu ranged from about 8 to 40. The data obtained here covers the "low-amplitude" range on the parameter map, with the goal being to cover the different expected regimes within this range. One of these is the attached flow regime with a fairly well developed theory (but with little experimental verification to date) which much of the data here attempts to cover. The other is a regime, which though of low-amplitude, is characterized by a separated flow behavior due to inherent large Reynolds number instabilities and resultant vortex shedding of the Honji-Hall type [11, 12]. Some of the data obtained in this study also covered this regime and is discussed further below.

The combined results have been presented in Fig. 2 in the form of a single plot of Nusselt number, Nu, vs the streaming Reynolds number, R_s. The data shows a $\sqrt{R_s}$ dependence and does indeed provide a good fit yielding a correlation that may be summarized as

$$\frac{Nu_d}{\sqrt{R_s}} = 0.90 \pm 10\ \% \text{ for } R_s > 125 - 150, \qquad (1)$$

The above behavior reaffirms the choice of R_s as the appropriate parameter for the boundary layer behavior in this regime and also confirms the expected laminar boundary layer nature of the flow.

The most extensive data in this study was gathered for the 585 Hz frequency value, which also provided the largest pressure amplitudes as indicated by the large range of R_s values (upto about 1100) that was achieved. As seen from the data for this frequency, there seem to be two clear trends for large values of R_s -- there's an initial $\sqrt{R_s}$ trend with a leading coefficient of 0.94 upto $R_s \approx 500$ which is consistent with the attached laminar flow behavior arguments made in the previous paragraph. This trend is followed by a steeper $R_s^{3/4}$ trend for even larger values of R_s and maybe correlated as

$$Nu_d = 0.20\, R_s^{0.75} \qquad (2)$$

and is an unexpected trend that has not been predicted before by theory. This behavior for very large R_s values seems to suggest a more vigorous heat transport mechanism that could not be induced by laminar boundary layer convective effects alone, and may be attributable to separation in the boundary layers leading to vortex shedding and the associated increased transport rates. These experimental observations are also consistent with the fluid mechanical studies of Honji, Hall and Sarpkaya in that they are clearly indicative of a change in the basic nature of the flow mechanics, possibly from an attached to a separated nature, as is evidenced here by the change in the power-law dependence of Nu_d on R_s.

9 Conclusions

The low-amplitude nominally attached flow regime of zero-mean oscillatory flow over a cylinder has been experimentally treated to develop some useful heat transfer correlations. The correlations developed are based on a large body of data that was gathered for the truly attached streaming flow regime, as well as (it appears) for its unstable counterpart at higher R_s characterized by possible vortex-shedding behavior. It may be noted that the actual magnitude of the relevant Reynolds number, R_s, involved is of $O(10^2 - 10^3)$ and can be considerably smaller than the values commonly encountered in conventional mean flows which may typically lie in the range $O(10^4 - 10^7)$. Nonetheless, as the values of the Nusselt number for these oscillatory flows indicate, the magnitudes of the heat transfer coefficients themselves are very much comparable in magnitude to those encountered in conventional mean flows, thus indicating the potential for significant convective heat transfer rates despite the zero-mean nature of the driving acoustic flow. It is suggested that when gases other than air are to be used, as is most likely the case in a thermoacoustic engine, a power-law dependence on the Prandtl number of the form $Pr^{0.7}$ established earlier by Davidson [13] and Gopinath & Mills [14] may be applied. This suggestion is based on the premise that such a dependence, although originally established strictly for the case of a cylinder or a sphere, should be equally suitable for other similar convex geometries which support essentially similar boundary layer mechanisms, as is also typically assumed in conventional mean flows.

References

[1] N. Rott, "Thermoacoustics," *Adv. Appl. Mech.* **20**, 135--175 (1980).

[2] N. Rott, "The heating effect connected with nonlinear oscillations in a resonance tube," *Z. Angew. Math. Phys.* **25**, 619--634 (1974).

[3] P. Merkli, & H. Thomann, "Thermoacoustic effects in a resonant tube," *J. Fluid Mech.* **70**, 161--177 (1975).

[4] E. S. Jeong, & J. L. Smith, Jr., "Secondary flow in reciprocating machinery," *National Heat Transfer Conference, San Diego*, ASME--HTD **204**, 105--113 (1992).

[5] J. Wheatley, T. Hofler, G. W. Swift, & A. Migliori, "An intrinsically irreversible thermoacoustic heat engine," *J. Acoust. Soc. Am.* **74**, 153--170 (1983).

[6] T. J. Hofler, "Thermoacoustic refrigerator design and performance," Ph. D. Thesis, University of California at San Diego (1986).

[7] G. W. Swift, "Thermoacoustic engines," *J. Acoust. Soc. Am.* **84**, 1145--1180 (1988).

[8] A. Gopinath, N. L. Tait, & S. L. Garrett, "Thermoacoustic streaming in a resonant channel: The time-averaged temperature distribution," *J. Acoust. Soc. Am.* **103**, 1388--1405 (1998).

[9] A. Gopinath & D. H. Harder, "An experimental study of heat transfer from a cylinder in low-amplitude oscillatory flows," *submitted Int. J. Heat Mass Transfer* (1998).

[10] P. D. Richardson, "Effects of sound and vibration on heat transfer," *Appl. Mech. Rev.* **20**, 201--217 (1967).

[11] H. Honji, "Streaked flow around an oscillating cylinder," *J. Fluid Mech.* **107**, 509--520 (1981).

[12] P. Hall, "On the stability of the unsteady boundary layer on a cylinder oscillating transversely in a viscous fluid," *J. Fluid Mech.* **146**, 347--367 (1984).

[13] B. J. Davidson, "Heat transfer from a vibrating circular cylinder," *Int. J. Heat Mass Transfer* **16**, 1703--1727 (1973).

[14] A. Gopinath & A. F. Mills, "Convective heat transfer from a sphere due to acoustic streaming," *J. Heat Transfer* **115**, 332--341 (1993).

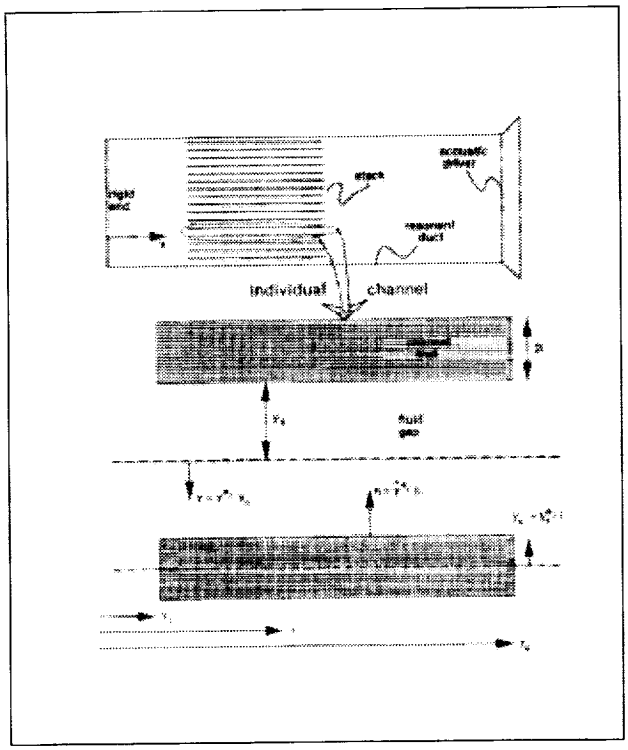

Figure 1: Study I: Definition sketch of the problem statement showing the stack of plane parallel channels in the resonant duct

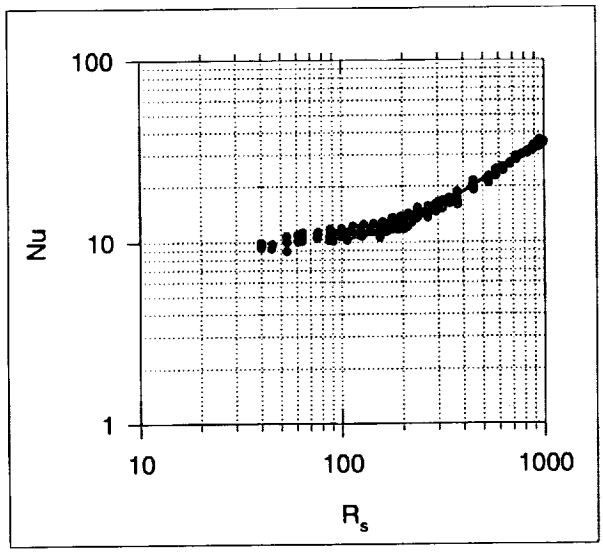

Figure 2: Study II: Plot of Nu_d vs R_s for all frequencies

DAMPING OF DROP OSCILLATIONS BY SURFACTANTS AND SURFACE VISCOSITY

Brian M. Rush, Ali Nadim, Dept. Aero. and Mech. Engr., Boston University, Boston, MA 02215 USA

Abstract

The roles played by surfactants and interfacial rheology on damping the shape oscillations of liquid drops are analyzed for the case of axisymmetric shape oscillations of a nearly spherical liquid drop surrounded by another fluid in the absence of gravity. Both fluids are taken to be viscous, although the Reynolds number associated with the shape oscillations is assumed large enough that deviations from inviscid flow are only present in thin Stokes boundary layers near the no-slip interface. Also, an insoluble surfactant is assumed to be present at the interface and surface tension is taken to be a linearly decreasing function of local surfactant concentration. This surfactant layer is further assumed to behave as a two-dimensional Newtonian fluid layer characterized by surface shear and dilatational viscosities.

Under these conditions, several sources can be identified for mechanical dissipation and the ultimate damping of the shape oscillations of the drop. These include viscous effects associated with the bulk fluids that appear in two distinct forms: one associated with the oscillatory viscous boundary layers which form near the interface between the drop and surrounding fluid, and the other associated with the flows far from the interface which resemble potential flow although they dissipate energy through weak viscous action. Surfactants and surface rheology additionally contribute to dissipation in other ways. The surface shear and dilatational viscosities dissipate energy within the interface in much the same way as the viscous dissipation in the three-dimensional bulk fluids just mentioned. Moreover, as various parts of the interface locally increase or decrease in area during shape oscillations, the concentration of surfactants locally decreases or increases. This leads to gradients in surfactant concentration on the interface where the process of gradient diffusion of surfactants within the interface, itself an irreversible process, leads to energy dissipation. Also, the Marangoni flow resulting from this non-uniformity in surface tension contributes to viscous damping.

This paper outlines the derivation of a general mechanical energy equation for such a system. It contains dissipation terms accounting for each of the mechanisms described above. The energy equation is applied to a slightly perturbed axisymmetric drop oscillating in a low-density surrounding fluid to derive an approximate ordinary differential equation (resembling that of a damped harmonic oscillator) which describes the time evolution of pure shape modes.

In parallel to the analytical treatment, the implementation of a boundary integral method for potential (i.e. inviscid) flow is presented for the case of a two-dimensional drop oscillating in vacuum. The effect of a constant surface dilatational viscosity is included in the computations by combining the tangential and normal components of the dynamic boundary condition into a single equivalent expression. This expression, combined with Bernoulli's equation for the pressure, the kinematic boundary condition and the regularized Fredholm integral equation of the second kind representing Laplace's equation for potential flow, produces a coupled set of nonlinear equations that allow the time evolution of the drop's shape to be followed. Surface dilatational viscosity is shown to have a damping effect on the free oscillations of the drop.

1 Introduction

Shape oscillations of drops and bubbles have been studied since the works of Kelvin [6] and Rayleigh [15] who determined the linearized frequencies of inviscid shape modes. Their work was extended by Lamb [7], Reid [16] and Valentine *et al.* [19], who included estimates of damping by weak viscous effects in the bulk. Miller & Scriven [11] and Marston [10] further identified the important role played by the boundary layers near the interface in damping the oscillations. The additional effects of surfactants and surface rheology, known to have a strong influence on the base frequency and damping rates of drops [1] and bubbles [3], have been analyzed by Lu & Apfel [8] and Tian *et al.* [18]. Numerical studies, based upon the boundary integral method, of the dynamics of weakly viscous drops were initiated by Lundgren and Mansour [9] and have been extended to include surfactant effects by Tian *et al.* Apfel *et al.* [1] used numerical simulations in conjunction with experimental studies of drops in microgravity to quantify the important role of surfactants in such systems.

The present contribution also focuses on the role of surfactants and surface rheology on drop oscillations in the absence of gravity. In addition to Marangoni effects which arise due to non-uniformity of surface tension

along the interface in the presence of surfactants, the interfacial layer of adsorbed surfactants may also possess separate rheological properties [4] which change the dynamics. Our goal is to identify the specific mechanisms through which surfactants and surface rheology affect the system and quantify each of them. An approach based on a global mechanical energy balance is outlined and allows the damping rates of pure shape modes by bulk viscosity, surface viscosity, boundary layer dissipation, and surfactant transport to be quantified. This energy equation generalizes the work of Hsu & Apfel [5], who used a simplified energy equation to approximate the rate of damping of a viscous drop with a constant surface tension oscillating in the quadrupole mode. Supplementing the analytical treatment, a numerical implementation of the boundary integral method for potential flow is described which incorporates the effects of surface viscosity. The method is presented for the oscillations of two-dimensional liquid drops possessing a constant surface dilatational viscosity.

2 The Energy Equation

Consider a liquid drop of density $\hat{\rho}$ and viscosity $\hat{\mu}$ to be suspended in an infinite medium of density ρ and viscosity μ, in the absence of gravity. If both fluids are assumed to be incompressible and Newtonian, the continuity and momentum equations take the forms:

$$\nabla \cdot \mathbf{v} = 0\,, \quad \rho \frac{D\mathbf{v}}{Dt} = \nabla \cdot \mathbf{\Pi} \quad \text{for} \quad \mathbf{x} \in \mathcal{V}(t), \quad (1)$$

$$\nabla \cdot \hat{\mathbf{v}} = 0\,, \quad \hat{\rho} \frac{D\hat{\mathbf{v}}}{Dt} = \nabla \cdot \hat{\mathbf{\Pi}} \quad \text{for} \quad \mathbf{x} \in \hat{\mathcal{V}}(t), \quad (2)$$

where $\mathbf{v}$ and $\hat{\mathbf{v}}$ respectively refer to the medium and drop velocity fields, $\mathcal{V}(t)$ and $\hat{\mathcal{V}}(t)$ are the material volumes of the medium and drop, and the stress tensors $\mathbf{\Pi}$ and $\hat{\mathbf{\Pi}}$ are given by

$$\mathbf{\Pi} = -p\mathbf{I} + 2\mu\mathbf{E}\,, \qquad \mathbf{E} = \frac{1}{2}[(\nabla\mathbf{v}) + (\nabla\mathbf{v})^T], \quad (3)$$

$$\hat{\mathbf{\Pi}} = -\hat{p}\mathbf{I} + 2\hat{\mu}\hat{\mathbf{E}}\,, \qquad \hat{\mathbf{E}} = \frac{1}{2}[(\nabla\hat{\mathbf{v}}) + (\nabla\hat{\mathbf{v}})^T]. \quad (4)$$

Here p and $\hat{p}$ represent the pressures in the two fluids, $\mathbf{I}$ is the isotropic unit tensor, and $\mathbf{E}$ and $\hat{\mathbf{E}}$ are the symmetric and traceless rate-of-strain tensors.

These field equations need to be supplemented by boundary conditions at infinity – that the velocity field vanishes and the pressure tends to a constant value – and at the interface $S(t)$ between the drop and medium. The interface is assumed to be covered with surfactants and therefore possesses its own rheological properties, which may be characterized by the surface stress tensor $\mathbf{\Pi}_s$ [4]. The boundary conditions at the interface thus assume the respective forms [4]:

$$\left.\begin{aligned} \mathbf{v} = \hat{\mathbf{v}} &\equiv \mathbf{v}^s \\ \hat{\mathbf{n}} \cdot (\mathbf{\Pi} - \hat{\mathbf{\Pi}}) &= -\nabla_s \cdot \mathbf{\Pi}_s \end{aligned}\right\} \quad \text{for} \quad \mathbf{x} \in S(t). \quad (5)$$

The velocity at the interface is denoted by $\mathbf{v}^s$ and is equal to the fluid velocities in the medium and drop evaluated at S. The surface stress tensor is also assumed to be "Newtonian" and defined by a Boussinesq-Scriven constitutive relationship of the form [4, 12, 17]

$$\mathbf{\Pi}_s = \sigma\mathbf{I}_s + 2\mu_s\mathbf{E}_s + \kappa_s\mathbf{I}_s(\nabla_s \cdot \mathbf{v}^s). \quad (6)$$

In this expression, σ, μ_s, and κ_s respectively refer to interfacial tension, surface shear viscosity, and surface dilatational viscosity. Also, $\mathbf{I}_s = \mathbf{I} - \hat{\mathbf{n}}\hat{\mathbf{n}}$ is the surface unit tensor, $\nabla_s = \mathbf{I}_s \cdot \nabla$ is the surface gradient, and $\mathbf{E}_s$ is the symmetric and traceless surface rate-of-strain tensor defined by

$$\mathbf{E}_s = \frac{1}{2}[(\nabla_s\mathbf{v}^s) \cdot \mathbf{I}_s + \mathbf{I}_s \cdot (\nabla_s\mathbf{v}^s)^T] - \frac{1}{2}\mathbf{I}_s(\nabla_s \cdot \mathbf{v}^s). \quad (7)$$

The derivation of the mechanical energy equation begins by dot multiplying the momentum equation in (1) by $\mathbf{v}$, the momentum equation in (2) by $\hat{\mathbf{v}}$, integrating over the respective material volumes $\mathcal{V}(t)$ and $\hat{\mathcal{V}}(t)$, and adding the resulting equations. Assuming that the concentration of surfactants Γ varies only slightly from the equilibrium concentration Γ_o, the surface tension may be modeled as a linearly decreasing function of the form

$$\sigma(\Gamma) = \sigma_o + \beta(\Gamma - \Gamma_o)\,, \qquad \beta = \frac{d\sigma}{d\Gamma}(\Gamma_o) < 0. \quad (8)$$

With the aid of the boundary conditions (5), as well as the bulk and surface Reynolds Transport Theorems and Divergence Theorems [2, 12], the following energy equation is finally obtained [13]

$$\begin{aligned} \frac{d}{dt}\{K.E. + S.E.\} = & \\ & - \int_{\mathcal{V}(t)} 2\mu(\mathbf{E} : \mathbf{E})\, d\mathcal{V} - \int_{\hat{\mathcal{V}}(t)} 2\hat{\mu}(\hat{\mathbf{E}} : \hat{\mathbf{E}})\, d\hat{\mathcal{V}} \\ & - \int_{S(t)} \left[2\mu_s(\mathbf{E}_s : \mathbf{E}_s) + \kappa_s(\nabla_s \cdot \mathbf{v}^s)^2\right] dS \\ & - \int_{S(t)} \beta(\Gamma - \Gamma_o)(\nabla_s \cdot \mathbf{v}^s)\, dS, \end{aligned} \quad (9)$$

where

$$K.E. + S.E. = \int_{V(t)} \frac{1}{2}\rho v^2\, dV + \int_{\hat{V}(t)} \frac{1}{2}\hat{\rho}\hat{v}^2\, dV + \int_{S(t)} \sigma_o\, dS \qquad (10)$$

is the total kinetic energy plus surface potential energy of the system. The first two terms on the right-hand side of (9) represent dissipation in the two bulk fluids. The next two terms are similarly identified as dissipation terms arising from surface shear and dilatational viscosities. The last term on the right-hand side of (9) requires further attention. This term can be shown [13] to be either dissipative or provide an additional surface energy storage depending on the surface Peclet number characterizing surfactant transport. The complete surfactant transport equation for an insoluble surfactant is itself given by

$$\frac{\partial \Gamma}{\partial t} + \mathbf{v}^s \cdot \boldsymbol{\nabla}_s \Gamma + (\boldsymbol{\nabla}_s \cdot \mathbf{v}^s)\Gamma = \boldsymbol{\nabla}_s \cdot (D_s \boldsymbol{\nabla}_s \Gamma), \quad (11)$$

where D_s is the surface diffusivity of surfactants.

The mechanical energy equation obtained above may be used to derive an approximate ordinary differential equation (ODE) which describes the evolution of pure shape modes of three-dimensional axisymmetric liquid drops [13]. The key results are outlined here and the reader is referred to the original article [13] for details. The approximation involves using the potential flow solution to estimate the kinetic energy and the dissipation integrals in the bulk, the oscillatory Stokes boundary layer velocity field to estimate the dissipation rate in the thin layers surrounding the interface, and the surface velocity from this analysis to estimate the surface dissipation integrals. For the quadrupole mode of oscillation, with the radial coordinate of surface points given by

$$r = a_o[1 + f(t)P_2(\cos\theta)], \qquad (12)$$

and the surfactant concentration by

$$\Gamma(\theta, t) = \Gamma_o + g(t)P_2(\cos\theta), \qquad (13)$$

where a_o and Γ_o are the respective equilibrium radius and surfactant concentration, $f(t)$ and $g(t)$ the time-dependent amplitudes of deformation and concentration change (both assumed small), P_2 the second Legendre polynomial, and θ the polar angle measured from the axis of symmetry, the following system of ODEs may be obtained to describe the time-dependent dynamics:

$$\frac{\hat{\rho}a_o^3}{2}\ddot{f} + 4\sigma_o f = -\beta g - \left[5\hat{\mu}a_o + 12\mu_s + \kappa_s + \frac{25a_o^2}{12\sqrt{2}}\sqrt{\omega_{2,o}\mu\rho}\right]\dot{f},$$

$$\dot{g}(t) + \frac{6D_s}{a_o^2}g(t) = \Gamma_o \dot{f}(t).$$

Here, $\omega_{2,o}$ is the base frequency of the quadrupole shape mode given by $(8\sigma_o/\hat{\rho}a_o^3)^{1/2}$. The coefficient of $\dot{f}$ on the right-hand side of the first equation represents damping due to viscous dissipation in the bulk liquid inside the drop, due to surface shear and dilatational viscosities, and due to the Stokes boundary layer in the gas surrounding the drop. In addition, the term which couples that equation to surfactant concentration $g(t)$ can be partially dissipative, depending on the value of the surface Peclet number $\omega_{2,o}a_o^2/D_s$ [13]. These results are obtained in the limit where the density and viscosity of the drop phase are large compared with those of the surrounding fluid.

3 Boundary Integral Method

The numerical problem considers the shape oscillations of a *two*-dimensional inviscid drop in vacuum without gravity. It is assumed that the drop has an undeformed equilibrium radius a_o and the interface is highly contaminated with insoluble surfactants so that the interfacial properties σ_o, μ_s, and κ_s are constants. Parameterizing all the variables with arclength s, using the inviscid stress tensors $\hat{\mathbf{\Pi}} = -p\mathbf{I}$ and $\mathbf{\Pi} = 0$, and expressing the gradient $\boldsymbol{\nabla} = \hat{\mathbf{s}}\partial/\partial s + \hat{\mathbf{n}}\partial/\partial n$ and velocity of the interface $\mathbf{v}^s = \hat{\mathbf{s}}v_s + \hat{\mathbf{n}}v_n$ in terms of local coordinates $\hat{\mathbf{s}}$ and $\hat{\mathbf{n}}$, the tangential and normal components of the dynamic boundary condition in (5) take the respective forms:

$$0 = \frac{\partial}{\partial s}\left[\frac{\partial v_s}{\partial s} + v_n\mathcal{C}\right], \qquad (14)$$

$$p = \mathcal{C}\left\{\sigma_o + \kappa_s\left[\frac{\partial v_s}{\partial s} + v_n\mathcal{C}\right]\right\}, \qquad (15)$$

where $\mathcal{C}$ is the local curvature of the two-dimensional interface. By first noting that v_s is necessarily periodic in total arclength L and integrating (14) twice with respect to arclength around the drop these two components may be combined to obtain

$$p = \mathcal{C}\{\sigma_o + \kappa_s B(t)\}, \qquad (16)$$

where the time-dependent quantity $B(t)$ is defined by

$$B(t) = \frac{1}{L}\int_0^L v_n \mathcal{C}\, ds. \tag{17}$$

Nondimensionalizing time with $(\rho R^3/\sigma_o)^{1/2}$, length with a_o, and mass with ρa_o^3 the boundary integral formulation of the governing equations for this system at a particular instant in time are

$$\int_0^L K_1(s_i,s)[q(s)-q(s_i)]\,ds = \phi(s_i), \tag{18}$$

$$\psi(s_i) = -\int_0^L K_2(s_i,s)[q(s)-q(s_i)]\,ds\,\hat{\mathbf{k}}, \tag{19}$$

$$\frac{D\phi}{Dt}(s) = \frac{1}{2}|\mathbf{v}^s(s)|^2 - \mathcal{C}(s)\{1+\kappa_s^* B\}, \tag{20}$$

$$\frac{d\mathbf{x}}{dt}(s) = \mathbf{v}^s(s). \tag{21}$$

Equation (18) represents the regularized double-layer potential boundary integral formulation of Laplace's equation for potential flow [14]. K_1 is the weakly singular kernel defined as the projection of the gradient of the two-dimensional Green's function for Laplace's equation in the direction normal to the interface, $q(s)$ is a distribution of dipole densities around the drop interface, and ϕ is the scalar velocity potential. $\psi = \psi\hat{\mathbf{k}}$ is the vector velocity potential perpendicular to the plane and is related to the velocity of the surface through its curl, $\nabla\times\psi = \mathbf{v}^s$. This vector velocity potential also relates to the distribution of dipole densities through an integral containing the weakly singular kernel K_2, which is defined as the cross product of the unit normal with the gradient of the two-dimensional Green's function.

The dynamic boundary condition (16) has been used with Bernoulli's unsteady equation for pressure to obtain (20), where the time derivative is with respect to an observer moving with the velocity of the interface $\mathbf{v}^s$ and $\kappa_s^* = \kappa_s(\sigma_o/\rho R^3)^{1/2}$ is the nondimensional surface dilatational viscosity. Equation (21) represents the kinematic boundary condition.

The above equations were discretized by dividing the periodic boundary into N equally-spaced nodes in the interval $0 < s < L$. All derivatives were calculated using standard $\mathcal{O}[(\Delta s)^6]$ finite-difference schemes and the regularized integral relations in (18) and (19) were discretized into matrix relations using a trapezoidal quadrature rule between the nodes. The numerical scheme first initialized the shape of the drop $\mathbf{x}$ and the scalar velocity potential ϕ. The velocity of the interface was then calculated using LU decomposition to solve the matrix equivalent of (18), performing the matrix multiplication in (19), and taking derivatives of the vector velocity potential with respect to arclength. Using the updated velocity of the interface and curvature, the scalar velocity potential and drop shape could be integrated in time using a fourth-order Runge-Kutta scheme. To prevent clustering and allow for the calculation of the derivatives, the nodes were redistributed to equal spacing in arclength after each time-step. The accuracy of the numerical method was checked by calculating the conserved quantities of total energy and volume in time. Interestingly, the numerical problems reported by [9], arising from the instability of modes with wavelength twice the nodal spacing, did not appear in these two-dimensional calculations.

Figure 1 shows an example of the damping effects of surface dilatational viscosity for an initially perturbed two-dimensional inviscid drop. The calculation used 40 nodes to simulate nearly 40 oscillation periods in the quadrupole mode of moderate initial amplitude. Alternate plots of similar energy versus time curves reveal that the attenuation in time due to surface dilatational viscosity in two-dimensional drops cannot be represented by an exponential or power law.

4 Conclusions

An energy equation has been derived for the general case of a viscous drop suspended in a viscous medium with surfactants contaminating the interface. It contains terms clearly identifying dissipation contributions from the viscous effects in the bulk fluids, surface shear and dilatational viscosity effects in the interface, and surfactant transport.

An efficient numerical boundary integral method has been developed which incorporates the effects of a constant surface dilatational viscosity in simulations of an oscillating two-dimensional inviscid drop. Surface dilatational viscosity is shown to have a significant damping effect on the otherwise undamped inviscid oscillations. This damping was found to be neither an exponential nor a power law.

5 Acknowledgments

This research was supported by NASA under grant NAG3-1844.

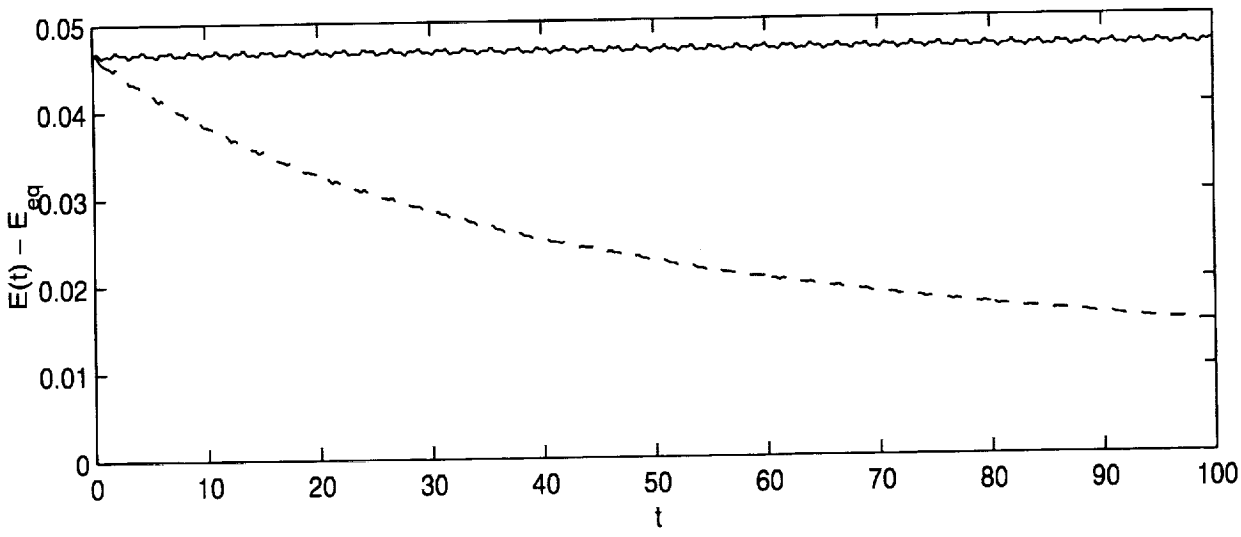

Figure 1: Total energy of the drop versus time after an initial condition $r = 1 + 0.1\cos(2\theta)$ and $\phi = 0$ for the cases $\kappa_s^* = 0$ (solid line), and $\kappa_s^* = 1$ (dashed).

References

[1] APFEL, R.E., TIAN, Y., JANKOVSKI, J., SHI., T. & CHEN, X., Free oscillations and surfactant studies of superdeformed drops in microgravity, *Phys. Rev. Letters*, **78**, 1912–1915 (1997).

[2] ARIS, R., *Vectors, Tensors and the Basic Equations of Fluid Mechanics*, Dover (1962).

[3] ASAKI, T.J., MARSTON, P.L. & TRINH, E.H., Free decay of shape oscillations of bubbles acoustically trapped in sea water, *J. Fluid Mech.*, **300**, 149–167 (1995).

[4] EDWARDS, D.A., BRENNER, H. & WASAN, D.T., *Interfacial Transport Processes and Rheology*, Butterworth-Heinemann (1991).

[5] HSU, C.J. & APFEL, R.E., Model for the quadrupole oscillations of drops for determining interfacial tension, *J. Acoust. Soc. Am.*, **82**, 2135–2144 (1987).

[6] KELVIN, LORD, Oscillations of a liquid sphere, *Mathematical Papers*, Clay & Sons (1890).

[7] LAMB, H., *Hydrodynamics*, 6th ed., Cambridge University Press (1932). (Reprinted by Dover, 1945.)

[8] LU, H.L. & APFEL, R.E., Shape oscillations of drops in the presence of surfactants, *J. Fluid Mech.*, **222**, 351–368 (1991).

[9] LUNDGREN, T.S. & MANSOUR, N.N., Oscillation of drops in zero gravity with weak viscous effects, *J. Fluid Mech.*, **194**, 479–510 (1988).

[10] MARSTON, P.L., Shape oscillation and static deformation of drops and bubbles driven by modulated radiation stresses — theory, *J. Acoust. Soc. Am.*, **67**, 15–26 (1980). [Erratum **71**, 511–512, (1982).]

[11] MILLER, C.A. & SCRIVEN, L.E., The oscillations of a fluid droplet immersed in another fluid, *J. Fluid Mech.*, **32**, 417–435 (1968).

[12] NADIM, A. Introduction to surface rheology with application to dilute emulsions of viscous drops, *Chem. Eng. Commun.*, **148–150**, 391–407 (1996).

[13] NADIM, A. & RUSH B. M. Mechanisms contributing to the damping of shape oscillations of liquid drops. In *Third International Conference on Multiphase Flow*, Lyon, France, June 8–12, (1998).

[14] POZRIKIDIS, C., *Introduction to Theoretical and Computational Fluid Dynamics*, Oxford University Press (1997).

[15] RAYLEIGH, LORD, *The Theory of Sound*, 2nd ed., Macmillan (1894). (Reprinted by Dover, 1945.)

[16] REID, W.H., The oscillations of a viscous liquid drop, *Quart. Appl. Math.*, **18**, 86–89 (1960).

[17] SCRIVEN, L.E., Dynamics of a fluid interface, *Chem. Eng. Sci.*, **12**, 98–108 (1960).

[18] TIAN, Y., HOLT, G., APFEL, R.E., Investigations of liquid surface rheology of surfactant solutions by droplet shape oscillations: Theory, *Phys. Fluids*, **7** (12), 2938–2949 (1995).

[19] VALENTINE, R.S., SATHER, N.F. & HEIDEGER, W.J., The motion of drops in viscous media, *Chem. Eng. Sci.*, **20**, 719–728 (1965).

Conference Schedule

Fourth Microgravity Fluid Physics & Transport Phenomena Conference
Cleveland, Ohio

Tuesday, August 11, 1998

2-5 PM	Tour of NASA Lewis (advance reservation required). Buses leaving from Sheraton.
5-7 PM	Registration and cash bar: Sheraton City Centre Hotel (Grand Ballroom Lobby)

Wednesday, August 12, 1998

7:30 AM	Registration: Sheraton City Centre Hotel (Grand Ballroom Lobby)
8:30	Opening Plenary Session (Grand Ballroom) Chair: Jack Salzman, Chief, Microgravity Science Division, NASA Lewis Research Center
8:30	Welcome: Martin P. Kress, Deputy Director, NASA Lewis Research Center
8:45	Keynote: Dr. John-David Bartoe, Manager, Research, International Space Station Program, NASA Johnson Space Center
9:50	Conference Objectives: Dr. Simon Ostrach, Director, National Center for Microgravity Research on Fluids and Combustion
10:10	Break
10:40	NASA Research Announcement - Fluid Physics & Transport Phenomena Discipline: Dr. Brad Carpenter, Lead Enterprise Scientist, Microgravity Research Division, Office of Life & Microgravity Science and Applications, NASA Headquarters
11:00	Fluid Physics & Transport Phenomena Research Thrusts: Dr. G. Paul Neitzel, Georgia Institute of Technology/Chairman, Microgravity Fluid Physics and Transport Phenomena Discipline Working Group
11:20	Fluid Physics Research on the International Space Station Planned Utilization of ISS US Fluids and Combustion Facility ESA Fluids Science Module NASDA Fluid Physics Facility
12:00 noon	Lunch
1:30 PM	Parallel Sessions 1A-C
3:10	Break
3:40	Parallel Sessions 2A-C
5:40	Free time

Thursday, August 13, 1998

8:00 AM	Thursday Plenary Session: Chair: Dr. David Weitz ,University of Pennsylvania (Grand Ballroom) Plenary Lecturer: Dr. Dudley Saville, Princeton University: Electrohydrodynamics & Electrokinetics: Moving Fluids & Particles with Electric Fields
8:40	Featured Speakers: Dr. Paul Chaikin and Dr. William Russel, Princeton University: The Dynamics Of Disorder-Order Transitions In Hard Sphere Colloidal Dispersions
9:20	Break
9:30	Parallel Sessions 3A-C
10:50	Break
11:15	Parallel Sessions 4A-C
12:35 PM	Lunch
2:00	Exposition: New Principal Investigators & Diagnostics Exhibits(Grand Ballroom)
5:00	Free time
6:15	Shuttle service to Great Lakes Science Center - Lolly the Trolley
6:30	Cash bar
7:30	OMNIMAX® Movie: Mission to Mir
8:15	Dinner
9:30	Shuttle service to Sheraton City Centre Hotel

Friday, August 14, 1998

8:00 AM	Friday Plenary Session: Chair: Dr. Iwan Alexander, Senior Scientist (Fluids), National Center for Microgravity Research on Fluids and Combustion/Case Western Reserve University (Grand Ballroom) Plenary Lecturer: Dr. Ronald Probstein, Massachusetts Institute of Technology: Micro-scale and Meso-scale Effects on Macroscopic Fluid Dynamics
8:40	Featured Speaker: Dr. Stein Sture, University of Colorado: Mechanics of Granular Materials at Low Effective Stresses
9:10	Dr. Robert Rhome, Director, Microgravity Research Division, Office of Life and Microgravity Sciences and Applications, NASA Headquarters: Microgravity Research Program and Human Exploration and Development of Space
9:40	Break
9:55	Parallel Sessions 5A-C
10:55	Break
11:25	Parallel Sessions 6A-C
12:25 PM	Luncheon: Speaker: Dr. Norman Thagard, M.D., Professor and Bernard F. Sliger Eminent Scholar Chair, Florida A&M University/Florida State University College of Engineering, NASA Astronaut (retired)
2:00	Parallel Sessions 7A-C
3:40	Adjourn

Tuesday, August 11, 1998

2:00-5:00 P.M. Tour of NASA Lewis Research Center

5:00-7:00 P.M. Registration and Cash Bar
Sheraton City Centre Hotel
(Grand Ballroom Lobby)

Wednesday, August 12, 1998
Morning

7:30 A.M.	Registration: Sheraton City Centre Hotel (Grand Ballroom Lobby)
8:30-12:00 noon	Opening Plenary (Grand Ballroom) Chair: Jack Salzman, Chief, Microgravity Science Division, NASA Lewis Research Center (Grand Ballroom)
8:30	Welcome: Martin P. Kress, Deputy Director, NASA Lewis Research Center
8:45	Keynote: Dr. John-David Bartoe, Manager, Research, International Space Station Program, NASA Johnson Space Center
9:50	Conference Objectives Dr. Simon Ostrach, Director, National Center for Microgravity Research on Fluids and Combustion
10:10	Break
10:40	NASA Research Announcement - Fluid Physics & Transport Phenomena Discipline Dr. Brad Carpenter, Lead Enterprise Scientist, Microgravity Research Division, Office of Life & Microgravity Science and Applications, NASA Headquarters
11:00	Fluid Physics & Transport Phenomena Research Thrusts Dr. G. Paul Neitzel, Georgia Institute of Technology Chairman, Microgravity Fluid Physics & Transport Phenomena Discipline Working Group
11:20	Fluid Physics Research on the International Space Station Planned Utilization of ISS US Fluids and Combustion Facility ESA Fluids Science Module NASDA Fluid Physics Facility
12:00 noon	Lunch

Wednesday Afternoon

Parallel Sessions 1A-1C

1:30-3:10 P.M.

Multiphase Flow I
Session Chair: Hasan Oguz, Johns Hopkins University

1:30 Paper #307
Mark McCready, University of Notre Dame: Mechanism of Atomization in a Two Layer Couette Flow

1:50 Paper #199
Vermuri Balakotaiah, University of Houston: Studies on Normal & Microgravity Annular Two-Phase Flows

2:10 Paper #220
Davood Abdollahian, S. Levi, Inc. : Experimental And Analytical Study Of Two-Phase Flow In Microgravity

2:30 Paper #403
Edward Keshock, Cleveland State University: Measurement of Two-Phase Flow Characteristics Under Microgravity Conditions

2:50 Paper #299
Simon Ostrach, NCMR/Case Western Reserve University: Industrial Processes Affected by Gravity

Electric And Magnetic Effects
Session Chair: Robert Davis, University of Colorado at Boulder

1:30 Paper #347
John Hart/Daniel Ohlsen, University of Colorado at Boulder: Waves In Radial Gravity Using Magnetic Fluids

1:50 Paper #385
George Bankoff, Northwestern University: Control Of Flowing Liquid Films By Electrostatic Fields In Space

2:10 Paper #413
Robert Davis, University of Colorado at Boulder: Cell And Particle Interactions And Aggregation During Electrophoretic Motion

2:30 Paper #263
Boyd Edwards, West Virginia University: Magnetic Control of Convection In Electrically Nonconducting Fluids

2:50 Paper #275
Robert Kusner, NASA Lewis Research Center: Electric Field Induced Interfacial Instabilities

G-Jitter And Stochastic Flow
Session Chair: Iwan Alexander, NCMR/Case Western Reserve University

1:30 Paper #161
Jorge Vinals, Florida State University: Fluid Physics In A Fluctuating Acceleration Environment

1:50 Paper #149
George Homsy, Stanford University: Thermocapillary Flows with Low-Frequency g-Jitter

2:10 Paper #437
Michael Schatz, University of Texas at Austin: Ground-Based Experiments On Vibrational Thermal Convection

2:30 Paper #471
Seth Putterman, University of California at Los Angeles: Diffusing Light Photography of Containerless Ripple Turbulence

2:50 Paper #369
Eric Shaqfeh, Stanford University: Drop Breakup In Fixed Bed Flows As Model Stochastic Flow Fields

3:10-3:40 P.M. Break

Wednesday Afternoon
Parallel Sessions 2A-2C
3:40-5:40 P.M

Multiphase Flow II
Session Chair: Mark McCready, University of Notre Dame

3:40 Paper #467
Yasuhiro Kamotani, Case Western Reserve University: Bubble Generation In A Flowing Liquid Medium And Resulting 2-Phase Flow In Microgravity

4:00 Paper #355
Hasan Oguz, Johns Hopkins University: Production Of Gas Bubbles In Reduced-G Environments

4:20 Paper #492
Luis Bernal, University of Michigan:
Vortex Droplet Formation by a Vortex Ring in Microgravity

4:40 Paper #361
Chris Rogers, Tufts University: Decoupling The Role Of Inertia And Gravity On Particle Dispersion

5:00 Paper #411
Mohammad Kassemi, NCMR: Bubble Dynamics On A Heated Surface

5:20 Paper #406
Sanjoy Banerjee, University of California at Santa Barbara:
A Three-Dimensional Level Set Method for Direct Simulation Of Two-Phase Flows in Variable Gravity Environments

Colloids
Session Chair: Paul Chaikin, Princeton University

3:40 Paper #235
Douglas Durian, University of California at Los Angeles:
Shear-Induced Melting Of Aqueous Foams

4:00 Paper #339
Jing Liu, California State University at Long Beach: Dynamics of Single Chains of Suspended Ferrofluid Particles

4:20 Paper #427
Alice Gast, Stanford University:
Chain Dynamics in Magnetorheological Suspensions

4:40 Paper #486
David Weitz, University of Pennsylvania: Physics of Colloids in Space

5:00 Paper #183
Penger Tong, Oklahoma State University: Analogies Between Colloidal Sedimentation and Turbulent Convection at High Prandtl Numbers

5:20
Noel Clark, University of Colorado
Structure, Hydrodynamics, And Phase Transitions Of Freely Suspended Liquid Crystals

Interfacial Phenomena I
Session Chair: Dan Rosner, Yale University

3:40 Paper #289
Enrique Ramé/Stephen Garoff, NCMR/Carnegie Mellon University: The Influence of Thin Films on the Hydrodymanics Near Moving Contact Lines

4:00 Paper #273
Leonard Schwartz, University of Delaware: Direct Numerical Simulation of Wetting and Spreading Behavior on Heterogeneous and Roughened Substrates

4:20 Paper #379
Ziyuan Liu/Marc Perlin, University of Michigan:
On The Boundary Conditions At An Oscillating Contact Line

4:40 Paper #395
Seth Lichter, Northwestern University: The Micromechanics Of The Moving Contact Line

5:00 Paper #185
Ain Sonin, Massachusetts Institute of Technology: Dynamics Of The Molten Contact Line

5:20 Paper #167
Jayanth Banavar/Joel Koplik, Pennsylvania State University/ City College of the City University of New York: Effective Forces Between Colloidal Particles

Wednesday Evening
Free Time

Thursday, August 13, 1998
Morning

8:00 A.M. Thursday Plenary
Chair: Dr. David Weitz, University of Pennsylvania
(Grand Ballroom)

Plenary Lecturer:
Electrohydrodynamics & Electrokinetics: Moving Fluids & Particles with Electric Fields
Dr. Dudley Saville, Princeton University

Featured Speakers:
The Dynamics Of Disorder-Order Transitions In Hard Sphere Colloidal Dispersions
Dr. Paul Chaikin and Dr. William Russel/Princeton University

9:20 A.M. Break

Parallel Sessions 3A-3C
9:30-10:50 A.M.

Phase Change I-Boiling
Session Chair:
Andrea Prosperetti,
Johns Hopkins University

9:30 Paper #163
Peter Wayner, Jr., Rensselaer Polytechnic Institute: Constrained Vapor Bubble

9:50 Paper #397
Kevin Hallinan, University of Dayton: Comments on the Operation of Capillary Pumped Loops In Low Gravity

10:10 Paper #287
Herman Merte, University of Michigan: A Study Of Nucleate Boiling With Forced Convection

10:30 Paper #297
Cila Herman, Johns Hopkins University: Experimental Investigation Of Pool Boiling Heat Transfer Enhancement In Microgravity In The Presence Of E Fields

Near Critical Point Flows
Session Chair: Joe Goddard, University of California at San Diego

9:30 Paper #295
Robert Berg, National Institute of Standards and Technology: Critical Viscosity Of Xenon: Surprises and Scientific Results

9:50 Paper #433
John Hegseth, University of New Orleans: Growth And Morphology Of Phase Separating Supercritical Fluids (GMSF), Boiling in Subcritical Fluids, and Critical Fluctuations

10:10 Paper #489
John Hegseth, University of New Orleans: A Compressible Geophysical Flow Experiment

10:30 Paper #491
Eric Kaler, University of Delaware: Phase Separation Kinetics in IsoPycnic Mixtures of H_2O/CO_2/Ethoxylated Alcohol Surfactants

Interfacial Phenomena II
Session Chair: Joel Koplik, City College of the City University of New York

9:30 Paper #241
James Maher, University of Pittsburgh: The Dissolution of an Interface Between Miscible Liquids

9:50 Paper #455
Daniel Mackowski, Auburn University: Investigation Of Thermal Stress Convection In Nonisothermal Gases Under Microgravity Conditions

10:10 Paper #343
E. James Davis, University of Washington: Phoretic Forces

10:30 Paper #305
Kathleen Stebe, Johns Hopkins University: Surfactants on a Droplet in an Extensional Flow: Stresses Created by Monolayer-Forming Surfactants

10:50 A.M. Break

Thursday Morning
Parallel Sessions 4A-4C
11:15 A.M.-12:35 P.M.

Phase Change II: Solidification
Session Chair: Ain Sonin, Massachusetts Institute of Technology

11:15 Paper #181
Sam Coriell, National Institute for Standards and Technology: Interface Morphology During Crystal Growth: Effects Of Anisotropy And Fluid Flow

11:35 Paper #203
Stephen Davis, Northwestern University: Directional Solidification of a Binary Alloy into a Cellular Convection Flow: Localized Morphologies

11:55 Paper #335
Dino Megaridis, University of Illinois at Chicago: Fluid Dynamics And Solidification Of Molten Solder Droplets Impacting On A Substrate

12:15 Paper #479
Saleh Tanveer, Ohio State University: Two-Dimensional Dendritic Crystal Growth for Weak Undercooling

Granular Media
Session Chair: Ashok Sangani, Syracuse University

11:15 Paper #405
James Jenkins, Cornell University: Particle Segregation in Collisional Shearing Flows

11:35 Paper #450
Joe Goddard, University of California at San Diego: Material Instabilities In Particulate Systems

11:55 Paper #265
Robert Behringer, Duke University: Gravity and Granular Materials

12:15 Paper #447
Masami Nakagawa, Colorado School of Mines: MRI Measurements And Granular Dynamics Simulation Of Segregation Of Granular Mixtures

Thermocapillary Flows I
Session Chair: Y . Kamotani, Case Western Reserve University

11:15 Paper #205
Simon Ostrach, NCMR/Case Western Reserve University: Surface Tension Driven Convection Experiment -2

11:35 Paper #353
Hossein Haj-Hariri, University of Virginia: Thermally-Driven Interfacial Flows In Multi-Layered Fluid Structures

11:55 Paper #429
Robert Kelly, University of California at Los Angeles: Studies In Thermocapillary Convection Of The Marangoni-Benard Type

12:15 Paper #319
Sindo Kou, University of Wisconsin: Thermocapillary Convection in a Low Pr Material Under Simulated Reduced Gravity

12:35 - 2:00 P.M. Lunch

Thursday Afternoon

Exposition

2:00-5:00 P.M.

Grand Ballroom

Poster	Presenter/Affiliation
Phase Diagrams of Electric-Field Induced Aggregation In Conducting Colloids	Andreas Acrivos, City College of the City University of New York
Ultrasonic Thermal Field Imaging of Opaque Fluids	C. David Andereck, Ohio State University
A Novel Acousto-Electric Levitator for Studies of Drop and Particle Clusters and Arrays	Robert E. Apfel, Yale University
Fluid Physics of Foam Evolution and Flow	Hassan Aref, University of Illinois at Urbana-Champaign
Inertial Effects in Suspension Dynamics	John F. Brady, California Institute of Technology
Marangoni Effects on Near-Bubble Microscale Transport During Boiling of Binary Fluid Mixtures	Van P. Carey, University of California at Berkeley
Dynamics of Dust in Photoelectron Layers Near Surfaces in Space	Joshua E. Colwell, University of Colorado at Boulder
Scaling of Multiphase Flow Regimes and Interfacial Behavior at Microgravity	Christopher J. Crowley, Creare, Inc.
Thermocapillary-Induced Phase Separation with Coalescence	Robert H. Davis, University of Colorado
Simulation of Rotating Thermal Convection and Comparison With Space-Laboratory Experiments	Anil Deane, University of Maryland
Attenuation of Gas Turbulence by a Nearly Stationary Dispersion of Fine Particles	John K. Eaton, Stanford University
A Dust Aggregation and Concentration System (DACS) for the Microgravity Space Environment	Frank J. Giovane, Naval Research Laboratory
Plasma Dust Crystallization	John A. Goree, University of Iowa
Determination of the Accommodation Coefficient Using Vapor/Gas Bubble Dynamics in an Acoustic Field	Nail Gumerov, Dynaflow, Inc.
Engineering of Novel Biocolloidal Suspensions	Daniel A. Hammer, University of Pennsylvania
Sonoluminescence in Space: the Critical Role of Buoyancy in Stability and Emission Mechanisms	R. Glynn Holt, Boston University
Rheology of Foam Near the Order-Disorder Phase Transition	R. Glynn Holt, Boston University
Fluid Flow in an Evaporating Droplet	Ronald G. Larson, University of Michigan
Studies of Gas - Particle Interactions in a Microgravity Flow Cell	Michel Y. Louge, Cornell University
Microgravity Experiments to Evaluate Electrostatic Forces in Controlling Cohesion and Adhesion of Granular Materials	John R. Marshall, SETI/NASA Ames Research Center
Single Bubble Sonoluminescence in Low Gravity and Optical Radiation Pressure Positioning of the Bubble	Philip Marston, Washington State University
An Interferometric Investigation of Contact Line Dynamics in Spreading Polymer Melts and Solutions	Gareth H. McKinley, Massachusetts Institute of Technology
Numerical Simulation of Parametric Instability in Two and Three-Dimensional Fluid Interfaces	Constantine Pozrikidis, University of California at San Diego
Complex Dynamics in Marangoni Convection with Rotation	Hermann Riecke, Northwestern University

Exposition, Continued

Poster	Presenter/Affiliation
The Effect of Surface Induced Flows on Bubble and Particle Integration	Paul J. Sides, Carnegie Mellon University
Modeling of Transport Processes in a Solid Oxide Electrolyzer Generating Oxygen on Mars	K.R. Sridhar, University of Arizona
Computations of Boiling in Microgravity	Gretar Tryggvason, University of Michigan
Entropic Surface Crystals and Crystal Binary Growth in Binary Hard-Sphere Colloids	Arjun G. Yodh, University of Pennsylvania
Enhanced Boiling on Micro-Configured Composite Surfaces Under Microgravity Conditions	Nengli Zhang, Ohio Aerospace Institute
The Small-Scale Structure of Turbulence	Gregory Zimmerli, National Center for Microgravity Research on Fluids and Combustion
Paramagnetic Liquid Bridge in a Gravity-Compensating Magnetic Field	Charles Rosenblatt, Case Western Reserve University

Exhibits

Throughout Conference Meeting Area

Note: Exhibits Are Available Throughout the Duration of the Conference

Exhibit Title	Presenter
Compact Fiber Optic Probes for Static and Dynamic Light Scattering and Biomedical Applications	R. Ansari National Center for Microgravity Research on Fluids and Combustion NCMR
Compact Laser Light Scattering Multiangle Apparatus	R. Ansari National Center for Microgravity Research on Fluids and Combustion NCMR
On-line particle sizing in fluids under flow	R. Ansari National Center for Microgravity Research on Fluids and Combustion NCMR
Fluids Integrated Rack	R. Corban, NASA Lewis Research Center
Acceleration Measurement Discipline	R. DeLombard NASA Lewis Research Center
Optical Tweezers	D. Griffin, NASA Lewis Research Center
ERE	N. Hall, NASA Lewis Research Center
Laser Light Scattering with Multiple Scattering Suppression	W. Meyer National Center for Microgravity Research on Fluids and Combustion
Surface Light Scattering	W. Meyer National Center for Microgravity Research on Fluids and Combustion
CDOT	W. Meyer National Center for Microgravity Research on Fluids and Combustion
National Center for Microgravity Research On Fluids and Combustion	A. Heyward National Center for Microgravity Research on Fluids and Combustion
Laser Feedback Interferometry	B. Ovryn National Center for Microgravity Research on Fluids and Combustion
Common-Path Interferometry for Fluid Measurements	N. Rashidnia National Center for Microgravity Research on Fluids and Combustion
MSD K-12 Education Program	M. Rogers National Center for Microgravity Research on Fluids and Combustion
Optical Microscopy of Colloids	R. Rogers NASA Lewis Research Center LeRC
International Space Station Telescience	K. Schubert NASA Lewis Research Center
Mechanics of Granular Materials	S. Sture, University of Colorado
Astrotech Space Operations	M. Windsor, Astrotech Burkhardt Franke, Daimler-Benz Aerospace, Bremen, Germany
Microgravity Program Performance Goals	D. Woodard, Marshall Space Flight Center
Microgravity Principal Investigator Locations	D. Woodard, Marshall Space Flight Center
Slowly Rotating Optical Breadboard	G. Zimmerli National Center for Microgravity Research on Fluids and Combustion

Thursday Evening

5:00 P.M.: Free time

6:15 P.M.: Shuttle service begins to Great Lakes Science Center (Lolly the Trolley)

6:30 P.M.: Cash Bar, Great Lakes Science Center

7:30 P.M.: OMNIMAX® Movie: Mission to Mir, Great Lakes Science Center

8:15 P.M.: Dinner, Great Lakes Science Center

9:45-10:30 P.M.: Shuttle service return to Sheraton City Centre Hotel

Friday, August 14, 1998
Morning

8:00 A.M. Friday Plenary
Chair: Dr. Iwan Alexander, Senior Scientist, National Center for Microgravity Research On Fluids and Combustion/Case Western Reserve University
(Grand Ballroom)

Plenary Lecturer:
8:00-8:40 A.M.
Micro-scale and Meso-scale Effects on Macroscopic Fluid Dynamics
Dr. Ronald Probstein, Massachusetts Institute of Technology

Featured Speaker:
8:40-9:10 A.M.
Mechanics Of Granular Materials at Low Effective Stresses
Dr. Stein Sture, University of Colorado

9:10-9:40 A.M.
Microgravity Research Program and Human Exploration and Development of Space
Dr. Robert Rhome, Director, Microgravity Science Division, Office of Life and Microgravity Sciences and Applications, NASA Headquarters

9:40 -9:55 A.M. Break

Friday Morning, 1998

Parallel Sessions 5A-5C

9:55-10:55 A.M.

Phase Change III: Boiling
Chair: Peter Wayner
Rensselaer Polytechnic Institute

9:55 Paper #459
Vijay Dhir, University of California at Los Angeles: Investigation Of Nucleate Boiling Mechanisms Under Microgravity Conditions

10:15 Paper #367
Jungho Kim, University of Denver: Boiling Heat Transfer Measurements on Highly Conductive Surfaces Using Microscale Heater and Temperature Arrays

10:35 Paper #445
Marc Smith, Georgia Institute of Technology: Vibration-Induced Droplet Atomization

Suspensions
Session Chair: Alice Gast, Stanford University

9:55 Paper #393
S. E. Elghobashi, University of California at Irvine: Effects Of Gravity On Sheared Turbulence Laden With Bubbles And Droplets

10:15 Paper #456
R.J. Hill/A. Sangani
Cornell University/Syracuse University: Buoyancy Driven Shear Flows of Bubble Suspensions

10:35 Paper #449
Michael Loewenberg, Yale University: Direct Numerical Simulation of Drop Breakup in Isotropic Turbulence

Special Topics I
Session Chair: Gareth McKinley, Massachusetts Institute of Technology

9:55 Paper #461
Paul Neitzel, Georgia Institute of Technology: Non-Coalescence Effects In Microgravity

10:15 Paper #215
Josh Colwell, University of Colorado at Boulder: Collide: Microgravity Experiment on Collisions in Planetary Rings and Protoplanetary Disks

10:35 Paper #179
Edgar Knobloch, University of California at Berkeley: Weakly Nonlinear Description of Parametric Instabilities in Vibrating Flows

10:55 A.M. Break

Friday Morning

Parallel Sessions 6A-6C

11:25 A.M.- 12:25 P.M.

Phase Change IV: Boiling
Session Chair: Vijay Dhir, University of California at Los Angeles

11:25 Paper #325
Andrea Prosperetti, Johns Hopkins University: Pressure Radiation Forces on Vapor Bubbles

11:45 Paper #463
Amir Faghri, University of Connecticut: Condensation of Forced Convection Two-Phase Flow in a Miniature Tube

12:05 Paper #349
Eugene Trinh, Jet Propulsion Laboratory: Acoustic Shearing In Microgravity: Flow Stability And Heat Transfer Enhancement

Special Topics II
Session Chair: Eric Shaqfeh, Stanford University

11:25 Paper #485
Gareth McKinley, Massachusetts Institute of Technology: Extensional Rheometry of Polymer Solutions And the Uniaxial Elongation of Viscoelastic Filaments

11:45 Paper #351
Jeff Mackey, NYMA, Inc.: Flow-Induced Birefringence Measurement System Using Dual-Crystal Transverse Electro-Optic Modulator for Microgravity Fluid Physics Applications

12:05 Paper #497
Ben Ovryn, NCMR: Phase Shifted Laser Feedback Interference Microscopy: Applications to Fluid Physics Phenomena

Convective Instability
Session Chair: Hossein Haj-Hariri, University of Virginia

11:25 Paper #303
J.B. Swift/H. Swinney, University of Texas at Austin: Long Wavelength Rupturing Instability in Surface-Tension-Driven Benard Convection

11:45 Paper #391
Jeffrey Jacobs, University of Arizona: PLIF Flow Visualization of Incompressible Richtmeyer-Meshokov Instability

12:05 Paper #169
Sung Lin, Clarkson University: Absolute And Convective Instability Of A Liquid Jet

12:35 - 2:00 P.M. Lunch

Luncheon Speaker: Dr. Norman Thagard, M.D., Professor & Bernard F. Sliger Eminent Scholar Chair, FAMU/FSU College of Engineering, and NASA Astronaut (retired)

Friday Afternoon

Parallel Sessions 7A-7C

2:00 P.M.- 3:40 P.M.

Bubbles and Drops
Session Chair: Luis Bernal, University of Michigan

2:00 Paper #321
Osman Basaran, Purdue University: Drop Ejection from an Oscillating Rod

2:20 Paper #477
A. Esmaeeli/V. Arpaci/An-Ti Chai, University of Michigan/NASA Lewis Research Center: Numerical Modeling of Three-Dimensional Fluid Flow with Phase Change

2:40 Paper #382
L.G. Leal, University of California at Santa Barbara: The Breakup and Coalescence of Gas Bubbles Driven by the Velocity Gradients of Non-Uniform Flow

3:00 Paper #389
Eugene Trinh/Satwindar Sadhal, Jet Propulsion Laboratory/University of Southern California: Ground-Based Studies Of Thermocapillary Flows In Levitated Laser-Heated Drops

3:20 Paper #285
R. Balasubramaniam, NCMR: Thermocapillary Migration and Interactions Of Bubbles And Drops

Liquid Bridges
Session Chair: Mike Schatz, University of Texas at Austin

2:00 Paper #409
Iwan Alexander, NCMR/Case Western Reserve University: Stability Limits And Dynamics Of Nonaxisymmetric Liquid Bridges

2:20 Paper #261
Philip Marston, Washington State University: Radiation and Maxwell Stress Stabilization Of Liquid Bridges

2:40 Paper #377
Paul Steen, Cornell University: Stability Of Shapes Held By Surface Tension And Subjected To Flow

3:00 Paper #253
Dudley Saville, Princeton University: Electrohydrodynamic Stability of a Liquid Bridge

3:20 Paper #327
Jeremiah Brackbill, Los Alamos National Laboratory: Dynamic Modelling Of Microgravity Flow

Interfacial Phenomena III
Session Chair: Kathleen Stebe, Johns Hopkins University

2:00 Paper #257
Daniel Rosner, Yale University: Fluid/Solid Boundary Conditions in Nonisothermal Systems

2:20 Paper #473
Paul Concus, University of California at Berkeley: A Symmetry Breaking Experiment Aboard Mir and the Stability of Rotating Liquid Films

2:40 Paper #225
Michael Dreyer/Hans Rath, University of Bremen: Critical Velocities In Open Capillary Flows

3:00 Paper #481
Ashok Gopinath, Naval Postgraduate School: Thermoacoustic Effects At A Solid-Fluid Boundary

3:20 Paper #371
Ali Nadim, Boston University: Damping of Drop Oscillations by Surfactants

3:40 P.M. Adjourn

Thank you for your participation in the 4th Microgravity Fluid Physics and Transport Phenomena Conference

AUTHOR INDEX

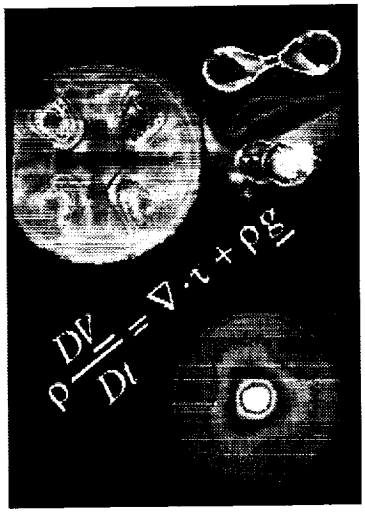

WE'VE SAVED SOME TREES

This CD ROM of the 1998 Fourth Microgravity Fluid Physics and Transport Phenomena Conference is a compendium of over 130 papers totaling about 800 pages. In it's production we have attempted to bring the process into the 21st century.

The Internet and the World Wide Web provided the primary means of communication. Well over 90 percent of all papers, posters and abstracts were electronically submitted via the National Center for Microgravity Research's server.

The different operating systems (MAC, WINDOWS, UNIX) along with the various software applications used by the authors (Microsoft Word, TeX, Postscript) provided the major challenge in putting together this CD ROM.

Thanks go out to those NCMR, CWRU, NASA LeRC and LPI staff personnel, who were instrumental in this project. A special thank you to all the authors who worked with us in the submission process to assure that this work would have a unified look and feel.

NCMR